The international journal of science / 18 May 2023

nature



RAGING BULLS

Tusk-growth record reveals male mammoths had testosterone surges

Collective agreement
Meet the researchers putting scientific consensus to the test

Cleaning up
How innovative climate action by the G7 could drive decarbonization

Industrial evolution
Organic catalyst offers improved efficiency for chlorine synthesis

VISIT…

LANZAROTE Caliente.com

Nature.2023.05.20

[Sat, 20 May 2023]

- [This Week]
- [News in Focus]
- [Opinion]
- [Work]
- [Research]
- [Amendments & Corrections]

This Week

- **Research assessment exercises are necessary — but we need to learn to do them better** [16 May 2023]
  • Australia is overhauling its research evaluation system — an opportunity for it, and other countries, to review what makes a system work for everyone.
- **For chemists, the AI revolution has yet to happen** [17 May 2023]
  • Machine-learning systems in chemistry need accurate and accessible training data. Until they get it, they won't achieve their potential.
- **Audit AI search tools now, before they skew research** [16 May 2023]
  • Generative AI could be a boon for literature search, but only if independent groups scrutinize its biases and limitations.

- EDITORIAL
- 16 May 2023

Research assessment exercises are necessary — but we need to learn to do them better

Australia is overhauling its research evaluation system — an opportunity for it, and other countries, to review what makes a system work for everyone.



The University of Sydney says that participating in each ERA exercise costs it 40,000 hours in staff time and Aus$2 million in salaries.Credit: Hongjie Han/Getty

Research evaluation at the Australian Research Council (ARC), one of the country's main funding bodies, is set to get a makeover. Last month, an

independent expert review recommended that the ARC scrap its 13-year-old research-scoring system, known as Excellence in Research for Australia (ERA), and its companion exercise, the Engagement and Impact assessment, which grades the real-world benefits of institutions' work. Both had been on hold since last August, awaiting the findings of the review.

This is a rare case in which an evaluation system can be rewritten from scratch. The ARC should take this opportunity to improve how it measures and communicates the value of Australia's research workforce, on the basis of not just lessons learnt from the ERA's deficiencies, but also principles that have been developed and implemented elsewhere in the world. In doing so, it will help to create a research culture that reflects the best possible values that research should represent.

Between 2010 and 2018, there were four ERA exercises scoring outputs from Australia's 42 universities and publicly funded research institutions. Research is given a rating from 1, for "well below world standard", to 5, for "well above world standard". For most science and engineering disciplines, citation metrics are the primary measure; for humanities, social sciences, computing and mathematics, the reliance is on peer review.



[Australian researchers welcome plan to curb politicians' power to veto research grants]

Last month's expert review of the ERA, initiated by the Australian government, concludes that the evaluation has meant Australia performs

favourably on international benchmarks. But this has come at a cost. Submissions to the review confirmed that the ERA process was onerous, owing to the time taken to compile the information required. This took a toll on both individuals and institutions. At the University of Sydney, for instance, upwards of 40,000 hours of staff time was spent on the ERA process, costing the university more than Aus$2 million (US$1.3 million) in salaries alone, according to its submission.

These efforts came without much discernible reward. The results of the ERA — unlike, say, the Research Excellence Framework in the United Kingdom — are not used to decide university funding. Instead, they are used for such purposes such as setting research strategy, benchmarking and evaluating trends. At the same time, pitting institutions against each other encourages them to poach academics and duplicate expertise, rather than fostering a collaborative, cross-disciplinary research culture.

The review wisely resists suggesting that the ERA be replaced with a purely metrics-based exercise to reduce overheads. Using metrics such as citations and journal impact factors is problematic, to say the least. For one thing, they do not capture replication studies and meta-analyses, which journals are increasingly publishing. Furthermore, studies in the social sciences and humanities — more frequently published in national, rather than international publications — are especially disadvantaged by such measures. And just counting citations in well-known journals doesn't do justice to other important work, such as building databases and software, and engaging with the public.

Ten years ago this month, the San Francisco Declaration on Research Assessment (DORA) enshrined the principle that evaluations should not rely too heavily on journal impact factors as a measure of research quality. The declaration, developed during the 2012 Annual Meeting of the American Society for Cell Biology, urges, among other things, that journal-based metrics not be used as a surrogate measure of research quality for assessing an individual scientist's contributions, or in hiring, promotion or funding decisions. More than 20,000 individuals and 2,800 institutions across 160 countries have signed DORA so far.



Elite university strategies might boost profile and rankings, but at what cost?

More has happened in the decade since. The 2015 Leiden Manifesto recommends that assessors anticipate how appraisal systems can be gamed (D. Hicks *et al. Nature* **520**, 429–431; 2015). The 2019 Hong Kong Principles aim to build trust in science by including transparency, open-science and responsible-research practices in evaluations (D. Moher *et al. PLoS Biol.* **18**, e3000737; 2020). In 2021, the International Network of Research Management Societies developed the SCOPE Framework, a how-to guide for conducting assessments that embed these desirable principles.

Australia is not alone in reconsidering how it does appraisals. The Swedish Research Council, for instance, avoids the pressure of evaluating its entire research workforce in a single all-encompassing exercise by assessing specific disciplines as required, rather than according to a set cycle. The Netherlands, too, has a less onerous process that doesn't just capture research institutions' previous outputs, but looks forwards by identifying future plans and capacity, to pinpoint strengths and areas for improvement ahead of time.

The ERA's replacement should also not downgrade the expertise of research managers. Many are researchers themselves, and their role extends far beyond administering the ERA. Through their work, universities are continually striving to improve policies surrounding research ethics, public

engagement and publishing, seeking to become more diverse and more welcoming places. It would be folly to lose that expertise.

It’s important to score the quality of publicly funded research. There’s no perfect system, but the ARC and other national funding agencies should take care to adopt principles and practices that work. Evaluation has the power to shape research culture for good and ill. It needs to be done well.

Nature **617**, 437 (2023)

doi: https://doi.org/10.1038/d41586-023-01611-y

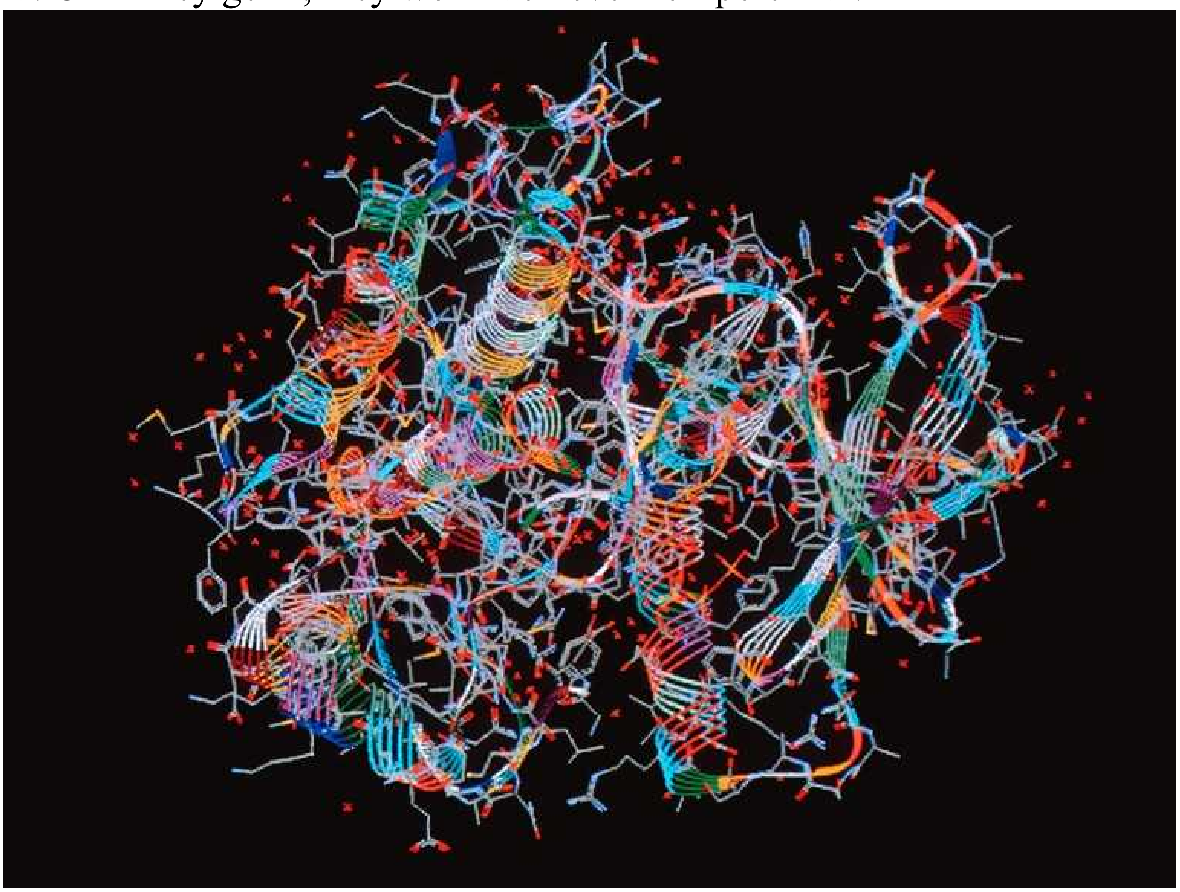
This article was downloaded by **calibre** from https://www.nature.com/articles/d41586-023-01611-y

| Section menu | Main menu |

- EDITORIAL
- 17 May 2023

For chemists, the AI revolution has yet to happen

Machine-learning systems in chemistry need accurate and accessible training data. Until they get it, they won’t achieve their potential.



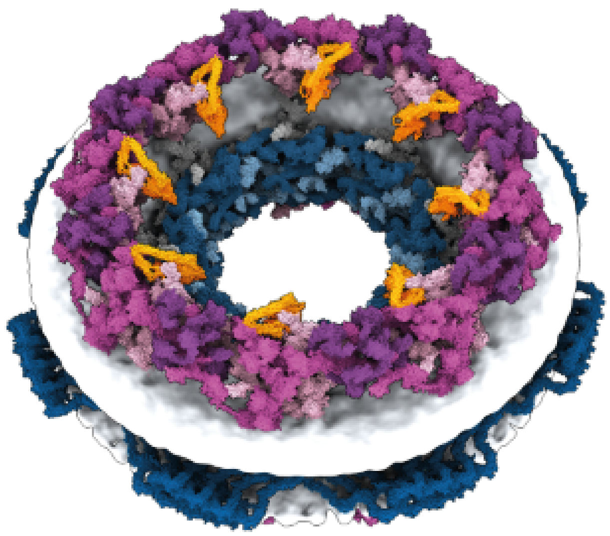
More than 20 years ago, the Cancer Research Screensaver harnessed distributed computing power to assess anti-cancer activity in molecules.Credit: James King-Holmes/SPL

Many people are expressing fears that artificial intelligence (AI) has gone too far — or risks doing so. Take Geoffrey Hinton, a prominent figure in AI, who recently resigned from his position at Google, citing the desire to speak out about the technology's potential risks to society and human well-being.

But against those big-picture concerns, in many areas of science you will hear a different frustration being expressed more quietly: that AI has not yet gone far enough. One of those areas is chemistry, for which machine-learning tools promise a revolution in the way researchers seek and synthesize useful new substances. But a wholesale revolution has yet to happen — because of the lack of data available to feed hungry AI systems.

Any AI system is only as good as the data it is trained on. These systems rely on what are called neural networks, which their developers teach using training data sets that must be large, reliable and free of bias. If chemists want to harness the full potential of generative-AI tools, they need to help to establish such training data sets. More data are needed — both experimental and simulated — including historical data and otherwise obscure knowledge, such as that from unsuccessful experiments. And researchers must ensure that the resulting information is accessible. This task is still very much a work in progress.

Take, for example, AI tools that conduct retrosynthesis. These begin with a chemical structure a chemist wants to make, then work backwards to determine the best starting materials and sequence of reaction steps to make it. AI systems that implement this approach include 3N-MCTS, designed by researchers at the University of Münster in Germany and Shanghai University in China[1]. This combines a known search algorithm with three neural networks. Such tools have attracted attention, but few chemists have yet adopted them.



What's next for AlphaFold and the AI protein-folding revolution

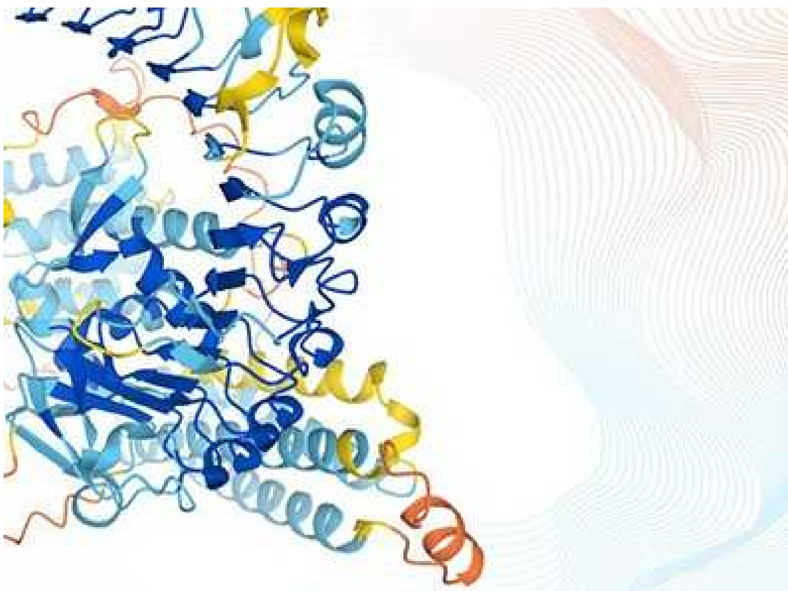
To make accurate chemical predictions, an AI system needs sufficient knowledge of the specific chemical structures that different reactions work with. Chemists who discover a new reaction usually publish results exploring this, but often these are not exhaustive. Unless AI systems have comprehensive knowledge, they might end up suggesting starting materials with structures that would stop reactions working or lead to incorrect products[2].

An example of mixed progress comes in what AI researchers call ‘inverse design’. In chemistry, this involves starting with desired physical properties and then identifying substances that have these properties, and that can, ideally, be made cheaply. For example, AI-based inverse design helped scientists to select optimal materials for making blue phosphorescent organic light-emitting diodes[3].

Computational approaches to inverse design, which ask a model to suggest structures with the desired characteristics, are already in use in chemistry, and their outputs are routinely scrutinized by researchers. If AI is to outperform pre-existing computational tools in inverse design, it needs enough training data relating chemical structures to properties. But what is meant by ‘enough’ training data in this context depends on the type of AI used.

A generalist generative-AI system such as ChatGPT, developed by OpenAI in San Francisco, California, is simply data-hungry. To apply such a generative-AI system to chemistry, hundreds of thousands — or possibly even millions — of data points would be needed.

A more chemistry-focused AI approach trains the system on the structures and properties of molecules. In the language of AI, molecular structures are graphs. In molecules, chemical bonds connect atoms — just as edges connect nodes in graphs. Such AI systems fed with 5,000–10,000 data points can already beat conventional computational approaches to answering chemical questions[4] . The problem is that, in many cases, even 5,000 data points is far more than are currently available.



Artificial intelligence in structural biology is here to stay

The AlphaFold protein-structure-prediction tool[5], arguably the most successful chemistry AI application, uses such a graph-representation approach. AlphaFold's creators trained it on a formidable data set: the information in the Protein Data Bank, which was established in 1971 to collate the growing set of experimentally determined protein structures and currently contains more than 200,000 structures. AlphaFold provides an excellent example of the power AI systems can have when furnished with sufficient high-quality data.

So how can other AI systems create or access more and better chemistry data? One possible solution is to set up systems that pull data out of published research papers and existing databases, such as an algorithm created by researchers at the University of Cambridge, UK, that converts chemical names to structures[6]. This approach has accelerated progress in the use of AI in organic chemistry.

Another potential way to speed things up is to automate laboratory systems. Existing options include robotic materials-handling systems, which can be set up to make and measure compounds to test AI model outputs[7,8]. However, at present this capability is limited, because the systems can carry out only a relatively narrow range of chemical reactions compared with a human chemist.

AI developers can train their models using both real and simulated data. Researchers at the Massachusetts Institute of Technology in Cambridge have used this approach to create a graph-based model that can predict the optical properties of molecules, such as their colour[9].



How AlphaFold can realize AI's full potential in structural biology

There is another, particularly obvious solution: AI tools need open data. How people publish their papers must evolve to make data more accessible. This is one reason why *Nature* requests that authors deposit their code and

data in open repositories. It is also yet another reason to focus on data accessibility, above and beyond scientific crises surrounding the replication of results and high-profile retractions. Chemists are already addressing this issue with facilities such as the Open Reaction Database.

But even this might not be enough to allow AI tools to reach their full potential. The best possible training sets would also include data on negative outcomes, such as reaction conditions that don't produce desired substances. And data need to be recorded in agreed and consistent formats, which they are not at present.

Chemistry applications require computer models to be better than the best human scientist. Only by taking steps to collect and share data will AI be able to meet expectations in chemistry and avoid becoming a case of hype over hope.

Nature **617**, 438 (2023)

doi: https://doi.org/10.1038/d41586-023-01612-x

References

1. Segler, M. H. S., Preuss, M. & Waller, M. P. *Nature* **555**, 604–610 (2018).
2. Struble, T. J. *et al. J. Med. Chem.* **63**, 8667–8682 (2020).
3. Kim, K. *et al. npj Comp. Mater.* **4**, 67 (2018).
4. Yang, K. *et al. J. Chem. Inf. Model.* **59**, 3370–3388 (2019).
5. Jumper, J. *et al. Nature* **596**, 583–589 (2021).
6. Lowe, D. M., Corbett, P. T., Murray-Rust, P. & Glen, R. C. *J. Chem. Inf. Model.* **51**, 739–753 (2011).
7. Coley, C. W. *et al. Science* **365**, eaax1566 (2019).

8. Angello, N. H. *et al.* *Science* **378**, 399–405 (2022).

9. Greenman, K. P., Green, W. H. & Gómez-Bombarelli, R. *Chem. Sci.* **13**, 1152–1162 (2022).

This article was downloaded by **calibre** from https://www.nature.com/articles/d41586-023-01612-x

- WORLD VIEW
- 16 May 2023

Audit AI search tools now, before they skew research



Generative AI could be a boon for literature search, but only if independent groups scrutinize its biases and limitations.

- Michael Gusenbauer

Search tools assisted by large language models (LLMs) are changing how researchers find scholarly information. One tool, scite Assistant, uses GPT-3.5 to generate answers from a database of millions of scientific papers. Another, Elicit, uses an LLM to write its answers to searches for articles in a scholarly database. Consensus finds and synthesizes research claims in papers, whereas SciSpace bills itself as an 'AI research assistant' that can explain mathematics or text contained in scientific papers. All of these tools give natural-language answers to natural-language queries.

Search tools tailored to academic databases can use LLMs to offer alternative ways of identifying, ranking and accessing papers. In addition, researchers can use general artificial intelligence (AI)-assisted search systems, such as Bing, with queries that target only academic databases such as CORE, PubMed and Crossref.

All search systems affect scientists' access to knowledge and influence how research is done. All have unique capabilities and limitations. I'm intimately familiar with this from my experience building Search Smart, a tool that allows researchers to compare the capabilities of 93 conventional search tools, including Google Scholar and PubMed. AI-assisted, natural-language search tools will undoubtedly have an impact on research. The question is: how?

The time remaining before LLMs' mass adoption in academic search must be used to understand the opportunities and limitations. Independent audits of these tools are crucial to ensure the future of knowledge access.



Tools such as ChatGPT threaten transparent science; here are our ground rules for their use

All search tools assisted by LLMs have limitations. LLMs can 'hallucinate': making up papers that don't exist, or summarizing content inaccurately by making up facts. Although dedicated academic LLM-assisted search

systems are less likely to hallucinate because they are querying a set scientific database, the extent of their limitations is still unclear. And because AI-assisted search systems, even open-source ones, are ‘black boxes’ — their mechanisms for matching terms, ranking results and answering queries aren’t transparent — methodical analysis is needed to learn whether they miss important results or systematically favour specific types of papers, for example. Anecdotally, I have found that Bing, scite Assistant and SciSpace tend to yield different results when a search is repeated, leading to irreproducibility. The lack of transparency means there are probably many limitations still to be found.

Already, Twitter threads and viral YouTube videos promise that AI-assisted search can speed up systematic reviews or facilitate brainstorming and knowledge summarization. If researchers are not aware of the limitations and biases of such systems, then research outcomes will deteriorate.

Regulations exist for LLMs in general, some within the sphere of the research community. For example, publishers and universities have hammered out policies to prevent LLM-enabled research misconduct such as misattribution, plagiarism or faking peer review. Institutions such as the US Food and Drug Administration rate and approve AIs for specific uses, and the European Commission is proposing its own legal framework on AI. But more-focused policies are needed specifically for LLM-assisted search.



Why open-source generative AI models are an ethical way forward for science

In working on Search Smart, I developed a way to assess the functionalities of databases and their search systems systematically and transparently. I often found capabilities or limitations that were omitted or inaccurately described in the search tools' own frequently asked questions. At the time of our study, Google Scholar was researchers' most widely used search engine. But we found that its ability to interpret Boolean search queries, such as ones involving OR and AND, was both inadequate and inadequately reported. On the basis of these findings, we recommended not relying on Google Scholar for the main search tasks in systematic reviews and meta-analyses (M. Gusenbauer & N. R. Haddaway *Res. Synth. Methods* **11**, 181–217; 2020).

Even if search AIs are black boxes, their performance can still be evaluated using 'metamorphic testing'. This is a bit like a car-crash test: it asks only whether and how passengers survive varying crash scenarios, without needing to know how the car works internally. Similarly, AI testing should prioritize assessing performance in specific tasks.

LLM creators should not be relied on to do these tests. Instead, third parties should conduct a systematic audit of these systems' functionalities. Organizations that already synthesize evidence and advocate for evidence-based practices, such as Cochrane or the Campbell Collaboration, would be ideal candidates. They could conduct audits themselves or jointly with other entities. Third-party auditors might want to partner with librarians, who are likely to have an important role in teaching information literacy around AI-assisted search.

The aim of these independent audits would not be to decide whether or not LLMs should be used, but to offer clear, practical guidelines so that AI-assisted searches are used only for tasks of which they are capable. For example, an audit might find that a tool can be used for searches that help to define the scope of a project, but can't reliably identify papers on the topic because of hallucination.

AI-assisted search systems must be tested before researchers inadvertently introduce biased results on a large scale. A clear understanding of what these systems can and cannot do can only improve scientific rigour.

Nature **617**, 439 (2023)

doi: https://doi.org/10.1038/d41586-023-01613-w

This article was downloaded by **calibre** from https://www.nature.com/articles/d41586-023-01613-w

News in Focus

- **First UK children born using three-person IVF: what scientists want to know** [10 May 2023]
  • British fertility regulator reveals that at least one child has been born using mitochondrial replacement therapy, but details are scant.
- **First human ‘pangenome’ aims to catalogue genetic diversity** [10 May 2023]
  • Researchers release draft results from an ongoing effort to capture the entirety of human genetic variation.
- **Physicists create long-sought topological quantum states** [09 May 2023]
  • Exotic particles called nonabelions could fix quantum computers’ error problem.
- **Saudi universities entice top scientists to switch affiliations — sometimes with cash** [05 May 2023]
  • Some institutions arrange for highly cited researchers to change their main affiliations, which boosts their position in global university rankings.
- **FDA advisers unanimously back over-the-counter birth control pill** [10 May 2023]
  • Panellists say that making the contraceptive available in the United States without a prescription will benefit women’s health.
- **NIH reinstates grant for controversial coronavirus research** [08 May 2023]
  • EcoHealth Alliance lost funding during the Trump administration, but can now proceed with its research — under extensive restrictions.
- **The ocean is hotter than ever: what happens next?** [10 May 2023]
  • Record temperature combined with an anticipated El Niño could devastate marine life and increase the chances of extreme weather.
- **Can giant surveys of scientists fight misinformation on COVID, climate change and more?** [17 May 2023]
  • Shocked by the COVID-19 infodemic, several efforts have launched to gather researchers’ consensus views, with the hope of improving public debate and policymaking.

- **GISAID in crisis: can the controversial COVID genome database survive?** [04 May 2023]
  • The most popular repository for sharing SARS-CoV-2 sequence data has come under increasing scrutiny. Scientists and funders around the world must now consider what lies ahead for the open sharing of genome data.

- NEWS
- 10 May 2023

First UK children born using three-person IVF: what scientists want to know

British fertility regulator reveals that at least one child has been born using mitochondrial replacement therapy, but details are scant.

- Ewen Callaway



Mitochondrial replacement therapy is an *in vitro* fertilization technique that involves the DNA of three people.Credit: Zephyr/Science Photo Library

Eight years after the United Kingdom became the first country to regulate the reproductive technique known as mitochondrial replacement, news has emerged that children have been born using the procedure.

The Human Fertilisation and Embryology Authority (HFEA), the UK fertility regulator, confirmed that fewer than five UK children had been born using the procedure as of April 2023. The confirmation came in response to a freedom of information request by the *Guardian* newspaper. The HFEA provided no further information about the procedure or the children.

“It’s exciting news, but at the same time it doesn’t tell us anything about whether the method has actually worked,” says Dagan Wells, a reproductive geneticist at the University of Oxford, UK. “There are open questions, and we need to get answers as soon as possible.”

Mitochondrial replacement therapy (MRT), which was legalized in the United Kingdom in 2015, is intended to prevent the inheritance of serious health conditions caused by mutations to mitochondria, cells’ energy-producing organelles; such mutations often affect the heart, brain and muscles.

The procedure — sometimes called three-person *in vitro* fertilization (IVF) — involves moving nuclear genetic material from an egg or single-cell embryo with disease-causing mitochondria to a donor egg or embryo that has had its nuclear genetic material removed.

Grey regulation

The procedure has been performed in other countries, where its use is not regulated. In 2016, a US doctor announced that he had used MRT successfully to prevent mitochondrial disease in a baby, in a procedure conducted in Mexico. Children have also been born through mitochondrial transfers conducted in Greece and Ukraine to treat infertility. Last year, Australia became the second country to approve MRT. But the procedure remains restricted in many other countries, including the United States.

The mitochondrial transfers uncovered by *The Guardian* were done at the Newcastle Fertility Centre, the only UK clinic with a licence to conduct MRT. Under current regulations, the HFEA must approve each use on a case-by-case basis.

Researchers are anxious to learn more from the UK procedures as they start to conduct their own trials. “If there are any negative things to be considered, we need to know about those sooner rather than later,” says Wells.

Knowing how well the procedures worked and whether the babies are free of mitochondrial disease is crucial, says Robin Lovell-Badge, a developmental biologist at the Francis Crick Institute in London, who gave a statement to the UK Science Media Centre. Lovell-Badge also wants to know “whether there is any risk of them developing problems later in life or, if female, if their offspring are at risk of having the disease”.

This risk could arise during the procedure — when, inevitably, a small number of mitochondria are transferred into the donor egg or embryo. Wells wants to know the extent of this ‘carry-over’ in the UK cases and whether or not very low levels of mutation-bearing mitochondria cause health problems.

Mutant mitochondria

Scientists also want to know whether the levels of mutant mitochondria that are transferred remain stable over time. Animal and cell studies have found that in some cases the carried-over mitochondria can increase markedly over time, replacing donor mitochondria in cells — a phenomenon known as reversal[1].

And this can happen in humans. This year, Wells and his colleagues observed reversal after using MRT to treat infertility in a trial of 25 couples in Greece. Of the 6 children born, 5 had mitochondrial DNA that came almost entirely from the donor in cells from blood, umbilical cord and other tissues sampled. However, one child’s cells had high levels of mitochondria inherited from the mother — 30–60% of the total. When the embryo was

implanted, less than 1% of its mitochondria were carried over from the maternal egg[2].

The reversal seems to have had no effect on the child's health. "If we had been doing the same procedure to avoid a mitochondrial DNA disorder, then this might be a cause for concern," says Wells. "So that's a big question we have: has any reversal been seen in any of these children?"

It's not clear why the proportion of potentially disease-causing mitochondria can increase so dramatically after mitochondrial transfer and during development. One possibility is that genetic factors enable the maternal mitochondrial lineage to replicate more efficiently than mitochondria in the donor egg or embryo, says Wells. If so, it might be worth matching donor and recipient on the basis of similarities in their mitochondrial DNA, he adds; this would potentially reduce the ability of one lineage to out-replicate another.

There may be other ways to prevent reversal, says Shoukhrat Mitalipov, a reproductive biologist at the Oregon Health & Science University in Portland who was part of the infertility trial. In the five children who gained nearly all their mitochondria from a donor, the researchers had frozen the mother's eggs before transferring the nuclear genetic material into fresh donor eggs. Both eggs were fresh during the transfer that created the child in which reversal occurred. "We're still puzzled as to whether freezing the mother's egg is actually beneficial," he says.

The first UK births from MRT also provide an opportunity to take stock of the country's cautious approach to allowing the procedure.

"It gives the general public some reassurance that these kinds of cutting-edge procedures — which push scientific but also ethical boundaries — are being done with appropriate oversight," says Wells. But the fact that just one UK clinic can perform MRT has probably created a bottleneck for treatment, he adds. "There are pluses and minuses."

Nature **617**, 443-444 (2023)

doi: https://doi.org/10.1038/d41586-023-01585-x

References

1. Kang, E. *Nature* **540**, 270–275 (2016).
2. Costa-Borges, N. *et al. Fertil. Steril*. https://doi.org/10.1016/j.fertnstert.2023.02.008 (2023).

This article was downloaded by **calibre** from https://www.nature.com/articles/d41586-023-01585-x

- NEWS
- 10 May 2023

First human ‘pangenome’ aims to catalogue genetic diversity

Researchers release draft results from an ongoing effort to capture the entirety of human genetic variation.

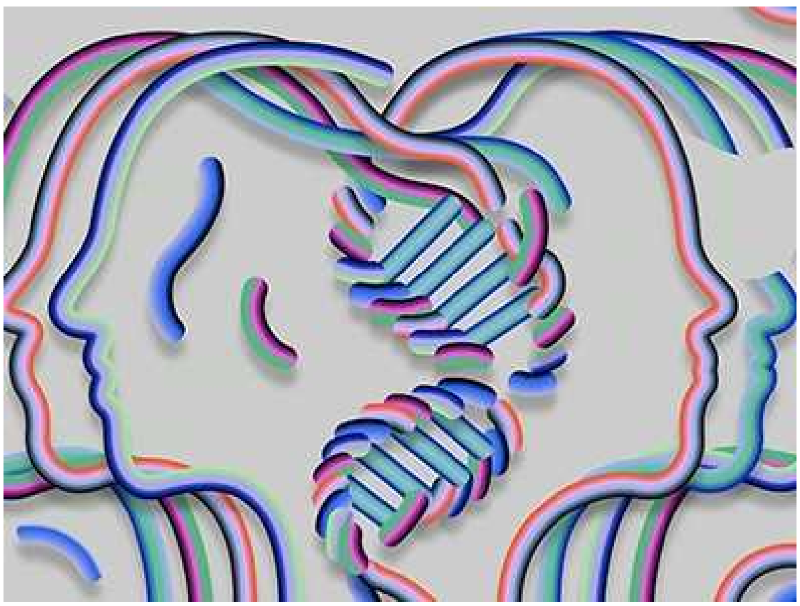
- Layal Liverpool



The human pangenome represents a collection of genetic sequences from a diverse cohort of people.Credit: Gideon Mendel/Corbis via Getty

More than 20 years after the release of the first draft genome from the landmark Human Genome Project, researchers have published a draft human 'pangenome' — a snapshot of what is poised to become a new reference for genetic research that captures more of human diversity than has been previously available. Geneticists have welcomed the milestone, while also highlighting key ethical considerations surrounding the effort to make genome research more inclusive.

"This is like going from black-and-white television to 1080p," says Keolu Fox, a genome scientist at the University of California, San Diego.



A more-inclusive genome project aims to capture all of human diversity

"It's something that we have all been waiting for," says Aimé Lumaka, a geneticist who holds a joint position at the University of Liège in Belgium and the University of Kinshasa in the Democratic Republic of the Congo. "The current reference genome is missing not only part of the genomic information but, most importantly, it's missing diversity," he says.

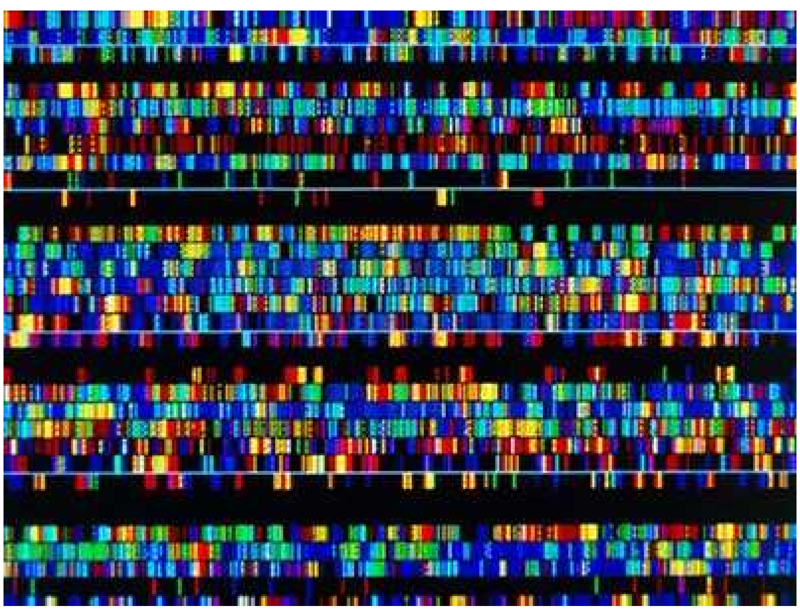
The draft genome, published in *Nature* on 10 May[1], was produced by the Human Pangenome Reference Consortium. Launched in 2019, the international project aims to map the entirety of human genetic variation, to create a comprehensive reference against which geneticists will be able to

compare other sequences. Such a reference would aid studies investigating potential links between genes and disease.

The draft pangenome follows the 2022 publication of the first complete sequence of the human genome[2], which filled gaps that had been left by the original Human Genome Project. But unlike the original draft genome and its successor, both of which were derived mostly from the DNA of just one person, the draft pangenome represents a collection of sequences from a diverse selection of 47 people from around the globe, including individuals from Africa, the Americas, Asia and Europe.

Genetic Tube map

Eimear Kenny, a geneticist at the Icahn School of Medicine at Mount Sinai in New York City, and her colleagues aligned all these sequences computationally to form a ‘pangenome graph’ — conceptually similar to a London Underground map, in which branching paths indicate genetic variation. The researchers found that the pangenome enabled them to identify twice as many structural variants — large genomic alterations such as gene duplications or deletions — per person than is possible using the original, linear reference genome. The team aims to analyse sequences from 350 people by mid-2024.



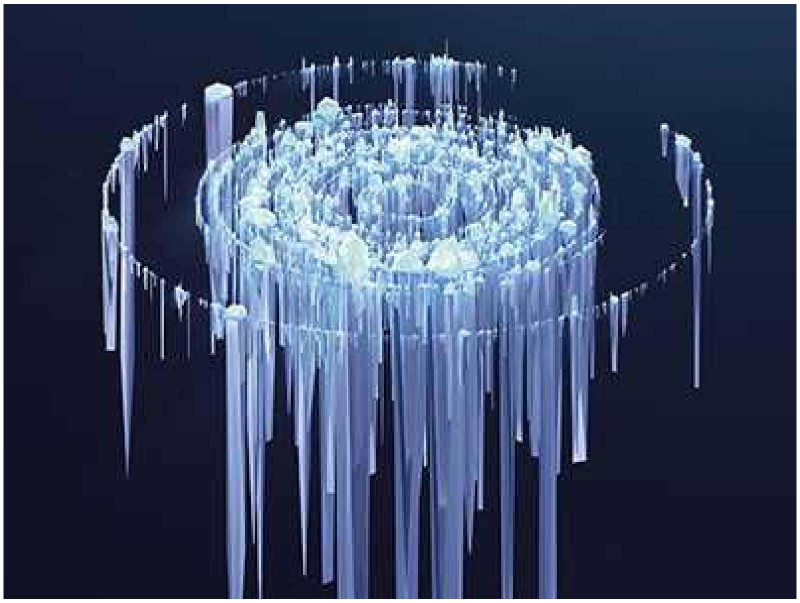
A complete human genome sequence is close: how scientists filled in the gaps

Many of the samples being analysed are from people who took part in the 1000 Genomes Project, a sequencing effort initiated in 2008 to map genetic variation across 26 diverse populations. The participants' frozen DNA samples are being defrosted and reanalysed by the pangenome consortium using a more detailed technique called 'long-read sequencing'. This analyses longer sections of DNA at a time, compared with older sequencing methods, and can distinguish between chromosome pairs from the same person. "It's a much higher-resolution approach," says Fox.

Consent forms signed by the participants at the time of the 1000 Genomes Project cover the reanalysis of their samples and, during a press conference, Kenny and other researchers from the pangenome consortium said that the project was taking further measures to ensure ethical collection and use of the genetic data. For instance, the consortium has committed not to include people who are members of Indigenous or other ethnic groups that have formal policies preventing contribution of samples, said Kenny.

Ethical considerations

However, some researchers — including Fox — are concerned that the project risks repeating ethically questionable practices from other large-scale genetic-diversity projects. For instance, the Human Genome Diversity Project in the 1990s and the ongoing All of Us Research Program received criticism, including from US-based ethnic groups, for failing to engage sufficiently with members of the communities whose DNA they were sampling. These included people belonging to marginalized groups usually under-represented in human genetic research.



A wealth of discovery built on the Human Genome Project — by the numbers

“We will, of course, advance knowledge of human structural variation with new data sets and new tools. The progress we should be striving for, however, is the equitable engagement of under-represented communities in this work from the ground up,” says Krystal Tsosie, a genetic epidemiologist and bioethicist at Arizona State University in Tempe. Tsosie is also co-founder of the Native BioData Consortium, a non-profit research institute in Eagle Butte, South Dakota, led by Indigenous scientists and members of ethnic groups. “If the research is not benefiting the diverse communities first and foremost, then we are doing something fundamentally wrong here,” she says.

Fox, who is on the board of the Native BioData Consortium, agrees. He is concerned that data from the Human Pangenome Reference Project, which is funded by the US National Institutes of Health, could be used by the pharmaceutical industry for commercial purposes — as has happened in the past[3] — without tangible benefits to the study participants or their communities.

Revisiting consent

Latifa Jackson, a geneticist at Howard University in Washington DC, points out that the 1000 Genomes Project relied partly on samples collected many years before it launched. “I am concerned that many of the participating pangenome locations have samples that were collected in the 1980s under very different political and social structures,” she says. “We need to revisit ideas of consent, especially for samples collected 30–40 years ago under very different power structures.”

“We recognize that this work is at the forefront of genomic research and has specific features, including open access of data, that warrant a great deal of consideration, and that the applications can raise ethical, legal and social issues,” Kenny said at the press conference. “We have drawn not only from our own expertise, but also built on the work of scholars and organizations throughout the world, to be aware of the many pitfalls and to systematically review other efforts for lessons learned, that we can bring into this new initiative.”

Kenny added that the pangenome consortium is hoping to recruit new study participants as part of its effort to maximize diversity among the planned 350 genomes. These will include participants obtained “through a large health system in an urban city like New York, which has people from almost every country of the world through processes of diaspora and migration”, said Kenny.

Nature **617**, 444-445 (2023)

doi: https://doi.org/10.1038/d41586-023-01576-y

References

1. Liao, W.-W. *et al. Nature* **617**, 312–324 (2023).
2. Nurk, S. *et al. Science* **376**, 44–53 (2022).
3. Fox, K. *N. Engl. J. Med.* **383**, 411–413 (2020).

This article was downloaded by **calibre** from https://www.nature.com/articles/d41586-023-01576-y

- NEWS
- 09 May 2023

Physicists create long-sought topological quantum states

Exotic particles called nonabelions could fix quantum computers’ error problem.

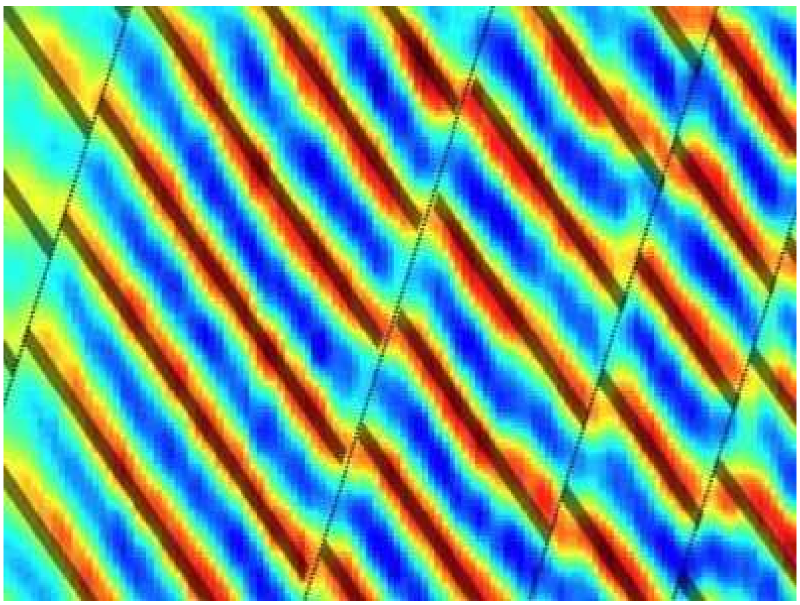
- Davide Castelvecchi



Borromean rings depicted in a church in Florence, Italy. If any one of the three rings is removed, the other two are no longer joined.Credit: Raphael Salzedo/Alamy

The coat of arms of Italy’s aristocratic House of Borromeo contains an unsettling symbol: an arrangement of three interlocking rings that cannot be pulled apart but doesn’t contain any linked pairs.

That same three-way linkage is an unmistakable signature of one of the most coveted phenomena in quantum physics — and it has now been observed for the first time. Researchers have used a quantum computer to create virtual particles and move them around so that their paths formed a Borromean-ring pattern.



Welcome anyons! Physicists find best evidence yet for long-sought 2D structures

The exotic particles are called non-Abelian anyons, or nonabelions for short, and their Borromean rings exist only as information inside the quantum computer. But their linking properties could help to make quantum computers less error-prone, or more ‘fault-tolerant’ — a key step to making them outperform even the best conventional computers. The results, revealed in a preprint on 9 May[1], were obtained on a machine at Quantinuum, a quantum-computing company in Broomfield, Colorado, that formed as the result of a merger between the quantum computing unit of Honeywell and a start-up firm based in Cambridge, UK.

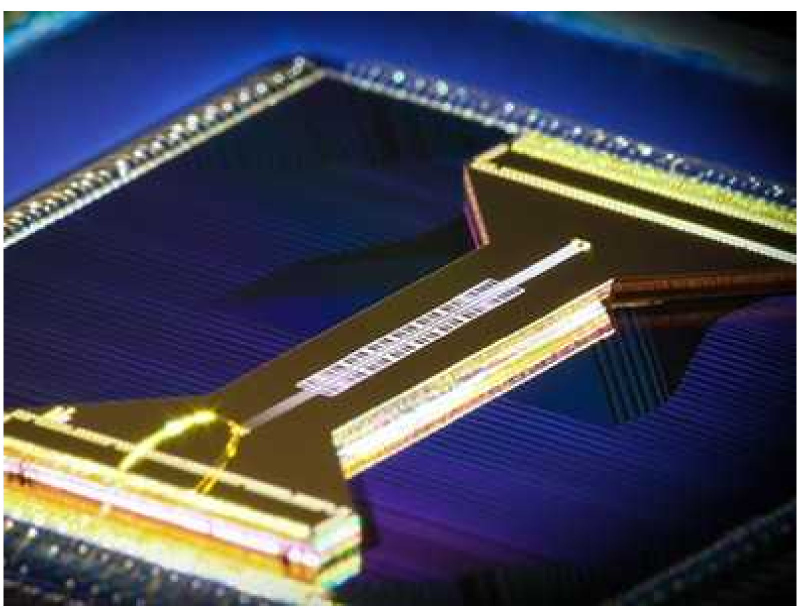
“This is the credible path to fault-tolerant quantum computing,” says Tony Uttley, Quantinuum’s president and chief operating officer.

Other researchers are less optimistic about the virtual nonabelions’ potential to revolutionize quantum computing, but creating them is seen as an achievement in itself. “There is enormous mathematical beauty in this type of physical system, and it’s incredible to see them realized for the first time, after a long time,” says Steven Simon, a theoretical physicist at the University of Oxford, UK.

Basket-weave doughnut

In the experiment, Henrik Dreyer, a physicist at Quantinuum’s office in Munich, Germany, and his collaborators used the company’s most advanced machine, called H2, which has a chip that can produce electric fields to trap 32 ions of the element ytterbium above its surface. Each ion can encode a qubit, a unit of quantum computation that can be ‘0’ or ‘1’ like ordinary bits, but also a superposition of both states simultaneously.

Quantinuum’s approach has an advantage: compared with most other types of qubit, the ions in its trap can be moved around and brought to interact with each other, which is how quantum computers perform computations.



Quantum computer race intensifies as alternative technology gains steam

The physicists exploited this flexibility to create an unusually complex form of quantum entanglement, in which all 32 ions share the same quantum state. And by engineering those interactions, they created a virtual lattice of entanglement with the structure of a kagome — a pattern used in Japanese basket-weaving that resembles the repeated overlapping of six-pointed stars — folded to form a doughnut shape. The entangled states represented the lowest-energy states of a virtual 2D universe — essentially, the states that contain no particles at all. But with further manipulation, the kagome can be put in excited states. These correspond to the appearance of particles that should have the properties of nonabelions.

To prove that the excited states were nonabelions, the team performed a series of tests. The most conclusive one consisted of moving the excited states around to create virtual Borromean rings. The appearance of the pattern was confirmed by measurements of the state of the ions during and after the operation, Dreyer says.

“No two particles are taken around each other, but all together they are linked,” says Ashvin Vishwanath, a theoretical physicist at Harvard University in Cambridge, Massachusetts, and a co-author of the paper. “It’s really an amazing state of matter that we don’t have a very clear realization of in any other set-up.”

Michael Manfra, an experimental physicist at Purdue University in West Lafayette, Indiana, says that although the results are impressive, the Quantinuum machine does not truly create nonabelions, but merely simulates some of their properties. But the authors say that the particles’ behaviour satisfies the definition, and that for practical purposes they could still form a basis for quantum computing.

Quantum pedigree

Like the Borromeo family, nonabelions come with a storied genealogy in both physics and mathematics, including work that has led to several Nobel prizes and Fields medals. Nonabelions are a type of anyon, a particle that

can exist only in a 2D universe or in situations where matter is trapped in a 2D surface — for example at the interface of two solid materials.

The strange topology that is reshaping physics

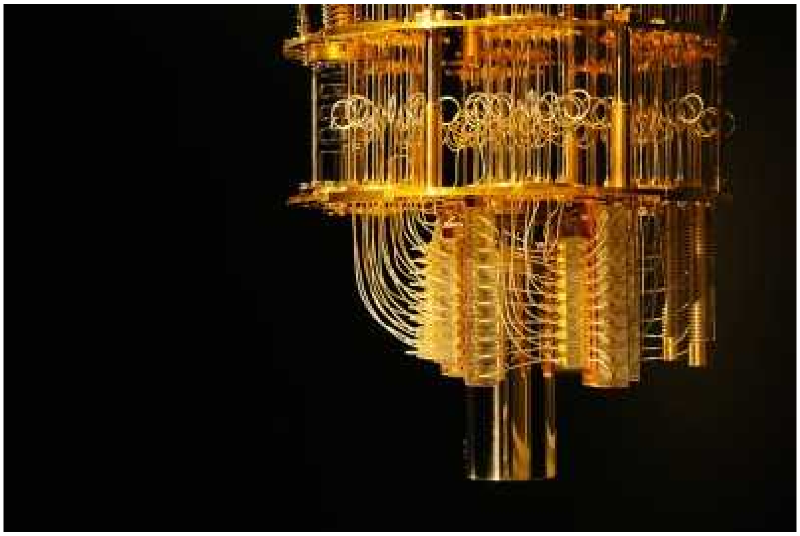
Anyons defy one of physicists' most cherished assumptions: that all particles belong to one of two categories, fermions or bosons. When two identical fermions switch positions, their quantum state, called the wavefunction, is flipped by 180 degrees (in a mathematical space called Hilbert space). But when bosons are switched, their wavefunction is unchanged.

When two anyons are switched, on the other hand, neither of these two options applies. Instead, for standard, 'Abelian' anyons, the wavefunction is shifted by a certain angle, different from fermions' 180 degrees. Non-Abelian anyons respond by changing their quantum state in a more complex way — which is crucial because it should enable them to perform quantum computations that are non-Abelian, meaning that the calculations produce different outcomes if performed in a different order.

Topological robustness

Nonabelions could also offer an advantage over most other ways of doing quantum computing. Ordinarily, the information in an individual qubit tends to degrade quickly, producing errors — something that has limited progress towards useful quantum computing. Physicists have developed various error-correction schemes that would require encoding a qubit in the collective quantum state of many atoms, potentially thousands.

But nonabelions should make that task a lot easier, because the paths they trace when they are looped around one another should be robust to errors. Perturbations such as magnetic disturbances might slightly move the paths around without changing the qualitative nature of their linking, called their topology.



Underdog technologies gain ground in quantum-computing race

The concept of nonabelions and their potential as ‘topological qubits’ was first proposed 20 years ago by theoretical physicist Alexei Kitaev, now at the California Institute of Technology in Pasadena[2]. Physicists including Manfra have been aiming to create states of matter that naturally contain nonabelions and can therefore serve as the platform for topological qubits. Microsoft has made topological qubits its preferred approach to developing a quantum computer.

Vishwanath says that the nonabelions in Quantinuum’s machine are an important initial step. “To get into that game — to be even a contender for a topological quantum computer — the first step you need to take is to create such a state,” he says.

Simon says that the virtual nonabelion approach could be useful for quantum computations, but that it remains to be seen whether it will be more efficient than other error-correction schemes — some of which are also topologically inspired. The physical anyons that both Manfra and Microsoft are working on would be topologically robust out of the box. Dreyer says that, at the moment, it is still unclear how efficient his team’s nonabelions will turn out to be.

Nature **617**, 445-446 (2023)

doi: https://doi.org/10.1038/d41586-023-01574-0

References

1. Iqbal, M. *et al.* Preprint at https://arxiv.org/abs/2305.03766 (2023).

2. Kitaev, A. Y. *Ann. Phys.* **303**, 2–30 (2003).

This article was downloaded by **calibre** from https://www.nature.com/articles/d41586-023-01574-0

- NEWS
- 05 May 2023

Saudi universities entice top scientists to switch affiliations — sometimes with cash

Some institutions arrange for highly cited researchers to change their main affiliations, which boosts their position in global university rankings.

- Michele Catanzaro



Riyadh, Saudi Arabia.Credit: Abdullah Al-Eisa/Getty

Research institutions in Saudi Arabia are gaming global university rankings by encouraging top researchers to change their main affiliations, sometimes

in exchange for cash, and often with little obligation to do meaningful work. That's the conclusion of a report that shows how, over the past decade, dozens of the world's most highly cited researchers have switched their primary affiliations to universities in the country. That, in turn, has boosted the standing of Saudi Arabian institutions in university ranking tables, which consider the citation impacts of an institution's researchers.

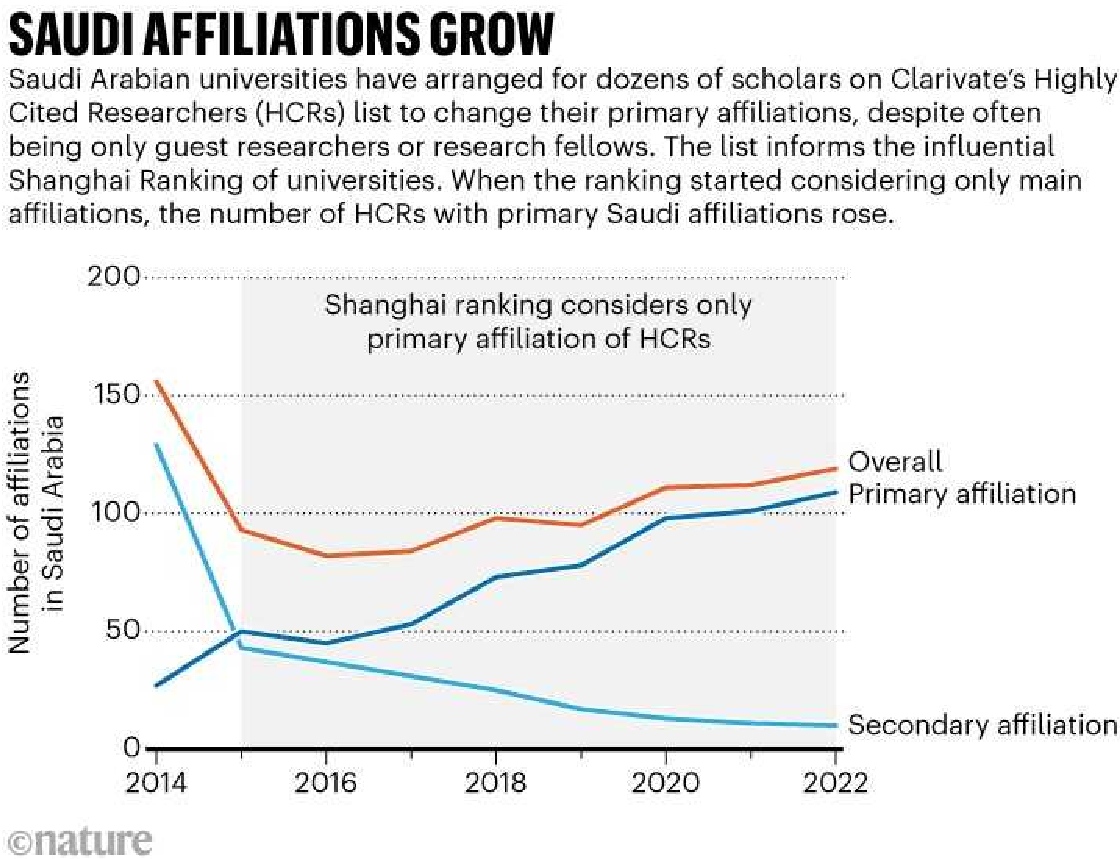
"We have found a pattern of sudden appearance of a Saudi primary affiliation," says Yoran Beldengrün, who co-authored the report, published on 4 May by SIRIS Academic, a consultancy in Barcelona, Spain. "Gaming practices and misleading affiliations feed suspicions about the reliability of science," says the report.

"Stating an affiliation that does not correspond to a work relation, with the objective of increasing the ranking of an institution, is not in agreement with good scientific practices," says Pere Puigdomènech, a plant molecular biologist and member of the European Science Foundation's Forum on Research Integrity. "The manipulation of indicators is a by-product of the idolatry of ranking and indexes, that has been repeatedly denounced as misguided."

The analysis looked at the list of highly cited researchers (HCRs) maintained by publishing-analytics firm Clarivate, based in London, which features scholars whose papers rank in the top 1% most cited papers in Clarivate's Web of Science database for a given field or year. The number of researchers on the list who have a primary affiliation in Saudi Arabia increased from 27 to 109 between 2014 and 2022, the report found. These researchers work in a range of disciplines, and many have secondary affiliations in countries including Spain, China, the United Kingdom, Germany and India. The trend means that Saudi Arabia is disproportionately flush with HCRs: in 2022, 0.44% of its researchers were HCRs, compared with 0.19% of US scholars and 0.08% of German researchers.

"The high number of highly cited researchers is the main reason why some Saudi universities are ranked among the top 150 worldwide," says Domingo Docampo, a mathematician at the University of Vigo in Spain who consults for SIRIS, but was not involved in the report. In a 2013 paper[1], Docampo used public data, including researcher affiliations, to reproduce the results of

the Academic Ranking of World Universities, also known as the Shanghai Ranking — a leading league table that takes into account Clarivate’s HCR list.



Source: SIRIS Academic. *The affiliation game of Saudi Arabian higher education & research institutions* (2023).

SIRIS’s report follows revelations in Spanish in newspaper *El País*, which in April reported that chemist Raphael Luque had been suspended from the University of Cordoba in Spain, where he was employed full-time, after switching his primary affiliation to King Saud University (KSU) in Riyadh. The change is thought to have reduced the University of Cordoba’s position in the Shanghai Ranking by more than 140 places. Luque, who did not respond to *Nature*’s request for comment, told El País that he didn’t receive money directly from Saudi institutions, beyond funding for his research and premium travel and hotels.

Other Spanish researchers told *El País* that they have received money. Some have been forced by their Spanish universities to give up their Saudi positions, or are being investigated amid concerns that they moved their affiliations in exchange for money.

Cash offers

Although the analysis of affiliation switches is new, awareness of the practice isn't. SIRIS's report does not detail specific financial arrangements between institutions and researchers, but since the early 2010s, leading researchers worldwide have reported being approached by Saudi universities with offers of cash in exchange for being added to a researcher's affiliations. The arrangements often seem to require minimal contributions to the institution's research.

In 2011, *Science* reported that 61 researchers had signed such contracts with King Abdulaziz University in Jeddah, with varying financial terms and levels of contribution. At the time, King Abdulaziz University and KSU, also mentioned in the *Science* story, responded by acknowledging they had programmes to recruit top international scientists, but said they used best practice for international collaborations; neither responded to *Nature*'s requests for comment for this story.

In 2014, apparently wise to the idea that institutions could game its table through multiple affiliations, the Shanghai Ranking started to consider only primary affiliations of researchers in Clarivate's HCR list. (Representatives of the Shanghai Ranking did not reply to *Nature*'s requests for comment.) But the practice continued, this time concentrated on primary affiliations. In the following years, Saudi primary affiliations rose, and academics with secondary affiliations in the country dropped from 130 to 10 in the same period, found SIRIS's report (see 'Saudi affiliations grow').

In 2019, shortly after she appeared on Clarivate's 2018 HCR list, chemist Mira Petrović at the Catalan Institute for Water Research in Girona, Spain, received an e-mail from KSU inviting her to form a collaboration. "I thought they wanted to propose a real collaboration," says Petrović. But after a brief exchange, she received an e-mail bluntly asking to change her affiliation in

exchange for cash. “Your primary affiliation should be King Saud University on https://hcr.clarivate.com,” says the e-mail. “Once your affiliation has been changed,” it adds, “you will receive 70,000 Euro.” Petrovic declined. “What they were proposing was devoid of any academic content,” she says.

Clear pattern

Although some of the 109 HCRs on the 2022 list with a primary Saudi affiliation are based in the nation, many do not have what would typically be considered formal academic employment at a Saudi institution. At least 44 (40%) have only a research fellowship or are guest researchers; Clarivate marks them on its online list with an asterisk. (There were 46 asterisks in the 2022 list — two corresponded to affiliations in China, and the rest to Saudi ones.) “Most researchers follow the established tradition of using the secondary affiliation for such appointments and reserve the primary affiliation slot for their main employer,” wrote David Pendlebury, Clarivate’s head of research analysis, in an e-mail to *Nature*.

The SIRIS report says that many affiliation changes follow a pattern: a scholar enters the HCR list with one main affiliation, then switches to a Saudi one in later years (affiliations are self-reported to Clarivate). In some cases, researchers switch back to their original institution after a year or two.

Three-quarters of Saudi-affiliated HCRs have a secondary affiliation in a different country. That is markedly higher than those based in other countries: only 2% of HCRs with a primary affiliation in the United States have a secondary affiliation elsewhere, as do 13% with a primary affiliation in Spain.

Many in the research community criticize reliance on rankings, because they distort a university’s priorities and cannot capture an institution’s true value. “All the quantitative indicators based on bibliometrics are very delicate in use, and subject to gaming,” says Ghislaine Filliatreau, research-integrity officer at INSERM, the French national institute for health and medical research, who sits on the Shanghai Ranking’s international advisory board. “So, for all those types of indicators, better to never use quantifications as measurements, but as indications.”

The Saudi ministry of education did not reply to *Nature*’s request for comment.

Nature **617**, 446-447 (2023)

doi: https://doi.org/10.1038/d41586-023-01523-x

References

1. Docampo, D. *Scientometrics* **94**, 567–587 (2013).

This article was downloaded by **calibre** from https://www.nature.com/articles/d41586-023-01523-x

- NEWS
- 10 May 2023
- Correction 11 May 2023

FDA advisers unanimously back over-the-counter birth control pill

Panellists say that making the contraceptive available in the United States without a prescription will benefit women's health.

- Mariana Lenharo



Some types of birth control pill must be taken every day around the same time for them to be effective.Credit: Isabel Pavia/Getty

An advisory committee for the US Food and Drug Administration (FDA) has unanimously endorsed the agency making an oral contraceptive available over the counter. If the FDA follows this advice, the medication, sold under the name Opill, will be the first birth-control pill available without prescription in the United States. A final decision by the agency is expected in the coming months.



US lawsuit threatens access to abortion drug: the science behind the case

Because the FDA often follows its advisers' recommendations, the two-day meeting, which ended on 10 May, was hotly anticipated. Associations such as the American College of Obstetricians and Gynecologists (ACOG) and the American Medical Association have been urging the agency to make oral contraceptives available over the counter.

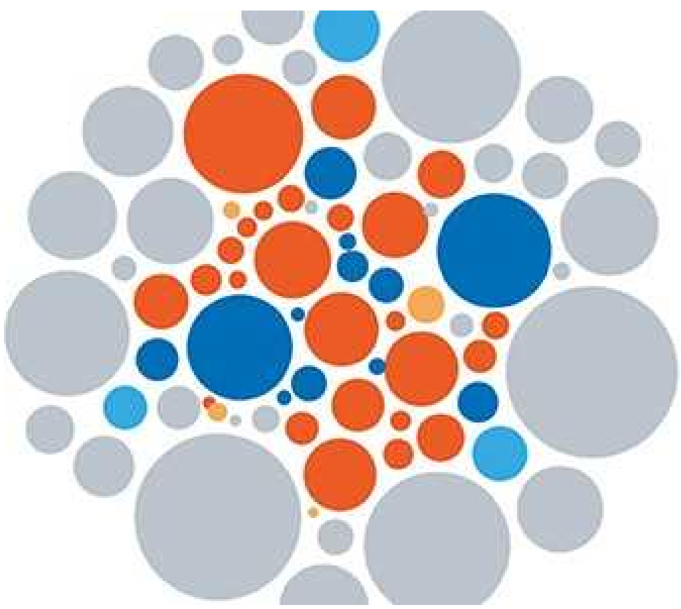
"The scientific evidence is clear that over-the-counter access to contraception without age restrictions can be accomplished safely, and the benefit of increased access is significant," said Kristyn Brandi, a gynaecologist representing ACOG at the meeting. She pointed out that many people seeking medication to prevent unwanted pregnancies face obstacles, including cost barriers and difficulties in obtaining an appointment with a physician. "People from marginalized communities, including racial and ethnic minorities, uninsured people and those who don't speak English, are more likely to face these barriers," she said.

The decision is especially important in the light of recent restrictions on abortion access in the United States, says Daniel Grossman, director of Advancing New Standards in Reproductive Health (ANSIRH), a research programme at the University of California, San Francisco. “People in about one-third of the country can’t access abortion care,” he says. “Now it’s even more important that remaining barriers to effective contraception are removed.”

Oral contraceptives are available over the counter in many other countries, although access to some requires a conversation with a pharmacist. In 2021, two brands of contraceptive pill became available without prescription in the United Kingdom, with only this requirement.

No prescription needed

There are two types of hormone-based birth control: one contains progestin, a synthetic form of the hormone progesterone, and the other uses a combination of progestin and the hormone oestrogen.



Women’s health research lacks funding — these charts show how

Opill, known by the generic name norgestrel, is a progestin-only medication. This type of drug has fewer risks compared with the combination pills,

which have been associated with blood clots, for example. Norgestrel was first approved by the FDA in 1973. In June 2022, Opill’s maker, HRA Pharma, based in Paris, filed an application to switch the medication from requiring a health-care provider’s prescription to not needing one.

To be sold over the counter in the United States, a drug must meet certain criteria. It should be used for a condition that the recipient can self-diagnose — in this case, the desire to prevent an unwanted pregnancy. The user should also be able to administer the drug safely and effectively without the help of a health-care provider. With Opill, that means taking one pill every day at the same time. The last criterion is that the drug should have a low potential for misuse and abuse.

In applying for the switch to non-prescription status, HRA Pharma submitted data to the FDA from studies probing whether consumers understand how to use Opill without supervision and can correctly identify whether they have any contraindications. These are medical conditions, such as a history of breast cancer, that would preclude them from taking the drug.

Concerns raised

During the advisory meeting, FDA scientists criticized the data presented by HRA Pharma, especially the results of the study evaluating how the drug might be used in a real-world setting. About one-third of the study participants reported taking more pills than were made available to them, which prompted the scientists to question the study’s conclusions. The scientists were also not completely convinced that users were capable of recognizing that they had contraindications for the pill.



[After Roe v. Wade: US researchers warn of what's to come]

The agency scientists even questioned the efficacy and safety of the drug. They noted that the clinical trials that led to its approval in 1973 might have had different results if they were conducted today, citing an increased incidence of obesity that could potentially lower the medication's efficacy.

It is unusual to bring up this issue, Grossman says. "With this kind of application to move a medication to non-prescription status, the only thing you should be looking at is whether people use it appropriately, according to the instructions and whether they can appropriately select for use or not," he says.

The scientists' intense scrutiny comes at a time when a lawsuit is [challenging the agency's decades-ago approval of the abortion pill mifepristone] — as well as its authority. It's unclear whether these concerns will affect the FDA's final decision on Opill.

During the portion of the meeting when members of the public could participate, some pushed back on the concerns. "Women can understand labels, including contraindications," said Caroline Renko, a manager at PharmedOut, a project at Georgetown University in Washington DC that educates physicians about how pharmaceutical companies influence prescribing. "Birth-control pills are so commonly used that information

regarding the importance of not missing doses or taking doses late is common knowledge,” she said. “These patronizing concerns are not grounds to take away a woman’s choice from her.”

During the advisory committee’s discussion, panellists acknowledged some of the limitations of the HRA Pharma data but ultimately concluded that enough evidence exists that the benefits of having an over-the-counter contraceptive pill outweigh the risks.

”Do I think that we’ve got perfect data? No,” said committee member Cynthia Baur, a health literacy and health-communication specialist at the University of Maryland in College Park. “Do I think it was a perfect study? No. Do I think it was adequate to feel reassured that a large number of people can use this drug as intended? Yes.”

Nature **617**, 448 (2023)

doi: https://doi.org/10.1038/d41586-023-01580-2

Updates & Corrections

- **Correction 11 May 2023**: An earlier version of this story said that Opill’s maker filed an application for switching the drug to over-the-counter use in July 2022. It was June 2022.

This article was downloaded by **calibre** from https://www.nature.com/articles/d41586-023-01580-2

- NEWS
- 08 May 2023

NIH reinstates grant for controversial coronavirus research

EcoHealth Alliance lost funding during the Trump administration, but can now proceed with its research — under extensive restrictions.

- Max Kozlov



Research organization EcoHealth Alliance plans to investigate coronaviruses in bats.Milehightraveller/Getty

The US National Institutes of Health (NIH) has reinstated a grant to a highly scrutinized research organization that studies bat coronaviruses — but the agency has placed several stipulations on the scope of the research and on the organization's accounting practices.

The move caps a years-long saga that has thrust the EcoHealth Alliance, a small non-profit organization in New York City, into the political fray for its collaborations with the Wuhan Institute of Virology (WIV) in China. In April 2020, after then-US-president Donald Trump hinted that SARS-CoV-2 originated in a WIV laboratory, the NIH terminated EcoHealth's grant. Its goal was to study how coronaviruses, such as SARS-CoV-2, jump from bats to humans. A few months later, the NIH reinstated and immediately suspended the award until certain conditions were met that, at the time, EcoHealth said were impossible to complete.



The shifting sands of 'gain-of-function' research

Researchers who spoke to *Nature* applaud the renewal, adding that this type of research is essential to avert the next pandemic. They claim that the NIH's termination and subsequent suspension were politically motivated, and that, although long overdue, this renewal ends — for now — a drama-filled exchange between the agency and EcoHealth.

"It's about goddam time," says Gerald Keusch, associate director of the National Emerging Infectious Diseases Laboratory at Boston University in Massachusetts, who organized researchers to push back against EcoHealth's grant termination in 2020. "The integrity of science requires a barrier against political interference," he says.

The NIH "routinely considers processes and measures for strengthening [its] oversight over federal funds" and has been working with EcoHealth to strengthen its "administrative processes to meet NIH's expectations", says Amanda Fine, a spokesperson for the NIH in Washington DC.

Lengthy list of conditions

Although the organization will now be able to continue its bat coronavirus research for the first time since the saga began, the NIH placed an extensive list of restrictions on the four-year, US$2.9-million award. None of the researchers who spoke to *Nature* had ever seen a grant with so many stipulations.

Among other things, EcoHealth is specifically forbidden from performing any in-country research in China, including with the WIV, or collecting any new samples from vertebrates — such as bats. The revised grant also mandates greater scrutiny of EcoHealth's finances and accounting practices, driven in part by a federal watchdog report, released in January, finding that EcoHealth had misreported about $90,000 in expenses. The report also faulted the NIH for improperly terminating EcoHealth's grant.

Furthermore, EcoHealth will be forbidden from performing any work that is deemed by the NIH's parent organization, the Department of Health and Human Services (HHS), to have the potential to enhance the virulence or transmission of a virus. This restriction stems, in part, from criticism that research done at the WIV and funded by an EcoHealth subaward qualified as 'gain of function' research.

Disputed research

Congressional Republicans have alleged that this research, which involved attaching spike proteins from wild bat coronaviruses to an unrelated virus to determine whether the wild pathogens could infect human airway cells, should have undergone HHS review. Anthony Fauci, then-director of the National Institute for Allergy and Infectious Diseases, has said the agency concluded that these experiments did not meet the bar to undergo such review, and noted that the WIV did not intend to enhance the viruses.



[Tens of thousands of people exposed to bat coronaviruses each year]

Virologists say this type of research is essential for developing vaccines and therapeutics against emerging pathogens and for understanding how likely a pathogen is to spark a pandemic. The NIH and HHS have been finalizing guidance that will probably tighten the oversight of such research in the United States.

“I don’t know if any other single grantee from NIH has been subjected to this level of oversight,” says Peter Daszak, president of the EcoHealth Alliance. Yet he is “positive and optimistic” about the grant restart, despite all the restrictions. A key priority for the newly released funds will be analysing nearly 300 partial or complete genomes of SARS-related coronaviruses from samples that the organization collected before the funding halt, he says.

Third rail of virology

These restrictions seem reasonable, in light of the enormous public attention to and scrutiny of gain-of-function research, says Lawrence Gostin, a health-law and policy specialist at Georgetown University in Washington DC. Still, Gostin says he is surprised the agency restarted its funding for EcoHealth, given that it has been the “third rail of politics” the past few years.

Angela Rasmussen, a virologist at the University of Saskatchewan in Saskatoon, Canada, says she is pleasantly surprised to see the grant renewed, but worries about the “terrible precedent” that the NIH set by “arbitrarily” terminating an award on the basis of “unfounded rumours” regarding the origins of SARS-CoV-2. She hopes that these same restrictions will not apply to other scientists doing similar work, but is encouraged by the number of research groups that are now studying coronaviruses following the COVID-19 pandemic.

Nature **617**, 449 (2023)

doi: https://doi.org/10.1038/d41586-023-01566-0

This article was downloaded by **calibre** from https://www.nature.com/articles/d41586-023-01566-0

- NEWS EXPLAINER
- 10 May 2023

The ocean is hotter than ever: what happens next?

Record temperature combined with an anticipated El Niño could devastate marine life and increase the chances of extreme weather.

- Nicola Jones



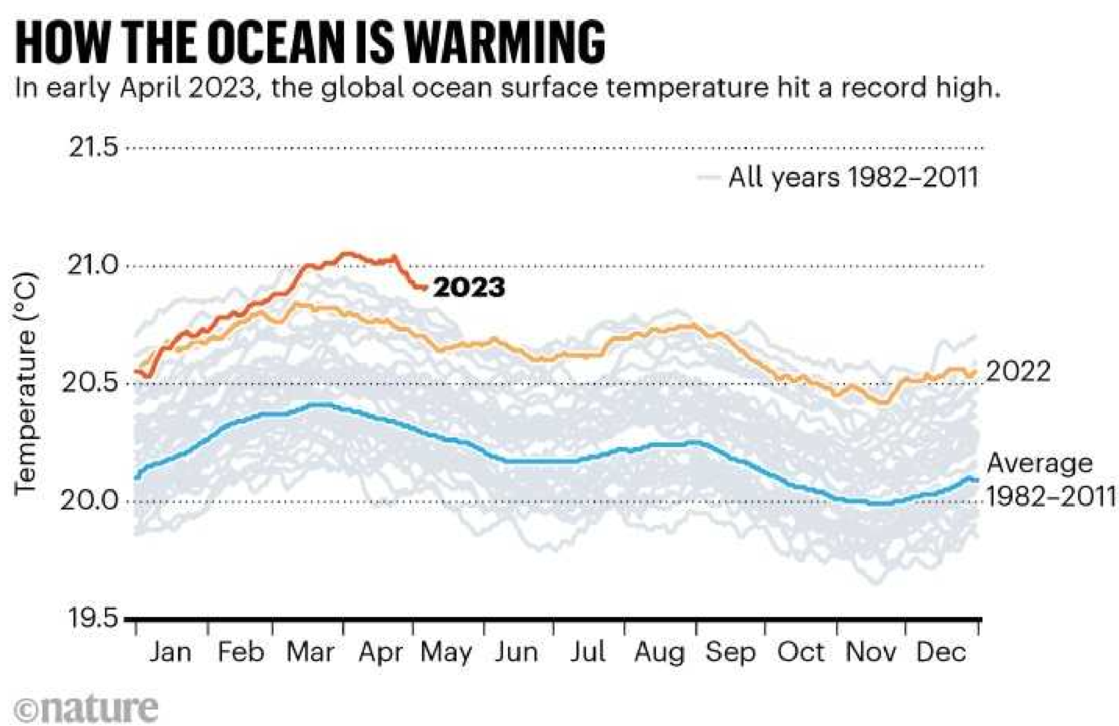
Warm oceans can bleach and kill corals.Credit: Juergen Freund/NPL

The global ocean hit a new record temperature of 21.1 ºC in early April, 0.1 ºC higher than the last record in March 2016. Although striking, the figure

(see 'How the ocean is warming') is in line with the ocean warming anticipated from climate change. What is remarkable is its occurrence ahead of — rather than during — the El Niño climate event that is expected to bring warmer, wetter weather to the eastern Pacific region later this year.

That means warmer-than-average ocean temperatures are likely to persist or even intensify, bringing with them more-extreme weather and marine heatwaves, which spell problems for marine life from corals to whales.

“We are probably looking at a string of record highs over the next year or so,” says Josh Willis, an oceanographer at NASA’s Jet Propulsion Laboratory in Pasadena, California. “This coming year is gonna be a wild ride if the El Niño really takes off.”



Source: climatereanalyzer.org; NOAA Optimum Interpolation SST (OISST)

The El Niño Southern Oscillation (ENSO) is a natural, cyclical climate pattern. During the El Niño phase, winds over the Pacific are weakened or reversed, allowing warm waters to slosh eastwards in the Pacific. El Niño tends to coincide with warmer years both in the ocean and on land. The

previous record of 21.0 ºC, for example, occurred during a very strong El Niño event.

ENSO is currently in a neutral phase, coming out of a rare extended three-year period of La Niña (the opposite phase to El Niño). But El Niño is expected to kick in this year: according to the World Meteorological Organization, there is a 60% chance of it developing between May and July, and an up to 80% chance of it happening by October.

Return of 'the Blob'

Andrew Leising, an oceanographer at the Southwest Fisheries Science Center of the US National Oceanographic and Atmospheric Administration (NOAA) in La Jolla, California, expects to see unusually warm waters in the Pacific off the west coast of the United States during the summer and autumn. If the El Niño develops as expected, he adds, "this could create a situation like 2014 to 2015, when we got smacked by the Blob heatwave", a particularly big and damaging marine heatwave.

Marine heatwaves can be devastating for wildlife, and fisheries. Large heatwaves on the US Pacific coast tend to compress the habitable zone for many species into a narrow strip along the coast, Leising says. That can bring whales closer to shore as they chase food, which can increase ship strikes and entanglements in fishing gear. When warm waters butt up against the shore, he adds, they can host harmful algal blooms that close crab and mussel fisheries. But at the moment, Leising says, there is some unusually strong upwelling of cold water occurring along the US west coast, which could protect against some warming this year.

In the lead-up to April's record ocean temperature, some regions in the Southern Hemisphere experienced marine heatwaves, starting in February — among them, waters off Peru's coast and in the Southern Ocean, says Boyin Huang, an oceanographer who works on sea surface temperature data for NOAA's National Centers for Environmental Information in Asheville, North Carolina.

Unusually warm waters bring particular stress for corals. Almost all coral regions are currently experiencing remarkably high temperatures, says Matthew England, a physical oceanographer at the University of New South Wales in Sydney, Australia. “What we’re seeing now for coral reefs is they’re getting pushed to extreme temps, and they don’t get to regrow because it doesn’t come back to cooler temperatures.”

The last record-breaking ocean temperature year of 2016 coincided with an unusual global bleaching event for corals, only the third ever known to have happened. Bleached corals — which have expelled the algae that give them their colour — have poorer health, and many die.

“It’s fairly likely that we can expect another global bleaching event this year,” says Christian Voolstra, who studies corals at the University of Konstanz in Germany. Even if an El Niño doesn’t settle in this year, he adds, it will come soon enough. “It’s bad news no matter what.”

Heating planet

Warm waters are also physically less capable of holding dissolved oxygen, adding to the stress for marine life. “With ocean warming and deoxygenation, the available habitats for many species are decreasing,” says William Cheung, a marine biologist at the University of British Columbia in Vancouver, Canada.

And high ocean temperatures can trigger extreme weather. The unusually warm waters off Peru this year have helped to feed intense rainfall and Tropical Cyclone Yaku — the first such storm to hit the area in decades.

The ocean temperature spike — recorded by NOAA and probably the highest in more than 100,000 years — coincides with other warming trends. For example, in the Southern Hemisphere, the sea ice extent hit a new all-time low in February 2023. The ocean absorbs about 90% of the extra heat in the climate system resulting from global warming. But because it takes more energy to heat water than air, the surface water temperature is rising more slowly than the surface air temperature is.

“This wouldn’t have happened without climate change,” tweeted Jens Terhaar, an ocean biogeochemical modeller at the Woods Hole Oceanographic Institution in Massachusetts, in response to the news of the new temperature record. “We are in a new climate state, extremes are the new normal.”

Nature **617**, 450 (2023)

doi: https://doi.org/10.1038/d41586-023-01573-1

This article was downloaded by **calibre** from https://www.nature.com/articles/d41586-023-01573-1

- NEWS FEATURE
- 17 May 2023

Can giant surveys of scientists fight misinformation on COVID, climate change and more?

Shocked by the COVID-19 infodemic, several efforts have launched to gather researchers' consensus views, with the hope of improving public debate and policymaking.

- David Adam



Illustration by Antonio Rodríguez

In the next few weeks, some 20,000 researchers will receive an e-mail asking them if COVID-19 is caused by a virus. It might seem a futile exercise, given that the answer is obvious. But that's not the point.

The e-mails are a test for a project by Peter Vickers, a philosopher of science at the University of Durham, UK, to assess scientific consensus. He wants to set up a tool that widely probes degrees of scientific agreement on issues in public health, climate change and other topics in the public eye to help support evidence-based policymaking.

He is not alone. Rocked by the hugely visible impact of misinformation during the COVID-19 pandemic, several researchers are launching efforts to survey scientists' thinking on issues from vaccine safety to climate change.

Whereas Vickers favours giant, general surveys, other projects want to focus on smaller groups of specialists, and even to have them talk to each other to establish why they agree or disagree. But all of these projects aim to make scientific debate, arguments and degrees of consensus both more visible and transparent — which, their creators argue, will benefit public conversation and policymaking. Observers, however, caution that the projects might merely further politicize public debate.

"I think the world just needs a dedicated institute that actually measures scientific consensus across the world in a really serious way," Vickers says.

The power of big numbers

Vickers became interested in consensus after writing a book on what science can confidently say is true — a state of knowledge he labels as future-proof (*Identifying Future-Proof Science*, 2022).



Peter Vickers.Credit: Mike Vickers

Frustrated by the gap between what scientists know about anthropogenic climate change and public surveys that suggest many people remain unconvinced, he wants to create a university institute to establish where scientists stand on this and other issues.

Vickers's idea is to use surveys to assess agreement among tens of thousands of researchers in many scientific disciplines: physics, biology, chemistry, Earth sciences and health sciences. This vision differs from other kinds of consensus report, such as those from the Intergovernmental Panel on

Climate Change, which don't use surveys to query whether scientists agree with specific statements.

Although other studies have used surveys to judge consensus, Vickers says those efforts lacked global scale. Asking a select number of experts — a few hundred, say — leaves the conclusion open to criticisms of cherry-picking opinions, he argues. And sceptics might find it easier to claim that their minority positions counterbalance consensus views if, he says, the full extent of scientific agreement hasn't been made visible.

"There'll be some people who say they don't care if a physicist believes that COVID is caused by a virus," he says. "But that's how you get big numbers of scientists, and you'll be able to have this big statistic which may have influence over some people."

Vickers has set up his system by signing up coordinators at 31 institutions across 12 countries, who will distribute e-mailed questions to scientists in many disciplines. Each will be presented with statements and asked simply whether they strongly agree, agree, disagree, strongly disagree or are neutral. It should take researchers only a minute to read and respond to the e-mail, Vickers says.

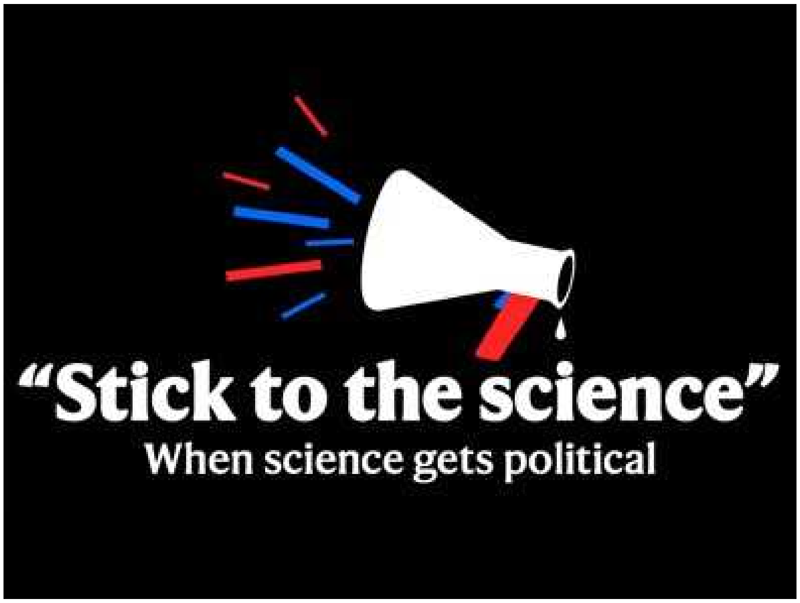
The results will be anonymous, but tagged to show institution and scientific area. Exactly how they will be tallied and reported is yet to be decided. The project was set up with £20,000 (US$25,200) from his university, and Vickers hopes to use the pilot results to win a much larger grant to establish a full-time research unit.



Top climate scientists are sceptical that nations will rein in global warming

Consensus, of course, says nothing about truth — just that there is broad agreement on something. And there is no consensus about how broad that needs to be. “Probably above 75%, or above 80% I would call consensus. That’s a wide-open question. But I think when you get into the nineties, it’s all consensus,” says Peter Doran, a geophysicist at Louisiana State University in Baton Rouge who has published studies demonstrating the levels of scientific consensus among climate-change experts (K. F. Myers *et al. Environ. Res. Lett.* **16**, 10430; 2021).

Vickers has set his own bar for declaring consensus at 95%, something he argues counts as beyond reasonable doubt. “You want to set a bar that’s so high that there isn’t a single counter-example from history. You’ve never reached that bar before and then been wrong,” he says. It’s a provocative statement, but Vickers argues his book research shows that documented near-unanimous levels of scientific agreement — at least relating to issues based on data from experiments — are relatively rare throughout scientific history, and, when reached, have not yet been proved wrong.



‘Stick to the science’: Nature’s podcast series on science and politics

“The trajectory I’m talking about is where somebody has a hypothesis and it turns into a theory and then, eventually, people start calling it a fact,” he says.

However, the 20,000 scientists he has signed up so far are predominantly based at Western institutions — a bias he wants to address if the idea catches on. Groupthink can be a powerful corrupting force, Vickers acknowledges, as can prejudice. He brings up the example of continental drift. In the mid-twentieth century, many US and UK geologists insisted that drift was impossible, but many others, including those in South Africa and India, disagreed, Vickers notes. “There was a prejudice there.”

Helping or hurting?

Vickers argues that showing how scientists agree should help to fight disinformation and support evidence-based policymaking. But James Evans, a sociologist at the University of Chicago in Illinois, warns that efforts to deliberately find and promote scientific consensus in this way could be counterproductive. “It feels manipulative. It doesn’t feel scientific,” he says. “If we push too hard the narrative that you don’t believe this, but all scientists do, it could have the reverse effect.”

Scientists who are not experts in the field under discussion are likely to respond on the basis of their personal values, he says, which could alienate rather than engage many members of the public. “I feel like it’s a weaponization of scientific voices,” Evans says.

In response, Vickers says Evans’s sociological critique doesn’t concern him. From his point of view, he’s just working to correct misconceptions. He argues that scientists have expertise in judging scientific statements, including those outside their field. “They often have to use second-order evidence as a proxy for first-order evidence,” he says.

And he points to a study on vaccine take-up in the Czech Republic as an example of how consensus can help (V. Bartoš *et al*. *Nature* **606**, 542–549; 2022). In early 2021, reports suggested that people thought that only half the country’s doctors believed that available COVID-19 vaccines were safe. But a team of economists led by Vojtěch Bartoš at the University of Munich, Germany, surveyed 9,650 doctors in the Czech Republic and found that was a massive underestimate. In fact, 90% of the doctors trusted the vaccines.



Are repeat COVID infections dangerous? What the science says

When the researchers asked a sample of around 2,000 people in the Czech Republic whether they intended to get vaccinated, they found that mentioning the consensus among doctors about vaccine safety significantly raised the number of people who said they would. Intended uptake rose by about four percentage points compared with a control group that was not

told about the doctors' views. And those intentions carried through into a similar difference for actual vaccination between the two groups, as measured some nine months after vaccines became widely available.

"It really seems that these people took this information seriously, even though we just provided it once," Bartoš says.

The four-point difference is more important than it might sound. By the end of the study, around 25% of the control group had not been vaccinated. "If we think about it as a reduction of the group of people who do not get vaccinated, then we have actually reduced this group by about a fifth," Bartoš adds.

Haixin Dang, a philosopher at the University of Nebraska Omaha who studies how researchers work together to generate scientific knowledge, says Vickers's project could make a positive contribution.

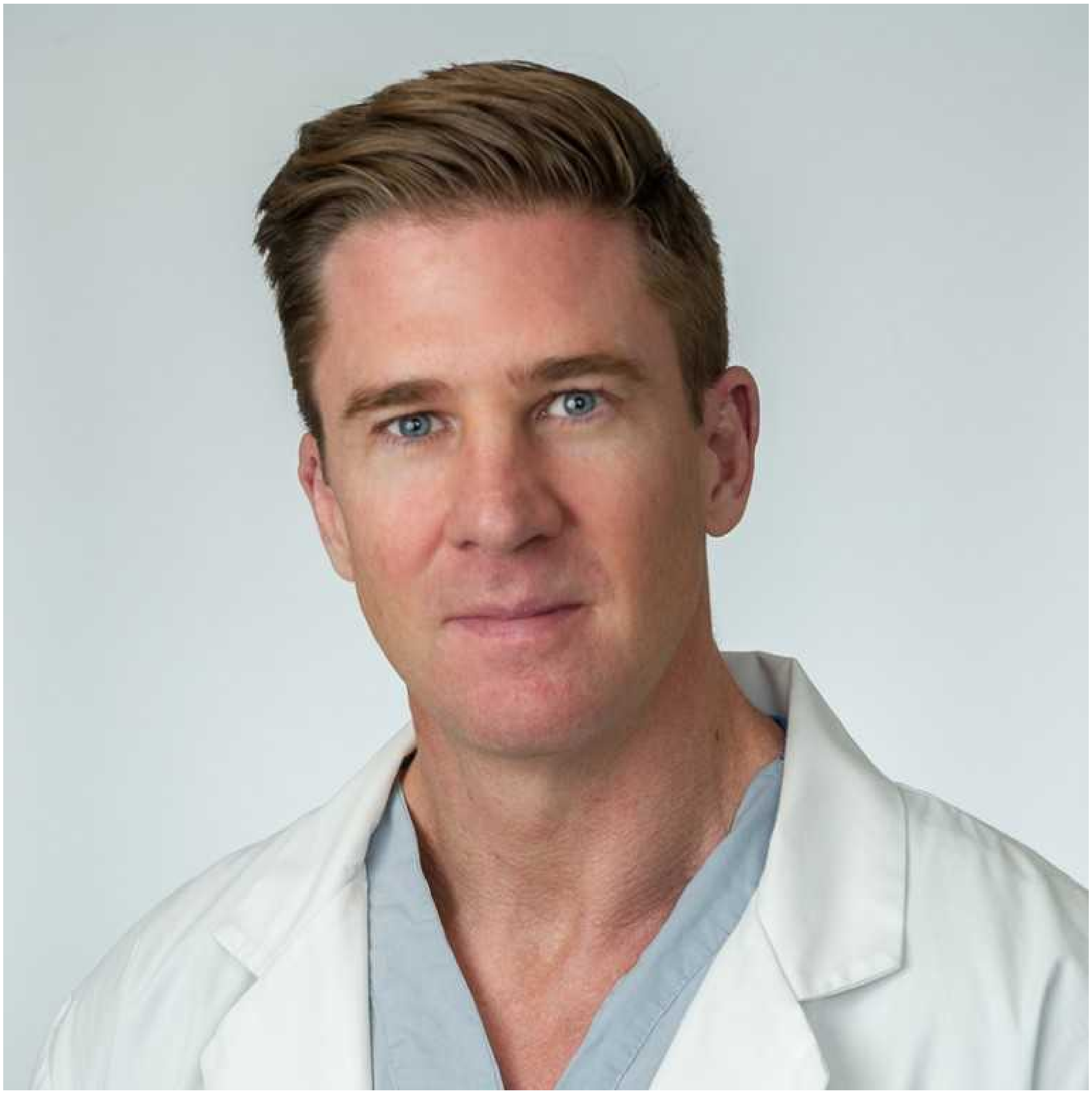
One issue with asking scientists to establish levels of consensus, she cautions, is that questions that the most people are able to agree on will be the least interesting. "The consensus view has to be bland. Because the more specific it is, the more idiosyncratic a statement becomes, then the fewer and fewer people will be able to agree," she says. "Often, consensus hides the diversity of views underneath the consensus."

Countering misinformation

Two other projects that kicked off this year have related ambitions to Vickers's, but with contrasting methods and goals. One, a non-profit organization called the Clarity Foundation, is based in British Columbia, Canada. The other, a website called comCensus, is the work of Daniele Fanelli, a metascientist at Heriot-Watt University in Edinburgh, UK. Both projects are interested in establishing degrees of consensus, but will survey the views of much smaller groups of experts, at least at first.

David Sweet, a critical-care doctor at Vancouver General Hospital in Canada, co-founded the Clarity Foundation after witnessing the impact of misinformation on people's attitudes to treatments and vaccine safety at first hand during the pandemic. "I'd have patients in the ICU dying and then

learning that their family members had convinced them not to get vaccinated," he says. "And the reason they had done that is because of the misinformation that was being spread on social media and the Internet. And I saw that repeatedly and it was heartbreaking."



David Sweet.Credit: David D. Sweet

His experiences suggested to him that much of the public has lost trust in institutions. The Clarity Foundation intends to work on ways to fix the situation.

“We need to blast society with the good, the same way that the misinformation is being blasted from the other side,” he says. The group’s co-founders include entrepreneur Thomas Lamb (chief executive of the mining firm Myriad Uranium in Vancouver), infectious-diseases specialist Jolanta Piszczek at the University of British Columbia in Vancouver and neuroscientist Jay Van Bavel at New York University.

Working on the principle that people still trust members of professional organizations, in April, Sweet’s group asked physician members of the British Columbia infectious-diseases and critical-care societies about the safety of COVID-19 vaccines.

They asked the 199 experts to agree or disagree with 7 statements, such as “I would recommend COVID-19 vaccinations to my family and friends.” Some 135 (68%) responded, with the results showing that, for example, 99% of the doctors thought that the vaccines were safe and effective in adults.

Follow-up questions to other specialist professional groups could feature topics including climate change, microplastics and even conspiracy theories, Sweet says. His group is less interested in proving (or disproving) consensus, he says, and more in gauging levels of agreement and disagreement, then later probing the reasons why.

After gathering responses to questions, the project plans to use the results to generate videos and other social-media-friendly content, with the idea of combating misinformation. “It then has the ability to go viral, just like all the misinformation out there,” Sweet says.

To promote its COVID-19 vaccine poll results, the foundation has produced a video featuring Canadian actor Jewel Staite. “So much of what you see on social media and the Internet conflicts [with] what public institutions are telling us,” she says in the video. “Many people don’t know what to believe, but there are new solutions coming.”

Website debate

Fanelli also plans to invite only experts to weigh in on questions at the comCensus website. His project is specifically not seeking the average

scientist's view, because researchers without direct experience in a field won't have first-hand expertise of it.

Those invited (perhaps a few dozen to a few hundred) get a password to access a question on the site, so that no one can comment without being invited. Fanelli's system, which could be closed or open for the public to view, depending on the issue, aims to encourage participants to articulate their evidence and to vote on others' contributions, such as which comment they found most insightful or got them to reconsider. It also allows participants to change their minds on the question over time.



Daniele Fanelli.Credit: M. Minelli & C.

The result, Fanelli hopes, is a website that will empower people to find out how experts think and to reflect on the rationales driving different answers, with the help of data visualizations that show, for instance, which answers were voted most helpful or most convincing.

“By the end, one has a better, worked-out picture of what the true consensus is, because everybody who could have changed their mind — or made someone else change their mind with good arguments — has had a chance to do so,” he says.

Fanelli had the idea for his site after seeing how claims of scientific consensus were used to stifle debate during the pandemic. Specifically, he says, he did not like the way in which questions on the origins of the coronavirus SARS-CoV-2, and whether it could have escaped from a laboratory, were dismissed by many high-profile voices as unscientific and off-limits.

With no dedicated funding, Fanelli launched a basic version of the website in April to show how it could work (www.comcensus.org). In pilot studies, he has invited virologists to comment on whether the database GISAID is the best venue for sharing information on pathogens in a public-health emergency, and asked researchers in artificial intelligence (AI) about the merits of a moratorium on the development of advanced AI systems. In these pilots, the platform creates pseudonyms for commenters, so that it is not possible to see who holds each view.

Rather than suggest questions himself, Fanelli has created a model in which individuals or organizations would pay a nominal fee for administration costs (perhaps £100 or so) and use his site to ask questions of their own devising. Those sponsors would decide whether the question, answers and discussions are available for anyone to read, or restricted to a limited group.

Fanelli has built it, but will people come? “People wanting to use it, that would definitely be a marker of success,” he says. The ultimate mission, he says, is for the platform to play a part in public conversations.

Many social scientists have already established robust methodologies to assess degrees of scientific and medical consensus — for instance, to help policymakers understand the evidence for the cost-effectiveness of a drug or a social policy. And if Vickers, Sweet or Fanelli envisage their work being used to guide authoritative advice on high-stakes policy issues, such as in public health, more-rigorous survey methods might be needed, says Sean Grant, who studies the generation and use of evidence at the University of Oregon in Eugene. “How they think [their findings] will be used is really important for me,” he says.

At this stage, it’s unclear how the three projects will pan out. But they could prove useful to inform and influence public discussion, says Dang. Scientific consensus has an important social role: besides driving policymaking, it can help to communicate science and connect with people outside science, she says. “It depends on what the goal is, what you think consensus does for you.”

Nature **617**, 452-454 (2023)

doi: https://doi.org/10.1038/d41586-023-01614-9

This article was downloaded by **calibre** from https://www.nature.com/articles/d41586-023-01614-9

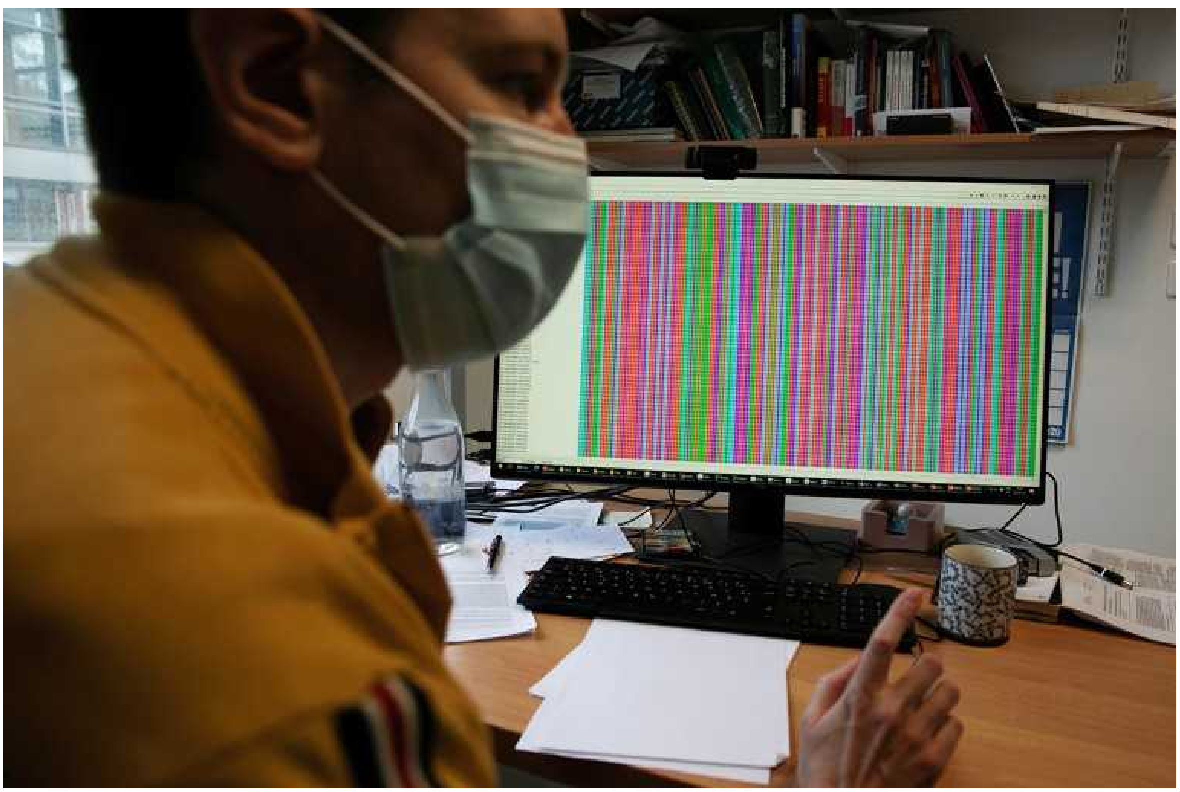
| Section menu | Main menu |

- NEWS FEATURE
- 04 May 2023

GISAID in crisis: can the controversial COVID genome database survive?

The most popular repository for sharing SARS-CoV-2 sequence data has come under increasing scrutiny. Scientists and funders around the world must now consider what lies ahead for the open sharing of genome data.

- Mariana Lenharo

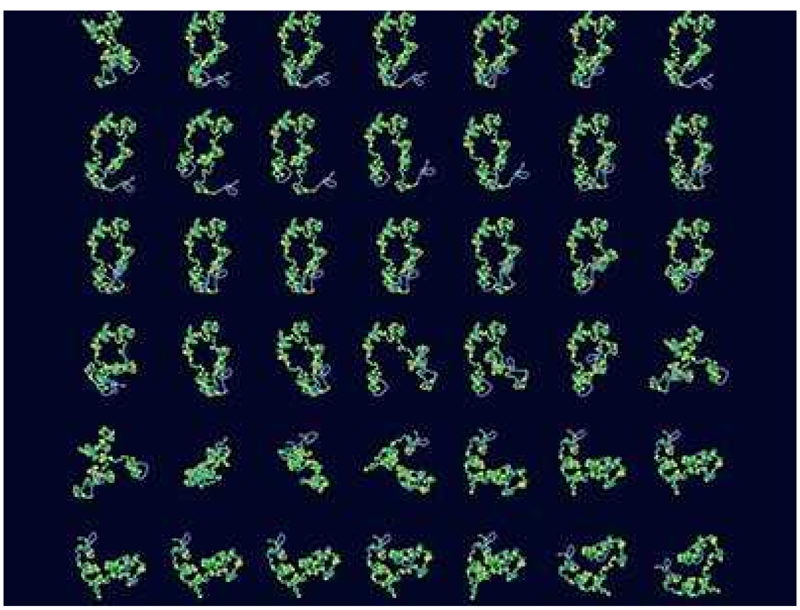


Scientists uploaded 15.5 million SARS-CoV-2 sequences to GISAID since the start of the pandemic. Credit: Baptiste Giroudon/Paris Match via Getty

During the COVID-19 pandemic, one online platform emerged as the main repository for viral genome data. GISAID, an initiative launched in 2008 to improve the global sharing of influenza data, earned the trust of scientists by ensuring that they would be credited for the data they generated. It now hosts more than 15 million SARS-CoV-2 genome sequences, more than any other existing database, as well as around 2 million influenza sequences.

But several scientists have raised concerns about the platform's lack of transparency, how it mediates disputes over credit and how it sanctions scientists who have allegedly violated its terms and conditions.

Given the importance of pathogen-genome data for tracking the emergence of viral variants and developing strategies and vaccines to combat them, it is crucial to discuss how researchers can continue to share these sequences going forward. *Nature* spoke to scientists in eight countries about what they see as the future of pathogen-genome sharing, and of GISAID.



Scientists call for fully open sharing of coronavirus genome data

The researchers acknowledged the key part that GISAID has played during the COVID-19 pandemic and stressed the need to preserve the platform. But

many of them said that drastic changes are necessary, particularly in light of an investigation by *Science* in April into GISAID's founder, Peter Bogner, who has a large role in the platform's operations. "GISAID has lost enormous credibility in recent weeks and appears to be untenable in its current form with its current leadership," says Edward Holmes, a virologist at the University of Sydney in Australia. The scientists also discussed the limitations of other models of genome data sharing and how these limitations mainly affect academics in low-income countries.

In a statement sent to *Nature*, GISAID says the organization recognizes the need to transform. "Over the coming weeks and months, we will be announcing additional steps the initiative will be taking regarding our work towards our governance and related practices," the statement says.

What is the origin of GISAID?

There are many data-sharing platforms that allow scientists to quickly disseminate genome-sequence data to the research community. Some of them are public-domain databases which provide unrestricted access to data. The largest include GenBank in the United States, the European Nucleotide Archive (ENA) and the DNA Data Bank of Japan, which are all part of the International Nucleotide Sequence Database Collaboration.

Once a genome is available on one of these sites, almost any scientist can access and analyse the data. Although this lack of restrictions might be good for science, it discourages some researchers from sharing their data until they've had sufficient opportunity to publish their own findings. Anderson Brito, a virologist at the All for Health Institute (ITpS) in São Paulo, Brazil, says that researchers in low-income countries are particularly vulnerable. "When research groups from these countries submit their data to fully open databases, well-resourced groups may quickly analyse and take most of the credit," he says.



GISAID provided a mechanism to help prevent scientists from ‘scooping’ one another.Credit: Christophe Archambault/AFP via Getty

GISAID was conceived during the global spread of avian influenza in 2006 as another model for sharing genome data, one that ensured due credit[1].

The acronym originally stood for the Global Initiative on Sharing Avian Influenza Data, but its mission expanded to encompass all influenza viruses and, eventually, other pathogens. In contrast to the fully open platforms, the data shared on GISAID are available to registered users, who agree not to republish the sequences without permission. And those who wish to publish analyses of data housed in GISAID must offer to collaborate with the scientists who produced the sequences.

Many academics also saw the platform as a way of creating equitable access to the broader spoils of genome research. GISAID supporters argued that if scientists from low- or middle-income countries provided influenza sequence data that enabled the development of an improved vaccine, for example, then they should be compensated, or, at the very least, their nations should have guaranteed access to the resulting vaccine.

GISAID never offered a mechanism to make that happen, but the arguments were important to many countries. Indonesia, for example, stopped sharing virus samples in 2007 amid a deadly avian influenza outbreak in protest of the limited access to vaccines many countries face. It reversed that position in 2008 when it reportedly began sharing influenza data with GISAID.

In the early days of the COVID-19 pandemic, GISAID aimed to be the main repository for SARS-CoV-2 data. The GISAID team proactively reached out to politicians around the world to garner support, and to researchers to provide training and resources. The database quickly gained popularity.

Why is GISAID under scrutiny?

GISAID originally intended to enforce data sharing limits only temporarily. Bogner, an entrepreneur based in Santa Monica, California, and the scientists who first presented the idea stated that the sequences submitted to GISAID would be deposited in fully open data repositories such as GenBank, “with a maximum delay of six months”.



COVID-origins report sparks debate over major genome hub GISAID

That promise was never fulfilled, however. GISAID lacks a mechanism to move the data to open-access databases, and that’s one of its main flaws according to critics. In its response to *Nature*, GISAID said it is already accessible to the public and therefore it doesn’t plan to provide a mechanism to transfer data. Researchers could, in theory, upload their sequences to an

open database after depositing them on GISAID, but that would mean double the work. In practice, data get trapped under strong restrictions indefinitely. This motivated a group of scientists in 2021 to publish an open letter urging other academics to publish their SARS-CoV-2 genome data on fully open-access platforms.

Many scientists also say that the way GISAID controls access for different users seems to be arbitrary. Vinod Scaria and Bani Jolly, biologists at the CSIR Institute of Genomics and Integrative Biology in New Delhi, say that even within their own laboratory, users have different levels of access to the data. GISAID says that “everyone with valid access credentials has access to all data shared via GISAID”, but that “there are additional services that GISAID may provide to individuals who are affiliated with organizations with a proven record of using data under the proper and agreed upon guidelines”.

Some have pointed out that GISAID has been, at times, unfair in applying sanctions to users. Theo Sanderson, a pathogen genome researcher at the Francis Crick Institute in London, says that there have been “profound failures to date, in which access to data seems to have been withdrawn to punish users for perceived slights to GISAID”. Such slights might include public criticism or failure to acknowledge GISAID’s contributions. According to the organization, “in the vast majority of cases where a user’s access to GISAID was temporarily suspended, the user had materially breached GISAID’s terms of access”.



A dispute arose around access to sequence data from a market that sold live animals.Credit: Alex Plavevski/EPA-EFE/Shutterstock

In March, GISAID temporarily revoked access to the platform for a group of scientists involved in trying to uncover the origins of the COVID-19 pandemic. The group had published an online report describing genomic data[2] from swabs taken throughout the seafood market in Wuhan, China, where one of the first large outbreaks of the disease had been recorded. The platform said the publication violated its terms of use. The authors have disputed this, saying that they had credited the scientists who provided the data and reached out to them with an offer to collaborate.

“The GISAID compliance policy seems to have grey areas, which ultimately raise more questions and doubts,” wrote Scaria and Jolly in a joint statement to *Nature*.

The *Science* story describes episodes of scientists losing access to GISAID in apparent retaliation for public criticism of the platform, claims which GISAID refutes. It also discusses Bogner’s unconventional background and financial disputes with a vendor providing services to GISAID. “The

revelations in the article are pretty shocking. And I do think that they highlight some real concerns about GISAID, and in particular GISAID’s governance,” says Emma Hodcroft, a molecular epidemiologist at the University of Bern in Switzerland.



[Wuhan market samples fail to shed further light on COVID origins]

GISAID says it has “never taken any retaliatory action or imposed suspensions” for any reason other than violations of its terms and conditions. It adds that its processes could be improved: “As part of our steps to address governance and operating structure, we consider it a top priority to ensure a fair process for appeals and address the concerns of our users around suspensions.”

GISAID’s governance page lists a scientific advisory council of 12 people, but it is unclear how the council operates. In practice, according to sources close to the platform, Bogner seems to make most of the decisions. “If you have massively important data sets that have untransparent governance structures that allow for unpredictable retaliation and erratic behaviour — that’s just not the way that a level playing field should work,” says biologist Amber Hartman Scholz, head of the science policy department at Leibniz Institute DSMZ, a collection of microorganisms and cell cultures, in Brunswick, Germany.

Why don’t scientists switch to another platform?

If some researchers are dissatisfied with GISAID's governance, why don't they simply start uploading their viral sequences to other existing databases?

One of the reasons is that it's easier to upload data to GISAID. "Data submitters often praise its submission system, which is more intuitive and flexible than what is offered by other databases," Brito says. "GISAID also invests in expert data curators, which — in close interaction with data submitters — help ensure the quality of the data."

Another reason is that scientists want their data to be where everyone else's sequences are. "My sequences are most useful when they can be combined with sequences that came from somewhere else in my country or the world," says Hodcroft.

Furthermore, the fear of uploading data to open-access databases and of being scooped — having other scientists publish studies using those sequences first — is real. "Whether we like it or not," says Hodcroft, "the currency of science is publication."

What are the possible ways forward?

Despite the problems, the scientists agree that GISAID is likely to remain an important resource for viral genomes. "It's in the best interest of public health that GISAID and the innovations it has promoted over the past years survive," says Brito. Jeremy Kamil, a virologist at LSU Health Shreveport in Louisiana, agrees. "To lose GISAID would be unequivocally a tragedy."

But if GISAID is to have a future, it requires drastic reform and new leadership, its critics say. "A new and transparent governance structure is required, and one that should not be at the whim of a single individual," says Holmes. That would translate into having clear criteria on who gets access to the platform and which actions would result in sanctions.

The platform also needs to provide mechanisms for scientists submitting sequences to release their data to public-domain archives if they want to do so, says Sanderson. Furthermore, the scientists urge GISAID to acknowledge when the platform collects data from public data sets and to clearly identify those sequences. Currently, scientists who download data

from multiple platforms can’t verify whether they are working with duplicate sequences.

To implement those changes, GISAID would need to ideally bring in outside experts in ethics and governance, says Kamil. That would require Bogner to “hand over the keys and back off”, he says.



[The broken promise that undermines human genome research]

In its statement, GISAID says the organization recognizes the need to evaluate aspects of its governance, but didn’t provide details around potential changes. “I expect that funding agencies will put pressure to improve, significantly, the governance of such an important institution,” says Gustavo Palacios, a virologist at the Icahn School of Medicine at Mount Sinai in New York.

The only current funder listed on GISAID’s website is The Rockefeller Foundation. Although representatives there did not respond directly to *Nature*’s questions, they sent a statement by Bruce Gellin, chief of global public-health strategy, based in Washington DC, noting that GISAID was one of the few platforms making the rapid sharing of genome data possible in the early days of the pandemic. “The Rockefeller Foundation believes global data sharing platforms should be based on principles of trust, collaboration, and discussion,” the statement says. “To support this, data

generators, users, platforms, and expert groups must be accountable and transparent."

If GISAID doesn't change, some scientists think that a new organization might have to be built from scratch, but that such a database shouldn't be very different from the current one. "From a platform perspective, it did actually do a pretty good job in addressing that balance between rapid and open sharing versus retention of some form of ownership over the data," says Richard Webby, an infectious-disease scientist at St. Jude Children's Research Hospital in Memphis, Tennessee, and a former member of GISAID's scientific advisory council.

Ewan Birney, joint director of the European Molecular Biology Laboratory's European Bioinformatics Institute near Cambridge, UK, which runs the open data platform ENA, says that a pathogen database endorsed by the World Health Organization is "an important part of the future". Such a platform would "give assurance to low- and middle-income countries that they can share data in a controlled way for public health, while still having assurances that rules will be followed", he says. "And then there should be a time at which such public-health data is transitioned to fully open data so that researchers can look at the data as a whole."

The possibility that fully accessible data platforms completely take over seems unlikely for the immediate future because of scientists' concerns about authorship. Birney says that open platforms such as ENA can recommend and encourage proper citation, but they don't have the mechanisms to enforce it. "Rather, we think that's better done through similar things to patent law, an international law where access and benefits are controlled."

Ultimately, Holmes says, the goal should be to do everything possible to encourage people to share their data. "The key lesson from the COVID-19 pandemic is that data sharing is the single most important thing we can do to help prevent and control pandemics."

Nature **617**, 455-457 (2023)

doi: https://doi.org/10.1038/d41586-023-01517-9

References

1. Bogner, P. *et al. Nature* **442**, 981 (2006).
2. Crits-Christoph, A. *et al.* Preprint at Zenodo https://doi.org/10.5281/zenodo.7754299 (2023).

This article was downloaded by **calibre** from https://www.nature.com/articles/d41586-023-01517-9

Opinion

- **Three climate policies that the G7 must adopt — for itself and the wider world** [16 May 2023]
  • By taking the lead in innovative climate action, the seven richest economies can create a virtuous circle to help the world decarbonize faster.
- **Create an IPCC-like body to harness benefits and combat harms of digital tech** [17 May 2023]
  • Emerging information technologies, including ChatGPT, require proper stewardship. An intergovernmental panel to synthesize the evidence offers the best path forward.

- COMMENT
- 16 May 2023

Three climate policies that the G7 must adopt — for itself and the wider world

By taking the lead in innovative climate action, the seven richest economies can create a virtuous circle to help the world decarbonize faster.

- Edward B. Barbier



A solar-power facility at the Fukushima Hydrogen Energy Research Field in Namie, Japan. Credit: Philip Fong/AFP via Getty

This week, the leaders of the Group of Seven (G7) economies — Canada, France, Germany, Italy, Japan, the United Kingdom and the United States, plus the European Union — will assemble in Hiroshima, Japan, for their 49th summit. Climate action will, rightly, be high on the agenda. With climate impacts mounting and the transition to low-carbon energy at a crossroads, the group must make sure that the action it takes is swift and decisive, and works both in its member countries' best interests and in those of the wider world.

Global leadership from the G7 is crucial for cutting greenhouse-gas emissions quickly to keep planetary warming within the 1.5–2 °C threshold of the Paris climate agreement[1]. G7 actions matter because the group accounts for more than half of global gross domestic product (GDP), 28% of carbon dioxide emissions from fossil fuels and 13% of the world's population, as well as a large share of historical emissions[2]. It also has the financial means to assist other countries in developing more-ambitious decarbonization goals.

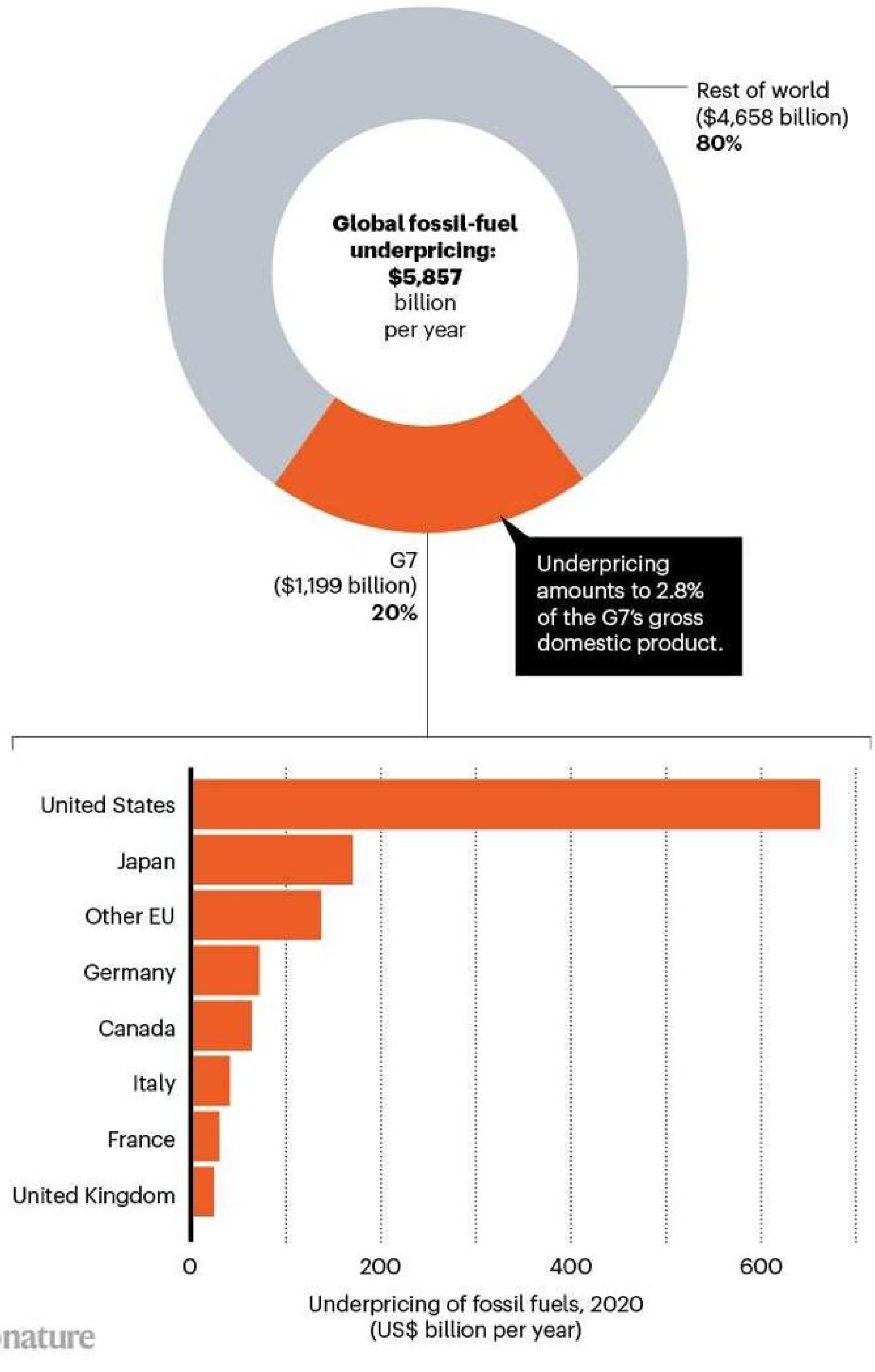
Climate commitments already made by the G7 need to be expanded and market distortions hindering the green transition should be removed. In 2020 and 2021, the group spent more than US$725 billion on green measures, such as clean energy, energy efficiency, electric vehicles and green-innovation research, as part of packages for economic recovery from the global slowdown that accompanied the COVID-19 pandemic[3].

But at the same time, market distortions favouring fossil fuels remain[4]. Across the G7 countries, subsidies — such as incentives for increased production, write-offs and tax deductions and reducing prices paid by consumers — for oil, coal and gas amount to $63 billion per year, or $62 per person, on average[5]. Artificially depressed prices deter fast growth of low-carbon energy and have helped to spur a post-pandemic surge in fossil-fuel consumption and greenhouse-gas emissions[6]. But the true cost is much greater. Adding in the environmental and health costs of fossil-fuel use, including climate impacts, pollution, traffic congestion and road accidents, as well as forgone tax revenues, underpricing fossil fuels is costing the G7 nations almost $1.2 trillion each year — 2.8% of the G7's GDP and $1,186

per person[5]. For the rest of the world, the cost is $4.7 trillion (see ‘The true price of fossil fuels’).

THE TRUE PRICE OF FOSSIL FUELS

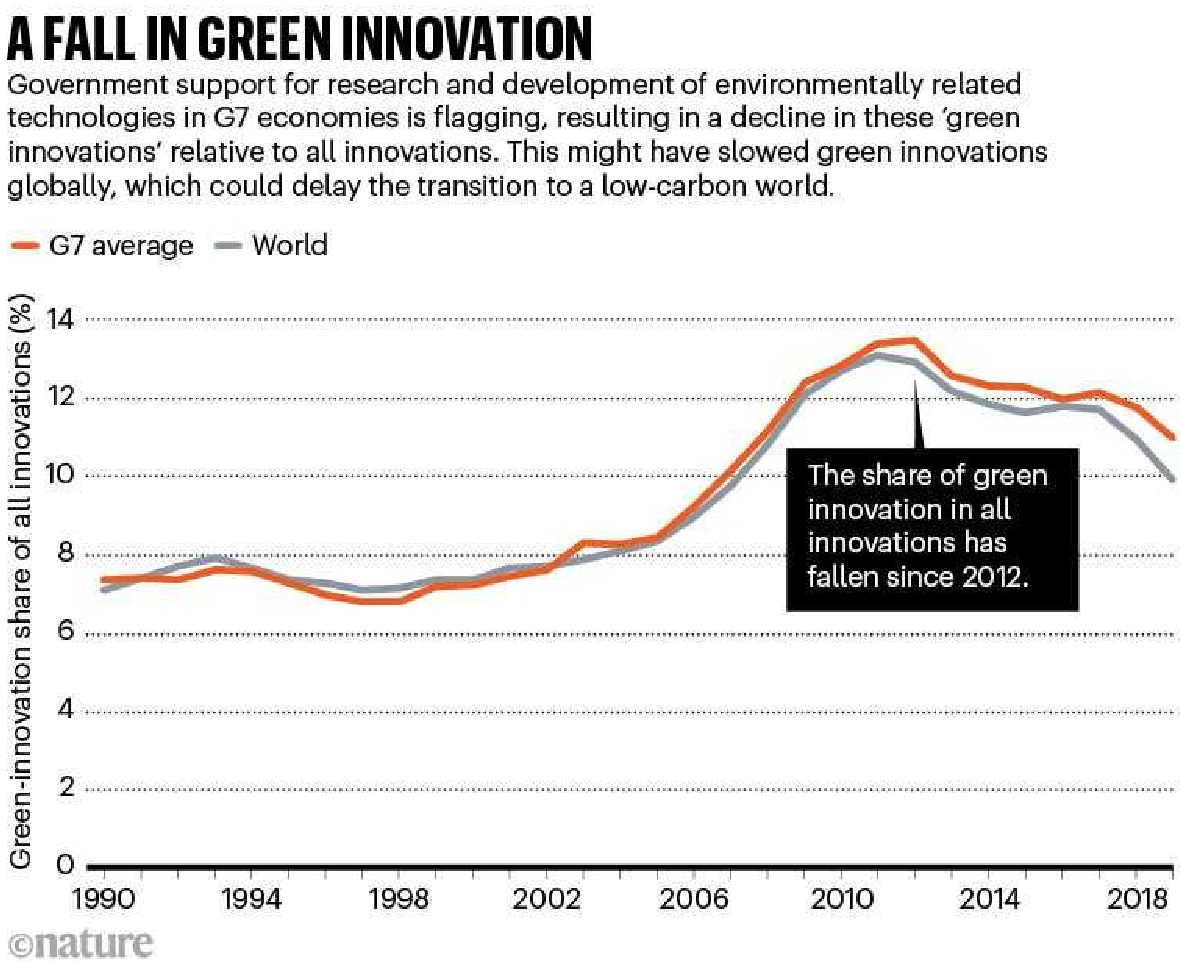
Underpricing oil, coal and gas is costing the G7 economies almost US$1.2 trillion each year when environmental costs such as climate impacts, pollution and traffic congestion are included — much more than the $63 billion it spends annually on subsidies. The G7 is thus responsible for 20% of global costs.



©nature

Source: IMF (go.nature.com/3KKHML)

Government investment in green tech research and development (R&D) is flagging in G7 nations just when it is needed most. Although renewables took a growing share of energy R&D public spending from the 1990s to the 2000s, reaching a peak of 15–30% of the total in all 7 economies in 2010, since 2015 that share has fallen to around 10–20% of the total[7]. Government-funded R&D related to the environment is stuck at 1.5–3% for 6 of the G7 economies and at just 0.3% in the United States in 2021[7]. Lapsing innovation in the G7 might have slowed environmental-technology development globally (see 'A fall in green innovation'). Over 2016–19, the G7 accounted for 70% of global green innovation, with the United States and Japan each producing 21% and Germany 11%[7].



Source: OECD

The G7 has taken some positive steps. At the 2022 summit in Germany, the group agreed to form a 'Climate Club' to spur the introduction of more-ambitious climate policies; its formal launch is expected later this year. Eventually, the group intends other countries to join, and the G7 and other members are considering whether or not to impose levies on imported goods, on the basis of their embodied carbon emissions. The aim would be to decarbonize emission-intensive and trade-exposed industries, such as cement, chemicals, iron and steel, while protecting these industries from competition in countries that have not adopted similar initiatives.

But the G7 can and should do much more, within its own borders and in the wider world. Last month, I outlined a three-tiered low-carbon strategy in a policy paper for the Hiroshima summit (see go.nature.com/3lduqd2). The gist of it, outlined here, is that the G7 should adopt three core sets of policies: to overcome market distortions favouring fossil fuels; to foster a more-inclusive version of the Climate Club; and to assist emerging-market and developing economies to attain climate, poverty-alleviation and development goals.

Remove market distortions favouring fossil fuels

All G7 members should start by implementing three green policies to reduce greenhouse-gas emissions from fossil-fuel use. First, they should phase out all subsidies for consuming and producing fossil fuels over the next five years. This would save money and make economies more sustainable, energy independent and secure.

Second, they should phase in more-comprehensive carbon-pricing mechanisms. These involve either carbon taxes or emission-trading schemes, both of which effectively put a charge on each tonne of carbon produced. A tax imposes this charge directly, whereas emission trading places an overall cap on pollution and allows polluters to trade their allocated emission permits. The resulting traded price for permits becomes the charge for emitting carbon. Although several G7 economies have introduced carbon taxes and emission trading to limit greenhouse-gas emissions, in general carbon prices remain too low to incentivize changes in behaviour, and the scope of these mechanisms is too narrow.



Why we need a new economics of water as a common good

To be on track for net zero emissions by 2050, high-income and large emitters such as those in the G7 should attain a carbon price of at least $75 per tonne of carbon dioxide emitted and extend the pricing to cover more sectors[8]. No G7 member does both (see Supplementary Table 1). For example, the European Union Emissions Trading System has reached higher price levels but covers only power, manufacturing and aviation. Japan's carbon price is extremely low — $2 per tonne of carbon dioxide equivalent (tCO_2e) — but does cover all sectors (with some exemptions)[9]. The United States currently has no national carbon pricing scheme but it could encourage states and cities to tax and trade carbon more widely, as California, Oregon, Washington and the Regional Greenhouse Gas Initiative of 12 eastern states currently do.

Third, G7 countries should direct the revenues raised towards green priorities, including investments in clean-energy R&D and transport infrastructure. Governments should offset adverse effects on income, employment and inequality by raising the minimum wage, providing payments or retraining for displaced workers, and targeting income dividends and tax rebates to vulnerable households. Policies along these lines in Italy, France, Germany, Spain, Norway and Estonia cushioned the impacts of the energy-price surge following the Russian invasion of Ukraine,

for example[10]. Fully compensating the bottom 20% of all European households for the 2021–22 energy-price surge would have cost each nation, on average, 0.4% of GDP[10].

Make the Climate Club globally inclusive

The G7's Climate Club initiative is a step in the right direction, but from a global perspective, its success will hinge on how effectively other nations can be brought in. In the second key set of actions I propose, the G7 should extend its Climate Club with a more-inclusive framework. To be effective in encouraging members to reduce emissions, a climate club must agree on a minimum carbon price for participants and impose penalties on countries that don't participate[11]. But the G7, and the world, will reap more benefits by also allowing other countries to join. If other large emitters remain outside, industries based in the G7 might become less competitive and some will switch production to nations with fewer restrictions, reducing emissions savings[8].



A wind turbine spins in front of the cooling towers at the Jänschwalde coal-fired power station in Germany.Credit: Sean Gallup/Getty

Committing to remove market distortions favouring fossil fuels should be the main precondition for any nation joining the Climate Club. As an incentive, minimum carbon prices should be set lower for emerging-market and developing economies that become members. For example, prices could be set at $75 per tCO_2e emitted for high-income countries, $50 per tonne for middle-income countries and $25 per tonne for low-income countries[8,12]. Such a differentiated price floor is progressive because it will induce proportionally more carbon mitigation by high-income countries.

Participants in the club could achieve the price floor through either pricing carbon or equivalent policies, such as regulations that limit emissions and expand the sectors covered and by commitments from states, provinces, cities and businesses. Initially, the carbon price floor could be just for power generation and carbon-intensive industries such as cement, iron, steel and chemicals. Later, it would be extended to other sectors and sources from industry, services, transport and agriculture. Individual countries could set higher carbon prices to achieve more-ambitious mitigation pledges and targets.



Energy crisis: five questions that must be answered in 2023

The G7 Climate Club will also need to impose a carbon import levy — a charge on the carbon embodied in imports from regions that have yet to adopt the club's minimum carbon pricing. Therefore, a 'border carbon adjustment' is necessary to protect the collective policies and competitiveness of carbon-intensive industries of club members[13]. Combined with a differentiated carbon price floor, the import levy would allow economies in the club to implement ambitious mitigation policies for their carbon-intensive industries and encourage others to join the club[8]. Emerging-market and developing economies are likely to respond by imposing a carbon price on their own industrial sectors and eventually participate in the club[8].

Assist developing economies to decarbonize

The G7 should go further in assisting emerging-market and developing economies with adopting the policies and investments needed to participate in the Climate Club. That entails scaling up and broadening G7 initiatives such as the Just Energy Transition Partnerships (JETPs) and the Partnership for Global Infrastructure and Investment (PGII).

The JETPs are a financing cooperation mechanism created by the G7 in which donors help to fund specific investments in emerging economies, with the aim of reducing fossil-fuel dependency and over-reliance on coal, to accelerate a clean-energy transition. The first partnership was established between G7 members and South Africa at COP26 in Glasgow, UK, in 2021. Two more partnerships were launched with Indonesia and Vietnam last year, and two more are planned with Senegal and India. However, these plans are still vague. Some G7 partners — the EU, France, Germany, the United Kingdom and the United States — have pledged $8.5 billion in technical and financial assistance to South Africa for clean electricity, electric vehicles and green hydrogen projects, but with few specifics[14].



[Degrowth can work — here's how science can help]

The PGII, announced at the 2022 G7 summit in Germany, seeks to mobilize $600 billion in global infrastructure investments from public and private sources by 2027; the United States has pledged $200 billion already, and further details on implementing the fund are likely to emerge at the Hiroshima summit. It should prioritize investments that complement and support those made through the JETPs. This might include improving transmission grids to support clean energy, more-sustainable urban development, decarbonizing industries and creating charging networks for electric vehicles.

In return, partner nations should adopt carbon pricing and other policies necessary to join the Climate Club. The G7 should assist them with finance and the design and implementation of climate policies. This might be coordinated through the World Bank's Partnership for Market Implementation Facility, which aims to put carbon-pricing policies and programmes in place in at least 30 emerging and developing economies; G7 support would enable more countries to be brought in.

Such policies should ideally be designed to achieve poverty alleviation, development and climate-mitigation goals simultaneously, especially in rural areas. Two promising policies are swapping out fossil-fuel subsidies to provide expansion of renewable-energy services in underserved rural areas;

and using revenues from carbon pricing to fund nature-based solutions, such as planting forests, that create jobs and livelihoods in poor regions.

By all these means, creating the conditions for an inclusive Climate Club will enable the G7 to accelerate a low-carbon transition of their economies and encourage more nations to do the same.

Nature **617**, 459-461 (2023)

doi: https://doi.org/10.1038/d41586-023-01586-w

References

1. IPCC. *AR6 Synthesis Report: Climate Change 2023* (IPCC, 2023).
2. World Bank. *World Development Indicators* (World Bank, 2023).
3. Nahm, J. M., Miller, S. M. & Urpelainen, J. *Nature* **603**, 28–31 (2022).
4. Barbier, E. B. *Nature* **565**, 6 (2019).
5. Parry, I. W. H., Black, S. & Vernon, N. *Still Not Getting Energy Prices Right: A Global and Country Update of Fossil Fuel Subsidies* (International Monetary Fund, 2021).
6. REN21. *Renewables 2022 Global Status Report* (REN21, 2022).
7. OECD. *Green Growth Indicators* (OECD, 2023).
8. Chateau, J., Jaumotte, F. & Schwerhoff, G. *Economic and Environmental Benefits from International Cooperation on Climate Policies* (International Monetary Fund, 2022).
9. World Bank. *Carbon Pricing Dashboard* (World Bank, 2023).
10. Ari, A. *et al. Surging Energy Prices in Europe in the Aftermath of the War: How to Support the Vulnerable and Speed up the Transition Away from Fossil Fuels* (International Monetary Fund, 2022).

11. Nordhaus, W. *Am. Econ. Rev.* **105**, 1339–1370 (2015).

12. Parry, I., Black, S. & Roaf, J. *Proposal for an International Carbon Price Floor Among Large Emitters* (International Monetary Fund, 2021).

13. Böhringer, C., Fischer, C., Rosendahl, K. E. & Rutherford, T. F. *Nature Clim. Change* **12**, 22–29 (2022).

14. Wemanya, A. & Adow, M. *Implementation of the Just Energy Transition Partnership in South Africa* (Germanwatch, 2022).

This article was downloaded by **calibre** from https://www.nature.com/articles/d41586-023-01586-w

- COMMENT
- 17 May 2023

Create an IPCC-like body to harness benefits and combat harms of digital tech

Emerging information technologies, including ChatGPT, require proper stewardship. An intergovernmental panel to synthesize the evidence offers the best path forward.

- Joseph Bak-Coleman ,
- Carl T. Bergstrom,
- Jennifer Jacquet,
- James Mickens,
- Zeynep Tufekci &
- …
- Timmons Roberts

Show authors



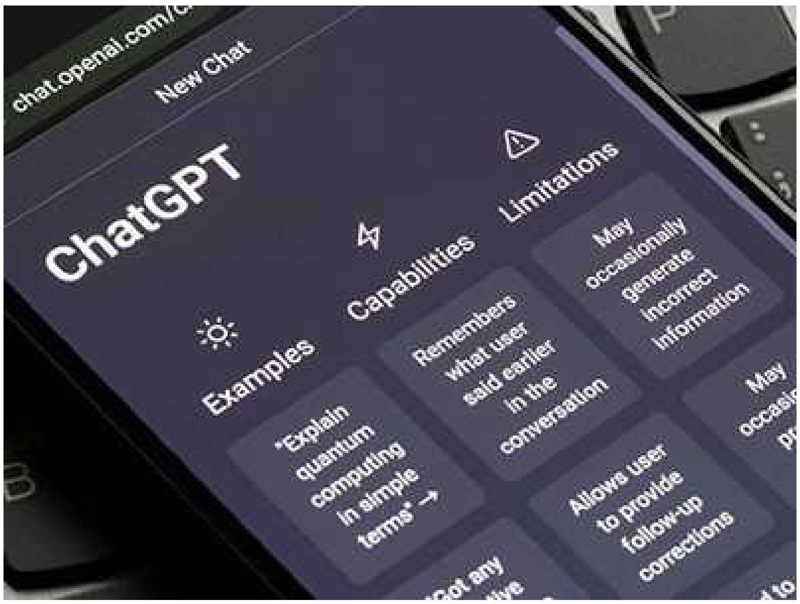
People protesting against Facebook's policies hold aloft an inflatable angry emoji outside the firm's 2019 shareholders meeting in California. Credit: Stephen Lam/Reuters

Search engines, online banking, social-media platforms and large-language models, such as ChatGPT, are among the many computational systems that offer (or could offer) tremendous benefits. They provide people with unprecedented access to information. They help to connect hundreds of millions of individuals. And they could make all sorts of tasks easier, from writing computer code to preparing scientific manuscripts.

Such innovations also come with risks.

The speed at which content can be generated and shared creates new possibilities for amplifying hate speech, misinformation and disinformation[1,2]. Decision-making that is augmented by algorithms can exacerbate existing societal biases and create new forms of inequity, for instance in policing and health care[3]. And generative artificial-intelligence (AI) systems that create visual and written content at scale could be used in ways for which the world is not prepared, culturally or legally.

Although an increasing number of universities, institutes, think tanks and government organizations are attempting to make sense of and improve the digital world, technology companies are, in our view, deploying a range of tactics to influence debate about the tools they are developing. As independent researchers studying the societal impacts of digital information technologies, we continually weigh the risks of corporations taking legal action against us for the most basic scholarly activities: collecting and sharing data, analysing findings, publishing papers and distributing results. Also, the type of data made available tends to focus research efforts on the behaviour of users, rather than on the design of the platforms themselves.



[Tools such as ChatGPT threaten transparent science; here are our ground rules for their use]

The challenges of climate change and ecosystem degradation have similarities to those now stemming from the global information ecosystem in terms of complexity, scale and importance. In the same way as bodies such as the United Nations Intergovernmental Panel on Climate Change (IPCC) conduct assessments of global environmental change that inform evidence-based policy, an analogous panel is now needed to understand and address the impact of emerging information technologies on the world's social, economic, political and natural systems.

An Intergovernmental Panel on Information Technology would have more leverage when it comes to persuading technology companies to share their data than would independent researchers or non-profit groups, such as the Coalition for Independent Technology Research, which defends the right of researchers to study the impact of technology on society. A panel would also have credibility in non-Western countries — this will be increasingly crucial as the impacts of digital communication technologies play out in different cultural contexts.

We are aware that a non-profit organization called PeaceTech Lab in Washington DC — headed by current and former technology, media and telecommunications executives who have partnered with Microsoft, Amazon and Facebook — is assembling a panel with a similar charge to that of the body we are proposing (see go.nature.com/3vctvmb). We question, however, whether such a group can operate with independence.

Help or harm?

It is often straightforward to understand the short-term incentives that lead people to adopt digital information technologies. It is much harder to predict long-term responses and understand what harms could need to be mitigated down the road, while increasing the potential benefits.

Machine-learning algorithms designed to guide landlords on rental pricing, for example, have supported cartel-like dynamics with respect to rent pricing and supply restrictions. And algorithms that direct police towards 'high-crime areas', using data on the locations of past arrests, can exacerbate existing biases in the criminal justice system.

Meanwhile, generative AI threatens the workplace structure of entire industries, and challenges people's ideas of proof, evidence and veracity. Using generative AI systems for text, such as ChatGPT, could undermine public understanding of science by driving the industrial-scale production of texts containing falsehoods and irrelevancies. Conversely, such systems could also level the playing field in international science by reducing or eliminating language barriers.



A kiosk in Accra, Ghana, selling money-transfer services for mobile phones.Credit: Ernest Ankomah/Bloomberg via Getty

Various groups have been trying to gain insights about the impacts of digital information technologies on society, but their efforts have often been stymied by threats of legal action or actual lawsuits. Our own experiences, and those of many others working in this area, suggest to us that technology companies are increasingly using various tactics to hamper external scientific study and influence public discourse.

Access to data about even basic quantitative patterns of use and user behaviour are often tightly restricted by technology platforms. In 2021 Meta, the owner of Facebook, sent a cease-and-desist notice to researchers at New York University after they had created a browser extension to gather data on targeted advertising on the platform. From conversations with colleagues, we know that others have since been dissuaded from conducting this type of work.

Technology corporations are also selective in what they publish from their own research teams. For example, with external collaborators, Meta has

published findings on the benefits of Facebook when people are grieving[4], and the platform's tendency to encourage altruism[5]. Yet we hear little about Meta's own research on potential harms. Documents made available to the US Securities and Exchange Commission in 2021 reveal that Facebook's ranking algorithm scored emoji reactions as five times more valuable than 'likes' for three years — even while internal data showed that posts that sparked the angry emoji were more likely to include potentially harmful and false content, such as incorrect claims about vaccines.



ChatGPT listed as author on research papers: many scientists disapprove

We think that as awareness of the issues around potentially harmful and misleading content has grown, companies have steered research agendas, putting responsibility for problems more frequently on individual users. Twitter, Facebook and Jigsaw (a think tank within Google) have cooperated extensively with academic researchers working on warning labels for misleading content, for instance. Without any other intervention, this essentially suggests that the burden of responsibility for stopping the spread of misinformation is on the user. (Research so far suggests that although these labels raise awareness and can reduce sharing by individuals, when used in isolation they are unlikely to make a significant dent in the spread of false information overall[6].)

What is not interrogated — or reported publicly — is how the core capabilities of a platform result in harmful outcomes, or how design choices intended to increase engagement and revenue also exacerbate the spread of inflammatory, sensationalized, false and even violence-inciting content.

Most companies require a specified project description before they will share any data, which effectively gives corporations full editorial discretion. In combination with companies providing limited information about platform design, the net result is that the data that independent investigators need to measure and mitigate harms is generally unavailable.

A consolidated approach

Since 1988, the IPCC has brought together international experts to improve understanding of the causes and impacts of greenhouse-gas emissions, and what might be done to manage them. Likewise, the Intergovernmental Science-Policy Platform on Biodiversity and Ecosystem Services (IPBES), established in 2012, has improved knowledge and raised awareness about the world's failing ecosystems and their importance to human development and health. These bodies are tasked with consolidating existing information, collecting more data as needed, synthesizing that knowledge and sharing it with decision makers. Although the bodies do not have regulatory authority, their global assessment reports increase awareness and enable evidence-based policy.

As a society, we are failing to adequately address the use of digital information technologies as a global challenge that affects nearly every aspect of modern life. Similarly to climate change and ecosystem degradation, the use of these technologies has difficult-to-predict consequences that span generations and continents.

So far, efforts to better manage online information ecosystems have largely involved implementing guard rails. The US AI Bill of Rights, for instance, promises to provide individuals with options for privacy, and freedom from harm caused by AI, but is vague on how harm could be reliably assessed and averted. A first step towards proper stewardship is creating an infrastructure that can consolidate and summarize the state of knowledge on the potential

societal impacts of digital communications technologies — in a format that is digestible and accessible for policymakers around the world.



AI bot ChatGPT writes smart essays — should professors worry?

An Intergovernmental Panel on Information Technology, including experts in policy, law, physical and social sciences, engineering, the humanities, government and ethics, offers the best possibility for achieving this. As with the IPCC and the IPBES, the goal would not be to establish international consensus on how to manage the digital world, or to hand down regulatory recommendations — but to provide a knowledge base to underpin the decisions of actors such as governments, humanitarian groups and even businesses.

Such an organization will face challenges that are distinct from those of the IPCC and the IPBES. Climate change and ecosystem degradation are problems characterized by rich data, comparatively well understood causes and consequences, and measurable and obvious economic harm in the long term. As such, the IPCC and the IPBES can base their reports on shared assumptions regarding food security, natural disasters and sustainability.

By contrast, most researchers investigating the impacts of digital technologies are severely limited in their access to data about the systems that they study. Researchers are also confronting a rapidly moving target:

many firms, from social-media platforms and search engines to ride-sharing services and news outlets, are constantly running suites of A–B tests on their users — adjusting some feature in the interface, and assessing what effect this has on user behaviour.

An intergovernmental panel, representing the interests of UN member states, could identify where current levels of transparency are not generating sufficient insight. It could also galvanize research and motivate regulators to enact policy that engenders increased transparency, accountability and auditing. Although countries such as China, Russia and the United States might not agree on how various platforms and services should be deployed or constrained, as the consequences of the digital world play across international borders, any hope of negotiation between nations requires a clearer picture of what is happening and why, and what policy responses are available.

Working with ethicists and human-rights organizations, such a panel would be guided by shared goals, such as those enshrined in international human-rights treaties and norms. It would also be guided by emerging formulations of people's rights in the face of a fast-changing digital environment — such as rights to meaningful privacy and consent, a healthier information ecology and better safety online. With this framing, an Intergovernmental Panel on Information Technology could, for example, agree to gather information on the prevalence and economic consequences of fraud or the effects of social media on adolescent mental health. It could gather reliable indicators of illegitimate interference or manipulation in elections, or assess the downstream effects of unregulated financial dynamics.

Progress will require nations to negotiate. In many cases, progress might be at odds with the short-term interests of some of the world's largest corporations — and with some of its most powerful governments. But this is nothing new for an intergovernmental organization. Certainly, the problems emerging from the online information ecosystem will not be fixed at national scales, within distinct academic disciplines or through a network of academic and non-profit institutions with little power and conflicting incentives.

The ongoing transformation of the digital public sphere is characterized by risks, benefits and trade-offs. The COVID-19 pandemic has demonstrated the power of the online information ecosystem when it comes to mobilizing thousands of researchers across all of science to solve a societal problem. But as with other historical transformations, such as those brought by the Industrial Revolution, management and adaptation are key to ensuring that digital communication technologies promote beneficial dynamics.

Nature **617**, 462-464 (2023)

doi: https://doi.org/10.1038/d41586-023-01606-9

References

1. Bail, C. A. *et al. Proc. Natl Acad. Sci. USA* **115**, 9216–9221 (2018).
2. Juul, J. L. & Ugander, J. *Proc. Natl Acad. Sci. USA* **118**, e2100786118 (2021).
3. Panch, T., Mattie, H. & Atun, R. *J. Glob. Health* **9**, 020318 (2019).
4. Hobbs, W. R. & Burke, M. K. *Nature Hum. Behav.* **1**, 0092 (2017).
5. Kizilcec, R. F., Bakshy, E., Eckles, D. & Burke, M. *Proc. Conf. Hum. Factors Comput. Syst*. https://doi.org/10.1145/3173574.3173700 (2018).
6. Bak-Coleman, J. B. *et al. Nature Hum. Behav.* **6**, 1372–1380 (2022).

This article was downloaded by **calibre** from https://www.nature.com/articles/d41586-023-01606-9

Work

- **How geoscientists are making their field more welcoming**
  [15 May 2023]
  • Grassroots initiatives aim to make the discipline more inclusive of researchers from under-represented communities.
- **Brain imaging: fMRI advances make scans sharper and faster** [15 May 2023]
  • Researchers are finding ways to improve one of neuroscientists' favourite tools: functional magnetic resonance imaging.
- **I was deathly afraid of the sea — now I work to protect it**
  [15 May 2023]
  • Conservationist Loyiso Dunga aims to guard kelp, a crucial resource in South African waters that is home to invertebrates, fish and mammals.

- CAREER FEATURE
- 15 May 2023

How geoscientists are making their field more welcoming

Grassroots initiatives aim to make the discipline more inclusive of researchers from under-represented communities.

- Virginia Gewin

Find a new job



Vashan Wright co-founded a programme to improve equity in the geosciences.Credit: Koobakile Kgosiemang

The broad fields of Earth- and geosciences continue to be the least diverse in academic science research. However, the lack of diversity can, in part, be explained by hostile and exclusionary behaviour, according to a February survey by the ADVANCEGeo Partnership, a network of societies that aims to improve workplace conditions in the Earth sciences (E. Marín-Spiotta *et al. Earths Future* **11**, e2022EF002912; 2023). Racism, sexism and ableism continue to be problems in both education and workplace environments. For example, the number of people of colour receiving a PhD in geosciences in the United States has not risen much beyond about 10% in the past 46 years.

During 2019, US-based geoscientists distributed the workplace-climate survey to more than 2,100 members of 5 Earth- and space-science organizations. They found that, whereas most participants experienced positive behaviours, those in historically excluded groups were exposed mainly to negative behaviours. The authors concluded that deeply entrenched historical biases in these workplaces had led to the ongoing patterns of exclusionary conduct, which contributes to the loss of diverse talent.



Collection: Diversity and scientific careers

People of colour, women, scientists with disabilities, non-binary and lesbian, gay, bisexual, queer, pansexual and asexual (LGBQPA+) scientists experienced interpersonal mistreatment, devaluation of work, discriminatory language and sexual harassment more frequently than did people not identifying as part of those groups. Of the 14% who experienced sexual harassment, the vast majority were from historically excluded groups.

More than one-third of those surveyed — notably, half of Black respondents – considered leaving their institution or making a career change. “This is a snapshot. It shows a lot of people leaving disciplines, but the survey doesn’t capture those who already left,” says study co-author Erika Marín-Spiotta, a biogeochemist at the University of Wisconsin– Madison. In recent years, university departments, federal granting agencies and other US institutions have invested tens of millions of dollars in efforts to improve workplace climates throughout the geosciences. *Nature* spoke to five researchers spearheading programmes that they hope will make geosciences a more welcoming space.

VASHAN WRIGHT: Book-club champions of change

Geophysicist at the University of California, San Diego’s Scripps Institution of Oceanography in La Jolla.

I noticed many people starting book clubs to discuss racism and explore actions that they could take after the 2020 murder of George Floyd, a Black man killed by a police officer in Minneapolis, Minnesota. Unconvinced that a typical book club would be effective at the scale needed to effect change, I contemplated what would have to be done to assemble the national leadership necessary to make policy-level changes. The US National Science Foundation (NSF) funded my proposal to start an international book club that would go beyond reading books to meaningfully centre the voices of geoscientists of colour and explore ways to dismantle the structural barriers that prevent their full participation in the field.

My colleagues and I founded Unlearning Racism in Geoscience (URGE) as a guided effort, across a range of participating institutions, to update the

policies that control access to hiring and admissions, the resources available to people of colour and how department demographic data are tracked and made accessible. To do that, URGE invited geoscientists to form participating groups, or pods, associated with an organization or academic unit. Almost 4,000 participants formed pods at 310 university departments, federal agencies and even in industry. The pods discussed a range of journal articles, heard oral presentations of lived experiences and discussed codes of behavioural conduct in advance of drafting anti-racist policies that they plan to adopt at their institutions. Whereas several pods have already instituted their changes, others are still reviewing them.



US geoscience programmes drop controversial admissions test

Some of the policy changes involved removing or lowering graduate admission fees and requirements for high test-scores, which can be barriers to diversity. Others included providing a directory of self-care and mental-health resources for people of colour, adding pronouns to e-mail signatures or on social media and acknowledging stolen Indigenous lands in papers and presentations.

It takes time to do this type of networked, interactive discussion well. It's important to continually centre people of colour, without worrying about how white people will respond. It's also important to encourage and invite a wide range of people to share their ideas. I was particularly impressed by the

fascinating ideas that early-career researchers brought to the table. For example, at a summit planning an URGE conference, they expressed interest in encouraging presenters to share art, music or dance, so that attendees could bring their whole selves, including their full cultural context, to a conference.

ERIKA MARÍN-SPIOTTA: Keep the conversations going

Biogeochemist at the University of Wisconsin–Madison and lead principal investigator of the ADVANCEGeo Partnership.

Our first NSF ADVANCEGeo Partnership grant was funded in 2017 to provide workshops on identifying sexual harassment and on creating, implementing and enforcing ethical codes of conduct. We quickly realized that we would need to address other behaviours as well. Sexual harassment doesn't happen in a vacuum. Places that allow other harmful behaviours to happen — even if not illegal — can also cause a great deal of damage to workers. When we started offering workshops, we thought we'd deliver around ten. Already, we've conducted more than 200 at scientific conferences and university departments. Participants learn to identify sexual harassment and related bullying and microaggressions, and about the health and economic impacts of tolerating them. They are then guided through real-world scenarios to identify and address harms, and explore actions that can be done ahead of time to reduce them.

We are training more people, and have produced a website of resources for academics who want to address these issues. In 2022, we received our second ADVANCEGeo grant, of US$1.2 million, to address broader forms of identity-based harassment, bullying and microaggressions. Expanding the workshops' scope helped us to connect with wider audiences. For example, men became more interested because they can recognize when people are being bullied.

What's become clear is that a three-hour, standalone workshop isn't going to solve the problem. Departments want more. We can't prevent every

exclusionary behaviour, but we can give people the tools to reduce the harm caused when they do happen.

We're trying to focus on the systems and structures that allow these kinds of behaviour to persist. Places of higher education are competitive. There is a mindset of "if you win, I lose". As a result, our system doesn't incentivize treating each other well. In fact, it can be penalizing. It feels silly saying this, but we have to work out how to reward being respectful of each other.



Elizabeth Smith is working to improve accessibility for people conducting fieldwork.Credit: Tyler Bell/OU CIWRO/NOAA/NSSL

ELIZABETH SMITH: Build a climate based on values

Research meteorologist at the National Oceanic and Atmospheric Administration's National Severe Storms Laboratory in Norman, Oklahoma.

Over the past few years, I have led a series of sessions to collaboratively update the US National Weather Center protocol, including the rules that make fieldwork physically safe. We are now building on that to make fieldwork more accessible for people from different backgrounds. The centre's building, in Norman, Oklahoma, houses both the National Severe Storms Laboratory, where I work, and the University of Oklahoma School of Meteorology. As a result, we can have a variety of people out in the field together — from first-year university students to senior government-agency scientists. The sessions are now more of a two-way conversation than a sterile one-sided training course that people sit through, often begrudgingly. As a result, people are more engaged. For example, our high-level static field protocol document now includes team-created standards for behaviour, as well as the consequences for engaging in unacceptable actions. The team took ownership as we built this for ourselves.

In 2022, I noticed that student volunteers at the centre were from much more diverse backgrounds than in previous years. For example, the university received an NSF supplement for a hearing-impaired student who needed a sign-language interpreter for multiple weeks in the field. It was great to foster this level of accessibility in the field, which is uncommon.

As a federal agency, the US National Oceanic and Atmospheric Administration, is also actively working on building formal training requirements for fieldwork, which most often takes place, for example, on its research ships and aircraft. Some of our work has informed its effort.

Overall, we've had a positive response to this participatory approach, even though discussions can get uncomfortable. As part of the training, we conduct a survey asking, among other things: have you experienced harassment? Have you witnessed harassment? The numbers match the statistics we see in the literature: 20–30% of employees have witnessed harassment. Session attendees are always surprised to see that. They think that these behaviours must only be happening elsewhere. It's eye-opening to see it is in your own workplace.



Asmeret Asefaw Berhe has designed programmes to encourage disadvantaged researchers.Credit: Teamrat A. Ghezzehei

ASMERET ASEFAW BERHE: Pay a living wage to encourage inclusivity

Director of the Office of Science for the US Department of Energy in Washington DC.

The US Department of Energy (DOE) is a large funding organization that supports 10 national labs, 28 user facilities and around 300 universities. Our efforts to create a vibrant scientific workforce start by making science more equitable and inclusive. We designed granting programmes to ensure that we are paying attention to groups of people who have been disproportionately disadvantaged in science, technology, engineering and mathematics (STEM)

or who historically have received very little of our publicly funded resources.

We have three new programmes to further improve inclusivity and equity. The Reaching a New Energy Workforce training programme, or RENEW, is designed to attract communities that have been historically under-represented or minoritized. We partner with emerging research institutions, including historically Black colleges and universities (HBCUs), other minority-serving institutions, as well as smaller, rural higher-education institutions. In the first year of the RENEW initiative, we gave out 41 awards totalling US$32 million to 37 institutions, including 24 minority-serving ones. The focus is on building lasting partnerships between these institutions and the DOE's national labs.

Funding for Accelerated Inclusive Research (FAIR) is an initiative that will expand collaborations between emerging institutions, minority-serving organizations and DOE labs and facilities to build research capacity for further DOE missions. Both RENEW and FAIR aim to increase the diversity of research groups and institutions. The third prong, Promoting Inclusive Equitable Research (PIER), requires all DOE grant applicants to submit a PIER plan, outlining, for example, how they will recruit and include individuals from diverse backgrounds, cultivate a safe, respectful work environment and provide equitable access to professional-development opportunities, as part of their proposal.

After holding a series of listening sessions, we raised the DOE Office of Science graduate-student compensation to $45,000 — and we encourage the same from all recipients paid through Office of Science funding. We made the change because if we want an engaged, vibrant scientific workforce, we have to pay people a living wage. In addition, we expanded the eligibility for early-career award proposals, from 10 years to 12 for untenured professors. It was a conscious effort to acknowledge the career impacts of the COVID-19 pandemic. So, either we stand by and watch some people miss their chance to receive these potentially career-altering awards, or we can expand that opportunity for them. Removing barriers that prevent early-career researchers from moving forward in STEM can go a long way.

JULIET CRIDER: Create a virtual field experience

Geoscientist at the University of Washington in Seattle.

At some point, geology students get out of the classroom to look at rocks in the field. Often, that involves a lot of driving, overnight travel, camping or hiking — and frequently in unfamiliar or uncomfortable outdoor conditions. In recent years, there's been a community recognition that these field excursions are not always accessible for individuals with physical disabilities, but that is also the case for people without previous outdoor experience or who don't have the gear to be comfortable in the field.



What Black scientists want from colleagues and their institutions

At the same time, the technology used to turn photographs into accurate, measurable 3D models has become more advanced, as have digital tools for video-game development. As a result, my lab group — notably PhD student Max Needle — created a virtual field-trip experience. The first one was based on exposed folds of bedrock near Shamokin, Pennsylvania, informally called the Whaleback anticline. It's possible to build high-resolution digital models of landforms and outcrops for research purposes, and it's also an opportunity to make field representations that students can explore and

measure digitally. Max recognized that video-game interfaces would allow students to traverse this particular site in the world. There's even a jet-pack mode to collect information from locations that would be impossible to access in real life.

We're not the only ones creating these resources. Groups at the University of Milano-Biccoca in Milan, Italy, have produced similar tools that enable students to interact with digital rock formations, and colleagues at the University of Aberdeen, UK, created eRock, an open-source repository of virtual 3D rock formations from around the world.

One reason geology is not very diverse is this stereotype of rugged geologists who climb mountains. That is unappealing and intimidating to a lot of people. In our department, we are changing the nature of our capstone project requirements, including alternative tracks that emphasize lab science — an increasingly important element of our discipline. Digital field trips are part of a larger cultural shift to illuminate the many paths into geosciences — which do not always require going to remote mountains — to hopefully attract a wider range of prospective students.

Nature **617**, 637-639 (2023)

doi: https://doi.org/10.1038/d41586-023-01615-8

These interviews have been edited for length and clarity.

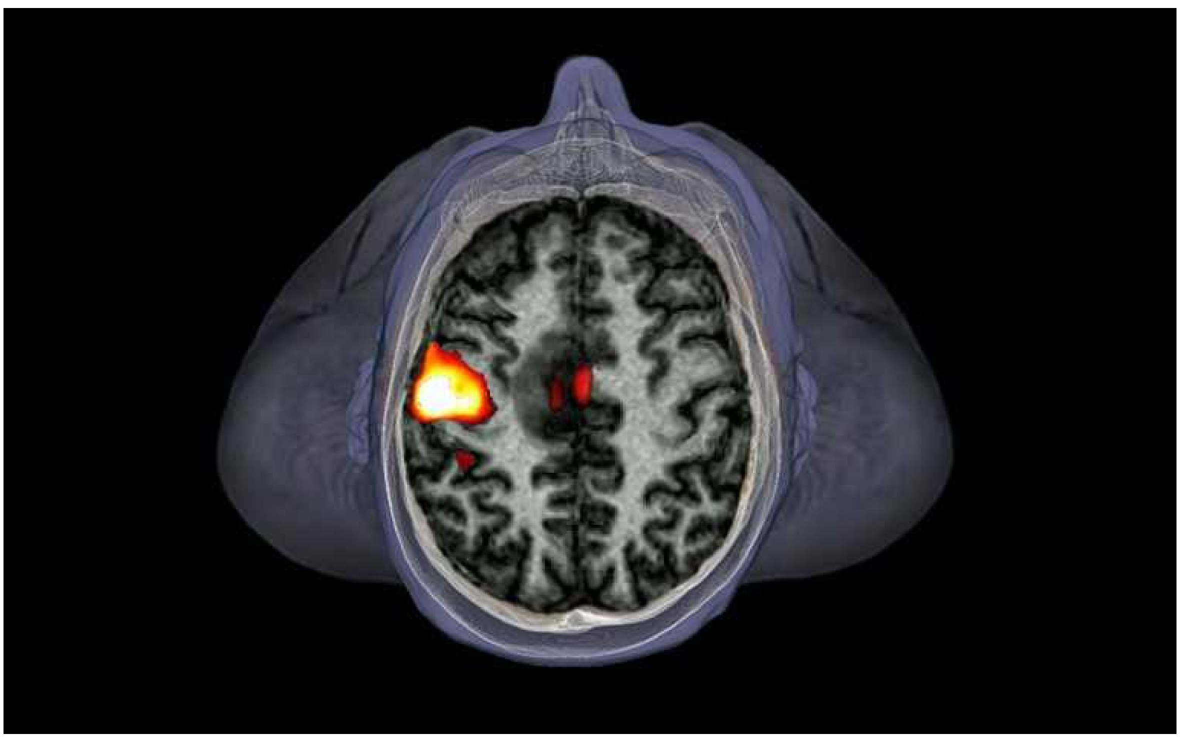
This article was downloaded by **calibre** from https://www.nature.com/articles/d41586-023-01615-8

- TECHNOLOGY FEATURE
- 15 May 2023

Brain imaging: fMRI advances make scans sharper and faster

Researchers are finding ways to improve one of neuroscientists' favourite tools: functional magnetic resonance imaging.

- Diana Kwon



A top-down fMRI scan of the brain shows neuronal activity (red and yellow) in the left hemisphere's motor cortex as the person moves a hand. Credit: Zephyr/Science Photo Library

Last October, the neuroimaging community was abuzz with excitement. Researchers in South Korea seemed to have overcome one of the biggest

limitations of functional magnetic resonance imaging (fMRI), a popular method for studying the human brain[1].

Jang-Yeon Park, an author of the study, had been pondering the limitations of fMRI since his graduate student days at the University of Minnesota in Minneapolis. While conducting his PhD in medical physics, Park had developed a fascination for neuroscience. He found himself in seminars where researchers described studies of the human brain they had conducted with fMRI.

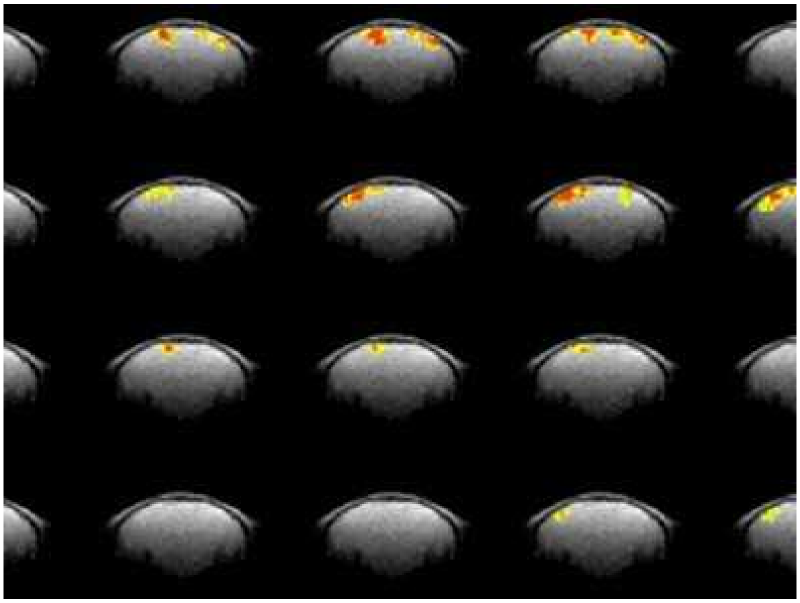
The technique works by picking up on changes in blood oxygen levels, which fluctuate with neuronal activity. But these blood-flow-related — or haemodynamic — changes are relatively slow compared with the neurons that they represent. To Park, this was a clear limitation. To reveal how the brain works, he thought, fMRI had to become much faster.

Typically, fMRI acquires brain slices as complete images — a process that limits how quickly the method can gather data. Instead, Park and his team at Sungkyunkwan University in Seoul tweaked the software to capture brain image data in segments, then used a computer algorithm to reconstruct the image. Using this modification — and a powerful MRI scanner — the researchers could track brain activity on the millisecond timescale, a temporal precision much greater that of conventional fMRI. This enabled them to detect the activity of mouse neurons from repeated stimulation of their whisker pads. The researchers published their technique[1], which they dubbed direct imaging of neuronal activity (DIANA), in October 2022.

The rise of fMRI

DIANA is just one approach researchers have developed to improve fMRI. Some, such as Park, are devising ways to get closer to the neurons they wish to measure, rather than relying on the proxy measure of blood flow through the brain. Others have found improvements to fMRI's spatial and temporal resolution — still relying on the blood-based signal — to capture more accurate snapshots of the brain in action.

“There are many promising avenues” that researchers have been exploring, says Noam Shemesh, an interdisciplinary MRI scientist at the Champalimaud Centre for the Unknown in Lisbon. “It’s all very exciting.”



Faster MRI scan captures brain activity in mice

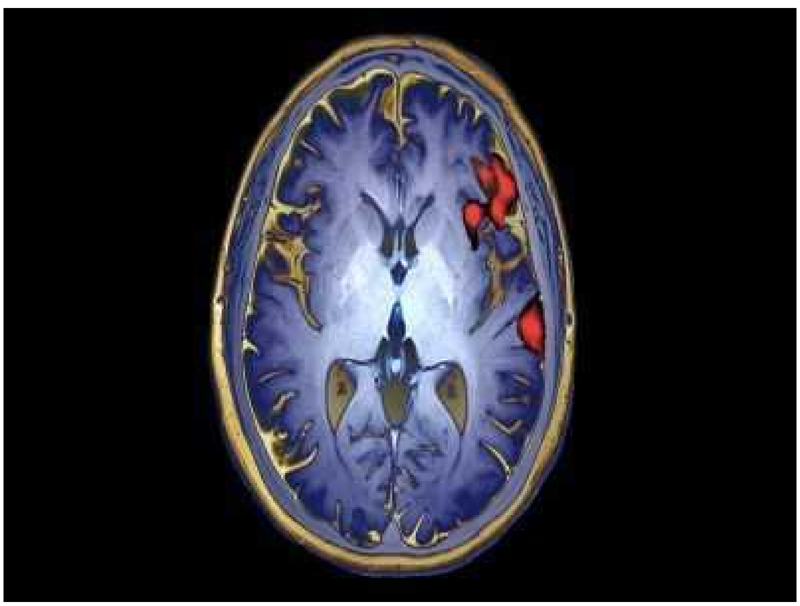
The foundational principle of fMRI is neurovascular coupling — the idea that brain activity and blood flow are linked[2]. In 1880, the Italian physiologist Angelo Mosso, studying blood-flow variations in people with skull defects, observed that cognitive tasks could induce changes in blood flow[3]. Ten years later, British scientists Charles Roy and Charles Sherrington observed the effects of injecting brain extracts into the bloodstreams of animals. They hypothesized that metabolites produced by neuronal activity could increase blood flow to the brain[4].

In 1990, Seiji Ogawa, then an investigator at AT&T Bell Laboratories in Murray Hill, New Jersey, and his colleagues noticed dark lines in the images of brains of rats and mice they had taken using MRI. These lines, they discovered, were blood vessels — the shadowy contours had formed because of deoxygenated haemoglobin (a protein that, when oxygenated, transports oxygen to cells throughout the body)[5]. Oxygenated and deoxygenated haemoglobin have different magnetic properties, and the drop in oxygenated blood led to an accompanying decrease in the MRI signal where the vessels were found. The researchers proposed that this blood-

oxygen-level dependent (BOLD) signal could be exploited to measure brain activity[5].

A few years later, three groups — including Ogawa and his colleagues — independently demonstrated that BOLD could detect brain activation in humans in MRI scanners[6–8], yielding the method researchers now call fMRI.

It provided a clear advantage over other neuroimaging techniques. Although electroencephalography (EEG), which measures brain electrical activity, and magnetoencephalography (MEG), which records magnetic fields produced by neuronal activity, collect data much more rapidly than fMRI does — picking up signals on a millisecond, rather than second, timescale — fMRI is better at pinpointing where in the brain the activity occurred. And unlike with positron emission tomography, there is no need to inject radioactive substances into the bloodstream.



Can brain scans reveal behaviour? Bombshell study says not yet

MRI was already a popular tool for creating detailed anatomical images in medicine, and MRI scanners were available in hospitals around the world. fMRI could be conducted simply by applying new software to these existing machines. “We could just ride on the back of the success that MRI was already experiencing,” says Peter Bandettini, a physicist and neuroscientist at the National Institute of Mental Health in Bethesda, Maryland. “The field

propagated so quickly and easily because of that." Now, researchers publish more than 10,000 academic articles mentioning fMRI annually.

Still, the technique has limitations. One is that it does not directly measure brain activity. It can take seconds for blood oxygenation changes to occur, whereas neurons fire on millisecond timescales. This raises the question of how exactly neural activity leads to changes in blood oxygen levels — and whether the relationship between neuronal activity and blood oxygenation is the same throughout the brain.

fMRI also struggles to image diseases in which blood flow is affected, such as cardiovascular disease or Alzheimer's disease. Because BOLD-based fMRI measures changes in blood flow, it cannot distinguish a vascular abnormality from a neuronal one. This poses a problem for both understanding and treating disease, says Shella Keilholz, an MRI physicist and neuroscientist at Emory University and the Georgia Institute of Technology, both in Atlanta.

Imaging at the neuronal level

Some researchers are searching for alternative ways to measure brain function — and especially, to detect neuronal activity directly.

One method, neural current imaging, measures the electromagnetic fields generated by neuronal electrical activity, similar to what EEG or MEG can do. The fields produced are much smaller than that created by the BOLD effect, says Bruce Rosen, a physicist and radiologist at Harvard Medical School in Boston, Massachusetts, making them hard to spot using MRI. Researchers have demonstrated that the approach is theoretically possible — showing, for example, that electromagnetic signals can be detected using MRI in post-mortem turtle brains[9–10]. In human brains, however, scientists have had little success.

Researchers have also tried to detect neuronal function by tracking physiological changes. When neurons receive input from other activated neurons, they swell temporarily. This can be detected using diffusion MRI, a technique that measures the movement of water molecules. Denis Le Bihan,

a neuroscientist and physicist at NeuroSpin, a research institute in Paris aimed at advancing MRI, says that although the exact mechanism through which diffusion MRI detects changes in neuronal swelling remains an open question, one potential explanation is that cell swelling alters how water molecules organize around neuronal membranes.



Increasingly powerful scanners for magnetic resonance imaging are becoming available, enabling improved resolution in brain scans.Credit: Jens Schlueter/DDP/AFP via Getty

Diffusion MRI, which Le Bihan developed in the 1980s[11], is used in the clinic to detect strokes and other brain diseases. It is also the basis for diffusion tensor imaging, which researchers use to map the organization of white matter in the brain. But the ability to detect neuronal function with this method, dubbed diffusion fMRI — which Le Bihan and his colleagues first reported in the 2000s[12,13] — has faced scepticism. Researchers have questioned whether diffusion fMRI is identifying the morphological changes that occur with neuronal firing, or if it is simply picking up on changes in blood flow.

Le Bihan and others have worked to convince the neuroimaging community that diffusion fMRI can indeed pick up on cell swelling that is linked to neuronal activity. Shemesh, for instance, says that work from his group in the past few years[5] provides clear evidence of this. “We saw signals that are just too fast to be related to blood flow — and they coincide with measurements of morphological changes of activity,” he explains.

Still, the technique has yet to be adopted widely. For one thing, diffusion fMRI produces a weaker signal than BOLD-based imaging does. It also requires scientists to learn how to use new software. More to the point, researchers have yet to be convinced of the utility of diffusion fMRI, says Keilholz. Demonstrating that this technique produces different results to BOLD in patients with diseases such as Alzheimer’s could drive adoption, she says.

A new view of the brain

For her part, Keilholz is convinced of diffusion fMRI’s potential. She says she regarded the method as the most promising for directly detecting neuronal activity — until Park’s method from South Korea came along, that is.

As Park explains, the technical background for his approach dates back to 2014. Soon after he joined the faculty at Sungkyunkwan University in Seoul, he came across a paper by researchers at the National Institute of Neurological Disorders and Stroke in Bethesda that reported a unique way of acquiring fMRI data[14]. It enabled the researchers to gather data with 40- to 50-millisecond resolution — much faster than conventional fMRI — and they used it to study neuronal activity in specific cortical layers of the rat brain. Park thought he might be able to apply the method to push the temporal resolution further, up to the speed at which neuronal firing occurs.



Neuroscience in court: The painful truth

His modifications to the imaging software led to an increase in temporal resolution to 5 milliseconds. This enabled the team to detect neuronal activity generated by repeatedly stimulating the animal’s whisker pads in two regions — the somatosensory cortex, which processes sensory inputs, and the thalamus, a relay station for sensory and motor inputs[1].

According to Yen-Yu Shih, a neuroimaging scientist at the University of North Carolina School of Medicine in Chapel Hill, DIANA could represent a breakthrough in temporal resolution in fMRI. Although more work needs to be done before the method can be widely adopted, Shih says, “even showing that there’s a possibility is already a tremendous contribution to the field”.

Still, experts caution that it is still too early to determine how useful the technique will be.

First, there are its limitations, Bandettini says. The signal that DIANA produces is small relative to BOLD-based fMRI, meaning it can be difficult to detect. The technique is also highly sensitive to motion — the animals in Park’s study were anaesthetized — and requires the stimulus (in this case, the electrical stimulation of whisker pads) to be precisely synchronized with data acquisition. That could limit the method’s applications to processes

such as vision, hearing or touch, in which it is possible to provide stimuli at regular intervals. Higher-level cognitive functions, such as memory, might be more difficult to capture in this manner.

There is also the question of what the researchers are detecting with DIANA. Park and his colleagues suggest that they are picking up on changes to the water molecules on the surface of neurons. Park says that changes in the membrane ‘potential’ — the concentration of charged ions on either side of the cellular membrane — alter the hydration on the cell surface. An MRI scanner, which senses changes in water molecules, might be able to detect that difference. Another possibility, he says, is cell swelling, which diffusion MRI can also detect. Le Bihan notes that both effects could be happening, because cell swelling might be related to the water layer around the cell membrane. However, he and other specialists say that the jury is still out on which, if either, of these factors underlies the effects that Park and his team observed.

Technical improvements could theoretically resolve these issues, Bandettini says, but the biggest question right now is whether other groups are able to replicate Park’s results independently. “I think the enthusiasm about this should be tempered until we know more about the nature of the signal we’re looking at and we can get some reproducing results,” Bandettini says. However, he adds, “if we figure out a way to make DIANA work well, it would be huge”.

Park says he and his team are now working to optimize data acquisition and analysis — and to implement DIANA fMRI in humans. “That’s the highest priority,” he says.

Building better BOLD

In the meantime, researchers have also devised ways to improve fMRI without abandoning neurovascular coupling.

One key advance comes down to the hardware. More powerful magnets mean researchers can collect better data, because they reduce the signal-to-noise ratio and enable images to be obtained at higher spatial and temporal

resolutions. Some of the first human fMRI studies were done using magnets with field strengths of 1.5 tesla, about 30,000 times stronger than Earth's magnetic field. Scientists have now used magnets of up to 10.5 tesla in human neuroimaging studies, and ever more powerful ones are being built. In February, a consortium of research institutions in the Netherlands announced that it would construct the world's strongest human MRI scanner so far, a machine with a magnetic field strength of 14 tesla.



NatureTech hub

Researchers have also varied the ways in which they observe blood flow through the brain. Because BOLD depends on changes in blood oxygen levels, it's more sensitive to blood flow through large veins, which drain deoxygenated blood away from the sites where brain activity occurred, than through regions with smaller vessels, such as capillaries. This becomes an issue when researchers want to look at the brain in finer detail. To get around this problem, researchers developed techniques such as vascular space occupancy[15], which measure changes in blood volume rather than blood oxygenation. Such tools have enabled neuroscientists to obtain better spatial resolution than with standard BOLD fMRI, making it possible to look at differences in neuronal activity across various layers of the brain's cortex[16].

Other improvements include updating data-collection techniques and using machine learning to improve image reconstruction. Some scientists are working on improving their understanding of the BOLD signal itself. Even after 30 years, many questions about BOLD-based imaging remain, Shih says, such as whether neurovascular coupling occurs in the same way across brain regions, and how the haemodynamic signal is influenced by the activity of different cell types or molecules such as neurotransmitters.

Anna Devor, a biomedical engineer at Boston University in Massachusetts, and her colleagues are looking at how changes in blood flow are linked to fluctuations in neurotransmitters. “Today, if you look at the functional MRI maps, you’ll see where the activity is happening, but you don’t know what the activity is,” Devor says. “We’re trying to figure out how these patterns of haemodynamics are related to specific neuronal circuits.”

The reality is that, although techniques such as DIANA stir up excitement in the neuroimaging field, BOLD is here to stay, at least for the foreseeable future. “We’re always looking for something that works better than BOLD,” Bandettini says. But BOLD has been “amazingly robust” for so many neuroscience questions. “I think that there will still be more surprises and insights to be gained,” he says.

Nature **617**, 640-642 (2023)

doi: https://doi.org/10.1038/d41586-023-01616-7

References

1. Toi, P. T. *et al. Science* **378**, 160–168 (2022).

2. Iadecola, C. *Neuron* **96**, 17–42 (2017).

3. Sandrone, S. *et al. Brain* **137**, 621–633 (2014).

4. Roy, C. S. & Sherrington, C. S. *J. Physiol.* **11**, 85–108 (1890).

5. Nunes, D., Gil, R. & Shemesh, N. *NeuroImage* **231**, 117862 (2021).

6. Kwong, K. K. *et al. Proc. Natl Acad. Sci. USA* **89**, 5675–5679 (1992).

7. Bandettini, P. A., Wong, E. C., Hinks, R. S., Tikofsky, R. S. & Hyde, J. S. *Magn. Reson. Med.* **25**, 390–397 (1992).

8. Ogawa, S. *et al. Proc. Natl Acad. Sci. USA* **89**, 5951–5955 (1992).

9. Sundaram, P. *et al. NeuroImage* **132**, 477–490 (2016).

10. Luo, Q. *et al. NeuroImage* **47**, 1268–1276 (2009).

11. Le Bihan, D. *Nature Rev. Neurosci.* **4**, 469–480 (2003).

12. Darquié, A., Poline, J.-B., Poupon, C., Saint-Jalmes, H. & Le Bihan, D. *Proc. Natl Acad. Sci. USA* **98**, 9391–9395 (2001).

13. Le Bihan, D., Urayama, S., Aso, T., Hanakawa, T. & Fukuyama, H. *Proc Natl Acad. Sci. USA* **103**, 8263–8268 (2006).

14. Yu, X., Qian, C., Chen, D., Dodd, S. J. & Koretsky, A. P. *Nature Methods* **11**, 55–58 (2014).

15. Huber, L. *et al. NeuroImage* **164**, 131–143 (2018).

16. Yang, J., Huber, L., Yu, Y. & Bandettini, P. A. *Neurosci. Biobehav. Rev.* **128**, 467–478 (2021).

This article was downloaded by **calibre** from https://www.nature.com/articles/d41586-023-01616-7

- WHERE I WORK
- 15 May 2023

I was deathly afraid of the sea — now I work to protect it

Conservationist Loyiso Dunga aims to guard kelp, a crucial resource in South African waters that is home to invertebrates, fish and mammals.

- Virginia Gewin



Loyiso Dunga is a conservationist and marine biologist based in Cape Town, South Africa, working for Parley for the Oceans, a non-profit environmental organization based in New York City. Credit: Barry Christianson for *Nature*

I grew up deathly afraid of the ocean. But that changed in 2016, when I began mapping South Africa's kelp forests for my biology master's degree. I used satellite imagery to find the kelp; then I assessed the potential environmental threats that the forests face, such as unsustainable offshore mining, pollution and even shadows from coastal development.

As I began this survey across the 1,300-kilometre kelp-rich stretch of South Africa's coastline, I wanted to see the kelp that was below the ocean's surface. I vividly recall floating on my stomach looking down at this golden, waving forest. I was amazed by the biodiversity that exists underneath this big, blue blanket, including invertebrates, fish and mammals.

In this image, taken near where I first encountered kelp forests off the coast of Windmill beach, south of Cape Town, I am looking for the different types of animal, including limpets, sea urchins and octopuses, that live in these forests. In my advocacy work, I use films and social media to educate the public about how, for example, over half of the atmosphere's oxygen comes from kelp forests.

So far, we have mapped only coastal kelp because it is visible to satellites during low tide. We hope to use remotely operated vehicles to map the underwater extent of it.

South Africa's natural kelp forests are among the few that are still expanding. Others around the world are endangered because of over-harvesting or coastal development. In response to increased demand for kelp, for use in products such as toothpaste and possibly as a biodegradable alternative to plastic, my team is building sustainable kelp farms. The government supports a non-lethal harvesting approach in which we collect only the tops of the stalks, allowing the plant to regrow as it continues to provide habitat.

Perhaps the kelp forests' biggest threat is the lack of awareness or appreciation of how many species call them home. It's a spiritual place.

Nature **617**, 644 (2023)

doi: https://doi.org/10.1038/d41586-023-01617-6

This article was downloaded by **calibre** from https://www.nature.com/articles/d41586-023-01617-6

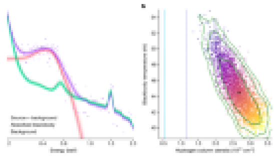
| Section menu | Main menu |

Research

- **A radio-detected type Ia supernova with helium-rich circumstellar material** [17 May 2023]
  • A type Ia supernova shows the presence of helium-rich circumstellar material, as demonstrated by its spectral features, infrared emission and a radio counterpart, that probably originates from a single-degenerate system in which a white dwarf accretes material from a helium donor star.
- **Photochemically produced SO2 in the atmosphere of WASP-39b** [26 Apr 2023]
  • Observations from the JWST show the presence of a spectral absorption feature at 4.05 μm arising from SO2 in the atmosphere of the gas giant exoplanet WASP-39b, which is produced by photochemical processes and verified by numerical models.
- **Photochromism from wavelength-selective colloidal phase segregation** [17 May 2023]
  • A simple spectral selective active colloidal system is designed in which TiO2 colloidal species are coded with dyes to form a photochromic swarm that adapts the appearance of incident light due to layered phase segregation.
- **A 3D printable alloy designed for extreme environments** [19 Apr 2023]
  • The authors develop a new oxide-dispersion-strengthened NiCoCr-based alloy using a model-driven alloy design approach and laser-based additive manufacturing, showing how such designs can provide superior compositions using far fewer resources than previous methods.
- **Widespread somatic L1 retrotransposition in normal colorectal epithelium** [10 May 2023]
  • This study illustrates long interspersed nuclear element-1 retrotransposition-induced somatic mosaicism in normal cells and provides insights into the genomic and epigenomic regulation of transposable elements over the human lifetime.
- **Long-range inhibition synchronizes and updates prefrontal task activity** [26 Apr 2023]
  • Rule-shift behavioural experiments in mice demonstrate that callosal projections of parvalbumin-expressing neurons switch prefrontal circuits from maintenance mode to rule-learning mode by gating inputs from other callosal inputs that maintain previous rule representations.

- **[Adeno-associated virus 2 infection in children with non-A–E hepatitis]** [30 Mar 2023]
  • A case–control study investigating the causes of recent cases of acute hepatitis of unknown aetiology in 32 children identifies an association between adeno-associated virus infection and host genetics in disease susceptibility.
- **[Genomic investigations of unexplained acute hepatitis in children]** [30 Mar 2023]
  • An investigation using various methods reports an association between adeno-associated virus 2 and paediatric hepatitis of unknown aetiology.
- **[Adeno-associated virus type 2 in US children with acute severe hepatitis]** [30 Mar 2023]
  • A retrospective analysis using PCR testing, viral enrichment-based sequencing and agnostic metagenomic sequencing finds an association between adeno-associated virus type 2 and paediatric hepatitis of unknown cause.
- **[Profiling the human intestinal environment under physiological conditions]** [10 May 2023]
  • Variations in microbial composition, phage induction, antimicrobial resistance genes and bile acid profiles are identified by using an ingestible device for site-specific sampling along the intestines.
- **[SARS-CoV-2 Omicron boosting induces de novo B cell response in humans]** [03 Apr 2023]
  • COVID-19 booster immunizations aimed at spike protein from new SARS-CoV-2 variants induce robust germinal centre B cell responses against the original spike protein, as well as de novo B cell responses against the variant spike protein.
- **[Glioblastoma remodelling of human neural circuits decreases survival]** [03 May 2023]
  • High-grade gliomas functionally remodel neural circuits in the human brain, promoting tumour progression and impairing cognition.
- **[The electron–proton bottleneck of photosynthetic oxygen evolution]** [03 May 2023]
  • Microsecond infrared spectroscopy together with quantum chemistry reveal the rate-determining proton and electron movements and identify an oxygen-radical state of the manganese cluster as the S4 state.
- **[Structural evidence for intermediates during O2 formation in photosystem II]** [03 May 2023]
  • Using serial femtosecond X-ray cystallography, we provide structural insights into the final reaction step of Kok’s photosynthetic water oxidation cycle, specifically the S3→[S4]→S0

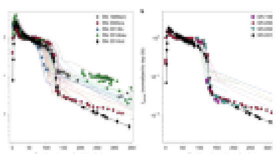
transition where O_2 is formed.



A helium-burning white dwarf binary as a supersoft X-ray source

22 March 2023

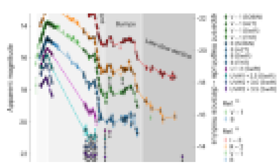
J. Greiner, C. Maitra, … R. Vanderspek



The electron-capture origin of supernova 2018zd

28 June 2021

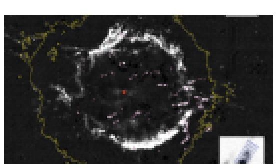
Daichi Hiramatsu, D. Andrew Howell, … Koichi Itagaki



A superluminous supernova lightened by collisions with pulsational pair-instability shells

01 May 2023

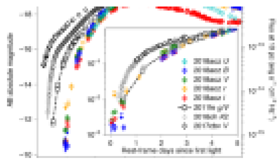
Weili Lin, Xiaofeng Wang, … Lingjun Wang



Detection of pristine circumstellar material from the Cassiopeia A supernova progenitor

20 January 2020

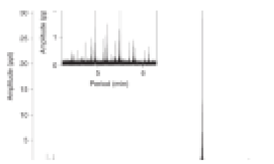
Bon-Chul Koo, Hyun-Jeong Kim, … Daniel T. Jaffe



Infant-phase reddening by surface Fe-peak elements in a normal type Ia supernova

17 February 2022

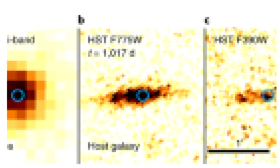
Yuan Qi Ni, Dae-Sik Moon, … Sheng Yang



A hot subdwarf–white dwarf super-Chandrasekhar candidate supernova Ia progenitor

12 July 2021

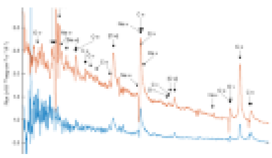
Ingrid Pelisoli, P. Neunteufel, … B. N. Barlow



An extremely energetic supernova from a very massive star in a dense medium

13 April 2020

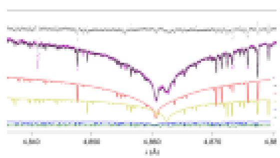
Matt Nicholl, Peter K. Blanchard, … Kerry Paterson



[A WC/WO star exploding within an expanding carbon–oxygen–neon nebula](#)

12 January 2022

A. Gal-Yam, R. Bruch, … N. Knezevic



[A spectroscopic quadruple as a possible progenitor of sub-Chandrasekhar type Ia supernovae](#)

12 May 2022

Thibault Merle, Adrian S. Hamers, … C. Clare Worley

- Article
- Open Access
- Published: 17 May 2023

A radio-detected type Ia supernova with helium-rich circumstellar material

- Erik C. Kool ,
- Joel Johansson,
- Jesper Sollerman,
- Javier Moldón,
- Takashi J. Moriya,
- Seppo Mattila,
- Steve Schulze,
- Laura Chomiuk,
- Miguel Pérez-Torres,
- Chelsea Harris,
- Peter Lundqvist,
- Matthew Graham,
- Sheng Yang,
- Daniel A. Perley,
- Nora Linn Strotjohann,
- Christoffer Fremling,
- Avishay Gal-Yam,
- Jeremy Lezmy,
- Kate Maguire,
- Conor Omand,
- Mathew Smith,
- Igor Andreoni,
- Eric C. Bellm,
- Joshua S. Bloom,
- Kishalay De,
- Steven L. Groom,
- Mansi M. Kasliwal,
- Frank J. Masci,
- Michael S. Medford,
- Sungmin Park,
- Josiah Purdum,
- Thomas M. Reynolds,
- Reed Riddle,
- Estelle Robert,
- Stuart D. Ryder,
- Yashvi Sharma &
- …

- Daniel Stern

Show authors

Nature **volume 617**, pages 477–482 (2023)

- 383 Altmetric

- Metrics details

Abstract

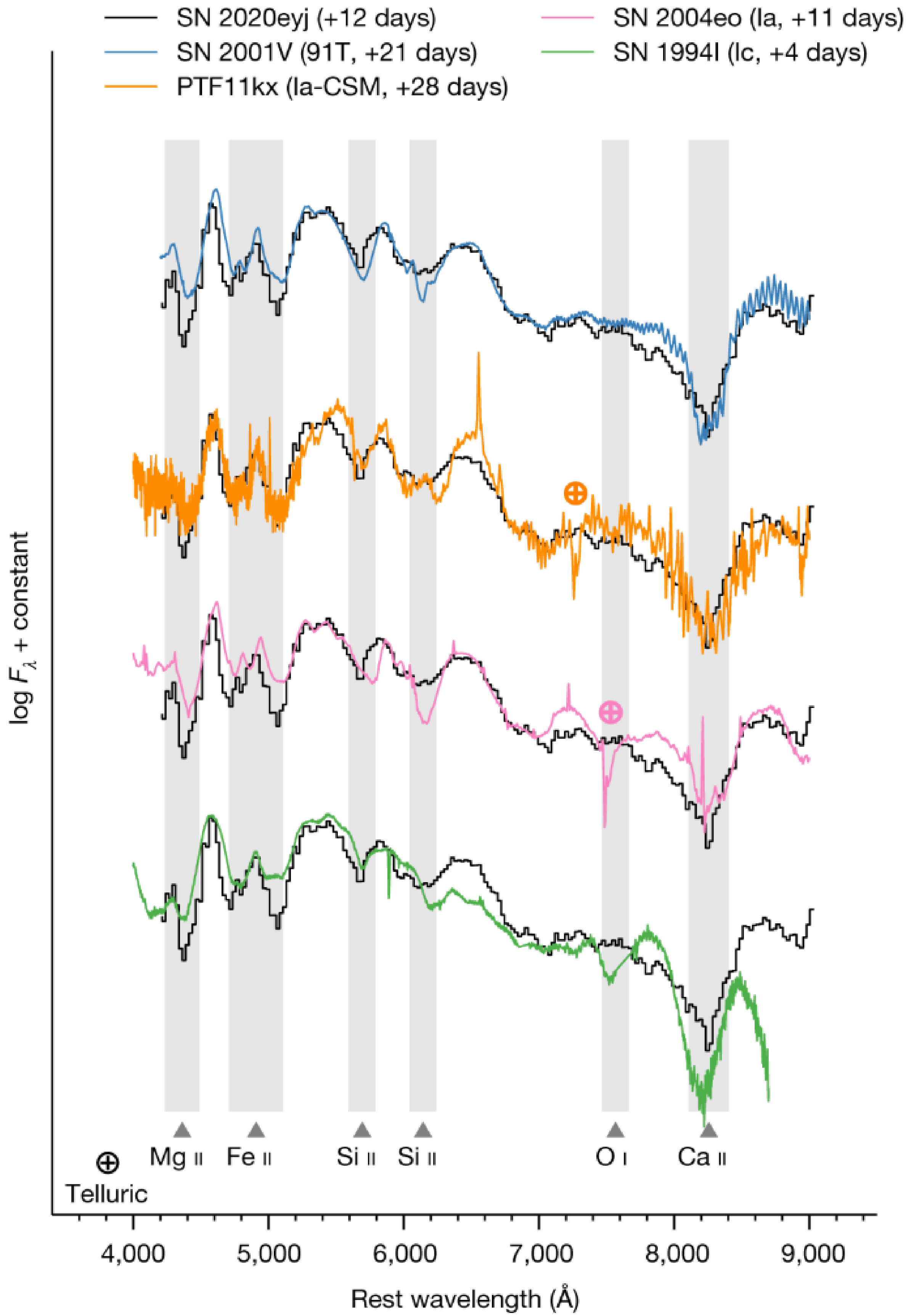
Type Ia supernovae (SNe Ia) are thermonuclear explosions of degenerate white dwarf stars destabilized by mass accretion from a companion star[1], but the nature of their progenitors remains poorly understood. A way to discriminate between progenitor systems is through radio observations; a non-degenerate companion star is expected to lose material through winds[2] or binary interaction[3] before explosion, and the supernova ejecta crashing into this nearby circumstellar material should result in radio synchrotron emission. However, despite extensive efforts, no type Ia supernova (SN Ia) has ever been detected at radio wavelengths, which suggests a clean environment and a companion star that is itself a degenerate white dwarf star[4,5]. Here we report on the study of SN 2020eyj, a SN Ia showing helium-rich circumstellar material, as demonstrated by its spectral features, infrared emission and, for the first time in a SN Ia to our knowledge, a radio counterpart. On the basis of our modelling, we conclude that the circumstellar material probably originates from a single-degenerate binary system in which a white dwarf accretes material from a helium donor star, an often proposed formation channel for SNe Ia (refs. [6,7]). We describe how comprehensive radio follow-up of SN 2020eyj-like SNe Ia can improve the constraints on their progenitor systems.

Main

SN 2020eyj was first detected on 7 March 2020 UT (modified Julian date (MJD) = 58,915.12; see ‘Observations’ section in Methods), at α = 11 h 11

min 47.19 s, $\delta = 29° 23' 06.5''$ (J2000). The SN was classified as a SN Ia (ref. [8]) based on a low-resolution spectrum obtained on 2 April 2020, 25 days after the first detection. Comparisons with type Ia and Ibc spectra from the literature support the SN Ia classification (see ‘SN Ia classification’ section in Methods and Fig. 1). Unusual evolution of the later light curve prompted us to obtain a second spectrum on 20 July 2020, 131 days after first detection. The second spectrum was very similar to those of type Ibn SNe (SNe Ibn), which are SNe that interact with helium-rich circumstellar material (CSM) and have spectra characterized by narrow (roughly a few 10^3 km s^{-1}) He i emission lines while showing little to no H i (refs. [9,10]).

Fig. 1: The first spectrum of SN 2020eyj is consistent with a type Ia(–CSM).

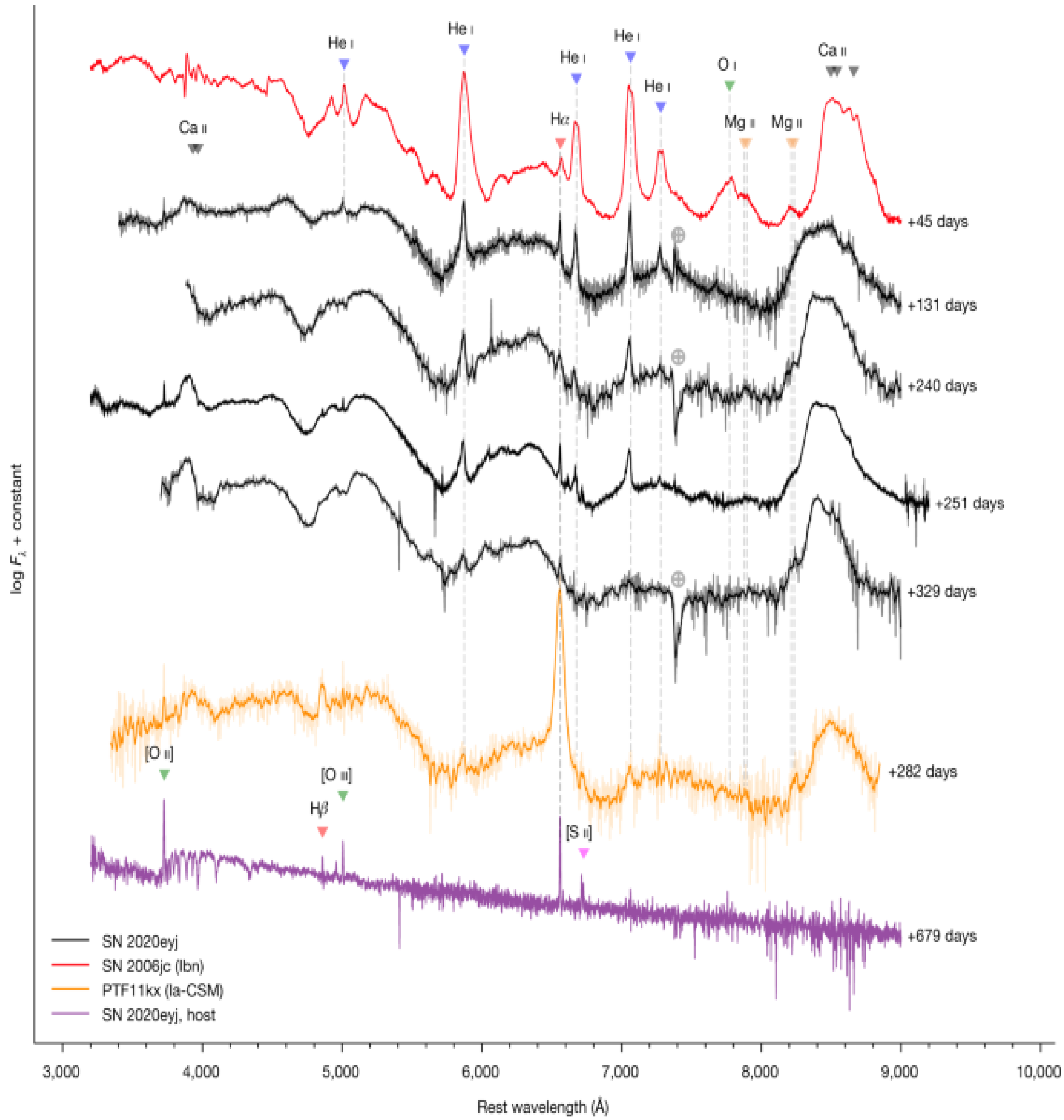


SN 2020eyj (+12 days)
SN 2001V (91T, +21 days)
PTF11kx (Ia-CSM, +28 days)
SN 2004eo (Ia, +11 days)
SN 1994I (Ic, +4 days)
log F_λ + constant
Mg II
Fe II
Si II
Si II
O I
Ca II
⊕
Telluric
4,000
5,000
6,000
7,000
8,000
9,000
Rest wavelength (Å)

The SEDM classification spectrum of SN 2020eyj, obtained about 12 days after peak and shown in black, is compared with type Ia-91T SN 2001V, type Ia–CSM PTF11kx, type Ia SN 2004eo and type Ic SN 1994I. Phases are relative to peak, which—in the case of SN 2020eyj—has an uncertainty of a couple of days. Several important absorption features are indicated at the expected wavelengths. Notably, the spectrum of SN 2020eyj lacks any sign of O i 7,774 Å absorption. Spectra have been corrected for MW reddening. Telluric features are indicated by crossed circles.

On the basis of the late-time (tail-phase) CSM-interaction-dominated spectra (Fig. 2), SN 2020eyj falls in the category of the rare subclass of SNe Ia that show evidence of CSM interaction in their optical spectra (SNe Ia–CSM; ref. [11]). The narrow emission lines in the spectra of such interacting SNe arise from shock interaction between the fast-moving SN ejecta and the slow-moving CSM[12]. SNe Ia–CSM are strong contenders for the single-degenerate (SD) SN Ia formation channel on account of the CSM, which is commonly assumed to originate from a non-degenerate donor star through stellar or accretion winds. Before SN 2020eyj, all of the discovered SNe Ia–CSM exhibited prominent Balmer emission lines and only weak He emission features[11].

Fig. 2: The spectra of SN 2020eyj in the tail phase are dominated by CSM interaction.

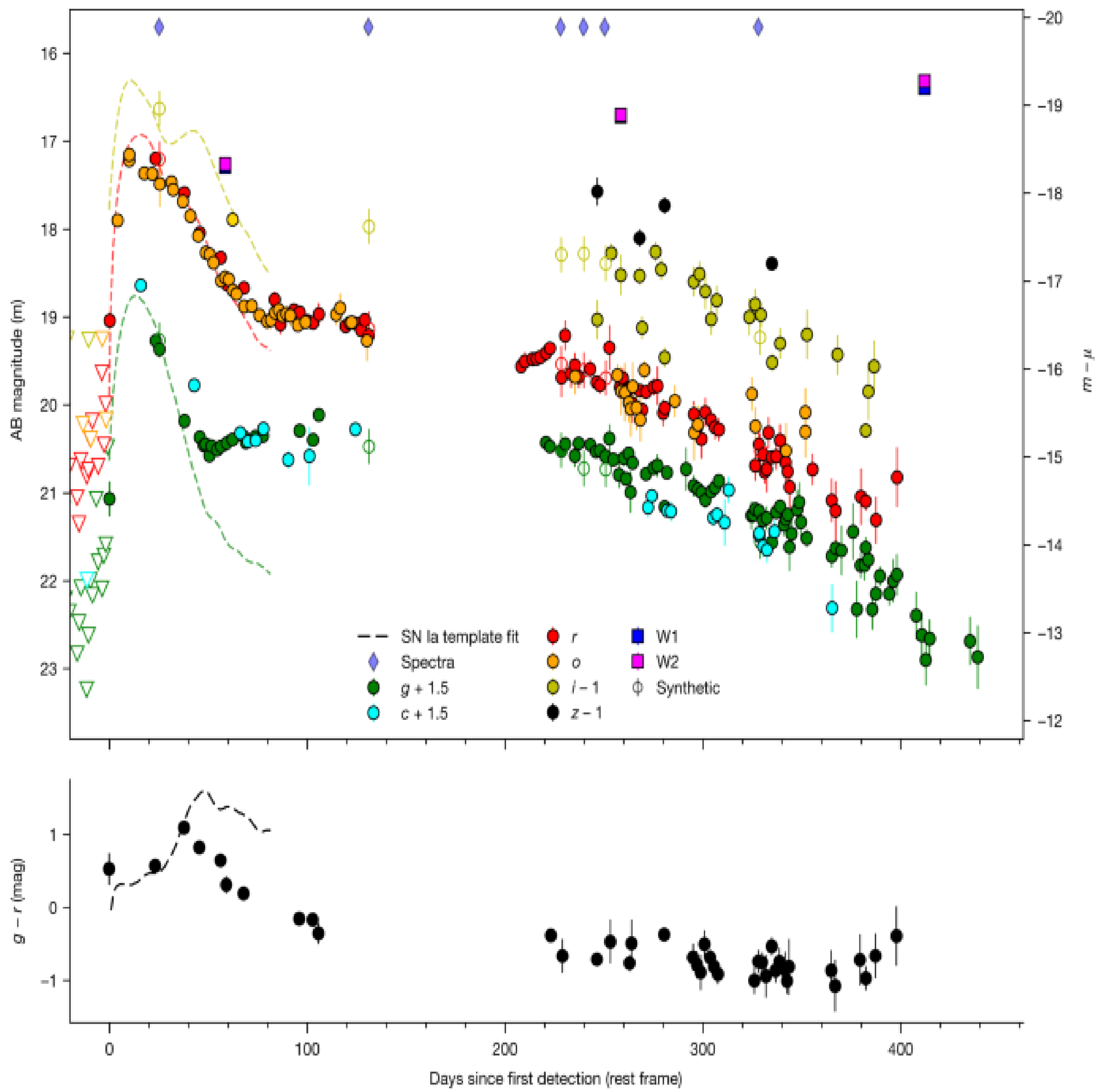


The spectra of SN 2020eyj at late phases (in black) are compared with the prototypical type Ibn SN 2006jc and the type Ia–CSM SN PTF11kx. The spectra show features common to SNe Ia–CSM, such as the quasi-continuum blueward of 5,700 Å and broad Ca ii emission. The main SN emission features are identified in the top spectrum. The emission lines in SN 2020eyj show strong asymmetry, with attenuated red wings (Extended Data Fig. 3). The bottom spectrum is of the host of SN 2020eyj, obtained at 679 days, some 300 days after the SN had faded below the detection limit of the ZTF. Some unresolved galaxy lines are marked. Phases are relative to

first detection, which—in the case of SN 2006jc—was at or after the peak. Spectra have been corrected for MW reddening. Telluric features are indicated by crossed circles.

Typically, CSM interaction contributes substantially to or even dominates the spectral and light-curve evolution of SNe Ia–CSM from the beginning, hindering unambiguous classification as SNe Ia (ref. [13]). However, in some rare cases, SNe Ia–CSM have shown a delay in CSM interaction[14,15,16], suggesting that the CSM was located far ($>10^{15}$ cm) from the binary system at the time of explosion. Notably, PTF11kx cemented SNe Ia–CSM as a bona fide SN Ia subclass by virtue of a delay of about 60 days, allowing for an indisputable SN Ia classification before CSM interaction[15]. SN 2020eyj follows a similar evolution as PTF11kx, initially showing a typical SN Ia bell-shaped light curve (Fig. 3) and a spectrum consistent with a SN Ia of the 91T subgroup[17] without clear evidence for CSM interaction (Fig. 1). Then, at 50 days after first detection, the *g*-band light curve of SN 2020eyj diverges from a steady decline into a plateau that lasts for roughly 200 days. Such an evolution and colour change is not expected for a normal SN Ia (Fig. 3) but is driven by the emergence of spectral features associated with CSM interaction (see 'Light-curve analysis' section in Methods). We interpret the start of the plateau at 50 days as the epoch when CSM interaction starts to contribute substantially or even dominate the light curve of SN 2020eyj. Assuming a SN ejecta velocity of 10^4 km s^{-1} (ref. [18]), the delay corresponds to an inner boundary to the CSM of about 4×10^{15} cm. Except for the presence of He emission lines, the late-time spectra of SN 2020eyj are typical for the SN Ia–CSM class, with prominent broad Ca ii emission from the near-infrared (NIR) triplet and without any sign of O iλ7774 emission (Fig. 2). The compact and star-forming host galaxy of SN 2020eyj (see 'Host galaxy' section in Methods) is also consistent with those of other SNe Ia–CSM[11].

Fig. 3: The multiband light curve of SN 2020eyj can be divided into a diffusion-peak phase and a long-lived interaction-powered tail phase.



The light curves of SN 2020eyj are shown with overplotted SN Ia template fits to the initial peak (see 'Light-curve analysis' section in Methods). The most recent mid-infrared epoch (W1 and W2) is outside the date range plotted here and is shown in Extended Data Fig. 2 . Open circles indicate synthetic photometry derived from the spectra. Phase is in rest-frame days since first detection. Apparent magnitudes on the left *y* axis, absolute magnitudes on the right *y* axis, in which μ is the distance modulus. Non-detections with 5σ upper limits are indicated by triangles. The photometry has been binned into one-night bins and has been corrected for MW reddening. The diamond markers at the top indicate the epochs of spectroscopy. The bottom panel shows the $g-r$ colour for the nights in

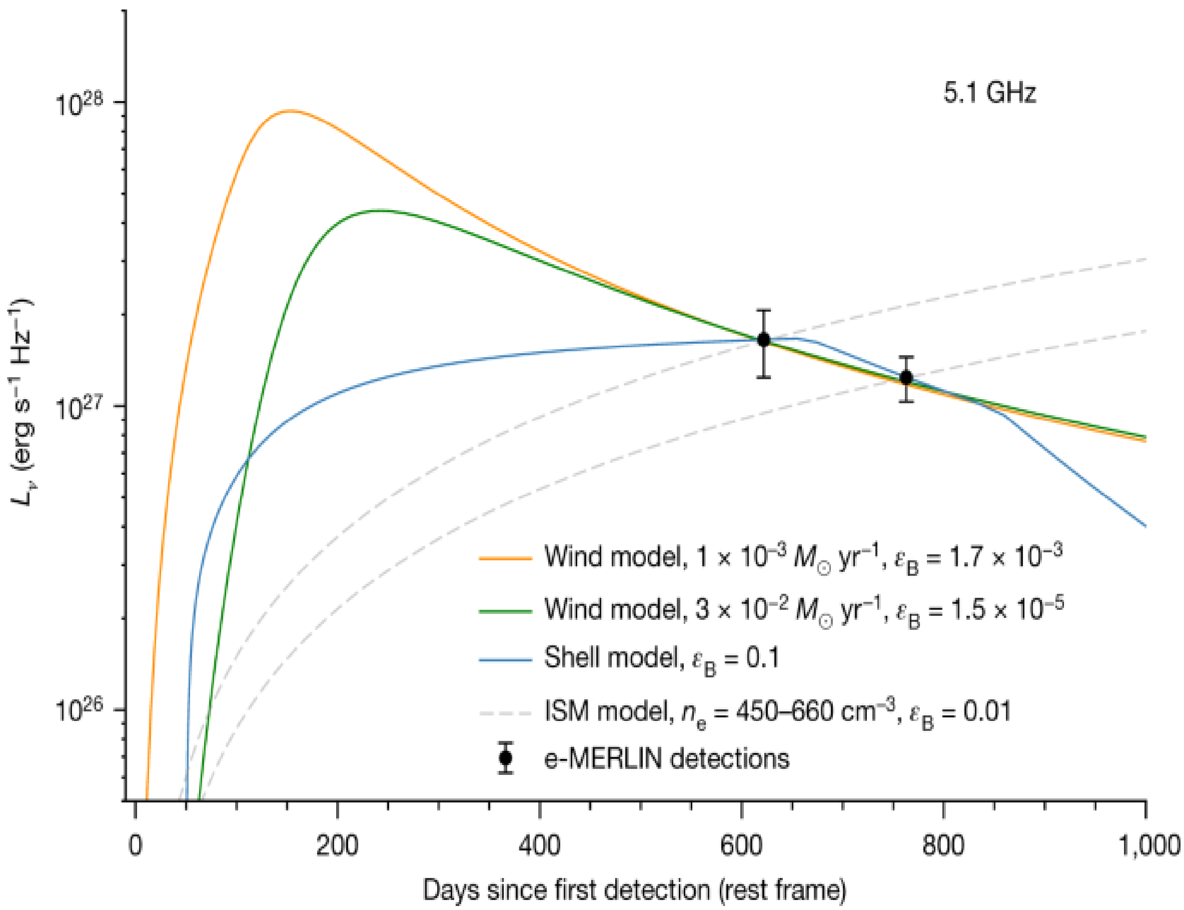
which both g and r photometry was obtained, overplotted with the colour evolution of a typical SN Ia. The error bars represent 1σ uncertainties.

Despite the similarities between SN 2020eyj and other SNe Ia–CSM, the presence of He i lines and absence of prominent H i lines remains a striking difference with profound implications for the progenitor system. As H i is easier to ionize than He i, the absence of the lines indicates that the CSM around SN 2020eyj, and thus the companion star, is He-rich and H-poor. Although the late-time spectra of SN 2020eyj are similar to those of SNe Ibn, these SNe are presumed to arise from the core collapse of massive (>10 $M_{\odot}$) stars[9,19,20], which are unlikely to be in a binary system with a white dwarf (WD), as they would undergo core collapse long before the WD formed. A merger involving a degenerate He WD donor star is also disfavoured, because in such merger models, only a small amount of unburned He (about 0.03 $M_{\odot}$ (ref. [21])) is present close to ($\lesssim 10^{12}$ cm) the WD (ref. [22]), whereas the CSM around SN 2020eyj resides at $>10^{15}$ cm. Instead, a strong candidate for the donor star in the SN 2020eyj progenitor system is a non-degenerate He star (initial mass 1–2 $M_{\odot}$, for example, ref. [23]). WD + He star systems can be formed by means of binary evolution[24] and this SD channel for SNe Ia has garnered recent interest because the very restrictive limits placed by radio non-detections and deep optical imaging[25] that exclude most H-rich donor star models still allow for low-CSM-density WD + He star systems[25,26]. The possible detection in pre-explosion Hubble Space Telescope imaging of the progenitor system of the type Iax (SNe Ia similar to SN 2002cx (ref. [27])) SN 2012Z, a blue compact source interpreted as a He-star donor[28], has further strengthened this hypothesis, although the thermonuclear nature of type Iax SNe is debated[29].

The CSM interaction in SN 2020eyj is also confirmed, for the first time in a SN Ia, through the detection of a radio counterpart, at a frequency of 5.1 GHz at 605 and 741 days after the first detection (see ‘Radio’ section in Methods). Follow-up in the X-rays did not yield a detection (see ‘X-ray’ section in Methods). We model the radio synchrotron emission, which results from the shock interaction between the ejecta and the CSM, assuming two basic CSM configurations expected in a SD progenitor system; a constant density shell and a wind-like density profile with density $\rho \propto r^{-2}$

(Fig. 4). A constant density shell could result from a mass ejection event such as a nova, whereas a wind-like CSM profile would be expected from an optically thick wind, in which the mass-transfer rate from the donor star to the WD exceeds the maximum accretion rate of He-rich material that the WD can burn on its surface[26,30]. As well as CSM material resulting from a SD scenario, we consider synchrotron emission resulting from the interaction of a SN Ia from a double-degenerate (DD) WD merger interacting with the local interstellar medium (ISM)[31]. For the SD shell model, the radio detections are best explained with a CSM mass of $M_{csm} = 0.36\,M_{\odot}$ (see 'CSM shells' section in Methods), with the expectation that the radio light curve will start to drop off rapidly at around 900 days. For the SD optically thick wind model, the bolometric light-curve tail (see 'Bolometric light curve' section in Methods) and radio detections of SN 2020eyj are well fitted with a mass-transfer rate of 10^{-3}–$10^{-2}\,M_{\odot}\,yr^{-1}$, microphysics parameter $\epsilon_B = 10^{-5}$–10^{-3} and a CSM mass within 10^{17} cm of $M_{csm} = 0.3$–$1.0\,M_{\odot}$. The DD ISM model (the dashed lines in Fig. 4) requires unusually high ISM densities and does not recover the observed decline in flux, ruling out the DD formation channel for SN 2020eyj (see 'ISM' section in Methods). The best fit radio light curves of the shell and wind models differ in particular at early phases (Fig. 4), but no radio data were obtained at these epochs. Instead, multifrequency monitoring of the radio counterpart of SN 2020eyj until late phases (>1,000 days) will allow to discriminate between the rapid drop-off of the shell model and a shallower decline expected in the case of a wind-like CSM.

Fig. 4: The radio detections of SN 2020eyj at 5.1 GHz can be reconciled with CSM interaction.



For the wind model, in which the CSM follows a density profile of $\rho \propto r^{-2}$, we assume a pre-SN wind velocity of 1,000 km s^{-1} and adopt a mass-transfer rate as inferred from fitting the bolometric light curve of SN 2020eyj. Depending on the level of line-of-sight extinction affecting the bolometric light curve (see ‘Bolometric light curve’ section in Methods), the wind model fits the observations (in black, with 1σ uncertainties) well for the microphysics parameter $\epsilon_B = 1.7 \times 10^{-3}$ (1.5×10^{-5}) and a CSM mass of $M_{csm} = 0.3\ M_\odot$ ($1\ M_\odot$) within 10^{17} cm (see ‘Optically thick wind’ section in Methods) when $E(B - V) = 0$ mag (0.5 mag). For the shell model, in which the CSM is concentrated in a constant-density CSM shell, we assume ϵ_B = 0.1 and obtain a best estimate for the CSM mass of $M_{csm} = 0.36\ M_\odot$ and a CSM interaction end time of t_{end} = 665 days (a width of 8.6×10^{16} cm; see ‘CSM shells’ section in Methods). In both the wind and shell model fits, ϵ_e = 0.1 is assumed. We also show radio light curves from a model involving a DD SN Ia interacting with the ISM (see ‘ISM’ section in Methods). To fit

the individual radio detections, this model requires unusually high ISM densities and neither fit reproduces the observed decline in flux, ruling out the DD scenario.

A viable progenitor scenario for SN 2020eyj needs to explain not only the presence and properties of a He-rich CSM but also its detached configuration. For the delayed type Ia–CSM SN 2002ic, the CSM-free cavity was attributed to a possible drop-off in mass-transfer rate or the emergence of a low-density fast wind evacuating the CSM[32]. In the case of PTF11kx, the delayed CSM interaction was explained by a scenario involving a symbiotic nova progenitor, in which recurrent novae on the surface of the WD sweep up the wind-deposited CSM into shells[15]. SN 2020eyj shows strong similarities to PTF11kx, which may hint at a common progenitor scenario. Their light curves are virtually identical up until day 50 (Extended Data Fig. 1) with risetimes of about 14 days in the *g* band, which is fast for a SN Ia (ref. [33]). And, except for the nature of the narrow emission lines, both SNe have similar spectra throughout their evolution (Figs. 1 and 2). For SN 2020eyj, a nova progenitor could look like V445 Puppis (V445 Pup; see 'V445 Puppis' section in Methods), the only known nova system that showed He-rich, but H-free, ejecta[34,35]. Notably, the V445 Pup system is considered a prime candidate progenitor system for the He star + WD SN Ia channel, as it is claimed to be host to a WD with a mass close to the Chandrasekhar limit[36]. Furthermore, a prominent carbon-rich equatorial dusty disk such as that in V445 Pup (refs. [34,35]) could explain (see 'V445 Puppis' section in Methods) the luminous infrared counterpart of SN 2020eyj (Extended Data Fig. 2), which we attribute to an infrared echo from radiatively heated pre-existing dust with a dust mass of order $10^{-2}\ M_{\odot}$ (see 'Dust properties' section in Methods). The initial models invoking recurrent novae for the origin of PTF11kx (ref. [15]) were challenged by the CSM masses involved[37], which were too large by orders of magnitude for symbiotic nova mass build-up models[38]. Similarly, the mass resulting from a V445 Pup-like nova outburst ($\lesssim 10^{-3}\ M_{\odot}$; see 'V445 Puppis' section in Methods) is insufficient to explain the CSM mass observed in SN 2020eyj. However, a recent study of the radio evolution of V445 Pup suggests that the equatorial disk could have pre-dated (and survived) the nova outburst[39], which would allow for mass build-up in the disk between nova eruptions.

This scenario would require the SN to occur soon after the nova outburst and before the resumption of mass transfer between the donor and WD reforms the disk at small radii. We note that a nova similar to the year 2000 event of V445 Pup would not have been detectable at the distance of SN 2020eyj (see ‘Precursor search’ section in Methods).

SN 2020eyj represents the first observational example of the previously speculated class of SNe Ia–He CSM (ref. [40]). The presence of a dense CSM, supported by a radio detection, offers strong evidence for the SD scenario for SN 2020eyj, in particular for the He star + WD formation channel. It is estimated that about 10% of all SD SNe Ia arise from this channel[7], which is probably the dominant source of SNe Ia with short delay times[41]. Understanding the timescale of SN Ia activity is important for the chemical evolution of galaxies. The confirmed presence of a He-rich CSM in a SN Ia system also affects SN Ia explosion modelling, as He plays a vital role in double detonation models in which the WD explosion is triggered by the ignition of a massive ($\lesssim 0.2\,M_\odot$) He shell on its surface[30]. Constraining the rate of SNe Ia similar to SN 2020eyj would require systematic spectroscopic follow-up of SNe Ia with long-lived light curves, as monitoring at present often stops after a seemingly normal SN Ia has been classified. Observational properties that SN 2020eyj share with its H-analogue PTF11kx, such as a fast rise and a 91T-like peak spectrum, can potentially guide such follow-up efforts and allow for the discovery and study of more SN 2020eyj-like SNe Ia, including at radio wavelengths.

Methods

Observations

Discovery

SN 2020eyj was discovered by the Asteroid Terrestrial-impact Last Alert System (ATLAS)[42,43] on 23 March 2020 UT (ref. [44]) and subsequently detected as part of the Zwicky Transient Facility (ZTF) survey[45,46], at $\alpha = 11$ h 11 min 47.19 s, $\delta = 29°\,23'\,06.5''$ (J2000). Pre-discovery detections were recovered in the ZTF data on 7 March 2020 UT (MJD = 58,915.12) in both g

and *r* filters. For reference, we list some key characteristics of SN 2020eyj in Extended Data Table 1.

Optical photometry

Follow-up photometry was obtained as part of public and partnership ZTF survey observations[47] with the ZTF camera[48] on the Palomar 48-in. telescope (P48) telescope in the *g* and *r* bands, and later phases were also covered in the *i* band. The P48 data were reduced and host subtracted using the ZTF reduction and image-subtraction pipeline[49], which makes use of the ZOGY algorithm[50] for reference-image subtraction. Following the rationale illustrated in ref. [51], we apply the difference image zero point magnitude to convert fluxes from units in detector data number (DN) to μJy and translate fluxes to AB magnitudes. We apply a detection threshold of signal-to-noise ratio (S/N) $\gtrsim 3$ and for non-detections we compute 5σ upper limits. The Supplementary Information lists the ZTF magnitudes and upper limits.

Further photometric epochs were obtained with the Liverpool Telescope[52], the Spectral Energy Distribution Machine (SEDM) on the Palomar 60-in. telescope (P60), the Las Cumbres Observatory telescopes (programme ID NOAO2020B-012) and the Alhambra Faint Object Spectrograph and Camera (ALFOSC) on the Nordic Optical Telescope (NOT), with data reduced and host subtracted using the pipelines described in refs. [53,54] or standard methods. In this work, we also make use of the forced photometry service from the ATLAS survey[42,55], which contained valuable photometry in the *o* and *c* bands. One *i*-band epoch was obtained from the Pan-STARRS1 data archive[56].

ZTF and ATLAS also obtained observations of the location of SN 2020eyj in the nights immediately preceding the first detection, with limiting magnitudes in the ZTF *g* band on 5 and 6 March 2020 UT of 20.8 and 19.7, respectively, and the (binned) observations in the *o* band from ATLAS on 5 March 2020 UT correspond to a limiting magnitude of 20.2. Phases in this study are relative to the first ZTF detection (MJD = 58,915.212, 7 March 2020 UT) in rest-frame days, unless stated otherwise. Given the excellent constraints on the nights before, this epoch is also close to the time of first light.

All magnitudes are reported in the AB system. The extinction in the Milky Way (MW) was obtained from ref. [57] as $E(B-V) = 0.024$ mag. MW reddening corrections are applied using the extinction law with $R_V = 3.1$ (ref. [58]), whereas SN reddening corrections are applied using $R_V = 2$. The photometric magnitudes of SN 2020eyj are listed in the Supplementary Information. The ATLAS and P48 light curves are shown in Fig. 3, binned into one-night bins to enhance the S/N.

Optical spectroscopy

The first optical spectrum of SN 2020eyj was obtained with the SEDM (ref. [59]) mounted on the P60 (ref. [60]), 25 days after first detection. All SEDM spectra are automatically reduced and calibrated with pysedm (ref. [61]) and the quality of the SEDM spectrum of SN 2020eyj was further improved using hypergal (ref. [62]). Follow-up spectroscopy was obtained from 131 days onward with the Low-Resolution Imaging Spectrometer (LRIS)[63] on the Keck I telescope and the ALFOSC on the NOT (ref. [64]). A host spectrum was obtained at 678 days, after the SN had fully faded from view. The spectra were reduced in a standard manner, using LPipe (ref. [65]) and PypeIt[66,67] for Keck/LRIS and NOT/ALFOSC, respectively.

A log of the obtained spectra is provided in Extended Data Table 2 and the epochs of spectroscopy are indicated by the diamond markers on top of the light curves in Fig. 3. The spectra were absolute-flux-calibrated against the *r*-band magnitudes using the Gaussian process interpolated magnitudes and then corrected for MW extinction. All spectral data and corresponding information will be made available through the WISeREP public database[68]. We present the peak SEDM spectrum in Fig. 1 and the later sequence of spectra in Fig. 2.

The initial spectrum obtained with SEDM is characterized by broad absorption features (see 'SN Ia classification' section). The later spectra are shaped by broad Fe ii lines, in particular the quasi-continuum blueward of 5,700 Å (refs. [69,70,71,72,73]) and a prominent Ca ii NIR triplet. Superimposed on the continuum are narrow He i emission lines, as well as Hα. We measure full width at half maximum (FWHM) velocities of the He i emission lines

and Hα in the spectra obtained with Keck at 131 and 251 days by fitting a Lorentzian profile to the complete lines, as well as to just the blue wings. The red wings in the He and Hα lines are markedly attenuated (see Extended Data Fig. 3 and ‘Dust properties’ section), so the intrinsic FWHM velocities are better represented by (double) the blue-wing FWHM. We report these FWHM velocities in Extended Data Table 2. The FWHM velocities of the He i emission lines range from 1,100 to 2,700 km s^{-1} (corrected for the red wings), with no sign of a narrow (<1,000 km^{-1}) component detected in some SNe Ibn and interpreted as coming from the unshocked CSM[71,74]. There is also no sign of material stripped from the donor star by the SN ejecta[75,76], which is predicted to show up as narrow emission (<1,000 km^{-1} (ref. [77])).

The asymmetric line profile we associate with the SN also applies to the Hα emission line, suggesting the presence of H in the CSM. In the spectrum obtained at 131 days, Hα has an equivalent width of 14 Å, not corrected for contribution by the host. By comparison, the He i emission lines at 5,876 Å, 6,678 Å and 7,065 Å in the same spectrum have equivalent widths of 47 Å, 43 Å and 61 Å, respectively. As H is easier to ionize than He, the more prominent He lines means that the CSM must predominantly consist of He. By epoch 329 days, the Hα luminosity has dropped to the luminosity of the Hα narrow emission line in the host spectrum obtained at 678 days (see ‘Host galaxy’ section).

Infrared photometry

Following a report[78] of a mid-infrared detection of SN 2020eyj in the 2021 data release of the NEOWISE Reactivation (NEOWISE-R)[79] survey, we queried the IPAC Infrared Science Archive for any NEOWISE-R detections at the position of SN 2020eyj. After filtering poor-quality data and binning individual exposures following the method described in ref. [80], the SN was recovered in both W1 and W2 filters (3.4 and 4.6 μm, respectively) in all four 2020 and 2021 epochs, with the earliest detection at 59 days after first detection (Fig. 3 and Extended Data Table 3). The host is not detected in (stacked) WISE data before the SN explosion (Extended Data Fig. 2, top panels), so we assume that the contribution from the host is negligible and all observed flux is because of the SN.

Radio

We observed SN 2020eyj with the electronic Multi-Element Radio Linked Interferometer Network (e-MERLIN) in two epochs. The first epoch, with a duration on target and phase calibrator of about 16 h, was conducted on 19 November 2021 (centred on MJD 59,538.29), 605 days after first detection and included six e-MERLIN telescopes (Mk2, Kn, De, Cm, Da and Pi). The second epoch was conducted during six consecutive days between 6 and 12 April 2022 (mean MJD 59,678.59, 741 days after first detection). Between fix and six telescopes (including the Lovell) participated, with some antennae missing part of the runs owing to technical problems. Owing to the much smaller field of view of the Lovell telescope, the pointing centre of the second epoch was shifted by 1 arcmin to include an in-beam calibrator in the primary beam of this telescope. 3C 286 and OQ 208 were used as amplitude and band-pass calibrators, respectively. The phase calibrator, J1106+2812, was correlated at position $\alpha_{J2000.0}$ = 11 h 06 min 07.2617 s and $\delta_{J2000.0}$ = 28° 12′ 47.065″, at a separation of 1.7° from the target, and was detected with a flux density of 150 mJy. We centred our observations at a frequency of 5.1 GHz, using a bandwidth of 512 MHz. The data were correlated with the e-MERLIN correlator at Jodrell Bank Observatory, using four spectral windows, each of 512 channels, with 1-s integrations and four polarizations.

We calibrated and processed the data using the e-MERLIN CASA pipeline[81] version v1.1.19 running on CASA version 5.6.2. We used the 10-mJy in-beam source to self-calibrate the residual phases and amplitudes of the target source. Cleaning was done with the software package wsclean[82]. Final images of the target were produced with a synthesized beam of 80 mas × 35 mas at a position angle of 28° and 94 mas × 71 mas at a position angle of −71°, in the first and second epochs, respectively. The 1σ root mean squares of the images is 17 and 8 μJy beam^{-1}, respectively. The target is detected in both epochs as an unresolved source as characterized with task IMFIT. We estimate the uncertainty of the peak flux density to be a quadratic sum of the image root mean square and a conservative 10% amplitude scale calibration error. The final flux density of the source is 80 ± 20 and 60 ± 10 μJy beam^{-1} in the first and second epochs, respectively. The radio source is located at an average position of $\alpha_{J2000.0}$ = 11 h 11 min 47.1763 s and $\delta_{J2000.0}$ = 29° 23′ 06.45″, with an estimated uncertainty of 10 mas.

The average position of the e-MERLIN detections relative to the optical positions of SN 2020eyj is shown in Extended Data Fig. 4. The radio detection is consistent with the position of the SN in the ALFOSC epoch at 382 days (*r* band) and the position reported in GaiaAlerts of the detection of SN 2020eyj in the *G* band at 42 days.

X-ray

On 27 April 2022, 758 days after first detection, we observed SN 2020eyj for 3.8 ks with the X-ray telescope XRT between 0.3 and 10 keV aboard the Neil Gehrels Swift Observatory[83,84]. We analysed the data with the online tools of the UK Swift team (https://www.swift.ac.uk/user_objects/) that use the methods described in refs. [85,86] and the software package HEASoft version 6.26.1. SN 2020eyj evaded detection down to a count rate of 0.003 count s^{-1} (3σ limit). To convert the count-rate limit into a flux limit, we assumed a power-law spectrum with a photon index Γ of 2 and a galactic neutral hydrogen column density of 1.9×10^{20} cm^{-2} (ref. [87]). Here the photon index Γ is defined as the power-law index of the photon flux density ($N(E) \propto E^{-\Gamma}$). Between 0.3 and 10 keV, the count-rate limit corresponds to an unabsorbed flux of 1.1×10^{-13} erg cm^{-2} s^{-1} and a luminosity $<2.4 \times 10^{41}$ erg s^{-1}. It is possible that a deeper observation would have yielded a detection, as the type Ia–CSM SN 2012ca was detected in X-rays at a similar epoch, with a luminosity on the order 10^{40} erg s^{-1} (ref. [88]).

SN Ia classification

During the peak phase of SN 2020eyj, an optical spectrum was obtained with the low-resolution ($R \approx 100$) SEDM on the P60, 25 days after first detection. This high S/N spectrum was characterized by broad absorption features (Fig. 1), based on which SN 2020eyj was classified as a SN Ia at redshift $z = 0.03$ (ref. [8]). Using SNIascore, a deep-learning-based classifier of SNe Ia based on low-resolution spectra[89], it was noted that the SN could be a type Ibc SN erroneously classified as SN Ia because of the degeneracy between peak spectra of SNe Ibc with those of SNe Ia at post-peak phases, but their classifier favoured a SN Ia classification anyway. In general, based on the comparison study in ref. [13], type Ibc SNe erroneously classified as

type Ia(–CSM/91T) are much less common than the inverse. Here we scrutinize the SEDM spectrum using comparisons with SNe from the literature, based on spectral matching with the SuperNova IDentification (SNID)[90] and Superfit[91] classification tools, for which the SNID template library has been supplemented with the type Ibc templates from ref. [92]. We adopt a g-band peak epoch of MJD = 58,929 ± 2, based on the light-curve fitting described in the 'Light-curve fit' section, with the uncertainty driven by the poor sampling of our photometry around peak.

The top 10 SNID (rlap > 10) and Superfit matches are all of type Ia (Fig. 1) and include normal SNe Ia such as SN 2004eo (ref. [93]) and 91T-like SNe such as SN 2001V (ref. [94]). The best matching SN of type Ibc (rlap = 8) is the type Ic SN 1994I (refs. [95,96,97,98]). The phases corresponding to the matched SNe Ia are all post-peak, ranging from 12 days to about 50 days post-maximum, whereas the matching SN Ibc spectra are all within a few days from peak. The phase of the SEDM spectrum of SN 2020eyj is 12 days post-maximum, which corroborates the SN Ia classification.

In terms of spectral features, the SEDM spectrum shows broad absorption lines that, based on the spectral comparisons, can be unambiguously identified as Si ii, Fe ii and Ca ii (Fig. 1). Compared with normal SNe Ia as exemplified by SN 2004eo, the Si ii features in SN 2020eyj are shallow. Diluted Si ii absorption is common for 91T-like SNe Ia, as in the spectrum of SN 2001V. Type Ia–CSM are known to show 91T-like spectra around peak[13]. As a SN strongly interacting with a CSM, the presence of diluted Si ii in the SEDM spectrum of SN 2020eyj is consistent with a type Ia(–CSM) classification. In terms of expansion velocity, the velocity of the Si iiλ6355 absorption feature in the SEDM spectrum is 8,900 ± 600 km s^{-1}. This velocity is on the slow side for the SN Ia sample described in ref. [99] but consistent with the SN Ia sample in ref. [100] and comparable with, for example, SN 2004eo (Fig. 1).

Another notable feature in the SEDM spectrum is the complete lack of O i 7,774 Å absorption (Fig. 1), even though O i absorption in SNe Ia is common, in particular 91T-like SNe Ia can have shallow or non-existent O i (ref. [101]). This is clearly visible in the matched spectrum of SN 2001V. By contrast, SNe Ibc that lack O i absorption are extremely uncommon,

especially at about 12 days post-peak[102,103], as exemplified by type Ic SN 1994I in Extended Data Fig. 5. In this figure, we have also included the type Ibn SN 2006jc at a phase similar to that of the SEDM spectrum, to highlight that SN 2020eyj does not show any sign of He i emission lines or the quasi-continuum expected for a type Ibn at this phase.

An absence of oxygen lines is typical for type Ia–CSM spectra, both as an absorption feature around peak and as emission in later epochs[11,104], as seen in the early and late spectra of PTF11kx in Figs. 1 and 2, respectively. Similarly, the late spectra of SN 2020eyj lack any sign of O iλ7774 emission (Fig. 2). Other features in the late-time spectra of SN 2020eyj that are typical for type Ia–CSM include prominent broad Ca ii emission and a high Hα/Hβ Balmer ratio, which indicates that the emission lines are probably produced through collisional excitation rather than recombination[11]. The high S/N spectrum at 251 days shows both Hα and Hβ emission, but after correcting for contribution by the host, only Hα shows some residual flux related to the transient. We note that, at this late phase, SN 2020eyj is about four magnitudes brighter than expected from a normal SN Ia, such as SN 2004eo (ref. [93]), and the spectrum is dominated by CSM-interaction features.

In conclusion, based on its spectral features, we classify SN 2020eyj as a type Ia(–CSM) SN. Furthermore, as we discuss in the 'Light-curve fits' section, the light curves of SN 2020eyj show strong similarities to those of PTF11kx, the SN that cemented SNe Ia–CSM as a subclass.

Light-curve analysis

Light-curve fits

The light curve of SN 2020eyj (Fig. 3) can be divided into two phases, similar to its spectral evolution. In the first phase, lasting around 50 days, the light curve follows a fairly typical bell-like shape, peaking at $m \approx 17.2$ in both the r band and the ATLAS bands, which—at a luminosity distance of 131.4 Mpc (see 'Host galaxy' section)—corresponds to $M \approx -18.4$, not accounting for host extinction. During the first phase, the light curve has a red $g - r$ colour, consistent with the classification spectrum. The second phase, the tail phase from 50 days onward, is characterized by a slowly

evolving light curve with spectra that are dominated by CSM interaction. Although the r-band light curve continues to fade, albeit at a slower rate of about 0.6 mag per 100 days between days 50 and 251, the g-band light curve plateaus. This results in a $g-r$ colour change to blue (see bottom panel of Fig. 3), which—based on the spectra—is driven by the pseudo-continuum blueward of 5,700 Å. This Fe ii feature, typical for CSM-interaction-powered spectra, is well traced by the ZTF g band (4,100–5,500 Å). From 251 days onward, the light curve fades in all bands at a rate of about 1 mag per 100 days.

The transition between the two phases is well captured by the photometry at 50 days, when the decline in the g band is abruptly halted and changes to a plateau lasting around 200 days. This divergence of the g-band light curve from a smooth decline is probably the epoch in which CSM interaction starts contributing (substantially) to the light curve and in which the spectra start to look like those of SNe Ibn. But even though the late spectra may be similar to SNe Ibn, the light curve is unlike those of documented SNe Ibn. SNe Ibn are characterized by uniform, rapidly evolving blue light curves[105], peaking at $M_r \approx -19.5$. There is a handful of long-lived, slowly evolving SNe Ibn reported in the literature, but they are either much brighter than SN 2020eyj (refs. [106,107]) or have a much longer risetime[108]. None of the literature SNe Ibn show a long-duration (>300 days), slowly evolving light-curve tail such as that observed in SN 2020eyj. It is worth noting that there have been suggestions in the literature that some SNe Ibn may come from thermonuclear explosions, hidden by a dense CSM[109]. The discovery of SN 2020eyj seemingly supports that notion.

The post-peak decline rates and peak magnitudes of SNe Ia are strongly correlated (the Phillips relation[110]), with brighter (fainter) SNe Ia evolving slower (faster). We fit the first phase of the multiband light curves with SNooPy[111], to determine whether the width (stretch) of SN 2020eyj is consistent with the expected peak luminosity. The light curve of SN 2020eyj up to 50 days is well described by a SN Ia light curve with an adopted stretch of $s_{BV} = 1.2 \pm 0.1$ and an extinction of $E(B-V) = 0.5 \pm 0.1$ mag (adopting a total-to-selective extinction ratio $R_V = 2.0$), resulting in a peak magnitude approximately 0.06 mag fainter than expected from the Phillips relation. The required line-of-sight extinction is considerable but is

consistent with the host extinction of $E(B-V)=0.5{4}_{-0.12}^{+0.14}\,{\rm{mag}}$ derived from host galaxy Balmer lines (see ‘Host galaxy’ section). We apply the same fitting method to the light curve of PTF11kx, consisting of published and previously unpublished photometry. For PTF11kx, we adopt the same stretch factor of 1.2 and obtain an extinction of $E(B-V) = 0.27 \pm 0.02$ mag, consistent with the extinction $A_V \approx 0.5$ mag derived in ref. [15]. After correcting for the fitted host extinction, the resulting absolute-magnitude light curves of SN 2020eyj and PTF11kx are practically identical in the *g* and *r* bands for the first approximately 45 days, even though the fits are independent (Extended Data Fig. 1). The *r*-band light curves peak at $M_r \approx -19.3$ for both SNe, consistent with both SNe Ia and SNe Ia–CSM, although both SNe are on the fainter end of the sample of SNe Ia–CSM described in ref. [11]. From the light-curve fits, we obtain for SN 2020eyj risetimes in the *g* and *r* bands of 14 ± 2 and 16 ± 2 days since first detection, respectively. This is fast for a SN Ia (ref. [33]) but similar to PTF11kx (Extended Data Fig. 1).

An important caveat about the light-curve fit is that the intrinsic decline rate of SN 2020eyj could seem slower because of the contribution by CSM interaction. On the basis of the colour evolution of the light curve, we know from day 50 onward that the CSM contribution is notable, but it is reasonable to assume that some CSM interaction already contributes to the light curve at earlier epochs. This means that the stretch parameter we measure should be regarded as an upper limit and, as a result, so is the peak luminosity of the fit. SN 2020eyj, but also PTF11kx, are not typical SNe Ia, so the colours and peak magnitude could (to some extent) also be a property intrinsic to the class.

Bolometric light curve

The light curve of SN 2020eyj around peak has limited photometric coverage, in both wavelength and cadence, which hinders the construction of a precise, full bolometric light curve. Instead, we compute the bolometric light curve based on the SN Ia light-curve template fit obtained in the ‘Light-curve fits’ section, for epochs when the photometry (notably the *g* band) still matches well with the fitted light curve (up to 38 days after first detection; Extended Data Fig. 1). From the fitted optical light curves, we

flux calibrate, correct for host extinction and integrate the spectral time series from ref. [112] from the ultraviolet (UV) to the NIR (1,000–25,000 Å). For the tail phase, we integrate the Keck spectra at 131 and 251 days from 3,000 to 10,000 Å and apply a linear extrapolation in the UV to zero flux at 2,000 Å. There is little spectroscopic (Fig. 2) and colour (Fig. 3) evolution between the Keck spectrum at 251 days and the NOT spectrum at 328 days, so we extend the pseudo-bolometric light curve to the final photometric epoch at 383 days obtained with ALFOSC on the NOT assuming a constant bolometric correction applied to the *g*-band magnitude. Extended Data Fig. 6 shows the bolometric luminosity inferred from the template fit, the Keck spectra and the final photometric epoch. The template fit to the initial peak included considerable line-of-sight extinction of $E(B-V)=0.5$ mag (see 'Light-curve fits' section). To account for the possibility that SN 2020eyj may be intrinsically faint rather than a normal SN Ia substantially dust-extincted, we also include a bolometric light curve for $E(B-V)=0$. Depending on dust extinction, the total integrated energy radiated across the bolometric light curve amounts to 0.6–1.2 × 10^{50} erg.

Host galaxy

The host of SN 2020eyj is a faint and compact galaxy with designation SDSS J111147.15+292305.9 (Extended Data Fig. 4). We retrieved science-ready co-added images from the Galaxy Evolution Explorer (GALEX) general release 6/7 (ref. [113]), the Sloan Digital Sky Survey data release 9 (SDSS DR 9; ref. [114]) and the Panoramic Survey Telescope and Rapid Response System (Pan-STARRS, PS1) DR1 (ref. [56]) and measured the brightness of the host using LAMBDAR (Lambda Adaptive Multi-Band Deblending Algorithm in R; ref. [115]) and the methods described in ref. [116]. We augment this dataset with an optical *r*-band image obtained with ALFOSC on the NOT on 2 May 2022 and UV observations from Swift/UVOT from 27 April 2022. The photometry on the UVOT images was done with uvotsource in HEASoft and an aperture encircling the entire galaxy (aperture radius 8″). Extended Data Table 4 lists all measurements. We fit the host galaxy spectral energy distribution (SED) with the software package Prospector version 0.3 (ref. [117]) to determine the host galaxy properties. We assumed a Chabrier initial mass function[118] and approximated the star formation history (SFH) by a linearly increasing SFH

at early times followed by an exponential decline at late times (functional form $t \times \exp(-t/\tau)$, in which t is the age of the SFH episode and τ is the e-folding timescale). The model was attenuated with the model in ref. [119]. The priors were set identical to those in ref. [116]. The fit resulted in a low host-galaxy mass of $\log (M/{M}_{\odot })=7.7{9}_{-0.34}^{+0.15}$.

We obtained a host galaxy spectrum with LRIS/Keck after SN 2020eyj had faded from view, at 678 days. We identify unresolved ($\lesssim$150 km s^{-1}) host-galaxy lines in the spectrum, such as numerous Balmer lines in emission and absorption, [N ii] $\lambda\lambda$6548,6583, [O ii] $\lambda\lambda$3726,3729, [O iii] $\lambda\lambda$4959,5007 and [S ii] $\lambda\lambda$6716,6731, based on which we measure a redshift of $z = 0.0297 \pm 0.0001$. Adopting a flat cosmology with $H_0 = 70$ km s^{-1} Mpc^{-1} and $\Omega_M = 0.3$, this redshift corresponds to a luminosity distance to SN 2020eyj of 131.4 Mpc, which we use throughout this paper. Correcting for MW extinction, the adopted distance results in a host galaxy absolute magnitude of $M_r = -15.8$.

On the basis of the Balmer decrement measured in the host spectrum, we estimate a host extinction with $E(B-V)=0.5{4}_{-0.12}^{+0.14}\,{\rm{mag}}$, in agreement with the extinction obtained by fitting the light curves of SN 2020eyj with a SN Ia template (see ‘Light-curve fits’ section). The line ratios of $\log_{10}$([O iii] λ5007/Hβ) = 0.39 and $\log_{10}$([N ii] λ6583/Hα) = −1.26 put the host galaxy well into the regime of star-forming galaxies on the Baldwin–Phillips–Terlevich diagram[120]. Adopting the parameterization of the empirical oxygen calibration O3N2 by ref. [121], we obtain an oxygen abundance of $12 + \log(O/H) = 8.14 \pm 0.03$. Such a low oxygen abundance is expected for a low-mass galaxy[122].

The host properties of 16 SNe Ia–CSM were reported in refs. [11,123]. The authors concluded that all objects in their samples exploded in star-forming late-type galaxies (spiral and dwarf galaxies) with absolute magnitudes between $M_r = -20.6$ and −18.1 mag. The hosts of three SNe in this sample evaded detection in archival SDSS images, implying an absolute magnitude $M_r > -18$ mag. SN 2020eyj exploded in a markedly low-luminosity star-forming dwarf galaxy with an absolute r-band magnitude of only $M_r = -15.8$ mag (not corrected for host attenuation). However, the modelling of the host-galaxy SED and the Balmer decrement show non-negligible

attenuation of $0 < E(B-V) < 0.55$ mag (3σ confidence interval from host SED modelling) or $0.2 < E(B-V) < 1$ mag (3σ confidence interval from the Balmer decrement), which would alleviate the apparent extremeness of the host galaxy.

Dust properties

Infrared emission is commonly observed in interacting SNe and can be attributed to the condensation of dust in the SN ejecta or in the shocked CSM, or to pre-existing dust in the CSM that is heated radiatively by the SN emission or by the ejecta–CSM shock interaction[124,125,126,127]. The mid-infrared luminosity of SN 2020eyj is at a similar level as for the most infrared-luminous interacting SNe, such as type IIn– and Ia–CSM SNe, and at 4.5 μm is 6–10 magnitudes brighter than normal type Ia SNe and ≳4 magnitudes brighter than the type Ibn SN 2006jc (Extended Data Fig. 2, bottom panel).

Assuming optically thin dust, the flux F_ν can be written as[128]:

$${F}_{\nu }=\frac{{M}_{{\rm{d}}}\,{B}_{\nu }({T}_{{\rm{d}}}){\kappa }_{\nu }(a)}{{d}^{2}},$$
(1)

in which $M_{\rm d}$ is the mass of the dust, B_ν the Planck blackbody function, $T_{\rm d}$ the temperature of the dust, $\kappa_\nu(a)$ the dust absorption coefficient as a function of dust particle radius a and d is the distance to the observer. For simplicity, we assume a simple dust population of a single size composed entirely of amorphous carbon with a grain size of 0.1 μm with the corresponding absorption coefficient κ as in refs. [129,130] and fit the WISE data to obtain an estimate of the dust temperature and mass. We note that the dust mass depends on assumed grain size, which we cannot constrain on the available data. Varying the grain size from 0.01 to 1.0 μm changes the derived dust mass by an order of magnitude[129]. Over the first three epochs, up to 412 days, we derive a constant dust temperature of around 800 K (Extended Data Table 3), consistent with a lack of colour evolution in the WISE photometry (Fig. 3). Only at the fourth WISE epoch (614 days) do we see a marked decrease in the dust temperature, to 608 ± 23 K. These dust temperatures are

well below the expected evaporation temperature of dust (1,500 K for silicates and 1,900 K for graphite grains[127]). As well as the dust temperatures, we obtain dust mass estimates of $(1.8 \pm 0.3) \times 10^{-3}\, M_{\odot}$ to $(9.9 \pm 2.1) \times 10^{-3}\, M_{\odot}$ for the first and final WISE epochs, respectively (Extended Data Table 3). The dust mass estimated for the final epoch corresponds to a CSM mass of $1 \times (0.01/r_{dg})\, M_{\odot}$, in which r_{dg} is the dust-to-gas ratio. The total integrated energy emitted in the infrared is 9×10^{49} erg (Extended Data Table 3), which is similar to the integrated energy emitted in the optical (see 'Bolometric light curve' section).

In the case of optically thin dust that we consider here, the blackbody radius can be interpreted as a lower limit to the radius at which the dust resides. In the case of SN 2020eyj, the blackbody radius is $(2.5 \pm 0.2) \times 10^{16}$ cm in the first epoch and increases thereafter to $(6.4 \pm 0.6) \times 10^{16}$ cm at 614 days (Extended Data Table 3). Assuming a SN ejecta velocity of 10^4 km s^{-1}, by 59 days, the ejecta would only have travelled about 20% of the distance inferred from the blackbody fit at that epoch. Combined with the constant dust temperature, this suggests that the infrared emission of SN 2020eyj is dominated by pre-existing dust being radiatively heated by CSM interaction emission, as was the case in type Ia–CSM SN 2005gj (ref. [130]). Furthermore, because the dust reached a temperature of 800 K as early as 59 days and showed no notable evolution afterwards, it is unlikely that any surrounding dust was evaporated owing to the SN, because such hot dust would have dominated the infrared flux. For a peak SN luminosity of roughly 10^{43} erg s^{-1} (Extended Data Fig. 6), the dust evaporation radius is $R_{evap} = (0.34\text{–}2.6) \times 10^{17}$ cm, depending on dust grain size and composition[127]. The lack of dust at the sublimation temperature implies that the immediate region surrounding the SN was devoid of dust, much like the CSM-free cavity inferred from the SN light curve.

The He i and Hα emission-line profiles show the red wing being attenuated with time (Extended Data Fig. 3). Such an evolution in the line profiles has been interpreted to result from condensation of dust in the ejecta or the shocked CSM, obscuring the red wing of the emission line[126,131,132]. Similar line profiles have been observed in many SNe Ia–CSM[11] and in the prototypical type Ibn SN 2006jc, in which the evolution of the line profiles

was attributed to dust condensing in a cool dense shell produced by the interaction of the ejecta with CSM also producing a substantial infrared excess[125]. Notably, such line-profile evolution has also been observed in the He nova V445 Pup, which was attributed to dust obscuration within the shell[35]. In particular, for type Ia–CSM SN 2005gj, dust formation was inferred from line profiles[11], whereas the bulk of the infrared emission was also attributed to pre-existing dust[130]. Although the line asymmetry in the spectra of SN 2020eyj is consistent with dust formation, it must be noted that asymmetric line profiles can also arise from optical depth effects, for example, in SNe Ibn (ref. [20]). A substantial contribution to the infrared flux by newly formed dust is also not consistent with the lack of colour evolution in the light curve of SN 2020eyj from day 100 onward. The dust formation in SN 2006jc was accompanied by a reddening of the optical light curve[125], which we do not observe in SN 2020eyj past 100 days. So, we attribute the bright infrared counterpart of SN 2020eyj predominantly to pre-existing dust, similar to the conclusion drawn for the infrared counterpart of the prototypical type Ia–CSM SN 2002ic (ref. [124]).

CSM origin

Optically thick wind

Using progenitor models for the He star donor SN Ia channel from ref. [6], Moriya et al.[26] investigated the CSM properties resulting from this channel, in which accretion from a non-degenerate He star allows the accompanying WD to reach the Chandrasekhar limit. The study by Moriya et al.[26] focused on the low-circumstellar-density regime, in which the CSM properties in the WD + He star systems still adhere to the stringent CSM constraints imposed by radio non-detections of SNe Ia (refs. [4,5,133,134]). Here we explore if the models with sufficiently dense CSM, with a wind-like density profile ($\rho \propto r^{-2}$), can explain the interaction-powered light-curve tail of SN 2020eyj and the detections at radio wavelengths. To quantify the properties of the CSM, we fit the CSM-interaction-powered tail of the bolometric light curve using the analytical model from ref. [26] and use the resulting mass-transfer rates to fit the radio detections.

Extended Data Fig. 6 shows the bolometric light curve of SN 2020eyj, with the initial peak described by the SN Ia template fit (solid line), and for the tail phase the luminosities inferred from the Keck spectra at 131 and 251 days and the ALFOSC epoch at 383 days (see 'Light-curve fits' section). From the light curve described by the SN Ia component alone (solid and dotted lines), it is also clear that the late-time light curve of SN 2020eyj cannot be powered by ^{56}Ni decay, as the flux integrated across the Keck spectrum at 131 days is already at least ten times larger than what the radioactive decay delivers. Also plotted are the CSM-interaction model fits to the light-curve tail, for both $E(B-V)=0$ and 0.5 mag, as discussed in the 'Light-curve fits' section. Assuming a pre-SN wind velocity of 1,000 km s^{-1}, the CSM-powered tail of SN 2020eyj is consistent with mass-transfer rates between $10^{-3}\,M_\odot$ yr^{-1} ($E(B-V)=0$ mag) and $3\times10^{-2}\,M_\odot$ yr^{-1} ($E(B-V)=$ 0.5 mag), which is 1–2 orders of magnitude larger than that considered in the original study[26]. At these very high mass-transfer rates, the critical mass accretion rate by the WD is exceeded and the excess is ejected as an optically thick wind, resulting in an extended He envelope[26]. In the model, the forward shock reaches approximately 10^{17} cm in 800 days. If we assume a wind velocity of 1,000 km s^{-1}, the CSM mass within 10^{17} cm in the models range from 0.3 $M_\odot$ to 1 $M_\odot$, for $E(B-V)=0$ and 0.5 mag, respectively.

Extended Data Fig. 6 shows the wind model radio light curves fitted to the radio detections at 5.1 GHz, adopting $\epsilon_e=0.1$ and mass-transfer rates of $10^{-3}\,M_\odot$ yr^{-1} and $3\times10^{-2}\,M_\odot$ yr^{-1}, for $E(B-V)=0$ and 0.5 mag, respectively. We consider both synchrotron emission with synchrotron self-absorption and free–free absorption but note that, at the late phase of the radio detection, free–free absorption has only a minor impact. The radio light curve with an adopted mass-transfer rate of $10^{-3}\,M_\odot$ yr^{-1} is consistent with the radio detections of SN 2020eyj at 5.1 GHz, with microphysics parameter $\epsilon_B=1.7\times10^{-3}$. For the high-extinction scenario, with a mass-transfer rate of $3\times10^{-2}\,M_\odot$ yr^{-1}, the model fits when $\epsilon_B=1.5\times10^{-5}$. In either case, the late time evolution follows the observed power-law decline rate of the observed radio luminosity of $\beta=-1.6$, which is comparable with that for hydrogen-free SNe Ibc (ref. [135]).

It is worth noting that the bolometric light curve only extends to 400 days, whereas the first detection of SN 2020eyj at 5 GHz took place at 605 days. Furthermore, it has been argued that the mass-transfer rates associated with the optically thick wind phase ($>10^{-7}\,M_{\odot}\,{\rm yr}^{-1}$) do not lead to SNe Ia but rather to accretion-induced collapse of the WD (refs. [136,137]), although alternative wind models have been suggested to overcome this problem[138].

CSM shells

The CSM surrounding the H-rich analogue of SN 2020eyj, PTF11kx, was argued to be concentrated in shells[15]. Other SNe Ia have shown evidence for CSM concentrated in thin shells, albeit at distances (about 10^{16} cm) that no interaction with the ejecta is expected[139,140,141,142]. Shells have also been invoked for the configuration of the CSM in core-collapse H-rich type IIn SNe and typically attributed to ejection events by their massive progenitors. One noteworthy example is the well-studied SN 2014C, which transitioned from a stripped-envelope SN to a type IIn SN owing to interaction with a distant shell, and was detected in the radio[143,144]. Models for the radio emission of SNe Ia colliding with a constant-density shell of CSM have been previously presented in the literature, along with approximate functional forms to describe the evolution of the optically thick synchrotron light curve[145]. Because those models assume hydrogen-rich material, for our calculations, we modify $n_{\rm e}=\rho/m_{\rm p}$ to $n_{\rm e}=\rho/(2m_{\rm p})$; otherwise, we use the default parameters, notably $\epsilon_{\rm B}=0.1$. We explore shell models with a range of CSM masses $M_{\rm csm}=(0.01\text{–}1)\,M_{\odot}$ and interaction end times from $t_{\rm end}=$ 328 days (the spectrum that does not show prominent He i lines) to $t_{\rm end}=$ 763 days (the second radio detection)—in this model, interaction must have ended before the second radio detection for the radio emission to have declined between the two observations. We assume a shell inner radius of $R_{\rm in}=(30{,}000\ {\rm km\ s^{-1}})(50\ {\rm days})=1.3\times10^{16}$ cm to close the system of equations in the model; then, the ranges of $M_{\rm csm}$ and $t_{\rm end}$ correspond to a range of shell widths $\Delta R/R_{\rm in}=3.4\text{–}7.5$. For each model, we calculate the representative model error as ${\sigma }_{{\rm{mod}}}=\max \left(\left|{L}_{\nu ,{\rm{obs}}}({t}_{i})-{L}_{\nu ,{\rm{mod}}}({t}_{i})\right|/\Delta {L}_{\nu ,{\rm{obs}}}({t}_{i})\right)$, in which

subscripts ‘obs’ and ‘mod’ refer to observed and modelled values, respectively, L_ν is spectral luminosity and ΔL_ν is the error on the luminosity (flux error only; error in distance is not included). The best-fit model by this metric has $M_{csm} = 0.36\, M_\odot$ and $t_{end} = 665$ days, which is a very similar mass to what is found for PTF11kx based on analysis of its optical spectra[146]. We find that models with $\sigma_{mod} \leq 3$ have $t_{end} \approx (500–763)$ days and $M_{csm} \approx (0.2–0.5)\, M_\odot$, whereas those with $\sigma_{mod} \leq 1$ (that is, a better fit) have $t_{end} \gtrsim 580$ days and $M_{csm} \approx (0.3–0.4)\, M_\odot$. The best-fit shell model is shown in Fig. 4.

V445 Puppis

The nova outburst of V445 Pup in the year 2000 lacked any Balmer emission in the spectra of its ejecta, but instead was characterized by He and carbon emission lines[34,147], making it the first and so far only known He nova system. On the basis of light-curve modelling, a mass ($\geq 1.35\, M_\odot$) close to the Chandrasekhar limit was inferred for the WD in V445 Pup (ref. [36]), consistent with the observed high ejecta velocities up to 8,450 km s^{-1} (ref. [35]). Combined with a high mass-transfer rate $>10^{-7}\, M_\odot\, yr^{-1}$, in which half of the accreted matter remains on the WD (ref. [36]), V445 Pup is considered to be a prime candidate progenitor for the SD He + WD SN Ia progenitor channel.

On the basis of infrared spectra showing prominent carbon lines[34,148] and a rapid decline in the light curve of V445 Pup, it was shown that a carbon-rich thick dust shell must have formed in the nova ejecta[34,147]. High-resolution NIR images resolved the nova event into an expanding narrow bipolar shell with bulk velocities of about 6,700 km s^{-1} and a perpendicular central dust disk that strongly attenuates the optical He i emission lines arising from the receding shell[35]. Seven years after the outburst, the bipolar shell of V445 Pup, as imaged in the NIR, extended to around 10^{17} cm and the central dust torus had an outer radius (perpendicular to the lobes) of $\gtrsim 10^{16}$ cm (ref. [35]). An outer dust shell in a V445 Pup-like system could survive dust sublimation from a SN Ia explosion, depending on peak luminosity and grain composition[127]. A recent study of the long-lived radio evolution of V445 Pup showed that the system was continuously synchrotron luminous

for years after the outburst[39]. The synchrotron emission originated from the inner edge of the equatorial disk and was interpreted as interaction between a wind coming off the WD from nuclear burning and the surviving disk. The persistence of the disk through the nova outburst suggests that the disk is at least comparable in mass with the mass of the nova ejecta, which was estimated to be about $10^{-4}\,M_{\odot}$ (ref. [36]). In turn, the mass of the WD in V445 Pup, close to the Chandrasekhar limit, limits the ejecta mass in the system to not more than about $10^{-3}\,M_{\odot}$ (Fig. 7 in ref. [36]).

ISM

Radio emission can potentially arise from a SN Ia in the DD scenario as a result of interaction with the ISM. We have modelled the radio light curve from such a merger scenario in the same way as in refs. [31,134], that is, we assume that the supernova is the result of two merging WDs with masses 0.9 and 1.1 $M_{\odot}$, as described in ref. [149]. The outermost ejecta has a density slope $\propto \rho^{-n}$ with $n = 13$ (see ref. [31] for a discussion on n). The microphysics parameters are the standard values $\epsilon_e = 0.1$ and $\epsilon_B = 0.01$. The modelled radio emission increases with time (Fig. 4) and, to agree with the observed 5.1-GHz fluxes at 605 and 741 days, the ISM electron density has to be 660 cm^{-3} and 450 cm^{-3}, respectively, assuming fully ionized hydrogen and helium with He/H = 0.1. For $n = 13$ and fixed ϵ_e, the electron density scales roughly as \({{\epsilon }}_{{\rm{B}}}^{-0.74}\), so other ISM densities are possible accordingly. For a probable upper limit on ϵ_B of 0.1, the ISM density would be $n_e = 85$ cm^{-3} to fit the flux at the second epoch, and for ϵ_B of 0.001, $n_e = 2{,}570$ cm^{-3}. The increase in radio flux with time is opposite to what is observed and is a property for all our ISM models with $n > 7.1$. Lower n values are not expected[31] and the densities required in our ISM models are much higher than normal ISM densities. Moreover, for the $n = 13$, $\epsilon_B = 0.01$ model, in which $n_e = 450$ cm^{-3}, the modelled flux for the first epoch undershoots by 2σ (Fig. 4). In summary, our radio observations and their modelling argue strongly against an ISM scenario, which arises from a DD progenitor system. Furthermore, the observed strong helium lines are also at odds with an ISM scenario[150]. We therefore conclude that SN 2020eyj did not result from the thermonuclear runaway of a WD in a DD progenitor system, leaving the SD scenario as the only viable alternative.

Precursor search

The CSM surrounding SN 2020eyj could have originated from one or more novae, such as observed in V445 Pup. We investigate if a similar outburst at the location of SN 2020eyj can be found in ZTF data going back more than

2 years. The position of SN 2020eyj was observed 772 times (after quality cuts) in the *g*, *r* and *i* bands across 202 different nights in the final 2.29 years before the SN explosion. There are no notable pre-explosion detections in unbinned or binned light curves (1-day-long to 90-day-long bins) following the search method described in ref. [151]. When combining observations in week-long bins, we reach a median limiting absolute magnitude of −14.28 in the *r* band (−14.26 in the *g* band). We can, hence, rule out precursors that are brighter than −14 magnitude 21% of the time in the *r* band (16% of the time in the *g* band). Precursors brighter than magnitude −15 can be ruled out 49% of the time in the *r* band (39% for the *g* band) in the final 2.29 years before the SN. The nova outburst of V445 Pup peaked at $m_V = 8.6$ (ref. [152]), which—at a distance of 8.2 kpc (ref. [35])—equates to an absolute magnitude of $M_V = -1$, far below the detection threshold of the ZTF.

Data availability

The optical spectra of SN 2020eyj that support the findings of this study have been made available through the WISeREP archive (https://www.wiserep.org/object/14508). The ZTF photometry is listed in the Supplementary Information. Radio data from the electronic Multi-Element Radio Linked Interferometer Network (e-MERLIN) have been made available on the Zenodo repository with identifier https://doi.org/10.5281/zenodo.7665246. Data from the NEOWISE-R mission are available from the NASA/IPAC Infrared Science Archive with identifier https://doi.org/10.26131/IRSA124. Photometry from the Asteroid Terrestrial-impact Last Alert System (ATLAS) were obtained from a public source (https://fallingstar-data.com/forcedphot/).

Code availability

On request, the corresponding author will provide the code used to produce the figures. The details of the models used in the 'Light-curve fits' and 'Optically thick wind' sections can be found in refs. [26,31,145] and references therein.

References

1. Whelan, J. & Iben, I.Jr Binaries and supernovae of Type I. *Astrophys. J.* **186**, 1007–1014 (1973).

2. Seaquist, E. R. & Taylor, A. R. The collective radio properties of symbiotic stars. *Astrophys. J.* **349**, 313–327 (1990).

3. Hachisu, I., Kato, M. & Nomoto, K. A new model for progenitor systems of Type Ia supernovae. *Astrophys. J. Lett.* **470**, L97 (1996).

4. Horesh, A. et al. Early radio and X-ray observations of the youngest nearby Type Ia supernova PTF 11kly (SN 2011fe). *Astrophys. J.* **746**, 21 (2012).

5. Pérez-Torres, M. A. et al. Constraints on the progenitor system and the environs of SN 2014J from deep radio observations. *Astrophys. J.* **792**, 38 (2014).

6. Wang, B., Meng, X., Chen, X. & Han, Z. The helium star donor channel for the progenitors of Type Ia supernovae. *Mon. Not. R. Astron. Soc.* **395**, 847–854 (2009).

7. Ruiter, A. J., Belczynski, K. & Fryer, C. Rates and delay times of Type Ia supernovae. *Astrophys. J.* **699**, 2026–2036 (2009).

8. Dahiwale, A. & Fremling, C. ZTF transient classification report for 2020-04-02. Transient Name Server Classification Report 2020-947, 1 (2020).

9. Foley, R. J. et al. SN 2006jc: a Wolf-Rayet star exploding in a dense He-rich circumstellar medium. *Astrophys. J. Lett.* **657**, L105–L108 (2007).

10. Pastorello, A. et al. A giant outburst two years before the core-collapse of a massive star. *Nature* **447**, 829–832 (2007).

11. Silverman, J. M. et al. Type Ia supernovae strongly interacting with their circumstellar medium. *Astrophys. J. Suppl. Ser.* **207**, 3 (2013).

12. Smith, N. in *Handbook of Supernovae* (eds Alsabti, A. & Murdin, P.) 403–429 (Springer, 2017).

13. Leloudas, G. et al. Supernova spectra below strong circumstellar interaction. *Astron. Astrophys.* **574**, A61 (2015).

14. Hamuy, M. et al. An asymptotic-giant-branch star in the progenitor system of a type Ia supernova. *Nature* **424**, 651–654 (2003).

15. Dilday, B. et al. PTF 11kx: a Type Ia supernova with a symbiotic nova progenitor. *Science* **337**, 942–945 (2012).

16. Graham, M. L. et al. Delayed circumstellar interaction for Type Ia SN 2015cp revealed by an HST ultraviolet imaging survey. *Astrophys. J.* **871**, 62 (2019).

17. Branch, D. et al. Comparative direct analysis of Type Ia supernova spectra. II. Maximum light. *Publ. Astron. Soc. Pac.* **118**, 560–571 (2006).

18. Wilk, K., Hillier, D. J. & Dessart, L. Ejecta mass diagnostics of Type Ia supernovae. *Mon. Not. R. Astron. Soc.* **474**, 3187–3211 (2018).

19. Pastorello, A. et al. Massive stars exploding in a He-rich circumstellar medium – I. Type Ibn (SN 2006jc-like) events. *Mon. Not. R. Astron. Soc.* **389**, 113–130 (2008).

20. Dessart, L., Hillier, D. J. & Kuncarayakti, H. Helium stars exploding in circumstellar material and the origin of Type Ibn supernovae. *Astron. Astrophys.* **658**, A130 (2022).

21. Boyle, A., Sim, S. A., Hachinger, S. & Kerzendorf, W. Helium in double-detonation models of type Ia supernovae. *Astron. Astrophys.* **599**, A46 (2017).

22. Kromer, M. et al. Double-detonation sub-Chandrasekhar supernovae: synthetic observables for minimum helium shell mass models. *Astrophys. J.* **719**, 1067–1082 (2010).

23. Yoon, S. C. & Langer, N. The first binary star evolution model producing a Chandrasekhar mass white dwarf. *Astron. Astrophys.* **412**, L53–L56 (2003).

24. Iben, I.Jr & Tutukov, A. V. Helium-accreting degenerate dwarfs as presupernovae and scenarios for the ultrasoft X-ray sources. *Astrophys. J.* **431**, 264 (1994).

25. Li, W. et al. Exclusion of a luminous red giant as a companion star to the progenitor of supernova SN 2011fe. *Nature* **480**, 348–350 (2011).

26. Moriya, T. J., Liu, D., Wang, B. & Liu, Z.-W. Circumstellar properties of Type Ia supernovae from the helium star donor channel. *Mon. Not. R. Astron. Soc.* **488**, 3949–3956 (2019).

27. Li, W. et al. SN 2002cx: the most peculiar known Type Ia supernova. *Publ. Astron. Soc. Pac.* **115**, 453–473 (2003).

28. McCully, C. et al. A luminous, blue progenitor system for the type Iax supernova 2012Z. *Nature* **512**, 54–56 (2014).

29. Valenti, S. et al. A low-energy core-collapse supernova without a hydrogen envelope. *Nature* **459**, 674–677 (2009).

30. Nomoto, K. Accreting white dwarf models for type I supernovae. II. Off-center detonation supernovae. *Astrophys. J.* **257**, 780–792 (1982).

31. Kundu, E., Lundqvist, P., Pérez-Torres, M. A., Herrero-Illana, R. & Alberdi, A. Constraining magnetic field amplification in SN shocks using radio observations of SNe 2011fe and 2014J. *Astrophys. J.* **842**, 17 (2017).

32. Wood-Vasey, W. M., Wang, L. & Aldering, G. Photometry of SN 2002ic and implications for the progenitor mass-loss history.

Astrophys. J. **616**, 339–345 (2004).

33. Miller, A. A. et al. ZTF early observations of Type Ia supernovae. II. First light, the initial rise, and time to reach maximum brightness. *Astrophys. J.* **902**, 47 (2020).

34. Ashok, N. M. & Banerjee, D. P. K. The enigmatic outburst of V445 Puppis - a possible helium nova? *Astron. Astrophys.* **409**, 1007–1015 (2003).

35. Woudt, P. A. et al. The expanding bipolar shell of the helium nova V445 Puppis. *Astrophys. J.* **706**, 738–746 (2009).

36. Kato, M., Hachisu, I., Kiyota, S. & Saio, H. Helium nova on a very massive white dwarf: a revised light-curve model of V445 Puppis (2000). *Astrophys. J.* **684**, 1366–1373 (2008).

37. Soker, N., Kashi, A., García-Berro, E., Torres, S. & Camacho, J. Explaining the Type Ia supernova PTF 11kx with a violent prompt merger scenario. *Mon. Not. R. Astron. Soc.* **431**, 1541–1546 (2013).

38. Moore, K. & Bildsten, L. Circumstellar shell formation in symbiotic recurrent novae. *Astrophys. J.* **761**, 182 (2012).

39. Nyamai, M. M. et al. Radio light curves and imaging of the helium nova V445 Puppis reveal seven years of synchrotron emission. *Mon. Not. R. Astron. Soc.* **501**, 1394–1412 (2021).

40. Nomoto, K. & Leung, S.-C. Single degenerate models for Type Ia supernovae: progenitor's evolution and nucleosynthesis yields. *Space Sci. Rev.* **214**, 67 (2018).

41. Wang, B., Chen, X., Meng, X. & Han, Z. Evolving to Type Ia supernovae with short delay times. *Astrophys. J.* **701**, 1540–1546 (2009).

42. Tonry, J. L. et al. ATLAS: a high-cadence all-sky survey system. *Publ. Astron. Soc. Pac.* **130**, 064505 (2018).

43. Smith, K. W. et al. Design and operation of the ATLAS transient science server. *Publ. Astron. Soc. Pac.* **132**, 085002 (2020).

44. Tonry, J. et al. ATLAS transient discovery report for 2020-03-24. Transient Name Server Discovery Report 2020-863, 1 (2020).

45. Bellm, E. C. et al. The Zwicky Transient Facility: system overview, performance, and first results. *Publ. Astron. Soc. Pac.* **131**, 018002 (2019).

46. Graham, M. J. et al. The Zwicky Transient Facility: science objectives. *Publ. Astron. Soc. Pac.* **131**, 078001 (2019).

47. Bellm, E. C. et al. The Zwicky Transient Facility: surveys and scheduler. *Publ. Astron. Soc. Pac.* **131**, 068003 (2019).

48. Dekany, R. et al. The Zwicky Transient Facility: observing system. *Publ. Astron. Soc. Pac.* **132**, 038001 (2020).

49. Masci, F. J. et al. The Zwicky Transient Facility: data processing, products, and archive. *Publ. Astron. Soc. Pac.* **131**, 018003 (2019).

50. Zackay, B., Ofek, E. O. & Gal-Yam, A. Proper image subtraction—optimal transient detection, photometry, and hypothesis testing. *Astrophys. J.* **830**, 27 (2016).

51. Yao, Y. et al. ZTF early observations of Type Ia supernovae. I. Properties of the 2018 sample. *Astrophys. J.* **886**, 152 (2019).

52. Steele, I. A. et al. The Liverpool Telescope: performance and first results. *Proc. SPIE* **5489**, 679–692 (2004).

53. Fremling, C. et al. PTF12os and iPTF13bvn. Two stripped-envelope supernovae from low-mass progenitors in NGC 5806. *Astron. Astrophys.* **593**, A68 (2016).

54. De, K. et al. The Zwicky Transient Facility census of the local universe. I. Systematic search for calcium-rich gap transients reveals three related spectroscopic subclasses. *Astrophys. J.* **905**, 58 (2020).

55. Smith, K. W. et al. Design and operation of the ATLAS Transient Science Server. *Publ. Astron. Soc. Pac.* **132**, 085002 (2020).

56. Chambers, K. C. et al. The Pan-STARRS1 surveys. Preprint at https://arxiv.org/abs/1612.05560 (2016).

57. Schlafly, E. F. & Finkbeiner, D. P. Measuring reddening with Sloan Digital Sky Survey stellar spectra and recalibrating SFD. *Astrophys. J.* **737**, 103 (2011).

58. Cardelli, J. A., Clayton, G. C. & Mathis, J. S. The relationship between infrared, optical, and ultraviolet extinction. *Astrophys. J.* **345**, 245–256 (1989).

59. Blagorodnova, N. et al. The SED Machine: a robotic spectrograph for fast transient classification. *Publ. Astron. Soc. Pac.* **130**, 035003 (2018).

60. Cenko, S. B. et al. The automated Palomar 60 inch telescope. *Publ. Astron. Soc. Pac.* **118**, 1396–1406 (2006).

61. Rigault, M. et al. Fully automated integral field spectrograph pipeline for the SEDMachine: pysedm. *Astron. Astrophys.* **627**, A115 (2019).

62. Lezmy, J., Copin, Y., Rigault, M., Smith, M. & Neill, J. D. HyperGal: hyperspectral scene modeling for supernova typing with the SED Machine integral field spectrograph. *Astron. Astrophys.* **668**, A43 (2022).

63. Oke, J. B. et al. The Keck low-resolution imaging spectrometer. *Publ. Astron. Soc. Pac.* **107**, 375 (1995).

64. Djupvik, A. A. & Andersen, J. in *Highlights of Spanish Astrophysics V. Astrophysics and Space Science Proceedings* (eds Diego, J., Goicoechea, L., González-Serrano, J. & Gorgas, J.) 211–218 (Springer, 2010).

65. Perley, D. A. Fully automated reduction of longslit spectroscopy with the Low Resolution Imaging Spectrometer at the Keck Observatory. *Publ. Astron. Soc. Pac.* **131**, 084503 (2019).

66. Prochaska, J. et al. PypeIt: the Python spectroscopic data reduction pipeline. *J. Open Source Softw.* **5**, 2308 (2020).

67. Prochaska, J. X. et al. pypeit/PypeIt: release 1.0.0. *Zenodo* https://zenodo.org/record/3743493 (2020).

68. Yaron, O. & Gal-Yam, A. WISeREP—an interactive supernova data repository. *Publ. Astron. Soc. Pac.* **124**, 668–681 (2012).

69. Chugai, N. N. Circumstellar interaction in type Ibn supernovae and SN 2006jc. *Mon. Not. R. Astron. Soc.* **400**, 866–874 (2009).

70. Kiewe, M. et al. Caltech Core-Collapse Project (CCCP) observations of Type IIn supernovae: typical properties and implications for their progenitor stars. *Astrophys. J.* **744**, 10 (2012).

71. Smith, N. et al. SN 2011hw: helium-rich circumstellar gas and the luminous blue variable to Wolf–Rayet transition in supernova progenitors. *Mon. Not. R. Astron. Soc.* **426**, 1905–1915 (2012).

72. Stritzinger, M. et al. Multi-wavelength observations of the enduring Type IIn supernovae 2005ip and 2006jd. *Astrophys. J.* **756**, 173 (2012).

73. Pastorello, A. et al. Massive stars exploding in a He-rich circumstellar medium – IV. Transitional Type Ibn supernovae. *Mon. Not. R. Astron. Soc.* **449**, 1921–1940 (2015).

74. Pastorello, A. et al. Massive stars exploding in a He-rich circumstellar medium – II. The transitional case of SN 2005la. *Mon. Not. R. Astron. Soc.* **389**, 131–140 (2008).

75. Botyánszki, J., Kasen, D. & Plewa, T. Multidimensional models of Type Ia supernova nebular spectra: strong emission lines from stripped

companion gas rule out classic single-degenerate systems. *Astrophys. J. Lett.* **852**, L6 (2018).

76. Dessart, L., Leonard, D. C. & Prieto, J. L. Spectral signatures of H-rich material stripped from a non-degenerate companion by a Type Ia supernova. *Astron. Astrophys.* **638**, A80 (2020).

77. Pan, K.-C., Ricker, P. M. & Taam, R. E. Impact of Type Ia supernova ejecta on a helium-star binary companion. *Astrophys. J.* **715**, 78–85 (2010).

78. Thévenot, M., Kabatnik, M. & Gantier, J. M. Supernovae detected in NEOWISE-R 2021. Transient Name Server AstroNote 2021-212, 1 (2021).

79. Mainzer, A. et al. Initial performance of the NEOWISE reactivation mission. *Astrophys. J.* **792**, 30 (2014).

80. Kool, E. C. et al. AT 2017gbl: a dust obscured TDE candidate in a luminous infrared galaxy. *Mon. Not. R. Astron. Soc.* **498**, 2167–2195 (2020).

81. Moldon, J. eMCP: e-MERLIN CASA pipeline. Astrophysics Source Code Library, record ascl:2109.006 (2021).

82. Offringa, A. R. et al. WSCLEAN: an implementation of a fast, generic wide-field imager for radio astronomy. *Mon. Not. R. Astron. Soc.* **444**, 606–619 (2014).

83. Gehrels, N. et al. The Swift gamma-ray burst mission. *Astrophys. J.* **611**, 1005–1020 (2004).

84. Burrows, D. N. et al. The Swift X-Ray Telescope. *Space Sci. Rev.* **120**, 165–195 (2005).

85. Evans, P. A. et al. An online repository of Swift/XRT light curves of γ-ray bursts. *Astron. Astrophys.* **469**, 379–385 (2007).

86. Evans, P. A. et al. Methods and results of an automatic analysis of a complete sample of Swift-XRT observations of GRBs. *Mon. Not. R. Astron. Soc.* **397**, 1177–1201 (2009).

87. HI4PI Collaboration et al. HI4PI: a full-sky H I survey based on EBHIS and GASS. *Astron. Astrophys.* **594**, A116 (2016).

88. Bochenek, C. D. et al. X-ray emission from SN 2012ca: a Type Ia-CSM supernova explosion in a dense surrounding medium. *Mon. Not. R. Astron. Soc.* **473**, 336–344 (2018).

89. Fremling, C. et al. SNIascore: deep-learning classification of low-resolution supernova spectra. *Astrophys. J. Lett.* **917**, L2 (2021).

90. Blondin, S. & Tonry, J. L. Determining the type, redshift, and age of a supernova spectrum. *Astrophys. J.* **666**, 1024–1047 (2007).

91. Howell, D. A. et al. Gemini spectroscopy of supernovae from the Supernova Legacy Survey: improving high-redshift supernova selection and classification. *Astrophys. J.* **634**, 1190–1201 (2005).

92. Modjaz, M. et al. Optical spectra of 73 stripped-envelope core-collapse supernovae. *Astron. J.* **147**, 99 (2014).

93. Pastorello, A. et al. ESC and KAIT observations of the transitional Type Ia SN 2004eo. *Mon. Not. R. Astron. Soc.* **377**, 1531–1552 (2007).

94. Vinkó, J. et al. The Type Ia supernova 2001V in NGC 3987. *Astron. Astrophys.* **397**, 115–120 (2003).

95. Nomoto, K. et al. A carbon–oxygen star as progenitor of the type Ic supernova 1994I. *Nature* **371**, 227–229 (1994).

96. Sasaki, M. et al. Optical spectra of the supernova 1994I in M51 around the maximum light phase. *Publ. Astron. Soc. Jpn.* **46**, L187–L190 (1994).

97. Wheeler, J. C. et al. SN 1994I in M51 and the nature of type Ibc supernovae. *Astrophys. J. Lett.* **436**, L135–L138 (1994).

98. Filippenko, A. V. et al. The Type Ic supernova 1994I in M51: detection of helium and spectral evolution. *Astrophys. J. Lett.* **450**, L11 (1995).

99. Wang, X. et al. Improved distances to Type Ia supernovae with two spectroscopic subclasses. *Astrophys. J. Lett.* **699**, L139–L143 (2009).

100. Folatelli, G. et al. Spectroscopy of Type Ia supernovae by the Carnegie Supernova Project. *Astrophys. J.* **773**, 53 (2013).

101. Silverman, J. M., Kong, J. J. & Filippenko, A. V. Berkeley Supernova Ia Program – II. Initial analysis of spectra obtained near maximum brightness. *Mon. Not. R. Astron. Soc.* **425**, 1819–1888 (2012).

102. Liu, Y.-Q., Modjaz, M., Bianco, F. B. & Graur, O. Analyzing the largest spectroscopic data set of stripped supernovae to improve their identifications and constrain their progenitors. *Astrophys. J.* **827**, 90 (2016).

103. Fremling, C. et al. Oxygen and helium in stripped-envelope supernovae. *Astron. Astrophys.* **618**, A37 (2018).

104. Fox, O. D. et al. On the nature of Type IIn/Ia-CSM supernovae: optical and near-infrared spectra of SN 2012ca and SN 2013dn. *Mon. Not. R. Astron. Soc.* **447**, 772–785 (2015).

105. Hosseinzadeh, G. et al. Type Ibn supernovae show photometric homogeneity and spectral diversity at maximum light. *Astrophys. J.* **836**, 158 (2017).

106. Pastorello, A. et al. Massive stars exploding in a He-rich circumstellar medium – V. Observations of the slow-evolving SN Ibn OGLE-2012-SN-006. *Mon. Not. R. Astron. Soc.* **449**, 1941–1953 (2015).

107. Kool, E. C. et al. SN 2020bqj: a Type Ibn supernova with a long-lasting peak plateau. *Astron. Astrophys.* **652**, A136 (2021).

108. Karamehmetoglu, E. et al. OGLE-2014-SN-131: a long-rising Type Ibn supernova from a massive progenitor. *Astron. Astrophys.* **602**, A93

(2017).

109. Hosseinzadeh, G. et al. Type Ibn supernovae may not all come from massive stars. *Astrophys. J. Lett.* **871**, L9 (2019).

110. Phillips, M. M. The absolute magnitudes of Type IA supernovae. *Astrophys. J. Lett.* **413**, L105 (1993).

111. Burns, C. SNooPy. *Carnegie Science* https://users.obs.carnegiescience.edu/cburns/SNooPyDocs/html/ (2015).

112. Hsiao, E. Y. et al. K-corrections and spectral templates of Type Ia supernovae. *Astrophys. J.* **663**, 1187–1200 (2007).

113. Martin, D. C. et al. The Galaxy Evolution Explorer: a space ultraviolet survey mission. *Astrophys. J.* **619**, L1 (2005).

114. Ahn, C. P. et al. The ninth data release of the Sloan Digital Sky Survey: first spectroscopic data from the SDSS-III Baryon Oscillation Spectroscopic Survey. *Astrophys. J. Suppl. Ser.* **203**, 21 (2012).

115. Wright, A. H. et al. Galaxy And Mass Assembly: accurate panchromatic photometry from optical priors using LAMBDAR. *Mon. Not. R. Astron. Soc.* **460**, 765–801 (2016).

116. Schulze, S. et al. The Palomar Transient Factory core-collapse supernova host-galaxy sample. I. Host-galaxy distribution functions and environment dependence of core-collapse supernovae. *Astrophys. J. Suppl. Ser.* **255**, 29 (2021).

117. Johnson, B. D., Leja, J., Conroy, C. & Speagle, J. S. Stellar population inference with Prospector. *Astrophys. J. Suppl. Ser.* **254**, 22 (2021).

118. Chabrier, G. Galactic stellar and substellar initial mass function. *Publ. Astron. Soc. Pac.* **115**, 763 (2003).

119. Calzetti, D. et al. The dust content and opacity of actively star-forming galaxies. *Astrophys. J.* **533**, 682–695 (2000).

120. Baldwin, J. A., Phillips, M. M. & Terlevich, R. Classification parameters for the emission-line spectra of extragalactic objects. *Publ. Astron. Soc. Pac.* **93**, 5–19 (1981).

121. Marino, R. A. et al. The O3N2 and N2 abundance indicators revisited: improved calibrations based on CALIFA and T_e-based literature data. *Astron. Astrophys.* **559**, A114 (2013).

122. Sánchez, S. F. et al. The mass-metallicity relation revisited with CALIFA. *Mon. Not. R. Astron. Soc.* **469**, 2121–2140 (2017).

123. Prieto, J. L. et al. A study of the Type Ia/IIn supernova 2005gj from X-ray to the infrared: paper I. Preprint at https://arxiv.org/abs/0706.4088 (2007).

124. Kotak, R., Meikle, W. P. S., Adamson, A. & Leggett, S. K. On the nature of the circumstellar medium of the remarkable Type Ia/IIn supernova SN 2002ic. *Mon. Not. R. Astron. Soc.* **354**, L13–L17 (2004).

125. Mattila, S. et al. Massive stars exploding in a He-rich circumstellar medium – III. SN 2006jc: infrared echoes from new and old dust in the progenitor CSM. *Mon. Not. R. Astron. Soc.* **389**, 141–155 (2008).

126. Fox, O. D. et al. A Spitzer survey for dust in Type IIn supernovae. *Astrophys. J.* **741**, 7 (2011).

127. Fransson, C. et al. High-density circumstellar interaction in the luminous Type IIn SN 2010jl: the first 1100 days. *Astrophys. J.* **797**, 118 (2014).

128. Hildebrand, R. H. The determination of cloud masses and dust characteristics from submillimetre thermal emission. *Q. J. R. Astron. Soc.* **24**, 267–282 (1983).

129. Fox, O. D. et al. Disentangling the origin and heating mechanism of supernova dust: late-time Spitzer spectroscopy of the Type IIn SN 2005ip. *Astrophys. J.* **725**, 1768–1778 (2010).

130. Fox, O. D. & Filippenko, A. V. The late-time rebrightening of Type Ia SN 2005gj in the mid-infrared. *Astrophys. J. Lett.* **772**, L6 (2013).

131. Pozzo, M. et al. On the source of the late-time infrared luminosity of SN 1998S and other Type II supernovae. *Mon. Not. R. Astron. Soc.* **352**, 457–477 (2004).

132. Smith, N. et al. Systematic blueshift of line profiles in the Type IIn supernova 2010jl: evidence for post-shock dust formation? *Astron. J.* **143**, 17 (2012).

133. Chomiuk, L. et al. A deep search for prompt radio emission from thermonuclear supernovae with the Very Large Array. *Astrophys. J.* **821**, 119 (2016).

134. Lundqvist, P. et al. The deepest radio observations of nearby SNe Ia: constraining progenitor types and optimizing future surveys. *Astrophys. J.* **890**, 159 (2020).

135. Weiler, K. W., Panagia, N., Montes, M. J. & Sramek, R. A. Radio emission from supernovae and gamma-ray bursters. *Annu. Rev. Astron. Astrophys.* **40**, 387–438 (2002).

136. Wang, B., Podsiadlowski, P. & Han, Z. He-accreting carbon-oxygen white dwarfs and Type Ia supernovae. *Mon. Not. R. Astron. Soc.* **472**, 1593–1599 (2017).

137. Wong, T. L. S. & Schwab, J. Evolution of helium star-white dwarf binaries leading up to thermonuclear supernovae. *Astrophys. J.* **878**, 100 (2019).

138. Meng, X. & Podsiadlowski, P. A common-envelope wind model for Type Ia supernovae – I. Binary evolution and birth rate. *Mon. Not. R. Astron. Soc.* **469**, 4763–4787 (2017).

139. Patat, F. et al. Detection of circumstellar material in a normal type Ia supernova. *Science* **317**, 924–926 (2007).

140. Simon, J. D. et al. Constraints on circumstellar material around the Type Ia supernova 2007af. *Astrophys. J.* **671**, L25–L28 (2007).

141. Maguire, K. et al. A statistical analysis of circumstellar material in Type Ia supernovae. *Mon. Not. R. Astron. Soc.* **436**, 222–240 (2013).

142. Sternberg, A. et al. Multi-epoch high-spectral-resolution observations of neutral sodium in 14 Type Ia supernovae. *Mon. Not. R. Astron. Soc.* **443**, 1849–1860 (2014).

143. Milisavljevic, D. et al. Metamorphosis of SN 2014C: delayed interaction between a hydrogen poor core-collapse supernova and a nearby circumstellar shell. *Astrophys. J.* **815**, 120 (2015).

144. Margutti, R. et al. Ejection of the massive hydrogen-rich envelope timed with the collapse of the stripped SN 2014C. *Astrophys. J.* **835**, 140 (2017).

145. Harris, C. E., Chomiuk, L. & Nugent, P. E. Tumbling dice: radio constraints on the presence of circumstellar shells around Type Ia supernovae with impact near maximum light. *Astrophys. J.* **912**, 23 (2021).

146. Graham, M. L. et al. PTF11kx: a Type Ia supernova with hydrogen emission persisting after 3.5 years. *Astrophys. J.* **843**, 102 (2017).

147. Kato, M. & Hachisu, I. V445 Puppis: helium nova on a massive white dwarf. *Astrophys. J.* **598**, L107–L110 (2003).

148. Iijima, T. & Nakanishi, H. Spectroscopic observations of the first helium nova V445 Puppis. *Astron. Astrophys.* **482**, 865–877 (2008).

149. Pakmor, R. et al. Normal Type Ia supernovae from violent mergers of white dwarf binaries. *Astrophys. J. Lett.* **747**, L10 (2012).

150. Osterbrock, D. E. & Ferland, G. J. *Astrophysics of Gaseous Nebulae and Active Galactic Nuclei* (University Science Books, 2006).

151. Strotjohann, N. L. et al. Bright, months-long stellar outbursts announce the explosion of interaction-powered supernovae. *Astrophys. J.* **907**, 99 (2021).

152. Kato, T., Kanatsu, K., Takamizawa, K., Takao, A. & Stubbings, R. Possible nova in Puppis. *IAU Circular* **7552**, 1 (2000).

153. Kasliwal, M. M. et al. The GROWTH Marshal: a dynamic science portal for time-domain astronomy. *Publ. Astron. Soc. Pac.* **131**, 038003 (2019).

154. Szalai, T. et al. Spitzer's last look at extragalactic explosions: long-term evolution of interacting supernovae. *Astrophys. J.* **919**, 17 (2021).

155. Johansson, J. et al. Spitzer observations of SN 2014J and properties of mid-IR emission in Type Ia supernovae. *Mon. Not. R. Astron. Soc.* **466**, 3442–3449 (2017).

Acknowledgements

We thank L. Dessart, M. Barlow and J. Nordin for helpful feedback and discussions and T. Szalai for providing us with their mid-infrared Spitzer light curves. E.C.K. acknowledges support from the G.R.E.A.T. research environment, financed by Vetenskapsrådet, the Swedish Research Council, project number 2016-06012; the research project grant 'Understanding the Dynamic Universe' financed by the Knut and Alice Wallenberg Foundation under Dnr KAW 2018.0067; and The Wenner-Gren Foundations.J.M. and M.P.-T. acknowledge financial support from the grant CEX2021-001131-S, funded by MCIN/AEI/ 10.13039/501100011033, and from the grant IAA4SKA (ref. R18-RT-3082) from the Economic Transformation, Industry, Knowledge and Universities Council of the Regional Government of Andalusia and the European Regional Development Fund from the European Union. M.P.-T also acknowledges financial support through grant PID2020-117404GB-C21, funded by MCIN/AEI/ 10.13039/501100011033. J.M. also acknowledges financial support from the grant PID2021-123930OB-C21 funded by MCIN/AEI/ 10.13039/501100011033, by "ERDF A way of making Europe" and by the "European Union". J.M. and

M.P.-T. acknowledge the Spanish Prototype of an SRC (SPSRC) service and support financed by the Spanish Ministry of Science, Innovation and Universities, by the Regional Government of Andalusia, by the European Regional Development Funds and by the European Union NextGenerationEU/PRTR. T.J.M. is supported by the Grants-in-Aid for Scientific Research of the Japan Society for the Promotion of Science (JP20H00174, JP21K13966, JP21H04997). L.C. and C.H. acknowledge support from NSF grants AST-1751874, AST-1907790 and AST-2107070. S.M. acknowledges support from the Academy of Finland project 350458. The research of A.G.-Y. is supported by the EU through European Research Council (ERC) grant no. 725161, the ISF GW excellence centre, an IMOS space infrastructure grant and BSF/Transformative and GIF grants, as well as the André Deloro Institute for Advanced Research in Space and Optics, the Schwartz/Reisman Collaborative Science Program and the Norman E Alexander Family M Foundation ULTRASAT Data Center Fund, The Kimmel Center for Planetary Sciences, Minerva and Yeda-Sela; A.G.-Y. is the incumbent of the Arlyn Imberman Professorial Chair. N.L.S. is financed by the Deutsche Forschungsgemeinschaft (DFG, German Research Foundation) through the Walter Benjamin programme—461903330. K.M. is supported by H2020 ERC Starting Grant no. 758638 (SUPERSTARS). E.R. has received funding from the ERC under the European Union's Horizon 2020 research and innovation programme (grant agreement no 759194—USNAC). Based on observations obtained with the Samuel Oschin Telescope 48-in. and the 60-in. Telescope at the Palomar Observatory as part of the Zwicky Transient Facility (ZTF) project. The ZTF is supported by the National Science Foundation under grant no. AST-2034437 and a collaboration including Caltech, IPAC, the Weizmann Institute of Science, the Oskar Klein Centre at Stockholm University, the University of Maryland, Deutsches Elektronen-Synchrotron and Humboldt University, the TANGO Consortium of Taiwan, the University of Wisconsin at Milwaukee, Trinity College Dublin, Lawrence Livermore National Laboratories, IN2P3, France, the University of Warwick, the University of Bochum and Northwestern University. Operations are conducted by COO, IPAC and UW. This work was supported by the GROWTH Marshal project[153] financed by the National Science Foundation under grant no. 1545949. SED Machine is based on work supported by the National Science Foundation under grant no. 1106171. The ZTF forced-photometry

service was financed under the Heising-Simons Foundation grant no. 12540303 (principal investigator: M. Graham). Based on observations made with the Nordic Optical Telescope, owned in collaboration by the University of Turku and Aarhus University, and operated jointly by Aarhus University, the University of Turku and the University of Oslo, representing Denmark, Finland and Norway, the University of Iceland and Stockholm University at the Observatorio del Roque de los Muchachos, La Palma, Spain, of the Instituto de Astrofisica de Canarias. The data presented here were obtained in part with ALFOSC, which is provided by the Instituto de Astrofisica de Andalucia (IAA) under a joint agreement with the University of Copenhagen and NOT. The Liverpool Telescope is operated on the island of La Palma by Liverpool John Moores University in the Spanish Observatorio del Roque de los Muchachos of the Instituto de Astrofisica de Canarias with financial support from the UK Science and Technology Facilities Council. e-MERLIN is a National Facility operated by the University of Manchester at Jodrell Bank Observatory on behalf of STFC. This work has made use of data from the Asteroid Terrestrial-impact Last Alert System (ATLAS) project. The ATLAS project is primarily funded to search for near-Earth asteroids through NASA grants NN12AR55G, 80NSSC18K0284 and 80NSSC18K1575; by-products of the NEO search include images and catalogues from the survey area. This work was partially financed by Kepler/K2 grant J1944/80NSSC19K0112 and HST GO-15889 and STFC grants ST/T000198/1 and ST/S006109/1. The ATLAS science products have been made possible through the contributions of the University of Hawaii Institute for Astronomy, Queen's University Belfast, the Space Telescope Science Institute, the South African Astronomical Observatory and the Millennium Institute of Astrophysics (MAS), Chile. The Pan-STARRS1 Surveys (PS1) and the PS1 public science archive have been made possible through contributions by the Institute for Astronomy, the University of Hawaii, the Pan-STARRS Project Office, the Max Planck Society and its participating institutes, the Max Planck Institute for Astronomy, Heidelberg and the Max Planck Institute for Extraterrestrial Physics, Garching, Johns Hopkins University, Durham University, the University of Edinburgh, Queen's University Belfast, the Harvard–Smithsonian Center for Astrophysics, the Las Cumbres Observatory Global Telescope Network Incorporated, the National Central University of Taiwan, the Space Telescope Science Institute, the National Aeronautics

and Space Administration under grant no. NNX08AR22G issued through the Planetary Science Division of the NASA Science Mission Directorate, the National Science Foundation grant no. AST-1238877, the University of Maryland, Eötvös Loránd University (ELTE), the Los Alamos National Laboratory and the Gordon and Betty Moore Foundation. We acknowledge ESA Gaia, DPAC and the Photometric Science Alerts Team (http://gsaweb.ast.cam.ac.uk/alerts).

Funding

Open access funding provided by Stockholm University.

Author information

Authors and Affiliations

1. The Oskar Klein Centre, Department of Astronomy, Stockholm University, AlbaNova, Stockholm, Sweden

   Erik C. Kool, Joel Johansson, Jesper Sollerman, Peter Lundqvist, Sheng Yang & Conor Omand

2. The Oskar Klein Centre, Department of Physics, Stockholm University, AlbaNova, Stockholm, Sweden

   Joel Johansson & Steve Schulze

3. Instituto de Astrofísica de Andalucía, Consejo Superior de Investigaciones Científicas (CSIC), Granada, Spain

   Javier Moldón & Miguel Pérez-Torres

4. Jodrell Bank Centre for Astrophysics, School of Physics and Astronomy, The University of Manchester, Manchester, UK

   Javier Moldón

5. National Astronomical Observatory of Japan, National Institutes of Natural Sciences, Mitaka, Japan

   Takashi J. Moriya

6. School of Physics and Astronomy, Faculty of Science, Monash University, Clayton, Victoria, Australia

   Takashi J. Moriya

7. Tuorla Observatory, Department of Physics and Astronomy, University of Turku, Turku, Finland

   Seppo Mattila

8. School of Sciences, European University Cyprus, Nicosia, Cyprus

   Seppo Mattila

9. Center for Data Intensive and Time Domain Astronomy, Department of Physics and Astronomy, Michigan State University, East Lansing, MI, USA

   Laura Chomiuk & Chelsea Harris

10. Facultad de Ciencias, Universidad de Zaragoza, Zaragoza, Spain

    Miguel Pérez-Torres

11. Division of Physics, Mathematics and Astronomy, California Institute of Technology, Pasadena, CA, USA

    Matthew Graham, Christoffer Fremling, Mansi M. Kasliwal, Reed Riddle & Yashvi Sharma

12. Henan Academy of Sciences, Zhengzhou, China

    Sheng Yang

13. Astrophysics Research Institute, Liverpool John Moores University, Liverpool, UK

Daniel A. Perley

14. Department of Particle Physics and Astrophysics, Weizmann Institute of Science, Rehovot, Israel

Nora Linn Strotjohann & Avishay Gal-Yam

15. Univ. Lyon, Univ. Claude Bernard Lyon 1, CNRS/IN2P3, IP2I Lyon, UMR 5822, Villeurbanne, France

Jeremy Lezmy, Mathew Smith & Estelle Robert

16. School of Physics, Trinity College Dublin, The University of Dublin, Dublin, Ireland

Kate Maguire

17. School of Physics and Astronomy, University of Southampton, Southampton, UK

Mathew Smith

18. Joint Space-Science Institute, University of Maryland, College Park, MD, USA

Igor Andreoni

19. Department of Astronomy, University of Maryland, College Park, MD, USA

Igor Andreoni

20. Astrophysics Science Division, NASA Goddard Space Flight Center, Greenbelt, MD, USA

Igor Andreoni

21. DIRAC Institute, Department of Astronomy, University of Washington, Seattle, WA, USA

Eric C. Bellm

22. Department of Astronomy, University of California, Berkeley, Berkeley, CA, USA

Joshua S. Bloom & Michael S. Medford

23. Lawrence Berkeley National Laboratory, Berkeley, CA, USA

Joshua S. Bloom & Michael S. Medford

24. Kavli Institute for Astrophysics and Space Research, Massachusetts Institute of Technology, Cambridge, MA, USA

Kishalay De

25. Infrared Processing and Analysis Center (IPAC), California Institute of Technology, Pasadena, CA, USA

Steven L. Groom & Frank J. Masci

26. Ulsan National Institute of Science and Technology, Ulsan, South Korea

Sungmin Park

27. Caltech Optical Observatories, California Institute of Technology, Pasadena, CA, USA

Josiah Purdum

28. The Cosmic Dawn Center (DAWN), Niels Bohr Institute, University of Copenhagen, Copenhagen, Denmark

Thomas M. Reynolds

29. School of Mathematical and Physical Sciences, Macquarie University, Sydney, New South Wales, Australia

Stuart D. Ryder

30. Astronomy, Astrophysics and Astrophotonics Research Centre, Macquarie University, Sydney, New South Wales, Australia

Stuart D. Ryder

31. Jet Propulsion Laboratory, California Institute of Technology, Pasadena, CA, USA

Daniel Stern

Contributions

E.C.K. led the follow-up observations and is the primary author of the manuscript. J.J. conducted the spectral analysis and SN Ia light-curve modelling, and contributed to the source and infrared analysis. J.S. contributed substantially to the writing of the manuscript and the source analysis, and conducted follow-up observations with the NOT. J.M. and M.P.-T. led the radio observations and data analysis. T.J.M., L.C., C.H. and P.L. conducted the radio light-curve modelling. S.S. conducted the host-galaxy analysis. M.G. conducted follow-up observations with Keck. S.M. contributed to the writing and the infrared interpretation. S.Y. contributed to the data analysis. D.A.P. conducted follow-up observations with the Liverpool Telescope. N.L.S. conducted the precursor search. C.F., K.D. and Y.S. conducted follow-up observations. A.G.-Y. contributed to the writing and source analysis. J.L. and M.S. conducted the SEDM spectrum analysis. K.M., C.O., T.M.R. and S.D.R. contributed to the writing and source analysis. I.A., E.C.B., J.S.B., S.L.G., M.M.K., F.J.M., M.S.M., S.P., J.P., R.R. and D.S. are ZTF builders. All authors contributed to edits to the manuscript.

Corresponding author

Correspondence to Erik C. Kool.

Ethics declarations

Competing interests

The authors declare no competing interests.

Peer review

Peer review information

Nature thanks Ferdinando Patat and the other, anonymous, reviewer(s) for their contribution to the peer review of this work. Peer reviewer reports are available.

Additional information

Publisher's note Springer Nature remains neutral with regard to jurisdictional claims in published maps and institutional affiliations.

Extended data figures and tables

Extended Data Fig. 1 The light curves of SN 2020eyj are consistent with a SN Ia and its H-rich analogue SN Ia-CSM PTF11kx.

We simultaneously fit the *g*, *r* and *i* light curves of the initial peak phases of both SN 2020eyj and PTF11kx with the SN Ia light curve fitter SNooPy. SN 2020eyj is well fit with stretch factor 1.2 and $E(B-V) = 0.5 \pm 0.1$ mag. Similarly, PTF11kx is well fit with stretch factor 1.2 and $E(B-V) = 0.25 \pm 0.02$ mag. Panels show the absolute-magnitude light curves of SN 2020eyj and PTF11kx, after correcting for the host extinction derived from the fit. **a**, *g* band. **b**, *r* band for SN 2020eyj and *r*/*R* band for PTF11kx. **c**, *i* band.

Open circles indicate synthetic photometry derived from the spectra. The error bars represent 1σ uncertainties.

Extended Data Fig. 2 SN 2020eyj was accompanied by a bright mid-infrared counterpart.

a, A co-added image of the last NEOWISE-R epoch before the SN explosion, without any sign of the SN host. **b**, The co-added image in the W1 filter of the November 2020 NEOWISE-R epoch, 261 days after first detection, with SN 2020eyj clearly visible. **c**, A mid-infrared light-curve comparison of SN 2020eyj in the W2 filter (4.6 μm) to a sample of SNe observed with Spitzer at 4.5 μm, adapted from ref. [154], including Type IIn SNe (in black), Type Ia-CSM SNe (in red) and Type Ibn SN 2006jc (in lilac). Furthermore, the light curves of a sample of SNe Ia from ref. [155] is plotted in green. SN 2020eyj (large pink circles) is among the brightest SNe observed in the mid-infrared and is 6–10 magnitudes brighter than normal SNe Ia, depending on the phase. The error bars represent 1σ uncertainties.

Extended Data Fig. 3 The He and Hα emission-line profiles in the late spectra of SN 2020eyj show notable asymmetry.

The He i emission lines at 5,876 Å, 6,678 Å and 7,065 Å all show strong attenuation in the red wings and an apparent blue shift over time between the 131 and 251 days epochs. Such line asymmetry is commonly observed in SNe Ia-CSM (ref. [11]) and is interpreted as resulting from the condensation of dust in the ejecta or shocked CSM, obscuring the red wing (see ‘Dust properties’ section in Methods), but may also be a result of optical depth effects[20]. The Hα emission line at 131 days also shows asymmetry and there is a (minor) decline in flux between the two epochs shown here. By 329 days, the Hα luminosity has dropped to the level of the line emission in the host spectrum (see ‘Optical spectroscopy’ section in Methods).

Extended Data Fig. 4 The position of the radio detection is consistent with the position of SN 2020eyj in the optical.

a, The average position of the e-MERLIN detections (black circle, 0.01″ uncertainty), the position reported in GaiaAlerts (*G* band, green circle, 0.06″ uncertainty) and the position of SN 2020eyj in the ALFOSC epoch at 382 days (*r* band, red circle, 0.1″ uncertainty), overlaid on a 4″ × 4″ Pan-STARRS1 *i*-band dataset of the host. **b**, A 3′ × 3′ colour composite image, obtained with NOT/ALFOSC, of the compact star-forming host galaxy of SN 2020eyj and its environment.

Extended Data Fig. 5 The spectra of SN 2020eyj do not match Type Ic or Ibn SNe at early epochs.

The SEDM classification spectrum of SN 2020eyj compared with Type Ibn SN 2006jc and Type Ic SN1994I at similar epochs, about 12 days after peak. At 15 days post-peak, SN 2006jc already showed strong He emission lines and developed the quasi-continuum typical for CSM-interaction-dominated spectra. These features are not observed in SN 2020eyj at 12 days post-peak but do become prominent at late phases (Fig. 2). At 13 days post-peak, SN 1994I has grown redder compared with its peak spectrum shown in Fig. 1 and the O i 7,774 Å absorption feature has become more prominent, whereas in SN 2020eyj, this feature is not present.

Extended Data Fig. 6 The bolometric light curve of SN 2020eyj can be described with a radioactive decay model for the peak phase and an optically thick wind for the tail phase.

For the initial SN Ia peak of SN 2020eyj, we adopt the bolometric light curve (solid lines) accompanying the SN Ia template fit to the *gri* photometry (see ‘Light-curve fits’ section in Methods), assuming no line-of-sight extinction (in green) and an extinction of $E(B-V) = 0.5$ mag (in orange). Overplotted are the associated bolometrically corrected luminosities up to 40 days. From epoch 46 days onward, the SN Ia template fit no longer accurately describes the observed (*g*-band) photometry (Extended Data Fig. 1). The dotted lines show the continuation of the bolometric light curve of the underlying SN Ia. The three measurements in the tail phase are based on the integration of the two Keck spectra, extrapolated to the UV, and a bolometrically corrected photometric

ALFOSC epoch. The dashed lines represent the fits to the tail-phase measurements using the analytical model from ref. [26], following the same colour scheme for the level of extinction. In the transition region from the diffusion peak to the CSM-interaction-powered tail, between 50 and 100 days, the sum of the models would overestimate the luminosity, suggesting that the CSM configuration is more complicated than a simple wind-like density profile. The red diamonds show the infrared luminosity of SN 2020eyj (Extended Data Table 3), which are not included in the model fits.

Extended Data Table 1 Key characteristics of SN 2020eyj
Extended Data Table 2 Log of spectroscopic observations of SN 2020eyj and its host and FWHM velocity measurements of prominent emission lines in the 131 and 251 days Keck spectra
Extended Data Table 3 Mid-infrared photometry from the WISE telescope and infrared and dust properties of SN 2020eyj
Extended Data Table 4 Host-galaxy photometry

Supplementary information

Supplementary Table 1

Optical photometry of SN 2020eyj from the ZTF and affiliated programmes. The values are in observed magnitudes and not corrected for galactic extinction. Phase is relative to the first detection epoch, in rest-frame days.

Peer Review File

Rights and permissions

Open Access This article is licensed under a Creative Commons Attribution 4.0 International License, which permits use, sharing, adaptation, distribution and reproduction in any medium or format, as long as you give appropriate credit to the original author(s) and the source, provide a link to the Creative Commons licence, and indicate if changes were made. The images or other third party material in this article are

included in the article's Creative Commons licence, unless indicated otherwise in a credit line to the material. If material is not included in the article's Creative Commons licence and your intended use is not permitted by statutory regulation or exceeds the permitted use, you will need to obtain permission directly from the copyright holder. To view a copy of this licence, visit http://creativecommons.org/licenses/by/4.0/.

Reprints and Permissions

About this article

Cite this article

Kool, E.C., Johansson, J., Sollerman, J. *et al.* A radio-detected type Ia supernova with helium-rich circumstellar material. *Nature* **617**, 477–482 (2023). https://doi.org/10.1038/s41586-023-05916-w

- Received: 30 September 2022
- Accepted: 02 March 2023
- Published: 17 May 2023
- Issue Date: 18 May 2023
- DOI: https://doi.org/10.1038/s41586-023-05916-w

Share this article

Anyone you share the following link with will be able to read this content:

Get shareable link

Sorry, a shareable link is not currently available for this article.

Copy to clipboard

Provided by the Springer Nature SharedIt content-sharing initiative

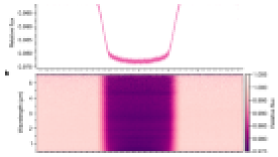
Radio show for rare type Ia

- Paul Woods

Nature Astronomy Research Highlight 19 May 2023

This article was downloaded by **calibre** from https://www.nature.com/articles/s41586-023-05916-w

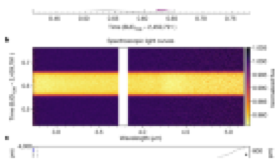
| Section menu | Main menu |



Early Release Science of the exoplanet WASP-39b with JWST NIRSpec PRISM

09 January 2023

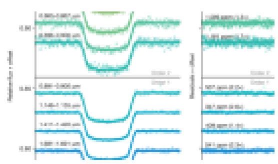
Z. Rustamkulov, D. K. Sing, … S. Zieba



Early Release Science of the exoplanet WASP-39b with JWST NIRSpec G395H

09 January 2023

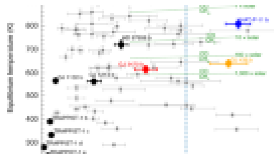
Lili Alderson, Hannah R. Wakeford, … Xi Zhang



Early Release Science of the exoplanet WASP-39b with JWST NIRISS

09 January 2023

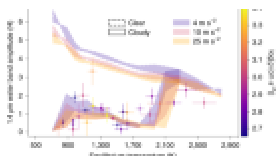
Adina D. Feinstein, Michael Radica, … Xi Zhang



A sub-Neptune exoplanet with a low-metallicity methane-depleted atmosphere and Mie-scattering clouds

01 July 2019

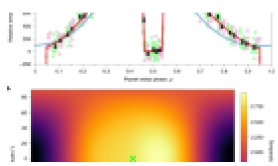
Björn Benneke, Heather A. Knutson, … Joshua Kammer



Aerosol composition of hot giant exoplanets dominated by silicates and hydrocarbon hazes

25 May 2020

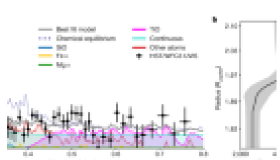
Peter Gao, Daniel P. Thorngren, … Xi Zhang



Diurnal variations in the stratosphere of the ultrahot giant exoplanet WASP-121b

21 February 2022

Thomas Mikal-Evans, David K. Sing, … Jessica J. Spake



[UV absorption by silicate cloud precursors in ultra-hot Jupiter WASP-178b]

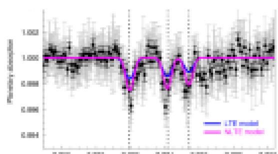
06 April 2022

Joshua D. Lothringer, David K. Sing, … Autumn T. Winch

[A reflective, metal-rich atmosphere for GJ 1214b from its JWST phase curve]

10 May 2023

Eliza M.-R. Kempton, Michael Zhang, … Peter McGill



[High-resolution detection of neutral oxygen and non-LTE effects in the atmosphere of KELT-9b]

22 December 2021

Francesco Borsa, Luca Fossati, … Denis Shulyak

- Article
- Open Access
- Published: 26 April 2023

Photochemically produced SO_2 in the atmosphere of WASP-39b

- Shang-Min Tsai ,
- Elspeth K. H. Lee,

- Diana Powell,
- Peter Gao,
- Xi Zhang,
- Julianne Moses,
- Eric Hébrard,
- Olivia Venot,
- Vivien Parmentier,
- Sean Jordan,
- Renyu Hu,
- Munazza K. Alam,
- Lili Alderson,
- Natalie M. Batalha,
- Jacob L. Bean,
- Björn Benneke,
- Carver J. Bierson,
- Ryan P. Brady,
- Ludmila Carone,
- Aarynn L. Carter,
- Katy L. Chubb,
- Julie Inglis,
- Jérémy Leconte,
- Michael Line,
- Mercedes López-Morales,
- Yamila Miguel,
- Karan Molaverdikhani,
- Zafar Rustamkulov,
- David K. Sing,
- Kevin B. Stevenson,
- Hannah R. Wakeford,
- Jeehyun Yang,
- Keshav Aggarwal,
- Robin Baeyens,
- Saugata Barat,
- Miguel de Val-Borro,
- Tansu Daylan,
- Jonathan J. Fortney,
- Kevin France,

- Jayesh M. Goyal,
- David Grant,
- James Kirk,
- Laura Kreidberg,
- Amy Louca,
- Sarah E. Moran,
- Sagnick Mukherjee,
- Evert Nasedkin,
- Kazumasa Ohno,
- Benjamin V. Rackham,
- Seth Redfield,
- Jake Taylor,
- Pascal Tremblin,
- Channon Visscher,
- Nicole L. Wallack,
- Luis Welbanks,
- Allison Youngblood,
- Eva-Maria Ahrer,
- Natasha E. Batalha,
- Patrick Behr,
- Zachory K. Berta-Thompson,
- Jasmina Blecic,
- S. L. Casewell,
- Ian J. M. Crossfield,
- Nicolas Crouzet,
- Patricio E. Cubillos,
- Leen Decin,
- Jean-Michel Désert,
- Adina D. Feinstein,
- Neale P. Gibson,
- Joseph Harrington,
- Kevin Heng,
- Thomas Henning,
- Eliza M.-R. Kempton,
- Jessica Krick,
- Pierre-Olivier Lagage,
- Monika Lendl,

- Joshua D. Lothringer,
- Megan Mansfield,
- N. J. Mayne,
- Thomas Mikal-Evans,
- Enric Palle,
- Everett Schlawin,
- Oliver Shorttle,
- Peter J. Wheatley &
- …
- Sergei N. Yurchenko

Show authors

Nature **volume 617**, pages 483–487 (2023)

- 2603 Accesses
- 20 Altmetric
- Metrics details

Abstract

Photochemistry is a fundamental process of planetary atmospheres that regulates the atmospheric composition and stability[1]. However, no unambiguous photochemical products have been detected in exoplanet atmospheres so far. Recent observations from the JWST Transiting Exoplanet Community Early Release Science Program[2,3] found a spectral absorption feature at 4.05 μm arising from sulfur dioxide (SO_2) in the atmosphere of WASP-39b. WASP-39b is a 1.27-Jupiter-radii, Saturn-mass (0.28 M_J) gas giant exoplanet orbiting a Sun-like star with an equilibrium temperature of around 1,100 K (ref. [4]). The most plausible way of generating SO_2 in such an atmosphere is through photochemical processes[5,6]. Here we show that the SO_2 distribution computed by a suite of photochemical models robustly explains the 4.05-μm spectral feature identified by JWST transmission observations[7] with NIRSpec PRISM (2.7σ)[8] and G395H

(4.5σ)[9]. SO_2 is produced by successive oxidation of sulfur radicals freed when hydrogen sulfide (H_2S) is destroyed. The sensitivity of the SO_2 feature to the enrichment of the atmosphere by heavy elements (metallicity) suggests that it can be used as a tracer of atmospheric properties, with WASP-39b exhibiting an inferred metallicity of about 10× solar. We further point out that SO_2 also shows observable features at ultraviolet and thermal infrared wavelengths not available from the existing observations.

Main

JWST observed WASP-39b as part of its Transiting Exoplanet Community Early Release Science Program (ERS Program 1366), with the goal of explaining its atmospheric composition[2,3]. Data from the NIRSpec PRISM and G395H instrument modes showed a distinct absorption feature between 4.0 µm and 4.2 µm, peaking at around 4.05 µm, that atmospheric radiative–convective–thermochemical equilibrium models could not explain with metallicity and C/O values typically assumed of gas giant planets (1–100× solar and 0.3–0.9, respectively[8,9]). After excluding instrument systematics and stellar variability, a thorough search for gases has shown SO_2 as a promising candidate with the best-fit absorption feature (see Methods), although ad hoc spectra with injected SO_2 were used in the analysis.

Sulfur shares some chemical similarities with oxygen but uniquely forms various compounds with a wide range of oxidation states (−2 to +6 (ref. [10])). Although SO_2 is ubiquitously outgassed and associated with volcanism on terrestrial worlds (for example, Earth, Venus and Jupiter's satellite Io), the source of SO_2 is fundamentally different on gas giants. Under thermochemical equilibrium, sulfur chiefly exists in the reduced form, such that H_2S is the primary sulfur reservoir in a hydrogen/helium-dominated gas giant[11,12,13,14]. At the temperature of WASP-39b, the equilibrium mixing ratio of SO_2 in the observable part of the atmosphere is less than about 10^{-12} for 10× solar metallicity and less than about 10^{-9} for even 100× solar metallicity (see Extended Data Fig. 1). This equilibrium abundance of SO_2 is several orders of magnitude smaller than the values needed to produce the spectral feature observed by JWST (volume mixing ratios (VMRs) of 10^{-6}–

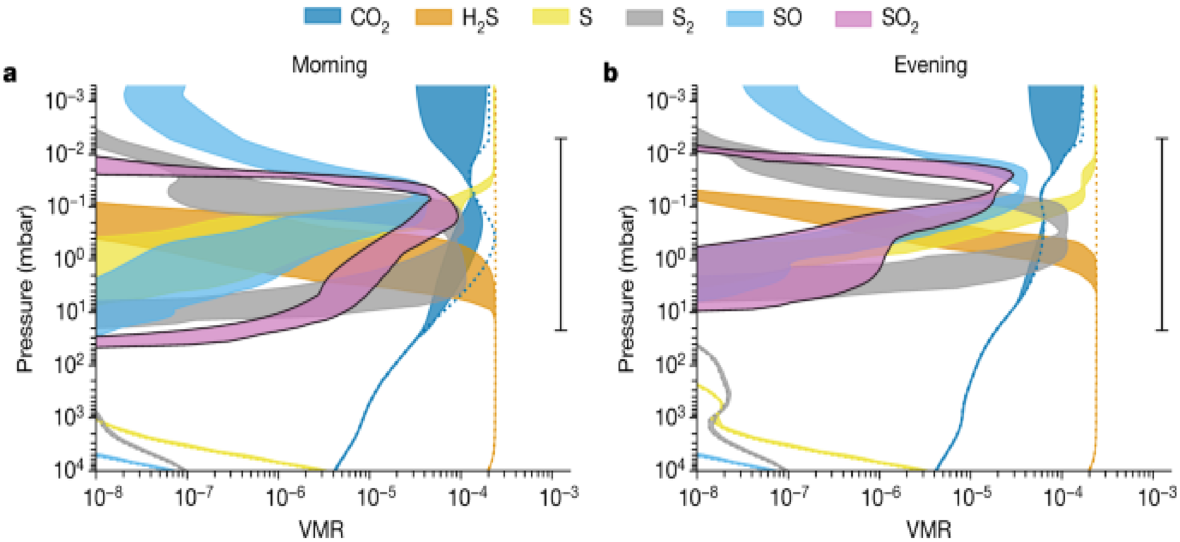
10^{-5})[8,9]. By contrast, under ultraviolet (UV) irradiation, SO_2 can be oxidized from H_2S as a photochemical product. H and OH radicals, generated by photolysis processes, are key to liberating SH radicals and atomic S from H_2S and subsequently oxidizing them to SO and SO_2. Although previous photochemical modelling studies have shown that substantial SO_2 can be produced in hydrogen-rich exoplanet atmospheres in this way[5,6,13,15,16], the extent to which such a model could reproduce the current WASP-39b observations remained unverified.

We have performed several independent, cloud-free 1D photochemical model calculations of WASP-39b using the ARGO, ATMO, KINETICS and VULCAN codes (see Methods for model details). All models included sulfur kinetic chemical networks and were run using the same vertical temperature–pressure profiles of the morning and evening terminators adopted from a 3D WASP-39b atmospheric simulation with the Exo-FMS general circulation model (GCM)[17] (see Extended Data Fig. 2). The nominal models assumed a metallicity of 10× solar (ref. [18]) with a solar C/O ratio of 0.55, whereas we explored the sensitivity to atmospheric properties.

The peak mixing ratios of the main sulfur species produced by the different photochemical models are largely consistent with each other to within an order of magnitude, as shown in Fig. 1. The SO_2 mixing ratio profiles are highly variable with altitude and strongly peaked at 0.01–1 mbar with a value of 10–100 ppm. SO_2 (along with CO_2) is more favoured at the cooler morning terminator, at which H_2S is less stable against reaction with atomic H at depth (with SO_2 abundance peak of 50–90 ppm at the morning terminator and 15–30 ppm at the evening terminator). Although the peak SO_2 abundance from the photochemical models is greater than that estimated from fitting to the PRISM and G395H data, which assumed vertically constant mixing ratios of about 1–10 ppm and about 2.5–4.6 ppm, respectively, the column-integrated number densities above 10 mbar are highly consistent (see Methods). Our models indicate that S, S_2 and SO, which are precursors of SO_2, also reach high abundances in the upper atmosphere above the pressure level at which H_2S is destroyed.

Nevertheless, they are not expected to manifest observable spectral features in the PRISM/G395H wavelength range.

Fig. 1: Simulated vertical distribution of sulfur species and CO_2.



a,**b**, The colour-shaded areas indicate the span (enclosed by the maximum and minimum values) of VMRs of CO_2 (blue), SO_2 (pink with black borders) and other key sulfur species (H_2S, orange; S, yellow; S_2, grey; SO, light blue) computed by an ensemble of photochemical models (ARGO, ATMO, KINETICS and VULCAN) for the morning (**a**) and evening (**b**) terminators. The thermochemical equilibrium VMRs are indicated by the dotted lines, with SO_2 not within the x-axis range owing to its very low abundance in thermochemical equilibrium. The range bar on the right represents the main pressure ranges of the atmosphere investigated by JWST NIRSpec spectroscopy. Photochemistry produces SO_2 and other sulfur species above the 1-mbar level with abundances several orders of magnitude greater than those predicted by thermochemical equilibrium.

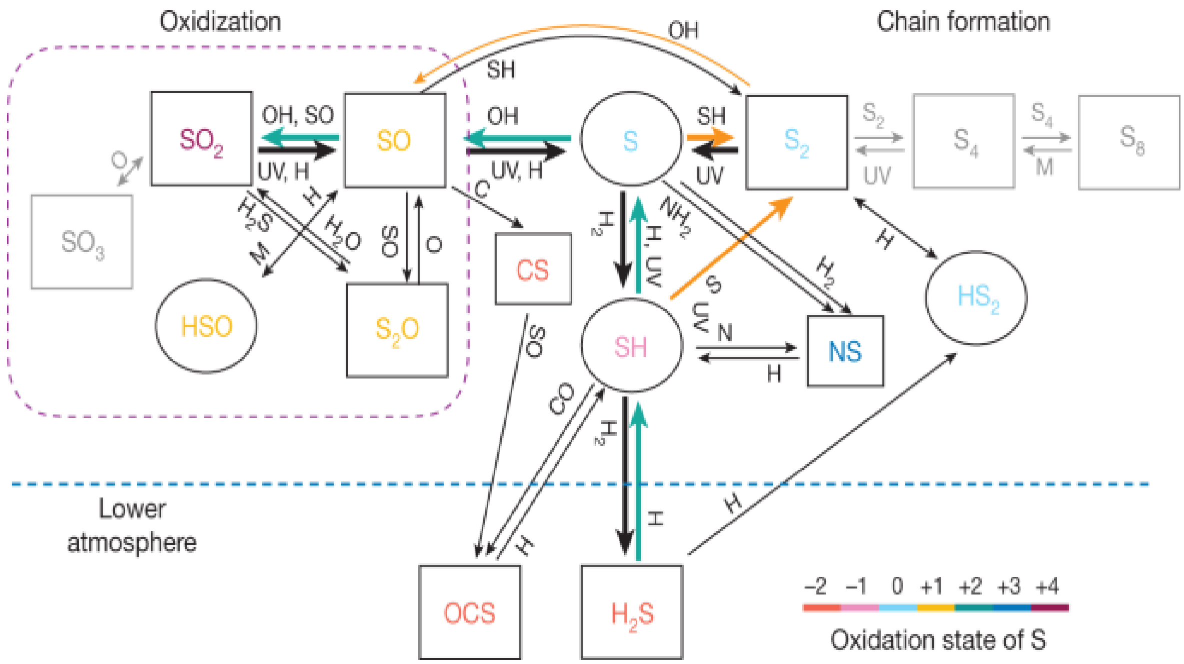
The important pathways of sulfur kinetics in the atmosphere of WASP-39b from our models are summarized in Fig. 2. The photochemical production paths of SO_2 from H_2S around the SO_2 peak are as follows:

$$\begin{array}{c}\,\,\,{{\rm{H}}}_{2}
{\rm{O}}\,\mathop{\longrightarrow }\limits^{h\nu }\,{\rm{O}}{\rm{H}}+
{\rm{H}}\\ \,\,\,{{\rm{H}}}_{2}{\rm{O}}+{\rm{H}}\,\longrightarrow \,

{\rm{O}}{\rm{H}}+{{\rm{H}}}_{2}\\ \,\,\,{{\rm{H}}}_{2}{\rm{S}}+{\rm{H}}\,\longrightarrow \,{\rm{S}}{\rm{H}}+{{\rm{H}}}_{2}\\ \,\,\,{\rm{S}}{\rm{H}}+{\rm{H}}\,\longrightarrow \,{\rm{S}}+{{\rm{H}}}_{2}\\ \,\,\,{\rm{S}}+{\rm{O}}{\rm{H}}\,\longrightarrow \,{\rm{S}}{\rm{O}}+{\rm{H}}\\ \frac{\,\,\,{\rm{S}}{\rm{O}}+{\rm{O}}{\rm{H}}\,\longrightarrow \,{\rm{S}}{{\rm{O}}}_{2}+{\rm{H}}}{{\rm{net:}}\,{{\rm{H}}}_{2}{\rm{S}}+2{{\rm{H}}}_{2}{\rm{O}}\,\longrightarrow \,{\rm{S}}{{\rm{O}}}_{2}+3{{\rm{H}}}_{2}}\end{array}$$
(1)

Water photolysis in equation (1) is an important source of atomic H that initiates the pathway. The last step of oxidizing SO into SO_2 is generally the rate-limiting step. The oxidization of SO and photolysis of SO_2 account for the main sources and sinks of SO_2, which lead to altitude-varying distribution that peaks around 0.1 mbar (see Extended Data Fig. 4). At high pressures with less available OH, reactions involving S_2 become important in oxidizing S (see Methods). The growth of elemental sulfur allotropes beyond S_2 effectively stops for temperatures higher than approximately 750 K (refs. [5,6]).

Fig. 2: A simplified schematic of the chemical pathways of sulfur species.

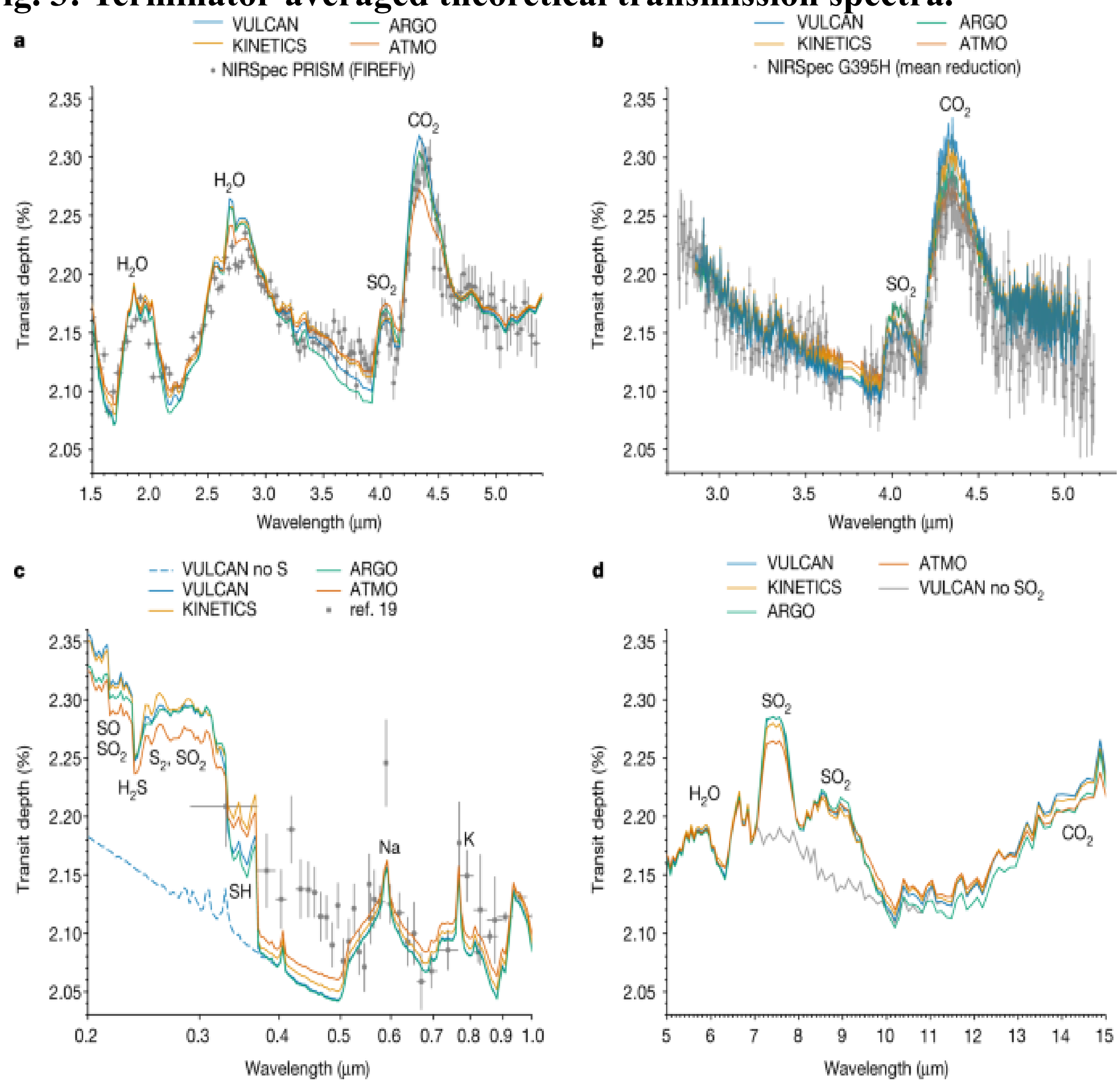


H_2S, which is the stable sulfur-bearing molecule at thermochemical equilibrium in an H_2 atmosphere, readily reacts with atomic H to form SH radicals and, subsequently, atomic S in the photochemical region (above about 0.1 mbar). Reaction of S with photochemically generated OH then produces SO, which is further oxidized to SO_2. The thick arrows denote efficient reactions and M denotes any third body. Inefficient reactions and inactive paths in the temperature regime of WASP-39b are greyed out. The cyan arrows mark the main path from H_2S to SO_2, whereas the orange arrows mark the paths that are important at higher pressures. Sulfur species are colour-coded by the oxidation states of S. Rectangles indicate stable molecules, whereas ovals indicate free radicals.

Figure 3 shows the morning/evening averaged transmission spectra resulting from the different photochemical models. All models are able to reproduce the strength and shape of the 4.05-µm SO_2 feature seen in the NIRSpec PRISM and G395H modes. The scatter in the model spectra is on par with the uncertainties of the data and is attributed to the spread in the vertical VMR structure of SO_2 and CO_2 produced by each model (Fig. 1). Also shown in Fig. 3 are the predicted spectra in the MIRI LRS wavelength range (5–12 µm), which exhibit prominent SO_2 features around 7.5 µm and 8.8 µm, as well as an upward slope redward of 12 µm owing to CO_2. Furthermore,

our models predict a strong UV (0.2–0.38 μm) transmission signal from the presence of S species: H_2S, S_2, SO_2 and SH produce a sharp opacity gradient shortward of 0.38 μm (Extended Data Fig. 7), at which the room-temperature UV cross-sections are used except those at 800 K for SH. The discrepancy between the models and previous HST STIS and VLT/FORS2 observations[19] (see Fig. 3) within 0.38–0.5 μm could potentially be because of enhanced UV opacities at high temperatures and/or aerosol particles. Further characterization of the sulfur species spectral features in the UV is promising with the scheduled HST/UVIS observation (Program 17162, principal investigators: Z. Rustamkulov and D. Sing).

Fig. 3: Terminator-averaged theoretical transmission spectra.

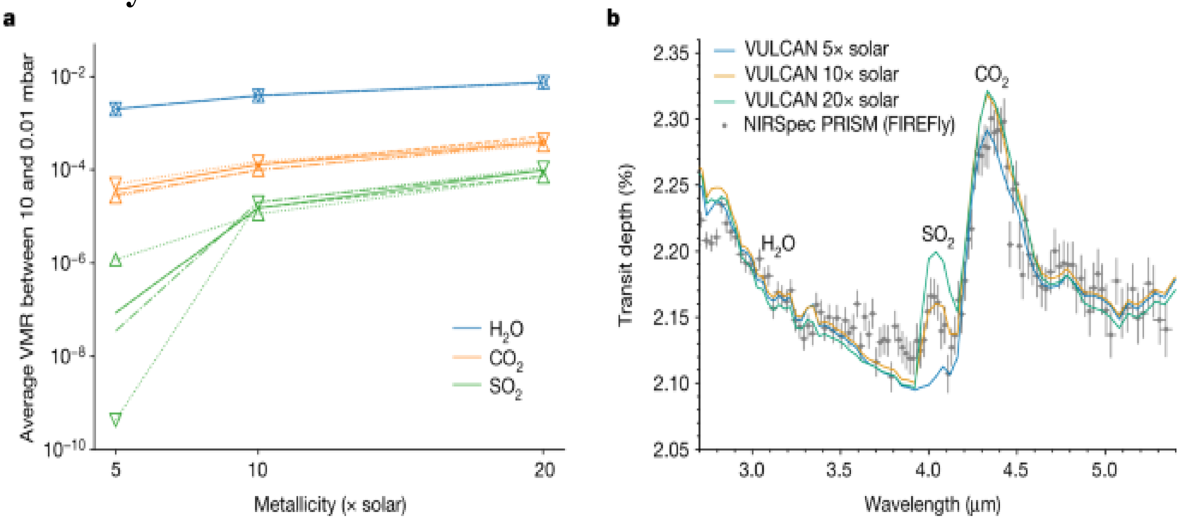


We show the transmission spectra averaged over the morning and evening terminators generated from 1D photochemical model results. **a**, Comparison with the NIRSpec PRISM FIREFly reduction[8]. **b**, Comparison with the NIRSpec G395H weighted-mean reduction[9]. **c**, Comparison with the current HST and VLT/FORS2 optical wavelength data[19,37]. The models show pronounced features at UV wavelengths owing to sulfur species compared with the model without S-bearing species (dashed blue line). **d**, Predicted spectra across the MIRI LRS wavelength range, with SO_2 removed from the VULCAN output shown in grey to indicate its contribution. All of the spectral data show 1σ error bars and the standard deviations averaged (unweighted) over all reductions are shown for the NIRSpec G395H data.

SO_2 has recently been suggested as a promising tracer of metallicity in giant exoplanet atmospheres[16]. To test this and show trends in atmospheric properties, we have conducted sensitivity analysis on metallicity as well as temperature and vertical mixing using VULCAN (see Methods for details and further tests on C/O and stellar UV flux). Figure 4a summarizes these results for SO_2, along with H_2O and CO_2, which are more commonly used as proxies for atmospheric metallicity[13,20,21,22]. Overall, the average abundance of SO_2 in the pressure region relevant for such observation is not strongly sensitive to temperature or vertical mixing once SO_2 has reached observable ppm levels and is mildly sensitive to C/O (see Extended Data Fig. 5). By contrast, SO_2 shows either a similar or a stronger dependence on metallicity compared with H_2O and CO_2. This sensitivity to metallicity can be understood from the net reaction (equation (1)), in which it takes one molecule of H_2S and two molecules of H_2O to make one SO_2. Although SO_2 can be further oxidized into SO_3, which requires extra oxygen, SO_3 is rarely produced to an observable level in a H_2-dominated atmosphere. Therefore, SO_2 can be an ideal tracer of heavy-element enrichment for giant planets, with given constraints on the temperature and stellar far-ultraviolet (FUV) flux. The applicability of SO_2 as a tracer of metallicity is further shown in Fig. 4b, in which the increase in the SO_2 feature amplitude between 5× and 20× solar metallicity is much greater than that of CO_2 and H_2O. As such, retrieval analyses seeking to evaluate the atmospheric metallicity of warm

giant exoplanets can substantially benefit from both CO_2 and SO_2 measurements.

Fig. 4: The metallicity trends and synthetic spectra with varying metallicity.



a, The averaged VMR of H_2O, CO_2 and SO_2 in the atmosphere between 10 and 0.01 mbar examined by transmission spectroscopy as a function of atmospheric metallicity. The nominal model is shown by solid lines, whereas the eddy diffusion coefficient (K_{zz}) scaled by 0.1 and 10 are shown by dashed and dashed-dotted lines, respectively. The models with the whole temperature increased and decreased by 50 K are indicated by the upward-facing and downward-facing triangles connected by dotted lines, respectively. **b**, The morning and evening terminator-averaged theoretical transmission spectra with different metallicities (relative to solar value) compared with the NIRSpec observation. The error bars show 1σ standard deviations.

Our results demonstrate the importance of considering photochemistry—and sulfur chemistry in particular—in warm exoplanet atmospheres when interpreting exoplanet atmospheric observations. Exoplanet photochemistry has been investigated using numerical models since the detection of an atmosphere on a transiting exoplanet[23,24], followed by a diverse set of subsequent studies explaining the interplay of carbon, oxygen, nitrogen, hydrogen and sulfur (see, for example, ref. [25] for a review). It has been further pointed out that sulfur can affect other nonsulfur species, such as

atomic H, CH_4 and NH_3 (refs. [6,15]; also see Extended Data Fig. 6). Temperature trends in the photochemical production of sulfur species (Extended Data Fig. 10) in exoplanet atmospheres are potentially observable with features in the UV and infrared (Fig. 3 and Extended Data Fig. 7). At temperatures higher than that of WASP-39b, SH and SO may become relatively more abundant than SO_2 (refs. [6,13,15]). Observing these compositional variations with temperature in H_2-dominated atmospheres, modulated by the atmospheric metallicity, could substantially improve our understanding of high-temperature chemical networks and atmospheric properties. The observational effort should also be complemented by a more accurate determination of key chemical reaction rate constants and UV cross-sections at the relevant temperatures (for example, refs. [26,27]), as well as photochemical modelling development beyond 1D that includes horizontal transport (for example, refs. [28,29,30]).

The accessibility of sulfur species in exoplanet atmospheres through the aid of photochemistry allows for a new window into planet-formation processes, whereas in the Solar System gas giants, the temperature is sufficiently low that sulfur is condensed out as either H_2S clouds or together with NH_3 as ammonium hydrosulfide (NH_4SH) clouds[31], making it more difficult to observe. Sulfur has been detected in protoplanetary disks[32], in which it may be primarily in refractory form[33], making it a reference element showing the metallicity contributions of accreted solid and gas[34,35,36]. Such efforts for warm giant exoplanets are now a possibility thanks to the observability of photochemically produced SO_2. Thus, the detection of SO_2 offers valuable insights into further atmospheric characterization and planet formation.

Methods

4.05-µm feature

A list of gas species that have been compared with the 4.05-µm absorption feature in the transit observation of WASP-39b can be found in ref. [8]. In particular, species with absorption features at similar wavelengths but are ruled out include H_2S, HCN, HBr, PH_3, SiO and SiO_2. H_2S and HCN absorb

shortward of the feature at 4.05 µm, whereas SiO_2 absorbs longward of that, and HBr, SiO and PH_3 have wider absorption bands than the observed feature. Chemically, SiO and SiO_2 are also expected to rain out at the temperature of WASP-39b and the solar elemental abundances have little bromine ($Br/H \approx 4 \times 10^{-10}$). Ultimately, the injection tests of SO_2 provide 2.7σ detection with NIRSpec PRISM (ref. [8]) and 4.8σ with G395H (ref. [9]).

The temperature–pressure and eddy diffusion coefficient profiles derived from the Exo-FMS GCM

To provide inputs to the 1D photochemical models, a cloud-free WASP-39b GCM was run using the Exo-FMS GCM[17]. We computed the transmission spectra derived from our photochemical model results using gCMCRT (ref. [40]) and the ExoAmes high-temperature SO_2 line list[41]. System parameters were taken from ref. [7]. We assume a 10× solar metallicity atmosphere in thermochemical equilibrium and use two-stream, correlated-*k* radiative transfer without optical and UV wavelength absorbers such as TiO, VO and Fe, which are assumed to have rained out from the atmosphere given the atmospheric temperatures of WASP-39b. The assumption about thermochemical equilibrium in radiative-transfer calculations will be discussed in the next section.

Although the temperatures of WASP-39b cross several condensation curves of sulfide clouds, such as Na_2S and ZnS, the gas composition is not expected to be markedly affected. The elemental abundances of Na and Zn are less abundant than S ($Na/S \approx 0.13$, $Zn/S \approx 0.0029$), which would at most reduce approximately 20% of the total sulfur, similar to how oxygen is being sequestered in silicates and metals[42]. Furthermore, this full condensation is unlikely because sulfide condensates generally have high surface energies[43,44] that inhibit efficient nucleation, consistent with the detection of gaseous sodium on WASP-39b (ref. [8]).

The radius of WASP-39b is inflated notably and we assume an internal temperature of 358 K, taken from the relationship between irradiated flux and internal temperature found in ref. [45]. Extended Data Fig. 2a shows the latitude–longitude map of the temperature at a pressure level of 10 mbar.

The input to the photochemical models are the temperature–pressure profiles at the morning and evening limbs (Extended Data Fig. 2), which we compute by taking the average of the profiles over all latitudes and ±10° (as estimated from the opening-angle calculations from ref. [46]) of the morning (western) and evening (eastern) terminators (that is, the region between the grey curves in Extended Data Fig. 2a. The cooler morning terminator as a result of the horizontal heat transport facilitated by the global circulation can be seen in the figure.

Vertical mixing in 1D chemical models is commonly parameterized by eddy diffusion. For exoplanets, the eddy diffusion coefficient (K_{zz}) is in general a useful but loosely constrained parameter. For the 1D photochemical models used in this work, we assume that K_{zz} follows an inverse square-root dependence with pressure in the stratosphere (for example, ref. [29]) as

$${K}_{{\rm{zz}}}({{\rm{cm}}}^{2}\,{{\rm{s}}}^{-1})=5\times 1{0}^{7}{\left(\frac{5{\rm{bar}}}{P}\right)}^{0.5}$$
(2)

and held constant below the 5-bar level in the convective zone. The eddy diffusion profile generally fits the root-mean-squared vertical wind multiplied by 0.1 scale height as the characteristic length scale from the GCM. The resulting K_{zz} profile is presented in Extended Data Fig. 2.

Radiative feedback of disequilibrium composition

The temperature profiles adopted from the GCM assume chemical equilibrium abundances. To evaluate the radiative feedback from disequilibrium chemical abundances, we first performed self-consistent 1D calculations, coupling the radiative-transfer and photochemical-kinetics models using HELIOS (ref. [47]) and VULCAN (ref. [6]), for which the opacity sources in HELIOS include H_2O, CH_4, CO, CO_2, NH_3, HCN, C_2H_2, SH, H_2S, SO_2, Na, K, H^-, CIA H_2–H2 and H_2–He (see references in ref. [47]). Yet we found negligible differences between the temperature profile computed from equilibrium abundances and that from disequilibrium abundances. This is probably because water, as the predominant infrared opacity source,

remains unaffected by disequilibrium processes. Meanwhile, a few opacities are missing in our radiative-transfer calculation. In particular, the opacity of SO_2 (ref. [48]) does not extend into the visible and UV wavelength range. Previous works[13,49] indicated that SH and S_2 have strong absorption in the UV–visible and can potentially affect the thermal structure. To quantify the radiative effect of these sulfur species, we calculated the shortwave heating rate with

$${c}_{{\rm{P}}}\frac{{\rm{d}}T}{{\rm{d}}t}=\frac{F{\kappa }_{i}\Delta {m}_{i}}{\Delta {m}_{{\rm{air}}}}$$
(3)

in which c_P is the specific heat capacity of the air, F is the stellar flux associated with the direct beam and Δm_i and Δm_{air} are the column mass of species i and air of an atmospheric layer, respectively. Extended Data Fig. 3 illustrates the shortwave heating owing to SH, S_2 and SO_2. Our estimate shows that SO_2 contributed the most in our WASP-39b model, rather than SH and S_2 being the main shortwave absorbers for atmospheres with solar-like metallicity[13,49]. The peak of heating owing to SO_2 is comparable with a grey opacity of 0.05 $cm^2\ g^{-1}$ over 220–800 nm and could potentially raise the temperatures around 0.1 mbar (the visible grey opacity for the irradiation of WASP-39b irradiation is about 0.005 $cm^2\ g^{-1}$ (ref. [50])). Nevertheless, this heating effect does not change our main conclusions about photochemically forming SO_2 on WASP-39b. As long as temperatures do not fall below roughly 750 K, at which sulfur allotrope formation starts to take over, SO_2 is not too sensitive to temperature increases up to 100 K.

The stellar spectrum of WASP-39

We require the high-energy spectral energy distribution (SED) of the WASP-39 host star as input to drive our set of photochemical models. However, as an inactive mid G-type star (T_{eff} = 5,485 ± 50 K; ref. [51]) at a distance of 215 pc (Gaia DR3), WASP-39 is too faint for high-S/N UV spectroscopy with HST. To approximate the stellar radiation incident on WASP-39b, we created a custom stellar SED that combines direct spectroscopy of WASP-39

in the optical (with HST/STIS G430L and G750L modes; GO 12473, principal investigator: D. Sing) with representative spectra from analogous stars at shorter wavelengths.

Our approach to estimating the UV stellar SED was based on two factors: (1) in the near-ultraviolet (NUV; 2,300–2,950 Å), in which the flux is dominated by the photosphere, we chose a proxy with a similar spectral type to WASP-39 and (2) in the extreme ultraviolet (XUV) and FUV (1–2,300 Å), in which the stellar flux is dominated by chromospheric, transition region and coronal emission lines, we chose a proxy star with similar chromospheric activity indicators and used spectral type as a secondary consideration. In the NUV, we used HST/STIS E230M spectra of HD 203244, a relatively active (Ca II log($({R}_{{\rm{H}}{\rm{K}}}^{{\prime} })$) = −4.4 (ref. [52])), nearby (that is, unreddened, d = 20.8 pc; Gaia DR2), G5 V star ($T_{\rm eff}$ = 5,480 K (ref. [53])) from the STARCat archive[54]. Although HD 203244 is a suitable proxy at photospheric wavelengths, WASP-39 is a relatively old (about 7 Gyr) star with low chromospheric activity (log($({R}_{{\rm{H}}{\rm{K}}}^{{\prime} })$) = −4.97 ± 0.06) and a long rotation period ($P_{\rm rot}$ = 42.1 ± 2.6 days; ref. [51]), suggesting substantially lower high-energy flux than HD 203244. Therefore, we elected to use a lower-activity G-type star, the Sun, at wavelengths shorter than 2,300 Å. The Sun has high-quality archival data available across the UV and X-rays and similar chromospheric activity to WASP-39 (the average solar Ca II log($({R}_{{\rm{H}}{\rm{K}}}^{{\prime} })$) value is −4.902 ± 0.063 and ranges from approximately −4.8 to −5.0 from solar maximum to solar minimum[55,56]). With the components in hand, we first corrected the observed STIS spectra of WASP-39 for interstellar dust extinction of $E(B-V) = 0.079$ (ref. [57]) using a standard $R_V = 3.1$ interstellar reddening curve[58] and then interpolated all spectra onto a 0.5-Å-pixel^{-1} grid. The NUV spectrum of HD 203244 was scaled to the reddening-corrected WASP-39 observations in the overlap region between 2,900 and 3,000 Å and the XUV + FUV spectrum of the quiet Sun[59] was scaled to the blue end of the combined SED. The flux scaling between two spectral components is defined as $((F_{\rm ref} - \alpha \times F_{\rm proxy})/\sigma_{\rm ref})^2$ in the overlap region, in which 'proxy' is the spectrum being scaled, 'ref' is the spectrum to which we are scaling and α is the scale factor applied to the proxy spectrum. α is varied until the above

quantity is minimized ($\alpha = 2.04 \times 10^{-16}$ and 7.58×10^{-3} for the FUV and NUV components, respectively). The final combined spectrum was convolved with a 2-Å full width at half maximum Gaussian kernel and wavelengths longer than 7,000 Å were removed to avoid the near-infrared fringing in the STIS G750L mode. We show the stellar spectrum at the surface of the star used for our photochemical models in Extended Data Fig. 2.

We compared our estimated SED for WASP-39 against archival GALEX observations from Shkolnik[60], who found the NUV (1,771–2,831 Å) flux density to be 168.89 μJy, or an average NUV spectral flux of $F_\lambda = 9.8 \times 10^{-16}$ erg cm^{-2} s^{-1} Å^{-1} at 2,271 Å. Correcting this value by the average extinction correction in the GALEX NUV bandpass, a factor of 1.79, and comparing it with the average flux of our estimated SED over the same spectral range (1.66×10^{-15} erg cm^{-2} s^{-1} Å^{-1}), we find the agreement between the GALEX measurement of WASP-39 and our stellar proxy to be better than 6%.

Simulated transmission spectra from gCMCRT

To post-process the 1D photochemical model output and produce transmission spectra, we use the 3D Monte Carlo radiative-transfer code gCMCRT[40].

For processing 1D columns, gCMCRT uses 3D spherical geometry but with a constant vertical profile across the globe in latitude and longitude. In this way, spectra from 1D outputs can be computed. We process the morning and evening terminator vertical 1D chemical profiles of each photochemical model separately, taking the average result of the two transmission spectra to produce the final spectra that are compared with the observational data.

In the transmission spectra model, we use opacities generated from the following line lists: H_2O (ref. [61]), OH (ref. [62]), CO (ref. [63]), CO_2 (ref. [64]), CH_4 (ref. [65]), CH_3 (ref. [66]), HCN (ref. [67]), C_2H_2 (ref. [68]), C_2H_4 (ref. [69]), C_2H_6 (ref. [70]), C_4H_2 (ref. [70]), C_2 (ref. [71]), CN (ref. [72]), CH (ref. [73]), SO_2 (ref. [41]),

SH (ref. [48]), SO (ref. [74]), H_2S (ref. [75]), NO (ref. [76]), N_2O (ref. [76]), NO_2 (ref. [76]), HCl (ref. [70]), Na (ref. [77]), K (ref. [77]).

Description of photochemical models

We use the following 1D thermo-photochemical models to produce the steady-state chemical abundance profiles for the terminators of WASP-39b. All models assume cloud-free conditions and adopt the same temperature profiles, stellar UV flux, eddy diffusion coefficient profile (Extended Data Fig. 2) and zero-flux (closed) boundary conditions. A zenith angle of 83° (an effective zenith angle that matches the terminator-region-mean actinic flux for near-unity optical depth) is assumed for the terminator photochemical modelling.

VULCAN

The 1D kinetics model VULCAN treats thermochemical[78] and photochemical[6] reactions. VULCAN solves the Eulerian continuity equations, including chemical sources/sinks, diffusion and advection transport, and condensation. We applied the C-H-N-O-S network (https://github.com/exoclime/VULCAN/blob/master/thermo/SNCHO_photo_network.txt) for reduced atmospheres containing 89 neutral C-bearing, H-bearing, O-bearing, N-bearing and S-bearing species and a total of 1,028 thermochemical reactions (that is, 514 forward–backward pairs) and 60 photolysis reactions. The sulfur allotropes are simplified into a system of S, S_2, S_3, S_4 and S_8. The sulfur kinetics data are drawn from the NIST and KIDA databases, as well as modelling[5,79] and ab initio calculations published in the literature (for example, ref. [80]). For simplicity and cleaner model comparison, the temperature-dependent UV cross-sections[6] are not used in this work. The pathfinding algorithm described in ref. [81] is used to identify the important chemical pathways. We note that the paths presented in this study are mainly based on VULCAN output (see Extended Data Table 1). Although detailed reactions might differ between different photochemical models, the main paths remain robust.

KINETICS

The KINETICS 1D thermo-photochemical transport model[42] uses the Caltech/JPL KINETICS model[82,83] to solve the coupled 1D continuity equations describing the chemical production, loss and vertical transport of atmospheric constituents of WASP-39 b. The model contains 150 neutral C-bearing, H-bearing, O-bearing, N-bearing, S-bearing and Cl-bearing species that interact with each other through a total of 2,350 reactions (that is, 1,175 forward–reverse reaction pairs). These reactions have all been fully reversed through the thermodynamic principle of microscopic reversibility[84], such that the model would reproduce thermochemical equilibrium in the absence of transport and external energy sources, given sufficient integration time. The chemical reaction list involving C-bearing, H-bearing, O-bearing and N-bearing species is taken directly from ref. [22]. Included for the first time here are 41 sulfur and chlorine species: S, S(1D), S_2, S_3, S_4, S_8, SH, H_2S, HS_2, H_2S_2, CS, CS_2, HCS, H_2CS, CH_3S, CH_3SH, SO, SO_2, SO_3, S_2O, $HOSO_2$, H_2SO_4 (gas and condensed), OCS, NS, NCS, HNCS, Cl, Cl_2, HCl, ClO, HOCl, ClCO, $ClCO_3$, ClS, ClS_2, Cl_2S, ClSH, OSCl, $ClSO_2$ and SO_2Cl_2. The thermodynamic data of several chlorine-bearing and sulfur-bearing species are not available in the previous literature and we performed ab initio calculations for these species. We first carried out electronic-structure calculations at the CBS-QB3 level of theory using Gaussian 09 (ref. [85]) to determine geometric conformations, energies and vibrational frequencies of the target molecules. Then the thermodynamic properties of these molecules were calculated by Arkane (ref. [86]), a package included in the open-source software RMG v3.1.0 (refs. [87,88]), with atomic-energy corrections, bond corrections and spin–orbit corrections, based on the CBS-QB3 level of theory as the model chemistry. The reaction rate coefficients and photolysis cross-sections for these S and Cl species are derived from Venus studies[89,90,91,92,93,94], interstellar medium studies[95], Io photochemical models[96,97], Jupiter cometary-impact models[98,99], the combustion-chemistry literature[100,101,102,103], terrestrial stratospheric compilations[104,105] and numerous individual laboratory or computational kinetics studies (such as refs. [106,107,108,109,110]).

ARGO

The 1D thermochemical and photochemical kinetics code ARGO originally[111,112] used the Stand2019 network for neutral hydrogen, carbon, nitrogen and oxygen chemistry. ARGO solves the coupled 1D continuity equation including thermochemical-photochemical reactions and vertical transport. The Stand2019 network was expanded by Rimmer et al. [113] by updating several reactions, incorporating the sulfur network developed by ref. [15], and supplementing it with reactions from refs. [93,114], to produce the Stand2020 network. The Stand2020 network includes 2,901 reversible reactions and 537 irreversible reactions, involving 480 species composed of H, C, N, O, S, Cl and other elements.

ATMO

The C-H-N-O chemical kinetics scheme from ref. [115] is implemented by ref. [116] in the standard 1D atmosphere model ATMO, which solves for the chemical disequilibrium steady state. As of the time of writing of this article, the sulfur kinetic scheme of ATMO, derived from applied combustion models, is still at the development and validation stage. Hence, for WASP-39b, we performed ATMO with the C-H-N-O-S thermochemical network from VULCAN (ref. [6]) along with the photochemical scheme from ref. [117] (an update of the native photochemical scheme from ref. [115]), with another 71 photolysis reactions of H_2S, S_2, S_2O, SO, SO_2, CH_3SH, SH, H_2SO and COS.

Sensitivity tests

We examine the sensitivity of our chemical outcomes to essential atmospheric properties using VULCAN. For models with various metallicity and C/O ratios, we explore the sensitivity to temperature and vertical mixing by systematically varying the temperature–pressure and eddy diffusion coefficient profiles. Specifically, the temperature throughout the atmosphere is shifted by 50 K and the eddy diffusion coefficients are multiplied/divided by 10. These variations span a range comparable with the temperature differences among radiative transfer models[47] and the uncertainties in parameterizing vertical mixing with eddy diffusion coefficients[118,119]. On our choice of internal heat, we have further conducted tests with different

internal temperatures and found that the compositions above 1 bar are not sensitive to internal temperature, because the quench levels of the main species are at higher levels given the adopted eddy diffusion coefficient. We have also verified that the temperature above the top boundary of the GCM (about 5×10^{-5} bar; Extended Data Fig. 2) does not affect the composition below.

Sensitivity to C/O is summarized in Extended Data Fig. 5, in which the nominal model has a C/O ratio of 0.55, as in the main text. The averaged abundance of both SO_2 and H_2O in the pressure region relevant for transmission spectrum observations show similar dependencies on C/O, decreasing by a few factors as the C/O increased from sub-solar (0.25) to super-solar (0.75) values. The averaged abundance of SO_2 is not very sensitive to temperature and vertical mixing either, except for C/O = 0.75, for which the SO_2 concentration is at roughly the ppm level, similar to what is found in Fig. 4.

Finally, we performed sensitivity tests to the UV irradiation—the ultimate energy source of photochemistry. We first tested the sensitivity to the assumed stellar spectra by performing the same models with the solar spectrum (close to WASP-39) and found negligible differences in the photochemical results. Because the UV spectrum shortward of 295 nm is constructed from stellar proxies rather than directly measured, we then focused on varying the stellar flux in the FUV (1–230 nm) and NUV (230–295 nm) separately. Extended Data Fig. 8 shows that the resulting sulfur species abundances are almost identical when the UV flux is reduced by a factor of 10, broadly consistent with what Zahnle et al.[5] suggested that the photochemical destruction of H_2S only becomes photon-limited when the stellar UV flux is reduced by about two orders of magnitude (for a directly imaged gas giant). On the other hand, although SO and SO_2 are not sensitive to increased NUV, they are substantially depleted with increased FUV. This is because the photodissociation of SO and SO_2 mainly operates in the FUV and the enhanced FUV can destroy SO and SO_2, even with the same amount of available OH radicals.

Spectral effects of assuming a vertically uniform SO_2 distribution

Minor species commonly have VMR varying with altitude in the observable region of the atmosphere, especially those produced or destroyed by photochemistry. Extended Data Fig. 9 demonstrates that assuming a vertically constant VMR of SO_2 can lead to underestimating its abundances by about an order of magnitude. This is verified by comparing the column-integrated number density from the pressure level relevant for transmission spectroscopy. For example, the terminator-averaged column-integrated number density of SO_2 above 10 mbar by VULCAN is about 1.4×10^{19} molecules cm^{-2}, which is equal to a vertically uniform SO_2 with a concentration around 4 ppm. Hence modelling frameworks that assume vertically uniform composition should be treated with caution and would benefit from comparisons with photochemical models, especially for photochemically active species that can exhibit large vertical gradients.

Opacities of sulfur species

The opacities of sulfur species illustrated in Extended Data Fig. 7 are compiled from UV cross-sections and infrared line lists. The room-temperature UV cross-sections are taken from the Leiden Observatory database[120] (http://home.strw.leidenuniv.nl/~ewine/photo). The infrared opacities include SO_2 (ref. [121]), H_2S (refs. [122,48]), CS (ref. [123]) and a newly computed high-temperature line list for SO (ref. [74]). The opacity from OCS (ref. [124]) is only available up to room temperature at present, hence its coverage is probably incomplete in our region of interest.

Alternative SO_2 production pathways

S_2 formation can compete with SO_2 production, as we will explore in detail in the next section. On WASP-39b, reactions involving S_2 are found to be important in oxidizing S at high pressures at which less OH is available. S and SH would first react to form S_2 by $SH + S \rightarrow H + S_2$ before getting

oxidized through $S_2 + OH \rightarrow SO + SH$. The scheme is similar to that in equation (1) except SH and S_2 play the role of the catalyst to oxidize S into SO, whereas SO can also self-react to form SO_2 in this regime (references of important reactions are listed in Extended Data Table 1).

Implications of observing sulfur photochemistry

The temperature of WASP-39b resides within the sweet spot of producing SO_2 (ref. [16]). Previous photochemical modelling works suggested that, at lower temperatures, sulfur allotropes would be favoured over SO_2, whereas SH can prevail at higher temperatures[5,6]. Here we briefly explain the general temperature trends of sulfur photochemical products.

After S is liberated from H_2S, sulfur can follow either the oxidization or the chain polymerization paths, as illustrated in Fig. 2. The competing of the two paths is essentially controlled by the abundance of the oxidizing radical OH relative to atomic H. We can estimate the OH to H ratio by assuming that OH is in quasi-equilibrium with H_2O, that is, ${k}_{{{\rm{H}}}_{2}{\rm{O}}}[{{\rm{H}}}_{2}{\rm{O}}][{\rm{H}}]={k}_{{{\rm{H}}}_{2}{\rm{O}}}^{{\prime} }[{\rm{OH}}][{{\rm{H}}}_{2}]$, in which ${k}_{{{\rm{H}}}_{2}{\rm{O}}}$ and ${k}_{{{\rm{H}}}_{2}{\rm{O}}}^{{\prime} }$ are the forward and backward rate constants of $H_2O + H \rightarrow OH + H_2$, respectively. Then, ${\rm{[OH]/[H]}}\approx 2\frac{{k}_{{{\rm{H}}}_{2}{\rm{O}}}}{{k}_{{{\rm{H}}}_{2}{\rm{O}}}^{{\prime} }}\times {\rm{O}}/{\rm{H}}$, because most of the O is in H_2O. Extended Data Fig. 10a shows that the [OH]/[H] ratio strongly depends on temperature. When the temperature drops below about 750 K, the scarcity of OH makes S preferably react with SH to form S_2. SO and SO_2 could only be produced at higher altitudes, at which more OH is available from water photolysis (for example, refs. [5,6]).

We further perform photochemical calculations using VULCAN with a grid of temperature profiles across planetary equilibrium temperatures 600–2,000 K, adopted from the 1D radiative–convective equilibrium models applied in ref. [39], in which an internal temperature of 100 K with perfect heat

redistribution and gravity $g = 1{,}000\ \mathrm{cm\ s^{-2}}$ are assumed. Apart from the thermal profiles, we keep the rest of the planetary parameters the same as the WASP-39b model in this work, including stellar UV irradiation. Extended Data Fig. 10b reveals the observation of sulfur photochemistry on other irradiated exoplanets, summarizing the averaged abundances of the key sulfur molecules produced by photochemistry as a function of equilibrium temperature. For 10× solar metallicity, the sweet-spot temperature for producing observable SO_2 is $1{,}000\ \mathrm{K} \lesssim T_{eq} \lesssim 1{,}600\ \mathrm{K}$. For $T_{eq} \lesssim 1{,}000\ \mathrm{K}$, SO_2 production below the 0.01-mbar level ceased and S_x (sulfur allotropes; mainly S_2 and S_8 here) is more favoured. For $T_{eq} \gtrsim 1{,}600\ \mathrm{K}$, SH becomes the predominant sulfur-bearing molecular (apart from atomic S) around mbar levels. Although observing SH is challenging in the infrared, it can potentially be identified in the near-UV (300–400 nm)[125].

Data availability

The data used in this paper are associated with JWST ERS Program 1366 and are available from the Mikulski Archive for Space Telescopes (https://mast.stsci.edu), which is operated by the Association of Universities for Research in Astronomy, Inc., under NASA contract NAS 5-03127 for JWST. The chemical networks and abundance output of the photochemical models (ARGO, ATMO, KINETICS and VULCAN) presented in this study are available at https://doi.org/10.5281/zenodo.7542781.

Code availability

The codes VULCAN and gCMCRT used in this work to simulate composition and produce synthetic spectra are publicly available: VULCAN[6,78] (https://github.com/exoclime/VULCAN); gCMCRT[40] (https://github.com/ELeeAstro/gCMCRT).

References

1. Yung, Y. L. & DeMore, W. B. *Photochemistry of Planetary Atmospheres* (Oxford Univ. Press, 1999).

2. Stevenson, K. B. et al. Transiting exoplanet studies and community targets for JWST's Early Release Science Program. *Publ. Astron. Soc. Pac.* **128**, 094401–094411 (2016).

3. Bean, J. L. et al. The Transiting Exoplanet Community Early Release Science Program for JWST. *Publ. Astron. Soc. Pac.* **130**, 114402–114421 (2018).

4. Faedi, F. et al. WASP-39b: a highly inflated Saturn-mass planet orbiting a late G-type star. *Astron. Astrophys.* **531**, A40 (2011).

5. Zahnle, K., Marley, M. S., Morley, C. V. & Moses, J. I. Photolytic hazes in the atmosphere of 51 ERI b. *Astrophys. J.* **824**, 137 (2016).

6. Tsai, S.-M. et al. A comparative study of atmospheric chemistry with VULCAN. *Astrophys. J.* **923**, 264 (2021).

7. JWST Transiting Exoplanet Community Early Release Science Team. Identification of carbon dioxide in an exoplanet atmosphere. *Nature* **614**, 649–652 (2023).

8. Rustamkulov, Z. et al. Early Release Science of the exoplanet WASP-39b with JWST NIRSpec PRISM. *Nature* **614**, 659–663 (2023).

9. Alderson, L. et al. Early Release Science of the exoplanet WASP-39b with JWST NIRSpec G395H. *Nature* **614**, 664–669 (2023).

10. Seinfeld, J. H. & Pandis, S. N. *Atmospheric Chemistry and Physics: From Air Pollution to Climate Change* (Wiley, 2016).

11. Atreya, S. et al. A comparison of the atmospheres of Jupiter and Saturn: deep atmospheric composition, cloud structure, vertical mixing, and origin. *Planet. Space Sci.* **47**, 1243–1262 (1999).

12. Visscher, C., Lodders, K. & Fegley, B.Jr Atmospheric chemistry in giant planets, brown dwarfs, and low-mass dwarf stars. II. Sulfur and phosphorus. *Astrophys. J.* **648**, 1181–1195 (2006).

13. Zahnle, K., Marley, M. S., Freedman, R. S., Lodders, K. & Fortney, J. J. Atmospheric sulfur photochemistry on hot Jupiters. *Astrophys. J.* **701**, L20–L24 (2009).

14. Wang, D., Miguel, Y. & Lunine, J. Modeling synthetic spectra for transiting extrasolar giant planets: detectability of H_2S and PH_3 with the James Webb Space Telescope. *Astrophys. J.* **850**, 199 (2017).

15. Hobbs, R., Rimmer, P. B., Shorttle, O. & Madhusudhan, N. Sulfur chemistry in the atmospheres of warm and hot Jupiters. *Mon. Not. R. Astron. Soc.* **506**, 3186–3204 (2021).

16. Polman, J., Waters, L. B. F. M., Min, M., Miguel, Y. & Khorshid, N. H_2S and SO_2 detectability in hot Jupiters: sulfur species as indicator of metallicity and C/O ratio. *Astron. Astrophys*. **670**, A161 (2023).

17. Lee, E. K. H. et al. Simulating gas giant exoplanet atmospheres with Exo-FMS: comparing semigrey, picket fence, and correlated-*k* radiative-transfer schemes. *Mon. Not. R. Astron. Soc.* **506**, 2695–2711 (2021).

18. Lodders, K. Solar elemental abundances. Oxford Research Encyclopedia of Planetary Science (2020).

19. Wakeford, H. R. et al. The complete transmission spectrum of WASP-39b with a precise water constraint. *Astron. J.* **155**, 29 (2018).

20. Lodders, K. & Fegley, B. Atmospheric chemistry in giant planets, brown dwarfs, and low-mass dwarf stars. I. Carbon, nitrogen, and oxygen. *Icarus* **155**, 393–424 (2002).

21. Madhusudhan, N. & Seager, S. High metallicity and non-equilibrium chemistry in the dayside atmosphere of hot-Neptune GJ 436b. *Astrophys. J.* **729**, 41 (2011).

22. Moses, J. I. et al. Compositional diversity in the atmospheres of hot Neptunes, with application to GJ 436b. *Astrophys. J.* **777**, 34 (2013).

23. Charbonneau, D., Brown, T. M., Noyes, R. W. & Gilliland, R. L. Detection of an extrasolar planet atmosphere. *Astrophys. J.* **568**, 377–384 (2002).

24. Liang, M.-C., Parkinson, C. D., Lee, A. Y.-T., Yung, Y. L. & Seager, S. Source of atomic hydrogen in the atmosphere of HD 209458b. *Astrophys. J.* **596**, L247–L250 (2003).

25. Moses, J. I. Chemical kinetics on extrasolar planets. *Philos. Trans. R. Soc. Lond. Ser. A* **372**, 20130073 (2014).

26. Venot, O. et al. VUV-absorption cross section of carbon dioxide from 150 to 800 K and applications to warm exoplanetary atmospheres. *Astron. Astrophys.* **609**, A34 (2018).

27. Fortney, J. et al. The need for laboratory measurements and ab initio studies to aid understanding of exoplanetary atmospheres. Preprint at https://arxiv.org/abs/1905.07064 (2019).

28. Tsai, S.-M. et al. Inferring shallow surfaces on sub-Neptune exoplanets with JWST. *Astrophys. J. Lett.* **922**, L27 (2021).

29. Moses, J. I., Tremblin, P., Venot, O. & Miguel, Y. Chemical variation with altitude and longitude on exo-Neptunes: predictions for ariel phase-curve observations. *Exp. Astron* **53**, 279–322 (2022).

30. Baeyens, R., Konings, T., Venot, O., Carone, L. & Decin, L. Grid of pseudo-2D chemistry models for tidally locked exoplanets - II. The role of photochemistry. *Mon. Not. R. Astron. Soc.* **512**, 4877–4892 (2022).

31. Atreya, S. K. et al. Deep atmosphere composition, structure, origin, and exploration, with particular focus on critical in situ science at the icy giants. *Space Sci. Rev.* **216**, 18 (2020).

32. Semenov, D. et al. Chemistry in disks. XI. Sulfur-bearing species as tracers of protoplanetary disk physics and chemistry: the DM Tau case. *Astron. Astrophys.* **617**, A28 (2018).

33. Kama, M. et al. Abundant refractory sulfur in protoplanetary disks. *Astrophys. J.* **885**, 114 (2019).

34. Öberg, K. I. & Wordsworth, R. Jupiter's composition suggests its core assembled exterior to the N_2 snowline. *Astron. J.* **158**, 194 (2019).

35. Turrini, D. et al. Tracing the formation history of giant planets in protoplanetary disks with carbon, oxygen, nitrogen, and sulfur. *Astrophys. J.* **909**, 40 (2021).

36. Pacetti, E. et al. Chemical diversity in protoplanetary disks and its impact on the formation history of giant planets. *Astrophys. J.* **937**, 36 (2022).

37. Nikolov, N. et al. VLT FORS2 comparative transmission spectroscopy: detection of Na in the atmosphere of WASP-39b from the ground. *Astrophys. J.* **832**, 191 (2016).

38. Stock, J. W., Kitzmann, D. & Patzer, A. B. C. FastChem 2: an improved computer program to determine the gas-phase chemical equilibrium composition for arbitrary element distributions. *Mon. Not. R. Astron. Soc.* **517**, 4070–4080 (2022).

39. Ohno, K. & Fortney, J. J. Nitrogen as a tracer of giant planet formation. I.: a universal deep adiabatic profile and semi-analytical predictions of disequilibrium ammonia abundances in warm exoplanetary atmospheres. Preprint at https://arxiv.org/abs/2211.16876 (2022).

40. Lee, E. K. H. et al. 3D radiative transfer for exoplanet atmospheres. gCMCRT: a GPU-accelerated MCRT code. *Astrophys. J.* **929**, 180 (2022).

41. Underwood, D. S. et al. ExoMol molecular line lists - XIV. The rotation–vibration spectrum of hot SO_2. *Mon. Not. R. Astron. Soc.* **459**, 3890–3899 (2016).

42. Moses, J. I. et al. Disequilibrium carbon, oxygen, and nitrogen chemistry in the atmospheres of HD 189733b and HD 209458b.

Astrophys. J. **737**, 15 (2011).

43. Gao, P. et al. Aerosol composition of hot giant exoplanets dominated by silicates and hydrocarbon hazes. *Nat. Astron.* **4**, 951–956 (2020).

44. Yu, X. et al. Haze evolution in temperate exoplanet atmospheres through surface energy measurements. *Nat. Astron.* **5**, 822–831 (2021).

45. Thorngren, D., Gao, P. & Fortney, J. J. The intrinsic temperature and radiative–convective boundary depth in the atmospheres of hot Jupiters. *Astrophys. J. Lett.* **884**, L6 (2019).

46. Wardenier, J. P., Parmentier, V. & Lee, E. K. H. All along the line of sight: a closer look at opening angles and absorption regions in the atmospheres of transiting exoplanets. *Mon. Not. R. Astron. Soc.* **510**, 620–629 (2022).

47. Malik, M. et al. Self-luminous and irradiated exoplanetary atmospheres explored with HELIOS. *Astron. J.* **157**, 170 (2019).

48. Gorman, M. N., Yurchenko, S. N. & Tennyson, J. ExoMol molecular line lists XXXVI: X $^2\Pi$ – X $^2\Pi$ and A $^2\Sigma^+$ – X $^2\Pi$ transitions of SH. *Mon. Not. R. Astron. Soc.* **490**, 1652–1665 (2019).

49. Lavvas, P. & Arfaux, A. Impact of photochemical hazes and gases on exoplanet atmospheric thermal structure. *Mon. Not. R. Astron. Soc.* **502**, 5643–5657 (2021).

50. Guillot, T. On the radiative equilibrium of irradiated planetary atmospheres. *Astron. Astrophys.* **520**, A27–A39 (2010).

51. Mancini, L. et al. The GAPS programme with HARPS-N at TNG. XVI. Measurement of the Rossiter–McLaughlin effect of transiting planetary systems HAT-P-3, HAT-P-12, HAT-P-22, WASP-39, and WASP-60. *Astron. Astrophys.* **613**, A41 (2018).

52. Boro Saikia, S. et al. Chromospheric activity catalogue of 4454 cool stars. Questioning the active branch of stellar activity cycles. *Astron. Astrophys.* **616**, A108 (2018).

53. Casagrande, L. et al. New constraints on the chemical evolution of the solar neighbourhood and Galactic disc(s). Improved astrophysical parameters for the Geneva-Copenhagen Survey. *Astron. Astrophys.* **530**, A138 (2011).

54. Ayres, T. R. StarCAT: a catalog of space telescope imaging spectrograph ultraviolet echelle spectra of stars. *Astrophys. J. Suppl.* **187**, 149–171 (2010).

55. Mamajek, E. E. & Hillenbrand, L. A. Improved age estimation for solar-type dwarfs using activity-rotation diagnostics. *Astrophys. J.* **687**, 1264–1293 (2008).

56. Fossati, L. et al. Suppressed far-UV stellar activity and low planetary mass loss in the WASP-18 system. *Astron. J.* **155**, 113 (2018).

57. Schlegel, D. J., Finkbeiner, D. P. & Davis, M. Maps of dust infrared emission for use in estimation of reddening and cosmic microwave background radiation foregrounds. *Astrophys. J.* **500**, 525–553 (1998).

58. Cardelli, J. A., Clayton, G. C. & Mathis, J. S. The relationship between infrared, optical, and ultraviolet extinction. *Astrophys. J.* **345**, 245 (1989).

59. Woods, T. N. et al. Solar Irradiance Reference Spectra (SIRS) for the 2008 Whole Heliosphere Interval (WHI). *Geophys. Res. Lett.* **36**, L01101 (2009).

60. Shkolnik, E. L. An ultraviolet investigation of activity on exoplanet host stars. *Astrophys. J.* **766**, 9 (2013).

61. Polyansky, O. L. et al. ExoMol molecular line lists XXX: a complete high-accuracy line list for water. *Mon. Not. R. Astron. Soc.* **480**, 2597–2608 (2018).

62. Hargreaves, R. J., Gordon, I. E., Kochanov, R. V. & Rothman, L. S. HITEMP: extensive molecular line lists for high-temperature exoplanet atmospheres. In *EPSC-DPS Joint Meeting 2019* Vol. 13, EPSC-DPS2019-919-1 (2019).

63. Li, G. et al. Rovibrational line lists for nine isotopologues of the CO molecule in the X $^1\Sigma^+$ ground electronic state. *Astrophys. J. Suppl. Ser.* **216**, 15 (2015).

64. Yurchenko, S. N., Mellor, T. M., Freedman, R. S. & Tennyson, J. ExoMol line lists – XXXIX. Ro-vibrational molecular line list for CO_2. *Mon. Not. R. Astron. Soc.* **496**, 5282–5291 (2020).

65. Hargreaves, R. J. et al. An accurate, extensive, and practical line list of methane for the HITEMP database. *Astrophys. J. Suppl.* **247**, 55 (2020).

66. Adam, A. Y., Yachmenev, A., Yurchenko, S. N. & Jensen, P. Variationally computed IR line list for the methyl radical CH_3. *J. Phys. Chem. A* **123**, 4755–4763 (2019).

67. Barber, R. J. et al. ExoMol line lists – III. An improved hot rotation-vibration line list for HCN and HNC. *Mon. Not. R. Astron. Soc.* **437**, 1828–1835 (2014).

68. Chubb, K. L., Tennyson, J. & Yurchenko, S. N. ExoMol molecular line lists – XXXVII. Spectra of acetylene. *Mon. Not. R. Astron. Soc.* **493**, 1531–1545 (2020).

69. Mant, B. P., Yachmenev, A., Tennyson, J. & Yurchenko, S. N. ExoMol molecular line lists – XXVII. Spectra of C_2H_4. *Mon. Not. R. Astron. Soc.* **478**, 3220–3232 (2018).

70. Gordon, I. E. et al. The HITRAN2020 molecular spectroscopic database. *J. Quant. Spectrosc. Radiat. Transf.* **277**, 107949 (2022).

71. Yurchenko, S. N., Szabó, I., Pyatenko, E. & Tennyson, J. ExoMol line lists XXXI: spectroscopy of lowest eights electronic states of C_2. *Mon. Not. R. Astron. Soc.* **480**, 3397–3411 (2018).

72. Syme, A.-M. & McKemmish, L. K. Full spectroscopic model and trihybrid experimental-perturbative-variational line list for CN. *Mon. Not. R. Astron. Soc.* **505**, 4383–4395 (2021).

73. Masseron, T. et al. CH in stellar atmospheres: an extensive linelist. *Astron. Astrophys.* **571**, A47 (2014).

74. Brady, R. P., Yurchenko, S. N., Kim, G. S., Somogyi, W. & Tennyson, J. An ab initio study of the rovibronic spectrum of sulphur monoxide (SO): diabatic vs. adiabatic representation. *Phys. Chem. Chem. Phys.* **24**, 24076–24088 (2022).

75. Azzam, A. A. A., Tennyson, J., Yurchenko, S. N. & Naumenko, O. V. ExoMol molecular line lists – XVI. The rotation-vibration spectrum of hot H_2S. *Mon. Not. R. Astron. Soc.* **460**, 4063–4074 (2016).

76. Hargreaves, R. J. et al. Spectroscopic line parameters of NO, NO_2, and N_2O for the HITEMP database. *J. Quant. Spectrosc. Radiat. Transf.* **232**, 35–53 (2019).

77. Kurucz, R. L. & Bell, B. Atomic line data. Kurucz CD-ROM no. 23 (Smithsonian Astrophysical Observatory, 1995).

78. Tsai, S.-M. et al. VULCAN: an open-source, validated chemical kinetics Python code for exoplanetary atmospheres. *Astrophys. J. Suppl. Ser.* **228**, 20 (2017).

79. Moses, J. I. Sl9 impact chemistry: long-term photochemical evolution. *Int. Astron. Union Colloq.* **156**, 243–268 (1996).

80. Du, S., Francisco, J. S., Shepler, B. C. & Peterson, K. A. Determination of the rate constant for sulfur recombination by quasiclassical trajectory calculations. *J. Chem. Phys.* **128**, 204306 (2008).

81. Tsai, S.-M. et al. Toward consistent modeling of atmospheric chemistry and dynamics in exoplanets: validation and generalization of the chemical relaxation method. *Astrophys. J* **862**, 31 (2018).

82. Allen, M., Yung, Y. L. & Waters, J. W. Vertical transport and photochemistry in the terrestrial mesosphere and lower thermosphere (50–120 km). *J. Geophys. Res.* **86**, 3617–3627 (1981).

83. Yung, Y. L., Allen, M. & Pinto, J. P. Photochemistry of the atmosphere of Titan: comparison between model and observations. *Astrophys. J. Suppl. Ser.* **55**, 465–506 (1984).

84. Visscher, C. & Moses, J. I. Quenching of carbon monoxide and methane in the atmospheres of cool brown dwarfs and hot Jupiters. *Astrophys. J.* **738**, 72 (2011).

85. Frisch, M. J. et al. Gaussian 09, revision E.01 (Gaussian Inc., 2009).

86. Allen, J. W., Goldsmith, C. F., Green, W. H. & West, R. H. Automatic estimation of pressure-dependent rate coefficients. *Phys. Chem. Chem. Phys.* **14**, 1131–1155 (2012).

87. Gao, C. W., Allen, J. W., Green, W. H. & West, R. H. Reaction Mechanism Generator: automatic construction of chemical kinetic mechanisms. *Comput. Phys. Commun.* **203**, 212–225 (2016).

88. Liu, M. et al. Reaction Mechanism Generator v3.0: advances in automatic mechanism generation. *J. Chem. Inf. Model* **61**, 2686–2696 (2021).

89. Yung, Y. L. & Demore, W. B. Photochemistry of the stratosphere of Venus: implications for atmospheric evolution. *Icarus* **51**, 199–247 (1982).

90. Mills, F. P. *I. Observations and Photochemical Modeling of the Venus Middle Atmosphere. II. Thermal Infrared Spectroscopy of Europa and Callisto* (California Inst. Technol., 1998).

91. Mills, F. P. & Allen, M. A review of selected issues concerning the chemistry in Venus' middle atmosphere. *Planet. Space Sci.* **55**, 1729–1740 (2007).

92. Krasnopolsky, V. A. Chemical kinetic model for the lower atmosphere of Venus. *Icarus* **191**, 25–37 (2007).

93. Zhang, X., Liang, M. C., Mills, F. P., Belyaev, D. A. & Yung, Y. L. Sulfur chemistry in the middle atmosphere of Venus. *Icarus* **217**, 714–

739 (2012).

94. Bierson, C. J. & Zhang, X. Chemical cycling in the Venusian atmosphere: a full photochemical model from the surface to 110 km. *J. Geophys. Res.* **125**, e06159 (2020).

95. Vidal, T. H. G. et al. On the reservoir of sulphur in dark clouds: chemistry and elemental abundance reconciled. *Mon. Not. R. Astron. Soc.* **469**, 435–447 (2017).

96. Moses, J. I., Zolotov, M. Y. & Fegley, B.Jr Alkali and chlorine photochemistry in a volcanically driven atmosphere on Io. *Icarus* **156**, 107–135 (2002).

97. Moses, J. I., Zolotov, M. Y. & Fegley, B.Jr Photochemistry of a volcanically driven atmosphere on Io: sulfur and oxygen species from a Pele-type eruption. *Icarus* **156**, 76–106 (2002).

98. Moses, J. I., Allen, M. & Gladstone, G. R. Nitrogen and oxygen photochemistry following SL9. *Geophys. Res. Lett.* **22**, 1601–1604 (1995).

99. Moses, J. I., Allen, M. & Gladstone, G. R. Post-SL9 sulfur photochemistry on Jupiter. *Geophys. Res. Lett.* **22**, 1597–1600 (1995).

100. Sendt, K., Jazbec, M. & Haynes, B. S. Chemical kinetic modeling of the H/S system: H_2S thermolysis and H_2 sulfidation. *Proc. Combust. Inst.* **29**, 2439–2446 (2002).

101. Zhou, C., Sendt, K. & Haynes, B. S. Experimental and kinetic modelling study of H_2S oxidation. *Proc. Combust. Inst.* **34**, 625–632 (2013).

102. Zeng, Z., Altarawneh, M., Oluwoye, I., Glarborg, P. & Dlugogorski, B. Z. Inhibition and promotion of pyrolysis by hydrogen sulfide (H_2S) and sulfanyl radical (SH). *J. Phys. Chem. A* **120**, 8941–8948 (2016).

103. Alzueta, M. U., Pernía, R., Abián, M., Millera, A. & Bilbao, R. CH_3SH conversion in a tubular flow reactor. Experiments and kinetic modelling. *Combust. Flame* **203**, 23–30 (2019).

104. Sander, S. P. et al. Chemical kinetics and photochemical data for use in atmospheric studies. JPL publication no. 10-6 (2011).

105. Burkholder, J. B. et al. Chemical kinetics and photochemical data for use in atmospheric studies. Evaluation number 19. JPL publication 19-5 (2020).

106. Jourdain, J. L., Le Bras, G. & Combourieu, J. Kinetic study of some elementary reactions of sulfur compounds including reactions of S and SO with OH radicals. *Int. J. Chem. Kinetics* **11**, 569–577 (1979).

107. Shiina, H., Miyoshi, A. & Matsui, H. Investigation on the insertion channel in the $S(^3P) + H_2$ reaction. *J. Phys. Chem. A* **102**, 556–3559 (1998).

108. Peng, J., Hu, X. & Marshall, P. Experimental and ab initio investigations of the kinetics of the reaction of H atoms with H_2S. *J. Phys. Chem. A* **103**, 5307–5311 (1999).

109. Du, S., Francisco, J. S., Shepler, B. C. & Peterson, K. A. Determination of the rate constant for sulfur recombination by quasiclassical trajectory calculations. *J. Chem. Phys.* **128**, 204306 (2008).

110. Woon, D. E., Maffucci, D. M. & Herbst, E. Theoretical kinetic studies of Venus chemistry. Formation and destruction of SCl, SCl_2, and HSCl. *Icarus* **354**, 114051 (2021).

111. Rimmer, P. B. & Helling, C. A chemical kinetics network for lightning and life in planetary atmospheres. *Astrophys. J. Suppl. Ser.* **224**, 9 (2016).

112. Rimmer, P. B. & Rugheimer, S. Hydrogen cyanide in nitrogen-rich atmospheres of rocky exoplanets. *Icarus* **329**, 124–131 (2019).

113. Rimmer, P. B. et al. Hydroxide salts in the clouds of Venus: their effect on the sulfur cycle and cloud droplet pH. *Planet. Sci. J.* **2**, 133 (2021).

114. Krasnopolsky, V. A. Chemical kinetic model for the lower atmosphere of Venus. *Icarus* **191**, 25–37 (2007).

115. Venot, O. et al. A chemical model for the atmosphere of hot Jupiters. *Astron. Astrophys.* **546**, A43 (2012).

116. Drummond, B. et al. The effects of consistent chemical kinetics calculations on the pressure-temperature profiles and emission spectra of hot Jupiters. *Astron. Astrophys.* **594**, A69 (2016).

117. Venot, O. et al. New chemical scheme for giant planet thermochemistry. Update of the methanol chemistry and new reduced chemical scheme. *Astron. Astrophys.* **634**, A78 (2020).

118. Parmentier, V., Fortney, J. J., Showman, A. P., Morley, C. & Marley, M. S. Transitions in the cloud composition of hot Jupiters. *Astrophys. J.* **828**, 22 (2016).

119. Komacek, T. D., Showman, A. P. & Parmentier, V. Vertical tracer mixing in hot Jupiter atmospheres. *Astrophys. J.* **881**, 152 (2019).

120. Heays, A. N., Bosman, A. D. & van Dishoeck, E. F. Photodissociation and photoionisation of atoms and molecules of astrophysical interest. *Astron. Astrophys.* **602**, A105 (2017).

121. Underwood, D. S. et al. ExoMol line lists XIV: a line list for hot SO_2. *Mon. Not. R. Astron. Soc.* **459**, 3890–3899 (2016).

122. Azzam, A. A. A., Yurchenko, S. N., Tennyson, J. & Naumenko, O. V. ExoMol line lists XVI: a hot line list for H_2S. *Mon. Not. R. Astron. Soc.* **460**, 4063–4074 (2016).

123. Paulose, G., Barton, E. J., Yurchenko, S. N. & Tennyson, J. ExoMol molecular linelists – XII. Line lists for eight isotopologues of CS. *Mon. Not. R. Astron. Soc.* **454**, 1931–1939 (2015).

124. Gordon, I. E. et al. The HITRAN2020 molecular spectroscopic database. *J. Quant. Spectrosc. Radiat. Transf.* **277**, 107949 (2021).

125. Evans, T. M. et al. An optical transmission spectrum for the ultra-hot Jupiter WASP-121b measured with the Hubble Space Telescope. *Astron. J.* **156**, 283 (2018).

Acknowledgements

This work is based on observations made with the NASA/ESA/CSA JWST. The working groups are associated with programme JWST-ERS-01366. The initial manuscript was improved by the constructive comments from L. Mancini, J. Mendonça, A. Saba and X. Tan. S.-M.T. is supported by the European Research Council advanced grant EXOCONDENSE (no. 740963; principal investigator: R. T. Pierrehumbert). E.K.H.L. is supported by the SNSF Ambizione Fellowship grant (no. 193448). X.Z. is supported by NASA Exoplanet Research grant 80NSSC22K0236. O.V. acknowledges funding from the ANR project ‘EXACT’ (ANR-21-CE49-0008-01), from the Centre National d’Études Spatiales (CNES) and from the CNRS/INSU Programme National de Planétologie (PNP). L.D. acknowledges support from the European Union H2020-MSCA-ITN-2109 under grant no. 860470 (CHAMELEON) and the KU Leuven IDN/19/028 grant Escher. This work benefited from the 2022 Exoplanet Summer Program at the Other Worlds Laboratory (OWL) at the University of California, Santa Cruz, a programme financed by the Heising-Simons Foundation. T.D. is an LSSTC Catalyst Fellow. J.K. is an Imperial College Research Fellow. B.V.R. is a 51 Pegasi b Fellow. L.W. is an NHFP Sagan Fellow. A.D.F. is an NSF Graduate Research Fellow.

Author information

Authors and Affiliations

1. Atmospheric, Oceanic and Planetary Physics, Department of Physics, University of Oxford, Oxford, UK

   Shang-Min Tsai & Jake Taylor

2. Department of Earth Sciences, University of California, Riverside, Riverside, CA, USA

Shang-Min Tsai

3. Center for Space and Habitability, University of Bern, Bern, Switzerland

Elspeth K. H. Lee

4. Center for Astrophysics | Harvard & Smithsonian, Cambridge, MA, USA

Diana Powell, Mercedes López-Morales & James Kirk

5. Earth and Planets Laboratory, Carnegie Institution for Science, Washington, DC, USA

Peter Gao, Munazza K. Alam & Nicole L. Wallack

6. Department of Earth and Planetary Sciences, University of California, Santa Cruz, Santa Cruz, CA, USA

Xi Zhang

7. Space Science Institute, Boulder, CO, USA

Julianne Moses & Channon Visscher

8. University of Exeter, Exeter, UK

Eric Hébrard

9. Université de Paris Cité and Univ. Paris Est Creteil, CNRS, LISA, Paris, France

Olivia Venot

10. Université Côte d’Azur, Observatoire de la Côte d’Azur, CNRS, Laboratoire Lagrange, Nice, France

Vivien Parmentier

11. Institute of Astronomy, University of Cambridge, Cambridge, UK

Sean Jordan & Oliver Shorttle

12. Jet Propulsion Laboratory, California Institute of Technology, Pasadena, CA, USA

Renyu Hu & Jeehyun Yang

13. Division of Geological and Planetary Sciences, California Institute of Technology, Pasadena, CA, USA

Renyu Hu, Julie Inglis & Nicole L. Wallack

14. School of Physics, University of Bristol, Bristol, UK

Lili Alderson, Hannah R. Wakeford & David Grant

15. Department of Astronomy and Astrophysics, University of California, Santa Cruz, Santa Cruz, CA, USA

Natalie M. Batalha, Aarynn L. Carter, Jonathan J. Fortney, Sagnick Mukherjee & Kazumasa Ohno

16. Department of Astronomy and Astrophysics, University of Chicago, Chicago, IL, USA

Jacob L. Bean & Adina D. Feinstein

17. Department of Physics and Institute for Research on Exoplanets, Université de Montréal, Montreal, Quebec, Canada

Björn Benneke & Jake Taylor

18. School of Earth and Space Exploration, Arizona State University, Tempe, AZ, USA

Carver J. Bierson, Michael Line & Luis Welbanks

19. Department of Physics and Astronomy, University College London, London, UK

Ryan P. Brady & Sergei N. Yurchenko

20. Space Research Institute, Austrian Academy of Sciences, Graz, Austria

Ludmila Carone & Patricio E. Cubillos

21. Centre for Exoplanet Science, University of St Andrews, St Andrews, UK

Katy L. Chubb

22. Department of Physics & Astronomy, Johns Hopkins University, Baltimore, MD, USA

Julie Inglis & David K. Sing

23. Laboratoire d’Astrophysique de Bordeaux, Université de Bordeaux, Pessac, France

Jérémy Leconte

24. Leiden Observatory, University of Leiden, Leiden, the Netherlands

Yamila Miguel, Amy Louca & Nicolas Crouzet

25. SRON Netherlands Institute for Space Research, Leiden, the Netherlands

Yamila Miguel

26. Universitäts-Sternwarte München, Ludwig-Maximilians-Universität München, Munich, Germany

Karan Molaverdikhani & Kevin Heng

27. Exzellenzcluster Origins, Munich, Germany

Karan Molaverdikhani

28. Department of Earth & Planetary Sciences, Johns Hopkins University, Baltimore, MD, USA

Zafar Rustamkulov & David K. Sing

29. Johns Hopkins Applied Physics Laboratory, Laurel, MD, USA

Kevin B. Stevenson

30. Indian Institute of Technology Indore, Indore, India

Keshav Aggarwal

31. Anton Pannekoek Institute for Astronomy, University of Amsterdam, Amsterdam, the Netherlands

Robin Baeyens, Saugata Barat & Jean-Michel Désert

32. Planetary Science Institute, Tucson, AZ, USA

Miguel de Val-Borro

33. Department of Astrophysical Sciences, Princeton University, Princeton, NJ, USA

Tansu Daylan

34. Laboratory for Atmospheric and Space Physics, University of Colorado Boulder, Boulder, CO, USA

Kevin France & Patrick Behr

35. School of Earth and Planetary Sciences (SEPS), National Institute of Science Education and Research (NISER), Homi Bhabha National Institute (HBNI), Odisha, India

Jayesh M. Goyal

36. Department of Physics, Imperial College London, London, UK

James Kirk

37. Max Planck Institute for Astronomy, Heidelberg, Germany

Laura Kreidberg, Evert Nasedkin, Thomas Henning & Thomas Mikal-Evans

38. Lunar and Planetary Laboratory, University of Arizona, Tucson, AZ, USA

Sarah E. Moran

39. Department of Earth, Atmospheric and Planetary Sciences, Massachusetts Institute of Technology, Cambridge, MA, USA

Benjamin V. Rackham

40. Kavli Institute for Astrophysics and Space Research, Massachusetts Institute of Technology, Cambridge, MA, USA

Benjamin V. Rackham

41. Astronomy Department and Van Vleck Observatory, Wesleyan University, Middletown, CT, USA

Seth Redfield

42. Maison de la Simulation, CEA, CNRS, Univ. Paris-Sud, UVSQ, Université Paris-Saclay, Gif-sur-Yvette, France

Pascal Tremblin & Pierre-Olivier Lagage

43. Chemistry and Planetary Sciences, Dordt University, Sioux Center, IA, USA

Channon Visscher

44. NASA Goddard Space Flight Center, Greenbelt, MD, USA

Allison Youngblood

45. Centre for Exoplanets and Habitability, University of Warwick, Coventry, UK

Eva-Maria Ahrer & Peter J. Wheatley

46. Department of Physics, University of Warwick, Coventry, UK

Eva-Maria Ahrer, Kevin Heng & Peter J. Wheatley

47. NASA Ames Research Center, Moffett Field, CA, USA

Natasha E. Batalha

48. Department of Astrophysical and Planetary Sciences, University of Colorado Boulder, Boulder, CO, USA

Zachory K. Berta-Thompson

49. Department of Physics, New York University Abu Dhabi, Abu Dhabi, United Arab Emirates

Jasmina Blecic

50. Center for Astro, Particle, and Planetary Physics (CAP3), New York University Abu Dhabi, Abu Dhabi, United Arab Emirates

Jasmina Blecic

51. School of Physics and Astronomy, University of Leicester, Leicester, UK

S. L. Casewell

52. Department of Physics & Astronomy, University of Kansas, Lawrence, KS, USA

Ian J. M. Crossfield

53. INAF - Turin Astrophysical Observatory, Pino Torinese, Italy

Patricio E. Cubillos

54. Institute of Astronomy, Department of Physics and Astronomy, KU Leuven, Leuven, Belgium

Leen Decin

55. School of Physics, Trinity College Dublin, Dublin, Ireland

Neale P. Gibson

56. Planetary Sciences Group, Department of Physics and Florida Space Institute, University of Central Florida, Orlando, FL, USA

Joseph Harrington

57. Department of Astronomy, University of Maryland, College Park, MD, USA

Eliza M.-R. Kempton

58. Infrared Processing and Analysis Center (IPAC), California Institute of Technology, Pasadena, CA, USA

Jessica Krick

59. Département d'Astronomie, Université de Genève, Sauverny, Switzerland

Monika Lendl

60. Department of Physics, Utah Valley University, Orem, UT, USA

Joshua D. Lothringer

61. Steward Observatory, University of Arizona, Tucson, AZ, USA

Megan Mansfield & Everett Schlawin

62. Department of Physics and Astronomy, Faculty of Environment, Science and Economy, University of Exeter, Exeter, UK

N. J. Mayne

63. Instituto de Astrofísica de Canarias (IAC), Tenerife, Spain

Enric Palle

Contributions

All authors played a notable role in the JWST Transiting Exoplanet Community Early Release Science Program, including the original proposal, preparatory work, tool development, coordinating meetings and so on. Some specific contributions are listed as follows. S.-M.T., P.G., D.P., X.Z., E.K.H.L. and V.P. designed the project and drafted the article. E.K.H.L. and L.C. performed 3D GCMs. S.-M.T., J.M., E.H., O.V., S.J., R.H., J.Y., K.M., R.B., C.J.B. and A.L. developed and/or performed photochemical models. S.-M.T., J.M., E.H., O.V., S.J., R.H., K.O. and P.T. contributed substantially to model comparisons and chemical analysis. K.L.C. and S.-M.T. compiled the sulfur opacities and E.K.H.L. computed the synthetic spectra. Z.R., D.K.S., J.K., E.S., and A.L.C. reduced and analysed the NIRSpec PRISM data. L.A., H.R.W., M.K.A., S.B., D.G., J.I., T.M.-E. and N.L.W. reduced and analysed the NIRSpec G395H data, with further contributions from J.B. and T.D. B.V.R., J.J.F., S.E.M., S.R., Y.M., K.L.C. and L.D. provided substantial feedback, with E.H. coordinating comments from all other authors, to improve the manuscript.

Corresponding author

Correspondence to Shang-Min Tsai.

Ethics declarations

Competing interests

The authors declare no competing interests.

Peer review

Peer review information

Nature thanks Panayotis Lavvas and the other, anonymous, reviewer(s) for their contribution to the peer review of this work. Peer reviewer reports are available.

Additional information

Publisher's note Springer Nature remains neutral with regard to jurisdictional claims in published maps and institutional affiliations.

Extended data figures and tables

Extended Data Fig. 1 Chemical equilibrium abundances in the atmosphere of WASP-39b.

VMR profiles of H_2O (blue), CO_2 (orange), H_2S (green) and SO_2 (red), as computed by FastChem (ref. [38]) based on the morning terminator temperature profile, are given for 10× (solid lines) and 100× (dashed lines) solar metallicity.

Extended Data Fig. 2 The temperature–wind map of the WASP-39b Exo-FMS GCM and input for 1D photochemical models.

a, The colour scale represents temperature across the planet and arrows denote the wind direction and magnitude at 10 mbar. The ±10° longitudinal regions with respect to the morning and evening terminators are indicated with solid grey lines. The '+' symbol denotes the sub-stellar point. **b**, 1D temperature–pressure profiles adopted from the morning and evening terminators averaging all latitudes and ±10° longitudes (regions enclosed by grey lines in **a**) and the K_{zz} profile (equation (2) and held constant below the 5-bar level) overlaying the root-mean-squared vertical wind multiplied by 0.1 scale height from the GCM (grey). The temperatures are kept isothermal

from those at the top boundary of the GCM around 5×10^{-5} bar when extending to lower pressures (about 10^{-8} bar) for photochemical models. **c**, Input WASP-39 stellar flux at the surface of the star. The pink-shaded region indicates the optical wavelength range at which the stellar spectrum is directly measured, whereas the blue-shaded and green-shaded regions are those constructed from the Sun and HD 203244, respectively.

Extended Data Fig. 3 Shortwave radiative heating of sulfur species.

Radiative heating rates (erg s^{-1} g^{-1}) of SO_2, SH and H_2S to demonstrate their potential impact on the temperature structure. Heating owing to a vertically constant grey opacity of 0.05 cm^2 g^{-1} is shown for comparison. All heating rates are integrated over 220–800 nm.

Extended Data Fig. 4 The main source and sink profiles of SO_2 in our WASP-39b model.

The reaction rates of the main sources and sinks of SO_2 in the VULCAN morning-terminator model for WASP-39b. The dashed lines of the same colour are the corresponding reverse reactions and the dotted black line indicates the distribution profile (arbitrarily scaled) of SO_2.

Extended Data Fig. 5 The C/O trends and synthetic spectra.

Same as Fig. 4 but as a function of C/O ratio at 10× solar metallicity. **a**, The averaged VMR of H_2O, CO_2 and SO_2 between 10 and 0.01 mbar as a function of C/O ratio, in which the solar C/O is 0.55. The nominal model is shown by solid lines, whereas the eddy diffusion coefficient (K_{zz}) scaled by 0.1 and 10 are shown by dashed and dashed-dotted lines, respectively. The models for which the whole temperature increased and decreased by 50 K are indicated by the upward-facing and downward-facing triangles connected by dotted lines, respectively. **b**, The morning and evening terminator-averaged theoretical transmission spectra with different C/O

ratios compared with the NIRSpec PRISM observation. The error bars show 1σ standard deviations.

Extended Data Fig. 6 The impact of sulfur on other nonsulfur species.

VMR profiles of some species in our WASP-39b model that exhibit differences from VULCAN including sulfur kinetics (solid lines) and without sulfur kinetics (dashed lines).

Extended Data Fig. 7 The opacities of several sulfur species.

Opacities of several sulfur species at 1,000 K and 1 mbar, except that those in the UV and of OCS are at room temperature. The opacities in the infrared are binned down to $R \approx 1{,}000$ for clarity.

Extended Data Fig. 8 The main sulfur species abundances with reduced and enhanced UV irradiation.

VMR profiles of the main sulfur species in the VULCAN morning-terminator model with 0.1× (**a**) and 10× (**b**) UV. Our nominal model is shown by solid lines for comparison, whereas the model with varying FUV (1–230 nm) is shown by the dashed lines and that with varying NUV (230–295 nm) is shown by dashed-dotted lines.

Extended Data Fig. 9 The effects of assuming a vertically uniform distribution of SO_2.

Terminator-averaged theoretical transmission spectra generated from abundance distribution computed by the photochemical model VULCAN compared with assuming constant 1, 5 and 10 ppm of SO_2. As before, the NIRSpec PRISM observation is shown with 1σ error bars.

Extended Data Fig. 10 The OH to H ratio and the temperature trends for sulfur molecules produced by photochemistry.

a, ${k}_{{{\rm{H}}}_{2}{\rm{O}}}/{k}_{{{\rm{H}}}_{2}{\rm{O}}}^{{\prime} }\times {\rm{O/H}}$ as a proxy of OH to H ratio at 10× solar metallicity, in which ${k}_{{{\rm{H}}}_{2}{\rm{O}}}$ and ${k}_{{{\rm{H}}}_{2}{\rm{O}}}^{{\prime} }$ are the forward and backward rate constants of $H_2O + H \rightarrow OH + H_2$, respectively. When OH becomes scarce relative to H as temperature decreases, the chain-forming path (does not require OH) is favoured over the oxidization path (requires OH). **b**, The average VMR between 10 and 0.01 mbar as a function of planetary equilibrium temperature with temperature profiles adopted from ref. [39] (see text for the setup). The dotted grey line marks approximately the required SO_2 concentration to be detectable with WASP-39b parameters. S_x denotes the allotropes S_2 and S_8 and SO_x denotes the oxidized species SO and SO_2.

Extended Data Table 1 Important reactions for SO_2 production

Supplementary information

Peer Review File

Rights and permissions

Open Access This article is licensed under a Creative Commons Attribution 4.0 International License, which permits use, sharing, adaptation, distribution and reproduction in any medium or format, as long as you give appropriate credit to the original author(s) and the source, provide a link to the Creative Commons licence, and indicate if changes were made. The images or other third party material in this article are included in the article's Creative Commons licence, unless indicated otherwise in a credit line to the material. If material is not included in the article's Creative Commons licence and your intended use is not permitted by statutory regulation or exceeds the permitted use, you will need to obtain permission directly from the copyright holder. To view a copy of this licence, visit http://creativecommons.org/licenses/by/4.0/.

Reprints and Permissions

About this article

Cite this article

Tsai, SM., Lee, E.K.H., Powell, D. *et al.* Photochemically produced SO_2 in the atmosphere of WASP-39b. *Nature* **617**, 483–487 (2023). https://doi.org/10.1038/s41586-023-05902-2

- Received: 11 November 2022
- Accepted: 28 February 2023
- Published: 26 April 2023
- Issue Date: 18 May 2023
- DOI: https://doi.org/10.1038/s41586-023-05902-2

Share this article

Anyone you share the following link with will be able to read this content:

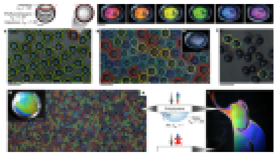
Get shareable link

Sorry, a shareable link is not currently available for this article.

Copy to clipboard

Provided by the Springer Nature SharedIt content-sharing initiative

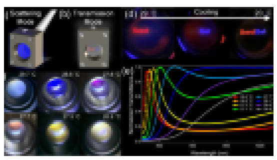
This article was downloaded by **calibre** from https://www.nature.com/articles/s41586-023-05902-2



Colouration by total internal reflection and interference at microscale concave interfaces

27 February 2019

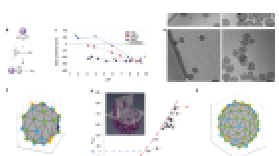
Amy E. Goodling, Sara Nagelberg, … Lauren D. Zarzar



Finely tunable dynamical coloration using bicontinuous micrometer-domains

24 June 2022

Yuyin Xi, Fan Zhang, … Yun Liu



Spontaneous organization of supracolloids into three-dimensional structured materials

28 January 2021

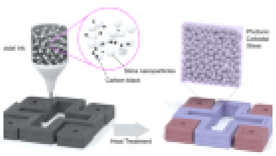
Mohammad-Amin Moradi, E. Deniz Eren, … Joseph P. Patterson



Light-switchable propulsion of active particles with reversible interactions

26 May 2020

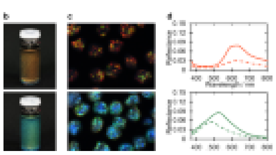
Hanumantha Rao Vutukuri, Maciej Lisicki, … Jan Vermant



Three-dimensional printing of photonic colloidal glasses into objects with isotropic structural color

29 July 2022

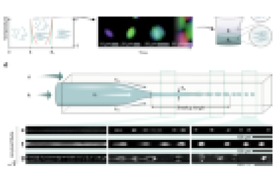
Ahmet F. Demirörs, Erik Poloni, … André R. Studart



Cellulose photonic pigments

13 June 2022

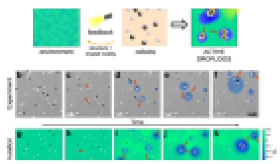
Richard M. Parker, Tianheng H. Zhao, … Silvia Vignolini



Disentangling kinetics from thermodynamics in heterogeneous colloidal systems

04 February 2023

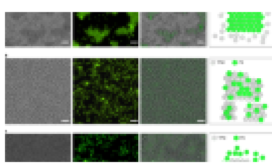
Hamed Almohammadi, Sandra Martinek, … Raffaele Mezzenga



Active droploids

14 October 2021

Jens Grauer, Falko Schmidt, … Benno Liebchen



Tunable assembly of hybrid colloids induced by regioselective depletion

27 July 2020

Mingzhu Liu, Xiaolong Zheng, … Marcus Weck

- Article
- Open Access
- Published: 17 May 2023

Photochromism from wavelength-selective colloidal phase segregation

- Jing Zheng,
- Jingyuan Chen,
- Yakang Jin,
- Yan Wen,
- Yijiang Mu,
- Changjin Wu,
- Yufeng Wang,
- Penger Tong,
- Zhigang Li,
- Xu Hou &
- …
- Jinyao Tang

Show authors

Nature **volume 617**, pages 499–506 (2023)

- 55 Altmetric

- Metrics details

Abstract

Phase segregation is ubiquitously observed in immiscible mixtures, such as oil and water, in which the mixing entropy is overcome by the segregation enthalpy[1,2,3]. In monodispersed colloidal systems, however, the colloidal–colloidal interactions are usually non-specific and short-ranged, which leads to negligible segregation enthalpy[4]. The recently developed photoactive colloidal particles show long-range phoretic interactions, which can be readily tuned with incident light, suggesting an ideal model for studying phase behaviour and structure evolution kinetics[5,6]. In this work, we design a simple spectral selective active colloidal system, in which TiO_2 colloidal species were coded with spectral distinctive dyes to form a photochromic colloidal swarm. In this system, the particle–particle interactions can be programmed by combining incident light with various wavelengths and intensities to enable controllable colloidal gelation and segregation. Furthermore, by mixing the cyan, magenta and yellow colloids, a dynamic

photochromic colloidal swarm is formulated. On illumination of coloured light, the colloidal swarm adapts the appearance of incident light due to layered phase segregation, presenting a facile approach towards coloured electronic paper and self-powered optical camouflage.

Main

The macroscopic properties of materials are fundamentally determined by interactions between their basic composition units. For example, in a mixture of molecules with similar interactions, the mixing entropy dominates and leads to a well-mixed solution, whereas a distinct intermolecular interaction leads to the enthalpy penalty and causes phase segregation[1,2,3,7]. Colloid solution is an excellent model system for studying phase transition and self-assembly at the atomic scale, in which the colloidal particles are regarded as gigantic artificial atoms[8,9]. Classical paths to phase segregation in colloidal mixtures have been demonstrated by changing thermodynamic variables such as temperature and/or solvent interactions[10,11,12,13].

On the other hand, the active matter offers a new approach for realizing complex phase behaviours beyond thermodynamic equilibrium[4,14]. The segregation of active colloids has been proposed as motility-induced phase separation[15,16], in which the dispersed self-propulsion particles condense due to particles' mobility and repulsive interaction. Theoretically, the active colloidal mixture can self-phase separate due to distinctive diffusivity[16], temperature[17] and activity[18,19].

Most recently, the light-powered microswimmers[20,21,22] have been developed with respect to a controllable nanorobot, which offers potential for biomedical application and functional new materials[23,24] as the swimmer activity, alignment direction and interparticle interaction can be readily modulated with incident light. Owing to its flexibility, the light-powered active colloidal system has recently been applied to active matter research[5,6], in which the particle interactions can be repeatedly turned on and off. On the other hand, one unique feature of light-powered active colloids is that the particles can be designed to respond to different wavelengths and

polarization states of light[25,26], enabling selective excitation of one colloidal species within a colloidal mixture solution. Here, we present a simple spectra-selective active colloidal system composed of photosensitive TiO_2 colloidal particles suspended in redox shuttle solution. On photoexcitation, the redox reaction on TiO_2 particles generates chemical gradient, which tunes the effective particle–particle interaction. By mixing several otherwise identical TiO_2 colloidal species loaded with dyes of different absorption spectra and adjusting the incident light spectra, the on-demand colloidal phase segregation is realized.

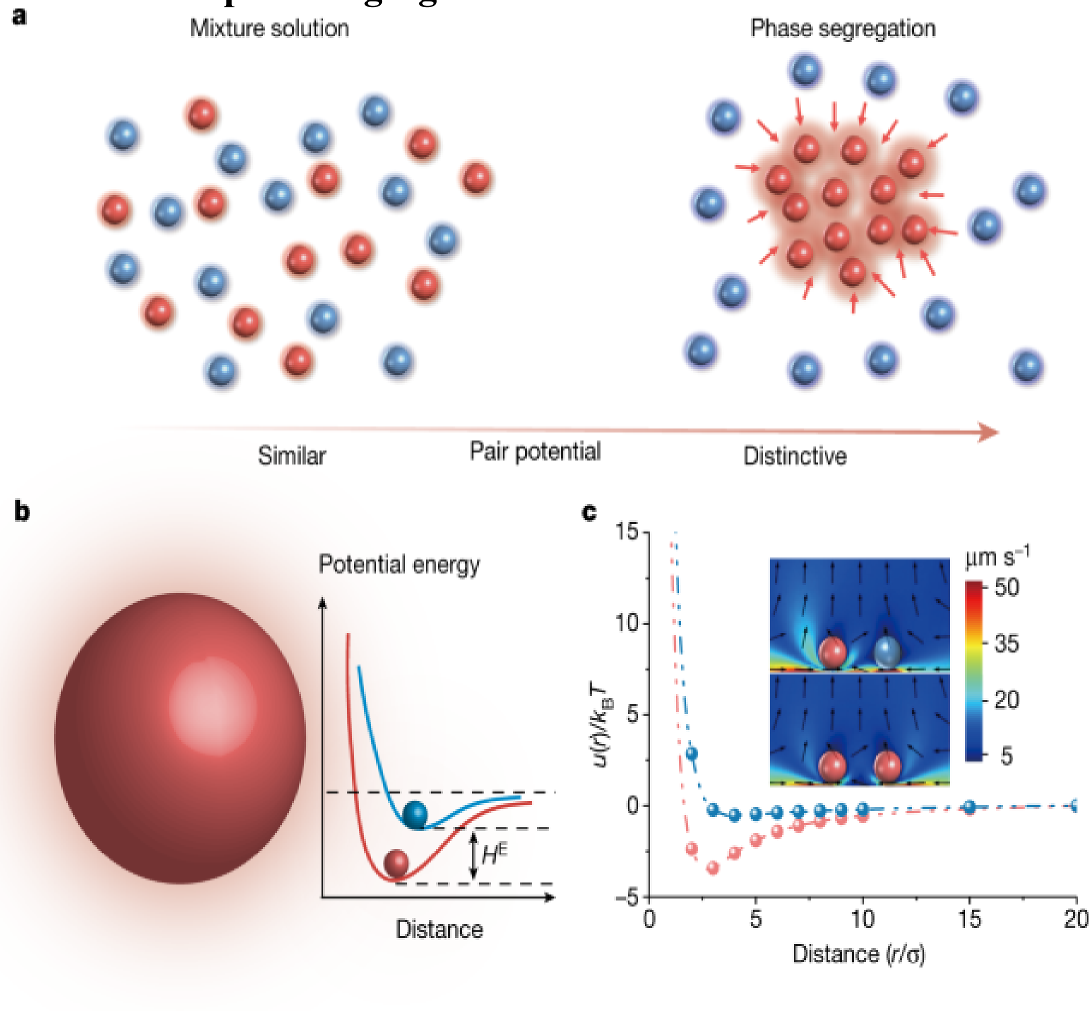
At high concentration, the light-induced segregation in this active colloidal mixture is vertically layered, corresponding to the incident light spectra, and produces a coloured colloidal enrichment accordingly. At the macroscopic scale, the photoactive colloidal mixture is photochromic as different colour-enriched layers are exposed. This new colour-shifting colloidal swarm relies on the rearrangement of existing pigment rather than the in situ generation of the new chromophore, which is similar to the action of pigment cells (chromatophores) in cephalopod's skin[27,28]. We expect this new programmable photochromic ink can be developed towards electronic ink[29], displays[30] and active optical camouflage[31].

Particle interaction tunability in spectral sensitive colloidal system

To study the phase segregation process, it is necessary to use colloids with tuneable potential. Previously, the attractive potential for colloid self-assembly[32] has been realized with polymer interactions[33], DNA strand grafting[34], depletion force[35] and so on. However, none of these approaches offers independent control of particle potential, which makes it difficult to explore the phase kinetics in the colloidal mixture. Here we adapt the simple dye-sensitized colloid to realize this interaction tuneability based on our previously demonstrated microswimmer system[25]. On photoexcitation of dyes, the redox reaction results in diffusiophoretic flow[36] and effective attractive potential. As illustrated in Fig. 1a, the segregation process can be monitored in two steps by selectively tuning the interparticle potential in the

binary colloidal mixture. First, with similar particle interactions applied to two components (red and blue particles), a well-mixed dispersed phase can be prepared. Then, one component's (red particles) attractive potential is tuned to be significantly greater than another (blue particles), which contributes to the effective excess enthalpy (Fig. 1b) and leads to the segregation.

Fig. 1: Schematic of phase segregation in colloidal mixture.



a, Illustration of the evolution from well-mixed colloidal solution to phase segregation by adjusting the interparticle potential. **b**, Illustration of tuneable particle interaction in the dark (blue) and under photoexcitation (red), which leads to the excess enthalpy (H^E). **c**, Simulated phoretic flow field and effective potential of the active–active particle (red curve and bottom of the

inset) and active–passive particle (blue curve and top of the inset). The particle–particle distance *r* is normalized by particle diameter *σ*.

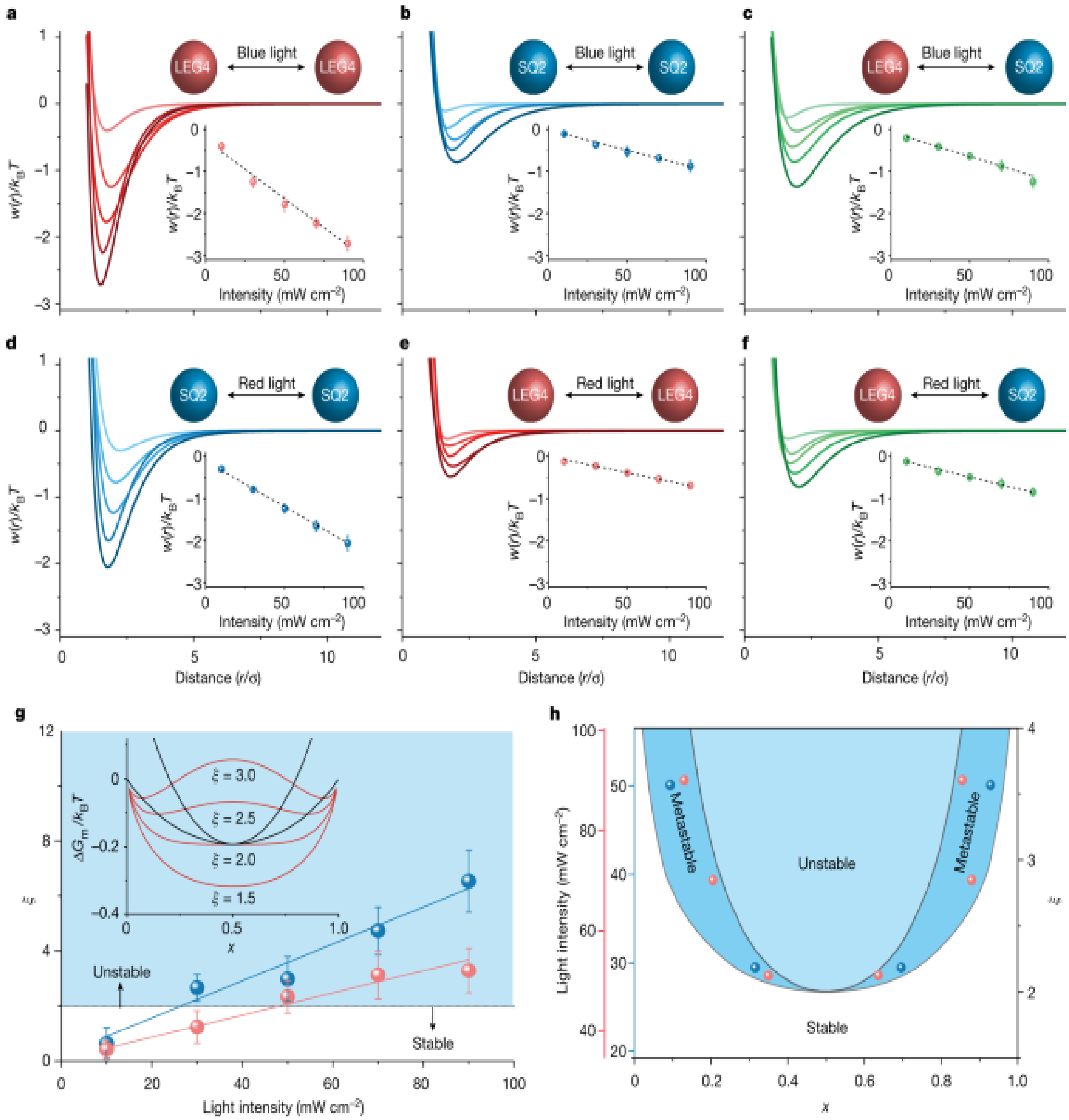
Source data

This photochemistry-powered phoretic flow has been previously used to form photoresponsive colloidal crystal[33] and active swarm[5,37,38]. Here, we denoted the unexcited particle as the ‘passive’ one, whereas the photoexcited particle is ‘active’. The numerical simulation (Methods) is used to visualize the phoretic flow field and the interaction between active–active and active–passive particle pairs. Although the active particle interaction is non-reciprocal by nature, we assume our system’s quasistatic state may be treated as a quasi-equilibrium system, which significantly simplifies the numerical treatment and facilitates understanding. As shown in the inset of Fig. 1c, the relatively long-range attraction and short-range repulsion can be predicted, which contributed to the effective attractive potential. Notably, the flow field and resulting apparent pair potential between two active particles are stronger than the active–passive pair, which contributes to the excess enthalpy for phase segregation.

In our system, TiO_2 colloids sensitized with spectral distinctive dyes (Methods) are used, enabling not only easy identity switching between active and passive, but also access to all the intermediate states by controlling the relative activity with illumination intensity. Experimentally, the light-induced interactions between dye-sensitized colloids as represented by the apparent pair potential $w(r)$ can be characterized by measuring the static radial distribution function $g(r)$ under varied incident light intensity. In our binary colloidal system, the dye SQ2 (λ_{max} = 650 nm) and LEG4 (λ_{max} = 480 nm) were selected to sensitize the TiO_2 colloids, respectively, then the $g(r)$ and $w(r)$ were measured in diluted conditions (area fraction $\phi \cong 1\%$) and illuminated with a wavelength variable source (Methods), whereas $w(r)$ is further fitted by standard Morse potential $u\left(r\right)={D}_{0}[{{\rm{e}}}^{-2a\left(r-{r}_{0}\right)}-{2{\rm{e}}}^{-a\left(r-{r}_{0}\right)}]$. As shown in Fig. 2a,d, $w(r)$ of the active–active particles can be tuned with incident light intensity, and the apparent bonding strength ($u_{{\rm{Active}}-{\rm{Active}}}={w}_{\min}\left(r\right)$) scales linearly with illumination intensity, whereas the bonding strength of

passive–passive particles (${u}_{{\rm{Passive}}-{\rm{Passive}}}$), Fig. 2b,e) and active–passive particles (${u}_{{\rm{Active}}-{\rm{Passive}}}$), Fig. 2c,f) are both much less sensitive to the illumination condition. This linear dependence may be attributed to the linear photochemistry kinetics dependence on photon flux, as reported previously in a light-powered nanomotor system[39].

Fig. 2: Spectral selective effective potential of dye-sensitized-colloid modulated with illumination.



a–**c**, The fitted apparent pair potentials of LEG4–LEG4 sensitized (**a**), SQ2–SQ2 sensitized (**b**) and LEG4–SQ2 sensitized TiO_2 colloids (**c**) under blue light (440–480 nm) illumination with various intensity (10, 30, 50, 70 and 90 mW cm^{-2}). **d**–**f**, The fitted apparent pair potentials of SQ2–SQ2 sensitized (**d**), LEG4–LEG4 sensitized (**e**) and LEG4–SQ2 sensitized TiO_2 colloids (**f**) under red light (640–660 nm) illumination with various intensities (10, 30, 50, 70 and 90 mW cm^{-2}). The particle–particle distance r is normalized by particle diameter σ. Insets show the linear dependence of particle's bonding strength to the illumination intensity. **g**, The ξ dependence on blue (blue line) and red (red line) light intensity, where $\xi = 2$ is the phase stability boundary. Inset shows the ξ variation of the Gibbs energy of the binary mixture. **h**, The theoretical phase diagram of the active binary mixture with respect to red and blue light intensities (left axis) and ξ (right axis). Inset points show the obtained phase compositions as observed experimentally, where red and blue points represent the condensed phases with red and blue light illumination, respectively.

Source data

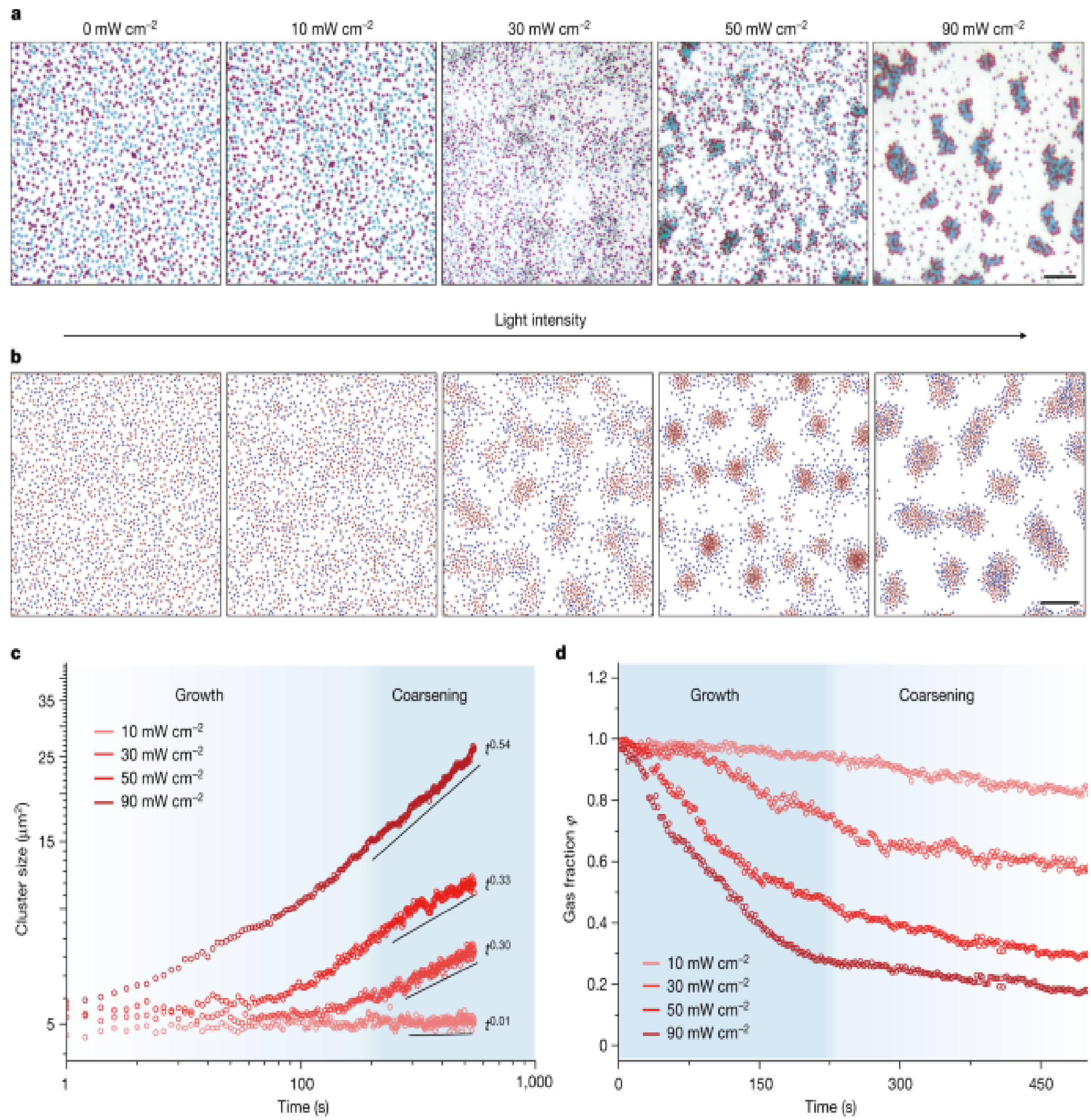
This unique property enables us to control the phase segregation process by tuning the particle–particle interaction with light. In classical binary mixture, the phase stability is determined by the excess enthalpy, ${H}^{{\rm{E}}}=n\xi {\rm{RT}}{x}_{{\rm{A}}}{x}_{{\rm{B}}}$, where $\xi =\frac{z}{{k}_{{\rm{B}}}T}\left({u}_{{\rm{AB}}}-\frac{{u}_{{\rm{AA}}}+{u}_{{\rm{BB}}}}{2}\right)$ is a dimensionless parameter representing the interaction potential difference between two components, n is the number of particles, R is the gas constant, T is the temperature, z is the effective coordination number, k_B is the Boltzmann constant, u is the apparent bonding strength, and x_A, x_B are mole fractions of A and B, respectively. In our active binary mixture, the ξ increases linearly with the illuminated light intensity (Fig. 2g). As the particle's Brownian motion, corresponding to the apparent system temperature, is not enhanced proportionally (Extended Data Fig. 1), the overall effective molar free energy of segregation ${\Delta }_{{\rm{mix}}}{G}_{{\rm{m}}}={\rm{RT}}({x}_{{\rm{A}}}{\rm{ln}}{x}_{{\rm{A}}}+{x}_{{\rm{B}}}{\rm{ln}}{x}_{{\rm{B}}}+{\xi x}_{{\rm{A}}}{x}_{{\rm{B}}})$ turns negative with increasing ξ under strong illumination, which leads to

phase segregation. When $\xi >$ 2, the overall effective free energy has a double minimum (inset of Fig. 2g), leading to phase instability. As shown in Fig. 2h, the phase diagram representing the phases under various illumination intensities (scales with ξ) can be constructed. In this phase diagram, the outer line is the minimum ${\Delta }_{{\rm{mix}}}{G}_{{\rm{m}}}$ line corresponding to the coexistence phase, whereas the inner spinodal curve ($\frac{{{\rm{d}}}^{2}G}{{\rm{d}}{x}^{2}}=0$) defines the metastable mixture phase. The phase segregation is expected within the spinodal curve, as will be discussed later in our experiment.

Spectral selective light-induced phase segregation kinetics

To study the phase kinetics of colloidal mixture, the well-mixed colloidal solution with a one to one LEG4 to SQ2 ratio was prepared and confined in a rectangle capillary with a medium area fraction ($\varphi \approx 15 \%$), and subjected to uniform illumination to activate one colloidal species selectively. As shown in Fig. 3a and Supplementary Video 1, under dark conditions, both LEG4 and SQ2 sensitized TiO_2 colloids show indistinctive potential with apparent bonding strength less than 0.5 k_BT, which leads to the colloidal mixture behaving as a well-mixed gas. With increasing red light illumination (640–660 nm and 10, 30, 50 and 90 mW cm^{-2}), the SQ2 sensitized TiO_2 colloids were tuned from a passive to increasingly active state, while the LEG4 sensitized TiO_2 colloids remained passive due to their much weaker absorption. As stated previously, ${\rm{\xi }}$ scales with the light intensity (Fig. 2g), which leads to phase instability under high illumination. On the other hand, because the passive–passive (LEG4–LEG4) particle bonding strength is less sensitive to the illumination condition (Fig. 2e), and passive particle condensation is only obvious under high illumination intensity. It is worth noting that under all-illumination conditions, the observed phase composition is close to the metastable spinodal curve, which aligns with the thermodynamics of binary mixture.

Fig. 3: Experimental and Brownian dynamics simulation of light-induced binary mixture phase segregation.



a, Experimental evolution of active particle (SQ2 sensitized TiO_2 colloid) and passive particle (LEG4 sensitized TiO_2 colloid) under various red light illumination levels (640–660 nm and 10, 30, 50 and 90 mW cm^{-2}). Scale bar, 10 µm. **b**, The Brownian dynamic simulation result of active (red) and passive (blue) particle binary mixture evolution under apparent pair potential fitted from experimental result. Scale bar, 20 µm. **c**, Experimental results of cluster size evolution of the binary colloidal system show increasing exponents with higher illumination intensity. **d**, The gas fraction of the binary mixture decreases over time under different light illumination conditions, showing the growth and coarsening stage of the phase evolution.

Source data

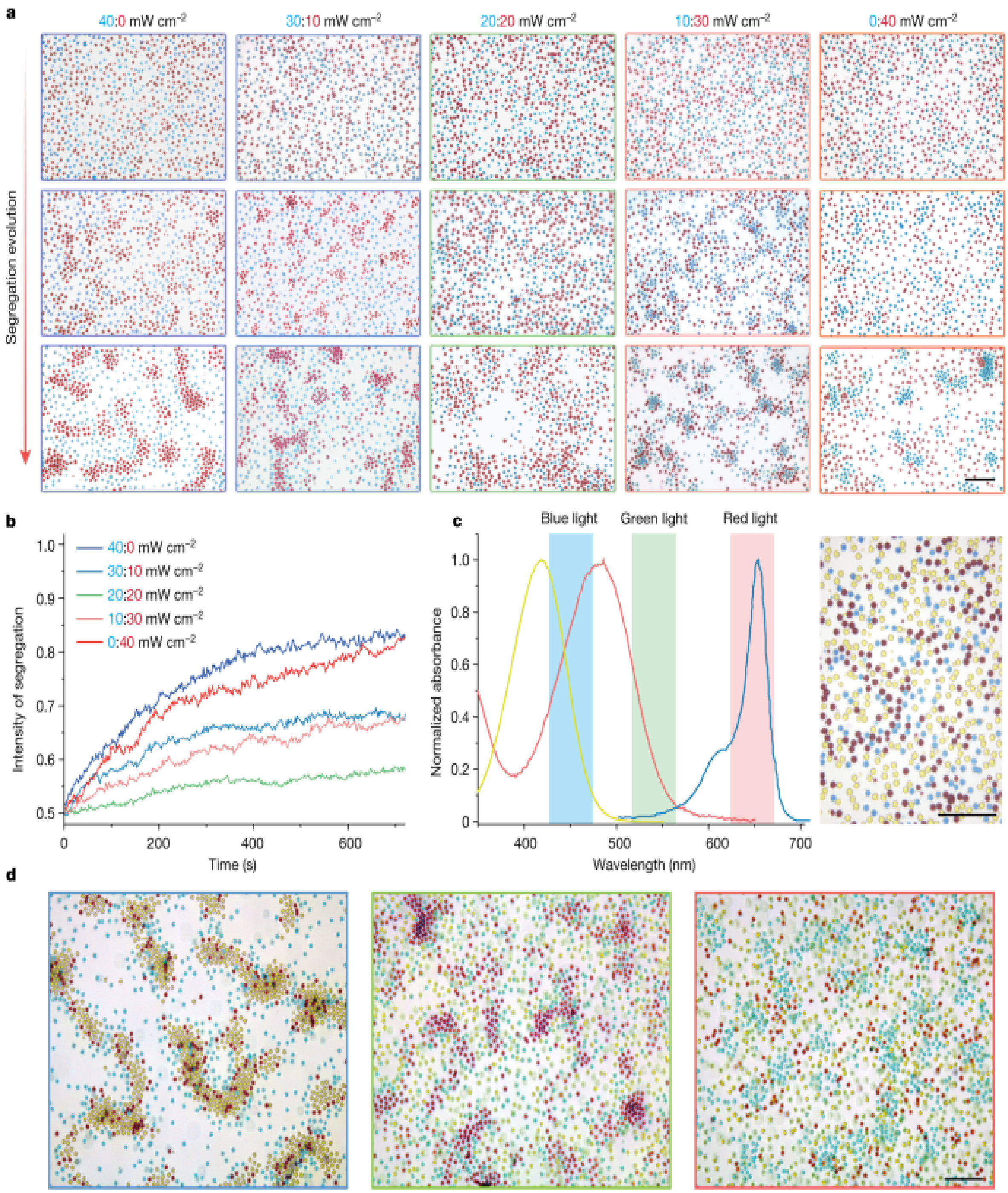
To facilitate the understanding of the observed segregation dynamics, we use Brownian dynamics simulations to corroborate our experiment and test whether the non-equilibrium nature plays an essential role in the observed segregation. In our Brownian dynamics simulation, the potential parameters are adopted by fitting the experimentally measured $w(r)$ with standard Morse potential (Supplementary Tables 1 and 2). In the simulation, all particles diffuse freely in two-dimensional (2D) space and are only subjected to the aforementioned effective potential. As no further non-reciprocal interactions, such as self-propulsion and diffusiophoresis from chemical gradient, are considered, the Brownian dynamics simulation represents the simplest physical pictures in the thermodynamic system. As shown in Fig. 3b and Supplementary Video 2, the Brownian dynamics simulation successfully catches the essence of the observed phase segregation, verified that our dye-sensitized colloid system can be regarded as the quasi-equilibrium system and may be used as a model system for the thermodynamic and kinetic study of mixture phase transition.

In active matter physics, it is prudent to ask to what degree the classic models of nucleation, growth and coarsening from irreversible thermodynamics can be applied to predict the kinetics and static properties of the active matter system[40]. For phase transition, the domain dynamics have been well-established on the basis of the premise of self-similar growth, which leads to the power-law kinetics: $S\propto {t}^{\nu }$ (where S is the averaged size of the cluster, t is the time and ν is growth exponent)[41]. The cluster coarsening in our binary system also follows self-similar growth mechanism (Extended Data Fig. 2). Here, we define cluster with a simple minimum separation criterion: all particles with centre-to-centre distance smaller than 1.5 particles in diameter are considered within the same cluster, and analyse our experimental data from Fig. 3a. As shown in Fig. 3c, the light-induced phase segregation indeed follows the power law after around 200 s of incubation delay. Furthermore, the gas fraction (the percentage of isolated particles in all particles) decreases immediately on illumination and gradually saturates after roughly 200 s (Fig. 3d), which can be regarded as the growth and coarsening stage of the phase evolution, respectively. We extracted the coarsening stage exponents ν of colloid segregation under different illumination conditions, as shown in Fig. 3c.

Under mid-range light intensity (30 and 50 mW cm^{-2}), the growth exponents are stable around a third and increased to roughly 0.5 under strong illumination (90 mW cm^{-2}), in agreement with our simulation result (Extended Data Figs. 7 and 8), suggesting other growth mechanisms may play a role as the system is biased far away from equilibrium. A similar exponent increase has been reported previously in active and passive system[42,43], whereas further investigation will be needed to explain the exact cause in our light-activated mixture.

As stated previously, optical activation enables an attractive tuneable potential between different components, in which the identity of active and/or passive particles can be easily switched with different illumination conditions. As shown in Fig. 4a and Supplementary Video 3, the illumination gradually transited from pure blue (40 mW cm^{-2}) to combined blue to red (30:10, 20:20 and 10:20 mW cm^{-2}) and pure red (40 mW cm^{-2}), which gradually switched the active and/or passive identity of LEG4 and SQ2 sensitized particles. The corresponding light absorption induces the clustering of active particles, while the passive particles largely remain in the dispersed phase with the exception of the combined illumination, where both colloidal particles are active. The light-induced process under various illumination spectra can be quantified with the intensity of segregation. Here, considering a binary system composed of A and B particles, for simplicity, we define the intensity of segregation *I* as $I=\frac{{N}_{{\rm{AA}}}+{N}_{{\rm{BB}}}}{{N}_{{\rm{AA}}}+{N}_{{\rm{BB}}}+{N}_{{\rm{AB}}}}$, where $N_{\rm AA}$, $N_{\rm BB}$ and $N_{\rm AB}$ represent the number of pairs for every particle's nearest three neighbouring particles. As shown in Fig. 4b, in a binary mixture of active and passive particles (that is, the system is only illuminated with red or blue light), the system quickly segregates while blending red and blue illumination at different ratios leads to slower and weaker segregation as both colloidal components are activated, which decreases the ξ.

Fig. 4: Spectral tuneable binary and ternary mixture segregation.



a, The optical colloidal segregation evolution of LEG4 and SQ2 sensitized TiO_2 colloids under illumination with various blue to red ratios (40:0, 30:10, 20:20, 10:30 and 0:40 mW cm^{-2}). Scale bar, 10 μm. **b**, The time dependence of the intensity of segregation of the binary system under different illumination conditions. **c**, The normalized absorbance of ethanolic solution of dyes (L0 (yellow), LEG4 (magenta) and SQ2 (cyan)) with distinctive

absorption spectra covering the visible spectrum. The inset shows the spectral range of illuminating RGB light source. The photograph on the right shows the colours of SQ2, LEG4 and L0 sensitized TiO_2 colloids under microscope. Scale bar, 10 µm. **d**, The ternary colloidal mixture composed of L0, LEG4 and SQ2 sensitized TiO_2 colloids shows spectra-selective phase segregation. Scale bar, 10 µm.

Source data

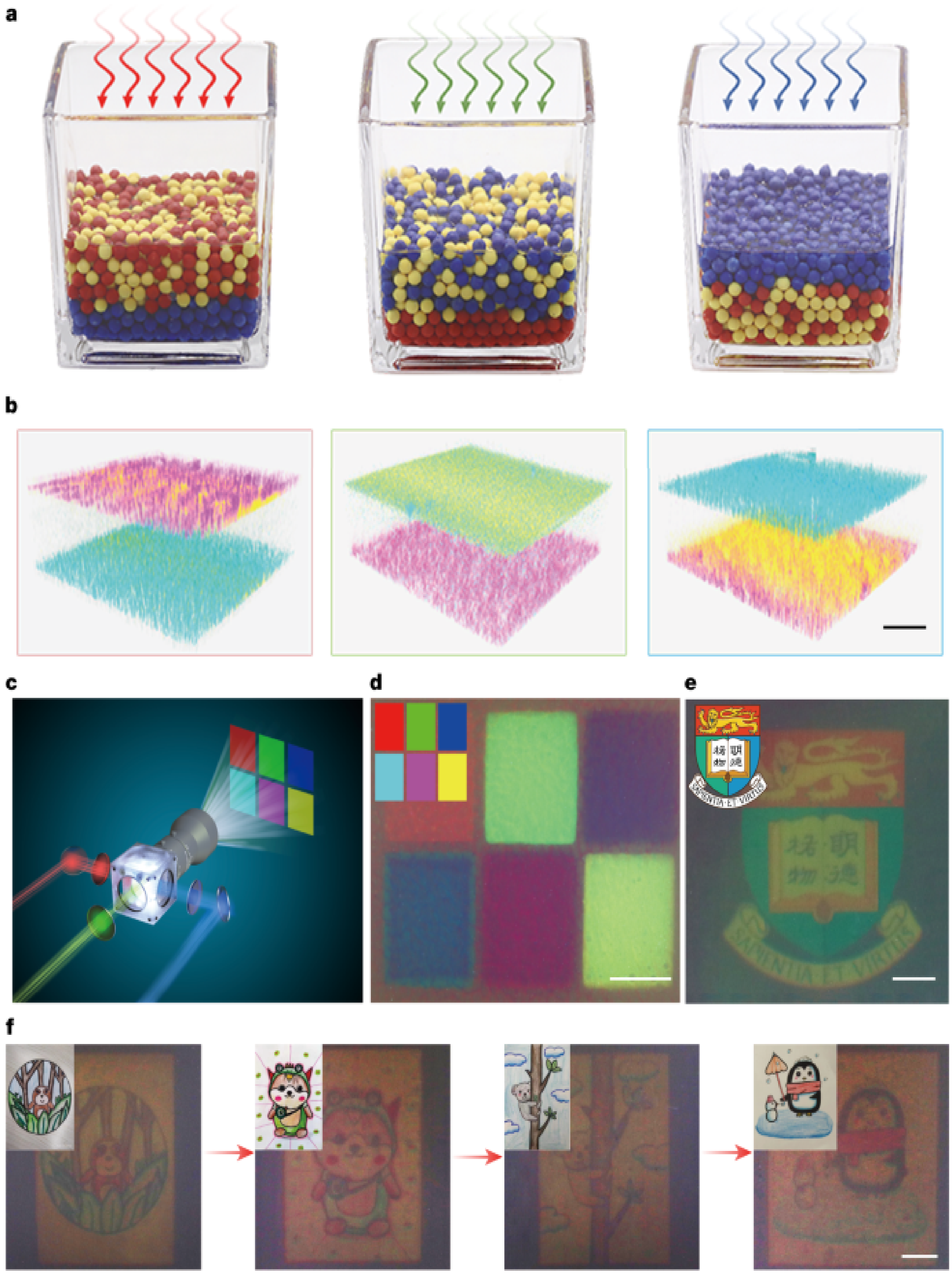
As our dye-sensitized active colloids share the same energy cascade mechanism with well-studied dye-sensitized solar cell[44], a plethora of organic and metalorganic dyes are readily available with tuneable absorption. We expand our binary colloidal mixture to a ternary system to cover the entire visible spectrum. In this case, the dye L0 (\({\lambda }_{\max }=420\,{\rm{nm}}\)) is used to sensitize TiO_2 colloid and offers an extra yellow channel. Under the optical microscope (Fig. 4c), the three sensitized TiO_2 particles show distinctive vivid colours as cyan (SQ2), magenta (LEG4) and yellow (L0), respectively. In this ternary mixture, phase segregation is still triggered by the aggregation of active particles on excitation with the corresponding light. A red, green, blue (RGB) light source with centre wavelengths of 450, 530 and 650 nm is used to activate different particles selectively (Fig. 4c). As shown in Fig. 4d, under blue illumination, both L0 and LEG4 sensitized TiO_2 colloids are activated, whereas the SQ2 sensitized TiO_2 remains passive, which leads to the cocondensation of L0 and LEG4 sensitized particles (yellow and magenta particles) from the mixture (left Fig. 4d). In the meantime, under green or red light illumination, the active species are switched to LEG4 or SQ2 sensitized TiO_2, where the corresponding condensation of magenta particles (LEG4 sensitized TiO_2) or cyan particles (SQ2 sensitized TiO_2) can be observed.

Three-dimensional phase segregation and photochromic colloidal swarm

A cephalopod's skin demonstrates unmatched camouflage ability, in which the chromatophore can sense the environment's light condition and change its appearance with the actions of pigment cells accordingly[45]. Although intricate in nature, the colour-shifting ability of chromatophores is fundamentally based on a mechanical mechanism, where the pigment granules are folding and unfolding under the control of the radial muscles. Compared to the artificial chemistry-based photochromic material, this mechanical mechanism is more reliable and programmable as no chemical change is needed for the appearance shifting.

As shown previously, the ternary dye-sensitized-colloid mixture can respond to light spectra to induce selective segregation. Here, we further explore the colour-shifting ability of this active mixture. In a high-concentration mixture, the previously negligible vertical flow of individual active particles overlapped with each other and started to overcome the gravity and lead to layer segregation as illustrated in Fig. 5a and Supplementary Fig. 1a, which can be further validated by COMSOL and Brownian dynamics simulations (Extended Data Fig. 3). To verify the vertical stratification, the active colloidal mixture with close to unity area fraction ($\varphi \approx 100 \%$) is exposed to red, green and blue light, respectively, while the particle's distribution is visualized with the confocal microscope. As shown in Fig. 5b, under red light illumination, the SQ2 sensitized TiO_2 is active, which induces the aggregation at the bottom, while passive L0 and LEG4 sensitized colloids are carried to the top due to their weak interaction with the active colloids. Likewise, with green or blue light illumination, the mixture undergoes a similar stratification process, in which the active particles predominantly reside at the bottom and passive particles atop (Supplementary Table 3).

Fig. 5: 3D phase segregation and photochromic colloidal swarm.



a, The illustration of spectral sensitive layered segregation in the ternary colloidal system, where different illumination spectra resulted in distinctive

vertical stratification. **b**, The 3D distribution of ternary colloidal particles as imaged by confocal microscope after red, green and blue light illumination. The SQ2, LEG4 and L0 sensitized TiO_2 colloids are represented in cyan, magenta and yellow, respectively. Scale bar, 50 µm. **c**, A modified projector is used to project designed colour images. **d**, Six colour blocks emerged on the surface of photochromic ink after 2 min of exposure. The inset shows the projected pattern. Scale bar, 2 mm. **e**, The university logo emerged on the surface of photochromic ink after 2 min of exposure. Scale bar, 2 mm. **f**, Sequential patterning of the photochromic ink with different colour paintings with 2 min exposure. The inset shows the original projected patterns. Scale bar, 2 mm.

This layered stratification can be used to formulate active photochromic ink. It is worth noting that, at 100% area fraction, the mixture is still too dilute and the optical density of top layer colloids is far from realizing colloidal colourization, while the excessively high particle concentration also deteriorates the colourization ability as the interstitial space between particles diminishes, which is necessary for three-dimensional (3D) colloidal rearrangement. In addition, particle sizes need to be optimized to achieve high image quality and enhanced responsivity.

To formulate the colloidal swarm ink, we further increase the colloidal concentration to $C_0 = 4 \times 10^{11}$ per cm^3, which corresponds to area fraction $\phi \cong$ 3,000%. The ratio of L0, LEG4 and SQ2 sensitized colloids is tuned to around 1:2:1 to balance the reflectance (Supplementary Fig. 2a). The colloidal swarm ink is sealed into a parallel plate glass cell with a depth of roughly 100 µm. A modified commercial projector with bandpass filters is used to project the colour image onto the colloidal swarm ink to demonstrate the photochromic ability (Fig. 5c and Supplementary Fig. 2b).

First, six colour blocks of red, green, blue, cyan, magenta and yellow are projected onto the colloidal swarm ink and exposed for 120 s. As shown in Fig. 5d, the colloidal mixture acts as a positive photochromic colloidal swarm, which agrees well with our previously observed layered stratification (Fig. 5b). We further optimize the image quality and sensitivity of the colloidal swarm ink by selecting different particle sizes and concentrations

(Extended Data Figs. 4 and 5), in which the optimal performance is achieved with 500 nm particles and particle concentration at 1×10^{12} per cm^3.

To demonstrate, we project a university logo on the optimized colloidal swarm with 20 mW cm^{-2} illumination. As shown in Fig. 5e, an accurate colour pattern is impregnated on the colloidal swarm, and this image is quasistable up to 30 min, before the segregated colloids remix due to Brownian motion. As the colloidal swarm ink's photochromic ability is rooted in the redistribution of photoactive colloids, the colour pattern can be easily erased and repatterned with light. As shown in Fig. 5f, 120 s exposure is applied to simultaneously erase the existing image and imbed new patterns, in which various paintings are sequentially patterned into colloidal swarm ink by projecting new images over the existing ones without losing pattern quality. Furthermore, the photochromic ability of colloidal swarm ink can be further programmed by tuning the particle interactions with surface modification[46]. For instance, by controlling the surface charge polarity, the colloidal swarm ink can be programmed to show the negative colour image of the incident pattern, which manifests the flexibility of colloidal swarm ink (Extended Data Fig. 6 and Supplementary Table 4). We summarize some key features of existing photochromic materials and compare them with our new photoactive colloidal swarm ink (Supplementary Table 5).

It is worth noting that the colloidal swarm ink's sensitivity and colour contrast could be further optimized by enhancing the colloidal swarm photoactivity with the same strategies used in dye-sensitized solar cells[47], and replacing TiO_2 particles with density-matched photoactive particles, in which the same design principle and physics shown in this study can be applied. On the other hand, as colloidal photochromism results from the pigment particle rearrangement, the ultimate response time should be comparable with the current e-ink system (roughly 1,000 ms), which is intrinsically slower than the LCD and OLED displays. Thus this new photochromic material is not competing with LCD or OLED technology and should target other emerging applications.

Conclusion

In summary, we demonstrated a spectra-selective active colloidal mixture system, in which particle–particle interaction can be readily tuned by controlling the illumination spectra and intensity. The specific colloidal component can be selectively activated on excitation with corresponding light. This active mixture undergoes phase segregation that can be well predicted with phase stability thermodynamics. On the basis of this mechanism, we further demonstrate a new photochromic colloidal swarm, which self-adapts its appearance to incident light by inducing layered phase segregation. As this colloidal swarm is entirely self-sustained and simple to make, it promises wide applications from optical camouflage, smart-window for building thermal management, to full-colour electronic ink for e-readers, on further enhanced sensitivity and response time.

Methods

Synthesis of dye-sensitized monodisperse TiO_2 microsphere

The synthesis of the monodisperse TiO_2 microsphere was carried out by a modified sol-gel procedure[48]. In a typical process, 0.28 g dodecylamine was dissolved in a mixture solution containing 0.12 ml of deionized water, 50 ml of acetonitrile and 100 ml of methanol. After stirring for 5 min, 1 ml of titanium (IV) isopropoxide was added to the transparent solution and further stirred for 12 h to obtain a suspension. The suspension was centrifuged, washed with ethanol and dispersed in 15 ml of ethanol. Supplementary Fig. 3 shows the scanning electron microscopy image of the as-prepared monodisperse TiO_2 microsphere.

Commercial dyes SQ2 (5-carboxy-2-((3-((2,3-dihydro-1,1-dimethyl-3-ethyl-1*H*-benzo(e)indol-2-ylidene)methyl)-2-hydroxy-4-oxo-2-cyclobuten-1-ylidene)methyl)-3,3-dimethyl-1-octyl-3*H*-indolium, as received from Solaronix), LEG4 (3-(6-(4-(bis(2′,4′-dibutyloxybiphenyl-4-yl)amino-)phenyl)-4,4-dihexyl-cyclopenta-(2,1-b:3,4-b’)dithiophene-2-yl)-2-cyanoacrylic acid, as received from Dyenamo) and L0 (4-(diphenylamino) phenylcyanoacrylic acid, as received from Dyenamo) were used to stain the as-prepared TiO_2 microsphere. The absorbance of these selected dyes was measured by ultraviolet-visible light spectroscopy,

showing the distinctive absorbance (Supplementary Fig. 4). In a typical staining process, 5 ml of TiO_2 suspension solution was centrifuged to remove the solvent and then dispersed in 5 ml fo saturated ethanolic solution of dye. The colloidal concentration can be measured by counting the number of colloids after several rounds of dilution. After 2 days of loading, the dye-sensitized TiO_2 colloids were centrifuged and washed with ethanol to remove excess dye and redispersed in hydroquinone (100 mM) and benzoquinone (1 mM) aqueous solution with colloidal concentration of roughly 4×10^{11} per cm^3.

Simulation of electric field and fluid flow

The particle–particle interaction is numerically simulated by the COMSOL Multiphysics package. To simulate the diffusiosmotic flow around the particle and the apparent pair potential, the interactions between the activated–passive particle pair and the activated–activated particle pair are considered. Generally, when the light with a certain wavelength is illuminated from the top, the particle is activated and the oxidation products are generated from the illuminated side. As light cannot penetrate through the particle, we only consider the illuminated hemisphere to be the oxidation reaction site, in which the chemical reaction involved is $QH_2 \rightarrow BQ + 2H^+$ and the counter reduction reaction $BQ + 2H_2O \rightarrow QH_2 + 2OH^-$ proceed at the shaded side. Owing to the different diffusion coefficients of H^+ and OH^-, an uneven distribution of charged species will be produced, resulting in a local electric field. Such self-generated electric fields drive the motion of the charged species in the electrical double layer of both the particle surface and the substrate, producing a fluid flow that drags the particle.

To build the model, three different modules will be used. The diffusion of dilute species module is used to simulate the diffusion of H^+ and OH^-, the electrostatic module is used to simulate the electric field that is generated by the competing diffusion between H^+ and OH^-, and the fluid flow module is used to simulate the diffusio-osmotic flow generated by the movement of ions in electrical double layer. For the diffusion of dilute species, the distribution of H^+ and OH^- can be affected by the diffusion, convection and

electrophoresis under the electric field. Such behaviour can be fully described by the continuity equation at a steady state,

$${\rm{\nabla }}\,{{\bf{J}}}_{{\boldsymbol{i}}}=U\,{\rm{\nabla }}{{\bf{c}}}_{{\bf{i}}}-{{D}}_{{i}}{{\rm{\nabla }}}^{{\rm{2}}}{{\bf{c}}}_{{\bf{i}}}-\frac{{{\bf{z}}}_{{\bf{i}}}{\rm{F}}{{D}}_{{i}}{\rm{\nabla }}({{\bf{c}}}_{{\bf{i}}}{{\rm{\nabla }}}_{{\boldsymbol{\phi }}})}{{\rm{R}}{\rm{T}}}$$
(1)

where J_i is the flux of ion i, U is the fluidic velocity, F is the Faraday constant, φ is the electrostatic potential, R is the gas constant, T is the temperature and c_i, D_i and z_i are the concentration, diffusion coefficient and charge of species i, respectively. The electrostatic potential ($E=-\nabla \phi$) can be calculated from the Poisson equation,

$$-{\varepsilon }_{0}{\varepsilon }_{{\rm{r}}}{\nabla }^{2}\phi ={\rho }_{e}=F\left({Z}_{+}{c}_{+}+{Z}_{-}{c}_{-}\right)$$
(2)

where ε_0 is the vacuum permittivity, $\varepsilon_{\rm r}$ is the relative permittivity of water, ρ_e is the charge density, Z_+ and c_+ are the charge and concentration of H^+ ions, and $Z{\rm{_}}$ and c_- are the charge and concentration of OH^-.

The fluid flow outside the electric double layer is governed by two equations, the Stokes equation at steady state equation (3) and the continuity equation for the incompressible fluid equation (4), respectively.

$$-\nabla p+u{\nabla }^{2}U=0$$
(3)
$${\rm{\nabla }}\,{\bf{U}}={\bf{0}}$$
(4)

where u, U and p are the dynamic viscosity of water, velocity and pressure, respectively. The initial value of U and p are zero in our simulation.

The boundary condition on the activated particle is set to be the release or consumption of ions, representing the continuity of ion flux on the reaction hemisphere. On the reaction hemisphere, H^+ and OH^- will both be released from the surface, so the flux of both species will be set as positive.

In the fluid flow module, the boundary condition of both the particle surface and the substrate is set to be the electro-osmotic boundary. Electro-osmotic flow is then dominated by the tangential component of the electric field,

$${E}_{{\rm{t}}}=E-(E-n)\,\bullet \,n$$
(5)

where E_t is the tangential component of the electric field strength E. The electro-osmotic velocity is then governed by

$${u}_{{\rm{p}}}=-\frac{{\varepsilon }_{{\rm{r}}}{\varepsilon }_{0}{\zeta }_{{\rm{p}}}}{\mu }{E}_{{\rm{t}}}$$
(6)
$${u}_{{\rm{sub}}}=-\frac{{\varepsilon }_{{\rm{r}}}{\varepsilon }_{0}{\zeta }_{{\rm{sub}}}}{\mu }{E}_{{\rm{t}}}$$
(7)

$ {\zeta }_{{\rm{p}}}$, ${\zeta }_{{\rm{sub}}}$ here represent the zeta potential of the particle and the substrate, u_p and u_{sub} are the velocity of the electro-osmotic flow on the particle and the substrate, respectively.

Extended Data Fig. 7 shows the simulation results for activated–passive (above) and activated–activated (below). The concentration distribution of H^+ is shown as an example of the transport of dilute species simulation. Together with the distribution of OH^-, the generated electric field is produced as shown in Extended Data Fig. 7b.

To calculate the apparent pair potential, we modify the model of Morse potential to be the sum of an attractive potential exerted by diffusio-osmotic flow and an electrostatic repulsion potential. The apparent attraction force exerted on the particle generated by total electro-osmotic flow is first calculated. We consider the attraction force $F_a(x)$ as a function of separation

distance x, so that the attraction potential ${u}_{{\rm{a}}}(x)$ can be calculated by performing an integration from the particle surface x_0 to ∞,

$${u}_{{\rm{a}}}(x)=-{\int }_{{x}_{0}}^{{\rm{\infty }}}{F}_{{\rm{a}}}(x){\rm{d}}x$$
(8)

The attraction force at differential x can be calculated by performing a volumetric integration of the pressure P on the electric double layer. As our simulation is in 2D, the volumetric integration will become areal integration,

$${F}_{{\rm{a}}}(x)=\iint P{\rm{d}}x{\rm{d}}y$$
(9)

The integration area is an annular area around the particle representing the electric double layer with a thickness of 30 nm, which is estimated for an ionic concentration of 7×10^{-4} mol m^{-3}. The result shows the total force exerted on a particle, we only consider the x component because the y component does not contribute to the attraction interaction. Attraction force on the x axis is calculated by $F \times \cos(\theta)$, where θ is the included angle between the x and y components of the velocity. The attraction force at different separation distances can be calculated by performing a parametric sweep in COMSOL. A potential can be plotted by performing integration on the curve in commercial package Origin with equation (8),

For the repulsion potential $u_r(x)$, we adopted the equation of electrostatic repulsion between two charged spherical colloids with the Derjaguin approximation,

$${u}_{{\rm{r}}}(x)=\frac{{Q}^{2}}{4\pi {\varepsilon }_{0}{\varepsilon }_{{\rm{r}}}}{\left(\frac{{{\rm{e}}}^{-\kappa r}}{1+\kappa r}\right)}^{2}\frac{{{\rm{e}}}^{-\kappa x}}{x}$$
(10)

$$Q=4\pi {r}^{2}{\varepsilon }_{0}{\varepsilon }_{{\rm{r}}}\zeta \kappa $$
(11)

where Q is the surface charge, κ is the inversion of Debye length, r is the radius of the particle and ζ is the zeta potential of the particle.

The simulated apparent pair potential can thus be calculated by

$$w(x)={u}_{{\rm{a}}}(x)+{u}_{{\rm{r}}}(x)$$
(12)

Measurement of the apparent pair potential

The area fraction ϕ occupied by the interfacial particles is defined as $\varphi =\frac{N\pi {r}^{2}}{A}$. To measure the apparent pair potential, the as-prepared LEG4-loaded TiO_2 and SQ2-loaded TiO_2 were mixed with a ratio of 1:1, and diluted 3,000 times in QH2/BQ aqueous solution. Then the mixture solution was loaded into a wax-sealed capillary (Arte Glass Associates Co., Ltd, the path length is 100 μm), with area fraction $\phi \cong 1\%$. The supercontinuum laser (SC-Pro, Wuhan Yangtze Soton Laser Co., Ltd) coupled with the variable linear filter was used as the light source. The dynamic interaction of the colloids was observed with Olympus BX51M optical microscope and recorded by a digital video camera (Canon EOS M50) at 1,920 × 1,080 resolution at 30 fps. As shown in Supplementary Fig. 5, the radial distribution function $g(r)$ can be calculated from scores of statistical location information from the recorded data, according to the general expression equation (13)[49,50,51].

$$g(r)=\frac{2N(r)}{A{\rho }^{2}(2\pi r{\rm{d}}r)}$$
(13)

where r is separation distance, $N(r)$ is the number of colloidal pairs at separation distance r, N is the total number of colloids in each frame, A is the area of the frame, $\rho = N/A$ is the number density of the particles, $2\pi r\mathrm{d}r$ is the bin area. In this binary mixture, α and β represent the two components. The equation (14) is derived to calculate the radial distribution function between species α and β, where the number of them is denoted as N_α and N_β, respectively.

$${g}_{{\alpha \beta }}\left(r\right)=\frac{A}{{N}_{{\alpha }}{N}_{{\beta }}} < \mathop{\sum }\limits_{i=1}^{{N}_{\alpha }}\mathop{\sum }\limits_{j=1}^{{N}_{\beta }}\delta \left(r-\left({r}_{i}-{r}_{j}\right)\right) > $$
(14)

With finite concentration, the radial distribution function can reflect the interaction between neighbouring colloids. Generally, the apparent pair potential (Supplementary Fig. 6) can be determined by equation (15):

$$w\left(r\right)=-{k}_{{\rm{B}}}T{\rm{ln}}g\left(r\right)$$
(15)

Brownian dynamics simulation

Numerical fitting to the above apparent pair potential using homemade MATLAB codes was carried out to determine the particle–particle interaction potential and showed the standard Morse potential:

$$U\left(r\right)={D}_{0}\left[{{\rm{e}}}^{-2a\left(r-{r}_{0}\right)}-{2{\rm{e}}}^{-a\left(r-{r}_{0}\right)}\right]$$
(16)

where D_0 is the depth of the potential well, a controls the ‘width’ of the potential and r_0 is the equilibrium distance. The fitting parameters will be used to describe the corresponding particle–particle interactions in Brownian dynamics simulations.

The Brownian dynamics simulations were conducted using the LAMMPS package[1]. The simulation system is 2D ($6.0 \times 6.0\ \mu m^2$) and consists of 2,178 active and 2,178 passive particles. Periodic boundary conditions are used in lateral directions. The cut-off distance is set to 5.0 µm. A standard velocity-Verlet integrator with a time step of 1.0 µs is adopted to integrate the equation of motion:

$$m\frac{\partial v}{\partial t}={F}_{{\rm{c}}}-\frac{m}{\tau }v+{F}_{{\rm{r}}}$$
(17)

where m is the particle mass, v is the particle velocity, τ ranging from 1.0 to 1,000.0 μs is the damping factor, F_c is the conservative force from the interparticle interactions and ${F}_{{\rm{r}}}\propto \sqrt{\frac{m{k}_{{\rm{B}}}T}{\tau {\rm{d}}t}}$ is the force due to solvent atoms at a temperature T randomly bumping into the particle. The interaction among particles is described using the Morse potential equation (16) with the obtained parameters. Active and passive particles of the same size were uniformly dispersed at the initial state. The system was first relaxed for 2.0 s under consideration of identical particles, that is, active and passive particles are considered the same. After that, the system reached an equilibrium state, in which both active and passive particles were uniformly distributed. Then the system was run for 2.0 s (2×10^6 time steps) using various interparticle interactions in Supplementary Table 1.

Determination of Brownian dynamics of TiO_2 particles under light illumination

The SQ2 sensitized TiO_2 colloid was selected to illustrate the influence of light intensity on the mean squared displacement (MSD). The experiment process was similar to the measurement of pair potential, with decreased area fraction ϕ of 0.5%. The MSD under various red light intensities (10, 30, 50, 70 and 90 mW cm^{-2}) was then calculated using homemade MATLAB codes. As shown in Extended Data Fig. 1, the intensity of light had negligible effect on the MSD.

2D phase separation and coarsening of binary mixture

To study the phase behaviour of binary mixture, first a well-mixed solution of as-prepared LEG4-loaded-TiO_2 and SQ2-loaded-TiO_2 with a 1:1 ratio was diluted 200 times in QH2/BQ aqueous solution. Then it was sealed into a rectangle capillary and rested for 2 min to make sure all suspending colloid precipitated on the bottom surface with a roughly 15% area fraction.

To investigate the influence of light intensity on phase kinetics, red light with various intensities (640–660 nm; 10, 30, 50 and 90 mW cm^{-2}) was illuminated on the binary mixture solution from the top, with weak white

backlight. In our definition, cluster was determined by connecting all particles with centre-to-centre separation smaller than 1.5 particle diameter, and the cluster size was averaged over all clusters in the field of view. Then the gas fraction, the percentage of isolated colloids in all colloids, was calculated. The method was also applied to the Brownian dynamics simulation of phase evolution. As shown in Extended Data Fig. 8, the simulated phase segregation result matched well with the experiment (Fig. 3) except for the growth exponent at high illumination intensity, in which the simulated growth exponent was 0.85 compared to 0.54 in the experiment. This deviation may be attributed to the inaccurate potential of applied Morse potential, which is accurate in long range, but less accurate in the short range for describing particle–particle interaction. In high illumination, the particle–particle distance is small, which manifests this potential inaccuracy, and the growth exponents discrepancy is observed.

Furthermore, uniform light with various red-to-blue ratios (40:0, 30:10, 20:20, 10:30 and 0:40 mW cm^{-2}) was illuminated to the binary solution to further study the effect of incident light spectrum on the phase segregation. As shown in Fig. 4a, the various illumination spectra result in various intensities of segregation, which is defined by the following equation:

$$I=\frac{{N}_{{\rm{AA}}}+{N}_{{\rm{BB}}}}{{N}_{{\rm{AA}}}+{N}_{{\rm{BB}}}+{N}_{{\rm{AB}}}}$$
(18)

For simplicity, the two components in the binary mixture are denoted as A and B, where N_{AA}, N_{BB} and N_{AB} represent the number of pairs for every particle's nearest three neighbouring particles.

In a ternary system, L0 sensitized TiO_2 colloids were introduced to offer a third colour channel. The area fraction of the ternary mixture was also tuned to 15%. The ternary phase segregation was also observed under top blue, green and red light illumination with fixed intensity (50 mW cm^{-2}). Obvious segregation appeared under about 2 min of top light illumination.

To quantitatively characterize the self-similarity during the phase segregation process, the chord length distribution function[43,52], \(P(l/\langle

l\rangle)\), was measured for a different temporal snapshot. Briefly, a straight line was randomly generated across a snapshot. The chord length l was then determined by the length of the line segment inside the cluster. By varying the starting point and the orientation of the straight line randomly, a series of l values from different straight lines was obtained and then normalized by the mean value (characteristic length) <*l*>, from which the chord length distribution function \(P(l/\langle l\rangle)\) was yielded.

As shown in Extended Data Fig. 2. The chord length distribution functions are independent of time, indicating a self-similar growth mechanism, which is also the origin of the power-law dependence and very similar to the phase separation in a classical thermodynamic mixture.

3D phase segregation

To study the vertical phase segregation of the ternary colloidal system, the 3D particle distribution was mapped by optical microscope and confocal laser scanning microscope (LEICA TCS SP8), respectively. Specifically, a colloidal mixture solution of L0, LEG4 and SQ2-loaded TiO_2 (the ratio for them was 1:1:1) was sealed into a parallel plated glass cell separated with parafilm ($\phi \cong$ 100%). Then the cell was exposed to the blue, green and red light (Supplementary Fig. 1a) in turn, and illuminated from the top with a fixed intensity (100 mW cm^{-2}). The optical microscope (the magnification and numerical aperture of the objective were ×40 and 0.9, respectively) was focused at different depths ($Z = 0$ to 80 μm), and the distribution of varying colour colloids at each depth layer was tracked. As shown in Supplementary Fig. 1b and Supplementary Video 4, the active SQ2-loaded colloids aggregated at the bottom under red light illumination, while passive L0 and LEG4-loaded colloids were pushed to the top. Conversely, under green and blue light top illumination (Supplementary Video 4), the active and passive couples were switched to LEG4/(SQ2+L0) and (L0+LEG4)/SQ2, respectively (Supplementary Table 3).

This light-inducing vertical segregation can also be visualized with a confocal microscope (Fig. 5b). Experimentally, the ternary mixture solution sealed in the homemade cell was placed under the inverted confocal microscope and exposed to blue, green and red light illumination from the

top, in turn, at a fixed intensity (100 mW cm^{-2}). After about 2 min of illumination, the 3D confocal images were captured in which the fluorescence signals of SQ2, LEG4 and L0 were set as cyan, magenta, and yellow, respectively.

3D simulation of the phase segregation

To simulate the 3D phase segregation, COMSOL Multiphysics was used to simulate the detailed flow field in the particle matrix, while all the particles' top parts received higher light intensity than the bottom due to scattering and shadowing of the particle matrix. As shown in Extended Data Fig. 3a, on illumination, a vertical flow was generated between particles by diffusiophoresis, which was the origin of the attractive potential. Under this attractive potential, active particles clustered together and the vertical flows overlapped with each other and intensified (Extended Data Fig. 3b).

In the 3D phase separation experiment, there were roughly 30–50 layers of particles in the colloidal solution, and the lower particles served as the pseudo-substrate for the upper layers. As shown in simulation (Extended Data Fig. 3c), when passive particles (blue) settled below a layer of active particles (red), the upwards electro-osmotic flow was generated similarly to the particle monolayer. As more layers of active particles stacked, the upwards flow increased, which brought passive particles to the top, while the active particles made a sediment at the bottom due to the counteraction of the upwards fluid flow generation (Extended Data Fig. 3d,e).

We further explain this 3D layering process in crowded conditions with 3D Brownian dynamics simulations, where the light-dependent Morse potential, $u={D}_{0}\left[{{\rm{e}}}^{-2\alpha \left(r-{r}_{0}\right)}-2{{\rm{e}}}^{-\alpha \left(r-{r}_{0}\right)}\right]$ describing the particle interaction and the light-dependent vertical force describing the upwards flow field is adopted. Here, the parameters of potential function, that is, the depth of the potential well D_0 and α controlling the 'width' of the potential, were obtained from fitting the apparent pair potentials, as measured in our experiment (Fig. 2). Besides, according to the experimental observation and former diffusiophoresis simulations, a vertical force that varied with the average vertical distance h

was added, and the magnitudes of imposed vertical forces applied on the two distinct particles were proportional to the particle activity. Initially, it was assumed that active and passive particles were uniformly distributed in the simulated domain. A 3D simulation with constant temperature, volume and number of particles (*N*, *V* and *T*) was then carried out. As shown in Extended Data Fig. 3f, active and passive particles spontaneously separated under the light illumination, which is consistent with our experimental observation.

Macroscopic photochromic ink and characterization

To formulate the photochromic colloidal swarm ink, the as-prepared L0-loaded-TiO_2, LEG4-loaded-TiO_2 and SQ2-loaded-TiO_2 solutions were mixed at a 1:2:1 ratio (Supplementary Fig. 2a). A commercial 3LCD projector was chosen to project designed colour textures onto the as-prepared colloidal swarm ink. To obtain pure blue, green and red light, three optical filters were placed between the dichroic combiner cube and the original RGB light source to narrow the default broader output wavelength range for non-overlapping output (Supplementary Fig. 2b,c). To project high-resolution image, the projector lens was inverted.

In the macroscopic imaging demonstration, the colloidal swarm ink was injected into a parallel plate glass cell separated with parafilm, while the designed textures were projected onto the ink and exposed for 120 s. The obtained colour images were recorded with a digital camera (Canon EOS M50). The colour gamut was measured to characterize the performance of the photochromic ink. First, a series of images were obtained by projecting six colour blocks (Fig. 5d) with different times and intensities. Then all the samples were placed under the pinhole of the integrating sphere, and the simulated sunlight was illuminated into the integrating sphere. The spectrometer and commercial software (Oceanview) were used to draw the received reflected light spectrum into the colour gamut diagram (polytetrafluoroethylene is selected as a white Lambertian diffuser).

Particle size dependence of photochromic ink performance

To study the influence of the particle size on the photochromic performance of the active ink, we investigated the photochromic performance of colloidal

swarm with 500 nm, 1 μm and 2 μm TiO_2 particles, respectively. As shown in Extended Data Fig. 4, smaller particles resulted in much-enhanced photosensitivity, in which the brightness and contrast of the resulting image improved, whereas the larger particles showed much deteriorated image quality. To quantify the photosensitivity, characteristic curves of colloidal swarms with 500 nm, 1 μm and 2 μm TiO_2 were measured and plotted as contrast versus light intensity and contrast versus exposure time. From the characteristic curves, we concluded that the minimum light intensity and exposure time were 20 mW cm^{-2} and 1 min, respectively.

We speculate that the photosensitivity is determined by the balance of upwards flow generated by active particles and the gravity of passive particles. As a result, the photosensitivity is not fundamentally limited by the working mechanism. Instead, lower density particles (such as high porosity TiO_2 (ref. [53]) or polystyrene-TiO_2 core-shell particles[54]) with less gravitational drag may further enhance colloidal swarm photosensitivity. In addition, new photosensitive dyes with high absorption coefficients or better dye loading strategies, such as shown in recent publication[47] may also enhance the photochromic performance of colloidal swarm.

Performance of the photochromic ink with different particle concentrations

Owing to thermal fluctuation, the colloidal swarm behaves as a liquid in which interstitial space allows the particle rearrangement for segregation. On the other hand, this interstitial space shrinks as particle density decreases, which prevents the segregation process. As shown in Extended Data Fig. 5, the segregation is observed in diluted ink, while the image contrast is not high as there are insufficient particles in the swarm. The colloidal swarm image quality gradually improves with particle concentration and an optimal concentration is achieved at 1×10^{12} per cm^3. Further increasing particle concentration leads to deteriorated contrast and brightness, suggesting incomplete segregation.

Performance of the photochromic ink with different zeta potentials

As the colour image of the photochromic ink is a result of phase segregation, the response can be easily tuned with simple surface modification or doped with different dyes. As shown in Extended Data Fig. 6 and Supplementary Table 4, a negative colour image is achieved with positively charged particles instead of positive colour images for negatively charged particles.

We also compared the key features of current available photochromic materials, which are mainly based on the valence transition in material or photoisomerization of chromophore molecules. As shown in Supplementary Table 5, the performance of our colloidal swarm ink offers full-colour rendering ability and immediate repatterning ability with high sensitivity and response speed[55,56,57,58,59,60].

Data availability

The data that support the findings of this study are available from the corresponding author upon reasonable request. Source data are provided with this paper.

References

1. Mahynski, N. A. et al. Assembly of multi-flavored two-dimensional colloidal crystals. *Soft Matter* **13**, 5397–5408 (2017).

2. Fox, J. M. et al. The molecular origin of enthalpy/entropy compensation in biomolecular recognition. *Annu. Rev. Biophys.* **47**, 223–250 (2018).

3. Balazs, A. C., Emrick, T. & Russell, T. P. Nanoparticle polymer composites: where two small worlds meet. *Science* **314**, 1107–1110 (2006).

4. Wu, C. et al. Ion-exchange enabled synthetic swarm. *Nat. Nanotechnol.* **16**, 288–295 (2021).

5. Palacci, J. et al. Living crystals of light-activated colloidal surfers. *Science* **339**, 936–940 (2013).

6. Lavergne, F. A., Wendehenne, H., Bäuerle, T. & Bechinger, C. Group formation and cohesion of active particles with visual perception–dependent motility. *Science* **364**, 70–74 (2019).

7. Xu, B. et al. Rigidity enhances a magic-number effect in polymer phase separation. *Nat. Commun.* **11**, 1561 (2020).

8. Gnan, N. & Zaccarelli, E. The microscopic role of deformation in the dynamics of soft colloids. *Nat. Phys.* **15**, 683–688 (2019).

9. Hueckel, T., Hocky, G. M., Palacci, J. & Sacanna, S. Ionic solids from common colloids. *Nature* **580**, 487–490 (2020).

10. Dijkstra, M., van Roij, R. & Evans, R. Phase behavior and structure of binary hard-sphere mixtures. *Phys. Rev. Lett.* **81**, 2268–2271 (1998).

11. Schulz, M. & Keddie, J. L. A critical and quantitative review of the stratification of particles during the drying of colloidal films. *Soft Matter* **14**, 6181–6197 (2018).

12. Chen, M. et al. Observation of isotropic–isotropic demixing in colloidal platelet–sphere mixtures. *Soft Matter* **11**, 5775–5779 (2015).

13. Liu, W. et al. Segregation in drying binary colloidal droplets. *ACS Nano* **13**, 4972–4979 (2019).

14. Yan, J. et al. Reconfiguring active particles by electrostatic imbalance. *Nat. Mater.* **15**, 1095–1099 (2016).

15. Geyer, D., Martin, D., Tailleur, J. & Bartolo, D. Freezing a flock: motility-induced phase separation in polar active liquids. *Phys. Rev. X* **9**, 031043 (2019).

16. Großmann, R., Aranson, I. S. & Peruani, F. A particle-field approach bridges phase separation and collective motion in active matter. *Nat. Commun.* **11**, 5365 (2020).

17. Grosberg, A. Y. & Joanny, J. F. Nonequilibrium statistical mechanics of mixtures of particles in contact with different thermostats. *Phys. Rev. E*

92, 032118 (2015).

18. Stenhammar, J., Wittkowski, R., Marenduzzo, D. & Cates, M. E. Activity-induced phase separation and self-assembly in mixtures of active and passive particles. *Phys. Rev. Lett.* **114**, 018301 (2015).

19. Curatolo, A. I. et al. Cooperative pattern formation in multi-component bacterial systems through reciprocal motility regulation. *Nat. Phys.* **16**, 1152–1157 (2020).

20. Šípová-Jungová, H., Andrén, D., Jones, S. & Käll, M. Nanoscale inorganic motors driven by light: principles, realizations, and opportunities. *Chem. Rev.* **120**, 269–287 (2020).

21. Kochergin, Y. S. et al. Hybrid inorganic–organic visible-light-driven microrobots based on donor–acceptor organic polymer for degradation of toxic psychoactive substances. *ACS Nano* **15**, 18458–18468 (2021).

22. Chen, C. et al. Chemical/light-powered hybrid micromotors with 'on-the-fly' optical brakes. *Angew. Chem. Int. Ed.* **57**, 8110–8114 (2018).

23. Wang, J. et al. Light-driven micro/nanomotor for promising biomedical tools: principle, challenge, and prospect. *Acc. Chem. Res.* **51**, 1957–1965 (2018).

24. Xu, L. et al. Light-driven micro/nanomotors: from fundamentals to applications. *Chem. Soc. Rev.* **46**, 6905–6926 (2017).

25. Zheng, J. et al. Orthogonal navigation of multiple visible-light-driven artificial microswimmers. *Nat. Commun.* **8**, 1438 (2017).

26. Xuan, M. et al. Noncontinuous super-diffusive dynamics of a light-activated nanobottle motor. *Angew. Chem. Int. Ed.* **57**, 6838–6842 (2018).

27. Reiter, S. et al. Elucidating the control and development of skin patterning in cuttlefish. *Nature* **562**, 361–366 (2018).

28. Barnett, J. B. et al. Imperfect transparency and camouflage in glass frogs. *Proc. Natl Acad. Sci. USA* **117**, 12885 (2020).

29. Comiskey, B., Albert, J. D., Yoshizawa, H. & Jacobson, J. An electrophoretic ink for all-printed reflective electronic displays. *Nature* **394**, 253–255 (1998).

30. Dumanli, A. G. & Savin, T. Recent advances in the biomimicry of structural colours. *Chem. Soc. Rev.* **45**, 6698–6724 (2016).

31. Chen, K. et al. Bioinspired dynamic camouflage from colloidal nanocrystals embedded electrochromics. *Nano Lett.* **21**, 4500–4507 (2021).

32. Min, Y. et al. The role of interparticle and external forces in nanoparticle assembly. *Nat. Mater.* **7**, 527–538 (2008).

33. Yi, C. et al. Self-limiting directional nanoparticle bonding governed by reaction stoichiometry. *Science* **369**, 1369–1374 (2020).

34. Rogers, W. B. & Manoharan, V. N. Programming colloidal phase transitions with DNA strand displacement. *Science* **347**, 639–642 (2015).

35. Li, B. et al. Modes of surface premelting in colloidal crystals composed of attractive particles. *Nature* **531**, 485–488 (2016).

36. Keh, H. J. Diffusiophoresis of charged particles and diffusioosmosis of electrolyte solutions. *Curr. Opin. Colloid Interface Sci.* **24**, 13–22 (2016).

37. Mou, F. et al. Phototactic flocking of photochemical micromotors. *iScience* **19**, 415–424 (2019).

38. Singh, D. P., Choudhury, U., Fischer, P. & Mark, A. G. Nonequilibrium assembly of light-activated colloidal mixtures. *Adv. Mater.* **29**, 1701328 (2017).

39. Wang, J. et al. Rational design of reversible redox shuttle for highly efficient light-driven microswimmer. *ACS Nano* **14**, 3272–3280 (2020).

40. Mallory, S. A., Valeriani, C. & Cacciuto, A. An active approach to colloidal self-assembly. *Annu. Rev. Phys. Chem.* **69**, 59–79 (2018).

41. Onuki, A. *Phase Transition Dynamics* (Cambridge Univ. Press, 2002).

42. Redner, G. S., Hagan, M. F. & Baskaran, A. Structure and dynamics of a phase-separating active colloidal fluid. *Phys. Rev. Lett.* **110**, 055701 (2013).

43. Tateno, M. & Tanaka, H. Power-law coarsening in network-forming phase separation governed by mechanical relaxation. *Nat. Commun.* **12**, 912 (2021).

44. Muñoz-García, A. B. et al. Dye-sensitized solar cells strike back. *Chem. Soc. Rev.* **50**, 12450–12550 (2021).

45. Williams, T. L. et al. Dynamic pigmentary and structural coloration within cephalopod chromatophore organs. *Nat. Commun.* **10**, 1004 (2019).

46. Dai, B. et al. Programmable artificial phototactic microswimmer. *Nat. Nanotechnol.* **11**, 1087–1092 (2016).

47. Ren, Y. et al. Hydroxamic acid pre-adsorption raises the efficiency of cosensitized solar cells. *Nature* **613**, 60–65 (2023).

48. Tanaka, S., Nogami, D., Tsuda, N. & Miyake, Y. Synthesis of highly-monodisperse spherical titania particles with diameters in the submicron range. *J. Colloid Interface Sci.* **334**, 188–194 (2009).

49. Pliego-Pastrana, P. & Carbajal-Tinoco, M. D. Two-component polypeptides modeled with effective pair potentials. *J. Phys. Chem. B* **110**, 24728–24733 (2006).

50. Chen, W. et al. Attraction between weakly charged silica spheres at a water-air interface induced by surface-charge heterogeneity. *Phys. Rev.*

E **79**, 041403 (2009).

51. Behrens, S. H. & Grier, D. G. Pair interaction of charged colloidal spheres near a charged wall. *Phys. Rev. E* **64**, 050401 (2001).

52. Lu, B. & Torquato, S. Chord-length and free-path distribution functions for many-body systems. *J. Chem. Phys.* **98**, 6472–6482 (1993).

53. Liu, Y. et al. Radially oriented mesoporous TiO_2 microspheres with single-crystal–like anatase walls for high-efficiency optoelectronic devices. *Sci. Adv.* **1**, e1500166 (2015).

54. Xue, Y., Wang, F., Luo, H. & Zhu, J. Preparation of noniridescent structurally colored PS@TiO_2 and Air@C@TiO_2 core–shell nanoparticles with enhanced color stability. *ACS Appl. Mater. Interfaces* **11**, 34355–34363 (2019).

55. Fan, J. et al. Flexible, switchable and wearable image storage device based on light responsive textiles. *Chem. Eng. J.* **404**, 126488 (2021).

56. Wales, D. J. et al. 3D-printable photochromic molecular materials for reversible information storage. *Adv. Mater.* **30**, 1800159 (2018).

57. Zhang, X. et al. Self-accelerating photocharge separation in BiOBr ultrathin nanosheets for boosting photoreversible color switching. *Chem. Eng. J.* **428**, 131235 (2022).

58. Dong, J. & Zhang, J. Photochromic and super anti-wetting coatings based on natural nanoclays. *J. Mater. Chem. A* **7**, 3120–3127 (2019).

59. Jeong, W. et al. Full color light responsive diarylethene inks for reusable paper. *Adv. Funct. Mater.* **26**, 5230–5238 (2016).

60. Jin, Y. et al. Photo-chromeleon: re-programmable multi-color textures using photochromic dyes. In *Proc. 2019 ACM User Interface and Technology Symposium* 701–712 (Association for Computing Machinery, 2019).

Acknowledgements

We thank T.Y. Tang for contributing personal artwork for the photochromic demonstration in Fig. 5f. This work was supported in part by the Hong Kong Research Grants Council (RGC) General Research Fund (grant nos. GRF17307221, GRF16300421, GRF17304618 and GRF16300421), the Collaborative Research Fund (grant no. C7082-21G), RGC Research Fellowship (grant no. RFS2122-7S06), Croucher Foundation Senior Research Fellowship (2022), Croucher Innovation Award (2019), the Shenzhen-Hong Kong Innovation Circle Program (grant no. SGDX2019081623341332), the National Natural Science Foundation of China (grant nos. 22275156, T2241022, 52025132, 21975209 and 22121001), the Fundamental Research Funds for the Central Universities of China (grant no. 20720220019) and the Tencent Foundation (The XPLORER PRIZE).

Author information

Authors and Affiliations

1. State Key Laboratory of Physical Chemistry of Solid Surfaces, College of Chemistry and Chemical Engineering, Xiamen University, Xiamen, China

   Jing Zheng & Xu Hou

2. Department of Chemistry, The University of Hong Kong, Pokfulam, Hong Kong, China

   Jing Zheng, Jingyuan Chen, Yijiang Mu, Changjin Wu, Yufeng Wang & Jinyao Tang

3. Department of Mechanical and Aerospace Engineering, The Hong Kong University of Science and Technology, Clear Water Bay, Hong Kong, China

   Yakang Jin & Zhigang Li

4. School of Physics, University of Electronic Science and Technology of China, Chengdu, China

Yakang Jin

5. Department of Physics, The Hong Kong University of Science and Technology, Clear Water Bay, Hong Kong, China

Yan Wen & Penger Tong

6. Department of Physics, Research Institute for Biomimetics and Soft Matter, Fujian Provincial Key Laboratory for Soft Functional Materials Research, Jiujiang Research Institute, College of Physical Science and Technology, Xiamen University, Xiamen, China

Xu Hou

7. Innovation Laboratory for Sciences and Technologies of Energy Materials of Fujian Province (IKKEM), Xiamen, China

Xu Hou

8. State Key Laboratory of Synthetic Chemistry, The University of Hong Kong, Hong Kong, China

Jinyao Tang

Contributions

J.T. and J.Z. conceived and designed the project. J.Z. prepared the samples and conducted most of the measurement. Y.W. and J.Z. calculated the apparent pair potential. Y.J. performed the Brownian dynamic simulation. J.C. helped with COMSOL simulation. J.T., J.Z. and X.H. wrote the manuscript. All authors discussed the results and commented on the manuscript.

Corresponding author

Correspondence to Jinyao Tang.

Ethics declarations

Competing interests

The authors declare no competing interests.

Peer review

Peer review information

Nature thanks Jianguo Guan, Monica Olvera de la Cruz and the other, anonymous, reviewer(s) for their contribution to the peer review of this work. Peer reviewer reports are available.

Additional information

Publisher's note Springer Nature remains neutral with regard to jurisdictional claims in published maps and institutional affiliations.

Extended data figures and tables

Extended Data Fig. 1 Mean squared displacement in varies illumination intensity.

Mean squared displacement (MSD) as a function of time for SQ2 sensitized TiO_2 colloids under red light (640–660 nm) illumination with various intensities (10 mW/cm^2, 30 mW/cm^2, 50 mW/cm^2, 70 mW/cm^2, 90 mW/cm^2).

Extended Data Fig. 2 The time evolution of the chord length distribution.

The chord length distribution functions for the colloid-poor phase at different times (300 s, 360 s, 420 s and 480 s) after being scaled by the characteristic length ⟨l⟩.

Extended Data Fig. 3 Simulation of Passive/Active particle mixture.

a–b, Flow field simulation around active particles (red) and passive (blue) particles shows **a**, inward fluid flow that pushes the particles together when well separated and **b**, the upward fluid flow intensified after cluster formation. **c–e**, Simulations of fluid flow on particles under different conditions. **c**: Active particles located on multiple layers of passive particles, referring to the initial state of the active particles; **d**: One active particle suspended in solution, moving downwards due to the self-generated upward flow in light gradient; **e**: Active particles located below passive particles, referring to the final state of the active particles. **f**. Evolution of active (red) and passive (blue) particles in the binary mixture from 3D Brownian dynamics simulations.

Extended Data Fig. 4 The performance of photochromic active colloidal with various particle diameters.

a, The optical images of the texture of different particle sizes. Scale bar: 2 mm. **b**, Characteristic curve of different photochromic nanoswarm under different light intensity and time.

Extended Data Fig. 5 Concentration dependence of the photochromic property of the colloidal swarm.

performance of photonic nanoswarm with different concentrations of the particle mixture. Scale bar: 2 mm.

Extended Data Fig. 6 Photochromic colloidal swarm with different charge polarity.

Positive and negative images of photochromic nanoswarm modulated by zeta potential. Scale bar: 2 mm.

Extended Data Fig. 7 Ion and electric field distribution around active and passive colloidal.

a, Simulated concentration distribution of H^+ ions produced by the chemical reaction between active and passive particles. **b**, The electric field of the active-passive species. **c**, Simulated concentration distribution of H^+ ions produced by the chemical reaction between two active particles. **d**, The electric field of the active–active species.

Extended Data Fig. 8 Brownian dynamics simulation of colloidal mixture.

a, The Brownian dynamics simulated cluster size evolution of the binary colloidal system under various apparent pair potentials fitted from experimental results under different red light illumination (640-660 nm, 10 mW/cm^2, 30 mW/cm^2, 50 mW/cm^2, 90 mW/cm^2), corresponding to the Fig. 3b. The cluster sizes are compatible with the relation of $S(t) \sim t^{0.02}$, $S(t) \sim t^{0.36}$, $S(t) \sim t^{0.36}$, $S(t) \sim t^{0.85}$, respectively. **b**, The simulated gas fraction of binary mixture decreases over time under various apparent pair potential fitting from experimental results.

Supplementary information

Supplementary Information

This file contains Supplementary Figs. 1–6 and Tables 1–5.

Peer Review File

Supplementary Video 1

Phase segregation of binary mixture. Phase segregation of binary mixture under various red light illumination intensities (640–660 nm; 10, 30, 50 and 90 mW cm^{-2}).

Supplementary Video 2

Brownian dynamic simulated phase segregation. Brownian dynamic simulated phase segregation of binary mixture under apparent pair potential fitted from experimental result under various red light illumination intensities (640–660 nm; 10, 30, 50 and 90 mW cm^{-2}).

Supplementary Video 3

The optical colloidal phase evolution. The optical colloidal phase evolution of LEG4 and SQ2 sensitized TiO_2 colloids under illumination with various blue/red light ratios (40:0, 30:10, 20:20, 10:30 and 0:40 mW cm^{-2}).

Supplementary Video 4

The vertical phase segregation. The vertical phase segregation of a ternary colloidal mixture containing L0, LEG4 and SQ2 sensitized TiO_2 colloids under top red, green and blue light illumination.

Source data

Source Data Figs. 1–4.

Rights and permissions

Open Access This article is licensed under a Creative Commons Attribution 4.0 International License, which permits use, sharing, adaptation, distribution and reproduction in any medium or format, as long as you give appropriate credit to the original author(s) and the source, provide a link to the Creative Commons licence, and indicate if changes were made. The images or other third party material in this article are included in the article's

Creative Commons licence, unless indicated otherwise in a credit line to the material. If material is not included in the article's Creative Commons licence and your intended use is not permitted by statutory regulation or exceeds the permitted use, you will need to obtain permission directly from the copyright holder. To view a copy of this licence, visit http://creativecommons.org/licenses/by/4.0/.

Reprints and Permissions

About this article

Cite this article

Zheng, J., Chen, J., Jin, Y. *et al.* Photochromism from wavelength-selective colloidal phase segregation. *Nature* **617**, 499–506 (2023). https://doi.org/10.1038/s41586-023-05873-4

- Received: 13 December 2021
- Accepted: 21 February 2023
- Published: 17 May 2023
- Issue Date: 18 May 2023
- DOI: https://doi.org/10.1038/s41586-023-05873-4

Share this article

Anyone you share the following link with will be able to read this content:

Get shareable link

Sorry, a shareable link is not currently available for this article.

Copy to clipboard

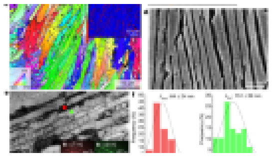
Provided by the Springer Nature SharedIt content-sharing initiative

Ink that mimics the colour of incoming light

- Hector Lopez-Rios
- Monica Olvera de la Cruz

Nature News & Views 17 May 2023

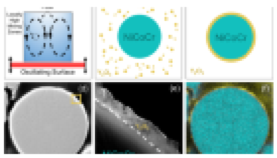
This article was downloaded by **calibre** from https://www.nature.com/articles/s41586-023-05873-4



Strong yet ductile nanolamellar high-entropy alloys by additive manufacturing

03 August 2022

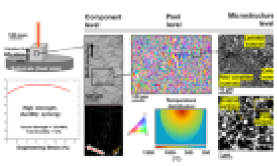
Jie Ren, Yin Zhang, … Wen Chen



Efficient production of a high-performance dispersion strengthened, multi-principal element alloy

15 June 2020

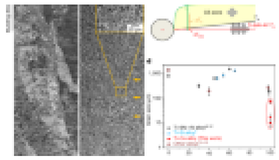
T. M. Smith, A. C. Thompson, … C. A. Kantzos



Multiscale hierarchical and heterogeneous mechanical response of additively manufactured novel Al alloy investigated by high-resolution nanoindentation mapping

31 October 2022

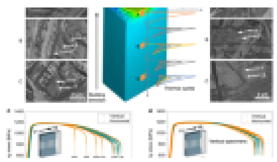
Abhijeet Dhal, Saket Thapliyal, … Rajiv S. Mishra



[Additive manufacturing of ultrafine-grained high-strength titanium alloys]

04 December 2019

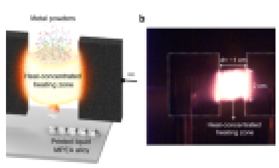
Duyao Zhang, Dong Qiu, … Mark A. Easton



[Designing against phase and property heterogeneities in additively manufactured titanium alloys]

09 August 2022

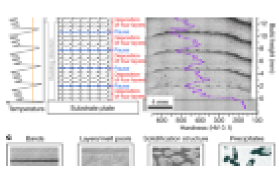
Jingqi Zhang, Yingang Liu, … Ming-Xing Zhang



[Ultrahigh-temperature melt printing of multi-principal element alloys]

07 November 2022

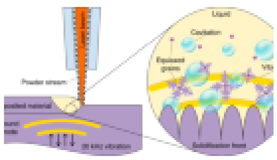
Xizheng Wang, Yunhao Zhao, … Liangbing Hu



[High-strength Damascus steel by additive manufacturing](#)

24 June 2020

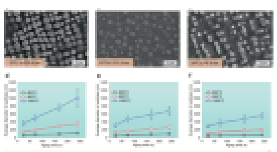
Philipp Kürnsteiner, Markus Benjamin Wilms, … Dierk Raabe



[Grain structure control during metal 3D printing by high-intensity ultrasound](#)

09 January 2020

C. J. Todaro, M. A. Easton, … M. Qian



[Achieving thermally stable nanoparticles in chemically complex alloys via controllable sluggish lattice diffusion](#)

18 August 2022

Bo Xiao, Junhua Luan, … Tao Yang

- Article
- Open Access
- Published: 19 April 2023

A 3D printable alloy designed for extreme environments

- Timothy M. Smith ,
- Christopher A. Kantzos,
- Nikolai A. Zarkevich,
- Bryan J. Harder,
- Milan Heczko,
- Paul R. Gradl,
- Aaron C. Thompson,
- Michael J. Mills,
- Timothy P. Gabb &
- …
- John W. Lawson

Show authors

Nature **volume 617**, pages 513–518 (2023)

- 26k Accesses
- 1 Citations
- 176 Altmetric
- Metrics details

Abstract

Multiprincipal-element alloys are an enabling class of materials owing to their impressive mechanical and oxidation-resistant properties, especially in extreme environments[1,2]. Here we develop a new oxide-dispersion-strengthened NiCoCr-based alloy using a model-driven alloy design approach and laser-based additive manufacturing. This oxide-dispersion-strengthened alloy, called GRX-810, uses laser powder bed fusion to disperse nanoscale Y_2O_3 particles throughout the microstructure without the use of resource-intensive processing steps such as mechanical or in situ alloying[3,4]. We show the successful incorporation and dispersion of nanoscale oxides throughout the GRX-810 build volume via high-resolution characterization of its microstructure. The mechanical results of GRX-810

show a twofold improvement in strength, over 1,000-fold better creep performance and twofold improvement in oxidation resistance compared with the traditional polycrystalline wrought Ni-based alloys used extensively in additive manufacturing at 1,093 °C[5,6]. The success of this alloy highlights how model-driven alloy designs can provide superior compositions using far fewer resources compared with the 'trial-and-error' methods of the past. These results showcase how future alloy development that leverages dispersion strengthening combined with additive manufacturing processing can accelerate the discovery of revolutionary materials.

Main

High-entropy alloys, also commonly referred to as multi-principal element alloys (MPEAs), are a class of materials that are currently of interest among the metallurgical community[1,2,7,8,9]. In the past decade numerous scientific investigations have uncovered remarkable properties exhibited by these alloys[7,10,11,12,13]. One of the most heavily investigated MPEA family is the Cantor alloy CoCrFeMnNi and its derivatives[2,8,14]. This group of alloys showed excellent strain hardening, resulting in high tensile strength and ductility[7,15,16,17,18]. Overcoming the strength–ductility trade-off is a result of atomic-scale deformation mechanisms[16], such as locally variable stacking-fault energies[19] and magnetically driven phase transformations[20]. This class of alloys has also proven to be robust, resisting hydrogen environment embrittlement[21], exhibiting improved irradiation properties[22] and providing superior strength at cryogenic temperatures[23]. As a result, these alloys show great potential for numerous aerospace and energy applications in elevated-temperature and corrosive environments, allowing for weight reduction and higher performance operation.

One Cantor alloy derivative of special interest is the medium-entropy alloy NiCoCr. This alloy family provides the highest strength at room temperature among the Cantor alloy and its derivatives[2,24]. Recently, this alloy was shown to provide impressive tensile properties (1,100 MPa room temperature yield strength) when undergoing partial recrystallization heat treatment after cold rolling[17]. These properties are also attributed to strain-induced, face-centred cubic (FCC) to hexagonal close-packed (HCP) phase

transformations and local stacking-fault variations. Alloying and doping of NiCoCr with refractory elements and interstitials have also been explored recently. Seol et al. found that doping the high-entropy alloy, NiCoCrFeMn, with 30 ppm of boron resulted in significant improvements in strength and ductility attributed to both grain boundary and interstitial strengthening from the boron[25]. Recent studies have also found that the addition of carbon to MPEAs resulted in improved strength[26,27,28]. Lastly, Wu et al.[29] found that three atomic percentage (at.%) additions of W in NiCoCr created a finer grain structure (average grain size 1 μm), resulting in a large increase in yield strength of the alloy (over 1,000 MPa, compared with 500 MPa for nonalloyed NiCoCr) while maintaining exceptional ductility of over 50% (ref. [29]). These results suggest that significant improvements in FCC MPEA systems can still be realized through additional alloying.

Investigations of oxide-dispersion-strengthened (ODS) MPEAs have shown improved high-temperature properties (strength and creep)[4] and irradiation properties[30]. Similarly, multiple recent studies have successfully produced ODS alloys through laser powder bed fusion (L-PBF) using a variety of techniques[3,4,31]. These methods have relied on mechanical alloying[4,31], in situ alloying[3] or chemical reactions[32] to introduce and incorporate oxides into the three-dimensional (3D) printed matrix. However, all these processes introduce complexity and repeatability issues when trying to produce similar material through different additive manufacturing (AM) methods or machines. Recent work by Smith et al. produced ODS NiCoCr through L-PBF in which nanoscale Y_2O_3 nanoparticles were coated onto NiCoCr metal powder through a high-energy mixing process that does not require any binders, fluids or chemical reactions. This process did not deform or impact powder spherical morphology, which is important in regard to high-quality AM components. Using this approach these authors produced an ODS alloy that provided a 35% increase in tensile strength and threefold improvement in ductility at 1,093 °C compared with its non-ODS counterpart[33].

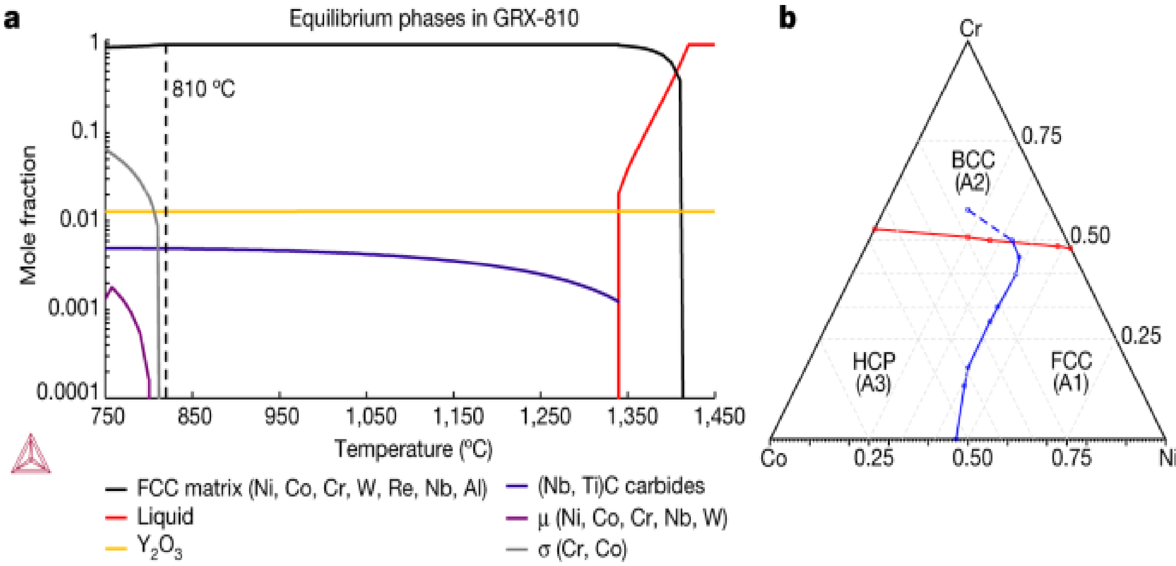
Building on the work and using the same coating process performed by Smith et al.[33], a model-driven alloy design approach was employed to optimize the NiCoCr alloy system for high-temperature applications using AM for complex components. This effort resulted in a new composition that was built using L-PBF to include nanoscale Y_2O_3 dispersoids for further

high-temperature strength/stability above 810 °C. The characterization of this new alloy, Glenn Research Center Extreme Temperature above 810 °C (GRX-810), showed orders of magnitude better creep strength and twofold higher tensile strength compared with commercially available high-temperature alloys used in AM[34,35] and with other alloys explored in this study (NiCoCr, NiCoCr-ODS, NiCoCr-ODS with minor additions of Re (1.5 wt%) and B (0.03wt%) (ODS-ReB)). This study confirms the maturity of both model-driven alloy design and AM processes to produce next-generation materials with properties not feasible through previous, conventional manufacturing technologies.

Microstructure characterization of GRX-810

Figure 1 provides the predicted phase equilibrium of the model-optimized GRX-810 alloy and its composition, based on percentage by weight. A full description of the modelling approach and microstructure analysis of GRX-810 can be found in Methods. The phase diagram in Fig. 1b shows that, for a large segment of the NiCoCr compositional space, HCP is the most energetically stable phase at 0 K. However, due to the higher symmetry and entropy associated with the FCC phase, this is expected to be observed at elevated temperatures, as reported for decades in NiCoCr-based alloys[36,37,38,39]. Figure 2 provides the high-resolution microstructural characterization of untested hot isostatic pressurized (HIP) GRX-810 after the powder was coated and consolidated through AM as shown in Extended Data Figs. 1 and 2.

Fig. 1: Modelling of GRX-810 and the NiCoCr compositional space.

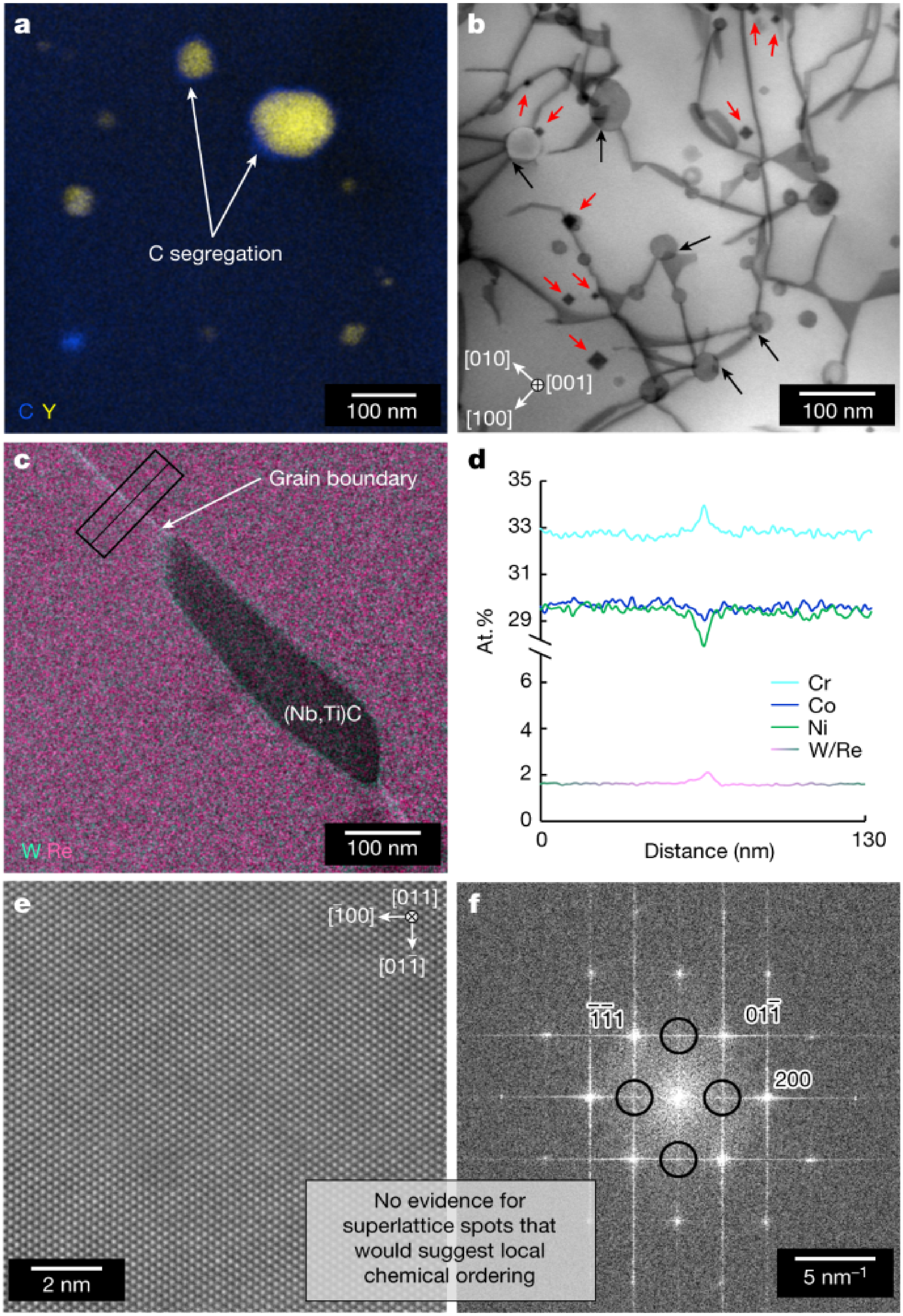


Alloy	Ni	Co	Cr	Re	Al	Ti	Nb	W	C
New composition (GRX-810)	Bal.	33	29	1.5	0.3	0.25	0.75	3.0	0.05

a, Predicted phase stability in GRX-810. **b**, Calculated NiCoCr ternary phase diagram at 0 K. **a**, The body-centred cubic (BCC) Cr-rich phase has lower energy than FCC or HCP above the red line; dashed blue line indicates *E*(HCP) = *E*(FCC) for metastable HCP and FCC, which are higher in energy than BCC. Solid blue line separates the lowest energy HCP Co-rich and FCC Ni-rich phases. Points are assessed from density functional theory (DFT) as shown in Extended Data Fig. 3. Values are at.%. Table shows nominal composition of GRX-810 (in wt%).

Source Data

Fig. 2: High-resolution characterization of GRX-810 microstructure.


a
C segregation
C Y
100 nm
b
[010]
[001]
[100]
100 nm
c
Grain boundary
(Nb,Ti)C
W Re
100 nm
d
35
33
31
29
6
4
2
0
At. %
0
Distance (nm)
130
Cr
Co
Ni
W/Re
e
[011]
[$\bar{1}$00]
[01$\bar{1}$]
2 nm
No evidence for superlattice spots that would suggest local chemical ordering
f
$\bar{1}\bar{1}$1
01$\bar{1}$
200
5 nm^{-1}

a, Scanning transmission electron microscopy–energy dispersive X-ray spectroscopy (STEM–EDS) combined Y and C map showing C segregation at the oxide–matrix interface. **b**, BF–STEM diffraction contrast image (DCI) micrograph (electron beam is parallel with [001] zone axis of matrix) of dislocation interaction with oxides (black arrows) and the presence of stacking-fault tetrahedra (red arrows). **c**, STEM–EDS combined W and Re map showing segregation at grain boundary and surrounding the carbide. **d**, Integrated line scans (at.%), from the rectangle outlined in **c**, showing segregation of Cr, W and Re and depletion of Co and Ni at the grain boundary. Elements not measuring any change across the boundary are not shown. **e**, Atomic resolution [011] zone axis HAADF–STEM image of GRX-810 lattice. **f**, Fast Fourier transformation of the image in **e** showing the absence of any additional superlattice spots. Both **d** and **e** suggest that local chemical ordering is not present.

Source Data

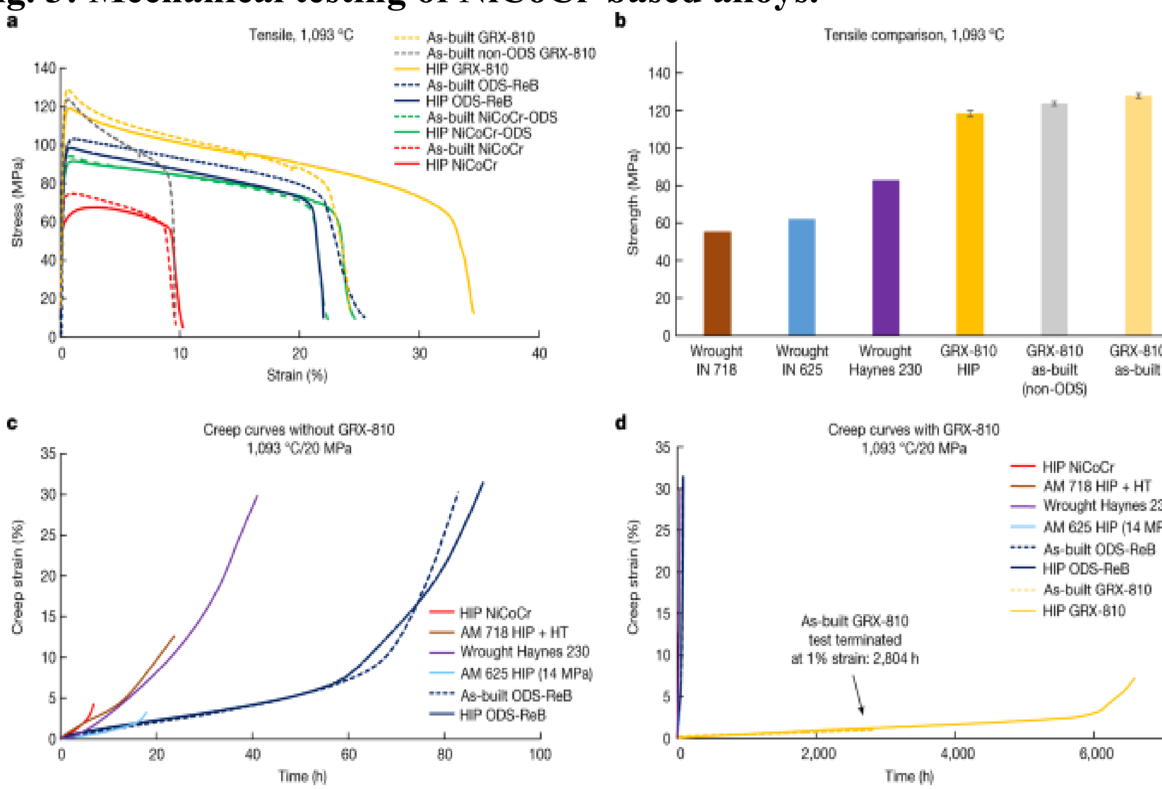
One notable observation in Fig. 2a is the presence of carbon segregation along some, but not all, oxide–matrix interfaces. The additional low-angle annular dark-field (LAADF)–STEM DCI analysis shown in Fig. 2b shows a representative defect microstructure. It consists of network of 1/2<110> dislocations mostly dissociated into observable intrinsic stacking faults bound by 1/6<112> Shockley partials. Dissociated dislocations mutually interact and form numerous extended stacking-fault node configurations. The density of these dissociated dislocations and grain structure of GRX-810 is better shown in the lower resolution microstructural characterization shown in Extended data Fig. 4. In addition, the presence of numerous stacking-fault tetrahedra and prevalent dislocation interaction with oxides is observed. Stacking-fault tetrahedra have been found to further inhibit dislocation motion and may further improve the creep and tensile properties of this alloy[40]. Figure 2c,d shows solute segregation of Cr, W and Re at the grain boundary, with Ni and Co depleted. The EDS map in Fig. 2c also shows the presence of Nb/Ti-rich metal carbides predicted by the thermodynamic models to be stable up to alloy melting temperature. This analysis was further validated through SEM as shown in Extended Data Fig. 5. High-resolution high-angle annular dark-field (HAADF)–STEM analysis of the GRX-810 lattice was performed to explore whether local chemical ordering exists in this alloy, as has been found in other high-entropy

alloys[41,42]. The analysis in Fig. 2e,f shows that, despite possessing $L1_2$-forming elements such as Al, Ti and Nb, the lattice maintained a perfect solid solution with no short-range elemental ordering present[43].

Mechanical properties of GRX-810

Five different MPEA alloys (NiCoCr, NiCoCr-ODS, ODS-ReB, GRX-810 and non-ODS GRX-810) under both as-built and HIP conditions were tensile and/or creep tested at 1,093 °C to compare their overall high-temperature mechanical properties. Tests were also performed on AM 718, AM 625 and wrought Haynes 230 for comparison with conventional wrought superalloys used extensively in AM. Figure 3 shows the tensile and 20 MPa creep performance of these alloys at 1,093 °C.

Fig. 3: Mechanical testing of NiCoCr-based alloys.



a, Engineering stress–strain curves at 1,093 °C for as-built and HIP alloys. **b**, Comparison of ultimate tensile strength between different alloys. Wrought 718 and 625 strengths were provided by the literature.[44] **c**, 1,093 °C creep curves for as-built and HIP NiCoCr, NiCoCr-ODS and ODS-ReB at 20 MPa.

d, The same tests with GRX-810 curves included. Additional tests of AM 718, 625 and H230 are shown at 20 MPa for a better comparison with conventional high-temperature superalloys. Error bars correspond to 1 s.d.

Source Data

Figure 3a shows the elevated-temperature tensile tests (1,093 °C) that highlight the strength and elongation differences of the five alloys tested. The non-ODS NiCoCr sample was found to have lower strength and ductility than the NiCoCr-ODS sample. In fact, by simply incorporating Y_2O_3 particles the strength of NiCoCr was increased and ductility improved twofold. This highlights the strengthening effect provided by these oxides at elevated temperatures. The minor additions of Re and B to NiCoCr-ODS appear to have improved the strength of the alloy marginally. Notably, GRX-810 showed higher strength and ductility when compared with the other ODS alloys; indeed, compared with NiCoCr (where this study began[33]), GRX-810 provided twice the strength and over three times the ductility, making it a much more robust high-temperature alloy. One surprising result is the strength of non-ODS GRX-810, which appears to be comparable to that of as-built GRX-810 although it has limited ductility (comparable to the non-ODS NiCoCr alloy). This finding suggests that the improvement in strength is due to base composition, whereas the oxides are the source of improved ductility. Additional alloys are compared in Fig. 3b, showing the strength of GRX-810 and non-ODS GRX-810 compared with the wrought Haynes 230 tested in this study (Supplementary Fig. 1), and compared with wrought 625 and 718 from the literature[44]. Extended Data Fig. 6a,b shows the as-built room temperature tensile tests. These curves present little difference in regard to strength and elongation between the different alloys, although GRX-810 did provide slightly higher tensile strength compared with the three other alloys. The HIP room temperature tests provide some variation in strength, because the ODS alloys were able to retain higher strength after this processing step. This is most probably attributed to the finer grain structure maintained in the ODS alloys compared with the larger grain growth and more equi-axed grain structure in the non-ODS NiCoCr sample[45]. Notably, the transverse (*x*–*y*) GRX-810 sample provided significantly higher strength compared with those tested in the vertical (*z*) direction, a typical result found with L-PBF materials[46]. This finding

highlights the anisotropy present in the AM samples that can not be recrystallized through conventional means such as a HIP step, but also suggests that print direction provides less strength than other orientations for these ODS materials. Lastly, Extended Data Table 1 shows the tensile properties of as-built and HIP GRX-810 at varying temperatures. Two notable observations are shown in this table. First, as-built GRX-810 consistently offers higher strength compared with HIP GRX-810; and second, GRX-810 provides unexpected cryogenic tensile properties (as-built GRX-810 provides 1.3 GPa of tensile strength), showing that nanoscale oxides are not detrimental to alloy strength at these low temperatures. These high cryogenic strengths have been noted in NiCoCr in past studies, and are suggested to be due to a FCC-to-HCP phase transformation[13,20,23]. The data in Extended Data Table 1 also show that GRX-810 remains ductile from cryogenic to elevated (1,093 °C) temperature.

Creep tests were also performed at 1,093 °C to compare the properties of these alloys, and are shown in Fig. 3c,d. Figure 3c,d also shows the impact of the combination of the oxide-strengthening and model-driven composition of GRX-810 for high-temperature creep strength. At 1,093 °C and 20 MPa, HIP GRX-810 ruptured after 6,500 h of creep whereas the as-built test was terminated at 1% strain (over 2,800 h). All other non-ODS alloys considered, namely NiCoCr, AM superalloy 718, AM superalloy 625 (at 14MPa) and wrought Haynes 230, ruptured in under 40 h. The orders of magnitude improvement in creep performance by GRX-810 is also shown in Table 1, with time to reach 1% strain at 1,093 °C under 20 MPa of stress for each alloy[5,47,48,49].

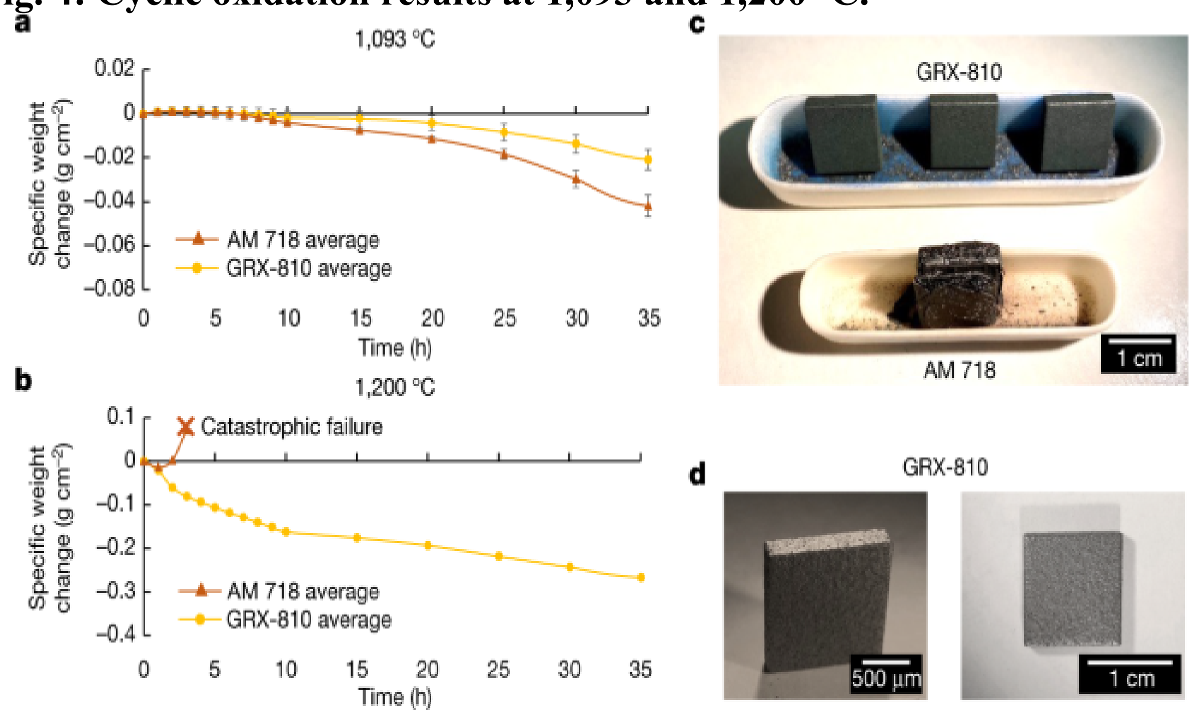
Table 1 Time to reach 1% creep strain for GRX-810

From Table 1 it can be seen that as-built GRX-810 required more than 500-fold longer to reach 1% strain compared with wrought Haynes 230, and over 1,000-fold longer compared with AM superalloy 718. Also, as observed from the tensile results, as-built GRX-810 exhibited better high-temperature properties compared with HIP GRX-810. GRX-810 even provided better creep strength in this regime compared with wrought Nb-based alloy C-103 tested in a high-vacuum environment[50]. At the higher 31 MPa stress level shown in Extended Data Fig. 6c,d, as-built GRX-810 lasted for almost

2,500 h compared with NiCoCr, which lasted just over 1 h—an almost 2,000-fold improvement in life span.

One explanation for the improved tensile and creep properties of GRX-810 may be the improvement observed in oxidation resistance compared with Superalloy 718. In Fig. 4, the results from cyclic oxidation tests conducted on GRX-810 and Superalloy 718 are shown up to 35 h at 1,100 and 1,200 °C. During exposure at 1,093 °C, the weight loss observed for each alloy was attributed to oxide spallation on air quenching from the test temperature. Nevertheless, the results shown here indicate that GRX-810 has oxidative durability superior to AM superalloy 718 at 1,093 °C, and significantly better at 1,200 °C, in which AM superalloy 718 offered little to no life. More complete oxidation analysis is provided in Extended Data Fig. 7.

Fig. 4: Cyclic oxidation results at 1,093 and 1,200 °C.



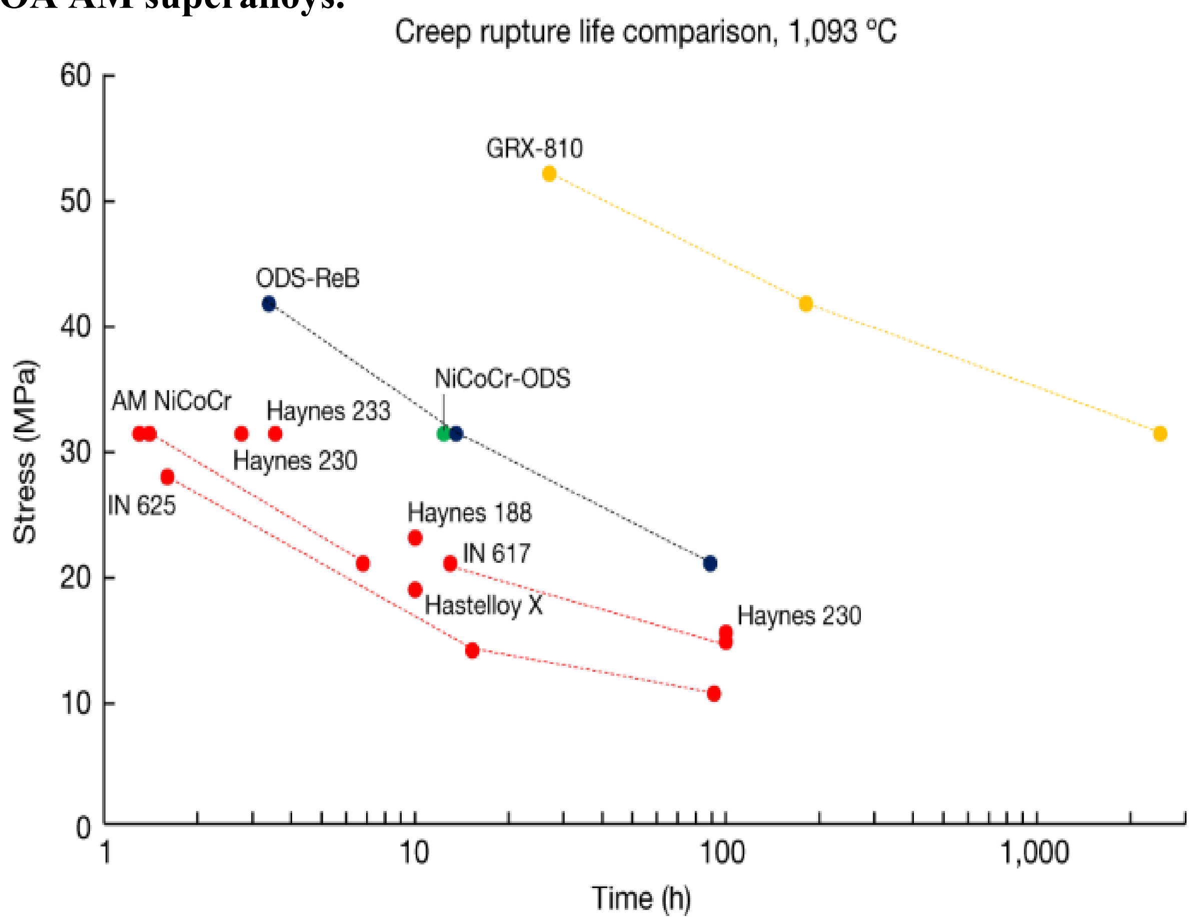
a,**b**, Cyclic oxidation results for GRX-810 and superalloy 718 at 1,093 °C (**a**) and 1,200 °C (**b**) for up to 35 h. **c**, Optical images of oxidation samples after 100 h at 1,093 °C and 3 h at 1,200 °C, at which the superalloy 718 sample presented catastrophic oxidation. The three samples above are all GRX-810. **d**, GRX-810 samples after thermal cycling for 100 h at 1,093 and 1,200 °C. Error bars represent 1 s.d.

Source Data

Comparison with current SOA AM alloys

Figure 3 and Extended Data Fig. 6 show that GRX-810 exhibits markedly improved creep rupture properties over baseline NiCoCr and NiCoCr-ODS alloys. Furthermore, compared with current state-of-the-art (SOA) AM high-temperature alloys (superalloy 718, superalloy 625 and Haynes 230), GRX-810 can provide orders of magnitude better creep life at 1,093 °C. To further illustrate this improvement, the 1,093 °C creep rupture lives of these alloys and other commercially available superalloys are plotted together in Fig. 5 (refs. [44,51,52,53,54,55]).

Fig. 5: Creep rupture life of as-built GRX-810 compared with current SOA AM superalloys.



Scatter plot of superalloy creep rupture life at 1,093 °C. GRX-810 presents superior creep properties compared with wrought alloys currently used in 3D printed high-temperature applications.

The plot in Fig. 5 compares the high-temperature properties of both NiCoCr-ODS (green) and NiCoCr with Re and B additions (ODS-ReB) (blue), GRX-810 (gold) and conventional wrought superalloys used commonly in AM (red). In Fig. 3, although GRX-810 clearly shows improvement in tensile strength, its creep performance is even more pronounced and notable. Additional creep tests were performed, and results can be found in Extended Data Fig. 8. It is evident that the addition of nanoscale oxide dispersoids provided sufficient strength in the matrix to avoid dislocation motion (Supplementary Fig. 2), thereby leading to improvement in both mechanical and oxidation properties. However, STEM analysis of ODS-ReB and GRX-810 did not show any significant differences in oxide size or spatial distributions that could explain the differences in creep performance between the two alloys. Therefore, to better explain the creep strength of GRX-810, longitudinal sections taken from two 1,093 °C air creep tests at 20 MPa were analysed, as shown in Extended Data Fig. 9. Whereas other ODS alloys (for example, ODS-ReB) failed through a combination of grain boundary creep void coalescence and shear failure, GRX-810 appears to have suppressed these failure mechanisms because no apparent grain boundary voids/defects were observed after much longer test times. One contributory factor is that non-ODS GRX-810 has higher strength than even previous ODS alloys, and thus creep stress is a lower fraction of the alloy's yield stress. Nevertheless, the grain boundary failure modes in other ODS alloys suggest that in GRX-810 the stable MC carbides and solute segregation of W, Cr and Re along grain boundaries are factors contributing significantly to the protection of the alloy from grain boundary failure mechanisms. Previous studies have suggested that carbide stability at high temperature will influence grain boundary crack initiation during creep[56]. In addition, grain boundary diffusivity was reported to be correlated to the rate of void formation during creep[57,58]. Therefore, the addition of W and Re (known slow diffusors) should further inhibit creep void formation along grain boundaries whereas Cr segregation is expected to improve grain boundary corrosion and oxidation properties[59]. Stress-induced nitride formation was also observed in both the ODS-ReB (Cr-rich nitrides) and

GRX-810 (Al- and Cr-rich nitrides) alloys. Whereas the formation of these internal nitrides is considered detrimental to both alloys' properties[60], the nitrides in GRX-810 did not appear to contribute to grain boundary failure as observed in the ODS-ReB alloy.

In conclusion we present the design, characterization and properties of a new NiCoCr-based ODS alloy, GRX-810, which provides superior performance in extreme environments compared with current AM alloys. The use of computational modelling in alloy design led to a composition that balances properties and processability, with advanced characterization giving insights into the underlying microstructure and mechanisms. Creep performance of GRX-810 at 1,093 °C showed orders of magnitude improvement compared with currently used high-temperature alloys, thereby enabling the use of AM for complex components in extreme environments.

Methods

Materials

Three batches of pre-alloyed, gas-atomized powder feedstock (compositions given in Supplementary Table 1) were purchased from Praxair, Inc. The powders were sieved using +270 and −325 mesh (10–53 µm) to acquire an average particle diameter of around 15 µm as determined using a Horiba PSA300 Static Image Analysis System. The dispersoid used in the AM process was nanoscale Y_2O_3 powder (diameter 100–200 nm; American Elements). The powder was certified 99.999% pure yttrium oxide. These dispersoids were subsequently coated onto the base alloy powder using a high-energy acoustic mixer. Examples of powder morphology pre- and postmixed (coated), using the method described in ref. [33], are shown in Extended Data Fig. 1. Postmixed powder was then sieved using a 230 mesh screen to remove any large oxide or metallic powder particles. Unmixed powder (NiCoCr), mixed NiCoCr (NiCoCr-ODS) powder, NiCoCr-ReB (ODS-ReB), mixed GRX-810 and unmixed GRX-810 (non-ODS) samples were built using powder bed fusion to produce microstructural and mechanical test components on an EOS M100 L-PBF machine (40 µm beam diameter). For GRX-810 builds on the EOS M280, optimal densities were

achieved with a laser energy density of 90–110 J mm^{-3}. Vertical test specimens (height 55.0 mm, diameter 6.35 mm) were built on 304 stainless steel build plates. All samples were then removed from the build plates using electrical discharge machining. Supplementary Table 1 provides a list of each alloy and its corresponding composition.

Mechanical testing

After removal of test coupons from their respective build plates, selected specimens underwent a HIP cycle at 1,185 °C while wrapped in Ta foil to mitigate oxidation. The HIP cycle also had the benefit of removal of residual stresses. This provides a better comparison between ODS and non-ODS samples because residual stress has been shown to convolute structure–property relationships[61]. Both as-built and HIP specimens of each alloy type were tensile tested at room and elevated temperature using a cylindrical specimen with a 3.175-mm-diameter-gauge section. Cryogenic tensile testing at liquid N temperature (−196 °C) was also performed on GRX-810 samples. Testing was performed at Metcut Research, Inc. Tensile tests were performed at room temperature, at 0.127 mm min^{-1} for the first 1.5% strain followed by an increase to 1.016 mm s^{-1} until failure in accordance with the ASTM E8/E8M-21 standard, and at 1,093 °C at a constant strain rate of 1.016 mm min^{-1} in accordance with the ASTM E21-17 standard. Following tensile tests, creep tests were performed at 1,093 °C by Metcut in accordance with the ASTM E139-11 standard. Testing of creep samples was continued until rupture (unless otherwise stated), after which they were then rapidly air cooled to maintain the fracture surface. All specimens were tested in the print direction unless otherwise specified in the description.

Oxidation testing

Samples of AM 718 and the GRX-810 alloy were cut into samples of nominal size 12.5 × 12.5 × 3.5 mm^3, which provided a total surface area of around 487.5 mm^2. Surfaces were polished to a smooth finish with 1 μm diamond paste. Samples were oxidized in a laboratory airbox furnace at 1,093 °C for progressively longer dwell times. Exposure started at 1 h intervals for the first 10 h then at 5 h intervals for the next 25 h, followed by a 25 h duration and finally a 40 h duration for a total of 100 h at that

temperature. Sample weights were measured after each interval for a total of 18 data points for each sample over the entire thermal exposure. After samples had reached the conclusion of the 100 h test at 1,093 °C, half underwent a second oxidation heat treatment at 1,200 °C for the same time period and intervals as the 1,093 °C test.

At 1,093 °C, the AM superalloy 718 and GRX-810 both underwent similar mass gain over the first few hours, indicating oxidation. However, both samples had exhibited mass loss by 7 h, which was accompanied by a spallation of oxide during each subsequent air quench to room temperature by removal from the box furnace. Specific weight change appeared to be linear in both AM superalloy 718 and GRX-810 from 5 to 10 h, with the rate of loss in the former roughly twice that of the latter. From 10–40 h, 5 h intervals were implemented and specific weight change per hour slowed, supporting the observation of oxide spallation during air quench to room temperature. The rate of loss in specific weight for AM superalloy 718 was again roughly twice that of GRX-810. Over the 25 and 40 h cycles shown in Extended Data Fig. 7, specific weight change rate slowed further and both alloys underwent equivalent weight change after air quenching to room temperature. A more significant level of spallation was observed at these longer intervals (as indicated by the larger drop in specific weight), but specific weight change per hour was lower than for the 1 and 5 h intervals.

After the 1,093 °C tests, half of the samples were removed and the remainder underwent additional progressive oxidation exposure at 1,200 °C following the same approach. In the case of AM superalloy 718, the sample lasted for only three 1 h cycles before undergoing catastrophic oxidation and complete disintegration and thus testing was ended. Runaway oxidation in the AM superalloy:718 sample can be seen in Fig. 4c, with significant weight gain observed after 1 h. The GRX-810 alloy exhibited similar behaviour to that at 1,093 °C exposure, although the specific weight change rate was around 40-fold more rapid over the 1 h heat treatment cycle. Over the 5, 25 and 40 h cycles, specific weight was only three- to fourfold more rapid than that at 1,093 °C over the same time intervals.

Microstructural characterization

For SEM analysis, samples were polished using SiC grit paper followed by 0.5 µm diamond suspension. Afterwards, a final polish using 50 nm colloidal silica for 24 h was employed on samples used for electron backscatter diffraction (EBSD) analysis. EBSD orientation mapping was performed using an EDAX Hikari EBSD detector with 800 nm spot size. Postprocessing of maps was completed using TSL OIM Data Collection 7 software. High-resolution SEM imaging of the Y_2O_3 coating on NiCoCr powder was performed using a Tescan MAIA3 in ultrahigh-resolution configuration at 15 kV. Chemical maps were obtained with an Oxford Ultim Max Silicon Drift Detector and Aztec Software, and were used to determine phases in postcrept samples. STEM disc samples (diameter 3 mm) were extracted from metallographic samples of GRX-810 and ODS-ReB. STEM samples were thinned manually to 130 µm using 600 grit SiC polishing paper. To achieve electron transparency, polished STEM discs were electropolished with a solution of 90% methanol and 10% perchloric acid at −40 °C and 12 V using a Struers twin-jet polisher. Microstructural analysis was performed on an FEI Talos at 200 kV using a HAADF detector. Defect analysis was performed using S-CORR probe aberration-corrected and monochromated Thermo Fisher Scientific Themis-Z STEM at an acceleration voltage of 300 kV. STEM diffraction contrast imaging was performed with BF and HAADF detectors by selection of the appropriate camera length. Atomic resolution of the microstructure was performed by tilting of the thin disc foils into specific low-index crystallographic zones. High-resolution EDS data were collected by a Super-X energy dispersive X-ray spectroscopy detector in Themis-Z. Data were collected and processed using Thermo Fisher Scientific Velox software. In particular, raw data in the original spectral maps were quantified using standard Cliff–Lorimer (k-factor) fit (default k-factors available in Velox were used, as well as the Brown–Powell empirical ionization cross-section model) including background subtraction. STEM micrographs were corrected for potential sample drift and scanning beam distortions using the drift-corrected frame integration function of Velox.

The Archimedes method with deionized water as the immersion fluid was used to determine the density of the additively manufactured GRX-810 material. Specimens with surface-breaching networks of cracks and porosity allow water infiltration that can be observed as bubbling during submersion;

no bubbling was observed during submersion of GRX-810. Measurements of a part's mass in air (M_a) and in water (M_w) were taken on a Mettler Toledo XS205 system. Density of the AM part was calculated by

$$p=\left(\frac{{M}_{{\rm{a}}}}{({M}_{{\rm{a}}}-{M}_{{\rm{w}}})}\right)\times \left({p}_{{\rm{w}}}-{p}_{0}\right)+{p}_{0}$$
(1)

where p_w is the temperature-dependent density of water and p_0 is air density. The reported density value is an average of three independent measurements.

Powder feedstock (15–45 µm) of the optimized composition shown in Fig. 1 was obtained, coated with Y_2O_3 nanoparticles and built with L-PBF using the steps detailed above. Successful production of GRX-810 using AM L-PBF allowed for the characterization of GRX-810 in both as-built and post-HIP states. Extended Data Fig. 2 shows the high density (over 99.97%) that can be achieved with optimized print parameters for GRX-810 based on optical microscopy analysis. Relative density measurements further confirmed this value, showing 99.96% density value for the same sample. From the SEM analysis shown in Extended Data Fig. 5, the major difference in microstructure between as-built and HIP GRX-810 samples is the presence of fine MC carbides along grain boundaries after the HIP processing step. These grain boundary phases were confirmed as Ti/Nb-rich carbides through both SEM and TEM EDS, for which the results of the former can be found in Supplementary Fig. 3. No other phases were present in either material state, validating the accuracy of thermodynamic calculations in prediction of stable microstructures in the compositional space. The intragranular dark contrast 'dot-like' features observed in Extended Data Fig. 5b are Y_2O_3 particles sufficiently large to be observed by SEM using secondary electron imaging mode. The lack of bulk oxide formation provides further evidence that the coated GRX-810 powder can be successfully printed using L-PBF to form an optimized oxide dispersion-strengthened alloy.

From Extended Data Fig. 4a, little to no variations in grain structure and average grain diameter between as-built and HIP conditions were observed in GRX-810. This finding suggests that the distribution of fine oxides sufficiently suppresses dislocation and grain boundary movement at high temperatures. The grain texture usually associated with AM melting processes is apparent between the *x*–*y* and *x*–*z* planes[23,46]. Extended Data Fig. 4b illustrates LAADF–STEM DCI showing defect configurations and corresponding EDS chemical maps. The yttrium map confirms the presence of Y_2O_3 particles evenly distributed throughout the GRX-810 matrix. In fact, this distribution of oxides appears to have pinned the dislocations produced during the L-PBF build step as a high-dislocation density that can be observed in the LAADF–STEM DCI micrograph. The Cr and Ni maps represent chemical maps of the other elements, showing no local segregation or ordering at 500 nm length scale.

Modelling of the next-generation MPEA

Thermodynamic modelling (CALPHAD) was employed to produce a superior composition using equi-atomic NiCoCr as a foundation[62,63]. Simulations were completed adding specific elements (for example, B, C, Al, Ti, V, Mn, Fe, Zr, Nb, Mo, Hf, Ta, W and Re) to an equi-atomic composition of NiCoCr. Therefore, as new elements were included in the simulation, the atomic percentages of Ni, Co and Cr remained equal. Thresholds were used to better constrain the models and guide optimization. The thresholds included (1) maximized solid solution strengthening; (2) the FCC solid-solution matrix should be maintained; for this constraint it was assumed that any undesired phases stable above 810 °C would not be acceptable; (3) enabling of MC carbide formation along grain boundaries stable above 1,200 °C; and (4) the temperature difference associated with a composition solidification temperature range (STR) must remain below 100 °C for AM printability. This reduction in STR has been used by welding engineers to predict an alloy's susceptibility to solidification cracking, dendritic segregation (which requires remedial postprocessing), residual stress and hot cracking[33,64]. These constraints allowed the alloy compositional space to be manageable and reduced the number of overall simulations, thereby leading to the optimized composition and predicted equilibrium phases shown in Fig. 1a. Simulations were performed using

Thermo-Calc v.2020b with the Ni alloy database TCNI8. Upwards of 10^7 equilibrium calculations were performed across composition and temperature space. Y and O were not considered in the composition search, because the Y_2O_3 phase is expected to be inert and is not well described in the TCNI8 database[62]. The Y_2O_3 line shown in Fig. 1 is approximate and is included here for visual clarity.

To better understand the phase stability and properties of the NiCoCr compositional space, a full overview using DFT calculations was performed[65]. Extended Data Fig. 3 shows the computed electronic spin density of states of the FCC (A1), BCC (A2) and HCP (A3) phases of the equi-atomic NiCoCr alloy system. Interestingly, from Extended Data Fig. 3, the formation energy of equi-atomic NiCoCr (relative to elemental solids) is positive. At this composition, energies of the FCC and HCP phases are quite comparable, suggesting there is a crossover from the HCP to FCC ground state nearby. Both FCC and HCP phases are close packed and the computed equilibrium volumes per atom for FCC and HCP at any composition are rather close, with the equilibrium volume of BCC differing significantly. In the close-packed phase (such as FCC), the stacking-fault energy increases with the absolute value of the energy difference E(HCP) – E(FCC). Creep properties are influenced by stacking-fault energy, which depends on composition. For future guidance on NiCoCr-based alloy development, the results from Extended Data Fig. 3 are organized into a predicted ternary phase diagram at 0 K in Fig. 1b. Although this phase diagram may not represent stable phases at high temperatures due to entropy, these calculations have important implications in the properties of the NiCoCr system at cryogenic temperatures. Recent papers have found excellent mechanical properties for NiCoCr-based medium-entropy alloys at these low temperatures in which the phase transformation from FCC to HCP during deformation is the principal contributing factor[23,66]. Therefore, these low-temperature properties may be further improved by moving the composition of NiCoCr into the more stable HCP phase regime while maintaining an FCC phase. Future work is planned to explore this possibility.

DFT calculations

For this study, the all-electron DFT KKR-coherent potential approximation (CPA) Green's function code[67] was employed to calculate energies of disordered structures. Within the KKR method[68,69], atomic sphere approximation[70] was used with periodic boundary corrections[71]. The basis of atomic orbitals within the atomic sphere approximation spheres included *s*, *p*, *d* and *f* orbitals ($l_{max} = 3$). In addition, the PBEsol GGA-type exchange correlation functional[72] was used. Self-consistency was achieved using a modified Broyden's second method[73]. Integration in a complex energy plane was performed using the Chebyshev quadrature semicircular contour with 20 points. Homogeneous atomic disorder was addressed by CPA[65]. Crystal structures considered included A1 (FCC), A2 (BCC) and A3 (HCP). The ideal $c/a = (8/3)^{1/2} = 1.632993$ was chosen for the HCP phase. A special k-point mesh[74] for Brillouin zone integration included 18^3 k-points for FCC and BCC one-atom primitive cells and $16 \times 16 \times 8$ for the HCP two-atom unit cell; an auxiliary secondary 12^3 mesh was used for FCC and BCC and $10 \times 10 \times 6$ for HCP in KKR-CPA code[67].

Data availability

The experimental data that support the findings of this study are available from the corresponding author on reasonable request. Source data are provided with this paper.

References

1. Cantor, B., Chang, I. T. H., Knight, P. & Vincent, A. J. B. Microstructural development in equiatomic multicomponent alloys. *Mater. Sci. Eng. A* **375–377**, 213–218 (2004).

2. Miracle, D. B. & Senkov, O. N. A critical review of high entropy alloys and related concepts. *Acta Mater.* **122**, 448–511 (2017).

3. Chen, P., Yang, C., Li, S., Attallah, M. M. & Yan, M. In-situ alloyed, oxide-dispersion-strengthened CoCrFeMnNi high entropy alloy fabricated via laser powder bed fusion. *Mater. Des.* **194**, 108966 (2020).

4. Hadraba, H. et al. Oxide dispersion strengthened CoCrFeNiMn high-entropy alloy. *Mater. Sci. Eng. A* **689**, 252–256 (2017).

5. Amato, K. et al. Microstructure and mechanical behavior of Inconel 718 fabricated by selective laser melting. *Act Mater.* **60**, 2229–2239 (2012).

6. Blakey-Milner, B. et al. Metal additive manufacturing in aerospace: a review. *Mater. Des.* **209**, 110008 (2021).

7. Gali, A. & George, E. P. Tensile properties of high- and medium-entropy alloys. *Intermetallics* **39**, 74–78 (2013).

8. Miracle, D. B. et al. Exploration and development of high entropy alloys for structural applications. *Entropy* **16**, 494–525 (2014).

9. Miracle, D. B. High entropy alloys as a bold step forward in alloy development. *Nat. Commun.* **10**, 1805 (2019).

10. Wu, Z., Bei, H., Pharr, G. M. & George, E. P. Temperature dependence of the mechanical properties of equiatomic solid solution alloys with face-centered cubic crystal structures. *Acta Mater.* **81**, 428–441 (2014).

11. Senkov, O. N., Wilks, G. B., Scott, J. M. & Miracle, D. B. Mechanical properties of Nb25Mo25Ta25W25 and V20Nb20Mo20Ta20W20 refractory high entropy alloys. *Intermetallics* **19**, 698–706 (2011).

12. Zaddach, A. J., Niu, C., Koch, C. C. & Irving, D. L. Mechanical properties and stacking fault energies of NiFeCrCoMn high-entropy alloy. *JOM* **65**, 1780–1789 (2013).

13. Gludovatz, B. et al. A fracture-resistant high-entropy alloy for cryogenic applications. *Science* **345**, 1153–1158 (2014).

14. Coury, F. G., Zepon, G. & Bolfarini, C. Multi-principal element alloys from the CrCoNi family: outlook and perspectives. *J. Mater. Res. Technol.* **15**, 3461–3480 (2021).

15. Jin, K., Gao, Y. F. & Bei, H. Intrinsic properties and strengthening mechanism of monocrystalline Ni-containing ternary concentrated solid solutions. *Mater. Sci. Eng. A* **695**, 74–79 (2017).

16. Miao, J. et al. The evolution of the deformation substructure in a Ni-Co-Cr equiatomic solid solution alloy. *Acta Mater.* **132**, 35–48 (2017).

17. Slone, C. E., Miao, J., George, E. P. & Mills, M. J. Achieving ultra-high strength and ductility in equiatomic CrCoNi with partially recrystallized microstructures. *Acta Mater.* **165**, 496–507 (2019).

18. Slone, C. E. et al. Influence of deformation induced nanoscale twinning and FCC-HCP transformation on hardening and texture development in medium-entropy CrCoNi alloy. *Acta Mater.* **158**, 38–52 (2018).

19. Smith, T. M. et al. Atomic-scale characterization and modeling of 60 dislocations in a high-entropy alloy. *Acta Mater.* **110**, 352–363 (2016).

20. Niu, C., LaRosa, C. R., Miao, J., Mills, M. J. & Ghazisaeidi, M. Magnetically-driven phase transformation strengthening in high entropy alloys. *Nat. Commun.* **9**, 1363 (2018).

21. Luo, H., Li, Z. & Raabe, D. Hydrogen enhances strength and ductility of an equiatomic high-entropy alloy. *Sci. Rep.* **7**, 9892 (2017).

22. Granberg, F. et al. Mechanism of radiation damage reduction in equiatomic multicomponent single phase alloys. *Phys. Rev. Lett.* **116**, 135504 (2016).

23. Gludovatz, B. et al. Exceptional damage-tolerance of a medium-entropy alloy CrCoNi at cryogenic temperatures. *Nat. Commun.* **7**, 10602 (2016).

24. Laplanche, G. et al. Reasons for the superior mechanical properties of medium-entropy CrCoNi compared to high-entropy CrMnFeCoNi. *Acta Mater.* **128**, 292–303 (2017).

25. Seol, J. B. et al. Boron doped ultrastrong and ductile high-entropy alloys. *Acta Mater.* **151**, 366–376 (2018).

26. Zhou, R. et al. Microstructures and mechanical properties of C-containing FeCoCrNi high-entropy alloy fabricated by selective laser melting. *Intermetallics* **94**, 165–171 (2018).

27. Huang, T. et al. Effect of carbon addition on the microstructure and mechanical properties of CoCrFeNi high entropy alloy. *Sci. China Technol. Sci.* **61**, 117–123 (2018).

28. Wu, Z., Parish, C. M. & Bei, H. Nano-twin mediated plasticity in carbon-containing FeNiCoCrMn high entropy alloys. *J. Alloys Compd.* **647**, 815–822 (2015).

29. Wu, Z. et al. Enhanced strength and ductility of a tungsten-doped CoCrNi medium-entropy alloy. *J. Mater. Res.* **33**, 3301–3309 (2018).

30. Lu, C. et al. High radiation tolerance of an ultrastrong nanostructured NiCoCr alloy with stable dispersed nanooxides and fine grain structure. *J. Nucl. Mater*. **557**, 153316 (2021).

31. Li, M., Guo, Y., Li, W., Zhang, Y. & Chang, Y. Property enhancement of CoCrNi medium-entropy alloy by introducing nano-scale features. *Mater. Sci. Eng. A* **817**, 141368 (2021).

32. Martin, J. H. et al. 3D printing of high-strength aluminium alloys. *Nature* **549**, 365–369 (2017).

33. Smith, T. M., Thompson, A. C., Gabb, T. P., Bowman, C. L. & Kantzos, C. A. Efficient production of a high-performance dispersion element alloy. *Sci. Rep*. **10**, 9663 (2020).

34. GaoLe, Z., XiaoAn, H., Jia, H., JinWu, W. & Yun, W. High-temperature mechanical properties of nickel-based superalloys manufactured by additive manufacturing. *Mater. Sci. Technol.* **36**, 1523–1533 (2020).

35. Schneider, J., Lund, B. & Fullen, M. Effect of heat treatment variations on the mechanical properties of Inconel 718 selective laser melted specimens. *Addit. Manuf.* **21**, 248–254 (2018).

36. Sims, C. T. A history of superalloy metallurgy for superalloy metallurgists. *Superalloys* https://doi.org/10.7449/1984/Superalloys_1984_399_419 (1984).

37. Sabol, G. P. & Stickler, R. Microstructure of nickel-based superalloys. *Phys. Status Solidi B Basic Solid State Phys*. **35**, 11–52 (1969).

38. Jena, A. K. & Chaturvedi, M. C. The role of alloying elements in the design of nickel-base superalloys. *J. Mater. Sci.* **19**, 3121–3139 (1984).

39. Reed, R. *The Superalloys* (Cambridge Univ. Press, 2006).

40. Wirth, B. D., Bulatov, V. V. & Diaz de la Rubia, T. Dislocation-stacking fault tetrahedron interactions in Cu. *J. Eng. Mater. Technol.* **124**, 329–334 (2002).

41. Zhang, R. et al. Short-range order and its impact on the CrCoNi medium-entropy alloy. *Nature* **581**, 283–287 (2020).

42. Walsh, F., Asta, M. & Ritchie, R. O. Magnetically driven short-range order as an explanation for anomalous measurements in CrCoNi. *Proc. Natl Acad. Sci. USA* **118**, e2020540118 (2020).

43. Miao, J. et al. Ordering effects on deformation substructures and strain hardening behavior of a CrCoNi based medium entropy alloy. *Acta Mater.* **210**, 116829 (2021).

44. The International Nickel Company. in *High Temperature, High Strength Nickel Base Alloys* 1–19 (Nickel Development Institute, 1995).

45. Dunstan, D. J. & Bushby, A. J. Grain size dependence of the strength of metals: the Hall-Petch effect does not scale as the inverse square root of grain size. *Int. J. Plast.* **53**, 56–65 (2014).

46. Gradl, P. R., Mireles, O. R., Protz, C. S. & Garcia, C. P. *Metal Additive Manufacturing for Propulsion Applications* (American Institute of Aeronautics and Astronautics, 2022).

47. Sudbrack, C. K. et al. Impact of powder variability on the microstructure and mechanical behavior of selective laser melted alloy 718. *Miner. Met. Mater. Ser.* **2018-June**, 89–113 (2018).

48. Gradl, P. R. & Protz, C. S. Technology advancements for channel wall nozzle manufacturing in liquid rocket engines. *Acta Astronaut*. **174**, 148–158 (2020).

49. Gradl, P. et al. Robust metal additive manufacturing process selection and development for aerospace components. *J. Mater. Eng. Perform.* **31**, 6013–6044 (2022).

50. Titran, R. H. & Klopp, W. D. Long-time creep behavior of the niobium alloy C-103. *NASA Tech. Pap.* **1727**, 1–9 (1980).

51. Davis, J. R. *Heat-Resistant Materials* (ASM Int., 1999).

52. Moon, J.-H., Yoon, M.-G. & Ha, T. K. Microstructure and high temperature deformation behavior of cast 310S alloy. *Int. J. Ind. Manuf. Eng.* **8**, 533–536 (2014).

53. Korb, G., Ruhle, M. & Martinz, H.-P. New iron-based ODS-superalloys for high demanding applications. *Am. Soc. Mech. Eng.* **91**, 1–8 (1991).

54. Special Metals. *Product Handbook of High-Performance Nickel Alloys* 1–43 (https://www.specialmetals.com/documents/nickel-alloy-handbook.pdf; 2019).

55. Millan, P. P. & Mays, J. C. Oxide-dispersion-strengthened turbine blades (MA6000). *NASA Contract. Rep*. (1986).

56. Yang, J., Zheng, Q., Sun, X., Guan, H. & Hu, Z. Relative stability of carbides and their effects on the properties of K465 superalloy. *Mater. Sci. Eng. A* **429**, 341–347 (2006).

57. Garosshen, T. J., Tillman, T. D. & Mccarthy, G. P. Effects of B, C, and Zr on the structure and properties of a PM nickel base superalloy. *Metall. Trans. A* **18**, 69–77 (1987).

58. Kontis, P. et al. On the effect of boron on grain boundary character in a new polycrystalline superalloy. *Acta Mater.* **103**, 688–699 (2016).

59. Joshi, A. & Stein, D. F. Chemistry of grain boundaries and its relation to intergranular corrosion of austenitic stainless steel. *Corrosion* **28**, 321–330 (1972).

60. Wang, Y. et al. Internal nitridation during creep of IN617 superalloy. *Corros. Sci.* **209**, 110763 (2022).

61. Chen, W. et al. Microscale residual stresses in additively manufactured stainless steel. *Nat. Commun.* **10**, 4338 (2019).

62. Andersson, J. O., Helander, T., Höglund, L., Shi, P. & Sundman, B. Thermo-Calc & DICTRA, computational tools for materials science. *CALPHAD* **26**, 273–312 (2002).

63. Andersson, J. O., Helander, T., Hoglund, L., Shi, P. F. & Sundman, B. Thermo-Calc and Dictra, computational tools for materials science. *CALPHAD* **26**, 273–312 (2016).

64. Thavamani, R., Balusamy, V., Nampoothiri, J., Subramanian, R. & Ravi, K. R. Mitigation of hot cracking in Inconel 718 superalloy by ultrasonic vibration during gas tungsten arc welding. *J. Alloys Compd.* **740**, 870–878 (2018).

65. Johnson, D. D., Nicholson, D. M., Pinski, F. J., Gyorffy, B. L. & Stocks, G. M. Density-functional theory for random alloys: total energy within the coherent-potential approximation. *Phys. Rev. Lett.* **56**, 2088–2091 (1986).

66. Liu, D. et al. Exceptional fracture toughness of CrCoNi-based medium- and high-entropy alloys at 20 Kelvin. *Science* **983**, 978–983 (2022).

67. Johnson, D. D., Smirnov, A. V. & Khan, S. N. *MECCA: Multiple-Scattering Electronic-Structure Calculations for Complex Alloys* (KKR-CPA Program, ver. 2.0) (Iowa State University and Ames Laboratory, 2015).

68. Kohn, W. & Rostoker, N. Solution of the Schrödinger equation in periodic lattices with an application to metallic lithium. *Phys. Rev.* **94**, 1111–1120 (1954).

69. Korringa, J. On the calculations of the energy of a Bloch wave in a metal. *Phys. XIII* **6–7**, 392–400 (1947).

70. Alam, A. & Johnson, D. D. Optimal site-centered electronic structure basis set from a displaced-center expansion: Improved results via a priori estimates of saddle points in the density. *Phys. Rev. B* **80**, 125123 (2009).

71. Christensen, N. E. & Satpathy, S. Pressure-induced cubic to tetragonal transition in Csl. *Phys. Rev. Lett.* **55**, 600–603 (1985).

72. Perdew, J. P. et al. Restoring the density-gradient expansion for exchange in solids and surfaces. *Phys. Rev. Lett.* **100**, 136406 (2008).

73. Johnson, D. D. Modified Broyden's method for accelerating convergence oin self-consistent calculations. *Phys. Rev. Lett.* **38**, 12807–12813 (1988).

74. Monkhorst, H. J. & Pack, J. D. Special points for Brillouin-zone integrations. *Phys. Rev. B* **13**, 5188–5192 (1976).

Acknowledgements

Funding for this study was provided by NASA's Aeronautics Research Mission Directorate—Transformational Tools and Technologies Project Office and NASA's Space Technology Mission Directorate Game Changing Development Program under the optimized and Repeatable Components in Additive Manufacturing project. M.H. and M.J.M. acknowledge the support of the National Science Foundation and the DMREF programme under grant no. 1922239. For more information on this technology, and to discuss licencing and partnering opportunities, please contact grc-techtransfer@mail.nasa.gov and reference LEW-19886-1 and LEW-20020-1.

Author information

Authors and Affiliations

1. NASA Glenn Research Center, Cleveland, OH, USA

   Timothy M. Smith, Christopher A. Kantzos, Bryan J. Harder & Timothy P. Gabb

2. NASA Ames Research Center, Moffett Field, CA, USA

   Nikolai A. Zarkevich & John W. Lawson

3. Department of Materials Science and Engineering, The Ohio State University, Columbus, OH, USA

   Milan Heczko & Michael J. Mills

4. Propulsion Department, NASA Marshall Space Flight Center, Huntsville, AL, USA

   Paul R. Gradl

5. HX5 LLC, Fort Walton Beach, FL, USA

   Aaron C. Thompson

Contributions

T.M.S. wrote the manuscript. T.M.S., C.A.K., T.P.G. and P.R.G. designed experiments and performed microstructural/mechanical characterization. T.M.S., M.H. and M.J.M. performed TEM analysis. T.M.S. produced the powder feedstock, both coated and uncoated. A.C.T. operated the EOS M100 and developed the build parameters. B.J.H. performed cyclic oxidation tests. C.A.K., N.A.Z. and J.W.L. performed the CALPAHD and DFT models.

Corresponding author

Correspondence to Timothy M. Smith.

Ethics declarations

Competing interests

The authors declare no competing interests.

Peer review

Peer review information

Nature thanks Meurig Thomas and the other, anonymous, reviewer(s) for their contribution to the peer review of this work. Peer reviewer reports are available.

Additional information

Publisher's note Springer Nature remains neutral with regard to jurisdictional claims in published maps and institutional affiliations.

Extended data figures and tables

Extended Data Fig. 1 Powder Characterization.

a,**b**, Secondary electron SEM images of an uncoated ReB metal powder particle (**a**) and a coated ReB metal powder particle (**b**). **c**, A higher-resolution image of the coating in **b**.

Extended Data Fig. 2 Defect characterization of As-built GRX-810.

Optical microscopy image of as-built GRX-810 with optimized print parameters. Image segmentation analysis suggests that the density of the as-built part is above 99.97%.

Extended Data Fig. 3 Density functional theory computed formation energies of the Ni-Co-Cr system.

a–**i**, Computed formation energies of A1 (FCC), A2 (BCC), and A3 (HCP) phases at zero pressure versus composition along the selected lines (**a**) for: **b**, quaternary $(NiCoCr)_{(1-x)/3}Re_x$; **c**–**f**, ternary; and **g**,**i**, binary alloys.

Extended Data Fig. 4 Microstructural characterization of HIP GRX-810.

a, Electron back scatter diffraction (EBSD) inverse pole figure maps of the X-Y build plane and the Y-Z build plane where the Z-axis represents the build direction. Represented are maps from as-built and HIP samples. No significant difference was observed between the as-built and post-HIP grain structure. **b**, STEM-EDS Y, Cr, and Ni maps and corresponding LAADF-DCI micrograph of untested HIP GRX-810.

Extended Data Fig. 5 Scanning electron microscopy analysis of as-built and HIP GRX-810.

a,**b**, Secondary electron SEM images revealing the microstructure of (**a**) as-built GRX-810 and (**b**) HIP GRX-810 transverse to the build direction (X-Y). In the higher resolution image in **b**, both MC carbides and nanoscale Y_2O_3 particles can be observed.

Extended Data Fig. 6 Mechanical tests of NiCoCr-based alloys.

a,**b**, Engineering stress-strain curves at room temperature for the as-built alloys (**a**) and for HIP alloys (**b**). The step between 1 % and 2 % strain results from an increase in the tensile strain rate which is consistent with ASTM E8 standard. **c**, 1,093 °C creep curves for as-built and HIP NiCoCr, NiCoCr-ODS, ODS-ReB at 30MPa. **d**, The same tests with GRX-810 curves included.

Extended Data Fig. 7 Cyclic oxidation results at 1,093 °C and 1,200 °C.

a,**b**, Cyclic oxidation results for GRX-810 and superalloy 718 at 1,093 °C (**a**) and 1,200 °C (**b**) up to 100 h. Error bars correspond to 1 standard deviation.

Extended Data Fig. 8 Creep results at 1,093 °C / 41MPa.

Creep results at higher stress. Creep curves of ReB-ODS and HIP GRX-810 at 41 MPa / 1,093 °C.

Extended Data Fig. 9 Optical analysis of creep deformation.

a, An optical cross-section of the as-built ODS-ReB sample tested at 1,093 °C / 20 MPa. **b**, Creep pores/overload cracking along with a Cr-rich nitride in a high plasticity region of the sample. **c**, A region removed from the fracture surface that reveals creep void formation and lack of nitride formation. **d**, A representative micrograph of the microstructure in the as-built GRX-810 sample tested at 1,093 °C / 20 MPa that was terminated at 1% strain after 2,800 h. No creep void formation is observed but the presence of Al-rich and Cr-rich nitride phases along grain boundaries can be seen. **e**, A representative micrograph of the microstructure from the grip section of the same as-built GRX-810 sample revealing that nitrides did not form in an area under no stress. These results suggest that the nitride phases are creep induced.

Extended Data Table 1 Overview of tensile results for As-built and HIP GRX-810

Supplementary information

Supplementary Information

Supplementary Figs. 1–3 and Table 1.

Peer Review File

Source data

Source Data Fig. 1

Source Data Fig. 2

Source Data Fig. 3

Source Data Fig. 4

Rights and permissions

Open Access This article is licensed under a Creative Commons Attribution 4.0 International License, which permits use, sharing, adaptation, distribution and reproduction in any medium or format, as long as you give appropriate credit to the original author(s) and the source, provide a link to the Creative Commons licence, and indicate if changes were made. The images or other third party material in this article are included in the article's Creative Commons licence, unless indicated otherwise in a credit line to the material. If material is not included in the article's Creative Commons licence and your intended use is not permitted by statutory regulation or exceeds the permitted use, you will need to obtain permission directly from the copyright holder. To view a copy of this licence, visit http://creativecommons.org/licenses/by/4.0/.

Reprints and Permissions

About this article

Cite this article

Smith, T.M., Kantzos, C.A., Zarkevich, N.A. *et al.* A 3D printable alloy designed for extreme environments. *Nature* **617**, 513–518 (2023). https://doi.org/10.1038/s41586-023-05893-0

- Received: 07 October 2022
- Accepted: 27 February 2023

- Published: 19 April 2023
- Issue Date: 18 May 2023
- DOI: https://doi.org/10.1038/s41586-023-05893-0

Share this article

Anyone you share the following link with will be able to read this content:

Get shareable link

Sorry, a shareable link is not currently available for this article.

Copy to clipboard

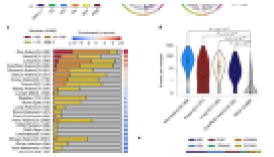
Provided by the Springer Nature SharedIt content-sharing initiative

This article is cited by

- **A 3D-printed alloy that can face extreme environments**
  - Charlotte Allard

  Nature Reviews Materials (2023)

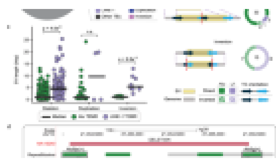
This article was downloaded by **calibre** from https://www.nature.com/articles/s41586-023-05893-0



Pan-cancer analysis of whole genomes identifies driver rearrangements promoted by LINE-1 retrotransposition

05 February 2020

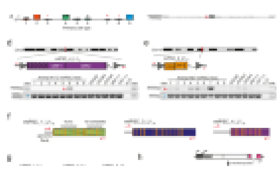
Bernardo Rodriguez-Martin, Eva G. Alvarez, … PCAWG Consortium



Transposable element-mediated rearrangements are prevalent in human genomes

19 November 2022

Parithi Balachandran, Isha A. Walawalkar, … Christine R. Beck



Retrotransposon instability dominates the acquired mutation landscape of mouse induced pluripotent stem cells

03 December 2022

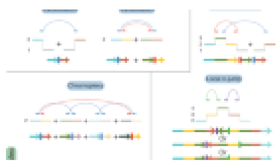
Patricia Gerdes, Sue Mei Lim, … Geoffrey J. Faulkner



[Transposable elements in human genetic disease]

12 September 2019

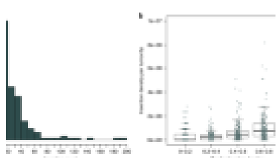
Lindsay M. Payer & Kathleen H. Burns



[Patterns of somatic structural variation in human cancer genomes]

05 February 2020

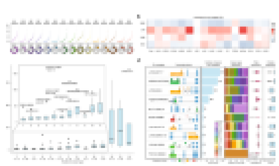
Yilong Li, Nicola D. Roberts, … PCAWG Consortium



[Retrotransposon insertions can initiate colorectal cancer and are associated with poor survival]

06 September 2019

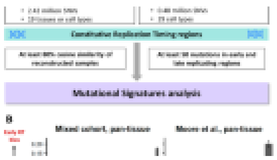
Tatiana Cajuso, Päivi Sulo, … Lauri A. Aaltonen



Transposable elements drive widespread expression of oncogenes in human cancers

29 March 2019

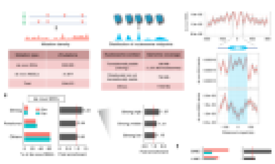
Hyo Sik Jang, Nakul M. Shah, … Ting Wang



Mutational signatures association with replication timing in normal cells reveals similarities and differences with matched cancer tissues

15 May 2023

Adar Yaacov, Shai Rosenberg & Itamar Simon



Nucleosome positioning stability is a modulator of germline mutation rate variation across the human genome

13 March 2020

Cai Li & Nicholas M. Luscombe

- Article
- Open Access
- Published: 10 May 2023

Widespread somatic L1 retrotransposition in normal colorectal epithelium

- Chang Hyun Nam,
- Jeonghwan Youk,
- Jeong Yeon Kim,
- Joonoh Lim,
- Jung Woo Park,
- Soo A Oh,
- Hyun Jung Lee,
- Ji Won Park,
- Hyein Won,
- Yunah Lee,
- Seung-Yong Jeong,
- Dong-Sung Lee,
- Ji Won Oh,
- Jinju Han,
- Junehawk Lee,
- Hyun Woo Kwon ,
- Min Jung Kim &
- …
- Young Seok Ju

Show authors

Nature **volume 617**, pages 540–547 (2023)

- 95 Altmetric

- Metrics details

Abstract

Throughout an individual’s lifetime, genomic alterations accumulate in somatic cells[1,2,3,4,5,6,7,8,9,10,11]. However, the mutational landscape induced by retrotransposition of long interspersed nuclear element-1 (L1), a widespread mobile element in the human genome[12,13,14], is poorly understood in normal cells. Here we explored the whole-genome sequences of 899 single-cell clones established from three different cell types collected from 28 individuals. We identified 1,708 somatic L1 retrotransposition events that were enriched in colorectal epithelium and showed a positive relationship with age. Fingerprinting of source elements showed 34 retrotransposition-competent L1s. Multidimensional analysis demonstrated that (1) somatic L1 retrotranspositions occur from early embryogenesis at a substantial rate, (2) epigenetic on/off of a source element is preferentially determined in the early organogenesis stage, (3) retrotransposition-competent L1s with a lower population allele frequency have higher retrotransposition activity and (4) only a small fraction of L1 transcripts in the cytoplasm are finally retrotransposed in somatic cells. Analysis of matched cancers further suggested that somatic L1 retrotransposition rate is substantially increased during colorectal tumourigenesis. In summary, this study illustrates L1 retrotransposition-induced somatic mosaicism in normal cells and provides insights into the genomic and epigenomic regulation of transposable elements over the human lifetime.

Main

Somatic mutations spontaneously accumulate in normal cells throughout an individual’s lifetime, from the first cell division[2,3,4,5]. Previous studies on somatic mosaicism have primarily focused on nucleotide variants[6,7,8,9,10,11]. More complex structural events remain less explored owing, in part, to their relative paucity and technical challenges in detection, particularly at single-cell resolution.

Long interspersed nuclear element-1 (L1) retrotransposons are widespread transposable elements representing approximately 17% of the human genome[12,13,14]. Evolutionally, L1 retrotransposons are a remarkably successful parasitic unit in the germline through ‘copying and pasting’ themselves at new genomic sites[15]. However, most of the approximately 500,000 L1s in the human reference genome are unable to transpose further

because they are truncated and have lost their functional potential. To date, 264 retrotransposition-competent L1 (rc-L1) sources have been discovered in cancer genomes[16,17] or other experimental studies[12,13,18,19,20,21]. Occasionally L1 retrotranspositions have been found in genetic analysis of tissues in several diseases[22,23], implying their role in the development of human diseases and necessitating a more systematic characterization.

Somatic L1 retrotransposition events (soL1Rs) have been systematically explored in cancer tissues[16,17,24]. Specific cancer types, including oesophageal and colorectal adenocarcinomas, showed a higher burden of soL1Rs, which often leads to alteration of cancer genes[17]. In polyclonal normal tissues, soL1R has not yet been clearly studied because it is challenging to detect instances limited to a small fraction of cells. Although several techniques have been previously employed to show soL1Rs in normal neurons, inconsistent soL1R rates have been reported across studies, ranging from 0.04 to 13.7 soL1Rs per neuron[25,26,27,28,29,30].

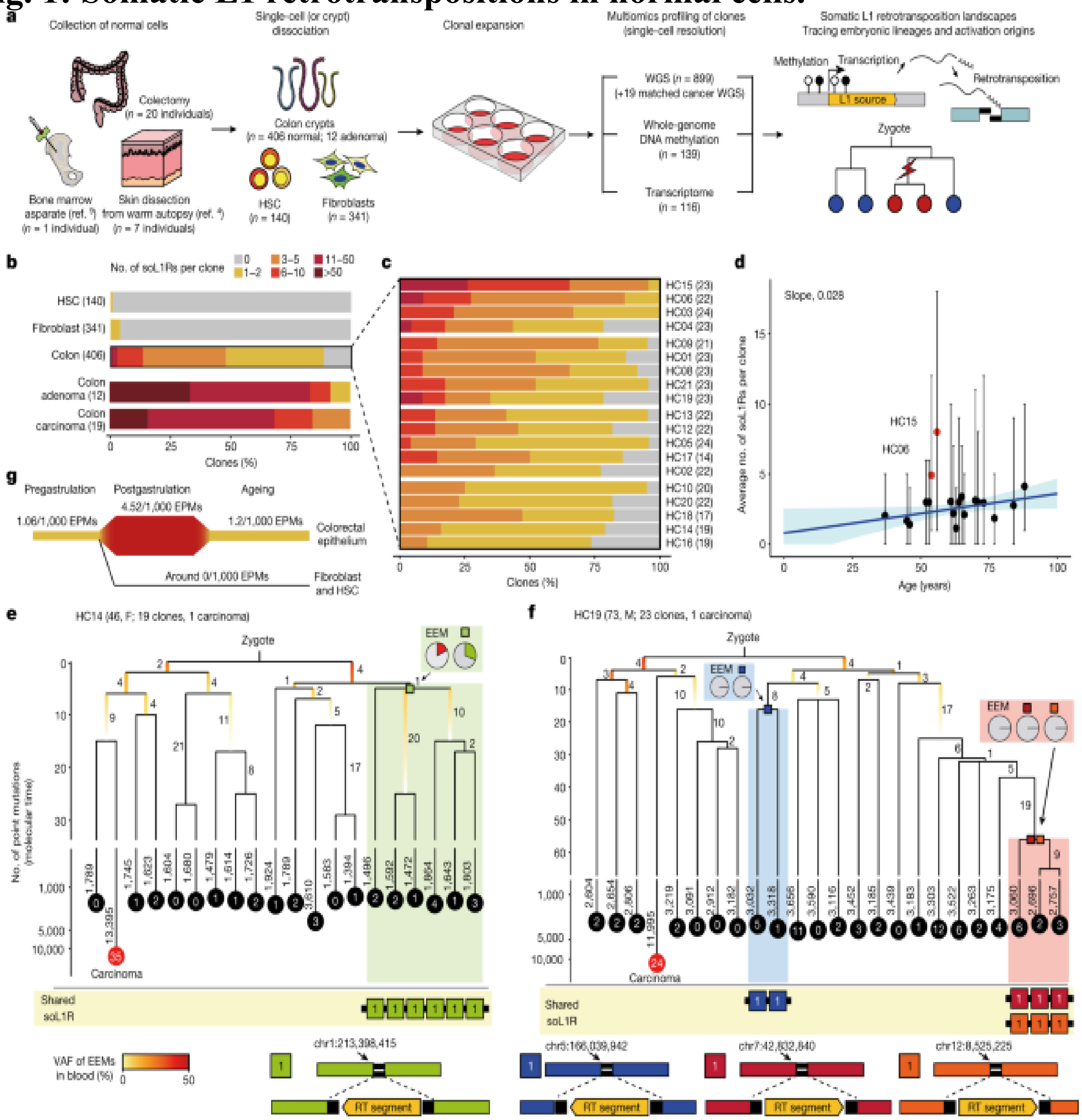
To systematically explore soL1R-induced mosaicism in normal cells, we investigated whole-genome sequences of colonies expanded from single cells (hereafter referred to as clones)[2,4]. Our approaches further allowed for simultaneous multi-omics profiling from identical clones[31] and accurate detection of early embryogenic events shared by multiple clones[2,4,5].

SoL1R in normal colorectal epithelium

In total, we explored 899 whole-genome sequences from clones (Fig. 1a) established from colorectal epithelium (406 clones from 19 donors), fibroblasts collected from various locations (341 clones from seven donors)[4], haematopoietic stem and progenitor cells (140 clones from one donor)[9] and MUTYH-associated adenomatous polyps in the colon (12 clones from four polyps of a donor). Additionally we investigated 19 matched colorectal cancer tissues from donors of normal colorectal clones (Supplementary Table 1). From these sequences we assessed somatically acquired mutations, including single-nucleotide variants (SNVs), indels, structural variations and soL1Rs (Supplementary Table 1). These mutations confirmed that the vast

majority of the clones were established from a single non-neoplastic founder cell without frequent culture-associated artefacts (Extended Data Figs. 1a,b).

Fig. 1: Somatic L1 retrotranspositions in normal cells.



a, Experimental design of the study. HSC, haematopoietic stem and progenitor cells. **b**, Proportion of clones with various numbers of soL1Rs across different cell types (number of clones shown in parentheses). **c**, Proportion of normal colorectal clones with various numbers of soL1Rs across 19 individuals (number of clones shown in parentheses). **d**, Linear regression of the average number of soL1Rs per clone on age in 19

individuals with normal colorectal clones. Vertical line crossing each dot indicates the range of soL1R burden per clone in each individual. Blue line represents the regression line, and shaded areas indicate its 95% confidence interval. Two outlier individuals (HC15 and HC06) are highlighted in red. **e**,**f**, Early clonal phylogenies of HC14 (**e**) and HC19 (**f**) reconstructed by somatic point mutation. Branch lengths are proportional to the numbers of somatic mutations, which are shown by numbers next to the branches. Early embryonic branches are coloured by variant allele fraction (VAF) of early embryonic mutations (EEMs) in the blood. The numbers of soL1Rs detected are shown in the filled circles at the tips of branches. Pie charts indicate the proportion of blood cells harbouring the EEM or soL1R. RT segment, retrotransposed segment. **g**, Normalized soL1R rates in various stages and cell types.

Among the 887 normal and 12 MUTYH-associated adenomatous clones we identified 1,250 and 458 soL1Rs, respectively, by a combined analysis using four different bioinformatics tools (Extended Data Fig. 1c and Supplementary Tables 1 and 2). Of note, soL1R events were clearly distinguished from other genomic rearrangements owing to the two canonical features of retrotransposition—the poly-A tail and target site duplication (TSD; Extended Data Fig. 1d,e). Multiple evidence indicated that most soL1Rs in clones were true somatic events rather than culture-induced events (Supplementary Discussion 1 and Supplementary Fig. 1). In addition, we further found 572 soL1Rs from the 19 matched cancers, 97.2% of which ($n = 556$) were clonal events shared by all cancer cells in the tissue. For the other retrotransposon types we additionally detected nine somatic Alu insertions in normal clones (Supplementary Table 2).

Of the 1,250 soL1Rs in the 887 healthy clones, 98.9% ($n = 1,236$) were detected from colorectal epithelium, showing extreme cell-type specificity ($P = 9.0 \times 10^{-173}$, two-sided Fisher's exact test). Most normal colorectal clones ($n = 359$, 88%) harboured at least one soL1R, on average three events per clone (Fig. 1b). Remarkably, soL1Rs were more abundant than other classical types of somatic structural variation in clones (Extended Data Fig. 1f).

In colorectal epithelium we found substantial variations in soL1R burden across clones and individuals. The soL1R burden in colorectal clones was

between zero and 18 per clone (Fig. 1c). When averaged, soL1R burdens showed a broad but positive relationship with the age of individuals (0.028 soL1Rs per clone per year; Fig. 1d), similar to the clock-like property of endogenous somatic SNVs and indels (Extended Data Fig. 2a)[32]. This implies that soL1Rs are acquired at a more-or-less constant background rate throughout life in colorectal epithelium. Two outlier individuals further suggest genetic predisposition and/or environmental exposures that stimulate L1 activities (Fig. 1d).

The soL1R burdens were not strongly associated with other features, such as sex and anatomical location of clones in the colon (Extended Data Fig. 2b,c). At the individual clone level, the soL1R burden did not show marked association with other genomic features such as point mutation burden, telomere length, activity of cell-endogenous SNV processes[33] (SBS1 and SBS5/40; standard signatures in the COSMIC database), exposure to reactive oxygen species (SBS18) or colibactin from *pks*$^{+}$ *Escherichia coli*[34] (SBS88) (Extended Data Fig. 2d–i).

SoL1Rs in normal cells are not confined to the colorectal epithelium, because we detected an additional 37 in 259 laser-capture microdissected (LCM) patches from 13 organs[5,11] (Extended Data Fig. 2j and Supplementary Table 3). However, these burdens should not be directly compared to those from colorectal clones because soL1R detection sensitivity is compromised in LCM-based whole-genome sequencing (WGS; Supplementary Discussion 2 and Supplementary Figs. 2 and 3).

High soL1R activity in embryogenesis

Of the 1,250 soL1Rs in normal clones, 30 were shared by two or more clones in an individual (ten events when collapsed), implying that these events were present in the most recent common ancestral cells of the clones. Developmental phylogenies of the clones, reconstructed using postzygotic mutations as previously reported[4,5] (Fig. 1e,f and Extended Data Figs. 3 and 4), clearly demonstrated that these soL1Rs were embryonic events. For example, a soL1R event in HC14, shared by six colorectal clones (six out of 19 clones, 32% clonal frequency), was acquired in an ancestral cell at the second-generation node in the phylogeny (Fig. 1e). In addition to the

position of the node, the number of postzygotic point mutations ($n = 5$) in the ancestral node supported the idea that the event occurred at the four-cell-stage embryo, given that the first two cell generations in human development generate 2.4–3.8 mutations per cell per cell division (pcpcd) and later cell generations generate 0.7–1.2 mutations pcpcd[4,5]. As expected for a pregastrulation event, soL1R was observed in an approximately 200× whole-genome sequence of peripheral blood (mesodermal origin) with around 34% cellular frequency beyond colorectal epithelium (endodermal origin; Fig. 1e). Similarly one somatic Alu insertion, found in HC04, was also probably obtained at the pregastrulation stage (Extended Data Fig. 4).

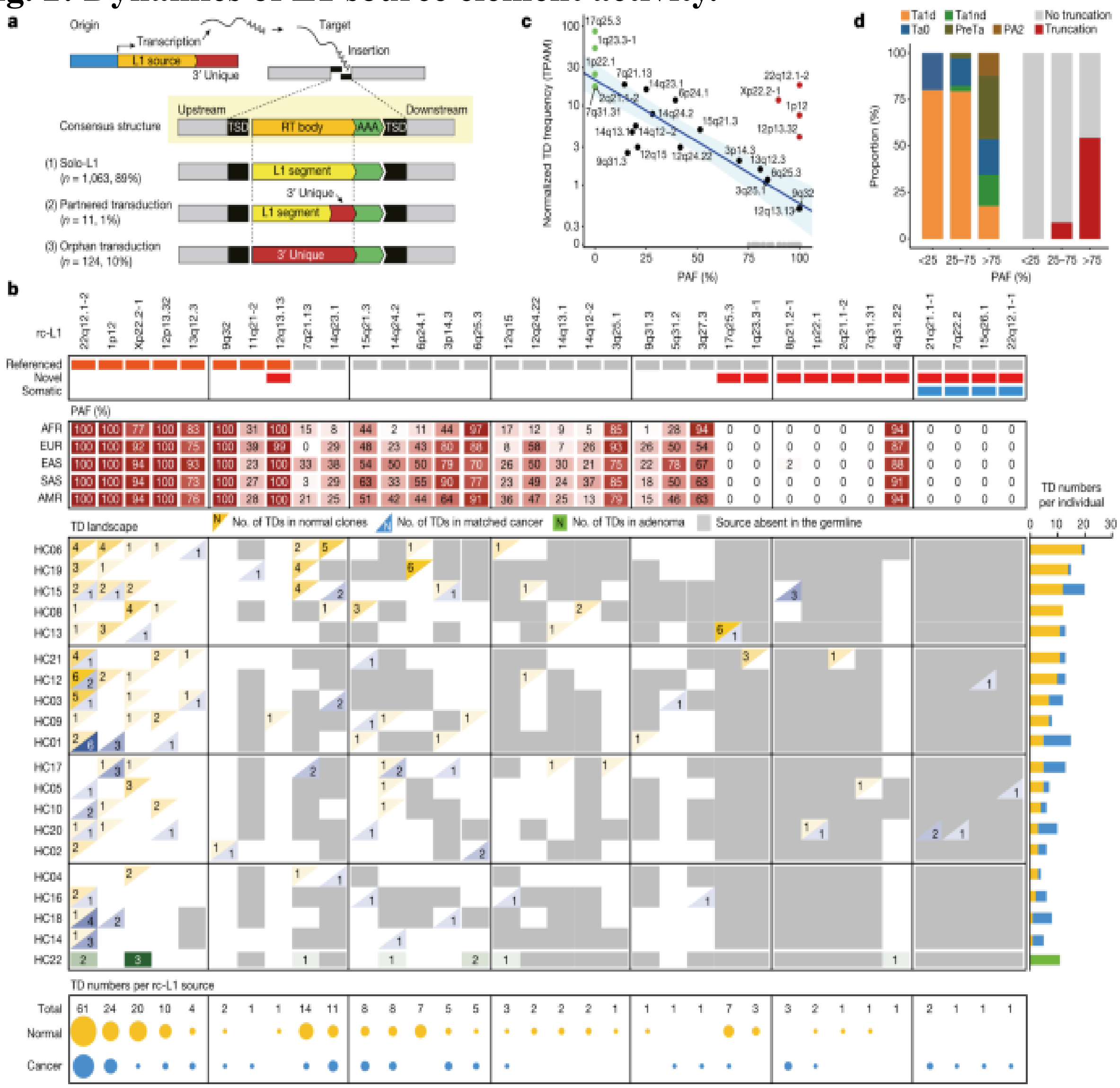
The other nine shared soL1Rs were probably postgastrulation embryonic events, given the downstream positions and molecular time of their ancestral nodes in the phylogeny (16−56 point mutations of molecular time, equivalent to the 11th–78th cell generations assuming the aforementioned fixed point mutation rate in embryogenesis)[4,5] and the absence of soL1Rs in around 200× whole-genome sequences of blood (Fig. 1f and Extended Data Figs. 3 and 4).

For comparison of various stages and cell types we calculated soL1R rates by counting the number of soL1R events per number of endogenous point mutations[32,33] (EPMs; defined as SBS1 and SBS5/40 SNVs and ID1 and ID2 indels). The soL1R rate in terminal colorectal branches (postdevelopmental colorectal epithelium) was 1.2 per 1,000 EPMs (Fig. 1g). This rate was about four times higher in postgastrulation embryonic branches differentiating to colorectal epithelium (4.52 per 1,000 EPMs, $P = 8.4 \times 10^{-4}$, two-sided Poisson exact test), equivalent to between 1.1×10^{-3} and 9.0×10^{-3} soL1R pcpcd (assuming a fixed early endogenous point mutation rate[4,5]). Point estimate for the soL1R rate in pregastrulation branches was 1.06 per 1,000 EPMs, although we found one such instance in 28 individuals (Fig. 1e). By contrast, the rates were close to zero per 1,000 EPMs for blood and fibroblast lineages, regardless of embryonic and postdevelopmental stages (Fig. 1g).

Tracing the source element of soL1Rs

The retrotransposed segments in soL1Rs of normal colorectal clones were mostly the 3' fraction of repetitive L1 sequences ($n = 1{,}063$, 89%; known as solo-L1; Fig. 2a)[16]. Occasionally the unique downstream sequences of L1 sources were retrotransposed with or without L1 sequences (known as partnered ($n = 11$, 1%) and orphan transductions ($n = 124$, 10%), respectively; Fig. 2a)[16]. In transduction events, fingerprinting of their source elements is possible using the unique sequences as a barcode of L1 sources[16].

Fig. 2: Dynamics of L1 source element activity.



a, Schematic diagram of three classes of L1 retrotransposition: solo-L1, partnered transduction and orphan transduction. **b**, The landscape of

transduction events with the features of 34 rc-L1s. TD, transduction; AFR, Africans; EUR, Europeans; EAS, East Asians; SAS, South Asians; AMR, Americans. **c**, Relationship between the population allele frequency of rc-L1s and their normalized retrotransposition activity. Green dots indicate private sources found in just one individual; red dots indicate prevalent-active sources; black and grey dots indicate common sources contributing any and no transduction events in our study, respectively. Blue line represents the regression line of active, but not prevalent, sources and shaded areas indicate its 95% confidence interval. TPAM, number of transductions per L1 allele per 1 million endogenous point mutations of molecular time. **d**, Proportion of L1 subfamily and prevalence of truncating mutations of rc-L1 sources across their PAF. Groups with PAF < 25, 25 < PAF < 75 and PAF > 75 have ten, 34 and 90 L1 sources, respectively.

Combining colorectal clones and cancer tissues, we found 217 transduction events with 34 L1 sources encompassing these, confirming their retrotransposition competency (Fig. 2b and Supplementary Table 4). Of these, 12 (35%) were new rc-L1s because they did not overlap with 264 active sources previously known[12,13,16,17,18,19,20,21]. The new rc-L1 sources include three types: (1) one referenced-germline source (present in both the human reference genome and the germline of the individual), (2) seven non-referenced-germline sources (absent in the reference genome but present in the germline) and (3) four postzygotically acquired sources absent in both the reference genome and germline (Extended Data Fig. 5). Of note, four new non-referenced-germline sources (17q25.3, 1q23.3-1, 1p22.1 and 2q21.1-2; Fig. 2b and Supplementary Table 4) were private to an individual, not being observed in our germline panel encompassing 2,860 individuals from five ancestries. This indicates that the acquisition of new rc-L1 sources is ongoing in the human genome pool, as suggested by population-based genome studies[12,21,35].

SoL1R activity across source elements

Each of the 34 rc-L1 sources contributed to a different number of transductions in colorectal clones (Fig. 2b). For example, four L1 sources (22q12.1-2, 1p12, Xp22.2-1 and 12p13.32) affected a large fraction (at least 50%) of individuals, causing approximately 50% of the somatic transduction

events in our study. These four rc-L1s were prevalent in the population, showing around 100% population allele frequency (PAF) in the human genome pool (Fig. 2b).

Except for these four 'prevalent-active' rc-L1s, high PAF rc-L1s showed low soL1R activity in colorectal epithelium. Most of the 90 rc-L1s with PAF over 75% contributed either none (81, 90%) or one soL1R event (4, 4%) in the 406 colorectal clones. By contrast, rare source elements were often retrotransposed in multiple clones of an individual having the source in the germline. For example, the private source 17q25.3 contributed six events across 22 colorectal clones of HC13 (Fig. 2b).

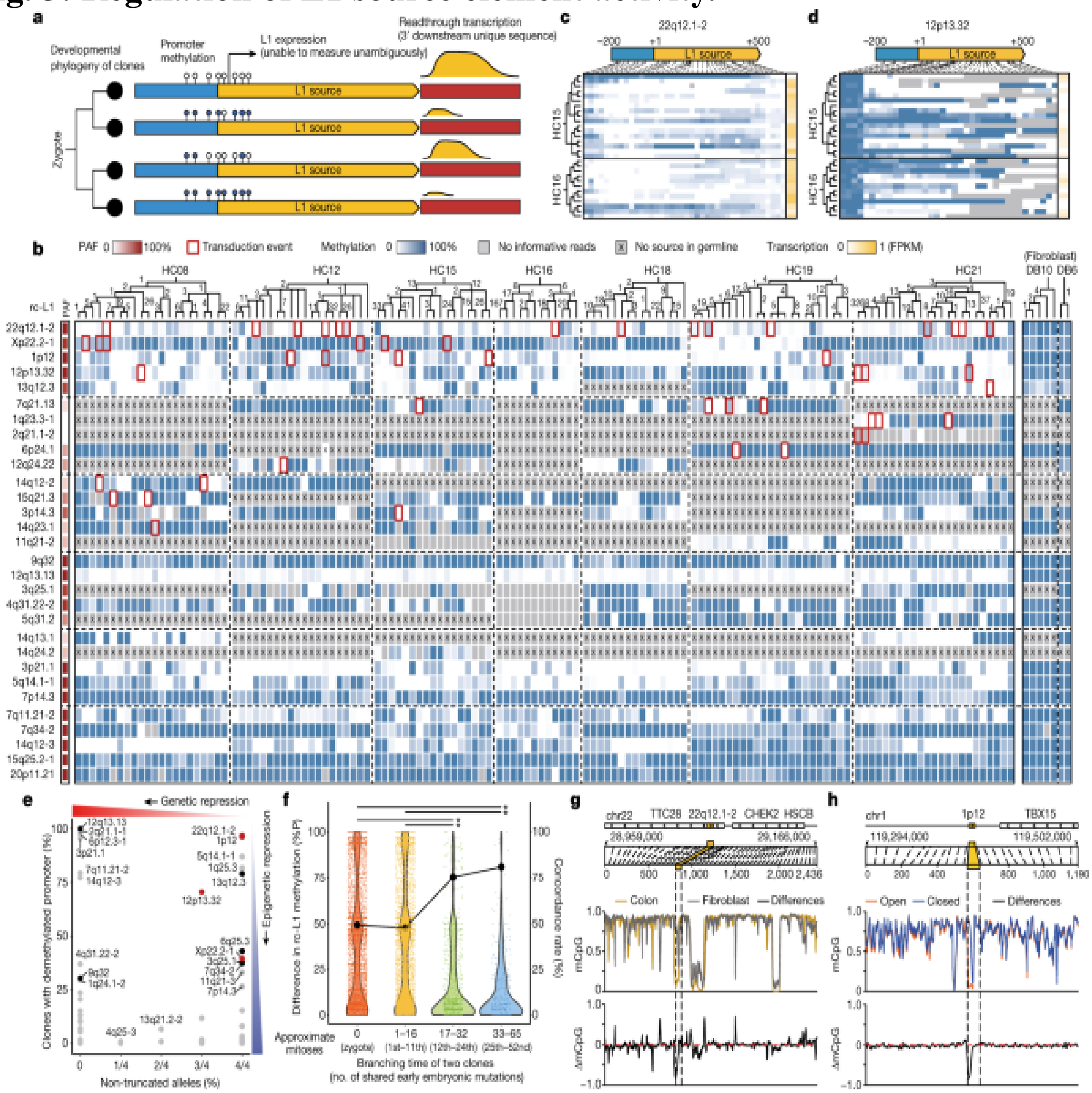
To compare retrotransposition activities across different source elements, transductions from each rc-L1 were counted per L1 allele per 1 million EPMs of molecular time (referred to as TPAM) in normal colorectal lineages in individuals harbouring the source. Intriguingly, TPAM rates generally showed a negative correlation with the PAF of rc-L1s (Fig. 2c). Rare sources showed higher retrotransposition activities than prevalent sources, except for the four prevalent-active rc-L1s. These features are in line with the inverse relationship between the prevalence and penetrance of human genomic variants[36]. Because rc-L1s can cause insertional mutagenesis, which is potentially damaging, its activity should be repressed through genetic and/or epigenetic mechanisms. Ultrarare sources probably precede sufficient negative selection because they emerged in the human population relatively recently[12].

To understand the genetic foundation of the differential activities across rc-L1s, we explored sequence polymorphisms of the source elements using long-read WGS of two colorectal clones. Population-prevalent source elements were predominantly in the older L1 subfamilies (such as pre-Ta and PA2), as suggested previously[12], and harboured open reading frame-disrupting mutations more frequently than rare source elements (Fig. 2d and Supplementary Table 4).

Dynamics of L1 promoter demethylation

To explore the epigenetic foundation of differential rc-L1 activities in normal cells, we combined whole-genome DNA methylation (in 139 clones) and RNA expression profiles (in 116 clones) in a subset of clones established (Figs. 1a and 3a). As reported for bulk tissues[16,37], these clones represented a strong negative correlation between locus-specific L1 promoter methylation and transcription (Extended Data Fig. 6), suggesting that L1 promoter demethylation is a main switch for L1 transcription.

Fig. 3: Regulation of L1 source element activity.



a, Schematic diagram of the multidimensional analysis. **b**, Panorama of DNA methylation status of 30 rc-L1s with developmental phylogenies for

132 normal colorectal clones and seven fibroblast clones from nine individuals. It includes 14 rc-L1s contributing any transduction events in these clones and 16 additional rc-L1s showing demethylated promoters in at least five clones. Numbers of branch-specific point mutations are shown in the phylogenies. **c**,**d**, DNA methylation status and readthrough transcription level of rc-L1 at 22q12.1-2 (**c**) and 12p13.32 (**d**). **e**, Proportion of non-truncation and promoter demethylation of 90 population-prevalent rc-L1s. Red dots, prevalent-active sources; black and grey dots, common sources showing any and no transduction events in our study, respectively. **f**, Differences in rc-L1 promoter methylation in clone pairs according to their embryonic branching time. The top 30 rc-L1s showing substantial variation in promoter methylation were considered. A fixed mutation rate[4] was used to convert mutation time to embryonic cell generation. %P, percentage point; $^*P < 2.2 \times 10^{-16}$ (two-sample Kolmogorov–Smirnov test). **g**,**h**, Methylation profile of 100 kb upstream and downstream regions of rc-L1 at 22q12.1-2 (**g**) and 1p12 (**h**). The rc-L1 loci are highlighted by yellow rectangles. Top, genomic coordinates and order of CpG sites. Middle, fraction of methylated CpG in colorectal (gold) and fibroblast (silver) clones (**g**), and in colorectal clones with open (orange) and closed (blue) promoters (**h**). Bottom, differences in fraction of methylated CpG depicted in middle panel. mCpG, methylated CpG.

The frequency of promoter demethylation (and the resultant transcription) varied across cell types and source elements (Fig. 3b, Extended Data Fig. 7, Supplementary Discussion 3 and Supplementary Figs. 4 and 5). Although predominantly methylated in fibroblast clones, rc-L1 promoters were often markedly demethylated in colorectal clones. For instance, promoters of prevalent-active sources 22q12.1-2 and 12p13.32 showed frequent biallelic demethylation (and resultant RNA transcription) in colorectal clones (Fig. 3b–d). Occasionally the clonal frequency of an rc-L1 promoter demethylation was more prevalent in specific individuals, as observed in sources 5q14.1-1 and 14q12-3 (Fig. 3b). Whole-genome DNA methylation profiles from various bulk tissues[38] suggest that colon tissue has a higher frequency of rc-L1 promoter demethylation than any other cell type (Extended Data Fig. 8a).

Of note, we observed that population-prevalent rc-L1s were frequently repressed through promoter methylation and/or genetic truncation. Of the 90 population-prevalent rc-L1s (PAF > 75%), 68 (75.6%) showed predominant promoter methylation in more than 75% of colorectal clones (Fig. 3e). Of the other 22 rc-L1s not preferentially promoter methylated (such as 12q13.13), ten harboured open reading frame-truncating mutations in all informative alleles from the long-read sequencing. The remaining 12 rc-L1s, particularly the four prevalent-active sources (22q12.1-2, Xp22.2-1, 1p12 and 12p13.32), escaped from both genetic and epigenetic repression, which may indicate the functional roles of the sources[39].

Multidimensional analysis further provided four insights into the epigenetic regulation of source elements and subsequent soL1R activity. First, rc-L1 promoter demethylation is a prerequisite condition for soL1Rs. A source element causing any transduction events in a clone was always promoter demethylated in the corresponding clone (Fig. 3b; 47 out of 47, highlighted by red rectangles; 37 homozygous and ten heterozygous demethylations). This further indicates that the demethylated rc-L1 promoter is stable in somatic lineages over time, because its reverse methylation would disrupt such an exclusive association.

Second, the L1 promoter epigenotype is primarily determined in embryogenesis. Autosomal rc-L1 promoter demethylation was predominantly homozygous (Fig. 3b–d), suggesting that it is directly inherited from pregastrulation epigenetic reprogramming, which globally removes DNA methylations in the genome[40,41,42]. An alternative scenario, stochastic loss of methylation in the ageing process, is less likely because it will preferentially shape demethylation in one allele. Rather, our findings suggest that fully demethylated rc-L1 promoters shaped in the earliest embryonic stage are not sufficiently remethylated subsequently in colorectal epithelial lineages (Fig. 3b). Remethylation should be more thorough in fibroblast lineages because fibroblast clones showed almost complete rc-L1 promoter methylation (Fig. 3b). Molecular time in the clonal phylogenies also indicates that the rc-L1 promoter remethylation process is operational predominantly in the postgastrulation stage. Colorectal clones having their most recent common ancestral cell in the 17–65 embryonic mutations of molecular time (12th–90th cell generations, assuming the above-mentioned

fixed early mutation rate[4,5]; near gastrulation to organogenesis) exhibited a higher concordance of promoter epigenotypes for an rc-L1 source (77% concordance rate, 1,446 out of 1,885 clone–L1 pairs) than did clones that diverged earlier (Fig. 3b–d,f).

Third, the range of insufficient remethylation is localized to the promoter of rc-L1 and is independent of other genomic regions. For example, despite the extreme difference in the promoter methylation level of the prevalent-active 22q12.1-2 source between fibroblast and colorectal clones, its 100 kb upstream and downstream regions showed highly similar DNA methylation profiles (Fig. 3g). Likewise, DNA methylation levels of neighbouring and genome-wide regions were largely concordant between colorectal clones, regardless of L1 promoter epigenotype (Fig. 3h and Extended Data Fig. 8b,c).

Last, most L1 transcripts are unproductive regarding soL1Rs in normal cells. A colorectal clone has 17–42 rc-L1 alleles with promoter demethylation (Fig. 3b), and their transcriptome sequences suggest that a colorectal epithelial lineage is continuously exposed to several rc-L1 transcripts over a lifetime (average 0.6 fragments per kilobase of transcript per million mapped reads (FPKM) when all rc-L1s are aggregated; Extended Data Fig. 7)[43]. However, a clone acquires around three soL1Rs in its lifetime, implying the presence of an active defence mechanism that protects the retrotransposition of L1 transcripts in normal cells.

Genomic regions of soL1R insertions

The target sites of soL1Rs were broadly distributed genome wide in both normal and cancer cells (Extended Data Fig. 9a). SoL1Rs in normal clones were more frequently inserted in regions of L1 endonuclease target site motifs (190-fold; 95% confidence interval (CI) 78.8–459) and late-replicating regions (5.89-fold; 95% CI 4.48–7.74) as previously observed in cancers[17], although chromatin states and transcriptional levels showed a relatively small effect (Extended Data Fig. 9b).

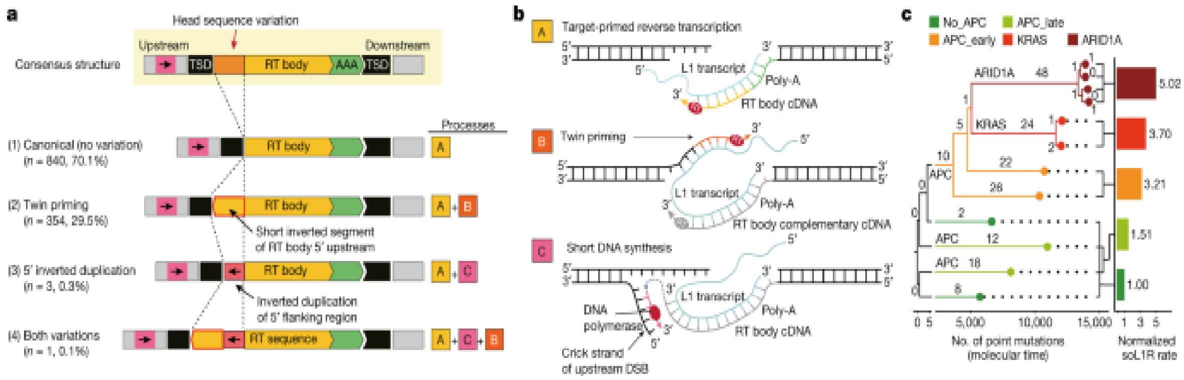
We observed a substantial level of soL1R depletion in the functional regions of the genome as observed in germline L1s[44]. Among the 1,250 soL1Rs in

normal clones we found only one event involving an exon of a protein-coding gene, which showed 29-fold lower frequency than random expectation ($P = 1.9 \times 10^{-11}$, two-sided Poisson exact test). Similarly, soL1Rs were more frequently observed in gene-sparse regions (Extended Data Fig. 9c). SoL1R-combined genomic rearrangements, which represented 1% of soL1Rs in cancer tissues[17], were not observed in normal clones. Our data further demonstrated that soL1R events did not induce additional mutations, gene expression/splicing changes or DNA methylation alterations in nearby regions from retrotransposition sites (Extended Data Fig. 9d–f). We speculate that clones with functionally damaging soL1Rs were negatively selected in normal cells.

Breakpoints of soL1R events

We further investigated breakpoint sequences at soL1R target sites to infer the mechanistic processes of L1 insertions. In addition to the two canonical features (TSD and poly-A tail), which are acquired by target-primed reverse transcription (process A; Fig. 4a,b), a substantial fraction of soL1Rs showed sequence variations in the 5' head part of the retrotransposed segments, characterized by (1) short inversion in the intraretrotransposed (intraRT) body ($n = 354$; 29.5%), (2) short foldback inversion (inverted duplication) in the 5′ upstream of the target site ($n = 3$; 0.3%) or (3) both ($n = 1$; 0.1%). These sequence variations can be explained by the twin priming mechanism (process B; Fig. 4b)[45] and additional DNA synthesis (around 52–220 base pairs (bp)) potentially by DNA polymerases in the final resolution of L1-mediated insertional mutagenesis (process C; Fig. 4b), respectively. An additional occasional event was observed in a clone established from adenoma, in which part of the precursor mRNA, transcribed in the vicinity of the insertion site, was reverse transcribed and co-inserted into the genome, suggesting strand switching of the reverse transcriptase (Extended Data Fig. 9g). These features collectively illustrate that soL1Rs are not acquired by fully ordered and linear processes, but several optional events can be engaged stochastically[46].

Fig. 4: Breakpoint and rate acceleration of somatic L1 retrotranspositions.



a,**b**, Schematic diagrams of genomic structures of canonical and complex L1 insertions (**a**) and underlying mechanisms (**b**). RT body, retrotransposed body; DSB, double-strand break. **c**, Phylogeny of MUTYH-associated adenomatous clones with normalized L1 rates in groups of lineages classified by driver mutations. Branch lengths are proportional to molecular time, as measured by the number of somatic point mutations. Numbers of branch-specific soL1Rs and branch-specific driver mutations are shown.

Interestingly, we found two clones, each of which had transductions at different genomic target sites but with exactly the same length of unique sequences (Extended Data Fig. 9h). Given that poly-A tailing is a random event in readthrough transcription, our findings suggest that multiple soL1R events from a single L1 transcript are possible.

SoL1R acceleration in tumourigenesis

The soL1R burden in the 19 matched colorectal carcinomas showed considerable variance, between four and 105 (Fig. 1b). On average soL1R burden was 30 per cancer, approximately tenfold more frequent than that observed in normal colorectal clones. The soL1R rate in colorectal carcinomas was 3.47 per 1,000 EPMs, which is around threefold higher than in normal colorectal epithelium (Extended Data Fig. 10a). Qualitatively, soL1Rs in tumours shaped more profound changes, including longer insert length (1,031 versus 453 bp for solo-L1, $P = 8.6 \times 10^{-20}$, two-sided *t*-test; 755 versus 615 bp for partnered transductions, $P = 0.59$, two-sided Wilcoxon rank-sum test; and 530 versus 242 bp for orphan transductions, $P = 0.004$, two-sided *t*-test; Extended Data Fig. 10b) and a higher frequency of head sequence variations (41.8 vesus 29.9%, $P = 9.6 \times 10^{-7}$, two-sided Fisher's

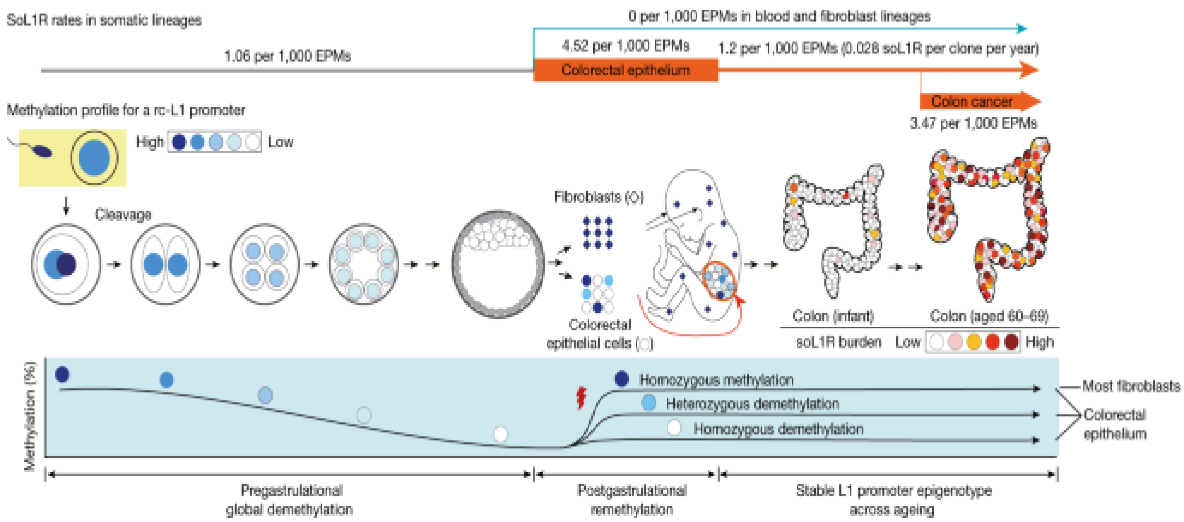
exact test; Extended Data Fig. 10c). Our findings suggest a permissive condition for L1 retrotransposition in tumour development, not necessarily equivalent to the classical genome instability in cancers. For example, TP53-inactivating mutations and microsatellite and chromosomal instability did not show a robust correlation with soL1R burdens in colorectal cancers (Extended Data Fig. 10d,e). Although chromosomal instability was significant in pancancers encompassing over 2,600 cancer cases[17] (Extended Data Fig. 10f,g), the association was weak and inconsistent in each tumour histologic type (Extended Data Fig. 11).

Acceleration of soL1R rate during tumour development was observed in MUTYH-associated adenomatous clones. In the developmental tree of adenomatous polyps, soL1R rate increased as lineages became closer to carcinoma with an accumulation of more driver mutations. For example, soL1R rate in lineages with three driver mutations (loss-of-function mutations in *APC* and *ARID1A* and a gain-of-function mutation in *KRAS*) was three- to fivefold higher than that in lineages with no marked drivers (Fig. 4c).

Discussion

Our findings demonstrate that cell-endogenous L1 elements lead to retrotransposition in normal somatic lineages and that colon epithelial cells acquire 0.028 soL1R events per year. Mobilization starts from early human embryogenesis, even before gastrulation, as observed previously[13,47]. The repertoire of rc-L1 is inherited from the parents, and their epigenetic activation is predominantly determined in the postgastrulation embryonic stage, which is then robustly transmitted in the somatic lineage during ageing (Fig. 5). Given the number of crypts in the colon (10 million)[48], individuals in their 60s would collectively have 20 million retrotransposition events in the colorectal epithelium. A small fraction of these L1 insertions can confer phenotypic changes in mutant cells and contribute to human diseases such as cancer[17].

Fig. 5: Landscape of somatic L1 retrotranspositions.



Schematic diagram illustrating factors influencing the soL1R landscape. Genetic composition of rc-L1s is inherited from the parents. The methylation landscape of rc-L1 promoters is predominantly determined by global DNA demethylation, followed by remethylation processes in the developmental stages. Then, when an rc-L1 is promoter demethylated in a specific cell lineage, the source expresses L1 transcripts thus making possible the induction of soL1Rs.

Several complementary methods, including deep sequencing[6], whole-genome amplification[8], duplex DNA sequencing[49], LCM[5,10,11] and in vitro single-cell expansions[2,4,7,9], can be used to explore somatically acquired genomic changes in normal cells. Although clonal expansions are labour intensive and applicable only to dividing cells, they have fundamental advantages[31] including (1) implementation of sensitive and precise mutation detection at the absolute single-cell level, (2) facilitation of additional multi-omics profiling in the same single clones, and (3) permitting the exploration of early developmental relationships of clones.

Although our analyses hint at some mechanisms, many things are yet to be discovered in the dynamics of L1 retrotransposition in normal cells. Owing to their repetitive nature, sequences of source elements and soL1Rs are largely inaccessible by short reads. The mechanistic basis of locus- and cell-type specificity in differential promoter demethylation is puzzling. More comprehensive panoramas on a more significant number of single cells of diverse cell types, from various time points in ageing and disease

progression and by more innovative sequencing techniques[50], are warranted to answer these questions.

Methods

Human tissues

For the in vitro establishment of clonal organoids from colorectal tissues, healthy mucosal tissues were obtained from surgical specimens of 19 patients undergoing elective tumour-removal surgery (Supplementary Table 1). Normal tissues (approximately $1 \times 1 \times 1\ cm^3$ in size) were cut from a region more than 5 cm away from the primary tumour. Matched blood and colorectal tumour tissues from the same patients were also collected for bulk-tissue WGS.

Fresh biopsies from one patient with MUTYH-associated familial adenomatous polyposis were obtained by colonoscopy. Tissues (approximately $0.5 \times 0.5 \times 0.5\ cm^3$ in size) were cut from four polyps. Matched blood and buccal mucosa tissue from the same patient were also collected.

All tissues were transported to the laboratory for organoid culture experiments within 8 h of the collection procedure. All procedures in this study were approved by the Institutional Review Board of Seoul National University Hospital (approval no. 1911-106-1080) and KAIST (approval no. KH2022-058), and informed consent was obtained from all study participants. This study was conducted in accordance with the Declaration of Helsinki and its later amendments. No statistical methods were used to predetermine sample size. The experiments were conducted without randomization and the investigators were not blinded during the experimental procedures and data analysis.

Publicly available datasets

We included publicly available whole-genome sequences of single-cell expanded clones to reach a more complete picture of L1 retrotransposition in various human tissues. We included 474 whole-genome sequences from two

previous datasets, one for haematopoietic cells (140 clones from one individual)[9] and one for mesenchymal fibroblasts from our previous work (334 clones from seven individuals)[4]. In addition, we included 259 whole-genome sequences produced from LCM-based patches dissected from 13 organs investigated in a previous study[5,11]. Furthermore, we explored 578 whole-genome sequences generated from LCM-based patches of colorectal tissues[51] to investigate differences in sensitivity for soL1R detection between LCM and clonal expansion methods.

To understand the PAF of rc-L1s we collected 2,852 publicly available whole-genome sequences of normal tissues with known ethnicity information. These data were collected from various studies[52,53,54,55,56,57].

To understand the impact of the level of genome instability on the frequency of soL1Rs in tumours, we further explored variant calls from the ICGC/TCGA Pan-Cancer Analysis of Whole-Genome (PCAWG) Consortium, which included 2,677 cancer and matched normal whole-genome sequences across around 40 tumour types[17,53]. SoL1Rs from PCAWG samples can be found in a previous paper[17]. Other somatic mutation calls (including TP53-inactivating mutations, structural variations and mutational signatures) generated by the consortium are available for download at https://dcc.icgc.org/releases/PCAWG. Our matrix used in the analysis is available in Supplementary Table 5, which includes driver mutations of 19 matched colorectal cancers identified using CancerVision (Genome Insight).

Organoid culture of colorectal crypts

All organoid establishment procedures and media compositions were adopted from the literature, with slight modifications[58]. Mucosal tissues were cut into sections of approximately 5 mm and washed with PBS. Tissues were transferred to 10 mM EDTA (Invitrogen) in 50 ml conical tubes, followed by shaking incubation for 30 min at room temperature. After incubation, the tubes were gently shaken to separate crypts from connective tissues. The supernatant was collected, and 20 µl of suspension was observed under a stereomicroscope to check for the presence of crypts. Crypt suspension was centrifuged at 300 relative centrifugal force for 3 min,

and the pellet was washed once with PBS to reduce ischaemic time. Isolated crypts were embedded in growth-factor-reduced Matrigel (Corning) and plated on a 12-well plate (TPP). Plating of crypts was performed at limited dilution by modification of the protocol from a previous study[59]. In brief, approximately 2,000 crypts were transferred to 900 µl of Matrigel and 3 × 150 µl of droplets were plated in three wells of a 12-well plate. Next, 450 µl of Matrigel was added to the remaining dilution and plating of three droplets in three wells was repeated. Serial dilution was performed at least four times and the final remaining dilution was plated in six wells. Plates were transferred to an incubator at 37 °C for 5–10 min to solidify the Matrigel. Each well was overlaid with 1 ml of organoid culture media, the compositions of which are described in Supplementary Table 6.

Clonal expansion of single-crypt-derived organoid

Primary culture of bulk and diluted crypts was maintained for at least 10 days to ensure the initial mass of single-crypt-origin organoid. After growth of organoids, a single example was manually picked using a 200 µl pipette under an inverted microscope. The picked organoid was placed in an Eppendorf tube and dissociated using a 1 ml syringe with a 25 G needle under TrypLE Express (Gibco). Next, blocking of TrypLE by ADF+++ (Advanced DMEM/F12 with 10 mM HEPES, 1× GlutaMAX and 1% penicillin-streptomycin) was followed by centrifugation and washing. The pellet was placed in a single well of a 24-well plate. Plates were transferred to a humidified 37 °C/5% CO_2 incubator and medium changed every 2–3 days. After successful passage, clonal organoids were transferred to a 12-well plate and further expanded. Confluent clones were collected for nucleic acid extraction and organoid stock.

Reclonalization of single-crypt-derived organoid

Cultured single-crypt-derived organoids were harvested and dissociated using TrypLE Express. After blocking of TrypLE and washing, organoids were resuspended using ADF+++. Organoid suspensions were filtered through a 40 µm strainer (Falcon), then single cells were sorted into a FACS tube by cell sorter (FACSMelody, BD Biosciences). Single cells were selected based on forward- and side-scatter characteristics according to the

manufacturer’s protocol. Sorted cells were sparsely seeded with growth-factor-reduced Matrigel (500 per well) in 12-well plates. Grown reclonalized single organoids were manually picked and expanded by the methods described above.

Primary culture of skin fibroblasts

We obtained seven fibroblast clones for methylation analysis. Dermal skin fibroblasts were cultured by a method described previously[4]. In brief, skin samples were washed with PBS (Gibco) and adipose tissue and blood vessels removed. The remaining tissues were cut into small pieces (1–2 mm^2) and treated with 1 mg ml^{-1} collagenase/dispase solution (Roche) at 37 °C for 1 h. After treatment, the epidermal layer was separated from the dermal layer and the latter washed with DMEM medium containing 20% FBS (Gibco) to inhibit collagenase/dispase activity. Dermal tissue was then minced into small pieces and cultured in collagen I-coated 24-well plates (Corning) with 200 µl of medium in a humidified incubator at 37 °C with 5% CO_2 concentration.

Library preparation and WGS

For Illumina sequencing we extracted genomic DNA materials from clonally expanded cells, matched peripheral blood and colorectal tumour tissues using either the DNeasy Blood and Tissue kit (Qiagen) or the Allprep DNA/RNA kit (Qiagen) according to the manufacturer’s protocol. DNA libraries were generated using Truseq DNA PCR-Free Library Prep Kits (Illumina) and sequenced on either the Illumina HiSeq X Ten platform or the NovaSeq 6000 platform. Colorectal clones were whole-genome sequenced with a mean 17-fold depth of coverage. Matched peripheral blood and colorectal tumour tissues were sequenced with a mean coverage of 181- and 35-fold, respectively. For PacBio sequencing we extracted genomic DNA from colon organoids using the Circulomics Nanobind Tissue Big DNA kit (Circulomics) according to the manufacturer’s protocol. DNA libraries were prepared using the MRTbell express template prep kit 2.0 (PacBio) and sequenced on a PacBio Sequel IIe platform.

Whole-transcriptome sequencing of organoids

Total RNA was extracted from clonally expanded cells using the Allprep DNA/RNA kit (Qiagen). The total RNA sequencing library was constructed using the Truseq Stranded Total RNA Gold kit (Illumina) according to the manufacturer's protocol.

Whole-genome DNA methylation sequencing of organoids

Genomic DNA was extracted from clonally expanded cells using either the DNeasy Blood and Tissue kit (Qiagen) or the Allprep DNA/RNA kit (Qiagen). The libraries were prepared from 200 ng of input DNA with control DNA (CpG methylated pUC19 and CpG unmethylated lambda DNA) using the NEBNext Enzymatic Methylation-seq kit (NEB) according to the manufacturer's protocol. Paired-end sequencing was performed using the NovaSeq 6000 platform (Illumina).

Variant calling and filtering of WGS data

Sequenced reads were mapped to the human reference genome (GRCh37) using the Burrows–Wheeler aligner (BWA)–MEM algorithm[60]. Duplicated reads were removed by either Picard (available at http://broadinstitute.github.io/picard) or SAMBLASTER[61]. We identified SNVs and short indels as previously reported[4]. Briefly, base substitutions and short indels were called using Haplotypecaller2 (ref. [62]) and VarScan2 (ref. [63]). To establish high-confidence variant sets we removed variants with the following features: (1) 1% or more VAF in the panel of normal, (2) high proportion of indels or clipping (over 70%), (3) three or more mismatched bases in the variant reads and (4) frequent existence of error reads in other clones.

Calling structural variations

We identified somatic structural variations in a similar way to our previous report[4]. We called structural variations using DELLY[64] with matched blood samples and phylogenetically distant clones to retain both early embryonic and somatic mutations. We then discarded variants with the following features: (1) the presence in the panel of normals, (2) insufficient number of supporting read pairs (fewer than ten read pairs with no supporting SA tag or

fewer than three discordant read pairs with one supporting SA tag) and (3) many discordant reads in matched blood samples. To remove any remaining false-positive events and rescue false-negative events located near breakpoints, we visually inspected all the rearrangements passing the filtering process using Integrative Genomics Viewer[65].

Calling L1 retrotransposition and other mobile element insertions

We called L1 retrotranspositions using MELT[20], TraFiC-mem[16], DELLY[64] and xTea[66] with matched blood samples and phylogenetically distant clones to retain both early embryonic and somatic mutations. Potential germline calls, overlapping with events found in unmatched blood samples, were removed. To confirm the reliability of calls and remove remaining false-positive events we visually inspected all soL1R candidates focusing on two supporting pieces of evidence: (1) poly-A tails and (2) target site duplications using Integrative Genomics Viewer[65]. Additionally we excluded variants with a low number of supporting reads (fewer than 10% of total reads) to exclude potential artefacts. We obtained the 5′ and 3′ ends of the inserted segment to both calculate the size of soL1Rs and determine whether L1-inversion or L1-mediated transduction was combined. When both ends of the insert were mapped on opposite strands, the variant was considered to be inverted. When the inserted segment was mapped to unique and non-repetitive genomic sequences, where a full-length L1 element is located within a 15 kb upstream region, we determined that the L1 insertion was combined with the 3′ transduction and derived from the L1 element on the upstream region of unique sequences. To calculate the VAF of soL1Rs we divided the number of L1-supporting read pairs by the total number of informative read pairs around insertion sites. A read pair was considered informative if the region covering its start and end spanned the insertion breakpoint. Furthermore, we counted the number of reference-supporting read pairs twice when calculating the total number of informative read pairs, because insertion is supported by reads pairs at both ends of the insert. To identify clonal L1 insertions in cancer samples we established a cutoff based on the minimum cell fraction value of shared soL1Rs in normal colorectal clones, because shared soL1Rs are considered true variants. We used the same approach for other mobile element insertions, including Alu and SVA.

Mutational signature analysis

To extract mutational signatures in our samples we used three different tools (in-house script, SigProfiler[67] and hierarchical dirichlet processes[68]) to achieve a consensus set of mutational signatures for each type of colon sample, including normal epithelial cells, adenoma and carcinoma. In brief, our in-house script is based on non-negative matrix factorization with or without various mathematical constraints, and borrows core methods from the predecessor of SigProfiler[69] such as using a measure of stability and reconstruction error for model selection; however, it provides greater flexibility in examining a broader set of possible solutions, including those that can be missed by SigProfiler, and enables a deliberate approach for determining the number of presumed mutational processes. As a result, we selected a subset of signatures that best explain the given mutational spectrum: SBS1, SBS5, SBS18, SBS40, SBS88, SBS89, ID1, ID2, ID5, ID9, ID18 and IDB for normal colorectal epithelial cells; SBS1, SBS5, SBS18, SBS36, SBS40, ID1, ID2, ID5 and ID9 for MUTYH-associated adenoma; and SBS1, SBS2, SBS5, SBS13, SBS15, SBS17a, SBS17b, SBS18, SBS21, SBS36, SBS40, SBS44, SBS88, ID1, ID2, ID5, ID9, ID12, ID14 and ID18 for colorectal cancers. All signatures are attributed to known mutational signatures available from v.3.2 of the COSMIC mutational signature (available at https://cancer.sanger.ac.uk/cosmic/signatures) and IDB, which is a newly found signature from previous research on normal colorectal epithelial cells[51] but not yet catalogued in COSMIC mutational signature.

Reconstruction of early phylogenies

We reconstructed the phylogenetic tree of the colonies and the major clone of cancer tissue from an individual by generating an $n \times m$ matrix representing the genotype of n mutations of m samples, as previously conducted[4]. Briefly, SNVs and short indels from all samples of an individual were merged and only variants with five or more mapped reads in all samples were included to avoid incorrect genotyping for low coverage. Additionally, variants with VAF < 0.25 in all samples were removed to exclude potential sequencing artefacts. If the VAF of the ith mutation in the jth sample was more than 0.1, M_{ij} was assigned 1; otherwise, 0. Mutations

shared in all samples were regarded as germline variants and discarded. We grouped all mutations according to the types of samples in which they were found and established the hierarchical relationship between mutation groups. In short, if the samples of mutation group A contain all the samples of mutation group B in addition to other samples, mutation group B is subordinate to mutation group A. We then reconstructed the phylogenetic tree that best explains the hierarchy of the mutation groups. The final phylogenetic tree is a rooted tree in which each sample (colony) is attached to one terminal node of the tree, with the number of mutations in the corresponding mutation group being the length of the branch. For cancer samples, the length of branches represents clonal point mutations with cancer cell fractions greater than 0.7. To convert molecular time (number of early mutations) to physical cell generations we used a mutation rate of 2.4–3.8 pcpcd for the first two cell divisions and then 0.7–1.2 pcpcd, which were estimated from a previous work[4,5].

Estimation of soL1R rates in various stages

When calculating soL1R rates we classified point mutations on phylogenetic trees into four different stages: pregastrulation, postgastrulation, ageing (postdevelopment) and tumourigenesis. Mutations shared by multiple clones and detected in bulk blood whole-genome sequences (mesodermal origin) were considered pregastrulational. Mutations in early branches[4,51,70] but not found in bulk blood whole-genome sequences were considered postgastrulational. All other mutations in normal clones were considered to have accumulated during the ageing process. For mutations in ageing and tumourigenesis we counted those attributable to endogenous mutational processes (SBS1 and SBS5/40 for SNVs, ID1 and ID2 for indels), to exclude extra mutations by external carcinogen exposure. For mutations in tumours we counted clonal point mutations (cancer cell fractions greater than 0.7) to exclude subclonal mutations. Finally we calculated soL1R rates in each stage by dividing the number of soL1Rs by the total number of endogenous point mutations. The calculation of soL1R rate for tumourigenesis included only non-hypermutated tumours.

Population allele frequency of L1 sources

To calculate the PAF of rc-L1 sources we collected 2,852 publicly available and eight in-house (overall 2,860) whole-genome sequences of normal tissues with known ethnicity information (714 Africans, 588 Europeans, 538 South Asians, 646 East Asians and 374 Americans)[52,53,54,55,56,57]. Initially we determined whether individuals had rc-L1s in their genome. Briefly, we calculated the proportion of L1-supporting reads for non-reference L1 and the proportion of reads with small insert size opposing L1 deletion for reference L1, respectively. Only rc-L1s with a proportion of 15% or more were considered to exist in the genome. We then calculated the PAF of a specific rc-L1 as the proportion of individuals with the L1 in the population.

Long-read, whole-genome sequence analysis

Sequenced reads were mapped to the human reference genome (GRCh37) using pbmm2 (https://github.com/PacificBiosciences/pbmm2), a wrapper for minimap2 (ref. [71]). Sequences for L1-supporting reads near source elements were extracted and mapped to the L1HS consensus sequences[18] using BWA[60]. We next identified sequence variations of source elements, including truncating mutations, and assigned each source element to corresponding L1 subfamilies[21].

Methylation analysis

Sequenced reads were processed using Cutadapt[72] to remove adaptor sequences. Trimmed reads were mapped using Bismark[73] to the genome combining human reference genome (GRCh37) modified by the incorporation of L1 consensus sequences at the non-reference L1 source sites, pUC19 and lambda DNA sequences. For a single CpG site, the number of reads supporting methylation (C or G), the number of reads supporting demethylation (A or T) and the proportion of former reads among total reads (methylation fraction) were calculated using Bismark. Conversion efficacy was estimated with reads mapped on CpG methylated pUC19 and CpG unmethylated lambda DNA. To observe overall methylation status we examined the methylation fraction in regions ranging from 600 bp upstream to 600 bp downstream from L1 transcription start site for each L1 source element. We then focused on CpG sites located between the L1 transcription start site and the 250 bp downstream region (+1 to +250) and classified each

CpG site into one of three categories according to methylation fraction: homozygous demethylation (methylation fraction below 25%), heterozygous (methylation fraction at least 25% and methylation fraction below 75%) and homozygous methylation (methylation fraction at least 75%). Next, methylation scores were assigned to CpG sites (0 for homozygous demethylation, 5 for heterozygous and 10 for homozygous methylation) and summarized by averaging the score of all CpG sites on the +1 to +250 region of the L1 element. Finally we compared the methylation score across every sample and every known source element to determine the relationship between methylation status and source activation.

For the analysis of L1 promoter methylation level in bulk tissues we downloaded whole-genome bisulfite sequencing data of 16 different tissues from Roadmap Epigenomics[74]. The Roadmap codes are E050 BLD.MOB.CD34.PC.F (Mobilized_CD34_Primary_Cells_Female), E058 SKIN.PEN.FRSK.KER.03 (Penis_Foreskin_Keratinocyte_Primary_Cells_skin03), E066 LIV.ADLT (Adult_Liver), E071 BRN.HIPP.MID (Brain_Hippocampus_Middle), E079 GI.ESO (Esophagus), E094 GI.STMC.GAST (Gastric), E095 HRT.VENT.L (Left_Ventricle), E096 LNG (Lung), E097 OVRY (Ovary), E098 PANC (Pancreas), E100 MUS.PSOAS (Psoas_Muscle), E104 HRT.ATR.R (Right_Atrium), E105 HRT.VNT.R (Right_Ventricle) E106 GI.CLN.SIG (Sigmoid_Colon), E109 GI.S.INT (Small_Intestine) and E112 THYM (Thymus). The methylation fractions of CpG sites in referenced L1 sources were collected and summarized by averaging the fraction of all CpG sites on the +1 to +250 region of the L1 element, then compared the averaged L1 promoter methylation level across different tissues.

Gene expression analysis

Sequenced reads were processed using Cutadapt[72] to remove adaptor sequences. Trimmed reads were mapped to the human reference genome (GRCh37) using the BWA–MEM algorithm[60]. Duplicated reads were removed by SAMBLASTER[61]. To identify the expression level of each L1 source element we collected reads mapped on regions up to 1 kb downstream from the 3′ end of the source element, and calculated the FPKM value. Only reads in the same direction with the source element were

considered. If the source element was located on the gene and both were on the same strand, the FPKM value was not calculated because the origin of reads on the downstream region is ambiguous.

Association with genome features

The L1 insertion rate was calculated as the total number of soL1Rs per sliding window of 10 Mb, with an increment of 5 Mb. To examine the relationship between L1 insertion rate and other genomic features at single-nucleotide resolution we used a statistical approach described previously[17,75]. In brief, we divided the genome into four bins (0–3) for each of the genomic features, including replication time, DNA hypersensitivity, histone mark (H3K9me3 and H3K36me3), RNA expression and closeness to the L1 canonical endonuclease motif (here defined as either TTTT|R (where R is A or G) or Y|AAAA (where Y is C or T)). By comparison of breakpoint sequences with the L1 endonuclease motif, we assigned genomics regions with more than four (most dissimilar), three, two and fewer than one (most similar) mismatches to the L1 endonuclease motif into bins 0, 1, 2 and 3, respectively. DNA hypersensitivity and histone mark data from the Roadmap Epigenomics Consortium were summarized by averaging fold-enrichment signal across eight cell types. Genomic regions with fold-enrichment signal lower than 1 belonged to bin 0, and the remainder were divided into three equal-sized bins: bin 1 (least enriched), bin 2 (moderately enriched) and bin 3 (most enriched). RNA sequencing data were also obtained from Roadmap and FPKM and averaged across eight cell types. Regions with no expression (FPKM = 0) belong to bin 0 and the remainder were divided into three equal-sized bins: bin 1 (least expressed), bin 2 (moderately expressed) and bin 3 (most expressed). Replication time was processed by averaging eight ENCODE cell types, and genomic regions were stratified into four equal-sized regions: bin 0 contained regions with the latest replicating time and bin 3 contained regions with the earliest replicating time. For every feature, enrichment scores were calculated by comparison of bins 1–3 against bin 0. Therefore, the log value of the enrichment score for bin 0 should be equal to 0 and is not described on plots.

Reporting summary

Further information on research design is available in the Nature Portfolio Reporting Summary linked to this article.

Data availability

Whole-genome, DNA methylation and transcriptome sequencing data are deposited in the European Genome-phenome Archive with accession no. EGAS00001006213 and are available for general research use. The human reference genome GRCh37 is available at https://www.ncbi.nlm.nih.gov/data-hub/genome/GCF_000001405.13.

Code availability

In-house scripts for analyses are available on GitHub (https://github.com/ju-lab/colon_LINE1).

References

1. Stratton, M. R., Campbell, P. J. & Futreal, P. A. The cancer genome. *Nature* **458**, 719–724 (2009).

2. Behjati, S. et al. Genome sequencing of normal cells reveals developmental lineages and mutational processes. *Nature* **513**, 422–425 (2014).

3. Ju, Y. S. et al. Somatic mutations reveal asymmetric cellular dynamics in the early human embryo. *Nature* **543**, 714–718 (2017).

4. Park, S. et al. Clonal dynamics in early human embryogenesis inferred from somatic mutation. *Nature* **597**, 393–397 (2021).

5. Coorens, T. H. H. et al. Extensive phylogenies of human development inferred from somatic mutations. *Nature* **597**, 387–392 (2021).

6. Martincorena, I. et al. Tumor evolution. High burden and pervasive positive selection of somatic mutations in normal human skin. *Science* **348**, 880–886 (2015).

7. Blokzijl, F. et al. Tissue-specific mutation accumulation in human adult stem cells during life. *Nature* **538**, 260–264 (2016).

8. Lodato, M. A. et al. Aging and neurodegeneration are associated with increased mutations in single human neurons. *Science* **359**, 555–559 (2018).

9. Lee-Six, H. et al. Population dynamics of normal human blood inferred from somatic mutations. *Nature* **561**, 473–478 (2018).

10. Moore, L. et al. The mutational landscape of normal human endometrial epithelium. *Nature* **580**, 640–646 (2020).

11. Moore, L. et al. The mutational landscape of human somatic and germline cells. *Nature* **597**, 381–386 (2021).

12. Ebert, P. et al. Haplotype-resolved diverse human genomes and integrated analysis of structural variation. *Science* **372**, eabf7117 (2021).

13. Sanchez-Luque, F. J. et al. LINE-1 evasion of epigenetic repression in humans. *Mol. Cell* **75**, 590–604 (2019).

14. Lander, E. S. et al. Initial sequencing and analysis of the human genome. *Nature* **409**, 860–921 (2001).

15. Kazazian, H. H. Jr Mobile elements: drivers of genome evolution. *Science* **303**, 1626–1632 (2004).

16. Tubio, J. M. C. et al. Mobile DNA in cancer. Extensive transduction of nonrepetitive DNA mediated by L1 retrotransposition in cancer genomes. *Science* **345**, 1251343 (2014).

17. Rodriguez-Martin, B. et al. Pan-cancer analysis of whole genomes identifies driver rearrangements promoted by LINE-1 retrotransposition. *Nat. Genet.* **52**, 306–319 (2020).

18. Brouha, B. et al. Hot L1s account for the bulk of retrotransposition in the human population. *Proc. Natl Acad. Sci. USA* **100**, 5280–5285

(2003).

19. Beck, C. R. et al. LINE-1 retrotransposition activity in human genomes. *Cell* **141**, 1159–1170 (2010).

20. Gardner, E. J. et al. The Mobile Element Locator Tool (MELT): population-scale mobile element discovery and biology. *Genome Res.* **27**, 1916–1929 (2017).

21. Chuang, N. T. et al. Mutagenesis of human genomes by endogenous mobile elements on a population scale. *Genome Res.* **31**, 2225–2235 (2021).

22. Kazazian, H. H. Jr et al. Haemophilia A resulting from de novo insertion of L1 sequences represents a novel mechanism for mutation in man. *Nature* **332**, 164–166 (1988).

23. Ostertag, E. M. & Kazazian, H. H. Jr Biology of mammalian L1 retrotransposons. *Annu. Rev. Genet.* **35**, 501–538 (2001).

24. Lee, E. et al. Landscape of somatic retrotransposition in human cancers. *Science* **337**, 967–971 (2012).

25. Coufal, N. G. et al. L1 retrotransposition in human neural progenitor cells. *Nature* **460**, 1127–1131 (2009).

26. Baillie, J. K. et al. Somatic retrotransposition alters the genetic landscape of the human brain. *Nature* **479**, 534–537 (2011).

27. Evrony, G. D. et al. Single-neuron sequencing analysis of L1 retrotransposition and somatic mutation in the human brain. *Cell* **151**, 483–496 (2012).

28. Evrony, G. D. et al. Cell lineage analysis in human brain using endogenous retroelements. *Neuron* **85**, 49–59 (2015).

29. Upton, K. R. et al. Ubiquitous L1 mosaicism in hippocampal neurons. *Cell* **161**, 228–239 (2015).

30. Erwin, J. A. et al. L1-associated genomic regions are deleted in somatic cells of the healthy human brain. *Nat. Neurosci.* **19**, 1583–1591 (2016).

31. Youk, J., Kwon, H. W., Kim, R. & Ju, Y. S. Dissecting single-cell genomes through the clonal organoid technique. *Exp. Mol. Med.* **53**, 1503–1511 (2021).

32. Alexandrov, L. B. et al. Clock-like mutational processes in human somatic cells. *Nat. Genet.* **47**, 1402–1407 (2015).

33. Alexandrov, L. B. et al. The repertoire of mutational signatures in human cancer. *Nature* **578**, 94–101 (2020).

34. Pleguezuelos-Manzano, C. et al. Mutational signature in colorectal cancer caused by genotoxic *pks E. coli*. *Nature* **580**, 269–273 (2020).

35. Stewart, C. et al. A comprehensive map of mobile element insertion polymorphisms in humans. *PLoS Genet.* **7**, e1002236 (2011).

36. McCarthy, M. I. et al. Genome-wide association studies for complex traits: consensus, uncertainty and challenges. *Nat. Rev. Genet.* **9**, 356–369 (2008).

37. Iskow, R. C. et al. Natural mutagenesis of human genomes by endogenous retrotransposons. *Cell* **141**, 1253–1261 (2010).

38. ENCODE Project Consortium. An integrated encyclopedia of DNA elements in the human genome. *Nature* **489**, 57–74 (2012).

39. Jachowicz, J. W. et al. LINE-1 activation after fertilization regulates global chromatin accessibility in the early mouse embryo. *Nat. Genet.* **49**, 1502–1510 (2017).

40. Messerschmidt, D. M., Knowles, B. B. & Solter, D. DNA methylation dynamics during epigenetic reprogramming in the germline and preimplantation embryos. *Genes Dev.* **28**, 812–828 (2014).

41. Guo, H. et al. The DNA methylation landscape of human early embryos. *Nature* **511**, 606–610 (2014).

42. Smith, Z. D. et al. DNA methylation dynamics of the human preimplantation embryo. *Nature* **511**, 611–615 (2014).

43. Mortazavi, A., Williams, B. A., McCue, K., Schaeffer, L. & Wold, B. Mapping and quantifying mammalian transcriptomes by RNA-Seq. *Nat. Methods* **5**, 621–628 (2008).

44. Medstrand, P., van de Lagemaat, L. N. & Mager, D. L. Retroelement distributions in the human genome: variations associated with age and proximity to genes. *Genome Res.* **12**, 1483–1495 (2002).

45. Ostertag, E. M. & Kazazian, H. H. Jr Twin priming: a proposed mechanism for the creation of inversions in L1 retrotransposition. *Genome Res.* **11**, 2059–2065 (2001).

46. Gilbert, N., Lutz, S., Morrish, T. A. & Moran, J. V. Multiple fates of L1 retrotransposition intermediates in cultured human cells. *Mol. Cell. Biol.* **25**, 7780–7795 (2005).

47. van den Hurk, J. A. et al. L1 retrotransposition can occur early in human embryonic development. *Hum. Mol. Genet.* **16**, 1587–1592 (2007).

48. Nguyen, H. et al. Deficient Pms2, ERCC1, Ku86, CcOI in field defects during progression to colon cancer. *J. Vis. Exp.* **28**, 1931 (2010).

49. Abascal, F. et al. Somatic mutation landscapes at single-molecule resolution. *Nature* **593**, 405–410 (2021).

50. Ewing, A. D. et al. Nanopore sequencing enables comprehensive transposable element epigenomic profiling. *Mol. Cell* **80**, 915–928 (2020).

51. Lee-Six, H. et al. The landscape of somatic mutation in normal colorectal epithelial cells. *Nature* **574**, 532–537 (2019).

52. Lee, J. J.-K. et al. Tracing oncogene rearrangements in the mutational history of lung adenocarcinoma. *Cell* **177**, 1842–1857 (2019).

53. ICGC/TCGA Pan-Cancer Analysis of Whole Genomes Consortium. Pan-cancer analysis of whole genomes. *Nature* **578**, 82–93 (2020).

54. 1000 Genomes Project Consortium et al. A global reference for human genetic variation. *Nature* **526**, 68–74 (2015).

55. Mallick, S. et al. The Simons Genome Diversity Project: 300 genomes from 142 diverse populations. *Nature* **538**, 201–206 (2016).

56. Bergström, A. et al. Insights into human genetic variation and population history from 929 diverse genomes. *Science* **367**, eaay5012 (2020).

57. Lorente-Galdos, B. et al. Whole-genome sequence analysis of a Pan African set of samples reveals archaic gene flow from an extinct basal population of modern humans into sub-Saharan populations. *Genome Biol.* **20**, 77 (2019).

58. Fujii, M., Matano, M., Nanki, K. & Sato, T. Efficient genetic engineering of human intestinal organoids using electroporation. *Nat. Protoc.* **10**, 1474–1485 (2015).

59. Jager, M. et al. Measuring mutation accumulation in single human adult stem cells by whole-genome sequencing of organoid cultures. *Nat. Protoc.* **13**, 59–78 (2018).

60. Li, H. & Durbin, R. Fast and accurate short read alignment with Burrows-Wheeler transform. *Bioinformatics* **25**, 1754–1760 (2009).

61. Faust, G. G. & Hall, I. M. SAMBLASTER: fast duplicate marking and structural variant read extraction. *Bioinformatics* **30**, 2503–2505 (2014).

62. Van der Auwera, G. A. et al. From FastQ data to high confidence variant calls: the Genome Analysis Toolkit best practices pipeline. *Curr. Protoc. Bioinformatics* **43**, 11.10.11–11.10.33 (2013).

63. Koboldt, D. C. et al. VarScan 2: somatic mutation and copy number alteration discovery in cancer by exome sequencing. *Genome Res.* **22**,

568–576 (2012).

64. Rausch, T. et al. DELLY: structural variant discovery by integrated paired-end and split-read analysis. *Bioinformatics* **28**, i333–i339 (2012).

65. Robinson, J. T. et al. Integrative genomics viewer. *Nat. Biotechnol.* **29**, 24–26 (2011).

66. Chu, C. et al. Comprehensive identification of transposable element insertions using multiple sequencing technologies. *Nat. Commun.* **12**, 3836 (2021).

67. Islam, S. M. A. et al. Uncovering novel mutational signatures by de novo extraction with SigProfilerExtractor. *Cell Genomics* **2**, 100179 (2022).

68. Teh, Y. W., Jordan, M. I., Beal, M. J. & Blei, D. M. Hierarchical Dirichlet Processes. *J. Am. Stat. Assoc.* **101**, 1566–1581 (2006).

69. Alexandrov, L. B., Nik-Zainal, S., Wedge, D. C., Campbell, P. J. & Stratton, M. R. Deciphering signatures of mutational processes operative in human cancer. *Cell Rep.* **3**, 246–259 (2013).

70. Mitchell, E. et al. Clonal dynamics of haematopoiesis across the human lifespan. *Nature* **606**, 343–350 (2022).

71. Li, H. Minimap2: pairwise alignment for nucleotide sequences. *Bioinformatics* **34**, 3094–3100 (2018).

72. Martin, M. Cutadapt removes adapter sequences from high-throughput sequencing reads. *EMBnet J* **17**, 10 (2011).

73. Krueger, F. & Andrews, S. R. Bismark: a flexible aligner and methylation caller for Bisulfite-Seq applications. *Bioinformatics* **27**, 1571–1572 (2011).

74. Kundaje, A. et al. Integrative analysis of 111 reference human epigenomes. *Nature* **518**, 317–330 (2015).

75. Supek, F. & Lehner, B. Clustered mutation signatures reveal that error-prone DNA repair targets mutations to active genes. *Cell* **170**, 534–547 (2017).

Acknowledgements

We thank S. Park, R. Kim, B.-K. Koo and G. J. Faulkner for their comments and discussions. This work was supported by the National Research Foundation of Korea funded by the Korean Government (nos. NRF-2020R1A3B2078973 to Y.S.J. and NRF-2021R1G1A1009606 to H.W.K.); a grant from the MD-PhD/Medical Scientist Training Programme through the Korea Health Industry Development Institute, funded by the Ministry of Health & Welfare of Republic of Korea; and by the Suh Kyungbae Foundation (no. SUHF-18010082 to Y.S.J.).

Author information

Author notes

1. These authors contributed equally: Chang Hyun Nam, Jeonghwan Youk

Authors and Affiliations

1. Graduate School of Medical Science and Engineering, Korea Advanced Institute of Science and Technology, Daejeon, Republic of Korea

   Chang Hyun Nam, Jeonghwan Youk, Joonoh Lim, Soo A Oh, Hyein Won, Yunah Lee, Jinju Han & Young Seok Ju

2. Genome Insight, Inc., Daejeon, Republic of Korea

   Jeonghwan Youk, Jeong Yeon Kim, Joonoh Lim & Young Seok Ju

3. Department of Internal Medicine, Seoul National University Hospital, Seoul, Republic of Korea

   Jeonghwan Youk & Hyun Jung Lee

4. Korea Institute of Science and Technology Information, Daejeon, Republic of Korea

   Jung Woo Park & Junehawk Lee

5. Department of Surgery, Seoul National University College of Medicine, Seoul, Republic of Korea

   Ji Won Park, Seung-Yong Jeong & Min Jung Kim

6. Department of Life Science, University of Seoul, Seoul, Republic of Korea

   Dong-Sung Lee

7. Department of Anatomy, School of Medicine, Kyungpook National University, Daegu, Republic of Korea

   Ji Won Oh

8. Department of Anatomy, Yonsei University College of Medicine, Seoul, Republic of Korea

   Ji Won Oh

9. Department of Nuclear Medicine, Korea University College of Medicine, Seoul, Republic of Korea

   Hyun Woo Kwon

Contributions

J.Y. and Y.S.J. conceived the study. J.Y., H.W.K., J.Y.K., H.W. and Y.L. developed the entire protocol of clonal expansion of colorectal epithelial cells and conducted experiments. H.J.L., Ji.W.P., S.-Y.J. and M.J.K. collected colorectal samples and clinical histories from patients. S.A.O. conducted genome sequencing. C.H.N. and J.Y. conducted most genome and statistical analyses, with contributions from J.Lim, H.W.K. and Y.S.J. Ju.W.P. and J.Lee contributed to large-scale genome data management. D.-

S.L., J.W.O. and J.H. participated in data interpretation. C.H.N., H.W.K. and Y.S.J. wrote the manuscript with contributions from all authors. Y.S.J. supervised the overall study.

Corresponding authors

Correspondence to Hyun Woo Kwon, Min Jung Kim or Young Seok Ju.

Ethics declarations

Competing interests

Y.S.J. is a cofounder and chief executive officer of Genome Insight, Inc. The remaining authors declare no competing interests.

Peer review

Peer review information

Nature thanks Trevor Graham, Jose Tubio and the other, anonymous, reviewer(s) for their contribution to the peer review of this work. Peer reviewer reports are available.

Additional information

Publisher's note Springer Nature remains neutral with regard to jurisdictional claims in published maps and institutional affiliations.

Extended data figures and tables

Extended Data Fig. 1 Clones for detection of soL1Rs.

a, A scatter plot showing mean sequencing coverage of clones and peak VAF of somatic mutations. Most clones showed their peak VAFs around 0.5, indicating that they were established from a single founder cell. **b**,

Chromosome level copy number changes of the 887 normal clones. No significant genome-wide aneuploidy was detected, supporting genomic stability during clonal expansion of normal single cells. **c**, A Venn diagram showing the number of soL1Rs detected by each bioinformatics tool. **d**, A schematic plot describing two genomic footprints of retrotransposition, the poly-A tail and target site duplication. RT body, retrotransposed body; TSD, target site duplication. **e**, The distribution of target site lengths at insertion sites. Positive and negative target site lengths indicate target site duplication and deletion, respectively. soL1R, somatic L1 retrotransposition. **f**, Number of structural variations in 406 clones from normal colon epithelial cells. T-T inversion, tail-to-tail inversion; H-H inversion, head-to-head inversion.

Extended Data Fig. 2 Associations between soL1R burden and other genomic features of clones.

a, Linear regression between the average number of endogenous point mutations in the colorectal clones and the age of sampling in 19 individuals. Blue line represents the regression line (44.6 point mutations per year), and shaded areas indicate its 95% confidence interval. The rate is consistent with the rate previously estimated in the colon (43.6 mutations per year from Lee-Six et al., Ref. [51]). **b**,**c**, Comparison of the average number of soL1Rs per individual across sex (b) and anatomical location of the colorectal crypts (c) in 19 individuals with normal colorectal clones with two-sided Wilcoxon rank-sum test. Box plots illustrate median values with interquartile ranges (IQR) with whiskers (1.5 x IQRs). ns, not significant. **d**–**i**, Relationship between the number of soL1R for each colorectal clone and the number of somatic point mutations (d), telomere length (e), the number of somatic SBS1 SNVs (f, clock-like mutations by deamination of 5-methylcytosine), the number of somatic SBS5+SBS40 SNVs (g, clock-like mutations by unknown process), the number of somatic SBS18 SNVs (h, possibly damage by reactive oxygen species), and the number of somatic SBS88 SNVs (i, damage by colibactin from *pks+ E. coli*). No obvious association was found. **j**, Number of LCM-based patches with various numbers of soL1Rs across different organs. LCM, laser-capture microdissection.

Extended Data Fig. 3 SoL1Rs on the developmental phylogenies of the clones from the seven individuals with early embryonic

soL1R events.

Early phylogenies of colorectal clones and the matched cancer tissue are shown in seven individuals who have shared soL1Rs among clones. Branch lengths are proportional to the molecular time measured by the number of somatic point mutations. The numbers of branch-specific point mutations are shown with numbers. The filled circles at the ends of branches represent normal clones (black-filled circles) and cancer clones (red-filled circles). The numbers within the filled circles show the number of soL1Rs detected from the clones. Shaded areas indicate somatic lineages with shared soL1Rs. The genomic location of the shared soL1R insertions and the proportion of the blood cells carrying the soL1Rs are shown by genomic coordinates and pie charts. Coloured bars on the right side represent the proportion of mutational signatures attributable to the somatic point mutations. Orange diamonds show L1 sources (origin), which caused transduction events across the colorectal clones.

Extended Data Fig. 4 SoL1Rs on the developmental phylogenies of the clones from the 12 individuals without early embryonic soL1R events.

Early phylogenies of colorectal clones and the matched cancer tissue are shown in 12 individuals who have no shared soL1Rs among clones. Branch lengths are proportional to the molecular time measured by the number of somatic point mutations. The numbers of branch-specific point mutations are shown with numbers. The filled circles at the ends of branches represent normal clones (black-filled circles) and cancer clones (red-filled circles). The numbers within the filled circles show the number of soL1Rs detected from the clones. Shaded area indicates somatic lineages with shared Alu insertion. The genomic location of the shared Alu insertion and the proportion of the blood cells carrying the Alu insertion are shown by genomic coordinates and a pie chart. Coloured bars on the right side represent the proportion of mutational signatures attributable to the somatic point mutations. Orange diamonds show L1 sources (origin), which caused transduction events across the colorectal clones.

Extended Data Fig. 5 An example of a soL1R event induced from a somatically acquired L1 source.

HC05 tumour has a rc-L1 in 22q12.1 (middle) which is not found in the germline of HC05 (blood; left). The rc-L1 (22q12.1-1) caused a transduction event at 5q31.1 (right) in the tumour, suggesting secondary transduction from the new somatically acquired rc-L1. The proposed order of events is summarised in the lower-left panel. SoL1R, somatic L1 retrotransposition.

Extended Data Fig. 6 Relationship between DNA methylation status and readthrough RNA expression levels.

Relationship between DNA methylation status in the promoter region and readthrough RNA expression level of rc-L1s, which have variable methylation and expression levels, is described in each individual. It only includes cases where there are more than 10 clones with information on methylation and expression levels for a specific rc-L1 in an individual. Correlation coefficient and P-value from Pearson's test is described. Blue line represents the regression line, and the shaded areas indicate its 95% confidence interval. FPKM, fragments per kilobase of transcript per million.

Extended Data Fig. 7 Panorama of DNA methylation status and readthrough RNA expression levels of 48 rc-L1s.

DNA methylation status, readthrough RNA expression levels, and developmental phylogenies of 48 rc-L1s in 132 normal colorectal clones and 7 fibroblast clones from 9 patients are displayed. It includes 27 rc-L1s that were active in our colorectal cohort and 21 rc-L1s that harbour demethylated promoters in at least five colorectal clones. The phylogenies are shown on the left side with the number of point mutations (molecular time). PAF, population allele frequency; FPKM, fragments per kilobase of transcript per million; rc-L1, retrotransposition-competent L1.

Extended Data Fig. 8 DNA methylation levels in various tissues and differences in DNA methylation in the regions nearby source elements and whole-genomes of colorectal clones.

a, Average level of L1 promoter DNA methylation across different tissues from ENCODE. Among 30 rc-L1s described in Fig. 3b, only 12 rc-L1s with sufficient reads in all tissues were selected. **b**, Methylation profiles of 100 kb upstream and downstream regions of 6 reference rc-L1s with variable methylation levels in colorectal clones. The region for rc-L1 is highlighted with yellow boxes. The genomic coordinates and order of CpG sites are depicted in the top panel. Middle panel shows the fraction of methylated CpG in colorectal clones with open (orange) and closed (blue) promoters. Bottom panel shows the differences in the fraction of methylated CpG depicted in the middle panel. mCpG, methylated CpG. **c**, A scatter plot showing genome-wide methylation levels of normal colorectal clones in each individual.

Extended Data Fig. 9 Characteristics of soL1R insertion sites and examples of soL1Rs providing insights into the L1 dynamics in somatic cells.

a, Genome-wide distribution of soL1R target sites in normal colorectal clones and 19 matched colorectal cancers. Bars represent the number of L1 insertions in a 10 Mb sliding window with a 5-Mb-sized step. **b**, Association between L1 insertion rate and various genomic features. Dots represent the log value of enrichment scores calculated by comparing bins 1–3 against bin 0 for each feature. L1 EN motif, L1 endonuclease target motif; DHS, DNase I hypersensitivity site. **c**, Distribution of distances to the nearest gene from L1 insertion sites and those from random sites. **d**–**f**, Distribution of distances to the nearest point mutations (d), gene expression level (e), and methylation fraction of nearby region (f) in colorectal clones with and without L1 insertions. TPM, transcripts per million. **g**, An example of a soL1R co-inserted with an expressed gene in the vicinity of the insertion site. A suggestive mechanism is shown in the bottom panel. SoL1R, somatic L1 retrotransposition; TSD, target site duplication; RT body, retrotransposed body. **h**, An example of a clone with two transduction events at different genomic target sites but with the same length of the unique sequences. A suggestive mechanism is shown in the bottom panel.

Extended Data Fig. 10 Differences in genomic features of somatic L1 insertion between normal colorectal clones and

colorectal cancers.

a, The soL1R rate is accelerated during tumourigenesis in colorectal lineages. EPM, endogenous point mutation. **b**, Distribution of L1 insertion size in 406 normal colorectal clones and 19 matched colorectal cancers. **c**, Proportion of soL1Rs events with head variations in 406 normal colorectal clones and 19 matched colorectal cancers. **d**–**g**, The number of soL1Rs between colorectal cancers with or without TP53 inactivating mutations (left), microsatellite instability (middle) and genomic instability (chromosomal instability; right). Sample numbers are shown in the parentheses. P values from two-sided t-test (left, middle) and linear regression (right) were shown. Box plots illustrate median values with interquartile ranges (IQR) with whiskers (1.5 x IQRs). Blue lines represent the regression lines, and the shaded areas indicate their 95% confidence intervals. P values from two-sided multivariate regression were represented in the right space. ns, not significant. d. In 19 matched colorectal cancer tissues. e. In 19 matched colorectal cancer tissues and 52 PCAWG colorectal cancer tissues. f. In 19 matched colorecal cancer tissues and 4 cancer types (colorectal adenocarcinomas, oesophageal adenocarcinomas, lung squamous cell carcinomas, and head and neck squamous cell carcinomas) showing a higher soL1R burden among 40 histologic types in PCAWG. g. In 19 matched colorectal cancer tissues with all whitelist PCAWG samples.

Extended Data Fig. 11 SoL1Rs in cancer and classical genome instability.

Relationship between soL1R burden and classical genome instability, such as TP53-inactivating mutations and chromosomal instability, was analysed in PCAWG whitelist samples (n = 2,677) and 19 matched colorectal cancers in this study. Cancer types with less than 10 cases were not considered. **a**, Somatic TP53-inactivating mutations and the number of soL1R events. Box plots illustrate median values with interquartile ranges (IQR) with whiskers (1.5 x IQRs). Number of cases in each histology type were shown in parentheses. P values from two-sided t-test were shown. NA, not available. **b**, Linear regression between the chromosomal instability (genomic rearrangements) and the number of soL1R events in each cancer type. Blue lines represent the regression lines, and the shaded areas indicate their 95%

confidence intervals. R-squared and P values from linear regression were represented in each panel.

Supplementary information

Supplementary Information

This file contains Supplementary Discussion 1 (potential culture-associated L1 retrotransposition events in the clones), Supplementary Discussion 2 (genomics techniques for sensitive detection of soL1Rs), Supplementary Discussion 3 (panorama of promoter methylation and readthrough expression of rc-L1s), Supplementary References, Supplementary Figs. 1–5 and legends for Supplementary Tables 1–6.

Reporting Summary

Peer Review File

Supplementary Table 1

Demographic and mutational characteristics of samples. The table presents information on each sample in the study, including patients' age and sex, the anatomical location where the samples were obtained and the mutational burden and signatures for each sample.

Supplementary Table 2

Annotation of somatic retrotranspositions identified in this study. The table presents detailed information on each somatic retrotransposition event identified in the study, including genomic coordinates, strand orientation, insertion size and type and the number of supporting reads for each insertion.

Supplementary Table 3

Annotation of somatic retrotranspositions identified in LCM-based patches. The table presents detailed information on each somatic retrotransposition event identified in LCM-based patches, including genomic coordinates, strand orientation, insertion size and type and the number of supporting reads for each insertion.

Supplementary Table 4

List of source elements with characteristics. The table contains information on 276 rc-L1s analysed in the study, including genomic coordinates, cytoband, strand orientation, population allele frequency, L1 subfamily information and a list of truncating mutations. Additionally, the table shows the number of transduction events from each rc-L1 in every colorectal sample examined in the study.

Supplementary Table 5

Association of soL1R and genome instability features in cancer. The table presents information on colorectal cancer samples analysed in the study and PCAWG whitelisted cancers, including histology information, the number of somatic L1 retrotransposition and structural variations, whether the samples harbour TP53-inactivating mutations or microsatellite instability and a list of canonical driver mutations.

Supplementary Table 6

Organoid culture media composition for colorectal epithelial cells. The table presents organoid culture medium composition for colorectal epithelial cells.

Rights and permissions

Open Access This article is licensed under a Creative Commons Attribution 4.0 International License, which permits use, sharing, adaptation, distribution and reproduction in any medium or format, as long as you give appropriate credit to the original author(s) and the source, provide a link to the Creative Commons licence, and indicate if changes were made. The images or other third party material in this article are included in the article's

Creative Commons licence, unless indicated otherwise in a credit line to the material. If material is not included in the article's Creative Commons licence and your intended use is not permitted by statutory regulation or exceeds the permitted use, you will need to obtain permission directly from the copyright holder. To view a copy of this licence, visit http://creativecommons.org/licenses/by/4.0/.

Reprints and Permissions

About this article

Cite this article

Nam, C.H., Youk, J., Kim, J.Y. *et al.* Widespread somatic L1 retrotransposition in normal colorectal epithelium. *Nature* **617**, 540–547 (2023). https://doi.org/10.1038/s41586-023-06046-z

- Received: 18 May 2022
- Accepted: 04 April 2023
- Published: 10 May 2023
- Issue Date: 18 May 2023
- DOI: https://doi.org/10.1038/s41586-023-06046-z

Share this article

Anyone you share the following link with will be able to read this content:

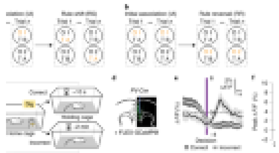
Get shareable link

Sorry, a shareable link is not currently available for this article.

Copy to clipboard

Provided by the Springer Nature SharedIt content-sharing initiative

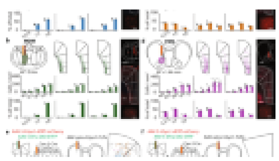
This article was downloaded by **calibre** from https://www.nature.com/articles/s41586-023-06046-z



Cross-hemispheric gamma synchrony between prefrontal parvalbumin interneurons supports behavioral adaptation during rule shift learning

25 May 2020

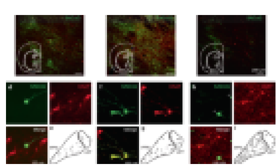
Kathleen K. A. Cho, Thomas J. Davidson, … Vikaas S. Sohal



Bi-directional regulation of cognitive control by distinct prefrontal cortical output neurons to thalamus and striatum

31 March 2021

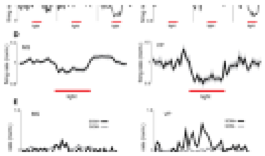
Sybren F. de Kloet, Bastiaan Bruinsma, … Huibert D. Mansvelder



Cholinergic midbrain afferents modulate striatal circuits and shape encoding of action strategies

08 April 2020

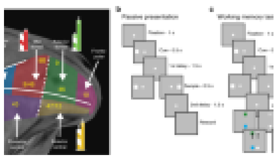
Daniel Dautan, Icnelia Huerta-Ocampo, … Juan Mena-Segovia



[Basal forebrain somatostatin cells differentially regulate local gamma oscillations and functionally segregate motor and cognitive circuits]

22 February 2019

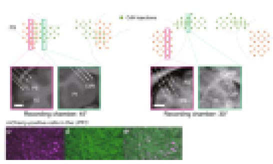
Nelson Espinosa, Alejandra Alonso, … Pablo Fuentealba



[Anterior-posterior gradient of plasticity in primate prefrontal cortex]

17 September 2018

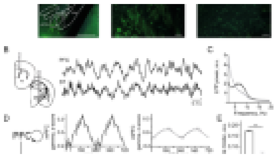
Mitchell R. Riley, Xue-Lian Qi, … Christos Constantinidis



[Chemogenetic inactivation reveals the inhibitory control function of the prefronto-striatal pathway in the macaque brain]

16 September 2021

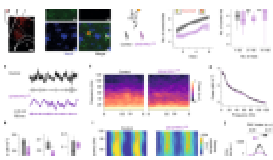
Mineki Oguchi, Shingo Tanaka, … Masamichi Sakagami



[Prefrontal - subthalamic pathway supports action selection in a spatial working memory task]

26 June 2020

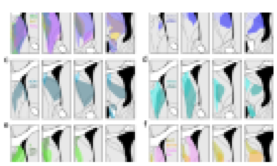
Carla Heikenfeld, Sara Mederos, … Alexey Ponomarenko



[GABAergic signaling to astrocytes in the prefrontal cortex sustains goal-directed behaviors]

07 December 2020

Sara Mederos, Cristina Sánchez-Puelles, … Gertrudis Perea



[Top-down regulation of motivated behaviors via lateral septum sub-circuits]

18 May 2022

Antoine Besnard & Felix Leroy

- Article
- [Open Access]
- [Published: 26 April 2023]

Long-range inhibition synchronizes and updates prefrontal task activity

- Kathleen K. A. Cho ,
- Jingcheng Shi,
- Aarron J. Phensy,
- Marc L. Turner &
- …
- Vikaas S. Sohal

Show authors

Nature **volume 617**, pages 548–554 (2023)

- 8306 Accesses
- 249 Altmetric
- Metrics details

Abstract

Changes in patterns of activity within the medial prefrontal cortex enable rodents, non-human primates and humans to update their behaviour to adapt to changes in the environment—for example, during cognitive tasks[1,2,3,4,5]. Parvalbumin-expressing inhibitory neurons in the medial prefrontal cortex are important for learning new strategies during a rule-shift task[6,7,8], but the circuit interactions that switch prefrontal network dynamics from maintaining to updating task-related patterns of activity remain unknown. Here we describe a mechanism that links parvalbumin-expressing neurons, a new callosal inhibitory connection, and changes in task representations. Whereas nonspecifically inhibiting all callosal projections does not prevent mice from learning rule shifts or disrupt the evolution of activity patterns, selectively inhibiting only callosal projections of parvalbumin-expressing neurons impairs rule-shift learning, desynchronizes the gamma-frequency

activity that is necessary for learning[8] and suppresses the reorganization of prefrontal activity patterns that normally accompanies rule-shift learning. This dissociation reveals how callosal parvalbumin-expressing projections switch the operating mode of prefrontal circuits from maintenance to updating by transmitting gamma synchrony and gating the ability of other callosal inputs to maintain previously established neural representations. Thus, callosal projections originating from parvalbumin-expressing neurons represent a key circuit locus for understanding and correcting the deficits in behavioural flexibility and gamma synchrony that have been implicated in schizophrenia and related conditions[9,10].

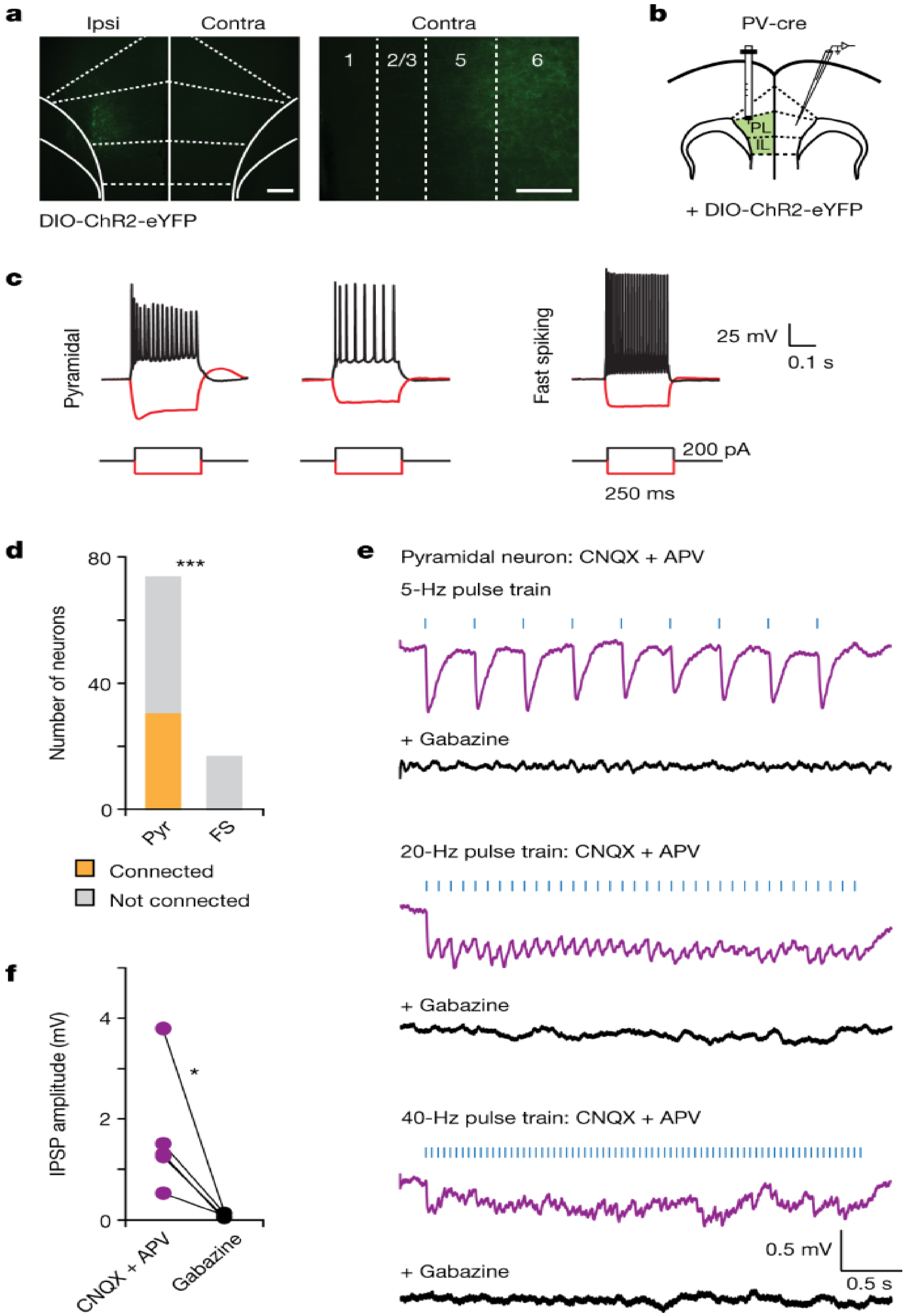
Main

Organisms must continually update their behavioural strategies to adapt to changes in the environment. Inappropriate perseveration on outdated strategies is a hallmark of conditions such as schizophrenia and bipolar disorder, and classically manifests in the Wisconsin card sorting task[11] (WCST). It is well documented that the prefrontal cortex is responsible for such flexible cognitive control, by providing active maintenance of rule or goal representations[12,13,14], adaptive gating of these representations[15], and the top-down biasing of sensory processing via extensive interconnectivity with other brain regions[16,17]. Studies have shown that within the medial prefrontal cortex (mPFC), normal parvalbumin-expressing (PV) interneuron function is required for mice to perform 'rule-shift' tasks, which, similar to the WCST, involve identifying uncued rule changes and learning new rules that use cues that were previously irrelevant to trial outcomes[6,7]. Moreover, PV interneurons have a key role in generating synchronized rhythmic activity in the gamma-frequency (around 40 Hz) range[18,19]. Indeed, during rule-shift tasks, the synchrony of gamma-frequency activity between PV interneurons in the left and right mPFC increases after error trials—that is, when mice receive feedback that a previously learned rule has become outdated—and optogenetically disrupting this synchronization causes perseveration[8]. Nevertheless, the basic relationships between circuits (synaptic connections), network dynamics (interhemispheric gamma synchrony) and neural representations (task-dependent changes in activity patterns) remain unknown.

Callosal projections from PFC PV neurons

Gamma synchrony is commonly assumed to be transmitted across regions by excitatory synapses[20], which are the predominant form of long-range communication in the cortex. However, we explored an alternative hypothesis suggested by recent descriptions of long-range γ-aminobutyric-acid-releasing (GABAergic) connections originating from PV neurons in mPFC[21]. Specifically, we first demonstrated that PV-expressing neurons in the mPFC give rise to callosal GABAergic synapses in the contralateral mPFC (Fig. 1). We identified this anatomical link by injecting AAV-EF1α-DIO-ChR2-eYFP into one mPFC of PV-cre mice and observed virally labelled PV terminals in the contralateral PFC, particularly in deep layers 5 and 6 (Fig. 1a). To characterize this callosal PV projection and its recipient neurons, we performed recordings in the contralateral mPFC (Fig. 1b). We found that callosal PV projections innervate pyramidal neurons (identified on the basis of their morphology and non-fast spiking physiology; 31 out of 75 connected) but not fast-spiking neurons (0 out of 18 connected) (Fig. 1d). Rhythmic trains of PV-terminal optogenetic stimulation elicited time-locked inhibitory postsynaptic potentials (IPSPs) in ChR2-negative pyramidal neurons (Fig. 1e), which were not blocked by the glutamatergic receptor antagonists 6-cyano-7-nitroquinoxaline-2,3-dione disodium salt (CNQX) (10 μM) and d-2-amino-5-phosphonopentanoic acid (APV) (50 μM), but were completely abolished by bath application of the type A γ-aminobutyric acid ($GABA_A$) receptor antagonist gabazine (10 μM; Fig. 1e,f). To further characterize the specific targets of callosal mPFC PV synapses, we injected fluorescent dye-conjugated cholera toxin subunit B (CTb) into four downstream targets of mPFC, then recorded from retrogradely labelled mPFC neurons that project to the contralateral mPFC (that is, contralateral to where recordings were performed and ipsilateral to the AAV-DIO-ChR2 injection), dorsal striatum, mediodorsal (MD) thalamus, or nucleus accumbens (NAc) (Extended Data Fig. 1b–k). After a single 5-ms light pulse to optogenetically activate callosal PV^+ terminals in the presence of glutamatergic antagonists (20 μM 6,7-dinitroquinoxaline-2,3-dione (DNQX) and 50 μM APV), we observed time-locked IPSPs in 22 out of 22 MD-projecting pyramidal neurons, compared with 0 out of 18 callosally projecting pyramidal neurons, 0 out of 21 accumbens-projecting pyramidal neurons, and 7 out of 24 dorsal striatum-projecting pyramidal neurons.

Fig. 1: Callosal mPFC PV projections preferentially target pyramidal neurons.



a
Ipsi
Contra
Contra
1
2/3
5
6
DIO-ChR2-eYFP
b
PV-cre
PL
IL
+ DIO-ChR2-eYFP
c
Pyramidal
Fast spiking
25 mV
0.1 s
200 pA
250 ms
d
80
40
0
Number of neurons
***
Pyr
FS
Connected
Not connected
e
Pyramidal neuron: CNQX + APV
5-Hz pulse train
+ Gabazine
20-Hz pulse train: CNQX + APV
+ Gabazine
40-Hz pulse train: CNQX + APV
0.5 mV
0.5 s
+ Gabazine
f
4
2
0
IPSP amplitude (mV)
*
CNQX + APV
Gabazine

a, Injection of AAV-DIO-ChR2-eYFP in one (ipsilateral (ipsi)) mPFC of PV-cre mice enabled visualization of $eYFP^+$ terminals in the contralateral (contra) mPFC. Scale bars: 250 µm (**a**, left) and 100 µm (**a**, right). **b**, Experimental design schematic. Whole-cell recordings were made contralateral to the virus injection in prefrontal brain slices. **c**, Example current-clamp responses from potential recipient neurons during injection of hyperpolarizing or depolarizing current. **d**, During optogenetic stimulation of callosal PV terminals, we observed synaptic responses in pyramidal (Pyr) neurons but not in fast-spiking (FS) interneurons (two-sided chi-square test, $P = 0.0008$; $n = 93$ cells, 14 mice). **e**, Rhythmic trains of blue light flashes (5 ms, 470 nm; denoted as blue bars) delivered through the 40× objective were used to optogenetically stimulate callosal PV terminals. Example recordings from a recipient pyramidal neuron showing optogenetically evoked IPSPs in the presence of CNQX and APV that are abolished with gabazine. **f**, IPSPs are blocked by gabazine application (two-tailed paired *t*-test, $P = 0.0419$; $n = 5$ cells, 4 mice). $*P < 0.05$, $***P < 0.001$.

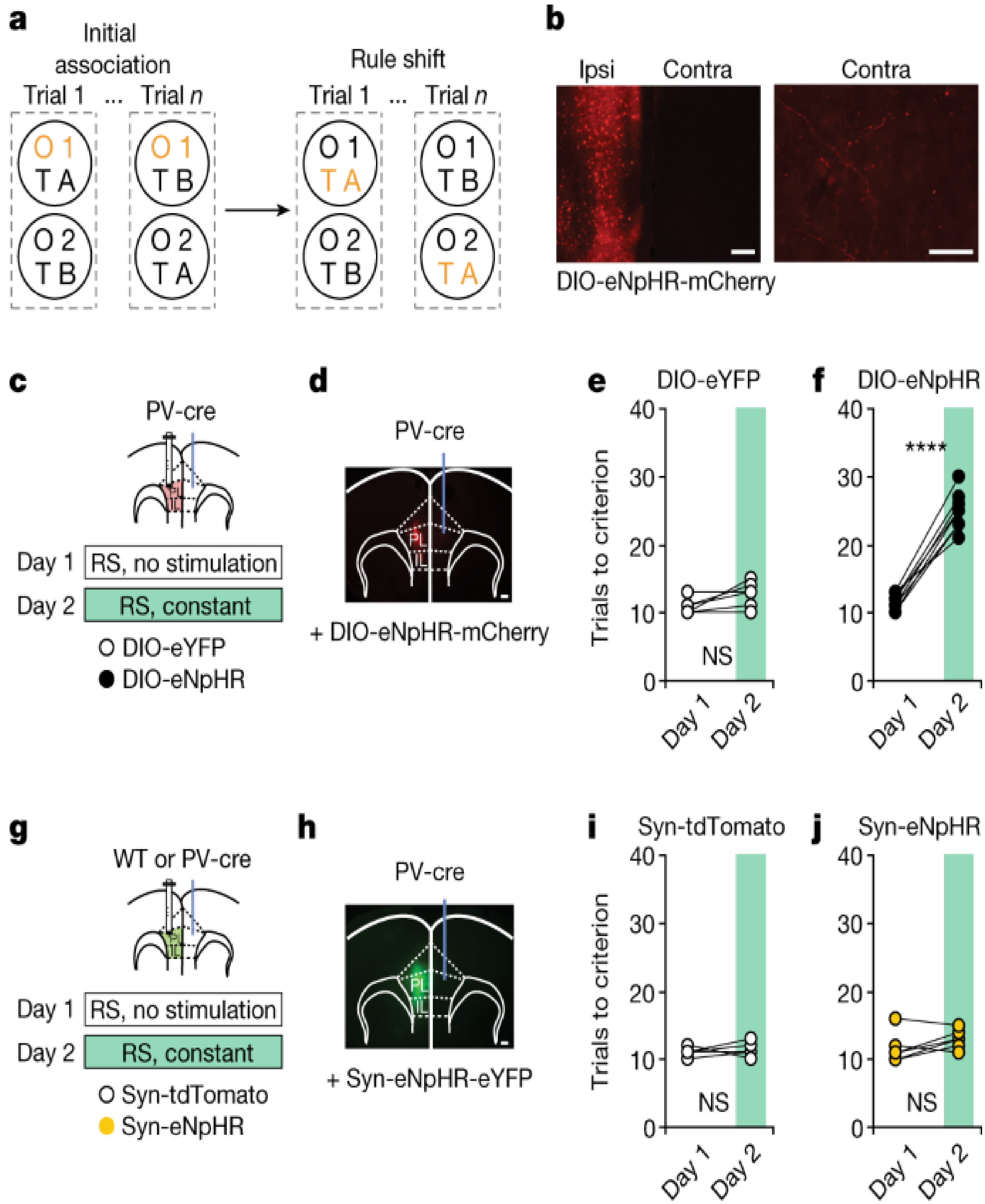
Source data

Rule-shift learning

Although we identified a long-range inhibitory anatomical connection between the prefrontal cortices, the function of this input was not defined. We next explored the role of these callosal mPFC PV^+ projections as mice performed a task involving the type of behavioural adaptations involved in the WCST. Variants of this task have previously been characterized[6,7,22] in which mice are first required to associate one set of sensory cues with the location of a hidden food reward (initial association). After learning the initial association, the mice must then learn to attend to a set of sensory cues that were previously present, but irrelevant to the outcome of each trial, and make decisions based on these previously irrelevant cues (rule shift) (Fig. 2a and Extended Data Fig. 2). Because cross-hemispheric gamma synchrony between PV interneurons is essential for learning the rule shift[8], callosal PV^+ projections may be a good candidate to effectively coordinate activity across hemispheres. To investigate this, we injected AAV-EF1α-DIO-eNpHR-mCherry or control virus into one mPFC of PV-cre mice, then optogenetically silenced callosal PV^+ terminals in the contralateral mPFC

during the rule-shift portion of the task (Fig. 2b–f and Extended Data Figs. 2b and 5). Selective inhibition of callosal PV^{+} terminals is sufficient to impair rule-shift learning and induce perseveration (relative to PV-cre mice injected with a control virus; Fig. 2e,f and Extended Data Figs. 3a and 5a–h). Notably, nonspecific inhibition of all callosal projections (both GABAergic and excitatory connections) did not affect rule-shift performance (Fig. 2g–j and Extended Data Figs. 3b and 5i–p). As controls, we verified that selective inhibition of callosal PV+ terminals did not affect gross motor behaviour during rule shifts (Extended Data Fig. 4a–c,j–m and Supplementary Video 1) or performance in an intra-dimensional rule reversal (which has similar task mechanics to the rule shift but differs in that it does not depend on mPFC gamma synchrony[8]) (Extended Data Fig. 6).

Fig. 2: Optogenetic inhibition of callosal mPFC PV projections impairs cognitive flexibility.



a, Schematic of the rule-shift task. On each trial, a mouse chooses one of two bowls, each scented with a different odour (O1 or O2) and filled with a different textured digging medium (TA or TB), to find a food reward. Mice first learn an initial association between one of these sensory cues (for example, O1) and food reward (the cue associated with reward is indicated

in orange). Once mice reach the learning criterion (8 out of 10 consecutive trials correct), this association undergoes an extra-dimensional rule shift (RS; for example, from O1 to TA being rewarded). **b**, Representative images showing AAV-DIO-eNpHR-mCherry (DIO-eNpHR) expression in ipsilateral mPFC and callosal PV terminals in contralateral mPFC. Scale bars: 100 µm (left) and 50 µm (right). **c**,**g**, Experimental design with DIO-eYFP or DIO-eNpHR (**c**) or Syn-tdTomato or Syn-eNpHR (**g**) mice. Day 1, no light delivery; day 2, continuous light for inhibition during the rule shift. **d**, Representative image showing DIO–eNpHR expression in one mPFC and a fibre-optic cannula implanted in contralateral mPFC. Scale bar, 100 µm. **e**,**f**, Optogenetic inhibition of mPFC callosal PV terminals impairs rule-shift performance in DIO-eNpHR mice ($n = 8$) compared with controls ($n = 7$) (two-way ANOVA (task day × virus); interaction: $P < 0.0001$). **e**, Performance of DIO-eYFP controls did not change ($P = 0.11$). **f**, Inhibition disrupts rule-shift performance in DIO-eNpHR mice ($P < 0.0001$). **h**, Representative image showing Syn–eNpHR expression in one mPFC and a fibre-optic cannula implanted in contralateral mPFC. Scale bar, 100 µm. **i**,**j**, Performance of Syn-tdTomato controls ($n = 4$) is similar to Syn-eNpHR mice ($n = 6$; two-way ANOVA (task day × virus); interaction: $P = 0.38$). Two-way ANOVA with Bonferroni post hoc comparisons. ****$P < 0.0001$; NS, not significant.

Source data

Next we tested whether the behavioural deficits induced by inhibiting callosal PV$^+$ projections might be persistent and reversible. For this, we took advantage of an intersectional strategy that used a Flp- and Cre-dependent AAV in PV-cre mice to drive NpHR3.3 (NpHR) and ChR2 expression specifically in callosally projecting PV neurons[23]. To label and manipulate callosal PV$^+$ projections, we injected AAVretro-Flp in one mPFC of PV-cre mice, and in the contralateral mPFC we implanted an optical fibre and injected the NpHR and ChR2 Flp- and Cre-dependent AAVs (Extended Data Fig. 7). Once again, silencing callosal PV$^+$ projections impaired rule-shift performance on day 1 (Extended Data Fig. 7h–j). Unexpectedly, the impairments in rule-shift performance persisted on day 2, in the absence of any further optogenetic inhibition. On day 3, 40-Hz stimulation of callosal PV$^+$ projections rescued perseveration and these effects persisted in the

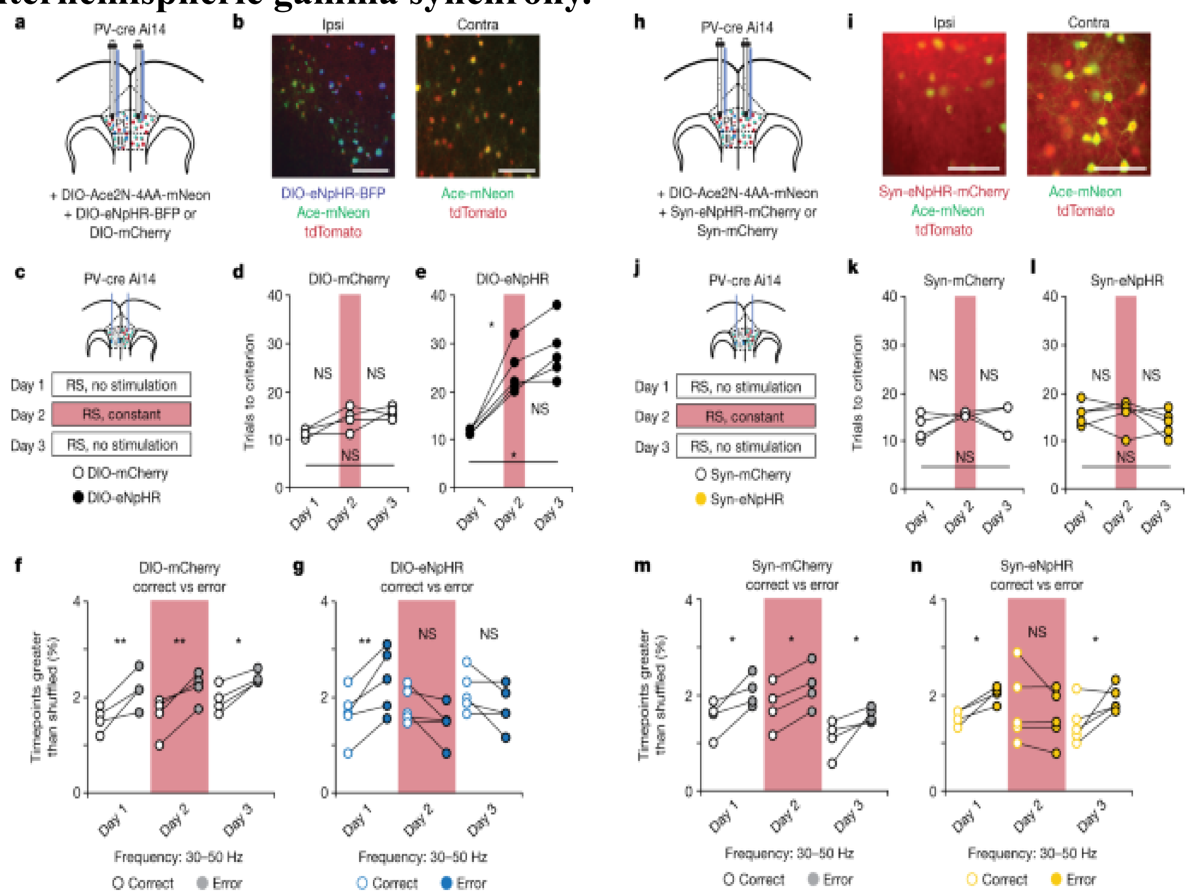
absence of further optogenetic manipulations on day 4 of testing (which occurred at least 1 week later). In ChR2-negative controls (PV-cre mice injected with Flp- and Cre-dependent NpHR but mCherry instead of ChR2), rule-shift deficits induced by inhibiting callosal PV^+ projections persisted across days (Extended Data Fig. 7e–g). These results identify callosal PV^+ projections as powerful bi-directional drivers of network plasticity. Notably, long-range GABAergic projections have been hypothesized to have a role in the temporal coordination of neuronal activity[24,25]. On this basis, we hypothesized that the behavioural deficits that we observed may reflect the fact that when callosal PV^+ projections are selectively inhibited, callosal communication (mediated largely by excitatory connections) becomes uncoordinated, disrupting normal information processing.

Gamma synchrony

To test this possibility, we studied how callosal PV^+ projections influence the cross-hemispheric gamma synchrony in PV interneurons that we previously found to be essential for re-appraising the behavioural salience of sensory cues during rule shifts. For this, we injected AAV-EF1α-DIO-eNpHR-BFP or control virus into one mPFC of PV-cre Ai14 mice (Fig. 3a,b and Extended Data Fig. 8a,b). To track transmembrane voltage activity patterns of PV neurons, we also injected virus expressing the Cre-dependent, genetically encoded voltage indicator Ace-mNeon (AAV-DIO-Ace2N-4AA-mNeon) into both mPFCs. We then implanted multimode optical fibres to excite and measure fluorescence from both Ace-mNeon and a control fluorophore (tdTomato) expressed in PV interneurons in the left and right mPFC as well as to optogenetically silence PV^+ callosal terminals (Fig. 3a,b and Extended Data Fig. 2c). Using this method, we had previously found that gamma synchrony between PV interneurons in the left and right mPFC increases during rule shifts when mice make errors—that is, when they do not receive an expected reward and therefore receive feedback that the previously learned association is no longer valid[8]. We confirmed this result on day 1 (Fig. 3c–g), in the absence of any optogenetic silencing. On day 2, optogenetic inhibition of callosal PV^+ terminals disrupted performance in the rule-shift task, compared with PV-cre Ai14 mice given control virus (Fig. 3c–e and Extended Data Fig. 8a–h). This behavioural deficit, which

was consistent with our earlier experiments, correlated with deficits in cross-hemispheric gamma synchrony: specifically, the increase in cross-hemispheric PV neuron gamma synchrony observed after rule-shift errors on day 1 was abolished on day 2 (Fig. 3f–g). Moreover, the impairments in both rule-shift performance and gamma synchrony persisted on day 3, in the absence of any additional optogenetic inhibition (Fig. 3e,g).

Fig. 3: Optogenetic inhibition of callosal mPFC PV projections disrupts interhemispheric gamma synchrony.



a, PV-cre Ai14 mice had bilateral AAV-DIO-Ace2N-4AA-mNeon injections, an ipsilateral AAV-DIO-eNpHR-BFP or control virus (AAV-DIO-mCherry) injection and fibre-optic implants in both prefrontal cortices. **b**, Representative images of DIO-eNpHR, Ace-mNeon and tdTomato expression in the ipsilateral (ipsi) versus contralateral (contra) mPFC. Scale bars, 50 µm. **c**, Experimental design: day 1, no light; day 2, continuous light (in contra) for inhibition during the rule shift; day 3, no light. **d**, Performance of DIO-mCherry mice ($n = 4$) did not change. **e**, Performance

was impaired in DIO-eNpHR mice ($n = 5$). **f**, Gamma synchrony was higher after rule-shift errors than after rule-shift correct decisions across days in controls ($n = 4$ mice). **g**, Gamma synchrony was higher after rule-shift errors for DIO-eNpHR mice on day 1 (no light) but not on day 2 or day 3 ($n = 5$ mice). **h**, PV-cre Ai14 mice had bilateral Ace-mNeon injections, an ipsilateral injection of AAV-Syn-eNpHR-mCherry or AAV-Syn-mCherry (control), and fibre-optic implants in both prefrontal cortices. **i**, Representative images of Syn-eNpHR, Ace-mNeon and tdTomato expression in ipsilateral and contralateral mPFC. Scale bars, 25 µm. **j**, Experiments using Syn-eNpHR with the same design as **c**. **k**,**l**, Performance of controls ($n = 4$ mice) and Syn-eNpHR mice ($n = 5$) did not change across days. **m**, Gamma synchrony was higher after rule-shift errors across days in controls ($n = 4$ mice). **n**, Gamma synchrony was higher after rule-shift errors for Syn-eNpHR mice on day 1 (no light). This was abolished with light on day 2, then restored on day 3 (no light) ($n = 5$ mice). Full statistics are provided in the Methods. Two-way ANOVA followed by Bonferroni post hoc comparisons. $^*P < 0.05$, $^{**}P < 0.01$.

Source data

Given that inhibiting all callosal projections, using the synapsin promoter, does not affect rule-shift performance, we tested how it would affect gamma synchrony. Again, we observed that this manipulation did not affect rule-shift performance (Fig. 3h–l and Extended Data Fig. 8i–p). Notably, silencing all callosal communication did disrupt normal increases in interhemispheric gamma synchrony following error trials on day 2 (Fig. 3m–n). However, this deficit did not persist in the absence of further optogenetic inhibition on day 3 (Fig. 3m–n). This is consistent with our model, in which the function of long-range GABA projections and gamma synchrony is not to facilitate essential inter-regional communication, but rather to prevent such communication from occurring in an aberrant manner that deleteriously impacts the normal evolution of prefrontal network activity during rule shifts. In this model, the transient loss of gamma synchrony that occurs during nonspecific inhibition of all callosal projections is not problematic because all callosal communication is suppressed. Furthermore, in this case, deficits in gamma synchrony do not persist, indicating that these persistent deficits reflect circuit plasticity that is triggered by inhibiting callosal PV^+ projections but requires the presence of activity in other callosal projections.

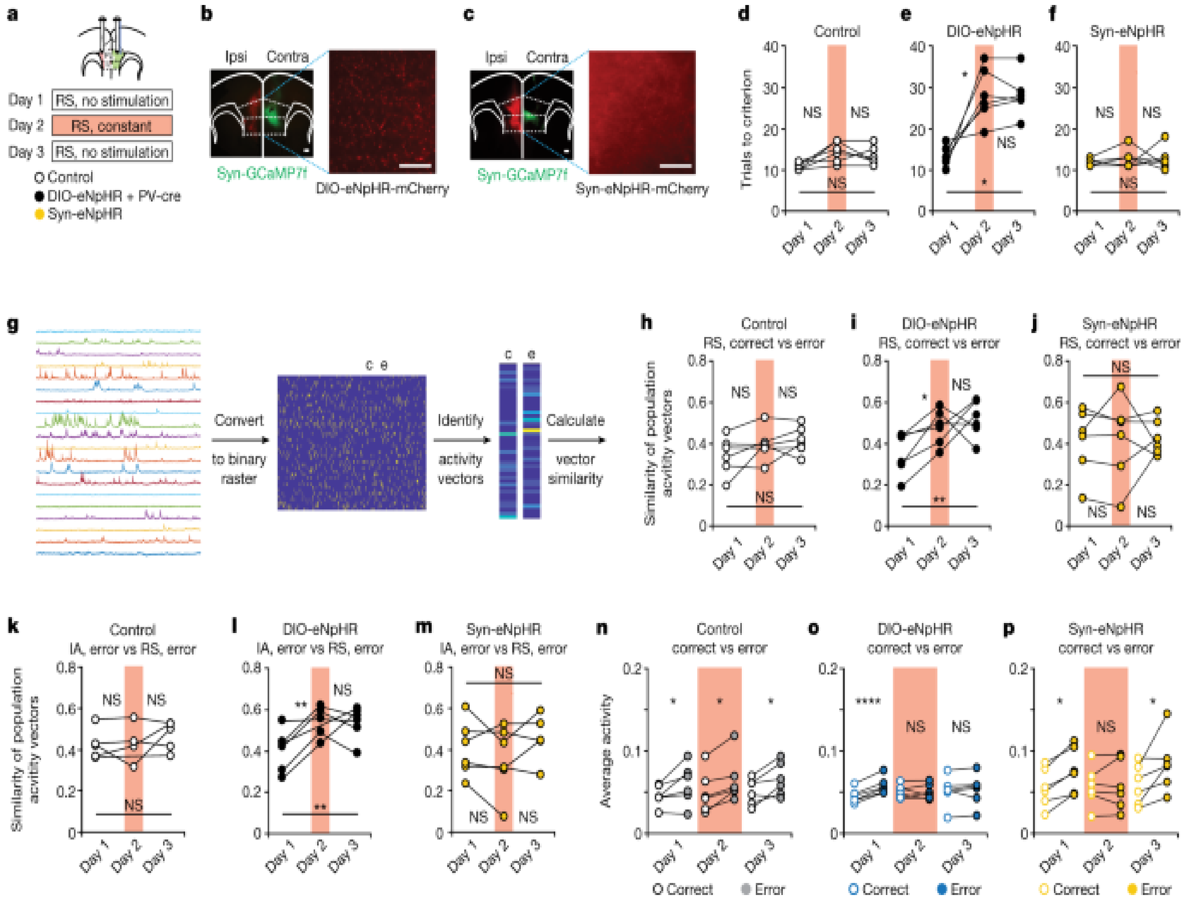
In addition, inhibiting callosal PV^+ projections also disrupts increases in gamma synchrony occurring during inter-trial intervals (ITI) following rule-shift errors (Extended Data Fig. 9e).

Updating of activity patterns

We specifically hypothesized that the inhibition of callosal PV^+ projections and consequent deficits in gamma synchrony would disrupt the changes in prefrontal activity patterns that normally serve to update behavioural strategies[3]. In particular, during normal rule-shift learning, gamma synchrony increases specifically following rule-shift errors. Therefore, we hypothesized that prefrontal activity patterns might begin to diverge from previously established representations specifically during this period, and that inhibiting callosal PV^+ projections would disrupt this process. First, using an alternative method to quantify gamma synchrony within TEMPO measurements on shorter time frames (Methods), we confirmed that interhemispheric gamma synchrony between mPFC PV neurons is higher specifically after digging on error trials compared with correct trials, and that inhibiting callosal PV^+ projections specifically disrupts increases in gamma synchrony during this period (Extended Data Fig. 9f–i). Then, to quantify the divergence of activity patterns during and immediately after this period of increased gamma synchrony, we measured the similarity between activity patterns during the 10 s following a choice on correct versus error trials. We measured these activity patterns using microendoscopic calcium imaging in PV-cre mice injected with AAV-synapsin-GCaMP7f (Syn-GCaMP7f) and implanted with a gradient-index (GRIN) lens in one mPFC, and injected in the other mPFC with either AAV-EF1α-DIO-eNpHR-mCherry (DIO-eNpHR), AAV-synapsin-eNpHR-mCherry (Syn-eNpHR) or a control virus (AAV-DIO-mCherry in PV-cre mice or AAV-synapsin-mCherry in wild-type mice) (Fig. 4a–c and Extended Data Fig. 10). We measured Syn-GCaMP7f fluorescence while mice performed a rule shift on three consecutive days (Fig. 4a). On the second day, we also delivered red light to activate eNpHR in callosal terminals (Extended Data Fig. 2d). As in previous experiments, specifically inhibiting callosal PV^+ terminals significantly increased the number of trials needed to learn a rule shift in eNpHR-expressing mice (whereas there was no effect in controls) (Fig. 4d,e

and Extended Data Fig. 10f–i). This was accompanied by a significant increase in the similarity between activity patterns occurring after error trials and those after correct trials (by contrast, no such increase occurred in controls) (Fig. 4d,e,h,i). To confirm that this reflects a suppression of changes in activity patterns that normally occur after rule-shift errors, we also computed the similarity between activity patterns after rule-shift errors and those occurring after errors during learning of the initial association (Fig. 4g,k–m and Extended Data Figs. 3e,f and 10t,u). Activity patterns following rule-shift errors also became more similar to those observed during the initial association. Finally, analysing activity on faster timescales (1 s), we found that inhibiting callosal PV^+ projections also makes fast-timescale patterns occurring after incorrect decisions during the rule shift more similar to those occurring after correct decisions during the rule shift (Extended Data Fig. 10v–x). Furthermore, inhibiting callosal PV^+ projections also disrupts the evolution of fast-timescale activity patterns that normally occurs over the course of a single error trial (Extended Data Fig. 10q–s). This suggests that inhibiting callosal PV^+ projections disrupts learning that occurs, at least in part, during each trial. Consistent with this, inhibiting callosal PV+ projections only during ITIs did not affect rule-shift learning (Extended Data Fig. 2l–o).

Fig. 4: Optogenetic inhibition of callosal PV projections disrupts prefrontal activity patterns.



a, Mice had AAV-DIO-eNpHR-mCherry (in PV-cre mice) or AAV-Synapsin-eNpHR-mCherry (in wild-type mice) or control viruses AAV-DIO-mCherry (PV-cre mice) or AAV-Syn-mCherry (wild-type mice) injected in the ipsilateral mPFC, AAV-synapsin-GCaMP7f injected in the contralateral mPFC, and a GRIN lens (for microendoscope imaging) implanted in the contralateral mPFC. Experimental design: day 1, no light; day 2, continuous light for inhibition during the rule shift; day 3, no light. **b**, Left, representative images showing DIO-eNpHR in ipsilateral mPFC and Syn-GCaMP7f in contralateral mPFC. Right, DIO-eNpHR in callosal PV^{+} axonal fibres. **c**, Left, representative images of Syn-eNpHR in ipsilateral mPFC and Syn-GCaMP7f in contralateral mPFC. Right, Syn-eNpHR in callosal axonal fibres. **d**,**f**, Performance of controls and Syn-eNpHR mice ($n = 6$ per group) did not change across days. **e**, Performance was impaired in DIO-eNpHR mice ($n = 6$) on day 2 and day 3. **g**, Overview of Ca^{2+} imaging analysis and example data from one experiment. dF/F traces for a subset of neurons and 10 min. We detected events in dF/F traces to generate a binary activity raster, identify periods immediately following correct choices (c) or errors

(e), compute population activity vectors, and calculate the similarity between vectors. **h**,**j**, For controls and Syn-eNpHR mice ($n = 6$ per group), the similarity of activity vectors following rule-shift errors and those following rule-shift correct trials did not change across days. **i**, In DIO-eNpHR mice ($n = 6$ mice), the similarity between activity vectors following rule-shift errors and those following rule-shift correct trials was higher on days 2 and day 3 than on day 1. **k**,**m**, In controls and Syn-eNpHR mice ($n = 6$ per group) the similarity of activity vectors following initial association errors and those following rule-shift errors did not change across days. **l**, In DIO-eNpHR mice ($n = 6$), the similarity of activity vectors following initial association errors and those following rule-shift errors was higher on day 2 and day 3 than on day 1. **n**, Controls ($n = 6$) had higher average activity (fraction of active frames, averaged across neurons) during the 10 s following rule-shift errors compared with the 10 s following rule-shift correct decisions on all days. Two-way ANOVA with Bonferroni post hoc comparisons. **o**, In DIO-eNpHR mice ($n = 6$), the increase in average activity after rule-shift errors depends on the day. Average activity increased after rule-shift errors on day 1, but not on days 2 or day 3. Two-way ANOVA with Bonferroni post hoc comparisons. **p**, In Syn-eNpHR mice ($n = 6$), there is an overall increase in average activity following rule-shift errors. This occured on day 1 and day 3, but not on day 2. Two-way ANOVA with Bonferroni post hoc comparisons. Full statistics are provided in the Methods. Two-way ANOVA followed by Tukey's post hoc comparisons unless otherwise noted. *$P < 0.05$, **$P < 0.01$, **$P < 0.0001$. **b**,**c**, Scale bars: 100 µm (left) and 50 µm (right).

Source data

As in previous experiments, deficits in learning a rule shift observed after inhibiting callosal PV^+ projections persisted on the next day (day 3) without any additional light delivery to activate eNpHR (Fig. 4e). The increased similarity between activity patterns following rule-shift errors and those following correct trials and between rule-shift errors and initial association errors also persisted at this later time point (Fig. 4i,l). By contrast, there was no change in rule-shift performance nor in the similarity of activity patterns after correct versus error rule-shift trials across days in eNpHR-negative controls (Fig. 4d,h,k).

Consistent with our earlier findings, nonspecifically inhibiting all callosal projections (using Syn-eNpHR) did not disrupt rule-shift learning (Fig. 4f). Nonspecifically inhibiting all callosal projections also had no effect on the similarity of activity after rule-shift errors to activity after rule-shift correct trials (Fig. 4j) or initial association errors (Fig. 4m). Thus, callosal inputs can inappropriately maintain previously established neural representations, specifically when callosal PV^+ projections and gamma synchrony are suppressed. Furthermore, callosal PV^+ projections and interhemispheric PV gamma synchrony seem to be specifically involved in regulating callosal communication—when all callosal communication is suppressed, there is no longer a behavioural consequence of inhibiting callosal PV^+ projections and suppressing gamma synchrony.

Discussion

Changes in patterns of activity within the prefrontal cortex are presumed to drive behavioural adaptation. However, the neural mechanisms that switch the mPFC from maintaining previously learned representations and strategies to updating them have not been known. Previous work had suggested the involvement of PV neurons and long-distance gamma synchrony. Here we characterize a novel callosal projection from prefrontal PV neurons, and reveal the multifaceted mechanism whereby this specific synapse modulates particular targets (that is, MD-projecting pyramidal neurons) and network dynamics (gamma oscillations) to regulate circuit interactions (callosal communication) that shape emergent patterns of activity (population activity vectors following error trials) and guide behaviour. Three aspects of this mechanism are particularly notable.

First, the fact that neocortical GABAergic neurons give rise to long-range connections capable of eliciting physiologically meaningful postsynaptic responses has only recently become appreciated, and the behavioural functions of these long-range GABAergic projections are not well understood. Here we show that in mPFC, callosal GABAergic projections from PV^+ neurons promote interhemispheric gamma synchrony, which has previously been shown to be necessary for learning rule shifts. This directly supports a hypothesized role of long-range GABAergic projections in synchronizing rhythmic activity interhemispherically[24], and contrasts with

earlier findings from hippocampal slices which suggested that excitatory synapses on PV interneurons synchronize gamma oscillations across long distances[26]. One limitation is that we cannot directly infer the number of PV interneurons driving these increases in synchrony, because they are based on bulk measurements of fluorescence. However, these measures of synchrony increase by around 50%, making it unlikely that they are driven solely by a small fraction of cells. Whereas many long-range GABAergic projections target mainly downstream GABAergic neurons[21], callosal PV^+ projections innervate a large fraction of layer 5 and layer 6 pyramidal neurons. Furthermore, callosal PV^+ synapses have the same subtype-specificity previously observed for local PV interneuron synapses[27], preferentially inhibiting thalamically projecting rather than callosally projecting pyramidal neurons. This specificity is particularly notable given that we previously found that this mPFC output pathway to MD thalamus is essential for behavioural flexibility[28].

Second, in this task, gamma synchrony does not appear to act via the most basic form of the 'communication through coherence' mechanism[29]. The communication through coherence mechanism proposes that when two regions are synchronized in a coherent manner, they benefit from enhanced effective connectivity. However, in this case, connectivity between the two hemispheres is not actually necessary for rule-shift learning, as activity patterns evolve appropriately and learning is unperturbed when we nonspecifically inhibit all callosal projections. By contrast, when PV^+ callosal projections are selectively inhibited, sparing excitatory callosal communication, mice become perseverative and previously learned representations are inappropriately maintained. In this scenario, excitatory communication between the two hemispheres is intact, but gamma synchrony is lost (Fig. 3g). We previously showed that optogenetically perturbing gamma synchrony (using out-of-phase stimulation across hemispheres) disrupts rule-shift learning[8]. Thus, inter-regional communication is not necessary for normal behaviour; however, when gamma synchrony is lost, inter-regional communication occurs in an aberrant manner that interferes with normal learning. This could occur because, during a gamma cycle, high levels of inhibition gradually fall, producing corresponding changes in excitatory neuron firing[8]. In this way, rhythmic inhibition periodically resets network activity; this reset could

allow the emergence of new representations that diverge from the previously established ones that are stored within patterns of recurrent connections. By contrast, when excitatory input from the contralateral cortex is not appropriately synchronized by PV-driven inhibition, it could arrive prematurely, inappropriately reinforcing previously learned representations and thereby disrupting normal learning. Appropriately timed callosal inhibition might also counterbalance the influence of callosal and recurrent excitation on a specific neuronal population (for example, mPFC–MD projection neurons) that otherwise maintains previously learned associations.

A third surprising feature is that inhibiting callosal PV^+ projections leads to persistent changes in gamma synchrony, neural representations and rule-shift performance. Furthermore, stimulating the same projections can then reverse this behavioural impairment. This reveals a novel form of network plasticity, whereby transiently disrupting connectivity between two brain regions leads to persistent deficits in their ability to synchronize, process information and contribute to behaviour. Notably, the resulting network state, characterized by cognitive inflexibility and deficient task-evoked gamma synchrony, captures key cognitive and circuit endophenotypes of schizophrenia. In many respects, this deleterious network plasticity represents the inverse of our earlier finding that transiently enhancing gamma synchrony (using synchronizing optogenetic stimulation) can persistently rescue rule-shift learning in mutant (heterozygous for *Dlx5* and *Dlx6*) mice[6,8]. Our new findings show that prefrontal circuit plasticity resulting from transient modulations of gamma synchrony is bi-directional, occurs even in previously normal mice, and can be triggered by a previously unappreciated long-range GABAergic projection. It will be important to explore how this plasticity depends on changes in callosal PV^+ projections, callosally projecting PV^+ neurons, and/or additional circuit elements. Future studies could also explore the role of callosal PV^+ projections (and potential plasticity) using behavioural paradigms that differ from those used here in key respects (for example, automated lever-press tasks).

In summary, our results show how a novel connection switches the prefrontal cortex from maintaining to updating behavioural strategies by gating the ability of callosal communication to maintain previously established activity patterns. Furthermore, this connection can trigger a

novel bi-directional form of network plasticity. Thus, callosal connections originating from prefrontal PV neurons represent a critical circuit locus for understanding and potentially correcting deficits in gamma synchrony and behavioural flexibility that are major features of schizophrenia[9,10].

Methods

Mice

All animal care, procedures and experiments were conducted in accordance with NIH guidelines and approved by the Administrative Panels on Laboratory Animal Care at the University of California, San Francisco as well as followed French and European guidelines for animal experimentation and in compliance with the institutional animal welfare guidelines of the Paris Brain Institute. Mice were group housed (2–5 siblings) in a temperature-controlled environment (22–24 °C), had ad libitum access to food and water, and reared in normal lighting conditions (12-h light-dark cycle), until rule-shift experiments began. All experiments were done using PV-cre, wild-type C57/Bl6, and PV-cre Ai14 lines (The Jackson Laboratory). Both male and female adult mice (8–10 weeks and 10–20 weeks old at time of experiment) were used for slice electrophysiology and behavioural experiments, respectively.

Surgery

Male and female mice were anaesthetized using isoflurane (2.5% induction, 1.2–1.5% maintenance, in 95% oxygen) and placed in a stereotaxic frame (David Kopf Instruments). Body temperature was maintained using a heating pad. An incision was made to expose the skull for stereotaxic alignment using bregma and lambda as vertical references. The scalp and periosteum were removed from the dorsal surface of the skull and scored with a scalpel to improve implant adhesion. Viruses were infused at 100–150 nl min^{-1} through a 35-gauge, beveled injection needle (World Precision Instruments) using a microsyringe pump (World Precision Instruments, UMP3 UltraMicroPump). After infusion, the needle was kept at the injection site for 5–10 min and then slowly withdrawn. After surgery, mice were

allowed to recover until ambulatory on a heated pad, then returned to their home cage.

For slice electrophysiology experiments using optogenetic opsins, mice were injected unilaterally in the mPFC, near the border between the prelimbic and infralimbic cortices (1.7 anterior-posterior (AP), + or −0.3 mediolateral (ML), and −2.75 dorsoventral (DV) mm relative to bregma) with 0.4 µl of AAV5-EF1α-DIO-ChR2-eYFP (UNC Vector Core) to selectively target neurons expressing Cre. To allow for virus expression, experiments began at least 3 weeks after injection. For retrograde labelling of mPFC neurons that project callosally versus to mediodorsal (MD) thalamus, cholera toxin subunit B (CTb) conjugated with Alexa Fluor 488 (CTb-488, Invitrogen; 0.2% w/v, 400 nl) was injected in the PFC ipsilateral to the previous AAV-DIO-ChR2 injection (1.7 AP, −0.4 ML, and −2.5 DV mm relative to bregma) and Alexa Fluor 594-conjugated CTb (CTb-594, Invitrogen; 0.2% w/v, 400 nl) was injected in the MD thalamus (contralateral to the AAV-DIO-ChR2 injection) (−1.7 AP, +0.35 ML, −3.5 DV mm relative to bregma). For retrograde labelling of mPFC neurons projecting to the NAc versus dorsal striatum, CTb-488 (0.2% w/v, 400 nl) was injected in the NAc (contralateral to the AAV-DIO-ChR2 injection) (1.34 AP, −1.0 ML, and −4.6 DV mm relative to bregma) and CTb-594 (0.2% w/v, 600 nl) was injected in the dorsal striatum (also contralateral to the AAV-DIO-ChR2 injection) (+0.9 AP, +1.16 ML, −3.0 DV mm relative to bregma). To allow time for retrograde transport of CTb, experiments began one week after CTb injection.

For behavioural experiments using eNpHR and control optogenetics, mice were injected unilaterally in the mPFC, near the border between the prelimbic and infralimbic cortices (1.7 AP, + or −0.3 ML, and −2.75 DV mm relative to bregma) with 1 µl of AAV2-EF1α-DIO-eNpHR3.0-mCherry (UNC Vector Core), 1 µl of AAV5-EF1α-DIO-eYFP (UNC Vector Core), AAV5-hSynapsin-eNpHR3.0-eYFP (UNC Vector Core) or AAV5-hSynapsin-tdTomato (UNC Vector Core), to selectively target Cre-expressing cells or non-selectively target prefrontal neurons. After injecting virus, a 200/240 µm (core/outer) diameter, NA = 0.22, mono fibre-optic cannula (Doric Lenses, MFC_200/240-0.22_2.3mm_FLT) was slowly inserted into mPFC until the tip of the fibre reached a DV depth of −2.25. Implants were affixed onto the skull using Metabond Quick Adhesive

Cement (Parkell). To allow for virus expression, behavioural experiments began at least five weeks after injection.

For behavioural experiments using both NpHR and ChR2 optogenetics, mice were injected unilaterally in the mPFC, near the border between the prelimbic and infralimbic cortices (1.7 AP, −0.3 ML, and −2.75 DV mm relative to bregma) with 0.75 µl of AAV8-nEF-Con/Fon-NpHR3.3-eYFP (Addgene) and 0.75 µl of AAV8-nEF-Con/Fon-ChR2-mCherry (Addgene) or 0.75 µl of AAV8-EF1α-Con/Fon-mCherry (Addgene) and contralaterally in PFC (1.7 AP, +0.3 ML, −2.75 DV mm relative to bregma) with 0.7 µl AAVrg-EF1α-FlpO (Addgene), to selectively target Cre-expressing cells in ipsilateral PFC that send projections to contralateral PFC. After injecting virus, a 200/240 µm (core/outer) diameter, NA = 0.22, mono fibre-optic cannula (Doric Lenses, MFC_200/240-0.22_2.3mm_FLT) was slowly inserted into mPFC until the tip of the fibre reached a DV depth of −2.25. Implants were affixed onto the skull using Metabond Quick Adhesive Cement (Parkell). To allow for virus expression, behavioural experiments began at least five weeks after injection.

For behavioural experiments that combined dual-site voltage indicator imaging with optogenetics, mice were injected bilaterally at 3 depths (DV: −2.5, −2.25 and −2.0) at the following AP/ML for mPFC: 1.7 AP, ±0.3 ML with 3 × 0.2 µl of AAV1-CAG-DIO-Ace2N-4AA-mNeon (Virovek). Mice were also injected unilaterally in the mPFC (1.7 AP, −0.3 ML, and −2.75 DV mm relative to bregma) with either 1 µl of AAV2-EF1α-DIO-eNpHR3.0-BFP (Virovek) or 1 µl of AAV5-EF1α-DIO-mCherry (UNC Vector Core), 1 µl of AAV2-hSynapsin-eNpHR3.0-mCherry (UNC Vector Core) or 1 µl of AAV2-hSynapsin-mCherry (UNC Vector Core). After injection of virus, two 400/430 µm (core/outer) diameter, NA = 0.48, multimode fibre implants (Doric Lenses, MFC_400/430-0.48_2.8mm_ZF1.25_FLT) were slowly inserted into the mPFC at a ±12° angle using the following coordinates: 1.7 (AP), ±0.76 (ML), −2.14 (DV). To allow for virus expression, behavioural experiments began at least five weeks after injection.

For behavioural experiments that combined in vivo calcium imaging with optogenetics, mice were injected unilaterally at 4 depths (DV: −2.75, −2.5, −2.25, −2.0) at the following AP/ML for mPFC: 1.7 AP, +0.4 ML with diluted (1:3; Addgene) 4 × 0.15 µl of AAV9-synapsin-jGCaMP7f-WPRE

(Addgene). Mice were also injected unilaterally in the contralateral mPFC (1.7 AP, −0.3 ML, and −2.75 DV mm relative to bregma) with either 1 µl of AAV2-EF1α-DIO-eNpHR3.0-mCherry (UNC Virus Core), 1 µl of AAV5-EF1α-DIO-mCherry (UNC Virus Core), 1 µl of AAV2-hSynapsin-eNpHR3.0-mCherry (UNC Virus Core) or 1 µl of AAV2-hSynapsin-mCherry (UNC Virus Core). After injection of virus, a 0.5 mm × 4.0 mm-long integrated GRIN lens (Inscopix) was slowly advanced into the mPFC until the tip was placed at 1.7 AP, +0.4 ML, DV −2.25 and cemented in place with Metabond Quick Adhesive Cement (Parkell). To allow for virus expression, behavioural experiments began at least five weeks after injection.

Slice preparation and analysis

Adult mice were anaesthetized using isoflurane and decapitated, and their brains were rapidly removed. Coronal slices (250 µm thick) were cut from adult mice of either sex using a vibratome (VT1200S Leica Microsystems) and a chilled slicing solution in which Na^+ was replaced by sucrose, then incubated in warmed artificial cerebrospinal fluid (ACSF) at 30-31 °C for 15 min and then at least 1 h at room temperature before being used for recordings. ACSF contained (in mM): 126 NaCl, 26 $NaHCO_3$, 2.5 KCl, 1.25 NaH_2PO_4, 1 $MgCl_2$, 2 CaCl and 10 glucose. Slices were secured by placing a harp along the midline between the two hemispheres.

Somatic whole-cell patch recordings were obtained from ChR2-negative neurons amid ChR2-positive axonal fibres in the mPFC contralateral to the site of virus injection, on an upright microscope (BX51WI; Olympus). Recordings were made using a Multiclamp 700A (Molecular Devices). Patch electrodes (tip resistance = 2–6 MOhms) were filled with the following (in mM): 130 potassium gluconate, 10 KCl, 10 HEPES, 10 EGTA, 2 $MgCl_2$, 2 MgATP, and 0.3 NaGTP (pH adjusted to 7.3 with KOH). All recordings were at 32.5 ± 1 °C. Series resistance was usually 10–20 MΩ, and experiments were discontinued above 30 MΩ.

Intrinsic properties were calculated based on the current-clamp responses to a series of 250 msec current pulse injections from −200 to 450 pA (50 pA per increment). Spiking properties were calculated based on the response to

a current pulse that was 100 pA above the minimal level that elicited spiking. Neurons were classified as fast spiking if they met 3 out of the 4 following criteria: action potential (AP) half-width was < 0.5 ms, firing frequency > 50 Hz, fast after hyperpolarization (fAHP) amplitude > 14 mV, and spike-frequency accommodation (SFA) index < 2.

In vitro ChR2 stimulation

Stimulation of channelrhodopsin (ChR2) in callosal PV terminals was performed using ~4–5 mW flashes of light generated by a Lambda DG-4 high-speed optical switch with a 300 W Xenon lamp (Sutter Instruments) or by an LED (Cairn Research OptoLED Lite), and an excitation filter set centred around 470 nm, delivered to the slice through a 40× objective (Olympus). Illumination was delivered across a full high-power (40×) field. To measure IPSPs, current-clamp recordings were performed while stimulating ChR2 using trains of light pulses (5 ms light pulses at 5 Hz, 20 Hz, and 40 Hz). In experiments in which glutamatergic and $GABA_A$ receptors were blocked, drugs were bath applied at the following concentrations (in μM): 10 CNQX (Tocris) or 20 DNQX (Tocris), 50 APV (Tocris), and 10 gabazine (Sigma). Drugs were prepared as concentrated stock solutions and were diluted in ACSF on the day of the experiment.

Rule-shift task

This cognitive flexibility task has been described previously[6]. In brief, mice are singly housed and habituated to a reverse light/dark cycle, and food intake is restricted until the mouse is 80–85% of the ad libitum feeding weight. After mice reached their target weight, they underwent one day of habituation. On this day, mice were given ten consecutive trials with the baited food bowl to ascertain that they could reliably dig and that only one bowl contained food reward. All mice were able to dig for the reward, and started the task the next day. At the start of each trial, the mouse was placed in its home cage to explore two bowls, each containing one odour and one digging medium, until it dug in one bowl, signifying a choice. As soon as a mouse began to dig in the incorrect bowl, the other bowl was removed, so there was no opportunity for ‘bowl switching’ (digging is defined as the sustained displacement of the medium within a bowl). The bait was a piece

of a peanut butter chip (approximately 5–10 mg in weight) and the cues, either olfactory (odour) or somatosensory and visual (texture of the digging medium which hides the bait), were altered and counterbalanced. All cues were presented in small animal food bowls (All Living Things Nibble bowls, PetSmart) that were identical in colour and size. Digging media were mixed with the odour (0.01% by volume) and peanut butter chip powder (0.1% by volume). All odours were ground dried spices (McCormick or Alpi Nature garlic and McCormick or Albert Ménès coriander), and unscented digging medium (Mosser Lee White Sand Soil Cover or Scalare Sable de Rivière, Natural Integrity Clumping Clay or Monoprix cat litter).

After mice reached their target weight, they underwent one day of habituation. On this day, mice were given ten consecutive trials with the baited food bowl to ascertain that they could reliably dig and that only one bowl contained food reward. Specifically, the habituation trials are used to train the mouse on the mechanics of the task, there is no association made between food reward and cue. All mice were able to dig for the reward. Mice do not undergo any other specific training before being tested on the task. Then, on days 1 and 2 (and in some cases, on additional days as well), mice performed the task (this was the testing done for experiments). After the task was done for the day, the bowls were filled with different odour–medium combinations and food was evenly distributed among these bowls and given to the mouse so that no specific cue was rewarded greater than the other cues present. The same stimuli were used across days—only the cue that is associated with the food reward changed.

Mice were tested through a series of trials. The determination of which odour and medium to pair and which side (left or right) contained the baited bowl was randomized (subject to the requirement that the same combination of pairing and side did not repeat on more than three consecutive trials) using https://www.random.org. On each trial, while the particular odour–medium combination present in each of the two bowls may have changed, the particular stimulus (for example, a particular odour or medium) that signalled the presence of food reward remained constant over each portion of the task (initial association and rule shift). If the initial association paired a specific odour with food reward, then the digging medium would be considered the irrelevant dimension. The mouse is considered to have learned the initial association between stimulus and reward if it makes eight

correct choices during ten consecutive trials. Each portion of the task ended when the mouse met this criterion. Following the initial association, the rule-shift portion of the task began, and the particular stimulus associated with reward underwent an extra-dimensional shift. For example, if an odour had been associated with reward during the initial association, then a digging medium was associated with reward during the rule-shift portion of the task. The mouse is considered to have learned this extra-dimensional rule shift if it makes 8 correct choices during ten consecutive trials. When a mouse makes a correct choice on a trial, it is allowed to consume the food reward before the next trial. Following correct trials, the mouse is transferred from the home cage to a holding cage for about 10 s while the new bowls were set up (ITI). After making an error on a trial, a mouse was transferred to the holding cage for about 2 min (ITI). For Extended Data Fig. 4p–z, the ITI following errors was 30 s in the holding cage. All animals performed the initial association in a similar number of trials (average: 10–15 trials). Experiments were performed blind to the virus injected. Videos were manually scored with a temporal resolution of 1 s.

For analyses (described below), the onset of digging was chosen as the time of a decision for two reasons. First, as noted above, once a mouse began to dig in the incorrect bowl, the other (correct) bowl was removed. Second, only upon the commencement of digging could a mouse determine whether reward was present in the chosen bowl and obtain feedback about whether or not it had made a correct choice. The time windows used for analysis excluded periods when the mouse moved from the home cage to the holding cage and vice versa.

Rule-reversal task

This cognitive flexibility task was described previously[6,8]. Similarly to the mechanics of the rule-shift task described above, after the initial association, the rule-reversal portion of the task began, and the particular stimulus associated with reward underwent an intra-dimensional reversal. For example, if an odour had been associated with reward during the initial association, then the previously unrewarded odour became associated with reward during the rule-reversal portion of the task. The mouse was

considered to have learned the intra-dimensional rule reversal when it made eight correct choices out of ten consecutive trials.

In vivo optogenetic stimulation

For behavioural experiments using optogenetic eNpHR stimulation: A 532 nm green laser (OEM Laser Systems) was coupled to the mono fibre-optic cannula (Doric Lenses) with a zirconia sleeve (Doric Lenses) through a 200-µm-diameter mono fibre-optic patch cord (Doric Lenses) and adjusted such that the final light power was 2.5 mW. For behavioural experiments using optogenetic ChR2 stimulation: A 473 nm blue laser (OEM Laser Systems) was coupled to the mono fibre-optic cannula (Doric Lenses) with a zirconia sleeve (Doric Lenses) through a 200 µm diameter mono fibre-optic patch cord (Doric Lenses, Inc.) and adjusted such that the final light power was 0.5 mW. A function generator (Agilent 33500B Series Waveform Generator) connected to the laser generated a 40-Hz train of 5-ms pulses.

Extended Data Fig. 2 shows experiments designed to control for potential behavioural effects of scattered light from one hemisphere activating eNpHR in PV neuron cell bodies in the contralateral hemisphere. These experiments used a final light power of 0.1 mW when connected to the 532 nm green laser (OEM Laser Systems) or 638 nm red laser (Doric Lenses). To determine the appropriate light power for these experiments, a mouse was implanted with a dual fibre-optic cannula (Doric Lenses; DFC_200/240-0.22_2.3mm_GS0.7_FLT) without virus injection in order to measure light scattering from one mPFC to the contralateral hemisphere. Using a dual fibre-optic patch cord (Doric Lenses; DFP_200/240/900-0.22_2m_GS0.7-2FC), light was delivered to the mPFC on one side, and the light coming through the other side was measured using a light meter (ThorLabs, PM100D). The final light power delivered to one mPFC was 2.5 mW, across wavelengths 532 nm, 594 nm, and 638 nm—similar to what was used in the optogenetic and optogenetic and dual-site voltage indicator experiments. Measurements of 40 nW, 20 nW, and 50 nW at the contralateral fibre were observed, respectively. Accounting for transmission loss of the patch cord (for example, only 80% of the light is transmitted from end to end), the scattered light power entering the fibre tip would be 50 nW, 25 nW and 62.5 nW respectively. This measurement likely overestimates the actual light

entering via the fibre tip located in brain parenchyma since it will include both scattered light within the brain and contamination from ambient room light. Conversely, this measurement only includes light located in the vicinity of the fibre tip that is traveling at an appropriate angle to enter the fibre (which has numerical aperture 0.22 implying a 25.4° acceptance angle). Therefore, to be extremely conservative, experiments in Extended Data Fig. 2 utilized a final light power of 0.1 mW, which is >1,000 times stronger than the measured scattered light power. Both 532 nm and 638 nm at this final light power ipsilateral to the viral injection site was used.

Experiments in Extended Data Fig. 2l–o were similar to other experiments using optogenetic eNpHR stimulation except in the following respects: mice were injected with 0.7 µl of AAV2-EF1α-DIO-eNpHR3.0-mCherry (UNC Vector Core) and 0.4 µl of AAV5-EF1α-DIO-ChR2-eYFP (UNC Vector Core), to selectively target Cre-expressing cells (although ChR2 stimulation was not ultimately used in these experiments). Light for optogenetic eNpHR stimulation was specifically switched on on day 2 during ITIs (when the mouse was in the holding cage) and switched off during the trial in the home cage.

For all optogenetic experiments, light stimulation began once mice reached the 80% criterion during the initial association portion of the task. Mice then performed three additional initial association trials with the light stimulation before the rule-shift portion of the task began. The light stimulation did not alter the performance or behaviour of the mice during these three extra trials of the initial association. Experiments were performed blind to virus injected.

Combined dual-site voltage indicator imaging and optogenetic eNpHR stimulation

High-bandwidth, time-varying bulk fluorescence signals were measured at each recording site using the dual-site voltage-indicator technique[8], with some modifications as described below.

Optical apparatus

A fibre-optic stub (400 μm core, NA = 0.48, low-autofluorescence fibre; Doric Lenses, MFC_400/430-0.48_2.8mm_ZF1.25_FLT) was stereotaxically implanted in each targeted brain region. A matching fibre-optic patch cord (Doric Lenses, MFP_400/430/1100-0.48_2m_FC-ZF1.25) provided a light path between the animal and a miniature, permanently aligned optical bench, or 'mini-cube' (Doric Lenses, FMC5_E1(460-490)_F1(500-540)_E2(555-570)_F2(580-600)_S). One fibre on the ipsilateral side of the viral injection of either 1 μl of AAV2-EF1α-DIO-eNpHR3.0-BFP (Virovek) or 1 μl of AAV5-EF1α-DIO-mCherry (UNC Vector Core) was used to both deliver excitation light to and collect emitted fluorescence from that recording site. The fibre contralateral to the viral injection site was connected to a separate mini-cube (Doric Lenses, FMC6_E1(460-490)_F1(500-540)_E2(555-570)_F2(580-600)_O(628-642)_S) that was attached to a 638 nm laser (Doric Lenses) and was used to deliver excitation light and optogenetic stimulation to and collect emitted fluorescence from that recording site. The far end of the patch cord and each 1.25 mm diameter zirconia optical implant ferrule were cleaned with isopropanol before each recording, then securely attached via a zirconia sleeve.

For the first mini-cube sans laser port, optics allow for the simultaneous monitoring of two spectrally separated fluorophores, with dichroic mirrors and cleanup filters chosen to match the excitation and emission spectra of the voltage sensor and reference fluorophores in use ('mNeon' voltage sensor channel: excitation 460–490 nm, emission 500–540 nm; 'red' control fluorophore: excitation 555–570 nm, emission 580–600 nm). The mini-cube optics are sealed and permanently aligned and all five ports (sample to animal, two excitation lines and two emission lines) are provided with matched coupling optics and FC connectors to allow for a modular system design.

For the second mini-cube that contains a port for optogenetic stimulation, a 565 nm LED and 555–570 nm filter is used to excite tdTomato, a 580–600 nm filter is used for tdTomato emission, and a 638 nm laser with 628–642 nm filter is used to excite eNpHR. The light used to excite eNpHR does not interfere with the genetically encoded voltage indicator based measurements of synchrony, and the light used to excite tdTomato does not activate eNpHR enough to affect rule-shift performance. This is due to two factors. First, the

eNpHR and tdTomato excitation spectra are offset—for example, at 605 nm, eNpHR activation is near its peak whereas relative excitation of tdTomato is <1%. Second, the intensity used to excite tdTomato is just ~0.1 mW, which is ~50-fold less than what was used to activate eNpHR and disrupt rule-shift performance. The mini-cube optics are sealed and permanently aligned and all six ports (sample to animal, three excitation lines and two emission lines) are provided with matched coupling optics and FC connectors to allow for a modular system design.

To perform dual-site voltage indicator recordings, excitation light for each of the two colour channels was provided by a fibre-coupled LED (Center wavelengths 490 nm and 565 nm, Thorlabs M490F3 and M565F3) connected to the mini-cube by a patch cord (200 μm, NA = 0.39; Thorlabs M75L01). Using a smaller diameter for this patch cord than for the patch cord from the cube to the animal is critical to reduce the excitation spot size on the output fibre face and thus avoid cladding autofluorescence. LEDs were controlled by a 4-channel, 10-kHz-bandwidth current source (Thorlabs DC4104). LED current was adjusted to give a final light power at the animal (averaged during modulation, see below) of approximately 200 μW for the mNeon channel (460–490 nm excitation), and 100 μW for the Red channel (555–570 nm excitation).

Each of the two emission ports on the mini-cube was connected to an adjustable-gain photoreceiver (Femto, OE-200-Si-FC; Bandwidth set to 7 kHz, AC-coupled, 'low'gain of $\sim 5 \times 10^7$ V W^{-1}) using a large-core high-NA fibre to maximize throughput (600 μm core, NA = 0.48 (Doric lenses, MFP_600/630/LWMJ-0.48_0.5m_FC-FC).

Note that, for dual-site voltage indicator recordings and optogenetics experiments, two completely independent optical setups were employed, with separate implants, patch cords, mini-cubes, LEDs, a separate laser, photoreceivers, and lock-in amplifiers.

Modulation and lock-in detection

At each recording site, each of the two LEDs was sinusoidally modulated at a distinct carrier frequency to reduce crosstalk due to overlap in fluorophore spectra. The corresponding photoreceiver outputs were then demodulated

using lock-in amplification techniques. A single instrument (Stanford Research Systems, SR860) was used to generate the modulation waveform for each LED and to demodulate the photoreceiver output at the carrier frequency. To further reduce crosstalk between recording sites, distinct carrier frequencies (2, 2.5, 3.5 and 4 kHz) were used across sites. Low-pass filters on the lock-in amplifiers were selected to reject noise above the frequencies under study (cascade of 4 Gaussian FIR filters with 84 Hz equivalent noise bandwidth; final attenuation of signals are approximately −1dB (89% of original magnitude) at 20 Hz, −3dB (71% of original magnitude) at 40 Hz, and −6dB (50% of original magnitude) at 60 Hz).

In vivo dual-site voltage indicator imaging

Analogue signals were digitized by a multichannel real-time signal processor (Tucker-Davis Technologies; RX-8). The commercial software Synapse (Tucker-Davis Technologies) running on a PC was used to control the signal processor, write data streams to disk, and to record synchronized video from a generic infrared USB webcam (Ailipu Technology, ELP-USB100W05MT-DL36). Lock-in amplifier outputs were digitized at 3 kHz.

Combined dual-site voltage indicator imaging and optogenetics analysis

Analysis of voltage indicator data was described previously[8] and was facilitated using the signal processing toolbox and MATLAB (Mathworks), using the following functions: fir1, filtfilt, and regress. All four signals during the entire time series of the experiment (left mNeon, left tdTomato, right mNeon, right tdTomato) were first filtered around a frequency of interest. To quantify zero-phase lag cross-hemispheric synchronization between left and right mNeon signals, a linear regression analysis was performed to predict the right mNeon signal using the following inputs: left mNeon signal, left tdTomato signal, and right tdTomato signal. The goodness of fit is compared to how well the regression works if the left mNeon signal is shuffled, i.e., if a randomly chosen segment of the original left mNeon signal is used, instead of the segment recorded at the same time as the right mNeon signal. R^2 values are calculated as a function of time using one second segments and compared to the 99th percentile of the

distribution of R^2 values obtained from 100 fits to randomly shuffled data. The fraction of time points at which the R^2 obtained from actual data exceeds the 99th percentile of the R^2 values obtained from shuffled data was used to measure zero-phase lag synchronization between the left and right mNeon signals.

This analysis was performed at the time of the decision (for example, immediately following the beginning of digging in one bowl, until the end of digging), and smoothed measurements over a 5-min time window following the time point of interest. The first five trials of the rule shift were analysed. Experiments were performed, scored and analysed blind to virus injected.

Shorter-timeframe resolution dual-site voltage indicator imaging and optogenetics analysis

For high temporal resolution quantification of synchrony between signals from dual-site voltage indicator recordings, we first bandpass-filtered Ace-mNeon and tdTomato signals as described above. Then, we 'corrected' the filtered Ace-mNeon signal (to minimize artefacts and noise) by fitting the ipsilateral filtered tdTomato signal via robust linear regression using the robustfit function in Matlab and a time windows of 250 ms. Then, we subtracted off this fit of the tdTomato signal from the filtered Ace-mNeon signal to obtain a corrected Ace-mNeon signal. We then calculated zero-lag cross-correlation between the corrected Ace-mNeon signals from the left and right mPFC across the whole session using 1-s windows.

Combined calcium imaging and optogenetics

Imaging data were collected using a miniaturized one-photon microscope (nVoke2; Inscopix). GCaMP7f signals (calcium activity) were detected using 435–460 nm excitation LED (0.1–0.2 mW), and optogenetic stimulation of eNpHR-expressing axons was performed using a second 590–650 nm excitation LED (1–2 mW light power). nVoke2 software (Inscopix) was used to control the microscope and collect imaging data. Images were acquired at 20 frames per second, spatially downsampled (4×), and were stored for offline data processing. An input TTL from a separate ANY-maze computer

(Stoelting Europe) to the nVoke2 acquisition software were used to synchronize calcium imaging and mouse behaviour movies.

Combined calcium-imaging and optogenetics analysis

Calcium-imaging movies were preprocessed using Inscopix Data Processing Software (IDPS; Inscopix). The video frames were spatially filtered (bandpass) with cut-offs set to 0.008 pixel^{-1} (low) and 0.3 pixel^{-1} (high) followed by frame-by-frame motion correction for removing movement artefacts associated with respiration and head-unrestrained behaviour. The mean image over the imaging session was computed, and the d*F/F* was computed using this mean image. The resultant preprocessed movies were then exported into MATLAB, and cell segmentation was performed using an open-source calcium-imaging software (CIAPKG)[30]. Specifically, a principal component analysis/independent component analysis (PCA/ICA) approach was used to detect and extract regions of interest (presumed neurons) per field of view[31]. For each movie, the extracted output neurons were then manually sorted to remove overlapping neurons, neurons with low signal-to-noise ratio, and neurons with aberrant shapes. Accepted neurons and their calcium activity traces were exported to MATLAB for further analysis using custom scripts as previously described[32]. In brief, the s.d. (σ) of the calcium movie was calculated and this was used to perform threshold-based event detection on the traces by first detecting increases in d*F/F* exceeding 2 (over 1 s). Subsequently, events were detected that exceeded 10 for over 2 s and had a total area under the curve higher than 150σ. The peak of the event was estimated as the local maximum of the entire event. For an extracted output neuron, active frames were marked as the period from the beginning of an event until the calcium signal decreased 30% from the peak of the event (up to a maximum of 2 s).

We calculated the similarity of population activity vectors using the ‘cosine similarity’, which is equivalent to computing the normalized dot product between the two vectors, that is:

$$(\sum {x}_{i}\,{y}_{i})\,/\,{[(\sum {{x}_{i}}^{2})(\sum {{y}_{i}}^{2})]}^{1/2}$$

where x_i and y_i represent the average activity of the ith neuron in the two population activity vectors. Each vector was the average of activity during the 10 s immediately following a choice. We computed the similarity between each pair of vectors, then averaged this similarity across all the pairs from one mouse.

The first five trials of the rule shift were analysed. For Extended Data Fig. 10t–u, the last five initial association trials and the additional initial association trials during optogenetic inhibition were analysed.

Histology and imaging

All mice used for behavioural and imaging experiments were anaesthetized with Euthasol and transcardially perfused with 30 ml of ice-cold 0.01 M PBS followed by 30 ml of ice-cold 4% paraformaldehyde in PBS. Brains were extracted and stored in 4% paraformaldehyde for 24 h at 4 °C before being stored in PBS. Slices 70–100 μm thick were obtained on a Leica VT100S and mounted on slides. All imaging was performed on an Olympus MVX10, Nikon Eclipse 90i, Zeiss LSM510, Zeiss Axioskop2, Zeiss ApoTome.2, and Keyence BZ-X All-in-One Fluorescence Microscope. All mice were verified to have virus-driven expression and optical fibres located in the mPFC. For mice used in parvalbumin immunohistochemistry, 60-μm slices from PV-cre mice injected with AAV2-EF1α-DIO-ChR2-eYFP unilaterally in PFC were obtained on a Leica VT100S and were rinsed twice at room temperature (10 min each) in PBS and incubated overnight at 4 °C with 0.3% Triton X-1000, 0.1% normal donkey serum (NDS) and monoclonal anti-PV antibody (1:1,000; Sigma). Slices were then rinsed twice in PBS (10 min each) at room temperature and incubated with Alexa 688 goat anti-mouse antibody (1:500; Invitrogen) for 3 h at room temperature. Slices were then rinsed twice in PBS (10 min each) at room temperature and coverslipped in mounting medium. Immunofluorescence was then observed with Zeiss ApoTome.2 and images were acquired.

Data analyses and statistics

Statistical analyses were performed using Prism 8 (GraphPad) and detailed in the corresponding figure legends. Quantitative data are expressed as the

mean and error bars represent the s.e.m. Group comparisons were made using two-way ANOVA followed by Bonferroni post hoc tests to control for multiple comparisons unless otherwise noted. Paired and unpaired two-tailed Student's *t*-tests were used to make single-variable comparisons. Similarity of variance between groups was confirmed by the *F* test. Measurements were taken from distinct samples and from samples that were measured repeatedly. *$P < 0.05$, **$P < 0.01$, ***$P < 0.001$, ****$P < 0.0001$. Comparisons with no asterisk or 'NS' had $P > 0.05$ and were considered not significant. No statistical methods were used to pre-determine sample sizes but our sample size choice was based on previous studies[6,8] and are consistent with those generally employed in the field. Data distribution was assumed to be normal, but this was not formally tested.

For Fig. 3d,e,k,l, full statistics are: optogenetic inhibition of callosal mPFC PV terminals impairs rule shifts in DIO-eNpHR mice ($n = 5$) compared to DIO-mCherry controls ($n = 4$) on days 2 and 3 (two-way ANOVA (task day × virus); interaction: $P = 0.0009$). **d**, DIO-mCherry performance did not change (day 1 to 2: $P = 0.28$; day 1 to 3: $P = 0.094$; day 2 to 3: $P > 0.99$). **d**,**e**,**k**,**l**, Two-way ANOVA (task day × virus) comparing rule-shift (RS) performance across groups (interaction: $P < 0.0001$), showed no group difference on day 1 but significant impairment on days 2 and 3 for DIO-eNpHR compared to DIO-mCherry and Syn-tdTomato. **e**, Optogenetic inhibition of mPFC callosal PV terminals impairs rule shifts in DIO-eNpHR mice compared to DIO-mCherry controls (day 1 to 2: $P = 0.014$; day 1 to 3: $P = 0.012$; day 2 to 3: $P = 0.075$). For Fig. 3f,g, full statistics are: 30–50 Hz synchronization is higher after RS errors than after RS correct decisions across task days in controls ($n = 4$ mice; two-way ANOVA; main effect of trial type: $P = 0.0056$; day 1: $P = 0.004$; day 2: $P = 0.005$; day 3: $P = 0.022$). **g**, Gamma synchrony is higher after RS errors than after RS correct decisions for DIO-eNpHR mice on day 1 (no light), but not days 2 and 3 ($n = 5$ mice; two-way ANOVA (trial type × task day); interaction: $P = 0.0039$; day 1: $P = 0.0056$; day 2: $P = 0.16$; day 3: $P = 0.23$). Differences in gamma synchrony between RS errors and correct trials are also significantly lower in DIO-eNpHR mice compared to controls on days 2 (two-way ANOVA (trial type × virus); interaction: $P = 0.018$) and 3 (two-way ANOVA (trial type × virus); interaction: $P = 0.034$). We then performed two-way ANOVA (task day × virus, type of error) comparing gamma synchrony across groups

with appropriate post hoc tests corrected for multiple comparisons; gamma synchrony is lower for DIO-eNpHR mice compared to matched controls on error (interaction: $P = 0.049$), but not correct trials (interaction: $P = 0.93$) on both days 2 ($P = 0.0089$) and 3 ($P = 0.016$). For Fig. 3k–n, full statistics are: inhibiting callosal terminals does not affect rule shifts in Syn-eNpHR mice ($n = 5$) compared to controls ($n = 4$) across days (two-way ANOVA (task day × virus); $P = 0.37$). **k**, Performance of controls did not change across days (day 1 to 2: $P = 0.48$; day 1 to 3: $P > 0.99$; day 2 to 3: $P > 0.99$). **l**, Performance of Syn-eNpHR mice did not change across days (day 1 to 2: $P > 0.99$; day 1 to 3: $P = 0.96$; day 2 to 3: $P = 0.85$). **m**, Interhemispheric 30–50 Hz synchronization is higher after RS errors than RS correct decisions across days in controls ($n = 4$ mice; two-way ANOVA; main effect of trial type: $P = 0.020$; day 1: $P = 0.015$; day 2: $P = 0.049$; day 3: $P = 0.025$). **n**, Gamma synchrony is higher after RS errors than RS correct decisions for Syn-eNpHR mice on day 1 (no light). This was abolished with light on day 2, then restored in the absence of light on day 3 ($n = 5$ mice; two-way ANOVA; (trial type × task day); interaction: $P = 0.011$; day 1: $P = 0.037$; day 2: $P = 0.46$; day 3: $P = 0.021$). Gamma synchrony is lower for Syn-eNpHR mice compared to matched controls on error (two-way ANOVA; interaction: $P = 0.045$) but not correct trials (interaction: $P = 0.74$) on day 2 ($P = 0.043$), but not on day 3 ($P = 0.58$). Two-way ANOVA followed by Bonferroni post hoc comparisons was used.

For Fig. 4d–f, full statistics are: optogenetic inhibition of callosal PV terminals impairs rule shifts in DIO-eNpHR mice ($n = 6$) compared to controls ($n = 6$) and Syn-eNpHR mice ($n = 6$) on days 2 and 3 (two-way ANOVA (task day × virus); interaction: $P < 0.0001$). **d**, Performance of controls did not change (day 1 to 2: $P = 0.057$; day 1 to 3: $P = 0.12$; day 2 to 3: $P = 0.67$). **e**, Optogenetic inhibition of callosal PV terminals impairs rule shifts in DIO-eNpHR mice (day 1 to 2: $P = 0.020$; day 1 to 3: $P = 0.010$; day 2 to 3: $P > 0.99$). **f**, Performance of Syn-eNpHR mice did not change (day 1 to 2: $P = 0.58$; day 1 to 3: $P = 0.82$; day 2 to 3: $P > 0.99$). For Fig. 4h,j, full statistics are: optogenetic inhibition changes the similarity of activity vectors specifically in DIO-eNpHR mice (two-way ANOVA, main effect of task day: $P = 0.017$; task day × group interaction: $P = 0.32$). **h**, For controls ($n = 6$ mice), there is no change across days in the similarity between activity vectors after RS errors and those after correct decisions (day 1 to 2: $P = 0.57$; day 1 to 3: $P = 0.32$; day 2 to 3: $P = 0.90$). **i**, In DIO-eNpHR mice ($n =$

6 mice), there is an increase in the similarity between activity vectors after RS errors and those after correct decisions from day 1 (before optogenetic inhibition) to days 2 and 3 (during and after inhibition, respectively) (day 1 to 2: $P = 0.044$; day 1 to 3: $P = 0.0067$; day 2 to 3: $P = 0.71$). **j**, For Syn-eNpHR mice ($n = 6$ mice), there is no change across days in the similarity between activity vectors after RS errors and those after correct decisions (day 1 to 2: $P = 0.99$; day 1 to 3: $P = 0.93$; day 2 to 3: $P = 0.98$). Two-way ANOVA to compare the change in activity vector similarity from day 1 to 2 in the DIO-eNpHR group to a group consisting of the eNpHR-negative and synapsin-eNpHR mice, using mouse, day, and day × group interaction as factors revealed a significant day × group interaction ($P = 0.040$). **k**–**m**, The similarity between activity vectors after decisions on error trials during the initial association (IA) and those during the RS. There is increased similarity across days in DIO-eNpHR mice ($n = 6$; two-way ANOVA (task day × virus); interaction: $P = 0.025$). **k**, There is no change in the similarity of population activity vectors after IA errors and RS errors across days in controls ($n = 6$; day 1 to 2: $P = 0.99$; day 1 to 3: $P = 0.52$; day 2 to 3: $P = 0.50$). **l**, During and following optogenetic inhibition on days 2 and 3 in DIO-eNpHR mice, there is an increase in the similarity of population activity vectors following IA versus RS error trials (day 1 to 2: $P = 0.0038$; day 1 to 3: $P = 0.0045$; day 2 to 3: $P = 0.95$). **m**, In Syn-eNpHR mice, there is no change in the similarity of population activity vectors following IA versus RS errors trials across days ($n = 6$; day 1 to 2: $P = 0.41$; day 1 to 3: $P = 0.90$; day 2 to 3: $P = 0.24$). **n**, Controls have increases in average activity (fraction of frames in which a neuron is active, averaged across all neurons) during the 10 s following RS errors compared to the 10 s following RS correct decisions on all days ($n = 6$; two-way ANOVA, main effect of trial type: $P = 0.010$; day 1: Bonferroni $P = 0.022$; day 2: Bonferroni $P = 0.015$; day 3: Bonferroni $P = 0.016$). **o**, DIO-eNpHR mice have an increase in average activity after errors that depends on the day ($n = 6$; two-way ANOVA (task day × trial type); interaction: $P = 0.0003$). This difference occurs on day 1 (Bonferroni $P < 0.0001$), but is abolished with light delivery on day 2 (Bonferroni $P > 0.99$), and continues to be absent even without further light delivery on day 3 (Bonferroni $P > 0.99$). **p**, In Syn-eNpHR mice, there is an overall increase in average activity following error trials ($n = 6$; two-way ANOVA, main effect of trial type: $P = 0.0088$). This occurs on days 1 (Bonferroni $P = 0.038$) and 3 (Bonferroni $P = 0.016$), but not with

light delivery on day 2 (Bonferroni $P > 0.99$). Two-way ANOVA followed by Tukey post hoc comparisons was used unless otherwise noted.

Reporting summary

Further information on research design is available in the Nature Portfolio Reporting Summary linked to this article.

Data availability

The data that support the findings of this study are available from the corresponding author upon reasonable request. The underlying physiological data (trial-by-trial measurements of synchrony and population activity vectors) and associated MATLAB code are available on Zenodo at https://doi.org/10.5281/zenodo.7709805. Source data are provided with this paper.

Code availability

Custom codes for analysis and modelling were written in MATLAB and are available on Zenodo (https://doi.org/10.5281/zenodo.7709805) as well as from the corresponding author upon request.

References

1. Miller, E. K. & Cohen, J. D. An integrative theory of prefrontal cortex function. *Annu. Rev. Neurosci.* **24**, 167–202 (2001).

2. Durstewitz, D., Vittoz, N. M., Floresco, S. B. & Seamans, J. K. Abrupt transitions between prefrontal neural ensemble states accompany behavioral transitions during rule learning. *Neuron* **66**, 438–448 (2010).

3. Karlsson, M. P., Tervo, D. G. R. & Karpova, A. Y. Network resets in medial prefrontal cortex mark the onset of behavioral uncertainty. *Science* **338**, 135–139 (2012).

4. Seo, H., Cai, X., Donahue, C. H. & Lee, D. Neural correlates of strategic reasoning during competitive games. *Science* **346**, 340–343 (2014).

5. Domenech, P., Rheims, S. & Koechlin, E. Neural mechanisms resolving exploitation-exploration dilemmas in the medial prefrontal cortex. *Science* **369**, eabb0184 (2020).

6. Cho, K. K. A. et al. Gamma rhythms link prefrontal interneuron dysfunction with cognitive inflexibility in *Dlx5/6*$^{+/-}$ mice. *Neuron* **85**, 1332–1343 (2015).

7. Canetta, S. et al. Maternal immune activation leads to selective functional deficits in offspring parvalbumin interneurons. *Mol. Psychiatry* **21**, 956–968 (2016).

8. Cho, K. K. A. et al. Cross-hemispheric gamma synchrony between prefrontal parvalbumin interneurons supports behavioral adaptation during rule shift learning. *Nat. Neurosci.* **23**, 892–902 (2020).

9. Dienel, S. J. & Lewis, D. A. Alterations in cortical interneurons and cognitive function in schizophrenia. *Neurobiol. Dis.* **131**, 104208 (2019).

10. Hirano, Y. & Uhlhaas, P. J. Current findings and perspectives on aberrant neural oscillations in schizophrenia. *Psychiatry Clin. Neurosci.* **75**, 258–268 (2021).

11. Green, M. F. Cognitive impairment and functional outcome in schizophrenia and bipolar disorder. *J. Clin. Psychiatry* **67**, 36–42 (2006).

12. Schmitt, L. I. et al. Thalamic amplification of cortical connectivity sustains attentional control. *Nature* **545**, 219–223 (2017).

13. Bolkan, S. S. et al. Thalamic projections sustain prefrontal activity during working memory maintenance. *Nat. Neurosci.* **20**, 987–996 (2017).

14. Lundqvist, M. et al. Gamma and beta bursts underlie working memory. *Neuron* **90**, 152–164 (2016).

15. Rikhye, R. V., Gilra, A. & Halassa, M. M. Thalamic regulation of switching between cortical representations enables cognitive flexibility. *Nat. Neurosci.* **21**, 1753–1763 (2018).

16. Wimmer, R. D. et al. Thalamic control of sensory selection in divided attention. *Nature* **526**, 705–709 (2015).

17. Nakajima, M., Schmitt, L. I. & Halassa, M. M. Prefrontal cortex regulates sensory filtering through a basal ganglia-to-thalamus pathway. *Neuron* **103**, 445–458.e10 (2019).

18. Sohal, V. S., Zhang, F., Yizhar, O. & Deisseroth, K. Parvalbumin neurons and gamma rhythms enhance cortical circuit performance. *Nature* **459**, 698–702 (2009).

19. Cardin, J. A. et al. Driving fast-spiking cells induces gamma rhythm and controls sensory responses. *Nature* **459**, 663–667 (2009).

20. Schneider, M. et al. A mechanism for inter-areal coherence through communication based on connectivity and oscillatory power. *Neuron* **109**, 4050–4067.e12 (2021).

21. Lee, A. T., Vogt, D., Rubenstein, J. L. R. & Sohal, V. S. A class of GABAergic neurons in the prefrontal cortex sends long-range projections to the nucleus accumbens and elicits acute avoidance behavior. *J. Neurosci.* **34**, 11519–11525 (2014).

22. Bissonette, G. B. et al. Double dissociation of the effects of medial and orbital prefrontal cortical lesions on attentional and affective shifts in mice. *J. Neurosci.* **28**, 11124–11130 (2008).

23. Fenno, L. E. et al. Comprehensive dual- and triple-feature intersectional single-vector delivery of diverse functional payloads to cells of behaving mammals. *Neuron* **107**, 836–853.e11 (2020).

24. Caputi, A., Melzer, S., Michael, M. & Monyer, H. The long and short of GABAergic neurons. *Curr. Opin. Neurobiol.* **23**, 179–186 (2013).

25. Melzer, S. & Monyer, H. Diversity and function of corticopetal and corticofugal GABAergic projection neurons. *Nat. Rev. Neurosci.* **21**, 499–515 (2020).

26. Fuchs, E. C. et al. Genetically altered AMPA-type glutamate receptor kinetics in interneurons disrupt long-range synchrony of gamma oscillation. *Proc. Natl Acad. Sci. USA* **98**, 3571–3576 (2001).

27. Lee, A. T. et al. Pyramidal neurons in prefrontal cortex receive subtype-specific forms of excitation and inhibition. *Neuron* **81**, 61–68 (2014).

28. Marton, T. F. et al. Role of prefrontal cortex and mediodorsal thalamus in task engagement and behavioral flexibility. *J. Neurosci.* **38**, 2569–2578 (2018).

29. Fries, P. Rhythms for cognition: communication through coherence. *Neuron* **88**, 220–235 (2015).

30. Corder, G. et al. An amygdalar neural ensemble that encodes the unpleasantness of pain. *Science* **363**, 276–281 (2019).

31. Mukamel, E. A., Nimmerjahn, A. & Schnitzer, M. J. Automated analysis of cellular signals from large-scale calcium imaging data. *Neuron* **63**, 747–760 (2009).

32. Frost, N. A., Haggart, A. & Sohal, V. S. Dynamic patterns of correlated activity in the prefrontal cortex encode information about social behavior. *PLoS Bio.* **19**, e3001235 (2021).

Acknowledgements

V.S.S. is supported by grants from the US National Institute of Health (R01MH121342 and R01NS116594), the McKnight Endowment Fund for Neuroscience (Memory and Cognitive Disorders award), and the Brain Research Foundation (Scientific Innovations Award BRF-SIA-2019-02).

K.K.A.C. is supported by the Institut National de la Santé et de la Recherche Médicale (Inserm) and the Marie Skłodowska-Curie Individual Fellowship (MSCA-IF). The authors thank O. Lavielle for providing PV-cre heterozygous mice; L. Frank and M. Brainard for feedback on earlier versions of this manuscript; members of the Alberto Bacci laboratory for discussions; and the ICM technical staff of the facilities PHENO-ICMice and Histomics. This work was also supported by 'Investissements d'avenir' ANR-10-IAIHU-06.

Author information

Author notes

1. Kathleen K. A. Cho

   Present address: Institut du Cerveau-Paris Brain Institute, Sorbonne Université, Inserm U1127–CNRS UMR 7225, Paris, France

Authors and Affiliations

1. Department of Psychiatry and Behavioral Sciences, Weill Institute for Neurosciences, University of California, San Francisco, San Francisco, CA, USA

   Kathleen K. A. Cho, Jingcheng Shi, Aarron J. Phensy, Marc L. Turner & Vikaas S. Sohal

2. Kavli Institute for Fundamental Neuroscience, University of California, San Francisco, San Francisco, CA, USA

   Kathleen K. A. Cho, Jingcheng Shi, Aarron J. Phensy, Marc L. Turner & Vikaas S. Sohal

Contributions

K.K.A.C. and V.S.S. designed the study. K.K.A.C. conducted all experiments and analyses, with the exception of Flp- and Cre-dependent

AAV-NpHR experiments with or without ChR2, synapsin-eNpHR dual-site voltage indicator experiments and controls, synapsin-eNpHR and synapsin-mCherry microendoscopic calcium-imaging experiments, and experiments in Extended Data Fig. 2e–h, which were performed by J.S. A.J.P. analysed the shorter-timeframe dual-site voltage indicator recordings in Extended Data Fig. 9f–l. M.L.T. performed surgeries for synapsin–eNpHR and synapsin–mCherry microendoscopic calcium-imaging experiments. K.K.A.C. and V.S.S. wrote the paper.

Corresponding authors

Correspondence to Kathleen K. A. Cho or Vikaas S. Sohal.

Ethics declarations

Competing interests

The authors declare no competing interests.

Peer review

Peer review information

Nature thanks Thomas McHugh and the other, anonymous, reviewer(s) for their contribution to the peer review of this work. Peer review reports are available.

Additional information

Publisher's note Springer Nature remains neutral with regard to jurisdictional claims in published maps and institutional affiliations.

Extended data figures and tables

Extended Data Fig. 1 Callosal PV+ projections innervate mPFC neurons projecting to mediodorsal thalamus and dorsal striatum.

a, Example immunohistochemistry image showing staining for parvalbumin (PV, red) and eYFP expression after a unilateral injection of AAV-DIO-ChR2-eYFP in the mPFC of *PV-Cre* mice. ChR2-eYFP expression is 96.7% specific for PV colabeled neurons. **b**, Experimental design: AAV-DIO-ChR2-eYFP was injected into one mPFC of *PV-Cre* mice to express ChR2 in callosal PV terminals. To retrogradely-label neurons that project to the contralateral mPFC or mediodorsal (MD) thalamus, cholera toxin subunit B conjugated with Alexa Fluor 488 (CTb Alexa-488) was injected in the mPFC ipsilateral to the AAV-DIO-ChR2 injection, and Alexa Fluor 594-conjugated cholera toxin subunit B (CTb Alexa-594) was injected in MD thalamus (contralateral to the site of AAV-DIO-ChR2 injection) ($n = 3$ mice). Whole-cell recordings were made from labeled neurons (contralateral to the AAV-DIO-ChR2 injection) within prefrontal brain slices. **c**, Example current-clamp responses to hyperpolarizing or depolarizing current pulses in retrogradely-labeled pyramidal neurons projecting to contralateral mPFC and MD thalamus. **d**, Experimental design: Injection of AAV-DIO-ChR2-eYFP in one mPFC of *PV-Cre* mice to express channelrhodopsin in callosal PV terminals. To retrogradely-label neurons that project to nucleus accumbens (NAc) or dorsal striatum, CTb Alexa-488 was injected in NAc and CTb Alexa-594 was injected in dorsal striatum (both contralateral to the AAV-DIO-ChR2 injection) ($n = 3$ mice). Whole-cell recordings were made from labeled neurons within prefrontal brain slices. **e**, Example current-clamp responses to hyperpolarizing or depolarizing current pulses in retrogradely-labeled neurons projecting to NAc or dorsal striatum. A small number of fast-spiking (FS) neurons were present among retrogradely-labeled neurons projecting to dorsal striatum. **f**, During optogenetic stimulation of callosal PV terminals, we observed consistent synaptic responses in all MD-projecting neurons and a fraction of dorsal striatum-projecting pyramidal neurons. **g**, Representative images showing CTb labeling of mPFC neurons projecting to the contralateral mPFC, ipsilateral MD thalamus, ipsilateral NAc, or ipsilateral dorsal striatum. **h**–**k**, A blue light flash (5 ms, 470 nm; denoted as a blue bar) delivered through the 40x objective were used to optogenetically stimulate callosal PV terminals.

Example recordings from mPFC pyramidal neurons projecting to MD thalamus or dorsal striatum, showing optogenetically-evoked inhibitory postsynaptic potentials (IPSPs) in the presence of DNQX and APV. Scale bars, 100 µm, unless otherwise indicated.

Source data

Extended Data Fig. 2 Rule shift task description and control experiments using weak light delivery or weak viral expression.

a, Trial timeline. A mouse begins each trial when it is placed in the home cage, then makes a decision, indicated by digging in one bowl. If the mouse is correct, the food reward is consumed. The mouse is then transferred to the holding cage until the next trial. The intertrial interval (ITI) is longer after errors. **b**, For optogenetic inhibition behavior experiments in Fig. 2, Day 1: no light delivery during the initial association (IA), nor during the rule shift (RS); Day 2: no light is delivered while mice learn the IA, but once mice meet the criterion for learning (8/10 consecutive trials correct), we begin delivering continuous 532 nm light and test the animal for 3 additional IA trials, before switching to the RS portion of the task. **c**, For optogenetic inhibition dual-site voltage indicator experiments in Fig. 3, Day 1: no light delivery during the IA, nor during the RS; Day 2: no light delivery during the IA, but continuous light delivery of 638 nm begins during 3 additional IA trials, followed by the RS; Day 3: no light delivery during the IA, nor during the RS. **d**, For optogenetic inhibition + microendoscopic calcium imaging experiments in Fig. 4, Day 1: no light delivery during the IA, nor during the RS; Day 2: no light delivery during the IA, but continuous light delivery of 600 nm begins during 3 additional IA trials, followed by the RS; Day 3: no light delivery during the IA, nor during the RS. **e**, Control experiments to verify that weak light delivery does not affect RS learning. Experimental design: Day 1, no light delivery; Day 2, continuous 0.1 mW 532 nm light is delivered during the RS; Day 3, continuous light at 0.1 mW 638 nm for inhibition during the RS. **f**, Representative image showing AAV-DIO-eNpHR-mCherry (DIO-eNpHR) expression and a fiber-optic cannula in the same mPFC hemisphere in a *PV-Cre* mouse. Scale bar, 100 µm. **g**, **h**, Performance in the rule shift task did not vary across days in either controls ($n = 4$), or DIO-eNpHR-injected mice ($n = 5$; two-way ANOVA (task day ×

virus); interaction: $F_{(2,14)} = 0.01721$, $P = 0.983$). **i**, Experimental design: Day 1, no light delivery; Day 2, continuous 2.5 mW 532 nm light is delivered during the RS. **j**, Representative image showing diluted (200 nL in 800 nL saline) DIO-eNpHR expression and a fiber-optic cannula in the same mPFC hemisphere in a *PV-Cre* mouse. Scale bar, 250 µm. **k**, Light stimulation of PV cells infected with lower virus titer did not alter RS performance across days ($n = 2$ mice; two-tailed paired *t*-test, $P = 0.5000$). **l**, Experimental design: Day 1, no light delivery; Day 2, light delivery during the inter-trial interval (ITI) during the RS for optogenetic inhibition of callosal PV terminals; Day 3, no light was delivered; Day 4, continuous light during the RS. **m**, Representative image showing DIO-eNpHR-mCherry (DIO-eNpHR) expression in one mPFC and a fiber-optic cannula implanted in the contralateral mPFC. Scale bar, 100 µm. **n**, **o**, Optogenetic inhibition of mPFC callosal PV terminals impairs rule shift performance in DIO-eNpHR-expressing mice only when delivered during both the trial and inter-trial intervals of the RS ($n = 6$) compared to controls ($n = 3$; two-way ANOVA (task day × virus); interaction: $F_{(3,28)} = 23.31$, $P < 0.0001$). **n**, Performance of controls was not different from eNpHR-expressing mice on Day 1 (post hoc $t_{(28)} = 0.3489$, $P > 0.9999$), Day 2 (post hoc $t_{(28)} = 0.6978$, $P > 0.9999$), nor Day 3 (post hoc $t_{(28)} = 0.4652$, $P > 0.9999$). **o**, Inhibition disrupts rule shift performance in DIO-eNpHR-expressing mice compared to controls when light is delivered continuously throughout the RS on Day 4 (post hoc $t_{(28)} = 9.886$, $P < 0.0001$). Two-way ANOVA followed by Bonferroni post hoc comparisons was used. ****$P < 0.0001$.

Source data

Extended Data Fig. 3 Initial association performance.

a, Related to the experiments in Fig. 2, there is no difference in the number of trials needed to reach the criterion for learning the initial association (IA) for DIO-eYFP controls ($n = 7$) vs. DIO-eNpHR-expressing mice ($n = 8$; two-way ANOVA (task day × virus); interaction: $F_{(1,13)} = 1.936$, $P = 0.1874$). **b**, Related to the experiments in Fig. 2, there is no difference in the number of IA trials to reach the learning criterion for Syn-tdTomato controls ($n = 4$) vs. Syn-eNpHR-expressing mice ($n = 6$; two-way ANOVA (task day × virus);

interaction: $F_{(1,8)} = 0.05424$, $P = 0.8217$). **c**, Related to the experiments in Fig. 3, there is no difference in the number of IA trials needed to reach the learning criterion for DIO-mCherry controls ($n = 4$) vs. DIO-eNpHR-expressing mice ($n = 5$; two-way ANOVA (task day × virus); interaction: $F_{(2,14)} = 0.3027$, $P = 0.7435$). **d**, Related to the experiments in Fig. 3, there is no difference in the number of IA trials needed to reach the learning criterion for Syn-mCherry controls ($n = 4$) vs. Syn-eNpHR-expressing mice ($n = 5$; two-way ANOVA (task day × virus); interaction: $F_{(2,14)} = 2.131$, $P = 0.1557$). **e**, Related to the experiments in Fig. 4, there is no difference in the number of IA trials needed to reach the learning criterion for controls (DIO-mCherry or Syn-mCherry) ($n = 6$) vs. DIO-eNpHR-expressing mice ($n = 6$; two-way ANOVA (task day × virus); interaction: $F_{(2,20)} = 0.8831$, $P = 0.4290$). **f**, Related to the experiments in Fig. 4, there is no difference in the number of IA trials needed to reach the learning criterion for controls (DIO-mCherry or Syn-mCherry; $n = 6$) vs. Syn-eNpHR-expressing mice ($n = 6$; two-way ANOVA (task day × virus); interaction: $F_{(2,20)} = 1.372$, $P = 0.2764$). Two-way ANOVA followed by Bonferroni post hoc comparisons was used.

Source data

Extended Data Fig. 4 Motor and animal behavior during optogenetic manipulations.

a, We compared behavior between *PV-Cre* ± Ai14 mice injected with control virus (AAV-DIO-eYFP, AAV-DIO-mCherry, AAV-Syn-tdTomato, AAV-Syn-mCherry) vs. experimental eNpHR-expressing mice (injected with AAV-DIO-eNpHR-BFP, AAV-DIO-eNpHR-mCherry, AAV-Syn-eNpHR3.0-eYFP, or AAV-Syn-eNpHR-mCherry), for experiments in which light for optogenetic inhibition was delivered on Day 2. **b**, There is no bias in the fraction of choices made that were ipsilateral versus contralateral to the side of optogenetic inhibition ($n = 28$ DIO- and Syn-controls, $n = 41$ DIO- and Syn-eNpHR mice; two-way ANOVA (side bias × virus); interaction: $F_{(1,67)} = 0.7813$, $P = 0.3799$). For this, we specifically analyzed the final three initial association (IA) trials on Day 2. (On Day 2, after mice reach the learning criterion for the IA, we began delivering light for optogenetic

inhibition and performed three additional IA trials, followed by the rule shift). **c**, In experiments that included time-stamped behavior (dual-site voltage indicator and microendoscopic calcium imaging experiments), there is no difference in the latency to dig (aka, 'time to choice') when mice receive optogenetic inhibition during the first 5 rule shift (RS) trials vs. no optogenetic inhibition during the first 5 IA trials ($n = 8$ DIO-mCherry controls, $n = 11$ DIO-eNpHR mice; two-way ANOVA (type of task × virus); interaction: $F_{(1,17)} = 0.4236$, $P = 0.5239$). **d**–**e**, RS performance as a function of the type of cue shifts (odor to texture, texture to odor), task day (Day 1: no light; Day 2: light on for optogenetic inhibition), and group ($n = 17$ eNpHR-negative controls, $n = 19$ DIO-eNpHR mice) (two-way ANOVA (virus × task day); interaction: $F_{(3,64)} = 24.00$, $P < 0.0001$); there was no difference in performance for control mice on Day 1 vs. 2 for odor to texture shifts (Tukey's post hoc $q_{(64)} = 1.943$, $P = 0.5203$); there was not a significant difference in performance for control mice on Day 1 vs. 2 for texture to odor shifts (Tukey's post hoc $q_{(64)} = 3.559$, $P = 0.0668$); there was a marked significant difference in performance for DIO-eNpHR mice on Day 1 vs. 2 for odor to texture shifts (Tukey's post hoc $q_{(64)} = 16.16$, $P < 0.0001$); there was a marked significant difference in performance for DIO-eNpHR mice on Day 1 vs. 2 for texture to odor shifts (Tukey's post hoc $q_{(64)} = 13.3$, $P < 0.0001$). **f**–**g**, To determine whether the effects of optogenetic inhibition on the RS manifest immediately vs. only accrue after prolonged light delivery, we calculated the percentage of perseverative errors separately for the first 5 RS trials versus the next 5 RS trials, across control and experimental cohorts. Optogenetic inhibition of callosal PV projections causes mice to perseverate more on Day 2 compared to Day 1 for both the first 5 RS trials ($n = 19$ DIO-eNpHR mice; two-way ANOVA (trial type × task day); interaction: $F_{(1,18)} = 7.496$, $P = 0.0135$; post hoc $t_{(18)} = 2.581$, $P = 0.0376$) and the next 5 RS trials (post hoc $t_{(18)} = 6.453$, $P < 0.0001$). By contrast, there was no change from Day 1 to Day 2 in the percentage of perseverative choices within either the first 5 ($n = 15$ controls; two-way ANOVA (type of trial type × task day); interaction: $F_{(1,14)} = 0.09894$, $P = 0.7577$; post hoc $t_{(14)} = 1.557$, $P = 0.2836$) or next 5 RS trials in controls (post hoc $t_{(14)} = 2.002$, $P = 0.1302$). **h**, The proportion of correct vs. error decisions is plotted as a function of whether the cues that would be rewarded in the IA and RS are located in the same vs. different bowls,

during the first 5 RS trials ($n = 7$ DIO-mCherry controls, $n = 8$ DIO-eNpHR mice; same location two-way ANOVA (trial type × virus); interaction: $F_{(1,13)} = 0.02208$, $P = 0.8842$; same and correct post hoc $t_{(26)} = 0.1486$, $P > 0.9999$; same and incorrect post hoc $t_{(26)} = 0.1486$, $P > 0.9999$; different location two-way ANOVA (trial type × virus); interaction: $F_{(1,13)} = 13.87$, $P = 0.0026$; different and correct post hoc $t_{(26)} = 3.724$, $P = 0.0019$; different and incorrect post hoc $t_{(26)} = 3.724$, $P = 0.0019$). **i**, Same as **h** but for the next 5 RS trials ($n = 7$ DIO-mCherry control mice; same location two-way ANOVA (trial type × virus); interaction: $F_{(1,13)} = 3.214$, $P = 0.0963$; same and correct post hoc $t_{(26)} = 1.793$, $P = 0.1693$; same and incorrect post hoc $t_{(26)} = 1.793$, $P = 0.1693$; different location two-way ANOVA (trial type × virus); interaction: $F_{(1,13)} = 8.948$, $P = 0.0104$; different and correct post hoc $t_{(26)} = 2.991$, $P = 0.0120$; different and incorrect post hoc $t_{(26)} = 2.991$, $P = 0.0120$). **j**–**k**, The overall speed (meters per second) of mice during the first 5 IA and RS trials across days in the cohort of mice used for microendoscopic Ca^{2+} imaging ($n = 6$ eNpHR-negative controls; $n = 6$ DIO-eNpHR mice; two-way ANOVA (IA vs. RS × task day) for control mice: interaction: $F_{(1,10)} = 0.00271$, $P = 0.9595$; two way-ANOVA (IA vs. RS × task day) for DIO-eNpHR mice: interaction: $F_{(1,10)} = 1.378$, $P = 0.2677$). **l**–**m**, There is no difference in the amount of time (seconds) mice spent exploring bowls before making a decision during the first 5 IA and RS trials across days in the microendoscope experimental dataset ($n = 6$ eNpHR-negative controls; $n = 6$ DIO-eNpHR mice; two-way ANOVA (IA vs. RS × task day) for control mice: interaction: $F_{(1,10)} = 0.5053$, $P = 0.4934$; two way-ANOVA (IA vs. RS × task day) for DIO-eNpHR mice: interaction: $F_{(1,10)} = 0.1147$, $P = 0.7419$). **n**–**o**, The first move of the mouse toward the correct bowl (percent) during the first 5 IA and RS trials across days in the Ca^{2+} imaging experimental dataset ($n = 6$ eNpHR-negative controls; $n = 6$ DIO-eNpHR mice; two-way ANOVA (IA vs. RS × task day) for control mice: interaction: $F_{(1,10)} = 3.347$, $P = 0.0973$; two way-ANOVA (IA vs. RS × task day) for DIO-eNpHR mice: interaction: $F_{(1,10)} = 0.1316$, $P = 0.7244$). **p**–**z**, Effects of inhibiting callosal PV+ projections during a version of the RS task using a shorter (30 second) intertrial interval (ITI). **p**, Experimental design: Day 1, no light delivery; Day 2, continuous light during the RS for

optogenetic inhibition of callosal PV terminals ; Day 3, no light was delivered. **q**, Representative image showing DIO-eYFP expression in one mPFC and a fiber-optic cannula implanted in the contralateral mPFC in a *PV-Cre* mouse. **r**, Representative image showing DIO-eNpHR-mCherry (DIO-eNpHR) expression in one mPFC and a fiber-optic cannula implanted in the contralateral mPFC in a *PV-Cre* mouse. **s**,**w**, IA performance with a 30 s ITI in eNpHR-negative mice ($n = 6$) and eNpHR-expressing mice ($n = 8$; two-way ANOVA (task day × virus); interaction: $F_{(2,24)} = 0.1585$, $P = 0.8543$). **t**,**x**, Optogenetic inhibition of mPFC callosal PV terminals with a 30 s ITI impairs rule shift performance in DIO-eNpHR mice ($n = 8$) compared to controls ($n = 6$; two-way ANOVA (task day × virus); interaction: $F_{(2,24)} = 50.79$, $P < 0.0001$). **t**, Performance of DIO-eYFP controls did not change from Day 1 to Day 2 (Tukey's post hoc $q_{(5)} = 1.606$, $P = 0.5356$), Day 1 to Day 3 (Tukey's post hoc $q_{(5)} = 1.035$, $P = 0.7567$), nor Day 2 to Day 3 (Tukey's post hoc $q_{(5)} = 0.4344$, $P = 0.9498$). **x**, Inhibition disrupts rule shift performance in DIO-eNpHR mice from Day 1 to Day 2 (Tukey's post hoc $q_{(7)} = 15.34$, $P < 0.0001$), Day 1 to Day 3 (Tukey's post hoc $q_{(7)} = 21.75$, $P < 0.0001$), but not Day 2 to Day 3 (Tukey's post hoc $q_{(7)} = 2.679$, $P = 0.2101$). **u**, **y**, Optogenetic inhibition of callosal PV terminals increases perseverative errors in DIO-eNpHR mice ($n = 8$ mice) compared to DIO-eYFP controls ($n = 6$ mice; two-way ANOVA (task day × virus) interaction: $F_{(2,24)} = 19.79$, $P < 0.0001$). **v**, **z**, Optogenetic inhibition of callosal PV terminals has no effect on random errors in DIO-eNpHR mice ($n = 8$) compared to DIO-eYFP controls ($n = 6$; two-way ANOVA (task day × virus); interaction: $F_{(2,24)} = 1.079$, $P = 0.3559$). **u**, **v**, Light delivery does not affect the number of perseverative (post hoc $t_{(5)} = 0.000 – 1.000$, $P > 0.9999$) or random (post hoc $t_{(5)} = 0.4152 – 0.7906$, $P > 0.9999$) errors in DIO-eYFP controls across days. **y**, **z**, Optogenetic inhibition of callosal PV terminals on Day 2 increased the number of perseverative (post hoc $t_{(7)} = 6.008$, $P = 0.0016$ from Day 1 to Day 2; post hoc $t_{(7)} = 5.844$, $P = 0.0019$ from Day 1 to Day 3; but not from Day 2 to Day 3: post hoc $t_{(7)} = 1.111$, $P = 0.9093$) but not random (post hoc $t_{(7)} = 0.000 – 2.198$, $P = 0.1918 – > 0.9999$) errors compared to no stimulation. Two-way ANOVA followed by Bonferroni post hoc comparisons was used unless otherwise noted. Data

were expressed as mean ± s.e.m. ***P* < 0.01, *****P* < 0.0001; scale bar, 100 µm.

Source data

Extended Data Fig. 5 Optogenetic inhibition of callosal PV terminals (but not nonspecific inhibition of all callosal terminals) increases errors during rule shifts.

a, **e**, **i**, **m**, Experimental design: Day 1, no light delivery; Day 2, continuous light for optogenetic inhibition of callosal PV terminals during the rule shift (RS). **b**, **f**, **j**, **n**, Representative image showing viral expression in the mPFC ipsilateral to the injection (ipsi), and labeled callosal terminals in the contralateral mPFC (contra). **c**, **g**, Optogenetic inhibition of callosal PV terminals increases perseverative errors in DIO-eNpHR mice ($n = 8$ mice) compared to DIO-eYFP controls ($n = 7$ mice; two-way ANOVA (task day × virus); interaction: $F_{(1,13)} = 35.71$, $P < 0.0001$). **d**, **h**, Optogenetic inhibition of callosal PV terminals has a marginal effect on random errors in DIO-eNpHR mice ($n = 8$ mice) compared to DIO-eYFP controls ($n = 7$ mice; two-way ANOVA (task day × virus); interaction: $F_{(1,13)} = 4.617$, $P = 0.0511$). **c**, **d**, Light delivery does not affect the number of perseverative (post hoc $t_{(13)} = 1.877$, $P = 0.1662$) or random (post hoc $t_{(13)} = 0.0$, $P > 0.9999$) errors in DIO-eYFP controls. **g**, **h**, Optogenetic inhibition of callosal PV terminals on Day 2 increased the number of perseverative (post hoc $t_{(13)} = 10.75$, $P < 0.0001$) and random (post hoc $t_{(13)} = 3.145$, $P = 0.0155$) errors compared to no stimulation on Day 1. **k**, **l**, **o**, **p**, Optogenetic inhibition of all callosal projections has no effect on perseverative errors in Syn-eNpHR mice ($n = 6$) compared to controls ($n = 4$; two-way ANOVA (task day × virus); interaction: $F_{(1,8)} = 0.0$, $P > 0.9999$) nor on random errors (two-way ANOVA (task day × virus); interaction: $F_{(1,8)} = 0.07805$, $P = 0.787$). Two-way ANOVA followed by Bonferroni post hoc comparisons was used. **P* < 0.05, *****P* < 0.0001; scale bars, 250 µm and 100 µm, respectively.

Source data

Extended Data Fig. 6 Optogenetic inhibition of callosal PV terminals during a rule reversal does not impair reversal learning or induce persistent deficits in subsequent rule shifts.

a, Schematic illustrating the rule reversal task, in which mice chose one of two bowls, each baited by an odor (O1 or O2) and texture (TA or TB) cue, to find a hidden food reward (the stimulus associated with reward is indicated in orange). Mice first learn an initial association (IA) between either an odor or texture cue (odor O1 in this case) and food reward. Once mice reach the learning criterion (eight correct out of ten consecutive trials), this association undergoes an intra-dimensional rule reversal (RR; e.g., from O1 to O2). **b**, There is no difference in the number of IA trials needed to reach the learning criterion for control ($n = 3$ mice; AAV-DIO-eYFP injected; DIO-eYFP) vs. eNpHR-expressing ($n = 5$ mice; AAV-DIO-eNpHR-mCherry injected; DIO-eNpHR) mice across days (two-way ANOVA (task day × virus); interaction: $F_{(1,6)} = 1.127$, $P = 0.3292$). **c**, Experimental design: Day 1, continuous light for optogenetic inhibition of callosal PV terminals during the RR; Day 2, no light delivery during the rule shift (RS). **d**, **e**, Representative images showing viral expression in the mPFC ipsilateral to the injection (ipsi), and labeled callosal terminals in the contralateral mPFC (contra). Scale bars, 250 μm and 100 μm, respectively. **f**, **g**, Performance of DIO-eYFP controls ($n = 3$, **f**) is similar to DIO-eNpHR mice ($n = 5$, **g**) from Day 1 to Day 2 (two-way ANOVA (task day × virus); interaction: $F_{(1,6)} = 0.4286$, $P = 0.5370$). **h**, **i**, Optogenetic inhibition of callosal PV terminals does not change the total number of errors (perseverative and random) in DIO-eNpHR mice ($n = 5$ mice, **i**) compared to DIO-eYFP controls across days ($n = 3$ mice, **h**); two-way ANOVA (task day × virus); interaction: $F_{(1,6)} = 1.095$, $P = 0.3358$). Two-way ANOVA followed by Bonferroni post hoc comparisons was used.

Source data

Extended Data Fig. 7 Optogenetic inhibition of callosal PV terminals induces persistent perseveration during rule shifts that is reversed by 40 Hz stimulation of the same terminals.

a, Experimental design: Day 1, continuous green light was delivered for terminal inhibition during the rule shift (RS); Day 2, no light delivery; Day 3, 40 Hz blue light was delivered for terminal stimulation during the RS; on Day 4, which occurred 1 week later, no light was delivered. **b**, Representative images showing AAV-nEF-Con/Fon-NpHR3.3-eYFP (Con/Fon-NpHR-eYFP) and AAV-Con/Fon-mCherry (Con/Fon-mCherry) expression in one mPFC (ipsi) and callosal PV^{+} fibers and terminals in the contralateral mPFC (contra). **c**, Representative images showing AAV-nEF-Con/Fon-NpHR3.3-eYFP (Con/Fon-NpHR-eYFP) and AAV-nEF-Con/Fon-ChR2-mCherry (Con/Fon-ChR2-mCherry) expression in one mPFC (ipsi) and callosal PV terminals in the contralateral mPFC (contra). **d**, There is no difference in the number of initial association (IA) trials needed to reach the learning criterion between mice which express only NpHR ($n = 3$) and those expressing both NpHR and ChR2 ($n = 8$; two-way ANOVA (task day × virus); interaction: $F_{(3,27)} = 1.317$, $P = 0.2892$). **e**,**h**, In mice which express NpHR only (**e**; $n = 3$), optogenetic inhibition on Day 1 causes mice to take a large number of trials to learn the rule shift, and this does not change across subsequent days (post hoc $t_{(2)} = 0.3941$–1.732, $P > 0.9999$). By contrast, rule shift performance in mice expressing both NpHR and ChR2 (**h**; $n = 8$) is significantly different across days than that of mice which express NpHR-only (two-way ANOVA (task day × virus); interaction: $F_{(3,27)} = 6.747$, $P = 0.0015$). Optogenetic inhibition of mPFC callosal PV terminals causes NpHR+ChR2-expressing mice ($n = 8$) to take a large number of trials to learn rule shifts on Day 1 and this does not change on Day 2 (no light) (post hoc $t_{(7)} = 1.446$, $P > 0.9999$). However, RS learning is rescued by 40 Hz optogenetic stimulation on Day 3 (post hoc $t_{(7)} = 10.91$, $P < 0.0001$) and this improvement does not change on 'Day 4' of testing which occurs one week later (post hoc $t_{(7)} = 0.6394$, $P > 0.9999$). **f**, **i**: Optogenetic inhibition followed by stimulation of callosal PV terminals changes the number of perseverative errors in mice expressing both NpHR and ChR2 ($n = 8$ mice) compared to controls expressing only NpHR ($n = 3$ mice; two-way ANOVA; main effect of task day: $F_{(2.015,18.13)} = 7.167$, $P = 0.0050$; main effect of virus: $F_{(1,9)} = 14.31$, $P = 0.0043$; interaction: $F_{(3,27)} = 5.324$, $P = 0.0052$). By contrast, there is no difference in numbers of random errors (two-way ANOVA; main effect of task day: $F_{(1.491,13.42)} = 1.706$, $P = 0.2189$; main effect of virus: $F_{(1,9)} = 1.523$, $P = 0.2483$; interaction: $F_{(3,27)} = 0.2901$, $P =$

0.8322). **f**, Once mice expressing NpHR only receive optogenetic inhibition on Day 1, the number of perseverative errors is stable across days ($n = 3$ mice; Day 1 to Day 2: post hoc $t_{(2)} = 1.222$, $P > 0.9999$; Day 1 to Day 3: post hoc $t_{(2)} = 1.299$, $P > 0.9999$; Day 1 to Day 4: post hoc $t_{(2)} = 0.3111$, $P > 0.9999$; Day 2 to Day 3: post hoc $t_{(2)} = 0.3780$, $P > 0.9999$; Day 2 to Day 4: post hoc $t_{(2)} = 1.606$, $P > 0.9999$; Day 3 to Day 4: post hoc $t_{(2)} = 2.000$, $P > 0.9999$). **g**, In mice that express NpHR only ($n = 3$ mice), numbers of random errors are also stable across days (Day 1 to Day 2: post hoc $t_{(2)} = 1.387$, $P > 0.9999$; Day 1 to Day 3: post hoc $t_{(2)} = 1.732$, $P > 0.9999$; Day 1 to Day 4: post hoc $t_{(2)} = 1.000$, $P > 0.9999$; Day 2 to Day 3: post hoc $t_{(2)} = 1.000$, $P > 0.9999$; Day 2 to Day 4: post hoc $t_{(2)} = 1.000$, $P > 0.9999$; Day 3 to Day 4: post hoc $t_{(2)} = 0.3780$, $P > 0.9999$). **i**, 40 Hz stimulation of callosal PV terminals on Day 3 reduces the number of perseverative errors in mice expressing both NpHR and ChR2 ($n = 8$; Day 1 to Day 2: post hoc $t_{(7)} = 0.6494$, $P > 0.9999$; Day 1 to Day 3: post hoc $t_{(7)} = 5.218$, $P = 0.0074$; Day 1 to Day 4: post hoc $t_{(7)} = 6.416$, $P = 0.0022$; Day 2 to Day 3: post hoc $t_{(7)} = 4.822$, $P = 0.0115$; Day 2 to Day 4: post hoc $t_{(7)} = 12.33$, $P < 0.0001$; Day 3 to Day 4: post hoc $t_{(7)} = 0.4971$, $P > 0.9999$). **j**, 40 Hz stimulation on Day 3 does not affect the number of random errors in mice expressing both NpHR and ChR2 ($n = 8$ mice; Day 1 to Day 2: post hoc $t_{(7)} = 0.7061$, $P > 0.9999$; Day 1 to Day 3: post hoc $t_{(7)} = 0.6417$, $P > 0.9999$; Day 1 to Day 4: post hoc $t_{(7)} = 1.210$, $P > 0.9999$; Day 2 to Day 3: post hoc $t_{(7)} = 0.3140$, $P > 0.9999$; Day 2 to Day 4: post hoc $t_{(7)} = 0.4237$, $P > 0.9999$; Day 3 to Day 4: post hoc $t_{(7)} = 0.7977$, $P > 0.9999$). Two-way ANOVA followed by Bonferroni post hoc comparisons was used. $*P < 0.05$, $**P < 0.01$, $***P < 0.001$, $****P < 0.0001$; scale bars, 100 μm and 50 μm, respectively.

Source data

Extended Data Fig. 8 Optogenetic inhibition of callosal PV terminals, delivered while measuring signals from voltage indicators, increases errors during rule shifts (RS).

a, *PV-Cre* Ai14 mice had bilateral AAV-DIO-Ace2N-4AA-mNeon (Ace-mNeon) injections, an ipsilateral AAV-DIO-eNpHR-BFP (DIO-eNpHR) or AAV-DIO-mCherry injection and multimode fiber-optic implants in both prefrontal cortices. **b**, Representative images from mice injected with a control virus (DIO-mCherry), showing mCherry, Ace-mNeon, and tdTomato expression in the mPFC ipsilateral to the virus injection (ipsi), and Ace-mNeon and tdTomato in the contralateral hemisphere (contra). **c**, **f**, Experimental design: Day 1, no light delivery; Day 2, continuous light for inhibition during the rule shift (RS); Day 3, no light delivery. **d**, **e**, **g**, **h**, Optogenetic inhibition of callosal PV terminals increases perseverative errors in DIO-eNpHR-expressing mice ($n = 5$ mice, **g**-**h**) compared to DIO-mCherry-expressing controls ($n = 4$ mice, **d**-**e**; two-way ANOVA (task day × virus); interaction: $F_{(2,14)} = 5.226$, $P = 0.0202$), but has no effect on random errors (two-way ANOVA (task day × virus); interaction: $F_{(2,14)} = 0.4552$, $P = 0.6434$). **d**, **e**, Light delivery does not affect the number of perseverative (Day 1 to Day 2: post hoc $t_{(14)} = 1.392$, $P = 0.5566$; Day 1 to Day 3: post hoc $t_{(14)} = 1.392$, $P = 0.5566$; Day 2 to Day 3: post hoc $t_{(14)} = 0.0$, $P > 0.9999$) or random (Day 1 to Day 2: post hoc $t_{(14)} = 0.284$, $P > 0.9999$; Day 1 to Day 3: post hoc $t_{(14)} = 0.284$, $P > 0.9999$; Day 2 to Day 3: post hoc $t_{(14)} = 0.0$, $P > 0.9999$) errors in controls across days. **g**, **h**, Optogenetic inhibition of callosal PV terminals induces perseveration on Day 2 and Day 3 compared to no stimulation on Day 1 (Day 1 to Day 2: post hoc $t_{(14)} = 4.092$, $P = 0.0033$; Day 1 to Day 3: post hoc $t_{(14)} = 6.405$, $P < 0.0001$; Day 2 to Day 3: post hoc $t_{(14)} = 2.313$, $P = 0.1094$), but has no effect on random errors (Day 1 to Day 2: post hoc $t_{(14)} = 1.524$, $P = 0.4493$; Day 1 to Day 3: post hoc $t_{(14)} = 0.254$, $P > 0.9999$; Day 2 to Day 3: post hoc $t_{(14)} = 1.27$, $P = 0.6744$). **i**, *PV-Cre* Ai14 mice had bilateral AAV-DIO-Ace2N-4AA-mNeon (Ace-mNeon) injections, an ipsilateral AAV-Synapsin-eNpHR-BFP (Syn-eNpHR) or AAV-Synapsin-mCherry (Syn-mCherry) injection and multimode fiber-optic implants in both prefrontal cortices. **j**, Representative images from mice injected with a control virus (Syn-mCherry), showing mCherry, Ace-mNeon, and tdTomato expression in the mPFC ipsi to the virus injection, and Ace-mNeon and tdTomato in the contra hemisphere. **k**, **n**, Experimental design: Day 1, no light delivery; Day 2, continuous light for inhibition during the R; Day 3, no light delivery. **l**, **m**, **o**, **p**, Optogenetic inhibition of callosal terminals does not change the number of perseverative errors in

Syn-eNpHR mice ($n = 5$ mice, **l**-**m**) compared to Syn-mCherry controls ($n = 4$ mice, **l**-**m**; two-way ANOVA (task day × virus); interaction: $F_{(2,14)} = 1.933$, $P = 0.1814$), and has no effect on random errors (two-way ANOVA (task day × virus); interaction: $F_{(2,14)} = 0.3789$, $P = 0.6914$). **l**, **m**, Light delivery does not affect the number of perseverative (Day 1 to Day 2: post hoc $t_{(3)} = 1.464$, $P = 0.7183$; Day 1 to Day 3: post hoc $t_{(3)} = 0.8783$, $P > 0.9999$; Day 2 to Day 3: post hoc $t_{(3)} = 0.4804$, $P > 0.9999$) or random (Day 1 to Day 2: post hoc $t_{(3)} = 1.732$, $P = 0.5451$; Day 2 to Day 3: post hoc $t_{(3)} = 1.732$, $P = 0.5451$) errors in controls across days. **o**, **p**, Nonspecific optogenetic inhibition of all callosal projections does not affect the number of perseverative ($n = 5$ mice; Day 1 to Day 2: post hoc $t_{(4)} = 0.6882$, $P > 0.9999$; Day 1 to Day 3: post hoc $t_{(4)} = 2.108$, $P = 0.3081$; Day 2 to Day 3: post hoc $t_{(4)} = 1.121$, $P = 0.9752$) or random (Day 1 to Day 2: post hoc $t_{(4)} = 0.4082$, $P > 0.9999$; Day 1 to Day 3: post hoc $t_{(4)} = 1.000$, $P > 0.9999$; Day 2 to Day 3: post hoc $t_{(4)} = 0.000$, $P > 0.9999$) errors in Syn-eNpHR mice across days. Two-way ANOVA followed by Bonferroni post hoc comparisons was used. **$P < 0.01$, ****$P < 0.0001$; scale bars, 50 μm.

Source data

Extended Data Fig. 9 Additional analyses of gamma synchrony using dual-site voltage indicators.

a, Experimental design: Day 1, no optogenetic inhibition; Day 2, continuous light for optogenetic inhibition during the rule shift (RS); Day 3, no optogenetic inhibition (light for TEMPO was delivered on all days). **b**–**e**, Gamma synchrony during the intertrial interval (ITI). **b**–**c**, Gamma synchrony during ITIs does not change following correct or error trials during the initial association (IA) in either control ($n = 4$ mice; two-way ANOVA (trial type × task day); interaction: $F_{(1,7)} = 0.1143$, $P = 0.2111$) or DIO-eNpHR mice ($n = 5$ mice; two-way ANOVA (trial type × task day); interaction: $F_{(2,12)} = 1.903$, $P = 0.1915$) across days. **d**, Gamma synchrony during ITIs is higher after rule shift (RS) errors than after RS correct choices across days in control mice ($n = 4$ mice; Day 1: post hoc $t_{(9)} = 2.977$, $P = 0.047$; Day 2: post hoc $t_{(9)} = 2.969$, $P = 0.0472$; Day 3: post hoc $t_{(9)} = 4.039$,

$P = 0.0088$). **e**, In DIO-eNpHR mice, gamma synchrony during ITIs is higher after RS errors than after RS correct choices on Day 1 ($n = 5$ mice; Day 1: post hoc $t_{(12)} = 2.914$, $P = 0.039$), but not on Day 2 when mice receive optogenetic inhibition of callosal PV+ terminals (post hoc $t_{(12)} = 1.041$, $P = 0.9545$) nor on Day 3 (post hoc $t_{(12)} = 1.153$, $P = 0.8136$). **f**, We performed a shorter timeframe re-analysis of TEMPO data collected from *PV-Cre* Ai14 injected in one mPFC with AAV-DIO-eNpHR. This was originally collected for Fig. 3. Gamma synchrony was calculated as the zero-phase lag cross-correlation ('x-corr') between 'corrected' mNeon signals that had been filtered in the 30–50 Hz as described in the Methods. Synchrony was averaged over the 5 s following correct choices or errors during the rule shift (RS). This measure of interhemispheric gamma synchrony is higher after RS errors than RS correct choices on Day 1, but was not different after errors vs. correct choices on Days 2 and 3 ($n = 5$ mice; two-way ANOVA; main effect of type of decision: $F_{(1,8)} = 5.349$, $P = 0.0495$; Day 1: post hoc $t_{(24)} = 2.619$, $P = 0.0451$; Day 2: post hoc $t_{(24)} = 0.04492$, $P > 0.9999$; Day 3: post hoc $t_{(24)} = 1.763$, $P = 0.2717$). **g**–**i**, We also re-analyzed the TEMPO data collected from *PV-Cre* Ai14 mice injected in one mPFC with DIO-eNpHR to identify specific times when optogenetic inhibition of callosal PV+ projections disrupts gamma synchrony. We measured the change in gamma synchrony (calculated in 1 s windows for various time points relative to behavioral events) between Day 1 (control) and Day 2 (optogenetic inhibition) for both errors (filled circles) and correct choices (open circles) during the first 5 RS trials in *PV-Cre* mice expressing DIO-eNpHR. **g**, This change in gamma synchrony (change = Day 2 – Day 1) is not significantly different for error vs. correct trials around the time of trial start ($n = 5$ mice; two-way ANOVA (time point × error vs. correct); interaction: $F_{(15,64)} = 1.642$, $P = 0.0874$). **h**, This change in gamma synchrony is more negative for error vs. correct trials around the start of digging ($n = 5$ mice; two-way ANOVA (time point × error vs. correct); interaction: $F_{(15,64)} = 1.931$, $P = 0.0360$). **i**, This change in gamma synchrony is more negative for error vs. correct trials around the end of digging ($n = 5$ mice; two-way ANOVA (time point × error vs. correct); interaction: $F_{(10,44)} = 2.096$, $P = 0.0454$). **j**, Example traces of left (L) and right (R) Ace2n-4AA-mNeon (Ace-mNeon) traces (green and red, respectively), from 0–10 s after dig start on RS correct and error trials in a DIO-eNpHR-expressing mouse

and **k**, zoomed in on the period 6–7 s after dig start. **l**, The time course of gamma synchrony (correlation values calculated from filtered and cleaned Ace-mNeon signals) from 0–10 s after dig start for these two example trials. Two-way ANOVA followed by Bonferroni post hoc comparisons was used. Data were expressed as mean ± s.e.m. *$P < 0.05$, **$P < 0.01$.

Source data

Extended Data Fig. 10 Optogenetic inhibition of callosal terminals, delivered during concomitant calcium imaging, increases errors during rule shifts (RS). Finer timescale analysis of how optogenetic inhibition affects changes in activity patterns during RS.

a, **f**, **j**, *PV-Cre* or WT mice had AAV-DIO-eNpHR-mCherry (DIO-eNpHR) or AAV-Syn-eNpHR-mCherry (Syn-eNpHR) virus or a control virus (AAV-DIO-mCherry in *PV-Cre* mice or AAV-Synapsin-mCherry) injected in one mPFC and AAV-Synapsin-GCaMP7f (Syn-GCaMP7f) injected in the contralateral hemisphere. A GRIN lens, connected to a microendoscope, was implanted in contralateral to the site of eNpHR / control virus injection. Experimental design: Day 1, no light delivery for optogenetic inhibition; Day 2, continuous light for inhibition during the rule shift (RS); Day 3, no light delivery for optogenetic inhibition (light was delivered for calcium imaging on all days). **b**, Left: Representative image showing AAV-DIO-mCherry (DIO-mCherry) injected in the ipsilateral mPFC (ipsi) and Syn-GCaMP7f in the contralateral hemisphere (contra). Right: DIO-mCherry expression in callosal PV axonal fibers. **c**, Left: Representative image showing AAV-Syn-mCherry (Syn-mCherry) injected in the ipsilateral mPFC (ipsi) and Syn-GCaMP7f in the contralateral hemisphere (contra). Right: Syn-mCherry expression in callosal axonal fibers. **d**, **e**, **h**, **i**, **l**, **m**, Optogenetic inhibition of callosal PV terminals increases perseverative errors in DIO-eNpHR-expressing mice ($n = 6$ mice, panel **h**) compared to controls ($n = 6$ mice, panel **d**) and Syn-eNpHR-expressing mice ($n = 6$ mice, panel **l**) (two-way ANOVA (task day × virus); interaction: $F_{(4,30)} = 11.74$, $P < 0.0001$). However there is no effect on random errors (compare panels **e**, **i**, **m**) (two-way ANOVA (task day × virus); interaction: $F_{(4,30)} = 1.377$, $P =$

0.2654). **d**, Light delivery does not affect the number of perseverative errors in control mice across days (Day 1 to Day 2: post hoc $q_{(5)} = 2.936$, $P = 0.1896$; Day 1 to Day 3: post hoc $q_{(5)} = 3.457$, $P = 0.1235$; Day 2 to Day 3: post hoc $q_{(5)} = 1.257$, $P = 0.6700$). **e**, Similar to **d**, there is no change in random errors in control mice ($n = 6$ mice; Day 1 to Day 2: post hoc $q_{(5)} = 1.118$, $P = 0.7245$; Day 1 to Day 3: post hoc $q_{(5)} = 2.828$, $P = 0.2072$; Day 2 to Day 3: post hoc $q_{(5)} = 0.7670$, $P = 0.8547$). **g**, Left: Representative image showing AAV-DIO-eNpHR-mCherry (DIO-eNpHR) injected in the ipsi mPFC and Syn-GCaMP7f in the contra hemisphere. Right: DIO-eNpHR-mCherry expression in callosal PV axonal fibers. **h**, Optogenetic inhibition of callosal PV terminals increases the number of perseverative errors on Day 2 and Day 3 compared to no stimulation on Day 1 (Day 1 to Day 2: post hoc $q_{(5)} = 7.156$, $P = 0.0090$; Day 1 to Day 3: post hoc $q_{(5)} = 8.181$, $P = 0.0050$; Day 2 to Day 3: post hoc $q_{(5)} = 3.240$, $P = 0.1476$). **i**, Optogenetic inhibition of callosal PV terminals has no effect on random errors ($n = 6$ mice; Day 1 to Day 2: post hoc $q_{(5)} = 1.225$, $P = 0.6825$; Day 1 to Day 3: post hoc $q_{(5)} = 0.3147$, $P = 0.9732$; Day 2 to Day 3: post hoc $q_{(5)} = 1.414$, $P = 0.6083$). **k**, Left: Representative image showing AAV-Synapsin-eNpHR-mCherry (Syn-eNpHR) injected in the ipsi mPFC and Syn-GCaMP7f in the contra hemisphere. Right: Syn-eNpHR-mCherry expression in callosal axonal fibers. **l**, In Syn-eNpHR mice, optogenetic inhibition of all callosal terminals does not affect the number of perseverative errors across days (Day 1 to Day 2: post hoc $q_{(5)} = 2.739$, $P = 0.2231$; Day 1 to Day 3: post hoc $q_{(5)} = 0.4939$, $P = 0.9358$; Day 2 to Day 3: post hoc $q_{(5)} = 0.8687$, $P = 0.8190$). **m**, Similar to **l**, in Syn-eNpHR mice, optogenetic inhibition of all callosal terminals does not affect random errors ($n = 6$ mice; Day 1 to Day 2: post hoc $q_{(5)} = 2.236$, $P = 0.3350$; Day 1 to Day 3: post hoc $q_{(5)} = 1.257$, $P = 0.6700$; Day 2 to Day 3: post hoc $q_{(5)} = 1.651$, $P = 0.5192$). **n**, The number of cells in control (DIO-mCherry and Syn-mCherry) mice did not differ across days ($n = 6$ mice; one-way ANOVA; $P = 0.3100$; Day 1 to Day 2: post hoc $q_{(5)} = 2.068$, $P = 0.3818$; Day 1 to Day 3: post hoc $q_{(5)} = 1.155$, $P = 0.7101$; Day 2 to Day 3: post hoc $q_{(5)} = 1.421$, $P = 0.6057$). **o**, The number of cells in DIO-eNpHR-expressing mice did not differ across days ($n = 6$ mice; one-way ANOVA; $P = 0.7050$; Day 1 to Day 2: post hoc $q_{(5)} = 0.1767$, $P = 0.9914$;

Day 1 to Day 3: post hoc $q_{(5)} = 0.7532$, $P = 0.8594$; Day 2 to Day 3: post hoc $q_{(5)} = 1.131$, $P = 0.7192$). **p**, The number of cells in Syn-eNpHR mice decreased slightly from Day 1 (no optogenetic inhibition) to Day 2 (optogenetic inhibition of all callosal projections) ($n = 6$ mice; one-way ANOVA; $P = 0.0921$; Day 1 to Day 2: post hoc $q_{(5)} = 4.836$, $P = 0.0419$; Day 1 to Day 3: post hoc $q_{(5)} = 4.254$, $P = 0.0653$; Day 2 to Day 3: post hoc $q_{(5)} = 0.8008$, $P = 0.8431$). **q**–**s**, To quantify how activity evolves over the course of each RS error trial, we measured the similarity between population activity vectors (computed using a 2.5 s window) occurring at the beginning of the 10 s period following the start of digging, and those at the end of this period on the same trial, for each mouse on Day 1 versus Day 2. **q**, The similarity of activity patterns from the beginning to end of the post-dig period on RS error trials does not change from Day 1 to 2 in controls (two-tailed paired *t*-test, $t_{(5)} = 1.332$, $P = 0.2403$; $n = 6$); **r**, however this similarity increases from Day 1 to 2 for DIO-eNpHR mice (two-tailed paired *t*-test, $t_{(5)} = 3.921$, $P = 0.0112$; $n = 6$ mice); **s**, this similarity does not differ from Day 1 to 2 for Syn-eNpHR mice (two-tailed paired *t*-test, $t_{(5)} = 0.9724$, $P = 0.3755$; $n = 6$ mice). **t**, Optogenetic inhibition of callosal PV terminals does not affect the similarity between population activity vectors measured during correct IA trials preceding the rule shift. Mice had AAV-DIO-eNpHR-mCherry (DIO-eNpHR in *PV-Cre* mice) or a control virus (AAV-DIO-mCherry in *PV-Cre* mice or AAV-Syn-mCherry in WT mice) injected into one mPFC, and AAV-Synapsin-GCaMP7f injected and a GRIN lens implanted in the contralateral hemisphere. Experimental design: Day 1, no light for optogenetic inhibition; Day 2, continuous light for optogenetic inhibition was delivered during the rule shift (RS); Day 3, no light delivery for optogenetic inhibition (light was delivered for calcium imaging on all days). **u**, On Day 2, after mice reach the learning criterion for the IA, we began delivering light for optogenetic inhibition and performed three additional IA trials, followed by the rule shift. Optogenetic inhibition of callosal PV terminals did not affect the similarity between activity vectors recorded after correct choices during these three additional IA trials, and those recorded during the preceding five IA trials ($n = 6$ mice in each group; two-tailed, unpaired *t*-test, $t_{(10)} = 0.4958$, $P = 0.6307$). Thus, the effect of inhibiting callosal PV terminals to suppress changes in activity does not occur prior to the rule shift. **v**–**x**, The change from Day 1 to 2 (change = Day

2 value - Day 1 value) in the similarity of population activity vectors between correct trials and errors during the first 5 RS trials calculated using 1 s windows, for various time points relative to trial start (**v**), dig start (**w**), or dig end (**x**). **v**, There is a main effect of virus (two-way ANOVA; $F_{(2,285)} = 16.95$; $P < 0.0001$) between groups in the change in the population activity vector similarity from Day 1 to Day 2 around the time of trial start ($n = 6$ mice in each group). Tukey's post hoc tests reveal statistically significant differences at specific time points. **w**, There is a difference between groups (main effect of virus) for the change in population vector similarities following the start of digging ($n = 6$ mice in each group; two-way ANOVA; $F_{(2,285)} = 23.86$, $P < 0.0001$). Tukey's post hoc tests reveal statistically significant differences at specific time points. **x**, There is a difference between groups ($n = 6$ mice in each group; main effect of virus, two-way ANOVA; $F_{(2,285)} = 11.63$, $P < 0.0001$) for the change in population vector similarities around the end of digging. Tukey's post hoc tests reveal statistically significant differences at specific time points. Two-way ANOVA followed by Tukey post hoc comparisons was used unless other noted. Data were expressed as mean ± s.e.m. $^*P < 0.05$, $^{**}P < 0.01$; scale bars, 100 µm and 50 µm, respectively.

Source data

Supplementary information

Supplementary Video 1

Mouse behaviour before and after onset of optogenetic manipulation. Description: a representative video showing mouse behaviour before and after onset of optogenetic manipulation. This video starts with the mouse completing a correct trial during the initial association. Following transfer to the rest cage, the optogenetic stimulation begins for three additional initial association trials before the rule-shift portion of the task begins. Light stimulation does not alter the performance or behaviour of the mice during these three extra trials of initial association.

Reporting Summary

Peer Review File

Source data

Source Data Fig. 1

Source Data Fig. 2

Source Data Fig. 3

Source Data Fig. 4

Source Data Extended Data Fig. 1

Source Data Extended Data Fig. 2

Source Data Extended Data Fig. 3

Source Data Extended Data Fig. 4

Source Data Extended Data Fig. 5

Source Data Extended Data Fig. 6

Source Data Extended Data Fig. 7

Source Data Extended Data Fig. 8

Source Data Extended Data Fig. 9

Source Data Extended Data Fig. 10

Rights and permissions

Open Access This article is licensed under a Creative Commons Attribution 4.0 International License, which permits use, sharing, adaptation, distribution and reproduction in any medium or format, as long as you give appropriate credit to the original author(s) and the source, provide a link to the Creative Commons licence, and indicate if changes were made. The images or other third party material in this article are included in the article's Creative Commons licence, unless indicated otherwise in a credit line to the material. If material is not included in the article's Creative Commons licence and your intended use is not permitted by statutory regulation or exceeds the permitted use, you will need to obtain permission directly from the copyright holder. To view a copy of this licence, visit http://creativecommons.org/licenses/by/4.0/.

Reprints and Permissions

About this article

Cite this article

Cho, K.K.A., Shi, J., Phensy, A.J. *et al.* Long-range inhibition synchronizes and updates prefrontal task activity. *Nature* **617**, 548–554 (2023). https://doi.org/10.1038/s41586-023-06012-9

- Received: 07 December 2021
- Accepted: 24 March 2023
- Published: 26 April 2023
- Issue Date: 18 May 2023
- DOI: https://doi.org/10.1038/s41586-023-06012-9

Share this article

Anyone you share the following link with will be able to read this content:

Get shareable link

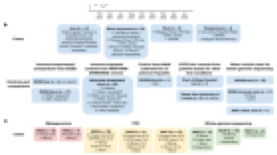
Sorry, a shareable link is not currently available for this article.

Copy to clipboard

Provided by the Springer Nature SharedIt content-sharing initiative

---

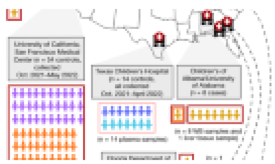
This article was downloaded by **calibre** from https://www.nature.com/articles/s41586-023-06012-9



Genomic investigations of unexplained acute hepatitis in children

30 March 2023

Sofia Morfopoulou, Sarah Buddle, … Judith Breuer



Adeno-associated virus type 2 in US children with acute severe hepatitis

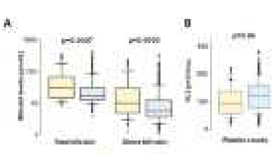
30 March 2023

Venice Servellita, Alicia Sotomayor Gonzalez, … Charles Y. Chiu

Prevalence of hepatitis B virus genotypes among patients with liver disease in Eritrea

31 May 2021

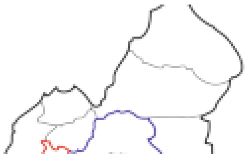
Mohammed Elfatih Hamida, Saud Mohammed Raja, … Freweini Tekle



HDV infection rates in northern Vietnam

23 May 2018

Mai Thanh Binh, Nghiem Xuan Hoan, … Thirumalaisamy P. Velavan



[High prevalence of hepatitis delta virus in Cameroon]

02 August 2018

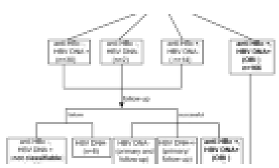
Emily K. Butler, Mary A. Rodgers, … Gavin Cloherty



[Prevalence of hepatitis E infection in HIV/HCV-coinfected patients in Spain (2012–2014)]

04 February 2019

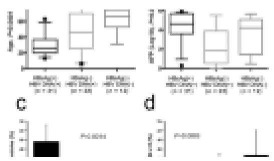
Sonia Vázquez-Morón, Juan Berenguer, … Salvador Resino



[Molecular characteristics of the full-length genome of occult hepatitis B virus from blood donors in China]

17 May 2022

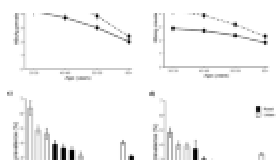
Min Wang, Ru Xu, … Yongshui Fu



[Early-onset liver cancer in South America associates with low hepatitis B virus DNA burden]

13 August 2018

Agnès Marchio, Juan Pablo Cerapio, … Pascal Pineau



[Conventional and genetic risk factors for chronic Hepatitis B virus infection in a community-based study of 0.5 million Chinese adults]

15 July 2022

Elizabeth Hamilton, Ling Yang, … Zhengming Chen

- Article
- Published: 30 March 2023

Adeno-associated virus 2 infection in children with non-A–E hepatitis

- Antonia Ho,
- Richard Orton,
- Rachel Tayler,
- Patawee Asamaphan,
- Vanessa Herder,

- Chris Davis,
- Lily Tong,
- Katherine Smollett,
- Maria Manali,
- Jay Allan,
- Konrad Rawlik,
- Sarah E. McDonald,
- Elen Vink,
- Louisa Pollock,
- Louise Gannon,
- Clair Evans,
- Jim McMenamin,
- Kirsty Roy,
- Kimberly Marsh,
- Titus Divala,
- Matthew T. G. Holden,
- Michael Lockhart,
- David Yirrell,
- Sandra Currie,
- Maureen O'Leary,
- David Henderson,
- Samantha J. Shepherd,
- Celia Jackson,
- Rory Gunson,
- Alasdair MacLean,
- Neil McInnes,
- Amanda Bradley-Stewart,
- Richard Battle,
- Jill A. Hollenbach,
- Paul Henderson,
- Miranda Odam,
- Primrose Chikowore,
- Wilna Oosthuyzen,
- Meera Chand,
- Melissa Shea Hamilton,
- Diego Estrada-Rivadeneyra,
- Michael Levin,

- Nikos Avramidis,
- Erola Pairo-Castineira,
- Veronique Vitart,
- Craig Wilkie,
- DIAMONDS Consortium,
- ISARIC4C Investigators,
- Massimo Palmarini,
- Surajit Ray,
- David L. Robertson,
- Ana da Silva Filipe,
- Brian J. Willett,
- Judith Breuer,
- Malcolm G. Semple,
- David Turner,
- J. Kenneth Baillie &
- …
- Emma C. Thomson

Show authors

Nature **volume 617**, pages 555–563 (2023)

- 13k Accesses

- 5 Citations

- 426 Altmetric

- Metrics details

Abstract

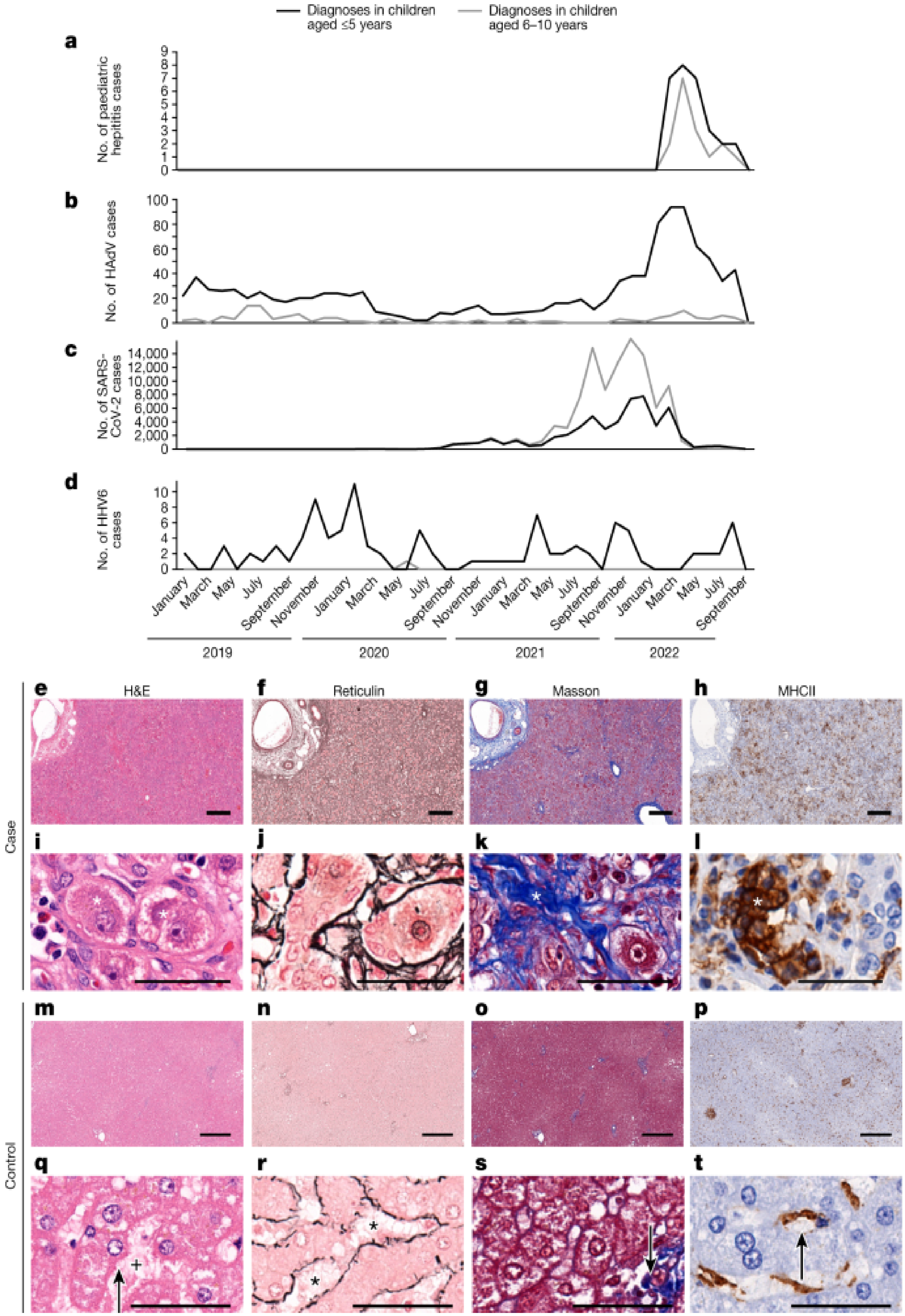
An outbreak of acute hepatitis of unknown aetiology in children was reported in Scotland[1] in April 2022 and has now been identified in 35 countries[2]. Several recent studies have suggested an association with human adenovirus with this outbreak, a virus not commonly associated with hepatitis. Here we report a detailed case–control investigation and find an

association between adeno-associated virus 2 (AAV2) infection and host genetics in disease susceptibility. Using next-generation sequencing, PCR with reverse transcription, serology and in situ hybridization, we detected recent infection with AAV2 in plasma and liver samples in 26 out of 32 (81%) cases of hepatitis compared with 5 out of 74 (7%) of samples from unaffected individuals. Furthermore, AAV2 was detected within ballooned hepatocytes alongside a prominent T cell infiltrate in liver biopsy samples. In keeping with a $CD4^+$ T-cell-mediated immune pathology, the human leukocyte antigen (HLA) class II *HLA-DRB1*04:01* allele was identified in 25 out of 27 cases (93%) compared with a background frequency of 10 out of 64 (16%; $P = 5.49 \times 10^{-12}$). In summary, we report an outbreak of acute paediatric hepatitis associated with AAV2 infection (most likely acquired as a co-infection with human adenovirus that is usually required as a 'helper virus' to support AAV2 replication) and disease susceptibility related to HLA class II status.

Main

In April 2022, several hospitals in Scotland reported that children were presenting to medical practitioners with acute severe hepatitis of unknown aetiology[1] (Fig. 1a). Elsewhere in the United Kingdom, 270 similar presentations were subsequently reported, for which 15 children required liver transplantation[3]. The World Health Organization (WHO) has now registered 1,010 probable cases that fulfil their definition of this illness in 35 countries[2]. Understanding the underlying cause of this new disease is a global public health imperative.

Fig. 1: Epidemiology and histological appearance of cases of paediatric hepatitis in Scotland.



Diagnoses in children aged ≤5 years
Diagnoses in children aged 6–10 years
a
No. of paediatric hepititis cases
b
No. of HAdV cases
c
No. of SARS-CoV-2 cases
d
No. of HHV6 cases
January
March
May
July
September
November
2019
2020
2021
2022
e
H&E
f
Reticulin
g
Masson
h
MHCII
Case
i
j
k
l
m
n
o
p
Control
q
r
s
t

a, The emergence of acute non-A–E hepatitis in children in March–September 2022 (ref. [3]). **b**–**d**, Cases of HAdV (**b**), SARS-CoV-2 (**c**) and HHV6 (**d**) infection in children aged ≤10 years in Scotland during the period January 2019 to September 2022. **e**–**t**, Histopathology of samples from cases of non-A–E hepatitis (**e**–**l**) and from healthy liver (**m**–**t**). **e**,**i**,**m**,**q**, Serial sections of formalin-fixed and paraffin-embedded liver tissue sections (one section for each stain per patient sample) stained with haematoxylin and eosin (H&E). **f**,**j**,**n**,**r**, Reticulin staining highlighting structural organization. **g**,**k**,**o**,**s**, Masson staining highlighting collagen fibres. **h**,**l**,**p**,**t**, Staining for MHCII$^+$ cells. **m**–**p**, The regular lobular structure of the liver from a healthy individual (identifier 145783) is not recognisable in **e**–**h**, which are sections collected from patient CVR35 who received a liver transplant. **h**, Immunohistochemistry showed an increase in MHCII$^+$ cells in tissue samples from patient CVR35 compared with healthy liver (**l**,**t**). **i**–**l**, Higher magnification micrographs of **e**–**h** showing details of liver histopathology. **i**,**q**, For patient CVR35 (**i**), enlarged (ballooned) and vacuolated hepatocytes (marked by asterisks) are evident compared with hepatocytes in healthy liver (**q**; from individual 145783) with regular morphology (indicated by the arrow) and regular sinus (indicated by the plus symbol). **j**,**r**, For the sample from patient CVR35 (**j**), reticulin staining shows destruction of the sinus structures and irregularly arranged fibres, whereas healthy liver (**r**) shows fibres lining the sinus (indicated by asterisks). **k**,**s**, For the sample from patient CVR35 (**k**), Masson staining shows an increase in collagen fibres (in blue, indicated by the asterisk) compared with minimal staining of fibres (indicated by the arrow) in healthy liver (**s**). **l**,**t**, High magnification image showing accumulation of MHCII$^+$ cells in the liver (indicated by the asterisk) of patient CVR35 (**l**), whereas healthy liver (**t**), staining is limited to Kupffer cells (indicated by the arrow). Scale bars, 50 µm (**i**–**l**,**q**–**t**) or 400 µm (**e**–**h**,**m**–**p**).

Source Data

Detailed clinical investigations carried out as part of the public health response excluded common causes of acute hepatitis, including viral hepatitis, drug toxicity and autoimmune hepatitis. However, recent or active human adenovirus (HAdV) infection was identified in a high proportion of cases in Scotland, England and the United States[4,5,6]. This finding was

notable because HAdV is not a common cause of hepatitis. An increase in HAdV diagnoses in Scotland directly preceded the outbreak of unexplained hepatitis in children of a similar age (Fig. 1a,b). SARS-CoV-2 had been circulating for 2 years and peaked several months before the increase in hepatitis cases[3] (Fig. 1c). Human herpesvirus 6 (HHV6A and HHV6B) infections were not detected at higher levels during 2021 or 2022 (Fig. 1d).

Research investigation

To investigate the aetiology of these cases of acute hepatitis, we recruited 32 affected children who presented to a hospital between 14 March 2022 and 20 August 2022 and met the Public Health Scotland case definition criteria for inclusion in the International Severe Acute Respiratory and Emerging Infections Consortium (ISARIC) WHO Clinical Characterization Protocol United Kingdom (CCP-UK) (ISRCTN66726260)[7]. Samples from unaffected children (control samples) were obtained from the Diagnosis and Management of Febrile Illness using RNA Personalised Molecular Signature Diagnosis (DIAMONDS) study cohort and from the NHS Greater Glasgow & Clyde (GG&C) Biorepository under appropriate ethics approval (Methods)

Clinical presentation

The median age of affected patients was 4.1 years (interquartile range (IQR) of 2.7–5.5 years) (Table 1). All patients were of white ethnicity, and 21 out of 32 (66%) were girls. Eighteen (56%) of the children reported a subacute history 2–12 weeks before acute hepatitis, which was characterized by an initial gastroenteritis-like illness followed by intermittent vomiting, abdominal pain and fatigue. The majority (23 out of 32) had no other medical conditions. One child had previously received a liver transplant, whereas none of the other patients were immunocompromised and none had received a COVID-19 vaccination. All routine blood tests for viral hepatitis, including hepatitis A, B, C and E, acute Epstein–Barr virus (EBV), cytomegalovirus (CMV), HHV6 and HHV7, and herpes simplex virus (HSV) were negative (Supplementary Table 1). Four patients had a low titre (1:80) of anti-nuclear antibodies and 3 patients had a low titre (1:40) of anti-

smooth muscle antibodies, but other markers of autoimmunity were negative (Table 1 and Supplementary Table 2).

Table 1 Demographic and clinical characteristics of the 32 patients with unexplained hepatitis

Following hospitalization, liver biopsy samples were obtained from five children. The samples showed evidence of lobular hepatitis with periportal and interface inflammation, intracellular inclusions, bile duct proliferation and ballooning of hepatocytes of varying severity (Fig. 1e–t). Mild-to-moderate fibrotic changes were noted, with no evidence of confluent fibrosis, and there was an inflammatory infiltrate that included cells expressing major histocompatibility complex class II (MHCII). Modified hepatic activity index scores (Ishak system)[8,9] ranged from 6 to 11 (Extended Data Table 1), and the biopsy samples stained negative for complement.

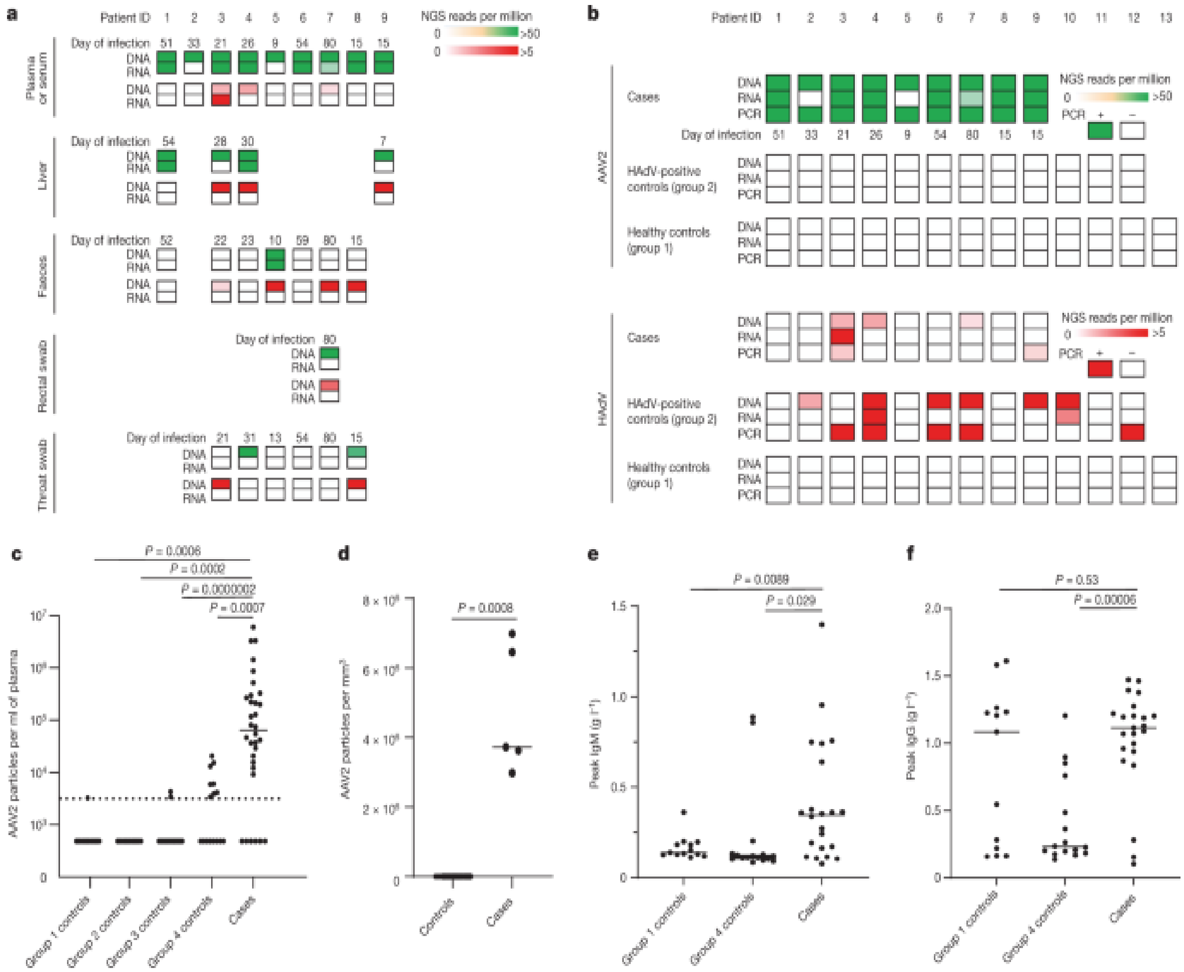
Four patients required transfer to a specialist liver unit owing to significant synthetic liver dysfunction. Two of the patients were treated with steroid therapy and improved. One patient received supportive care only and spontaneously improved. The fourth patient had severe disease and required liver transplantation and was treated with cidofovir for HAdV viraemia and steroids after the liver transplant. The remaining 28 patients received supportive care only, with no antiviral or steroid treatment, and all showed gradual resolution of hepatitis over 2–3 months. There were no deaths. The median duration of hospital stay was 6 days (range of 1–68 days) (Table 1). In the patients with weakly positive autoantibodies, all had normal or normalizing transaminase levels at last follow up in the absence of treatment with an anti-inflammatory or immunosuppressant.

Pathogen detection by sequencing

As the epidemiology was in keeping with the emergence of an infectious pathogen, we undertook metagenomics and target enrichment (TE) next-generation sequencing (NGS) on all available clinical samples from the first nine recruited patients. The samples included plasma ($n = 9$), liver biopsy samples ($n = 4$), throat swabs ($n = 6$), faecal samples ($n = 7$) and a rectal

swab ($n = 1$), and an average of 14 million sequence reads per sample were obtained (Fig. 2a–d). The samples were obtained between 7 and 80 days after initial symptom onset. Samples from the control group were restricted to children recruited in the United Kingdom between January 2020 and April 2022. Two comparison groups were used as controls: group 1 comprised serum or plasma samples from 13 age-matched healthy children (10 boys, 3 girls; age range of 3–5 years); and group 2 comprised serum or plasma samples from 12 children (8 boys, 4 girls; age range of 1–4 years) with HAdV infection confirmed by PCR and with normal transaminase levels. The children in group 2 had been diagnosed by nasopharyngeal aspirate ($n = 10$), by nose swab ($n = 1$) or by stool ($n = 1$) as part of the routine clinical investigation process and half of the patients required critical care. The difference in age between the patients with hepatitis and the healthy children in group 1 was not significant, but some samples from group 1 were obtained earlier than samples from the cases of hepatitis (January 2020–April 2022 compared with March–April 2022, respectively) (Extended Data Table 2a). The children in group 2 were younger (median age of 1.4 years, IQR of 1.1–3.1 years, $P < 0.001$), and samples were obtained between May 2020 and December 2021 (Extended Data Table 2b). Metagenomics NGS was carried out using protocols designed to identify both RNA and DNA viruses. Semi-agnostic TE sequencing was also performed using VirCapSeq-VERT Capture probes that target the genomes of 207 taxa of viruses known to infect vertebrates.

Fig. 2: Detection of AAV2 in cases of paediatric hepatitis.



a, Heatmap of HAdV and AAV2 reads detected in cases of hepatitis by TE sequencing. Samples obtained for routine clinical investigation (plasma, liver, faeces, rectal swab and throat swab) were retrospectively sequenced following DNA or RNA extraction. AAV2 read counts are shown from 0 to >50 reads per million in green (top rows) and HAdV read counts are shown from 0 to >5 reads per million in red (bottom rows). **b**, Heatmap of viral reads of plasma samples from cases of hepatitis and of plasma or sera samples from controls. Plasma samples from cases of hepatitis (cases), and plasma or sera samples from children with HAdV infection (group 2 controls) and from age-matched healthy children (group 1 controls) were sequenced following DNA or RNA extraction. AAV2 read counts are shown from 0 to >50 reads per million in green and HAdV read counts are shown from 0 to >5 reads per million in red. The number of days between initial symptom onset and sample are indicated. **c**, AAV2 real-time RT–qPCR of serum or plasma samples from 32 cases of hepatitis (cases) and from 74

controls in four groups: 13 in group 1 (healthy controls); 12 in group 2 (HAdV-positive controls); 33 in group 3 (hepatitis controls); and 16 in group 4 (contemporaneous controls). The detection threshold of the assay (3,200 copies per ml) is shown as a dotted line. Values are shown as a scatter plot with a median line. **d**, AAV2 real-time RT–qPCR of liver biopsy samples from 5 cases of hepatitis and from 19 controls. **e**, IgM responses determined by ELISA in 22 cases of hepatitis and in 29 controls (13 in group 3, 16 in group 4). **f**, IgG responses determined by ELISA in 22 cases of hepatitis cases and in 29 controls (13 in group 3, 16 in group 4). For **c**–**f**, statistical analysis was performed using Mann Whitney test (two-tailed), and experiments were performed in triplicate.

Source Data

TE sequencing reflected the metagenomics NGS results, but with higher sensitivity, and correlated with viral loads measured by quantitative PCR with reverse transcription (RT–qPCR) (Supplementary Figs. 1 and 2). The results from both methods showed that the viral genome detected most frequently in affected patient plasma samples was AAV2 (9 out of 9 cases) (Fig. 2a, Supplementary Table 3 and Extended Data Fig. 1). AAV2 was also detected in 4 out of 4 liver biopsy samples, and in 1 out of 7 faecal samples, 1 out of 1 rectal sample and 1 out of 6 throat swab samples. At lower read counts, HAdV-F41 or HAdV-C was detected in 6 out of 9 patients, whereas HHV6B was detected in 3 out of 4 plasma samples (Extended Data Fig. 1, Supplementary Tables 4 and 5, Supplementary Data 1 and Supplementary Fig. 3). HAdV types C1, 2, 5 and 6 could not be reliably distinguished owing to low read counts. The remaining clinical samples were excluded from analysis for HHV by sequencing because murine herpesvirus 1 had been added as an extraction control during routine clinical investigation.

Read counts of AAV2 by TE sequencing were high (median of 4,478 reads per million, IQR of 774–10,498 reads per million) in all 9 out of 9 cases of hepatitis compared with 0 out of 13 in group 1 healthy controls (IQR of 0–0 reads per million, $P < 0.001$) and 0 out of 12 in group 2 controls (children with HAdV infection and normal liver function tests; IQR of 0–0 reads per million, $P < 0.001$) (Supplementary Table 5). HAdV reads were detected in 6 out of 12 HAdV-positive samples from group 2 controls (median of 0.82 reads per million, IQR of 0–1,053 reads per million) despite plasma or sera

being a suboptimal sample type to detect HAdV. HAdV was detected in 3 out of 9 cases of hepatitis (median of 0 reads per million, IQR of 0–0.6 reads per million), whereas 0 out of 13 was detected in group 1 healthy controls (IQR of 0–0 reads per million, $P = 0.055$). HHV6B was also detected in 3 out of 4 cases of hepatitis compared with 0 out of 13 healthy controls (median of 1.9 reads per million, IQR of 0.3–3.5 reads per million and IQR of 0–0 reads per million, respectively, $P = 0.006$) (Supplementary Table 4). However, HHV6B read counts did not differ significantly between cases of hepatitis and group 2 controls (median of 0 reads per million, IQR of 0–0.04 reads per million, $P = 0.16$), which is in keeping with the occurrence of reactivation of HHV6B in the context of severe illness. The metagenomics and TE sequencing results from the 13 age-matched healthy control samples (group 1) revealed no evidence of AAV2, HAdV or HHV6B in plasma; however, low read counts of EBV, CMV and HHV6A were detected in a small number of samples (Supplementary Table 4). In samples from group 2 (children with HAdV infection and normal liver function tests), herpesviruses were detected in 9 out of 12 samples, including 2 out of 12 (as described above) with detectable numbers of HHV6B reads (1,050 and 5,062 reads per million), which was confirmed by PCR.

Sequence and phylogenetic analyses

Near-full genomes of AAV2 were obtained from all nine patients with hepatitis (GenBank accession numbers OP019741–OP019749), and in all cases, two large open reading frames corresponding to the *rep* and *cap* genes, flanked by inverted terminal repeat regions, were identified. Seven distinct sequences of AAV2 were noted (Extended Data Fig. 2), forming a single clade, alongside four AAV2 genomes previously detected in France between 2004 and 2015. Two out of three identical sequences were known to have come from individuals from the same household, therefore these two are epidemiologically linked. The third sequence was from a sample obtained around the same time but was not known to be linked to the other cases. Sequences from the liver samples matched those detected in plasma. Several mutations within the *VP1–VP3* genes were noted to be over-represented in the sequences derived from patients with hepatitis when compared with reference sequences (Extended Data Fig. 2). Notably, nine of the mutations in the capsid gene that were over-represented in the cases of

hepatitis (V151A, R447K, T450A, Q457M, S492A, E499D, F533Y, R585S and R588T) are associated with an AAV2 variant that has an altered phenotype. Characteristics of this variant include substantial evasion of neutralizing antibodies directed against wild-type AAV2, enhanced production yields, reduced heparin binding, increased virion stability and more localized spread in a mouse model[10].

A full genome of HAdV-F41 was obtained from a faecal sample (GenBank accession number OP019750) and was found to be closest phylogenetically to two genomes reported from Germany in 2019 and 2022 (Extended Data Fig. 2). Contigs matching to other human pathogens, including human coronavirus NL63, rhinovirus C, enterovirus B, human parainfluenza viruses 2 and 3, norovirus, and both betaherpesvirus and gammaherpesvirus were also detected across cases, albeit not consistently. These findings were confirmed by PCR (Supplementary Table 1).

Confirmatory PCR testing of cases of hepatitis

PCR testing for AAV2 was positive in all nine initial cases of hepatitis. Standards were used to estimate the viral loads of positive samples (Supplementary Fig. 2). All nine plasma samples tested negative by PCR for HHV6, HSV, CMV and EBV. Two out of the four liver biopsy specimens tested positive for HHV6 (cycle threshold (Ct) values of 33 and 36) (Supplementary Table 1). HAdV was detected in 3 out of 9 plasma samples, 3 out of 4 liver biopsy samples, 2 out of 6 throat swabs, 4 out of 7 faecal samples and 1 out of 1 rectal swab. The lower detection of HAdV and HHV6 by PCR compared with TE sequencing probably reflects a slightly lower sensitivity of the PCR assay. The low numbers of HAdV-positive samples detected using both assays may reflect the fact that plasma is a suboptimal sample type for HAdV detection (whole blood samples were unavailable).

Case–control study

To investigate the presence of AAV2 and the candidate helper viruses HAdV and HHV6B in plasma samples from cases of hepatitis, we undertook a

case–control study in which samples from 32 cases of hepatitis were compared with samples from the group 1 and group 2 controls described above and with samples from two additional control groups (Fig. 2a–f). Group 3 controls comprised 33 children (18 boys and 15 girls aged 2–16 years) with increased transaminase levels that had tested negative by PCR for HAdV. This group was used to test the hypothesis that reactivation of AAV2 may occur in children with severe hepatitis and may be a correlate of liver dysfunction. The children comprising group 3 were older (median age of 10.2 years, IQR of 7–13.6 years, $P < 0.001$) than the patients from the case group (Extended Data Table 2b) and 15 out of 33 had required critical care for ventilatory or cardiovascular support. Group 4 controls comprised residual plasma or serum samples from 16 children in Scotland aged 10 years and were attending hospital contemporaneously with the children with hepatitis between March and April 2022. The group 4 controls were used to determine whether AAV2 was circulating widely in children in healthcare facilities across Scotland at the time the children with hepatitis were admitted to hospital. Clinical details, including liver function were not available for this group. To ensure that the quantification of AAV2 was accurately performed, we confirmed standard curve concentrations using droplet digital PCR (Methods).

Significance differences between groups for viral loads in plasma samples were calculated using a Mann–Whitney test (two-tailed). RT–qPCR of plasma samples showed that 26 out of 32 cases of hepatitis were positive for AAV2, with a median estimated copy number of 66,100 copies per ml (IQR of 13,461– 300,277 copies per ml), a value higher than samples from all the control groups ($P < 0.001$ for all case–control comparisons). The median copy number in control groups 1–3 was below the detection limit. A median of 3,268 copies per ml (detection threshold of 3,200 copies per ml) was present in samples from control group 4, which suggested that AAV2 was circulating at low levels in children during March and April 2022 (Fig. 2c). Although five plasma samples from cases of hepatitis were positive for HAdV by PCR, and one tested positive by PCR for HHV6 DNA, these results were not significantly more common than in samples from the control group (Supplementary Fig. 3).

Next, five liver biopsy samples from cases of hepatitis were compared with 19 residual liver biopsy samples (controls) from children under 18 years old.

The median AAV2 viral load was 3,721,497 copies per mm^3 of liver (IQR of 3,308,243−6,717,616 copies per mm^3) in cases of hepatitis compared with 64 copies per mm^3 of liver (IQR of 20–83 copies per mm^3) in samples from the control group ($P < 0.001$; Fig. 2d). Glyceraldehyde-3-phosphate dehydrogenase was used as a marker of extraction efficiency in all samples, and results were similar between the case and control groups. When outliers were removed, significance was retained (Supplementary Data 2, Supplementary Fig. 4).

Longitudinal sampling

To investigate AAV2 viraemia and liver function values over time, longitudinal PCR testing was performed in 14 cases of hepatitis from whom multiple retrospective plasma samples were available (Supplementary Fig. 5). Spearman's rank correlation coefficients for the relationships between the trajectories of viral load and alanine transaminase and bilirubin were positive for most cases. However, overall statistical significance could not be confirmed owing to the sample size.

Where samples were available, we screened for the presence of AAV2-specific IgM and IgG antibodies within samples from patients and samples from the group 1 healthy controls and group 4 contemporaneous controls (Fig. 2e,f and Supplementary Fig. 6). Anti-AAV2 IgM was detected in 15 out of 23 (65.2%) samples from cases of hepatitis, but only 1 out of 13 (7.7%) samples from group 1 healthy controls and 2 out of 16 (12.5%) samples from the group 4 contemporaneous controls from Scotland. For the samples from cases of hepatitis that tested negative for AAV2-specific IgM, samples from four patients were noted to be obtained fewer than 3 days after the onset of illness and samples from two patients were obtained more than 77 days after the onset of illness. IgG was detected in 21 out of 23 (91.3%) samples from cases of hepatitis, in 8 out of 13 (61.5%) samples from age-matched healthy controls (group 1) and in 9 out of 16 (56.3%) samples from healthy controls from Scotland (group 4). Of the two samples from patients who tested seronegative, both were obtained at early time points, probably sampled before expected seroconversion (less than 3 days after the onset of illness).

SARS-CoV-2 infection

Routine clinical investigation detected SARS-CoV-2 nucleic acid in nasopharyngeal samples from 3 out of 31 (9.6%) children at the time of illness, 2 of whom were also seropositive. The third became infected after the onset of hepatitis. SARS-CoV-2 was not detected by PCR or by sequencing in any of the samples from cases or controls available for analysis, including liver samples. Nevertheless, to investigate the possibility that unexplained hepatitis in children might relate to a previous infection with SARS-CoV-2 or other seasonal coronaviruses, we carried out serological analysis of 23 available residual samples from cases. IgG antibody titres were quantitatively measured against the spike protein, the amino-terminal domain (NTD) and receptor binding domain (RBD) of the spike protein and the nucleocapsid of SARS-CoV-2. IgG antibody titres were also measured for human seasonal coronaviruses 229E, OC43, NL63 and HKU1. Electrochemiluminescence assays (MSD-ECL) for coronavirus-specific IgG revealed previous exposure to seasonal coronaviruses, with strong responses detected against NL63 (17 out of 23) and OC43 (21 out of 23) (Extended Data Fig. 3a). By comparison, plasma samples from 12 out of 23 children displayed high reactivity against HKU1, whereas only 3 out of 23 samples reacted strongly against 229E. Plasma samples from 11 children reacted with 2 or more SARS-CoV-2 antigens (nucleocapsid, spike protein, NTD or RBD). One of the samples reacted solely with the nucleocapsid antigen, which indicated that in total, 12 out of 23 patients displayed serological evidence of previous exposure to SARS-CoV-2 (Extended Data Fig. 3b). In summary, 12 out of 23 (52%) of the children with hepatitis displayed evidence of previous exposure to SARS-CoV-2. This level is lower than SARS-CoV-2 seroprevalence in children aged 5–11 years in Scotland between 14 March and 27 June 2022 (when Public Health Scotland enhanced surveillance for COVID-19 was discontinued), which was reported as between 59.0% (95% confidence interval (CI) of 50.6–71.2) and 72.4% (95% CI of 53.9–78.8)[11]. This result indicates that there is no direct link between COVID-19 and the outbreak of acute hepatitis studied here.

Host genetics and HLA typing

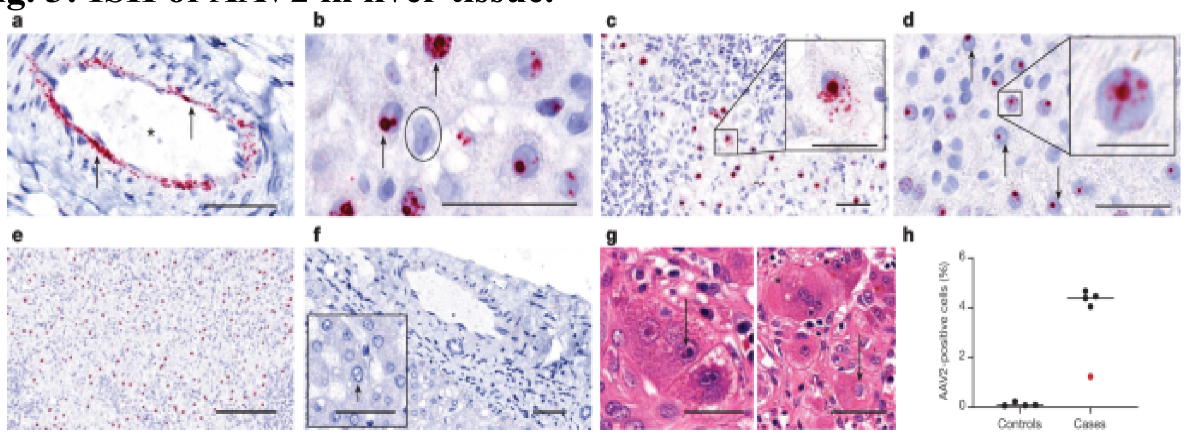
We next investigated whether some children might be genetically more susceptible to non-A–E hepatitis. To that end, 27 samples from cases of hepatitis and 64 platelet apheresis samples from local donors in Scotland (controls) were genotyped using high-resolution typing for all HLA loci (*HLA-A*, *HLA-B*, *HLA-C*, *HLA-DRB1*, *HLA-DRB3*, *HLA-DRB4*, *HLA-DRB5*, *HLA-DQA1*, *HLA-DQB1*, *HLA-DPA1* and *HLA-DPB1*). In total, 25 out of 27 (92.6%) samples from patients with hepatitis were positive for at least one copy of the *HLA-DRB1*04:01* allele compared with 10 out of 64 (15.6%) of samples from controls. The allele frequency in patients was 0.54 compared with 0.08 in controls (odds ratio (OR) of 13.7 (95% CI of 5.5–35.1), $P = 5.49 \times 10^{-12}$). The frequency of the *HLA-DRB1*04:01* allele (based on an imputation of HLA alleles) in a control set of unrelated participants from the UK Biobank ($n = 29{,}379$) was 0.11 (2,942 out of 29,379 allele carriers, OR of 112.3 (95% CI of 26.6–474.5), $P = 3.27 \times 10^{-23}$). The frequency was also 0.11 in British/Irish North-West European individuals from the Anthony Nolan charity register[11]. To check for cryptic relatedness among patients and population stratification, we performed genome-wide microarray genotyping in 19 cases of hepatitis and excluded participants with a conservative relatedness threshold (identity-by-state > 0.4). When compared with well-matched participants from the UK Biobank (Extended Data Fig. 4), similar signals for association with disease by allele frequency ($P = 8.96 \times 10^{-6}$) and across the three possible biallelic genotypes at this locus ($P = 1.2 \times 10^{-9}$) were obtained.

In addition to the association with the *DRB1* allele, 23 out of 27 samples from patients with hepatitis were positive for *HLA-DQA1*03:03* compared with 11 out of 64 samples from controls (allele frequency of 0.54 compared with 0.09, respectively, OR of 12.3 (5.1–30.7), $P = 1.9 \times 10^{-11}$). Moreover, 26 out of 27 samples from patients were positive for *HLA-DRB4*01:03* compared with 21 out of 64 samples from controls (allele frequency of 0.67 compared with 0.17, respectively, OR of 9.4 (4.4–21.3), $P = 1.8 \times 10^{-10}$). Owing to strong linkage disequilibrium in this region of the genome, it is not possible to be certain which is the causal susceptibility allele.

In situ hybridization and immune typing

To investigate the presence of AAV2, HAdV and HHV6 in liver biopsy samples, we carried out in situ hybridization (ISH). Liver biopsy samples of all patients were characterized by the presence of AAV2 RNA within the nuclei and cytoplasm of ballooned hepatocytes and in arterial endothelial cells, which is indicative of the presence of replicating virus (Fig. 3a–h). AAV2-positive cells were quantified at a high level in all cases using QuPath in biopsy samples from five non-A-non-E hepatitis, ranging from 1.2 to 4.7%. This level is similar to that seen in hepatitis associated with other viruses[12,13]. Consistent with low levels of HHV6B and HAdV sequence reads present in the biopsy samples from cases of hepatitis, negligible levels of viral RNA from these viruses were detected by ISH.

Fig. 3: ISH of AAV2 in liver tissue.



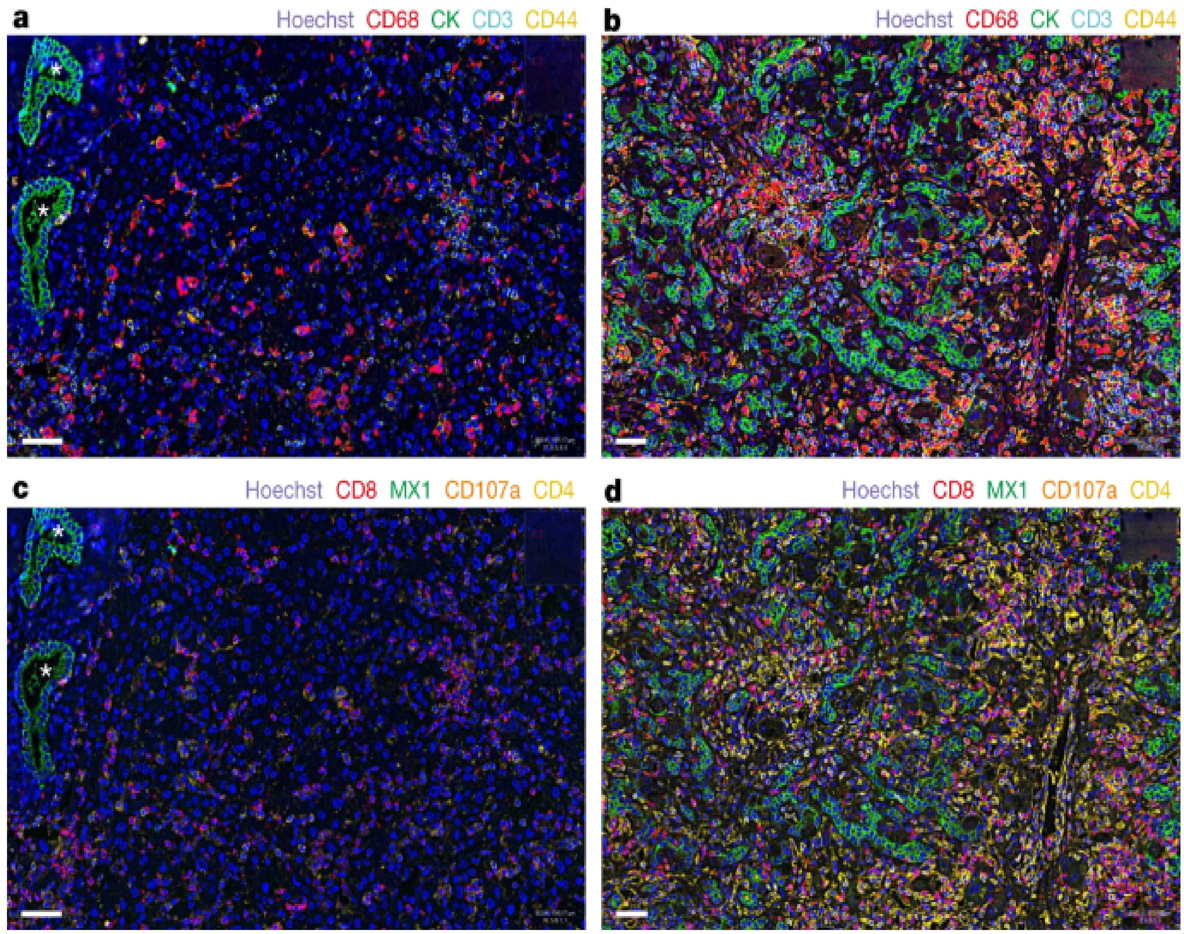
a–**g**, RNA ISH for the detection of AAV2 RNA in sections of formalin-fixed and paraffin-embedded liver tissues from children (one section per patient) with non A–E hepatitis. **a**, AAV2 RNA (red signal, indicated by an arrow) was detected in the endothelial cells of arteries in an explant liver section from patient CVR35. The vascular lumen is highlighted with by an asterisk. **b**, A positive AAV2 signal was detected in the nuclei of hepatocytes with vacuolated morphology from patient CVR4 (indicated by arrows) and in a negative cell (indicated by the circle). **c**,**d**, A liver section from patient CVR1 showed AAV2 RNA both in the nucleus and in the cytoplasm (**c**), whereas for patient CVR9 (**d**), AAV2 RNA was found only in the nucleus (indicated by arrows). **e**, A high percentage of hepatocytes with a positive signal for AAV2 was present predominantly in the nucleus of hepatocytes in the samples from patient CVR1. **f**, AAV2 was not detectable in liver sections from samples from healthy individuals in either the endothelial cells or

hepatocytes. **g**, Samples from patient CVR35 showed inclusion bodies in hepatocytes. Left, small, dark basophilic intranuclear inclusions next to the nucleolus (indicated by arrows). Right, a large, pale basophilic, diffuse intranuclear inclusion body (suggestive of adenovirus infection; indicated by an arrow) next to a multinucleated giant cell in the liver (indicated by the asterisk). **h**, AAV2-positive cells were quantified using QuPath in biopsy samples from five patients with non-A–E hepatitis (cases) and from controls. Patient CVR35 (who received a liver transplant) is highlighted in red. Using the entire section, cells were segmented to identify the nuclei and cytoplasm, and the algorithm was tuned to detect red signals. All samples were analysed using the same algorithm. Scale bars, 25 µm (insets of **c**,**d**), 50 µm (**a**–**d**,**f**,**g**) or 200 µm (**e**).

Source Data

To investigate the possibility of an immune-mediated pathogenesis of disease in the liver, multiplex analysis of liver samples was carried out using co-detection by indexing (CODEX) for various immune cellular markers, including CD3, CD4, CD8, PD-L1, CD107a, CD20, CD31, CD44, CD68, MX1 and PanCK (Fig. 4a–d and Supplementary Figs. 7 and 8). In the explant liver sample of patient CVR35, prominent disordered proliferation of epithelial cells throughout the liver tissue was evident, with increased numbers of $CD68^+$ macrophages, activated $CD4^+$ and $CD8^+$ T cells and $CD20^+$ B cells. High expression of the interferon-induced GTP-binding protein MX1 was also noted, which indicated that the innate immune response was activated.

Fig. 4: CODEX analysis of liver tissue.



a–**d**, Images of liver tissue from patient CVR35 (**b**,**d**) and a liver sample from an unaffected individual (control; **a**,**c**) show differences in cellular composition (**c**,**d**). **a**, Regularly structured bile ducts in the liver biopsy from the control are highlighted by asterisks, and epithelial cells are stained green using cytokeratin (CK). Scattered macrophages (CD68, red), T cells (CD3, cyan) and activated T cells (CD44, yellow) are also present. **b**, By contrast, the explant liver from patient CVR35 shows prominent proliferation of epithelial cells throughout the liver tissue (green), with increased macrophages (red), T cells (cyan) and activated T cells (yellow). **c**, The control liver shows scattered cytotoxic T cells (CD8, red), CD107a-positive cells (brown) and CD4-positive cells (yellow) cells and low expression of the interferon-induced GTP-binding protein MX1 (green). **d**, High numbers of all cell types and high MX1 expression are observed in the explant liver from patient CVR35. One section of liver was stained per individual, and the entire area was manually outlined. Cells were segmented to identify the nuclei and cytoplasm, and the algorithm was tuned to detect the colour

signal in the cells. All samples were analysed using the same algorithm for each stain. Scale bars, 50 µm.

Conclusions and final statements

In this study, we reported the association of AAV2 infection and the class II HLA allele *HLA-DRB1*04:01* with an outbreak of paediatric non-A–E hepatitis, with virus being detected independently by sequencing, real-time PCR and ISH. Liver biopsy tissue samples from all patients were characterized by the presence of AAV2 RNA (indicating replicating virus) within the nucleus and cytoplasm of ballooned hepatocytes and by a dense infiltrate of $CD4^+$ and $CD8^+$ T cells in the liver with an activated phenotype. A $CD4^+$ T-helper cell-mediated immunopathological response triggered by exposure to AAV2 infection is highly probable, consistent with the markedly increased frequency of the MHC class II *HLA-DRB1*04:01* allele in affected children.

AAV2 is a small non-enveloped virus with a single-stranded DNA genome of around 4,675 nucleotides in length and it belongs to the species adeno-associated dependoparvovirus A (genus *Dependoparvovirus*, family *Parvoviridae*)[14]. It was first described in 1965 and infects up to 80% of the adult population. Seroconversion occurs in early childhood following respiratory infection[15,16]. In a prospective study in the United States, the earliest seroconversion to AAV2 infection occurred in a 9-month-old child, and its seroprevalence increased from 24.2% to 38.7% in 3-year-old and 5-year-old children, respectively. This age range coincides with that of the cases in this study, which suggests that illness may be related to primary infection with AAV2 rather than its reactivation. In line with this hypothesis, anti-AAV2 IgM reactivity was observed in the majority of affected children. AAV2 relies on co-infection with a helper virus for replication, most commonly HAdV or a herpesvirus. Most clinical samples taken at presentation with hepatitis were obtained more than 20 days after initial symptom onset, which could explain the absence of a helper virus in some samples and low viral loads in positive samples. In an exploratory study using NGS, we detected two candidate helper viruses at low level in the cases of hepatitis: HAdV and HHV6B (in 6 out of 9 cases and in 3 out of 9 cases, respectively). These viruses were not confirmed to be higher in cases

than controls in plasma or liver samples in our larger case–control study. HHV6B was also present in two control groups that included children with severe HAdV infection and children with hepatitis of alternative aetiology. As HHV6 can establish latency and can integrate its genome into the human chromosome, it may reactivate following concomitant illness (or immunosuppression) and may represent either an opportunistic bystander or a pathogen.

We propose that AAV2 is directly implicated in the pathology of the 2022 outbreak of non-A–E hepatitis in children, which occurred following transmission as a co-infection with HAdV or less likely due to reactivation following HAdV or HHV6 infection. Our results also support an association between HLA class II haplotype and disease susceptibility. A $CD4^+$ T-cell-mediated response may direct maladaptive immunopathology mediated by T cytotoxic cells or B cells. In support of this notion, a $CD8^+$ cell-mediated response directed against the AAV2 viral capsid (VP1) in association with hepatitis was reported in early trials of AAV2 when used as a vector for gene therapy[17,18,19]. Hepatitis remains a common phenomenon in recipients of gene therapy vectored by AAV, and this side effect is usually treated pre-emptively with steroids before and for several weeks after the gene therapy; in rare cases, AAV-mediated gene therapy has been associated with deaths from fulminant hepatic failure[20,21]. As a result of this current study, further studies are needed investigate the association between HLA status with severe illness in gene therapy recipients. Notably, we did not find features of autoimmune hepatitis (AIH), either by serology or histology, in affected children. In a study of children from Scotland with AIH[22], the majority had evidence of seropositive disease (100% of patients with type II AIH tested positive for anti-LKM1). Furthermore, patients with AIH were older in age (median age of 11.4 years compared with 4.1 years in our cohort) and had significantly lower median alanine transaminase levels at diagnosis (444 IU per litre compared with 1,756 IU per litre). None of the AIH patients improved without treatment[22].

An alternative explanation for our findings is that AAV2 is not directly involved in pathology and is instead a biomarker of infection with HAdV. More than half of the patients with hepatitis in our study had subacute symptoms, with a median onset of 42 days before the onset of jaundice. The

opportunity to detect virus by sequencing was therefore reduced, as samples were collected after this stage of illness. Furthermore, whole blood samples might have increased the sensitivity of detection, but only serum or plasma samples were available. We consider this alternative hypothesis to be less likely because we did not detect AAV2 in a control group of children with HAdV infection who had normal liver function tests. However, HAdV41 is a common cause of diarrhoea in young children[23], and co-infection of AAV2 with HAdV41 may explain early gastrointestinal symptoms in affected children. By contrast, although adenovirus-associated hepatitis has been previously described, particularly among immunocompromised individuals[24], HAdV41 has not previously been associated with severe hepatitis. In the recent outbreaks of unexplained hepatitis in children, it has been inconsistently associated[4,5,6,25,26,27].

We also investigated the possibility that the unexplained cases of hepatitis were linked to a previous illness with COVID-19. Direct SARS-CoV-2-induced liver injury is unlikely though, as few of our cases of hepatitis (3 out of 31) were positive for SARS-CoV-2 by PCR on admission to hospital, and we did not identify SARS-CoV-2 by PCR or sequencing in any of the clinical samples from cases, including liver biopsies. Furthermore, the SARS-CoV-2 seroprevalence in cases of hepatitis was lower than in the community at that time. This result is in keeping with a case–control analysis by the UK Health Security Agency[3], who found no difference in SARS-CoV-2 PCR positivity between cases of hepatitis and children presenting to emergency departments between January and June 2022. Nevertheless, we cannot at this time fully exclude a post-COVID-19 immune-mediated phenomenon, for example, a link to HLA class II type, in susceptible children.

There are several limitations to this study. First, the presence of AAV2 in cases of hepatitis but not controls in groups 1–3 may have arisen because of seasonal variation in AAV2 transmission, as some children in the control groups were sampled earlier in the year than for cases. We included a contemporaneous control group (group 4) to address this possibility. Low viral loads of AAV2 were detected in a small number of samples from the group 4 controls, which is in keeping with the presence of the circulating virus in children at the time the cases of hepatitis occurred. Second, the

presence of AAV2 in the cases of hepatitis is an association and may not represent direct aetiology, and AAV2 may be a useful biomarker of recent HAdV (or less likely HHV6B) infection. We do not consider it probable that AAV2 simply represents a marker of liver damage because it was not present in cases of severe hepatitis of alternative aetiology and, significantly, we detected AAV2 in ballooned hepatocytes by ISH. The strong association of the *HLA-DRB1*04:01* allele, known to be associated with autoimmune hepatitis type 1[28] and extra-articular manifestations of rheumatoid arthritis[29], with the cases of hepatitis provides support for a large impact of host genetics on susceptibility. However, this analysis was affected by strong linkage disequilibrium, and larger studies are required to confirm a definitive association with this allele. The association between HLA status and the presence of an activated T cell infiltrate together with AAV2-infected cells in the liver is in keeping with a $CD4^+$ cell-mediated immune pathology[30]. We consider autoimmune disease to be less likely of a cause of the cases of hepatitis studied here because of the absence of autoantibodies and the absence of typical histology in liver specimens. It is also plausible that simultaneous HAdV infection with a co-infecting or reactivated AAV2 infection has resulted, for a proportion of children who are more susceptible (owing to the HLA class II allele *HLA-DRB1*04:01*), in a more severe outcome than might typically be expected for these commonly circulating viruses. Peptide mapping experiments are recommended in future studies to investigate the nature of the HLA class II-restricted T cell response.

The 2022 outbreak of AAV2-associated paediatric hepatitis that we described in this study may have arisen because of changes in exposure patterns to AAV2, HAdV and HHV6B as an indirect consequence of the COVID-19 pandemic. The circulation of common human viruses was interrupted in 2020 by the implementation of non-pharmaceutical interventions, including physical distancing and travel restrictions, instituted to mitigate SARS-CoV-2 transmission. Once restrictions were lifted, genetically susceptible children may have had a higher chance of being exposed to both HAdV and AAV2 for the first time, creating a synchronized wave of severe disease. Larger case–control studies are needed to confirm the role of AAV2 and HLA status in the aetiology of unexplained non-A–E paediatric hepatitis. Retrospective testing of samples from sporadic cases of unexplained hepatitis in children is also needed.

Methods

ISARIC CCP-UK recruitment, Biorepository and DIAMONDS studies

Ethics approval for the ISARIC CCP-UK study was given by the South Central–Oxford C Research Ethics Committee in England (13/SC/0149), the Scotland A Research Ethics Committee (20/SS/0028) and the WHO Ethics Review Committee (RPC571 and RPC572). Thirty-two children aged <16 years were prospectively recruited by written informed consent (parent or guardian) from the ISARIC WHO CCP-UK cohort admitted to hospital with increased transaminase levels (defined as alanine transaminase levels of >400 IU per litre and/or aspartate aminotransferase levels of >400 IU per litre) that was not due to viral hepatitis A–E, AIH or poisoning. Nine patients had available clinical samples for further investigation. Three additional patients had HLA typing performed, but samples were not available for further analysis. Samples for the control groups were obtained from children (aged <16 years) recruited to the DIAMONDS study, an ongoing multi-country study that aims to develop a molecular diagnostic test for the rapid diagnosis of severe infection and inflammatory diseases using personalized gene signatures (ISRCTN12394803). Ethics approval was given by the London-Dulwich Research Ethics Committee (20/HRA/1714). Controls included healthy individuals ($n = 13$; group 1), children with PCR-confirmed adenoviral infection with normal transaminase levels ($n = 12$; group 2), and children with increased transaminase levels without adenoviral infection ($n = 33$; group 3), recruited between 19 May 2020 to 8 January 2022. Surplus plasma samples from individuals in Scotland (aged <10 years; March to April 2022; group 4) and liver biopsy control samples (from individuals aged <18 years; January 2021 to July 2022) from the Diagnostic Pathology/Blood Sciences archive were obtained with NHS GG&C Biorepository approval (application no. 717; REC 22/WS/0020). Samples from adults that had tested negative by PCR for SARS-CoV-2 were used as an additional group for serological analysis of coronaviruses as a negative control group, also with NHS GG&C Biorepository approval. These adult samples were used without consent on the basis of Human Tissue Act legislation on consent exemption.

Viral PCR

RNA extraction was carried out using the protocol from Biomerieux Easymag. In total, 300 µl of plasma or sera was extracted and eluted into 80 µl of water.

AAV2 RT–qPCR was performed to detect a 62 bp amplicon of the AAV2 inverted terminal repeat region (ITR) as previously described[31] using the forward ITR primer (5′-GGAACCCCTAGTGATGGAGTT-3′) and the reverse ITR primer (5′-CGGCCTCAGTGAGCGA-3′). The AAV2 ITR hydrolysis probe was labelled with fluorescein (6FAM) and quenched with Black Hole quencher (BHQ) 5′-[6FAM]-CACTCCCTCTCTGCGCGCTCG-[BHQ1]3′). AAV2 primers and probe were synthesized by Merck Life Sciences. RT–qPCR analysis was performed using an ABI7500 Fast Real-Time PCR system (Applied Biosystems). A LUNA Universal One-Step RT PCR kit (New England Biolabs) was used for the amplification and detection of the AAV2 ITR target. RT–qPCR assays were performed in a 20 µl volume reaction (Luna Universal One-Step reaction mix, Luna WarmStart RT enzyme mix, 400 nM forward and reverse primers, 200 nM AAV2 ITR probe and 1–2.5 µl of template DNA) as per the manufacturer's instructions. To quantify the number of copies, serial dilutions of plasmid containing the 62 bp ITR product were used to generate a standard curve, which was then used to interpolate the copy number of AAV2 copies in the samples. Wells with no template were used as negative controls. RT–qPCR reactions were performed in triplicate. The RT–qPCR program consisted of an initial reverse transcription step at 55 °C for 10 min, an initial denaturation step at 95 °C for 1 min followed by 45 cycles of 95 °C denaturation for 10 s and extension at 58 °C for 1 min. A qPCR detection limit between 31 and 32 cycles was calculated as the threshold Ct value at the last dilution of DNA standards that were within the linear range. A PCR result was considered positive if all three reactions tested positive at ≤31 cycles.

Digital droplet PCR was performed according to the manufacturer's instructions using the digital droplet PCR supermix for probes (no dUTP) (Bio-Rad, 1863023) and analysed using a QX200 Droplet Digital PCR system (Bio-Rad, 1864001).

The West of Scotland Specialist Virology Centre, NHS Greater Glasgow and Clyde, conducted diagnostic real-time RT–PCR to detect HAdV, SARS-CoV-2-positive samples and other viral pathogens associated with hepatitis (for example, hepatitis A–E) following nucleic acid extraction utilizing the NucliSENS easyMAG and Roche MG96 platforms. HHV6 (ref. [32]) and HAdV41 (ref. [33]) were tested by qPCR as previously described using Invitrogen platinum qPCR mix (11730-025) and Quanta Biosciences qPCR mix mastermix (733-1273), respectively, on an ABI7500 system and amplified for 40 cycles. A 6 µl extract was amplified in a total reaction volume of 15 µl.

Measurement of antibody response to coronaviruses by electrochemiluminescence

IgG antibody titres were quantitatively measured against the spike protein, the NTD, the RBD or nucleocapsid of SARS-CoV-2, and against the spike glycoproteins of human seasonal coronaviruses 229E, OC43, NL63 and HKU1 using MSD V-PLEX COVID-19 Coronavirus Panel 2 (K15369) and Respiratory Panel 1 (K15365) kits. Multiplex meso scale discovery electrochemiluminescence (MSD-ECL) assays were performed according to manufacturer's instructions. Samples were diluted 1:5,000 in diluent and added to the plates along with serially diluted reference standard (calibrator) and serology controls 1.1, 1.2 and 1.3. Plates were read using a MESO Sector S 600 plate reader. Data were generated using Methodological Mind software and analysed using MSD Discovery Workbench (v.4.0). Results are expressed as MSD arbitrary units per ml (AU ml^{-1}). Adult negative and positive pools gave the following values: negative pool: spike, 56.6 AU ml^{-1}; NTD, 119.4 AU ml^{-1}; RBD, 110.5 AU ml^{-1}; and nucleocapsid, 20.7 AU ml^{-1}; SARS-CoV-2-positive pool: spike, 1,331.1 AU ml^{-1}; NTD, 1,545.2 AU ml^{-1}; RBD, 1,156.4 AU ml^{-1}; and nucleocapsid, 1,549.0 AU ml^{-1}. In the same assay, NIBSC 20/130 reference serum was used and the following values obtained: spike, 547.7 AU $ml^{-1;}$ NTD, 538.8 AU ml^{-1}; RBD, 536.9 AU ml^{-1}; and nucleocapsid 1,840.2 AU ml^{-1}.

Metagenomics sequencing

Full protocols on the detection of RNA and DNA viruses using metagenomics NGS and TE sequencing methods can be found in refs. [32,34].

In summary, residual nucleic acid from 27 samples from cases with hepatitis (from 9 patients with a combination of plasma, liver, faeces, rectal, and throat and nose samples), 12 samples from HAdV-positive individuals and 13 samples from healthy individuals (control samples were either plasma or sera) underwent metagenomics NGS sequencing at the MRC-University of Glasgow Centre for Virus Research Genomics facility. In brief, each nucleic acid sample was split into two library preparations to improve the chances of detecting RNA and DNA viruses. The protocol used to improve detection of RNA viruses included treatment with DNaseI (Ambion DNase I, ThermoFisher), ribosomal depletion (Ribo-Zero Plus rRNA Depletion Kit, Illumina), except for plasma samples, reverse transcription (SuperScript III, Invitrogen) and double-strand DNA synthesis (NEBNext Ultra II Non-Directional RNA Second Strand Synthesis Module, NEB). The protocol used to detect DNA viruses included partial removal of host DNA (NEBNext Microbiome DNA Enrichment Kit, NEB). Following this, both sets of samples were used to prepare libraries using a KAPA LTP kit (Roche) with unique dual indices (NEBNext Multiplex oligos for Illumina, NEB). The resulting libraries were pooled in equimolar amounts and sequenced using a NextSeq500 (Illumina) to obtain paired-end reads using 150 × 150 cycles.

TE sequencing

Following the library preparation step described above, DNA-derived and RNA-derived libraries were pooled separately and were incubated with VirCapSeq-VERT Capture Panel probes (Roche) following the manufacturer’s guidelines. The Roche VirCapSeq-VERT Capture Panel covers the genomes of 207 taxa of viruses known to infect vertebrates (including humans). Enriched DNA-derived and RNA-derived libraries were further amplified using 14 PCR cycles, then pooled and sequenced using a NextSeq500 (Illumina) to obtain paired-end reads using 150 × 150 cycles.

Bioinformatics analysis

Reads for each sample were first quality checked. Illumina adapters were trimmed using Trim Galore (https://github.com/FelixKrueger/TrimGalore) and then mapped to the human genome using BWA-MEM (https://github.com/lh3/bwa). Only reads that did not map to the human genome were used for metagenomics analyses. Reads per million were calculated as the number of viral reads per million reads sequenced to normalize for variation in sample sequencing depth. Non-human reads were then de novo assembled using MetaSPAdes (https://github.com/ablab/spades) to generate contigs for each sample. Contigs were compared against a protein database of all NCBI RefSeq organisms (including virus, bacteria and eukaryotes) with BLASTX using DIAMOND (https://github.com/bbuchfink/diamond). In addition, non-human reads for each sample were aligned to a small panel of HAdV NCBI RefSeq genomes (HAdV-A, HAdV-B1, HAdV-B2, HAdV-C, HAdV-D, HAdV-E, HAdV-F, HAdV-1, HAdV-2, HAdV-5, HAdV-7, HAdV-35, HAdV-54 and HAdV-F41).

The nine AAV2 near-complete genome contigs from the plasma samples were assembled and compared with sequences in GenBank using BLASTN (nucleotide database). Each of these AAV2 genomes had numerous close hits (exhibiting >95% similarity across 95% of the genome) with various existing AAV2 sequences; those most closely related were reported in a previous publication[35]. All linear complete AAV2 genomes returned from BLAST against the GenBank nucleotide database with a query coverage of >75% were selected and combined with the AAV sequences de novo assembled here and aligned using MAFFT. The terminal ends of this alignment were trimmed off, and IQ-TREE 2 was used (TIM+F+R3 model) to infer a phylogenetic tree. For the single HAdV41 genome de novo assembled, all available HAdV41 complete genomes were downloaded from GenBank, aligned with MAFFT and IQ-TREE2 was used (K2P+R2 model) to infer a phylogenetic tree.

Anti-AAV2 ELISA

AAV2 pAAV-CAG-tdTomato viral preparation (codon diversified) was a gift from E. Boyden (Addgene viral preparation number 59462-AAV2; http://n2t.net/addgene:59462; RRID:Addgene_59462).

AAV2 particles, obtained from Addgene (59462-AAV2) were diluted in PBS and used to coat a Immulon 2HB 96-well flat bottom plate (ImmunoChemistry Technologies) at a concentration of 1 × 10^8 particles per well. The plates were incubated on an orbital shaker overnight at 4 °C. Plates were then blocked with PBS-T (PBS with 0.1% Tween-20) containing 5% BSA for 1 h before the addition of samples. The plates were washed five times in PBS-T before serum samples, diluted 1:50 in PBS, were added in triplicate. A mouse anti-AAV2 (A20, Progen) was used as a positive control at a concentration of 1:50. Samples were incubated at room temperature on an orbital shaker for 90 min before washing five times in PBS-T and adding either anti-human IgM or anti-human IgG (Merck, A9794 and A1543, respectively) diluted 1:10,000. Goat anti-mouse IgG (Merck, A2429) was used as the secondary for the anti-AAV2 A20 positive control. The plates were incubated for 1 h before washing five times with PBS-T then 100 µl of alkaline phosphatase yellow (Merck, P7998) was added and incubated for 15 min before stopping the reaction with 3 M NaOH and the absorbance measured at 405 nm.

Immunohistochemistry, ISH and special staining

Formalin-fixed and paraffin-wax-embedded liver samples were cut at around 3 µm thickness and mounted on glass slides. A reticulin (1936) and Masson trichrome (1929) special staining method (Gordon and Sweets method (1936)) was performed. Antibodies used for immunohistochemistry are listed in Supplementary Table 6.

Detection of viral nucleic acids, ubiquitin and DapB-specific RNA (Advanced Cell Diagnostics, AAV2 (1195791), HHV6 (144565), adenovirus 41 (1192351), ubiquitin (310041) and DapB (310043)) was performed following the manufacturer's protocol with pretreatment with simmering in target solution (30 min) and additional proteinase K (30 min) treatment. A haematoxylin counterstain was performed, and slides were mounted with Vectamount mounting medium (H-500, Vector Laboratories) and scanned using a bright-field slide scanner (Leica, Aperio Versa 8).

Liver histopathology grading

Liver scoring was performed as previously described[8,9].

Quantification of immune cells

After scanning of the whole slide, liver tissue was outlined and the number of positively stained cells (DAB signal for immunohistochemistry or Fast Red signal for ISH) was assessed using software-assisted image analysis (QuPath, v.0.3.2)[36]. For each marker, the cell detection algorithm was tuned, and data were plotted using GraphPad Prism (v.9.4.1).

Spatial analysis (CODEX Phenocycler)

Formalin fixed, paraffin-wax-embedded liver samples (patient 228742A and patient 145808) were sectioned at 2–4 µm thickness on 22 × 22 mm glass coverslips (Akoya Biosciences, 7000005) coated in 0.1% poly-l-lysine (Sigma-Aldrich, P8920). Antigen retrieval was performed by pressure cooking with citrate buffer at pH 6. Carrier-free, pre-conjugated antibodies were purchased directly from Akoya Biosciences or purchased from other suppliers in preparation for custom conjugation. If carrier-free antibodies were not available, alternatives were purchased and purified using a Pierce antibody cleanup kit (44600, ThermoFisher). Antibodies were custom conjugated to a unique oligonucleotide barcode according to the manufacturer's instructions using an antibody conjugation kit (7000009, Akoya Biosciences) and stored at 4 °C for at least 48 h before use. Conjugated antibodies were stored at 4 °C.

Coverslips with tissue were rehydrated in an alcohol series and washed in distilled water before performing heat-induced antigen retrieval in a pressure cooker with citrate buffer (pH 6). Glass coverslips were then moved progressively between wells of a 6-well plate containing components of the CODEX staining kit (Akoya Biosciences, 7000008). This included 2 wells of hydration buffer (2 min each), 1 well of staining buffer (20 min), and then staining with 190 µl of an 11-marker antibody panel (Supplementary Table 7). Tissue sections of both samples were treated in the same way on the same day and were incubated with antibodies for 3 h at room temperature simultaneously. Following staining, tissue was incubated twice in staining buffer (2 min each) and transferred to a post-staining fixation solution made

from a 1:10 ratio of paraformaldehyde to storage buffer for 10 min. Tissue samples were then washed 3 times in 1× PBS (14190-094, Gibco), incubated in ice-cold methanol (M/4000/PC17, Fisher Scientific) for 5 min on ice, and again washed 3 times in PBS. Tissue sections were fixed in a fixative solution for 20 min, washed 3× in PBS and stored in storage buffer until image acquisition.

Image acquisition was achieved using a Keyence BZ-X710 microscope equipped with 4 fluorescent channels (1 nuclear stain, 3 for antibody visualization). In a 96-well plate (Akoya Biosciences, 7000006), a maximum of three oligonucleotide reporters were used per well (cycle) (5 µl each) and added to between 235 µl and 245 µl reporter stock solution that was made according to the manufacturer's instructions. Plates were sealed with aluminium film (Akoya Biosciences, 7000007) and stored at 4 °C until use. Pictures were captured using QuPath (v.0.3.2)[36].

Host genetics and HLA typing

High-resolution typing for all HLA loci (*HLA-A*, *HLA-B*, *HLA-C*, *HLA-DRB1*, *HLA-DRB3*, *HLA-DRB4*, *HLA-DRB5*, *HLA-DQA1*, *HLA-DQB1*, *HLA-DPA1* and *HLA-DPB1*) was performed using an AllType FASTplex NGS assay (One Lambda) run on an Illumina Mi-Seq platform. HLA typing was undertaken on 27 ISARIC participants who provided consent. One patient was omitted from analysis as they were a sibling of another case. HLA types from 64 Scottish National Blood Transfusion Service apheresis platelet donors, self-identified as white British ($n = 15$) or white Scottish ($n = 49$) were used as control samples for comparison with patient HLA allele frequencies. Genotyping was performed using Illumina Global Screening Array v.3.0 + multi-disease beadchips (GSAMD-24v3-0-EA) and Infinium chemistry. This consists of three steps: (1) whole genome amplification; (2) fragmentation followed by hybridization; and (3) single-base extension and staining. Arrays were imaged on an Illumina iScan platform, and genotypes were automatically called using GenomeStudio Analysis software (v.2.0.3), GSAMD-24v3-0-EA_20034606_A1.bpm manifest and a cluster file provided by the manufacturer.

Given the small sample size, it was not possible to implement quality control processes using GenomeStudio and the manufacturer's published recommendations. As genotyping was conducted using the same genotyping array used for the GenOMICC study, variants that passed quality control for the GenOMICC study were retained as previously described[37]. After further excluding variants with call rates of <95%, a total of 478,692 variants were used for downstream analysis.

Kinship and population structure

To identify close relatives up to third degree, King 2.1 was used, which confirmed the presence of a pair of siblings with no further close relatives identified. Genotypes of 19 patients were combined with imputed genotypes of a subset of unrelated participants from the UK Biobank, which was obtained by removing one individual in each pair with estimated kinship larger than 0.0442. The resulting genotypes were filtered to exclude variants with a mean allele frequency of <5%, a genotype missingness rate of <1.5% and Hardy–Weinberg equilibrium of $P < 10^{-50}$. Principal component analysis was conducted with gcta 1.955 in the set of unrelated individuals with pruned single nucleotide polymorphisms using a window of 1,000 markers, a step size of 50 markers and a r^2 threshold of 0.01. Analyses were performed once including all UK Biobank participants and once including only UK Biobank participants who were born in Scotland (UK Biobank data-field 1647) and of Caucasian genetic ancestry (UK Biobank data-field 22006).

Statistics

Differences between cases and control groups were tested using Fisher's exact test for categorical variables and Mann–Whitney (two tailed) for continuous variables using R studio (v.1.2.5033), R (v.4.1.2) and GraphPad (v.9.0.0).

For coronavirus serology experiments, comparisons were carried out using one-way analysis of variance (ANOVA) and Tukey's multiple comparison test, carried out in GraphPad (v.8.4.3).

HLA analysis used the Bridging ImmunoGenomic Data-Analysis Workflow Gaps (BIGDAWG) R package to derive OR and corrected *P* values for individual HLA alleles[38]. The Bonferroni-corrected *P* value significance threshold, adjusted for multiple comparisons (168 HLA alleles), was $P < 3.0 \times 10^{-4}$.

Figures

Figures were prepared using Microsoft Office Excel 2010, Microsoft Office PowerPoint 2010 and Adobe Illustrator 2022.

Reporting summary

Further information on research design is available in the Nature Portfolio Reporting Summary linked to this article.

Data availability

Datasets generated in the current study are appended as supplementary tables. Data, protocols and all documentation regarding this analysis may be made available to academic researchers after authorization from the independent data access and sharing committee. Clinical data and analysis scripts are available on request to the Independent Data Management and Access Committee at https://isaric4c.net/sample_access. Restrictions apply to the availability of identifiable clinical data. Owing to the relatively small number of cases, de-aggregation of data is potentially disclosive, as is the patient-level line list data. Therefore, a formal data-sharing agreement is required for data access. The Independent Data and Material Access Committee considers requests as they arrive; most responses are made within 28 days. Use of clinical samples are also restricted under ethical approvals obtained for their use. Genome sequences are available at GenBank with accession numbers OP019741–OP019749 for AAV2 and OP019750 for HAdV-F41. Source data are provided with this paper.

Code availability

Freely available bioinformatics and statistical software were used, see links in the Methods section.

References

1. Marsh, K. et al. Investigation into cases of hepatitis of unknown aetiology among young children, Scotland, 1 January 2022 to 12 April 2022. *Euro Surveill.* https://doi.org/10.2807/1560-7917.ES.2022.27.15.2200318 (2022).

2. Severe acute hepatitis of unknown aetiology in children—multi-country. *World Health Organization* (12 July 2022); https://www.who.int/emergencies/disease-outbreak-news/item/2022-DON400.

3. *Investigation into Acute Hepatitis of Unknown Aetiology in Children in England. Technical Briefing 4* (UK Health Security Agency, 2022).

4. Gutierrez Sanchez, L. H. et al. A case series of children with acute hepatitis and human adenovirus infection. *N. Engl. J. Med.* https://doi.org/10.1056/NEJMoa2206294 (2022).

5. Karpen, S. J. Acute hepatitis in children in 2022—human adenovirus 41? *N. Engl. J. Med*. https://doi.org/10.1056/NEJMe2208409 (2022).

6. Kelgeri, C. et al. Clinical spectrum of children with acute hepatitis of unknown cause. *N. Engl. J. Med.* https://doi.org/10.1056/NEJMoa2206704 (2022).

7. Dunning, J. W. et al. Open source clinical science for emerging infections. *Lancet Infect. Dis.* **14**, 8–9 (2014).

8. Knodell, R. G. et al. Formulation and application of a numerical scoring system for assessing histological activity in asymptomatic chronic active hepatitis. *Hepatology* **1**, 431–435 (1981).

9. Krishna, M. Histological grading and staging of chronic hepatitis. *Clin. Liver Dis.* **17**, 222–226 (2021).

10. Hsu, H. L. et al. Structural characterization of a novel human adeno-associated virus capsid with neurotropic properties. *Nat. Commun.* **11**, 3279 (2020).

11. Enhanced Surveillance of Covid-19 in Scotland (Population-based seroprevalence)—5 Week Rolling Estimate. *Public Health Scotland* (1 June 2022); https://publichealthscotland.scot/publications/enhanced-surveillance-of-covid-19-in-scotland/enhanced-surveillance-of-covid-19-in-scotland-population-based-seroprevalence-surveillance-1-june-2022/dashboard/.

12. Rodriguez-Inigo, E. et al. Percentage of hepatitis C virus-infected hepatocytes is a better predictor of response than serum viremia levels. *J. Mol. Diagn.* **7**, 535–543 (2005).

13. Tomlinson, J. E. et al. Tropism, pathology, and transmission of equine parvovirus-hepatitis. *Emerg. Microbes Infect.* **9**, 651–663 (2020).

14. Srivastava, A., Lusby, E. W. & Berns, K. I. Nucleotide sequence and organization of the adeno-associated virus 2 genome. *J. Virol.* **45**, 555–564 (1983).

15. Atchison, R. W., Casto, B. C. & Hammon, W. M. Adenovirus-associated defective virus particles. *Science* **149**, 754–756 (1965).

16. Li, C. et al. Neutralizing antibodies against adeno-associated virus examined prospectively in pediatric patients with hemophilia. *Gene Ther.* **19**, 288–294 (2012).

17. Martino, A. T. et al. Engineered AAV vector minimizes in vivo targeting of transduced hepatocytes by capsid-specific $CD8^+$ T cells. *Blood* **121**, 2224–2233 (2013).

18. Manno, C. S. et al. Successful transduction of liver in hemophilia by AAV-factor IX and limitations imposed by the host immune response. *Nat. Med.* **12**, 342–347 (2006).

19. Mingozzi, F. et al. $CD8^+$ T-cell responses to adeno-associated virus capsid in humans. *Nat. Med.* **13**, 419–422 (2007).

20. Ertl, H. C. J. Immunogenicity and toxicity of AAV gene therapy. *Front. Immunol.* **13**, 975803 (2022).

21. Chowdary, P. et al. Phase 1–2 trial of AAVS3 gene therapy in patients with hemophilia B. *N. Engl. J. Med.* **387**, 237–247 (2022).

22. Sebode, M., Weiler-Normann, C., Liwinski, T. & Schramm, C. Autoantibodies in autoimmune liver disease—clinical and diagnostic relevance. *Front. Immunol.* **9**, 609 (2018).

23. Rafie, K. et al. The structure of enteric human adenovirus 41—a leading cause of diarrhea in children. *Sci. Adv.* **7**, eabe0974 (2021).

24. Echavarria, M. Adenoviruses in immunocompromised hosts. *Clin. Microbiol. Rev.* **21**, 704–715 (2008).

25. Baker, J. M. et al. Acute hepatitis and adenovirus infection among children—Alabama, October 2021–February 2022. *MMWR Morb. Mortal. Wkly Rep.* **71**, 638–640 (2022).

26. Cooper, S. et al. Long COVID-19 liver manifestation in children. *J. Pediatr. Gastroenterol. Nutr.* https://doi.org/10.1097/MPG.0000000000003521 (2022).

27. Deep, A., Grammatikopoulos, T., Heaton, N., Verma, A. & Dhawan, A. Outbreak of hepatitis in children: clinical course of children with acute liver failure admitted to the intensive care unit. *Intensive Care Med.* https://doi.org/10.1007/s00134-022-06765-3 (2022).

28. van Gerven, N. M. et al. HLA-DRB1*03:01 and HLA-DRB1*04:01 modify the presentation and outcome in autoimmune hepatitis type-1. *Genes Immun.* **16**, 247–252 (2015).

29. Lanchbury, J. S. et al. Strong primary selection for the Dw4 subtype of DR4 accounts for the HLA-DQw7 association with Felty's syndrome. *Hum. Immunol.* **32**, 56–64 (1991).

30. Gay, D. et al. Functional interaction between human T-cell protein CD4 and the major histocompatibility complex HLA-DR antigen. *Nature* **328**, 626–629 (1987).

31. Aurnhammer, C. et al. Universal real-time PCR for the detection and quantification of adeno-associated virus serotype 2-derived inverted terminal repeat sequences. *Hum. Gene Ther. Methods* **23**, 18–28 (2012).

32. Tong, L. et al. Discovery of RNA and DNA viruses using next-generation sequencing: metagenomics. *protocols.io* https://doi.org/10.17504/protocols.io.261ge34zol47/v1 (2023).

33. van Maarseveen, N. M., Wessels, E., de Brouwer, C. S., Vossen, A. C. & Claas, E. C. Diagnosis of viral gastroenteritis by simultaneous detection of Adenovirus group F, Astrovirus, Rotavirus group A, Norovirus genogroups I and II, and Sapovirus in two internally controlled multiplex real-time PCR assays. *J. Clin. Virol.* **49**, 205–210 (2010).

34. Tong, L. et al. Discovery of RNA and DNA viruses using next-generation sequencing: targeted enrichment. *protocols.io* https://doi.org/10.17504/protocols.io.36wgqj3q3vk5/v1 (2023).

35. La Bella, T. et al. Adeno-associated virus in the liver: natural history and consequences in tumour development. *Gut* **69**, 737–747 (2020).

36. Bankhead, P. et al. QuPath: open source software for digital pathology image analysis. *Sci. Rep.* **7**, 16878 (2017).

37. Pairo-Castineira, E. et al. Genetic mechanisms of critical illness in COVID-19. *Nature* **591**, 92–98 (2021).

38. Pappas, D. J., Marin, W., Hollenbach, J. A. & Mack, S. J. Bridging ImmunoGenomic Data Analysis Workflow Gaps (BIGDAWG): an integrated case–control analysis pipeline. *Hum. Immunol.* **77**, 283–287 (2016).

39. Gautheret-Dejean, A. et al. Development of a real-time polymerase chain reaction assay for the diagnosis of human herpesvirus-6 infection

and application to bone marrow transplant patients. *J. Virol. Methods* **100**, 27–35 (2002).

Acknowledgements

We wish to acknowledge the contribution of the participating children and their parents who agreed to participate in the ISARIC CCP-UK and DIAMONDS studies, and the research teams who recruited the patients; S. Bennett-Slater from NHS Greater Glasgow and Clyde for assisting with sample location and testing; the histopathology team, Veterinary Diagnostic, University of Glasgow, for excellent technical assistance; P. Murcia for providing resources and advice; P. Olmo for administrative assistance; and E. J. Kremer from the Institut de Génétique Moléculaire de Montpellier, Université de Montpellier and A. Baker, University of Edinburgh, for advice. The work was funded by Public Health Scotland, the National Institute for Health Research (NIHR; award CO-CIN-01) and the Medical Research Council (MRC; grants MR/X010252/1, MC_UU_1201412, MC_UU_12018/12, MC_PC_19059, MC_PC_19025 and MC_PC_22004). DIAMONDS is funded by the European Union Horizon 2020 programme; grant 848196). M.P. acknowledges funding support from the Wellcome Trust (206369/Z/17/Z). M.G.S. acknowledges funding support from The Pandemic Institute, Liverpool and the NIHR Health Protection Research Unit (HPRU) in Emerging and Zoonotic Infections at University of Liverpool, and UK Health Security Agency. J.K.B. acknowledges funding support from a Wellcome Trust Senior Research Fellowship (223164/Z/21/Z), and MC_PC_20029, Sepsis Research (Fiona Elizabeth Agnew Trust), a BBSRC Institute Strategic Programme Grant to the Roslin Institute (BB/P013732/1, BB/P013759/1), and the Intensive Care Society of the United Kingdom. We acknowledge the support of Baillie Gifford and the Baillie Gifford Science Pandemic Hub at the University of Edinburgh. Parts of this research has been conducted using the UK Biobank Resource under project 788 and we would like to acknowledge the assistance of A. Tenesa in making this possible. Additional replication was also conducted using the UK Biobank Resource (Project 26041). This research was also funded by the National Institute for Health and Care Research (CO-CIN-01) and jointly by NIHR and UK Research and Innovation (CV220-169, MC_PC_19059). The views expressed in this article are those of the author(s) and not necessarily

those of UKRI, the NIHR, or the Department of Health and Social Care. We also acknowledge the support of NHS Research Scotland (NRS) Greater Glasgow and Clyde Biorepository team. For the purpose of open access, the author has applied a CC BY public copyright licence to any Author Accepted Manuscript version arising from this submission.

Author information

Author notes

1. These authors contributed equally: Antonia Ho, Richard Orton, Rachel Tayler, Patawee Asamaphan, Vanessa Herder, Chris Davis

2. These authors jointly supervised this work: David L. Robertson, Ana da Silva Filipe, Brian J. Willett, Judith Breuer, Malcolm G. Semple, David Turner, J. Kenneth Baillie, Emma C. Thomson

Authors and Affiliations

1. Medical Research Council–University of Glasgow Centre for Virus Research, Glasgow, UK

   Antonia Ho, Richard Orton, Patawee Asamaphan, Vanessa Herder, Chris Davis, Lily Tong, Katherine Smollett, Maria Manali, Jay Allan, Sarah E. McDonald, Elen Vink, Louisa Pollock, Emma C. Thomson, Massimo Palmarini, David L. Robertson, Ana da Silva Filipe, Brian J. Willett & Emma C. Thomson

2. Department of Paediatrics, Royal Hospital for Children, Glasgow, UK

   Rachel Tayler & Louisa Pollock

3. Pandemic Science Hub, Centre for Inflammation Research and Roslin Institute, University of Edinburgh, Edinburgh, UK

   Konrad Rawlik, Miranda Odam, Primrose Chikowore, Wilna Oosthuyzen, Nikos Avramidis, Erola Pairo-Castineira, Veronique

Vitart, Ivana Pennisi, Maggie Nyirenda, Lauren Obosi, Sara Clohisey, Andrew Law, Murray Wham & J. Kenneth Baillie

4. Department of Paediatrics, NHS Tayside, Dundee, UK

Louise Gannon

5. Department of Pathology, Queen Elizabeth University Hospital, Glasgow, UK

Clair Evans

6. Public Health Scotland, Glasgow, UK

Jim McMenamin, Kirsty Roy, Kimberly Marsh, Titus Divala, Matthew T. G. Holden, Michael Lockhart, David Yirrell, Sandra Currie, Maureen O'Leary, David Henderson & Sarah Tait

7. West of Scotland Specialist Virology Centre, Glasgow, UK

Samantha J. Shepherd, Celia Jackson, Rory Gunson, Alasdair MacLean & Neil McInnes

8. Virology Laboratory, Ninewells Hospital, Dundee, UK

Amanda Bradley-Stewart

9. Histocompatibility and Immunogenetics (H&I) Laboratory, Scottish National Blood Transfusion Service, Edinburgh Royal Infirmary, Edinburgh, UK

Richard Battle & David Turner

10. Department of Neurology and Department of Epidemiology and Biostatistics, University of California San Francisco, San Francisco, CA, USA

Jill A. Hollenbach

11. Child Life and Health, University of Edinburgh, Edinburgh, UK

Paul Henderson

12. UK Health Security Agency, London, UK

Meera Chand & Meera Chand

13. Section of Paediatric Infectious Disease, Department of Infectious Disease, Imperial College London, London, UK

Melissa Shea Hamilton, Diego Estrada-Rivadeneyra, Michael Levin, Aubrey Cunnington, Jethro Herberg, Myrsini Kaforou, Victoria Wright, Evangelos Bellos, Claire Broderick, Samuel Channon-Wells, Samantha Cooray, Tisham De, Giselle D'Souza, Leire Estramiana Elorrieta, Rachel Galassini, Dominic Habgood-Coote, Shea Hamilton, Heather Jackson, James Kavanagh, Mahdi Moradi Marjaneh, Stephanie Menikou, Samuel Nichols, Ruud Nijman, Harsita Patel, Ivana Pennisi, Oliver Powell, Ruth Reid, Priyen Shah, Ortensia Vito, Elizabeth Whittaker, Clare Wilson & Rebecca Womersley

14. MRC Human Genetics Unit, Institute for Genetics and Cancer, University of Edinburgh, Edinburgh, UK

Veronique Vitart & J. Kenneth Baillie

15. School of Mathematics and Statistics, University of Glasgow, Glasgow, UK

Craig Wilkie & Surajit Ray

16. University College London, London, UK

Judith Breuer

17. Pandemic Institute, University of Liverpool, Liverpool, UK

Malcolm G. Semple

18. Department of Clinical Research, London School of Hygiene and Tropical Medicine, London, UK

Shunmay Yeung, Manuel Dewez, Elizabeth Fitchett, Fiona Cresswell & Emma C. Thomson

19. Children's Clinical Research Unit, St Mary's Hospital, London, UK

Amina Abdulla, Sarah Darnell & Sobia Mustafa

20. Department of Electrical and Electronic Engineering, Imperial College London, South Kensington Campus, London, UK

Pantelis Georgiou & Nicolas Moser

21. Imperial College London, Department of Infectious Disease, Section of Adult Infectious Disease, Imperial College London, Hammersmith Campus, London, UK

Jesus-Rodriguez Manzano

22. Evelina London Children's Hospital, Guy's and St Thomas' NHS Foundation Trust, London, UK

Michael Carter, Shane Tibby, Jonathan Cohen, Francesca Davis, Julia Kenny, Paul Wellman & Marie White

23. Department of Women and Children's Health, School of Life Course Sciences, King's College London, London, UK

Michael Carter & Shane Tibby

24. Department of Infectious Diseases, School of Immunology and Microbial Sciences, King's College London, London, UK

Matthew Fish & Manu Shankar-Hari

25. Department of Intensive Care Medicine, Guy's and St Thomas' NHS Foundation Trust, London, UK

Aislinn Jennings & Manu Shankar-Hari

26. Royal Alexandra Children's Hospital, University Hospitals Sussex, Brighton, UK

    Katy Fidler & Vivien Richmond

27. Department of Infectious Diseases, University Hospitals Sussex, Brighton, UK

    Dan Agranoff & Mathew Seal

28. Research Nurse Team, University Hospitals Sussex, Brighton, UK

    Vivien Richmond

29. NIHR Southampton Clinical Research Facility, University Hospital Southampton NHS Foundation Trust and University of Southampton, Southampton, UK

    Saul Faust & Dan Owen

30. NIHR Southampton Clinical Research Facility, University Hospital Southampton NHS Foundation Trust, Southampton, UK

    Ruth Ensom & Sarah McKay

31. Department of R&D, University Hospital Southampton NHS Foundation Trust, Southampton, UK

    Diana Mondo, Mariya Shaji & Rachel Schranz

32. Royal London Hospital, London, UK

    Prita Rughnani, Amutha Anpananthar, Anna Riddell & Nosheen Khalid

33. Newham University Hospital, London, UK

    Prita Rughnani, Amutha Anpananthar & Susan Liebeschuetz

34. Whipps Cross University Hospital, London, UK

Prita Rughnani, Amutha Anpananthar, Nosheen Khalid, Ivone Lancoma Malcolm & Teresa Simagan

35. Great Ormond Street Hospital, London, UK

Mark Peters, Alasdair Bamford & Lauran O'Neill

36. UCL Great Ormond Street Institute of Child Health, London, UK

Mark Peters & Alasdair Bamford

37. Addenbrooke's Hospital, Cambridge, UK

Nazima Pathan, Esther Daubney & Deborah White

38. Department of Paediatrics, University of Cambridge, Cambridge, UK

Nazima Pathan

39. University College London Hospital, London, UK

Melissa Heightman, Sarah Eisen, Terry Segal & Lucy Wellings

40. St George's Hospital, London, UK

Simon B. Drysdale, Nicole Branch, Lisa Hamzah & Heather Jarman

41. University Hospital Lewisham, London, UK

Maggie Nyirenda, Lisa Capozzi & Emma Gardiner

42. Aintree University Hospital, Lower Lane, Liverpool, UK

Robert Moots & Michelle Linforth

43. Royal Liverpool Hospital, Prescot St, Liverpool, UK

Magda Nasher & Anita Hanson

44. Leeds Children's Hospital, Leeds, UK

Sean O'Riordan & Donna Ellis

45. Kings College Hospital, Denmark Hill, London, UK

Akash Deep & Ivan Caro

46. Sheffield Children's Hospital, Broomhall, Sheffield, UK

Fiona Shackley, Arianna Bellini & Stuart Gormley

47. Leicester General Hospital, Leicester, UK

Samira Neshat

48. Birmingham Children's Hospital, Steelhouse Lane, Birmingham, UK

Barnaby J. Scholefield, Ceri Robbins & Helen Winmill

49. John Radcliffe Hospital, Oxford University Hospitals NHS Foundation Trust, Oxford, UK

Stéphane C. Paulus, Andrew J. Pollard, Mark Anthony, Sarah Hopton, Danielle Miller, Zoe Oliver, Sally Beer & Bryony Ward

50. Department of Paediatrics, University of Oxford, Oxford, UK

Stéphane C. Paulus & Andrew J. Pollard

51. Oxford Vaccine Group, University of Oxford, Oxford, UK

Stéphane C. Paulus & Andrew J. Pollard

52. NIHR Oxford Biomedical Research Centre, Oxford, UK

Andrew J. Pollard & Andrew J. Pollard

53. Paediatric Research Unit, Patan Academy of Health Sciences, Kathmandu, Nepal

Shrijana Shrestha, Meeru Gurung, Puja Amatya, Bhishma Pokhrel & Sanjeev Man Bijukchhe

54. Oxford Vaccine Group, Department of Paediatrics, University of Oxford, Oxford, UK

Andrew J. Pollard, Tim Lubinda, Sarah Kelly & Peter O’Reilly

55. Translational Pediatrics and Infectious Diseases, Pediatrics Department, Hospital Clínico Universitario de Santiago, Santiago de Compostela, Galicia, Spain

Federico Martinón-Torres, Antonio Salas, Fernando Álvez González, Xabier Bello, Mirian Ben García, Sandra Carnota, Miriam Cebey-López, María José Curras-Tuala, Carlos Durán Suárez, Luisa García Vicente, Alberto Gómez-Carballa, Jose Gómez Rial, Pilar Leboráns Iglesias, Nazareth Martinón-Torres, José María Martinón Sánchez, Belén Mosquera Pérez, Jacobo Pardo-Seco, Lidia Piñeiro Rodríguez, Sara Pischedda, Sara Rey Vázquez, Irene Rivero Calle, Carmen Rodríguez-Tenreiro, Lorenzo Redondo-Collazo, Miguel Sadiki Ora, Sonia Serén Fernández, Cristina Serén Trasorras & Marisol Vilas Iglesias

56. GENVIP Research Group, Instituto de Investigación Sanitaria de Santiago, Universidad de Santiago de Compostela, Galicia, Spain

Federico Martinón-Torres, Antonio Salas, Fernando Álvez González, Xabier Bello, Mirian Ben García, Sandra Carnota, Miriam Cebey-López, María José Curras-Tuala, Carlos Durán Suárez, Luisa García Vicente, Alberto Gómez-Carballa, Jose Gómez Rial, Pilar Leboráns Iglesias, Nazareth Martinón-Torres, José María Martinón Sánchez, Belén Mosquera Pérez, Jacobo Pardo-Seco, Lidia Piñeiro Rodríguez, Sara Pischedda, Sara Rey Vázquez, Irene Rivero Calle, Carmen Rodríguez-Tenreiro, Lorenzo Redondo-Collazo, Miguel Sadiki Ora, Sonia Serén Fernández, Cristina Serén Trasorras & Marisol Vilas Iglesias

57. Unidade de Xenética, Departamento de Anatomía Patolóxica e Ciencias Forenses, Instituto de Ciencias Forenses, Facultade de Medicina, Universidade de Santiago de Compostela, and GenPop Research Group, Instituto de Investigaciones Sanitarias (IDIS), Hospital Clínico Universitario de Santiago, Galicia, Spain

Antonio Salas, María José Curras-Tuala, Alberto Gómez-Carballa, Jacobo Pardo-Seco & Sara Pischedda

58. Fundación Pública Galega de Medicina Xenómica, Servizo Galego de Saúde (SERGAS), Instituto de Investigaciones Sanitarias (IDIS), and Grupo de Medicina Xenómica, Centro de Investigación Biomédica en Red de Enfermedades Raras (CIBERER), Universidade de Santiago de Compostela (USC), Santiago de Compostela, Spain

Xabier Bello

59. Department of Clinical Infection, Microbiology and Immunology, University of Liverpool Institute of Infection, Veterinary and Ecological Sciences, Liverpool, UK

Enitan D. Carrol, Elizabeth Cocklin, Aakash Khanijau, Rebecca Lenihan, Nadia Lewis-Burke & Sam Romaine

60. Department of Infectious Diseases, Alder Hey Children's Hospital, Liverpool, UK

Enitan D. Carrol & Karen Newall

61. 2nd Department of Pediatrics, National and Kapodistrian University of Athens (NKUA), Children's Hospital "P, and A. Kyriakou", Athens, Greece

Maria Tsolia, Irini Eleftheriou, Nikos Spyridis, Maria Tambouratzi, Despoina Maritsi, Antonios Marmarinos & Marietta Xagorari

62. 1st Department of Infectious Diseases, Sotiria General Hospital, Athens, Greece

Lourida Panagiota & Pefanis Aggelos

63. Pathology Department, University of Patras, General Hospital “Panagia i Voithia”, Patras, Greece

Akinosoglou Karolina, Gogos Charalambos & Maragos Markos

64. Pathophysiology Department, Medical Faculty, National and Kapodistrian, Laiko General Hospital–University of Athens (NKUA), Athens, Greece

Voulgarelis Michalis & Stergiou Ioanna

65. Translational and Clinical Research Institute, Newcastle University, Newcastle upon Tyne, UK

Marieke Emonts, John Isaacs, Fabian J. S. van der Velden, Owen Treloar & Daisy Thomas

66. Great North Children’s Hospital, Paediatric Immunology, Infectious Diseases and Allergy, Newcastle upon Tyne Hospitals NHS Foundation Trust, Newcastle upon Tyne, UK

Marieke Emonts, Emma Lim, Fabian J. S. van der Velden, Owen Treloar & Daisy Thomas

67. NIHR Newcastle Biomedical Research Centre, Newcastle upon Tyne Hospitals NHS Trust and Newcastle University, Newcastle upon Tyne, UK

Marieke Emonts & Emma Lim

68. Population Health Sciences Institute, Newcastle University, Newcastle upon Tyne, UK

Emma Lim

69. Great North Children’s Hospital Research Unit, Newcastle upon Tyne, UK

Kathryn Bell, Stephen Crulley, Daniel Fabian, Evelyn Thomson, Diane Wallia, Caroline Miller & Ashley Bell

70. Great North Children's Hospital, Paediatric Oncology, Newcastle upon Tyne Hospitals NHS Foundation Trust, Newcastle upon Tyne, UK

Geoff Shenton

71. Department of Infection and Tropical Medicine, Newcastle upon Tyne Hospitals NHS Foundation Trust, Newcastle upon Tyne, UK

Ashley Price

72. NIHR Newcastle In Vitro Diagnostics Co-operative (Newcastle MIC), Newcastle upon Tyne, UK

Ashley Price

73. Servicio Madrileño de Salud (SERMAS), Pediatric Infectious Diseases Unit, Department of Pediatrics, Hospital Universitario 12 de Octubre, Madrid, Spain

Pablo Rojo, Cristina Epalza, Serena Villaverde & Ángela Manzanares

74. Department of Pediatrics, Faculty of Medicine, Universidad Complutense de Madrid, Madrid, Spain

Pablo Rojo

75. Fundación Biomédica del Hospital Universitario 12 de Octubre (FIB-H12O), Unidad Pediátrica de Investigación y Ensayos Clínicos (UPIC), Hospital Universitario 12 de Octubre, Instituto de Investigación Sanitaria Hospital 12 de Octubre (i+12), Madrid, Spain

Cristina Epalza, Sonia Márquez, Manuel Gijón, Fátima Machín, Laura Cabello, Irene Hernández & Lourdes Gutiérrez

76. Amsterdam UMC, Emma Children's Hospital, Department of Pediatric Immunology, Rheumatology and Infectious Disease, University of

Amsterdam, Amsterdam, The Netherlands

T. W. Taco Kuijpers, M. Martijn van de Kuip, A. M. Marceline van Furth, J. M. Merlijn van den Berg, Giske Biesbroek, Floris Verkuil, Carlijn C. W. van der Zee, Dasja Pajkrt, Michael Boele van Hensbroek, Dieneke Schonenberg, Mariken Gruppen, Sietse Nagelkerke & Machiel H. Jansen

77. Sanquin, Department of Molecular Hematology, University Medical Center, Amsterdam, The Netherlands

T. W. Taco Kuijpers, Sietse Nagelkerke & Ines Goetschalckx

78. Infectious Disease Unit, Academic Department of Pediatrics, Bambino Gesù Children's Hospital, IRCCS, Rome, Italy

Lorenza Romani, Maia De Luca, Sara Chiurchiù & Martina Di Giuseppe

79. Department of Paediatric Infectious Diseases and Immunology, Erasmus MC-Sophia Children's Hospital, Rotterdam, The Netherlands

Clementien L. Vermont

80. Department of General Paediatrics, Erasmus MC-Sophia Children's Hospital, Rotterdam, The Netherlands

Henriëtte A. Moll, Dorine M. Borensztajn, Nienke N. Hagedoorn, Chantal Tan, Joany Zachariasse & Medical students

81. Department of Immunology, Erasmus MC, Rotterdam, The Netherlands

W. Dik

82. Division of Infectious Disease, Department of Pediatrics, National Cheng Kung University Tainan, Tainan, Taiwan

Ching-Fen Kitty Shen

83. Riga Stradins University, Riga, Latvia

Dace Zavadska, Sniedze Laivacuma, Aleksandra Rudzate, Diana Stoldere, Arta Barzdina, Elza Barzdina & Monta Madelane

84. Children Clinical University Hospital, Riga, Latvia

Dace Zavadska, Aleksandra Rudzate, Diana Stoldere, Arta Barzdina, Elza Barzdina, Dagne Gravele & Dace Svile

85. Riga East Clinical University Hospital, Riga, Latvia

Sniedze Laivacuma & Monta Madelane

86. Service de Pédiatrie-Urgences, AP-HP, Hôpital Louis-Mourier, Colombes, France

Romain Basmaci, Noémie Lachaume, Pauline Bories, Raja Ben Tkhayat, Laura Chériaux, Juraté Davoust, Kim-Thanh Ong, Marie Cotillon, Thibault de Groc, Sébastien Le, Nathalie Vergnault, Hélène Sée, Laure Cohen, Alice de Tugny & Nevena Danekova

87. Université Paris Cité, Inserm, IAME, Paris, France

Romain Basmaci

88. BioMérieux–Open Innovation and Partnerships Department, Lyon, France

Marine Mommert-Tripon & Karen Brengel-Pesce

89. Department of Infectious diseases, University Medical Centre Ljubljana, Ljubljana, Slovenia

Marko Pokorn, Natalija Bahovec, Petra Bogovič, Mirijam Nahtigal, Lea Papst, Tina Plankar Srovin, Franc Strle & Katarina Vincek

90. University Children’s Hospital, University Medical Centre Ljubljana, Ljubljana, Slovenia

Marko Pokorn, Mojca Kolnik, Tadej Avčin, Tanja Avramoska, Lidija Kitanovski, Franc Strle & Anja Srpčič

91. Faculty of Medicine, University of Ljubljana, Ljubljana, Slovenia

Marko Pokorn, Tadej Avčin & Lidija Kitanovski

92. Pediatric Infectious Diseases and Immunology, University Medical Center Utrecht, Utrecht, The Netherlands

Michiel van der Flier, Louis J. Bont, Tom F. W. Wolfs & Coco R. Beudeker

93. Princess Maxima Center for Pediatric Oncology, Utrecht, The Netherlands

Michiel van der Flier, Louis J. Bont, Tom F. W. Wolfs & Coco R. Beudeker

94. Pediatric Intensive Care Unit, University Medical Center Utrecht, Utrecht, The Netherlands

Wim J. E. Tissing & Roelie M. Wösten-van Asperen

95. Pediatric Rheumatology, University Medical Center Utrecht, Utrecht, The Netherlands

Sebastiaan J. Vastert

96. Pediatric Neonatal Intensive Care, Wilhelmina Children’s Hospital, University Medical Center Utrecht, Utrecht, The Netherlands

Daniel C. Vijlbrief

97. Department of Pediatrics, Inselspital, Bern University Hospital, University of Bern, Bern, Switzerland

Philipp Agyeman, Christoph Aebi, Mariama Usman, Stefanie Schlüchter, Verena Wyss & Nina Schöbi

98. Department of Intensive Care and Neonatology, and Children's Research Center, University Children's Hospital Zurich, Zurich, Switzerland

Luregn Schlapbach, Elisa Zimmermann, Marion Meier, Kathrin Weber, Philipp Agyeman & Christoph Aebi

99. Child Health Research Centre, The University of Queensland, Brisbane, Queesnland, Australia

Luregn Schlapbach

100. Department of Intensive Care and Neonatology, and Children's Research Center, University Children's Hospital Zurich, Zurich, Switzerland

Luregn J. Schlapbach

101. Child Health Research Centre, The University of Queensland, Brisbane, Queensland, Australia

Luregn J. Schlapbach

102. Clinic of Neonatology, Department Mother-Woman-Child, Lausanne University Hospital and University of Lausanne, Lausanne, Switzerland

Eric Giannoni

103. Infectious Diseases Service, Department of Medicine, Lausanne University Hospital and University of Lausanne, Lausanne, Switzerland

Eric Giannoni

104. Department of Pediatrics, Children's Hospital Lucerne, Lucerne, Switzerland

Martin Stocker

105. Pediatric Infectious Diseases Unit, Children’s Hospital of Geneva, University Hospitals of Geneva, Geneva, Switzerland

Klara M. Posfay-Barbe

106. Infectious Diseases and Vaccinology, University of Basel Children’s Hospital, Basel, Switzerland

Ulrich Heininger

107. Children’s Hospital Aarau, Aarau, Switzerland

Sara Bernhard-Stirnemann

108. Division of Infectious Diseases and Hospital Epidemiology, Children’s Hospital of Eastern Switzerland St Gallen, St Gallen, Switzerland

Anita Niederer-Loher & Christian Kahlert

109. Department of Neonatology, University Hospital Zurich, Zurich, Switzerland

Giancarlo Natalucci

110. Division of Infectious Diseases and Hospital Epidemiology, and Children’s Research Center, University Children’s Hospital Zurich, Zurich, Switzerland

Christa Relly & Christoph Berger

111. Children’s Hospital Chur, Chur, Switzerland

Thomas Riedel

112. Micropathology, The Venture Center, University of Warwick Science Park, Coventry, UK

Colin Fink, Marie Voice, Leo Calvo-Bado, Michael Steele, Jennifer Holden, Benjamin Evans, Jake Stevens, Peter Matthews & Kyle Billing

113. Department of Pediatrics and Adolescent Medicine, Division of General Pediatrics, Medical University of Graz, Graz, Austria

Werner Zenz, Alexander Binder, Benno Kohlmaier, Daniela S. Kohlfürst, Nina A. Schweintzger, Christoph Zurl, Susanne Hösele, Manuel Leitner, Lena Pölz, Glorija Rajic, Bianca Stoiser, Martina Strempfl, Manfred G. Sagmeister, Sebastian Bauchinger, Astrid Ceolotto, Siegfried Gallistl, Harald Haidl, Almuthe Hauer, Christa Hude & Andrea Skrabl-Baumgartner

114. Department of Pediatric Pulmonology, Medical University of Graz, Graz, Austria

Alexandra Rusu, Ernst Eber & Andreas Pfleger

115. Department of Pediatric Hematooncology, Medical University of Graz, Graz, Austria

Martin Benesch & Volker Strenger

116. Paediatric Intensive Care Unit, Medical University of Graz, Graz, Austria

Andreas Kapper, Klaus Pfurtscheller & Siegfried Rödl

117. University Clinic of Pediatrics and Adolescent Medicine Graz, Medical University Graz, Graz, Austria

Markus Keldorfer, Sabine Löffler & Heidemarie Pilch

118. Clinical Institute of Medical and Chemical Laboratory Diagnostics, Medical University Graz, Graz, Austria

Tobias Niedrist

119. Department of Internal Medicine, State Hospital Graz II, Location West, Graz, Austria

Elmar Wallner

120. SkylineDx, Rotterdam, The Netherlands

Dennie Tempel, Danielle van Keulen & Annelieke M. Strijbosch

121. Biobanking and BioMolecular Resources Research Infrastructure–European Research Infrastructure Consortium (BBMRI-ERIC), Graz, Austria

Maike K. Tauchert

122. Division of Pediatric Infectious Diseases, Department of Pediatrics, Dr von Hauner Children's Hospital, University Hospital, LMU Munich, Munich, Germany

Ulrich von Both, Laura Kolberg & Patricia Schmied

123. German Center for Infection Research (DZIF), Partner Site Munich, Munich, Germany

Ulrich von Both

124. Department of Gynecology and Obstetrics, University Hospital, LMU Munich, Munich, Germany

Irene Alba-Alejandre

125. Division of Pediatric Rheumatology, Department of Pediatrics, Dr von Hauner Children's Hospital, University Hospital, LMU Munich, Munich, Germany

Katharina Danhauser

126. Department of Pediatric Cardiology and Pediatric Intensive Care, University Hospital, LMU Munich, Munich, Germany

Nikolaus Haas

127. Paediatric Intensive Care Unit, Department of Pediatrics, Dr von Hauner Children's Hospital, University Hospital, LMU Munich, Munich, Germany

Florian Hoffmann, Karl Reiter & Carola Schoen

128. Division of Pediatric Pulmonology, Department of Pediatrics, Dr von Hauner Children's Hospital, University Hospital, LMU Munich, Munich, Germany

Matthias Griese & Matthias Kappler

129. Division of Pediatric Haematology and Oncology, Department of Pediatrics, Dr von Hauner Children's Hospital, University Hospital, LMU Munich, Munich, Germany

Tobias Feuchtinger

130. Division of General Pediatrics, Department of Pediatrics, Dr von Hauner Children's Hospital, University Hospital, LMU Munich, Munich, Germany

Sabrina Juranek & Esther Maier

131. Division of Pediatric Gastroenterology, Department of Pediatrics, Dr von Hauner Children's Hospital, University Hospital, LMU Munich, Munich, Germany

Eberhard Lurz

132. Neonatal Intensive Care Unit, Department of Pediatrics, Dr von Hauner Children's Hospital, University Hospital, LMU Munich, Munich, Germany

Sebastian Schroepf

133. Department of Paediatrics, St Mary's Imperial College Hospital, London, UK

Shunmay Yeung

134. Department of Global Health and Development, Faculty of Public Health and Policy, London School of Hygiene and Tropical Medicine, London, UK

David Bath

135. Medical Research Council Unit, The Gambia at LSHTM, Banjul, The Gambia

Saidykhan Momodou, Effua Usuf, Ebrahim Ndure, Kalifa Bojang, Anna Roca & Isatou Sarr

136. NIHR Health Protection Research Unit, Institute of Infection, Veterinary and Ecological Sciences, Faculty of Health and Life Sciences, University of Liverpool, Liverpool, UK

Malcolm G. Semple, Lance C. W. Turtle, Tom Solomon & Hayley Hardwick

137. Respiratory Medicine, Alder Hey Children's Hospital, Institute in The Park, University of Liverpool, Alder Hey Children's Hospital, Liverpool, UK

Malcolm G. Semple

138. ISARIC Global Support Centre, Centre for Tropical Medicine and Global Health, Nuffield Department of Medicine, University of Oxford, Oxford, UK

Gail Carson & Laura Merson

139. National Heart and Lung Institute, Imperial College London, London, UK

Peter J. M. Openshaw & Jake Dunning

140. Imperial College Healthcare NHS Trust London, London, UK

Peter J. M. Openshaw

141. National Infection Service, Public Health England, London, UK

Jake Dunning, Maria Zambon & Samreen Ijaz

142. Centre for Inflammation Research, The Queen's Medical Research Institute, University of Edinburgh, Edinburgh, UK

Clark D. Russell

143. Edinburgh Pathology, University of Edinburgh, Edinburgh, UK

David Dorward

144. Blood Borne Virus Unit, Virus Reference Department, National Infection Service, Public Health England, London, UK

Richard S. Tedder

145. Transfusion Microbiology, National Health Service Blood and Transplant, London, UK

Richard S. Tedder

146. Department of Medicine, Imperial College London, London, UK

Richard S. Tedder

147. Department of Pharmacology, University of Liverpool, Liverpool, UK

Saye Khoo

148. Tropical and Infectious Disease Unit, Royal Liverpool University Hospital, Liverpool, UK

Lance C. W. Turtle

149. Walton Centre NHS Foundation Trust, Liverpool, UK

Tom Solomon

150. Liverpool School of Tropical Medicine, Liverpool, UK

Tom Fletcher

151. Centre for Clinical Infection and Diagnostics Research, Department of Infectious Diseases, School of Immunology and Microbial Sciences, King's College London, London, UK

Nicholas Price

152. Department of Infectious Diseases, Guy's and St Thomas' NHS Foundation Trust, London, UK

Nicholas Price

153. Division of Infection and Immunity, University College London and Great Ormond Street Hospital, London, UK

Judith Breuer

154. The Florey Institute for Host–Pathogen Interactions, Department of Infection, Immunity and Cardiovascular Disease, University of Sheffield, Sheffield, UK

Thushan de Silva

155. Liverpool Clinical Trials Centre, University of Liverpool, Liverpool, UK

Chloe Donohue

156. EPCC, University of Edinburgh, Edinburgh, UK

Lucy Norris

157. Edinburgh Clinical Research Facility, University of Edinburgh, Edinburgh, UK

Richard Clark, Audrey Coutts, Lorna Donnelly, Angie Fawkes, Tammy Gilchrist, Katarzyna Hafezi, Louise MacGillivray, Alan Maclean, Sarah McCafferty, Kirstie Morrice, Lee Murphy & Nicola Wrobel

158. Institute of Translational Medicine, University of Liverpool, Liverpool, UK

Victoria Shaw & Katie A. Ahmed

159. Sheffield Teaching Hospitals, Sheffield, UK

Jane A. Armstrong

160. University of Liverpool, Liverpool, UK

Lauren Lett

161. Royal Hospital for Children and Young People, Edinburgh, UK

Paul Henderson, Katherine Jack, Maxine Ramsay & Margaret Millar

162. Department of Paediatric Infectious Diseases and Immunology, Royal Hospital for Children, Glasgow, UK

Louisa Pollock

163. Royal Aberdeen Children's Hospital, Aberdeen, UK

Shyla Kishore, Maggie Connon & Catriona Ward

164. University Hospital Wishaw, North Lanarkshire, UK

Helen Brotherton, Thomas Jordan & Karen Leitch

165. Crosshouse and Ayr Hospital, Kilmarnock, UK

Lawrence Armstrong

166. Dumfries and Galloway Royal Infirmary, Dumfries, UK

Andrew Mitra & Janie Candlish

167. Borders General Hospital, Melrose, UK

Anna Dall, Lauren Finlayson & Joy Dawson

168. Forth Valley Royal Hospital, Larbert, UK

Kristyna Bohmova, Sheena Logan & Laura McGenily

169. Tayside Children’s Hospital, Ninewells Hospital, NHS Tayside, Dundee, UK

Louise Gannon & Susan MacFarlane

170. Ninewells Hospital, NHS Tayside, Dundee, UK

Louise Gannon & Susan MacFarlane

171. Doncaster and Bassetlaw Teaching Hospitals NHS Foundation Trust, Doncaster, UK NHS Foundation Trust, Doncaster, UK

Ken Agwuh & Sarah Farmer

172. Burnley General Teaching Hospital, Burnley, UK

Srikanth Chukkambotla

173. Hereford County Hospital, Hereford, UK

Ingrid DuRand

174. Leighton Hospital, Leighton, UK

Duncan Fullerton, Elijah Matovu & Amaryl Jones

175. Walsall Healthcare NHS Trust, Walsall, UK

Sanjeev Gar

176. Cumberland Infirmary, Cumberland, UK

Clive Graham

177. Paediatric Liver, GI & Nutrition Centre and MowatLabs, King's College Hospital, London, UK

Tassos Grammatikopoulos

178. Institute of Liver Studies, King's College London, London, UK

Tassos Grammatikopoulos

179. Birmingham Women's Children's Hospital, Birmingham, UK

Stuart Hartshorn, Tara Roome, Ruth Howman & Sara Burling

180. St Richards' Hospital, Chichester, UK

Luke Hodgson & Sharon Floyd

181. Airedale General Hospital, Keighley, UK

Paul Jennings

182. Hinchingbrooke Hospital, Huntingdon, UK

George Koshy & Tamas Leiner

183. Darlington Memorial Hospital, Darlington, UK

James Limb

184. Warrington Hospital, Kilmarnock, UK

Jeff Little & Sheena Logan

185. Leeds Teaching Hospitals NHS Trust, Leeds, UK

Fiona McGill & Collette Spencer

186. Queens Hospital Burton, Burton-on-Trent, UK

Craig Morris, Tim Reynolds & Holly Dickinson

187. Queen Margaret Hospital, Dunfermline, UK

John Morrice & Laura Beveridge

188. Royal Victoria Infirmary, Newcastle upon Tyne, UK

David Price

189. Poole University Hospital, Dorset, UK

Henrik Reschreiter, Lucy Rubick, Amy Roff & Sarah Mills

190. Bradford Royal infirmary, Bradford, UK

Paul Whittaker

191. Department of Paediatric Gastroenterology, Hepatology and Nutrition, Royal Hospital for Children, Glasgow, UK

Rachel Tayler

192. Avon and Wiltshire Mental Health Partnership NHS Trust, Bath, UK

Clare Irving

193. Queen Elizabeth University Hospital, Glasgow, UK

Barry Milligan & Naomi Hickey

194. University Hospital Crosshouse, Kilmarnock, UK

Claire Bell

195. Royal Free Hospital, London, UK

Cynthia Diaba

196. Diana Princess of Wales Hospital, Grimsby, UK

Jasmine Player

197. King's College Hospital, London, UK

Natassia Powell

198. Western General Hospital, Edinburgh, UK

Susie Ferguson

199. Barnsley Hospital, Barnsley, UK

Susan Hope

200. Bradford Teaching Hospitals NHS Foundation Trust, Bradford, UK

Rachel Swingler

201. Wye Valley NHS Trust, Hereford, UK

Emma Collins

202. Newcastle upon Tyne Hospitals NHS Foundation Trust, Newcastle upon Tyne, UK

Barbara Wilson

203. West Cumberland Hospital, Whitehaven, UK

Diane Armstrong & Rosemary Harper

204. University Hospital of North Durham, Durham, UK

Mark Birt

205. Worthing Hospital, Worthing, UK

Darran Martin

Consortia

DIAMONDS Consortium

- Michael Levin
- , Aubrey Cunnington
- , Jethro Herberg
- , Myrsini Kaforou
- , Victoria Wright
- , Evangelos Bellos
- , Claire Broderick
- , Samuel Channon-Wells
- , Samantha Cooray
- , Tisham De
- , Giselle D’Souza
- , Leire Estramiana Elorrieta
- , Diego Estrada-Rivadeneyra
- , Rachel Galassini
- , Dominic Habgood-Coote
- , Shea Hamilton
- , Heather Jackson
- , James Kavanagh
- , Mahdi Moradi Marjaneh
- , Stephanie Menikou
- , Samuel Nichols
- , Ruud Nijman
- , Harsita Patel
- , Ivana Pennisi
- , Oliver Powell
- , Ruth Reid
- , Priyen Shah
- , Ortensia Vito
- , Elizabeth Whittaker
- , Clare Wilson
- , Rebecca Womersley

- , Amina Abdulla
- , Sarah Darnell
- , Sobia Mustafa
- , Pantelis Georgiou
- , Jesus-Rodriguez Manzano
- , Nicolas Moser
- , Ivana Pennisi
- , Michael Carter
- , Shane Tibby
- , Jonathan Cohen
- , Francesca Davis
- , Julia Kenny
- , Paul Wellman
- , Marie White
- , Matthew Fish
- , Aislinn Jennings
- , Manu Shankar-Hari
- , Katy Fidler
- , Dan Agranoff
- , Vivien Richmond
- , Mathew Seal
- , Saul Faust
- , Dan Owen
- , Ruth Ensom
- , Sarah McKay
- , Diana Mondo
- , Mariya Shaji
- , Rachel Schranz
- , Prita Rughnani
- , Amutha Anpananthar
- , Susan Liebeschuetz
- , Anna Riddell
- , Nosheen Khalid
- , Ivone Lancoma Malcolm
- , Teresa Simagan
- , Mark Peters
- , Alasdair Bamford

- , Lauran O’Neill
- , Nazima Pathan
- , Esther Daubney
- , Deborah White
- , Melissa Heightman
- , Sarah Eisen
- , Terry Segal
- , Lucy Wellings
- , Simon B. Drysdale
- , Nicole Branch
- , Lisa Hamzah
- , Heather Jarman
- , Maggie Nyirenda
- , Lisa Capozzi
- , Emma Gardiner
- , Robert Moots
- , Magda Nasher
- , Anita Hanson
- , Michelle Linforth
- , Sean O’Riordan
- , Donna Ellis
- , Akash Deep
- , Ivan Caro
- , Fiona Shackley
- , Arianna Bellini
- , Stuart Gormley
- , Samira Neshat
- , Barnaby J. Scholefield
- , Ceri Robbins
- , Helen Winmill
- , Stéphane C. Paulus
- , Andrew J. Pollard
- , Mark Anthony
- , Sarah Hopton
- , Danielle Miller
- , Zoe Oliver
- , Sally Beer

- , Bryony Ward
- , Shrijana Shrestha
- , Andrew J. Pollard
- , Meeru Gurung
- , Puja Amatya
- , Bhishma Pokhrel
- , Sanjeev Man Bijukchhe
- , Tim Lubinda
- , Sarah Kelly
- , Peter O'Reilly
- , Federico Martinón-Torres
- , Antonio Salas
- , Fernando Álvez González
- , Xabier Bello
- , Mirian Ben García
- , Sandra Carnota
- , Miriam Cebey-López
- , María José Curras-Tuala
- , Carlos Durán Suárez
- , Luisa García Vicente
- , Alberto Gómez-Carballa
- , Jose Gómez Rial
- , Pilar Leboráns Iglesias
- , Federico Martinón-Torres
- , Nazareth Martinón-Torres
- , José María Martinón Sánchez
- , Belén Mosquera Pérez
- , Jacobo Pardo-Seco
- , Lidia Piñeiro Rodríguez
- , Sara Pischedda
- , Sara Rey Vázquez
- , Irene Rivero Calle
- , Carmen Rodríguez-Tenreiro
- , Lorenzo Redondo-Collazo
- , Miguel Sadiki Ora
- , Antonio Salas
- , Sonia Serén Fernández

- , Cristina Serén Trasorras
- , Marisol Vilas Iglesias
- , Enitan D. Carrol
- , Elizabeth Cocklin
- , Aakash Khanijau
- , Rebecca Lenihan
- , Nadia Lewis-Burke
- , Karen Newall
- , Sam Romaine
- , Maria Tsolia
- , Irini Eleftheriou
- , Nikos Spyridis
- , Maria Tambouratzi
- , Despoina Maritsi
- , Antonios Marmarinos
- , Marietta Xagorari
- , Lourida Panagiota
- , Pefanis Aggelos
- , Akinosoglou Karolina
- , Gogos Charalambos
- , Maragos Markos
- , Voulgarelis Michalis
- , Stergiou Ioanna
- , Marieke Emonts
- , Emma Lim
- , John Isaacs
- , Kathryn Bell
- , Stephen Crulley
- , Daniel Fabian
- , Evelyn Thomson
- , Diane Wallia
- , Caroline Miller
- , Ashley Bell
- , Fabian J. S. van der Velden
- , Geoff Shenton
- , Ashley Price
- , Owen Treloar

- , Daisy Thomas
- , Pablo Rojo
- , Cristina Epalza
- , Serena Villaverde
- , Sonia Márquez
- , Manuel Gijón
- , Fátima Machín
- , Laura Cabello
- , Irene Hernández
- , Lourdes Gutiérrez
- , Ángela Manzanares
- , T. W. Taco Kuijpers
- , M. Martijn van de Kuip
- , A. M. Marceline van Furth
- , J. M. Merlijn van den Berg
- , Giske Biesbroek
- , Floris Verkuil
- , Carlijn C. W. van der Zee
- , Dasja Pajkrt
- , Michael Boele van Hensbroek
- , Dieneke Schonenberg
- , Mariken Gruppen
- , Sietse Nagelkerke
- , Machiel H. Jansen
- , Ines Goetschalckx
- , Lorenza Romani
- , Maia De Luca
- , Sara Chiurchiù
- , Martina Di Giuseppe
- , Clementien L. Vermont
- , Henriëtte A. Moll
- , Dorine M. Borensztajn
- , Nienke N. Hagedoorn
- , Chantal Tan
- , Joany Zachariasse
- , Medical students
- , W. Dik

- , Ching-Fen Kitty Shen
- , Dace Zavadska
- , Sniedze Laivacuma
- , Aleksandra Rudzate
- , Diana Stoldere
- , Arta Barzdina
- , Elza Barzdina
- , Sniedze Laivacuma
- , Monta Madelane
- , Dagne Gravele
- , Dace Svile
- , Romain Basmaci
- , Noémie Lachaume
- , Pauline Bories
- , Raja Ben Tkhayat
- , Laura Chériaux
- , Juraté Davoust
- , Kim-Thanh Ong
- , Marie Cotillon
- , Thibault de Groc
- , Sébastien Le
- , Nathalie Vergnault
- , Hélène Sée
- , Laure Cohen
- , Alice de Tugny
- , Nevena Danekova
- , Marine Mommert-Tripon
- , Karen Brengel-Pesce
- , Marko Pokorn
- , Mojca Kolnik
- , Tadej Avčin
- , Tanja Avramoska
- , Natalija Bahovec
- , Petra Bogovič
- , Lidija Kitanovski
- , Mirijam Nahtigal
- , Lea Papst

- , Tina Plankar Srovin
- , Franc Strle
- , Anja Srpčič
- , Katarina Vincek
- , Michiel van der Flier
- , Wim J. E. Tissing
- , Roelie M. Wösten-van Asperen
- , Sebastiaan J. Vastert
- , Daniel C. Vijlbrief
- , Louis J. Bont
- , Tom F. W. Wolfs
- , Coco R. Beudeker
- , Philipp Agyeman
- , Luregn Schlapbach
- , Christoph Aebi
- , Mariama Usman
- , Stefanie Schlüchter
- , Verena Wyss
- , Nina Schöbi
- , Elisa Zimmermann
- , Marion Meier
- , Kathrin Weber
- , Philipp Agyeman
- , Luregn J. Schlapbach
- , Eric Giannoni
- , Martin Stocker
- , Klara M. Posfay-Barbe
- , Ulrich Heininger
- , Sara Bernhard-Stirnemann
- , Anita Niederer-Loher
- , Christian Kahlert
- , Giancarlo Natalucci
- , Christa Relly
- , Thomas Riedel
- , Christoph Aebi
- , Christoph Berger
- , Colin Fink

- , Marie Voice
- , Leo Calvo-Bado
- , Michael Steele
- , Jennifer Holden
- , Benjamin Evans
- , Jake Stevens
- , Peter Matthews
- , Kyle Billing
- , Werner Zenz
- , Alexander Binder
- , Benno Kohlmaier
- , Daniela S. Kohlfürst
- , Nina A. Schweintzger
- , Christoph Zurl
- , Susanne Hösele
- , Manuel Leitner
- , Lena Pölz
- , Alexandra Rusu
- , Glorija Rajic
- , Bianca Stoiser
- , Martina Strempfl
- , Manfred G. Sagmeister
- , Sebastian Bauchinger
- , Martin Benesch
- , Astrid Ceolotto
- , Ernst Eber
- , Siegfried Gallistl
- , Harald Haidl
- , Almuthe Hauer
- , Christa Hude
- , Andreas Kapper
- , Markus Keldorfer
- , Sabine Löffler
- , Tobias Niedrist
- , Heidemarie Pilch
- , Andreas Pflieger
- , Klaus Pfurtscheller

- , Siegfried Rödl
- , Andrea Skrabl-Baumgartner
- , Volker Strenger
- , Elmar Wallner
- , Dennie Tempel
- , Danielle van Keulen
- , Annelieke M. Strijbosch
- , Maike K. Tauchert
- , Ulrich von Both
- , Laura Kolberg
- , Patricia Schmied
- , Irene Alba-Alejandre
- , Katharina Danhauser
- , Nikolaus Haas
- , Florian Hoffmann
- , Matthias Griese
- , Tobias Feuchtinger
- , Sabrina Juranek
- , Matthias Kappler
- , Eberhard Lurz
- , Esther Maier
- , Karl Reiter
- , Carola Schoen
- , Sebastian Schroepf
- , Shunmay Yeung
- , Manuel Dewez
- , David Bath
- , Elizabeth Fitchett
- , Fiona Cresswell
- , Saidykhan Momodou
- , Effua Usuf
- , Ebrahim Ndure
- , Kalifa Bojang
- , Anna Roca
- & Isatou Sarr

ISARIC4C Investigators

- J. Kenneth Baillie
- , Malcolm G. Semple
- , Gail Carson
- , Peter J. M. Openshaw
- , Jake Dunning
- , Laura Merson
- , Clark D. Russell
- , David Dorward
- , Maria Zambon
- , Meera Chand
- , Richard S. Tedder
- , Saye Khoo
- , Lance C. W. Turtle
- , Tom Solomon
- , Samreen Ijaz
- , Tom Fletcher
- , Massimo Palmarini
- , Antonia Ho
- , Emma C. Thomson
- , Nicholas Price
- , Judith Breuer
- , Thushan de Silva
- , Chloe Donohue
- , Hayley Hardwick
- , Wilna Oosthuyzen
- , Miranda Odam
- , Primrose Chikowore
- , Lauren Obosi
- , Sara Clohisey
- , Andrew Law
- , Lucy Norris
- , Sarah Tait
- , Murray Wham
- , Richard Clark
- , Audrey Coutts
- , Lorna Donnelly
- , Angie Fawkes

- , Tammy Gilchrist
- , Katarzyna Hafezi
- , Louise MacGillivray
- , Alan Maclean
- , Sarah McCafferty
- , Kirstie Morrice
- , Lee Murphy
- , Nicola Wrobel
- , Sarah E. McDonald
- , Victoria Shaw
- , Katie A. Ahmed
- , Jane A. Armstrong
- , Lauren Lett
- , Paul Henderson
- , Louisa Pollock
- , Shyla Kishore
- , Helen Brotherton
- , Lawrence Armstrong
- , Andrew Mitra
- , Anna Dall
- , Kristyna Bohmova
- , Sheena Logan
- , Louise Gannon
- , Ken Agwuh
- , Srikanth Chukkambotla
- , Ingrid DuRand
- , Duncan Fullerton
- , Sanjeev Gar
- , Clive Graham
- , Tassos Grammatikopoulos
- , Stuart Hartshorn
- , Luke Hodgson
- , Paul Jennings
- , George Koshy
- , Tamas Leiner
- , James Limb
- , Jeff Little

- , Sheena Logan
- , Elijah Matovu
- , Fiona McGill
- , Craig Morris
- , John Morrice
- , David Price
- , Henrik Reschreiter
- , Tim Reynolds
- , Paul Whittaker
- , Thomas Jordan
- , Rachel Tayler
- , Clare Irving
- , Katherine Jack
- , Maxine Ramsay
- , Margaret Millar
- , Barry Milligan
- , Naomi Hickey
- , Maggie Connon
- , Catriona Ward
- , Laura Beveridge
- , Susan MacFarlane
- , Karen Leitch
- , Claire Bell
- , Lauren Finlayson
- , Joy Dawson
- , Janie Candlish
- , Laura McGenily
- , Tara Roome
- , Cynthia Diaba
- , Jasmine Player
- , Natassia Powell
- , Ruth Howman
- , Sara Burling
- , Sharon Floyd
- , Sarah Farmer
- , Susie Ferguson
- , Susan Hope

- , Lucy Rubick
- , Rachel Swingler
- , Emma Collins
- , Collette Spencer
- , Amaryl Jones
- , Barbara Wilson
- , Diane Armstrong
- , Mark Birt
- , Holly Dickinson
- , Rosemary Harper
- , Darran Martin
- , Amy Roff
- & Sarah Mills

Contributions

A.H., A.d.S.F., J.K.B. and E.C.T. conceived the study. A.H., R.O., D.L.R., P.A., V.H., C.D., B.J.W., D.T., R.B., N.A., J.K.B., J.H., P.H., S.R., C.W. and E.C.T. did the formal analysis. A.H., R.T., P.A., V.H., C.D., L.T., K.S., M.M., J.A., B.J.W., K.R., L.P., L.G., C.E., J.M., K.R., K.M., T.D., M.T.G.H., M.L., M.S.H., D.Y., S.C., M. O'Leary, M.P., D.H., A.M., N.M., A.d.S.F., J.B., D.T., R.B., P.H., M.O., P.C., W.O., M.C. and E.C.T. did the investigation. S.E.M., E.V., T.D., S.J.S., C.J., R.G., A.M., N.M., A.B.-S, M.T.G.H, D.E.-R., M.G.S. and M.L. provided resources. N.A., E.P.-C. and V.V. performed validation. A.H. and E.C.T. wrote the original draft of the manuscript. A.H., R.O., R.T., P.A., L.P., J.M., K.R., K.M., T.D., M.T.G.H., M.L., P.H., M.C., M.L., M.P., D.L.R., A.d.S.F., B.J.W., J.B., M.G.S., D.T., J.K.B. and E.C.T. reviewed and edited the manuscript. R.O., P.A., V.H., C.D., K.R., B.J.W. and E.C.T. visualized the data.

Corresponding author

Correspondence to Emma C. Thomson.

Ethics declarations

Competing interests

The authors declare no competing interests.

Peer review

Peer review information

Nature thanks Frank Tacke, Leif Sander and the other, anonymous, reviewer(s) for their contribution to the peer review of this work. Peer reviewer reports are available.

Additional information

Publisher's note Springer Nature remains neutral with regard to jurisdictional claims in published maps and institutional affiliations.

Extended data figures and tables

Extended Data Fig. 1 AAV2, HAdV and human herpesvirus detection by target enrichment sequencing in cases and controls.

Read counts per million are plotted for a) HAdV; b) AAV2; c) HHV6B; d) HSV1; e) HSV2; f) VZV; g) HHV6A; h) HHV7; i) HHV8; and j) CMV in cases, Group 1 healthy controls and Group 2 controls (HAdV positive children with normal liver function). Statistical significance was estimated using a Mann-Whitney test (two-sided).

Source Data

Extended Data Fig. 2 Phylogenetic and sequence analysis of AAV2 genomes.

a) Maximum likelihood phylogeny of AAV2 from hepatitis cases CVR1-9. The nine AAV2 genome sequences generated from the plasma samples via

target enrichment (highlighted in green) were aligned with a range of the closest AAV GenBank sequences[39]. AAV2 reference sequences are denoted by accession number, country and year of sampling b), Phylogeny of HAdV41 genome from case 5. The HAdV41 genome sequence from the faecal sample of patient 5 (red) was combined with complete genomes of HAdV41 from GenBank. Bootstrap values >70 are indicated. HAdV41 reference sequences are denoted by accession number, country and year of sampling; c), Key mutations and hierarchical clustering of AAV2 genomes. Mutations in published AAV2 sequences are highlighted in (blue) and case sequences (green); d) Mutations over-represented in hepatitis cases versus controls. Mutations in VP1-3, Rep78 and 52 and AAP are highlighted by % representation in case sequences (green) and published sequences (blue).

Extended Data Fig. 3 Reactivity of sera from paediatric hepatitis cases against human seasonal coronaviruses and SARS-CoV-2.

Sera from the paediatric hepatitis cases were screened for reactivity against spike proteins from **a)** seasonal coronaviruses 229E, OC43, NL63 and HKU1, and **b**) SARS-CoV-2 nucleocapsid (N), spike (S), and N-terminal domain (NTD) and receptor binding domain (RBD) of S by electrochemiluminescence (MSD-ECL). Reactivity of the 23 samples (Hepatitis) was compared with 16 sera from contemporaneous control samples from children (Group 4 Controls), and three groups of sera from adults of known SARS-CoV-2 status; Negatives (never tested positive for SARS-CoV-2; n = 30), Vaccinated two doses (n = 28) and Infected (n = 39).

Extended Data Fig. 4 Principal component analysis (PCA) plots.

PCA plots showing the first four genome-wide principal components to confirm genetic ancestry matching. **a)** Genomic PCA using full United Kingdom Biobank cohort as background population (grey), showing the subgroup of unrelated United Kingdom Biobank participants who were born in Scotland and of Caucasian ancestry (blue) and the hepatitis cases reported here (red). **b)** plots showing only the subgroup born in Scotland and of Caucasian ancestry.

Source Data

Extended Data Table 1 Modified hepatic activity index scores
Extended Data Table 2 Characteristics of cases and controls a) used in metagenomic and target enrichment analysis b) used in PCR analysis

Supplementary information

Supplementary Information

Supplementary clinical information, Supplementary Tables 1–7 and Supplementary Figs. 1–8.

Reporting Summary

Peer Review File

Supplementary Data 1

Source data for Supplementary Fig. 3.

Supplementary Data 2

Source data for Supplementary Fig. 4.

Source data

Source Data Fig. 1

Source Data Fig. 2

Source Data Fig. 3

Source Data Extended Data Fig. 1

Source Data Extended Data Fig. 4

Rights and permissions

Springer Nature or its licensor (e.g. a society or other partner) holds exclusive rights to this article under a publishing agreement with the author(s) or other rightsholder(s); author self-archiving of the accepted manuscript version of this article is solely governed by the terms of such publishing agreement and applicable law.

Reprints and Permissions

About this article

Cite this article

Ho, A., Orton, R., Tayler, R. *et al.* Adeno-associated virus 2 infection in children with non-A–E hepatitis. *Nature* **617**, 555–563 (2023). https://doi.org/10.1038/s41586-023-05948-2

- Received: 21 July 2022
- Accepted: 10 March 2023
- Published: 30 March 2023
- Issue Date: 18 May 2023
- DOI: https://doi.org/10.1038/s41586-023-05948-2

Share this article

Anyone you share the following link with will be able to read this content:

Get shareable link

Sorry, a shareable link is not currently available for this article.

Copy to clipboard

Provided by the Springer Nature SharedIt content-sharing initiative

This article is cited by

- **Adeno-associated virus type 2 in US children with acute severe hepatitis**
    - Venice Servellita
    - Alicia Sotomayor Gonzalez
    - Charles Y. Chiu

  Nature (2023)

- **Genomic investigations of unexplained acute hepatitis in children**
    - Sofia Morfopoulou
    - Sarah Buddle
    - Judith Breuer

  Nature (2023)

Adeno-associated virus type 2 in US children with acute severe hepatitis

- Venice Servellita
- Alicia Sotomayor Gonzalez
- Charles Y. Chiu

Nature Article 30 Mar 2023

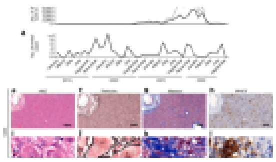
Severe hepatitis outbreak in children linked to AAV2 virus

- Frank Tacke

Nature News & Views 30 Mar 2023

This article was downloaded by **calibre** from https://www.nature.com/articles/s41586-023-05948-2

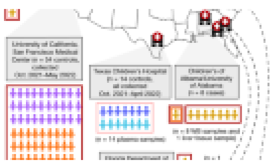
| Section menu | Main menu |



Adeno-associated virus 2 infection in children with non-A–E hepatitis

30 March 2023

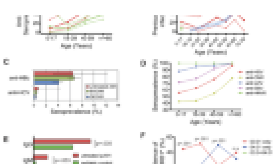
Antonia Ho, Richard Orton, … Emma C. Thomson



Adeno-associated virus type 2 in US children with acute severe hepatitis

30 March 2023

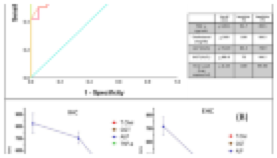
Venice Servellita, Alicia Sotomayor Gonzalez, … Charles Y. Chiu



Increased seroprevalence of HAV and parvovirus B19 in children and of HEV in adults at diagnosis of autoimmune hepatitis

28 November 2018

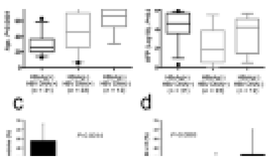
Richard Taubert, Jana Diestelhorst, … Elmar Jaeckel



[Insight into the distinctive paradigm of Human Cytomegalovirus associated intrahepatic and extrahepatic cholestasis in neonates]

28 September 2020

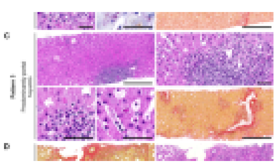
Aroni Chatterjee, Sumit Mukherjee, … Nilanjan Chakraborty



[Early-onset liver cancer in South America associates with low hepatitis B virus DNA burden]

13 August 2018

Agnès Marchio, Juan Pablo Cerapio, … Pascal Pineau



[The histologic presentation of hepatitis E reflects patients' immune status and pre-existing liver condition]

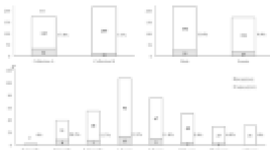
22 June 2020

Daniela Lenggenhager, Samuel Pawel, … Achim Weber

[Prevalence of hepatitis B virus genotypes among patients with liver disease in Eritrea]

31 May 2021

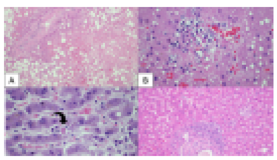
Mohammed Elfatih Hamida, Saud Mohammed Raja, … Freweini Tekle



[Identification of hepadnavirus in the sera of cats]

23 July 2019

Gianvito Lanave, Paolo Capozza, … Michele Camero



[Hepatic pathology in patients dying of COVID-19: a series of 40 cases including clinical, histologic, and virologic data]

13 August 2020

Stephen M. Lagana, Satoru Kudose, … Elizabeth C. Verna

- Article
- Open Access
- Published: 30 March 2023

Genomic investigations of unexplained acute hepatitis in children

- Sofia Morfopoulou,

- Sarah Buddle,
- Oscar Enrique Torres Montaguth,
- Laura Atkinson,
- José Afonso Guerra-Assunção,
- Mahdi Moradi Marjaneh,
- Riccardo Zennezini Chiozzi,
- Nathaniel Storey,
- Luis Campos,
- J. Ciaran Hutchinson,
- John R. Counsell,
- Gabriele Pollara,
- Sunando Roy,
- Cristina Venturini,
- Juan F. Antinao Diaz,
- Ala'a Siam,
- Luke J. Tappouni,
- Zeinab Asgarian,
- Joanne Ng,
- Killian S. Hanlon,
- Alexander Lennon,
- Andrew McArdle,
- Agata Czap,
- Joshua Rosenheim,
- Catarina Andrade,
- Glenn Anderson,
- Jack C. D. Lee,
- Rachel Williams,
- Charlotte A. Williams,
- Helena Tutill,
- Nadua Bayzid,
- Luz Marina Martin Bernal,
- Hannah Macpherson,
- Kylie-Ann Montgomery,
- Catherine Moore,
- Kate Templeton,
- Claire Neill,
- Matt Holden,

- Rory Gunson,
- Samantha J. Shepherd,
- Priyen Shah,
- Samantha Cooray,
- Marie Voice,
- Michael Steele,
- Colin Fink,
- Thomas E. Whittaker,
- Giorgia Santilli,
- Paul Gissen,
- Benedikt B. Kaufer,
- Jana Reich,
- Julien Andreani,
- Peter Simmonds,
- Dimah K. Alrabiah,
- Sergi Castellano,
- Primrose Chikowore,
- Miranda Odam,
- Tommy Rampling,
- Catherine Houlihan,
- Katja Hoschler,
- Tiina Talts,
- Cristina Celma,
- Suam Gonzalez,
- Eileen Gallagher,
- Ruth Simmons,
- Conall Watson,
- Sema Mandal,
- Maria Zambon,
- Meera Chand,
- James Hatcher,
- Surjo De,
- Kenneth Baillie,
- Malcolm Gracie Semple,
- DIAMONDS Consortium,
- PERFORM Consortium,
- ISARIC 4C Investigators,

- Joanne Martin,
- Ines Ushiro-Lumb,
- Mahdad Noursadeghi,
- Maesha Deheragoda,
- Nedim Hadzic,
- Tassos Grammatikopoulos,
- Rachel Brown,
- Chayarani Kelgeri,
- Konstantinos Thalassinos,
- Simon N. Waddington,
- Thomas S. Jacques,
- Emma Thomson,
- Michael Levin,
- Julianne R. Brown &
- …
- Judith Breuer

Show authors

Nature **volume 617**, pages 564–573 (2023)

- 9898 Accesses
- 5 Citations
- 557 Altmetric
- Metrics details

Abstract

Since its first identification in Scotland, over 1,000 cases of unexplained paediatric hepatitis in children have been reported worldwide, including 278 cases in the UK[1]. Here we report an investigation of 38 cases, 66 age-matched immunocompetent controls and 21 immunocompromised comparator participants, using a combination of genomic, transcriptomic, proteomic and immunohistochemical methods. We detected high levels of adeno-associated virus 2 (AAV2) DNA in the liver, blood, plasma or stool

from 27 of 28 cases. We found low levels of adenovirus (HAdV) and human herpesvirus 6B (HHV-6B) in 23 of 31 and 16 of 23, respectively, of the cases tested. By contrast, AAV2 was infrequently detected and at low titre in the blood or the liver from control children with HAdV, even when profoundly immunosuppressed. AAV2, HAdV and HHV-6 phylogeny excluded the emergence of novel strains in cases. Histological analyses of explanted livers showed enrichment for T cells and B lineage cells. Proteomic comparison of liver tissue from cases and healthy controls identified increased expression of HLA class 2, immunoglobulin variable regions and complement proteins. HAdV and AAV2 proteins were not detected in the livers. Instead, we identified AAV2 DNA complexes reflecting both HAdV-mediated and HHV-6B-mediated replication. We hypothesize that high levels of abnormal AAV2 replication products aided by HAdV and, in severe cases, HHV-6B may have triggered immune-mediated hepatic disease in genetically and immunologically predisposed children.

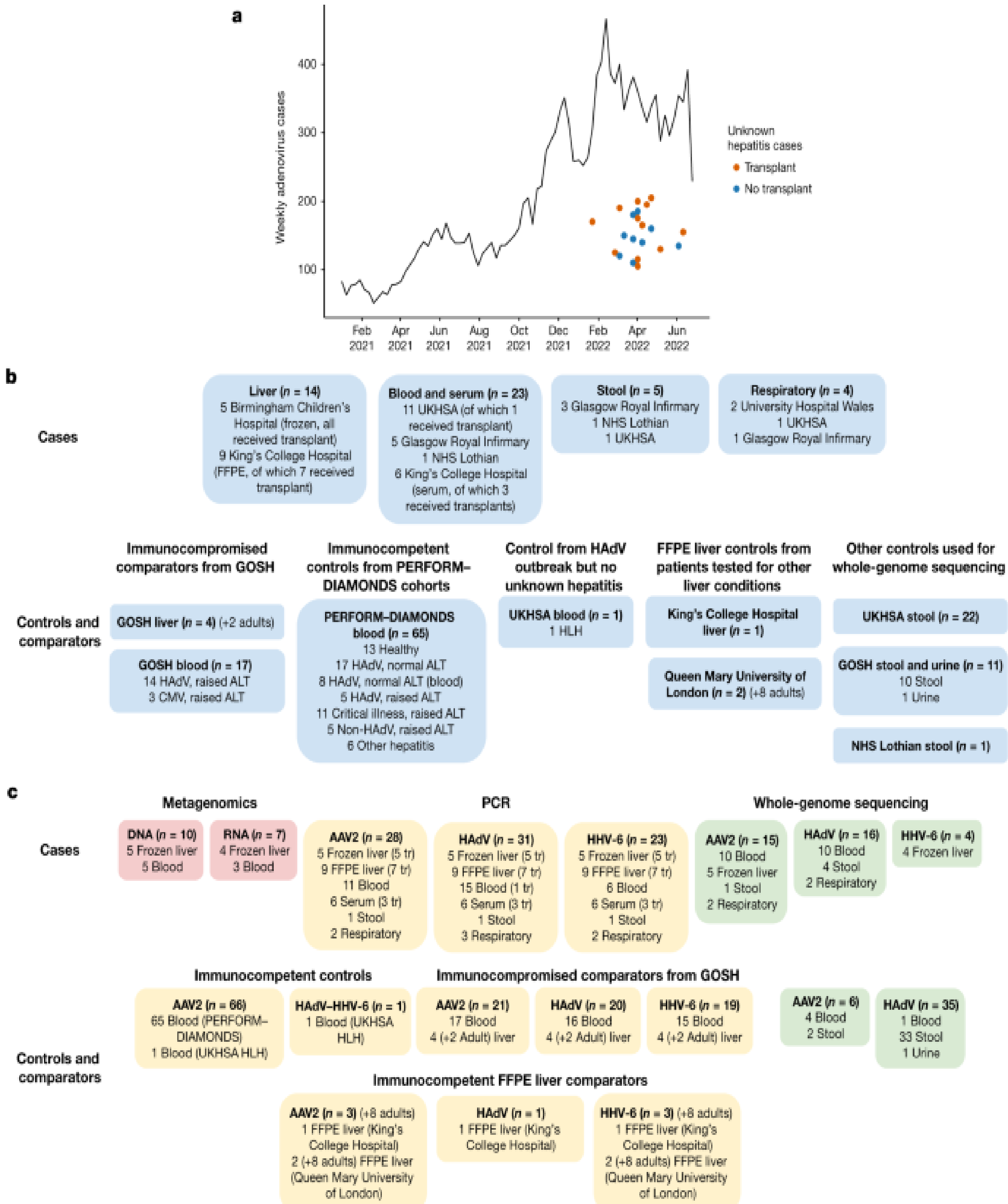
Main

In March 2022, the report of five cases of severe hepatitis of unknown aetiology led to the UK Health Security Agency (UKHSA) identifying 278 cases in total as of 30 September 2022[1]. Cases, defined as acute non-A–E hepatitis with serum transaminases of more than 500 IU in children under 10 years of age, were found to have been occurring since January 2022[2]. In the UK, 196 cases required hospitalization, 69 were admitted to intensive care and 13 required liver transplantation[1]. Case numbers have declined since April 2022[3].

UKHSA investigations identified HAdV to be commonly associated with the unexplained paediatric hepatitis, with 64.7% (156 of 241) testing positive in one or more samples from whole blood (the most sensitive sample type[4]) or mucosal swabs. HAdVs from the blood of 35 of 77 patients were typed as F41. Seven of eight patients in England who required liver transplantation tested HAdV positive in blood samples, with F41 found in five of five genotyped[2]. SARS-CoV-2 infection was detected in 8.9% (15 of 169) of UK and 12.8% (16 of 125) of English cases[2].

Given the uncertainty around the aetiology of this outbreak, and the potential that HAdV-F41, if implicated (Fig. 1a), could be a new or recombinant variant, we undertook untargeted metagenomic and metatranscriptomic sequencing of liver biopsies from five liver transplant cases and whole blood from five non-transplanted cases (Table 1 and Fig. 1b). The results were further verified by confirmatory PCRs of liver, blood, stool and nasopharyngeal samples from a total of 38 cases for which there was sufficient residual material. We compared our results with those from 13 healthy children and 52 previously healthy children presenting to hospital with other febrile illness, including HAdV, hepatitis unrelated to the current outbreak or a critical illness requiring admission to the intensive care unit. We also tested blood and liver biopsies from 17 profoundly immunosuppressed children with hepatitis who were not part of the current outbreak, in whom reactivation of latent infections might be expected.

Fig. 1: HAdV epidemiology and experimental outline.



a, HAdV in all sample types (epidemiology since January 2022). Source: second-generation surveillance system data, that is, laboratory reports to UKHSA of a positive HAdV result conducted by a laboratory in England and includes any sample type. Dots represent the day of presentation for the 28 of 38 cases for which we had data. **b**, Case and control specimens by source. CMV, cytomegalovirus; HLH, haemophagocytic

lymphohistiocytosis. **c**, Tests carried out by specimen type. More detail on samples tested and the results can be found in Tables 1 and 2. Not all tests were carried out on all samples due to lack of material. *n* refers to the total number of cases or controls. The numbers of each sample type may not sum to this total because samples of more than one type were sometimes taken from the same patient. For details, see Table 1. FFPE, formalin-fixed paraffin-embedded; tr, received liver transplant.

Table 1 Characteristics of unexplained paediatric hepatitis cases and related specimens

Cases

We received samples from 38 children meeting the case definition (Table 1). All cases were less than 10 years of age and 22 of 23 cases previously tested were positive by HAdV PCR (Table 2, Extended Data Table 1 and Supplementary Table 1). A summary of the samples received from these cases and the investigations carried out on them are shown in Fig. 1b,c.

Table 2 PCR, metagenomics and viral WGS results from cases in which metagenomic sequencing was performed

Clinical details

Pre-existing conditions, autoimmune, toxic and other infectious causes of hepatitis were excluded in 12 transplanted (cases 1–5, 28, 29, 31–34 and 36) and four non-transplanted (cases 30, 35, 37 and 38) children, investigated at two liver transplant units (Supplementary Table 1). The 12 transplanted cases reported gastrointestinal symptoms (nausea, vomiting and diarrhoea) preceding transplant by a median of 20 days (range 8–42 days). All 12 transplanted children survived, whereas the four children who did not receive liver transplants recovered without sequelae or evidence of chronic liver-related conditions. Five of the remaining 22 cases referred by Health Security Agencies, for whom this information was available, recovered without sequelae (Table 1 and Supplementary Table 1).

Metagenomic sequencing

We performed metagenomic and metatranscriptomic sequencing on samples of frozen explanted liver tissue from five cases who received liver transplants (median age of 3 years) and six blood samples from five non-transplanted hepatitis cases (median age of 5 years) (Table 1 and Fig. 1b). The liver samples had uniform and consistently high sequencing depth both for DNA sequencing (DNA-seq) and RNA-seq, whereas the blood samples had variable sequencing depth particularly for RNA-seq (Supplementary Table 2). We detected[5] abundant AAV2 reads in DNA-seq from five of five explanted livers and four of five blood samples from non-transplant cases (7–42 and 1.2–42 reads per million, respectively) (Table 2). Lower levels of HHV-6B were present in DNA-seq of all explanted liver samples (0.09–4 reads per million) but not in the six blood samples (Table 2). HAdV was detected (five reads) in one blood sample (Table 2).

Evidence of AAV2 replication

Metatranscriptomics revealed AAV2, but not HHV-6B or HAdV, RNA reads, in liver and blood samples (0.7–10 and 0–7.8 reads per million, respectively). Mapping liver RNA-seq data to the RefSeq AAV2 genome (NC_001401.2) identified high expression of the Cap open reading frame, particularly at the 3′ end of the capsid, suggesting viral replication[6] (Extended Data Fig. 1a), whereas reverse transcription (RT)–PCR of two livers confirmed the presence of AAV2 mRNA from the Cap open reading frame (Extended Data Fig. 1c). In the blood samples, which had not been treated to preserve RNA, we detected low levels of AAV2 RNA reads mapping throughout the genome (Extended Data Fig. 1b).

Nanopore sequencing of explanted livers

Ligation-based untargeted nanopore sequencing was applied to DNA from four of five frozen liver samples. All four samples were initially sequenced at a lower depth (average N50 of 8.37 kb). Six to sixteen AAV2 reads were obtained from each sample (5.57–22.24 million total reads; Supplementary Table 3). Mapping revealed concatenation of the 4-kb genome, compatible

with active AAV2 replication[7]. We observed alternating and head-to-tail concatemers, which could be consistent with both HAdV and human herpesvirus-mediated rolling hairpin and rolling circle replication, respectively[8]. Two of these samples were sequenced more deeply, resulting in 52 and 178 AAV2 reads in 82.9 and 122 million total (N50 of 4.40–8.52 kb) (Supplementary Table 3). Of the reads in the more deeply sequenced datasets, 42–48% comprised randomly linked, truncated and rearranged genomes, with few that were intact and of full length (Extended Data Fig. 2). The remaining reads were less than 3,000 bp long and may represent sections either of monomeric genomes or of more complex structures.

Integration analysis

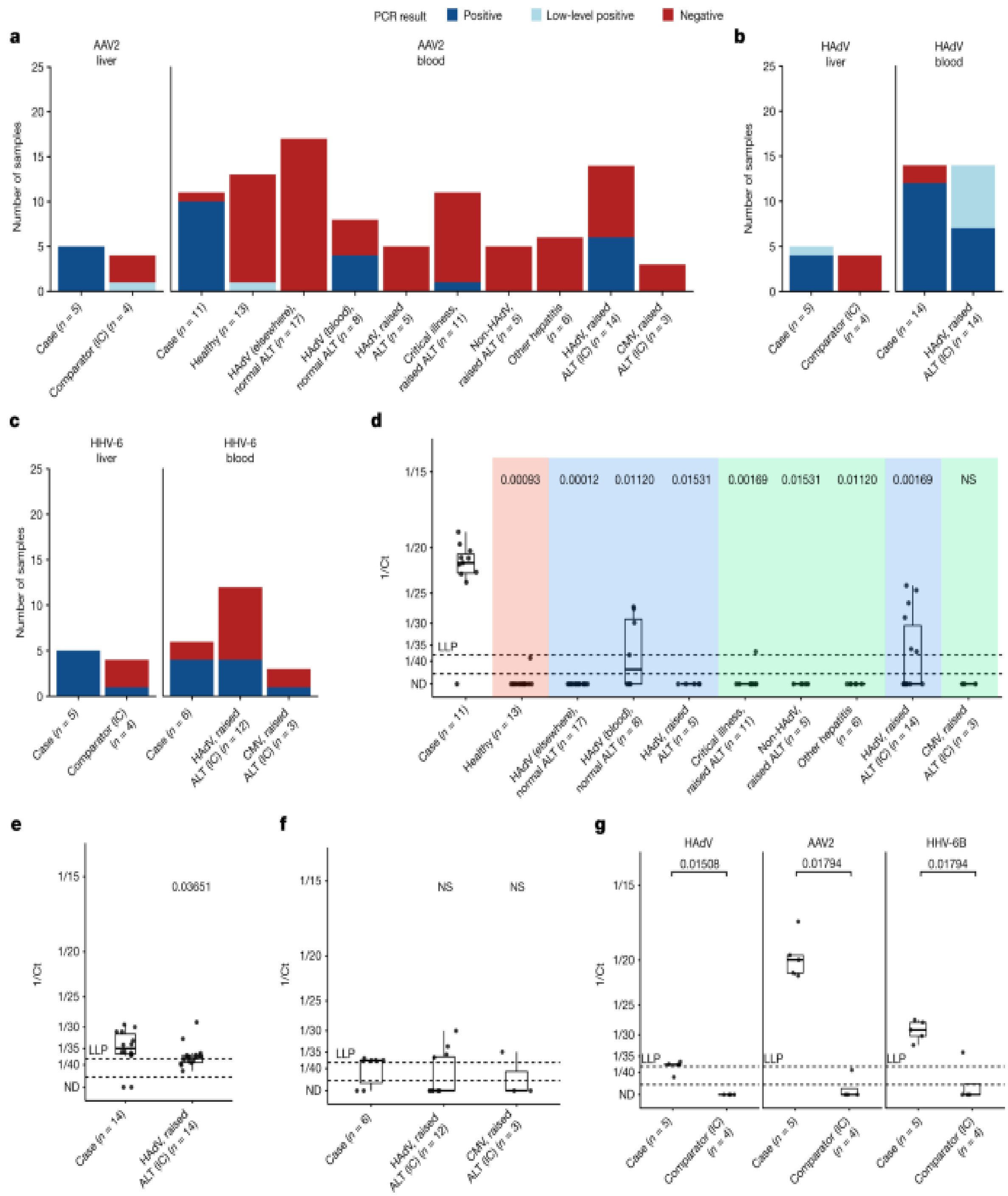
There was some evidence of AAV2 integration by deeper nanopore sequencing of explanted livers (Supplementary Table 3); however, none of the integration sites was confirmed by Illumina metagenomic or targeted AAV2 sequencing. The results are likely to represent artefacts of this library preparation method; chimeric reads have been described to occur in 1.7–3% of reads[9,10]. Given the number of human reads (72–120 million), we might expect to see this artefact occurring most commonly between AAV2 and human than between AAV2 reads.

Confirmatory real-time PCR

Where sufficient residual material was available, PCR tests were performed for AAV2 (28 of 38 cases), HAdV (31 of 38 cases) and HHV-6B (23 of 38 cases). The results confirmed high levels (cycle threshold (Ct) values: 17–21) of AAV2 DNA in all five frozen explanted livers that had undergone metagenomics (Table 2 and Fig. 2d), and lower levels of HHV-6B and HAdV DNA (Ct values: 27–32 and 37–42, respectively). AAV2 DNA was also detected (Ct values: 19–25) in blood samples from four of five cases that had undergone metagenomics, whereas HAdV, at levels too low to genotype, and HHV-6B were detected in two of four and three of four cases, respectively (one case had insufficient material) (Table 2). One of the blood metagenomics cases (case 9, JBB1) with insufficient material to test for HAdV and HHV-6B, tested positive for both viruses in the referring

laboratory. The AAV2-negative blood sample (case 10, JBB15) was also negative for HAdV but positive for HHV-6B (Table 2). A further ten of ten blood samples tested from cases were positive for HAdV by PCR. Sufficient material was available for AAV2 PCR in six of these (all positive; Ct values: 20–23) and HHV-6B PCR in two (one positive Ct value: 37) (Extended Data Table 1).

Fig. 2: Proportion of positive cases and viral loads (Ct values) for cases and controls.



a, Proportion of samples positive for AAV2. **b**, Proportion of samples positive for HAdV. **c**, Proportion of samples positive for HHV-6. Ct values less than 38 were defined as positive. Ct values more than 38 where the virus was detected within the maximum 45 cycles were defined as low-level positive (LLP). **d**, AAV2 in blood samples from cases, PERFORM–DIAMONDS immunocompetent controls and immunocompromised

comparators (IC). HAdV infection is in blue, non-HAdV hepatitis is in green and healthy is in red. **e**, HAdV levels in whole blood from cases and immunocompromised comparators. **f**, HHV-6 in whole blood from cases and immunocompromised comparators. **g**, HAdV, AAV2 and HHV-6 levels in frozen liver tissue from cases and immunocompromised comparators. In the box plots, the bold middle line represents the median and the upper and lower horizontal lines represent the upper (75th percentile) and lower (25th percentile) quartiles, respectively. The whiskers show maximum and minimum values. Each point represents one case or control. *n* Refers to the number of cases or controls. Where more than one sample for a case was tested, the midpoint of the Ct was plotted. All repeat tests had values if less than 2 Ct values apart, that is, within the limits of methodological error. The upper dashed line marked LLP indicates the LLP threshold (Ct = 38). Points below the second dashed line represent samples below the limit of PCR detection (Ct = 45). Wilcoxon non-parametric rank sum tests were conducted for **e** and **g** and a Kruskal–Wallis test followed by pairwise Wilcoxon tests with a Benjamini–Hochberg correction for multiple comparisons were used for **d** and **f**. All tests were two-tailed. Numbers show the *P* value compared with cases. ND, not determined (negative PCR result); NS, not significant.

AAV2 PCR was positive in nine formalin-fixed paraffin-embedded (FFPE) liver samples, including seven from transplanted cases (Ct values: 23–25) and two from non-transplanted cases (Ct values: 34–36; Extended Data Table 1). HHV-6B PCR was positive in six of seven FFPE samples (not case 32) from transplanted (Ct values: 30–37) and zero of two from non-transplanted (cases 30 and 35) cases, with positive HAdV (Ct values: 40–44) in four of nine cases. Three transplanted (cases 32, 34 and 36) and three non-transplanted (cases 35, 37 and 38) cases had serum available for testing. All were AAV2 positive (Ct values: 27–32) and HHV-6B negative, with one transplanted case and one non-transplanted case testing HAdV positive (Extended Data Table 1).

Together, 27 of 28 cases tested were AAV2 PCR positive, 23 of 31 were HAdV positive and 16 of 23 were HHV-6B positive. When results from referring laboratories were included, 33 of 38 cases were positive for HAdV and 19 of 26 cases were positive for HHV-6B (Table 2 and Extended Data Table 1).

Controls and comparators

To better contextualize the findings in cases with unexplained hepatitis, we selected control groups of children who were not part of the outbreak.

Blood from immunocompetent children

Whole blood from 65 immunocompetent children matched by age to cases (median age of 3.8 years) **(**Fig. 1b, Extended Data Table 2a and Supplementary Table 4) who were healthy, or had HAdV infection, hepatitis or critical illness, including requiring critical care, were selected from the PERFORM (personalised risk assessment in febrile illness to optimise real-life management; www.perform2020.org) and DIAMONDS (diagnosis and management of febrile illness using RNA personalised molecular signature diagnosis study; www.diamonds2020.eu) studies. Both studies recruited children presenting to hospital with an acute-onset febrile illness between 2017 and 2020 (PERFORM) and July 2020 to October 2021, during the COVID-19 pandemic (DIAMONDS) (Supplementary Table 4). Of the PERFORM–DIAMONDS control whole-blood samples, 6 of 65 (9.2%) were AAV2 PCR positive (Supplementary Table 5), compared with 10 of 11 (91%) whole-blood samples from cases (Fig. 2a; $P = 8.466 \times 10^{-8}$, Fisher's exact test). AAV2 DNA levels were significantly higher in whole-blood samples from cases than from controls (Fig. 2e; $P = 2.747 \times 10^{-11}$, Mann–Whitney test**)**.

One participant with an HAdV-F41-positive blood sample, originally thought to have unexplained paediatric hepatitis, was later found to have a previous condition that explained the hepatitis and was therefore reclassified as a control (referred to as 'reclassified control' or CONB40) (Supplementary Table 5). This blood sample was negative for AAV2 by PCR (Supplementary Table 5).

Liver from immunocompromised children

Frozen liver biopsy material from four immunocompromised children (median age of 10 years) (CONL1–4) who had been investigated for other

forms of hepatitis was also tested (Fig. 1b and Extended Data Table 2b). In three children, liver enzyme levels were raised (Supplementary Table 6); no results were available for CONL4. AAV2 was detected in CONL3 (Ct value: 39) and HHV-6B was detected in CONL2 (Ct value: 34), whereas HAdV was negative (Fig. 2d and Supplementary Table 5).

Blood from immunocompromised comparators

We also tested immunocompromised children who are more likely to reactivate latent viruses. Whole-blood samples from 17 immunocompromised children (median age of 1 year) with raised levels of liver transaminases (AST/ALT of more than 500 IU) and viraemia (HAdV or cytomegalovirus), all sampled in 2022 (Fig. 1b), were tested for AAV2, HHV-6B and HAdV (Extended Data Table 2b and Supplementary Table 5). The majority had received human stem cell or solid organ transplants, and none was linked to the recent hepatitis outbreak (Extended Data Table 2b). Five of 15 (33%) whole-blood samples were positive for HHV-6B, whereas 6 of 17 (35%) were positive for AAV2, significantly fewer than in cases ($P = 0.005957$, Fisher's exact test) and at significantly lower Ct levels ($P = 6.517 \times 10^{-5}$, Mann–Whitney test) (Fig. 2 and Supplementary Table 5). One HAdV-positive and AAV2-positive immunocompromised comparator (CONB23) was also positive for HHV-6B (Supplementary Table 5).

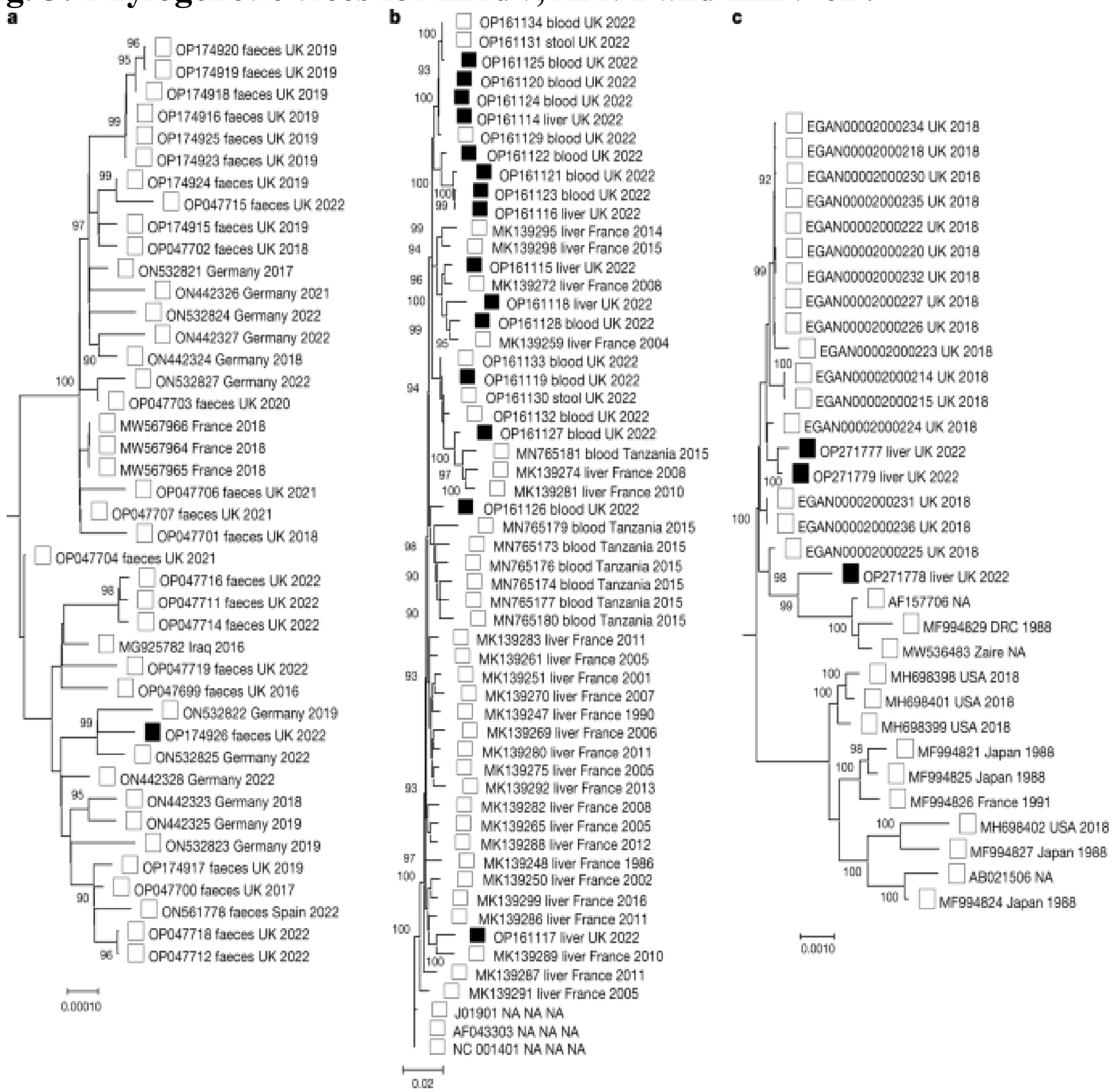
Four of the six AAV2-positive children from the PERFORM–DIAMONDS cohort (Fig. 2a and Supplementary Table 5) and all six of the AAV2-positive immunocompromised children (Fig. 2a and Supplementary Table 5) were also HAdV positive.

Viral whole-genome sequencing

One full HAdV-F41 genome sequence from the stool of one case (OP174926, case 22) (Supplementary Table 7) clustered phylogenetically with the HAdV-F41 sequence obtained from the reclassified control (CONB40) and with other HAdV-F41 sequences collected between 2015 and 2022, including 23 contemporaneous stool samples from children without the unexplained paediatric hepatitis (Figs. 1c and 3a). Sequencing

and *k*-mer analysis[11] of HAdV from 13 cases with partial sequences identified the genotype HAdV-F41 in 12 cases (Supplementary Tables 7 and 8). The partial sequences showed most similarity to the control sequence OP047699 (Supplementary Table 8), mapping across the entire viral genome, thus further excluding a recombinant virus.

Fig. 3: Phylogenetic trees for HAdV, AAV2 and HHV-6B.



Maximum likelihood phylogenetic trees combining reference sequences from the RefSeq database, publicly available complete genomes from GenBank, UK non-outbreak controls (open squares) and unexplained hepatitis cases (black squares) for the different viruses involved. **a**, HAdV. **b**,

AAV2. **c**, HHV-6B. HAdV and HHV-6B trees are midpoint rooted, whereas AAV2 is rooted from the RefSeq sequence NC_001401.2. Bootstrap values less than 90 are not shown. NA, value not known.

Single-nucleotide polymorphisms were largely shared between the single HAdV-positive stool from a case (OP174926) and control whole-genome sequences (Extended Data Fig. 3a). Given reported mutation rates for HAdV-F41 and other adenoviruses[12,13], any differences are likely to have arisen before the outbreak. No new or unique amino acid substitutions were noted in HAdV sequences from cases with only two substitutions overall (Extended Data Fig. 2d) and none in proteins critical for AAV2 replication.

AAV2 sequences from 15 cases, including five from the explanted livers and ten from whole blood from non-transplanted cases, clustered phylogenetically with control AAV2 sequences obtained from four immunocompromised HAdV-positive children with elevated levels of ALT in the comparator group (Extended Data Table 2b) and two healthy children with recent HAdV-F41 diarrhoea (Fig. 3b and Supplementary Table 9). The degree of diversity and lack of a unique common ancestor between case AAV2 genomes suggest that these are not specific to the hepatitis outbreak, but instead reflect the current viral diversity of the general population. Although comparison of the AAV2 sequences showed no difference between cases and controls, contemporary AAV2 sequences showed changes in the capsid compared with historic AAV2 (Extended Data Fig. 3c). None of these changes was shared with the hepatotropic AAV7 and AAV8 viruses (Extended Data Fig. 3b). The majority of the contemporary AAV2 genomes in cases and controls (20 of 21) contained a stop codon in the X gene, which is involved in viral replication[14], whereas historic AAV2 genomes contained this less frequently (11 of 35). The significance, if any, of this is currently unknown.

Although mean read depths for four HHV-6B genomes recovered from explanted livers were low (×5–10) (Supplementary Table 12), phylogeny (Fig. 3c) confirmed that all were different.

Transduction of AAV2 capsid mutants

Using a recombinant AAV2 (rAAV2) vector with a VP1 sequence (Extended Data Fig. 4a) containing the consensus amino acid sequence from AAV2 cases (AAV2Hepcase) (Extended Data Fig. 3b), we generated functional rAAV particles that transduced Huh-7 cells with comparable efficacy to both canonical AAV2 and the synthetic liver-tropic LK03 AAV vector[15]. Unlike canonical AAV2, the AAV2Hepcase capsid, which contains mutations (R585S and R588T) that potentially affect the heparin sulfate proteoglycan (HSPG)-binding domain, was unaffected by heparin competition, a feature that is associated with increased hepatotropism[16,17] (Extended Data Fig. 4b,c).

Histology and immunohistochemistry

Histological examination of the 12 liver explants and two liver biopsies showed nonspecific features of acute hepatitis with ballooning hepatocytes, disrupted liver architecture with varying degrees of perivenular, bridging or pan-acinar necrosis. There was no evidence of fibrosis suggestive of an underlying chronic liver disease. The appearances were similar to historic cases of seronegative hepatitis of unknown cause in children. There were no typical histological features of autoimmune hepatitis, notably no evidence of portal-based plasma cell-rich infiltrates. A cellular infiltrate was present in all cases, which on staining appeared to be predominantly of $CD8^+$ T cells but also included $CD20^+$ B cells. More widespread staining with the CD79a pan-B cell lineage, which also identifies plasma cells, was also observed (Extended Data Fig. 5). Macrophage lineage cells showed some C4d complement staining, whereas staining for immunoglobulins was nonspecific with disruption of the normal canalicular staining seen in controls due to the architectural collapse. MHC class I and class II staining, although increased in cases, was nonspecific and associated with sinusoid-containing blood cells and necrotic tissue (Extended Data Fig. 6a). No viral inclusions were observed and there were no features suggestive of direct viral cytopathic effect.

Immunohistochemistry was negative for adenovirus. Staining of the five explanted livers with AAV2 antibodies demonstrated evidence of nonspecific ingested debris but not the nuclear staining seen in the positive AAV2-infected cell lines and infected mouse tissue (Extended Data Fig. 6b).

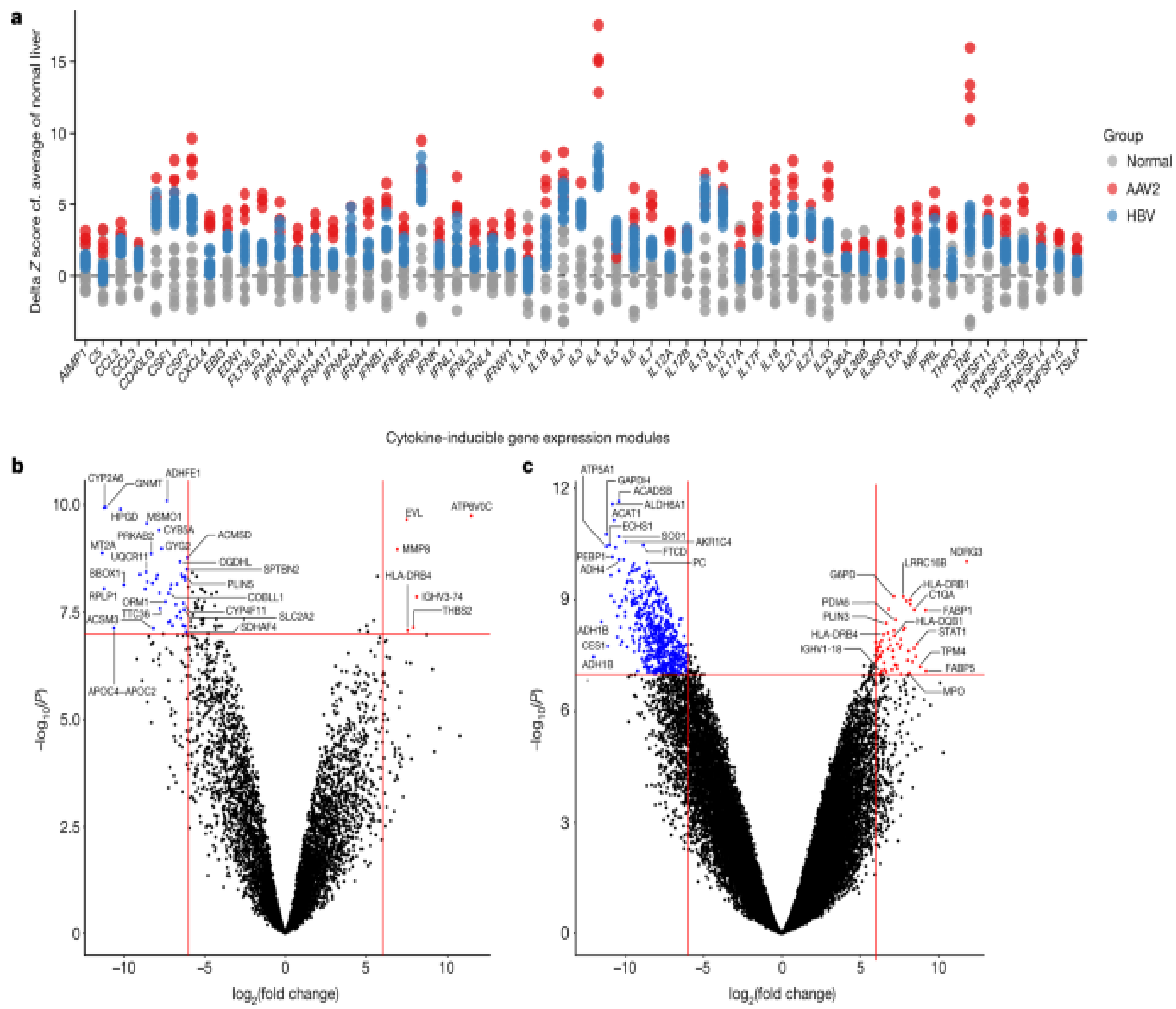
All five liver explants showed positive staining of macrophage-derived cells with antibody to HHV-6B, with no staining of negative control serial sections (Extended Data Fig. 6b). No specific HHV-6B staining was observed in 13 control liver biopsies from patients (including three children less than 18 years of age) with other viral hepatitis, toxic liver necrosis, autoimmune and other hepatitis, and normal liver. The control set was also negative for HAdV and AAV2 by immunohistochemistry.

Liver sections were morphologically suboptimal for electron microscopy, but no viral particles were identified in hepatocytes, blood vessel endothelial cells and Kupffer cells.

Transcriptomic analysis

We quantified functional cytokine activity by expression of independently derived cytokine-inducible transcriptional signatures of cell-mediated immunity (Supplementary Table 11) in bulk genome-wide transcriptional profiles from four of the frozen explanted livers. Results were compared with published data from normal adult livers ($n = 10$) and adult hepatitis B-associated acute liver failure ($n = 17$) (GSE96851)[18]. Data from the unexplained hepatitis cases revealed increased expression of diverse cytokines and pathways compared with normal liver. These pathways included prototypic cytokines associated with T cell responses, including IFNγ, IL-2, CD40LG, IL-4, IL-5, IL-7, IL-13 and IL-15 (Fig. 4a and Supplementary Table 12), as well as some evidence of innate immune type I interferon responses. Many of these responses showed substantially greater activity in unexplained hepatitis than in fulminant hepatitis B virus disease. The most striking enrichment was for TNF expression, and included other canonical pro-inflammatory cytokines including IL-1 and IL-6 (Extended Data Fig. 7). These data are consistent with an inflammatory process involving multiple pathways.

Fig. 4: Transcriptomic and proteomic analysis of case liver samples.



Transcriptomic analysis was conducted for the five frozen case liver samples from transplanted patients. **a**, Expressions of cytokine-inducible transcriptional modules in normal liver, and AAV2-associated ($n = 4$) or HBV-associated ($n = 17$) hepatitis requiring transplantation are shown as delta Z scores for the expression of each module, reflecting the difference from the average score from normal liver ($n = 10$) datasets, all from different patients. Each point represents the score form a single dataset or sample. **b**,**c**, Volcano plots of differentially expressed proteins (**b**) and peptides (**c**). The volcano plots illustrate fold changes and corresponding P values for the comparison between five liver explants from five patients and seven control healthy livers from seven controls. Each dot represents a protein or peptide. The P values were calculated by applying two-tailed empirical Bayes moderated t-statistics on protein-wise or peptide-wise linear models. Proteins (**b**) and peptides (**c**) differentially expressed (absolute $\log_2$(fold

change) > 6 and $P < 1 \times 10^{-7}$) are coloured red (upregulated) and blue (downregulated). The P values illustrated here are not adjusted for multiple comparisons. Full tables can be found in Supplementary Tables 12–14.

Proteomics

Proteomic analysis of the five frozen explanted livers did not detect AAV2 or HAdV proteins. Expression of HHV-6B U4, a protein of unknown function, was found in four of five cases; U43, part of the helicase primase complex, was found in two of five cases; and U84, a homologue of cytomegalovirus UL117, implicated in HHV-6B nuclear replication, was found in two of five cases (Extended Data Fig. 8).

The human proteome from the five frozen liver explants was compared with publicly available data from seven control 'normal' livers, taken from two different studies[19,20]. Both protein and peptide analyses (Fig. 4b,c and Supplementary Tables 13 and 14) found increased expression in unexplained hepatitis cases of HLA class II proteins and peptides (for example, HLADRB1 and HLADRB4), multiple peptides from variable regions of the heavy and light chains of immunoglobulin, complement proteins (such as C1q) and intracellular and extracellular released proteins from neutrophils and macrophages (MMP8 and MPO).

There was no evidence of HAdV, AAV2 or HHV-6B in any of the control livers.

Discussion

Despite reports implicating HAdV-F41 as causing the recent outbreak of unexplained paediatric hepatitis, we found very low levels of HAdV DNA, no proteins, inclusions or viral particles, including in explanted liver tissue from affected cases and no evidence of a change in the virus. By contrast, metagenomic and PCR analysis of liver tissue and blood identified high levels of DNA from AAV2, a member of the *Dependoparvovirus* genus, which has not been previously associated with clinical disease, in 27 of 28 cases. Replication of AAV2 requires co-infection with a helper virus, such as

HAdV, herpesviruses or papillomavirus[21], and can also be triggered in the laboratory by cellular damage[22], raising the possibility that the AAV2 detected was a bystander of previous HAdV-F41 infection and/or liver damage. Against this, we found little or no AAV2 in blood from age-matched, immunocompetent children including those with HAdV infection, hepatitis or critical illness (Fig. 2d). AAV2 has been reported to establish latency in the liver[23]; however, even in critically ill immunosuppressed children with hepatitis in whom reactivation might occur, we detected AAV2 infrequently and at significantly lower levels in the blood or in liver biopsies (Fig. 2d,g).

RNA transcriptomic and real-time PCR data from explanted livers point to active AAV2 infection, although we did not detect AAV2 proteins by immunohistochemistry (Extended Data Fig. 6b) or proteomics (Extended Data Fig. 8) or any viral particles. The abundant AAV2 genomes in the explanted liver are concatenated with many complex and abnormal configurations. AAV genome concatenation may occur during AAV2 replication[8], whereas abnormal AAV2 DNA complexes and rearrangements have been observed in the liver following AAV gene therapy[7]. Hepatitis following AAV gene therapy has been well described[24,25,26], with deaths occurring, albeit rarely[27]. The pattern of complexes typify both HAdV and herpesvirus (including HHV-6B)-mediated AAV2 DNA replication[6]. The presence of HHV-6B DNA in 11 of 12 explanted livers, but not in livers (0 of 2) of non-transplanted children, or control livers as well as the expression, in 5 of 5 cases tested, of HHV-6B proteins, including U43, a homologue of the HSV1 helicase primase UL52, which is known to aid AAV2 replication, highlight a possible role for HHV-6B as well as HAdV in the pathogenesis of AAV2 hepatitis, particularly in severe cases. Although AAV2 is also capable of chromosomal integration[28,29,30], we found little evidence of this by long read sequencing, computational analysis of metagenomics data or examination of unmapped reads, although further confirmatory studies may be required.

Although the pathogenesis of unexplained paediatric hepatitis and the role of AAV2 remain to be determined, our results point strongly to an immune-mediated process. Transcriptomic and proteomic data from the five explant livers identified significant immune dysregulation involving genes and

proteins that are strongly associated with activation of B cells and T cells, neutrophils and macrophages as well as innate pathways. The findings are supported by immunohistochemical staining showing infiltration into liver tissue of $CD8^+$, B cell and B cell lineage cells. Upregulation of canonical pro-inflammatory cytokines including lL-15, which has also been seen in a mouse model of AAV hepatitis[31], IL-4 and TNF occurred at levels greater even than are seen in fulminant liver failure following infection with hepatitis B virus. Increased levels in the same immunoglobulin variable region peptides and corresponding proteins from both immunoglobulin heavy and light chains across all five livers point to specific antibody involvement[32]. HLA-DRB1*04:01 (12 of 13 cases tested) (Supplementary Table 1) among children in our study supports the same genetic predisposition as mooted in a parallel study conducted in Scotland[33].

An immune-mediated process is consistent with studies of hepatitis following AAV gene therapy, in which raised AAV2 IgG and capsid specific cytotoxic T lymphocytes are observed in the affected patients; however, whether these directly mediate hepatitis remains unclear[26,34]. Although we did not find that AAV2 sequences in cases differed from those in AAV2 occurring as co-infections in HAdV-F41-positive stool collected from control children during the contemporary HAdV-F41 gastroenteritis outbreak (Fig. 3b), rAAV capsid expressing a consensus capsid sequence from the unexplained hepatitis cases (AAV2Hepcase) showed reduced HSPG dependency, compared with canonical AAV2 (Extended Data Fig. 4), while retaining hepatocyte transduction ability. This points to likely greater in vivo hepatotropism of currently circulating AAV2 than has hitherto been assumed from data on canonical AAV2 (ref. 17). Another member of the parvovirus family, equine parvovirus-hepatitis, has also been associated with acute hepatitis in horses (Theiler’s disease)[35].

There are several limitations to our study. Although other known infectious, autoimmune, toxic and metabolic aetiologies[3] have been excluded including by other studies[36,37], the number of cases investigated here is small, the study is retrospective, the immunocompromised controls were not perfectly age-matched, and only one immunocompetent and 17 immunocompromised controls were sampled during exactly the same period as the outbreak. Age-matched, immunocompetent controls contemporaneous with the outbreak

from the DIAMONDS study, although few in number, were however found to be AAV2 negative in a separate study carried out in Scotland[33].

Finally, our data alone are not sufficient on their own to rule out a contribution from SARS-CoV-2 Omicron, the appearance of which preceded the outbreak of unexplained hepatitis (Supplementary Table 1). We did not detect SARS-CoV-2 metagenomically even in three participants who tested positive on admission. Moreover, although seropositivity was higher in our cases (15 of 20) than in controls (3 of 10), this was not the case for another UK cohort[36] (38%) or in preliminary data from a UKHSA case–control study[3], which showed similar SARS-CoV-2 antibody prevalence between unexplained hepatitis cases and population controls (less than 5 years of age: 60.5% versus 46.3%, respectively; 5–10 years of age: 66.7% versus 69.6%, respectively). In line with UK national recommendations at the time, none of the children had received a COVID vaccine.

Although we found little evidence for SARS-CoV-2 directly causing the hepatitis outbreak, we cannot exclude the effect of the COVID-19 pandemic on child mixing and infection patterns. The contemporaneous development of unexplained paediatric hepatitis with a national outbreak of HAdV-F41 (ref. [2]) and the finding of HAdV-F41 in many cases suggest that the two are linked. Enteric HAdV infection is most common in those younger than 5 years of age[2], and infection is influenced by mixing and hygiene[38]. Few cases of HAdV-F41 occurred between 2020 and 2022 and no major outbreaks were recorded[2]. The current HAdV outbreak followed relaxation of restrictions due to the pandemic and represented one of many infections, including other enteric pathogens that occurred in UK children following return to normal mixing[39]. Under normal circumstances, the levels of AAV2 antibodies are high at birth, subsequently declining to reach their lowest point at 7–11 months of age, increasing thereafter through childhood and adolescence[40]. AAV2 is known to spread with respiratory HAdVs, infections that declined during the COVID-19 pandemic, and has not been detected by us in over 30 SARS-CoV-2-positive nasopharyngeal aspirates (data not shown). We also found AAV2 DNA to be present in HAdV-F41-positive stool from both cases and controls (Supplementary Table 5). With loss of child mixing during the COVID-19 pandemic, reduced spread of common respiratory and enteric viral infections and no evidence of AAV2 in SARS-

CoV-2-positive nasopharyngeal swabs, it is likely that immunity to both HAdV-F41 and AAV2 declined sharply in the age group affected by this unexplained hepatitis outbreak. Pre-existing antibody is known to reduce levels of AAV DNA in the liver of non-human primates following infusion of AAV gene therapy vectors[41]. The possibility that, in the absence of protective immunity, excessive replication of HAdV-F41 and AAV2 with accumulation of AAV2 DNA in the liver led to immune-mediated hepatic disease in genetically predisposed individuals needs further investigation. Evaluation of drugs that inhibit TNF and other cytokines massively elevated in this condition may identify important therapeutic options for future cases.

Methods

Ethics

Metagenomic analysis and HAdV sequencing were carried out by the routine diagnostic service at Great Ormond Street Hospital (GOSH). Additional PCRs, immunohistochemistry and proteomics on samples received for metagenomics are part of the GOSH protocol for confirmation of new and unexpected pathogens. The use for research of anonymized laboratory request data, diagnostic results and residual material from any specimen received in the GOSH diagnostic laboratory, including all cases received from Birmingham's Children Hospital UKHSA, Public Health Wales, Public Health Scotland as well as non-case samples from UKHSA, Public Health Scotland and GOSH research was approved by UCL Partners Pathogen Biobank under ethical approval granted by the NRES Committee London-Fulham (REC reference: 17/LO/1530).

Children undergoing liver transplant were consented for additional research under the International Severe Acute Respiratory and Emerging Infection Consortium (ISARIC) WHO Clinical Characterisation Protocol UK (CCP-UK) (ISRCTN 66726260) (RQ3001-0591, RQ301-0594, RQ301-0596, RQ301-0597 and RQ301-0598). Ethical approval for the ISARIC CCP-UK study was given by the South Central–Oxford Research Ethics Committee in England (13/SC/0149), the Scotland A Research Ethics Committee (20/SS/0028) and the WHO Ethics Review Committee (RPC571 and RPC572).

The UKHSA has legal permission, provided by regulation 3 of The Health Service (Control of Patient Information) Regulations 2002, to process patient confidential information for national surveillance of communicable diseases and, as such, individual patient consent is not required.

Control participants from the EU Horizon 2020 research and innovation program DIAMONDS–PERFORM (grant agreement nos. 668303 and 848196) were recruited according to the approved enrolment procedures of each study, and with the informed consent of parents or guardians: DIAMONDS (London-Dulwich Research Ethics Committee: 20/HRA/1714) and PERFORM (London-Central Research Ethics Committee: 16/LO/1684).

The sample IDs for the cases and controls are anonymized IDs that cannot reveal the identity of the study participants and are not known to anyone outside the research group, such as the patients or the hospital staff.

Samples

Initial diagnostic testing by metagenomics and PCR was performed at GOSH Microbiology and Virology clinical laboratories. Further WGS and characterization were performed at UCL.

Cases

Birmingham Children's Hospital provided us with explanted liver tissue from five biopsy sites from five cases, five whole blood 500 µl from four cases and serum plasma from one case (Table 1 and Fig. 1b). These were used in metagenomics testing (Table 2), followed by HAdV, HHV-6 and AAV2 testing by PCR and, depending on the Ct value, WGS (Supplementary Tables 7, 9 and 10). We subsequently received 25 additional specimens from UKHSA, Public Health Wales and Public Health Scotland/Edinburgh Royal Infirmary, including 16 additional blood samples, four respiratory specimens and five stool samples, for HAdV WGS and, depending on residual material, for AAV2 PCR testing followed by sequencing (Tables 1 and 2, Fig. 1b and Supplementary Tables 7, 9 and 10). We also received ten FFPE liver biopsy samples and six serum samples from

11 cases from King's College Hospital (Table 1). Of these cases, seven had received liver transplants.

Controls from DIAMONDS and PERFORM

PERFORM recruited children from ten EU countries (2016–2020). PERFORM was funded by the European Union's Horizon 2020 programme under GA no. 668303.

DIAMONDS is funded by the European Union Horizon 2020 programme grant number 848196. Recruitment commenced in 2020 and is ongoing. Both studies recruited children presenting with suspected infection or inflammation and assigned them to diagnostic groups according to a standardized algorithm.

Controls from GOSH for PCR

Blood samples from 17 patients not linked to the non-A–E hepatitis outbreak were tested by real-time PCR targeting AAV2 (Extended Data Table 2b). These comparators were patients with ALT/AST of more than 500 and HAdV or cytomegalovirus viraemia. These were purified DNA from residual diagnostic specimens received in the GOSH microbiology and virology laboratory in the previous year. All residual specimens were stored at −80 °C before testing and pseudo-anonymized at the point of processing and analysis. Viraemia was initially detected using targeted real-time PCR during routine diagnostic testing with UKAS-accredited laboratory-developed assays that conform to ISO:15189 standards.

In addition to the blood samples, four residual liver biopsies from four control patients referred for investigation of infection were tested by AAV2 and HHV-6B PCR. The liver biopsies were submitted to the GOSH microbiology laboratory for routine diagnosis by bacterial broad-range 16S rRNA gene PCR or metagenomics testing in 2021 and 2022. Three of four control patients were known to have elevated levels of liver enzymes. Two adult frozen liver samples previously tested by metagenomics were negative for AAV2 and positive for HHV-6B (Supplementary Table 5).

Controls from UKHSA

We received a blood sample from one patient with elevated levels of liver enzymes and HAdV infection. We also received one control stool sample from Public Health Scotland/Edinburgh Royal Infirmary and 22 control stool samples for sequencing.

Controls from King's College Hospital

A single FFPE liver biopsy control of normal marginal tissue from a hepatoblastoma from a child was negative for AAV2 and HAdV, but positive for HHV-6B (Ct = 37).

Controls from Queen Mary University of London

We received FFPE liver control samples from ten adults and three children (under 18 years of age) with other viral hepatitis, toxic liver necrosis, autoimmune and other hepatitis, and normal liver, from Queen Mary University of London. PCR gave valid results for samples from two children and eight adults, all of which were negative by PCR for AAV2 and HHV-6, apart from one adult sample, which was positive for HHV-6 at a high Ct value (Supplementary Table 5).

Metagenomic sequencing

Nucleic acid purification

Frozen liver biopsies were infused overnight at −20 °C with RNAlater-ICE. Up to 20 mg biopsy was lysed with 1.4-mm ceramic, 0.1-mm silica and 4-mm glass beads, before DNA and RNA purification using the Qiagen AllPrep DNA/RNA Mini kit as per the manufacturer's instructions, with a 30 µl elution volume for RNA and 50 µl for DNA.

Up to 400 µl whole blood was lysed with 0.5-mm and 0.1-mm glass beads before DNA and RNA purification on a Qiagen EZ1 instrument with an EZ1 virus mini kit as per the manufacturer's instructions, with a 60 µl elution volume.

For quality assurance, every batch of samples was accompanied by a control sample containing feline calicivirus RNA and cowpox DNA, which was processed alongside clinical specimens, from nucleic acid purification through to sequencing. All specimens and controls were spiked with MS2 phage RNA internal control before nucleic acid purification.

Library preparation and sequencing

RNA from whole-blood samples with an RNA yield of more than 2.5 ng μl^{-1} and from biopsies underwent ribosomal RNA depletion and library preparation with KAPA RNA HyperPrep kit with RiboErase, according to the manufacturer's instructions. RNA from whole blood with an RNA yield of less than 2.5 ng μl^{-1} did not undergo rRNA depletion before library preparation.

DNA from whole-blood samples with a DNA yield of more than 1 ng μl^{-1} and from biopsies underwent depletion of CpG-methylated DNA using the NEBNext Microbiome DNA Enrichment Kit, followed by library preparation with the NEBNext Ultra II FS DNA Library Prep Kit for Illumina, according to manufacturer's instructions. DNA from whole blood with a DNA yield of less than 1 ng μl^{-1} did not undergo depletion of CpG-methylated DNA before library preparation.

Sequencing was performed with a NextSeq High output 150 cycle kit with a maximum of 12 libraries pooled per run, including controls.

Metagenomics data analysis

Pre-processing pipeline

An initial quality control step was performed by trimming adapters and low-quality ends from the reads (Trim Galore![42] 0.3.7). Human sequences were then removed using the human reference GRCH38 p.9 (Bowtie2 (ref. [43]), version 2.4.1) followed by removal of low-quality and low-complexity sequences (PrinSeq[44], version 0.20.3). An additional step of human sequences removal followed (megaBLAST[45], version 2.9.0). For RNA-seq,

rRNA sequences were also removed using a similar two-step approach (Bowtie2 and megaBLAST). Finally, nucleotide similarity and protein similarity searches were performed (megaBLAST and DIAMOND[46] (version 0.9.30), respectively) against custom reference databases that consisted of nucleotide and protein sequences of the RefSeq collections (downloaded March 2020) for viruses, bacteria, fungi, parasites and human.

Taxonomic classification

DNA and RNA sequence data were analysed with metaMix[5] (version 0.4) nucleotide and protein analysis pipelines.

metaMix resolves metagenomics mixtures using Bayesian mixture models and a parallel Markov chain Monte Carlo search of the potential species space to infer the most likely species profile.

metaMix considers all reads simultaneously to infer relative abundances and probabilistically assign the reads to the species most likely to be present. It uses an 'unknown' category to capture the fact that some reads cannot be assigned to any species. The resulting metagenomic profile includes posterior probabilities of species presence as well as Bayes factor for presence versus absence of specific species. There are two modes: metaMix-protein, which is optimal for RNA virus detection, and metaMix-nucl, which is best for speciation of DNA microorganisms. Both modes were used for RNA-seq, whereas metaMix-nucl was used for DNA-seq.

For sequence results to be valid, MS2 phage RNA had to be detected in every sample and feline calicivirus RNA and cowpox DNA, with no additional unexpected organisms, detected in the controls.

Confirmatory mapping of AAV2

The RNA-seq reads were mapped to the AAV2 reference genome (NCBI reference sequence NC_001401) using Bowtie2, with the –very-sensitive option. Samtools[47] (version 1.9) and Picard (version 2.26.9; http://broadinstitute.github.io/picard/) were used to sort, deduplicate and

index the alignments, and to create a depth file, which was plotted using a custom script in R.

De novo assembly of unclassified reads

We performed a de novo assembly step with metaSPADES[48] (v3.15.5), using all the reads with no matches to the nucleotide database that we used for our similarity search. A search using megaBLAST with the standard nucleotide collection was carried out on all resulting contigs over 1,000 bp in length. All of the contigs longer than 1,000 bp matched to human, except two that mapped to Torque Teno virus.

Nanopore sequencing

DNA from up to 20 mg of liver was purified using the Qiagen DNeasy Blood & Tissue kit as per the manufacturer's instructions. Samples with limited amount of DNA were fragmented to an average size of 10 kb using a Megaruptor 3 (Diagenode) to reach an optimal molar concentration for library preparation. Quality control was perform using a Femto Pulse System (Agilent Technologies) and a Qubit fluorometer (Invitrogen). Samples were prepared for Nanopore sequencing using the ligation sequencing kit SQK-LSK110. DNA was sequenced on a PromethION using R9.4.1 flowcells (Oxford Nanopore Technologies). Samples were run for 72 h including a washing and reload step after 24 h and 48 h.

All library preparation and sequencing were performed by the UCL Long Read Sequencing facility.

Passed reads from Minknow were mapped to the reference AAV2 genome (NC_001401) using minimap2 (ref. [49]) using the default parameters. Reads were trimmed of adapters using Porechop v0.2.4 (https://github.com/rrwick/Porechop/), with the sequences of the adapters used added to adapters.py, and using an adapter threshold of 85. Reads that also mapped by minimap to the human genome (Ensemble GRCh38_v107), which could be ligation artefacts, were excluded from further analysis. The passed reads were also classified using Kraken2 (ref. [50]) with the PlusPF database (17 May 2021). The data relating to AAV2 reads in Supplementary

Table 3 refer to reads that were classified as AAV2 by both minimap2 and Kraken2 (version 2.0.8-beta), as the results from both methods were similar. Four reads across all four lower-depth samples were classified as HHV-6B by the EPI2ME WIMP[51] pipeline. No reads were classified as HAdV or HHV-6B by Kraken2 in the two higher-depth samples. Alignment dot plots were created for the AAV2 reads using redotable (version 1.1)[52], with a window size of 20. These were manually classified into possible complex and monomeric structures.

Integration analysis of Illumina data

We investigated potential integrations of AAV2 and HHV-6 viruses into the genome using the Illumina metagenomics data for five liver transplant cases. We first processed the pair-end reads (average sequence coverage per genome = 5×), quality checking using FastQC[53], with barcode and adaptor sequence trimmed by TrimGalore (phred-score = 20). Potential viral integrations were investigated with Vseq-Toolkit[54] (mode 3 with default settings except for high stringency levels). Predicted genomic integrations were visualized with IGV[55], requiring at least three reads supporting an integration site, spanning both human and viral sequences. Predicted integrations were supported by only one read, thus not fulfilling the algorithm criteria. Sequencing was performed at a lower depth than optimal for integration analysis, but no evidence was found for AAV2 or HHV-6B integration into the genomes of cases.

PCR

Real-time PCR targeting a 62-nt region of the AAV2 inverted terminal repeat sequence was performed using primers and probes previously described[56]. This assay has been predicted to amplify AAV2 and AAV6. The Qiagen QuantiNova probe PCR kit (PERFORM and DIAMONDS controls) or the Qiagen Quantifast probe PCR kit (all other samples) were used. Each 25-µl reaction consisted of 0.1 µM forward primer, 0.34 µM reverse primer and 0.1 µM probe with 5 µl template DNA.

Real-time PCR targeting a 74-bp region of the HHV-6 DNA polymerase gene was performed using primers and probes previously described[57] multiplexed with an internal positive control targeting mouse (*mus*) DNA spiked into each sample during DNA purification, as previously described[58]. In brief, each 25-µl reaction consisted of 0.5 µM of each primer, 0.3 µM HHV-6 probe, 0.12 µM of each *mus* primer, 0.08 µM *mus* probe and 12.5 µl Qiagen Quantifast Fast mastermix with 10 µl template DNA.

Real-time PCR targeting a 132-bp region of the HAdV hexon gene was performed using primers and probes previously described[59] multiplexed with an internal positive control targeting mouse (*mus*) DNA spiked into each sample during DNA purification, as previously described[58]. In brief, each 25-µl reaction consisted of 0.6 µM of each HHV-6 primer, 0.4 µM HHV-6 probe, 0.12 µM of each *mus* primer, 0.08 µM *mus* probe and 12.5 µl Qiagen Quantifast Fast mastermix with 10 µl template DNA.

PCR cycling for all targets, apart from the controls from the PERFORM and DIAMONDS studies, was performed on an ABI 7500 Fast thermocycler and consisted of 95 °C for 5 min followed by 45 cycles of 95 °C for 30 s and 60 °C for 30 s. For the PERFORM and DIAMONDS controls, PCR was performed on a StepOnePlus Real-Time PCR System and consisted of 95 °C for 2 min followed by 45 cycles of 95 °C for 5 s and 60 °C for 10 s. Each PCR run included a no template control and a DNA-positive control for each target.

Neat DNA extracts of the FFPE material were inhibitory to PCR, so PCR results shown were performed following a 1 in 10 dilution.

AAV2 quantitative PCR with reverse transcription

RNA samples were treated with the Turbo-DNA free kit (Thermo) to remove residual genomic DNA. Complementary DNA (cDNA) was synthesized using the QuantiTect Reverse Transcription kit. In brief, 12 µl of RNA was mixed with 2 µl of genomic DNA Wipeout buffer and incubated at 42 °C for 2 min and transferred to ice. For reverse transcription, 6 µl mastermix was used and incubated at 42 °C for 20 min followed by 3 min at 95 °C.

Real-time PCR targeting a 120-nt region of the AAV2 cap open reading frame sequence was performed using primers AAV2_cap _Fw-ATCCTTCGACCACCTTCAGT, AAV2_cap _Rv-GATT CCAGCGTTTGCTGTT and the probe AAV2_cap _Pr FAM-ACACAGTAT/ZEN/TCC ACGG GACAGGT-IBFQ. This assay has been predicted to amplify AAV2 and AAV6. The Qiagen QuantiNova probe PCR kit was used. Each 25-µl reaction consisted of 0.1 µM forward primer, 0.1 µM reverse primer and 0.2 µM probe with 2.5 µl template cDNA.

PCR was performed on a StepOnePlus Real-Time PCR System and consisted of incubation at 95 °C for 2 min followed by 45 cycles of 95 °C for 5 s and 60 °C for 10 s. Each PCR run included a no template control, a DNA-positive control and a RNA control from each sample to verify efficient removal of genomic DNA.

Immunohistochemistry

All immunohistochemistry was done on FFPE tissue cut at a thickness of 3 µm.

Adenovirus

AdV immunohistochemistry was carried out using the Ventana Benchmark ULTRA, Optiview Detection Kit, PIER with protease 1 for 4 min and antibody incubation for 32 min (AdV clone 2/6 and 20/11, Roche, 760-4870, pre-diluted). The positive control was a known HAdV-positive gastrointestinal surgical case.

Preparation of AAV2-positive controls

The plasmid used for transfection was pAAV2/2 (addgene, plasmid #104963; https://www.addgene.org/104963/), which expresses the genes encoding Rep/Cap of AAV2. This was delivered by tail-vein hydrodynamic injection[60] into albino C57BL/6 mice (5 mg in 2 ml PBS). Negative controls received PBS alone. At 48 h, mice were terminally exsanguinated and perfused by PBS. Livers were collected into 10% neutral buffered formalin

(CellPath UK). This was performed under Home Office License PAD4E6357.

AAV2 immunohistochemistry was carried out with four commercially available antibodies:

- Leica Bond-III, Bond Polymer Refine Detection Kit with DAB Enhancer, HIER with Bond Epitope Retrieval Solution 1 (citrate based pH 6) for 30 min and antibody incubation for 30 min (anti-AAV VP1/VP2/VP3 clone B1, PROGEN, 690058S, 1:100).

- Leica Bond-III, Bond Polymer Refine Detection Kit with DAB Enhancer, HIER with Bond Epitope Retrieval Solution 1 (citrate based pH 6) for 40 min and antibody incubation for 30 min (anti-AAV VP1/VP2/VP3 rabbit polyclonal, OriGene, BP5024, 1:100).

- Leica Bond-III, Bond Polymer Refine Detection Kit with DAB Enhancer, HIER with Bond Epitope Retrieval Solution 1 (citrate based pH 6) for 40 min and antibody incubation for 30 min (anti-AAV VP1 clone A1, OriGene, BM5013, 1:100).

- Leica Bond-III, Bond Polymer Refine Detection Kit with DAB Enhancer, HIER with Bond Epitope Retrieval Solution 1 (citrate based pH 6) for 40 min and antibody incubation for 30 min (anti-AAV VP1/VP2 clone A69, OriGene, BM5014, 1:100).

  HHV-6 immunohistochemistry straining was carried out with:

- Leica Bond-III, Bond Polymer Refine Detection Kit with DAB Enhancer, PIER with Bond Enzyme 1 Kit for 10 min and antibody incubation for 30 min (mouse monoclonal antibody (C3108-103) to HHV-6, ABCAM, ab128404, 1:100).

Negative reagent control slides were stained using the same antigen retrieval conditions and staining protocol incubation times using only BondTM Primary Antibody Diluent #AR9352 for the antibody incubation.

Electron microscopy

Samples of liver were fixed in 2.5% glutaraldehyde in 0.1 M cacodylate buffer followed by secondary fixation in 1.0% osmium tetroxide. Tissues were dehydrated in graded ethanol, transferred to an intermediate reagent, propylene oxide and then infiltrated and embedded in Agar 100 epoxy resin. Polymerization was undertaken at 60 °C for 48 h. Ultrathin sections of 90 nm were cut using a Diatome diamond knife on a Leica UC7 ultramicrotome. Sections were transferred to copper grids and stained with alcoholic urynal acetate and Reynold's lead citrate. The samples were examined using a JEOL 1400 transmission electron microscope. Images were captured on an AMT XR80 digital camera.

WGS

Bait design

To produce the capture probes for hybridization, biotinylated RNA oligonucleotides (baits) used in the SureSelectXT protocols for HAdV and HHV-6 WGS were designed in-house using Agilent community design baits with part numbers 5191-6711 and 5191-6713, respectively. They were synthesized by Agilent Technologies (2021) (available through Agilent's Community Designs programme: SSXT CD Pan Adenovirus and SSXT CD Pan HHV-6 and used previously[61,62]).

Library preparation and sequencing

For WGS of HAdV and HHV-6B, DNA (bulked with male human genomic DNA (Promega) if required) was sheared using a Covaris E220 focused ultrasonication system (PIP 75, duty factor of 10, 1,000 cycles per burst). End-repair, non-templated addition of 3′ poly A, adapter ligation, hybridization, PCR (pre-capture cycles dependent on DNA input and post-capture cycles dependent on viral load) and all post-reaction clean-up steps were performed according to either the SureSelectXT Low Input Target Enrichment for Illumina Paired-End Multiplexed Sequencing protocol (version A0), the SureSelectXT Target Enrichment for Illumina Paired-End Multiplexed Sequencing protocol (version C3) or the SureSelectXTHS Target Enrichment using the Magnis NGS Prep System protocol (version A0) (Agilent Technologies). Quality control steps were performed on the

4200 TapeStation (Agilent Technologies). Samples were sequenced using the Illumina MiSeq platform. Base calling and sample demultiplexing were performed as standard for the MiSeq platform, generating paired FASTQ files for each sample. A negative control was included on each processing run. A targeted enrichment approach was used due to the predicted high variability of the HHV-6 and HAdV genomes.

For AAV2 WGS, an AAV2 primer scheme was designed using primalscheme[63] with 17 AAV2 sequences from NCBI and one AAV2 sequence provided by GOSH from metagenomic sequencing of a liver biopsy DNA extract as the reference material. These primers amplify 15 overlapping 400-bp amplicons. Primers were supplied by Merck. Two multiplex PCRs were prepared using Q5 Hot Start High-Fidelity 2X Master Mix, with a 65 °C, 3 min annealing/extension temperature. Pools 1 and 2 multiplex PCRs were run for 35 cycles. Of each PCR, 10 µl was combined and 20 µl nuclease-free water was added. Libraries were prepared either manually or on the Agilent Bravo NGS workstation option B, following a reduced-scale version of the Illumina DNA protocol as used in the CoronaHiT protocol[64]. Equal volumes of the final libraries were pooled, bead purified and sequenced on the Illumina MiSeq. A negative control was included on each processing run.

All library preparation and sequencing were performed by UCL Genomics.

AAV2 sequence analysis

The raw fastq reads were adapted, trimmed and low-quality reads were removed. The reads were mapped to the NC_001401 reference sequence and then the amplicon primers regions were trimmed using the location provided in a bed file. Consensus sequences were then called at a minimum of 10× coverage. The entire processing of raw reads to consensus was carried out using the nf-core/viralrecon pipeline (https://nf-co.re/viralrecon/2.4.1; https://doi.org/10.5281/zenodo.3901628). Basic quality metrics for the samples sequenced are in Supplementary Table 9. All samples that gave 10× genome coverage over 90% were then used for further phylogenetic analysis. Samples were aligned along with known reference strains from GenBank using MAFFT[65] (version v7.271), and the trees were built with

IQ-TREE[66] (multicore version 1.6.12) with 1,000 rapid bootstraps and approximate likelihood-ratio test support. The samples were then labelled based on type and provider on the trees (Fig. 3a).

For each AAV2 sample, we aligned the consensus nucleotide sequence to the AAV2 reference sequence. From these alignments, the exact coordinates of the sample capsid were determined. We then used the coordinates to extract the corresponding nucleotide sequence and translated it to find the amino acid sequence. Next, we compared each sample to the reference to identify amino acid changes. Amino acid sequences from AAV capsid sequences were retrieved from GenBank for AAV1 to AAV12. Amino acid sequences of capsid constructs designed to be more hepatotropic were retrieved from refs. [16,67]. These sequence sets were then aligned to the AAV2 reference sequence using MAFFT[65]. We then compared each construct to the AAV2 reference to identify amino acid changes present, while retaining the AAV2 coordinate set.

HAdV and HHV-6B sequence analysis

Raw data quality control was performed using trim-galore (v.0.6.7) on the raw FASTQ files.

For HHV-6B, short reads were mapped with BWA mem[68] (0.7.17-r1188) using the RefSeq reference NC_000898.

For HAdV, genotyping is performed using AYUKA[11] (version 22-111). This novel tool is used to confidently assign one or more HAdV genotypes to a sample of interest, assessing inter-genotype recombination if more than one genotype is detected. The results from this screening step guide which downstream analyses are performed and which reference genome (or genomes) is used. If mixed infection is suspected, reads are separated using bbsplit (https://sourceforge.net/projects/bbmap/), and each genotype is analysed independently as normal. If recombination is suspected, a more detailed analysis is performed using Recombination Detection Program (RDP) and the sample is excluded from phylogenetic analysis. After genotyping, the cleaned read data are mapped using BWA to the relevant reference sequence (or sequences), and SNPs and small insertions and

deletions are called using bcftool (version1.15.1, https://github.com/samtools/bcftools) and a consensus sequence is generated also with bcftools, masking with Ns positions that do not have enough read support (15× by default). Consensus sequences generated with the pipeline are then concatenated to previously sequenced samples and a multiple sequence alignment is performed using the G-INS-I algorithm in the MAFFT software (MAFFT G-INS-I v7.481). The multiple sequence alignment is then used for phylogenetic analysis with IQ-TREE (IQ-TREE 2 2.2.0), using modelfinder and performing 1,000 rapid bootstraps.

Proteomics data generation

Liver explant tissue from cases was homogenized in lysis buffer, 100 mM Tris (pH 8.5), 5% sodium dodecyl sulfate, 5 mM tris(2-carboxyethyl)phosphine and 20 mM chloroacetamide then heated at 95 °C for 10 min and sonicated in an ultrasonic bath for another 10 min. The lysed proteins were quantified with NanoDrop 2000 (Thermo Fisher Scientific). One-hundred micrograms was precipitated with the methanol/chloroform protocol and then protein pellets were reconstituted in 100 mM Tris (pH 8.5) and 4% sodium deoxycholate (SDC). The proteins were subjected to proteolysis with 1:50 trypsin overnight at 37 °C with constant shaking. Digestion was stopped by adding 1% trifluoroacetic acid to a final concentration of 0.5%. Precipitated SDC was removed by centrifugation at 10,000*g* for 5 min, and the supernatant containing digested peptides was desalted on an SOLAμ HRP (Thermo Fisher Scientific). Of the desalted peptide, 50 μg was then fractionated on Vanquish HPLC (Thermo Fisher Scientific) using a Acquity BEH C18 column (2.1 × 50 mm with 1.7-μm particles from Waters): buffer A was 10 mM ammonium formiate at pH 10, whereas buffer B was 80% acetonitrile and the flow was set to 500 μl per minute. We used a gradient of 8 min to collect 24 fractions that were then concatenated to obtain 12 fractions. These 12 fractions were dried and dissolved in 2% formic acid before liquid chromatography–tandem mass spectrometry analysis. An estimated total of 2,000 ng from each fraction was analysed using an Ultimate3000 high-performance liquid chromatography system coupled online to an Eclipse mass spectrometer (Thermo Fisher Scientific). Buffer A consisted of water acidified with 0.1% formic acid, whereas buffer B was 80% acetonitrile and 20% water with 0.1% formic

acid. The peptides were first trapped for 1 min at 30 µl per minute with 100% buffer A on a trap (0.3 mm × 5 mm with PepMap C18, 5 µm, 100 Å; Thermo Fisher Scientific); after trapping, the peptides were separated by a 50-cm analytical column (Acclaim PepMap, 3 µm; Thermo Fisher Scientific). The gradient was 9–35% buffer B for 103 min at 300 nl per minute. Buffer B was then raised to 55% in 2 min and increased to 99% for the cleaning step. Peptides were ionized using a spray voltage of 2.1 kV and a capillary heated at 280 °C. The mass spectrometer was set to acquire full-scan mass spectrometry spectra (350:1,400 mass:charge ratio) for a maximum injection time set to auto at a mass resolution of 120,000 and an automated gain control target value of 100%. For a second, the most intense precursor ions were selected for tandem mass spectrometry. Higher energy collisional dissocation (HCD) fragmentation was performed in the HCD cell, with the readout in the Orbitrap mass analyser at a resolution of 15,000 (isolation window of 3 Th) and an automated gain control target value of 200% with a maximum injection time set to auto and a normalized collision energy of 30%. All raw files were analysed by MaxQuant[69] v2.1 software using the integrated Andromeda search engine and searched against the Human UniProt Reference Proteome (February release with 79,057 protein sequences) together with UniProt-reported AAV proteins and specific fasta created using EMBOSS Sixpack translating patient's virus genome. MaxQuant was used with the standard parameters with only the addition of deamidation (N) as variable modification. Data analysis was then carried out with Perseus[70] v2.05: proteins reported in the file 'proteinGroups.txt' were filtered for reverse and potential contaminants. Figures were created using Origin pro version 2022b.

Transduction of AAV2 capsid mutants

A transgene sequence containing enhanced green fluorescent protein (eGFP) was packaged into rAAV2 particles to track their expression in transduced cells, compared with rAAV capsids derived from canonical AAV2, AAV9 and a synthetic liver-tropic AAV vector called LK03 (ref. [15]).

rAAV vector particles were delivered to Huh-7 hepatocytes at a multiplicity of infection of 100,000 vector genomes per cell before analysing eGFP expression by flow cytometry 72 h later.

Recombinant AAV capsid sequence

The VP1 sequence was generated by generating a consensus sequence from a multiple sequence alignment of sequenced AAV2 genomes derived from patient samples, using the Biopython[71] package AlignIO. The designed VP1 sequence was then synthesized as a 'gBlock' (Integrated DNA Technologies) and incorporated into an AAV2 RepCap plasmid (AAV2/2 was a gift from M. Fan, Addgene plasmid #104963) between the SwaI and XmaI restriction sites, using InFusion cloning reagent (product 638948, Clontech).

AAV vector production

rAAV particles were generated by transient transfection of HEK 293T cells as previously described[72]. In brief, 1.8×10^7 cells were plated in 15-cm dishes before transfecting the pAAV-CAG-eGFP transgene plasmid (a gift from E. Boyden, Addgene plasmid #37825), the relevant RepCap plasmid and the pAdDeltaF6 helper plasmid (a gift from J. M. Wilson, Addgene plasmid #112867), at a ratio of 10.5 µg, 10.5 µg and 30.5 µg, respectively, using PEIPro transfection reagent (PolyPlus) at a ratio of 1 µl per 1 µg DNA. Seventy-two hours post-transfection, cell pellets and supernatant were harvested and rAAV particles were purified using an Akta HPLC platform. rAAV particle genome copy numbers were calculated by quantitative PCR targeting the vector transgene region. The rAAV2 vector

used in this study was purchased as ready-to-use AAV2 particles from Addgene (Addgene viral prep #37825-AAV2).

Analysis of rAAV transduction

Huh-7 hepatocytes (a gift from J. Baruteau, UCL) were plated in DMEM medium supplemented with 10% FBS and 1% penicillin–streptomycin supplement. The cell line was validated by testing for glypican-3 and was not tested for mycoplasma contamination. Cells were plated at a density of 1.5×10^3 cells per square centimetre and transduced with 1×10^5 viral genomes per cell. Transductions were performed in the presence or absence of 400 $\mu g\ ml^{-1}$ heparin, which was supplemented directly to cell media. Seventy-two hours after transduction, cells were analysed by microscopy using an EVOS Cell Imaging System (Thermo Fisher Scientific) before quantifying eGFP expression by flow cytometry using a Cytoflex Flow Cytometer (Beckman). eGFP-positive cells were determined by gating the live-cell population and quantifying the level of eGFP signal versus untransduced controls.

Human short-read data analysis

Cytokine transcriptomics analysis

Cytokine inducible gene expression modules were derived from previously published bulk tissue genome-wide transcriptomes of the tuberculin skin test that have been shown to reflect canonical human in vivo cell-mediated immune pathways[73] using a validated bioinformatic approach[74]. Cytokine regulators of genes enriched in the tuberculin skin[73] test (ArrayExpress accession number E-MTAB-6816) were identified using Ingenuity Pathway Analysis (Qiagen). Average correlation of $\log_2$-transformed transcripts per million data for every gene pair in each of the target gene modules were compared with 100 iterations of randomly selected gene modules of the same size, to select cytokine-inducible modules that showed significantly greater co-correlation (adjusted $P < 0.05$), representing co-regulated transcriptional networks for each 59 cytokines. We then used the average $\log_2$-transformed transcripts per million expression of all the genes in each

of these co-regulated modules to quantify the biological activity of the associated upstream cytokine within bulk genome-wide transcriptional profiles from AAV2-associated hepatitis ($n = 4$) obtained in the present study, compared with published $\log_2$-transformed and normalized microarray data from normal adult liver ($n = 10$) and hepatitis B adult liver ($n = 17$) (Gene Expression Omnibus accession number GSE96851)[18]. To enable comparison across the datasets, we transformed average gene expression values for each cytokine-inducible module to standardized (Z scores) using mean and standard deviation of randomly selected gene sets of the same size within each individual dataset. Statistically significant differences in Z scores between groups were identified by Student's t-tests with multiple testing correction (adjusted $P < 0.05$).

Proteomics differential expression

To compare the proteomics data from the explanted livers of cases with data from healthy livers, we downloaded the raw files from two studies[19,20] from PRIDE. The raw files were searched together with our files using the same settings and databases.

We performed differential expression analyses at the protein level and peptide level using a hybrid approach including statistical inference on the abundance (quantitative approach), as well as the presence or absence (binary approach) of proteins or peptides. DEP R package version 1.18.0 was used for quantitative analysis[75]. Proteins or peptides were filtered for those detected in all replicates of at least one group (case or control). The data were background corrected and variance was normalized using variance-stabilizing transformation. Missing intensity values were not distributed randomly and were biased to specific samples (either cases or controls). Therefore, for imputing the missing data, we applied random draws from a manually defined left-shifted Gaussian distribution using the DEP impute function with parameters fun:“man”, shift:1.8 and scale:0.3. The test_diff function based on linear models and the empirical Bayes method was used for testing differential expressions between the case and control samples.

HLA typing methods

Typing was undertaken in the liver centre units. Next-generation sequencing (sequencing by synthesis (Illumina) using AllType kits (VHBio/OneLambda), a high-resolution HLA typing method, was used.

Statistical analysis

Fisher's exact test and two-sided Wilcoxon (Mann–Whitney) non-parametric rank sum test were used for differences between case and control groups. Where multiple groups were compared, Kruskal–Wallis tests followed by Wilcoxon pairwise tests using a Benjamini–Hochberg correction were performed. All analysis were performed in R version 4.2.0.

Reporting summary

Further information on research design is available in the Nature Portfolio Reporting Summary linked to this article.

Data availability

The consensus genomes from viral WGS data are deposited in GenBank. IDs can be found in Supplementary Table 7 (HAdV), Supplementary Table 9 (AAV2) and Supplementary Table 10 (HHV6). The MS proteomics data have been deposited in the ProteomeXchange Consortium via the PRIDE partner repository with the dataset identifier PXD035925.

Code availability

The code for metagenomics and PCR analysis can be found at https://github.com/sarah-buddle/unknown-hepatitis. The transcriptomics analysis code is available at https://github.com/innate2adaptive/Bulk-RNAseq-analysis/tree/main/Zscore_gene_expression_module_analysis. The proteomics differential expression analysis code can be found at https://github.com/MahdiMoradiMarjaneh/proteomics_and_transcriptomics_of_hepatitis.

References

1. ECDC–WHO. Joint ECDC–WHO Regional Office for Europe hepatitis of unknown origin in children surveillance bulletin. *ECDC* https://cdn.ecdc.europa.eu/novhep-surveillance/ (2022).

2. UKHSA. Investigation into acute hepatitis of unknown aetiology in children in England: technical briefing 3 (UKHSA, 2022).

3. UKHSA. Investigation into acute hepatitis of unknown aetiology in children in England: technical briefing 4 (UKHSA, 2022).

4. Marsh, K. et al. Investigation into cases of hepatitis of unknown aetiology among young children, Scotland, 1 January 2022 to 12 April 2022. *Euro Surveill.* **27**, 2200318 (2022).

5. Morfopoulou, S. & Plagnol, V. Bayesian mixture analysis for metagenomic community profiling. *Bioinformatics* **31**, 2930–2938 (2015).

6. Berns, K. I. Parvovirus replication. *Microbiol. Rev.* **54**, 316–329 (1990).

7. Sun, X. et al. Molecular analysis of vector genome structures after liver transduction by conventional and self-complementary adeno-associated viral serotype vectors in murine and nonhuman primate models. *Hum. Gene Ther.* **21**, 750–762 (2010).

8. Meier, A. F. et al. Herpes simplex virus co-infection facilitates rolling circle replication of the adeno-associated virus genome. *PLoS Pathog.* **17**, e1009638 (2021).

9. Xu, Y. et al. Detection of viral pathogens with multiplex nanopore MinION sequencing: be careful with cross-talk. *Front. Microbiol.* **9**, 2225 (2018).

10. Eccles, D., White, R., Pellefigues, C., Ronchese, F. & Lamiable, O. Investigation of chimeric reads using the MinION. *F1000Res.* **6**, 631

(2017).

11. Guerra-Assunção, J. A., Goldstein, R. & Breuer, J. AYUKA: a toolkit for fast viral genotyping using whole genome sequencing. Preprint at *bioRxiv* https://doi.org/10.1101/2022.09.07.506755 (2022).

12. Risso-Ballester, J., Cuevas, J. M. & Sanjuán, R. Genome-wide estimation of the spontaneous mutation rate of human adenovirus 5 by high-fidelity deep sequencing. *PLoS Pathog.* **12**, e1006013 (2016).

13. Liu, L. et al. Genetic diversity and molecular evolution of human adenovirus serotype 41 strains circulating in Beijing, China, during 2010–2019. *Infect. Genet. Evol.* **95**, 105056 (2021).

14. Cao, M., You, H. & Hermonat, P. L. The X gene of adeno-associated virus 2 (AAV2) is involved in viral DNA replication. *PLoS ONE* **9**, e104596 (2014).

15. Lisowski, L. et al. Selection and evaluation of clinically relevant AAV variants in a xenograft liver model. *Nature* **506**, 382–386 (2014).

16. Cabanes-Creus, M. et al. Novel human liver-tropic AAV variants define transferable domains that markedly enhance the human tropism of AAV7 and AAV8. *Mol. Ther. Methods Clin. Dev.* **24**, 88–101 (2022).

17. Cabanes-Creus, M. et al. Restoring the natural tropism of AAV2 vectors for human liver. *Sci. Transl. Med.* **12**, eaba3312 (2020).

18. Chen, Z. et al. Role of humoral immunity against hepatitis B virus core antigen in the pathogenesis of acute liver failure. *Proc. Natl Acad. Sci. USA* **115**, E11369–E11378 (2018).

19. Wang, D. et al. A deep proteome and transcriptome abundance atlas of 29 healthy human tissues. *Mol. Syst. Biol.* **15**, e8503 (2019).

20. Niu, L. et al. Dynamic human liver proteome atlas reveals functional insights into disease pathways. *Mol. Syst. Biol.* **18**, e10947 (2022).

21. Timpe, J. M., Verrill, K. C. & Trempe, J. P. Effects of adeno-associated virus on adenovirus replication and gene expression during coinfection. *J. Virol.* **80**, 7807–7815 (2006).

22. Yakobson, B., Koch, T. & Winocour, E. Replication of adeno-associated virus in synchronized cells without the addition of a helper virus. *J. Virol.* **61**, 972–981 (1987).

23. la Bella, T. et al. Adeno-associated virus in the liver: natural history and consequences in tumour development. *Gut* **69**, 737–747 (2020).

24. Chowdary, P. et al. Phase 1–2 trial of AAVS3 gene therapy in patients with hemophilia B. *N. Engl. J. Med.* **387**, 237–247 (2022).

25. Chand, D. et al. Hepatotoxicity following administration of onasemnogene abeparvovec (AVXS-101) for the treatment of spinal muscular atrophy. *J. Hepatol.* **74**, 560–566 (2021).

26. Mullard, A. Gene therapy community grapples with toxicity issues, as pipeline matures. *Nat. Rev. Drug Discov.* **20**, 804–805 (2021).

27. Morales, L., Gambhir, Y., Bennett, J. & Stedman, H. H. Broader implications of progressive liver dysfunction and lethal sepsis in two boys following systemic high-dose AAV. *Mol. Ther.* **28**, 1753–1755 (2020).

28. Hüser, D. et al. Integration preferences of wildtype AAV-2 for consensus rep-binding sites at numerous loci in the human genome. *PLoS Pathog.* **6**, e1000985 (2010).

29. Nault, J. C. et al. Recurrent AAV2-related insertional mutagenesis in human hepatocellular carcinomas. *Nat. Genet.* **47**, 1187–1193 (2015).

30. Dalwadi, D. A. et al. AAV integration in human hepatocytes. *Mol. Ther.* **29**, 2898–2909 (2021).

31. Butterfield, J. S. S. et al. IL-15 blockade and rapamycin rescue multifactorial loss of factor VIII from AAV-transduced hepatocytes in

hemophilia A mice. *Mol. Ther.* **30**, 3552–3569 (2022).

32. Nathwani, A. C. Gene therapy for hemophilia. *Hematology Am. Soc. Hematol. Educ. Program* **2019**, 1–8 (2019).

33. Ho, A. et al. Adeno-associated virus 2 infection in children with non-A–E hepatitis. *Nature* https://doi.org/10.1038/s41586-023-05948-2 (2023).

34. Perrin, G. Q., Herzog, R. W. & Markusic, D. M. Update on clinical gene therapy for hemophilia. *Blood* **133**, 407–414 (2019).

35. Divers, T. J., Tomlinson, J. E. & Tennant, B. C. The history of Theiler's disease and the search for its aetiology. *Vet J.* **287**, 105878 (2022).

36. Kelgeri, C. et al. Clinical spectrum of children with acute hepatitis of unknown cause. *N. Engl. J. Med.* **387**, 611–619 (2022).

37. Sanchez, L. H. G. et al. A case series of children with acute hepatitis and human adenovirus infection. *N. Engl. J. Med.* **387**, 620–630 (2022).

38. Yang, W. X. et al. Prevalence of serum neutralizing antibodies to adenovirus type 5 (Ad5) and 41 (Ad41) in children is associated with age and sanitary conditions. *Vaccine* **34**, 5579–5586 (2016).

39. UKHSA. National norovirus and rotavirus bulletin. Week 28 report: data to week 26 (UKHSA, 2022).

40. Calcedo, R. et al. Adeno-associated virus antibody profiles in newborns, children, and adolescents. *Clin. Vaccine Immunol.* **18**, 1586–1588 (2011).

41. Nathwani, A. C. et al. Sustained high-level expression of human factor IX (hFIX) after liver-targeted delivery of recombinant adeno-associated virus encoding the hFIX gene in rhesus macaques. *Blood* **100**, 1662–1669 (2002).

42. Babraham Bioinformatics—Trim Galore! *Bioinformatiocs* https://www.bioinformatics.babraham.ac.uk/projects/trim_galore// (2019).

43. Langmead, B. & Salzberg, S. L. Fast gapped-read alignment with Bowtie 2. *Nat. Methods* **9**, 357–359 (2012).

44. Schmieder, R., Edwards, R. & Bateman, A. Quality control and preprocessing of metagenomic datasets. *Bioinformatics* **27**, 863–864 (2011).

45. Morgulis, A. et al. Database indexing for production MegaBLAST searches. *Bioinformatics* **24**, 1757–1764 (2008).

46. Buchfink, B., Xie, C. & Huson, D. H. Fast and sensitive protein alignment using diamond. *Nat. Methods* **12**, 59–60 (2015).

47. Li, H. et al. The Sequence Alignment/Map format and SAMtools. *Bioinformatics* **25**, 2078–2079 (2009).

48. Nurk, S., Meleshko, D., Korobeynikov, A. & Pevzner, P. A. metaSPAdes: a new versatile metagenomic assembler. *Genome Res.* **27**, 824–834 (2017).

49. Li, H. Minimap2: pairwise alignment for nucleotide sequences. *Bioinformatics* **34**, 3094–3100 (2018).

50. Wood, D. E., Lu, J. & Langmead, B. Improved metagenomic analysis with Kraken 2. *Genome Biol.* **20**, 257 (2019).

51. EPI2ME WIMP workflow: quantitative, real-time species identification from metagenomic samples. *Oxford Nanopore Technologies* https://nanoporetech.com/resource-centre/epi2me-wimp-workflow-quantitative-real-time-species-identification-metagenomic (accessed 2022).

52. Babraham Bioinformatics. re-DOT-able DotPlot tool. *Babraham Bioinformatics*

https://www.bioinformatics.babraham.ac.uk/projects/redotable/ (accessed 2022).

53. Babraham Bioinformatics. FastQC: a quality control tool for high throughput sequence data. *Babraham Bioinformatics* https://www.bioinformatics.babraham.ac.uk/projects/fastqc/ (accessed 2022).

54. Afzal, S., Fronza, R. & Schmidt, M. VSeq-Toolkit: comprehensive computational analysis of viral vectors in gene therapy. *Mol. Ther. Methods Clin. Dev.* **17**, 752–757 (2020).

55. Robinson, J. T. et al. Integrative genomics viewer. *Nat. Biotechnol.* **29**, 24–26 (2011).

56. Aurnhammer, C. et al. Universal real-time PCR for the detection and quantification of adeno-associated virus serotype 2-derived inverted terminal repeat sequences. *Hum. Gene Ther. Methods* **23**, 18–28 (2011).

57. Watzinger, F. et al. Real-time quantitative PCR assays for detection and monitoring of pathogenic human viruses in immunosuppressed pediatric patients. *J. Clin. Microbiol.* **42**, 5189–5198 (2004).

58. Tann, C. J. et al. Prevalence of bloodstream pathogens is higher in neonatal encephalopathy cases vs. controls using a novel panel of real-time PCR assays. *PLoS ONE* **9**, e97259 (2014).

59. Brown, J. R., Shah, D. & Breuer, J. Viral gastrointestinal infections and norovirus genotypes in a paediatric UK hospital, 2014–2015. *J. Clin. Virol.* **84**, 1–6 (2016).

60. Karda, R. et al. Production of lentiviral vectors using novel, enzymatically produced, linear DNA. *Gene Ther.* **26**, 86–92 (2019).

61. Myers, C. E. et al. Using whole genome sequences to investigate adenovirus outbreaks in a hematopoietic stem cell transplant unit. *Front. Microbiol.* **12**, 667790 (2021).

62. Gaccioli, F. et al. Fetal inheritance of chromosomally integrated human herpesvirus 6 predisposes the mother to pre-eclampsia. *Nat. Microbiol.* **5**, 901–908 (2020).

63. Quick, J. et al. Multiplex PCR method for MinION and Illumina sequencing of Zika and other virus genomes directly from clinical samples. *Nat. Protoc.* **12**, 1261–1267 (2017).

64. Baker, D. J. et al. CoronaHiT: high-throughput sequencing of SARS-CoV-2 genomes. *Genome Med.* **13**, 21 (2021).

65. Nakamura, T., Yamada, K. D., Tomii, K. & Katoh, K. Parallelization of MAFFT for large-scale multiple sequence alignments. *Bioinformatics* **34**, 2490–2492 (2018).

66. Minh, B. Q. et al. IQ-TREE 2: new models and efficient methods for phylogenetic inference in the genomic era. *Mol. Biol. Evol.* **37**, 1530–1534 (2020).

67. Hsu, H. L. et al. Structural characterization of a novel human adeno-associated virus capsid with neurotropic properties. *Nat. Commun.* **11**, 3279 (2020).

68. Li, H. & Durbin, R. Fast and accurate short read alignment with Burrows–Wheeler transform. *Bioinformatics* **25**, 1754–1760 (2009).

69. Cox, J. & Mann, M. MaxQuant enables high peptide identification rates, individualized p.p.b.-range mass accuracies and proteome-wide protein quantification. *Nat. Biotechnol.* **26**, 1367–1372 (2008).

70. Tyanova, S. et al. The Perseus computational platform for comprehensive analysis of (prote)omics data. *Nat. Methods* **13**, 731–740 (2016).

71. Cock, P. J. A. et al. Biopython: freely available Python tools for computational molecular biology and bioinformatics. *Bioinformatics* **25**, 1422–1423 (2009).

72. Ng, J. et al. Gene therapy restores dopamine transporter expression and ameliorates pathology in iPSC and mouse models of infantile parkinsonism. *Sci. Transl. Med.* **13**, eaaw1564 (2021).

73. Pollara, G. et al. Exaggerated IL-17A activity in human in vivo recall responses discriminates active tuberculosis from latent infection and cured disease. *Sci. Transl. Med.* **13**, eabg7673 (2021).

74. Chandran, A. et al. Rapid synchronous type 1 IFN and virus-specific T cell responses characterize first wave non-severe SARS-CoV-2 infections. *Cell Rep. Med.* **3**, 100557 (2022).

75. Zhang, X. et al. Proteome-wide identification of ubiquitin interactions using UbIA-MS. *Nat. Protoc.* **13**, 530–550 (2018).

Acknowledgements

UKHSA funded the metagenomics and HAdV sequencing. We thank A. Nathwani for helpful discussions. We acknowledge the considerable contribution from the GOSH microbiology laboratory. We thank the medical students who contributed to the DIAMOND consortium. All research at GOSH and UCL GOSH Institute of Child Health is made possible by the NIHR GOSH Biomedical Research Centre. The views expressed are those of the authors and not necessarily those of the NHS, the National Institute for Health Research (NIHR), the UKRI or the Department of Health and Social Care. The work was part funded by the NIHR Blood and Transplant Research Unit in Genomics to Enhance Microbiology Screening (GEMS), the National Institute for Health and Care Research (CO-CIN-01) or jointly by NIHR and UK Research and Innovation (CV220-169, MC_PC_19059). S. Morfopoulou is funded by a W.T. Henry Wellcome fellowship (206478/Z/17/Z). S.B. and O.E.T.M. are funded by the NIHR Blood and Transplant Research Unit (GEMS). M.M.M. and M.L. are supported in part by the NIHR Biomedical Research Centre of Imperial College NHS Trust. J.B. receives NIHR Senior Investigator Funding. M.N. and J.B. are supported by the Wellcome Trust (207511/Z/17/Z and 203268/Z/16/Z). M.N., J.B. and G.P. are supported by the NIHR University College London Hospitals Biomedical Research Centre. P. Simmonds is

supported by the NIHR (NIHR203338). T.S.J. is grateful for funding from the Brain Tumour Charity, Children with Cancer UK, GOSH Children's Charity, Olivia Hodson Cancer Fund, Cancer Research UK and the NIHR. DIAMONDS is funded by the European Union (Horizon 2020; grant 848196). PERFORM was funded by the European Union (Horizon 2020; grant 668303).

Author information

Author notes

1. These authors contributed equally: Sofia Morfopoulou, Sarah Buddle

Authors and Affiliations

1. Infection, Immunity and Inflammation Department, Great Ormond Street Institute of Child Health, University College London, London, UK

   Sofia Morfopoulou, Sarah Buddle, Oscar Enrique Torres Montaguth, José Afonso Guerra-Assunção, Sunando Roy, Cristina Venturini & Judith Breuer

2. Section for Paediatrics, Department of Infectious Diseases, Faculty of Medicine, Imperial College London, London, UK

   Sofia Morfopoulou, Mahdi Moradi Marjaneh, Andrew McArdle, Priyen Shah, Samantha Cooray, Evangelos Bellos, Claire Broderick, Samuel Channon-Wells, Tisham De, Giselle D'Souza, Leire Estramiana Elorrieta, Diego Estrada-Rivadeneyra, Rachel Galassini, Dominic Habgood-Coote, Shea Hamilton, Heather Jackson, James Kavanagh, Mahdi Moradi Marjaneh, Stephanie Menikou, Samuel Nichols, Ruud Nijman, Harsita Patel, Ivana Pennisi, Oliver Powell, Ruth Reid, Ortensia Vito, Elizabeth Whittaker, Clare Wilson, Rebecca Womersley, Ching-Fen Shen, Aubrey Cunnington, Jethro Herberg, Mysini Kaforou, Victoria

Wright, Lucas Baumard, Clive Hoggart, Sara Hourmat, Ian Maconochie, Naomi Lin, Ivonne Pena Paz & Michael Levin

3. Department of Microbiology, Virology and Infection Control, Great Ormond Street Hospital for Children NHS Foundation Trust, London, UK

   Laura Atkinson, Nathaniel Storey, Alexander Lennon, Jack C. D. Lee, James Hatcher, Surjo De, Julianne R. Brown & Judith Breuer

4. Section of Virology, Department of Infectious Diseases, Faculty of Medicine, Imperial College London, London, UK

   Mahdi Moradi Marjaneh

5. University College London Mass Spectrometry Science Technology Platform, Division of Biosciences, University College London, London, UK

   Riccardo Zennezini Chiozzi & Konstantinos Thalassinos

6. Histopathology Department, Great Ormond Street Hospital for Children NHS Foundation Trust, London, UK

   Luis Campos, J. Ciaran Hutchinson, Catarina Andrade, Glenn Anderson & Thomas S. Jacques

7. Research Department of Targeted Intervention, Division of Surgery and Interventional Science, University College London, London, UK

   John R. Counsell, Juan F. Antinao Diaz, Ala'a Siam, Luke J. Tappouni, Zeinab Asgarian & Killian S. Hanlon

8. Division of Infection and Immunity, University College London, London, UK

   Gabriele Pollara, Agata Czap, Joshua Rosenheim, Tommy Rampling, Catherine Houlihan & Mahdad Noursadeghi

9. Gene Transfer Technology Group, EGA-Institute for Women's Health, University College London, London, UK

Ala'a Siam, Joanne Ng & Simon N. Waddington

10. Genetics and Genomic Medicine Department, Great Ormond Street Institute of Child Health, University College London, London, UK

Rachel Williams, Charlotte A. Williams, Helena Tutill, Nadua Bayzid, Luz Marina Martin Bernal, Kylie-Ann Montgomery, Paul Gissen, Dimah K. Alrabiah & Sergi Castellano

11. Department of Neurodegenerative Disease, Queen Square Institute of Neurology, University College London, London, UK

Hannah Macpherson & Kylie-Ann Montgomery

12. Wales Specialist Virology Centre, Public Health Wales Microbiology Cardiff, University Hospital of Wales, Cardiff, UK

Catherine Moore

13. Department of Medical Microbiology, Edinburgh Royal Infirmary, Edinburgh, UK

Kate Templeton

14. Public Health Agency Northern Ireland, Belfast, UK

Claire Neill

15. School of Medicine, University of St. Andrews, St. Andrews, UK

Matt Holden

16. Public Health Scotland, Edinburgh, UK

Matt Holden & Sarah Tait

17. West of Scotland Specialist Virology Centre, Glasgow, UK

Rory Gunson & Samantha J. Shepherd

18. Micropathology Ltd, University of Warwick Science Park, Coventry, UK

Marie Voice, Michael Steele, Colin Fink, Jennifer Holden, Leo Calvo-Bado, Benjamin Evans, Jake Stevens, Peter Matthews & Kyle Billing

19. Molecular and Cellular Immunology, Great Ormond Street Institute of Child Health, University College London, London, UK

Thomas E. Whittaker & Giorgia Santilli

20. Institute of Virology, Freie Universität Berlin, Berlin, Germany

Benedikt B. Kaufer & Jana Reich

21. Nuffield Department of Medicine, University of Oxford, Oxford, UK

Julien Andreani & Peter Simmonds

22. Centre Hospitalier Universitaire (CHU) Grenoble–Alpes, Grenoble, France

Julien Andreani

23. National Centre for Biotechnology, King Abdulaziz City for Science and Technology, Riyadh, Saudi Arabia

Dimah K. Alrabiah

24. University College London Genomics, University College London, London, UK

Sergi Castellano

25. Roslin Institute, University of Edinburgh, Edinburgh, UK

Primrose Chikowore, Miranda Odam & Kenneth Baillie

26. UK Health Security Agency, London, UK

Tommy Rampling, Catherine Houlihan, Katja Hoschler, Tiina Talts, Cristina Celma, Suam Gonzalez, Eileen Gallagher, Ruth Simmons, Conall Watson, Sema Mandal, Maria Zambon, Meera Chand, Wilna Oosthuyzen, Lauren Obosi, Sara Clohisey & Andrew Law

27. Hospital for Tropical Diseases, University College London Hospitals NHS Foundation Trust, London, UK

Tommy Rampling

28. Department of Clinical Virology, University College London Hospitals, London, UK

Catherine Houlihan

29. Pandemic Institute, University of Liverpool, Liverpool, UK

Malcolm Gracie Semple

30. Respiratory Medicine, Alder Hey Children's Hospital NHS Foundation Trust, Liverpool, UK

Malcolm Gracie Semple

31. Centre for Genomics and Child Health, The Blizard Institute, Queen Mary University of London, London, UK

Joanne Martin

32. NHS Blood and Transplant, Bristol, UK

Ines Ushiro-Lumb

33. King's College Hospital, London, UK

Akash Deep, Ivan Caro, Natassia Powell, Maesha Deheragoda, Nedim Hadzic & Tassos Grammatikopoulos

34. Department of Cellular Pathology, University Hospitals Birmingham NHS Foundation Trust, Birmingham, UK

Rachel Brown

35. Liver Unit, Birmingham Women's and Children's NHS Foundation Trust, Birmingham, UK

Chayarani Kelgeri

36. Institute of Structural and Molecular Biology, Division of Biosciences, University College London, London, UK

Konstantinos Thalassinos

37. Institute of Structural and Molecular Biology, Birkbeck College, University of London, London, UK

Konstantinos Thalassinos

38. Medical Research Council Antiviral Gene Therapy Research Unit, Faculty of Health Sciences, University of the Witswatersrand, Johannesburg, South Africa

Simon N. Waddington

39. Developmental Biology and Cancer Department, Great Ormond Street Institute of Child Health, University College London, London, UK

Sarah E. McDonald & Thomas S. Jacques

40. Medical Research Council–University of Glasgow Centre for Virus Research, Glasgow, UK

Massimo Palmarini, Antonia Y. W. Ho & Emma Thomson

41. Children’s Clinical Research Unit, St. Mary’s Hospital, London, UK

Amina Abdulla, Sarah Darnell, Sobia Mustafa, Ladan Ali, Rikke Jorgensen & Salina Persand

42. Department of Electrical and Electronic Engineering, Imperial College London, London, UK

Pantelis Georgiou, Nicolas Moser, Molly Stevens, Eunjung Kim & Benjamin Pierce

43. Section of Adult Infectious Disease, Department of Infectious Disease, Imperial College London, London, UK

Jesus-Rodriguez Manzano

44. Evelina London Children’s Hospital, Guy’s and St. Thomas’ NHS Foundation Trust, London, UK

Michael Carter, Shane Tibby, Jonathan Cohen, Francesca Davis, Julia Kenny, Paul Wellman & Marie White

45. Department of Women and Children’s Health, School of Life Course Sciences, King’s College London, London, UK

Michael Carter & Shane Tibby

46. Department of Infectious Diseases, School of Immunology and Microbial Sciences, King’s College London, London, UK

Matthew Fish & Shankar-Hari

47. Department of Intensive Care Medicine, Guy’s and St. Thomas’ NHS Foundation Trust, London, UK

Aislinn Jennings & Shankar-Hari

48. Royal Alexandra Children’s Hospital, University Hospitals Sussex, Brighton, UK

Katy Fidler, Vivien Richmond, Julia Dudley & Emma Tavliavini

49. Department of Infectious Diseases, University Hospitals Sussex, Brighton, UK

Dan Agranoff & Matthew Seal

50. Research Nurse Team, University Hospitals Sussex, Brighton, UK

Vivien Richmond & Emma Tavliavini

51. National Institute for Health Research Southampton Clinical Research Facility, University Hospital Southampton NHS Foundation Trust, Southampton, UK

Saul Faust, Dan Owen, Ruth Ensom & Sarah McKay

52. University of Southampton, Southampton, UK

Saul Faust & Dan Owen

53. Department of Research and Development, University Hospital Southampton NHS Foundation Trust, Southampton, UK

Diana Mondo, Mariya Shaji & Rachel Schranz

54. Royal London Hospital, London, UK

Prita Rughnani, Amutha Anpananthar, Anna Riddell & Nosheen Khalid

55. Newham University Hospital, London, UK

Prita Rughnani, Amutha Anpananthar & Susan Liebeschuetz

56. Whipps Cross University Hospital, London, UK

Prita Rughnani, Amutha Anpananthar, Nosheen Khalid & Teresa Simagan

57. Barts Health NHS Trust, London, UK

Ivone Lancoma Malcolm

58. Great Ormond Street Hospital NHS Foundation Trust, London, UK

Mark Peters & Alasdair Bamford

59. Great Ormond Street Institute of Child Health, University College London, London, UK

Alasdair Bamford

60. Addenbrooke's Hospital, Cambridge, UK

Nazima Pathan, Esther Daubney & Deborah White

61. Department of Paediatrics, University of Cambridge, Cambridge, UK

Nazima Pathan

62. University College London Hospital, London, UK

Melissa Heightman, Sarah Eisen, Terry Segal & Lucy Wellings

63. St George's Hospital, London, UK

Simon B. Drysdale, Nicole Branch, Lisa Hamzah & Heather Jarman

64. University Hospital Lewisham, London, UK

Maggie Nyirenda, Lisa Capozzi & Emma Gardiner

65. Queen Elizabeth Hospital Greenwich, London, UK

Maggie Nyirenda

66. Aintree University Hospital, Liverpool, UK

Robert Moots & Michelle Linforth

67. Royal Liverpool Hospital, Liverpool, UK

Magda Nasher & Anita Hanson

68. Leeds Children's Hospital, Leeds, UK

Sean O'Riordan & Donna Ellis

69. Sheffield Children's Hospital, Sheffield, UK

Fiona Shackley, Arianna Bellini & Stuart Gormley

70. Leicester General Hospital, Leicester, UK

Samira Neshat

71. Birmingham Women's and Children's NHS Foundation Trust, Birmingham, UK

Barnaby J. Scholefield, Ceri Robbins, Helen Winmill, Stuart Hartshorn, Tara Roome, Ruth Howman & Sara Burling

72. John Radcliffe Hospital, Oxford University Hospitals NHS Foundation Trust, Oxford, UK

Stéphane C. Paulus, Andrew J. Pollard, Sarah Hopton, Danielle Miller, Zoe Oliver, Sally Beer & Bryony Ward

73. Department of Paediatrics, University of Oxford, Oxford, UK

Stéphane C. Paulus & Andrew J. Pollard

74. Oxford Vaccine Group, Department of Paediatrics, University of Oxford, Oxford, UK

Stéphane C. Paulus, Andrew J. Pollard, Tim Lubinda, Sarah Kelly, Peter O'Reilly, Rama Kandasamy, Stéphane Paulus, Michael J. Carter, Daniel O'Connor, Sagida Bibi & Dominic F. Kelly

75. National Institute for Health Research Oxford Biomedical Research Centre, Oxford, UK

Stéphane C. Paulus, Andrew J. Pollard, Rama Kandasamy, Stéphane Paulus, Michael J. Carter, Daniel O'Connor, Sagida Bibi & Dominic F. Kelly

76. Paediatric Research Unit, Patan Academy of Health Sciences, Kathmandu, Nepal

Shrijana Shrestha, Meeru Gurung, Puja Amatya, Bhishma Pokhrel, Sanjeev Man Bijukchhe, Stephen Thorson & Imran Ansari

77. Translational Paediatrics and Infectious Diseases, Paediatrics Department, Hospital Clínico Universitario de Santiago, Santiago de Compostela, Spain

Federico Martinón-Torres, Antonio Salas, Fernando Álvez González, Xabier Bello, Mirian Ben García, Sandra Carnota, Miriam Cebey-López, María José Curras-Tuala, Carlos Durán Suárez, Luisa García Vicente, Alberto Gómez-Carballa, Jose Gómez Rial, Pilar Leboráns Iglesias, Nazareth Martinón-Torres, José María Martinón Sánchez, Belén Mosquera Pérez, Jacobo Pardo-Seco, Lidia Piñeiro Rodríguez, Sara Pischedda, Sara Rey Vázquez, Irene Rivero Calle, Carmen Rodríguez-Tenreiro, Lorenzo Redondo-Collazo, Miguel Sadiki Ora, Sonia Serén Fernández, Cristina Serén Trasorras, Marisol Vilas Iglesias, Cristina Balo Farto, Ruth Barral-Arca & Maria Barreiro Castro

78. GENVIP Research Group, Instituto de Investigación Sanitaria de Santiago, Universidad de Santiago de Compostela, Galicia, Spain

Federico Martinón-Torres, Antonio Salas, Fernando Álvez González, Xabier Bello, Mirian Ben García, Sandra Carnota, Miriam Cebey-López, María José Curras-Tuala, Carlos Durán Suárez, Luisa García Vicente, Alberto Gómez-Carballa, Jose Gómez Rial, Pilar Leboráns Iglesias, Nazareth Martinón-Torres, José María Martinón Sánchez, Belén Mosquera Pérez, Jacobo Pardo-Seco, Lidia Piñeiro

Rodríguez, Sara Pischedda, Sara Rey Vázquez, Irene Rivero Calle, Carmen Rodríguez-Tenreiro, Lorenzo Redondo-Collazo, Miguel Sadiki Ora, Sonia Serén Fernández, Cristina Serén Trasorras, Marisol Vilas Iglesias, Cristina Balo Farto, Ruth Barral-Arca & Maria Barreiro Castro

79. Unidade de Xenética, Departamento de Anatomía Patolóxica e Ciencias Forenses, Instituto de Ciencias Forenses, Facultade de Medicina, Universidade de Santiago de Compostela, Galicia, Spain

Antonio Salas, Fernando Álvez González, Xabier Bello, María José Curras-Tuala, Alberto Gómez-Carballa, Jacobo Pardo-Seco, Sara Pischedda & Ruth Barral-Arca

80. GenPop Research Group, Instituto de Investigaciones Sanitarias (IDIS), Hospital Clínico Universitario de Santiago, Galicia, Spain

Antonio Salas, Fernando Álvez González, Xabier Bello, María José Curras-Tuala, Alberto Gómez-Carballa, Jacobo Pardo-Seco, Sara Pischedda & Ruth Barral-Arca

81. Department of Clinical Infection, Microbiology and Immunology, University of Liverpool, Institute of Infection, Veterinary and Ecological Sciences, Liverpool, UK

Enitan D. Carrol, Elizabeth Cocklin, Aakash Khanijau, Rebecca Lenihan, Nadia Lewis-Burke, Sam Romaine, Stéphane Paulus & Simon Leigh

82. Department of Infectious Diseases, Alder Hey Children’s Hospital, Liverpool, UK

Enitan D. Carrol

83. Liverpool Health Partners, Liverpool Science Park, Liverpool, UK

Enitan D. Carrol

84. Clinical Research Business Unit, Alder Hey Children's Hospital, Liverpool, UK

Karen Newal, Rebecca Jennings, Joanne Johnston & Karen Newall

85. Department of Paediatrics, National and Kapodistrian University of Athens (NKUA), P, and A. Kyriakou Children's Hospital, Athens, Greece

Maria Tsolia, Irini Eleftheriou, Nikos Spyridis, Maria Tambouratzi, Despoina Maritsi, Antonios Marmarinos, Marietta Xagorari, Antonis Marmarinos & Kelly Syggelou

86. Department of Infectious Diseases, Sotiria General Hospital, Athens, Greece

Lourida Panagiota & Pefanis Aggelos

87. Pathology Department, University of Patras, Panagia i Voithia General Hospital, Patras, Greece

Akinosoglou Karolina, Gogos Charalambos & Maragos Markos

88. Pathophysiology Department, Medical Faculty, National and Kapodistrian University of Athens (NKUA), Laiko General Hospital, Athens, Greece

Voulgarelis Michalis & Stergiou Ioanna

89. Translational and Clinical Research Institute, Newcastle University, Newcastle upon Tyne, UK

Marieke Emonts, John Isaacs, Fabian J. S. van der Velden, Owen Treloar & Daisy Thomas

90. Paediatric Immunology, Infectious Diseases and Allergy, Great North Children's Hospital, Newcastle upon Tyne Hospitals NHS Foundation Trust, Newcastle upon Tyne, UK

Marieke Emonts, Emma Lim, Fabian J. S. van der Velden, Owen Treloar, Daisy Thomas, Anne McDonnell, Ailsa Pickering, Bryan Baas, Lieke Kloosterhuis, Wilma Oosthoek, Joshua Bennet, Kalvin Collings, Ilona van der Giessen, Alex Martin, Emily Rowlands, Gabriella de Vries, Fabian van der Velden & Ravi Mistry

91. National Institute for Health Research Newcastle Biomedical Research Centre, Newcastle upon Tyne Hospitals NHS Foundation Trust and Newcastle University, Newcastle upon Tyne, UK

Marieke Emonts & Emma Lim

92. Population Health Sciences Institute, Newcastle University, Newcastle upon Tyne, UK

Emma Lim

93. Research Unit, Great North Children's Hospital, Newcastle upon Tyne Hospitals NHS Foundation Trust, Newcastle upon Tyne, UK

Kathryn Bell, Stephen Crulley, Daniel Fabian, Evelyn Thomson, Caroline Miller, Ashley Bell, Karen Allen, Adora Chan, Kirsty Devine, Sharon King, Paul McAlinden, Sam McDonald, Anne McDonnell, Ailsa Pickering, Amanda Wood, Diane Wallia, Phil Woodsford, Frances Baxter & Mathew Rhodes

94. Paediatric Oncology, Great North Children's Hospital, Newcastle upon Tyne Hospitals NHS Foundation Trust, Newcastle upon Tyne, UK

Geoff Shenton, Tasnim Arif & Aqeela Rashid

95. Department of Infection and Tropical Medicine, Newcastle upon Tyne Hospitals NHS Foundation Trust, Newcastle upon Tyne, UK

Ashley Price

96. National Institute for Health Research Newcastle In Vitro Diagnostics Co-operative (Newcastle MIC), Newcastle upon Tyne, UK

Ashley Price

97. Servicio Madrileño de Salud (SERMAS), Paediatric Infectious Diseases Unit, Department of Paediatrics, Hospital Universitario 12 de Octubre, Madrid, Spain

Pablo Rojo, Cristina Epalza, Serena Villaverde & Ángela Manzanares

98. Faculty of Medicine, Department of Paediatrics, Universidad Complutense de Madrid, Madrid, Spain

Pablo Rojo

99. Fundación Biomédica del Hospital Universitario 12 de Octubre (FIB-H12O), Unidad Pediátrica de Investigación y Ensayos Clínicos (UPIC), Hospital Universitario 12 de Octubre, Instituto de Investigación Sanitaria Hospital 12 de Octubre (i+12), Madrid, Spain

Cristina Epalza, Sonia Márquez, Manuel Gijón, Fátima Machín, Laura Cabello, Irene Hernández & Lourdes Gutiérrez

100. Department of Paediatric Immunology, Rheumatology and Infectious Disease, Amsterdam University Medical Centre, University of Amsterdam, Amsterdam, The Netherlands

Taco Kuijpers, Martijn van de Kuip, Marceline van Furth, Merlijn van den Berg, Giske Biesbroek, Floris Verkuil, Carlijn van der Zee, Dasja Pajkrt, Michael Boele van Hensbroek, Dieneke Schonenberg, Mariken Gruppen, Sietse Nagelkerke, Machiel H. Jansen, Taco Kuijpers, J. M. van den Berg, D. Schonenberg, A. M. Barendregt, D. Pajkrt, M. van der Kuip & A. M. van Furth

101. Sanquin Research Institute, Department of Molecular Hematology, University Medical Centre, Amsterdam, The Netherlands

Taco Kuijpers, Sietse Nagelkerke & Ines Goetschalckx

102. Infectious Disease Unit, Academic Department of Paediatrics, Bambino Gesù Children’s Hospital IRCCS, Rome, Italy

Lorenza Romani, Maia De Luca, Sara Chiurchiù & Martina Di Giuseppe

103. Department of Paediatric Infectious Diseases and Immunology, Erasmus Medical Centre–Sophia Children's Hospital, Rotterdam, The Netherlands

Clementien L. Vermont

104. Department of General Paediatrics, Erasmus Medical Centre–Sophia Children's Hospital, Rotterdam, The Netherlands

Henriëtte A. Moll, Dorine M. Borensztajn, Nienke N. Hagedoorn, Chantal Tan & Joany Zachariasse

105. Department of Immunology, Erasmus Medical Centre, Rotterdam, The Netherlands

W. Dik

106. Division of Infectious Disease, Department of Paediatrics, National Cheng Kung University, Tainan, Taiwan

Ching-Fen Shen

107. Riga Stradins University, Riga, Latvia

Dace Zavadska, Sniedze Laivacuma, Aleksandra Rudzate, Diana Stoldere, Arta Barzdina, Elza Barzdina, Sniedze Laivacuma, Monta Madelane, Anda Balode, Dārta Deksne, Ilze Grope, Anija Meiere, Ieva Nokalna, Jana Pavare, Zanda Pucuka, Katrina Selecka, Aleksandra Sidorova & Urzula Nora Urbane

108. Children's Clinical University Hospital, Riga, Latvia

Dace Zavadska, Sniedze Laivacuma, Aleksandra Rudzate, Diana Stoldere, Arta Barzdina, Elza Barzdina, Dagne Gravele, Dace Svile, Anda Balode, Dārta Deksne, Ilze Grope, Anija Meiere, Ieva

Nokalna, Jana Pavare, Zanda Pucuka, Katrina Selecka, Aleksandra Sidorova & Urzula Nora Urbane

109. Riga East Clinical University Hospital, Riga, Latvia

Sniedze Laivacuma & Monta Madelane

110. Service de Pédiatrie-Urgences, AP-HP, Hôpital Louis-Mourier, Colombes, France

Romain Basmaci, Noémie Lachaume, Pauline Bories, Raja Ben Tkhayat, Laura Chériaux, Juraté Davoust, Kim-Thanh Ong, Marie Cotillon, Thibault de Groc, Sébastien Le, Nathalie Vergnault, Hélène Sée, Laure Cohen, Alice de Tugny & Nevena Danekova

111. Université Paris Cité, INSERM, Paris, France

Romain Basmaci

112. Open Innovation and Partnerships, bioMérieux, Lyon, France

Marine Mommert-Tripon, Karen Brengel-Pesce, François Mallet, Alexandre Pachot & Marine Mommert

113. Joint Research Unit Hospice Civils de Lyon–bioMérieux, Centre Hospitalier Lyon Sud, Lyon, France

Karen Brengel-Pesce, François Mallet & Marine Mommert

114. Pathophysiology of Injury-induced Immunosuppression, University of Lyon, Lyon, France

Karen Brengel-Pesce & François Mallet

115. Department of Infectious Diseases, University Medical Centre Ljubljana, Ljubljana, Slovenia

Marko Pokorn, Mojca Kolnik, Tanja Avramoska, Natalija Bahovec, Petra Bogovic, Mirijam Nahtigal, Lea Papst, Tina Plankar

Srovin, Franc Strle, Katarina Vincek, Marko Pokorn, Petra Prunk & Veronika Osterman

116. University Children’s Hospital, University Medical Centre Ljubljana, Ljubljana, Slovenia

Marko Pokorn, Mojca Kolnik, Tadej Avcin, Tanja Avramoska, Lidija Kitanovski, Franc Strle, Anja Srpcic & Marko Pokorn

117. Faculty of Medicine, University of Ljubljana, Ljubljana, Slovenia

Marko Pokorn, Tadej Avcin & Lidija Kitanovski

118. Paediatric Infectious Diseases and Immunology, Wilhelmina Children’s Hospital, University Medical Centre Utrecht, Utrecht, The Netherlands

Michiel van der Flier, Louis J. Bont, Tom F. W. Wolfs & Coco R. Beudeker

119. Princess Maxima Centre for Paediatric Oncology, Utrecht, The Netherlands

Michiel van der Flier, Wim J. E. Tissing, Louis J. Bont, Tom F. W. Wolfs & Coco R. Beudeker

120. Paediatric Intensive Care Unit, Wilhelmina Children’s Hospital, University Medical Centre Utrecht, Utrecht, The Netherlands

Roelie M. Wösten-van Asperen

121. Paediatric Rheumatology, Wilhelmina Children’s Hospital, University Medical Centre Utrecht, Utrecht, The Netherlands

Sebastiaan J. Vastert

122. Paediatric Neonatal Intensive Care, Wilhelmina Children’s Hospital, University Medical Centre Utrecht, Utrecht, The Netherlands

Daniel C. Vijlbrief

123. Department of Paediatrics, Inselspital, Bern University Hospital, University of Bern, Bern, Switzerland

Philipp Agyeman, Christoph Aebi, Mariama Usman, Stefanie Schlüchter, Verena Wyss & Nina Schöbi

124. Department of Intensive Care and Neonatology, Children's Research Centre, University Children's Hospital Zurich, Zurich, Switzerland

Luregn Schlapbach, Elisa Zimmermann & Kathrin Weber

125. Child Health Research Centre, University of Queensland, Brisbane, Queensland, Australia

Luregn Schlapbach & Luregn J. Schlapbach

126. Clinic of Neonatology, Department Mother-Woman-Child, Lausanne University Hospital and University of Lausanne, Lausanne, Switzerland

Eric Giannoni

127. Infectious Diseases Service, Department of Medicine, Lausanne University Hospital and University of Lausanne, Lausanne, Switzerland

Eric Giannoni

128. Department of Paediatrics, Children's Hospital Lucerne, Lucerne, Switzerland

Martin Stocker

129. Paediatric Infectious Diseases Unit, Children's Hospital of Geneva, University Hospitals of Geneva, Geneva, Switzerland

Klara M. Posfay-Barbe

130. Infectious Diseases and Vaccinology, University of Basel Children's Hospital, Basel, Switzerland

Ulrich Heininger

131. Children's Hospital Aarau, Aarau, Switzerland

Sara Bernhard-Stirnemann

132. Division of Infectious Diseases and Hospital Epidemiology, Children's Hospital of Eastern Switzerland St. Gallen, St. Gallen, Switzerland

Anita Niederer-Loher & Christian Kahlert

133. Department of Neonatology, University Hospital Zurich, Zurich, Switzerland

Giancarlo Natalucci

134. Division of Infectious Diseases and Hospital Epidemiology, Children's Research Centre, University Children's Hospital Zurich, Zurich, Switzerland

Christa Relly & Christoph Berger

135. Children's Hospital Chur, Chur, Switzerland

Thomas Riedel

136. Department of Paediatrics and Adolescent Medicine, Division of General Paediatrics, Medical University of Graz, Graz, Austria

Werner Zenz, Alexander Binder, Benno Kohlmaier, Daniela S. Kohlfürst, Nina A. Schweintzger, Christoph Zurl, Susanne Hösele, Manuel Leitner, Lena Pölz, Alexandra Rusu, Glorija Rajic, Bianca Stoiser, Martina Strempfl, Manfred G. Sagmeister, Sebastian Bauchinger, Martin Benesch, Astrid Ceolotto, Siegfried Gallistl, Harald Haidl, Almuthe Hauer, Christa Hude, Andrea Skrabl-Baumgartner & Martin Benesch

137. Department of Paediatric Hematooncology, Medical University of Graz, Graz, Austria

Martin Benesch, Klaus Pfurtscheller, Siegfried Rödl, Volker Strenger, Martin Benesch & Larissa Krenn

138. Department of Paediatric Pulmonology, Medical University of Graz, Graz, Austria

Ernst Eber & Andreas Pfleger

139. Department of Internal Medicine, State Hospital Graz II, Graz, Austria

Andreas Kapper & Elmar Wallner

140. University Clinic of Paediatrics and Adolescent Medicine Graz, Medical University of Graz, Graz, Austria

Markus Keldorfer, Sabine Löffler, Heidemarie Pilch, Gunther Gores, Gudrun Nordberg, Laura Stampfer & Andreas Trobisch

141. Clinical Institute of Medical and Chemical Laboratory Diagnostics, Medical University of Graz, Graz, Austria

Tobias Niedrist

142. Paediatric Intensive Care Unit, Medical University of Graz, Graz, Austria

Klaus Pfurtscheller, Siegfried Rödl & Hinrich Baumgart

143. SkylineDx, Rotterdam, The Netherlands

Dennie Tempel, Danielle van Keulen & Annelieke M. Strijbosch

144. Biobanking and BioMolecular Resources Research Infrastructure–European Research Infrastructure Consortium (BBMRI-ERIC), Graz, Austria

Maike K. Tauchert

145. Division of Paediatric Infectious Diseases, Hauner Children's Hospital, University Hospital, Ludwig Maximilian University Munich, Munich, Germany

Ulrich von Both, Laura Kolberg, Patricia Schmied, Manuela Zwerenz & Judith Buschbeck

146. German Centre for Infection Research (DZIF), Partner Site Munich, Munich, Germany

Ulrich von Both

147. Department of Gynecology and Obstetrics, University Hospital, Ludwig Maximilian University Munich, Munich, Germany

Irene Alba-Alejandre

148. Division of Paediatric Rheumatology, Hauner Children's Hospital, University Hospital, Ludwig Maximilian University Munich, Munich, Germany

Katharina Danhauser

149. Department of Paediatric Cardiology and Paediatric Intensive Care, Hauner Children's Hospital, University Hospital, Ludwig Maximilian University Munich, Munich, Germany

Nikolaus Haas

150. Paediatric Intensive Care Unit, Hauner Children's Hospital, University Hospital, Ludwig Maximilian University Munich, Munich, Germany

Florian Hoffmann, Karl Reiter, Carola Schoen & Julia Keil

151. Division of Paediatric Pulmonology, Hauner Children's Hospital, University Hospital, Ludwig Maximilian University Munich, Munich, Germany

Matthias Griese & Matthias Kappler

152. Division of Paediatric Haematology and Oncology, Hauner Children's Hospital, University Hospital, Ludwig Maximilian University Munich, Munich, Germany

Tobias Feuchtinger & Vera Binder

153. Division of General Paediatrics, Hauner Children's Hospital, University Hospital, Ludwig Maximilian University Munich, Munich, Germany

Sabrina Juranek, Esther Maier & Christoph Bidlingmaier

154. Division of Paediatric Gastroenterology, Hauner Children's Hospital, University Hospital, Ludwig Maximilian University Munich, Munich, Germany

Eberhard Lurz

155. Neonatal Intensive Care Unit, Hauner Children's Hospital, University Hospital, Ludwig Maximilian University Munich, Munich, Germany

Sebastian Schroepf & Georg Muench

156. Faculty of Infectious and Tropical Disease, London School of Hygiene and Tropical Medicine, London, UK

Shunmay Yeung, Manuel Dewez, Elizabeth Fitchett, Fiona Cresswell, Juan Emmanuel Dewez, Martin Hibberd, Catherine Wedderburn & Anne Meierford

157. Department of Paediatrics, St. Mary's Hospital, London, UK

Shunmay Yeung & Ruud Nijman

158. Faculty of Public Health and Policy, London School of Hygiene and Tropical Medicine, London, UK

Shunmay Yeung, David Bath & Alec Miners

159. Centre of Clinical Medicine Research, National Cheng Kung University, Tainan, Taiwan

Ching-Chuan Liu & Shih-Min Wang

160. Medical Research Council Unit The Gambia at the London School for Hygiene and Tropical Medicine, Fajara, The Gambia

Effua Usuf, Kalifa Bojang, Syed M. A. Zaman, Fatou Secka, Suzanne Anderson, Anna RocaIsatou Sarr, Momodou Saidykhan, Saffiatou Darboe, Samba Ceesay & Umberto D'alessandro

161. Neonatal and Paediatric Intensive Care Unit, Children's Research Centre, University Children's Hospital Zurich, University of Zurich, Zurich, Switzerland

Luregn J. Schlapbach

162. Queensland Children's Hospital, Brisbane, Queensland, Australia

Luregn J. Schlapbach

163. Department of Paediatric Orthopedics, Medical University of Graz, Graz, Austria

Matthias Sperl

164. Department of Paediatric and Adolescence Surgery, Medical University of Graz, Graz, Austria

Holger Till

165. Faculty of Epidemiology and Population Health, London School of Hygiene and Tropical Medicine, London, UK

Baptiste Leurent

166. Radboud University Medical Centre, Nijmegen, The Netherlands

Ronald de Groot, Michiel van der Flier, Koen van Aerde, Wynand Alkema, Bryan van den Broek, Jolein Gloerich, Alain J. van Gool, Stefanie Henriet, Martijn Huijnen, Ria Philipsen, Esther Willems, L. de Haan & C. Neeleman

167. Amalia Children's Hospital, Nijmegen, The Netherlands

Michiel van der Flier, Koen van Aerde, Stefanie Henriet & L. de Haan

168. Wilhelmina Children's Hospital, University Medical Centre Utrecht, Utrecht, The Netherlands

Michiel van der Flier & Marien I. de Jonge

169. Canisius Wilhelmina Hospital, Nijmegen, The Netherlands

G. P. J. M. Gerrits & M. van Leur

170. St. Antonius Hospital, Nieuwegein, The Netherlands

J. Heidema

171. Catharina Hospital, Eindhoven, The Netherlands

C. J. Miedema

172. ETZ Elisabeth, Tilburg, The Netherlands

C. C. Obihara & G. A. Tramper-Stranders

173. Franciscus Gasthuis, Rotterdam, The Netherlands

G. A. Tramper-Stranders

174. Department of Pathology, University of Otago, Christchurch, New Zealand

David R. Murdoch

175. Newcastle University Business School, Centre for Knowledge, Innovation, Technology and Enterprise (KITE), Newcastle upon Tyne, UK

Lucille Valentine

176. Paediatric Intensive Care Unit, Great North Children's Hospital, Newcastle upon Tyne Hospitals NHS Foundation Trust, Newcastle upon Tyne, UK

Rachel Agbeko & Christine Mackerness

177. Northumbria University, Newcastle upon Tyne, UK

Mike Martin

178. Department of Infectious Diseases and Epidemiology, Faculty of Medicine, University of Ljubljana, Ljubljana, Slovenia

Marko Pokorn

179. Sanquin Research Institute, Landsteiner Laboratory at the AMC, University of Amsterdam, Amsterdam, The Netherlands

Taco Kuijpers, Ilse Jongerius, Evelien Sprenkeler, Judith Zandstra, G. van Mierlo & J. Geissler

180. Department of Paediatric Infectious Diseases and Immunology, Amsterdam University Medical Centre, Free University (VU) Amsterdam, Amsterdam, The Netherlands

M. van der Kuip & A. M. van Furth

181. ISARIC Global Support Centre, Centre for Tropical Medicine and Global Health, Nuffield Department of Medicine, University of Oxford, Oxford, UK

Gail Carson & Laura Merson

182. National Heart and Lung Institute, Imperial College London, London, UK

Peter J. M. Openshaw & Jake Dunning

183. Imperial College Healthcare NHS Foundation Trust, London, UK

Peter J. M. Openshaw

184. National Infection Service, Public Health England, London, UK

Jake Dunning

185. Centre for Inflammation Research, The Queen's Medical Research Institute, University of Edinburgh, Edinburgh, UK

Clark D. Russell

186. Edinburgh Pathology, University of Edinburgh, Edinburgh, UK

David Dorward

187. Blood Borne Virus Unit, Virus Reference Department, National Infection Service, Public Health England, London, UK

Richard S. Tedder

188. Transfusion Microbiology, National Health Service Blood and Transplant, London, UK

Richard S. Tedder

189. Department of Medicine, Imperial College London, London, UK

Richard S. Tedder

190. Department of Pharmacology, University of Liverpool, Liverpool, UK

Say Khoo

191. National Institute for Health Research Health Protection Research Unit, Institute of Infection, Veterinary and Ecological Sciences, Faculty of Health and Life Sciences, University of Liverpool, Liverpool, UK

Lance C. W. Turtle, Tom Solomon & Hayley Hardwick

192. Tropical and Infectious Disease Unit, Royal Liverpool University Hospital, Liverpool, UK

Lance C. W. Turtle

193. Walton Centre NHS Foundation Trust, Liverpool, UK

Tom Solomon

194. Virology Reference Department, National Infection Service, Public Health England, London, UK

Samreen Ijaz

195. Liverpool School of Tropical Medicine, Liverpool, UK

Tom Fletcher

196. Centre for Clinical Infection and Diagnostics Research, Department of Infectious Diseases, School of Immunology and Microbial Sciences, King's College London, London, UK

Nicholas Price

197. Department of Infectious Diseases, Guy's and St. Thomas' NHS Foundation Trust, London, UK

Nicholas Price

198. The Florey Institute for Host–Pathogen Interactions, Department of Infection, Immunity and Cardiovascular Disease, University of Sheffield, Sheffield, UK

Thushan de Silva

199. Liverpool Clinical Trials Centre, University of Liverpool, Liverpool, UK

Chloe Donohue

200. Edinburgh Parallel Computing Centre (EPCC), University of Edinburgh, Edinburgh, UK

Lucy Norris

201. Medical Research Council Human Genetics Unit, Medical Research Council Institute of Genetics and Molecular Medicine, University of Edinburgh, Edinburgh, UK

Murray Wham

202. Edinburgh Clinical Research Facility, University of Edinburgh, Edinburgh, UK

Richard Clark, Audrey Coutts, Lorna Donelly, Angie Fawkes, Tammy Gilchrist, Katarzyna Hafezi, Louise MacGillivray, Alan Maclean, Sarah McCafferty, Kirstie Morrice, Lee Murphy & Nicola Wrobel

203. Department of Histopathology, Great Ormond Street Hospital for Children NHS Foundation Trust, London, UK

Sarah E. McDonald

204. Institute of Translational Medicine, University of Liverpool, Liverpool, UK

Victoria Shaw

205. Sheffield Teaching Hospitals NHS Foundation Trust, Sheffield, UK

Jane A. Armstrong

206. University of Liverpool, Liverpool, UK

Lauren Lett

207. Royal Hospital For Children and Young People, Edinburgh, UK

Paul Henderson, Maxine Ramsay & Margaret Millar

208. Department of Paediatric Infectious Diseases and Immunology, Royal Hospital for Children Glasgow, Glasgow, UK

Louisa Pollock

209. Royal Aberdeen Children's Hospital, Aberdeen, UK

Shyla Kishore, Maggie Connon & Catriona Ward

210. Queen Margaret Hospital, Dumfermline, UK

Helen Brotherton, John Morrice & Laura Beveridge

211. Victoria Hospital, Kirkcaldy, UK

Helen Brotherton & John Morrice

212. University Hospital Crosshouse, Crosshouse, UK

Lawrence Armstrong & Claire Bell

213. University Hospital Ayr, Ayr, UK

Lawrence Armstrong

214. Dumfries and Galloway Royal Infirmary, Dumfries, UK

Andrew Mita & Janie Candlish

215. Borders General Hospital, Melrose, UK

Anna Dall, Lauren Finlayson & Joy Dawson

216. Forth Valley Hospital, Larbert, UK

Kristyna Bohmova, Sheena Logan & Laura McGenily

217. Tayside Children's Hospital and Ninewells Hospital, NHS Tayside, Dundee, UK

Louise Gannon

218. Doncaster and Bassetlaw NHS Foundation Trust, Doncaster, UK

Ken Agwuh & Sarah Farmer

219. Burnley General Hospital, Burnley, UK

Srikanth Chukkambotla

220. Hereford County Hospital, Hereford, UK

Ingrid DuRand

221. Leighton Hospital, Leighton, UK

Duncan Fullerton, Elijah Matovu & Amaryl Jones

222. Walsall Healthcare NHS Foundation Trust, Walsall, UK

Sanjeev Garg

223. Cumberland Infirmary, Cumberland, UK

Clive Graham

224. St. Richard's Hospital, Chichester, UK

Luke Hodgson & Sharon Floyd

225. Airedale Hospital, Keighley, UK

Paul Jennings

226. Hinchingbrooke Hospital, Huntingdon, UK

George Koshy & Tamas Leiner

227. Darlington Memorial Hospital, Darlington, UK

James Limb

228. Warrington Hospital, Warrington, UK

Jeff Little

229. Leeds Teaching Hospitals NHS Trust, Leeds, UK

Fiona McGill & Collette Spencer

230. Queen's Hospital Burton, Burton, UK

Craig Morris, Tim Reynolds & Holly Dickinson

231. Royal Victoria Infirmary, Newcastle upon Tyne, UK

David Price

232. University Hospitals Dorset NHS Foundation Trust, Dorset, UK

Henrik Reschreiter, Lucy Rubick, Amy Roff & Sarah Mills

233. Bradford Royal Infirmary, Bradford, UK

Paul Whittaker

234. Department of Paediatric Gastroenterology, Heptalogy and Nutrition, Royal Hospital for Children Glasgow, Glasgow, UK

Rachel Tayler

235. Avon and Wiltshire Mental Health Partnership NHS Foundation Trust, Bath, UK

Clare Irving

236. Queen Elizabeth University Hospital, Glasgow, UK

Barry Milligan & Naomy Hickey

237. Tayside Children’s Hospital, Dundee, UK

Susan MacFarlane

238. University Hospital Wishaw, Wishaw, UK

Karen Leitch

239. Royal Free Hospital, London, UK

Cynthia Diaba

240. Diana Princess of Wales Hospital, Grimsby, UK

Jasmine Player

241. Weston General Hospital, Weston-super-Mare, UK

Susie Ferguson

242. Barnsley Hospital, Barnsley, UK

Susan Hope

243. Bradford Teaching Hospitals NHS Foundation Trust, Bradford, UK

Rachel Swingler

244. Wye Valley NHS Foundation Trust, Hereford, UK

Emma Collins

245. Newcastle upon Tyne Hospitals, Newcastle upon Tyne, UK

Barbara Wilson

246. West Cumberland Hospital, Whitehaven, UK

Diane Armstrong & Rosemary Harper

247. University of North Durham, Durham, UK

Mark Birt

248. Worthing Hospital, Worthing, UK

Darran Martin

Consortia

DIAMONDS Consortium

- Michael Levin
- , Evangelos Bellos
- , Claire Broderick
- , Samuel Channon-Wells
- , Samantha Cooray
- , Tisham De
- , Giselle D’Souza
- , Leire Estramiana Elorrieta
- , Diego Estrada-Rivadeneyra
- , Rachel Galassini
- , Dominic Habgood-Coote
- , Shea Hamilton
- , Heather Jackson
- , James Kavanagh
- , Mahdi Moradi Marjaneh
- , Stephanie Menikou
- , Samuel Nichols
- , Ruud Nijman

- , Harsita Patel
- , Ivana Pennisi
- , Oliver Powell
- , Ruth Reid
- , Priyen Shah
- , Ortensia Vito
- , Elizabeth Whittaker
- , Clare Wilson
- , Rebecca Womersley
- , Amina Abdulla
- , Sarah Darnell
- , Sobia Mustafa
- , Pantelis Georgiou
- , Jesus-Rodriguez Manzano
- , Nicolas Moser
- , Michael Carter
- , Shane Tibby
- , Jonathan Cohen
- , Francesca Davis
- , Julia Kenny
- , Paul Wellman
- , Marie White
- , Matthew Fish
- , Aislinn Jennings
- , Shankar-Hari
- , Katy Fidler
- , Dan Agranoff
- , Vivien Richmond
- , Matthew Seal
- , Saul Faust
- , Dan Owen
- , Ruth Ensom
- , Sarah McKay
- , Diana Mondo
- , Mariya Shaji
- , Rachel Schranz
- , Prita Rughnani

- , Amutha Anpananthar
- , Susan Liebeschuetz
- , Anna Riddell
- , Nosheen Khalid
- , Ivone Lancoma Malcolm
- , Teresa Simagan
- , Mark Peters
- , Alasdair Bamford
- , Nazima Pathan
- , Esther Daubney
- , Deborah White
- , Melissa Heightman
- , Sarah Eisen
- , Terry Segal
- , Lucy Wellings
- , Simon B. Drysdale
- , Nicole Branch
- , Lisa Hamzah
- , Heather Jarman
- , Maggie Nyirenda
- , Lisa Capozzi
- , Emma Gardiner
- , Robert Moots
- , Magda Nasher
- , Anita Hanson
- , Michelle Linforth
- , Sean O’Riordan
- , Donna Ellis
- , Akash Deep
- , Ivan Caro
- , Fiona Shackley
- , Arianna Bellini
- , Stuart Gormley
- , Samira Neshat
- , Barnaby J. Scholefield
- , Ceri Robbins
- , Helen Winmill

- , Stéphane C. Paulus
- , Andrew J. Pollard
- , Sarah Hopton
- , Danielle Miller
- , Zoe Oliver
- , Sally Beer
- , Bryony Ward
- , Shrijana Shrestha
- , Meeru Gurung
- , Puja Amatya
- , Bhishma Pokhrel
- , Sanjeev Man Bijukchhe
- , Tim Lubinda
- , Sarah Kelly
- , Peter O'Reilly
- , Federico Martinón-Torres
- , Antonio Salas
- , Fernando Álvez González
- , Xabier Bello
- , Mirian Ben García
- , Sandra Carnota
- , Miriam Cebey-López
- , María José Curras-Tuala
- , Carlos Durán Suárez
- , Luisa García Vicente
- , Alberto Gómez-Carballa
- , Jose Gómez Rial
- , Pilar Leboráns Iglesias
- , Nazareth Martinón-Torres
- , José María Martinón Sánchez
- , Belén Mosquera Pérez
- , Jacobo Pardo-Seco
- , Lidia Piñeiro Rodríguez
- , Sara Pischedda
- , Sara Rey Vázquez
- , Irene Rivero Calle
- , Carmen Rodríguez-Tenreiro

- , Lorenzo Redondo-Collazo
- , Miguel Sadiki Ora
- , Sonia Serén Fernández
- , Cristina Serén Trasorras
- , Marisol Vilas Iglesias
- , Enitan D. Carrol
- , Elizabeth Cocklin
- , Aakash Khanijau
- , Rebecca Lenihan
- , Nadia Lewis-Burke
- , Karen Newal
- , Sam Romaine
- , Maria Tsolia
- , Irini Eleftheriou
- , Nikos Spyridis
- , Maria Tambouratzi
- , Despoina Maritsi
- , Antonios Marmarinos
- , Marietta Xagorari
- , Lourida Panagiota
- , Pefanis Aggelos
- , Akinosoglou Karolina
- , Gogos Charalambos
- , Maragos Markos
- , Voulgarelis Michalis
- , Stergiou Ioanna
- , Marieke Emonts
- , Emma Lim
- , John Isaacs
- , Kathryn Bell
- , Stephen Crulley
- , Daniel Fabian
- , Evelyn Thomson
- , Caroline Miller
- , Ashley Bell
- , Fabian J. S. van der Velden
- , Geoff Shenton

- , Ashley Price
- , Owen Treloar
- , Daisy Thomas
- , Pablo Rojo
- , Cristina Epalza
- , Serena Villaverde
- , Sonia Márquez
- , Manuel Gijón
- , Fátima Machín
- , Laura Cabello
- , Irene Hernández
- , Lourdes Gutiérrez
- , Ángela Manzanares
- , Taco Kuijpers
- , Martijn van de Kuip
- , Marceline van Furth
- , Merlijn van den Berg
- , Giske Biesbroek
- , Floris Verkuil
- , Carlijn van der Zee
- , Dasja Pajkrt
- , Michael Boele van Hensbroek
- , Dieneke Schonenberg
- , Mariken Gruppen
- , Sietse Nagelkerke
- , Machiel H. Jansen
- , Ines Goetschalckx
- , Lorenza Romani
- , Maia De Luca
- , Sara Chiurchiù
- , Martina Di Giuseppe
- , Clementien L. Vermont
- , Henriëtte A. Moll
- , Dorine M. Borensztajn
- , Nienke N. Hagedoorn
- , Chantal Tan
- , Joany Zachariasse

- , W. Dik
- , Ching-Fen Shen
- , Dace Zavadska
- , Sniedze Laivacuma
- , Aleksandra Rudzate
- , Diana Stoldere
- , Arta Barzdina
- , Elza Barzdina
- , Sniedze Laivacuma
- , Monta Madelane
- , Dagne Gravele
- , Dace Svile
- , Romain Basmaci
- , Noémie Lachaume
- , Pauline Bories
- , Raja Ben Tkhayat
- , Laura Chériaux
- , Juraté Davoust
- , Kim-Thanh Ong
- , Marie Cotillon
- , Thibault de Groc
- , Sébastien Le
- , Nathalie Vergnault
- , Hélène Sée
- , Laure Cohen
- , Alice de Tugny
- , Nevena Danekova
- , Marine Mommert-Tripon
- , Karen Brengel-Pesce
- , Marko Pokorn
- , Mojca Kolnik
- , Tadej Avcin
- , Tanja Avramoska
- , Natalija Bahovec
- , Petra Bogovic
- , Lidija Kitanovski
- , Mirijam Nahtigal

- , Lea Papst
- , Tina Plankar Srovin
- , Franc Strle
- , Anja Srpcic
- , Katarina Vincek
- , Michiel van der Flier
- , Wim J. E. Tissing
- , Roelie M. Wösten-van Asperen
- , Sebastiaan J. Vastert
- , Daniel C. Vijlbrief
- , Louis J. Bont
- , Tom F. W. Wolfs
- , Coco R. Beudeker
- , Philipp Agyeman
- , Luregn Schlapbach
- , Christoph Aebi
- , Mariama Usman
- , Stefanie Schlüchter
- , Verena Wyss
- , Nina Schöbi
- , Elisa Zimmermann
- , Kathrin Weber
- , Eric Giannoni
- , Martin Stocker
- , Klara M. Posfay-Barbe
- , Ulrich Heininger
- , Sara Bernhard-Stirnemann
- , Anita Niederer-Loher
- , Christian Kahlert
- , Giancarlo Natalucci
- , Christa Relly
- , Thomas Riedel
- , Christoph Berger
- , Marie Voice
- , Michael Steele
- , Colin Fink
- , Jennifer Holden

- , Leo Calvo-Bado
- , Benjamin Evans
- , Jake Stevens
- , Peter Matthews
- , Kyle Billing
- , Werner Zenz
- , Alexander Binder
- , Benno Kohlmaier
- , Daniela S. Kohlfürst
- , Nina A. Schweintzger
- , Christoph Zurl
- , Susanne Hösele
- , Manuel Leitner
- , Lena Pölz
- , Alexandra Rusu
- , Glorija Rajic
- , Bianca Stoiser
- , Martina Strempfl
- , Manfred G. Sagmeister
- , Sebastian Bauchinger
- , Martin Benesch
- , Astrid Ceolotto
- , Ernst Eber
- , Siegfried Gallistl
- , Harald Haidl
- , Almuthe Hauer
- , Christa Hude
- , Andreas Kapper
- , Markus Keldorfer
- , Sabine Löffler
- , Tobias Niedrist
- , Heidemarie Pilch
- , Andreas Pfleger
- , Klaus Pfurtscheller
- , Siegfried Rödl
- , Andrea Skrabl-Baumgartner
- , Volker Strenger

- , Elmar Wallner
- , Dennie Tempel
- , Danielle van Keulen
- , Annelieke M. Strijbosch
- , Maike K. Tauchert
- , Ulrich von Both
- , Laura Kolberg
- , Patricia Schmied
- , Irene Alba-Alejandre
- , Katharina Danhauser
- , Nikolaus Haas
- , Florian Hoffmann
- , Matthias Griese
- , Tobias Feuchtinger
- , Sabrina Juranek
- , Matthias Kappler
- , Eberhard Lurz
- , Esther Maier
- , Karl Reiter
- , Carola Schoen
- , Sebastian Schroepf
- , Shunmay Yeung
- , Manuel Dewez
- , David Bath
- , Elizabeth Fitchett
- & Fiona Cresswell

PERFORM Consortium

- Michael Levin
- , Aubrey Cunnington
- , Tisham De
- , Jethro Herberg
- , Mysini Kaforou
- , Victoria Wright
- , Lucas Baumard
- , Evangelos Bellos

- , Giselle D’Souza
- , Rachel Galassini
- , Dominic Habgood-Coote
- , Shea Hamilton
- , Clive Hoggart
- , Sara Hourmat
- , Heather Jackson
- , Ian Maconochie
- , Stephanie Menikou
- , Naomi Lin
- , Samuel Nichols
- , Ruud Nijman
- , Ivonne Pena Paz
- , Oliver Powell
- , Priyen Shah
- , Clare Wilson
- , Amina Abdulla
- , Ladan Ali
- , Sarah Darnell
- , Rikke Jorgensen
- , Sobia Mustafa
- , Salina Persand
- , Molly Stevens
- , Eunjung Kim
- , Benjamin Pierce
- , Katy Fidler
- , Julia Dudley
- , Vivien Richmond
- , Emma Tavliavini
- , Ching-Fen Shen
- , Ching-Chuan Liu
- , Shih-Min Wang
- , Federico Martinón-Torres
- , Antonio Salas
- , Fernando Álvez González
- , Cristina Balo Farto
- , Ruth Barral-Arca

- , Maria Barreiro Castro
- , Xabier Bello
- , Mirian Ben García
- , Sandra Carnota
- , Miriam Cebey-López
- , María José Curras-Tuala
- , Carlos Durán Suárez
- , Luisa García Vicente
- , Alberto Gómez-Carballa
- , Jose Gómez Rial
- , Pilar Leboráns Iglesias
- , Federico Martinón-Torres
- , Nazareth Martinón-Torres
- , José María Martinón Sánchez
- , Belén Mosquera Pérez
- , Jacobo Pardo-Seco
- , Lidia Piñeiro Rodríguez
- , Sara Pischedda
- , Sara Rey Vázquez
- , Irene Rivero Calle
- , Carmen Rodríguez-Tenreiro
- , Lorenzo Redondo-Collazo
- , Miguel Sadiki Ora
- , Sonia Serén Fernández
- , Cristina Serén Trasorras
- , Marisol Vilas Iglesias
- , Dace Zavadska
- , Anda Balode
- , Arta Barzdina
- , Dārta Deksne
- , Dagne Gravele
- , Ilze Grope
- , Anija Meiere
- , Ieva Nokalna
- , Jana Pavare
- , Zanda Pucuka
- , Katrina Selecka

- , Aleksandra Sidorova
- , Dace Svile
- , Urzula Nora Urbane
- , Effua Usuf
- , Kalifa Bojang
- , Syed M. A. Zaman
- , Fatou Secka
- , Suzanne Anderson
- , Anna RocaIsatou Sarr
- , Momodou Saidykhan
- , Saffiatou Darboe
- , Samba Ceesay
- , Umberto D’alessandro
- , Henriëtte A. Moll
- , Dorine M. Borensztajn
- , Nienke N. Hagedoorn
- , Chantal Tan
- , Clementien L. Vermont
- , Joany Zachariasse
- , W. Dik
- , Philipp Agyeman
- , Luregn J. Schlapbach
- , Christoph Aebi
- , Verena Wyss
- , Mariama Usman
- , Eric Giannoni
- , Martin Stocker
- , Klara M. Posfay-Barbe
- , Ulrich Heininger
- , Sara Bernhard-Stirnemann
- , Anita Niederer-Loher
- , Christian Kahlert
- , Giancarlo Natalucci
- , Christa Relly
- , Thomas Riedel
- , Christoph Berger
- , Enitan D. Carrol

- , Stéphane Paulus
- , Elizabeth Cocklin
- , Rebecca Jennings
- , Joanne Johnston
- , Simon Leigh
- , Karen Newall
- , Sam Romaine
- , Maria Tsolia
- , Irini Eleftheriou
- , Maria Tambouratzi
- , Antonis Marmarinos
- , Marietta Xagorari
- , Kelly Syggelou
- , Colin Fink
- , Marie Voice
- , Leo Calvo-Bado
- , Werner Zenz
- , Benno Kohlmaier
- , Nina A. Schweintzger
- , Manfred G. Sagmeister
- , Daniela S. Kohlfürst
- , Christoph Zurl
- , Alexander Binder
- , Susanne Hösele
- , Manuel Leitner
- , Lena Pölz
- , Glorija Rajic
- , Sebastian Bauchinger
- , Hinrich Baumgart
- , Martin Benesch
- , Astrid Ceolotto
- , Ernst Eber
- , Siegfried Gallistl
- , Gunther Gores
- , Harald Haidl
- , Almuthe Hauer
- , Christa Hude

- , Markus Keldorfer
- , Larissa Krenn
- , Heidemarie Pilch
- , Andreas Pfleger
- , Klaus Pfurtscheller
- , Gudrun Nordberg
- , Tobias Niedrist
- , Siegfried Rödl
- , Andrea Skrabl-Baumgartner
- , Matthias Sperl
- , Laura Stampfer
- , Volker Strenger
- , Holger Till
- , Andreas Trobisch
- , Sabine Löffler
- , Shunmay Yeung
- , Juan Emmanuel Dewez
- , Martin Hibberd
- , David Bath
- , Alec Miners
- , Ruud Nijman
- , Catherine Wedderburn
- , Anne Meierford
- , Baptiste Leurent
- , Ronald de Groot
- , Michiel van der Flier
- , Marien I. de Jonge
- , Koen van Aerde
- , Wynand Alkema
- , Bryan van den Broek
- , Jolein Gloerich
- , Alain J. van Gool
- , Stefanie Henriet
- , Martijn Huijnen
- , Ria Philipsen
- , Esther Willems
- , G. P. J. M. Gerrits

- , M. van Leur
- , J. Heidema
- , L. de Haan
- , C. J. Miedema
- , C. Neeleman
- , C. C. Obihara
- , G. A. Tramper-Stranders
- , Andrew J. Pollard
- , Rama Kandasamy
- , Stéphane Paulus
- , Michael J. Carter
- , Daniel O’Connor
- , Sagida Bibi
- , Dominic F. Kelly
- , Meeru Gurung
- , Stephen Thorson
- , Imran Ansari
- , David R. Murdoch
- , Shrijana Shrestha
- , Marieke Emonts
- , Emma Lim
- , Lucille Valentine
- , Karen Allen
- , Kathryn Bell
- , Adora Chan
- , Stephen Crulley
- , Kirsty Devine
- , Daniel Fabian
- , Sharon King
- , Paul McAlinden
- , Sam McDonald
- , Anne McDonnell
- , Ailsa Pickering
- , Evelyn Thomson
- , Amanda Wood
- , Diane Wallia
- , Phil Woodsford

- , Frances Baxter
- , Ashley Bell
- , Mathew Rhodes
- , Rachel Agbeko
- , Christine Mackerness
- , Bryan Baas
- , Lieke Kloosterhuis
- , Wilma Oosthoek
- , Tasnim Arif
- , Joshua Bennet
- , Kalvin Collings
- , Ilona van der Giessen
- , Alex Martin
- , Aqeela Rashid
- , Emily Rowlands
- , Gabriella de Vries
- , Fabian van der Velden
- , Mike Martin
- , Ravi Mistry
- , Ulrich von Both
- , Laura Kolberg
- , Manuela Zwerenz
- , Judith Buschbeck
- , Christoph Bidlingmaier
- , Vera Binder
- , Katharina Danhauser
- , Nikolaus Haas
- , Matthias Griese
- , Tobias Feuchtinger
- , Julia Keil
- , Matthias Kappler
- , Eberhard Lurz
- , Georg Muench
- , Karl Reiter
- , Carola Schoen
- , François Mallet
- , Karen Brengel-Pesce

- , Alexandre Pachot
- , Marine Mommert
- , Marko Pokorn
- , Mojca Kolnik
- , Katarina Vincek
- , Tina Plankar Srovin
- , Natalija Bahovec
- , Petra Prunk
- , Veronika Osterman
- , Tanja Avramoska
- , Taco Kuijpers
- , Ilse Jongerius
- , J. M. van den Berg
- , D. Schonenberg
- , A. M. Barendregt
- , D. Pajkrt
- , M. van der Kuip
- , A. M. van Furth
- , Evelien Sprenkeler
- , Judith Zandstra
- , G. van Mierlo
- & J. Geissler

ISARIC 4C Investigators

- Kenneth Baillie
- , Malcolm Gracie Semple
- , Gail Carson
- , Peter J. M. Openshaw
- , Jake Dunning
- , Laura Merson
- , Clark D. Russell
- , David Dorward
- , Maria Zambon
- , Meera Chand
- , Richard S. Tedder
- , Say Khoo

- , Lance C. W. Turtle
- , Tom Solomon
- , Samreen Ijaz
- , Tom Fletcher
- , Massimo Palmarini
- , Antonia Y. W. Ho
- , Emma Thomson
- , Nicholas Price
- , Judith Breuer
- , Thushan de Silva
- , Chloe Donohue
- , Hayley Hardwick
- , Wilna Oosthuyzen
- , Miranda Odam
- , Primrose Chikowore
- , Lauren Obosi
- , Sara Clohisey
- , Andrew Law
- , Lucy Norris
- , Sarah Tait
- , Murray Wham
- , Richard Clark
- , Audrey Coutts
- , Lorna Donelly
- , Angie Fawkes
- , Tammy Gilchrist
- , Katarzyna Hafezi
- , Louise MacGillivray
- , Alan Maclean
- , Sarah McCafferty
- , Kirstie Morrice
- , Lee Murphy
- , Nicola Wrobel
- , Sarah E. McDonald
- , Victoria Shaw
- , Jane A. Armstrong
- , Lauren Lett

- , Paul Henderson
- , Louisa Pollock
- , Shyla Kishore
- , Helen Brotherton
- , Lawrence Armstrong
- , Andrew Mita
- , Anna Dall
- , Kristyna Bohmova
- , Sheena Logan
- , Louise Gannon
- , Ken Agwuh
- , Srikanth Chukkambotla
- , Ingrid DuRand
- , Duncan Fullerton
- , Sanjeev Garg
- , Clive Graham
- , Tassos Grammatikopoulos
- , Stuart Hartshorn
- , Luke Hodgson
- , Paul Jennings
- , George Koshy
- , Tamas Leiner
- , James Limb
- , Jeff Little
- , Elijah Matovu
- , Fiona McGill
- , Craig Morris
- , John Morrice
- , David Price
- , Henrik Reschreiter
- , Tim Reynolds
- , Paul Whittaker
- , Rachel Tayler
- , Clare Irving
- , Maxine Ramsay
- , Margaret Millar
- , Barry Milligan

- , Naomy Hickey
- , Maggie Connon
- , Catriona Ward
- , Laura Beveridge
- , Susan MacFarlane
- , Karen Leitch
- , Claire Bell
- , Lauren Finlayson
- , Joy Dawson
- , Janie Candlish
- , Laura McGenily
- , Tara Roome
- , Cynthia Diaba
- , Jasmine Player
- , Natassia Powell
- , Ruth Howman
- , Sara Burling
- , Sharon Floyd
- , Sarah Farmer
- , Susie Ferguson
- , Susan Hope
- , Lucy Rubick
- , Rachel Swingler
- , Emma Collins
- , Collette Spencer
- , Amaryl Jones
- , Barbara Wilson
- , Diane Armstrong
- , Mark Birt
- , Holly Dickinson
- , Rosemary Harper
- , Darran Martin
- , Amy Roff
- & Sarah Mills

Contributions

J.B., S. Morfopoulou and S.B. conceived the study, analysed the data and wrote the manuscript. J.R.B., L.A., N.S., A.L., J.C.D.L., J.H. and S.D. coordinated samples and carried out the metagenomics and confirmatory PCRs. O.E.T.M., J.A.G.-A., S.R., C.V., L.M.M.B., R.W., C.A.W., H.T., N.B., H.M., K.-A.M., S.C.H. and D.K.A. carried out genome sequencing and analyses. M.M.M., M.N., G.P., A.C., A.M., C.V., J. Rosenheim and M.L. analysed transcriptomic data. K. Thalassinos, M.L., M.M.M. and R.Z.C. generated and analysed proteomic data. S.N.W., J.R.C., J.F.A.D., A.S., L.J.T., Z.A., J.N. and K.S.H. carried out AAV2 tropism experiments. G.S., P.G., T.E.W., S.N.W. and J.R.C. helped with AAV2 PCR development. L.C., R.B., M.D., J.M., J.C.H., C.A., G.A. and T.S.J. carried out histology, immunohistochemistry and electron microscopy. B.B.K. and J. Reich provided control HHV-6 material. P. Shah and J.A. provided control samples. M.L., P. Simmonds, S.C., M.V., C.F. and M.S. provided PERFORM and DIAMONDS control samples. K.B., M.G.S., P.C. and M.O. coordinated consent and data collection from ISARIC. T.G., N.H. and C.K. provided data and samples from KCH and Birmingham Liver Units. I.U.-L., M.C., M.Z., S. Mandal, C.W., R.S., E.G., S.G., C.C., T.T., K.H., C.H., T.R., C.M., K. Templeton, C.N., M.H., R.G. and S.J.S. provided data and samples from UKHSA and devolved nations. E.T. provided reagents and contributed helpful discussions.

Corresponding author

Correspondence to Judith Breuer.

Ethics declarations

Competing interests

.J.B. is a member of the MHRA COVID Vaccines and Therapeutics committees; holder of Wellcome Trust, UKRI and NIHR funding; and principal investigator on the GSK LUNAR study to provide MHRA with data on SARS-CoV-2 sequences in patients treated with sotrovimab.

Peer review

Peer review information

Nature thanks Frank Tacke and the other, anonymous, reviewer(s) for their contribution to the peer review of this work. Peer reviewer reports are available.

Additional information

Publisher's note Springer Nature remains neutral with regard to jurisdictional claims in published maps and institutional affiliations.

Extended data figures and tables

Extended Data Fig. 1 Evidence of AAV2 replication from meta-transcriptomics and RT-PCR.

Mapping of AAV2 reads to the reference genome for **a** liver RNA-Seq from 4 cases, **b** blood RNA-Seq from 2 cases. The horizontal lines in the same colour as the coverage graph are the predicted transcripts for each case. The horizontal lines in purple and green are the AAV2 genes. **c**, RT-PCR results for liver cases. N: Negative PCR result.

Extended Data Fig. 2 Examples of AAV2 complexes.

The y axis shows the coordinates of a full length AAV2 genome (rep gene in green and cap gene in yellow). X axis is the nanopore read with the length of the read indicated. Red dots indicate alignment to the forward strand and blue dots the reverse. **a**, indicative complexes based on literature[8] **b** and **c**. Examples of complex structures with both head to tail and alternating repeats, from a total of n = 25 and n = 75 such reads for cases 3 and 5 respectively. **b** shows the longest 2 reads for each case. **d**. Examples of truncated monomeric structures, from a total of n = 27 and n = 103 such reads for cases 3 and 5 respectively (Supplementary Table 3). The longest such read for each case is shown.

Extended Data Fig. 3 HAdV and AAV2 sequence analysis.

a, HAdV SNP plot: Visualisation of the multiple alignment of HAdV-F41 genomic sequences from the same clade as the single sequence from a case (highlighted in grey) (Fig. 3a). Includes both contemporary controls and publicly available HAdV-F41 genomes from GenBank. Consensus-level mutations differing from the reference sequence (bottom) are highlighted across the genome. Genomic position of the mutation is shown at the top of the plot. **b**, Variants between stool complete HAdV genome from case JBB27 and combined blood partial genomes from other cases. **c**, Frequency table of capsid residues in cases and historical controls. There is no difference between the capsid sequences of cases and contemporaneously circulating controls. However, there are changes compared with historical controls in all contemporary sequences. None of the recently acquired capsid changes are shared with known hepatotrophic strains in AAV7, 8 and 9. **d**, Amino acid differences between AAV2 capsid sequences from cases, contemporaneously circulating controls and historical publicly available sequences compared with the AVV2 reference sequence NC_001401.2. Also shown are the capsid sequences from known AAV7, 8 and 9 hepatotropic capsids compared to the reference sequence NC_001401.2.

Extended Data Fig. 4 AAV2 capsid analysis.

a, Amino acid sequence of novel AAV capsid variant. The consensus sequence of the VP1 sequence used for investigation of capsid transduction characteristics (AAVHepcase) is shown with alignment to canonical AAV2 VP1 (AAV2gp05). The alignment shows AAV2 amino acids that are different to the AAVHepcase sequence, with dots indicating matched amino acids sequence. **b**, In vitro analysis of AAV capsid transduction characteristics. Huh-7 hepatocytes were treated at MOI 100,000 with rAAV vectors containing capsid sequences derived from canonical AAV2, a consensus sequence derived from patient sequencing samples (Hepcase), LK03, or AAV9 (n = 3 each treatment). Transduction efficiency was determined by flow cytometry, based on the percentage of EGFP-positive cells, the EGFP fluorescence intensity in positive cells, and the ‘relative activity’ of EGFP expression (calculated by multiplying %GFP-positive cells by MFI/10070). Transductions were performed in the presence or

absence of 400 µg/mL heparin to investigate the role of HSPG interaction. rAAV2 was significantly affected by heparin competition, whereas other capsids, including that derived from AAV Hepcase, were not. Heparin competition significantly affected rAAV2 transduction in terms of percentage of GFP-positive cells ($P = 0.0016$), MFI ($P = 0.000008$), and relative activity ($P = 0.000008$), whereas other capsids, including that derived from AAV Hepcase, were not affected by heparin. All data were analysed by 2-sided t-test with Bonferroni post-hoc analysis. Error bars indicate standard deviation from the mean value. **c**, Images of Huh-7 cells treated with rAAV vectors *in vitro*. Images of transduced Huh-7 cells. Each cell population was treated with MOI 100,000 of the relevant viral vector, in the presence or absence of 400 µg/mL heparin and analysed by EGFP fluorescence 72-hours post-transduction. Scale bars = 300 µm.

Extended Data Fig. 5 Representative histology of case livers.

a & b, H&E sections x100 and x200 showing a pattern of acute hepatitis with parenchymal disarray, there is a normal, uninflamed, portal tract lower left image **a**. Spotty inflammation and apoptotic bodies are shown in **b** along with perivenular hepatocyte loss/necrosis. Immunohistochemistry shows fewer mature B lymphocytes (CD20 panel **c**) than T lymphocytes (CD3, panel **d**, pan T cell marker) most of which are cytotoxic CD8 lymphocytes (panel **e**). In conclusion the livers of these children have a distinctive pattern of damage which does not indicate a specific aetiology, it does not exclude but does not offer positive support for either autoimmune hepatitis or a direct cytopathic effect of virus on hepatocytes. Each image shows a representative result from histology carried out on a minimum of five cases.

Extended Data Fig. 6 Immunohistochemistry results for cases of unexplained hepatitis and control tissues.

a, Inflammatory markers (IgG, C4d, HLA-ABC, HLA-DR) in acute hepatitis cases and control liver. IgG, HLA-ABC and HLA-DR show a canalicular pattern in the control liver. This pattern is disrupted in the acute hepatitis cases due to the architectural collapse. In addition, there is increased staining associated with inflammatory cell/macrophage infiltrates.

C4d shows very weak staining in the acute hepatitis cases associated with macrophages but with without endothelial staining. All stains were undertaken on 5 affected cases and 13 control cases. **b**, Representative images of the immunohistochemistry (IHC). Acute hepatitis liver explant cases stained for HHV6, arrow shows staining of **A** representative cells, **B** adenovirus, AAV2 (**C** polyclonal antibody, **E** monoclonal antibody, clone A1). Paraffin embedded AAV2 transfected cell lines stained as positive controls for AAV2 (**D** polyclonal antibody, **F** monoclonal antibody, clone A1). All scale bars are 60 micrometres. HHV6, AAV2 (polyclonal) stains were undertaken on 15 affected cases and 13 controls. AAV2 (A1) stains were undertaken on 5 affected cases and 13 control cases. Staining for adenovirus was undertaken on 5 affected cases.

Extended Data Fig. 7 Cytokine inducible transcriptional modules.

Volcano plot of cytokine inducible transcriptional modules (n = 52) comparing their Z score expression in AAV2-associated hepatitis (n = 4) and HBV-associated hepatitis (n = 17) requiring transplantation using two-tailed unpaired t tests with Holm Sidak multiple testing correction for adjusted p values (n refers to number of patients). Each point represents a specific module listed in full in Supplementary Table 13. Labels for selected modules are shown.

Extended Data Fig. 8 HLA and HHV-6B proteins in case livers.

a & b Ranking of the quantified proteins using the log10 of iBAQ values for **a** JBL1, **b** JBL2, **c** JBL3, **d** JBL4, **e** JBL5. **f**, Scatter plot of quantified proteins in sample JBL4 versus JBL5. HLA proteins are highlighted in red. Red arrows denote HLA-DRB1 proteins. HHV6 proteins are highlighted in green and marked with green arrows.

Extended Data Table 1 PCR and whole genome sequencing for samples from cases where metagenomic sequencing was not performed

Extended Data Table 2 Controls and comparators

Supplementary information

Reporting Summary

Peer Review File

Supplementary Table 1

Clinical details of cases. 12 transplanted cases, 26 non-transplanted. Median age of cases where exact age is known is 3 years, with range 1.5-9. Case 10 was 9 years old. All other cases were aged 7 or under. Of 22 cases where the gender is known, 12 cases were female and 10 were male. Where known, all cases were of white ethnicity other than two.

Supplementary Table 2

Metagenomics summary statistics: raw read counts, human filtered and other findings. F: sequencing failed.

Supplementary Table 3

Nanopore sequencing. All four samples were sequenced to a lower depth. Case 3 and 5 underwent a second round of deeper sequencing. N50s across all sequencing runs were similar.

Supplementary Table 4

Clinical details for PERFORM/DIAMONDS immunocompetent controls and microbiological testing by referring laboratory for DIAMONDS controls. P: positive, N: negative, IC: inconclusive, VL: viral load.

Supplementary Table 5

PCR Results. Not all samples were tested for all viruses due to lack of remaining material. LLP: low level positive (Ct value > 38 and < 45), ND:

not determined (negative PCR results), NA: not tested due to lack of material.

Supplementary Table 6

Clinical details of liver controls and comparators

Supplementary Table 7

HAdV whole genome sequencing. OTR: on target reads, MRD: mean read depth, Coverage 1X: percentage of genome covered at depth 1, Coverage 30X: percentage of genome covered at depth 30.

Supplementary Table 8

Mapping of HAdV partial sequences.

Supplementary Table 9

AAV2 whole genome sequencing: OTR: on target reads, MRD: mean read depth, Coverage 1X: percentage of genome covered at depth 1, Coverage 10X: percentage of genome covered at depth 10.

Supplementary Table 10

HHV-6B whole genome sequencing from liver case samples. OTR: on target reads, MRD: mean read depth, Coverage 1X: percentage of genome covered at depth 1, Coverage 10X: percentage of genome covered at depth 10.

Supplementary Table 11

Cytokine modules - cytokine-inducible transcriptional signatures of cell-mediated immunity.

Supplementary Table 12

Summary statistics for multiple comparisons of cytokine transcriptional modules. Two-tailed unpaired t-tests with Holm Sidak multiple testing correction for adjusted p values were performed.

Supplementary Table 13

List of differentially expressed proteins between 5 cases and 7 controls. The p-values were calculated by applying two-tailed empirical Bayes moderated t-statistics on protein-wise linear models. P values were not adjusted for multiple comparisons.

Supplementary Table 14

List of differentially expressed peptides between 5 cases and 7 controls. The p-values were calculated by applying two-tailed empirical Bayes moderated t-statistics on peptide-wise linear models. P values were not adjusted for multiple comparisons.

Supplementary Table 15

HLA allele frequency of cases.

Rights and permissions

Open Access This article is licensed under a Creative Commons Attribution 4.0 International License, which permits use, sharing, adaptation, distribution and reproduction in any medium or format, as long as you give appropriate credit to the original author(s) and the source, provide a link to the Creative Commons licence, and indicate if changes were made. The images or other third party material in this article are included in the article's Creative Commons licence, unless indicated otherwise in a credit line to the material. If material is not included in the article's Creative Commons licence and your intended use is not permitted by statutory regulation or exceeds the permitted use, you will need to obtain permission directly from the copyright holder. To view a copy of this licence, visit http://creativecommons.org/licenses/by/4.0/.

Reprints and Permissions

About this article

Cite this article

Morfopoulou, S., Buddle, S., Torres Montaguth, O.E. *et al.* Genomic investigations of unexplained acute hepatitis in children. *Nature* **617**, 564–573 (2023). https://doi.org/10.1038/s41586-023-06003-w

- Received: 25 July 2022
- Accepted: 23 March 2023
- Published: 30 March 2023
- Issue Date: 18 May 2023
- DOI: https://doi.org/10.1038/s41586-023-06003-w

Share this article

Anyone you share the following link with will be able to read this content:

Get shareable link

Sorry, a shareable link is not currently available for this article.

Copy to clipboard

Provided by the Springer Nature SharedIt content-sharing initiative

This article is cited by

- **Adeno-associated virus type 2 in US children with acute severe hepatitis**

- Venice Servellita
- Alicia Sotomayor Gonzalez
- Charles Y. Chiu

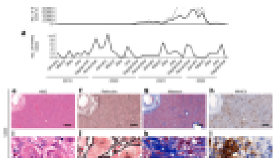
Nature (2023)

Severe hepatitis outbreak in children linked to AAV2 virus

- Frank Tacke

Nature News & Views 30 Mar 2023

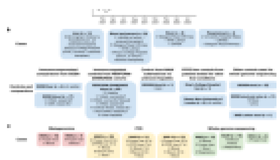
This article was downloaded by **calibre** from https://www.nature.com/articles/s41586-023-06003-w



Adeno-associated virus 2 infection in children with non-A–E hepatitis

30 March 2023

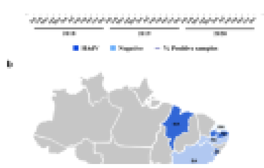
Antonia Ho, Richard Orton, … Emma C. Thomson



Genomic investigations of unexplained acute hepatitis in children

30 March 2023

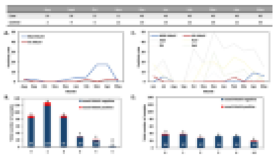
Sofia Morfopoulou, Sarah Buddle, … Judith Breuer



Human enteric adenovirus F40/41 as a major cause of acute gastroenteritis in children in Brazil, 2018 to 2020

02 July 2022

Lilian Gonçalves do Nascimento, Alexandre Madi Fialho, … Tulio Machado Fumian



[A Spanish case-control study in <5 year-old children reveals the lack of association between MLB and VA astrovirus and diarrhea](#)

04 February 2020

Diem-Lan Vu, Aurora Sabrià, … Susana Guix



[Genomic analyses of human adenoviruses unravel novel recombinant genotypes associated with severe infections in pediatric patients](#)

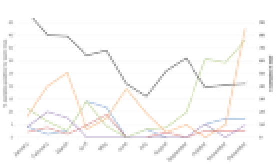
15 December 2021

Joyce Odeke Akello, Richard Kamgang, … Alban Ramette

[Seroprevalence of hepatitis E virus in risk populations and blood donors in a referral hospital in the south of Brazil](#)

16 March 2021

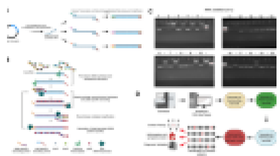
Marisa Boff Costa, Michele Soares Gomes Gouvêa, … Mário Reis Álvares-da-Silva



[Children Attending Day Care Centers are a Year-round Reservoir of Gastrointestinal Viruses]

01 March 2019

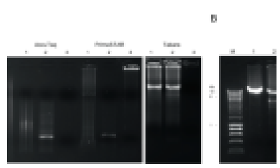
Betina Hebbelstrup Jensen, Pikka Jokelainen, … Karen A. Krogfelt



[Mass COVID-19 patient screening using UvsX and UvsY mediated DNA recombination and high throughput parallel sequencing]

08 March 2022

Dario Palmieri, Amanda Javorina, … Wayne O. Miles



[Amplification and next generation sequencing of near full-length human enteroviruses for identification and characterisation from clinical samples]

08 August 2018

Sonia R. Isaacs, Ki Wook Kim, … Maria E. Craig

- Article
- Published: 30 March 2023

Adeno-associated virus type 2 in US children with acute severe hepatitis

- Venice Servellita,
- Alicia Sotomayor Gonzalez,
- Daryl M. Lamson,
- Abiodun Foresythe,
- Hee Jae Huh,
- Adam L. Bazinet,
- Nicholas H. Bergman,
- Robert L. Bull,
- Karla Y. Garcia,
- Jennifer S. Goodrich,
- Sean P. Lovett,
- Kisha Parker,
- Diana Radune,
- April Hatada,
- Chao-Yang Pan,
- Kyle Rizzo,
- J. Bradford Bertumen,
- Christina Morales,
- Paul E. Oluniyi,
- Jenny Nguyen,
- Jessica Tan,
- Doug Stryke,
- Rayah Jaber,
- Matthew T. Leslie,
- Zin Lyons,
- Hayden D. Hedman,
- Umesh Parashar,
- Maureen Sullivan,
- Kelly Wroblewski,
- M. Steven Oberste,
- Jacqueline E. Tate,
- Julia M. Baker,

- David Sugerman,
- Caelin Potts,
- Xiaoyan Lu,
- Preeti Chhabra,
- Pediatric Hepatitis of Unknown Etiology Working Group,
- L. Amanda Ingram,
- Henry Shiau,
- William Britt,
- Luz Helena Gutierrez Sanchez,
- Caroline Ciric,
- Christina A. Rostad,
- Jan Vinjé,
- Hannah L. Kirking,
- Debra A. Wadford,
- R. Taylor Raborn,
- Kirsten St. George &
- …
- Charles Y. Chiu

Show authors

Nature **volume 617**, pages 574–580 (2023)

- 9592 Accesses
- 1 Citations
- 970 Altmetric
- Metrics details

Abstract

As of August 2022, clusters of acute severe hepatitis of unknown aetiology in children have been reported from 35 countries, including the USA[1,2]. Previous studies have found human adenoviruses (HAdVs) in the blood from patients in Europe and the USA[3,4,5,6,7], although it is unclear whether

this virus is causative. Here we used PCR testing, viral enrichment-based sequencing and agnostic metagenomic sequencing to analyse samples from 16 HAdV-positive cases from 1 October 2021 to 22 May 2022, in parallel with 113 controls. In blood from 14 cases, adeno-associated virus type 2 (AAV2) sequences were detected in 93% (13 of 14), compared to 4 (3.5%) of 113 controls ($P < 0.001$) and to 0 of 30 patients with hepatitis of defined aetiology ($P < 0.001$). In controls, HAdV type 41 was detected in blood from 9 (39.1%) of the 23 patients with acute gastroenteritis (without hepatitis), including 8 of 9 patients with positive stool HAdV testing, but co-infection with AAV2 was observed in only 3 (13.0%) of these 23 patients versus 93% of cases ($P < 0.001$). Co-infections by Epstein–Barr virus, human herpesvirus 6 and/or enterovirus A71 were also detected in 12 (85.7%) of 14 cases, with higher herpesvirus detection in cases versus controls ($P < 0.001$). Our findings suggest that the severity of the disease is related to co-infections involving AAV2 and one or more helper viruses.

Main

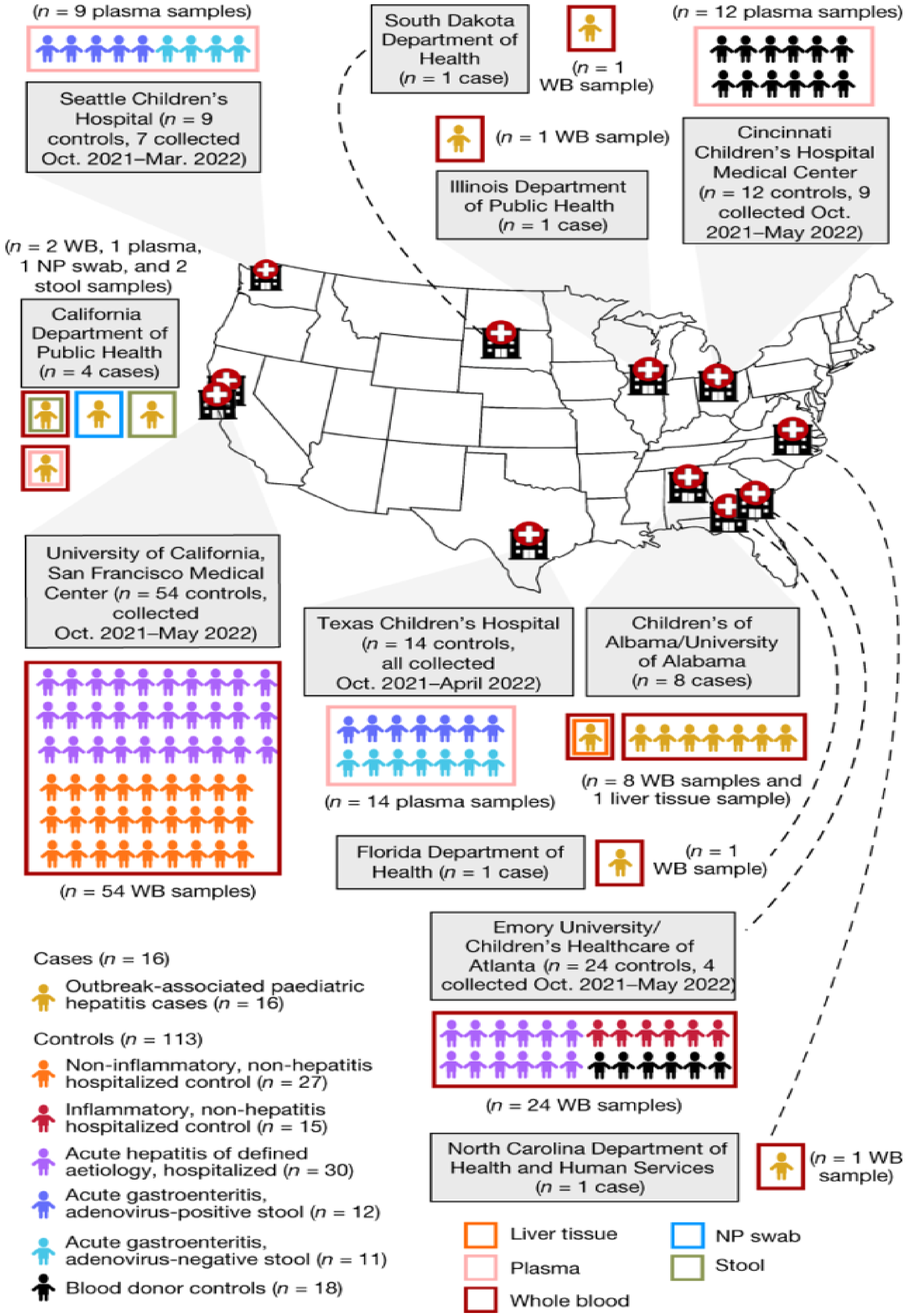
Viral hepatitis is an inflammation of the liver most commonly caused by one of the main hepatitis viruses (A–E). Since October 2021, clusters of acute non-A–E severe hepatitis of unknown aetiology in children have been reported in 35 countries, including the USA[1,2]. As of 17 August 2022, 358 people under investigation have been reported in the USA, of whom 22 (6%) required a liver transplant and 13 (4%) died[8].

HAdVs are non-enveloped, double-stranded DNA viruses that cause a variety of infections in both adults and children, including respiratory tract infection, conjunctivitis and gastroenteritis (mainly from HAdV type 40 (HAdV-40) and HAdV-41)[9]. Although a potentially life-threatening disease in immunocompromised patients[7,9], hepatitis from adenovirus infection has been thought to be rare in immunocompetent children without underlying comorbidities[10]. HAdVs, particularly HAdV-41, have been found in blood from clusters of acute severe hepatitis cases from Scotland, the UK and the USA[3,4,5,6,7], but whether the virus is causative remains unclear. Adeno-associated viruses (AAVs) are small, single-stranded DNA parvoviruses that are considered non-pathogenic in humans and for this reason have been

widely used as vectors for gene therapy[11]. Importantly, AAVs require a helper virus, such as a herpesvirus or adenovirus, for productive infection of liver tissue[12]. AAVs have previously been reported in children with acute severe hepatitis in a study of nine patients from the UK[13], often in association with adenovirus or human herpesvirus 6 (HHV-6) infection[14].

In this study, 27 samples (21 whole blood, 2 plasma, 1 liver tissue, 1 nasopharyngeal swab and 2 stool sample(s)) from 16 children with acute severe hepatitis of unknown aetiology were analysed (Fig. 1). All children met the clinical case definition established by the Centers for Disease Control and Prevention, including lack of a confirmed aetiology, liver enzyme levels (aspartate aminotransferase (AST) or alanine aminotransferase (ALT)) >500 U l^{-1}, age < 10 years and onset on or after 1 October 2021 (refs. [2,15]). Cases were enrolled from six states (Alabama, California, Florida, Illinois, North Carolina, and South Dakota) from 1 October 2021 to 22 May 2022. All 16 cases had positive testing for HAdV from blood, and thus HAdV infection was over-represented compared to the overall affected population, of which HAdV is detected in 45–90% (refs. [3,4,5,6,7]). The median age of affected children was 3 years; 56% were female and 44% male (Table 1). Mean elevations in ALT and AST were 2,293 ± 1,486 U l^{-1} (normal range: 4–36 U l^{-1}) and 2,652 ± 1,851 U l^{-1} (normal range: 8–33 U l^{-1}), respectively (Supplementary Table 1). A liver biopsy was carried out in eight patients; viral PCR testing of the liver biopsies for HAdVs, herpesviruses, enteroviruses and severe acute respiratory syndrome coronavirus 2 (SARS-CoV-2) was incomplete, but yielded positive results for HAdV in three patients with no other viruses detected (Fig. 2b and Supplementary Table 1). Two children underwent liver transplantation, but none died from complications of liver failure.

Fig. 1: Epidemiology of cases and controls.

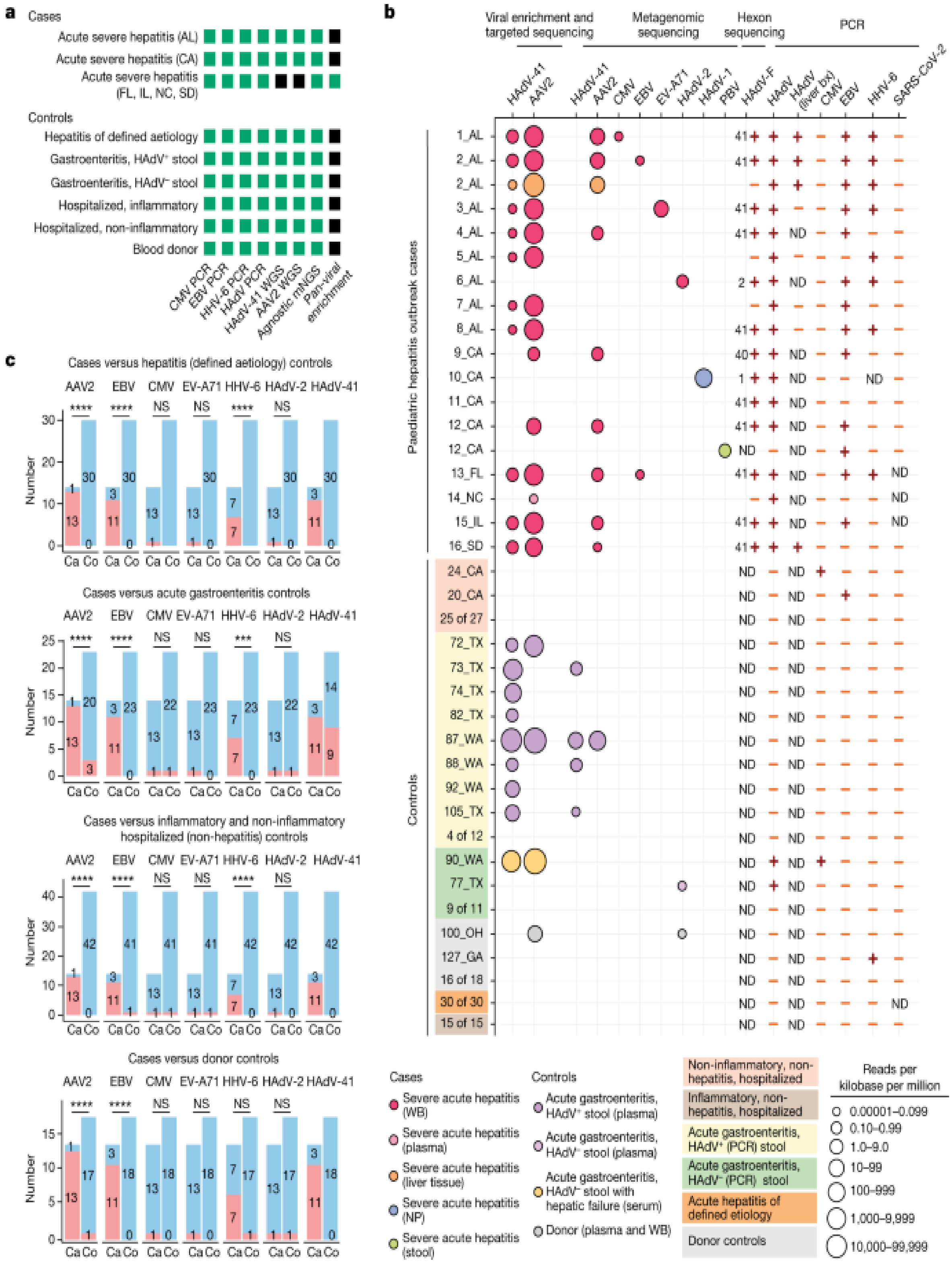


(n = 9 plasma samples)
Seattle Children's Hospital (n = 9 controls, 7 collected Oct. 2021–Mar. 2022)
South Dakota Department of Health (n = 1 case)
(n = 1 WB sample)
(n = 12 plasma samples)
(n = 1 WB sample)
Illinois Department of Public Health (n = 1 case)
Cincinnati Children's Hospital Medical Center (n = 12 controls, 9 collected Oct. 2021–May 2022)
(n = 2 WB, 1 plasma, 1 NP swab, and 2 stool samples)
California Department of Public Health (n = 4 cases)
University of California, San Francisco Medical Center (n = 54 controls, collected Oct. 2021–May 2022)
(n = 54 WB samples)
Texas Children's Hospital (n = 14 controls, all collected Oct. 2021–April 2022)
(n = 14 plasma samples)
Children's of Albama/University of Alabama (n = 8 cases)
(n = 8 WB samples and 1 liver tissue sample)
Florida Department of Health (n = 1 case)
(n = 1 WB sample)
Emory University/ Children's Healthcare of Atlanta (n = 24 controls, 4 collected Oct. 2021–May 2022)
(n = 24 WB samples)
North Carolina Department of Health and Human Services (n = 1 case)
(n = 1 WB sample)
Cases (n = 16)
Outbreak-associated paediatric hepatitis cases (n = 16)
Controls (n = 113)
Non-inflammatory, non-hepatitis hospitalized control (n = 27)
Inflammatory, non-hepatitis hospitalized control (n = 15)
Acute hepatitis of defined aetiology, hospitalized (n = 30)
Acute gastroenteritis, adenovirus-positive stool (n = 12)
Acute gastroenteritis, adenovirus-negative stool (n = 11)
Blood donor controls (n = 18)
Liver tissue
Plasma
Whole blood
NP swab
Stool

Geographic distribution of the 16 acute severe hepatitis cases and 113 controls in the study, showing the hospital or public health laboratory sites providing samples and associated clinical data from cases and/or controls. WB, whole blood; NP, nasopharyngeal.

Table 1 Demographic and clinical characteristics of cases and controls

Fig. 2: Sequencing and molecular-based testing for viruses carried out on cases and controls.



a, Analyses carried out on the different sample groups. The specific assays carried out for each group are shown in green whereas assays that were not

carried out are shaded in black. WGS, whole-genome sequencing. mNGS, metagenomic next-generation sequencing. **b**, Graphical chart showing results of sequencing or PCR-based assays for virus detection. Each circle represents a sequenced sample with at least three non-overlapping reads[29] aligning to a viral reference sequence. Circles are colour-coded on the basis of sample type and scaled according to normalized viral read counts. Viral PCR positive and negative results are denoted by plus and minus symbols, respectively. For the HAdV-F PCR, the HAdV subtype identified by hexon sequencing is shown to the left of the viral PCR result. PBV, picobirnavirus; bx, biopsy; ND, not determined. **c**, Associations between viruses detected in blood and cases of acute severe hepatitis of unknown aetiology in children. Red and blue shading indicate positive and negative detection, respectively. Uncorrected P values were calculated using two-tailed Fisher's exact test. A Bonferroni-corrected significance level of $P < 0.002$ was considered significant ($n = 24$ comparisons). Exact P values are provided in Supplementary Table 2. Ca, cases; Co, controls; AL, Alabama; CA, California; FL, Florida; GA, Georgia; IL, Illinois; NC, North Carolina; OH, Ohio; SD, South Dakota; TX, Texas; WA, Washington; NS, not significant; ***$P < 0.001$; ****$P < 0.0001$.

Controls ($n = 113$) consisted of 78 whole blood, 1 serum and 34 plasma samples. Many controls were enrolled from California ($n = 54$) and Georgia ($n = 24$) to be geographically similar to the cases, with the remaining controls enrolled from Ohio ($n = 12$), Texas ($n = 14$) and Washington ($n = 9$). Of the 113 controls, 69 (61.0%) were collected over the same time frame as that for the cases (that is, collected between 1 October 2021 and 22 May 22). The 113 controls consisted of 42 patients (37%) without hepatitis, 30 (26.5%) patients with acute hepatitis (ALT > 100 U l^{-1}) of defined aetiology, 23 (21%) patients with acute gastroenteritis (12 with positive HAdV stool testing) and 18 (16%) blood donors. Differences in age and sex between cases and controls were non-significant overall, although cases were significantly younger and older, respectively, than controls with hepatitis of defined aetiology and those with acute gastroenteritis (Table 1). Among reported symptoms, only jaundice was significantly more associated with cases than controls (Table 1). Mean elevations in ALT and AST in the 30 hepatitis controls were 291 ± 288 U l^{-1} and 455 ± 833 U l^{-1}, respectively, and

significantly lower than in cases ($P < 0.0001$; Table 1 and Supplementary Table 1).

Virus detection in hepatitis cases

Metagenomic sequencing for agnostic detection of all viruses[16], tiling multiplex PCR amplicon sequencing for AAV2 and HAdV-41 (ref. [17]), metagenomic sequencing with probe capture viral enrichment[18] and virus-specific polymerase chain reaction (PCR) testing for HAdV with genotyping by hexon gene sequencing were carried out to identify AAV2 and HAdV viruses in clinical samples from cases (Fig. 2a). We detected AAV2 from available whole-blood or plasma samples in 13 (93%) of 14 cases and confirmed detection of HAdV in all 14 cases (Fig. 2b). Of the 14 cases, 10 (71%) were typed as HAdV-41, 1 (7%) was typed as HAdV-40, and 1 (7%) was typed as HAdV-2; 1 (7%), sample NC_14, was untypable. AAV2 and HAdV-41 enrichment were carried out using either tiled multiplex PCR amplicon sequencing targeting the genomes of HAdV-41 and AAV ($n = 9$ samples, with a mean 6.6 ± 1.5 (s.d.) million raw reads generated per sample) or probe capture viral enrichment targeting 3,153 species ($n = 4$, with a mean 128 ± 34 (s.d.) million raw reads generated per sample). Mean normalized viral counts expressed as reads per kilobase per million mapped reads for AAV2 (\(\bar{x}\) = 4,063) were approximately 12.7 times greater than for HAdV-41 (\(\bar{x}\) = 320; Supplementary Table 1). AAV2 was detected in both liver tissue and whole blood from one case and in one of two plasma samples, but neither AAV2 nor HAdV-41 were detected in nasopharyngeal swab and stool samples. No reads from AAVs other than AAV2 were detected, despite using methods that would enrich for other AAV subtypes. Among the four cases analysed using metagenomic sequencing with probe capture viral enrichment (13_FL, 14_NC, 15_IL and 16_SD), Epstein–Barr virus (EBV) was also detected in the blood sample from 13_FL.

Metagenomic sequencing was less sensitive than viral enrichment and targeted sequencing for detection of AAV2 (8 of 14 cases, 57%) and HAdV-41 (0 of 13 cases, 0%; Fig. 2b and Supplementary Table 1). However, reads from additional viruses were identified including EBV ($n = 2$), cytomegalovirus (CMV; $n = 1$), HAdV-2 (adenovirus type C; $n = 1$) and

enterovirus A71 (EV-A71; $n = 1$) from whole blood, HAdV-1 (adenovirus type C; $n = 1$) from nasopharyngeal swab, and picobirnavirus ($n = 1$) from stool. EV-A71 was detected as a co-infection in an HAdV-41–AAV2 case, and HAdV-2 was detected in the single AAV2-negative case.

Among the 113 controls, AAV2 was detected in 4 (3.5%), including 2 (16.7%) of 12 children with acute HAdV-positive gastroenteritis, 1 (9.1%) of 11 hospitalized children with HAdV-negative gastroenteritis, and 1 donor control who was also positive for HAdV (Fig. 2b and Supplementary Table 1). The AAV2-positive child with HAdV-negative gastroenteritis was HAdV-negative from stool but both HAdV41-positive and CMV-positive from blood and had been discharged from the hospital with liver failure (although additional clinical details were not available). Of note, neither AAV2 nor HAdV-41 was detected among the 30 paediatric controls with acute hepatitis of defined aetiology and 42 hospitalized children without hepatitis.

We next carried out virus-specific PCR testing for EBV, CMV, HHV-6 and SARS-CoV-2 for all available cases and controls (Fig. 2b and Supplementary Table 1). EBV and HHV-6 were detected from blood in 11 (79%) of 14 and 7 (50%) of 14 cases, respectively, versus 1 (0.88%) of 113 controls for each virus. No tested cases were positive for CMV compared to 2 (1.8%) of 113 controls. SARS-CoV-2 was not detected in blood from cases or controls (Fig. 2b), or in liver biopsy tissue (Supplementary Table 1).

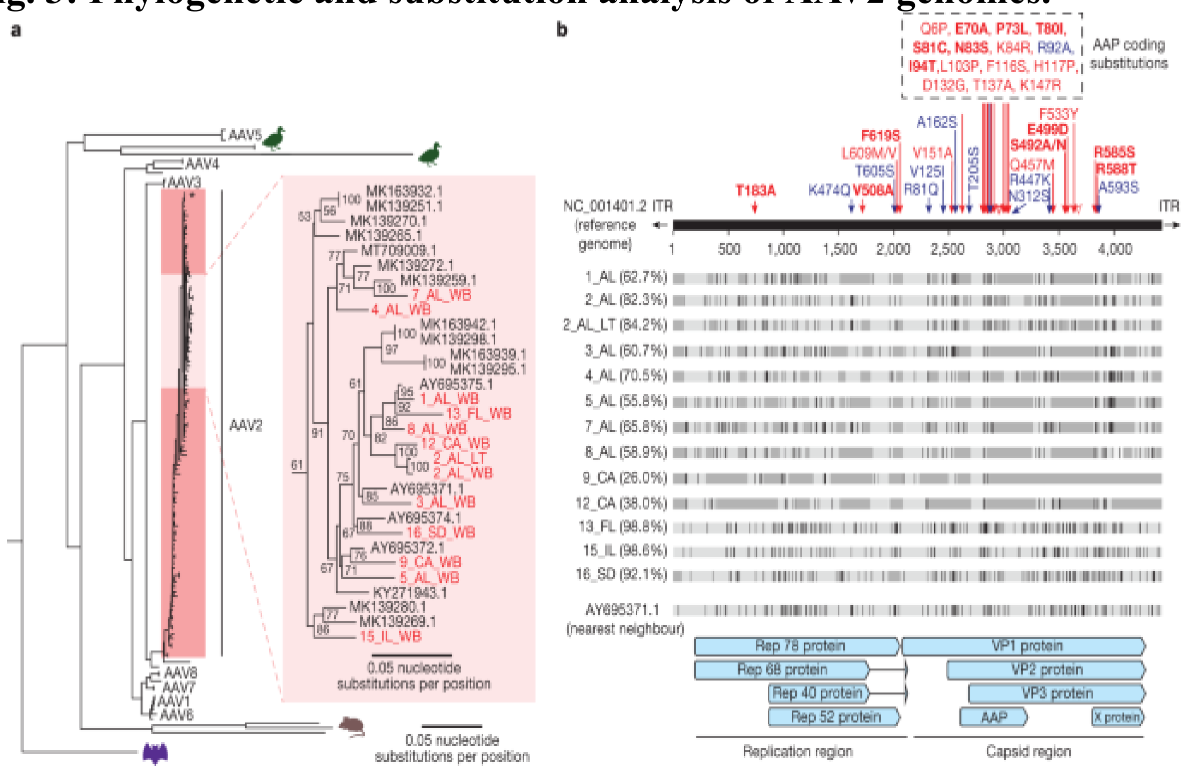
Virus associations with hepatitis cases

We used Fisher's exact test on cases ($n = 14$) and controls to investigate associations between detected viruses in blood and cases of acute severe hepatitis. Controls were stratified into four groups for comparison against cases (Fig. 2c and Supplementary Table 2). Three viruses, AAV2, EBV and HHV-6, were significantly associated with cases when compared to each control group, except for HHV-6 detection between cases and donors ($P = 0.010$, Bonferroni-corrected significance level of $P < 0.002$). As all 14 cases were known to be HAdV-positive a priori, statistical analysis was not carried out for HAdV-41.

Phylogenetic and substitution analyses

We carried out multiple sequence alignment and phylogenetic analysis of 13 recovered AAV2 genomes from 12 cases with >25% breadth of coverage (Fig. 3 and Extended Data Fig. 1). Multiple sequence alignment was carried out in parallel with all complete 119 AAV2 reference genomes deposited in GenBank as of 18 August 2022. A whole-genome nucleotide phylogenetic tree revealed that the 13 genomes were located within a distinct subgroup of a large human-infecting AAV2 clade (Fig. 3a). Other previously sequenced AAV2 genomes from France and the USA from patients without hepatitis were also found within this subgroup. Amino acid phylogenetic trees of the VP1 protein and the assembly-activating protein (AAP) showed slightly different topologies (Supplementary Fig. 1), but the 13 genomes were still positioned within a distinct subgroup.

Fig. 3: Phylogenetic and substitution analysis of AAV2 genomes.



a, Phylogenetic tree of 119 AAV2 genomes available from GenBank as of 18 August 2022. The 12 recovered genomes from this study with >25% coverage are denoted in red. The location of the AAV2 reference genome (NC_001401.2) is marked with a black asterisk. The phylogenetic tree was

constructed by multiple sequence alignment of the AAV genomes or amino acid sequences using the MAFFT algorithm[30], followed by maximum-likelihood-based tree construction using IQ-TREE[31]. **b**, Multiple sequence alignment of 13 AAV2 genomes recovered from cases. Nucleotide mismatches are represented by black-coloured vertical lines, whereas areas of missing coverage are represented by dark grey rectangles. Amino acid variants with respect to the reference genome (NC_001401.2) are denoted in blue and red arrows; red arrows indicate shared substitutions that were reported in another study from the UK and Scotland[14]. Substitution sites that were identified in 100% of cases with sufficient coverage in both studies are highlighted in bold red text. ITR, inverted terminal repeat.

To explore the underlying basis behind the observed phylogenetic clustering, we carried out multiple sequence alignment of the 13 genomes from cases. We then searched for shared coding substitutions relative to the AAV2 reference genome that were found in ≥50% of genomes with coverage at that substitution site. This analysis yielded 35 substitutions that were unevenly distributed across the viral genome, with 15 of 35 (42.9%) in the AAP, 14 of 35 (40%) in the VP1 protein, and 6 of 35 (17.1%) in the Rep78 protein (Fig. 3b and Supplementary Table 3). Clusters of substitutions were found to be located within hypervariable regions of the capsid VP1 and AAP proteins[13]. Of note, 25 (71.4%) of the 35 substitutions were shared with those identified in an independent study of severe paediatric hepatitis from the UK[14].

Discussion

Here we report virus findings from PCR, metagenomic and targeted sequencing of samples from 16 paediatric cases of acute severe hepatitis of unknown aetiology that were first identified in the USA in October 2021. After combining these three diagnostic modalities, AAV2 was detected in 93% (13 of 14) of cases for whom wholeblood or plasma samples were available ($P < 0.001$). Conversely, AAV2 was detected in only 4 (3.5%) of 113 controls and HAdV-41 was detected in 9 (8%) of 113. Notably, AAV2 was not detected in whole blood from 30 paediatric controls with hepatitis of defined aetiology. HAdV sequences were detected in all 14 cases, of which 11 (79%) were genotyped as HAdV-41. The 100% detection rate of HAdV is expected given that all 14 cases were known to be HAdV positive by clinical

testing a priori. Other co-infecting viruses, including EBV and HHV-6, were detected by PCR in many cases but rarely in controls ($P < 0.001$); EV-A71 was also detected by metagenomic sequencing in one case but not in any control. Taken together, these findings show a significant association between co-infection by AAV2 and one or more hepatotropic viral pathogens and the clinical manifestations of severe acute hepatitis, although a direct causal link has yet to be confirmed.

Initial epidemiological investigation and molecular testing have found adenovirus in 45–90% of severe acute hepatitis cases[3,4,5,6,7]. In the UK, 116 of 179 (64.8%) reported cases as of May 2022 have tested positive for HAdV (ref. [1]). This is in comparison to 8 of 9 (88.9%) positive cases in the USA corresponding to a cluster of cases who presented at a children's hospital in Alabama between October 2021 and March 2022 (ref. [5]), for which there is a substantial overlap with cases from our study. An expanded national investigation in the USA detected HAdV in slightly less than half (44.6%) of cases[3]. Consistent with previous reports[5,14], HAdV genotyping of our cases by sequencing confirmed that most of the detected serotypes were HAdV-41 (11 of 14, 79%).

Our results suggest that co-infection with AAV2 may cause more severe liver disease than infection by an adenovirus and/or herpesvirus alone. This condition may be analogous to the fulminant liver failure that can occur when hepatitis D virus (HDV, 'delta') infection is superimposed on a chronic hepatitis B virus (HBV) infection[19]. Notably, AAV2 was seen in only 2 (16.7%) of 12 paediatric controls with HAdV-associated acute gastroenteritis in the absence of liver inflammation, suggesting that co-infection with AAV2 may predispose patients to more severe disease. Here we also found that in cases of AAV2–HAdV co-infection, viral loads for AAV2 were higher than for HAdV, with an approximately 12.7× increase in mean normalized read counts by targeted sequencing. This observation may be partially explained by previously published data showing that AAVs can suppress the replication of other hepatotropic viruses, including adenoviruses and herpesviruses[12]. Similarly, patients co-infected with HDV usually exhibit low HBV viral loads owing to suppression of HBV replication by HDV-induced interferons[20].

Among the AAVs, AAV2 is the most well-characterized AAV and has been shown to replicate to high titres in the liver and spleen[11]. Seroprevalence data from infants, children and adults demonstrate that 30–80% of the general population is seropositive and that natural infection with AAV can occur at all ages[21]. However, there is a peak of AAV2 infection between the ages of 1 to 5 years old[22], consistent with the observed distribution of ages of cases in the current study.

Phylogenetic analysis reveals that the recovered AAV2 genomes from all cases map to a distinct subclade. The positioning is driven by groups of substitutions located within hypervariable regions of the capsid VP1 and AAP proteins[13]. Notably, two of these substitutions in the VP1 protein, R585S and R588T, are arginine-to-serine and arginine-to-threonine substitutions that probably impact receptor binding, as these residues are necessary for the interaction of AAV2 with its heparan sulfate proteoglycan receptor[23]. These are not only shared among the US genomes in the current study but also overlap substantially with the substitutions found in an independent study of acute severe hepatitis cases in children from the UK[14]. Notably, several of these shared capsid substitutions (V151A, Q457M, S492A, E499D, F533Y, R585S and R588T) are also found in a sublineage of AAV2 (AAVv66) that exhibits increased replication, virion stability, central nervous system transduction and evasion of neutralizing antibodies relative to wild-type AAV2 (ref. [24]). However, as other contemporary AAV2 genomes are not readily available, it is unclear whether the relatedness in AAV2 genomes across geographically dispersed regions and to AAVv66 merely represents detection of a predominant global circulating strain.

In the current study, hepatotropic viruses other than HAdV, including EBV, HHV-6 and EV-A71, were detected, albeit in a smaller proportion of cases. Infection by EBV or HHV-6 alone has been implicated in cases of liver failure requiring transplantation[25,26]. However, although we found substantial differences in the relative proportions of EBV and HHV-6 in cases compared to controls, we do not believe it likely that these viruses are the primary cause of acute severe hepatitis in these children. First, the viral loads for these herpesviruses were very low, with median PCR cycle threshold (C_t) values of 38.1 and 38 for EBV and HHV-6, respectively, and thus the borderline positive PCR results may represent detection of

integrated proviral DNA rather than bona fide low-level herpesvirus viraemia. Second, herpesvirus reactivation can be seen in various cytokine-associated inflammatory conditions such as coronavirus disease 2019 (COVID-19)[27], and whether such reactivation contributes to disease pathogenesis is unclear. Third, herpesviruses were not detected in available liver biopsy tissue from cases, and the only viruses detected were HAdV (two of six, 33%) and AAV2 (one of one, 100%). Nevertheless, it is striking that among the 16 cases, triple or quadruple infections with AAV2, adenovirus, EBV and/or HHV-6 were detected in whole blood from at least 12 cases (75%). We postulate that the COVID-19 pandemic and more than 2 years of school and childcare closures and decreased social interactions with other children may have generated a vulnerable population of young children who failed to develop broad immunity to common viral pathogens owing to lack of exposure. Notably, among the nine cases with available information, five of nine (55.6%) children had never attended school or a childcare centre, and the remaining four were probably hindered from interacting with other children by social isolation measures enacted at the onset of the pandemic. Decreased immunity from lack of exposure to common viral pathogens may have predisposed cases to infection by multiple viruses, thus increasing the likelihood of more severe disease manifestations such as hepatitis.

Limitations of the study include: lack of availability and/or incomplete testing of liver biopsies, particularly for the presence or absence of AAV2, making it difficult to ascertain the pathogenetic mechanisms underlying the viral infection; low titres associated with detected viral pathogens; and the retrospective study design and the inclusion of only cases that had previously tested positive for HAdV.

In summary, here we identify a distinct strain of AAV2 and co-infection with at least one helper virus in blood from US paediatric cases of acute severe hepatitis of unknown aetiology. These results are consistent with findings from independent and contemporary studies of acute severe hepatitis in children from Scotland and the UK[14,28]. AAV2 infection may contribute to the pathogenesis and/or severity of the hepatitis, or alternatively, may be a non-pathogenic marker of liver inflammation. Further studies including serologic surveillance, viral culture and animal models are needed to investigate the potential role that AAV2 infection may play in this disease.

Methods

Ethics statement

Remnant clinical samples from cases with acute severe hepatitis were collected and analysed under ‘no subject contact’ protocols with waiver of informed consent approved by the institutional review boards (IRBs) of the University of Alabama, Birmingham, the California Department of Public Health, the New York State Department of Health and the Centers for Disease Control and Prevention (CDC). Whole-blood samples from paediatric controls (age < 18) from Children’s Healthcare of Atlanta were prospectively collected and analysed under a protocol approved by the Emory IRB (STUDY00000723); parents or guardians of these children provided oral consent for study enrolment and collection and analysis of their samples. Remnant whole-blood samples from paediatric controls (age < 18) at University of California, San Francisco (UCSF) were collected, biobanked and analysed under a ‘no subject contact’ protocol with waiver of informed consent approved by the UCSF IRB (protocol no. 11-05519). A subset of the control samples was provided by the CDC from children enrolled in the National Vaccine Surveillance Network (NVSN) study. Approval for the NVSN study was obtained from the institutional review board at each participating site and from the CDC (protocol no. 6164). Parents or guardians of eligible children provided written informed consent for participant enrolment. Blood specimens were also collected as remnant samples from clinical procedures.

Participant recruitment and sample collection

This was a retrospective observational case–control study using all available samples from cases and controls. A severe acute hepatitis case enrolled in this study was a person under investigation by local, state or federal public health agencies, defined as a person <10 years of age with elevated (>500 U l^{-1}) AST or ALT, an unknown aetiology for the hepatitis, and onset on or after 1 October 2021 (ref. [8]). All cases ($n = 16$) were hospitalized with acute elevation in liver enzymes, AST or ALT, and one or more of the following symptoms on presentation: nausea, vomiting, jaundice, generalized

weakness and abdominal pain. Cases were selected for inclusion into the current study if blood samples had previously tested positive for adenovirus by clinical testing, resulting in a selection bias that made case–control comparisons related to adenovirus detection not meaningful. Blood samples from cases meeting the criteria for a person under investigation but testing negative for adenovirus were not available.

Controls from UCSF in California ($n = 54$) included children hospitalized with hepatitis of defined aetiology (>100 U l^{-1}) or another inflammatory or non-inflammatory condition. These controls were selected on the basis of availability of convenience samples from a study of biomarkers of acute inflammatory disease, including severe COVID-19, in hospitalized patients. Controls were selected to be geographically similar (located within the same state) to cases from California. Remnant whole-blood samples from controls from UCSF ($n = 54$) were retrospectively biobanked and aliquoted with addition of 2× DNA/RNA Shield (Zymo Research) in a 1:1 ratio by volume and stored at −80 °C until use.

Controls from Children's Healthcare of Atlanta ($n = 24$) in Georgia included children hospitalized with hepatitis of defined aetiology (>100 U l^{-1}) or another inflammatory or non-inflammatory condition ($n = 18$) or blood donors ($n = 6$). These controls were selected from available biobanked samples from consented participants enrolled in a prospective study of COVID-19 and multi-system inflammatory syndrome in children. Controls were selected to be geographically similar (located within a neighbouring state with similar demographic characteristics) to the cases from Alabama and Florida[32]. Collected samples were stored at −80 °C until use.

Serum or plasma samples from children enrolled in the NVSN study were also included as controls. Three groups of children were selected: children admitted for acute gastroenteritis who tested positive for adenovirus in the stool ($n = 12$), children admitted for acute gastroenteritis who tested negative for adenovirus in the stool ($n = 11$) and blood donors ($n = 12$). These children were enroled from three sites (Seattle, Houston and Cincinnati) from June 2021 to May 2022 and enrolment criteria have previously been described[33]. Collected samples were stored at −80 °C until use.

Nucleic acid extraction

Whole-blood and plasma samples collected from cases from Alabama were extracted at the Wadsworth Center laboratory using the NucliSENSÒ easyMAG 'specific B' protocol (bioMerieux) according to the manufacturer's instructions. Samples from cases from Florida, Illinois, North Carolina and South Dakota were extracted using the Zymo Direct-zol DNA/RNA Miniprep Kit (Zymo Research) following the manufacturer's instructions. Briefly, 200 µl of sample was extracted and total nucleic acid was eluted in 60 µl and stored at −80 °C until use.

Samples from cases from California were extracted at the California Department of Public Health. Whole-blood samples (200 µl) were extracted using the Qiagen Blood Mini Kit (Qiagen) according to the manufacturer's instructions. Total nucleic acid was eluted in 100 µl and stored at −80 °C until use. Respiratory samples, serum, plasma and clarified stool suspensions were extracted using the NucliSENS easyMAG instrument (bioMerieux). Briefly, 300 µl of nasopharyngeal swab, serum or plasma sample or 140 µl of clarified stool suspension was lysed with 1 ml of lysis buffer and incubated for 10 min at room temperature, followed by addition of 100 µl magnetic silica and transfer to the instrument to begin the automated extraction. Total nucleic acid was eluted in 110 µl for nasopharyngeal swab, serum or plasma or 60 µl for stool and stored at −80 °C before use.

For control samples from California, Georgia or the NVSN study, total nucleic acid was extracted at UCSF from the original sample using two different protocols for whole blood, plasma or serum. Whole-blood samples (400 µl) that had been pretreated with DNA/RNA Shield (Zymo Research) were extracted using the Quick-RNA Whole Blood Kit (Zymo Research) according to the manufacturer's instructions. Total nucleic acid was eluted in 15 µl and stored at −80 °C until use. Plasma or serum samples (200 µl) were extracted using the Mag-Bind Viral DNA/RNA 96 Kit (Omega Bio-Tek) on a KingFisher Flex instrument (Thermo-Fisher) according to the manufacturer's instructions. Total nucleic acid was eluted in 100 µl and stored at −80 °C until use.

Viral PCR testing

Samples from California cases were screened for adenovirus using a pan-adenovirus PCR targeting all HAdVs[34] and/or a group F adenovirus (HAdV-40 or HAdV-41) real-time PCR[35]. A cycle threshold cutoff of ≤40 was used to call a positive result by PCR. PCR and Sanger sequencing of the HAdV hexon gene targeting hypervariable regions 1–6 (ref. [36]) were carried out on all adenovirus-positive samples with purified PCR products sequenced in-house or sent to an outside laboratory (Sequetech, Mountain View, CA) for sequencing. Sanger sequences were assembled and edited in Sequencher 5.2.4 (Gene Codes) and analysed using the nucleotide BLAST aligner[37]. Samples from cases outside California and all control samples were screened for adenovirus using a pan-adenovirus PCR assay[34] and sequenced using a nested PCR assay targeting HAdV hexon hypervariable regions 1–6, followed by Sanger sequencing[38]. PCR testing for detection of CMV, EBV and HHV-6 was carried out as previously described[39].

Viral enrichment-based targeted sequencing

For cases from California and Alabama and all controls, viral enrichment followed by targeted sequencing of viral genomes was carried out using custom spiked primers designed to target HAdV-41 or AAV1–AAV8 genomes. Spiked primers were designed using the metagenomic sequencing with spiked primer enrichment (MSSPE) algorithm[17] as follows. For HAdV-41, 22 representative HAdV-41 genomes were aligned using MAFFT, and for AAV, 11 genomes representing AAV1–AAV8 were aligned using MAFFT. Next, automated primer design was carried out by running the MSSPE algorithm with the following parameters: kmer size = 25, segment window = 500, *e*-value = 0.1, dS = 2, dG = −9,000. The algorithm generated 219 HAdV and 150 AAV spiked primers (Supplementary Table 4). PCR amplification from extracted DNA was carried out as previously described[40], with the following modifications: the annealing temperature for PCR was 60 °C for HAdV and 53 °C for AAV. The HAdV primers were amplified in two different reactions using two different sets of primers (Supplementary Table 4, Set1 and Set2), whereas the AAV2 primers were amplified in a single reaction. NGS libraries were prepared using the NEBNext Ultra II DNA Kit (New England Biolabs) and Revelo DNA-Seq Mech Kit on the MagicPrep NGS system (Tecan Genomics). Final libraries were quantified using the Qubit Flex instrument (Invitrogen) with the

dsDNA HS Assay Kit (Invitrogen). Libraries were pooled and sequenced on an Illumina NextSeq using 300-base-pair (bp) single-end sequencing. Negative template controls were included in every run to monitor for contamination. No contamination from HAdV-41 or AAV2 reads was detected in the negative template control libraries.

For cases from Florida, Illinois, North Carolina and South Dakota, probe capture target enrichment of viral genomes was carried out on metagenomic libraries using the Twist Comprehensive Viral Research Panel (Twist Biosciences), which covers reference genomes of 3,153 viruses and 15,488 different strains[18]. Individual DNA libraries or cDNA libraries from RNA were hybridized to Comprehensive Viral Research Panel probes according to the manufacturer's instructions. Libraries were then barcoded and sequenced on an Illumina MiSeq (250-bp paired-end sequencing) or an Illumina NextSeq (150-bp paired-end sequencing). For plasma sample 14_NC, nucleic acid carrier, either bacteriophage lambda DNA (New England Biolabs) or HeLa total RNA (Thermo-Fisher), was added during the library preparation step according to the manufacturer's instructions.

Viral metagenomic sequencing and analysis

Metagenomic DNA and RNA libraries were prepared using the Revelo DNA-Seq Mech Kit on the MagicPrep NGS system (Tecan Genomics), NEBNext Ultra II DNA Library Prep Kit (New England Biolabs) and NEBNext Ultra II RNA Library Prep Kit (New England Biolabs), according to the manufacturer's instructions. Libraries were pooled and sequenced on a NextSeq 550 Sequencing System using 150-bp single-end sequencing. Potential contamination was monitored in each run by processing water and negative controls in parallel with samples.

Sequencing data from all cases and controls were analysed for viral nucleic acids using SURPI+ (v1.0.7-build.4)[41], an automated bioinformatics pipeline for pathogen detection and discovery from metagenomic data that has been modified to incorporate enhanced filtering and classification algorithms[29]. A threshold of ≥3 non-overlapping reads was used for calling a positive virus detection[29].

Phylogenetic analysis

Multiple sequence alignments were carried out using MAFFT algorithm (v7.388)[30] as implemented in Geneious (version 10.0.9)[42]. Nucleotide and amino acid phylogenetic trees were inferred using a maximum-likelihood method with ultrafast bootstrap approximation as implemented in IQ-TREE (version 1.6.1)[31] using 1,000 bootstrap replicates. Trees were visualized using FigTree (version 1.4.4).

Viral genome assembly and analysis

Binary base call (BCL) files generated by Illumina sequencers were simultaneously demultiplexed and converted to FASTQ files using bcl2fastq (version 2.20.0.422). Custom scripts were used to assemble AdV and AAV2 genomes as follows. Briefly, raw FASTQ reads were filtered using BBDuk (version 38.87)[43] for removal of adaptors, primer sequences and low-quality reads, and then HAdV-41 or AAV reads were identified by Bowtie2 (ref. [44]) alignment (parameters: -D 20 -R 3 -L11 -N 1) to a reference database consisting of 1,395 HAdV-41 or 3,600 AAV partial sequences or genomes, respectively. These aligned reads were then mapped to the HAdV-41 reference genome (accession DQ315364.2) or consecutively to AAV genomes 1–8. For all AAV genomes, the assembly with the highest breadth of coverage corresponded to the AAV2 reference genome (accession number NC_001401.2). Consensus assemblies were generated using iVar[45] (parameters: -t 0.5 -m 1). AAV consensus genomes were further analysed for shared alterations in the nucleotide and translated nucleotide (amino acid) sequences relative to the AAV2 reference by carrying out multiple sequence alignment using the MAFFT algorithm[30], followed by visualization of the alignment using Geneious software (version 10.0.9)[42].

Statistical analysis

Statistical analyses were carried out using the Python scipy package (version 1.5.2)[46] and rstatix package (version 0.7.0) in R (version 4.0.3)[47]. Uncorrected *P* values were calculated using two-tailed Fisher's exact test for categorical variables and two-tailed unpaired *t*-test for continuous variables,

with the significance level determined after a Bonferroni correction for multiple comparisons.

Data visualization

Plots were generated using matplotlib (version 3.3.2), seaborn (version 0.11.0) and plotly (version 5.6.0) packages in Python software (version 3.7.12), Jupyter notebook (version 6.1.4), RStudio (version 1.4) and Adobe Illustrator (version 26.4.1) software.

Reporting summary

Further information on research design is available in the Nature Portfolio Reporting Summary linked to this article.

Data availability

Raw metagenomic sequencing data with human reads removed have been deposited in the NCBI Sequence Read Archive (Bioproject accession number PRJNA918667, under umbrella BioProject accession number PRJNA171119). Detailed protocols for spiked primer enrichment and metagenomic library preparation, consensus genome files, alignment files, phylogenetic tree files and supplementary tables have been uploaded to a Zenodo data repository (https://doi.org/10.5281/zenodo.7089581).

Code availability

Custom scripts for HAdV-41 and AAV genome assembly are available in a Zenodo data repository (https://doi.org/10.5281/zenodo.7089581).

References

1. Khader, S., Foster, I., Dagens, A., Norton, A. & Sigfrid, L. Severe acute hepatitis of unknown aetiology in children-what is known? *BMC Med.* **20**, 280 (2022).

2. Severe acute hepatitis of unknown aetiology in children - multi-country. *WHO Disease Outbreak News* https://www.who.int/emergencies/disease-outbreak-news/item/2022-DON400 (2022).

3. Cates, J. et al. Interim analysis of acute hepatitis of unknown etiology in children aged <10 years - United States, October 2021-June 2022. *MMWR Morb. Mortal. Wkly Rep.* **71**, 852–858 (2022).

4. Elsheikh, R. et al. Acute hepatitis of unknown origin in children: Behind the statistics. *Hepatology* https://doi.org/10.1002/hep.32682 (2022).

5. Gutierrez Sanchez, L. H. et al. A case series of children with acute hepatitis and human adenovirus infection. *N. Engl. J. Med.* https://doi.org/10.1056/NEJMoa2206294 (2022).

6. Kelgeri, C. et al. Clinical spectrum of children with acute hepatitis of unknown cause. *N. Engl. J. Med.* https://doi.org/10.1056/NEJMoa2206704 (2022).

7. Marsh, K. et al. Investigation into cases of hepatitis of unknown aetiology among young children, Scotland, 1 January 2022 to 12 April 2022. *Euro Surveill.* **27**, 2200318 (2022).

8. *Technical Report: Acute Hepatitis of Unknown Cause* (CDC, 2022); https://www.cdc.gov/ncird/investigation/hepatitis-unknown-cause/technical-report.html.

9. Kager, J. et al. Fulminant adenoviral-induced hepatitis in immunosuppressed patients. *Viruses* **14**, 1459 (2022).

10. Hierholzer, J. C. Adenoviruses in the immunocompromised host. *Clin. Microbiol. Rev.* **5**, 262–274 (1992).

11. Wang, D., Tai, P. W. L. & Gao, G. Adeno-associated virus vector as a platform for gene therapy delivery. *Nat. Rev. Drug Discov.* **18**, 358–378 (2019).

12. Meier, A. F., Fraefel, C. & Seyffert, M. The interplay between adeno-associated virus and its helper viruses. *Viruses* **12**, 662 (2020).

13. Gao, G. et al. Adeno-associated viruses undergo substantial evolution in primates during natural infections. *Proc. Natl Acad. Sci. USA* **100**, 6081–6086 (2003).

14. Ho, A. et al. Adeno-associated virus 2 infection in children with non-A-E hepatitis. *Nature* https://doi.org/10.1038/s41586-023-05948-2 (2023).

15. Recommendations for adenovirus testing and reporting of children with acute hepatitis of unknown etiology. *CDC Health Alert Network* https://emergency.cdc.gov/han/2022/han00462.asp (2022).

16. Chiu, C. Y. & Miller, S. A. Clinical metagenomics. *Nat. Rev. Genet.* **20**, 341–355 (2019).

17. Deng, X. et al. Metagenomic sequencing with spiked primer enrichment for viral diagnostics and genomic surveillance. *Nat. Microbiol.* **5**, 443–454 (2020).

18. Kim, K. W. et al. Respiratory viral co-infections among SARS-CoV-2 cases confirmed by virome capture sequencing. *Sci. Rep.* **11**, 3934 (2021).

19. Negro, F. Hepatitis D virus coinfection and superinfection. *Cold Spring Harb. Perspect. Med.* **4**, a021550 (2014).

20. Urban, S., Neumann-Haefelin, C. & Lampertico, P. Hepatitis D virus in 2021: virology, immunology and new treatment approaches for a difficult-to-treat disease. *Gut* **70**, 1782–1794 (2021).

21. La Bella, T. et al. Adeno-associated virus in the liver: natural history and consequences in tumour development. *Gut* **69**, 737–747 (2020).

22. Calcedo, R. et al. Adeno-associated virus antibody profiles in newborns, children, and adolescents. *Clin. Vaccine Immunol.* **18**, 1586–1588 (2011).

23. Chen, C. L. et al. Molecular characterization of adeno-associated viruses infecting children. *J. Virol.* **79**, 14781–14792 (2005).

24. Hsu, H. L. et al. Structural characterization of a novel human adeno-associated virus capsid with neurotropic properties. *Nat. Commun.* **11**, 3279 (2020).

25. Chevret, L. et al. Human herpesvirus-6 infection: a prospective study evaluating HHV-6 DNA levels in liver from children with acute liver failure. *J. Med. Virol.* **80**, 1051–1057 (2008).

26. Mellinger, J. L. et al. Epstein-Barr virus (EBV) related acute liver failure: a case series from the US Acute Liver Failure Study Group. *Dig. Dis. Sci.* **59**, 1630–1637 (2014).

27. Brooks, B. et al. Epstein-Barr virus and human herpesvirus-6 reactivation in acute COVID-19 patients. *Viruses* **14**, 1872 (2022).

28. Morfopoulou, S. et al. Genomic investigations of unexplained acute hepatitis in children. *Nature* https://doi.org/10.1038/s41586-023-06003-w (2023).

29. Miller, S. et al. Laboratory validation of a clinical metagenomic sequencing assay for pathogen detection in cerebrospinal fluid. *Genome Res.* **29**, 831–842 (2019).

30. Katoh, K. & Standley, D. M. MAFFT multiple sequence alignment software version 7: improvements in performance and usability. *Mol. Biol. Evol.* **30**, 772–780 (2013).

31. Nguyen, L. T., Schmidt, H. A., von Haeseler, A. & Minh, B. Q. IQ-TREE: a fast and effective stochastic algorithm for estimating maximum-likelihood phylogenies. *Mol. Biol. Evol.* **32**, 268–274 (2015).

32. QuickFacts: Alabama. US *Census Bureau* https://www.census.gov/quickfacts/AL (2021).

33. Esona, M. D. et al. Rotavirus genotype trends and gastrointestinal pathogen detection in the United States, 2014-2016: results from the

New Vaccine Surveillance Network. *J. Infect. Dis.* **224**, 1539–1549 (2021).

34. Heim, A., Ebnet, C., Harste, G. & Pring-Akerblom, P. Rapid and quantitative detection of human adenovirus DNA by real-time PCR. *J. Med. Virol.* **70**, 228–239 (2003).

35. Lyman, W. H. et al. Prospective study of etiologic agents of acute gastroenteritis outbreaks in child care centers. *J. Pediatr.* **154**, 253–257 (2009).

36. Lu, X. & Erdman, D. D. Molecular typing of human adenoviruses by PCR and sequencing of a partial region of the hexon gene. *Arch. Virol.* **151**, 1587–1602 (2006).

37. Altschul, S. F., Gish, W., Miller, W., Myers, E. W. & Lipman, D. J. Basic local alignment search tool. *J. Mol. Biol.* **215**, 403–410 (1990).

38. Okada, M., Ogawa, T., Kubonoya, H., Yoshizumi, H. & Shinozaki, K. Detection and sequence-based typing of human adenoviruses using sensitive universal primer sets for the hexon gene. *Arch. Virol.* **152**, 1–9 (2007).

39. Dupuis, M. et al. Molecular detection of viral causes of encephalitis and meningitis in New York State. *J. Med. Virol.* **83**, 2172–2181 (2011).

40. Quick, J. et al. Multiplex PCR method for MinION and Illumina sequencing of Zika and other virus genomes directly from clinical samples. *Nat. Protoc.* **12**, 1261–1276 (2017).

41. Naccache, S. N. et al. A cloud-compatible bioinformatics pipeline for ultrarapid pathogen identification from next-generation sequencing of clinical samples. *Genome Res.* **24**, 1180–1192 (2014).

42. Kearse, M. et al. Geneious Basic: an integrated and extendable desktop software platform for the organization and analysis of sequence data. *Bioinformatics* **28**, 1647–1649 (2012).

43. Bushnell, B. BBMap: a fast, accurate, splice-aware aligner. https://www.osti.gov/servlets/purl/1241166 (2014).

44. Langmead, B. & Salzberg, S. L. Fast gapped-read alignment with Bowtie 2. *Nat. Methods* **9**, 357–359 (2012).

45. Grubaugh, N. D. et al. An amplicon-based sequencing framework for accurately measuring intrahost virus diversity using PrimalSeq and iVar. *Genome Biol.* **20**, 8 (2019).

46. Virtanen, P. et al. SciPy 1.0: fundamental algorithms for scientific computing in Python. *Nat. Methods* **17**, 261–272 (2020).

47. R Core Team. *R: A Language and Environmental for Statistical Computing* http://www.R-project.org (R Foundation for Statistical Computing, 2013).

Acknowledgements

We thank the public health officers who provided samples and patient metadata in support of this study: J. Kauerauf and L. Saathoff-Huber, Illinois Department of Public Health; S. Bunch, D. Dessi, A. Gent, C. Panzera, S. Vaccaro and J. Vergara Aguirre, Florida Department of Health; L. DiBiase, University of North Carolina Hospitals; L. Deyneka and R. Pelc, North Carolina Division of Public Health; and the North Carolina State Laboratory of Public Health. We thank H. Guevara, T. Padilla, E. Saguar, C. Wright, B. Molinar, L. Moua and A. Chen from the Respiratory and Gastroenteric Diseases Section of the Viral and Rickettsial Disease Laboratory, California Department of Public Health. We thank staff members at the UCSF Clinical Laboratories and the UCSF Clinical Microbiology Laboratories for their help in identifying and retrieving patient whole-blood samples for biobanking. We thank the Wadsworth Center HAdVanced Genomics Technology Core for carrying out the sequencing reactions, and S. Ogbamikael for carrying out the hexon gene-sequencing assays. We thank the Genomics group at the National Biodefense Analysis and Countermeasures Center for their efforts in creating the genomic libraries at short notice from the samples they were provided. This work was financially

supported in part by US CDC contracts 75D30121C12641 and 75D30121C10991 (C.Y.C.), BARDA contract 75A50122C00022 (C.Y.C.), the Chan-Zuckerberg Biohub (C.Y.C.) and National Institutes of Health/National Institute of Child Health and Human Development grant R61HD105618 (C.Y.C. and C.A.R.). This work was also financially supported in part under agreement number HSHQDC-15-C-00064 awarded to Battelle National Biodefense Institute (BNBI) by the Department of Homeland Security (DHS), Science and Technology Directorate, for the management and operation of the National Biodefense Analysis and Countermeasures Center (NBACC), a Federally Funded Research and Development Center. This manuscript has been authored in part by Battelle National Biodefense Institute, LLC under contract with DHS. The publisher, by accepting the article for publication, acknowledges that the US Government retains a non-exclusive, paid up, irrevocable, world-wide licence to publish or reproduce the published form of this manuscript, or allow others to do so, for US Government purposes. The funders had no role in the design and conduct of the study; collection, management, analysis and interpretation of the data; preparation, review or approval of the manuscript; and decision to submit the manuscript for publication. The findings and conclusions in this article are those of the authors and do not necessarily represent the views or opinions of the Alabama Department of Public Health, the California Department of Public Health, the California Health and Human Services Agency, the Florida Department of Health, the Illinois Department of Public Health, the New York State Department of Health/Wadsworth Center, the North Carolina Department of Public Health or the South Dakota Department of Health, nor do they reflect the official policy or position of the Federal Bureau of Investigation (FBI) or CDC. The views and conclusions contained in this article should not be interpreted as necessarily representing the official policies, either expressed or implied, of DHS or the US Government. DHS does not endorse any products or commercial services mentioned in this presentation. In no event shall DHS, BNBI or NBACC have any responsibility or liability for any use, misuse, inability to use or reliance upon the information contained herein. In addition, no warranty of fitness for a particular purpose, merchantability, accuracy or adequacy is provided regarding the contents of this document. This is publication #22.28 of the FBI Laboratory Division. Names of commercial manufacturers are provided for identification purposes alone,

and inclusion does not imply endorsement of the manufacturer, or its products or services by the FBI.

Author information

Author notes

1. These authors contributed equally: Venice Servellita, Alicia Sotomayor Gonzalez, Daryl M. Lamson

Authors and Affiliations

1. Department of Laboratory Medicine, University of California, San Francisco, San Francisco, CA, USA

   Venice Servellita, Alicia Sotomayor Gonzalez, Abiodun Foresythe, Hee Jae Huh, Paul E. Oluniyi, Jenny Nguyen, Jessica Tan, Doug Stryke, Miriam Oseguera, Robert Blattner & Charles Y. Chiu

2. Wadsworth Center, New York State Department of Health, David Axelrod Institute, Albany, NY, USA

   Daryl M. Lamson & Kirsten St. George

3. Department of Laboratory Medicine and Genetics, Samsung Medical Center, Sungkyunkwan University School of Medicine, Seoul, South Korea

   Hee Jae Huh

4. National Biodefense Analysis and Countermeasures Center (NBACC), Frederick, MD, USA

   Adam L. Bazinet, Nicholas H. Bergman, Karla Y. Garcia, Jennifer S. Goodrich, Sean P. Lovett, Kisha Parker, Diana Radune & R. Taylor Raborn

5. Federal Bureau of Investigation Laboratory Division/Scientific Response and Analysis Unit, Quantico, VA, USA

Robert L. Bull

6. California Department of Public Health, Richmond, CA, USA

April Hatada, Chao-Yang Pan, Kyle Rizzo, J. Bradford Bertumen, Christina Morales & Debra A. Wadford

7. Centers for Disease Control and Prevention, Atlanta, CA, USA

J. Bradford Bertumen, Hayden D. Hedman, Umesh Parashar, M. Steven Oberste, Jacqueline E. Tate, Julia M. Baker, David Sugerman, Caelin Potts, Xiaoyan Lu, Preeti Chhabra, Olivia Almendares, Neha Balachandran, Jordan E. Cates, Brandi Freeman, Anita Kambhampati, Rachel Marine, Everardo Vega, Mary E. Wikswo, Erin R. McKeever, Jan Vinjé & Hannah L. Kirking

8. Florida Department of Health, Tallahassee, FL, USA

Rayah Jaber & Natalia Cano

9. Illinois Department of Public Health, Chicago, IL, USA

Matthew T. Leslie & Maeve Marsh

10. North Carolina Department of Health and Human Services, Raleigh, NC, USA

Zin Lyons & Erin Ricketts

11. South Dakota Department of Health, Pierre, SD, USA

Hayden D. Hedman & Joshua L. Clayton

12. Association for Public Health Laboratories, Silver Spring, MD, USA

Maureen Sullivan & Kelly Wroblewski

13. Alabama Department of Public Health, Montgomery, AL, USA

L. Amanda Ingram

14. University of Alabama at Birmingham, Birmingham, AL, USA

David Kelly, Henry Shiau, William Britt & Luz Helena Gutierrez Sanchez

15. Department of Pediatrics, Emory University School of Medicine and Children's Healthcare of Atlanta, Atlanta, GA, USA

Caroline Ciric & Christina A. Rostad

16. Department of Biomedical Science, University at Albany, SUNY, Albany, NY, USA

Kirsten St. George

17. Department of Medicine, Division of Infectious Diseases, University of California, San Francisco, San Francisco, CA, USA

Charles Y. Chiu

18. Chan-Zuckerberg Biohub, San Francisco, CA, USA

Charles Y. Chiu

19. Baylor College of Medicine, Houston, TX, USA

Julie A. Boom & Leila C. Sahni

20. Seattle Children's Research Institute, Seattle, WA, USA

Janet A. Englund & Eileen J. Klein

21. Children's Hospital Medical Center, Cincinnati, OH, USA

Mary A. Staat

Consortia

Pediatric Hepatitis of Unknown Etiology Working Group

- Olivia Almendares
- , Neha Balachandran
- , Jordan E. Cates
- , Brandi Freeman
- , Anita Kambhampati
- , Rachel Marine
- , Everardo Vega
- , Mary E. Wikswo
- , Erin R. McKeever
- , David Kelly
- , Julie A. Boom
- , Leila C. Sahni
- , Janet A. Englund
- , Eileen J. Klein
- , Mary A. Staat
- , Maeve Marsh
- , Erin Ricketts
- , Joshua L. Clayton
- , Natalia Cano
- , Miriam Oseguera
- & Robert Blattner

Contributions

C.Y.C., J.V., R.T.R. and K.S.G. conceived and designed the study. C.Y.C., V.S. and A.S.G. coordinated the study. V.S., A.S.G., A.F., H.J.H., P.E.O. and J.T. carried out metagenomic sequencing and targeted viral enrichment experiments. V.S. and D. Stryke ran the SURPI computational pipeline for detection of viruses from metagenomic data. V.S. and C.Y.C. analysed metagenomic and targeted viral enrichment data, assembled AAV2 genomes and carried out phylogenetic and substitution analyses. A.L.B., N.H.B., R.L.B., K.Y.G., J.S.G., S.P.L., K.P., D.R. and R.T.R. carried out viral probe capture enrichment experiments and assembled AAV2 genomes. R.J.,

M.T.L., Z.L. and H.D.H. investigated acute severe hepatitis cases and collected samples and clinical metadata. U.P., M.S., K.W., M.S.O., J.E.T., J.M.B., D. Sugerman, C.P., X.L., P.C., J.V., H.L.K. and the CDC Pediatric Hepatitis of Unknown Etiology Working Group investigated acute severe hepatitis cases for the CDC and collected samples and clinical metadata. L.A.I., H.S., W.B. and L.H.G.S. investigated acute severe hepatitis cases in Alabama and collected samples and clinical metadata. C.C. and C.A.R. provided samples and clinical metadata from paediatric controls from Georgia. V.S., A.S.G., J.N. and C.Y.C. provided samples and clinical metadata from paediatric controls from California. A.H., C.-Y.P., K.R., J.B.B., C.M. and D.A.W. investigated acute severe hepatitis cases and carried out viral PCR testing and HAdV genotyping at the California Department of Public Health. D.M.L. and K.S.G. carried out viral PCR testing and HAdV genotyping at the Wadsworth Center/New York State Department of Public Health. C.Y.C. and V.S. wrote the initial draft of the manuscript and prepared the figures. C.Y.C., V.S., A.S.G., U.P., J.E.T., J.M.B., C.P., X.L., J.V., H.L.K. and R.T.R. edited the manuscript. All authors read the manuscript and agreed to its contents.

Corresponding author

Correspondence to Charles Y. Chiu.

Ethics declarations

Competing interests

C.Y.C. is a founder of Delve Bio and on the scientific advisory board for Delve Bio, Mammoth Biosciences, BiomeSense and Poppy Health. He is also a co-inventor on US patent 11380421, “Pathogen detection using next generation sequencing”, under which algorithms for taxonomic classification, filtering and pathogen detection are used by SURPI+ software. C.Y.C. receives research support unrelated to this manuscript from Abbott Laboratories, Inc. The institution of C.A.R. has received financial support to conduct clinical research unrelated to this manuscript from BioFire Inc., GSK, Janssen, MedImmune, Merck, Moderna, Novavax, PaxVax, Pfizer, Regeneron and Sanofi-Pasteur. She is co-inventor of

patented respiratory syncytial virus vaccine technology, which has been licensed to Meissa Vaccines, Inc. K.S.G. receives research support unrelated to this manuscript from Thermo-Fisher and has a royalty-generating collaborative agreement with Zeptometrix. The other authors declare no competing interests.

Peer review

Peer review information

Nature thanks Frank Tacke and the other, anonymous, reviewer(s) for their contribution to the peer review of this work. Peer reviewer reports are available.

Additional information

Publisher's note Springer Nature remains neutral with regard to jurisdictional claims in published maps and institutional affiliations.

Extended data figures and tables

Extended Data Fig. 1 Amino acid phylogenetic analysis of AAV2 genomes from cases, related to Fig. 3.

(**A**) Phylogenetic tree corresponding to the Assembly Activating Protein (AAP) protein. (**B**) Phylogenetic tree corresponding to the VP1 protein. Phylogenetic trees was constructed by multiple sequence alignment of the AAV genomes or amino acid sequences using the MAFFT algorithm[30], followed by maximum likelihood based tree construction using IQ-TREE[31].

Supplementary information

Reporting Summary

Peer Review File

Supplementary Table 1

Detailed demographic, clinical, laboratory and genomic characteristics for individual cases and controls.

Supplementary Table 2

Statistical associations of detected viruses in cases compared to controls.

Supplementary Table 3

Frequency of single nucleotide variants in AAV2 genomes from cases.

Supplementary Table 4

Primer sequences for detection and virus whole-genome sequencing of HAdV-41 and AAV2.

Rights and permissions

Springer Nature or its licensor (e.g. a society or other partner) holds exclusive rights to this article under a publishing agreement with the author(s) or other rightsholder(s); author self-archiving of the accepted manuscript version of this article is solely governed by the terms of such publishing agreement and applicable law.

Reprints and Permissions

About this article

Cite this article

Servellita, V., Sotomayor Gonzalez, A., Lamson, D.M. *et al.* Adeno-associated virus type 2 in US children with acute severe hepatitis. *Nature* **617**, 574–580 (2023). https://doi.org/10.1038/s41586-023-05949-1

- Received: 11 September 2022
- Accepted: 10 March 2023
- Published: 30 March 2023
- Issue Date: 18 May 2023
- DOI: https://doi.org/10.1038/s41586-023-05949-1

Share this article

Anyone you share the following link with will be able to read this content:

Get shareable link

Sorry, a shareable link is not currently available for this article.

Copy to clipboard

Provided by the Springer Nature SharedIt content-sharing initiative

[Adeno-associated virus 2 infection in children with non-A–E hepatitis](#)

- Antonia Ho
- Richard Orton
- Emma C. Thomson

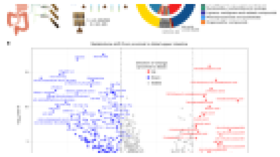
Nature Article 30 Mar 2023

[Severe hepatitis outbreak in children linked to AAV2 virus](#)

- Frank Tacke

Nature News & Views 30 Mar 2023

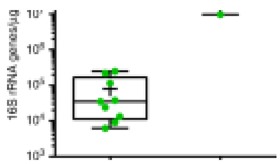
This article was downloaded by **calibre** from https://www.nature.com/articles/s41586-023-05949-1



Human metabolome variation along the upper intestinal tract

10 May 2023

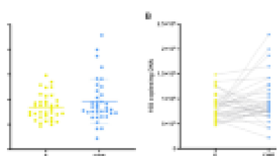
Jacob Folz, Rebecca Neal Culver, … Oliver Fiehn



The mucosal–luminal interface: an ideal sample to study the mucosa-associated microbiota and the intestinal microbial biogeography

04 February 2019

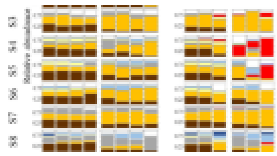
Walid Mottawea, James Butcher, … Alain Stintzi



Natural and after colon washing fecal samples: the two sides of the coin for investigating the human gut microbiome

25 October 2022

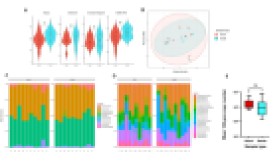
Elisabetta Piancone, Bruno Fosso, … Graziano Pesole



[Spatial distribution of live gut microbiota and bile acid metabolism in various parts of human large intestine]

04 March 2022

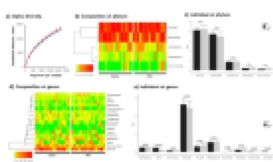
Daisuke Chinda, Toshihiko Takada, … Shinsaku Fukuda



[Rectal swabs as a viable alternative to faecal sampling for the analysis of gut microbiota functionality and composition]

10 January 2023

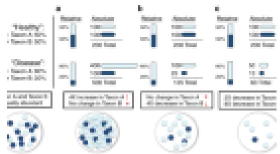
Shiva T. Radhakrishnan, Kate I. Gallagher, … Horace R. T. Williams



[Consumption of a Leuconostoc holzapfelii-enriched synbiotic beverage alters the composition of the microbiota and microbial extracellular vesicles]

01 August 2019

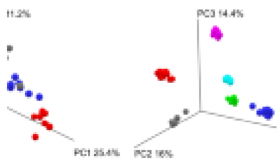
Jinho Yang, Andrea McDowell, … Yoon-Keun Kim



[A quantitative sequencing framework for absolute abundance measurements of mucosal and lumenal microbial communities]

22 May 2020

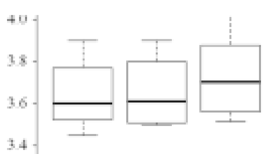
Jacob T. Barlow, Said R. Bogatyrev & Rustem F. Ismagilov



[Fecal sample collection methods and time of day impact microbiome composition and short chain fatty acid concentrations]

07 July 2021

Jacquelyn Jones, Stacey N Reinke, … Claus T. Christophersen



[Effects of bowel preparation on the human gut microbiome and metabolome]

11 March 2019

Naoyoshi Nagata, Mari Tohya, … Masahira Hattori

- Article
- Open Access

- Published: 10 May 2023

Profiling the human intestinal environment under physiological conditions

- Dari Shalon,
- Rebecca Neal Culver ,
- Jessica A. Grembi,
- Jacob Folz,
- Peter V. Treit,
- Handuo Shi,
- Florian A. Rosenberger,
- Les Dethlefsen,
- Xiandong Meng,
- Eitan Yaffe,
- Andrés Aranda-Díaz,
- Philipp E. Geyer,
- Johannes B. Mueller-Reif,
- Sean Spencer,
- Andrew D. Patterson,
- George Triadafilopoulos,
- Susan P. Holmes,
- Matthias Mann,
- Oliver Fiehn ,
- David A. Relman &
- …
- Kerwyn Casey Huang

Show authors

Nature **volume 617**, pages 581–591 (2023)

- 2 Citations

- 369 Altmetric
- Metrics details

Abstract

The spatiotemporal structure of the human microbiome[1,2], proteome[3] and metabolome[4,5] reflects and determines regional intestinal physiology and may have implications for disease[6]. Yet, little is known about the distribution of microorganisms, their environment and their biochemical activity in the gut because of reliance on stool samples and limited access to only some regions of the gut using endoscopy in fasting or sedated individuals[7]. To address these deficiencies, we developed an ingestible device that collects samples from multiple regions of the human intestinal tract during normal digestion. Collection of 240 intestinal samples from 15 healthy individuals using the device and subsequent multi-omics analyses identified significant differences between bacteria, phages, host proteins and metabolites in the intestines versus stool. Certain microbial taxa were differentially enriched and prophage induction was more prevalent in the intestines than in stool. The host proteome and bile acid profiles varied along the intestines and were highly distinct from those of stool. Correlations between gradients in bile acid concentrations and microbial abundance predicted species that altered the bile acid pool through deconjugation. Furthermore, microbially conjugated bile acid concentrations exhibited amino acid-dependent trends that were not apparent in stool. Overall, non-invasive, longitudinal profiling of microorganisms, proteins and bile acids along the intestinal tract under physiological conditions can help elucidate the roles of the gut microbiome and metabolome in human physiology and disease.

Main

The human intestinal tract harbours the vast majority of microorganisms residing in or on our bodies[1]; their genetic content and biochemical transformation capabilities are hundreds of times larger than those encoded by the human genome[8]. Humans depend on their gut microorganisms for

food digestion, immune system regulation and protection against pathogens, among other critical functions[1]. An important yet often overlooked aspect of the gut is regional heterogeneity and how it impacts local physiology[9]. Because of difficulties in accessing and sampling the intestinal tract, stool has been the main source of information for human gut microbiome studies[10]. However, stool reflects waste products and downstream effluent, within which regional variation is lost. For example, key metabolites such as bile acids are altered upstream by microbial transformations and then substantially absorbed by the host before excretion[4]. The regions of the gut distal to the stomach (duodenum, jejunum, ileum and colon) differ markedly in nutrient availability, pH, oxygen partial pressure, mucosal structure and flow rate[7]. As a result, distinct microbial communities with specialized functions, metabolomes, immune niches and proteomes are present in each intestinal region[3,4,11]. Thus, deeper understanding of how gut microorganisms impact human physiology and vice versa requires local sampling of the gut microbiome and its chemical environment in natural, unperturbed states.

Historically, sampling the human intestinal tract without disturbance or contamination has been challenging[10]. We recently discovered substantial regional variability in microbiota composition across spatial scales of only a few inches throughout the intestines of deceased organ donors[2]. However, organ donors have typically been treated with antibiotics, and, even in cases in which the intestinal tract has been sampled immediately after cessation of life support, the gut is often ischaemic or necrotic. Duodenal sampling from live individuals using upper endoscopy has a high probability of inadvertent contamination from oral, oesophageal or gastric contents. Endoscopic access to the mid-jejunum requires a ~2-h procedure involving general anaesthesia or sedation, performed under fasting[12,13]. Alternatively, a stoma from exteriorization of the ileum through the abdominal wall can provide intestinal samples, but this procedure is invasive and reflects altered gut anatomy and physiology, at a single location[14]. Despite the important effects on the microbiome and signalling properties of bile acids, studies on their chemical diversity and concentrations have relied on non-representative measurements of the few percent of bile acids in stool or the fraction of a percent in blood. Previously developed ingestible devices for sampling the human intestinal tract have important limitations such as complex

electronics[15], large size that risks device retention[15] or insufficient sampling volume for multi-omics analyses[16]. pH profiles, peristalsis, diet, physiology, gastrointestinal disorders and key metabolites such as bile acids[17] differ markedly between humans and animals[18], making human studies most relevant to human physiology and disease.

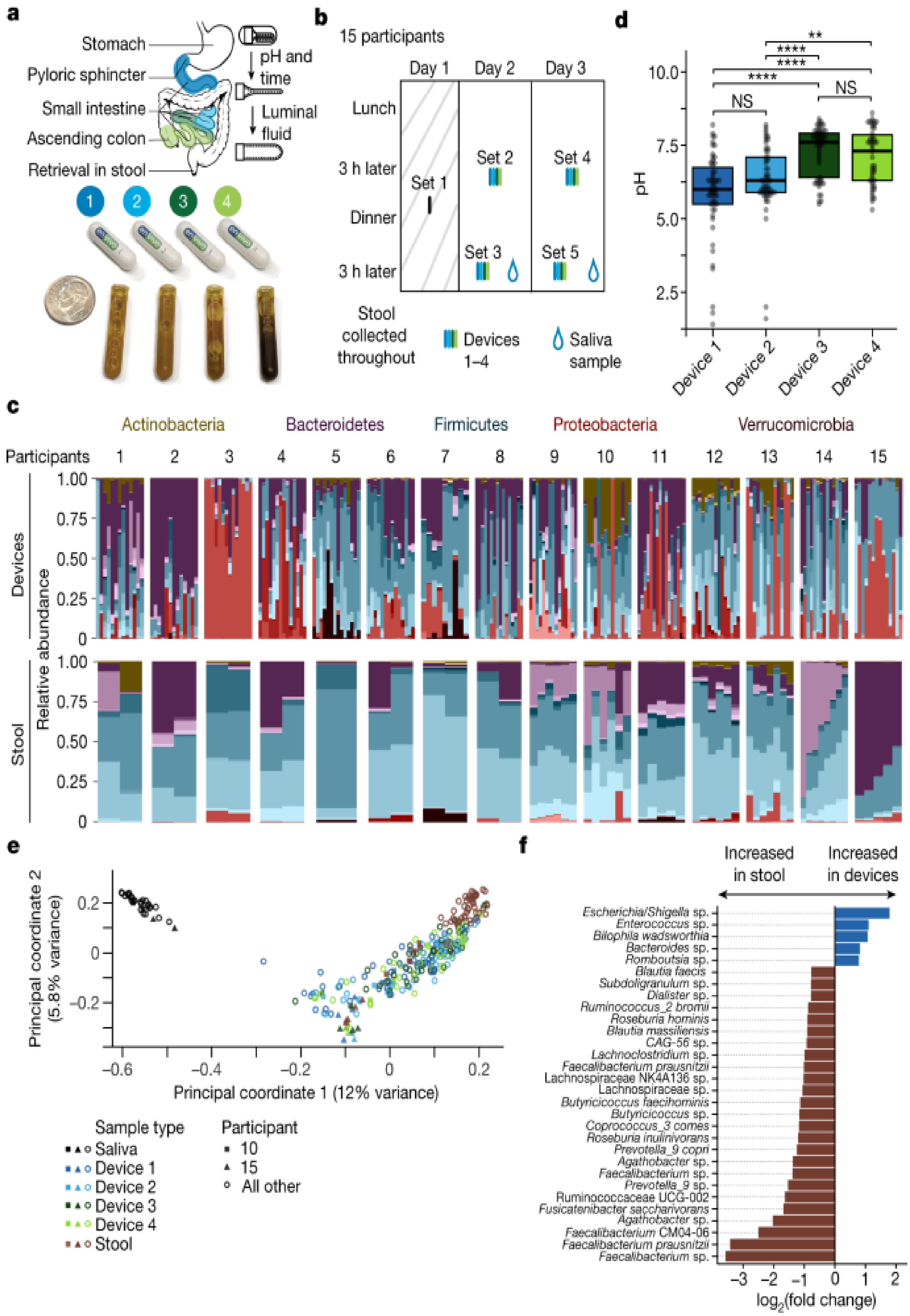
To measure microbial, viral, proteomic and bile acid profiles within the human intestines during normal digestion, we developed and evaluated a capsule device that collects luminal contents from the small intestine or ascending colon. The expanding bladder and lack of internal structure in our device allowed ~400 µl of liquid to be retrieved, enabling multi-omic analyses. We report differences in microbiome composition, gene class abundance, prophage induction and the host proteome between the intestines and stool. We discovered gradients of microbially transformed bile acids along the intestinal tract and identified correlations between the abundance of microbially modified bile acids and specific gut bacterial species. In a separate manuscript, we combined five metabolomics assays to identify spatial and temporal differences between stool and intestinal metabolomes, including diet-derived compounds and microbially linked metabolites such as sulfonolipids and fatty acid esters of hydroxy fatty acid lipids[19]. These discoveries illuminate biological properties of the intestinal tract that are inaccessible from stool or endoscopic sampling.

Device for sampling the human intestines

The sampling capsule is a single-use, passive device that collects fluid from the human intestines for ex vivo analysis. The device contains a collapsed collection bladder capped by a one-way valve inside a dissolvable capsule with an enteric coating (Fig. 1a). The enteric coating prevents contact between the collection bladder and the surrounding environment before entry into the intestines. The pH of the intestines typically rises from 4–6 in the duodenum to 7–8 in the ileum[15]. Once the device reaches a pre-set pH sufficient to dissolve the enteric coating, the collection bladder expands and draws in luminal contents through the one-way valve. To sample from four distinct regions of the intestinal tract, four devices were ingested as a set after an individual ate a meal of their choosing, wherein different device types in a set were designed to open at different, progressively higher pH

levels. Device type 4 included a time-delay coating to bias collection towards the ascending colon where the pH typically drops relative to the terminal ileum[15] (Methods and Fig. 1a). Each device collects up to 400 µl of luminal contents; bacterial density is higher in the lumen than at or within the mucosa[20], most mucosa-associated bacteria are represented in the luminal contents[21] and many metabolites of interest are in the lumen. After the bladder fills, the one-way valve prevents further entrance of liquid. The ingested devices are recovered from stool, and collected samples are extracted for analysis. These devices provide unique potential for multi-region collection of microorganisms and metabolites within the intestines during normal digestion.

Fig. 1: Devices enable longitudinal sampling of the human intestine.


a
Stomach
Pyloric sphincter
Small intestine
Ascending colon
Retrieval in stool
pH and time
Luminal fluid
1
2
3
4
b
15 participants
Day 1
Day 2
Day 3
Lunch
3 h later
Dinner
3 h later
Set 1
Set 2
Set 3
Set 4
Set 5
Stool collected throughout
Devices 1–4
Saliva sample
d
pH
10.0
7.5
5.0
2.5
NS
NS
****
****
****
**
Device 1
Device 2
Device 3
Device 4
c
Actinobacteria
Bacteroidetes
Firmicutes
Proteobacteria
Verrucomicrobia
Participants
1 2 3 4 5 6 7 8 9 10 11 12 13 14 15
Devices
Stool
Relative abundance
1.00
0.75
0.50
0.25
0
e
Principal coordinate 2 (5.8% variance)
Principal coordinate 1 (12% variance)
0.2
0
−0.2
−0.6
−0.4
−0.2
0
0.2
Sample type
Saliva
Device 1
Device 2
Device 3
Device 4
Stool
Participant
10
15
All other
f
Increased in stool
Increased in devices
Escherichia/Shigella sp.
Enterococcus sp.
Bilophila wadsworthia
Bacteroides sp.
Romboutsia sp.
Blautia faecis
Subdoligranulum sp.
Dialister sp.
Ruminococcus_2 bromii
Roseburia hominis
Blautia massiliensis
CAG-56 sp.
Lachnoclostridium sp.
Faecalibacterium prausnitzii
Lachnospiraceae NK4A136 sp.
Lachnospiraceae sp.
Butyricicoccus faecihominis
Butyricicoccus sp.
Coprococcus_3 comes
Roseburia inulinivorans
Prevotella_9 copri
Agathobacter sp.
Faecalibacterium sp.
Prevotella_9 sp.
Ruminococcaceae UCG-002
Fusicatenibacter saccharivorans
Agathobacter sp.
Faecalibacterium CM04-06
Faecalibacterium prausnitzii
Faecalibacterium sp.
−3
−2
−1
0
1
2
log2(fold change)

a, Overview of the intended sampling locations (top) of the four device types in packaged form for ingestion (middle) and as full collection bladders containing intestinal samples after retrieval from stool (bottom). A US dime is included for scale. Top right, the device contains a folded bladder capped with a one-way valve within a capsule with an enteric coating, which dissolves once the designated pH has been reached, enabling the bladder to unfold and draw in up to 400 µl of luminal fluid. **b**, Timeline for the collection of saliva, intestinal and stool samples from 15 healthy adults. Set 1 devices were not used for analyses. **c**, Family-level relative abundance for each sample by participant and location ($n = 268$). The colour of the ASV indicates the phylum, and the gradient of a given colour represents different families within the phylum. Only 16S rRNA gene ASVs with ≥3 reads in ≥5% of device and stool samples were used ($n = 399$ ASVs). **d**, The pH of the contents in devices designed to open at locations spanning the proximal to distal intestinal tract exhibited the expected increasing trend. Points represent individual devices ($n = 218$). P values from top to bottom: 0.018, 1.1×10^{-4}, 5.5×10^{-5}, 8.6×10^{-8}, 1 and 0.19. Boxplots show the median value and the first and third quartiles. NS, not significant; $^{**}P \leq 0.01$, $^{****}P \leq 0.0001$, Bonferroni-adjusted two-sided Wilcoxon rank-sum test. **e**, PCoA based on Canberra distance between microbial communities ($n = 297$). Read counts were $\log_2$ transformed. Each point represents an individual sample and is coloured by the sample type (stool, saliva and device types 1–4). Filled squares and triangles identify two outlier participants (10 and 15) who had taken oral antibiotics in the 5 months before intestinal sampling. Only 16S rRNA gene ASVs with ≥3 reads in ≥5% of samples (including saliva) were used ($n = 455$ ASVs). **f**, ASVs with $\log_2$(fold change) > 0.75 between devices and stool that were significantly differentially abundant ($n = 28$ ASVs across $n = 268$ analysed samples; limma-voom was used to calculate differential expression after size factors were estimated and normalized using DESeq2; $P < 0.05$, Benjamini–Hochberg correction).

We first sought to confirm whether the devices could be targeted to specific intestinal locations and would progress through the intestinal tract without contamination. In a feasibility study, we connected devices targeting the jejunum and ascending colon to a capsule endoscope and visualized successful in vivo sampling in a human (Supplementary Video 1). To assess

potential effects of incubation of the collected microorganisms in the device while it transited through the gut, we retrieved and incubated a set of four devices from a single bowel movement in an anaerobic chamber at 37 °C for up to 87 h (Methods). We found that major changes in microbiota composition did not occur in devices with a transit (incubation) time of ~58 h or less (Extended Data Fig. 1). Within these experimental limitations, we demonstrate below that microorganisms and metabolites display longitudinal gradients along the intestine and are highly distinct from the contents of stool samples.

Spatially distinct microbial communities

To assess compositional and functional differences within the intestinal microbiome, we carried out a clinical study with 15 healthy human participants (Supplementary Table 1). First, a single device was swallowed and retrieved to ensure that no complications arose during device passage through the gut (set 1; Fig. 1b); the contents of these devices were not analysed. Subsequently, sets of four devices (with each device type within a set having a different enteric coating) were ingested twice daily (3 h after lunch and 3 h after dinner) on two consecutive days (sets 2–5; Fig. 1b). All participants consumed their normal diets and kept a food log. All devices safely exited all participants and were successfully retrieved. No adverse events were reported. Participants collected contemporaneous saliva samples ($n = 2$, one on each day before ingesting devices 3 h after dinner) and 2–8 stool samples on or around the days when devices were recovered (Fig. 1b).

We obtained sufficient sampling volume and 16S rRNA gene sequencing depth from 210 devices, 29 saliva samples and 58 stool samples (Extended Data Fig. 2a and Methods). The pH profiles of the samples collected by the four device types (Fig. 1d) reasonably matched previously published measurements of pH along the human intestines, with a general increase in pH from the proximal to distal small intestine followed by a decrease in the ascending colon[15]. The time between device ingestion and recovery ranged from 8 to 67 h (Extended Data Fig. 2b), in line with previous reports of broadly distributed transit times[15]. Given typical gastric emptying times and the 3-h post-meal interval before devices were swallowed, the devices probably entered the small intestine with the final contents of the preceding

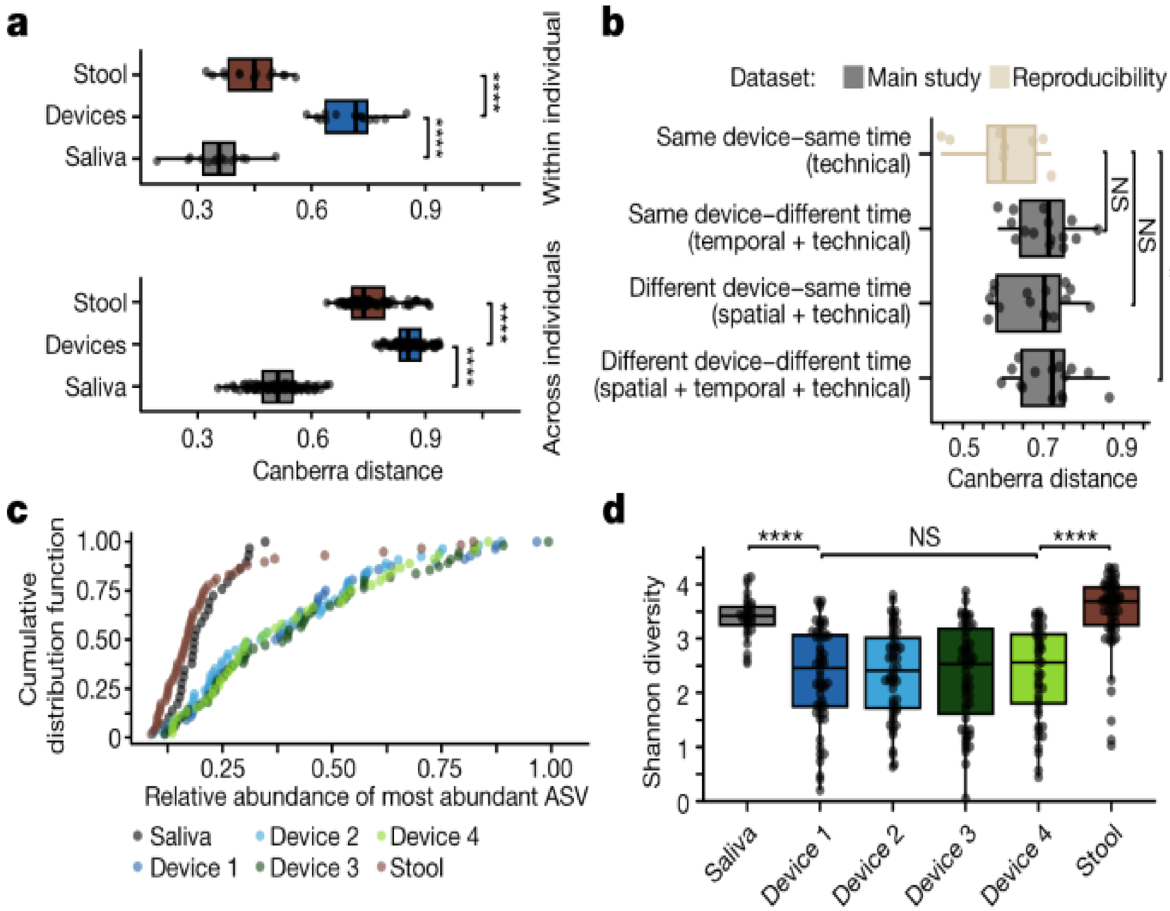
meal[22,23]. Nonetheless, the contents of the subsequent meal were more strongly associated with device transit time (Extended Data Fig. 2c,d).

A principal coordinate analysis (PCoA) based on Canberra distance identified location along the intestinal tract and across disparate sample types (saliva, intestines and stool) as an important latent variable. Saliva samples were significantly segregated from intestinal and stool samples across all participants (PERMANOVA, $P = 0.001$; Fig. 1e), indicating that the composition of the contents of all devices was distinct from the composition of the oral microbiota. Furthermore, we identified two participants (10 and 15; Fig. 1e) whose stool, and to some degree intestinal samples, clustered separately. On follow-up questioning, these participants reported taking antibiotics within the past 1 month (participant 10) and 5 months (participant 15). When considering each of the 15 participants individually, 23% ± 10% (137 ± 70 of 582 ± 85) of the amplicon sequence variants (ASVs, a proxy for species) detected in the devices were not detected in the participant's saliva or stool; the median relative abundance of these 137 ASVs was low (<0.4%). Similarly, 12% ± 8% of the ASVs in stool were not detected in the participant's intestinal samples, and the median relative abundance of these ASVs was low (<0.6%) in all but one outlier participant (participant 3) whose intestinal samples were dominated by a single species (and hence many abundant ASVs in stool were not detected in the intestinal samples). In line with previous studies[24], we observed higher relative abundance of the Proteobacteria phylum in the intestines than in stool (Extended Data Fig. 3a), including a *Bilophila wadsworthia* ASV, consistent with previous reports of *B. wadsworthia*'s key role in the small intestine[25]. Four additional ASVs, from the *Escherichia*/*Shigella*, *Enterococcus*, *Bacteroides* and *Romboutsia* genera, were significantly more abundant (adjusted $P < 0.05$ and $\log_2$(fold change) > 0.75) in intestinal samples than in stool (Fig. 1f). The *Romboutsia* genus was recently named following isolation of a species from rat ileal digesta[26], in line with this genus having a niche in the small intestine.

We observed more intra-individual microbiota variability among intestinal samples than among stool or saliva samples (Fig. 2a), suggesting that the devices collect from a more heterogenous habitat. Although device types 1–4 were designed to sample the intestines longitudinally, comparisons of

microbiota composition among devices of the same type but swallowed at different times are potentially confounded by variability in meal contents, periprandial neurohormonal variations, intestinal motility, pH and/or the intestinal microbiota itself. We therefore assessed technical and biological variability by having one participant ingest four devices of the same type simultaneously; this procedure was repeated twice for each device of types 1–4 over the course of 2 months. Devices of the same type ingested at the same time contained more similar microbial communities than devices of the same type ingested at different times (Fig. 2b). The increased variance in microbiota composition due to this temporal variability is comparable to the variance due to spatial variability along the intestine, as assessed using sets of four devices of distinct types ingested at the same time (Fig. 2b). Moreover, intestinal samples (unlike saliva or stool samples) were often dominated by a single ASV with relative abundance of >40% (Fig. 2c). Consequently, individual intestinal samples contained communities with lower alpha diversity relative to the intra-individual diversity represented by all samples from a device of a certain type or by all samples from devices swallowed at the same time (Fig. 2d and Extended Data Fig. 3b,c). Thus, much of the higher variability across intestinal samples relative to stool is probably due to the dynamic and heterogeneous nature of the microbiota along the intestinal tract.

Fig. 2: Microbiota variation across device types suggests patchy structure.



a, Microbiota composition varied significantly more between intestinal samples than between stool samples ($P = 1.5 \times 10^{-7}$ within participants and $P = 2.3 \times 10^{-22}$ across participants) or between saliva samples ($P = 1.5 \times 10^{-7}$ within participants and $P = 3.5 \times 10^{-35}$ across participants). Top, each point is the mean pairwise Canberra distance between all samples for a participant ($n = 14$, 15 and 14 for stool, devices and saliva, respectively). Bottom, each point is the mean of all pairwise comparisons between all samples from any two participants ($n = 105$, 105 and 105 for stool, devices and saliva, respectively). **b**, Combinations of spatial, temporal and technical ($n = 15$ each) variability in the microbiota composition of intestinal samples (gray) were higher than in technical replicates ($n = 8$; light brown) in which one participant swallowed four of the same device type simultaneously (the participant did so twice for each of the four device types). Each point represents the mean pairwise Canberra distance between intestinal samples from the same participant. Microbial communities from devices of the same type ingested at the same time were more similar than those from devices of the same type ingested at different times, although this difference was not

statistically robust ($P = 0.058$) given the small number of observations. **c**, Devices were more likely to be dominated by a single ASV as compared with stool or saliva. Each point is a single sample ($n = 29$ for saliva, $n = 56$, 54, 55 and 45 for device types 1–4, respectively, and $n = 58$ for stool). **d**, The Shannon diversity of saliva and stool samples was higher than that of intestinal samples (saliva to device type 1, $P = 5.3 \times 10^{-7}$; device type 4 to stool, $P = 2.9 \times 10^{-9}$). Each point is a single sample ($n = 29$ for saliva, $n = 56$, 54, 55 and 45 for device types 1–4, respectively, and $n = 58$ for stool). Boxplots show the median value and the first and third quartiles. *$P \leq 0.05$, ****$P \leq 0.0001$, Bonferroni-adjusted two-sided Wilcoxon rank-sum test. Canberra distances for **a**,**b** were computed from $\log_2$-transformed read counts of 16S rRNA gene ASVs with read count ≥3 in ≥5% of samples (including all repeatability samples) ($n = 446$).

Bacteria remain viable within devices

To determine whether the intestinal microorganisms collected by the capsule devices were viable, participant 1 ingested a device designed to collect from the proximal region of the intestines. An aliquot of the sample was retrieved under anaerobic conditions ex vivo and placed on an agarose pad with nutrients. The pad was sealed to prevent oxygen from diffusing to the cells and subjected to time-lapse imaging (Methods). Over 4 h, 20–50% of cells resumed growth (Supplementary Video 2); a similar regrowth fraction was observed in anaerobic resuspensions of fresh stool (Supplementary Video 3), indicating that the devices preserve live bacteria to the same degree as seen with fresh stool. The growing cells recovered from the device collectively displayed a wide range of morphologies (Extended Data Fig. 4a), suggesting that regrowth is not heavily biased towards a few taxa. Supporting this conclusion, we used plating and flow cytometry to obtain a library of 456 isolates from several intestinal samples from participant 1 and 31 isolates from stool samples from participant 1, comprising at least 51 unique species across four phyla (Methods and Supplementary Table 2). In our time-lapse imaging, we also noted occasional human cells (~0.1% of cell count; Extended Data Fig. 4b) that were probably epithelial cells on the basis of their morphology, in line with the small fraction of metagenomic reads from these samples that mapped to the human genome. Taking these findings

together, the devices enable culturomics experiments and may provide the opportunity to study host cells present in the lumen.

Genetic variation along the intestines

To evaluate functional differences between the intestinal and stool microbiota, we performed metagenomic sequencing on all device and stool samples (Methods). We obtained 696 dereplicated metagenome-assembled genomes (MAGs; >75% complete and <25% contamination) from these data (Methods and Supplementary Table 3), which enabled taxonomic identification for read-mapping applications. On the basis of the established role of the gut microbiota in carbohydrate degradation and its links to health and disease[27], we first focused on carbohydrate active enzyme (CAZyme) gene abundance in each region. The percentage of reads that mapped to CAZymes in devices exhibited greater variance than in stool (Extended Data Fig. 5a,b). Within devices, CAZyme gene abundance was positively correlated with the relative abundance of five ASVs: two unnamed *Bacteroides* species, two *Bacteroides vulgatus* strains and *Parabacteroides merdae* ($P < 0.001$, Benjamini–Hochberg corrected; Extended Data Fig. 5c). The *B. vulgatus* strains exhibited the highest slope and strongest correlation (Spearman's $\rho = 0.77$ and 0.75). By contrast, in stool, despite a correlation between the abundance of CAZyme genes and the Bacteroidaceae family (Extended Data Fig. 5d), there were no ASVs whose abundance correlated with CAZyme gene abundance, probably because of the greater evenness of the taxa observed in stool compared with intestinal samples (Fig. 2c).

To evaluate whether certain species explain CAZyme gene abundance in intestinal samples, we investigated the genomic content of our intestinal strain library of 456 isolates derived from device samples. Whole-genome sequencing of 74 phylogenetically diverse strains (completeness of >95%; Supplementary Table 2) from this library showed that the 35 members of the Bacteroidetes phylum typically contained more CAZyme genes than members of other phyla (Extended Data Fig. 5e). The dataset included ten *Parabacteroides* strains (eight *Parabacteroides distasonis* and two *P. merdae*). Each CAZyme gene was annotated with a CAZyme enzyme class and family to give a putative functional category. The CAZymes detected in the *P. merdae* strains were assigned to a mean of 107.5 unique CAZyme

functional categories out of a mean of 237.5 CAZymes, and *P. distasonis* enzymes were assigned to 95 unique CAZyme functional categories out of a mean of 237.5 CAZymes; thus, *P. distasonis* strains appear to contain greater redundancy than *P. merdae* strains (Supplementary Table 4). Furthermore, *P. merdae* strains contained seven additional unique CAZyme functional categories in the glycoside hydrolase family and five additional unique polysaccharide lyase functional categories compared with *P. distasonis* strains (Supplementary Table 4). We also investigated five strains of *B. vulgatus*: each possessed 301 or 302 CAZyme genes representing 131 unique functional categories, more than in any other non-*Bacteroides* isolate (Extended Data Fig. 5e and Supplementary Table 4). However, *B. vulgatus* was the *Bacteroides* species with the fewest CAZyme genes (Extended Data Fig. 5e and Supplementary Table 4), indicating that factors other than CAZyme abundance influence the dominance of *B. vulgatus* over other *Bacteroides* species in the intestines. These differences in CAZyme gene abundance and functional categories are an important consideration for how diet drives the growth of certain bacteria in the gastrointestinal tract and for which by-products of carbohydrate degradation may be available to the host.

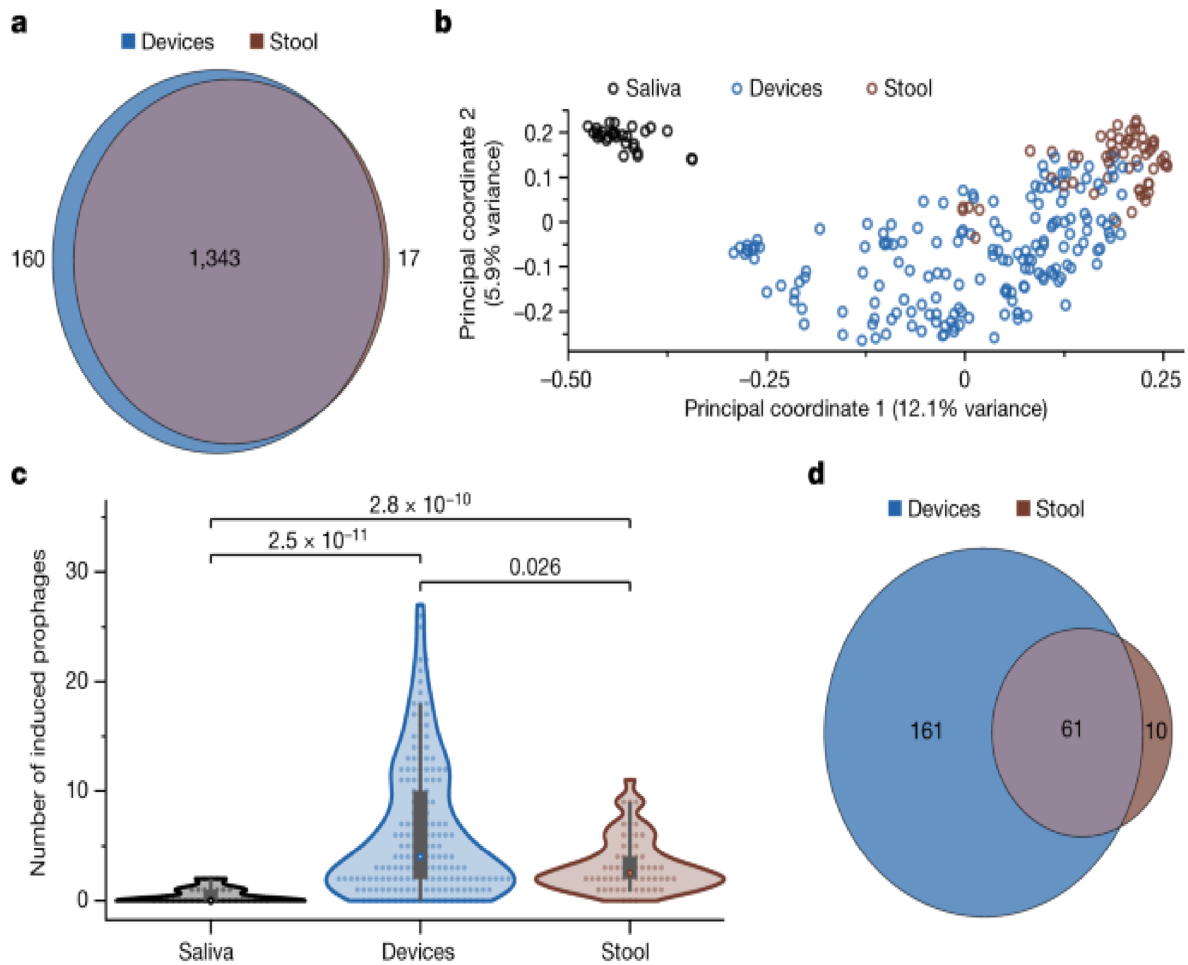
Given the substantial differences in microbiota compositions in the two participants who reported recently taking antibiotics compared with the other participants (Fig. 1e), we sought to determine whether metagenomic sequencing data could identify differences in antimicrobial resistance (AMR) potential. We focused on 6,453 AMR gene ontologies identified by the RGI algorithm on the basis of the Comprehensive Antibiotic Resistance Database (CARD, which uses a rigorously curated collection of peer-reviewed resistance determinants[28]; Methods) and calculated the percentage of reads in each sample that aligned to CARD. There were 9,596 AMR genes detected across all samples; 3,590 of these were unique and ≥90% the length of a reference AMR gene. By mapping reads from all samples to this database of 3,590 AMR genes, we found that intestinal samples had significantly higher percentages of reads that mapped to the CARD database than stool samples ($P = 0.03$, Wilcoxon rank-sum test; Extended Data Fig. 5f). In general, the frequency of AMR genes in stool was similar across participants, although some participants exhibited ~2- to 3-fold-higher mean frequencies of putative AMR genes in their intestinal samples than other participants (Extended Data Fig. 5g). Further analyses (Methods)

demonstrated that the abundance of *Escherichia*/*Shigella* species may result in larger reservoirs of AMR genes, particularly efflux-related genes, in the intestinal tract than was previously appreciated when assessing AMR in stool samples.

Increased prophage induction in intestines

Our metagenomics dataset also provided an opportunity to investigate the viral component of the intestinal microbiota. From the assembled contigs, we identified 1,607 viral operational taxonomic units (vOTUs) with >50% completeness, of which 629 were integrated prophages (Methods). Of these vOTUs, 83% (1,343/1,607) were present in both stool and intestinal samples (Fig. 3a), indicating that the intestines and stool have similar viromes. The abundance of these vOTUs as determined by read mapping was generally correlated between intestinal and stool samples (Extended Data Fig. 6a), although the intestinal samples had higher viral read mapping fractions (Extended Data Fig. 6b), perhaps owing to lower bacterial densities[1]. Viromes were more similar between stool and intestinal samples from the same participant (Jaccard distance of 0.40 ± 0.14, mean ± s.d.) than between stool (0.58 ± 0.09) or intestinal (0.62 ± 0.10) samples from different participants ($P < 10^{-10}$ in both cases, two-tailed Student's *t*-test), and PCoA of the viromes (Fig. 3b) showed similar clustering as with the microbiota (Fig. 1e).

Fig. 3: Prophage induction is more frequent in the intestines than in stool.



a, Stool and intestinal samples share most vOTUs. Only vOTUs at a depth of ≥1.0 were included. **b**, PCoA based on Canberra distance between profiles of vOTUs detected in samples coloured on the basis of sample type. **c**, Intestinal samples contained significantly higher numbers of induced prophages than stool ($P = 0.026$) or saliva ($P = 2.5 \times 10^{-11}$) samples. $n = 29$, 172 and 58 for saliva, intestinal and stool samples, respectively. P values are from a two-sided Wilcoxon rank-sum test. Density boxplots show the median value and the first and third quartiles. **d**, Most prophages induced in stool samples are also induced in the intestines, but many other induced prophages are unique to intestinal samples.

Quantification of prophage induction events based on the ratio of coverage of the viral and bacterial regions of the contig (Methods) showed significantly higher numbers of induced prophages in intestinal compared with stool samples (Fig. 3c). Most prophages (61/71) that were induced in the stool samples were also induced in the intestine; by contrast, 161 of the

222 induced prophages in intestinal samples were not observed in stool (Fig. 3d). Similar differences in prophage induction between intestinal and stool samples were observed in most participants (Extended Data Fig. 6c).

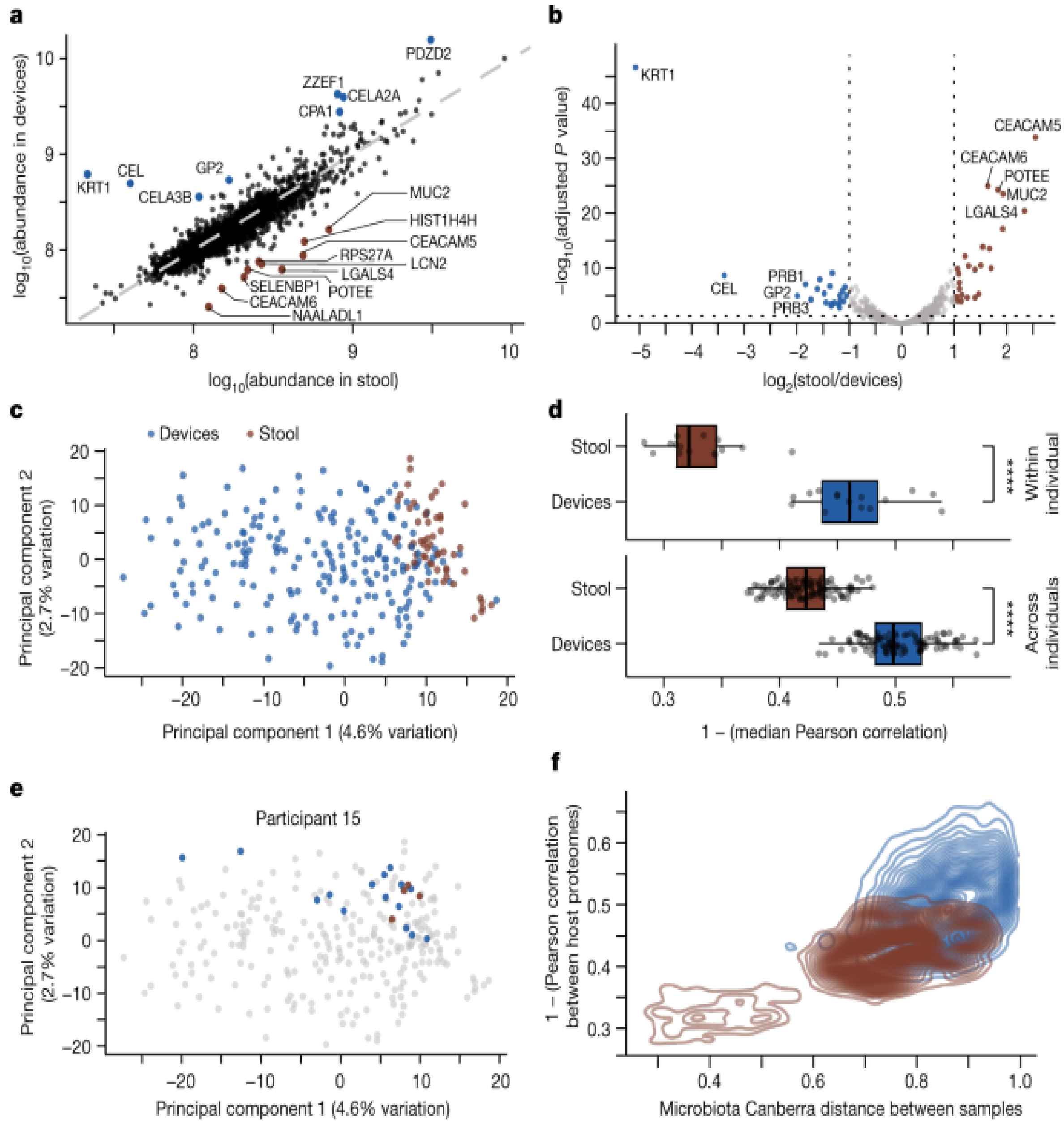
Of the contigs annotated as prophage, 279 of 629 were associated with a MAG and hence could be readily assigned taxonomy (Supplementary Table 5). Of the 328 induced prophages, the taxonomy of 138 could be assigned reliably and was collectively phylogenetically diverse, including Actinobacteria, Proteobacteria, Firmicutes and Bacteroidetes. The induced prophages were not strongly biased towards any MAG or taxon, with each MAG possessing a median of one induced prophage. Taxonomy was annotated for 141 (of 301) dormant phages, with each MAG possessing a median of one dormant phage, and these annotations were similarly diverse as the induced prophages. The number of prophage induction events was correlated with sample pH (Extended Data Fig. 6d), in line with a previous study demonstrating pH dependence of prophage induction in *Escherichia coli* strains from the bladder[29]. Taken together, our analyses indicate that the virome is individual specific but similar between the stool and intestines of the same individual, and that the intestinal environment favours prophage induction, highlighting the importance of in situ sampling for capturing phage dynamics.

Spatial variation of the host proteome

A previous study in mice showed that host protein abundance depends strongly on location within the intestinal tract[3], and our devices provide an unprecedented opportunity to quantify human host expression patterns in situ. We used liquid chromatography followed by tandem mass spectrometry (LC–MS/MS) to quantify human proteins in all intestinal and stool samples (Methods) and detected a comparable number to previous studies[30,31] (Extended Data Fig. 7a), with a similar number of detected proteins (Extended Data Fig. 7b) and coefficient of variation in the abundance of detected proteins (Extended Data Fig. 7c) across device types. The most abundant proteins in stool samples (Extended Data Fig. 7d) were consistent with previous studies[31]. Filtering for proteins detected in 70% of samples, we detected and analysed 2,276 ± 269 human proteins per sample and observed significant differences in the abundance of some proteins between

device samples and stool (Fig. 4a). A differential enrichment analysis identified sets of proteins that were indicators of regional specificity between the intestines and stool (Fig. 4b). We normalized abundance to the average across samples to account for the range of protein abundance and performed a principal component analysis (PCA). The human proteome clustered with similar qualitative features as the microbiota (Fig. 1e), with stool samples tightly clustering at high values of PC1 and intestinal samples displaying much greater variation along PC1 (Fig. 4c). Similar clustering was observed when considering only the 500 most abundant proteins (Extended Data Fig. 7e) or without normalization (Extended Data Fig. 7f). Moreover, the number of proteins with significantly different abundance between stool and each of the device types was highest between stool and type 1 devices and lowest between stool and type 4 devices (Extended Data Fig. 7g), probably reflecting longitudinal variation of the host proteome.

Fig. 4: Human protein abundance differs between stool and intestinal samples.



a, Median $\log_{10}$(abundance) of human proteins in stool samples ($n = 56$) compared with intestinal samples ($n = 212$). **b**, $\log_2$(fold change) of each protein abundance in stool relative to intestinal samples. A two-sample modified *t*-test with Benjamini–Hochberg correction was used. Proteins with absolute $\log_2$(fold change) > 1 and $P < 0.05$ are coloured on the basis of sample type and enrichment. **c**, PCA of normalized human protein abundance shows separation between intestinal and stool samples ($n = 212$ and 56, respectively). **d**, Human proteome composition varies significantly more between intestinal samples ($n = 212$) than between stool samples ($n =$

56), both within (top) and across (bottom) participants. Top, each circle is the median Pearson correlation coefficient of all sample pairs for a given participant. Bottom, each circle is the median of all correlation coefficients between all pairs of samples from any two participants ($n = 105$ for each intestinal and stool sample). ****$P \leq 0.0001$, Bonferroni-corrected two-tailed Wilcoxon rank-sum test. **e**, PCA from **c** highlighting the clustering of intestinal and stool samples from participant 15 ($n = 15$ and 4, respectively). **f**, Canberra distance between microbiota compositions was higher in samples with less similar human proteomes for all sample pairs of a given type ($n = 20,706$ pairwise comparisons for devices, $n = 1,485$ pairwise comparisons for stool).

On the basis of Pearson correlation coefficients, the host proteome in stool samples was more variable across individuals than within individuals (Fig. 4d). In intestinal samples, the host proteome was similarly variable across individuals as within individuals and was more variable than in stool samples (Fig. 4d), reflecting broad separation from stool sample proteomes (Fig. 4c). Nonetheless, in some cases (for example, in participant 15), the host proteome of intestinal samples clustered tightly with that of stool samples (Fig. 4e), similar to the microbiota-based clustering of samples from participant 15 (Fig. 1e).

To determine whether variation in the host proteome was globally related to the variation in microbiota composition across samples (Fig. 1e), we compared the Pearson correlation coefficient of the host proteome with the Canberra distance between the microbiota composition of pairs of samples. Sample pairs with more correlated proteomes had more closely related microbiota (Fig. 4f).

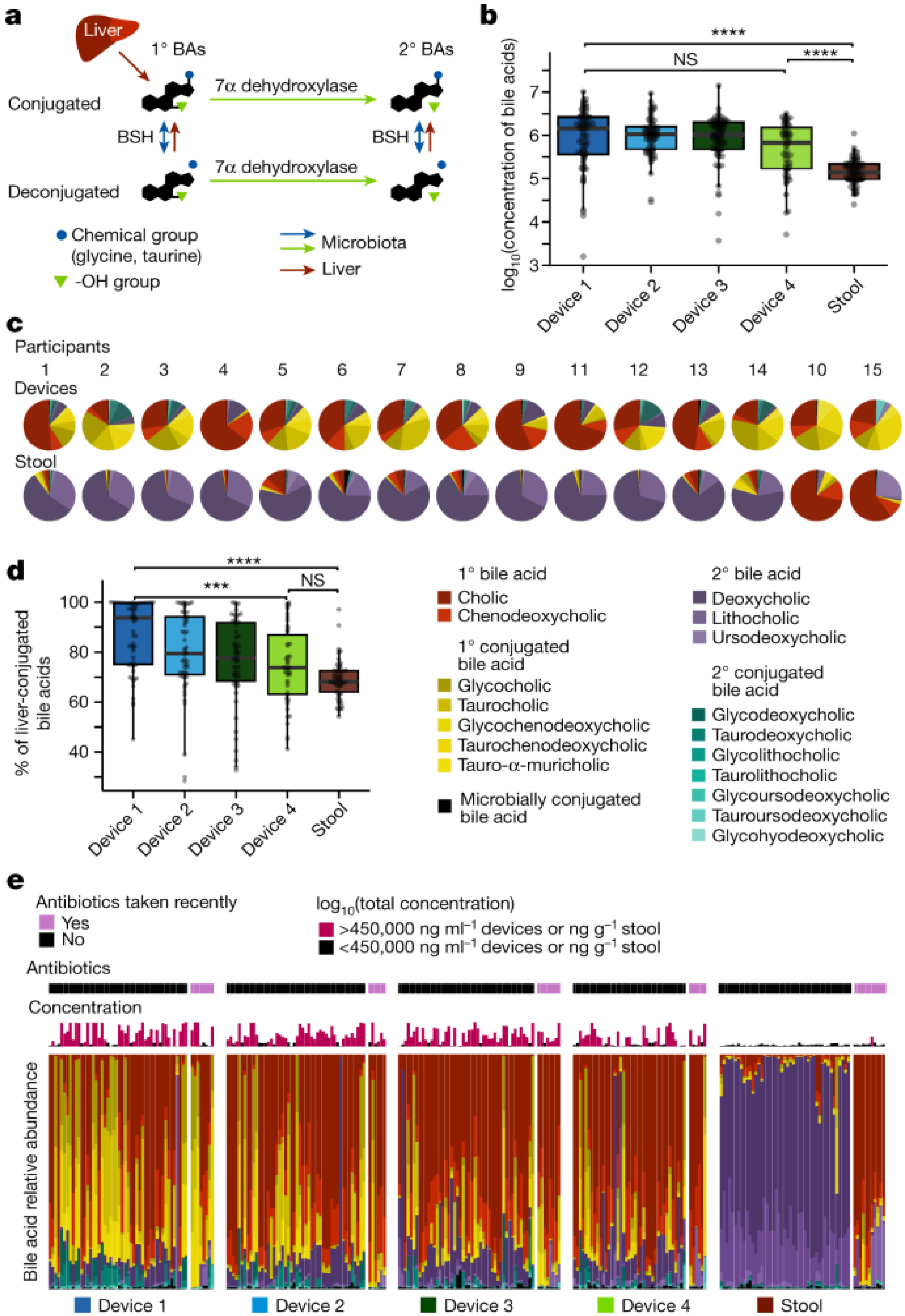
Thus, the host proteome determined from stool is not representative of the host proteome in the intestines, which is globally correlated with microbiota composition in the intestines.

Bile acid profiles along the intestinal tract

Bile acids are major chemical components of the human intestinal tract and are critical for food digestion, lipid absorption, host signalling and

neurohormonal regulation of diverse physiological processes[5]. Bile acids have been implicated in a wide range of disorders, including inflammatory bowel disease (IBD)[32], metabolic disorders[32] and neurological diseases[33,34]. Glycine- and taurine-conjugated forms of the primary bile acids cholic acid (CA) and chenodeoxycholic acid (CDCA) are secreted from the liver and gallbladder into the duodenum and are then subjected to various microbial transformations (Fig. 5a)[4,35]. Approximately 95% of bile acids that reach the distal ileum are transported through the epithelium into the portal vein and return to the liver[4], where they are transformed back into bile salts and re-secreted, creating the potential for longitudinal bile acid gradients along the intestinal tract. To quantify bile acid profiles along the intestinal tract, we performed targeted LC–MS/MS metabolomics with multiple-reaction monitoring (MRM) on 17 commonly investigated bile acids in the supernatants of all intestinal and stool samples. The total concentrations of bile acids and their relative levels in intestinal samples were highly variable (Fig. 5b), yet distinct trends were observed. The total concentration of bile acids was generally decreased by ~2-fold in samples collected by type 4 devices and ~10-fold in stool relative to samples collected by type 1 devices (Fig. 5b), probably reflecting active reabsorption of bile acids along the intestines[4].

Fig. 5: Devices capture different bile acid profiles along the intestinal tract compared with stool.



a
Liver
1° BAs
2° BAs
Conjugated
7α dehydroxylase
BSH
BSH
Deconjugated
7α dehydroxylase
Chemical group (glycine, taurine)
-OH group
Microbiota
Liver
b
log10(concentration of bile acids)
****
NS
****
Device 1
Device 2
Device 3
Device 4
Stool
c
Participants
1 2 3 4 5 6 7 8 9 11 12 13 14 10 15
Devices
Stool
d
% of liver-conjugated bile acids
****
***
NS
Device 1
Device 2
Device 3
Device 4
Stool
1° bile acid
Cholic
Chenodeoxycholic
1° conjugated bile acid
Glycocholic
Taurocholic
Glycochenodeoxycholic
Taurochenodeoxycholic
Tauro-α-muricholic
Microbially conjugated bile acid
2° bile acid
Deoxycholic
Lithocholic
Ursodeoxycholic
2° conjugated bile acid
Glycodeoxycholic
Taurodeoxycholic
Glycolithocholic
Taurolithocholic
Glycoursodeoxycholic
Tauroursodeoxycholic
Glycohyodeoxycholic
e
Antibiotics taken recently
Yes
No
log10(total concentration)
>450,000 ng ml−1 devices or ng g−1 stool
<450,000 ng ml−1 devices or ng g−1 stool
Antibiotics
Concentration
Bile acid relative abundance
Device 1
Device 2
Device 3
Device 4
Stool

a, Schematic of bile acid (BA) modifications by the liver and microbiota. The liver releases bile acids conjugated with glycine or taurine. Dehydroxylation by gut microorganisms converts primary (1°) to secondary (2°) bile acids. Microbial BSHs deconjugate amino acids from bile salts. **b**, The total concentration of all bile acids decreases along the intestinal tract (device type 1 to stool, $P = 2.0 \times 10^{-9}$; device type 4 to stool, $P = 5.6 \times 10^{-4}$; device type 1 to 4, $P = 0.18$). Shown are $\log_{10}$-transformed concentrations for intestinal ($n = 58$, 56, 57 and 47 for device types 1–4, respectively) or stool ($n = 57$) samples. **c**, The mean relative concentration of all bile acids for each participant in devices and stool. In all but two participants (10 and 15), DCA and LCA dominated the stool, but not the intestines. **d**, The percentage of liver-conjugated bile acids decreases significantly along the intestinal tract (device type 1 to stool, $P = 2.2 \times 10^{-10}$; device type 4 to stool, $P = 0.20$; device type 1 to 4, $P = 3.2 \times 10^{-4}$; $n = 58$, 56, 57 and 47 for device types 1–4, respectively, and $n = 57$ for stool samples). **e**, Relative abundance of bile acids for each sample arranged by device type. Participants are ordered 1–9, 11–14, 10, 15 within each device type. Antibiotic usage and $\log_{10}$(total concentration of bile acids) in the sample are also shown. Boxplots show the median and first and third quartiles. ***$P \leq 0.001$, ****$P \leq 0.0001$, Bonferroni-corrected two-sided Wilcoxon rank-sum test. Concentrations are in units of ng ml^{-1} or ng g^{-1} for devices and stool, respectively.

In contrast to all other participants, the stool bile acid profiles of two participants (10 and 15) were similar to their intestinal samples in that they contained a dominant fraction of CA (Fig. 5c). These are the two participants who reported recent antibiotic use and had substantially different microbiota composition to the other participants (Fig. 1e). The intestinal and stool samples from participants 10 and 15 also lacked deoxycholic acid (DCA) and lithocholic acid (LCA) (Fig. 5c), suggesting that the microorganisms necessary for the 7α-dehydroxylation reaction required to produce these bile acids may have been eliminated by the antibiotics.

In all other participants, the relative levels and dominant bile acid classes differed markedly between intestinal and stool samples. Intestinal samples were mostly dominated by the primary bile acid CA, whereas stool samples

were dominated by the secondary bile acid DCA (Fig. 5c), probably owing to prolonged exposure of bile acids to microbial enzymes in the colon. These results highlight that stool-based measurements do not reflect the true composition of bile acids along the intestinal tract.

Gradients of bile acid modifications

Bile acids are modified in the intestinal tract by microbial enzymes that deconjugate glycine or taurine or remove hydroxyl group(s) from the steroid backbone (Fig. 5a). Deconjugation is performed by bile salt hydrolases (BSHs), which cleave glycine and taurine from the bile acid backbone. BSH homologues are present in ~25% of bacterial strains sequenced from human stool samples[36]. Although there was only a small (albeit significant; $P = 0.03$, Wilcoxon rank-sum test) difference in the abundance of BSH genes between intestinal and stool samples (Extended Data Fig. 8a) and little variation in rank coverage between intestinal and stool samples (Extended Data Fig. 8b) or among device types based on metagenomic sequencing (Extended Data Fig. 8c), we observed a significant monotonic decrease in the percentage of liver-conjugated bile acids in samples from device type 1 to device type 4 (Fig. 5d), reflecting a trend of deconjugation along the intestinal tract and into stool[37].

Dehydroxylation reactions require several enzymes to transform primary to secondary bile acids and are thought to occur predominantly in the low-redox state of the colon[37]. In line with the majority of dehydroxylation occurring in the large intestine, we found that secondary bile acids did not change substantially across device types but were significantly increased in stool samples, which were dominated by secondary unconjugated bile acids (Fig. 5c and Extended Data Fig. 8d). The presence of secondary bile acids in intestinal samples is probably due to dehydroxylation of primary bile acids in the small intestine or re-introduction of secondary bile acids present in bile into the duodenum; secondary bile acids are expected to be in bile given previous evidence that they represent ~25% of the bile acids secreted from the gallbladder[37]. In sum, the variation in bile acid profiles that we detected throughout the intestinal tract (Fig. 5e) demonstrates regionality of the microbial activity and biochemical environment of the intestines, further

highlighting the limitations of relying on stool for microbiome and bile acid studies.

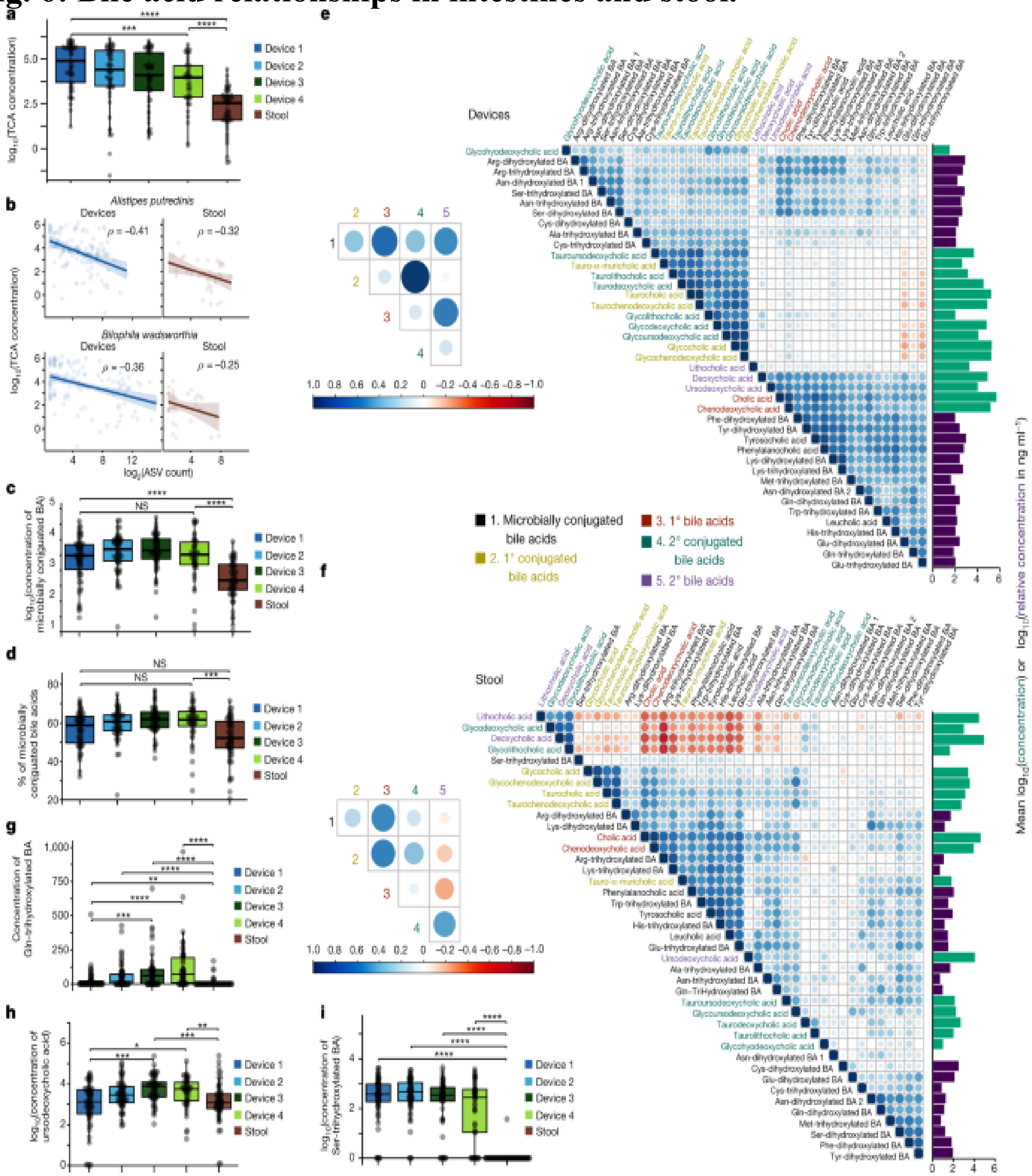
Microbial links to bile acid deconjugation

We sought to exploit the variation in conjugated bile acid concentrations across intestinal samples to identify candidate bacterial species responsible for deconjugation. Given the monotonic decrease in the fraction of liver-conjugated bile acids from device type 1 to 4 (Fig. 5d), we reasoned that the abundance of the microbial taxa most responsible for deconjugation might be inversely correlated with the concentration of conjugated bile acids, even against the background of potential regulation of deconjugation by the host or antimicrobial activity of bile acids.

We focused on primary bile acids, which dominate the pool of conjugated bile acids, namely glycocholic acid (GCA) and taurocholic acid (TCA). Previous studies have shown that diet can influence bile acid profiles in mice[25], motivating examination of whether certain types of food consumed during our study affected CA, GCA or TCA concentration in the human intestinal tract. The concentration of these bile acids was not significantly affected by diet, but participants who consumed vegetables during the study had a significantly higher ratio of TCA to GCA concentration ($P = 0.002$, Bonferroni-corrected Wilcoxon rank-sum test), and participants who had consumed dairy had a significantly higher ratio of GCA to TCA concentration ($P = 0.026$, Bonferroni-corrected Wilcoxon rank-sum test). A previous study linked milk-derived fat to TCA production in the gallbladder and *B. wadsworthia* expansion in the stool of mice[25], motivating investigation of the links between deconjugation and microbial taxa along the intestinal tract. The concentration of both GCA and TCA decreased from device type 1 to 4 and was significantly lower in stool (Fig. 6a and Extended Data Fig. 8e). GCA concentration was negatively correlated with the $\log_2$(abundance) of *Anaerostipes hadrus* and *Faecalibacterium prausnitzii* (Extended Data Fig. 8f), and TCA concentration was negatively correlated with the $\log_2$(abundance) of *Alistipes putredinis* and *B. wadsworthia* (Fig. 6b). Across all participants, we analysed our 440 high-quality MAGs (completeness of >90% and contamination of <10%, dereplicated to 99% average nucleotide identity (ANI)) and searched for the canonical BSH gene

in each using a hidden Markov model. We found putative BSH genes in *A. hadrus* (7 of 8 MAGs) and *A. putredinis* (4 of 4 MAGs), in accordance with previous literature[38]. By contrast, none of the 12 *F. prausnitzii* MAGs nor the 3 *B. wadsworthia* MAGs contained any putative BSH genes, suggesting that these taxa may use glycine and taurine[25] generated by other microbial deconjugation reactions.

Fig. 6: Bile acid relationships in intestines and stool.



a, TCA concentration decreases along the intestinal tract. Shown are $\log_{10}$-transformed concentrations. Device type 1 to 4, $P = 10^{-3}$; device type 1 to stool, $P = 6.2 \times 10^{-14}$; device type 4 to stool, $P = 5.5 \times 10^{-7}$. **b**, $\log_2$(read count) of an *A. putredinis* ASV and a *B. wadsworthia* ASV was negatively correlated ($P = 0.0020$ and $P = 0.0042$, respectively) with TCA concentration. Correlations were weaker in stool samples ($P = 0.36$ and $P = 0.56$, respectively). Correlations are Spearman correlations with Benjamini–Hochberg correction. Only ASVs with $P < 0.01$ after correction in devices are shown. Points are individual intestinal ($n = 210$) or stool ($n = 56$) samples for which both 16S rRNA sequencing and metabolomics data were available. **c**, The concentration of microbially conjugated bile acids is significantly higher in intestinal samples than in stool samples. The concentration did not differ significantly across device types. Device type 1 to 4, $P = 1$; device type 1 to stool, $P = 3.5 \times 10^{-6}$; device type 4 to stool, $P = 1.6 \times 10^{-6}$. **d**, The percentage of microbially conjugated bile acids increases along the intestinal tract and was significantly higher in intestinal samples than in stool. Device type 1 to 4, $P = 0.40$; device type 1 to stool, $P = 0.23$; device type 4 to stool, $P = 8.0 \times 10^{-4}$. **e**,**f**, Correlations between bile acid profiles differ between intestinal (**e**) and stool (**f**) samples. Shown are Pearson correlation coefficients using $\log_{10}$-transformed concentrations. Horizontal bars show the mean absolute concentration (green) or relative concentration (purple) (Methods). Bile acid ordering was determined by hierarchical clustering. Insets show the Pearson correlation coefficient for aggregated classes. **g**–**i**, Concentration of the respective bile acid across devices and stool. P values from top to bottom for **g**: 4.3×10^{-9}, 7.5×10^{-9}, 5.1×10^{-7}, 7.0×10^{-3}, 1.8×10^{-4} and 6.5×10^{-4}. P values from top to bottom for **h**: 0.001, 5.8×10^{-5}, 0.023 and 1.4×10^{-4}. P values from top to bottom for **i**: 5.9×10^{-13}, 1.5×10^{-16}, 8.5×10^{-20} and 6.2×10^{-19}. All boxplots show the median and first and third quartiles. Points are individual intestinal ($n = 58$, 56, 57 and 47 for device types 1–4, respectively) or stool ($n = 57$) samples, unless otherwise indicated. Concentrations in ng ml^{-1} (intestinal) or ng g^{-1} (stool). *$P \leq 0.1$, **$P \leq 0.01$, ***$P \leq 0.001$, ****$P \leq 0.0001$, Bonferroni-corrected two-sided Wilcoxon rank-sum test.

A number of negative correlations (implying potential microbial deconjugation) involving other taurine- and glycine-conjugated bile

acids were observed (Extended Data Fig. 8g–j). Taurochenodeoxycholic acid (TCDCA) concentration (Extended Data Fig. 8g) was also negatively correlated with *B. wadsworthia* and *A. putredinis* $\log_2$(abundance) (Extended Data Fig. 8i), and taurodeoxycholic acid (TDCA) was negatively correlated with *A. putredinis* $\log_2$(abundance) (Extended Data Fig. 8j), suggesting that these species interact with various taurine-conjugated bile acids. We focused mainly on *B. wadsworthia* because it was differentially abundant in intestinal samples compared with stool (Fig. 1f). The name of the *Bilophila* genus reflects its growth stimulation by high concentrations of bile[39], and the higher ratio of GCA to TCA concentration in participants who consumed dairy is potentially due to the ability of *B. wadsworthia* to deconjugate TCA to use taurine for growth[25]. Notably, in stool, the relative abundance of *B. wadsworthia* and *A. putredinis* was correlated only weakly or not at all with TCA concentration (Fig. 6b), indicating that the devices identify correlations between bile acids and microorganisms that would not be evident from stool.

Amino acid-specific bile acid conjugation

Bile acids conjugated to amino acids other than glycine and taurine (for example, tyrosocholic acid (TyroCA), leucocholic acid (LeuCA) and phenylalanocholic acid (PhenylCA)) were recently discovered in the gut of mice and stool of humans[35]. Synthesis of TyroCA, LeuCA and PhenylCA[35] by microorganisms that reside in the intestinal tract has been reported in vitro[40], and the levels of these conjugates differ significantly between healthy and disease states such as Crohn's and IBD[35,41]. Furthermore, these microbially conjugated bile acids are agonists of the human farnesoid X receptor[20]. Despite widespread interest in these conjugates, very few studies have measured their levels, particularly in host-relevant contexts such as the intestines, where longitudinal trends are completely unknown. Using untargeted LC–MS/MS analysis with data-dependent MS/MS acquisition, we detected 22 microbially conjugated bile acids in various hydroxylation forms across 13 amino acids in the intestinal samples of all participants (Supplementary Table 6). Microbially conjugated bile acids were at significantly higher concentrations (Fig. 6c) and accounted for a significantly higher fraction of the bile acid pool (Fig. 6d) in intestinal samples compared with stool.

The concentrations of primary and secondary liver-conjugated bile acids were highly correlated, while the total concentration of microbially conjugated bile acids was correlated with that of deconjugated bile acids across intestinal samples (Fig. 6e). In stool, the total concentration of microbially conjugated bile acids was correlated with the concentration of primary deconjugated bile acids and inversely correlated with the concentration of secondary deconjugated bile acids (Fig. 6f). These findings emphasize the effect of different anatomical regions and routes of formation and degradation on liver-conjugated bile acids (glycine and taurine conjugates) and microbially conjugated bile acids, further highlighting major differences in the metabolite environment of the intestines versus stool.

Across all intestinal samples in this study, the 22 microbially conjugated bile acids clustered into two groups: the concentration of cysteine-, serine- and alanine-conjugated bile acids exhibited strong correlation with the concentration of liver-conjugated bile acids such as GCA and TCA, while the concentration of glutamic acid-, glutamine-, tryptophan-, leucine-, arginine-, phenylalanine-, lysine- and tyrosine-conjugated bile acids correlated strongly with the concentration of unconjugated bile acids such as CA and CDCA (Fig. 6e). The clustering of correlation profiles of many di- and trihydroxylated bile acids of the same amino acid underscores the amino acid dependence of trends in microbially conjugated bile acids. This clustering was not present in stool samples (Fig. 6f); instead, both liver-conjugated and unconjugated bile acids correlated with various bile acid types conjugated with a given amino acid, which were sometimes largely uncorrelated with each other (for example, glutamate dihydroxlated and glutamate trihydroxylated; Fig. 6f).

Of the 22 microbially conjugated bile acids detected in intestinal samples, 20 were reliably detected in stool despite lower overall levels of bile acids in the stool (Fig. 6e,f). Even with variation in concentration, several microbially conjugated bile acids exhibited a gradient across device types and showed amino acid-specific trends. Glutamine-conjugated bile acids increased from type 1 to 4 devices (Fig. 6g) similarly to unconjugated secondary bile acids such as ursodeoxycholic acid (Fig. 6h), in line with the hypothesis that microbial conjugation along the small intestine causes some bile acids to increase in concentration. However, serine-conjugated bile acids decreased from type 1 to 4 devices (Fig. 6i), similar to trends in liver-

conjugated bile acids such as TCDCA (Extended Data Fig. 8g); this decrease in concentration is probably due to flow of microbially conjugated bile acids through enterohepatic circulation and deconjugation along the intestines when they are excreted in bile. Microbial deconjugation is the most parsimonious explanation for the decreases in concentration of certain microbially conjugated bile acids between device types 1 and 4 (Fig. 6c,d). Although PhenylCA, LeuCA and TyroCA are microbially conjugated, a previous study reported that PhenylCA, LeuCA and TyroCA are not deconjugated by intestinal microbiota[35]; we found that PhenylCA, LeuCA and TyroCA were not among the bile acids that decreased from device type 1 to 4. Together, these observations indicate that some microbially conjugated bile acids may be deconjugated by microorganisms while others are not. Previous studies did not detect these opposing longitudinal trends in microbially conjugated bile acids[41]. These data represent a spatial investigation of microbially conjugated bile acids in the human intestines and identify trends that are amino acid specific.

Discussion

Thus far, studies of the human gut microbiome and metabolites have relied mainly on stool. In this study, enabled by the development and implementation of an ingestible sampling device, we demonstrated that analysis of stool provides neither a complete nor an accurate representation of the longitudinal and temporal variability of the microbiota composition, virus activity, host proteome and bile acid contents within the intestines. The trends in microbially conjugated bile acids were strong and novel, and, although it remains unclear why bile acids exhibit distinct abundance profiles along the intestinal tract, our data provide the opportunity to identify the bacterial species and genes responsible for these transformations and profiles. The wide variability among intestinal samples, both within and across individuals, highlights the dynamic environment of the small intestine and the need for increased sampling (both longer term and in larger cohorts) to determine baseline variation expected in healthy individuals before studies of disease states can be robustly evaluated for differences in spatiotemporal variability or overall community composition. With that understanding, we envision interrogating how diet and disease differentially influence the intestinal microbiota, metabolome, virome and proteome.

Indeed, measurements from the proximal intestinal microbial ecosystem will be critical for future clinical studies of spatially restricted human intestinal diseases and therapeutic interventions directed at these disorders.

In a companion study[19], we interrogate spatial and temporal differences in intestinal metabolomes in further detail, including changes to dietary and lipid compounds. We report the detection in humans of sulfonolipids, which were associated with several microbial taxa, as well as an association of FAHFA lipids with *Blautia* species. Taken together, these studies demonstrate the feasibility and utility of a safe and non-invasive method for collection, characterization and quantification of the intestinal microbiota, metabolome, host proteins and bile acids along the human intestinal tract during normal digestion. This new capability, when deployed at scale, should improve understanding of the dynamic and intertwined nature of human metabolic pathways with our resident gut microorganisms and their potential involvement in normal physiology and disease.

Methods

Ingestible capsule sampling device

The capsule sampling device (CapScan, Envivo Bio) consists of a hollow elastic collection bladder capped by a one-way valve. The device is prepared for packaging by evacuating the collection bladder, folding it in half and packaging the folded device inside a dissolvable capsule measuring 6.5 mm in diameter and 23 mm in length, onto which an enteric coating is applied. The capsule and the enteric coating prevent contamination of the collection bladder from oral–pharyngeal and gastric microorganisms during ingestion. When the device reaches the target pH, the enteric coating and capsule disintegrate. The target pH is 5.5 for type 1, 6 for type 2 and 7.5 for type 3 and type 4, with type 4 also having a time delay coating to bias collection towards the ascending colon. After the enteric coating disintegrates, the collection bladder unfolds and expands into a tube 6 mm in diameter and 33 mm in length, thereby drawing in up to 400 µl of gut luminal contents through the one-way valve. The one-way valve maintains the integrity of the sample collected inside the collection bladder as the device moves through the colon and is exposed to stool.

In this study, participants concurrently ingested sets of four devices, each with distinct coatings to target the proximal to medial regions of the small intestine (coating types 1 and 2) and more distal regions (coating types 3 and 4). After sampling, the devices were passed in the stool into specimen-collection containers and immediately frozen. After completion of sampling, the stool was thawed and the devices were retrieved by study staff. The elastic collection bladders were rinsed in 70% isopropyl alcohol and punctured with a sterile hypodermic needle attached to a 1-ml syringe for sample removal. Samples were transferred into microcentrifuge tubes, and the pH was measured with an InLab Ultra Micro ISM pH probe (Mettler Toledo). A 40-µl aliquot was spun down for 3 min at 10,000 RCF, and its supernatant was used for metabolomics analysis while the pellet was used for proteomics analysis. The rest of the sample was frozen until being thawed for DNA extraction.

Study design

The study was approved by the WIRB-Copernicus Group institutional review board (study 1186513), and informed consent was obtained from each participant. Healthy volunteers were selected to exclude participants with clinically detectable gastrointestinal conditions or diseases that would potentially interfere with data acquisition and interpretation. There was no blinding, randomization, or statistical methods to determine sample size.

Participants met all of the following criteria for study inclusion: (1) age between 18 and 70 years; (2) American Society of Anesthesiologists (ASA) physical status class risk of 1 or 2; (3) for women of childbearing potential, a negative urine pregnancy test within 7 days of the screening visit and willingness to use contraception during the entire study period; and (4) fluency in English, with an understanding of the study protocol and ability to supply informed written consent, as well as compliance with study requirements.

Individuals with any of the following conditions or characteristics were excluded from the study: (1) a history of any of the following: prior gastric or oesophageal surgery, including lap banding or bariatric surgery, bowel obstruction, gastric outlet obstruction, diverticulitis, IBD, ileostomy or colostomy, gastric or oesophageal cancer, achalasia, oesophageal

diverticulum, active dysphagia or odynophagia, or active medication use for any gastrointestinal conditions; (2) pregnancy or planned pregnancy within 30 days of the screening visit or breast-feeding; (3) any form of active substance abuse or dependence (including drug or alcohol abuse), any unstable medical or psychiatric disorder, or any chronic condition that might, in the opinion of the investigator, interfere with conduct of the study; or (4) a clinical condition that, in the judgment of the investigator, could potentially pose a health risk to the individual while they were involved in the study.

Fifteen healthy individuals were enrolled in this study, and each swallowed at least 17 devices over the course of 3 days (for demographics, see Supplementary Table 1). Daily instructions included the following guidelines: record all foods and the time they were consumed throughout the day; if you work out, do so in the morning; eat breakfast and lunch as usual; swallow a set of four devices 3 h after lunch with up to two-thirds cup water; do not eat or drink anything for at least 2 h after swallowing the devices; if hungry after 2 h, snack lightly (up to 200 calories); do not drink any caffeinated beverages after lunch until the next morning; collect all stool starting 6 h after swallowing this set of devices until 48 h after swallowing the next set of devices; eat dinner as usual at least 6 h after lunch; swallow a set of four devices 3 h after dinner with two-thirds cup water; after swallowing this set, do not eat or drink anything until the morning. Alcohol consumption and diet contents were not restricted. All ingested devices were recovered, and no adverse events were reported during the study. Of the 255 ingested devices, 15 were set 1 safety devices (not included in analysis) and 22 contained gas or low sample volume. Saliva samples were collected after evening meals and immediately frozen at –20 °C. A sample of every bowel movement during the study was immediately frozen by the participant at −20 °C. A total of 306 samples (n = 29 saliva, n = 218 devices, n = 59 stool) provided sufficient material for multi-omic analyses (Extended Data Fig. 2a). Furthermore, participant 1 provided additional samples for assessment of replicability and microbial blooming.

Blooming analysis

To assess the effect of in-body incubation on the contents of the devices between the time of sample collection and sample retrieval, a set of four devices (one of each type) was ingested by participant 1. Following exit in a bowel movement at 32 h, the devices were immediately transferred to an anaerobic chamber and incubated at 37 °C. An aliquot of each sample was taken at 32 h (immediately after the bowel movement), 58 h and 87 h (with the latter two time points simulating lengthier gut transit times). These aliquots were subjected to 16S rRNA gene amplicon sequencing. The rank abundance of the 30 most abundant ASVs at 32 h shifted at 58 h by a median of 8–16 ranks and at 87 h by 12–30 ranks (Extended Data Fig. 1). The 9–17 ASVs that increased from below to above the detection limit during incubation collectively accounted for a relative abundance of 9.4–13.8% after 58 h and 5.2–18% after 87 h, presumably because of growth during incubation. Thus, although outgrowth can potentially alter assessments of microbiota composition, major changes are not expected for transit times of ~58 h or less.

Time-lapse imaging

Agarose (1%) pads with BHI medium were sealed using VALAP (1:1:1 Vaseline:lanolin:paraffin) and maintained at 37 °C using a heated environmental chamber (HaisonTech). Phase-contrast images were collected on a Nikon Ti-E epifluorescence microscope using μManager (v.1.4)[42].

DNA extraction and 16S rRNA gene sequence analysis

Of the 240 devices, 218 collected >50 μl of intestinal fluids and were subjected to DNA extraction and 16S rRNA gene and metagenomic sequencing; the remainder sampled <50 μl or were filled with gas, most likely from the colon.

For the 218 devices that sampled >50 μl, DNA was extracted using a Microbial DNA extraction kit (Qiagen)[43] and 50 μl from a device, 200 μl of saliva or 100 mg of stool.

16S rRNA amplicons were generated using Earth Microbiome Project-recommended 515F/806R primer pairs and 5PRIME HotMasterMix

(Quantabio, cat. no. 2200410) with the following programme in a thermocycler: 94 °C for 3 min; 35 cycles of 94 °C for 45 s, 50 °C for 60 s and 72 °C for 90 s; and 72 °C for 10 min. PCR products were cleaned, quantified and pooled using the UltraClean 96 PCR Cleanup kit (Qiagen, cat. no. 12596-4) and Quant-iT dsDNA High-Sensitivity Assay kit (Invitrogen, cat. no. Q33120). Samples were sequenced with 250-bp reads on a MiSeq instrument (Illumina).

Sequence data were demultiplexed using the Illumina bcl2fastq algorithm at the Chan Zuckerberg Biohub Sequencing facility. Subsequent processing was performed with the R statistical computing environment (v.4.0.3)[44] and DADA2 as previously described[43] using pseudo-pooling[45]. truncLenF and truncLenR parameters were set to 250 and 180, respectively. Taxonomy was assigned using the Silva rRNA database (v.132)[46]. Samples with >2,500 reads were retained for analyses. We obtained sufficient sequencing reads from 210 samples, which were the focus of subsequent analyses, along with sequencing data from 29 saliva and 58 stool samples (one participant provided only one saliva sample, and one stool sample had insufficient sequencing reads; Extended Data Fig. 2a).

A phylogenetic tree was constructed using phangorn as previously described[47]. Shannon diversity was calculated using the phyloseq::estimate_richness function, which is a wrapper for the vegan::diversity function[48,49]. Because intestinal samples were often dominated by a single ASV (Fig. 2c), the Canberra distance metric was used for pairwise beta-diversity comparisons. Only the 455 ASVs represented by ≥3 reads in ≥5% of samples were used to calculate distances.

Limitations and contamination analysis

One limitation of our study is that the exact location of sample collection within the intestines could not be clearly defined or validated. Variability in intestinal peristalsis and pH during normal digestion may cause devices within a set to experience different pH gradients; hence, they may open before or after their intended collection sites. Despite this limitation, analysis of 210 intestinal samples from 15 individuals showed consistent trends of biochemical and microbial activity in the human intestines. More consistent

sampling along a longitudinal gradient might be attained in future studies by collecting multiple sequential samples into a single device in a timed manner.

The significantly different bile acid profiles in intestinal compared with stool samples indicate that it is unlikely that stool contaminated the intestinal sampling devices during transit or sample recovery. However, because of the large increase in microbial density along the intestinal tract[37], even a minute amount of stool contamination could affect microbiota composition. We therefore used a statistical approach to identify samples as potentially contaminated on the basis of microbial community composition. Given the directional motility of the intestinal tract, one would expect intrinsic overlap between intestinal and stool microbial communities. Latent Dirichlet allocation with the topicmodels R package[50] was used to identify co-occurring groups of microorganisms ('topics'[51]) from intestinal and stool samples for each participant. For each intestinal sample, the cumulative probability of topics identified as derived from the same participant's stool was computed. Device samples with ≥10% of the total community identified as potentially originating from stool topics were flagged as possibly contaminated. Using this very conservative definition, 38 of the 210 intestinal samples with adequate sequencing read counts (originating from 12 of the study participants) were identified as possibly contaminated. All analyses presented in this study used all available data to avoid bias, but re-analysis of all data after removing the 38 samples that showed any signal of potential contamination from stool resulted in the same statistical trends as with the complete group of samples.

Metagenomic sequencing

Extracted DNA from all samples was arrayed in a 384-well plate, and concentrations were normalized after quantification using the PicoGreen dsDNA Quantitation kit (ThermoFisher). DNA was added to a tagmentation reaction, incubated for 10 min at 55 °C and immediately neutralized. Mixtures were added to ten cycles of a PCR that appended Illumina primers and identification barcodes to allow for pooling of samples during sequencing. One microlitre of each well was pooled, and the pooled library was purified twice using AMPure XP beads to select appropriately sized

bands. Finally, library concentration was quantified using a Qubit instrument (ThermoFisher). Sequencing was performed on a NovaSeq S4 instrument with read lengths of 2 × 146 bp.

Preprocessing of raw sequencing reads and metagenomic assembly

Skewer (v.0.2.2)[52] was used to remove Illumina adaptors, after which human reads were removed with Bowtie2 (v.2.4.1)[53]. Metagenomic reads from a single saliva, intestinal or stool sample were assembled with MEGAHIT (v.1.2.9)[54]. Assembled contigs were binned with MetaBAT 2 (v.2.15)[55] into 7,655 genome bins. checkM (v.1.1.3)[56] and quast (v.5.0.2)[57] were used to assess quality; bins with >75% completeness and <25% contamination were dereplicated at 99% ANI (strain level) with dRep (v.3.0.0)[58], resulting in 696 representative MAGs across all samples. GTDB-Tk was used to assign taxonomy[59]. Default parameters were used for all computational tools.

Strain isolation from intestinal and stool samples

Isolates were obtained directly from samples or from communities derived from passaging of samples[60] by either plating or fluorescence-activated cell sorting (FACS)[61]. For plating, samples were serially diluted tenfold onto BHI + 10% defibrinated horse blood (BHI-blood) plates and incubated for 72 h at 37 °C in an anaerobic chamber. Single colonies were re-streaked onto BHI-blood plates. This process was repeated an additional two times to ensure that the colony was axenic. Single colonies were then picked into a 2-ml deep-well plate containing 500 µl of BHI supplemented with menadione (vitamin K), cysteine and hemin (BHIS). In certain cases, Reinforced Clostridial Medium supplemented with menadione (vitamin K), cysteine and hemin (RCMS) was used instead. For FACS, single cells were sorted into BHIS using a previously described protocol that allows for isolation of strict anaerobes[61].

After 72 h of growth in an anaerobic chamber at 37 °C, frozen stocks of all isolates were made using a final concentration of 12% glycerol. To identify isolates, cultures were spun down and pellets were resuspended with PCR-

grade water in a 1:1 ratio. The primers 5′-AGAGTTTGATCCTGGCTCAG-3′ and 5′-GACGGGCGGTGWGTRCA-3′ were used to amplify the 16S rRNA gene. The PCR product was sent for Sanger sequencing, and sequences were filtered using sangeranalyseR with default parameters[62]. These sequences were searched against the rRNA/ITS BLAST database, and the top species hit was used to identify the strain.

Analysis of CAZyme and AMR content

Putative genes were called on assembled contigs for each sample or on assembled MAGs using Prodigal[63]. CAZyme genes were identified using run_dbcan.py (v.3.0.5)[64] with default parameters (searching with HMMER, eCAMI and DIAMOND). Genes identified in at least two of three programmes were dereplicated to create a curated database. Metagenomic reads for each sample were mapped against this database to calculate the percentage of reads mapped. AMR genes were identified using rgi (v.5.2.0)[28] with default parameters. All identified genes were filtered for >90% coverage and dereplicated to create a curated database of AMR genes. Metagenomic reads for each sample were mapped against this database to calculate the percentage of reads mapped.

CARD is known to be biased towards pathogens such as *Escherichia*/*Shigella* species[28], and indeed the relative abundance of *Escherichia*/*Shigella* species was highly positively correlated with the abundance of AMR genes in intestinal samples (Extended Data Fig. 5h). In stool samples, although no ASVs were positively correlated with the percentage of reads aligned to CARD, the abundance of the Enterobacteriaceae family was positively correlated, as was that of the Bacteroidaceae family (Extended Data Fig. 5i). To determine whether this correlation was driven by efflux activity, we recomputed AMR gene abundance while ignoring the 1,273 genes annotated as efflux pumps. In this analysis, intestinal samples did not exhibit significantly higher numbers of reads mapping to non-efflux AMR genes (Extended Data Fig. 5j). We identified AMR genes in each of our MAGs and found that Enterobacteriaceae possessed ~10- to 100-fold more AMR genes (normalized to the total number of genes) than other taxonomic families (Extended Data Fig. 5k).

Viral contig identification

After assembly, contigs >1 kb in length were analysed using VirSorter2 (ref. [65]), DeepVirFinder[66] and VIBRANT[67]. Contigs identified as viral by at least one algorithm (VirSorter2 score ≥0.9, or DeepVirFinder score ≥0.9 and $P < 0.05$, or VIBRANT score of medium quality or higher) were clustered using an ANI cut-off of 0.95 and coverage cut-off of 85%. The quality of the clustered contigs was analysed using CheckV[68], which also classified viral contigs as prophages if they contained both viral and bacterial regions.

Detection of prophage induction events

The algorithm PropagAtE[69] was used to identify active prophages with default parameters. In each sample, the total reads were first rarefied so that the number of reads mapped as viral was 5×10^5 (six device samples and ten saliva samples had fewer than 5×10^5 reads, and hence all reads from these samples were used for analyses). The reads were then mapped to the prophage contigs with a minimum per-cent identity of 97%. The algorithm identifies a prophage as active (induced) when the ratio of prophage to host depth for that contig is >2 and the prophage region has >50% coverage.

Proteomics sample preparation

After thawing samples, 20 µl of MS-grade water (Pierce) was added to each sample and the mixture was vortexed. Twenty microlitres of this mixture was transferred to a 96-well plate (AFA-TUBE TPX plate, cat. no. 520291, Covaris). Twenty microlitres of cell lysis buffer (containing Tris, CAA, TCEP and 8% SDS)[9] was added to each sample aliquot, and samples were boiled for 10 min in a PCR thermocycler (Eppendorf) to achieve reduction of disulfide bridges and alkylation of cysteines and to boost protein denaturation. Following boiling, samples were placed in a −80 °C freezer to ensure microbial capsule dissociation. Freeze–thaw cycles were repeated twice. Subsequently, samples were processed using the APAC protocol (https://d24ci5y4j5ezt1.cloudfront.net/wp/wp-content/uploads/2020/06/M020141.pdf). In brief, we applied Adaptive Focused Acoustics (AFA, Covaris) sonication in the 96-well plate for a total

duration of 300 s per column with an LE220-plus Focused ultrasonicator (Covaris) using the following parameters: peak power, 450 W; duty factor, 50%; cycles, 200; average power, 225 W.

In preparation for protein aggregation capture (PAC), magnetic carboxylate-modified particles (Sera-Mag, cat. no. 24152105050350, GE Healthcare/Merck) were washed three times with 1 ml of MS-grade water. Because the protein concentration of the samples varied over a large range, 500 µg of beads were added to each sample well to ensure sufficient beads regardless of the protein concentration. Protein precipitation was induced by the addition of acetonitrile at a final concentration of 70%.

Proteins were subsequently extracted from the solution through precipitation of the magnetic particles and purification by three steps of washing in 2-isopropanol. Following each wash, the plate was placed at 50 °C and shaken at 1,300 rpm for 10 min. To ensure complete precipitation, we incubated the suspension for a further 10 min at room temperature while shaking at 1,300 rpm and then allowed the beads to settle for 10 min without agitation.

To determine the concentration of enzymes needed during sample digestion, we measured the protein yield using a Nanodrop. Samples were then resuspended in digestion buffer, which contained 100 µl of 100 mM Tris (pH 8.5), supplemented with 0.5 µg trypsin and 0.5 µg LysC to achieve an enzyme:protein ratio of 1:20, and incubated overnight at 37 °C with shaking at 1,300 rpm.

Following digestion, the supernatant was removed by placing the 96-well plate on a magnetic rack (DynaMag-96 Side Skirted Magnet, cat. no. 12027, Invitrogen, ThermoFisher Scientific), allowing the supernatant to be easily transferred to a 96-well PCR plate (twin.tec PCR Plate LoBind, semi-skirted, 250 µl; cat. no. 0030129504, Eppendorf). The enzymatic reaction in the collected supernatant was quenched using trifluoracetic acid (TFA) at a final concentration of 1% (v/v). Peptides were purified using two-layer SDB–RPS (Empore SPE Disks; CDS Analytical, cat. no. 98-0604-0226-4) StageTips by three washing steps, twice in 1% TFA in 2-isopropanol and once in 0.2% TFA in water. Following the washing steps, peptides were eluted from the StageTips using elution buffer (80% acetonitrile and 1% NH_4^+)[70]. Purified samples were vacuum-dried in a SpeedVac (Eppendorf) at

60 °C for 1.5 h and resuspended in A* injection buffer (2% (v/v) acetonitrile and 0.1% (v/v) TFA in water). Protein concentration was measured in injection buffer for each sample using a Nanodrop, and samples were stored at −20 °C until MS measurement.

Proteomics UHPLC and mass spectrometry

Samples were analysed using LC–MS instrumentation, comprising an EASY-nLC 1200 ultra-high-pressure system coupled to an Exploris 480 with a nano-electrospray ion source (ThermoFisher Scientific). For each sample, the equivalent of 360 ng of purified peptides was separated on a custom 50-cm C18 LC column[71]. Peptides were eluted from the column using a linear gradient from 10% to 30% buffer B over 90 min at a constant flow rate of 300 nl min^{-1}, followed by a stepwise increase of buffer B to 60% for 5 min and an increase to 95% buffer B over the following 5 min. Afterwards, we applied a 5-min wash with 95% buffer B, followed by a decrease to 1% buffer B over 5 min and a 20-min wash.

The column temperature was kept constant at 50 °C using a custom oven, and HPLC parameters were monitored in real time using SprayQC software[72]. MS data were acquired with a Top15 data-dependent MS/MS method. The target values for the full-scan MS spectra were 3×10^6 charges in the *m*/*z* range 300–1,650, with a maximum injection time of 20 ms and a resolution of 60,000 at *m*/*z* 200. Fragmentation of precursor ions was performed by higher-energy C-trap dissociation (HCD) with a normalized collision energy of 27 eV. MS/MS scans were performed at a resolution of 15,000 at *m*/*z* 200 with a target value of 1×10^5 and a maximum injection time of 28 ms. Dynamic exclusion was set to 40 s to avoid repeated sequencing of identical peptides.

A HeLa sample was run approximately every 70 samples to ensure that the performance of the LC system and MS was maintained throughout the entire study. Technical replicates were collected for each plate in a random fashion to assess technical reproducibility. In all, 212 device samples and 56 stool samples passed quality control and were used for analyses (Extended Data Fig. 2a).

Proteomics data processing

MS raw files were analysed with MaxQuant software (v.2.1.0.0)[73], and peptide lists were searched against the UniProt human SwissProt and TREMBL FASTA database (version June 2022). A common contaminants database was also included[74]. Our search parameters included cysteine carbamidomethylation as a fixed modification and N-terminal acetylation and methionine oxidation as variable modifications. The false discovery rate (FDR) for proteins and peptides was set to 0 at a minimum peptide length of 7 amino acids. An in silico tryptic digest was used with a maximum of two missed cleavage sites. Peptide identification was performed at a precursor mass accuracy of 7 ppm and a fragment mass accuracy of 20 ppm. A reversed decoy database was used to estimate the fraction of false positive hits. Label-free quantification (LFQ) was performed at a minimum ratio count of 2 (ref. [75]). LFQ values, or non-normalized intensity values when indicated, were further processed in R (v.4.1.2). Proteins were filtered for 70% valid values in all samples. For PCA, missing values were imputed with the regularized method of the package missMDA (v.1.19), and PCA plots were generated with PCAtools (v.2.4.0). Statistical analysis was performed with limma (v.3.48.3) and a moderated *t*-test with FDR adjustment for multiple-hypothesis testing.

Sample preparation for LC–MS/MS metabolomics analysis

Supernatants from intestinal samples were extracted using a modified 96-well-plate biphasic extraction[76]. Samples in microcentrifuge tubes were thawed on ice, and 10 µl was transferred to the wells of a 2-ml polypropylene 96-well plate in a predetermined randomized order. A quality-control sample consisting of a pool of many intestinal samples from pilot studies was used to assess analytical variation. A quality-control sample matrix (10 µl) and blanks (10 µl of LC–MS-grade water) were included for every tenth sample. Further, 170 µl of methanol containing UltimateSPLASH Avanti Polar Lipids was added to each well as an internal standard. Then, 490 µl of methyl-*tert*-butyl-ether (MTBE) containing the internal standard cholesterol ester 22:1 was added to each well. Plates were sealed, vortexed vigorously for 30 s and shaken on an orbital shaking plate for 5 min at 4 °C. The plate was unsealed, and 150 µl of cold water was

added to each well. Plates were resealed, vortexed vigorously for 30 s and centrifuged at 4,000 RCF for 12 min at 4 °C.

From the top phase of the extraction wells, two aliquots of 180 µl each were transferred to new 96-well plates, and two aliquots of 70 µl each from the bottom phase were transferred to two other new 96-well plates. Plates were spun in a rotary vacuum until dry, sealed and stored at −80 °C until LC–MS/MS analysis. One of the 96-well plates containing the aqueous phase of extract was dissolved in 35 µl of HILIC-run solvent (8:2 acetonitrile/water). Five microlitres was analysed using non-targeted HILIC LC–MS/MS analysis. The autosampler temperature was kept at 4 °C. Immediately after HILIC analysis, the 96-well plates were spun in a rotary vacuum until dry, sealed and stored at −80 °C until targeted bile acid analysis.

Multiple dilutions were prepared for bile acid analysis as follows. The dried samples described above were dissolved in 60 µl of bile acid-run solvent (1:1 acetonitrile/methanol containing six isotopically labelled bile acid standards at 100 ng ml^{-1}) by 30 s of vortexing and 5 min of shaking on an orbital shaker. From this plate, 5 µl was transferred to a new 96-well plate and combined with 145 µl of bile acid-run solvent. Both dilutions were analysed for all samples, and samples that still presented bile acids above the highest concentration of the standard curve (1,500 ng ml^{-1}) were diluted 5:145 once more and re-analysed. A nine-point standard curve that ranged from 0.2 ng ml^{-1} to 1,500 ng ml^{-1} was used with all samples. The standard curve solutions were created by drying bile acid standard solutions to achieve the desired mass of bile acid standards and then dissolved in bile acid-run solvent. Three standard curve concentration measurements were analysed after every 20 samples during data acquisition along with one method blank.

For stool analyses, approximately 4 mg (±1 mg) of wet stool was transferred to 2-ml microcentrifuge tubes. Twenty microlitres of quality-control mix was added to the microcentrifuge tubes for quality-control samples. Blank samples were generated using 20 µl of LC–MS-grade water. To each tube, 225 µl of ice-cold methanol containing internal standards (as above) was added, followed by 750 µl of ice-cold MTBE with cholesterol ester 22:1. Two 3-mm stainless steel grinding beads were added to each tube, and tubes were processed in a Geno/Grinder automated tissue homogenizer and cell

lyser at 1,500 rpm for 1 min. Then, 188 μl of cold water was added to each tube. Tubes were vortexed vigorously and centrifuged at 14,000 RCF for 2 min. Two aliquots of 180 μl each of the MTBE layer and two aliquots of 50 μl each of the lower layer were transferred to four 96-well plates, and the plates were spun in a rotary vacuum until dry, sealed and stored at −80 °C until analysis with the intestinal samples. Stool samples were analysed using HILIC non-targeted LC–MS/MS and diluted in an identical manner to intestinal samples as described above. Stool samples were analysed in a randomized order after intestinal samples.

Metabolomics data acquisition

Samples were analysed using a Vanquish UHPLC system coupled to a TSQ Altis triple-quadrupole mass spectrometer (ThermoFisher Scientific). An Acquity BEH C18 column (1.7 μm, 2.1 mm × 100 mm) with an Acquity BEH C18 guard column (1.7 μm, 2.1 mm × 5 mm) was used for chromatographic separation with mobile phases A (LC–MS-grade water with 0.1% formic acid) and B (LC–MS-grade acetonitrile with 0.1% formic acid) and with a flow rate of 400 $\mu l\ min^{-1}$ and column temperature of 50 °C. The gradient began at 20% B for 1 min and shifted to 45% B between 1 and 11 min, to 95% B between 11 and 14 min and to 99% B between 14 and 14.5 min; 99% B was maintained until 15.5 min and transitioned to 20% B between 15.5 and 16.5 min; and 20% B was maintained until 18 min. The autosampler temperature was kept at 4 °C. The injection volume was 5 μl, and MRM scans were collected for all bile acids and internal standards (Supplementary Table 6).

Metabolomics data processing

MRM scans were imported to Skyline[77] software. Skyline performed peak integration for all analytes with given mass transitions and retention time windows optimized using authentic chemical standards (Supplementary Table 6). The chromatogram for each analyte was manually checked to confirm correct peak integration. Peak area was exported for all analytes. Analytes were omitted from further analysis if a convincing chromatographic peak was not observed in ≥1 sample (Supplementary Table 6). The ratio of analyte to its closest eluting internal standard was calculated and used for quantification. A linear model was fit to standard curve points for each bile acid ($R^2 > 0.995$ for all bile acids), and the model was applied to all samples and blanks to calculate concentrations. The average concentration reported for method blanks was subtracted from sample concentrations. Because multiple dilutions were analysed for each sample, the measurement closest to the centre of the standard curve (750 ng ml^{-1}) was used. Zero values were imputed with a concentration value between 0.001 and 0.1 ng ml^{-1}. Concentrations were reported as ng ml^{-1} for intestinal sample liquid supernatant and ng g^{-1} for wet stool. In all, 218 device samples and 57 stool samples passed quality control and were used for analyses (Extended Data Fig. 2a).

Non-targeted bile acid quantification

Bile acids conjugated to amino acids (for example, TyroCA, LeuCA and PhenylCA) were not included in the list for targeted analysis. Nonetheless, 22 microbially conjugated bile acids were detected during non-targeted data acquisition for intestinal and stool samples using HILIC chromatography as described previously[78]. Peaks corresponding to these microbially conjugated bile acids were annotated using m/z values for precursor mass, diagnostic MS/MS fragment ions (337.2526 for trihydroxylated and 339.2682 for dihydroxylated bile acids) and the corresponding amide conjugate fragment ion (Supplementary Table 7), as reported previously[40]. MS/MS spectra from synthetic standards for three microbially conjugated bile acids (Extended Data Fig. 9) served as positive controls based on

previously collected experimental MS/MS spectra[35]. Non-targeted HILIC analysis did not include bile acid standard curves to allow for direct quantification, so approximate quantification was achieved by comparing the concentration of GCA from targeted analysis to GCA peak height intensity from non-targeted analysis. A quadratic model was fit to GCA values from both analyses ($R^2 = 0.89$) and applied to the peak height intensity values of microbe-conjugated bile acids to calculate their approximate concentration. Approximate concentrations were used for analysis of bile acids measured with non-targeted analysis.

Reporting summary

Further information on research design is available in the Nature Portfolio Reporting Summary linked to this article.

Data availability

The 16S rRNA and metagenomics sequencing reads are available on NCBI under BioProject PRJNA822660. The mass spectrometry proteomics datasets are available through the ProteomeXchange Consortium in the PRIDE[79] partner repository with dataset identifier PXD038906. The targeted and non-targeted bile acid metabolomics datasets are available on Metabolomics Workbench under project numbers ST002073 and ST002075. The minimum datasets necessary for reproduction of figures or extended research related to this article are available on GitHub at https://github.com/jgrembi/capscan-profiling-human-intestine.

Code availability

Custom code for the generation of figures and statistical calculations in this manuscript is available on Zenodo at https://doi.org/10.5281/zenodo.7683655 (ref. [80]) and GitHub at https://github.com/jgrembi/capscan-profiling-human-intestine.

References

1. Hillman, E. T., Lu, H., Yao, T. & Nakatsu, C. H. Microbial ecology along the gastrointestinal tract. *Microbes Environ.* **32**, 300–313 (2017).

2. Tabula Sapiens, C. et al. The Tabula Sapiens: a multiple-organ, single-cell transcriptomic atlas of humans. *Science* **376**, eabl4896 (2022).

3. Lichtman, J. S. et al. The effect of microbial colonization on the host proteome varies by gastrointestinal location. *ISME J.* **10**, 1170–1181 (2016).

4. Chiang, J. Y. Bile acid metabolism and signaling. *Compr. Physiol.* **3**, 1191–1212 (2013).

5. Zhou, H. & Hylemon, P. B. Bile acids are nutrient signaling hormones. *Steroids* **86**, 62–68 (2014).

6. Lynch, S. V. & Pedersen, O. The human intestinal microbiome in health and disease. *N. Engl. J. Med.* **375**, 2369–2379 (2016).

7. Kastl, A. J. Jr., Terry, N. A., Wu, G. D. & Albenberg, L. G. The structure and function of the human small intestinal microbiota: current understanding and future directions. *Cell Mol. Gastroenterol. Hepatol.* **9**, 33–45 (2020).

8. Qin, J. et al. A human gut microbial gene catalogue established by metagenomic sequencing. *Nature* **464**, 59–65 (2010).

9. Zhang, X. & Figeys, D. Perspective and guidelines for metaproteomics in microbiome studies. *J. Proteome Res.* **18**, 2370–2380 (2019).

10. Tang, Q. et al. Current sampling methods for gut microbiota: a call for more precise devices. *Front. Cell Infect. Microbiol.* **10**, 151 (2020).

11. James, K. R. et al. Distinct microbial and immune niches of the human colon. *Nat. Immunol.* **21**, 343–353 (2020).

12. Spada, C. et al. Second-generation colon capsule endoscopy compared with colonoscopy. *Gastrointest. Endosc.* **74**, 581–589 (2011).

13. Leite, G. G. S. et al. Mapping the segmental microbiomes in the human small bowel in comparison with stool: a REIMAGINE study. *Dig. Dis. Sci.* **65**, 2595–2604 (2020).

14. Booijink, C. C. et al. High temporal and inter-individual variation detected in the human ileal microbiota. *Environ. Microbiol.* **12**, 3213–3227 (2010).

15. Maurer, J. M. et al. Gastrointestinal pH and transit time profiling in healthy volunteers using the IntelliCap system confirms ileo-colonic release of ColoPulse tablets. *PLoS ONE* **10**, e0129076 (2015).

16. Rezaei Nejad, H. et al. Ingestible osmotic pill for in vivo sampling of gut microbiomes. *Adv. Intel. Syst.* **1**, 1900053 (2019).

17. Li, J. & Dawson, P. A. Animal models to study bile acid metabolism. *Biochim. Biophys. Acta Mol. Basis Dis.* **1865**, 895–911 (2019).

18. Kararli, T. T. Comparison of the gastrointestinal anatomy, physiology, and biochemistry of humans and commonly used laboratory animals. *Biopharm. Drug Dispos.* **16**, 351–380 (1995).

19. Folz, J. et al. Human metabolome variation along the upper intestinal tract. *Nat. Metab.* https://doi.org/10.1038/s42255-023-00777-z (2023).

20. Earle, K. A. et al. Quantitative imaging of gut microbiota spatial organization. *Cell Host Microbe* **18**, 478–488 (2015).

21. Zmora, N. et al. Personalized gut mucosal colonization resistance to empiric probiotics is associated with unique host and microbiome features. *Cell* **174**, 1388–1405 (2018).

22. Datz, F. L., Christian, P. E. & Moore, J. Gender-related differences in gastric emptying. *J. Nucl. Med.* **28**, 1204–1207 (1987).

23. Goyal, R. K., Guo, Y. & Mashimo, H. Advances in the physiology of gastric emptying. *Neurogastroenterol. Motil.* **31**, e13546 (2019).

24. Vuik, F. et al. Composition of the mucosa-associated microbiota along the entire gastrointestinal tract of human individuals. *United Eur. Gastroenterol. J.* **7**, 897–907 (2019).

25. Devkota, S. et al. Dietary-fat-induced taurocholic acid promotes pathobiont expansion and colitis in *Il10*$^{-/-}$ mice. *Nature* **487**, 104–108 (2012).

26. Gerritsen, J. et al. Characterization of *Romboutsia ilealis* gen. nov., sp. nov., isolated from the gastro-intestinal tract of a rat, and proposal for the reclassification of five closely related members of the genus *Clostridium* into the genera *Romboutsia* gen. nov., *Intestinibacter* gen. nov., *Terrisporobacter* gen. nov. and *Asaccharospora* gen. nov. *Int. J. Syst. Evol. Microbiol.* **64**, 1600–1616 (2014).

27. Wardman, J. F., Bains, R. K., Rahfeld, P. & Withers, S. G. Carbohydrate-active enzymes (CAZymes) in the gut microbiome. *Nat. Rev. Microbiol.* https://doi.org/10.1038/s41579-022-00712-1 (2022).

28. Alcock, B. P. et al. CARD 2020: antibiotic resistome surveillance with the comprehensive antibiotic resistance database. *Nucleic Acids Res.* **48**, D517–D525 (2020).

29. Miller-Ensminger, T., Garretto, A., Stark, N. & Putonti, C. Mimicking prophage induction in the body: induction in the lab with pH gradients. *PeerJ* **8**, e9718 (2020).

30. Gold, L., Walker, J. J., Wilcox, S. K. & Williams, S. Advances in human proteomics at high scale with the SOMAscan proteomics platform. *New Biotechnol.* **29**, 543–549 (2012).

31. Lichtman, J. S., Marcobal, A., Sonnenburg, J. L. & Elias, J. E. Host-centric proteomics of stool: a novel strategy focused on intestinal responses to the gut microbiota. *Mol. Cell. Proteomics* **12**, 3310–3318 (2013).

32. Baars, A., Oosting, A., Knol, J., Garssen, J. & van Bergenhenegouwen, J. The gut microbiota as a therapeutic target in IBD and metabolic

disease: a role for the bile acid receptors FXR and TGR5. *Microorganisms* **3**, 641–666 (2015).

33. Bhargava, P. et al. Bile acid metabolism is altered in multiple sclerosis and supplementation ameliorates neuroinflammation. *J. Clin. Invest.* **130**, 3467–3482 (2020).

34. Ho, P. P. & Steinman, L. Obeticholic acid, a synthetic bile acid agonist of the farnesoid X receptor, attenuates experimental autoimmune encephalomyelitis. *Proc. Natl Acad. Sci. USA* **113**, 1600–1605 (2016).

35. Quinn, R. A. et al. Global chemical effects of the microbiome include new bile-acid conjugations. *Nature* **579**, 123–129 (2020).

36. Song, Z. et al. Taxonomic profiling and populational patterns of bacterial bile salt hydrolase (BSH) genes based on worldwide human gut microbiome. *Microbiome* **7**, 9 (2019).

37. Ridlon, J. M., Kang, D. J. & Hylemon, P. B. Bile salt biotransformations by human intestinal bacteria. *J. Lipid Res.* **47**, 241–259 (2006).

38. Connors, J. et al. The relationship between fecal bile acids and microbiome community structure in pediatric Crohn's disease. *ISME J.* **14**, 702–713 (2020).

39. Baron, E. J. et al. *Bilophila wadsworthia*, gen. nov. and sp. nov., a unique gram-negative anaerobic rod recovered from appendicitis specimens and human faeces. *J. Gen. Microbiol.* **135**, 3405–3411 (1989).

40. Lucas, L. N. et al. Dominant bacterial phyla from the human gut show widespread ability to transform and conjugate bile acids. *mSystems* https://doi.org/10.1128/mSystems.00805-21 (2021).

41. Dorrestein, P. et al. A synthesis-based reverse metabolomics approach for the discovery of chemical structures from humans and animals.

Preprint at *Research Square* https://doi.org/10.21203/rs.3.rs-820302/v1 (2021).

42. Edelstein, A. D. et al. Advanced methods of microscope control using µManager software. *J Biol. Meth.* **1**, e10 (2014).

43. Celis, A. I. et al. Optimization of the 16S rRNA sequencing analysis pipeline for studying in vitro communities of gut commensals. *iScience* **25**, 103907 (2022).

44. R Core Team. *R: A Language and Environment for Statistical Computing* (R Foundation for Statistical Computing, 2021).

45. Callahan, B. J. et al. DADA2: high-resolution sample inference from Illumina amplicon data. *Nat. Methods* **13**, 581–583 (2016).

46. Quast, C. et al. The SILVA ribosomal RNA gene database project: improved data processing and web-based tools. *Nucleic Acids Res.* **41**, D590–D596 (2013).

47. Schliep, K. P. phangorn: phylogenetic analysis in R. *Bioinformatics* **27**, 592–593 (2011).

48. McMurdie, P. J. & Holmes, S. phyloseq: an R package for reproducible interactive analysis and graphics of microbiome census data. *PLoS ONE* **8**, e61217 (2013).

49. Oksanen, J. et al. vegan: Community Ecology Package. R package version 2.5-7 https://CRAN.R-project.org/package=vegan (2020).

50. Grun, B. & Hornik, K. topicmodels: an R package for fitting topic models. *J Stat. Softw.* **40**, 1–30 (2011).

51. Sankaran, K. & Holmes, S. P. Latent variable modeling for the microbiome. *Biostatistics* **20**, 599–614 (2019).

52. Jiang, H., Lei, R., Ding, S. W. & Zhu, S. Skewer: a fast and accurate adapter trimmer for next-generation sequencing paired-end reads. *BMC Bioinformatics* **15**, 182 (2014).

53. Langmead, B. & Salzberg, S. L. Fast gapped-read alignment with Bowtie 2. *Nat. Methods* **9**, 357–359 (2012).

54. Li, D., Liu, C. M., Luo, R., Sadakane, K. & Lam, T. W. MEGAHIT: an ultra-fast single-node solution for large and complex metagenomics assembly via succinct de Bruijn graph. *Bioinformatics* **31**, 1674–1676 (2015).

55. Kang, D. D. et al. MetaBAT 2: an adaptive binning algorithm for robust and efficient genome reconstruction from metagenome assemblies. *PeerJ* **7**, e7359 (2019).

56. Parks, D. H., Imelfort, M., Skennerton, C. T., Hugenholtz, P. & Tyson, G. W. CheckM: assessing the quality of microbial genomes recovered from isolates, single cells, and metagenomes. *Genome Res.* **25**, 1043–1055 (2015).

57. Gurevich, A., Saveliev, V., Vyahhi, N. & Tesler, G. QUAST: quality assessment tool for genome assemblies. *Bioinformatics* **29**, 1072–1075 (2013).

58. Olm, M. R., Brown, C. T., Brooks, B. & Banfield, J. F. dRep: a tool for fast and accurate genomic comparisons that enables improved genome recovery from metagenomes through de-replication. *ISME J.* **11**, 2864–2868 (2017).

59. Chaumeil, P. A., Mussig, A. J., Hugenholtz, P. & Parks, D. H. GTDB-Tk: a toolkit to classify genomes with the Genome Taxonomy Database. *Bioinformatics* https://doi.org/10.1093/bioinformatics/btz848 (2019).

60. Aranda-Diaz, A. et al. Establishment and characterization of stable, diverse, fecal-derived in vitro microbial communities that model the intestinal microbiota. *Cell Host Microbe* **30**, 260–272 (2022).

61. Shiver, A. L., Culver, R., Deutschbauer, A. M. & Huang, K. C. Rapid ordering of barcoded transposon insertion libraries of anaerobic bacteria. *Nat. Protoc.* **16**, 3049–3071 (2021).

62. Chao, K. H., Barton, K., Palmer, S. & Lanfear, R. sangeranalyseR: simple and interactive processing of Sanger sequencing data in R. *Genome Biol. Evol.* https://doi.org/10.1093/gbe/evab028 (2021).

63. Hyatt, D. et al. Prodigal: prokaryotic gene recognition and translation initiation site identification. *BMC Bioinformatics* **11**, 119 (2010).

64. Huang, L. et al. dbCAN-seq: a database of carbohydrate-active enzyme (CAZyme) sequence and annotation. *Nucleic Acids Res.* **46**, D516–D521 (2018).

65. Guo, J. et al. VirSorter2: a multi-classifier, expert-guided approach to detect diverse DNA and RNA viruses. *Microbiome* **9**, 37 (2021).

66. Ren, J. et al. Identifying viruses from metagenomic data using deep learning. *Quant. Biol.* **8**, 64–77 (2020).

67. Kieft, K., Zhou, Z. & Anantharaman, K. VIBRANT: automated recovery, annotation and curation of microbial viruses, and evaluation of viral community function from genomic sequences. *Microbiome* **8**, 90 (2020).

68. Nayfach, S. et al. CheckV assesses the quality and completeness of metagenome-assembled viral genomes. *Nat. Biotechnol.* **39**, 578–585 (2021).

69. Kieft, K. & Anantharaman, K. Deciphering active prophages from metagenomes. *mSystems* **7**, e0008422 (2022).

70. Sielaff, M. et al. Evaluation of FASP, SP3, and iST protocols for proteomic sample preparation in the low microgram range. *J. Proteome Res.***16**, 4060–4072 (2017).

71. Müller-Reif, J. B. et al. A new parallel high-pressure packing system enables rapid multiplexed production of capillary columns. *Mol. Cell. Proteomics* **20**, 100082 (2021).

72. Scheltema, R. A. & Mann, M. SprayQc: a real-time LC–MS/MS quality monitoring system to maximize uptime using off the shelf components. *J. Proteome Res.* **11**, 3458–3466 (2012).

73. Cox, J. & Mann, M. MaxQuant enables high peptide identification rates, individualized p.p.b.-range mass accuracies and proteome-wide protein quantification. *Nat. Biotechnol.* **26**, 1367–1372 (2008).

74. Geyer, P. E. et al. Plasma proteome profiling to assess human health and disease. *Cell Syst.* **2**, 185–195 (2016).

75. Cox, J. et al. Accurate proteome-wide label-free quantification by delayed normalization and maximal peptide ratio extraction, termed MaxLFQ. *Mol. Cell. Proteomics* **13**, 2513–2526 (2014).

76. Matyash, V., Liebisch, G., Kurzchalia, T. V., Shevchenko, A. & Schwudke, D. Lipid extraction by methyl-*tert*-butyl ether for high-throughput lipidomics. *J. Lipid Res.* **49**, 1137–1146 (2008).

77. Adams, K. J. et al. Skyline for small molecules: a unifying software package for quantitative metabolomics. *J. Proteome Res.* **19**, 1447–1458 (2020).

78. Barupal, D. K. et al. A comprehensive plasma metabolomics dataset for a cohort of mouse knockouts within the International Mouse Phenotyping Consortium. *Metabolites* https://doi.org/10.3390/metabo9050101 (2019).

79. Perez-Riverol, Y. et al. The PRIDE database resources in 2022: a hub for mass spectrometry-based proteomics evidences. *Nucleic Acids Res.* **50**, D543–D552 (2022).

80. Grembi, J. et al. jgrembi/capscan-profiling-human-intestine: manuscript submission (v1.0.0). *Zenodo* https://doi.org/10.5281/zenodo.7683655 (2023).

Acknowledgements

The authors thank L. Symul and E. Costello for helpful discussions on statistical analyses. The authors acknowledge support from the National Science Foundation under grant no. 1936687 (to D.S.), the National Institutes of Health under awards RM1 GM135102 (to K.C.H.) and RO1 AI147023 (to D.A.R. and K.C.H.), the Bill and Melinda Gates Foundation under award INV-037857 (to D.A.R.) and the Thomas C. and Joan M. Merigan Endowment at Stanford University (to D.A.R.). R.N.C. was supported by an NDSEG graduate fellowship, J.A.G. was supported by a Stanford University School of Medicine Dean's Fellowship, H.S. was supported by a James S. McDonnell Postdoctoral Fellowship, F.A.R. was supported by EMBO Postdoctoral Fellowship ALTF 399-2021 and S.P.S. was supported by NIH T32 DK007056 and an A.P. Giannini Postdoctoral Fellowship. D.A.R. and K.C.H. were Chan Zuckerberg Biohub Investigators. We acknowledge the Stanford Research Computing Center for computational resources at the Sherlock high-performance cluster. D.S. acknowledges as inspiration Y. Shalon, who studied bile acids 50 years ago.

Author information

Author notes

1. These authors contributed equally: Dari Shalon, Rebecca Neal Culver, Jessica A. Grembi, Jacob Folz, David A. Relman, Kerwyn Casey Huang

Authors and Affiliations

1. Envivo Bio, Inc., San Francisco, CA, USA

   Dari Shalon

2. Department of Genetics, Stanford University School of Medicine, Stanford, CA, USA

   Rebecca Neal Culver

3. Department of Medicine, Stanford University School of Medicine, Stanford, CA, USA

Jessica A. Grembi, Les Dethlefsen, Eitan Yaffe & David A. Relman

4. West Coast Metabolomics Center, University of California, Davis, Davis, CA, USA

Jacob Folz & Oliver Fiehn

5. Department of Proteomics and Signal Transduction, Max-Planck Institute of Biochemistry, Martinsried, Germany

Peter V. Treit, Florian A. Rosenberger, Philipp E. Geyer, Johannes B. Mueller-Reif & Matthias Mann

6. Department of Microbiology and Immunology, Stanford University School of Medicine, Stanford, CA, USA

Handuo Shi, Sean Spencer, David A. Relman & Kerwyn Casey Huang

7. Department of Bioengineering, Stanford University, Stanford, CA, USA

Handuo Shi, Andrés Aranda-Díaz & Kerwyn Casey Huang

8. Chan Zuckerberg Biohub, San Francisco, CA, USA

Xiandong Meng, David A. Relman & Kerwyn Casey Huang

9. Division of Gastroenterology and Hepatology, Stanford University School of Medicine, Stanford, CA, USA

Sean Spencer & George Triadafilopoulos

10. Department of Veterinary and Biomedical Sciences, Pennsylvania State University, University Park, PA, USA

Andrew D. Patterson

11. Silicon Valley Neurogastroenterology and Motility Center, Mountain View, CA, USA

George Triadafilopoulos

12. Department of Statistics, Stanford University, Stanford, CA, USA

Susan P. Holmes

13. Department of Food Science and Technology, University of California, Davis, Davis, CA, USA

Oliver Fiehn

14. Infectious Diseases Section, Veterans Affairs Palo Alto Health Care System, Palo Alto, CA, USA

David A. Relman

Contributions

D.S. developed the CapScan device at Envivo Bio. R.N.C. curated the 16S rRNA and metagenomics sequencing libraries. J.F. curated all metabolomics datasets. J.B.M.-R., P.V.T. and P.E.G. curated the proteomics dataset. H.S. curated microscopy images. R.N.C. and J.A.G. analysed all datasets and curated figures, except that P.V.T. and F.A.R. analysed the proteomics data, H.S. curated the phage analysis and J.F. curated supplementary mass spectra. J.A.G. performed the contamination re-analysis, replicated all analyses and was responsible for the GitHub repository. L.D., X.M., E.Y., S.S., A.A.-D., A.D.P., S.P.H. and M.M. all provided intellectual insight. G.T. was the gastroenterologist overseeing the human study. O.F., D.A.R. and K.C.H. supervised and oversaw project execution. D.S., R.N.C., J.A.G., J.F. and K.C.H. wrote the original draft of the manuscript, and all authors reviewed and edited the manuscript before submission.

Corresponding authors

Correspondence to Rebecca Neal Culver, Oliver Fiehn, David A. Relman or Kerwyn Casey Huang.

Ethics declarations

Competing interests

D.S. is an employee of Envivo Bio, Inc. (San Francisco, CA) and owns stock in the company. D.S. is an inventor on pending patent application WO2018213729 covering the sampling device described in the manuscript, which is owned by Envivo Bio, Inc. All other authors declare no competing interests.

Peer review

Peer review information

Nature thanks Suzanne Devkota and the other, anonymous, reviewer(s) for their contribution to the peer review of this work.

Additional information

Publisher's note Springer Nature remains neutral with regard to jurisdictional claims in published maps and institutional affiliations.

Extended data figures and tables

Extended Data Fig. 1 Changes in intestinal microbiota composition during sample incubation.

Devices were collected from a bowel movement of a single subject 32 h after ingestion and placed immediately into an anaerobic chamber at 37 °C. Samples were collected from each device immediately (32 h) and again at 58 h and 87 h. Samples were then prepared for 16S rRNA gene sequencing.

Genus-level relative abundance is shown for all ASVs with read count ≥15 in any single sample.

Extended Data Fig. 2 Total gut transit time of devices varied across subjects and diets.

a) Subjects ($n = 15$) enrolled in the study ingested a total of 17 intestinal sampling devices each (set 1 consisted of a single device used as a safety test to ensure safe passage through the intestines). Subjects were also asked to provide two saliva samples and collect stool until all intestinal sampling devices were retrieved. Between two and eight stool samples from each subject were used for analysis. b) Device ($n = 240$) gut transit time was variable across subjects. Some subjects displayed differences in transit time dependent on the time of day the device was ingested. c) Device gut transit time varied according to certain types of food consumed in the meal prior to device ingestion (i.e., the food with which the devices presumably transited into the small intestines). *P*-values from left to right, top to bottom: 0.18, 0.00091, 0.24, 0.17, 0.29, 0.0049, 0.57, and 0.27. d) Device gut transit time varied according to the type of food consumed in the meal after devices were swallowed (i.e., the food that likely influenced gut motility while devices were passing through the large intestines). *P*-values from left to right, top to bottom: 0.68, 1.4×10^{-7}, 1.1×10^{-7}, 7.6×10^{-11}, 7×10^{-7}, 0.49, 0.25, and 0.3. Boxplots show the median and 1st and 3rd quartiles. Each dot is a device sample (b–d; $n = 60$ each for device types 1–4). ns: not significant, *: $P \leq 0.05$, **: $P \leq 0.01$, ***: $P \leq 0.001$, ****: $P \leq 0.0001$, Bonferroni-corrected two-sided Wilcoxon rank-sum test. Alcohol consumption and diet contents were not restricted. Subjects swallowed devices 3 h after lunch and dinner and were instructed not to consume any additional foods for at least 2 h after swallowing devices.

Extended Data Fig. 3 Diversity in phylum abundances and alpha and gamma diversity implicate a temporally and spatially heterogeneous intestinal tract.

a) Summed $\log_2$(read count) at the phylum level are shown for each sample by location. *P*-values from left to right: 0.57, 0.0035, 2.4×10^{-15}, 5.7 ×

10^{-7}, and 0.83. ASVs that did not have read count ≥3 in 5% of samples were ignored. Boxplots show the median and 1st and 3rd quartiles. Each dot represents a sample ($n = 210$ and 58 for devices and stool, respectively). ns: not significant, *: $P \leq 0.05$, **: $P \leq 0.01$, ***: $P \leq 0.001$, ****: $P \leq 0.0001$, Bonferroni-corrected two-sided Wilcoxon rank-sum test. b, c) The Shannon diversity of individual devices ($n = 210$ devices; alpha diversity, lighter points) was generally lower than that collectively of all devices from a single set (gamma diversity, bold points), indicating high spatial variation. Each subject (#1–#15) is shown separately. To ensure equal read depths for accurate comparisons, all intestinal samples were rarefied to the minimum sequencing depth of any device from that subject. Mean values and 95% confidence intervals for alpha and gamma diversity estimates were obtained by repeating the rarefaction procedure 1000 times.

Extended Data Fig. 4 Growing cells recovered from devices collectively displayed a wide range of morphologies.

a) A 2-µL sample was acquired from a single device and spotted onto an agarose pad with BHI medium. After 4 h of time-lapse imaging, growing cells displayed a wide range of morphological features, as highlighted by white arrows: 1. regular rods; 2. small rods; 3. wide rods; 4. branching; and 5. long/filamentous rods. Along with the sample shown, 3 other samples from devices ingested at the same time were imaged, and similar results were observed. b) Occasional human cells (white arrow) were observed during imaging.

Extended Data Fig. 5 Percent of reads mapping to CAZymes and antimicrobial resistance genes vary across the intestinal tract and are driven by distinct taxa.

a) The percent of reads that mapped to a database of CAZymes (Methods) was determined using metagenomic sequencing of each sample. b) Data from (a) separated by subject. c) In intestinal samples, the $\log_2$(read count) of eight ASVs was positively correlated (Spearman) with the percent of reads that mapped to the CAZyme database. Only ASVs with $P < 0.001$ are shown. P-values from left to right, top to bottom: 1.8×10^{-6}, 7.2×10^{-4}, 1.1

$\times 10^{-24}$, 3.7×10^{-4}, 3.7×10^{-4}, 2.6×10^{-5}, 3.7×10^{-4}, and 3.7×10^{-4}. d) The $\log_2$(ASV read count summed over family members) of the Bacteroidaceae family was significantly correlated (Spearman; $P = 6.4 \times 10^{-7}$) with the percent of reads from stool samples that mapped to the CAZyme database. No other families had $P < 0.01$. e) The number of CAZymes identified in strains isolated from the intestinal tract of subject 1, organized by species. Each circle represents a single strain, and horizontal lines (mostly hidden by the circles) represent the median. f) The percent of reads that mapped to a database of AMR genes (CARD, Methods) was determined using metagenomics sequencing of each sample and was higher in devices compared with stool ($P = 0.03$). g) Data from (f) separated by subject. h) In intestinal samples, the $\log_2$(read count) of two ASVs was positively correlated (Spearman) with the percent of reads that mapped to CARD. Only ASVs with $P < 0.001$ are shown. P-values from left to right, top to bottom: 5.7×10^{-8}, 1.5×10^{-4}, 4.1×10^{-7}, 2.5×10^{-4}, 6.4×10^{-5}, 2.0×10^{-8}, and 2.1×10^{-4}. i) In stool samples, the $\log_2$(ASV read count summed over family members) of families was significantly correlated (Spearman; $P = 5.7 \times 10^{-5}$, 1.5×10^{-3}, and 7.1×10^{-4}) with the percent of reads that mapped to a database of AMR genes. No other families had $P < 0.001$. j) The percent of reads that mapped to CARD ignoring all efflux pumps was similar between devices and stool ($P = 0.8$). k) $\log_{10}$(ratio of the number of AMR genes to bacterial genes) detected in each MAG, aggregated by family-level taxonomic assignment. Only MAGs with completion >75% and contamination <10% were included. In (a–d and f–j), each dot is a sample ($n = 175$ for devices and $n = 58$ for stool). All P-values reported are after Benjamini-Hochberg correction. Boxplots show the median and 1st and 3rd quartiles.

Extended Data Fig. 6 Intestinal samples have higher bacteriophage load.

a) The median sequencing depth of vOTUs ($n = 1343$) in intestinal samples was highly correlated with depth in stool samples (Pearson; $P < 2.2 \times 10^{-16}$). 481 vOTUs appeared in less than half of the intestinal samples and hence the median was 0 (represented as 10^{-4}). b) Intestinal samples had

significantly higher read fraction mapping to vOTUs. $n = 29$, 172, and 58 for saliva, intestinal, and stool samples, respectively. P-values are from two-tailed Student's t-tests. P-values from top to bottom, left to right: 4.7×10^{-14}, 2.2×10^{-16}, 2.3×10^{-7}. c) The number of induced prophages was generally higher in intestinal samples across subjects and was lowest in saliva samples. d) pH was correlated with the number of induced prophages in intestinal samples (Spearman; $P = 0.0015$).

Extended Data Fig. 7 Comparison of the human proteome in intestinal versus stool samples.

a) The number of host-associated proteins detected in each sample, colored by location (intestinal versus stool). Dotted line and number represent the mean. b) The number of host-associated proteins detected across samples from each device type and stool. Boxplot shows the median and 1st and 3rd quartiles. c) The distribution of coefficient of variation (CV) for all detected host proteins across device types and stool samples. d) Proteins were ranked based on mean $\log_{10}$(intensity) for intestinal and stool samples. The six most and five least abundant proteins are labelled for each location. e) A principal component analysis of the normalized abundance of the 500 most abundant host-associated proteins. Results are similar to Fig. 4c. Points are colored based on location of sample (intestinal versus stool). f) A principal component analysis of the non-normalized abundance of all host-associated proteins found in each sample. Results are qualitatively similar to Fig. 4c and e. Points are colored based on location of sample (intestinal versus stool). g) The number of host-associated proteins with significantly different abundance between stool and each device type based on a 5% false discovery rate (FDR). All panels used $n = 56$ stool and $n = 212$ device samples for analysis. In (b,c,g), $n = 56$ type 1, $n = 54$ type 2, $n = 56$ type 3, and $n = 46$ type 4 device samples were used.

Extended Data Fig. 8 Microbial bile salt hydrolase genes exhibited similar abundance and diversity in intestinal and stool samples despite differences in conjugated bile acids along the intestinal tract.

a) Open reading frames identified as bile salt (cholylglycine) hydrolase (BSH) enzymes via a hidden Markov model (HMM) search, normalized by the total number of open reading frames detected in the sample. b) The distribution of rank coverage of *bsh* genes was similar between intestinal and stool samples. c) Rank coverages of *bsh* genes in devices of each type and in stool are similar. (all $P > 0.90$). d) Percentage of primary (hydroxylated) bile acids was similar across device types and was lower in stool compared with intestinal samples (top to bottom: $P = 3.7 \times 10^{-13}$, 1.3×10^{-10}, and 0.91). e) Glycocholic acid (GCA) concentration decreased along the intestinal tract (top to bottom: $P = 1.6 \times 10^{-12}$, 0.035, and 0.003). f) The $\log_2$(ASV count) of *Alistipes putredinis*, *Anaerostipes hadrus*, and *Bilophila wadsworthia* was negatively correlated (Spearman; $P = 0.0068$, 0.0004, and 0.0068 in devices and $P = 0.63$, 0.84, and 0.70 in stool, respectively) with $\log_{10}$(GCA concentration). Only ASVs with $P < 0.01$ after a Benjamini-Hochberg correction in device samples are shown. g) Taurochenodeoxycholic acid (TCDCA) concentration decreased along the intestinal tract (top to bottom: $P = 0.0070$, 1.9×10^{-4}, 4.2×10^{-6}, 1.5×10^{-10}, and 0.0020). h) $\log_2$(ASV read count) of *Alistipes putredinis* and *Bilophila wadsworthia* in devices was negatively correlated (Spearman; $P = 2.5 \times 10^{-5}$ and 3.3×10^{-7}, respectively) with $\log_{10}$(TCDCA concentration). Only ASVs with $P < 0.01$ after a Benjamini-Hochberg correction in device samples are shown. i) $\log_2$(ASV read count) of *Bilophila wadsworthia* in devices was negatively correlated (Spearman; $P = 2.4 \times 10^{-5}$) with $\log_{10}$(concentration of taurodeoxycholic acid (TDCA)). Only ASVs with $P < 0.01$ after a Benjamini-Hochberg correction in device samples are shown. In (a–c), $n = 175$ device and $n = 58$ stool samples were used for analysis. In (d–h), $n = 210$ device samples and $n = 56$ stool samples were used for analysis. All boxplots show the median and 1st and 3rd quartiles. ns: not significant, ****: $P \leq 0.0001$, Bonferroni-corrected two-sided Wilcoxon rank-sum test. Bile acids shown are $\log_{10}$-transformed concentrations in units of ng/mL or ng/g for intestinal or stool samples, respectively.

Extended Data Fig. 9 Microbially conjugated bile acid identification.

Head-to-tail matches of experimental (top) to library (bottom) spectra from bile acids conjugated to tyrosine, phenylalanine, and leucine.

Supplementary information

Reporting Summary

Supplementary Tables

This file contains Supplementary Tables 1–7.

Supplementary Video 1

Devices targeting the jejunum and ascending colon were connected to a capsule endoscope, enabling visualization of successful in vivo sampling in a human participant.

Supplementary Video 2

Time-lapse imaging of a sample retrieved from a device. The field of view was biasedly chosen to contain one human epithelial cell.

Supplementary Video 3

Time-lapse imaging of a fresh stool sample.

Rights and permissions

Open Access This article is licensed under a Creative Commons Attribution 4.0 International License, which permits use, sharing, adaptation, distribution and reproduction in any medium or format, as long as you give appropriate credit to the original author(s) and the source, provide a link to the Creative Commons licence, and indicate if changes were made. The images or other third party material in this article are included in the article's Creative Commons licence, unless indicated

otherwise in a credit line to the material. If material is not included in the article's Creative Commons licence and your intended use is not permitted by statutory regulation or exceeds the permitted use, you will need to obtain permission directly from the copyright holder. To view a copy of this licence, visit http://creativecommons.org/licenses/by/4.0/.

Reprints and Permissions

About this article

Cite this article

Shalon, D., Culver, R.N., Grembi, J.A. *et al.* Profiling the human intestinal environment under physiological conditions. *Nature* **617**, 581–591 (2023). https://doi.org/10.1038/s41586-023-05989-7

- Received: 20 January 2022
- Accepted: 21 March 2023
- Published: 10 May 2023
- Issue Date: 18 May 2023
- DOI: https://doi.org/10.1038/s41586-023-05989-7

Share this article

Anyone you share the following link with will be able to read this content:

Get shareable link

Sorry, a shareable link is not currently available for this article.

Copy to clipboard

Provided by the Springer Nature SharedIt content-sharing initiative

This article is cited by

- **[A multi-omic trip through the human gut]**

    - Robert A. Quinn
    - Christian Martin
    - Douglas V. Guzior

    Nature Metabolism (2023)

- **[Human metabolome variation along the upper intestinal tract]**

    - Jacob Folz
    - Rebecca Neal Culver
    - Oliver Fiehn

    Nature Metabolism (2023)

Human metabolome variation along the upper intestinal tract

- Jacob Folz
- Rebecca Neal Culver
- Oliver Fiehn

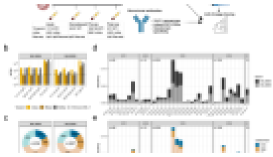
Nature Metabolism Letter Open Access 10 May 2023

A multi-omic trip through the human gut

- Robert A. Quinn
- Christian Martin
- Douglas V. Guzior

Nature Metabolism News & Views 10 May 2023

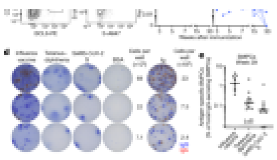
This article was downloaded by **calibre** from https://www.nature.com/articles/s41586-023-05989-7



Vaccination of SARS-CoV-2-infected individuals expands a broad range of clonally diverse affinity-matured B cell lineages

19 April 2023

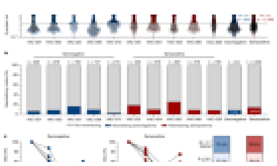
Mark Chernyshev, Mrunal Sakharkar, … Gunilla B. Karlsson Hedestam



Germinal centre-driven maturation of B cell response to mRNA vaccination

15 February 2022

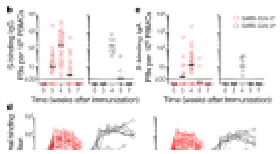
Wooseob Kim, Julian Q. Zhou, … Ali H. Ellebedy



Hybrid immunity improves B cells and antibodies against SARS-CoV-2 variants

20 October 2021

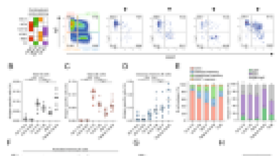
Emanuele Andreano, Ida Paciello, … Rino Rappuoli



[SARS-CoV-2 mRNA vaccines induce persistent human germinal centre responses]

28 June 2021

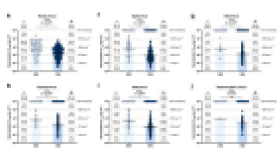
Jackson S. Turner, Jane A. O’Halloran, … Ali H. Ellebedy



[A public antibody class recognizes an S2 epitope exposed on open conformations of SARS-CoV-2 spike]

04 August 2022

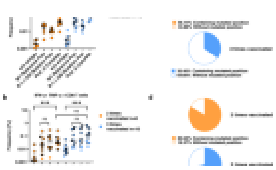
Mathieu Claireaux, Tom G. Caniels, … Marit J. van Gils



[B cell analyses after SARS-CoV-2 mRNA third vaccination reveals a hybrid immunity like antibody response]

04 January 2023

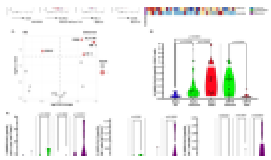
Emanuele Andreano, Ida Paciello, … Rino Rappuoli



Vaccines against the original strain of SARS-CoV-2 provide T cell memory to the B.1.1.529 variant

02 November 2022

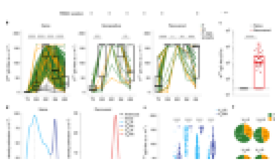
Charlyn Dörnte, Verena Traska, … Marc Schuster



Immune responses in Omicron SARS-CoV-2 breakthrough infection in vaccinated adults

18 July 2022

Hassen Kared, Asia-Sophia Wolf, … Siri Mjaaland



Memory CD8+ T cell diversity and B cell responses correlate with protection against SARS-CoV-2 following mRNA vaccination

22 September 2022

Nadia Brasu, Ines Elia, … Luigia Pace

- Article
- Published: 03 April 2023

SARS-CoV-2 Omicron boosting induces de novo B cell response in humans

- Wafaa B. Alsoussi,
- Sameer Kumar Malladi,
- Julian Q. Zhou,
- Zhuoming Liu,
- Baoling Ying,
- Wooseob Kim,
- Aaron J. Schmitz,
- Tingting Lei,
- Stephen C. Horvath,
- Alexandria J. Sturtz,
- Katherine M. McIntire,
- Birk Evavold,
- Fangjie Han,
- Suzanne M. Scheaffer,
- Isabella F. Fox,
- Senaa F. Mirza,
- Luis Parra-Rodriguez,
- Raffael Nachbagauer,
- Biliana Nestorova,
- Spyros Chalkias,
- Christopher W. Farnsworth,
- Michael K. Klebert,
- Iskra Pusic,
- Benjamin S. Strnad,
- William D. Middleton,
- Sharlene A. Teefey,
- Sean P. J. Whelan,
- Michael S. Diamond,
- Robert Paris,
- Jane A. O'Halloran,

- Rachel M. Presti,
- Jackson S. Turner &
- …
- Ali H. Ellebedy

Show authors

Nature **volume 617**, pages 592–598 (2023)

- 11k Accesses
- 3 Citations
- 140 Altmetric
- Metrics details

Abstract

The primary two-dose SARS-CoV-2 mRNA vaccine series are strongly immunogenic in humans, but the emergence of highly infectious variants necessitated additional doses and the development of vaccines aimed at the new variants[1,2,3,4]. SARS-CoV-2 booster immunizations in humans primarily recruit pre-existing memory B cells[5,6,7,8,9]. However, it remains unclear whether the additional doses induce germinal centre reactions whereby re-engaged B cells can further mature, and whether variant-derived vaccines can elicit responses to variant-specific epitopes. Here we show that boosting with an mRNA vaccine against the original monovalent SARS-CoV-2 mRNA vaccine or the bivalent B.1.351 and B.1.617.2 (Beta/Delta) mRNA vaccine induced robust spike-specific germinal centre B cell responses in humans. The germinal centre response persisted for at least eight weeks, leading to significantly more mutated antigen-specific bone marrow plasma cell and memory B cell compartments. Spike-binding monoclonal antibodies derived from memory B cells isolated from individuals boosted with either the original SARS-CoV-2 spike protein, bivalent Beta/Delta vaccine or a monovalent Omicron BA.1-based vaccine predominantly recognized the original SARS-CoV-2 spike protein.

Nonetheless, using a more targeted sorting approach, we isolated monoclonal antibodies that recognized the BA.1 spike protein but not the original SARS-CoV-2 spike protein from individuals who received the mRNA-1273.529 booster; these antibodies were less mutated and recognized novel epitopes within the spike protein, suggesting that they originated from naive B cells. Thus, SARS-CoV-2 booster immunizations in humans induce robust germinal centre B cell responses and can generate de novo B cell responses targeting variant-specific epitopes.

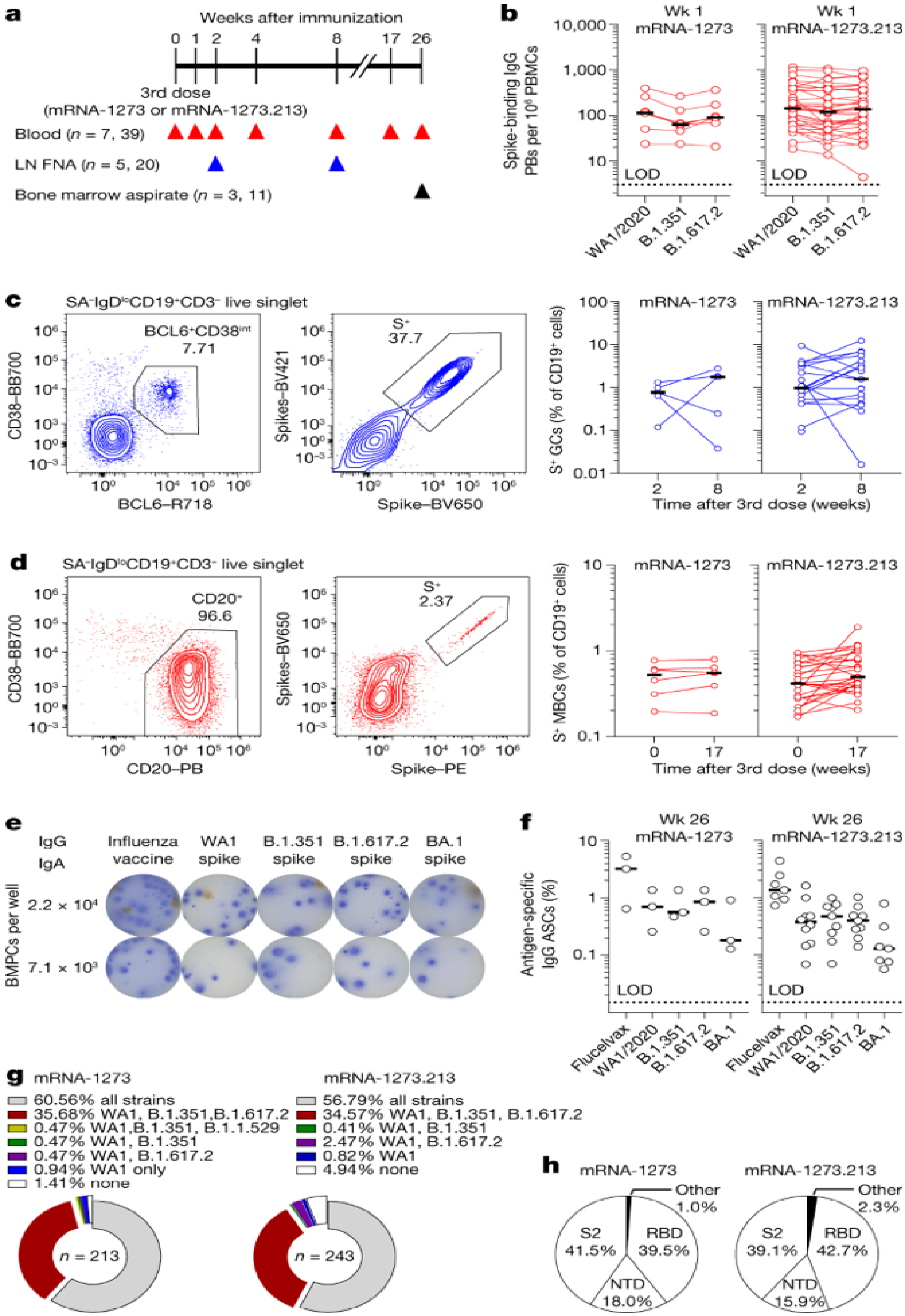
Main

The emergence of SARS-CoV-2 variants with increasing numbers of mutations in the spike (S) protein has decreased the effectiveness of primary series vaccinations and led to a recommendation for booster immunizations in most populations[10,11,12,13,14,15,16]. Multiple reports have documented that third-dose booster immunizations based on the ancestral Washington strain (WA1/2020) enhanced antibody responses to the ancestral strain as well as emerging variants of concern and correspondingly increased protective effectiveness[5,6,7,8,17,18,19,20,21]. In addition, new vaccines based on circulating variants have been developed to enhance the ability of induced antibodies to combat such variants. Indeed, recent evidence indicates that a B.1.351 (Beta)-containing booster can generate higher titres of neutralizing antibodies against both B.1.351 and B.1.1.529 (Omicron) BA.1 strains of SARS-CoV-2 compared with a booster based on the original strain alone[22]. Additionally, bivalent boosters encoding the original strain and either the BA.1 or BA.5 subvariant induced broader neutralizing antibody responses than the constituent monovalent vaccines[23]. Whether re-exposure to mRNA vaccines encoding S protein from the original SARS-CoV-2 strain or from variants of concern induce robust germinal centre reactions that are critical for refining high-affinity and durable antibody responses has not been examined in humans. To address this question, we conducted an immunization study of 46 healthy adults with no history of SARS-CoV-2 infection, all of whom had completed a primary two-dose vaccination course with either the Pfizer–BioNTech (BNT162b2) or Moderna (mRNA-1273) SARS-CoV-2 mRNA vaccines, both of which encode a prefusion-stabilized full-length SARS-CoV-2 S protein based on the WA1/2020 strain[24,25].

Recruited individuals received a third booster dose of 50 μg mRNA-1273 or mRNA-1273.213, which contains a total of 100 μg of mRNA encoding B.1.351 (Beta; sequence conservation of 99.1% for S protein and 98.7% for the receptor binding domain (RBD) compared with WA1/2020) and B.1.617.2 (Delta; sequence conservation of 99.2% for S protein and 99.1% for the RBD compared with WA1/2020) SARS-CoV-2 S proteins (Extended Data Tables 1 and 2), as a sub-study of an ongoing clinical trial (Clinical NCT04927065).

Seven of the participants received a booster immunization of mRNA-1273, and 39 received mRNA-1273.213. Blood samples were collected at baseline and weeks 1, 2, 4, 8, 17 and 26 after vaccination. Five participants from the mRNA-1273 cohort and twenty from the mRNA-1273.213 cohort consented to collection of fine needle aspirates (FNAs) of draining axillary lymph nodes at weeks 2 and 8. Three participants from the mRNA-1273 cohort and 11 from the mRNA-1273.213 cohort consented to collection of bone marrow aspirates 26 weeks after their third dose (Fig. 1a). Circulating S protein-specific antibody-producing plasmablasts were measured by enzyme-linked immune absorbent spot (ELISpot) assay. S protein-specific IgG- and IgA-producing plasmablasts were detected one week after the booster immunization from all participants in the mRNA-1273 cohort. Robust circulating IgG-producing plasmablast responses against the original WA1/2020 S protein and against the vaccine-encoded B.1.351 and B.1.617.2 S proteins were detected in all participants in the mRNA-1273.213 cohort 1 week after immunization, with lower IgA responses detectable in most participants (Fig. 1b and Extended Data Fig. 1a). Plasma IgG antibody titres against S protein from the WA1/2020, B.1.351, B.1.617.2 and BA.1 strains were measured by multiplex bead binding assay. In both cohorts, plasma antibody binding levels against all strains were increased 4 weeks after immunization and declined approximately 1.3- to 2-fold by 17 weeks (Extended Data Fig. 1b,c).

Fig. 1: B cell response to mRNA-1273 and mRNA-1273.213 booster immunizations.


a
Weeks after immunization
0 1 2 4 8 17 26
3rd dose
(mRNA-1273 or mRNA-1273.213)
Blood (n = 7, 39)
LN FNA (n = 5, 20)
Bone marrow aspirate (n = 3, 11)
b
Wk 1 mRNA-1273
Wk 1 mRNA-1273.213
Spike-binding IgG PBs per 10^6 PBMCs
LOD
WA1/2020
B.1.351
B.1.617.2
c
SA⁻IgD^lo CD19⁺CD3⁻ live singlet
BCL6⁺CD38^int 7.71
CD38–BB700
BCL6–R718
S⁺ 37.7
Spikes–BV421
Spike–BV650
S⁺ GCs (% of CD19⁺ cells)
mRNA-1273
mRNA-1273.213
Time after 3rd dose (weeks)
d
SA⁻IgD^lo CD19⁺CD3⁻ live singlet
CD20⁺ 96.6
CD38–BB700
CD20–PB
S⁺ 2.37
Spikes–BV650
Spike–PE
S⁺ MBCs (% of CD19⁺ cells)
mRNA-1273
mRNA-1273.213
Time after 3rd dose (weeks)
e
IgG
IgA
Influenza vaccine
WA1 spike
B.1.351 spike
B.1.617.2 spike
BA.1 spike
BMPCs per well
2.2 × 10^4
7.1 × 10^3
f
Wk 26 mRNA-1273
Wk 26 mRNA-1273.213
Antigen-specific IgG ASCs (%)
LOD
Flucelvax
WA1/2020
B.1.351
B.1.617.2
BA.1
g
mRNA-1273
60.56% all strains
35.68% WA1, B.1.351,B.1.617.2
0.47% WA1,B.1.351, B.1.1.529
0.47% WA1, B.1.351
0.47% WA1, B.1.617.2
0.94% WA1 only
1.41% none
n = 213
mRNA-1273.213
56.79% all strains
34.57% WA1, B.1.351, B.1.617.2
0.41% WA1, B.1.351
2.47% WA1, B.1.617.2
0.82% WA1
4.94% none
n = 243
h
mRNA-1273
Other 1.0%
S2 41.5%
RBD 39.5%
NTD 18.0%
mRNA-1273.213
Other 2.3%
S2 39.1%
RBD 42.7%
NTD 15.9%

a, Seven healthy adults received an mRNA-1273 booster and thirty-nine healthy adults received a mRNA-1273.213 booster. Blood was collected at baseline and at 1, 2, 4, 8, 17 and 26 weeks after the booster. FNAs of ipsilateral axillary lymph nodes were collected 2 and 8 weeks after the booster from 5 participants from the mRNA-1273 cohort and from 20 participants from the mRNA-1273.213 cohort; bone marrow aspirates were collected 26 weeks after the booster from 3 participants from the mRNA-1273 cohort and 11 participants from the mRNA-1273.213 cohort. LN, lymph node. **b**, Frequencies of IgG plasmablasts (PBs) specific for the indicated antigens measured by ELISpot in week (wk) 1 PBMCs from participants who received mRNA-1273 (left; $n = 7$) and mRNA-1273.213 (right; $n = 38$). **c**,**d**, Representative flow cytometry plots of BCL6 and CD38 (**c**) or CD20 and CD38 (**d**) on IgD^{lo} B cells in FNA (**c**) or PBMC (**d**) samples (left), pooled (WA1/2020, B.1.351, B.1.617.2 and BA.1) S protein probe (BV421 and BV650) staining on $BCL6^{+}CD38^{int}$ germinal centre B cells (**c**) and $CD20^{+}CD38^{lo/int}$ MBCs (**d**) (second from left), and frequencies of S^{+} germinal centre B cells from FNA (**c**) or S^{+} MBCs from PBMCs (**d**) from participants who received mRNA-1273 (second from right) and mRNA-1273.213 (right). **c**, mRNA-1273, $n = 5$; mRNA-1273.213, $n = 20$. **d**, mRNA-1273, $n = 6$; mRNA-1273.213, $n = 28$. **e**, Representative ELISpot wells coated with the indicated antigens, developed in blue (IgG) and red (IgA) after plating the indicated numbers of BMPCs. **f**, Frequencies of IgG BMPCs specific for the indicated antigens 26 weeks after participants received mRNA-1273 (left) or mRNA-1273.213 (right) boosters. Lines indicate medians. Symbols at each time point represent one sample. mRNA-1273, $n = 3$; mRNA-1273.213, $n = 10$. **g**,**h**, Binding of monoclonal antibodies from week 17 S^{+} MBCs from participants who received mRNA-1273 (left) and mRNA-1273.213 (right) to indicated antigens (**g**) and constituent domains of WA1/2020 S protein (**h**), measured by ELISA.

Ultrasonography was used to identify and guide FNA of accessible axillary lymph nodes on the same side as the site of immunization two and eight weeks after the booster. FNA samples were stained with pooled fluorescently labelled S protein probes from the WA1/2020, B.1.351, B.1.617.2 and BA.1 strains and then analysed by flow cytometry to detect S protein-specific B cells. We included BA.1 S protein probes in the pool to detect memory B cells (MBCs) that may have stochastically mutated to

better recognize the variant antigen[26]. Spike-recognizing (S^+) germinal centre B cells ($CD19^+CD3^-IgD^{lo}BCL6^+CD38^{int}$) and follicular helper T (T_{FH}) cells (defined as $CD3^+CD19^-CD4^+CD8^-CD14^-CXCR5^+PD\text{-}1^+BCL6^+FOXP3^-$) were detected in FNAs from all participants analysed at week 2. Frequencies of S^+ germinal centre B cells and T_{FH} cells correlated significantly and remained readily detectable in all but one participant from each cohort at week 8, consistent with the robust germinal centre response observed after primary vaccination with SARS-CoV-2 mRNA vaccines[2,27,28] (Fig. 1c and Extended Data Fig. 1d–f). Circulating S^+ MBCs in blood were identified as $CD19^+CD3^-IgD^{lo}CD20^+$ cells that bound the pooled fluorescently labelled S protein probes. S^+ MBCs were detected in all participants before the booster administration and at similar frequencies 17 weeks after the booster, with median frequencies of 0.52% and 0.55% of the total circulating B cells in the mRNA-1273 cohort, and 0.42% and 0.49% in the mRNA-1273.213 cohort (Fig. 1d). Consistent with sustained plasma antibody titres, bone marrow plasma cells (BMPCs) producing IgG that bound WA1/2020, B.1.351, B.1.617.2 and BA.1 S proteins were detected in all thirteen participants with enough BMPCs for ELISpot (3 from the mRNA-1273 and 10 from the mRNA-1273.213 cohort). Although the differences were not statistically significant, the frequencies of BMPCs that bound WA1/2020, B.1.351 and B.1.617.2 S proteins were approximately half of those of seasonal influenza vaccine-specific BMPCs, which accumulate over a lifetime of repeated antigen exposures. Similarly, the frequencies of BA.1-binding BMPCs were approximately one-quarter of those binding the other strains. S protein-binding IgA-producing BMPCs were considerably rarer or undetectable (Fig. 1e,f and Extended Data Fig. 1g,h).

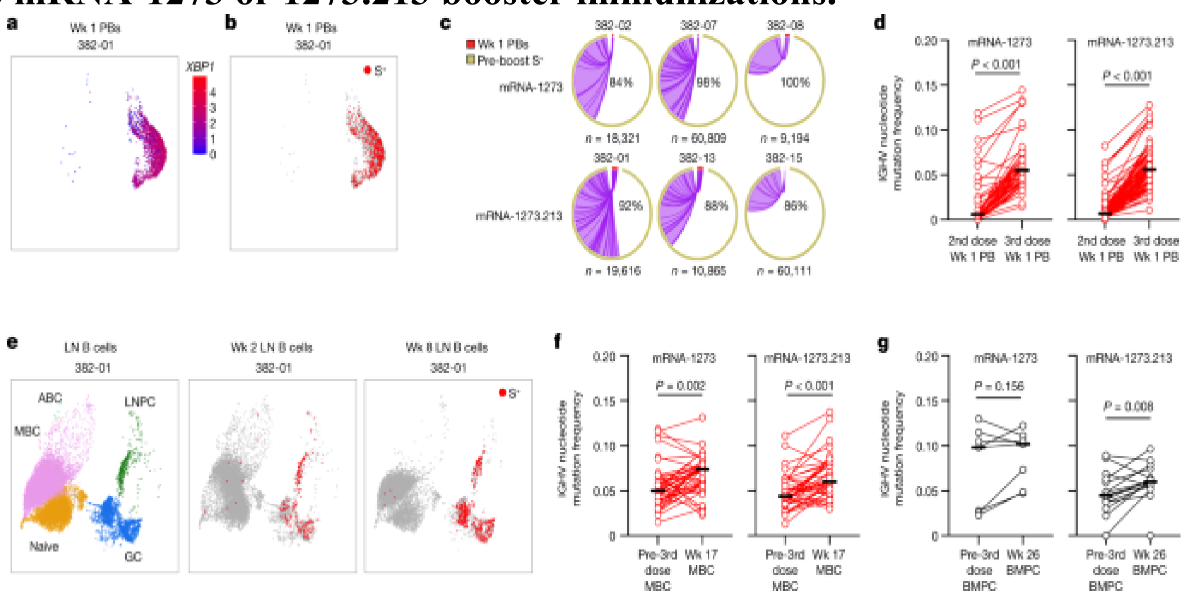
To characterize the breadth of the MBC repertoire after boosting, we selected three participants from each cohort for whom we had characterized the B cell response to the primary vaccination series: 382-02, 382-07 and 382-08 from the mRNA-1273 cohort and 382-01, 382-13 and 382-15 from the mRNA-1273.213 cohort[2,29]. For both cohorts, we stained week 17 post-boost peripheral blood mononuclear cells (PBMCs) with pooled fluorescently labelled S protein probes from the WA1/2020, B.1.351, B.1.617.2 and BA.1 strains, enabling us to sort MBCs for monoclonal

antibody generation independently of the S protein probe that they bound. We also bulk-sorted week 17 total MBCs for heavy chain immunoglobulin sequencing to broaden the clonal repertoire analyses (Extended Data Fig. 2a and Extended Data Table 3). We generated 81, 59, 73, 94, 90 and 59 clonally distinct monoclonal antibodies from participants 382-02, 382-07, 382-08, 382-01, 382-13 and 382-15, respectively. We next assessed the binding of these antibodies to S protein from the WA1/2020, 1.351, 1.617.2 and BA.1 strains by enzyme-linked immunosorbent assay (ELISA). In total, 205 out of 213 (96%) and 222 out of 243 (91%) monoclonal antibodies derived from the MBCs from the mRNA-1273 and mRNA-1273.213 cohorts, respectively, recognized the original WA1/2020, B.1.351 and B.1.617.2 S proteins, with 129 (61%) and 138 (57%), respectively, also recognizing BA.1 (Fig. 1g). Evaluation of the domains targeted by each monoclonal antibody revealed that 40%, 18% and 42% from the mRNA-1273 cohort and 43%, 16% and 39% from the mRNA-1273.213 cohort bound RBD, the N-terminal domain (NTD) and S2, respectively (Fig. 1h).

To track the clonal dynamics of the B cell response in the two cohorts, we performed single-cell RNA sequencing (scRNA-seq) on week 1 sorted plasmablasts and week 2 and week 8 FNA specimens from the same 6 participants and bulk-sorted germinal centre B cells and lymph node plasma cells (LNPCs) for heavy chain immunoglobulin sequencing (Fig. 2a,e, Extended Data Fig. 3a–g and Extended Data Tables 3–5). We then computationally inferred clonal relationships on the basis of common heavy chain *V* and *J* gene usage, CDR3 lengths and CDR3 similarity[30,31] to link the B cell receptor sequences to known S-specific clones identified among monoclonal antibodies derived from MBCs isolated 17 weeks after the third vaccine dose or from the previously characterized response to the primary vaccination series[2,29] (Fig. 2b,e, Extended Data Fig. 3h and Extended Data Table 6). The majority of S-specific plasmablasts identified by scRNA-seq after the booster dose were clonally related to MBCs, germinal centre B cells and/or plasma cells induced by primary vaccination (Fig. 2c). Multiple S-specific clones were detected in the plasmablast response after both the second dose of the primary vaccination series and the booster. Representatives of these clones participating in the booster plasmablast response had significantly higher somatic hypermutation (SHM) frequencies in their immunoglobulin heavy chain variable region (IGHV) genes than

those from the primary response, consistent with their recall from affinity-matured MBCs (Fig. 2d). S-specific plasmablast clones identified one week after the booster dose were identified in germinal centre responses in all six analysed participants, although the peak frequencies of the S-specific germinal centre clonal repertoire occupied by plasmablast clones varied from 17% to 100% among participants (Extended Data Fig. 3i,j). SHM frequencies among S-specific MBCs isolated 17 weeks after the booster were significantly higher than their clonally related counterparts isolated 6 months after the primary vaccination, consistent with additional rounds of germinal centre-driven maturation (Fig. 2f). Similar trends were observed among paired S-specific BMPC clones analysed 6 or 9 months after the primary immunization and 6 months after the booster. However, SHM did not increase in all clonal families, consistent with durable populations of MBCs and BMPCs generated by the primary vaccine response persisting through the booster response (Fig. 2f,g). mRNA-1273 and mRNA-1273.213 both elicited robust germinal centre responses and maturation of the MBC and BMPC responses, but we did not isolate any antibodies specifically targeting S proteins from the variant strains encoded by the mRNA-1273.213 vaccine that did not cross-react to the original WA1/2020 S protein. Thus, the B cell response after boosting with the mRNA-1273.213 vaccine was imprinted by the primary vaccination series with mRNA-1273, which encodes the ancestral S protein.

Fig. 2: Maturation of S protein-specific MBCs and BMPCs in response to mRNA-1273 or 1273.213 booster immunizations.

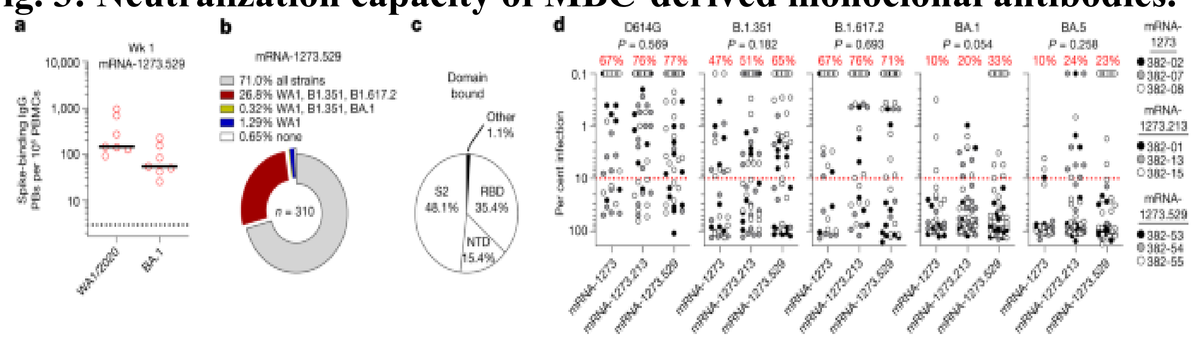


a,**b**,**e**, Uniform manifold approximation and projection (UMAP) of scRNA-seq transcriptional clusters of B cells from sorted circulating plasmablasts 1 week after booster immunization, with log-normalized *XBP1* gene expression (**a**) and S-specific clones (**b**) overlaid, or from FNAs of draining lymph nodes, with S-specific clones overlaid (**e**). Each dot represents a cell. **c**, Clonal overlap and percentages of S-specific plasmablast clones related to clones generated during the primary vaccine response among participants receiving mRNA-1273 (top) and mRNA-1273.213 (bottom). Peripheral arc lengths correspond to the number of B cell receptor sequences in the respective compartment and chord widths correspond to clone size. Purple chords connect clonally related sequences between plasmablast and pre-boost arcs. Percentages are of plasmablast clones related to pre-boost S-specific clones. The number of sequences is indicated below each plot. **d**,**f**,**g**, Paired median IGHV gene mutation frequencies of S-specific clones found among plasmablasts 1 week after the second dose of the primary vaccine series and 1 week after booster vaccination (**d**), MBCs identified 6 months after primary vaccination and 17 weeks after booster vaccination (**f**), and BMPCs identified 6 and/or 9 months after primary vaccination and 6 months after booster vaccination (**g**). Each symbol represents the median mutation frequency of a clone; horizontal lines indicate medians. *P* values from two-sided Wilcoxon test. **d**, mRNA-1273, $n = 52$; mRNA-1273.213, $n = 104$. **f**, mRNA-1273, $n = 42$; mRNA-1273.213, $n = 39$. **g**, mRNA-1273, $n = 7$; mRNA-1273.213, $n = 15$.

To determine whether a more antigenically divergent booster could generate a detectable response targeting novel epitopes, we recruited 8 participants who had received a 2-dose mRNA primary vaccination series and had no history of SARS-CoV-2 infection to receive 50 μg of mRNA-1273.529, which encodes BA.1 S protein (97.1% S protein and 93.3% RBD sequence conservation versus WA1/2020), as a first (third dose) or second (fourth dose at least 3 months after a third dose of mRNA-1273) booster (Extended Data Fig. 4a and Extended Data Tables 1 and 2). We analysed peripheral blood samples 1 and 17 weeks after the mRNA-1273.529 booster. All seven participants analysed one week after receiving the booster exhibited robust circulating IgG-producing plasmablast responses against the original WA1/2020 S protein as well as the vaccine-encoded BA.1 S protein, with lower IgA responses detectable in most participants (Fig. 3a and Extended Data Fig. 4b). To analyse the breadth of the MBC repertoire, we sorted

MBCs from PBMCs isolated 17 weeks after the booster from participants 382-53, 382-54 and 382-55 (all of whom received mRNA-1273.529 as a third dose booster) using the same pooled fluorescent S protein probes from the WA1/2020, B.1.351, B.1.617.2 and BA.1 strains to detect MBCs regardless of their strain specificity and to maintain consistency with the previously generated monoclonal antibodies. Similar to the monoclonal antibodies from the mRNA-1273 and mRNA-1273.213 cohorts, 303 out of 310 monoclonal antibodies (98%) were cross-reactive, binding S protein from WA1/2020, B.1.351 and B.1.617.2, including 220 (71%) that also recognized the BA.1 S protein encoded by the mRNA-1273.529 vaccine (Fig. 3b). Evaluation of the domains targeted by each monoclonal antibody revealed that 35% bound the RBD, 15% bound the NTD and 48% bound S2 (Fig. 3c). To assess the neutralization capacity of the MBC-derived monoclonal antibodies, we first screened all 730 S-binding monoclonal antibodies from the 3 cohorts with a high-throughput assay using chimeric vesicular stomatitis virus (VSV) in which the native envelope glycoprotein was replaced with S protein from the WA1/2020 strain with the D614G substitution[32]. Thirty monoclonal antibodies from the mRNA-1273 cohort, 49 from the mRNA-1273.213 cohort and 52 from the mRNA-1273.529 cohort neutralized infection by at least 80% at 5 μg ml^{-1} (Extended Data Fig. 4c). We then evaluated the neutralizing capacity of these 131 monoclonal antibodies against a panel of authentic, infectious SARS-CoV-2 variants, including WA1/2020 D614G, B.1.351, B.1.617.2, BA.1 and BA.5, against which 67%, 47%, 67%, 10% and 10% from the mRNA-1273 cohort, 76%, 51%, 76%, 20% and 24% from the mRNA-1273.213 cohort, and 77%, 65%, 71%, 33% and 23% from the mRNA-1273.529 cohort, respectively, reduced infection by at least 90% at 5 μg ml^{-1} (Fig. 3d).

Fig. 3: Neutralization capacity of MBC-derived monoclonal antibodies.

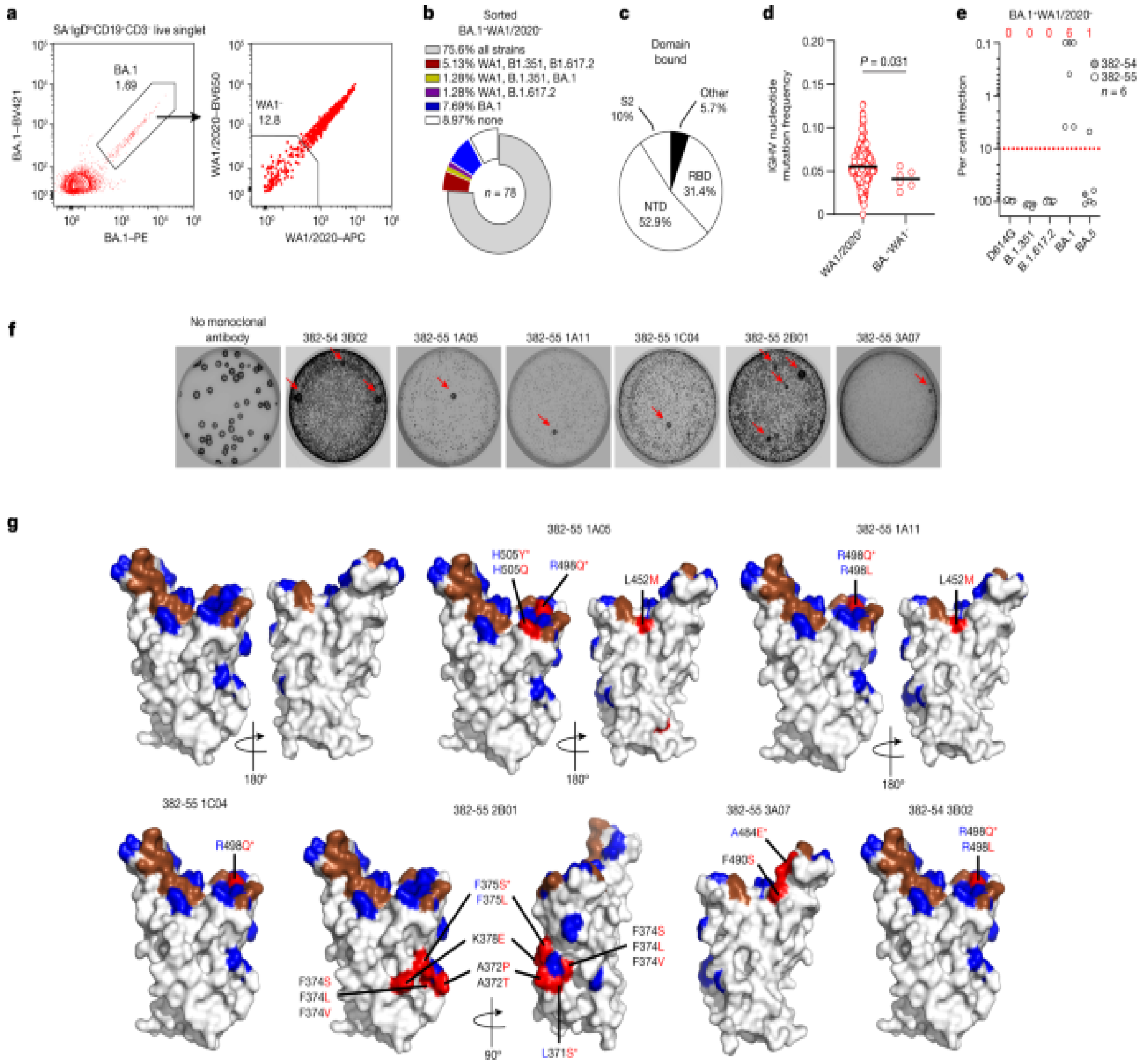


a, Frequencies of S-binding IgG-producing plasmablasts in PBMC 1 week after booster vaccination, measured by ELISpot in participants who received mRNA-1273.529. Horizontal lines indicate medians. Each symbol represents a sample; $n = 7$. **b**,**c**, Binding of monoclonal antibodies from S^+ MBCs 17 weeks after mRNA-1273.529 booster immunization to S proteins from indicated SARS-CoV-2 strains (**b**) and constituent domains of WA1/2020 S protein (**c**), measured by ELISA. **d**, Neutralizing activity of monoclonal antibodies from week 17 S^+ MBCs against indicated strains of authentic SARS-CoV-2 virus from participants who received indicated third-dose booster vaccines. Each symbol represents one monoclonal antibody. mRNA-1273, $n = 30$; mRNA-1273.213, $n = 49$; mRNA-1273.529, $n = 52$. Percentages indicate the proportion of monoclonal antibodies above the 90% infection reduction threshold. P values are from Chi-squared tests between the three vaccine cohorts.

Given the high frequency of cross-reactive monoclonal antibodies, we used a more targeted approach to sort MBCs specific for BA.1 S protein that did not bind WA1/2020 S protein from participants 382-53, 382-54 and 382-55 (Fig. 4a). Sixty-five out of the seventy-eight monoclonal antibodies (83%) isolated using this approach still cross-reacted with WA1/2020 S protein, indicating that the S-dependent sorting approach is not ideally sensitive for determining variant binding specificity. Out of the 78 monoclonal antibodies, 6 bound BA.1 S protein only, all of which were from participants 382-54 and 382-55 (Fig. 4b). Evaluation of the domains targeted by each monoclonal antibody revealed an increased proportion of NTD-targeting monoclonal antibodies at the expense of those specific for S2 compared with the monoclonal antibodies that were not sorted to exclude WA1/2020, with 31%, 53% and 10% binding RBD, NTD and S2, respectively (Fig. 4c). The SHM frequencies among the clonal families of the six monoclonal antibodies that bound BA.1 S protein but not WA1/2020 S protein were significantly lower than those from the same participants that cross-reacted with WA1/2020 S protein (Fig. 4d). We tested the neutralizing capacity of the six monoclonal antibodies that bound BA.1 but not WA1/2020 against the panel of SARS-CoV-2 variants. As expected, none of the six antibodies neutralized the ancestral D614G strain. Notably, all six neutralized BA.1, one also neutralized BA.5 (17%) and none neutralized B.1.351 or B.1.617.2 at 5 $\mu g\ ml^{-1}$ (Fig. 4e). All six of the BA.1-neutralizing monoclonal

antibodies targeted the RBD of S protein (Extended Data Fig. 4d). To identify the amino acid residues targeted by the six BA.1-specific monoclonal antibodies, we used VSV–SARS-CoV-2 S chimeric viruses (S from BA.1 strain) to select variants that escaped neutralization, as previously described[32,33]. We performed plaque assays on Vero E6 cells with the six neutralizing monoclonal antibodies in the overlay, purified the neutralization-resistant plaques, and sequenced the S genes (Fig. 4f and Extended Data Fig. 4e,f). Sequence analysis identified S protein escape mutations at R498 for monoclonal antibodies 382-54 3B02, 382-55 1A11 and 382-55 1C04; R498 and H505 for monoclonal antibody 382-55 1A05; L371, A372, F374, F375 and K378 for monoclonal antibody 382-55 2B01; and A484 and F490S for monoclonal antibody 382-55 3A07. Notably, many of the mutations were reversions to the ancestral strain of SARS-CoV-2. (Fig. 4g).

Fig. 4: Characterization of BA.1-specific monoclonal antibodies.



a, Gating strategy for sorting BA.1^{+} WA1/2020^{-} MBCs from PBMCs 17 weeks post booster. **b**,**c**, Binding of monoclonal antibodies from BA.1^{+} WA1/2020^{-} sorted MBCs to indicated strains of SARS-CoV-2 S protein (**b**), and constituent domains of S protein (**c**), measured by ELISA. **d**, IGHV mutation frequencies of clones related to monoclonal antibodies from participants 382-54 and 382-55 that bound WA1/2020 (left) and BA.1 but not WA1/2020 (right) S protein. Each symbol represents the median mutation frequency of a clone. WA1/2020^{+}, $n = 266$; BA.1^{+} WA1/2020^{-}, $n = 6$. Black lines indicate medians. P value from two-sided Mann–Whitney test. **e**, Neutralizing activity of BA.1^{+} WA1/2020^{-} S-binding monoclonal antibodies against indicated strains of authentic SARS-CoV-2 virus. Numbers above each virus are of monoclonal antibodies above the 90%

infection reduction threshold. **f**, Plaque assays on Vero E6 cells with indicated monoclonal antibody in the overlay to isolate escape mutants (red arrows). Images are representative of three experiments per monoclonal antibody. **g**, Structure of the RBD with the human ACE2 footprint highlighted in brown. BA.1 mutations are highlighted in blue and amino acids whose substitution confers resistance to indicated monoclonal antibodies in plaque assays are highlighted in red. Asterisks indicate substitutions that confer resistance to the indicated monoclonal antibody and are reversions from BA.1 to the WA1/2020 sequence.

Here we have evaluated antigen-specific B cell responses to SARS-CoV-2 mRNA-based booster immunizations in humans. We show that boosting with ancestral SARS-CoV-2 or bivalent B.1.351/B.1.617.2-matched vaccines induce robust S-specific germinal centre responses in draining axillary lymph nodes of all sampled participants that last until at least eight weeks after vaccination. S-specific plasmablasts and germinal centre B cells originate predominantly from pre-existing clonal lineages, consistent with most of the MBC-derived monoclonal antibodies that we isolated recognizing the original SARS-CoV-2 S protein. We also demonstrated that immunization with the monovalent B.1.1.529 BA.1-matched vaccine could induce rare de novo B cell responses against novel epitopes in the B.1.1.529 BA.1 S protein. These observations expand the large body of data showing improved potency and breadth of serum antibody responses after SARS-CoV-2 booster immunization in humans[5,6,7,8,9,18].

Several critical insights relevant to cellular immunity to SARS-CoV-2 and recall responses to vaccination can be drawn from this study. B cell clones comprising the plasmablast compartment induced after the booster immunization were significantly more mutated than the same clones detected one week after the completion of the primary vaccination series, a clear indication of the robust maturation process triggered by the primary vaccination[2,29]. Consistent with our previous work on B cell responses to seasonal influenza virus vaccination in humans[34], the data presented here show that pre-existing MBCs can be efficiently re-engaged into recall germinal centre reactions. The frequencies of IgG-secreting BMPCs specific for the original SARS-CoV-2 S protein were several fold higher than those measured seven months after mild SARS-CoV-2 infections or six months

after the primary mRNA vaccination series[29,35]. These increased frequencies are likely to be the result of the persistent germinal centre responses induced after the primary vaccination series and the new germinal centre reactions seeded by the booster immunization, highlighting the critical contribution of repeated antigen exposures to increasing antigen-specific BMPC frequency[36,37].

A key unexpected finding in our study was the exceptionally high percentage of circulating MBCs that recognize the S protein from the original SARS-CoV-2 strain in the individuals boosted with variant S antigens, particularly as the booster immunizations did not encode S protein from the original strain. Of note, none of the participants from whom the monoclonal antibodies were derived had documented SARS-CoV-2 infection or seroconverted against the virus nucleocapsid protein during the course of the study. These data are consistent with MBCs generated by the primary vaccination series dominating the recall response induced by the booster and potentially out-competing clones specific for novel epitopes. It is possible that we were unable to isolate more memory B cell-derived monoclonal antibodies specific for novel epitopes on the B.1.351, B.1.617.2 or B.1.1.529 BA.1 S proteins because their affinity for the probes was below the limit of detection. The high antigenic similarity between the variant-derived and original SARS-CoV-2 S antigens in the case of the bivalent B.1.351/B.1.617.2 vaccine may have contributed to the low frequency of de novo clones recognizing the variants, and our data lend support for the decision to not adopt this vaccine for clinical use. Given the degree of cross-reactivity in the response we observed to purely variant-based vaccines, it is likely that the recently licensed bivalent boosters encoding WA1/2020 and either BA.1 or BA.4/5 will elicit similarly cross-reactive responses. We also speculate that an additional immunization with a variant-based vaccine may be needed to amplify the exclusively variant-specific B cell clones, similar to what has been observed upon H5N1 influenza virus immunization in humans[38]. We note that many of the mutations selected when we cultured recombinant vesicular stomatitis virus expressing SARS-CoV-2 Omicron (BA.1) S protein in the presence of the de novo monoclonal antibodies were reverted to the residues in the original strain. This suggests that newly escaped viruses are likely to be sensitive to potently neutralizing antibodies, including some that were clinically approved for therapeutic use, that were

thought to be no longer useful because of the changes at the E484 residue, for example[39,40,41,42,43].

The high prevalence of MBCs recognizing the original SARS-CoV-2 S protein is evidence of antigenic imprinting, in which B cell responses to previously encountered antigens remain dominant even after exposure to different but antigenically related antigens[44,45]. Here we provide evidence that immunization with a distinct antigen can engage rare naive B cells that target novel epitopes, but the overall response remains dominated by clones that are cross-reactive to the original strain.

Methods

Sample collection, preparation and storage

All studies were approved by the Institutional Review Board of Washington University in St Louis. Written consent was obtained from all participants. Fifty-four healthy volunteers were enroled, of whom 26 and 15 provided axillary lymph node and bone marrow aspirate samples, respectively (Extended Data Table 1). Blood samples were collected in ethylenediaminetetraacetic acid (EDTA) evacuated tubes (BD), and PBMCs were enriched by density gradient centrifugation over Lymphopure (BioLegend). The residual red blood cells were lysed with ammonium chloride lysis buffer, washed with PBS supplemented with 2% fetal bovine serum (FBS) and 2 mM EDTA (P2), and PBMC were immediately used or cryopreserved in 10% dimethylsulfoxide (DMSO) in FBS. Ultrasound-guided FNA of axillary lymph nodes was performed by a radiologist. Lymph node dimensions and cortical thickness were measured, and the presence and degree of cortical vascularity and location of the lymph node relative to the axillary vein were determined prior to each FNA. For each FNA sample, six passes were made under continuous real-time ultrasound guidance using 22- or 25-gauge needles, each of which was flushed with 3 ml of RPMI 1640 supplemented with 10% FBS and 100 U ml^{-1} penicillin/streptomycin, followed by three 1-ml rinses. Red blood cells were lysed with ammonium chloride buffer (Lonza), washed with P2, and immediately used or cryopreserved in 10% DMSO in FBS. Participants reported no adverse effects from phlebotomies or serial FNAs. Bone marrow aspirates of

approximately 30 ml were collected in EDTA tubes from the iliac crest. Bone marrow mononuclear cells were enriched by density gradient centrifugation over Ficoll-Paque PLUS (Cytiva), and remaining red blood cells were lysed with ammonium chloride buffer (Lonza) and washed with P2. BMPCs were enriched from bone marrow mononuclear cells using the EasySep Human CD138 Positive Selection Kit II (StemCell Technologies) and immediately used for ELISpot or cryopreserved in 10% DMSO in FBS.

Cell lines

Expi293F cells were cultured in Expi293 Expression Medium (Gibco). Vero-TMPRSS2 cells[46] (a gift from S. Ding) were cultured at 37 °C in Dulbecco's modified Eagle medium (DMEM) supplemented with 10% FBS, 10 mM HEPES (pH 7.3), 1 mM sodium pyruvate, 1× nonessential amino acids, 100 U ml^{-1} of penicillin/streptomycin, and 5 μg ml^{-1} of blasticidin. Vero E6 cells were cultured at 37 °C in DMEM supplemented with 10% FBS, 10 mM HEPES (pH 7.3), 1 mM sodium pyruvate, 1× nonessential amino acids, and 100 U ml^{-1} of penicillin/streptomycin.

Antigens

Recombinant soluble S protein from WA1/2020, B.1.351, B.1.617.2 and B.1.1.529 (BA.1) strains of SARS-CoV-2 and their Avi-tagged counterparts were expressed as previously described[29,47]. In brief, mammalian cell codon-optimized nucleotide sequences coding for the soluble ectodomain of S (GenBank: MN908947.3, amino acids 1–1213) including a C-terminal thrombin cleavage site, T4 foldon trimerization domain, and hexahistidine tag were cloned into mammalian expression vector pCAGGS. The S sequences were modified to remove the polybasic cleavage site (RRAR to A), and two prefusion stabilizing proline mutations were introduced (K986P and V987P, wild type numbering). For expression of Avi-tagged variants, the CDS of pCAGGS vector containing the sequence for the relevant soluble S was modified to encode 3′ Avitag insert after the 6×His tag (5′-His tag-GGCTCCGGGCTGAACGACATCTTCGAAGCCCAGAAGATTGAGTGG CATGAG-Stop-3′; HHHHHHGSGLNDIFEAQKIEWHE-) using inverse PCR mutagenesis as previously described[48]. Recombinant proteins were produced in Expi293F cells (ThermoFisher) by transfection with purified

DNA using the ExpiFectamine 293 Transfection Kit (ThermoFisher). Supernatants from transfected cells were collected 3 days post-transfection, and recombinant proteins were purified using Ni-NTA agarose (ThermoFisher), then buffer exchanged into PBS and concentrated using Amicon Ultracel centrifugal filters (EMD Millipore). To biotinylate Avi-tagged S variants, the S-Avitag substrates were diluted to 40 μM and incubated for 1 h at 30°C with 15 μg ml^{-1} BirA enzyme (Avidity) in 0.05 M bicine buffer at pH 8.3 supplemented with 10 mM ATP, 10 mM magnesium acetate and 50 μM biotin. The protein was then concentrated and buffer exchanged with PBS using a 100 kDa Amicon Ultra centrifugal filter (EMD Millipore).

To generate antigen probes for flow cytometry staining and sorting, trimeric BirA-biotinylated recombinant S from WA1/2020, B.1.351. B.1.617.2, or B.1.1.529 (BA.1) were incubated with a 1.04-fold molar excess of BV421-, BV650-, or PE-conjugated streptavidin (BioLegend), on ice, with three equal additions of S spaced every 15 min. Fifteen minutes after the third S addition, d-biotin was added in sixfold molar excess to streptavidin to block any unoccupied biotin binding sites. Streptavidin-PE-Cy5 and streptavidin-APC-Fire750 (BioLegend) were blocked with a 6-fold molar excess of d-biotin and used as background staining controls. Bovine serum albumin (BSA) was biotinylated using the EZ-Link Micro NHS-PEG4-Biotinylation Kit (Thermo Fisher); excess unreacted biotin was removed using 7-kDa Zeba desalting columns (Pierce).

ELISpot assay

Wells were coated with Flucelvax Quadrivalent 2019/2020 seasonal influenza virus vaccine (Sequiris), recombinant S from the WA1/2020, B.1.351, B.1.617.2, or BA.1 strains of SARS-CoV-2, or pooled anti-κ and anti-λ light chain antibodies (Cellular Technology Limited). Direct ex vivo ELISpot assays were performed with non-cryopreserved PBMCs to determine the number of total, influenza vaccine-binding, or recombinant S-binding IgG- and IgA-secreting cells present in PBMC and non-cryopreserved enriched BMPC samples using IgG/IgA double-colour ELISpot Kits (Cellular Technology Limited) according to the manufacturer’s

instructions. ELISpot plates were analysed using an ELISpot counter (Cellular Technology Limited).

Fluorescent bead antigen binding assay

Recombinant biotinylated S from WA1/2020, B.1.351, B.1.617.2 and BA.1 strains of SARS-CoV-2 and biotinylated BSA were incubated for 30 min on ice with different fluorescence intensity peaks of the Streptavidin Coated Fluorescent Yellow Particle Kit (Spherotech) at 9.12 ng per µg beads. Beads were washed twice with 0.05% Tween 20 in PBS, resusupended in monoclonal antibodies diluted to 65 µg ml^{-1} or plasma samples diluted 1:80 in 0.05% Tween 20 in PBS, and incubated for 30 min on ice. Beads were washed twice with 0.05% Tween 20 in PBS, stained with IgG-APC-Fire750 (M1310G05, BioLegend, 1:100), incubated for 30 min on ice, washed twice with 0.05% Tween 20 in PBS, and resuspended in 2% FBS and 2 mM EDTA in PBS and acquired on an Aurora using SpectroFlo v2.2 (Cytek). Data were analysed using FlowJo v10 (Treestar). Background-subtracted median fluorescence intensities were calculated for each sample by subtracting its median fluorescence intensity plus two times robust standard deviation for BSA and the median fluorescence intensity of an influenza virus haemagglutinin-specific monoclonal antibody (for monoclonal antibody samples) or plasma collected prior to the SARS-CoV-2 pandemic (for plasma samples) for the respective spike variant (Extended Data Fig. 1b).

ELISA

Assays were performed in 96-well plates (MaxiSorp; Thermo) coated with 100 µl of recombinant S from WA1/2020, B.1.351, B.1.617.2 and BA.1 strains of SARS-CoV-2, NTD of WA1/2020 or BA.1, receptor binding domain of WA1/2020 or BA.1, or S2 domain of WA1/2020, or bovine serum albumin diluted to 1 µg ml^{-1} in PBS, and plates were incubated at 4 °C overnight. Plates then were blocked with 10% FBS and 0.05% Tween 20 in PBS. Purified monoclonal antibodies were serially diluted in blocking buffer and added to the plates. Plates were incubated for 90 min at room temperature and then washed 3 times with 0.05% Tween 20 in PBS. Goat anti-human IgG-HRP (goat polyclonal, Jackson ImmunoResearch, 1:2,500) was diluted in blocking buffer before adding to plates and incubating for 60

min at room temperature. Plates were washed 3 times with 0.05% Tween 20 in PBS and 3 times with PBS before the addition of *O*-phenylenediamine dihydrochloride peroxidase substrate (Sigma-Aldrich). Reactions were stopped by the addition of 1 M hydrochloric acid. Optical density measurements were taken at 490 nm.

VSV–SARS-CoV-2-$S_{\Delta 21}$ eGFP-reduction assay

The S gene of SARS-CoV-2 isolate WA1/2020 (with D614G mutation) was synthesized and replaced the native envelope glycoprotein of an infectious molecular clone of VSV, and resulting chimeric viruses expressing S protein from SARS-CoV-2 D614G were used for GFP reduction neutralization tests as previously described[32]. In brief, 10^3 PFU of VSV–SARS-CoV-2-$S_{\Delta 21}$ was incubated for 1 h at 37 °C with recombinant monoclonal antibodies diluted to 5 μg ml^{-1}. Antibody–virus complexes were added to Vero E6 cells in 96-well plates and incubated at 37 °C for 7.5 h. Cells were subsequently fixed in 2% formaldehyde (Electron Microscopy Sciences) containing 10 μg ml^{-1} Hoechst 33342 nuclear stain (Invitrogen) for 45 min at room temperature, when fixative was replaced with PBS. Images were acquired with an InCell 2000 Analyzer (GE Healthcare) automated microscope using the DAPI and FITC channels to visualize nuclei and infected cells (that is, eGFP-positive cells), respectively (4× objective, 4 fields per well, covering the entire well). Images were analysed using the Multi Target Analysis Module of the InCell Analyzer 1000 Workstation Software (GE Healthcare). GFP-positive cells were identified in the FITC channel using the top-hat segmentation method and subsequently counted within the InCell Workstation software. The sensitivity and accuracy of GFP-positive cell number determinations were validated using a serial dilution of virus. The percent infection reduction was calculated from wells to which no antibody was added. A background number of GFP-positive cells was subtracted from each well using an average value determined from at least four uninfected wells.

Focus reduction neutralization test

Each monoclonal antibody was incubated at 5 μg ml^{-1} in DMEM supplemented with 2% FBS, 10 mM HEPES, and 100 U ml^{-1}

penicillin/streptomycin with 10^2 focus-forming units of different of SARS-CoV-2 strains (WA1/2020 D614G, B.1.351, B.1.617.2, BA.1, and BA.5) for 1 h at 37 °C[49]. Antibody–virus complexes were added to Vero-TMPRSS2 cell monolayers in 96-well plates and incubated at 37 °C for 1 h. Subsequently, cells were overlaid with 1% (w/v) methylcellulose in MEM supplemented with 2% FBS. Plates were harvested 30 h (D614G, B.1.351, or B.1.617.2-infected) or 70 h (BA.1 or BA.5-infected) later by removing overlays and fixed with 4% PFA in PBS for 20 min at room temperature. Plates were washed and incubated with an oligoclonal pool of anti-S antibodies (SARS2-2, SARS2-11, SARS2-16, SARS2-31, SARS2-38, SARS2-57, and SARS2-71)[33], and an additional oligoclonal pool of anti-S antibodies with extended reactivity (SARS2-08, SARS2-09, SARS2-10, SARS2-13, SARS2-14, SARS2-17, SARS2-20, SARS2-26, SARS2-27, SARS2-28, SARS2-31, SARS2-41, SARS2-42, SARS2-44, SARS2-49, SARS2-62, SARS2-64, SARS2-65 and SARS2-67)[50] were included for staining BA.1- or BA.5-infected plates. Plates were subsequently incubated with HRP-conjugated goat anti-mouse IgG (Sigma 12–349) in PBS supplemented with 0.1% saponin and 0.1% bovine serum albumin. SARS-CoV-2-infected cell foci were visualized using TrueBlue peroxidase substrate (KPL) and quantitated on an ImmunoSpot microanalyzer (Cellular Technologies Limited).

Selection of monoclonal antibody escape mutants in SARS-CoV-2 S

We generated VSV–SARS-CoV-2-S (BA.1 variant) chimera by inserting the BA.1 spike gene into the VSV genome and using the resulting VSV–SARS-CoV-2 BA.1 chimeric virus to select for SARS-CoV-2 S variants that escape monoclonal antibody neutralization as described previously[32,33]. Antibody neutralization-resistant mutants were recovered by plaque isolation. In brief, plaque assays were performed to isolate the VSV–SARS-CoV-2 escape mutant on Vero cells with each tested monoclonal antibody in the overlay. The concentration of each monoclonal antibody in the overlay was determined by neutralization assays at a multiplicity of infection of 100. Escape clones were plaque-purified on Vero cells in the presence of monoclonal antibodies, and plaques in agarose plugs were amplified on MA104 cells with the monoclonal antibodies present in the medium. Viral

supernatants were collected after three days upon extensive cytopathic effect and clarified of cell debris by centrifugation at 1,000*g* for 5 min. Aliquots were maintained at −80 °C. Viral RNA was extracted from VSV–SARS-CoV-2 mutant viruses using RNeasy Mini kit (Qiagen), and the S gene was amplified using OneStep RT–PCR Kit (Qiagen). To sequence the 3,747-bp BA.1 spike gene, four sets of PCR were set up to efficiently cover the whole BA.1 spike gene in the virus as follows: first set of fragment PCR utilizing sequencing primers 15M (ctggattctatcagccac) and 369 (caatagattctgttggttgg); second set of fragment PCR utilizing sequencing primers 368 (ctctctcagaaacaaagtgt) and 372 (cctgcacgtgtttgaaaaa); third set of fragment PCR utilizing sequencing primers 370 (aactgcacagaagtccct) and 374 (agaacattctgtgtaactcc); and fourth set of fragment PCR utilizing sequencing primers 373 (tacaatcacttctggttgga) and 23L (cattgaactcgtcggtctc) (Extended Data Fig. 4f). The mutations were identified by Sanger sequencing (Genewiz).

Cell sorting and flow cytometry

Staining for flow cytometry analysis and sorting was performed using freshly isolated or cryopreserved FNA or PBMC samples. For analysis, PBMC were incubated for 30 min on ice with purified CD16 (3G8, BioLegend, 1:100), CD32 (FUN-2, BioLegend, 1:100), CD64 (10.1, BioLegend, 1:100) and PD-1-BB515 (EH12.1, BD Horizon, 1:100) in 2% FBS and 2 mM EDTA in PBS (P2), washed twice, then were stained for 30 min on ice with WA1/2020, B.1.351, B.1.617.2 and BA.1 spike probes pre-conjugated to SA–BV650 and SA–PE, $S_{167–180}$-PE-Cy7 tetramer, $S_{816–830}$-APC tetramer[51], biotin-saturated SA–PE-Cy5, ICOS-SB436 (ISA-3, Invitrogen, 1:50), IgG–BV480 (goat polyclonal, Jackson ImmunoResearch, 1:100), IgA–FITC (M24A, Millipore, 1:500), CD8a–A532 (RPA-T8, Thermo, 1:100), CD38–BB700 (HIT2, BD Horizon, 1:500), CD71-BV421 (CY1G4, 1:400), CD20–Pacific Blue (2H7, 1:400), CD4–Spark Violet 538 (SK3, 1:400), CD19–BV750 (HIB19, 1:100), IgD–BV785 (IA6-2, 1:200), CXCR5–PE-Dazzle 594 (J252D4, 1:50), CD14–PerCP (HCD14, 1:50), CD27–PE-Fire810 (O323, 1:200), CCR7-Spark 685 (G043H7, 1:100), IgM-A700 (MHM-88, 1:400), CD3–APC-Fire810 (SK7, 1:50), and Zombie NIR (all BioLegend) diluted in Brilliant Staining buffer (BD Horizon). For analysis, FNA samples were incubated for 30 min on ice with purified CD16

(3G8, BioLegend, 1:100), CD32 (FUN-2, BioLegend, 1:100), CD64 (10.1, BioLegend, 1:100) and PD-1-BB515 (EH12.1, BD Horizon, 1:100) in P2, washed twice, then stained for 30 min on ice with WA1/2020, B.1.351, B.1.617.2, and B.1.1.529 spike probes pre-conjugated to SA–BV421 and SA–BV650, $S_{167–180}$–APC tetramer, biotin-saturated SA–PE–Cy5, IgG–BV480 (goat polyclonal, Jackson ImmunoResearch, 1:100), IgA–FITC (M24A, Millipore, 1:500), CD8a–A532 (RPA-T8, Thermo, 1:100), CD38–BB700 (HIT2, BD Horizon, 1:500), CD20–Pacific Blue (2H7, 1:400), CD4–Spark Violet 538 (SK3, 1:400), IgM–BV605 (MHM-88, 1:100), CD19–BV750 (HIB19, 1:100), IgD–BV785 (IA6-2, 1:200), CXCR5–PE–Dazzle 594 (J252D4, 1:50), CD14–PerCP (HCD14, 1:50), CD71–PE–Cy7 (CY1G4, 1:400), CD27–PE–Fire810 (O323, 1:200), CD3–APC–Fire810 (SK7, 1:50) and Zombie NIR (all BioLegend) diluted in Brilliant Staining buffer (BD Horizon). Cells were washed twice with P2, fixed for 1 h at 25 °C using the True Nuclear fixation kit (BioLegend), washed twice with True Nuclear Permeabilization/Wash buffer, stained with Ki-67-BV711 (Ki-67, BioLegend, 1:200), Blimp1–PE (646702, R&D, 1:100), FOXP3–Spark 685 (206D, BioLegend, 1:200), and Bcl6–R718 (K112-91, BD Horizon, 1:200) for 1 h at 25 °C, and washed twice with True Nuclear Permeabilization/Wash buffer. Samples were resuspended in P2 and acquired on an Aurora using SpectroFlo v2.2 (Cytek). Flow cytometry data were analysed using FlowJo v10 (Treestar).

For sorting plasmablasts, PBMCs collected 1 week post-boost were stained for 30 min on ice with CD20–Pacific Blue (2H7, 1:400), CD71–FITC (CY1G4, 1:200), IgD–PerCP–Cy5.5 (IA6-2, 1:200), CD19–PE (HIB19, 1:200), CXCR5–PE–Dazzle 594 (J252D4, 1:50), CD38–PE–Cy7 (HIT2, 1:200), CD4–A700 (SK3, 1:400) and Zombie Aqua (all BioLegend) diluted in P2. Cells were washed twice, and plasmablasts (live singlet $CD4^{-}CD19^{+}IgD^{lo}CD20^{lo}CD38^{+}CXCR5^{lo}CD71^{+}$) were sorted using a Bigfoot (Invitrogen) into PBS supplemented with 0.05% BSA and immediately processed for scRNA-seq. For bulk sorting germinal centre and LNPC, lymph node FNA samples collected 2 or 8 weeks post-boost were stained for 30 min on ice with purified CD16 (3G8, BioLegend, 1:100), CD32 (FUN-2, BioLegend, 1:100), CD64 (10.1, BioLegend, 1:100) and PD-1–BB515 (EH12.1, BD Horizon, 1:100) in P2, washed twice, then stained for 30 min on ice with CD20–Pacific Blue (2H7, 1:400), CD19–BV750

(HIB19, 1:100), IgD–PerCP–Cy5.5 (IA6-2, 1:200), CD71–PE (CY1G4, 1:400), CXCR5–PE–Dazzle 594 (J252D4, 1:50), CD38–PE–Cy7 (HIT2, 1:200), CD4–A700 (SK3, 1:400) and Zombie Aqua (all BioLegend) diluted in P2. Cells were washed twice, and total germinal centre B cells (live singlet $CD4^{-}CD19^{+}IgD^{lo}CD20^{+}CD38^{int}CXCR5^{+}CD71^{+}$) and LNPC (live singlet $CD4^{-}CD19^{+}IgD^{lo}CD20^{lo}CD38^{+}CXCR5^{lo}CD71^{+}$) were sorted using a Bigfoot (Invitrogen) into Buffer RLT Plus (Qiagen) supplemented with 143 mM β-mercaptoethanol (Sigma-Aldrich) and immediately frozen on dry ice. For sorting memory B cells, PBMC collected 17 weeks post-boost were incubated for 10 min on ice with purified CD16 (3G8, BioLegend, 1:100), CD32 (FUN-2, BioLegend, 1:100), and CD64 (10.1, BioLegend, 1:100) in P2. For sorting S^{+} memory B cells, WA1/2020, B.1.351, B.1.617.2 and BA.1 spike probes pre-conjugated to SA–BV650 and SA–PE, biotin-saturated SA–PE–Cy5, CD20–Pacific Blue (2H7, 1:400), CD19–BV605 (HIB19, 1:100), IgD–BV785 (IA6-2, 1:200), CD3–FITC (HIT3a, 1:200), CD27–A700 (M-T271, 1:200) and Zombie NIR (all BioLegend) diluted in Brilliant Staining buffer (BD Horizon) were added and stained for an additional 30 min on ice. For sorting $BA.1^{+}$ $WA1/2020^{-}$ memory B cells, WA1/2020 probes pre-conjugated to SA–BV650 and SA–APC, BA.1 probes pre-conjugated to SA–BV421 and SA–PE, biotin-saturated SA–PE–Cy5, CD20–Pacific Blue (2H7, 1:400), IgD–BV785 (IA6-2, 1:200), CD19–FITC (HIB19, 1:100), CD27–PE–Fire810 (O323, 1:200), CD3–A700 (HIT3a, 1:100) and Zombie NIR (all BioLegend) diluted in Brilliant Staining buffer (BD Horizon) were added and stained for an additional 30 min on ice. Cells were washed twice, and pooled S-binding single memory B cells (live singlet $CD3^{-}CD19^{+}IgD^{lo}$SA–PE–$Cy5^{-}$ pooled spikes double positive) or $BA.1^{+}$ $WA1/2020^{-}$ single memory B cells (live singlet $CD3^{-}CD19^{+}IgD^{lo}$SA–PE-$Cy5^{-}$ $BA.1^{+}$ $WA1/2020^{-}$) were sorted using a Bigfoot (Invitrogen) into 96-well plates containing 2 μl Lysis Buffer (Clontech) supplemented with 1 U μl^{-1} RNase inhibitor (NEB), or total IgD^{lo} memory B cells were bulk sorted into Buffer RLT Plus (Qiagen) supplemented with 143 mM β-mercaptoethanol (Sigma-Aldrich) and immediately frozen on dry ice.

Monoclonal antibody generation

Antibodies were cloned as described previously[52]. In brief, VH, Vκ and Vλ genes were amplified by PCR with reverse transcription and nested PCR reactions from singly-sorted S^+ memory B cells using primer combinations specific for IgG, IgM/A, Igκ and Igλ from previously described primer sets[53] and then sequenced. To generate recombinant antibodies, restriction sites were incorporated via PCR with primers to the corresponding heavy and light chain V and J genes. The amplified VH, Vκ and Vλ genes were cloned into IgG1 and Igκ or Igλ expression vectors, respectively, as described previously[53,54,55]. Heavy and light chain plasmids were co-transfected into Expi293F cells (Gibco) for expression, and antibody was purified using protein A agarose chromatography (Goldbio). Sequences were obtained from PCR reaction products and annotated using the ImMunoGeneTics (IMGT)/V-QUEST database (http://www.imgt.org/IMGT_vquest/)[56,57]. Mutation frequency was calculated by counting the number of nonsynonymous nucleotide mismatches from the germline sequence in the heavy chain variable segment leading up to the CDR3, while excluding the 5′ primer sequences that could be error-prone.

scRNA-seq library preparation and sequencing

Sorted plasmablast and lymph node FNA samples were processed using the following 10x Genomics kits: Chromium Next GEM Single Cell 5′ Kit v2 (PN-1000263); Chromium Next GEM Chip K Single Cell Kit (PN-1000286); BCR Amplification Kit (PN-1000253); Dual Index Kit TT Set A (PN-1000215). Chromium Single Cell 5′ Gene Expression Dual Index libraries and Chromium Single Cell V(D)J Dual Index libraries were prepared according to manufacturer’s instructions. Both gene expression and V(D)J libraries were sequenced on a Novaseq S4 (Illumina), targeting a median sequencing depth of 50,000 and 5,000 read pairs per cell, respectively.

Bulk BCR library preparation and sequencing

RNA was purified from sorted plasmablasts and memory B cells from PBMC, germinal centre B cells and plasma cells from lymph node FNA (LNPC), and CD138-enriched BMPC using the RNeasy Plus Micro kit (Qiagen). Reverse transcription, unique molecular identifier (UMI)

barcoding, cDNA amplification, and Illumina linker addition to B cell heavy chain transcripts were performed using the human NEBNext Immune Sequencing Kit (New England Biolabs) according to the manufacturer's instructions. High-throughput 2× 300 bp paired-end sequencing was performed on the Illumina MiSeq platform with a 30% PhiX spike-in according to manufacturer's recommendations, except for performing 325 cycles for read 1 and 275 cycles for read 2.

Preprocessing of bulk sequencing BCR reads

Preprocessing of demultiplexed pair-end reads was performed using pRESTO v.0.6.2[58] as previously described[2], with the exception that sequencing errors were corrected using the UMIs as they were without additional clustering (Extended Data Table 3). Previously preprocessed unique consensus sequences from samples corresponding to participants in the current study and previously reported in ref. [29] were included without additional processing. Participants 382-01, 382-02, 382-07, 382-08, 382-13, and 382-15 correspond to previously reported 368-22, 368-20, 368-02a, 368-04, 368-01a and 368-10, respectively[2,29]. Previously preprocessed unique consensus sequences from samples corresponding to participants in the current study and reported in[2] were subset to those with at least two contributing reads and included.

Preprocessing of 10x Genomics single-cell BCR reads

Demultiplexed pair-end FASTQ reads were preprocessed using Cell Ranger v.6.0.1 as previously described[29] (Extended Data Table 4). Previously preprocessed single-cell BCR reads from samples corresponding to participants in the current study and reported in ref. [29] were included.

V(D)J gene annotation and genotyping

Initial germline V(D)J gene annotation was performed on the preprocessed BCRs using IgBLAST v.1.17.1[59] with the deduplicated version of IMGT/V-QUEST reference directory release 202113-2[56]. Further sequence-level and cell-level quality controls were performed as previously described[29].

Exceptions for monoclonal antibody sequences triggering QC filters were handled on a case-by-case basis upon inspection as follows. Indels detected in 382-01 1B04 heavy chain and 1F01 light chain and 382-53 2G07 heavy chain were accepted. The CDR3 annotations from IMGT/V-QUEST for 382-08 1G04 heavy chain, 382-54 1D09 heavy chain and 382-55 4H10 light chain were used in lieu of those from IgBLAST as the former had nucleotide lengths that were a multiple of 3 whereas the latter did not. Individualized genotypes were inferred based on sequences that passed all quality controls using TIgGER v.1.0.0[60] and used to finalize V(D)J annotations. Sequences annotated as non-productively rearranged by IgBLAST were removed from further analysis.

Clonal lineage inference

B cell clonal lineages were inferred on a by-individual basis based on productively rearranged sequences as previously described[29]. In brief, heavy chain-based clonal inference[31] was performed by partitioning the heavy chains of bulk and single-cell BCRs based on common V and J gene annotations and CDR3 lengths, and clustering the sequences within each partition hierarchically with single linkage based on their CDR3s[30]. Sequences whose CDR3 nucleotides were within 0.15 normalized Hamming distance from each other were clustered as clones. Following clonal inference, full-length clonal consensus germline sequences were reconstructed using Change-O v.1.0.2[61]. Within each clone, duplicate IMGT-aligned V(D)J sequences from bulk sequencing were collapsed using Alakazam v1.1.0[61] except for duplicates derived from different lymph nodes, time points, tissues, B cell compartments, isotypes, or biological replicates.

BCR analysis

B cell compartment labels were treated as previously described[29]. In brief, gene expression-based cluster annotation was used for single-cell BCRs; FACS-based sorting and magnetic enrichment were used for bulk BCRs, except that plasmablast sorts from lymph node FNA were labelled LNPCs; post-second dose week 2 IgD^{lo} enriched B cells from blood were labelled

activated; and post-second dose week 4 and post-third dose (booster) week 17 IgD^{lo} enriched B cells from blood were labelled memory. For analysis involving the memory compartment, the memory sequences were restricted to those from blood. A heavy chain-based B cell clone was considered S-specific if it contained any sequence corresponding to a S-binding monoclonal antibody that was previously reported[2,29] or from the current study. Clonal overlap between B cell compartments was visualized using circlize v.0.4.13[62]. SHM frequency was calculated for each heavy chain sequence using SHazaM v.1.0.2[61] as previously described[29] by counting the number of nucleotide mismatches from the germline sequence in the variable segment leading up to the CDR3, while excluding the first 18 positions that could be error-prone due to the primers used for generating the monoclonal antibody sequences.

Processing of 10x Genomics single-cell 5′ gene expression data

Demultiplexed pair-end FASTQ reads were first preprocessed on a by-sample basis and samples were subsequently subsampled to the same effective sequencing length and aggregated using Cell Ranger v.6.0.1 as previously described[29]. Quality control was performed on the aggregate gene expression matrix consisting of 336,960 cells and 36,601 features using SCANPY v.1.7.2[63]. In brief, to remove presumably lysed cells, cells with mitochondrial content greater than 17.5% of all transcripts were removed. To remove likely doublets, cells with more than 8,000 features or 80,000 total UMIs were removed. To remove cells with no detectable expression of common endogenous genes, cells with no transcript for any of a list of 34 housekeeping genes[29] were removed. The feature matrix was subset, based on their biotypes, to protein-coding, immunoglobulin, and T cell receptor genes that were expressed in at least 0.05% of the cells in any sample. The resultant feature matrix contained 15,751 genes. Finally, cells with detectable expression of fewer than 200 genes were removed. After quality control, there were a total of 312,242 cells from 39 single-cell samples (Extended Data Table 4).

Single-cell gene expression analysis

Transcriptomic data was analysed using SCANPY v.1.7.2[63] as previously described[29] with minor adjustments suitable for the current data. In brief, overall clusters were first identified using Leiden graph-clustering with resolution 0.50 (Extended Data Fig. 3b, Extended Data Table 5). UMAPs were faceted by participant and inspected for convergence to assess whether there was a need for integration (Extended Data Fig. 3c). Cluster identities were assigned by examining the expression of a set of marker genes[34] for different cell types (Extended Data Fig. 3d). To remove potential contamination by platelets, 205 cells with a log-normalized expression value of >2.5 for PPBP were removed. From a cluster consisting primarily of monocytes, 36 cells originating from lymph node FNA and with a log-normalized expression value of >0 for at least two of FDCSP, CXCL14[64], and FCAMR[65] were annotated FDCs. Cells from the overall B cell cluster were further clustered to identify B cell subsets using Leiden graph-clustering resolution 0.35 (Extended Data Fig. 3e and Extended Data Table 5). Cluster identities were assigned by examining the expression of a set of marker genes[34] for different B cell subsets (Extended Data Fig. 3f) along with the availability of BCRs. Despite being clustered with B cells during overall clustering, one group tended to have both BCRs and relatively high expression levels of CD2 and CD3E; one group tended to have no BCRs and relatively high CD2 and CD3E; and two unassigned groups tended to have no BCRs. These were excluded from the final B cell clustering. Ten cells that were found in the germinal centre B cell cluster but came from blood were labelled 'PB-like'[34]. Four-hundred and seven cells that were found in the PB cluster but came from lymph node FNA were re-assigned as LNPCs. One cell that was found in the LNPC cluster but came from blood was re-assigned as PB. Heavy chain SHM frequency and isotype usage of the B cell subsets were inspected for consistency with expected values to further confirm their assigned identities.

Reporting summary

Further information on research design is available in the Nature Portfolio Reporting Summary linked to this article.

Data availability

Antibody sequences have been deposited in GenBank under accession numbers OQ634308–OQ635939. Newly reported raw sequencing data and the transcriptomics count matrix are deposited at the Sequence Read Archive and Gene Expression Omnibus under BioProject PRJNA800176. Processed transcriptomics and BCR data are deposited at Zenodo (https://doi.org/10.5281/zenodo.7719030). Previously reported BCR data used in this study were deposited under BioProjects PRJNA731610, PRJNA741267 and PRJNA777934. The IMGT/V-QUEST database is accessible at http://www.imgt.org/IMGT_vquest/. Materials are available upon request through an interinstitutional materials transfer agreement.

References

1. Krause, P. R. et al. SARS-CoV-2 variants and vaccines. *N. Engl. J. Med.* **385**, 179–186 (2021).

2. Turner, J. S. et al. SARS-CoV-2 mRNA vaccines induce persistent human germinal centre responses. *Nature* **596**, 109–113 (2021).

3. Laidlaw, B. J. & Ellebedy, A. H. The germinal centre B cell response to SARS-CoV-2. *Nat. Rev. Immunol.* **22**, 7–18 (2022).

4. Amanat, F. et al. SARS-CoV-2 mRNA vaccination induces functionally diverse antibodies to NTD, RBD, and S2. *Cell* **184**, 3936–3948.e10 (2021).

5. Muecksch, F. et al. Increased memory B cell potency and breadth after a SARS-CoV-2 mRNA boost. *Nature* **607**, 128–134 (2022).

6. Goel, R. R. et al. Efficient recall of Omicron-reactive B cell memory after a third dose of SARS-CoV-2 mRNA vaccine. *Cell* **185**, 1875–1887.e8 (2022).

7. Rodda, L. B. et al. Imprinted SARS-CoV-2-specific memory lymphocytes define hybrid immunity. *Cell* **185**, 1588–1601.e14 (2022).

8. Pérez-Then, E. et al. Neutralizing antibodies against the SARS-CoV-2 Delta and Omicron variants following heterologous CoronaVac plus

BNT162b2 booster vaccination. *Nat. Med.* **28**, 481–485 (2022).

9. Sette, A. & Crotty, S. Immunological memory to SARS-CoV-2 infection and COVID-19 vaccines. *Immunol. Rev.* **310**, 27–46 (2022).

10. Lucas, C. et al. Impact of circulating SARS-CoV-2 variants on mRNA vaccine-induced immunity. *Nature* **600**, 523–529 (2021).

11. Wang, Z. et al. mRNA vaccine-elicited antibodies to SARS-CoV-2 and circulating variants. *Nature* **592**, 616–622 (2021).

12. Andrews, N. et al. Covid-19 vaccine effectiveness against the Omicron (B.1.1.529) variant. *N. Engl. J. Med.* **386**, 1532–1546 (2022).

13. Kuhlmann, C. et al. Breakthrough infections with SARS-CoV-2 omicron despite mRNA vaccine booster dose. *Lancet* **399**, 625–626 (2022).

14. Schmidt, F. et al. Plasma neutralization of the SARS-CoV-2 omicron variant. *N. Engl. J. Med.* **386**, 599–601 (2022).

15. Cameroni, E. et al. Broadly neutralizing antibodies overcome SARS-CoV-2 Omicron antigenic shift. *Nature* **602**, 664–670 (2022).

16. Cele, S. et al. Omicron extensively but incompletely escapes Pfizer BNT162b2 neutralization. *Nature* **602**, 654–656 (2022).

17. Falsey, A. R. et al. SARS-CoV-2 Neutralization with BNT162b2 vaccine dose 3. *N. Engl. J. Med.* **385**, 1627–1629 (2021).

18. Bowen, J. E. et al. Omicron spike function and neutralizing activity elicited by a comprehensive panel of vaccines. *Science* **377**, 890–894 (2022).

19. Muik, A. et al. Neutralization of SARS-CoV-2 Omicron by BNT162b2 mRNA vaccine–elicited human sera. *Science* **375**, 678–680 (2022).

20. Moreira, E. D. et al. Safety and efficacy of a third dose of BNT162b2 Covid-19 vaccine. *N. Engl. J. Med.* **386**, 1910–1921 (2022).

21. Barda, N. et al. Effectiveness of a third dose of the BNT162b2 mRNA COVID-19 vaccine for preventing severe outcomes in Israel: an observational study. *Lancet* **398**, 2093–2100 (2021).

22. Chalkias, S. et al. Safety, immunogenicity and antibody persistence of a bivalent Beta-containing booster vaccine against COVID-19: a phase 2/3 trial. *Nat. Med.* **28**, 2388–2397 (2022).

23. Scheaffer, S. M. et al. Bivalent SARS-CoV-2 mRNA vaccines increase breadth of neutralization and protect against the BA.5 Omicron variant in mice. *Nat. Med.* **29**, 247–257 (2023).

24. Jackson, L. A. et al. An mRNA vaccine against SARS-CoV-2—preliminary report. *N. Engl. J. Med.* **383**, 1920–1931 (2020).

25. Walsh, E. E. et al. Safety and immunogenicity of two RNA-based Covid-19 vaccine candidates. *N. Engl. J. Med.* **383**, 2439–2450 (2020).

26. Purtha, W. E., Tedder, T. F., Johnson, S., Bhattacharya, D. & Diamond, M. S. Memory B cells, but not long-lived plasma cells, possess antigen specificities for viral escape mutants. *J. Exp. Med.* **208**, 2599–2606 (2011).

27. Lederer, K. et al. Germinal center responses to SARS-CoV-2 mRNA vaccines in healthy and immunocompromised individuals. *Cell* **185**, 1008–1024.e15 (2022).

28. Röltgen, K. et al. Immune imprinting, breadth of variant recognition, and germinal center response in human SARS-CoV-2 infection and vaccination. *Cell* **185**, 1025–1040.e14 (2022).

29. Kim, W. et al. Germinal centre-driven maturation of B cell response to mRNA vaccination. *Nature* **604**, 141–145 (2022).

30. Gupta, N. T. et al. Hierarchical clustering can identify B cell clones with high confidence in Ig repertoire sequencing data. *J. Immunol.* **198**, 2489–2499 (2017).

31. Zhou, J. Q. & Kleinstein, S. H. Cutting edge: Ig H chains are sufficient to determine most B cell clonal relationships. *J. Immunol.* **203**, 1687–1692 (2019).

32. Case, J. B. et al. Neutralizing antibody and soluble ACE2 inhibition of a replication-competent VSV-SARS-CoV-2 and a clinical isolate of SARS-CoV-2. *Cell Host Microbe* **28**, 475–485.e5 (2020).

33. Liu, Z. et al. Identification of SARS-CoV-2 spike mutations that attenuate monoclonal and serum antibody neutralization. *Cell Host Microbe* **29**, 477–488.e4 (2021).

34. Turner, J. S. et al. Human germinal centres engage memory and naive B cells after influenza vaccination. *Nature* **586**, 127–132 (2020).

35. Turner, J. S. et al. SARS-CoV-2 infection induces long-lived bone marrow plasma cells in humans. *Nature* **595**, 421–425 (2021).

36. Radbruch, A. et al. Competence and competition: the challenge of becoming a long-lived plasma cell. *Nat. Rev. Immunol.* **6**, 741–750 (2006).

37. Weisel, F. J., Zuccarino-Catania, G. V., Chikina, M. & Shlomchik, M. J. A temporal switch in the germinal center determines differential output of memory B and plasma cells. *Immunity* **44**, 116–130 (2016).

38. Ellebedy, A. H. et al. Adjuvanted H5N1 influenza vaccine enhances both cross-reactive memory B cell and strain-specific naive B cell responses in humans. *Proc. Natl Acad. Sci. USA* **117**, 17957–17964 (2020).

39. Zost, S. J. et al. Potently neutralizing and protective human antibodies against SARS-CoV-2. *Nature* **584**, 443–449 (2020).

40. Chen, P. et al. SARS-CoV-2 neutralizing antibody LY-CoV555 in outpatients with COVID-19. *N. Engl. J. Med.* **384**, 229–237 (2021).

41. Hansen, J. et al. Studies in humanized mice and convalescent humans yield a SARS-CoV-2 antibody cocktail. *Science* **369**, 1010–1014

(2020).

42. Alsoussi, W. B. et al. A potently neutralizing antibody protects mice against SARS-CoV-2 infection. *J. Immunol.* **205**, 915–922 (2020).

43. Chen, R. E. et al. In vivo monoclonal antibody efficacy against SARS-CoV-2 variant strains. *Nature* **596**, 103–108 (2021).

44. Francis, T. On the doctrine of original antigenic sin. *Proc. Am. Philos. Soc.* **104**, 572–578 (1953).

45. Gostic, K. M., Ambrose, M., Worobey, M. & Lloyd-Smith, J. O. Potent protection against H5N1 and H7N9 influenza via childhood hemagglutinin imprinting. *Science* **354**, 722–726 (2016).

46. Zang, R. et al. TMPRSS2 and TMPRSS4 promote SARS-CoV-2 infection of human small intestinal enterocytes. *Sci. Immunol.* **5**, eabc3582 (2020).

47. Stadlbauer, D. et al. SARS-CoV-2 seroconversion in humans: a detailed protocol for a serological assay, antigen production, and test setup. *Curr. Protoc. Microbiol.* **57**, e100 (2020).

48. Fairhead, M. & Howarth, M. Site-specific biotinylation of purified proteins using BirA. *Methods Mol. Biol.* **1266**, 171–184 (2015).

49. Chen, R. E. et al. Resistance of SARS-CoV-2 variants to neutralization by monoclonal and serum-derived polyclonal antibodies. *Nat. Med.* **27**, 717–726 (2021).

50. VanBlargan, L. A. et al. A potently neutralizing SARS-CoV-2 antibody inhibits variants of concern by utilizing unique binding residues in a highly conserved epitope. *Immunity* **54**, 2399–2416.e6 (2021).

51. Mudd, P. A. et al. SARS-CoV-2 mRNA vaccination elicits a robust and persistent T follicular helper cell response in humans. *Cell* **185**, 603–613.e15 (2022).

52. Wrammert, J. et al. Broadly cross-reactive antibodies dominate the human B cell response against 2009 pandemic H1N1 influenza virus infection. *J. Exp. Med.* **208**, 181–193 (2011).

53. Smith, K. et al. Rapid generation of fully human monoclonal antibodies specific to a vaccinating antigen. *Nat. Protoc.* **4**, 372–384 (2009).

54. Wrammert, J. et al. Rapid cloning of high-affinity human monoclonal antibodies against influenza virus. *Nature* **453**, 667–671 (2008).

55. Nachbagauer, R. et al. Broadly reactive human monoclonal antibodies elicited following pandemic H1N1 influenza virus exposure protect mice against highly pathogenic H5N1 challenge. *J. Virol.* **92**, 1–17 (2018).

56. Brochet, X., Lefranc, M.-P. & Giudicelli, V. IMGT/V-QUEST: the highly customized and integrated system for IG and TR standardized V-J and V-D-J sequence analysis. *Nucleic Acids Res.* **36**, W503–W508 (2008).

57. Giudicelli, V., Brochet, X. & Lefranc, M.-P. IMGT/V-QUEST: IMGT standardized analysis of the immunoglobulin (IG) and T cell receptor (TR) nucleotide sequences. *Cold Spring Harb. Protoc.* **2011**, pdb.prot5633 (2011).

58. Vander Heiden, J. A. et al. pRESTO: a toolkit for processing high-throughput sequencing raw reads of lymphocyte receptor repertoires. *Bioinformatics* **30**, 1930–1932 (2014).

59. Ye, J., Ma, N., Madden, T. L. & Ostell, J. M. IgBLAST: an immunoglobulin variable domain sequence analysis tool. *Nucleic Acids Res.* **41**, W34–W40 (2013).

60. Gadala-Maria, D., Yaari, G., Uduman, M. & Kleinstein, S. H. Automated analysis of high-throughput B-cell sequencing data reveals a high frequency of novel immunoglobulin V gene segment alleles. *Proc. Natl Acad. Sci. USA* **112**, E862–E870 (2015).

61. Gupta, N. T. et al. Change-O: a toolkit for analyzing large-scale B cell immunoglobulin repertoire sequencing data. *Bioinformatics* **31**, 3356–3358 (2015).

62. Gu, Z., Gu, L., Eils, R., Schlesner, M. & Brors, B. circlize implements and enhances circular visualization in R. *Bioinformatics* **30**, 2811–2812 (2014).

63. Wolf, F. A., Angerer, P. & Theis, F. J. SCANPY: large-scale single-cell gene expression data analysis. *Genome Biol.* **19**, 15 (2018).

64. Haebe, S. et al. Single-cell analysis can define distinct evolution of tumor sites in follicular lymphoma. *Blood* **137**, 2869–2880 (2021).

65. Mourcin, F. et al. Follicular lymphoma triggers phenotypic and functional remodeling of the human lymphoid stromal cell landscape. *Immunity* **54**, 1788–1806.e7 (2021).

Acknowledgements

The authors thank all the donors for generously providing precious specimens; L. Kessels and the Washington University School of Medicine 382 Study Team (study coordinators A. Haile, R. Thompson, D. Carani, K. Gray and C. Ayres; pharmacists M. Royal and J. Tran; and laboratory technicians L. Blair, A. Afghanzada and N. Schodl) for assistance with scheduling participants and sample collection; P. Woodard, B. Thomas, M. Harrod, R. Hamlin, M. Rohn; the staff of the Center for Clinical Research Imaging at Washington University School of Medicine for assistance with sample collection; and C. Dalton and B. Roemmich for performing the nucleocapsid binding assay. The WU382 study was reviewed and approved by the Washington University Institutional Review Board (approval no. 202109021). This work was supported in part with funding from the US National Institutes of Health (NIH) and Moderna. The Ellebedy laboratory was supported by NIH grants U01AI141990, 1U01AI150747, 5U01AI144616-02 and R01AI168178-01. The Diamond laboratory was supported by NIH grant R01 AI157155. The Whelan laboratory was supported by NIH grant R01 AI163019. The content of this manuscript is

solely the responsibility of the authors and does not necessarily represent the official view of NIAID or NIH.

Author information

Author notes

1. These authors contributed equally: Wafaa B. Alsoussi, Sameer Kumar Malladi

Authors and Affiliations

1. Department of Pathology and Immunology, Washington University School of Medicine, St Louis, MO, USA

   Wafaa B. Alsoussi, Sameer Kumar Malladi, Julian Q. Zhou, Baoling Ying, Wooseob Kim, Aaron J. Schmitz, Tingting Lei, Stephen C. Horvath, Alexandria J. Sturtz, Katherine M. McIntire, Birk Evavold, Suzanne M. Scheaffer, Isabella F. Fox, Senaa F. Mirza, Christopher W. Farnsworth, Michael S. Diamond, Jackson S. Turner & Ali H. Ellebedy

2. Department of Molecular Microbiology, Washington University School of Medicine, St Louis, MO, USA

   Zhuoming Liu, Baoling Ying, Suzanne M. Scheaffer, Sean P. J. Whelan & Michael S. Diamond

3. Department of Emergency Medicine, Washington University School of Medicine, St Louis, MO, USA

   Fangjie Han

4. Division of Infectious Diseases, Department of Internal Medicine, Washington University School of Medicine, St Louis, MO, USA

   Luis Parra-Rodriguez, Michael S. Diamond, Jane A. O’Halloran & Rachel M. Presti

5. Moderna, Cambridge, MA, USA

Raffael Nachbagauer, Biliana Nestorova, Spyros Chalkias & Robert Paris

6. Infectious Disease Clinical Research Unit, Washington University School of Medicine, St Louis, MO, USA

Michael K. Klebert, Jane A. O’Halloran & Rachel M. Presti

7. Division of Oncology, Department of Medicine, Washington University School of Medicine, St Louis, MO, USA

Iskra Pusic

8. Mallinckrodt Institute of Radiology, Washington University School of Medicine, St Louis, MO, USA

Benjamin S. Strnad, William D. Middleton & Sharlene A. Teefey

9. Center for Vaccines and Immunity to Microbial Pathogens, Washington University School of Medicine, St Louis, MO, USA

Michael S. Diamond, Rachel M. Presti & Ali H. Ellebedy

10. The Andrew M. and Jane M. Bursky Center for Human Immunology and Immunotherapy Programs, Washington University School of Medicine, St Louis, MO, USA

Michael S. Diamond, Rachel M. Presti & Ali H. Ellebedy

Contributions

A.H.E., J.A.O., R.M.P., R.P., B.N. and S.C. conceived and designed the study. J.A.O., M.K.K. and R.M.P. wrote and maintained the IRB protocol, recruited participants and coordinated sample collection. W.B.A., W.K., F.H. and J.S.T. processed specimens. W.B.A., S.K.M., S.F.M. and J.S.T. performed multiplex bead array and ELISA. W.B.A., F.H. and J.S.T. performed ELISpot. W.B.A., S.K.M. and S.M. performed VSV

neutralization assays. W.B.A., S.K.M., W.K., A. J. Schmitz, T.L., S.C.H., A. J. Sturtz, K.M.M., B.E., I.F.F. and J.S.T. generated and characterized monoclonal antibodies. J.Q.Z. analysed scRNA-seq and BCR repertoire data. Z.L. rescued and produced the chimeric vesicular stomatitis viruses for neutralization assays and performed and analysed epitope mapping. B.Y. performed the SARS-CoV-2 virus neutralization assays. W.K. and A. J. Sturtz prepared libraries for scRNA-seq. A. J. Schmitz performed RNA extractions and library preparation for BCR bulk sequencing and expressed SARS-CoV-2 S and variant proteins. S.M.S. generated the authentic SARS-CoV-2 virus stocks. C.W.F. supervised the nucleocapsid binding assay. I.P. supervised bone marrow specimen collection. B.S.S. and W.D.M. performed FNA. B.S.S., W.D.M. and S.A.T. supervised lymph node evaluation prior to FNA and specimen collection and evaluated lymph node ultrasound data. J.S.T. sorted cells and collected and analysed the flow cytometry data. L.P.-R., R.P., R.N., J.S.T. and A.H.E. analysed data. A.H.E., M.S.D. and S.P.J.W. supervised experiments and obtained funding. J.S.T. and A.H.E. composed the manuscript. All authors reviewed and edited the manuscript.

Corresponding authors

Correspondence to Jackson S. Turner or Ali H. Ellebedy.

Ethics declarations

Competing interests

The Ellebedy laboratory and Infectious Disease Clinical Research Unit has received funding under sponsored research agreements from Moderna related to the data presented in the current study. The Ellebedy laboratory received funding from Emergent BioSolutions and AbbVie that are unrelated to the data presented in the current study. A.H.E. has received consulting and speaking fees from InBios International, Fimbrion Therapeutics, RGAX, Mubadala Investment Company, Moderna, Pfizer, GSK, Danaher, Third Rock Ventures, Goldman Sachs and Morgan Stanley and is the founder of ImmuneBio Consulting. W.B.A., A. J. Schmitz, S.P.J.W., M.S.D., J.S.T. and A.H.E. are recipients of a licensing agreement with Abbvie that is unrelated to the data presented in the current study. M.S.D. is a consultant for Inbios,

Vir Biotechnology, Senda Biosciences, Moderna, Sterne-Kessler and Immunome. The Diamond laboratory has received unrelated funding support in sponsored research agreements from Vir Biotechnology, Emergent BioSolutions and Moderna. S.P.J.W. is a consultant for Thylacine Bio. S.P.J.W. is a recipient of a licensing agreement with Vir Biotechnology and Merck. The Whelan laboratory has received unrelated funding support in sponsored research agreements from Vir Biotechnology. R.P., B.N., S.C. and R.N. are employees of and shareholders in Moderna. The other authors declare no competing interests.

Peer review

Peer review information

Nature thanks Sophie Valkenburg and the other, anonymous, reviewer(s) for their contribution to the peer review of this work. Peer review reports are available.

Additional information

Publisher's note Springer Nature remains neutral with regard to jurisdictional claims in published maps and institutional affiliations.

Extended data figures and tables

Extended Data Fig. 1 Robust GC and Tfh responses to mRNA-1273 and mRNA-1273.213 boosters.

(**a**) Frequencies of IgA plasmablasts specific for the indicated antigens measured by ELISpot in week-1 PBMC from participants who received mRNA-1273 (left) and mRNA-1273.213 (right). (**b**) Flow cytometry plots of influenza B/HA-specific mAb 321-05 6F05[34], cross-reactive mAb 382-08 1C11, and residue E484-specific mAb mu 2B04[42] binding to indicated strains of SARS-CoV-2 S by multiplex bead binding array. (**c**) Plasma IgG binding to indicated strains of SARS-CoV-2 S measured by multiplex bead

binding array in participants who received mRNA-1273 (left) and mRNA-1273.213 (right). (**d**) Gating strategy for analyzing S^+ germinal centre B cells and T follicular helper cells (T_{FH}) in FNA. (**e**) Frequencies of T_{FH} from FNA of draining lymph nodes. (**f**) Correlation between frequencies of S^+ germinal centre B cells and T_{FH}. *P* and *r* values from two-sided Spearman test. (**g**) Representative ELISpot wells coated with BSA, and developed in blue (IgG) and red (IgA) after plating the indicated numbers of BMPCs. (**h**) Frequencies of IgA-secreting BMPCs specific for the indicated antigens 26 weeks post-boost. Black lines indicate medians. Symbols at each time point represent one sample. For mRNA-1273 and mRNA-1273.213 respectively, $n = 7$ and 38 (a), $n = 6$ and 28 (c), $n = 5$ and 20 (e), $n = 3$ and 10 (h).

Extended Data Fig. 2 Breadth of MBC-derived mAbs after mRNA-1273 and mRNA-1273.213 boosters.

(**a**) Gating strategy for sorting S^+ MBC from PBMC.

Extended Data Fig. 3 Maturation of S-specific MBCs in response to mRNA-1273 or mRNA-1273.213 booster.

(**a**) Gating strategy for sorting plasmablasts from PBMC. (**b**,**c**,**e**,**g**) UMAPs showing scRNA-seq transcriptional clusters of total cells (b,c) or B cells (e,g) from all participants (b,e) or from each participant separately (c,g). (**d**,**f**) Dot plots for the marker genes used for identifying the annotated clusters in (b,c) (d) and in (e,g) (f). (**h**) SARS-CoV-2 S-specific clones visualized in red on UMAPs of B cells from each participant separately and faceted by time point. (**i**) Clonal overlap between S-binding plasmablasts and germinal centre B cells at indicated time points. Arc length corresponds to the number of BCR sequences and chord width corresponds to clone size. Purple chords correspond to clones spanning both compartments. Percentages are of germinal centre B cell clones related to plasmablasts at each time point. (**j**) Percentages of S-specific germinal centre clones related to week 1 plasmablasts. Symbols at each time point represent one sample, $n = 3$ for mRNA-1273 and $n = 3$ for mRNA-1273.213.

Extended Data Fig. 4 Characterization of BA.1-specific mAbs.

(**a**) Study design for mRNA-1273.529 vaccine cohort. Three and five healthy adult volunteers were enrolled and received an mRNA-1273.529 booster as a third or fourth dose, respectively. Blood was collected at baseline and at 1 and 17 weeks post-boost. (**b**) Frequencies of S-binding IgA-producing plasmablasts in PBMC 1 week post-boost measured by ELISpot in participants who received mRNA-1273.529. Black lines indicate medians. Symbols represent one sample; $n = 7$. (**c**) Neutralizing activity of mAbs from week 17 S^+ MBCs against chimeric vesicular stomatitis virus in which the native envelope glycoprotein was replaced with S from WA1/2020 (with D614G mutation). Each symbol represents one mAb, $n = 205$ for mRNA-1273, $n = 222$ for mRNA-1273.213, and $n = 303$ for mRNA-1273.529. Percentages are of mAbs above the 80% infection reduction threshold. (**d**) Binding of mAbs to constituent domains of BA.1 S by ELISA performed in duplicate, presented as mean OD_{490} values. S2-specific mAb 368-22 1B08 was described previously[2]. (**e**) Titration of mAbs to determine neutralizing concentrations against chimeric vesicular stomatitis virus in which the native envelope glycoprotein was replaced with S from SARS-CoV-2 BA.1. Data are representative of two independent experiments. (**f**) Plasmid map for chimeric vesicular stomatitis virus in which the native envelope glycoprotein was replaced with S from BA.1 with primers indicated in purple.

Extended Data Table 1 Study WU382 participant demographics
Extended Data Table 2 Booster (3rd or 4th dose) vaccine side effects[a]
Extended Data Table 3 Processing of BCR reads from bulk-seq
Extended Data Table 4 Processing of BCR and 5’ gene expression data from scRNA-seq. NS=no sorting
Extended Data Table 5 Cell counts and frequencies of overall and B cell transcriptional clusters from scRNA-seq
Extended Data Table 6 Counts of B cells found in S-binding clones and frequencies out of respective B cell transcriptional clusters

Supplementary information

Reporting Summary

Peer Review File

Rights and permissions

Springer Nature or its licensor (e.g. a society or other partner) holds exclusive rights to this article under a publishing agreement with the author(s) or other rightsholder(s); author self-archiving of the accepted manuscript version of this article is solely governed by the terms of such publishing agreement and applicable law.

Reprints and Permissions

About this article

Cite this article

Alsoussi, W.B., Malladi, S.K., Zhou, J.Q. *et al.* SARS-CoV-2 Omicron boosting induces de novo B cell response in humans. *Nature* **617**, 592–598 (2023). https://doi.org/10.1038/s41586-023-06025-4

- Received: 22 September 2022
- Accepted: 28 March 2023
- Published: 03 April 2023
- Issue Date: 18 May 2023
- DOI: https://doi.org/10.1038/s41586-023-06025-4

Share this article

Anyone you share the following link with will be able to read this content:

Get shareable link

Sorry, a shareable link is not currently available for this article.

Copy to clipboard

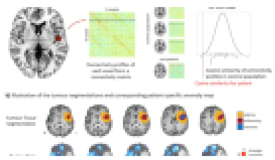
Provided by the Springer Nature SharedIt content-sharing initiative

This article is cited by

- **Evolution of antibody immunity following Omicron BA.1 breakthrough infection**
  - Chengzi I. Kaku
  - Tyler N. Starr
  - Laura M. Walker

  Nature Communications (2023)

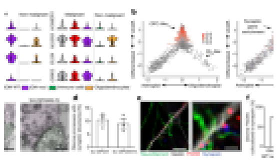
This article was downloaded by **calibre** from https://www.nature.com/articles/s41586-023-06025-4



Distributed changes of the functional connectome in patients with glioblastoma

27 October 2020

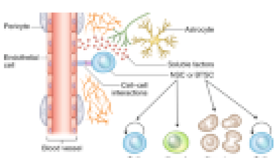
Karl-Heinz Nenning, Julia Furtner, … Georg Langs



Electrical and synaptic integration of glioma into neural circuits

18 September 2019

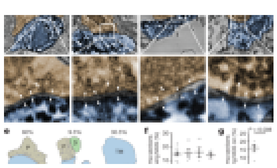
Humsa S. Venkatesh, Wade Morishita, … Michelle Monje



Emerging intersections between neuroscience and glioma biology

12 November 2019

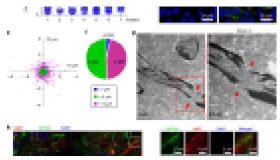
Erik Jung, Julieta Alfonso, … Frank Winkler



[Glutamatergic synaptic input to glioma cells drives brain tumour progression]

18 September 2019

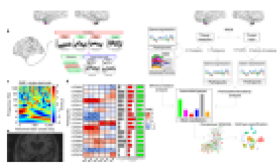
Varun Venkataramani, Dimitar Ivanov Tanev, … Thomas Kuner



[Invasion of white matter tracts by glioma stem cells is regulated by a NOTCH1–SOX2 positive-feedback loop]

17 December 2018

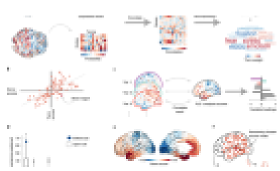
Jun Wang, Sen-Lin Xu, … Shi-Cang Yu



[Gene-expression correlates of the oscillatory signatures supporting human episodic memory encoding]

08 March 2021

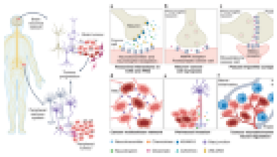
Stefano Berto, Miles R. Fontenot, … Genevieve Konopka



[Mapping gene transcription and neurocognition across human neocortex]

25 March 2021

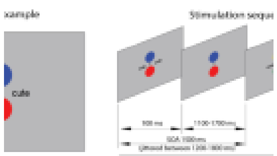
Justine Y. Hansen, Ross D. Markello, … Bratislav Misic



[Insights and opportunities at the crossroads of cancer and neuroscience]

12 September 2022

Chenchen Pan & Frank Winkler



[Formation of neocortical memory circuits for unattended written word forms: neuromagnetic evidence]

25 October 2018

Eino J. Partanen, Alina Leminen, … Yury Shtyrov

- Article
- Open Access
- Published: 03 May 2023

Glioblastoma remodelling of human neural circuits decreases survival

- Saritha Krishna,
- Abrar Choudhury,

- Michael B. Keough,
- Kyounghee Seo,
- Lijun Ni,
- Sofia Kakaizada,
- Anthony Lee,
- Alexander Aabedi,
- Galina Popova,
- Benjamin Lipkin,
- Caroline Cao,
- Cesar Nava Gonzales,
- Rasika Sudharshan,
- Andrew Egladyous,
- Nyle Almeida,
- Yalan Zhang,
- Annette M. Molinaro,
- Humsa S. Venkatesh,
- Andy G. S. Daniel,
- Kiarash Shamardani,
- Jeanette Hyer,
- Edward F. Chang,
- Anne Findlay,
- Joanna J. Phillips,
- Srikantan Nagarajan,
- David R. Raleigh,
- David Brang,
- Michelle Monje &
- …
- Shawn L. Hervey-Jumper

Show authors

Nature **volume 617**, pages 599–607 (2023)

- 28k Accesses
- 1 Citations
- 563 Altmetric

- Metrics details

Abstract

Gliomas synaptically integrate into neural circuits[1,2]. Previous research has demonstrated bidirectional interactions between neurons and glioma cells, with neuronal activity driving glioma growth[1,2,3,4] and gliomas increasing neuronal excitability[2,5,6,7,8]. Here we sought to determine how glioma-induced neuronal changes influence neural circuits underlying cognition and whether these interactions influence patient survival. Using intracranial brain recordings during lexical retrieval language tasks in awake humans together with site-specific tumour tissue biopsies and cell biology experiments, we find that gliomas remodel functional neural circuitry such that task-relevant neural responses activate tumour-infiltrated cortex well beyond the cortical regions that are normally recruited in the healthy brain. Site-directed biopsies from regions within the tumour that exhibit high functional connectivity between the tumour and the rest of the brain are enriched for a glioblastoma subpopulation that exhibits a distinct synaptogenic and neuronotrophic phenotype. Tumour cells from functionally connected regions secrete the synaptogenic factor thrombospondin-1, which contributes to the differential neuron–glioma interactions observed in functionally connected tumour regions compared with tumour regions with less functional connectivity. Pharmacological inhibition of thrombospondin-1 using the FDA-approved drug gabapentin decreases glioblastoma proliferation. The degree of functional connectivity between glioblastoma and the normal brain negatively affects both patient survival and performance in language tasks. These data demonstrate that high-grade gliomas functionally remodel neural circuits in the human brain, which both promotes tumour progression and impairs cognition.

Main

Malignant brain tumours such as glioblastomas exist within the context of complex neural circuitry. Neuronal activity promotes glioma growth through both paracrine signalling (neuroligin-3 and brain-derived neurotrophic factor

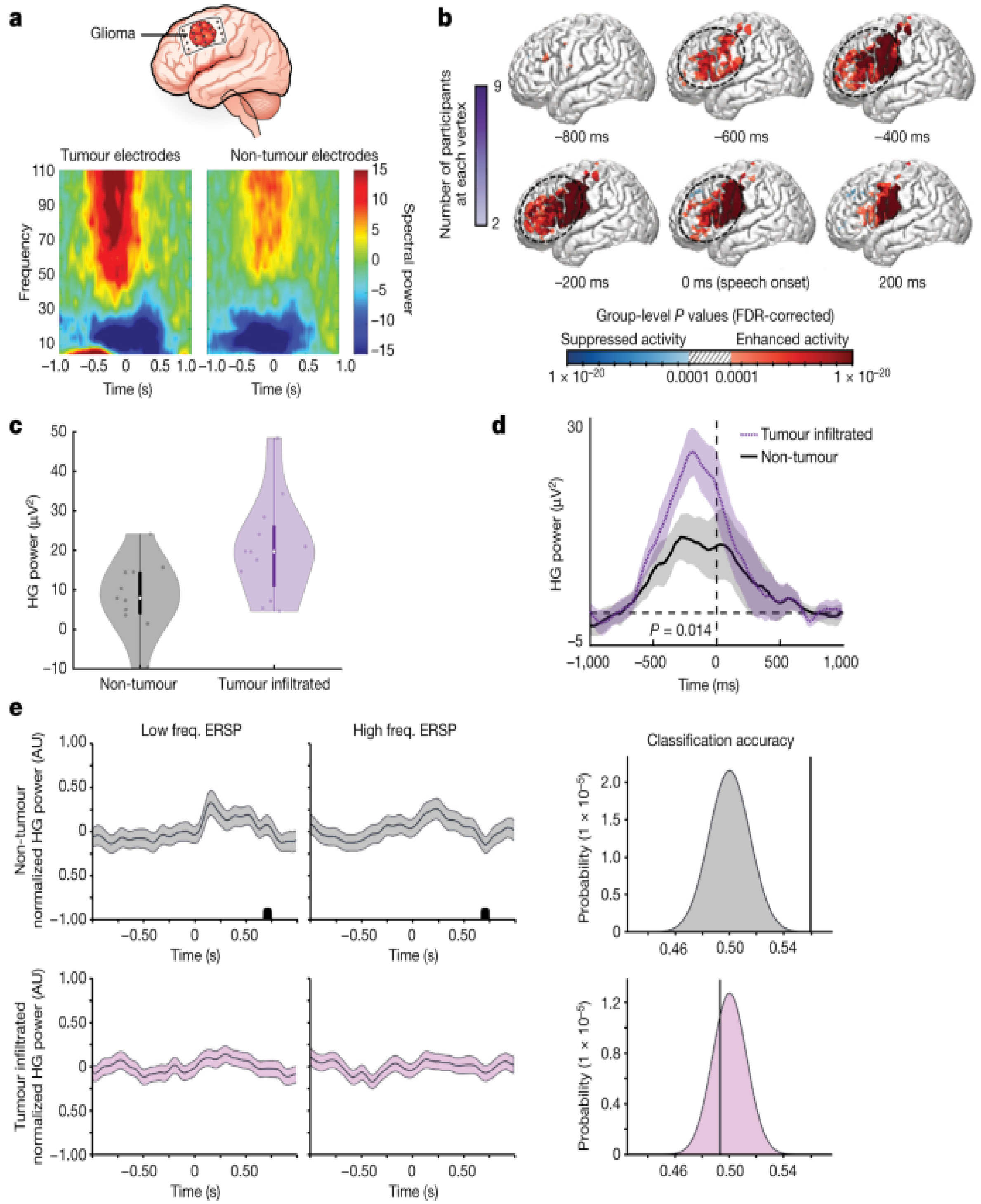
(BDNF)) and AMPAR (α-amino-3-hydroxy-5-methyl-4-isoxazole propionic acid receptor)-mediated excitatory electrochemical synapses[1,2,3,4].

Likewise, glioblastomas influence neurons, inducing neuronal hyperexcitability through the secretion of non-synaptic glutamate and synaptogenic factors[5,6] and reducing inhibitory interneurons[7]. Beyond preclinical models, we previously demonstrated in awake, resting patients that glioblastoma-infiltrated cortex exhibits increased neuronal excitability[2]. The mechanisms by which glioblastomas maintain the ability to engage with neuronal circuitry and alter cortical function remain incompletely understood[9]. Deciphering the processes by which gliomas remodel neural circuits may uncover therapeutic vulnerabilities for these lethal brain cancers. To address these gaps in knowledge, we performed intraoperative electrophysiology while patients engaged in language tasks: we analysed local field potentials in glioblastoma-infiltrated cortex during speech initiation, determined the decodability of neural responses and revealed biological drivers of synaptic enrichment in glioblastoma cells (Extended Data Fig. 1 and Supplementary Tables 1 and 2).

Glioblastomas remodel neural circuits

Glioblastomas and other high-grade gliomas interact with neural elements, resulting in cellular- and network-level changes[10,11,12,13]. While neurons within glioblastoma-infiltrated brain are hyperexcitable at rest, the extent of task-specific neuronal hyperexcitability and the ability to extract neural features from glioma-infiltrated cortex remain unclear. To examine cognitive task-specific neuronal activity from glioblastoma-infiltrated cortex, we selected a cohort of adult patients with cortically projecting tumours in the lateral prefrontal cortex (LPFC; Extended Data Fig. 2a). Electrocorticography (ECoG) electrodes were placed over tumour-infiltrated and normal-appearing cortex. ECoG signals filtered between 70–110 Hz were used for analysis of high-gamma band range power (HGp), which is strongly related to local neuronal population spikes[14,15] and is increased by cortical hyperexcitability[16]. Spectral data demonstrated clear separation of frequencies across tumour and non-tumour electrodes (Fig. 1a and Extended Data Fig. 3a).

Fig. 1: High-grade gliomas remodel long-range functional neural circuits.



a, In participants with dominant hemisphere glioblastomas, we applied subdural ECoG over the posterior lateral frontal cortex during an audiovisual speech initiation task to assess circuit dynamics. Spectral data show the

expected pattern of HGp increasing above 50 Hz in addition to clear separation of frequencies across tumour and non-tumour electrodes. **b**, The posterior lateral frontal cortex (outlined area) time series of HGp within tumour-infiltrated cortex between −600 ms and speech onset (0 ms). **c**, High-gamma (HG) recordings from averaged electrodes within each patient, while averaging the effect across the sampled region of cortex for an individual showing greater HG power within electrodes overlying tumour-infiltrated cortex ($n = 14$ patients, $F_{1,21} = 25.562$, $P = 0.00005$). Data are median (centre dot), first to third quartiles (bars) and the minimum and maximum points (whiskers). **d**, Electrodes were compared between non-tumour and tumour-infiltrated regions; the false-discovery rate (FDR)-corrected HGp demonstrates task-relevant hyperexcitability ($P = 0.016$). Data are mean ± s.e.m. **e**, Event-related spectral perturbations (ERSPs) during a naming task for low-frequency words (low freq., left column) and high-frequency words (high freq., middle column) in normal-appearing non-tumour regions (top row) and glioma-infiltrated (bottom row) cortex. Signals from high-frequency word trials were able to be decoded above chance in normal-appearing cortex (mean accuracy = 0.56, $P = 0.000089$) but not in glioma-infiltrated cortex (mean classifier accuracy = 0.49, $P = 0.72$) using a regularized logistic regression classifier with leave-one-participant-out cross-validation (right column). Data are mean ± 95% confidence interval. AU, arbitrary units. For **b**–**d**, statistical analysis was performed using two-sided linear mixed-effects models (**b**–**d**), and corrections for multiple comparisons were performed using FDR adjustment (**b** and **d**). For **e**, P values were determined using two-tailed Student's t-tests with Bonferroni multiple-comparison correction for the number of timepoints (left, ERSP) and one-sided Z-tests (right, classification accuracy).

Source data

ECoG was recorded from the dominant hemisphere LPFC during auditory and visual picture naming as an illustrative example of a well-defined cognitive neuronal circuit[17]. While patients were awake and speaking, HGp was recorded for single-electrode (Extended Data Fig. 3b) and group-level analysis. HGp data from control and non-tumour conditions demonstrate the expected neural time course of speech motor planning within the LPFC (Extended Data Figs. 2b and 3c,d), consistent with previously established

models of speech initiation demonstrated in non-human primates and humans[18,19]. We next performed the same analysis focused only on electrode arrays recording from tumour-infiltrated cortex. Countering the theory that glioblastoma–synaptic integration may result in physiologically disorganized neural responses, we found task-relevant neural activity within the entire region of the tumour-infiltrated cortex, including cortical regions that are not typically implicated in speech production (Fig. 1b)—a notable finding that indicates tumour-induced functional remodelling of language circuitry. Similarly, we found that, across WHO grade 2–4 glioma subtypes, task-specific neuronal responses for speech initiation are maintained within the LPFC (Extended Data Fig. 2c,d). These findings demonstrate that neuronal activity within tumour-affected cortex is physiologically organized, including neuronal activity elicited by speech tasks in regions that are outside of regions that are typically involved in speech production.

In light of this finding of preserved task-evoked neural responses from tumour-infiltrated cortex, we next examined whether the magnitude of neural responses may differ in tumour-affected cortical language areas. We therefore pair-matched tumour-infiltrated and normal-appearing cortex (Extended Data Fig. 3d,e), demonstrating increased HGp during speech production in glioblastoma-infiltrated cortex, consistent with hyperexcitability (Fig. 1c,d).

Neural computations for speech vary by condition. Vocalization of infrequently used (low frequency) words, for example, requires a more intricate coordination of articulatory elements than that of commonly used (high frequency) words[20,21]. We therefore determined the decodability of neuronal signals from normal-appearing and glioblastoma-infiltrated cortex using a logistic regression classifier to distinguish between low-frequency and high-frequency word trial conditions (Fig. 1e). We implemented identical training and leave-one-participant-out cross-validation paradigms for both conditions. Normal-appearing cortex produced above-chance decoding between low- and high-frequency word trials. By contrast, glioblastoma-infiltrated cortex did not decode word trials above chance. These data further demonstrate that glioblastoma infiltration into the human cortex maintains task-specific neuronal responses, including neuronal hyperexcitability, yet tumour-affected cortex loses the ability to decode complex word conditions.

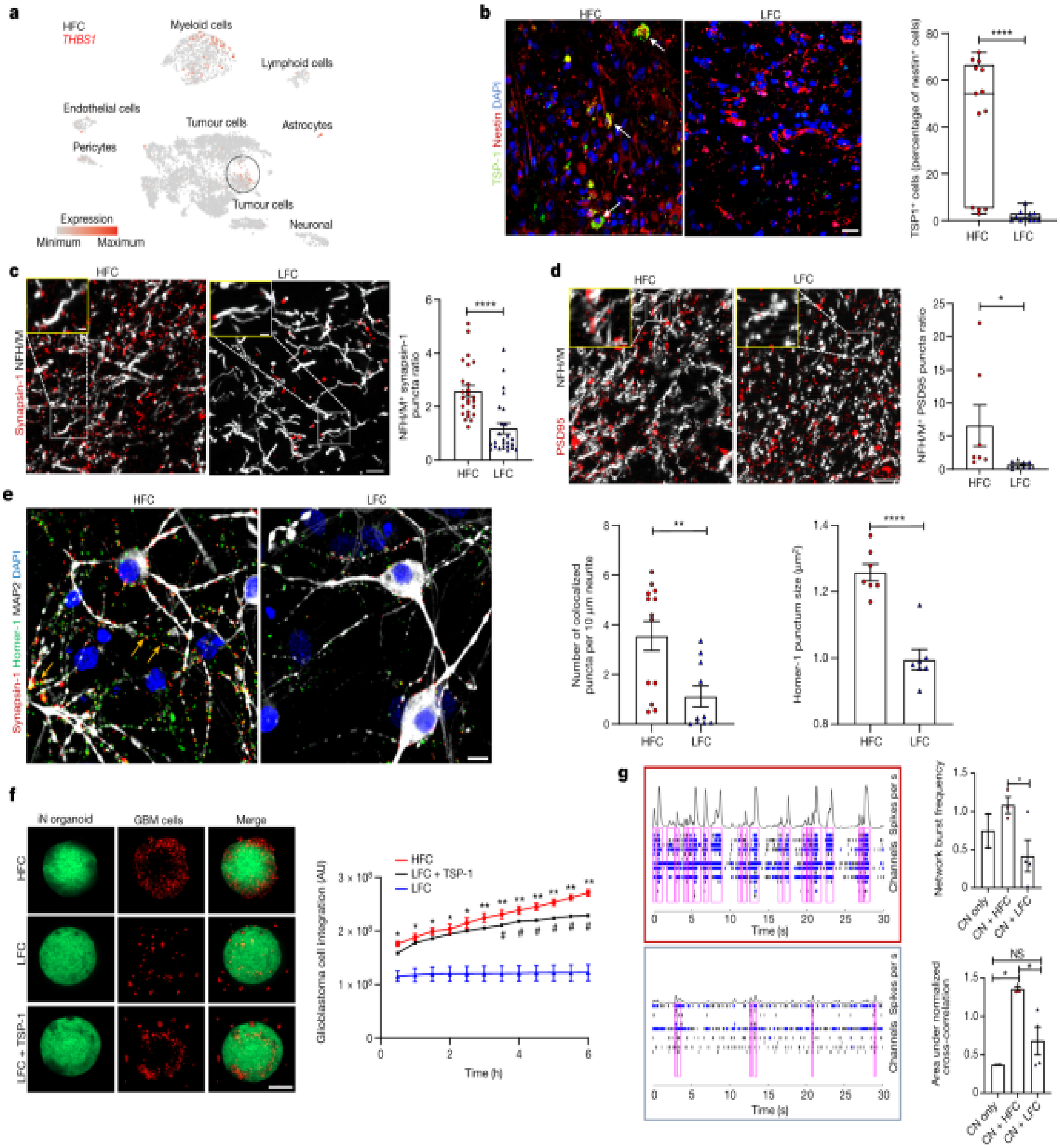
Synaptogenic tumour cells promote connectivity

Having demonstrated that gliomas remodel neuronal circuits, we next examined whether specific molecularly defined glioma cellular subpopulations influence functional integration of the tumour into neural circuitry. Glioblastoma cells are heterogeneous[22,23,24] and previous findings indicate that oligodendrocyte-precursor-cell-like subpopulations are enriched for synaptic gene expression[2], whereas astrocyte-like subpopulations secrete synaptogenic factors[8,25]. Thus, functionally connected regions may vary within tumours and differences in functional connectivity between tumour regions may be due at least in part to varying subpopulations of glioma cells. With the goal of sampling functionally connected regions within gliomas, we measured neuronal oscillations within glioma-infiltrated brain using magnetoencephalography (MEG) and sampled primary patient glioblastoma tissues with varying functional connectivity during surgical tumour resection[26,27,28]. The connectivity of an individual voxel was derived by the mean imaginary coherence between the index voxel and the rest of the brain[29,30,31]. Intratumoural functional connectivity correlated with neuronal activity within tumour-infiltrated cortex and high functional connectivity (HFC) voxels were identified both within tumour regions that were contrast-enhancing or T2/FLAIR hyperintense on magnetic resonance imaging (MRI; Extended Data Fig. 4).

To investigate the differences between functionally connected, HFC and non-functionally connected low functional connectivity (LFC) tumour regions, we performed bulk and single-cell RNA sequencing (RNA-seq) analyses. Bulk RNA-seq transcriptomic analysis revealed upregulation in HFC tumour regions of genes that are involved in the assembly of neural circuits, including axon pathfinding genes (*NTNG1*, also known as netrin G1), synapse-associated genes (for example, *SYNPO*, also known as synaptopodin) and synaptogenic factors including a sevenfold upregulation of thrombospondin-1 (*THBS1*, encoding TSP-1). *THBS1*, which encodes a known synaptogenic factor that is secreted in the healthy brain by astrocytes[32], was particularly interesting in the context of the observed remodelling of functional language circuitry described above (Extended Data Fig. 5a–c and Supplementary Table 3).

To further assess cellular subpopulation contribution to *THBS1* expression, we performed single-cell sequencing analysis of biopsy samples from HFC and LFC tumour regions (Supplementary Table 4). Malignant tumour cells were inferred on the basis of the expression programs and detection of tumour-specific genetic alterations, including copy-number variants (Extended Data Fig. 6a–e). We found that 2.44% of all tumour cells expressed *THBS1*, and that HFC tumour cells expressed higher levels of *THBS1* compared with LFC tumour cells (Fig. 2a and Extended Data Fig. 6g). Within LFC-region samples, *THBS1* expression primarily derives from a non-tumour astrocyte population (Extended Data Fig. 6e–g). This suggests that, within low-connectivity intratumoural regions, astrocytes chiefly express *THBS1*, whereas, within HFC regions, high-grade glioma cells express *THBS1* in addition to astrocytes and myeloid cells, which may promote the observed neural circuit remodelling (Extended Data Fig. 6h–j). Notably, myeloid cells, which include bone-marrow-derived macrophages, microglia, dendritic cells and neutrophils, chiefly comprise the glioblastoma tumour immune microenvironment (Extended Data Fig. 6d,e), and the microglial cell surface molecules CD36 and CD47 can function as TSP-1 receptors[33,34]. Although the role of TSP-1 in the tumour immune microenvironment is not yet clear, myeloid cell expression of TSP-1 suggests that multiple cell types in the tumour microenvironment of HFC regions may contribute to altered synaptic connectivity. Elevated expression of *THBS1* within HFC regions was confirmed by protein-level analysis using HFC and LFC patient-derived glioblastoma biopsy tissues. Concordant with transcriptomic profiles, immunohistochemistry analysis demonstrated increased TSP-1 expression within HFC tissues (Extended Data Fig. 7a). Immunofluorescence and confocal microscopy analysis confirmed that malignant tumour cells express TSP-1 in HFC tissue (Fig. 2b). The fact that a subpopulation of malignant tumour cells in HFC regions produce TSP-1 suggests a differential potential of tumour cells in the HFC regions to promote synaptogenesis and thereby connectivity, consistent with the cancer biology principal that cellular subpopulations assume distinct roles within the heterogenous cancer ecosystem, which may be defined at least in part by functional connectivity measures.

Fig. 2: Tumour-infiltrated circuits exhibit areas of synaptic remodelling characterized by glioma cells expressing synaptogenic factors.



a, Single-cell RNA-seq feature plot analysis of *THBS1* in HFC ($n = 6{,}666$ cells, 3 participants) tissues; within HFC samples, *THBS1* is primarily in glioblastoma cells (circled). **b**, TSP-1 immunofluorescence analysis of nestin-positive tumour cells in HFC and LFC tissues. $n = 13$ (HFC) and $n = 11$ (LFC) sections, 3 per group. $P = 0.000073$. Scale bar, 50 μm. The box plot shows the median (centre line), interquartile range (box limits) and minimum and maximum values (whiskers). **c**, The synapsin-1 puncta count in HFC and LFC glioblastoma tissue samples. $n = 25$ regions, 4 per group. $P = 0.000014$. Red, synapsin-1 (presynaptic puncta); white,

neurofilament heavy and medium (neurons). Scale bar, 10 µm. Inset: magnified view of synapsin-1 puncta on neurons. Scale bar, 3 µm. **d**, PSD95 puncta count. $n = 7$ (HFC) and $n = 9$ (LFC) sections, 3 per group. $P = 0.04$. Red, PSD95 (postsynaptic puncta); white, neurofilament heavy and medium chains (NFH/M) (neurons). Scale bar, 10 µm. Inset: magnified view of PSD95 puncta on neurons. Scale bar, 3 µm. **e**, Representative confocal images showing synaptic punctum colocalization (yellow arrows). Red, synapsin-1; green, homer-1 (postsynaptic puncta); white, MAP2 (neurons); blue, 4′,6-diamidino-2-phenylindole dihydrochloride (DAPI). Scale bar, 10 µm. Quantification of the number of colocalized pre- and postsynaptic puncta ($n = 13$ (HFC) and $n = 10$ (LFC) regions, 2 per group; $P = 0.005$) and homer-1 puncta size in neuron–glioma co-culture ($P = 0.000024$). **f**, TSP-1 rescue of induced neuron (iN) organoids in co-culture with HFC and LFC cells for 6 h. Scale bar, 300 µm. Quantification of glioblastoma (GBM) cell integration measured on the basis of the fluorescence intensity of RFP-positive glioblastoma cells in the organoids. Significant differences between HFC and LFC groups (asterisks) and LFC and LFC + TSP-1 (hash) are indicated. $n = 2$ (HFC and LFC groups) and $n = 1$ (LFC + TSP-1 group). Scale bar, 300 µm. **g**, Representative MEA raster plots showing individual spikes (tick mark), bursts (cluster of spikes in blue) and synchronized network bursts (pink) after 48 h co-culture of cortical neurons (CN) with HFC and LFC cells (outlined in red and blue, respectively). Quantification of network burst frequency (Hz) ($n = 2$ (CN only), $n = 3$ (CN + HFC) and $n = 4$ (CN + LFC); $P = 0.05$) and network synchrony (area under normalized cross-correlation; $n = 2$ (CN only), $n = 3$ (CN + HFC) and $n = 4$ (CN + LFC); $P = 0.0129$ (CN versus CN + HFC); $P = 0.0308$ (CN + HFC versus CN + LFC)). Data are mean ± s.e.m. (**b**–**g**). P values were determined using two-tailed Student's t-tests (**b**–**f**) and one-way analysis of variance (ANOVA) with Tukey's post hoc test (**g**). $^{*}P < 0.05$, $^{**}P < 0.01$, $^{****}P < 0.0001$; NS, not significant.

Source data

Hypothesizing that this subpopulation of HFC glioma cells may promote synaptogenesis and consequent remodelling of connectivity as observed in glioma-associated language networks above, we next examined whether HFC-associated glioma cells promote structural synapse formation, similar to normal astrocytes[35,36,37] and certain astrocyte-like glioblastoma cells[8,25].

We first analysed primary patient glioblastoma biopsies from HFC and LFC regions using immunohistochemistry and confocal microscopy. We found increased presynaptic neuronal puncta (synapsin-1; Fig. 2c) together with increased postsynaptic puncta density and cluster size on neurons ($PSD95^{+}neurofilament^{+}$), and synapsin–PSD95 puncta colocalization (Fig. 2d and Extended Data Fig. 7b) within HFC regions compared with LFC regions. Together, these data indicate increased synapse stability and/or synapse formation in high-connectivity regions of glioblastoma, supporting a role for TSP-1 in glioma-associated neural-circuit remodelling.

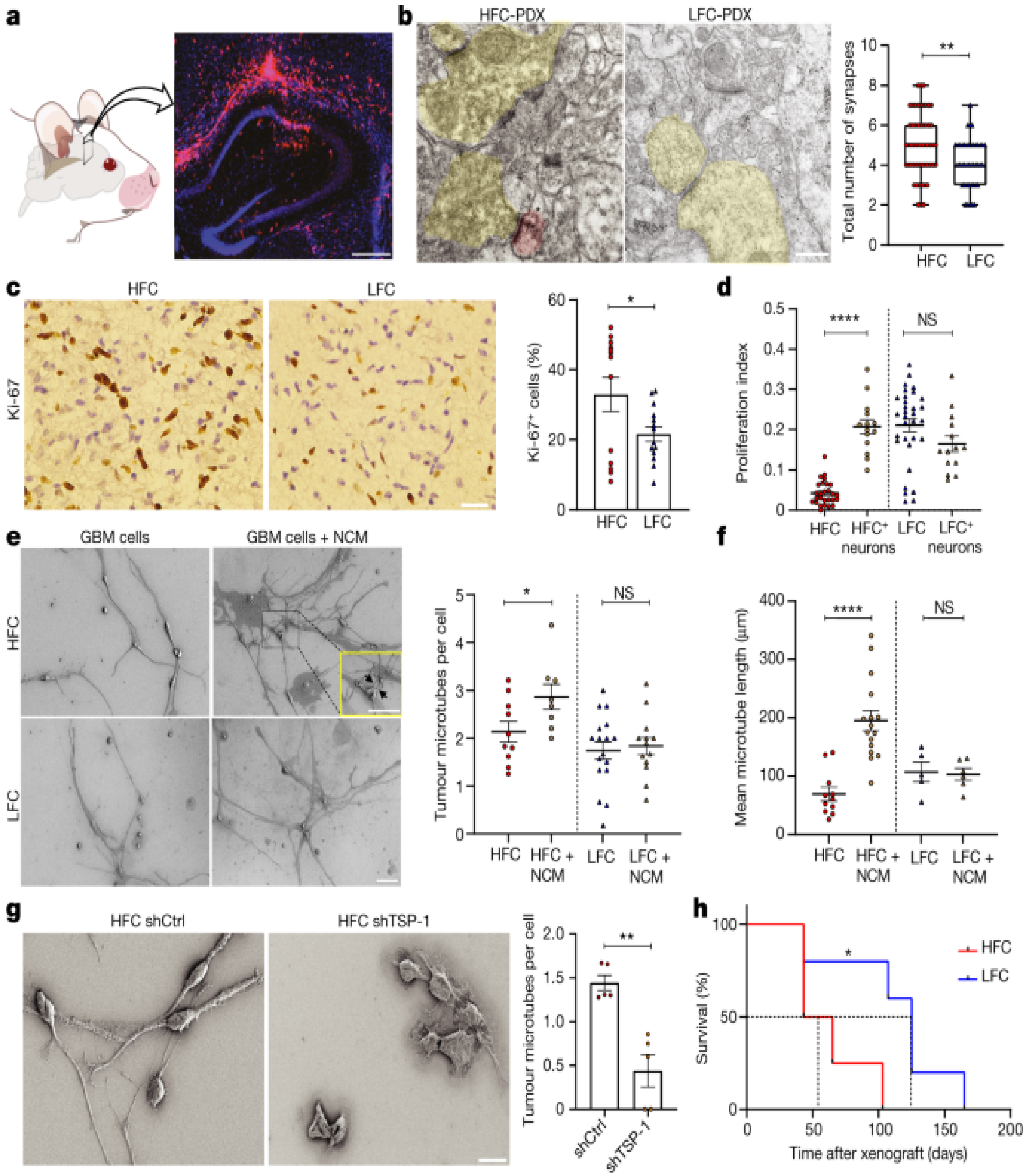
Primary patient-derived glioma cultures from HFC and LFC tumour regions were generated to perform further mechanistic experiments. We co-cultured high-grade glioma cells from HFC and LFC tumour regions with mouse hippocampal neurons to test the effects of $TSP\text{-}1^{high}$- and $TSP\text{-}1^{low}$-expressing primary patient-derived glioma cells on synaptic connectivity of neurons (Extended Data Fig. 7c,d). We then quantified the size of postsynaptic puncta (marked by the postsynaptic marker homer-1) and the number of colocalized pre- and postsynaptic puncta in HFC and LFC co-cultures with neurons. This demonstrated an increased number of colocalization points and postsynaptic $homer\text{-}1^{+}$ punctum size in glioma and neuronal processes in HFC–neuron co-cultures compared with LFC–neuron co-cultures (Fig. 2e), additionally indicating a role for HFC glioma cells in synaptogenesis.

To further investigate the functional distinctions between malignant subpopulations isolated from HFC and LFC regions, we tested neuron–glioma interactions in a neuronal organoid model. We co-cultured HFC and LFC glioma cells with GFP-labelled human neuron organoids generated from an induced pluripotent stem (iPS) cell line integrated with a doxycycline-inducible human *NGN2* transgene to drive neuronal differentiation[38]. Quantification of postsynaptic homer-1 in induced-neuron organoids revealed a relative increase in postsynaptic puncta density when co-cultured with HFC glioma cells compared with LFC glioma cells (Extended Data Fig. 7e). Live-cell imaging of neuronal organoids co-cultured with HFC and LFC glioma cells revealed that HFC glioma cultures exhibit prominent neuronal tropism and integrate extensively in the organoids, whereas LFC glioma cells displayed minimal integration with

neuron organoids (Fig. 2f and Supplementary Videos 1 and 2). Notably, exogenous administration of TSP-1 to induced-neuron–LFC co-culture reversed this phenotype and promoted robust LFC glioma integration into the neuronal organoid (Fig. 2f and Supplementary Video 3), further implicating TSP-1 in neuron–glioma interactions. The electrophysical properties of TSP-1^{high}-expressing cells in co-culture with neurons were analysed using multi-electrode array (MEA) electrophysiology. After co-culture for 48 h, the total number of network bursts (a measure of neuronal activity) from cortical neuron co-culture with TSP-1^{high}-expressing HFC cells was increased relative to cortical neurons alone or under LFC co-culture conditions. Neurons in co-culture with HFC glioma cells also demonstrated increased network synchrony as measured by the area under normalized cross-correlation (the area under interelectrode cross-correlation normalized to the autocorrelations; Fig. 2g and Extended Data Fig. 7f).

Gliomas exhibit intratumoural heterogeneity with subpopulations of cancer cells assuming particular roles[23,24]. The human data presented above demonstrate localizational heterogeneity of functional integration in glioblastoma with normal brain circuity and suggest that, within intratumoural regions of HFC, a tumour subpopulation with synaptogenic properties exists. We next examined the structural synapses in TSP-1^{high}-expressing HFC glioma cell-infiltrated mouse brain. RFP-labelled HFC or LFC glioma cells were stereotactically xenografted into the CA1 region of the mouse hippocampus[2] (Fig. 3a). After a period of engraftment and growth, immuno-electron microscopy analysis identified neuron-to-neuron and neuron-to-glioma synapses[2] (Fig. 3b). The total number of synapses (neuron-to-neuron and neuron-to-glioma combined) was significantly higher in HFC glioma xenografts than in LFC glioma xenografts (Fig. 3b and Extended Data Fig. 7g), further demonstrating a greater synaptogenic potential of glioma cells isolated from HFC patient tumour regions.

Fig. 3: High-grade gliomas exhibit bidirectional interactions with HFC brain regions.



a, Representative micrograph showing RFP-labelled glioblastoma xenografted into the mouse hippocampus. Scale bar, 500 μm. **b**, Immuno-electron microscopy analysis of HFC or LFC cell xenografts. The asterisk denotes immuno-gold particle labelling of RFP. Postsynaptic density in RFP^{+} tumour cells (pseudocoloured red), synaptic cleft and clustered synaptic vesicles in apposing presynaptic neuron (pseudocoloured yellow) identify both neuron–glioma synapses in HFC-PDX (left) and neuron–

neuron synapses in LFC-PDX (right). Quantification of the total number (neuron–neuron combined with neuron-glioma) of synapses per field of view in HFC/LFC xenografts. $n = 4$ mice per group. $P = 0.0019$. Scale bar, 1,000 nm. Data are median (centre line), with first and third quartiles (box limits) and the minimum and maximum points (whiskers). **c**, Representative immunohistochemistry images in glioblastoma tissues demonstrate increased Ki-67 protein expression in HFC samples. $n = 13$ (HFC) and $n = 14$ (LFC) regions, 4 per group. $P = 0.04$. Scale bar, 50 µm. **d**, Glioblastoma cells from HFC tissues show a marked increase in the proliferative index when co-cultured with mouse hippocampal neurons. $n = 27$ (HFC), $n = 14$ (HFC + neurons), $n = 32$ (LFC) and $n = 14$ regions (LFC + neurons), 3 per group. **e**, SEM images of HFC and LFC cells cultured in the presence or absence of neuronal conditioned medium (NCM) shows tumour microtubes (TMTs) that connect neighbouring cells through cytoplasmic extensions. Quantification of TMTs per cell. $n = 10$ (HFC), $n = 8$ (HFC + NCM), $n = 17$ (LFC) and $n = 13$ (LFC + NCM) regions, 2 per group. $P = 0.0455$. Scale bars, 20 µm (full fields) and 10 µm (magnified view). **f**, Quantification of the mean microtube length per spheroid. $n = 11$ (HFC), $n = 16$ (HFC + NCM), $n = 5$ (LFC) and $n = 6$ (LFC + NCM) spheroids, 1 per group. $P = 0.000011$. **g**, Representative SEM images showing TMTs and quantification of TMTs per cell from HFC shCtrl and HFC shTSP-1 conditions. $n = 5$ regions, 2 per group. $P = 0.0012$. Scale bar, 20 µm. **h**, Kaplan–Meier survival curves of mice bearing HFC or LFC xenografts. $n = 4$ (HFC) and $n = 5$ (LFC). $P = 0.03$. Data are mean ± s.e.m. (**b**–**h**). P values were determined using two-tailed Student’s t-tests (**b**–**g**) and two-tailed log-rank analysis (**h**).$^*P < 0.05$, $^{**}P < 0.01$, $^{****}P < 0.0001$; NS, not significant.

Source data

HFC promotes tumour progression

Neurons promote glioma cell proliferation[1,2,3,4] and we hypothesized that HFC cells may represent a cellular subpopulation within glioblastomas that are differentially regulated by neuronal factors. We found that primary patient biopsies from HFC and LFC regions demonstrated increased Ki-67 proliferative marker staining within HFC regions (Fig. 3c). To test whether HFC cells differentially proliferate in response to neuronal factors compared

with LFC primary patient cultures, patient-derived HFC and LFC cells cultured alone or in co-culture with mouse hippocampal neurons were treated with 5-ethynyl-2′-deoxyuridine (EdU) overnight. HFC glioma cells exhibit a fivefold increase in proliferation when cultured with neurons. By contrast, the LFC glioma in vitro cell proliferation index (determined as the fraction of DAPI cells co-expressing EdU) is similar with and without hippocampal neurons in vitro (Fig. 3d and Extended Data Fig. 8). These results indicate that the ability of HFC cells to proliferate is contingent on the presence of neuronally secreted factors and that, in the absence of neuronal signals, they tend to acquire a dormant tumour phenotype.

Given the neuronal tropism exhibited by HFC glioma cells together with the concept that neural network integration requires invasion of brain parenchyma to reach and colocalize with neuronal elements, we next tested the effects of neuronal conditioned medium on invasion of HFC and LFC glioma cells using a spheroid invasion assay. LFC glioma cells demonstrated no differences in spheroid volume in the presence or absence of neuronal conditioned medium; however, HFC glioma cells exhibited an increased spheroid invasion area in response to neuronal conditioned medium. In addition to increased invasion area, HFC glioma cells extended long processes representing tumour microtubes in response to neuronal conditioned medium (Extended Data Fig. 9a). Tumour microtubes connect glioma cells in a gap-junction-coupled network[1,39,40,41] through which neuronal-activity-induced currents are amplified[2]. Scanning electron microscopy (SEM) was performed on TSP-1^{high}-expressing HFC and LFC cells in the presence or absence of neuronal conditioned medium, demonstrating robust cytoplasmic extensions connecting HFC cells (Fig. 3e). We also quantified the change in mean spheroid volume. We found that neuronal conditioned medium increased both invasion and microtube length in HFC but not LFC cultures (Fig. 3f and Extended Data Fig. 9a). Concordantly, the invasive marker MET was increased within HFC samples compared with LFC samples (Extended Data Fig. 9b,c). Primary patient-derived HFC cells were then transduced with a short hairpin RNA (shRNA) control or shRNA against *THBS1* to knockdown TSP-1. Cell viability was confirmed using a live/dead assay with robust knockdown of our target protein (Extended Data Fig. 10a,b). Knockdown of *THBS1* in HFC cells decreased the number of tumour microtubes relative to the control

conditions (Fig. 3g), consistent with the known role for TSP-1 in tumour microtube formation[39].

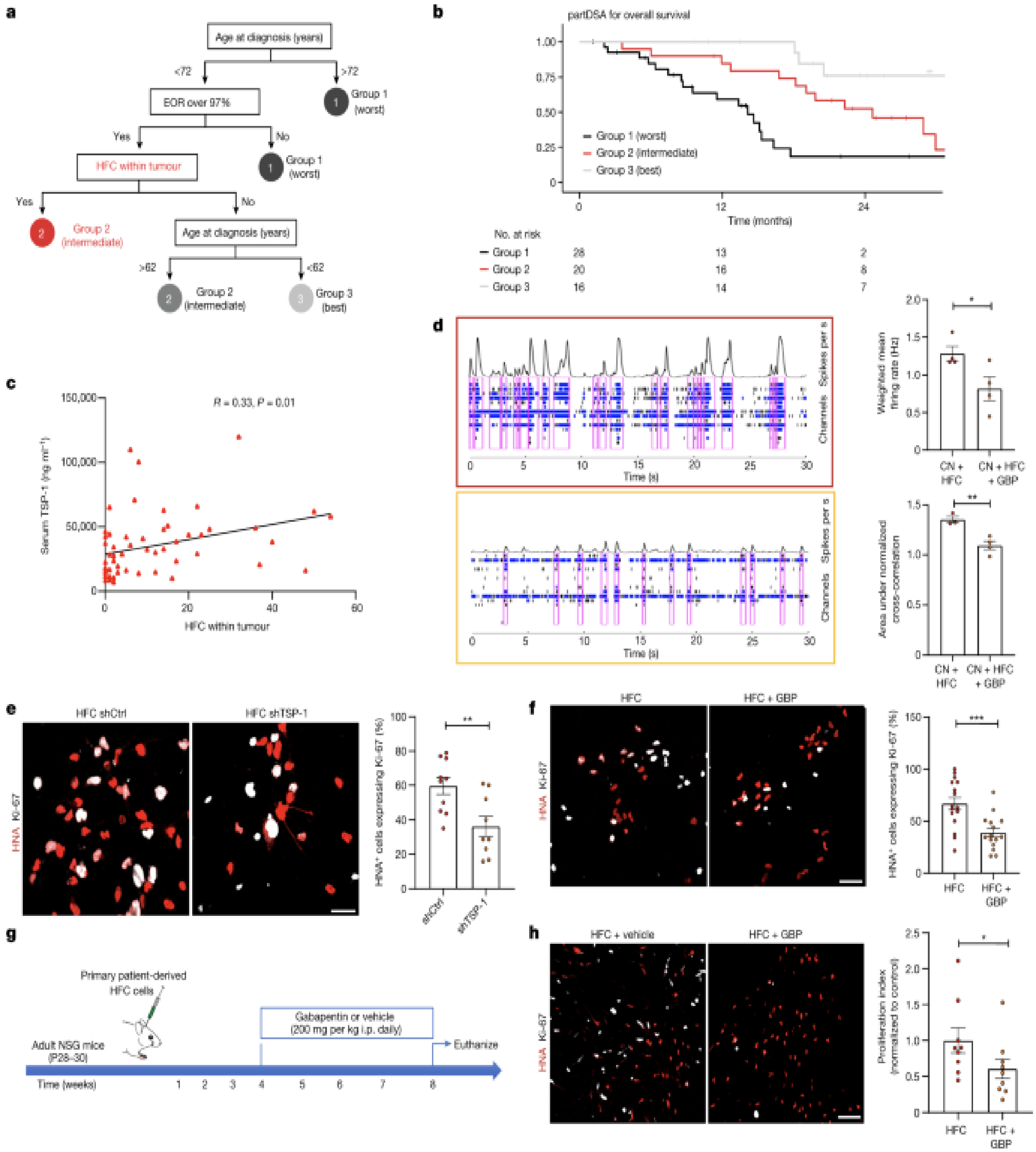
Glioblastoma cell invasion bears negative prognostic value. We therefore performed survival studies of mice that were orthotopically xenografted with patient-derived HFC or LFC glioma cells. Mice bearing HFC tumours exhibited greater tumour burden and shorter survival compared with LFC-tumour-xenografted mice (Fig. 3h and Extended Data Fig. 9d). Taken together, these results suggest that functionally connected intratumoural regions are enriched for a tumour cell population that is differentially responsive to neuronal signals and exhibits a proliferative, invasive and integrative phenotype in the neuronal microenvironment that negatively influences survival in a preclinical model.

Glioma connectivity shortens patient survival

We next investigated the effects of tumour-intrinsic functional connectivity on patient survival and cognition. First, we tested the hypothesis that gliomas exhibiting increased functional connectivity may be more aggressive, given the robust influence of neuronal activity on tumour progression[2,3,4]. We performed a human survival analysis of patients with newly diagnosed glioblastoma. After controlling for known correlates of survival (age, tumour volume, completion of chemotherapy and radiation, and extent of tumour resection)[42], neural oscillations and functional connectivity were measured within tumour-infiltrated brain using MEG (Supplementary Tables 2 and 5). A Kaplan–Meier survival analysis illustrates an overall survival of 71 weeks for patients with functional connectivity compared with an overall survival of 123 weeks for participants without HFC voxels, illustrating a striking inverse relationship between survival and functional connectivity of the tumour (mean follow-up time, 50.5 months) (Extended Data Fig. 11a). To identify clinically relevant survival risk groups, we next used recursive partitioning survival analysis using the partDSA algorithm[42,43,44]. Within this analysis we controlled for important prognostic variables such as MGMT promoter methylation status. Overall survival risk was based on the interactive effects of all known prognostic variables (for example, age at diagnosis, sex, tumour location, chemotherapy, radiotherapy, the presence of functional connectivity within

the tumour, pre- and post-operative tumour volume, and the extent of resection). The first division was based on known risk factors such as age and extent of tumour resection. Within this hierarchical model of partitioning, the degree of connectivity was identified as the next most important variable, which divided risk groups 2 and 3. Risk group 1 (black) had the worst outcomes and is the combination of patients older than 72 years or any age with less than 97% extent of tumour resection (subtotal resection). Risk group 3 (grey) had the best survival, and these are patients are younger than 62 years with over 97% extent of tumour resection and absence of functional connectivity in the tumour. Intermediate risk group 2 (red) revealed an interesting interaction between age and HFC. This group had two subsets: patients with over 97% resection of tumour and age younger than 72 years with intratumoural connectivity; and those between 62 and 72 years without functional integration (Fig. 4a,b). These results demonstrate the notable prognostic value of connectivity on survival. We next examined whether TSP-1, a secreted synaptogenic protein[32,35], can be identified in the patient serum and whether circulating TSP-1 is correlated with functional connectivity. Circulating TSP-1 levels in the patient serum exhibited a notable positive correlation with intratumoural functional connectivity (Fig. 4c).

Fig. 4: Intratumoural connectivity in patients with high-grade glioma is correlated with survival and TSP-1.



a,**b**, Schematic (**a**) and partDSA model (**b**) of overall survival in patients, incorporating the effects of glioblastoma intrinsic functional connectivity, therapeutic and clinical factors by recursive partitioning results into three risk groups. Risk group 1 (black) patients have the shortest survival, including a combination of (1) patients older than 72 and (2) patients younger than 72 with an extent of tumour resection (EOR) of less than 97%. Risk group 3 (grey) patients have the best survival, including patients who are younger than 62 with an extent of tumour resection of greater than 97%

and no intratumoural connectivity. Intermediate risk group 2 (red) comprises a combination of patients with greater than 97% extent of resection and (1) an age of younger than 72 with tumour intrinsic connectivity or (2) patients between 62 and 72 years without connectivity. **c**, Linear regression statistics illustrate that serum TSP-1 is correlated with the extent of intratumoural functional connectivity. $n = 56$. $P = 0.01$. **d**, Representative MEA raster plots showing neuronal spikes (black tick marks), bursts (cluster of spikes in blue) and synchronized network bursts (pink) of neuron–HFC co-cultures (outlined in red) and 24–48 h exposure of neuron–HFC co-culture to (50 μM) GBP (outlined in orange). Quantification of the weighted mean firing rate (Hz) and network synchrony (area under normalized cross-correlation) from HFC and HFC + GBP glioma–neuron co-culture (weighted mean firing rate: $n = 4$ well, 2 per group; $P = 0.04$; area under normalized cross-correlation: $n = 3$ (HFC) and $n = 4$ (HFC + GBP); $P = 0.007$). **e**, Representative confocal images from neuron–HFC glioma co-culture showing a decrease in HFC cell proliferation after *THBS1* knockdown using shRNA ($n = 10$ (HFC shCtrl) and $n = 9$ (HFC shTSP-1); $P = 0.0068$). Red, HNA (human nuclei); white, Ki-67. Scale bar, 30 μm. **f**, Representative confocal images from neuron–HFC glioma co-culture showing a decrease in HFC cell proliferation after gabapentin (32 μM) treatment for TSP-1 inhibition. $n = 16$ (HFC) and $n = 15$ (HFC + GBP), 2 per group. $P = 0.0007$. Red, HNA (human nuclei); white, Ki-67. Scale bar, 30 μm. **g**, Schematic for gabapentin treatment of HFC xenografted mice. i.p., intraperitoneal. **h**, Representative confocal images, and quantification demonstrating a decrease in the proliferation index (Ki-67^{+}HNA^{+}/HNA^{+}) after gabapentin treatment in mice bearing HFC xenografts. $n = 9$ mice per group. $P = 0.046$. Red, HNA (human nuclei); white, Ki-67. Scale bar, 70 μm. Data are mean ± s.e.m. (**d**–**f** and **h**). P values were determined using two-sided linear regression analysis (**c**), and two-tailed (**d**–**f**) and one-tailed (**h**) Student's *t*-tests. *$P < 0.05$, **$P < 0.01$, ***$P < 0.001$; NS, not significant.

Source data

We hypothesized that, beyond survival, intratumoural functional connectivity may also influence cognition. We therefore performed visual picture and auditory naming testing in our cohort of patients with dominant hemisphere glioblastoma, given their correlation with aphasia in clinical populations[45,46]. Linear regression of the number of HFC voxels within

tumours with language task performance demonstrated an inverse relationship between language cognitive performance and tumour functional connectivity (Extended Data Fig. 11b,c). Together, these findings suggest that functional integration of glioblastoma into neural circuits negatively influences cognition and survival.

TSP-1 as a therapeutic target

Given the premise that TSP-1 serves as a regulator of neuronal activity-driven glioma growth, we sought to target TSP-1 therapeutically using gabapentin (GBP), which blocks the thrombospondin receptor α2δ-1 (ref. [47]). In neuron–glioma co-cultures, individual spikes, bursts (cluster of spikes) and synchronized network bursts were reduced after 24–48 h exposure to GBP (Fig. 4d). Primary patient-derived HFC cells were transduced with shRNA-control or shRNA against *THBS1* or treated with GBP. Pharmacological TSP-1 inhibition using GBP did not influence the proliferation of HFC cells grown alone in culture, verifying that there were no tumour cell-intrinsic effects of GBP (Extended Data Fig. 12). By contrast, genetic or pharmacological targeting of TSP-1 resulted in a marked decrease in proliferation of HFC glioma cells co-cultured with neurons (Fig. 4e,f). GBP administration to mice bearing HFC patient-derived xenografts (PDX) resulted in a marked decrease in glioma proliferation (Ki-$67^{+}HNA^{+}/HNA^{+}$) in gabapentin-treated mice bearing HFC xenografts relative to vehicle-treated controls (Fig. 4g,h).

Discussion

Integration of high-grade glioma into neural networks is manifested by bidirectional interactions whereby neuronal activity increases glioma growth[1,2,3,4,48] and gliomas increase neuronal excitability[5,6,7,8]. To understand whether glioma–neuronal interactions influence neural circuit dynamics, we used short-range electrocorticography analysis of tumour-infiltrated cortex in humans to demonstrate language-task-specific activation as well as functional remodelling of language circuits. We further demonstrated that distinct intratumoural regions maintain functional connectivity through a subpopulation of TSP-1-expressing malignant cells

(HFC glioma cells). This molecularly distinct glioma subpopulation is differentially responsive to neuronal signals, exhibiting a synaptogenic, proliferative, invasive and integrative profile. Previous research has demonstrated that neuronal activity promotes glioma proliferation through paracrine and synaptic signalling[1,2,3,4], and we have now shown that patients with glioblastoma exhibiting functional connectivity between the tumour and the rest of the brain experience a shorter overall survival compared with patients without HFC. Pharmacological inhibition of TSP-1 decreases glioblastoma cell proliferation and network synchrony within the tumour microenvironment, highlighting a potential therapeutic strategy to be assessed in future clinical studies.

The neuronal microenvironment has emerged as a crucial regulator of glioma growth. Both paracrine signalling and connectivity remodelling may contribute to network-level changes in patients, affecting both cognition and survival. In patients, the role of neural network dynamics on survival and cognition remains poorly understood and how glioma–network interactions influence cognition remains unanswered. In fact, some studies using a heterogenous population of patients with both IDH wild type (WT) and mutant WHO grade III and IV gliomas have suggested that functional connectivity improves overall survival[49,50,51]; however, such previous research has been confounded by functional connectivity methods that are heavily influenced by the presence of tumour vascularity, limited spatial resolution and a heterogenous patient cohort. Nonetheless, the evidence in this study that glioblastomas remodel functional circuits and that functional connectivity negatively influences survival does not address direction of causality. It remains possible that glioma originating in functionally connected cortical regions are more strongly connected and may therefore exhibit greater network distribution, thereby encouraging distinct glioblastoma subpopulations with the ability to migrate[52]. A better understanding of the cross-talk between neurons and gliomas as well as how functional integration affects clinical outcomes may open the door to a range of pharmacological and neuromodulation therapeutic strategies focused on improving cognitive outcomes and survival.

Methods

Patients, samples, consent and ethics approval

Each participant in the study was recruited from a prospective registry of adults aged 18–85 with newly diagnosed frontal, temporal and parietal IDH-WT high-grade gliomas with detailed language assessments and baseline MEG recordings. Inclusionary criteria included the following: native English speaking, aged 18–85 years, and no previous history of psychiatric illness, neurological illness, or drug or alcohol abuse. All human electrocorticography data were obtained during lexical retrieval language tasks from 14 adult awake patients undergoing intraoperative brain mapping for surgical resection. Tumours from eight patients were used for RNA-seq experiments. Site-directed tumour biopsies from 19 patients were used for immunofluorescence/immunohistochemistry analysis and 24 patients were used for immunocytochemistry and cell-based functional assays. Tumours from eight patients were used for mouse xenograft experiments. All of the participants provided written informed consent to participate in this study, which was approved by the University of California, San Francisco (UCSF) institutional review board (IRB) for human research (UCSF CC-171027, CHR 17-23215) and performed in accordance with the Declaration of Helsinki.

We began by studying short-range circuit dynamics in a subset of 14 patients with dominant hemisphere glioblastoma infiltrating speech production areas of the inferior frontal lobe using ECoG in the intraoperative setting (Extended Data Fig. 1a). We then focused molecular studies on patients with surgically treated IDH-WT glioblastoma, performed extraoperative language assessments and imaginary coherence as a long-range measure of functional connectivity using MEG (Extended Data Fig. 1a,b). This enabled us to import functional connectivity data into the operating room in which we performed site-specific tissue biopsies of human glioma from regions with differing measures of functional connectivity for in vivo and in vitro cell biology experiments including primary patient cultures ($n = 19$ patients) and multimodal tissue profiling, including microscopy, sequencing, proteomics and patient-derived tumour xenografting (Extended Data Fig. 1c). This layered approach—combining clinical variables, cognition assessments, human and animal models of network dynamics, in addition to cell biology

—served as a platform to study the clinical implications of glioma–neuron interactions (Extended Data Fig. 1d and Supplementary Tables 1 and 2).

Human ECoG and data analyses

The hemisphere of language dominance was determined using baseline magnetic source imaging. In brief, the participants sat in a 275-channel whole-head CTF Omega 2000 system (CTF Systems) sampling at 1,200 Hz while they performed an auditory-verb generation task. The resulting time series were then reconstructed in source space with an adaptive spatial filter after registration with high-resolution MRI. Finally, changes in beta-band activity during verb generation were compared across hemispheres to generate an overall laterality index. All of the participants were left-dominant and underwent electrophysiological recording of the left hemisphere. We implemented an intraoperative testing paradigm that was previously established[9]. Noise in the operating room was minimized through rigorous enforcement of the following: (1) all personnel were requested to cease verbal communication; (2) telephones and alarms were muted; and (3) surgical suction and all other non-essential machinery were temporarily shut down. A 15 inch laptop computer (60 Hz refresh rate) running a custom MATLAB script integrated with PsychToolbox 3 (http://psychtoolbox.org/) was placed 30 cm away from each participant. The script initiated a picture-naming task that consisted of a single block of 48 unique stimuli, each depicting a common object or animal through coloured line drawings. Each stimulus was presented at the point of central fixation and occupied 75% of the display. After presentation of each stimulus, the participants were required to vocalize a single word that best described the item.

Intraoperative photographs with and without subdural electrodes present were used to localize each electrode contact combined with stereotactic techniques[9,53]. Images were registered using landmarks from gyral anatomy and vascular arrangement to preoperative T1- and T2-weighted MRI scans. Tumour boundaries were localized on MRI scans and electrodes within 10 mm of necrotic tumour core tissue were identified as ‘tumour’ contacts. Electrodes overlying the hypointense core of the tumour extending from the contrast enhancing rim to the edge of FLAIR were considered to be tumour electrodes, and electrodes completely outside of any T1 post gadolinium or

FLAIR signal were considered to be non-tumour or normal appearing by a trained co-author blinded to the electrophysiologic data[2]. Glioma-infiltrated regions were defined on the basis of two criteria previously established in the literature[9], including mass-like region of T2-weighted FLAIR sequences signal. Imaging was confirmed by gross inspection of the cortex confirming dilation and/or an abnormal vascular pattern. Previous research has shown that regions of non-enhancing disease consist of infiltrating tumour cells intermixed with neurons and normal glial cells[2,54]. These labels were reviewed by the study principal investigator (S.L.H.-J.) and compared to labels derived during intraoperative stereotactic neuronavigation to reach a consensus (Brainlab).

Each participant received a training session 2 days before participation to ensure familiarity with the task. ECoG signals were acquired during a period after stopping the administration of anaesthetics (minimum drug wash out period of 20 min) and the patient was judged to be alert and awake after an extensive post-emergence wakefulness assessment to ensure adequate arousal[55]. Intraoperative tasks consisted of naming pictorial representations of common objects and animals (picture naming) and naming common objects and animals through auditory descriptions (auditory naming)[56]. Post-operative videos were reanalysed to ensure that all data were collected and correct responses only were included for analysis. Audio was sampled at 44.1 kHz from a dual-channel microphone placed 5 cm from the participant and electrophysiological signals were amplified (g.tec). Recordings were acquired at 4,800 Hz and downsampled to 1,200 Hz during the initial stages of processing. During offline analyses, audio and electrophysiological recordings were manually aligned, resampled and segmented into epochs (speech-locked). These epochs set time = 0 ms as speech onset and included ±2,000 ms for a total of 4,000 ms of signal per trial. Trials were discarded if (1) an incorrect response was given (including fillers and interjections) or (2) there was a greater than 2 s delay between stimulus presentation and response so as to maintain consistent trial dynamics and ensure that the neural signal indeed reflected the experimental manipulations. Channels with excessive noise artifacts were visually identified and removed if their kurtosis exceeded 5.0. After the rejection of artifactual channels, data were referenced to a common average, high-pass filtered at 0.1 Hz to remove slow-drift artifacts, and bandpass filtered between 70–110 Hz using a 300-

Order FIR filter to focus the analyses on the high-gamma band range, which is strongly related to local mean population spiking rates. To extract the ERSPs, electrophysiological signals were first downsampled to 600 Hz, then high-pass filtered at 0.1 Hz to remove DC-offset and low-frequency drift, notch-filtered at 60 Hz and its harmonics to remove line noise, and bandpass-filtered between 70 and 170 Hz (that is, the high-gamma range) using a Hamming windowed sinc FIR filter. These signals were finally smoothed using a 100 ms Gaussian kernel, downsampled to 100 Hz and *z*-scored across each trial. Electrodes were subsequently rereferenced to the common average for each participant to facilitate group comparisons, and regions of interest were defined according to the Automated Anatomical Labelling Atlas (https://www.gin.cnrs.fr/en/tools/aal/). The location of grid implantation was solely directed by clinical indications. The accuracy of the final registration for each participant was independently confirmed using gyral and sulcal anatomy to triangulate the location of each electrode registered to the template surface and was then compared to intraoperative photographs of the actual cortex with the overlying grid(s)[57]. The HGp was then calculated using the square of the Hilbert transform on the filtered data. The HGp was then averaged across the resting-state time series, yielding a single measure of neural responsivity for each electrode contact. The HGp was then averaged across patients during the task response period, yielding a single measure of neuronal responsivity for each channel. The HGp levels were then compared between tumour and normal appearing channels. Linear mixed-effects modelling was used to perform statistical comparisons with repeated measures using the nlme package in R (v.3.1-161; https://cran.r-project.org/web/packages/nlme/citation.html). The signal's origin (that is, normal-appearing/glioma-infiltrated cortex) was modelled as a fixed effect and the participants were modelled as random effects. For continuous variables without repeated measures, *t*-tests were used. A threshold of $P < 0.05$ was used to denote statistical significance and corrections for multiple comparisons were made using the Bonferroni method.

To decode between low-frequency words (for example, rooster) and high-frequency words (for example, car), signals from normal-appearing and glioma-infiltrated electrodes were extracted from the anterior temporal lobe after participant-level registration to a common MNI atlas. Responses were time-locked to speech onset and the signal envelope was extracted using a

Hilbert transform after applying a bandpass filter in the high-gamma range (70–170 Hz). Subsequently, an l2-regularized logistic regression classifier was trained (cost of 1) to distinguish neural responses during vocalization of low-frequency words (for example, rooster) from high-frequency words (for example, car). Model performance was determined by taking the accuracy on a held-out participant and averaging it across all folds (that is, leave-one-participant-out cross-validation) and statistical significance was determined by testing this accuracy against a binomial distribution. This process was conducted separately for normal-appearing and glioma-infiltrated cortex using an identical preprocessing, training and testing paradigm.

MEG recordings and data analysis

MEG recordings were performed according to an established protocol[30,31]. In brief, the study participants had continuous resting state MEG recorded with a 275-channel whole-head CTF Omega 2000 system (CTF Systems) using a sampling rate of 1,200 Hz. During resting-state recordings, the participants were awake with their eyes closed. Surface landmarks were co-registered to structural magnetic resonance images to generate the head shape. Within the alpha frequency band, an artifact-free 1 min epoch was selected for further analysis if the patient's head movement did not exceed 0.5 cm. This artifact-free, 1 min epoch was then analysed using the NUTMEG software suite (v.4; UCSF Biomagnetic Imaging Laboratory) to reconstruct whole-brain oscillatory activity from MEG sensors so as to construct functional connectivity (imaginary coherence (IC)) metrics[54,58,59]. Spatially normalized structural magnetic resonance images were used to overlay a volume-of-interest projection (grid size = 8 mm; approximately 3,000 voxels per participant) such that each voxel contained the entire time series of activity for that location derived by all the MEG sensor recordings. The time series within each voxel was then bandpass-filtered for the alpha band (8–12 Hz) and reconstructed in source space using a minimum-variance adaptive spatial filtering technique[54,60]. The alpha frequency band was selected because it was the most consistently identified peak in the power spectra from this sampling window in our patient series. Functional connectivity estimates were calculated using IC, a technique known to reduce overestimation biases in MEG data generated from common references, cross-talk and volume conduction[26,28].

Resting-state MEG was also used to measure intratumoural gamma activity. A spatial beamformer was applied to extract neural signals at the voxel level from manually defined regions of interest corresponding to FLAIR signal abnormality (that is, within the infiltrative margin of the tumour)[61]. These source-space signals were then downsampled to 300 Hz, notch filtered at 60 Hz to remove line noise and rereferenced to the common average. Spectral activity from 1 to 50 Hz was estimated at each voxel using Thomson's multitaper method (pmtm in MATLAB R2021b) with 29 Slepian tapers. Next, gamma power from 30 to 50 Hz was computed at each voxel after subtracting the aperiodic component from each spectrum by fitting a Lorentzian function in semi-log space[62]. A point estimate of intratumoural gamma activity was subsequently computed by averaging the activity across all voxels for each participant and regressed against the corresponding number of manually counted intratumoural HFC nodes.

Functional connectivity map

The functional connectivity of an individual voxel was derived by the mean IC between the index voxel and the rest of the brain, referenced to its contralesional pair[30]. It is possible that there are regions within gliomas with varying amounts of functional connectivity. Moreover, there are individual patients with more or less functional connectivity. We have addressed these differences in our experimental model. Intratumoural differences in functional connectivity were addressed by the following: in comparison to contralesional voxels, we used a two-tailed *t*-test to test the null hypothesis that the *Z*-transformed connectivity IC between the index voxel and non-tumour voxel is equal to the mean of the *Z*-transformed connectivity between all contralateral voxels and the same set of voxels. The resultant functional connectivity values were separated into tertiles: upper tertile (HFC) and lower tertile (LFC). Functional connectivity maps were created by projecting connectivity data onto each individual patient's preoperative structural magnetic resonance images and imported into the operating room neuronavigation console. Stereotactic site-directed biopsies from HFC (upper tertile) and LFC (lower tertile) intratumoural regions were taken and x, y, z coordinates determined using Brainlab neuro-navigation. Thus, only the extremes of intratumoural connectivity (high and low connectivity, HFC and LFC, respectively) were analysed for these experiments. Rather than

raw values, each functional connectivity measure represents a *Z*-transformed value and it therefore remains likely that the HFC distinction for one patient does not perfectly coincide with the HFC distinction in another patient's tumour (intertumoural heterogeneity).

Measurement of tumour volume and calculation of volumetric extent of resection

Pre-operative and post-operative tumour volumes were quantified using BrainLab Smartbrush (v.2.6; Brainlab). Pre-operative MRI scans were obtained within 24 h before resection, and post-operative scans were all obtained within 72 h after resection. Total contrast-enhancing tumour volumes were measured at both pre-operative and post-operative timepoints. The total contrast-enhancing tumour volume was measured on T1-weighted post-contrast images, and the non- enhancing tumour volume was measured on T2 or FLAIR sequences. Manual segmentation was performed with region-of-interest analysis 'painting' inclusion regions based on fluid-attenuated inversion-recovery (FLAIR) sequences from pre- and post-operative MRI scans to quantify tumour volume. The extent of resection was calculated as follows: (pre-operative tumour volume − post-operative tumour volume)/pre-operative tumour volume × 100%. Manual segmentations were performed for which the tumour volumetric measurements were verified for accuracy after an initial training period. Volumetric measurements were performed blinded to patients' clinical outcomes. All of the patients in the cohort had available preoperative and postoperative MRI scans for analysis. To ensure that post-operative FLAIR signal was not surgically induced oedema or ischaemia, FLAIR pre- and post-operative MRIs were carefully compared alongside DWI sequences before including each region in the volume segmentation[42]. HFC voxels with T1 post gadolinium contrast enhancing tumour were considered to be HFC-positive for survival analysis.

Language assessments

One to two days before tumour resection, patients underwent baseline language evaluation, which consisted of naming pictorial representations of common objects and animals (picture naming) and naming common objects and animals through auditory descriptions (auditory naming). Visual picture

naming and auditory stimulus naming testing were used given their known significance and clinical correlation with outcomes in clinical patient population[63,64]. The correct answers for these tasks (delivered on a laptop with a 15 inch monitor (60 Hz refresh rate) positioned two feet away from the seated patient in a quiet clinical setting) were matched on word frequency (that is, commonality within the English language) using $SUBTLEX_{WF}$ scores provided by the Elixcon project and content category. Task stimuli were randomized and presented using PsychToolbox. The task order was randomly selected by the psychometrist for each participant. Slides were manually advanced by the psychometrist either immediately after the participant provided a response or after 6 s if no response was given. The tasks were scored on a scale from 0 to 4 by a trained clinical research coordinator who was initially blinded to all clinical data (including imaging studies). No participants had uncorrectable visual or hearing loss. Details of the administration and scoring of auditory and picture naming language tasks can be found in previous studies[27,55,65].

Isolation and culture of primary patient-derived glioblastoma cells

Tumour tissues with high (HFC) and low (LFC) functional connectivity sampled during surgery based on preoperative MEG were processed for quality control by a certified neuropathologist and were subsequently used to generate primary patient-derived cultures. Patient-matched samples were acquired from site-directed HFC and LFC intratumoural regions from the same patient. Intratumoural HFC and LFC tissues were dissociated both mechanically and enzymatically and then passed through a 40 µm filter to remove debris. The filtered cell suspension was then treated with ACK lysis buffer (Invitrogen) to remove red blood cells and subsequently cultured as free-floating neurospheres in a defined, serum-free medium designated tumour sphere culture medium, consisting of Dulbecco's modified Eagle's medium (DMEM-F12; Invitrogen), B27 (Invitrogen), N2 (Invitrogen), human-EGF (20 ng ml^{-1}; Peprotech), human-FGF (20 ng ml^{-1}; Peprotech). Normocin (InvivoGen) was also added to the cell culture medium in combination with penicillin–streptomycin (Invitrogen) to prevent mycoplasma, bacterial and fungal contaminations. Cell cultures were

routinely tested for mycoplasma (PCR Mycoplasma Test Kit I/C, PromoCell) and no positive results were obtained (Extended Data Fig. 7d).

Bulk RNA-seq and analysis

RNA was isolated from HFC (*n* = 3) and LFC (*n* = 4) tumour samples using the RNeasy Plus Universal Mini Kit (QIAGEN) and RNA quality was confirmed using the Advanced Analytical Fragment Analyzer. RNA-seq libraries were generated using the TruSeq Stranded RNA Library Prep Kit v2 (RS-122- 2001, Illumina) and 100 bp paired-end reads were sequenced on the Illumina HiSeq 2500 system to at least 26 million reads per sample at the Functional Genomics Core Facility at UCSF. Quality control of FASTQ files was performed using FASTQC (http://www.bioinformatics.babraham.ac.uk/projects/fastqc/). Reads were trimmed with Trimmomatic (v.0.32)[66] to remove leading and trailing bases with quality scores of less than 20 as well as any bases that did not have an average quality score of 20 within a sliding window of 4 bases. Any reads shorter than 72 bases after trimming were removed. Reads were subsequently mapped to the human reference genome GRCh38 (https://www.ncbi.nlm.nih.gov/assembly/GCF_000001405.39/)[67] using HISAT2[68] (v.2.1.0) with the default parameters. For differential expression analysis, we extracted exon-level count data from the mapped HISAT2 output using featureCounts[69]. Differentially expression analysis was performed using DESeq2[70] using the apeglm parameter[71] to accurately calculate log-transformed fold changes and setting a false-discovery rate of 0.05. Differentially expressed genes were identified as those with log-transformed fold changes of greater than 1 and an adjusted *P* value of less than 0.05. Unsupervised gene expression principal component analysis and volcano plots of IDH-WT glioblastoma (Extended Data Fig. 5b,c) revealed 144 differentially expressed genes between HFC and LFC tumour regions, including 40 genes involved in nervous system development (Supplementary Table 3).

Single-cell sequencing

Single-cell suspension generation

Fresh tumour samples were acquired from the operating room and transported to the laboratory space in PBS and on ice. Tumour tissue was minced with #10 scalpels (Integra LifeSciences) and then digested in papain (Worthington Biochemical, LK003178) for 45 min at 37 °C. Digested tumour tissue was then incubated in red blood cell lysis buffer (eBioscience, 00-4300-54) for 10 min at room temperature. Finally, the samples were sequentially filtered through 70 µm and 40 µm filters to generate a single-cell suspension.

Single-cell sequencing and analysis

Single-cell suspensions of three patient-matched HFC and LFC tumour tissues were generated as described above and processed for single-cell RNA-seq using the Chromium Next GEM Single Cell 3′ GEM, Library & Gel Bead Kit v3.1 on the 10x Chromium controller (10x Genomics) using the manufacturer's recommended default protocol and settings, at a target cell recovery of 5,000 cells per sample. Although single-cell sequencing does not capture all cell types within the central nervous system microenvironment, the sequencing pipeline used in this study has been demonstrated to identify neurons and was therefore chosen for use in physiologically annotated fresh glioblastoma samples, compared with single-nucleus RNA-seq, which is commonly applied for frozen archived tissues[72,73]. One hundred base pair paired-end reads were sequenced on the Illumina NovaSeq 6000 system at the Center for Advanced Technology at the University of California San Francisco, and the resulting FASTQ files were processed using the CellRanger analysis suite (v.3.0.2; https://github.com/10XGenomics/cellranger) for alignment to the hg38 reference genome, identification of empty droplets, and determination of the count threshold for further analysis. A cell quality filter of greater than 500 features but fewer than 10,000 features per cell, and less than 20% of read counts attributed to mitochondrial genes, was used. Single-cell UMI count data were preprocessed in Seurat (v.3.0.1)[74,75] using the sctransform workflow[76], with scaling based on the regression of UMI count and the percentage of reads attributed to mitochondrial genes per cell. Dimensionality reduction was performed using principal component analysis and then principal component loadings were corrected for batch effects using Harmony[77]. Uniform manifold approximation and projection was

performed on the reduced data with a minimum distance metric of 0.4 and Louvain clustering was performed using a resolution of 0.2. Marker selection was performed in Seurat using a minimum difference in the fraction of detection of 0.5 and a minimum log-transformed fold change of 0.5. We assessed the single-cell transcriptome from 6,666 HFC-region cells and 7,065 LFC-region cells (Supplementary Table 4).

Immunohistochemistry and immunofluorescence analysis

After rehydration, 5.0 µm paraffin-embedded sections were processed for antigen retrieval followed by blocking and primary antibody incubation overnight at 4 °C. The following primary antibodies were used: rabbit anti-synapsin 1 (1:1,000, EMD Millipore), mouse anti-PSD95 (1:100, UC Davis), mouse anti-nestin (1:500, Abcam), mouse anti-neurofilament (M+H; 1:1,000, Novus Biologicals), mouse anti-TSP-1 (1:20, Invitrogen), rabbit anti-TSP-1 (1:50, Abcam), rabbit anti-MET (1:100, Abcam) and rabbit anti-Ki-67 (1:100, Abcam). We used species-specific secondary antibodies: Alexa 488 goat anti-chicken IgG, Alexa 488 goat anti-rabbit IgG, Alexa 568 goat anti-rabbit IgG, Alexa 568 goat anti-mouse IgG, Alexa 647 goat anti-rabbit IgG, all used at 1:500 (Invitrogen). After DAPI nuclear counter staining (Vector Laboratories, 1:1,000), coverslips were mounted with Fluoromount-G mounting medium (SouthernBiotech) for immunofluorescence analysis. The number of synapsin-1 and PSD95 puncta was quantified using spots (with automatic intensity maximum spot detection thresholds and a spot diameter of 1.0 µm) detection function of Imaris. The ratio of pre- and postsynaptic puncta was calculated by dividing the total number of synapsin-1 or PSD95 puncta on neurofilament-positive neurons to the total number of cells stained with DAPI in 135 µm × 135 µm field areas for quantification. Alternatively, the sections were incubated in DAB horseradish peroxidase (Vector Laboratories) for chemical colorimetric detection after incubation in ImmPress anti-rabbit IgG (Novus Biologicals) and counterstained with Harris haematoxylin for immunohistochemistry analysis.

Glioma–mouse hippocampal neuron co-culture

Glioma cells were plated on poly-d-lysine and laminin-coated coverslips (Neuvitro) at a density of 10,000 cells per well in 24-well plates. Approximately 24 h later, 40,000 embryonic mouse hippocampal neurons (Gibco) were seeded on top of the glioma cells and maintained with serum-free Neurobasal medium supplemented with B27, gentamicin and GlutaMAX (Gibco). After 2 weeks of co-culture, cells were fixed with 4% paraformaldehyde (PFA) for 30 min at 4 °C and incubated in blocking solution (5% normal donkey and goat serum, 0.25% Triton X-100 in PBS) at room temperature for 1 h. Next, they were treated with primary antibodies diluted in the blocking solutions overnight at 4 °C. The following antibodies were used: rabbit anti-homer-1 (1:250, Pierce), mouse anti-synapsin-1 (1:200) and chicken anti-MAP2 (1:500, Abcam). The coverslips were then rinsed three times in PBS and incubated in secondary antibody solution (Alexa 488 goat anti-chicken IgG; Alexa 568 goat anti-mouse IgG, and Alexa 647 goat anti-rabbit IgG, all used at 1:500 (Invitrogen) in antibody diluent solution for 1 h at room temperature. The coverslips were rinsed three times in PBS and then mounted with VECTA antifade mounting medium with DAPI (Vector Laboratories).

Confocal imaging and quantification of synapsin-1 and homer-1 staining and colocalization analysis

Images were captured at 1,024 × 1,024 resolution using a ×10 objective on the Nikon C2 confocal microscope. The confocal microscope settings for the homer-1 Alexa488 and synapsin-1 Alexa647 channels were held constant across all of the samples that were used for the experiment. Collected images were then imported into Imaris software (Imaris v.9.2.1, Bitplane) and the threshold value for each channel was manually adjusted and the colocalized voxels of the synapsin-1 puncta with the homer-1 marker was detected by creating a colocalization channel using the built-in the colocalization module of the Imaris software. Furthermore, the colocalization events were quantified by running the built-in spot detection algorithm of Imaris in conjunction with the colocalization channel. Next, dendrites labelled by MAP2 was visualized in TRITC channel and reconstructed using the Filament tool of Imaris software; the number of colocalized puncta representing synapses were counted and presented as the number of synapsin-1- and homer-1-positive puncta per 10 μm of dendrite

length. Areas of homer-1 immunolabelled synaptic puncta were reconstructed using Imaris software Surface tool on maximal-intensity projections. Surfaces were built using a surface area detail level of 0.1 μm, thresholding by absolute intensity and taking all voxel >1.0 into account. The area sizes of individual anti-homer1-immunostained puncta were analysed and the mean values were calculated.

Induced neuron organoid and glioma co-culture

Induced neuron organoids were generated from a WTC11 iPS cell clone integrated by human NGN2 transgene induction as described previously[38,78]. In brief, iNeuron organoids were generated by the transgenic human iPS cell WTC11 line by NGN2 induction through addition of 2 μg ml^{-1} doxycycline in the 1:1 mixture of Neurobasal and BrainPhys neural medium containing 1% B-27 supplement, 0.5% GlutaMAX, 0.2 μM compound E, 10 ng ml^{-1} BDNF and 10 ng ml^{-1} NT-3 for 10 days to induce neuronal differentiation. Next, neuron maturation was triggered by feeding the organoids with approximately 8-month-old organoid conditioned medium derived from astrocytes. Astrocytes were differentiated from the human iPS cell WTC11 line and cultured in a medium consisting of DMEM/F12 containing GlutaMAX, sodium bicarbonate, sodium pyruvate, N-2 supplement, B-27 supplement (Gibco), 2 μg ml^{-1} heparin, 10 ng ml^{-1} EGF and 10 ng ml^{-1} FGF2. Neuron organoids were characterized as postmitotic and stained for MAP2 and βIII-tubulin to validate neuronal induction efficiency. After 14 days of neuronal differentiation, HFC/LFC glioma cells labelled with RFP were added to the neuron organoid culture at a ratio of 1:3. Before iNeuron induction, the transgenic human iPS cell line WTC11 was transduced with GFP lentivirus. A Zeiss Cell Observer spinning-disc confocal microscope (Carl Zeiss) fitted with a temperature- and carbon-dioxide-controlled chamber was used to record live interactions of glioma cells with neuron organoids. Organoids were imaged every 10 min for a 6 h period, starting at the time of co-culture initiation, using a 10× objective with 0.4 NA. To assess the effect of exogenous TSP-1 on the functional integration between glioma cells and neurons, human recombinant TSP-1 (R&D Systems) was applied at a dose of 5 μg ml^{-1} to the LFC-neuron organoid co-culture. Live-cell image analyses were performed using ImageJ. In brief, a region of interest was drawn around each GFP-positive neuron organoid and the

fluorescence intensity (integrated density) of the RFP-positive glioblastoma cells was measured in the outlined regions of interest for each of the indicated timepoints. At the end of two weeks, organoids from HFC and LFC co-cultures were embedded in OCT and sectioned at 10 μm thickness for homer-1 immunofluorescence staining. Determination of homer-1 expression was performed by analysing homer-1 puncta density of neuron-organoid-HFC and LFC co-cultures.

MEA recordings

Preparation of MEA plates

We prepared 24-well CytoView multi-electrode plates (Axion Biosystems) before the addition of cells by coating with poly-d-lysine (Thermo Fisher Scientific), laminin (Fisher Scientific) and fibronectin (Corning). In brief, 1 day before the establishment of cultures, a solution of 0.1 mg ml^{-1} of poly-d-lysine was added to the MEA plates at a volume of 100 μl per well and incubated at room temperature for 2 h. After 2 h, poly-d-lysine was aspirated and the plates were washed three times with sterile water, and allowed to air dry in a biosafety cabinet and stored at 4 °C. The next day, the plates were coated with 100 μl of 5 μg ml^{-1} laminin and 1 μg ml^{-1} fibronectin and incubated for 2 h at 37 °C before cell seeding.

Preparation of cortical cultures

Primary cortical cultures were established from E18 CD1 mice (Charles River Laboratories). Timed-pregnant CD1 dams were killed by CO_2 euthanasia in accordance with UCSF Institutional Animal Care and Use Committee (IACUC). Dissection of complete cortex from E18 embryos was performed in ice-cold HBSS (Gibco) under a dissecting microscope (Zeiss). Dissected cortices were minced to 1 mm^2 pieces and enzymatically digested in 5 ml of 0.25% trypsin reconstituted from 2.5% trypsin (Corning) in calcium- and magnesium-free Hank's Balanced Salt Solution (Worthington Biochemical Corporation) for 30 min at 37 °C. Then, 0.5 ml of 10 mg ml^{-1} of DNase (Sigma-Aldrich) was added in the last 5 min of dissociation. Mechanical dissociation was then carried about by trituration using fire-

polished glass Pasteur pipettes until tissue was homogeneously suspended with no visible sections/aggregates and subsequently filtered through a 40 μm cell strainer (Thermo Fisher Scientific). Cells were collected by centrifugation at 500*g* for 5 min and the resulting cell pellet was resuspended in fresh complete BrainPhys culture medium (1× BrainPhys culture medium (StemCell Technologies) supplemented with B27 (Invitrogen), N2 (Invitrogen) and penicillin–streptomycin antibiotics (Invitrogen). Then, 10 μl of cell suspension was mixed 1:1 with Trypan Blue, and the viable cell concentration was quantified using a haemocytometer. Further dilution was performed to bring viable cell concentration to 100,000 cells per 10 μl. Droplets of 10 μl were then added directly over the electrode field of each pretreated MEA well and stored in the cell culture incubator for 1 h to allow cell adhesion. The wells were then carefully flooded with 500 μl complete BrainPhys medium and the cultures were maintained and allowed to mature in a tissue culture incubator with semi-weekly half-volume medium changes.

Recordings of spontaneous neuronal activity and analysis

Spontaneous extracellular neuronal recordings were carried out using the Maestro Edge system with an integrated heating system and temperature controller (Axion Biosystems) in combination with the Axion 24-well CytoView MEA plates (each well housing a 4 × 4 16-channel electrode array that are 350 μm away from each other) and Axion Integrated Studio (AxIS) Navigator (v.3.5.2; Axion Biosystems). In brief, to record spontaneous neuronal activity, the Neural Real-Time module was used. The neuronal firing events/action potentials (herein referred to as the spike) was defined by applying an adaptive threshold crossing method, that sets the threshold for spike detection for each channel/electrode to 5 s.d. of the noise level[79]; activity exceeding this threshold was counted as a spike. Unless otherwise stated, all analysis considers only active channels, defined as channels exhibiting ≥5 spikes per min. Raw data files were obtained by sampling the channels simultaneously with a gain of 1,000× and a sampling frequency of 12.5 kHz per channel using a band-pass filter (200–3,000 Hz). To detect single-electrode bursting activity, an interspike interval threshold was used, setting the minimum number of spikes at 5 and the maximum interspike interval at 100 ms. The network bursting activity (simultaneous bursts at multiple MEA electrodes) was analysed by Neural Metric Tool (v.1.2.3;

Axion Biosystems). For this purpose, the Adaptive algorithm was selected using the following settings: minimum number of spikes = 50 and minimum electrodes = 35%. Quantification of network synchrony was computed through AxIS software by calculating the area under the normalized cross-correlogram (AUNCC) as described previously[80,81,82,83]. AUNCC represents the area under interelectrode cross-correlation normalized to the autocorrelations, with higher values indicating greater synchronicity of the network. For additional neural data analysis, including mean firing rate of each electrode (the ratio of the total number of spikes per second and the total duration of recording (1,800 s)) and weighted mean firing rate (defined as the spike rate per well multiplied by the number of active electrodes in the associated well), raw data files were processed offline using the Statistics Compiler function in AxIS. Statistics Compiler output files were processed in Microsoft Excel (Microsoft) and with custom Python scripts to organize and extract individual parameter data for each well of each MEA plate and for data normalization. Raster plots illustrating spike histogram and network bursts were generated using Neural Metric Tool (Axion Biosystems).

Glioma–neuron co-culture and gabapentin treatment

Spontaneous neuronal activity from cortical cultures grown on MEA plates was recorded in 30 min sessions on days in vitro 1 (DIV1), DIV7 and DIV15. Bright-field images were captured at each of the above timepoints to assess the neuronal cell density and electrode coverage. Primary cortical neurons showed a constant maturation trend from DIV7 to DIV15, and the co-culture experiments were initiated when neurons showed a synchronous activity pattern network at DIV15. Baseline data were therefore recorded on DIV15 immediately before addition of glioma cells in the presence or absence of gabapentin. For glioma cell co-culture, a single-cell suspension from cultured neurospheres of primary patient-derived HFC and LFC were prepared and diluted to a viable cell concentration of 20,000 cells per 5 µl. Droplets of 5 µl were then plated on top of differentiating neurons in the MEA plate. After plating, glioma cells were allowed to adhere for approximately 1 h after which HFC cultures were exposed for next 24–48 h to a working concentration of 50 µM gabapentin[84,85] diluted in complete BrainPhys medium or an equivalent amount of vehicle (sterile water) as a control. Each condition was run on two wells (experimental replicates).

Neurons from two different embryos were used as biological triplicates (n = 2). Presented data from MEA recordings reflects well-wide averages from active electrodes, with the number of wells per condition represented by n values.

Mice and housing conditions

All in vivo experiments were conducted in accordance with the protocols approved by the UCSF Institutional Animal Care and Use Committee (IACUC) and performed in accordance with institutional guidelines. Animals were maintained under pathogen-free conditions, in temperature- and humidity-controlled housing, with free access to food and water, under a 12 h–12 h light–dark cycle. For brain tumour xenograft experiments, the IACUC does not set a limit on maximal tumour volume but rather on indications of morbidity. These limits were not exceeded in any of the experiments as mice were euthanized if they exhibited signs of neurological morbidity or lost 15% or more of their body weight.

Orthotopic xenografting for neuronal circuit integration and mouse survival experiments

For all xenograft studies, NSG mice (NOD-SCID-IL2R gamma chain-deficient, The Jackson Laboratory) were used. Male and female mice were used equally. For immuno-electron microscopy experiments, a single-cell suspension from cultured neurospheres of HFC and LFC (n = 2 each) labelled with red fluorescent protein (RFP) were prepared in sterile DMEM immediately before the xenograft procedure. Mice (n = 8; 2 biological replicates per patient line) at postnatal day 28–30 were anaesthetized with 1–4% isoflurane and placed into a stereotactic apparatus. The cranium was exposed through a midline incision under aseptic conditions. Approximately 50,000 cells in 2 μl sterile PBS were stereotactically implanted into the CA1 region of the hippocampus through a 31-gauge burr hole, using a digital pump at infusion rate of 0.4 $\mu l\ min^{-1}$ and 31-gauge Hamilton syringe. Stereotactic coordinates used were as follows: 1.5 mm lateral to midline, 1.8 mm posterior to bregma, −1.4 mm deep to cranial surface. At the completion of infusion, the syringe needle was allowed to remain in place for a minimum of 2 min, then manually withdrawn at a rate of 0.875 $mm\ min^{-1}$ to

minimize backflow of the injected cell suspension. For survival studies, morbidity criteria used were either: reduction of weight by 15% initial weight, or clinical signs such as hunched posture, lethargy or persistent decumbency. Kaplan–Meier survival analysis using log-rank testing was performed to determine statistical significance.

Quantification of tumour cell burden

Cell quantification was performed by a blinded investigator at 10–20× magnification using the Zeiss LSM800 scanning confocal microscope and Zen 2011 imaging software (Carl Zeiss). The area for quantification was selected for a 1-in-6 series of 40 µm coronal sections (240 µm apart from one another). Immunohistochemistry was performed on brain sections from HFC and LFC xenografts to stain for human nuclear antigen (HNA)-positive tumour cells. The tumour burden was evaluated using blinded rank-order analysis as previously reported[86]. For each mouse, the section with the maximal amount of tumour burden was selected as defined by the number of HNA-positive cells. From this section, a tiled ×10 image of the centre of the section (3 × 3 tiles stitched together) was created, therefore generating a single image for each mouse that represents the maximal amount of tumour burden. Next, the images generated from each mouse were compared and ranked in order from the image with the least to maximum number of cells. Subsequently, scores were assigned and ranged from 1 to 24 with 1 and 24 representing images with the lowest and highest number of HNA-positive cells, respectively. After scoring, the experimenter was unblinded and the scores from each image were assigned to each of the respective HFC or LFC experimental conditions. Statistical differences between HFC and LFC scores were evaluated using two-tailed unpaired Mann–Whitney tests.

Sample preparation and image acquisition for electron microscopy

Twelve weeks after xenografting, mice were euthanized by transcardial perfusion with Karnovsky's fixative: 2% glutaraldehyde (EMS, 16000) and 4% PFA (EMS, 15700) in 0.1 M sodium cacodylate (EMS, 12300), pH 7.4. Transmission electron microscopy (TEM) was performed in the tumour mass within the CA1 region of the hippocampus for all xenograft analysis.

The samples were then post-fixed in 1% osmium tetroxide (EMS, 19100) for 1 h at 4 °C, washed three times with ultrafiltered water, then en bloc stained overnight at 4 °C. The samples were dehydrated in graded ethanol (50%, 75% and 95%) for 15 min each at 4 °C; the samples were then allowed to equilibrate to room temperature and were rinsed in 100% ethanol twice, followed by acetonitrile for 15 min. The samples were infiltrated with EMbed-812 resin (EMS, 14120) mixed 1:1 with acetonitrile for 2 h followed by 2:1 EMbed-812:acetonitrile overnight. The samples were then placed into EMbed-812 for 2 h, then placed into TAAB capsules filled with fresh resin, which were then placed into a 65 °C oven overnight. Sections were taken between 40 nm and 60 nm on a Leica Ultracut S (Leica) and mounted on 100-mesh Ni grids (EMS FCF100-Ni). For immunohistochemistry, microetching was done with 10% periodic acid and eluting of osmium with 10% sodium metaperiodate for 15 min at room temperature on parafilm. Grids were rinsed with water three times, followed by 0.5 M glycine quench, and then incubated in blocking solution (0.5% BSA, 0.5% ovalbumin in PBST) at room temperature for 20 min. Primary goat anti-RFP (1: 300, ABIN6254205) was diluted in the same blocking solution and incubated overnight at 4 °C. The next day, grids were rinsed in PBS three times, and incubated in secondary antibodies (1:10 10 nm gold-conjugated IgG, TED Pella, 15796) for 1 h at room temperature and rinsed with PBST followed by water. For each staining set, samples that did not contain any RFP-expressing cells were stained simultaneously to control for any non-specific binding. Grids were contrast stained for 30 s in 3.5% uranyl acetate in 50% acetone followed by staining in 0.2% lead citrate for 90 s. The samples were imaged using a JEOL JEM-1400 TEM at 120 kV and images were collected using a Gatan Orius digital camera.

Electron microscopy data analysis

Sections from the xenografted hippocampi of mice were imaged as above using TEM imaging. Here 101 sections of HFC xenografts across 4 mice and 104 sections of LFC xenografts across 3 mice were analysed. Electron microscopy images were taken at ×6,000 with a field of view of 15.75 μm^2. Glioma cells were counted and analysed after unequivocal identification of a cluster of immunogold particle labelling with 15 or more particles. The total number of synapses, including neuron-to-neuron and neuron-to-glioma

synapses (identified by: (1) the presence of synaptic vesicle clusters; (2) visually apparent synaptic cleft; and (3) identification of clear postsynaptic density in the glioma cell) were counted.

EdU assay

The EdU-incorporation assay was performed using an EdU assay kit (Invitrogen) according to the manufacturer's instructions. Patient-derived HFC/LFC glioma cells were seeded on poly-d-lysine- and laminin-coated coverslips at 10,000 cells per well of a 24-well plate. After 24 h of seeding, embryonic mouse hippocampal neurons were added to the glioma cells at 40,000 cells per well for the glioma-neuron co-culture group. After 72 h, glioma cells alone or in coculture with neurons were treated with 20 µM EdU overnight at 37 °C. Subsequently, the cells were fixed with 4% PFA and stained using the Click-iT EdU kit protocol. The proliferation index was then determined by quantifying the fraction of EdU-labelled cells/DAPI-labelled cells using confocal microscopy at ×10 magnification.

3D spheroid invasion assay

Glioma cell invasion was evaluated by performing an invasion assay using the Cultrex 3D Spheroid Cell Invasion Assay Kit (Trevigen) according to the manufacturer's protocol. In brief, 3,000 cells were resuspended in 50 µl of spheroid formation matrix solution (prepared in culture medium) in a round-bottom 96-well plate. Spheroids were allowed to form for 72 h and images were taken at ×10 magnification before addition of invasion matrix (0 h). Working on ice, 50 µl of invasion matrix was then added to each well and the plate was incubated at 37 °C. After 1 h of gel formation, for the glioma cell + mouse conditioned medium (mCM) group, 100 µl of mouse hippocampal neuron supernatant was added to the wells to assess the effect of neuronal secreted factors on the invasiveness of the glioma cells. After 24 h of incubation at 37 °C, invasions were observed under a microscope and images were taken at ×10. Microtube lengths as well as the area of each spheroid measured at 0 h (pre-invasion) and 24 h (post-invasion) were analysed using ImageJ and the difference was used to calculate the total area of cell invasion.

SEM analysis

SEM was performed as described previously[39] to investigate the tumour microtubes in greater detail. Primary patient-derived HFC/LFC glioma cells were seeded on poly-d-lysine- and laminin-coated coverslips (Neuvitro) at 10,000 cells per well of a 24-well plate. For the glioma cell + mCM and glioma cell + mCM + GBP groups, mouse neuronal conditioned medium was added to the wells in the absence or presence of gabapentin (32 μM), respectively, to assess the effect of neuronal secreted factors and gabapentin modulation on tumour microtube formation of glioma cells[47,87,88]. After culture for 1 week, the samples were fixed with 4% PFA for 30 min at 4 °C, washed with PBS and ultrafiltered water. After serial stepwise ethanol dehydration, coverslips were mounted on SEM stubs (TED Pella) using conductive adhesive tape (12 mm OD PELCO Tabs, TED Pella). The samples were then sputter-coated with a 2 nm layer of gold palladium. Tumour microtubes were observed under field emission SEM (Sigma 500; Carl Zeiss Microscopy) and micrographs were recorded at an accelerating voltage of 1.0 kV.

THBS1 shRNA knockdown

Primary patient-derived HFC glioma cells were seeded in 6-well plates at a density of 2×10^5 cells per well. After overnight incubation, cells were infected with lentiviral particles expressing a shRNA targeting *THBS1* or a control scramble construct expressing green fluorescent protein (GFP) according to the manufacturer's protocol using polybrene transfection reagent and subsequently kept in a 5% CO_2 incubator at 37 °C for 24 h. After 24 h, the medium was replaced with fresh complete culture medium. Cells were checked 72 h after transduction for GFP expression to evaluate the efficiency of the transduction. The lentiviral shRNA constructs targeting *THBS1* (5′-AGACATCTTCCAAGCATATAA-3′) and control scrambled shRNA (5′-CCTAAGGTTAAGTCGCCCTCG-3′) were designed and constructed by VectorBuilder.

Cell viability assay

The cell viability of primary patient-derived HFC cells after *THBS1* knockdown was evaluated using the Live/Dead Viability/Cytotoxicity kit (Molecular Probes). One-week after transduction, HFC cells expressing scramble shRNA or shRNA targeting *THBS1* were seeded on poly-d-lysine- and laminin-coated coverslips (Neuvitro) at 10,000 cells per well of a 24-well plate. After 1 week of culture, a 500 μl cell-staining solution at a final concentration of 2 μM calcein AM and 4 μM ethidium bromide (EthD-1) in DPBS was added to each well, and the plates were incubated for 45 min at room temperature in dark. As an indicator of cell viability, the calcein-AM is metabolically converted by intracellular esterase activity resulting in the green, fluorescent product, calcein. EthD-1 is excluded from live cells but is readily taken up by dead cells and stains the DNA emitting red fluorescence. Live and dead cells were imaged from four random fields per well and were visualized under a fluorescence microscope. The percentage of live cells was calculated as the number of live cells (in green) divided by the number of total cells (green + red) per image field.

In vitro cell proliferation assessment after *THBS1* shRNA knockdown

After 1 week of transduction, primary patient-derived high connectivity glioma cells expressing scramble shRNA or shRNA against *THBS1* were seeded on poly-d-lysine- and laminin-coated coverslips (Neuvitro) at 10,000 cells per well of a 24-well plate. Approximately 24 h later, 40,000 embryonic mouse hippocampal neurons (Gibco) were seeded on top of the glioma cells and maintained with serum-free Neurobasal medium supplemented with B27, gentamicin and GlutaMAX (Gibco). After 1 week of co-culture, cells were fixed with 4% PFA for 30 min at 4 °C and incubated in blocking solution (5% normal donkey and goat serum, 0.25% Triton X-100 in PBS) at room temperature for 1 h. Next, cells were treated with primary antibodies diluted in the blocking solutions overnight at 4 °C. The following antibodies were used: rabbit anti-Ki-67 (1:500, Abcam) and human nuclear antigen (HNA; mouse anti-human nuclei, 235-1; 1:100, Millipore). The coverslips were then rinsed three times in PBS and incubated in secondary antibody solution (Alexa 488 goat anti-rabbit IgG, and Alexa 647 goat anti-mouse IgG) all used at 1:500 (Invitrogen) in antibody diluent solution for 1 h at room temperature. The coverslips were

rinsed three times in PBS and then mounted with VECTA antifade mounting medium with DAPI (Vector Laboratories). To calculate the proliferation index, the total number of HNA-positive cells co-labelled with Ki-67 was divided by the total number of human nuclei-labelled cells per image field visualized using confocal microscopy at ×40 magnification.

In vitro cell proliferation assessment after pharmacological inhibition of TSP-1 by gabapentin

The effect of TSP-1 inhibition by gabapentin on glioma cell proliferation was evaluated by Ki-67 immunofluorescence staining, as described above. In brief, primary patient-derived high connectivity glioma cells were seeded on poly-d-lysine- and laminin-coated coverslips (Neuvitro) at 10,000 cells per well of a 24-well plate. Approximately 24 h later, 40,000 embryonic mouse hippocampal neurons (Gibco) were seeded on top of the glioma cells and maintained with serum-free Neurobasal medium supplemented with B27, gentamicin and GlutaMAX (Gibco). The next day, cultures were treated either with vehicle (sterile water) or 32 μM gabapentin followed by daily half-medium switches of fresh 32 μM gabapentin until 1 week of coculture[88]. Subsequently, cells were fixed and immunostained for Ki-67 and HNA labelling for proliferation assessment as described above.

Orthotopic xenografting for proliferation assessment and pharmacological inhibition of TSP-1 by gabapentin

A single-cell suspension from cultured neurospheres of primary patient-derived HFC and LFC were prepared in sterile HBSS immediately before the xenograft procedure by dissociation with TrypLE (Thermo Fisher Scientific). Mice (4–6 biological replicates per patient line) at postnatal day 28–30 were anaesthetized with 1–4% isoflurane and placed into a stereotactic apparatus. The cranium was exposed through midline incision under aseptic conditions. Approximately 150,000 cells in 3 μl sterile HBSS were stereotactically implanted into the premotor cortex (M2) through a 26-gauge burr hole, using a digital pump at infusion rate of 1.0 $\mu l\ min^{-1}$. Stereotactic coordinates used were as follows: 1.0 mm lateral to midline, 1.0 mm anterior to bregma, −1.0 mm deep to cortical surface. Four weeks after xenograft, HFC/LFC-bearing mice were treated with systemic

administration of gabapentin (200 mg kg^{-1}; Sigma-Aldrich; formulated in saline) through intraperitoneal injection for 28 consecutive days. Controls were treated with an identical volume of the relevant vehicle. At 8 weeks after xenograft, mice were euthanized and coronal brain sections at 40 µm were obtained for immunohistochemistry.

Confocal imaging and quantification of tumour burden and cell proliferation

Cell quantification was performed by a blinded investigator at ×10–20 magnification using the Zeiss LSM800 scanning confocal microscope and Zen imaging software (Carl Zeiss). The area for quantification was selected for a 1-in-6 series of 40 µm coronal sections (240 µm apart from one another). Within 3 sections of maximal tumour burden, all HNA-positive (mouse anti-human nuclei, 235-1; 1:100, Millipore) cells were quantified to determine the tumour burden within the areas quantified. HNA-positive tumour cells were then assessed for double-labelling with Ki-67. To calculate the proliferation index (the percentage of proliferating tumour cells for each animal), the total number of HNA-positive cells co-labelled with Ki-67 across all areas quantified was divided by the total number of human nuclei-positive cells counted across all areas quantified. Differences in proliferation indices were calculated using unpaired, one-tailed Student's *t*-tests.

ELISA

Peripheral blood samples from newly diagnosed patients with glioblastoma ($n = 56$) were collected and allowed to clot for 30 min at room temperature before centrifugation for 15 min at 1,000*g*. The serum was stored at −80 °C until analysis. The TSP-1 level was determined using the Quantikine immunosorbent assay kits according to the manufacturer's instructions (R&D Systems). To confirm the functional protein-level knockdown of *THBS1*, the TSP-1 level was also measured in cell culture supernatants collected from scramble and *THBS1*-shRNA transduced HFC cells (collected one-week after infection) using the Picokine ELISA kit (Boster Biological Technology).

Statistics and reproducibility

Statistical tests were conducted using Prism (GraphPad) software unless otherwise indicated. The significance test of different groups was determined using Student's *t*-tests and one-way ANOVA with Tukey's post hoc tests. $P \leq 0.05$ was considered to be statistically significant. Two-tailed unpaired Mann–Whitney tests were used to analyse the tumour cell burden of HFC and LFC hippocampal xenografts using the same significance denotation as above. Two-tailed log-rank analyses were used to analyse the statistical significance of Kaplan–Meier survival curves for human patients. All of the micrographs shown are representative of three independently conducted experiments, with similar results obtained. Statistical analyses for RNA-seq data are described above in the respective sections. The tumour volumes of patients with glioblastoma were calculated by manual segmentation with region-of-interest analysis 'painting' inclusion regions on the basis of FLAIR sequences. Volumetric measurements were made blinded to patients' clinical outcomes. Manual segmentations were performed by co-authors A.E., A.A. and A.L. with tumour volumetrics verified for accuracy after an initial training period. Student's *t*-tests and χ^2 tests were used to compare continuous and categorical variables between patient cohorts, respectively. Patient overall survival (OS) was defined as the time from the date of first surgery or original biopsy (if it occurred before surgery) until death or the last contact date. Alive patients were censored at the time of loss to follow-up or last follow-up date. Median follow-up was estimated using the reverse Kaplan–Meier method.

To identify clinically relevant survival risk groups in a multivariate setting, we used recursive partitioning analyses for survival data using the partDSA algorithm (v.0.9.14)[42,43,44]. Survival trees use recursive partitioning to divide patients into different risk groups. The Brier score was the chosen loss function for splitting and pruning. Such methods are nonparametric and, therefore, do not require the proportional hazards assumption. All known prognostic variables were included in the trees, including age at diagnosis, sex, MGMT promoter methylation status, tumour location, chemotherapy, radiotherapy, the presence of functional connectivity within the tumour, pre- and post-operative tumour volume and the extent of

resection. MGMT methylation status was included in both univariate Cox proportional-hazard modelling in addition to multivariate recursive partitioning survival analysis. The tree that minimized the fivefold cross-validated error as well as the most parsimonious tree within one standard error of the overall minimum error were selected for review. Leaves of the resulting trees defined the final risk groups from which the corresponding Kaplan–Meier curves were generated. Median OS times and hazard ratios were generated and compared between risk groups using the Kaplan–Meier method and the Cox proportional hazards model, respectively. The proportional hazards assumption was verified.

Reporting summary

Further information on research design is available in the Nature Portfolio Reporting Summary linked to this article.

Data availability

Bulk and single-cell RNA-seq data of primary patient-derived samples reported in this manuscript have been deposited at the NCBI Gene Expression Omnibus under the accession code GSE223065. The publicly available GRCh38 (hg38; https://www.ncbi.nlm.nih.gov/assembly/GCF_000001405.39/) was used in this study. Source data are provided with this paper.

References

1. Venkataramani, V. et al. Glutamatergic synaptic input to glioma cells drives brain tumour progression. *Nature* **573**, 532–538 (2019).

2. Venkatesh, H. S. et al. Electrical and synaptic integration of glioma into neural circuits. *Nature* **573**, 539–545 (2019).

3. Venkatesh, H. S. et al. Neuronal activity promotes glioma growth through neuroligin-3 secretion. *Cell* **161**, 803–816 (2015).

4. Venkatesh, H. S. et al. Targeting neuronal activity-regulated neuroligin-3 dependency in high-grade glioma. *Nature* **549**, 533–537 (2017).

5. Buckingham, S. C. et al. Glutamate release by primary brain tumors induces epileptic activity. *Nat. Med.* **17**, 1269–1274 (2011).

6. Campbell, S. L., Buckingham, S. C. & Sontheimer, H. Human glioma cells induce hyperexcitability in cortical networks. *Epilepsia* **53**, 1360–1370 (2012).

7. Campbell, S. L. et al. GABAergic disinhibition and impaired KCC2 cotransporter activity underlie tumor-associated epilepsy. *Glia* **63**, 23–36 (2015).

8. John Lin, C. C. et al. Identification of diverse astrocyte populations and their malignant analogs. *Nat. Neurosci.* **20**, 396–405 (2017).

9. Aabedi, A. A. et al. Functional alterations in cortical processing of speech in glioma-infiltrated cortex. *Proc. Natl Acad. Sci. USA* **118**, e2108959118 (2021).

10. Dalrymple, S. J. et al. Changes in proliferating cell nuclear antigen expression in glioblastoma multiforme cells along a stereotactic biopsy trajectory. *Neurosurgery* **35**, 1036–1044 (1994).

11. Hadjiabadi, D. H. et al. Brain tumors disrupt the resting-state connectome. *Neuroimage Clin.* **18**, 279–289 (2018).

12. Krishna, S. & Hervey-Jumper, S. L. Neural regulation of cancer: cancer-induced remodeling of the central nervous system. *Adv. Biol.* **6**, e2200047 (2022).

13. Stoecklein, V. M. et al. Resting-state fMRI detects alterations in whole brain connectivity related to tumor biology in glioma patients. *Neuro Oncol.* **22**, 1388–1398 (2020).

14. Crone, N. E., Boatman, D., Gordon, B. & Hao, L. Induced electrocorticographic gamma activity during auditory perception. *Clin. Neurophysiol.* **112**, 565–582 (2001).

15. Steinschneider, M., Fishman, Y. I. & Arezzo, J. C. Spectrotemporal analysis of evoked and induced electroencephalographic responses in primary auditory cortex (A1) of the awake monkey. *Cereb. Cortex* **18**, 610–625 (2008).

16. Yizhar, O. et al. Neocortical excitation/inhibition balance in information processing and social dysfunction. *Nature* **477**, 171–178 (2011).

17. Aabedi, A. A. & Hervey-Jumper, S. Convergence of heteromodal lexical retrieval in the lateral prefrontal cortex. *Sci. Rep.* **11**, 6305 (2020).

18. Chang, E. F. et al. Cortical spatio-temporal dynamics underlying phonological target detection in humans. *J. Cogn. Neurosci.* **23**, 1437–1446 (2011).

19. Romanski, L. M. et al. Dual streams of auditory afferents target multiple domains in the primate prefrontal cortex. *Nat. Neurosci.* **2**, 1131–1136 (1999).

20. Chartier, J., Anumanchipalli, G. K., Johnson, K. & Chang, E. F. Encoding of articulatory kinematic trajectories in human speech sensorimotor cortex. *Neuron* **98**, 1042–1054 (2018).

21. Criss, A. H., Aue, W. R. & Smith, L. The effects of word frequency and context variability in cued recall. *J. Mem. Lang.* **64**, 119–132 (2011).

22. Bhaduri, A. et al. Outer radial glia-like cancer stem cells contribute to heterogeneity of glioblastoma. *Cell Stem Cell* **26**, 48–63 (2020).

23. Neftel, C. et al. An integrative model of cellular states, plasticity, and genetics for glioblastoma. *Cell* **178**, 835–849 (2019).

24. Tirosh, I. & Suva, M. L. Tackling the many facets of glioblastoma heterogeneity. *Cell Stem Cell* **26**, 303–304 (2020).

25. Yu, K. et al. PIK3CA variants selectively initiate brain hyperactivity during gliomagenesis. *Nature* **578**, 166–171 (2020).

26. Guggisberg, A. G. et al. Mapping functional connectivity in patients with brain lesions. *Ann. Neurol.* **63**, 193–203 (2008).

27. Lee, A. T. et al. The impact of high functional connectivity network hub resection on language task performance in adult low- and high-grade glioma. *J. Neurosurg.* https://doi.org/10.3171/2020.1.JNS192267 (2020).

28. Nolte, G. et al. Identifying true brain interaction from EEG data using the imaginary part of coherency. *Clin. Neurophysiol.* **115**, 2292–2307 (2004).

29. Brookes, M. J. et al. Measuring functional connectivity using MEG: methodology and comparison with fcMRI. *Neuroimage* **56**, 1082–1104 (2011).

30. Tarapore, P. E. et al. Magnetoencephalographic imaging of resting-state functional connectivity predicts postsurgical neurological outcome in brain gliomas. *Neurosurgery* **71**, 1012–1022 (2012).

31. Tarapore, P. E. et al. Preoperative multimodal motor mapping: a comparison of magnetoencephalography imaging, navigated transcranial magnetic stimulation, and direct cortical stimulation. *J. Neurosurg.* **117**, 354–362 (2012).

32. Christopherson, K. S. et al. Thrombospondins are astrocyte-secreted proteins that promote CNS synaptogenesis. *Cell* **120**, 421–433 (2005).

33. Daubon, T. et al. Deciphering the complex role of thrombospondin-1 in glioblastoma development. *Nat. Commun.* **10**, 1146 (2019).

34. Jeanne, A., Schneider, C., Martiny, L. & Dedieu, S. Original insights on thrombospondin-1-related antireceptor strategies in cancer. *Front. Pharmacol.* **6**, 252 (2015).

35. Allen, N. J. & Eroglu, C. Cell biology of astrocyte-synapse interactions. *Neuron* **96**, 697–708 (2017).

36. Bushong, E. A., Martone, M. E., Jones, Y. Z. & Ellisman, M. H. Protoplasmic astrocytes in CA1 stratum radiatum occupy separate anatomical domains. *J. Neurosci.* **22**, 183–192 (2002).

37. Oberheim, N. A. et al. Uniquely hominid features of adult human astrocytes. *J. Neurosci.* **29**, 3276–3287 (2009).

38. Fernandopulle, M. S. et al. Transcription factor-mediated differentiation of human iPSCs into neurons. *Curr. Protoc. Cell Biol.* **79**, e51 (2018).

39. Joseph, J. V. et al. TGF-β promotes microtube formation in glioblastoma through thrombospondin 1. *Neuro Oncol.* **24**, 541–553 (2022).

40. Jung, E. et al. Tweety-homolog 1 drives brain colonization of gliomas. *J. Neurosci.* **37**, 6837–6850 (2017).

41. Osswald, M. et al. Brain tumour cells interconnect to a functional and resistant network. *Nature* **528**, 93–98 (2015).

42. Molinaro, A. M. et al. Association of maximal extent of resection of contrast-enhanced and non-contrast-enhanced tumor with survival within molecular subgroups of patients with newly diagnosed glioblastoma. *JAMA Oncol.* **6**, 495–503 (2020).

43. Lostritto, K., Strawderman, R. L. & Molinaro, A. M. A partitioning deletion/substitution/addition algorithm for creating survival risk groups. *Biometrics* **68**, 1146–1156 (2012).

44. Molinaro, A. M., Lostritto, K. & van der Laan, M. partDSA: deletion/substitution/addition algorithm for partitioning the covariate space in prediction. *Bioinformatics* **26**, 1357–1363 (2010).

45. Bell, B. D., Seidenberg, M., Hermann, B. P. & Douville, K. Visual and auditory naming in patients with left or bilateral temporal lobe epilepsy. *Epilepsy Res.* **55**, 29–37 (2003).

46. Hamberger, M. J., McClelland, S. 3rd, McKhann, G. M. 2nd, Williams, A. C. & Goodman, R. R. Distribution of auditory and visual naming sites in nonlesional temporal lobe epilepsy patients and patients with space-occupying temporal lobe lesions. *Epilepsia* **48**, 531–538 (2007).

47. Eroglu, C. et al. Gabapentin receptor α2δ-1 is a neuronal thrombospondin receptor responsible for excitatory CNS synaptogenesis. *Cell* **139**, 380–392 (2009).

48. Pan, Y. et al. NF1 mutation drives neuronal activity-dependent initiation of optic glioma. *Nature* **594**, 277–282 (2021).

49. Belgers, V. et al. Postoperative oscillatory brain activity as an add-on prognostic marker in diffuse glioma. *J. Neurooncol.* **147**, 49–58 (2020).

50. Daniel, A. G. S. et al. Functional connectivity within glioblastoma impacts overall survival. *Neuro. Oncol.* **23**, 412–421 (2020).

51. Derks, J. et al. Oscillatory brain activity associates with neuroligin-3 expression and predicts progression free survival in patients with diffuse glioma. *J. Neurooncol.* **140**, 403–412 (2018).

52. Venkataramani, V. et al. Glioblastoma hijacks neuronal mechanisms for brain invasion. *Cell* **185**, 2899–2917 (2022).

53. Delorme, A. & Makeig, S. EEGLAB: an open source toolbox for analysis of single-trial EEG dynamics including independent component analysis. *J. Neurosci. Methods* **134**, 9–21 (2004).

54. Dalal, S. S. et al. Five-dimensional neuroimaging: localization of the time-frequency dynamics of cortical activity. *Neuroimage* **40**, 1686–1700 (2008).

55. Aabedi, A. A. *et al*. Assessment of wakefulness during awake craniotomy to predict intraoperative language performance. *J. Neurosurg.* https://doi.org/10.3171/2019.2.JNS183486 (2019).

56. Chang, E. F., Raygor, K. P. & Berger, M. S. Contemporary model of language organization: an overview for neurosurgeons. *J. Neurosurg.* **122**, 250–261 (2015).

57. Rolls, E. T., Huang, C. C., Lin, C. P., Feng, J. & Joliot, M. Automated Anatomical Labelling Atlas 3. *Neuroimage* **206**, 116189 (2020).

58. Hinkley, L. B. et al. Cognitive impairments in schizophrenia as assessed through activation and connectivity measures of magnetoencephalography (MEG) data. *Front. Hum. Neurosci.* **3**, 73 (2010).

59. Wipf, D. & Nagarajan, S. A unified Bayesian framework for MEG/EEG source imaging. *Neuroimage* **44**, 947–966 (2009).

60. Vrba, J. & Robinson, S. E. Signal processing in magnetoencephalography. *Methods* **25**, 249–271 (2001).

61. Sekihara, K., Hild, K. E. 2nd & Nagarajan, S. S. A novel adaptive beamformer for MEG source reconstruction effective when large background brain activities exist. *IEEE Trans. Biomed. Eng.* **53**, 1755–1764 (2006).

62. Donoghue, T. et al. Parameterizing neural power spectra into periodic and aperiodic components. *Nat. Neurosci.* **23**, 1655–1665 (2020).

63. Emerton, B. C., Gansler, D. A., Sandberg, E. H. & Jerram, M. Functional anatomic dissociation of description and picture naming in the left temporal lobe. *Brain Imaging Behav.* **8**, 570–578 (2014).

64. Hamberger, M. J., Seidel, W. T., Goodman, R. R., Perrine, K. & McKhann, G. M. Temporal lobe stimulation reveals anatomic distinction between auditory naming processes. *Neurology* **60**, 1478–1483 (2003).

65. Wilson, S. M., Eriksson, D. K., Schneck, S. M. & Lucanie, J. M. A quick aphasia battery for efficient, reliable, and multidimensional assessment of language function. *PLoS ONE* **13**, e0192773 (2018).

66. Bolger, A. M., Lohse, M. & Usadel, B. Trimmomatic: a flexible trimmer for Illumina sequence data. *Bioinformatics* **30**, 2114–2120 (2014).

67. Schneider, V. A. et al. Evaluation of GRCh38 and de novo haploid genome assemblies demonstrates the enduring quality of the reference assembly. *Genome Res.* **27**, 849–864 (2017).

68. Kim, D., Paggi, J. M., Park, C., Bennett, C. & Salzberg, S. L. Graph-based genome alignment and genotyping with HISAT2 and HISAT-genotype. *Nat. Biotechnol.* **37**, 907–915 (2019).

69. Liao, Y., Smyth, G. K. & Shi, W. featureCounts: an efficient general purpose program for assigning sequence reads to genomic features. *Bioinformatics* **30**, 923–930 (2014).

70. Love, M. I., Huber, W. & Anders, S. Moderated estimation of fold change and dispersion for RNA-seq data with DESeq2. *Genome Biol.* **15**, 550 (2014).

71. Zhu, A., Ibrahim, J. G. & Love, M. I. Heavy-tailed prior distributions for sequence count data: removing the noise and preserving large differences. *Bioinformatics* **35**, 2084–2092 (2019).

72. Bakken, T. E. et al. Single-nucleus and single-cell transcriptomes compared in matched cortical cell types. *PLoS ONE* **13**, e0209648 (2018).

73. Couturier, C. P. et al. Single-cell RNA-seq reveals that glioblastoma recapitulates a normal neurodevelopmental hierarchy. *Nat. Commun.* **11**, 3406 (2020).

74. Butler, A., Hoffman, P., Smibert, P., Papalexi, E. & Satija, R. Integrating single-cell transcriptomic data across different conditions, technologies, and species. *Nat. Biotechnol.* **36**, 411–420 (2018).

75. Stuart, T. et al. Comprehensive integration of single-cell data. *Cell* **177**, 1888–1902 (2019).

76. Hafemeister, C. & Satija, R. Normalization and variance stabilization of single-cell RNA-seq data using regularized negative binomial regression. *Genome Biol.* **20**, 296 (2019).

77. Korsunsky, I. et al. Fast, sensitive and accurate integration of single-cell data with Harmony. *Nat. Methods* **16**, 1289–1296 (2019).

78. Krencik, R. et al. Systematic three-dimensional coculture rapidly recapitulates interactions between human neurons and astrocytes. *Stem Cell Rep.* **9**, 1745–1753 (2017).

79. Eisenman, L. N., Emnett, C. M., Mohan, J., Zorumski, C. F. & Mennerick, S. Quantification of bursting and synchrony in cultured hippocampal neurons. *J. Neurophysiol.* **114**, 1059–1071 (2015).

80. Eggermont, J. J. Properties of correlated neural activity clusters in cat auditory cortex resemble those of neural assemblies. *J. Neurophysiol.* **96**, 746–764 (2006).

81. Passaro, A. P., Aydin, O., Saif, M. T. A. & Stice, S. L. Development of an objective index, neural activity score (NAS), reveals neural network ontogeny and treatment effects on microelectrode arrays. *Sci. Rep.* **11**, 9110 (2021).

82. Pastore, V. P., Massobrio, P., Godjoski, A. & Martinoia, S. Identification of excitatory-inhibitory links and network topology in

large-scale neuronal assemblies from multi-electrode recordings. *PLoS Comput. Biol.* **14**, e1006381 (2018).

83. Ullo, S. et al. Functional connectivity estimation over large networks at cellular resolution based on electrophysiological recordings and structural prior. *Front. Neuroanat.* **8**, 137 (2014).

84. Cheng, J. K. & Chiou, L. C. Mechanisms of the antinociceptive action of gabapentin. *J. Pharmacol. Sci.* **100**, 471–486 (2006).

85. Roberto, M. et al. Cellular and behavioral interactions of gabapentin with alcohol dependence. *J. Neurosci.* **28**, 5762–5771 (2008).

86. Keough, M. B. et al. An inhibitor of chondroitin sulfate proteoglycan synthesis promotes central nervous system remyelination. *Nat. Commun.* **7**, 11312 (2016).

87. Cheng, C., Lau, S. K. & Doering, L. C. Astrocyte-secreted thrombospondin-1 modulates synapse and spine defects in the fragile X mouse model. *Mol. Brain* **9**, 74 (2016).

88. Crawford, D. C., Jiang, X., Taylor, A. & Mennerick, S. Astrocyte-derived thrombospondins mediate the development of hippocampal presynaptic plasticity in vitro. *J. Neurosci.* **32**, 13100–13110 (2012).

Acknowledgements

This study was supported by NIH grants K08NS110919 and P50CA097257; Robert Wood Johnson Foundation grant 74259; the UCSF LoGlio Collective and Resonance Philanthropies; and U19 CA264339, Tom Paquin Brain Cancer Research Fund to S.L.H.-J.; the Sullivan Brain Cancer Fund to S. Krishna; NIH grants F30CA246808 and T32GM007618 to A.C.; NIH grant K99CA252001 to H.S.V.; NIH grant R01NS100440 to S.N.; NIH grant R00DC013828 to D.B.; NIH grants R01NS092597, DP1NS111132, P50CA165962, R01CA258384, R01CA263500 and U19CA264504, a Robert J. Kleberg Jr and Helen C. Kleberg Foundation grant and funding from Cancer Research UK to M.M.;

American Brain Tumour Association grant MSSF1900021 and Lucien Rubinstein Award to N.A.; and the UCSF Physician Scientist Scholar Program, the UCSF Wolfe Meningioma Program Project, NIH grant K08CA212279 to D.R.R. We thank J. Phillips, A. Shai and the staff of the UCSF Brain Tumour Center Biorepository and Pathology Core; the staff within the Biological Imaging Development CoLab (BIDC) at UCSF for confocal microscopy and Imaris software support; T. Ozawa and R. Santos of the UCSF Brain Tumour Center Preclinical Therapeutics Core; N. Jumper for proofreading; and K. Probst for illustrations.

Author information

Authors and Affiliations

1. Department of Neurological Surgery, University of California, San Francisco, San Francisco, CA, USA

   Saritha Krishna, Abrar Choudhury, Kyounghee Seo, Sofia Kakaizada, Anthony Lee, Alexander Aabedi, Galina Popova, Caroline Cao, Cesar Nava Gonzales, Rasika Sudharshan, Andrew Egladyous, Nyle Almeida, Yalan Zhang, Annette M. Molinaro, Andy G. S. Daniel, Jeanette Hyer, Edward F. Chang, Joanna J. Phillips, David R. Raleigh & Shawn L. Hervey-Jumper

2. Department of Neurology, Stanford University, Stanford, CA, USA

   Michael B. Keough, Lijun Ni, Humsa S. Venkatesh, Kiarash Shamardani & Michelle Monje

3. Department of Psychology, University of Michigan, Ann Arbor, MI, USA

   Benjamin Lipkin & David Brang

4. Weill Institute for Neurosciences, University of California San Francisco, San Francisco, CA, USA

Edward F. Chang & Shawn L. Hervey-Jumper

5. Department of Radiology and Biomedical Imaging, University of California, San Francisco, San Francisco, CA, USA

Anne Findlay & Srikantan Nagarajan

6. Department of Pathology, University of California, San Francisco, San Francisco, CA, USA

Joanna J. Phillips & David R. Raleigh

7. Department of Radiation Oncology, University of California, San Francisco, San Francisco, USA

David R. Raleigh

8. Howard Hughes Medical Institute, Stanford, CA, USA

Michelle Monje

Contributions

S. Krishna and S.L.H.-J. designed, conducted and analysed experiments. M.M. contributed to study design, data analysis and manuscript editing. A.C. and D.R. contributed to bulk and single cell transcriptomic analyses. M.B.K. and K. Shamardani contributed to in vivo PDX gabapentin experiment. K. Seo contributed to in vitro organoid experiments. L.N. contributed to electron microscopy data acquisition and analyses. S. Kakaizada and N.A. contributed to language and cognitive assessments. Y.Z., A.M.M., A.L. and A.A. contributed to human survival analyses. G.P. and J.H. contributed to the MEA experiment. J.J.P., C.C., C.G. and R.S. contributed to quantitative imaging analysis. A.E., A.F. and S.N. contributed to MEG data acquisition and quantification. H.S.V. contributed to orthotopic xenografting. E.F.C., B.L., A.G.S.D. and D.B. contributed to intraoperative electrocorticography analysis. S. Krishna and S.L.H.-J. wrote the manuscript. S.L.H.-J. conceived the project and supervised all aspects of the work.

Corresponding author

Correspondence to Shawn L. Hervey-Jumper.

Ethics declarations

Competing interests

The authors declare no competing interests.

Peer review

Peer review information

Nature thanks Michael Taylor, Frank Winkler and the other, anonymous, reviewer(s) for their contribution to the peer review of this work. Peer reviewer reports are available.

Additional information

Publisher's note Springer Nature remains neutral with regard to jurisdictional claims in published maps and institutional affiliations.

Extended data figures and tables

Extended Data Fig. 1 Experimental workflow.

a, Schematic of study workflow. In human participants with dominant hemisphere gliomas, we applied subcortical high density electrocorticography during audiovisual speech initiation to assess tumour intrinsic neuronal circuit dynamics. Focusing on glioblastoma, we then assessed long-range functional connectivity using magnetoencephalography (MEG) imaginary coherence. **b**, Extra-operative language assessments were performed for correlation with biological assays. **c**, Long-range measure of tumour intrinsic functional connectivity identified regions of high and low

connectivity for site specific biopsies which were used for *in vivo* and *in vitro* cell biology experiments. **d**, Multiple layered approach including clinical variables, cognition assessments, human and animal model network dynamics, and cell biology experiments serves as a platform for glioma influence on neural circuit dynamics.

Extended Data Fig. 2 Electrode location and spectral data across cortically infiltrating diffuse glioma.

a, Electrodes overlying normal appearing and glioma-infiltrated regions a cohort of 14 adult patients with cortically projecting glioma in the lateral prefrontal cortex. Electrodes over non-tumour regions are shown in white and those over tumour-infiltrative regions in black. **b**, Positive control conditions included speech initiation responses within non-infiltrated cortex of the left lateral prefrontal cortex (LPFC) for non-cortically projecting glioblastoma. (Left) Axial FLAIR MRI demonstrates tumour location within insular cortex. Hemisphere of language dominance on the left was performed according to study protocol. (Middle) Black outline illustrates LPFC with ECoG recordings obtained from electrode A24, denoted by the red dot. White star represents frontal lobe motor cortex. (Right) Identical to non-tumour comparisons for cortically projecting gliomas, speech responses demonstrate elevate high gamma power (HGp) prior to speech onset consistent with speech motor planning. Dark line and shaded region represent mean and 95% confidence interval, respectively. **c**, Selectivity of maintained tumour intrinsic task-specific cortical responses is identified across diffuse glioma subtypes (adapted from Aabedi et al. 2021). Spectral data show clear separation of frequencies across tumour (glioma-infiltrated) and non-tumour (normal-appearing) electrodes. Group level analysis of participants (n = 12) demonstrates speech initiation responses across WHO 2–4 diffuse glioma. **d**, Glioma subtype-specific speech initiation spectral responses for electrodes above normal-appearing and glioma-infiltrated cortex showing conserved phenotype with task-specific hyperexcitability observed only in participants with glioblastoma. Subtypes: grade 2 and 3 oligodendroglioma (n = 4), grade 2 and 3 astrocytoma (n = 4), and glioblastoma (n = 4). *P* value determined by two-tailed Student's t-test and corrections for multiple comparisons were made using the FDR method (a).

Source data

Extended Data Fig. 3 Speech initiation neural activity in lateral prefrontal cortex (LPFC).

a, Spectral data of time vs frequency from 100–150 Hz for all tumour and non-tumour electrodes show the expected pattern of HgP increasing above 50 Hz. **b**, High gamma power (HGp) recording from single electrodes overlying tumour-infiltrated regions of brain. Dark line and shaded region represent mean and 95% confidence interval, respectively. **c**, Reconstructed time series of HGp from non-tumour electrodes demonstrating expected spatial and temporal pattern of neural activity within lateral prefrontal cortex. **d**, **e**, Electrodes matched to anatomical areas across tumour and non-tumour demonstrate hyperexcitability with glioma-infiltrated cortex. Plots are centred on median, with dark bars indicating the first and third quartiles, and whiskers the minimum and maximum points (n = 101 per group, $P = 0.0163$). P value determined by two-sided linear mixed-effects model with corrections for multiple comparisons made using the FDR method (b) and two-tailed Student's t-test (e). $^{*}P < 0.05$.

Source data

Extended Data Fig. 4 Gamma power and tumour-intrinsic connectivity imaging correlations.

a, Linear regression statistics illustrating that gamma power (a measure of neuronal activity) correlates with number of intratumoural high functional connectivity voxels in glioblastoma (n = 18 patients; $P = 0.00002$). Shaded area represents the 95% confidence interval predicted by the linear regression model. **b**, Sampling of functionally connected intratumoural regions using MEG was performed exclusively in participants with dominant hemisphere glioblastoma at the point of initial diagnosis. Site-directed tissue biopsies from HFC and LFC regions were taken as determined by MRI. Table illustrates site-specific sampling of each annotated specimen as it relates to contrast enhancing (CE) region and FLAIR tumour. Site-specific samples were acquired without regard for whether they originated from enhancing or FLAIR regions. **c**, While

samples were not acquired based on whether they originated from contrast enhancing or FLAIR regions, the stereotactic coordinates of each sample were acquired. While 57.78% of HFC samples originated from contrast enhancing regions, this did not reach statistical significance. P = 0.1923 two-sided chi square, P = 0.235 two-sided Fisher's exact test. *P* value determined by two-sided linear regression analysis (a). NS, not significant.

Source data

Extended Data Fig. 5 Neurogenic gene expression in glioblastoma.

a, Bulk RNA transcriptomic profile of HFC tissues showed a neurogenic signature including elevated (7-fold) expression of thrombospondin-1 (*TSP-1*) (n = 3-4 per group). **b**, Unsupervised principal component (PCA) analysis of bulk RNA sequencing data obtained from glioblastoma primary patient HFC (n = 3) and LFC (n = 4) samples. **c**, Volcano plots of IDH-WT glioblastoma samples revealed 144 differentially expressed genes between HFC and LFC tumour regions. The blue dots represent all differentially expressed genes, where differential expression is defined by the parameters: adjusted p-value < 0.05 and absolute log2fold change > 1. *P* value calculated using two-sided Wald test and adjusted for multiple comparisons with the Benjamini-Hochberg method.

Source data

Extended Data Fig. 6 TSP-1 expression in single-cell primary patient-derived glioblastoma.

a—**c**, Tumour cell validation using copy number variant assessment on three matched pairs of HFC and LFC samples from FC1 (SF#1), FC2 (SF#2), and FC3 (SF#3) glioblastoma patients. Trisomy 7 and monosomy 10 co-occur in most cells in FC1.Trisomy 7 is an early event, while monosomy 10 is a late event in FC2. FC3 patient sample contains no copy number variation but has high level amplification of *NTRK2* gene. **d**, Single-cell RNA transcriptomic profile UMAP confirms distinct cell populations including non-tumour astrocytes and neurons. **e**, Gene

enrichment profile used to identify each of the UMAP cell populations. **f**, **g**, Feature plot for *TSP-1* in combined (HFC + LFC) and LFC (n = 7,065 cells, 3 participants) population; within LFC samples, *TSP-1* expression is primarily from non-tumour astrocytes (suggesting that within low connectivity intratumoural regions, normal astrocytes secrete *TSP-1* to generate connectivity mirroring normal physiology). **h**, Dot plots showing *TSP-1* expression (grey to red scale) and percentage (number of cells expressing the gene) of *TSP-1*-positive cells in tumour cells and non-tumour astrocyte populations in HFC and LFC samples (n = 3 per group). Out of the total HFC tumour cells (n = 5325, 3 patients), 157 cells are *TSP-1* positive accounting for a percentage of 2.95, while only 1.59% (51 cells out of a total of 3212 LFC tumour cells [n = 3 patients]) express *TSP-1*. However, in the non-tumour astrocyte population, the number of *TSP-1*-positive cells are higher in LFC (n = 34 out of a total of 41 astrocytes, accounting for 82.9%) compared to HFC (n = 15 out of a total of 20 astrocytes, accounting for 75%) samples. **i**, Violin plots illustrating significantly increased TSP-1 expression within HFC region glioblastoma cells relative to LFC regions ($P = 1.4*10^{-7}$). **j**, Compared to HFC, slight trend of increased TSP-1 expression within non-tumour astrocytes of LFC population. However, this trend did not reach statistical significance, likely due to the small number of non-tumour astrocytes captured ($P = 0.45$). *P* values determined by two-tailed Student's t-test.

Source data

Extended Data Fig. 7 TSP-1 expression, synaptic puncta colocalization in primary patient-derived glioblastoma tissues, neuron organoid-glioblastoma co-culture model and structural synapse formation in patient-derived xenograft models.

a, TSP-1 (immunohistochemistry) expression in arbitrary units (A.U.) in HFC and LFC tissues (n = 16 regions; 3 per group; $P = 0.04$). Scale bar, 50 µm. **b**, Representative confocal images of primary patient-derived HFC and LFC tissues showing regions of synaptic puncta colocalization (white arrows). Orange, synapsin-1 (presynaptic puncta); red, PSD95 (postsynaptic puncta); green, neurofilament (neurons). Scale bar, 15 µm. Quantification of

the number of colocalized pre- and postsynaptic puncta (HFC: n = 7; LFC: n = 10 regions, 2 per group; $P = 0.05$). Quantification of postsynaptic PSD95 puncta size (HFC: n = 6; LFC: n = 9, 2 per group; $P = 0.0441$). Scale bar, 15 µm. **c**, Primary patient-derived cultures and mouse hippocampal neuron controls. Neurofilament (heavy and medium chains) and nestin antibodies used as specific markers to label mouse hippocampal neurons and glioblastoma cells, respectively in glioma-neuron co-culture. Left panel: mouse hippocampal neurons alone in culture for 14 days only express neurofilament (green) and not nestin (orange). Right panel: Nestin (orange) expression in GBM cells co-cultured with neurofilament (green) labelled mouse hippocampal neurons for 14 days. Scale bar, 100 µm. **d**, Cell cultures tested for mycoplasma using a commercially available kit (PCR Mycoplasma Test Kit I/C, PromoCell, Heidelberg, Germany) shows absence of a positive band at ~270 bp. Tested primary patient-derived lines shows internal control DNA at ~479 bp indicated a successfully performed PCR. **e**, Neuron organoids (GFP labelled) were generated from an iPSC cell line integrated with doxycycline inducible human NGN2 transgene and co-cultured with RFP labelled HFC and LFC cells (pseudo-coloured white) for two weeks. Quantification of postsynaptic Homer-1 puncta density (calculated by dividing the number of puncta measured with the area of the image field) in 2-week induced neuron (iN) organoid sections (n = 8 per group; $P = 0.0009$). Scale bar, 10 µm. **f**, Multi-electrode array of glioma-neuron co-culture and control conditions. Magnified view of multi-electrode array (MEA), showing RFP-labelled glioblastoma cells in co-culture with neurons (top row). Scale bar, 100 µm. Representative raster plot showing individual spikes/extracellular action potentials (tick mark), bursts (cluster of spikes in blue) and synchronized network bursts (pink) of mouse cortical neuron (DIV 18) only condition (bottom row). The cumulative trace above the raster plots depicts the population spike time histogram indicating the synchronized activity between the different electrodes (network burst). **g**, Structural synapses in primary patient-derived glioblastoma xenografts. Quantification of neuron-to-neuron ($P = 0.1381$) and neuron-glioma synapses ($P = 0.0005$) per high power field (hpf) in HFC and LFC xenografts (top row). Specificity negative controls for immuno-gold labelling (bottom row). (Left) HFC xenograft with secondary antibody only (no primary antibody) control and (right) non-glioma bearing negative control tissue demonstrating few randomly distributed immunogold

particles across the tissue specimen. Scale bar, 1000 nm. Data presented as mean ± s.e.m. *P* values determined by two-tailed Student's t-test. **P* < 0.05; ***P* < 0.01; ****P* < 0.001; NS, not significant.

Source data

Extended Data Fig. 8 Proliferation of primary patient-derived glioblastoma cell monoculture and neuron co-culture conditions.

Primary patient glioblastoma cells from HFC regions illustrate marked increase in proliferation when co-cultured with mouse hippocampal neurons. **a**, Quantification of proliferation indices of HFC (n = 4) and LFC (n = 4) glioma cells alone in culture (in the absence of neurons) from individual patient lines, determined by quantifying the fraction of EdU labelled cells/DAPI labelled cells; *P* = 0.00005). **b**, Representative confocal images illustrating proliferating HFC and LFC glioma cells (EdU^+, green) in the absence or presence of mouse hippocampal neurons (72h co-culture). Scale bar, 100 μm. Data presented as mean ± s.e.m. *P* value determined by two-tailed Student's t-test. *****P* < 0.0001.

Source data

Extended Data Fig. 9 Activity-dependent invasion of TSP-1 positive HFC cells.

a, 3D spheroid invasion assay showing representative micrographs imaged 24 h after addition of invasion matrix. Analysis includes quantification of mean spheroid invasion area normalized for each sample to the initial (0 h) spheroid area (HFC: n = 11; HFC + NCM: n = 16; LFC: n = 5; LFC + NCM: n = 6 spheroids, 1 per group; *P* = 0.02). Scale bar, 200 μm. Data presented as mean ± s.e.m. *P* values determined by two-tailed Student's t-test. **b**, Representative confocal images of primary patient-derived HFC and LFC tissues showing MET-positive glioma cells (white arrows). Red, MET; orange, Nestin (HFC/LFC-GBM cells); blue, DAPI. Scale bar, 30 μm. Quantification of MET-positive glioma cells per high-power field (HFC: n

= 8; LFC: n = 11, 3 per group; *P* = 0.0005). **c**, Representative immunohistochemistry images of MET staining in HFC and LFC tissues demonstrate increased tissue level protein expression (HFC: n = 26; LFC: n = 24 regions, 4 per group; *P* = 0.0329). Scale bar, 50 µm. Data presented as mean ± s.e.m. *P* values determined by two-tailed Student's t-test. **d**, Representative confocal images showing the diffuse infiltrative pattern of HFC cells in the hippocampus in comparison to the LFC cells. Quantification of tumour burden of HFC and LFC hippocampal xenografts using rank order analysis (HFC: n = 13; LFC: n = 11 regions; *P* = 0.002). Scale bar, 100 µm. Data presented as mean ± s.e.m. *P* value determined by two-tailed Mann-Whitney test. *P < 0.05; **P < 0.01; ***P < 0.001; NS, not significant.

Source data

Extended Data Fig. 10 Cell viability and TSP-1 knockdown validation.

a, Cell viability determined by live/dead cell assay. Representative images illustrating no significant cell death 2 weeks post-transduction of HFC cells with control (shCont) or TSP-1 shRNAs. Live (green) and dead (red) cells were imaged from four random fields per well and were visualized under a fluorescence microscope. The percentage of live cells were calculated as the number of live cells (in green) divided by the total number of cells (green + red) per image field (n = 4 regions per group; *P* = 0.0720). Scale bar, 100 µm. **b**, ELISA experiments performed on cell culture supernatants demonstrating strong reduction of TSP-1 expression after knockdown of TSP-1 in two different primary patient-derived HFC cell lines compared to the control scramble condition (n = 2 per group). Data presented as mean ± s.e.m. *P* values determined by two-tailed Student's t-test. N.S., not significant.

Source data

Extended Data Fig. 11 Patient survival and language task performance.

a, Kaplan-Meier human survival analysis illustrates 71-week overall survival for patients with HFC voxels as determined by contrast-enhanced T1-weighted images as compared to 123-weeks for participants without HFC voxels within their glioblastoma (mean follow-up months 50.5, range 4.9–155.9 months). **b**, Picture and auditory naming language task performance across the study population. **c**, Linear regression statistics illustrating a negative correlation between the number of intratumoural high functional connectivity voxels and baseline auditory and picture naming scores (n = 31, $P = 0.0181$). P value determined by two-tailed linear regression analysis.

Source data

Extended Data Fig. 12 Anti-proliferative effects of TSP-1 inhibition in glioblastoma is limited to activity-dependent mechanisms.

Representative confocal images from HFC glioma monoculture showing no significant change in proliferation (as measured by the number of human nuclear antigen (HNA)-positive cells co-labelled with Ki67 divided by the total number of HNA-positive tumour cells counted across all areas quantified) upon pharmacological TSP-1 inhibition using (32 µM) gabapentin (HFC: n = 7; LFC: n = 9 regions, 2 per group; $P = 0.50$). Red, HNA (human nuclei); white, Ki67. Scale bar, 30 µm. Data presented as mean ± s.e.m. *P* values determined by two-tailed Student’s t-test. NS, not significant.

Source data

Supplementary information

Supplementary Information

Supplementary Tables 1–5.

Reporting Summary

Peer Review File

Supplementary Video 1

3D co-culture of HFC glioma cells with induced neuron organoids.

Supplementary Video 2

3D co-culture of LFC glioma cells with induced neuron organoids.

Supplementary Video 3

3D co-culture of LFC glioma cells with induced neuron organoids in the presence of TSP-1.

Source data

Source Data Fig. 1

Source Data Fig. 2

Source Data Fig. 3

Source Data Fig. 4

Source Data Extended Data Fig. 2

Source Data Extended Data Fig. 3

Source Data Extended Data Fig. 4

Source Data Extended Data Fig. 5

Source Data Extended Data Fig. 6

[Source Data Extended Data Fig. 7]

[Source Data Extended Data Fig. 8]

[Source Data Extended Data Fig. 9]

[Source Data Extended Data Fig. 10]

[Source Data Extended Data Fig. 11]

[Source Data Extended Data Fig. 12]

Rights and permissions

Open Access This article is licensed under a Creative Commons Attribution 4.0 International License, which permits use, sharing, adaptation, distribution and reproduction in any medium or format, as long as you give appropriate credit to the original author(s) and the source, provide a link to the Creative Commons licence, and indicate if changes were made. The images or other third party material in this article are included in the article's Creative Commons licence, unless indicated otherwise in a credit line to the material. If material is not included in the article's Creative Commons licence and your intended use is not permitted by statutory regulation or exceeds the permitted use, you will need to obtain permission directly from the copyright holder. To view a copy of this licence, visit http://creativecommons.org/licenses/by/4.0/.

Reprints and Permissions

About this article

Cite this article

Krishna, S., Choudhury, A., Keough, M.B. *et al.* Glioblastoma remodelling of human neural circuits decreases survival. *Nature* **617**, 599–607 (2023).

https://doi.org/10.1038/s41586-023-06036-1

- Received: 18 February 2021
- Accepted: 31 March 2023
- Published: 03 May 2023
- Issue Date: 18 May 2023
- DOI: https://doi.org/10.1038/s41586-023-06036-1

Share this article

Anyone you share the following link with will be able to read this content:

Get shareable link

Sorry, a shareable link is not currently available for this article.

Copy to clipboard

Provided by the Springer Nature SharedIt content-sharing initiative

How thought itself can drive tumour growth

- George M. Ibrahim
- Michael D. Taylor

Nature News & Views 03 May 2023

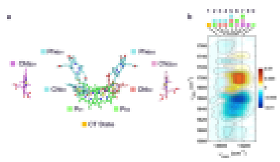
This article was downloaded by **calibre** from https://www.nature.com/articles/s41586-023-06036-1



Structural evidence for intermediates during O2 formation in photosystem II

03 May 2023

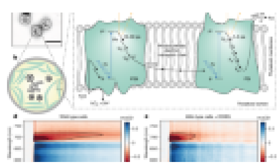
Asmit Bhowmick, Rana Hussein, … Vittal K. Yachandra



The initial charge separation step in oxygenic photosynthesis

27 April 2022

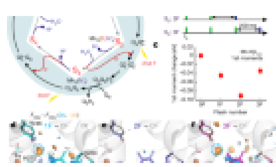
Yusuke Yoneda, Eric A. Arsenault, … Graham R. Fleming



Photosynthesis re-wired on the pico-second timescale

22 March 2023

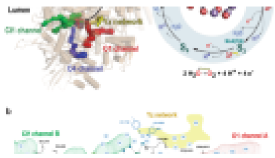
Tomi K. Baikie, Laura T. Wey, … Jenny Z. Zhang



[Structures of the intermediates of Kok's photosynthetic water oxidation clock](#)

07 November 2018

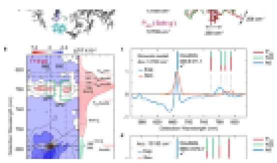
Jan Kern, Ruchira Chatterjee, … Vittal K. Yachandra



[Structural dynamics in the water and proton channels of photosystem II during the S2 to S3 transition](#)

11 November 2021

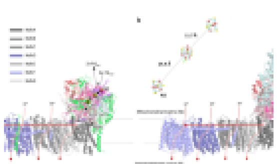
Rana Hussein, Mohamed Ibrahim, … Junko Yano



[Excitonic structure and charge separation in the heliobacterial reaction center probed by multispectral multidimensional spectroscopy](#)

14 May 2021

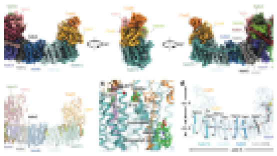
Yin Song, Riley Sechrist, … Jennifer P. Ogilvie



[Functional basis of electron transport within photosynthetic complex I](#)

10 September 2021

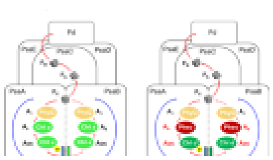
Katherine H. Richardson, John J. Wright, … Maxie M. Roessler



[Redox-coupled proton pumping drives carbon concentration in the photosynthetic complex I]

24 January 2020

Jan M. Schuller, Patricia Saura, … Ville R. I. Kaila



[Structure of the far-red light utilizing photosystem I of Acaryochloris marina]

20 April 2021

Tasuku Hamaguchi, Keisuke Kawakami, … Yasuhiro Kashino

- Article
- Open Access
- Published: 03 May 2023

The electron–proton bottleneck of photosynthetic oxygen evolution

- Paul Greife,
- Matthias Schönborn,

- Matteo Capone,
- Ricardo Assunção,
- Daniele Narzi,
- Leonardo Guidoni &
- …
- Holger Dau

Show authors

Nature **volume 617**, pages 623–628 (2023)

- 14k Accesses
- 110 Altmetric
- Metrics details

Abstract

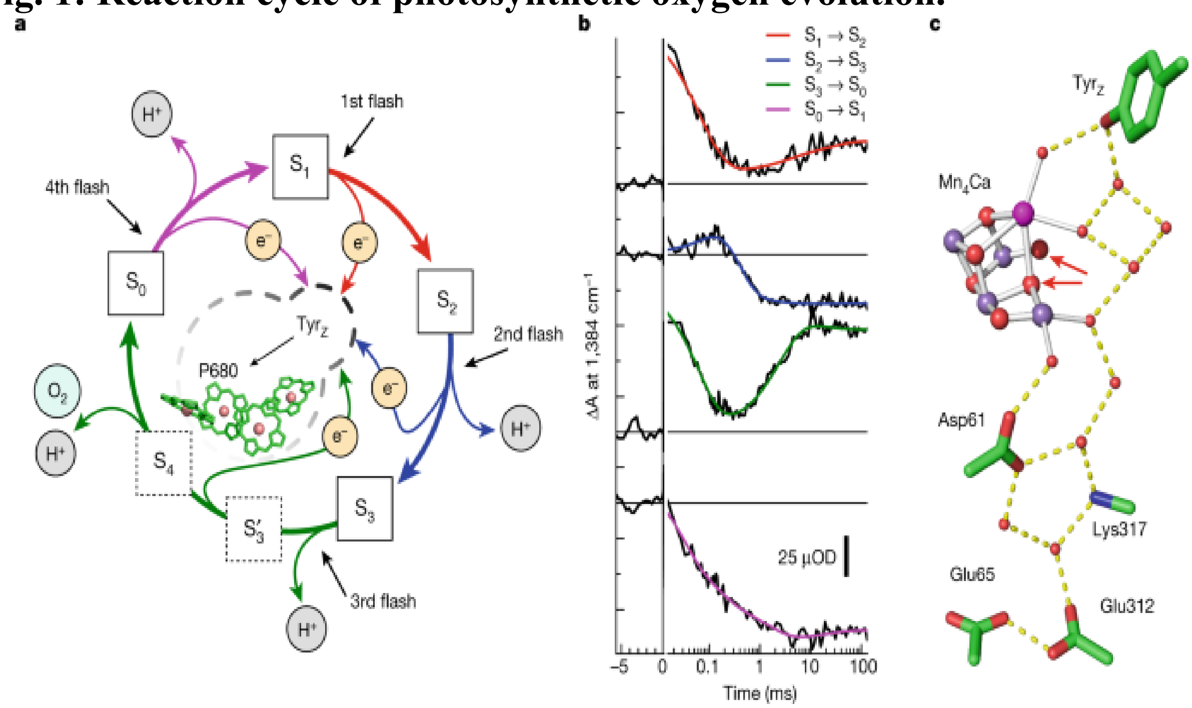
Photosynthesis fuels life on Earth by storing solar energy in chemical form. Today's oxygen-rich atmosphere has resulted from the splitting of water at the protein-bound manganese cluster of photosystem II during photosynthesis. Formation of molecular oxygen starts from a state with four accumulated electron holes, the S_4 state—which was postulated half a century ago[1] and remains largely uncharacterized. Here we resolve this key stage of photosynthetic O_2 formation and its crucial mechanistic role. We tracked 230,000 excitation cycles of dark-adapted photosystems with microsecond infrared spectroscopy. Combining these results with computational chemistry reveals that a crucial proton vacancy is initally created through gated sidechain deprotonation. Subsequently, a reactive oxygen radical is formed in a single-electron, multi-proton transfer event. This is the slowest step in photosynthetic O_2 formation, with a moderate energetic barrier and marked entropic slowdown. We identify the S_4 state as the oxygen-radical state; its formation is followed by fast O–O bonding and O_2 release. In conjunction with previous breakthroughs in experimental and computational investigations, a compelling atomistic picture of

photosynthetic O_2 formation emerges. Our results provide insights into a biological process that is likely to have occurred unchanged for the past three billion years, which we expect to support the knowledge-based design of artificial water-splitting systems.

Main

In all plants, algae and cyanobacteria, sunlight drives the splitting of water molecules into energized electrons and protons, both of which are needed for the reduction of CO_2 and eventually carbohydrate formation[2]. Molecular oxygen (O_2) is formed during this process, which transformed the Earth's atmosphere during the 'great oxygenation event'[3], which began about 2.4 billion years ago. Light-driven water oxidation occurs at the oxygen-evolving complex, a Mn_4CaO_5 cluster bound to the proteins of photosystem II[2,4] (PSII). The relationship between electron and proton transfer in the bottleneck steps of O_2 formation has remained incompletely understood. We address this key step here using time-resolved Fourier transform infrared (FTIR) experiments (Fig. 1).

Fig. 1: Reaction cycle of photosynthetic oxygen evolution.



a, Model of the S-state cycle with sequential electron and proton removal from the oxygen-evolving site[10,11,50]. Starting in the dark-stable S_1 state, each laser flash initiates oxidation of the primary chlorophyll donor ($P680^+$ formation) followed by electron transfer from a tyrosine sidechain (Tyr_Z oxidation) and—in three of the four S-state transitions—manganese oxidation, until four electron holes (oxidizing equivalents) are accumulated by the Mn_4Ca-oxo cluster in its S_4 state. **b**, Example of tracing S-state transitions using IR absorption changes after excitation with visible-wavelength laser flashes (at zero on the time axis). The absorption changes (ΔA) are provided in optical density (OD) units. The IR transients at 1,384 cm^{-1} reflect symmetric stretching vibrations of carboxylate protein sidechains that sense changes in the oxidation state of manganese in the microsecond and millisecond time domain (coloured lines are simulations with time constants provided in Supplementary Table 2). Note that the scale on the *x* axis is linear below $t = 0$ and logarithmic above $t = 0$. **c**, The Mn_4Ca cluster (Mn, violet; Ca, pink) in the S_3 state with six bridging oxygens, the redox-active tyrosine (Tyr_Z), and further selected protein sidechains as well as water molecules (red spheres), based on crystal structures[25]. Assignment to polypeptide chains, numbering of the atoms of Mn_4Ca-oxo and water molecules and hydrogen-bond distances are indicated in Supplementary Fig. 1. The two oxygens atoms that form the O–O bond in the oxygen-evolving $S_3 \rightarrow S_0$ transition are indicated by red arrows.

Source data

Time-resolved tracking of O_2 transition

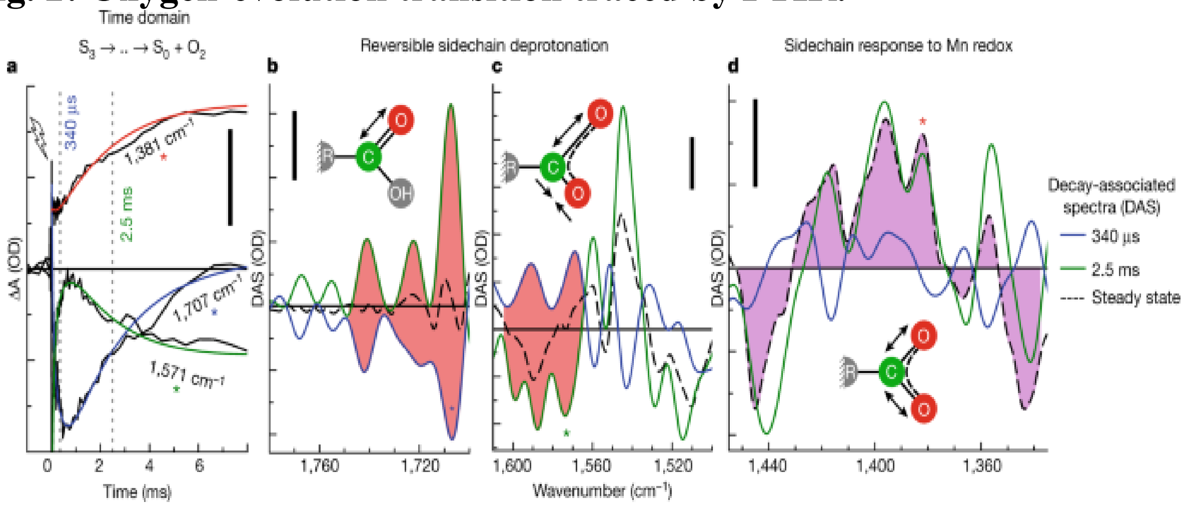
To perform time-resolved infrared spectroscopy on PSII, we developed an FTIR step-scan experiment with automated exchange of dark-adapted PSII particles (Methods), thereby expanding previous experiments at individual wavenumbers[5,6,7] towards detection of complete fingerprint spectra. The sample exchange system was refilled about every 60 h using PSII membrane particles with about 1.5 g of chlorophyll prepared from 40 kg of fresh spinach leaves for day and night data collection over a period of 7 months. We initiated the transitions between semi-stable S states by 10 visible light

(532 nm) nanosecond laser flashes applied to the dark-adapted photosystems (Extended Data Fig. 1). Using a specific deconvolution approach based on Kok's standard model[1] (Fig. 1a), we obtained time-dependent S-state difference spectra for each of the individual transitions between the four semi-stable reaction-cycle intermediates S_1, S_2, S_3 and S_0 (for selected time courses see Extended Data Fig. 2).

We focus on the oxygen-evolution transition, $S_3 \rightarrow S_4 \rightarrow S_0 + O_2$, predominantly induced by the third laser flash, for which time courses at selected wavenumbers are shown in Fig. 2a (time-resolved spectra are shown in Extended Data Fig. 3). Multiexponential simulations of the time courses provided 5 time constants describing acceptor- and donor-side PSII processes, including the expected time constants of 340 µs and 2.5 ms. The 2.5-ms time constant ($t_{{\rm{O}}_{2}}$) corresponds to the reciprocal rate constant of the rate-determining step in O–O bond formation and O_2 release[8,9]. The 340 µs time constant ($t_{{\rm{H}}^{+}}$) corresponds to an obligatory step of proton removal from the oxygen-evolving complex of PSII, as shown recently by time-resolved detection of X-ray absorption, UV-visible spectroscopy, recombination fluorescence and photothermal signals[10,11,12], resulting in a specific Mn(iv)$_4$ $({\rm{Tyr}}_{\rm{Z}}^{{\rm{ox}}\bullet})$ metalloradical intermediate that was also trapped in low-temperature magnetic resonance experiments[13,14]. 'Obligatory' here signifies that the O–O bond formation chemistry can proceed only after proton removal is complete, as verified by the delayed onset of signals that trace manganese oxidation states or, generally, the O_2 formation chemistry[8,10,12,15,16], which is also visible in the top time course of Fig. 2a. For systematic analysis of the 2D time–wavenumber data array obtained by the FTIR step-scan experiment, we exploited that the requirement for wavenumber independence of the time constants of proton removal ($t_{{\rm{H}}^{+}} = 340$ µs) and the electron transfer associated with O_2 formation ($t_{{\rm{O}}_{2}}$ = 2.5 ms), because they always reflect the same reaction (the same rate constant). The time constants can thus serve as a kinetic tag of the reaction in the time-resolved spectroscopic data. By simultaneous simulation of the time courses at 2,582 wavenumbers (1,800 cm^{-1} to 1,200 cm^{1}) using the same set of time constants at each wavenumber, we obtained the amplitude

spectra shown in Fig. 2b–d, which are denoted as decay-associated spectra (DAS).

Fig. 2: Oxygen-evolution transition traced by FTIR.



a, IR time traces at selected wavenumbers, demonstrating the delayed onset of O–O bond formation (1,381 cm^{-1}) and reversible changes assignable to transient sidechain deprotonation (1,571 cm^{-1} and 1,707 cm^{-1}). The corresponding wavenumbers in the spectra in **b**–**d** are marked with coloured asterisks. **b**–**d**, DAS corresponding to the proton release phase (\({t}_{{{\rm{H}}}^{+}}\) = 340 µs, blue line) and the oxygen-evolution phase (\({t}_{{{\rm{O}}}_{2}}\) = 2.5 ms, green) as well as the steady-state difference spectrum of the $S_3 \rightarrow S_0 + O_2$ transition (dashed black line). Red areas **b**,**d** mark inverted 340 µs DAS and 2.5 ms DAS, indicating reversible behaviour; purple shaded areas in **c** highlight the similarity of the 2.5 ms DAS and the steady-state spectrum, in line with the assignment to non-transient changes in Mn oxidation state. Scale bars, 50 µOD.

Source data

Pivotal sidechain deprotonation

Conventional steady-state S-state difference spectra collected hundreds of milliseconds after the laser flash could reflect the changes directly coupled to the stable light-induced oxidation-state changes of manganese ions and sensed by the coordinated protein sidechains, as often assumed[17,18] (but see

also ref. [19]). Then, the steady-state difference spectrum should correspond to the DAS of the t_{O_2} component (2.5 ms), as indeed visible in Fig. 2d, supporting assignment to the Mn- or Ca-binding carboxylate sidechains. In other spectral regions, however, we observed a different behaviour: in the t_{O_2} amplitude spectrum, (1) positive peaks at 1,700–1,750 cm^{-1} (Fig. 2b) and (2) negative peaks at 1,565–1,605 cm^{-1} (Fig. 2c) are not matched by counterparts in the steady-state spectrum. These peaks are probably assignable to (1) vibrations of protonated carboxylate sidechains (C=O vibrations of Asp- or Glu-associated carboxylic acid groups) and (2) deprotonated sidechains of carboxylates[20] (asymmetric O–C–O vibrations of Asp- or Glu-associated carboxylate ions). The mismatch between t_{O_2} amplitudes and the near-zero steady-state spectrum is explainable by carboxylate sidechain deprotonation early in the $S_3 \rightarrow S_4 \rightarrow S_0$ transition, which is subsequently reversed by reprotonation in parallel with O_2 formation, as indicated by the inverted amplitude spectra of the t_{H^+} and t_{O_2} components (marked by red areas). On these grounds, and supported by further analyses including experiments in deuterated water (Supplementary Figs. 9 and 10), we conclude that carboxylate deprotonation coincides with the relocation of a proton towards the aqueous solvent (t_{H^+}) and carboxylate reprotonation paralleling the O_2 formation step (t_{O_2}).

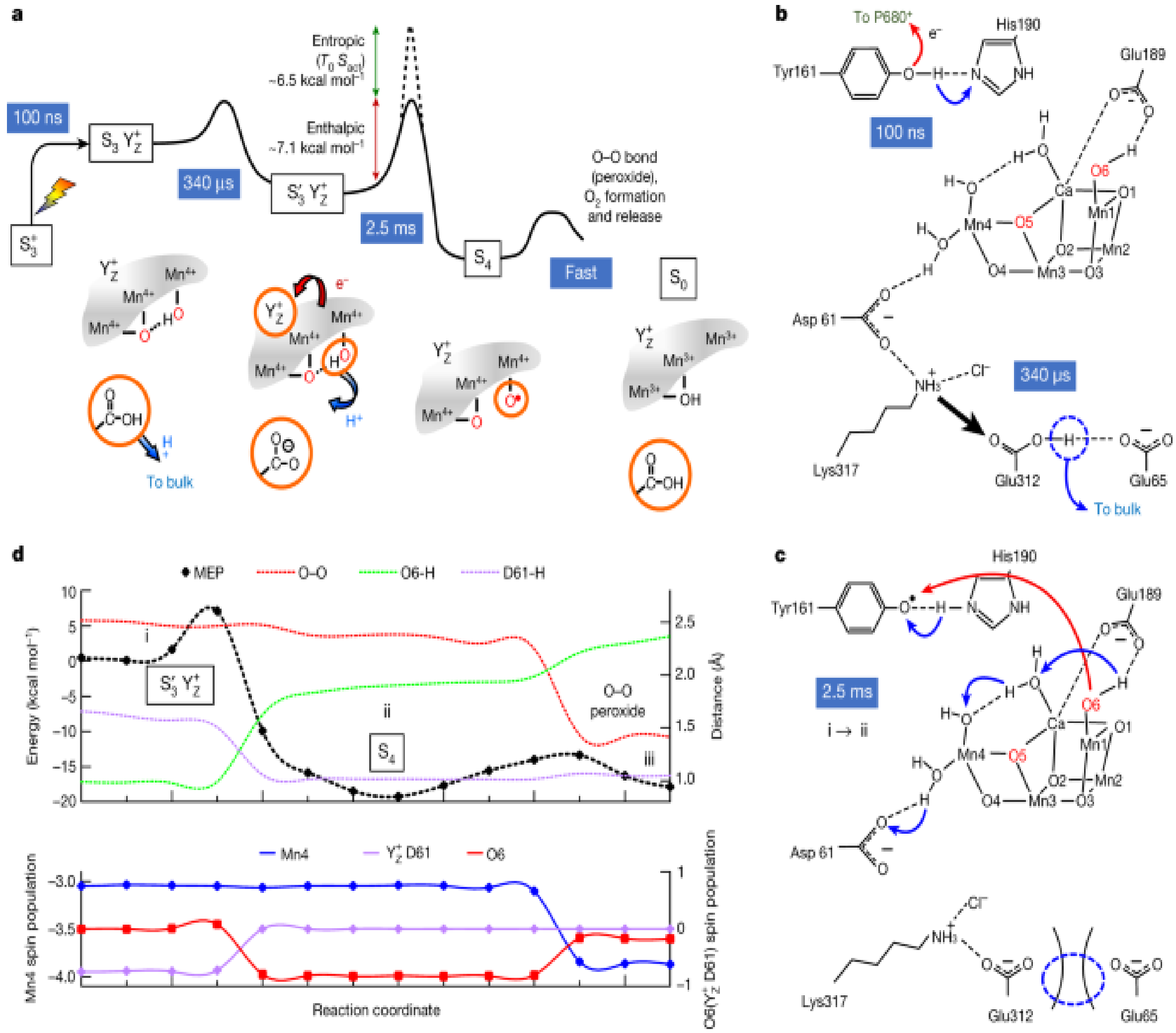
The presence of the three well-resolved bands at 1,707, 1,723 and 1,744 cm^{-1} (Fig. 2b and Extended Data Fig. 4) is attributed to a specific pair of carboxylate residues with fluctuating hydrogen-bond configurations: the Glu65–Glu312 pair in Fig. 1c, which may be described as a proton gate[21] or proton-loading site[22,23]. In analogy to the proton-loading site of cytochrome *c* oxidase[24], fractional protonation state changes of further groups might also be involved. Next, on the basis of a recent crystallographic model of the oxygen-evolving complex in its S_3 state[25], we explore a plausible carboxylate assignment and track the O–O bond formation computationally, starting from the $\mathrm{Tyr}_{\mathrm{Z}}^{\mathrm{ox}}$ S_3 state.

Atomistic scenario by quantum chemistry

We investigated the reaction path leading to O–O bond formation using density functional theory (DFT)-based minimum energy path (MEP) calculations (see Methods). The computational tracing of O–O bond formation starts with an oxidized redox-active tyrosine (Tyr_Z), and the $\mathrm{Mn}_4\mathrm{Ca}$ cluster still in its S_3-state conformation[26] (Extended Data Fig. 6), which has previously been determined by serial free-electron laser crystallography[25,27]. Moreover, it is assumed that the transition from the S_{3} to the $\mathrm{S}_{3}^{\prime}$ state has been completed (with time constant of 340 µs), resulting in a deprotonated state of a carboxylate group, which is the prerequisite for the subsequent reactions leading via the S_4 state to O–O bond formation and O_2 release.

The calculated MEP comprises three metastable states (i, ii and iii) and two transitions as shown in Fig. 3. In the first transition (i → ii), electron transfer (to $\mathrm{Tyr}_{\mathrm{Z}}^{\mathrm{ox}}$) is coupled to proton transfer from a Mn-bound hydroxide (Mn1(iv)-O6H) to a specific water molecule (W2), resulting in an oxyl radical terminally bound to a Mn ion (Mn1(iv)-O6$^{\bullet}$). The transfer of the $\mathrm{Tyr}_{\mathrm{Z}}^{\mathrm{ox}}$ hole to O6 constitutes oxidation of a substrate-water oxygen by one electron. The thereby reached S_4 state cannot be considered a transition state, but rather a reaction intermediate which is stable (minimally) over the 10-ps trajectory of the ab initio molecular dynamics simulations[28]. Eventually, the final state (iii) is reached by oxo–oxyl coupling and peroxide formation. In contrast to previous investigations[26,29,30,31], our MEP calculations on the i → ii transition are not restricted to the local events at the $\mathrm{Mn}_4\mathrm{Ca}$-oxo cluster and its immediate ligand environment. They also include the electron transfer step (Supplementary Information)—that is, the simultaneous Tyr_Z reduction and O6 oxidation, as well as the coupled shift of four protons from initial hydrogen-bond donor to hydrogen-bond acceptor. The nuclear rearrangements around Tyr_Z and the $\mathrm{Mn}_4\mathrm{Ca}$-oxo cluster are not isolated events, but are interlinked via a cluster of hydrogen-bonded water molecules that is included in the quantum region of the MEP calculations.

Fig. 3: Proton and electron transfer steps of the oxygen-evolution transition.



a, Schematic summary of experimental findings on reaction intermediates, time constants (reciprocal rate constants), enthalpic and entropic contribution of the activation energy (see Extended Data Fig. 5), and S-state assignment. The entropic contribution is the product of the entropy of activation (S_{act}) and the absolute temperature that corresponds to 20 °C (T_0 = 293.15 K). Key features are highlighted with orange circles, the two oxygen atoms from ‘substrate water’ are shown in red, and charge-transfer events are indicated with arrows (red, electron transfer; blue, proton transfer). Out of the four Mn ions of the Mn_4Ca cluster, only the three Mn ions (Mn1, Mn3 and Mn4) that have accumulated oxidizing equivalents (holes) in preceding S-state transitions and are ‘discharged’ concomitantly with O_2 formation are

shown. The fourth hole transiently residing on the oxidized Tyr_Z (denoted here as ${{\rm{Y}}}_{{\rm{Z}}}^{+}$) is filled by electron transfer from a substrate-water oxygen in the ${{\rm{S}}}_{3}^{{\prime} }\to {{\rm{S}}}_{4}$ transition. **b**,**c**, The rate-constant processes depicted in **a**, ${{\rm{S}}}_{3}^{+}\to {{\rm{S}}}_{3}\to {{\rm{S}}}_{3}^{{\prime} }$ (**b**) and ${{\rm{S}}}_{3}^{{\prime} }\to {{\rm{S}}}_{4}$ (**c**), are assigned to atomistic events, facilitated by computational results. The dotted blue circles highlight the creation of a proton vacancy induced by Tyr_Z oxidation and activating Asp61 as a proton acceptor in the ${{\rm{S}}}_{3}^{{\prime} }\to {{\rm{S}}}_{4}$ transition via movement of the Lys317 sidechain. **d**, Energy values associated with MEP calculations and internuclear distances (top graph, dashed lines) as well as spin populations of the Mn ions, atoms and residues species (bottom graph, solid lines) that characterize the peroxide formation. See Extended Data Figs. 7 and 8, for structures complementing **d** and describing the complete oxygen-evolution transition.

The obvious mechanistic problem of the ${{\rm{S}}}_{3}^{{\prime} }\to {{\rm{S}}}_{4}$ transition is that both (1) Mn(iv)-OH deprotonation without previous hole transfer to ${{\rm{Tyr}}}_{{\rm{Z}}}^{{\rm{ox}}}$ and (2) hydroxyl radical formation without previous deprotonation would involve an energetically unfavourable intermediate state (Supplementary Information). Now our MEP calculations show how this mechanistic problem can be solved via the coupled (concerted) movement of one electron (to ${{\rm{Tyr}}}_{{\rm{Z}}}^{{\rm{ox}}}$) and three protons (Fig. 3c,d and Supplementary Video). This proton movement can be viewed as a Grotthus-type proton transfer: the individual protons are shifted within a hydrogen bond by only about 1 Å, whereas overall the protonation is moved over a distance of approximately 7 Å, from O6 to Asp61. Additional structural information about these and further steps of the $S_3 \rightarrow S_0$ transition are reported in Extended Data Fig. 8. We emphasize that the reaction coordinates presented here extend previous computational investigations[30,31,32,33,34] by including both the pivotal protonation and hydrogen-bond dynamics associated with Tyr_Z reduction and oxyl-radical formation, thereby enabling a plausible connection to the experimentally detected entropy of activation (Supplementary Information).

The MEP calculation results in an energetic barrier of Mn(iv)-O□ formation in the ${{\rm{S}}}_{3}^{{\prime} }\to {{\rm{S}}}_{4}$ transition of only 7 kcal mol^{-1} (300 meV). This figure agrees surprisingly well with the experimental value of 7.1 kcal mol^{-1} (310 meV) that we determined for the crystallographically characterized cyanobacterial photosystems from *Thermosynechococcus elongatus* from the temperature dependence of the rate constant of O_2 formation (Arrhenius plot) by applying Eyring's transition-state theory (Extended Data Fig. 5). Assuming a purely enthalpic free energy of activation, these values would imply a time constant below 1 μs, whereas we detected a millisecond time constant. The experimental findings thus indicate a substantial entropic contribution to the free energy of activation of about 6.5 kcal mol^{-1} (285 meV), which corresponds to a slowdown by a factor exceeding 10,000. The pronounced entropic slowdown is most plausibly explained by many approximately isoenergetic conformations of the hydrogen-bonded protein–water network at the active site, with rapid interconversion between these networks. Out of these conformations, a subset of specific arrangements of the atoms and hydrogen-bond interactions is required for the rate-determining reaction to proceed. Pronounced variations in water positions and hydrogen-bonded chains of water molecules, which are coupled to protein dynamics, have indeed been observed in classical molecular dynamics simulation of PSII in the time range of tens of nanoseconds[35]. This suggests a strong entropic contribution to the activation energy of any reaction that relies on a specific location of water molecules and hydrogen-bond interactions, as is the case for the ${{\rm{S}}}_{3}^{{\prime} }\to {{\rm{S}}}_{4}$ transition shown in Fig. 3. The crystallographic analysis of semi-stable intermediates in the water oxidation cycle also supports reaction steps coupled to rearrangement of water molecules[25,36].

Our MEP calculations suggest protonation of the Asp61 carboxylate group in an electron transfer step that is coupled to a Grotthus-type movement of three protons, with the unconventional feature of a metal ion (Mn4) acting as a relay. This single-electron—multi-proton step facilitates the critical step of Mn^{IV}-O□ formation (S_4) before O–O bond formation. The transient carboxylate deprotonation and reprotonation that we detected in the IR experiment might be assignable to the sidechain of Asp61. However, Asp61

is probably already deprotonated in the S_3 steady state of the Kok cycle[37,38,39,40] (Supplementary Information), possibly sharing a delocalized proton with the nearby Mn-bound water molecule[41]. In an alternative scenario, we identify a proton-carrying carboxylate ‘dyad’, Glu312 and Glu65, as the site of deprotonation within about 300 μs after the flash. Here we assume that Glu312 is initially protonated[42] (Supplementary Information) and transiently deprotonated during the oxygen-evolution transition. Other computational work suggests that Glu65 is initially protonated[43], but this difference is of minor importance. A shift of the nearby Lys317 sidechain could have a role in promoting Glu312–Glu65 deprotonation and increasing the proton affinity of Asp61, as shown in Extended Data Fig. 9 and Supplementary Information. Notably, Yano and coworkers[21] suggested that the Glu65–Glu312 pair serves as a proton-transport gate, on the basis of transient conformational changes during the $S_2 \rightarrow S_3$ transition detected by serial crystallography. They did not investigate the oxygen-evolution transition itself. Furthermore, they could not demonstrate deprotonation of the carboxylate dyad. Nonetheless, assuming they are transferable to the $S_3 \rightarrow S_4 \rightarrow S_0$ transition, their finding of conformational changes of Glu65 provides support to our conclusion that Tyr_Z oxidation induces residue rearrangements and Glu65–Glu312 deprotonation.

Conclusions

Our study differs from previous studies in that it establishes a close connection between the sequence of events and reaction kinetics derived from experimental findings and those from computational analyses. We identify the rate-determining step in photosynthetic water oxidation as the formation of a Mn(iv)-O radical, which corresponds to a one-electron oxidation of a substrate water molecule. The close coupling between electron transfer and Mn-OH deprotonation via Grotthus-type relocation of three protons facilitates the low enthalpic reaction barrier, with a computed barrier height that is as low as found experimentally. The concerted electron–proton reaction requires that the nuclei and hydrogen-bond pattern at the active site are perfectly arranged, which provides a plausible explanation for reaction slowdown by entropic factors. Computationally, we

identify a low-energy path for the subsequent peroxide formation which is in line with a mechanistic idea pursued by Siegbahn and others[30,31,32,33,34,44], but we find that this is not the overall rate-determining step. However, we cannot completely exclude further low-energy routes towards O–O bond formation[40]—as they have also been discussed in relation to substrate–water exchange rates[45]—because an exhaustive search covering all conceivable reaction paths is unachievable. Previous investigations[30,31,32,33,34,40,44,46] did not consider the mechanistic features of a combined enthalpic—entropic barrier associated with the Mn-OH deprotonation and Mn(iv)-O$^{\bullet}$ radical formation, which we identify as the kinetically most demanding, overall bottleneck step in photosynthetic water oxidation.

The formation of ${\rm{Tyr}}_{\rm{Z}}^{\rm{ox}}$, which provides the fourth electron hole at the active site, is insufficient to start the reactions leading to O_2 formation; the creation of a proton vacancy by the removal of a further proton from the active site is required[10]. Here we find that the proton is removed not from a substrate water molecule, but from a nearby base, which is identified as a carboxylate sidechain. This is the prerequisite for the subsequent concerted electron–proton transfer reaction that facilitates in the direct one-electron oxidation of a substrate water molecule, resulting in a Mn(iv)-O$^{\bullet}$ radical without formation of a Mn(v) intermediate. This last experimentally detectable state before the onset of water oxidation is thus formed in the presence of four accumulated electron holes (three Mn(iii/iv) plus one ${\rm{Tyr}}_{\rm{Z}}^{\rm{ox}}$) and an essential proton vacancy. Its characteristics might justify assignment to the S_4 state, as previously proposed[10]. However, this state is better classified as ${\rm{S}}_3^{\prime}{\rm{Tyr}}_{\rm{Z}}^{\rm{ox}}$, to clarify the placement of the four electron holes and not to obscure the role of the tyrosine residue as an electron relay. Here we identify the S_4 state—whose identity had remained unknown since Bessel Kok developed the S-state cycle paradigm 50 years ago[1]—as an oxyl-radical state, with the four electron holes needed for O_2 formation available at the Mn_4Ca-oxo cluster itself (three Mn(iii/iv) plus one O$^{\bullet}$). It is identified as a real reaction intermediate transiently formed before O–O bond formation—not a transition state, but experimentally undetectable for kinetic reasons.

An important development in photo- and electrocatalytic water oxidation for use in CO_2-neutral fuel production is the use of oxide materials based on earth-abundant metals (such as Mn, Fe, Co and Ni). These often share structural motifs with biological catalysts and frequently undergo metal-centred oxidation-state changes, which allows the accumulation of oxidizing equivalents before the onset of O_2 formation[47,48]—for example, by Mn(iii/iv) oxidation[49]. Given our knowledge of photosynthetic water oxidation, we consider it plausible that in inorganic oxide materials, the formation of a reactive metal-O radical is the kinetically most demanding rate-determining step, which can proceed efficiently by coupled electron–proton transfer. Following the biological paragon, we expect that tuning the inorganic material for (1) extensive hole accumulation by metal oxidation at low overpotentials and (2) metal radical formation facilitated by proton-coupled electron transfer can lead to improved oxygen-evolution reaction catalyst materials based on earth-abundant resources.

Methods

Preparation of PSII particles

High-activity PSII membrane particles (>1,000 μmol O_2 per mg chlorophyll and hour) were prepared from spinach leaves as described[51]—with the Triton incubation time reduced[52] to 1 min—and stored at −80 °C in a betaine-rich cryo-buffer (1 M glycinebetaine, 25 mM 2-morpholin-4-yl ethanesulfonic acid (MES), 15 mM NaCl, 5 mM $MgCl_2$, 5 mM $CaCl_2$, pH 6.2 adjusted with NaOH) with a final chlorophyll concentration of about 2 mg ml^{-1}. Starting with 4 kg of spinach leaves, each PSII preparation yielded PSII membrane particles corresponding to about 200 mg chlorophyll. In total, about 40 kg of fresh spinach leaves were processed for this work, resulting in about PSII membrane particles corresponding to more than 1,500 mg of chlorophyll.

Before measurement, the PSII membrane particles were thawed, resuspended and washed twice by centrifugation at 50,000*g* for 12 min in betaine-free variant of the cryo-buffer. The resulting pellet was mixed with an artificial electron acceptor (about 30 μl of a stock solution of 700 mM

phenyl-p-benzoquinone (PPBQ) dissolved in dimethyl sulfoxide (DMSO)) yielding a final ratio of 7 μmol PPBQ per mg chlorophyll of the PSII membrane particles.

Realization of 1,800 irradiation spots

The FTIR measurement cells consisted of two CaF_2 plates (diameter of 25 mm) sealed with vacuum grease. A small amount of PSII suspension with added electron acceptor sample was placed on one plate, with the second plate pressed firmly on top. The thickness of the sample was set using a self-made device using rotation and pneumatic pressure to press the plates together; simultaneous measurement of the absorbance at 1,650 cm^{-1} allowed for the reasonably homogenous samples with an absorbance of 1 ± 0.2 absorbance units. Following thickness adjustment, two saturating laser flashes were applied (5-ns pulse width, 532 nm). These pre-flashes and the subsequent dark-relaxation period ensure a reproducible synchronization of the photosystems in the dark-stable S_1 state with the tyrosine residue denoted as Tyr_D in its oxidized form[53].

Approximately 45 CaF_2 'sandwiches', prepared as described above, were loaded into an automated sample change plate and mounted within a modified commercial FTIR spectrometer (Bruker Vertex 70, detector D317/BF) with an extended sample chamber and temperature control device, as shown in Extended Data Fig. 1 and detailed in the Supplementary Information. Concave focusing mirrors further focused the IR beam to a spot with a diameter of about 1.6 mm on the PSII sample. Each of the 45 CaF_2 sandwiches can have about 40 unique sample spots, resulting in about 1,800 individual spots per refill of the automated sample exchange system. Before measurement, the absorbance of each spot is sampled, and those not meeting the criteria of 1 ± 0.2 absorbance units are excluded from further measurement. This typically resulted in the exclusion of about 10% of the spots.

Execution of the step-scan FTIR experiment

The temperature was regulated to 10 °C and a constant stream of dry air kept the sample chamber humidity below 2%. S-state cycling of the PSII membrane particles was achieved using saturating flashes from an excitation laser (5-ns flashes, 532 nm, Continuum Minilight II) coupled into the sample chamber through a transmission window. Spot size was adjusted using an iris to be larger than the diameter of the IR beam.

After loading the spectrometer and before start of the step-scan FTIR experiment, the samples were dark-adapted for at least 1 h. In the FTIR experiment, dark-adapted spots of the PSII sample were irradiated with 10 excitation laser flashes with a flash spacing of 700 ms. For each flash, the detector signal was recorded for 136 ms, with 24-bit analogue-to-digital conversion every 6 µs (sampling frequency of about 170 kHz), 6 ms before the flash and 130 ms after the flash, as illustrated by the timing diagram in Extended Data Fig. 1. Once data collection for the 10th flash had been completed, the sample holder moved a 'fresh' sample spot into the IR beam path before initiation of the next flash sequence. At least 1 h of dark adaptation passed before the same sample spot was measured again. For the step-scan dataset, 334 interferogram mirror positions were repeatedly sampled, resulting in a spectral resolution of about 10 cm^{-1}. For signal averaging, about 230,000 measurement cycles where performed, meaning about 2,300,000 excitation flashes were applied and recorded within about 7 months. During this period, the experimental setup was repeatedly refilled with fresh PSII FTIR samples and data for total measurement time of about 60 days was recorded. After extensive assessment of the loss of functional stability over extended time periods, we decided to expose the FTIR PSII samples to laser flash sequences for typically 50–60 h (Supplementary Fig. 3). The primary data analysis as well as the correction for thermal artefacts are described in the Supplementary Information. Averaged time-resolved interferograms for all ten applied flashes and relevant Python analysis code has been made available[54,55].

For comparison, rapid-scan S-state difference spectra were recorded using the same type FTIR samples and automated sample exchange system as used for the step-scan data. The individual rapid-scan interferograms were collected within 37 ms, at a spectral resolution of 4 cm^{-1}. The steady-state

spectrum was calculated by averaging spectra from 300 ms to 1 s after each laser flash.

Decay-associated spectra

The time evolution of the obtained spectra was simulated with a standard exponential model:

$${F}_{\nu }\left(t\right)=\sum _{i}{A}_{\nu ,i}\cdot (1-{{\rm{e}}}^{-t/{\tau }_{i}})+{B}_{\nu },$$
(1)

where $F_v(t)$ provides spectrum at a specific time, t, after the laser flash and v indicates discrete wavenumbers spaced by 0.23 cm^{-1}. The time constants (τ_i) and amplitude coefficients, $A_{v,i}$, were obtained by a simultaneous least-square fit of 2,582 transients corresponding to wavenumbers ranging from 1,800 cm^{-1} to 1,200 cm^{-1}.

The amplitude coefficients, $A_{v,i}$, when plotted with respect to the wavenumber, represents the change in the recorded spectrum associated with time constant τ_i, the DAS of the τ_i process. Note that according to equation (1), a positive value for $A_{v,i}$ represents a positive contribution the final steady-state spectrum. The offset B_v represents the spectrum of all flash-induced changes that are faster than the time resolution of our experiment (sum of changes occurring within nanoseconds up to about 5 µs after the laser flash). Simulations begin 9 µs after the excitation flash. A Python toolbox written for this analysis has been made available[55].

Acceptor-side correction

In the DAS of the $S_3 \rightarrow S_0$ transition, the amplitude of the millisecond phase is a combination (sum) of a minor contribution from the quinone reactions at the PSII acceptor side and major contribution of the oxygen-evolution step. For improved DAS of the oxygen-evolution step, we corrected for the quinone contribution based on the following rationale: the two-electron chemistry at the PSII acceptor side results in binary oscillation of the flash-

number-dependent acceptor-side contribution, with one type of acceptor-side contributions dominating on odd flash numbers and a second type dominating on even flash numbers. This is supported by the clear similarity between the millisecond DAS of the $S_2 \rightarrow S_3$ and $S_0 \rightarrow S_1$ transitions (Supplementary Fig. 4). Consequently, we assume that the DAS of the millisecond phase in the $S_1 \rightarrow S_2$ transition also contributes to the millisecond DAS in the $S_3 \rightarrow S_0$ transition.

For the $S_1 \rightarrow S_2$ transition, DAS were obtained for 4 time constant components: 33 µs, 91 µs, 3.1 ms and 25 ms. The DAS of the 3.1 ms phase was subtracted from the corresponding DAS of the $S_3 \rightarrow S_0$ transition, without further scaling. We note that the acceptor-side correction is uncritical to our conclusion, as demonstrated in Supplementary Fig. 5, but improves the precision of the DAS shown in Fig. 2.

Activation energies from O_2 polarography

Thylakoid membranes from *T. elongatus* cells were prepared as described elsewhere[56]. After storage at −80 °C, the thylakoid suspension was thawed on ice for 60 min in complete darkness. After resuspension in an electrolyte buffer (150 mM NaCl, 25 mM MES, 1 M glycinebetaine, 5 mM $MgCl_2$, 5 mM $CaCl^2$, pH 6.2 adjusted with NaOH), an aliquot of 10 µl with a PSII concentration corresponding to 10 µg of chlorophyll was placed into the cavity of a centrifugable two-electrode assembly followed by centrifugation in a swingout rotor at 10,000*g*. We used a custom-made centrifugable static ring-disk electrode assembly of a bare platinum and silver-ring electrodes to perform time-resolved oxygen polarography measurements[56,57]. A custom-made potentiostat provided the polarization voltage (−0.95 V at the Pt electrode versus the Ag ring electrode) for O_2-reduction at the bare Pt electrode, which was switched-on 15 s before the first excitation flash. The current signal was recorded for 500 ms (20 ms before and 480 ms after each flash, for 80 flashes with 900 ms spacing) using a first-order high-pass filter (time constant of 100 ms) for suppression of slow drift contributions in the current signal. The S-state transitions were induced by saturating flashes of red light (613 nm, 40 µs of flash duration). The light source was a high-power light-emitting diode (LED) operated at a maximum current density of

around 150 A, as facilitated by capacitor discharge. The temperature during data acquisition was set using Peltier elements and monitored by a miniature temperature sensor immersed in the sample buffer.

For accurate (correct) and precise determination of the O_2 formation rate constant, the recorded current transients were simulated by numerical integration of the one-dimensional O_2 diffusion equation, involving light-induced O_2 production within the PSII layer covering the electrode (source terms), O_2-consumption at the electrode (sink terms), and accounting for the high-pass filter characteristics (see refs. [56,57], software developed by I. Zaharieva). By variation of model parameters, the recorded O_2 transients were simulated until optimal agreement between experimental and simulated transients was reached (least-squares curve fitting).

After determination of the activation energy (E_{act}) and pre-exponential factor (A) following the classical approach of Arrhenius, the enthalpy of activation (H_{act}) and entropy of activation (S_{act}) were determined using the Eyring equation of transition-state theory[58] (also called Eyring–Polanyi equation) with a transmission coefficient of unity, analogous to the treatment in refs. [59,60].

In Extended Data Fig. 5e, at each temperature the data points (filled circles) indicate the average of three values of the time constant of oxygen evolution (τ_{ox}) obtained by simulation of the O_2 transients of three independent experiments with averaging of 70–80 flash-induced O_2 transients per experiment; the error bars indicate the corresponding standard deviation ($n = 3$). The value of E_{act} and its uncertainty range result from determination of the slope of the regression line for ln (τ_{ox}) versus $(k_B T)^{-1}$ (shown as a dotted line; k_B, Boltzmann constant; T, temperature in Kelvin) without weighting by standard deviations; the provided uncertainty range of E_{act} corresponds to the 1σ confidence interval of the slope value. The uncertainty ranges for H_{act} and S_{act} were estimated such that their relative uncertainty corresponds to the relative uncertainty in E_{act} resulting in ranges of about ±9 meV for H_{act} and $T_0 S_{act}$. Alternatively, the uncertainty ranges could be estimated by assuming the same absolute uncertainty in E_{act}, H_{act}

and T_0S_{act}, which would result in uncertainty ranges of about ±10 meV for both H_{act} and T_0S_{act}.

QM/MM molecular dynamics simulations

The model used for quantum mechanics/molecular mechanics (QM/MM) calculations is the same adopted in previous studies[26,28]. The model consists of the D1, D2 and CP43 protein domains, the respective cofactors, the Mn_4Ca cluster, and water molecules present in this region. (D1, D2 and CP43 indicate the protein subunits of PSII, which correspond to the *PsbA*, *PsbB* and *PsbC* gene products.) The Mn_4Ca cluster, with its ligands present in the first shell (D1-Asp170, D1-Glu189, D1-His332, D1-Glu333, D1-Asp342, D1-Ala344 and CP43-Glu354), plus additional residues in the second shell (D1-Asp61, D1-Tyr161, D1-His190, D1-His337, D1-Asn181, D1-Ile60, D1-Ser169 and CP43-Arg357) were treated at the DFT level. Additionally, the first 14 water molecules closest or directly coordinated to the Mn_4Ca cluster, and the chloride anion close to Glu333 were also treated at DFT level. See Supplementary Fig. 18 for graphical representation of the DFT region. The rest of the system was treated at classical level using AMBER99SB force field[61] to describe the protein residues and the general AMBER force field (GAFF)[62] for the description of the other cofactors present in the investigated region of PSII.

QM/MM calculations reported in this study have been carried out using the CP2K package[63]. QM/MM molecular dynamics simulations were performed in the NVT ensemble using a Nose–Hoover thermostat[64,65] (time constant τ = 0.1 ps) to couple the system with a thermal bath at $T = 298.15$ K. A cutoff for the plane-wave expansion of 320 Rydberg was used to treat the quantum region with a cubic cell 28.0 × 28.0 × 28.0 A. The PBE+U scheme[66] was employed using the DZVPMOLOPT-SR-GTH Gaussian basis set optimized for molecular systems[67]. Electrostatic coupling between the classical and quantum regions of the system was treated by means of fast Gaussian expansion of the electrostatic potential[63]. A time step of 0.5 fs was used.

To study the effect of the protonation of Asp61 by W1 water molecule, we applied a position restraint on the proton between Asp61 and W1 to force

the protonation of Asp61. The O-H equilibrium distance for the restraint was set to 1 A with a force constant of 0.01 internal units. The restraint has been applied for a limited amount of time and the results are described in the Supplementary Information.

MEP calculations

MEP calculations have been performed on a PSII gas-phase model directly extracted from the QM-treated region of the QM/MM simulations described in ref. [26]. The B3LYP[68,69] functional with TZVP-MOLOPT-SR-GTH Gaussian basis set has been employed for all the gas-phase calculations. A 28.0 Å side cubic cell and a cutoff for the plane-wave expansion of 320 Rydberg was used to treat the quantum region. The systems have been simulated following the 'high oxidation-state paradigm' of the S_3 state, consistent with previous computational work[26,30,33,40,70,71] and in line with most experimental analyses, as reviewed in ref. [72]. The 'high oxidation-state paradigm' in the S_3 state corresponds to an oxidation pattern of the four Mn ions equal to iv, iv, iv and iv. The spin multiplicity, M, equals 6 with a spin moment of 5/2 as determined experimentally[73].

The rationale of the MEP calculations and the specific nudged elastic band (NEB) approach is illustrated in Supplementary Fig. 19. To calculate the MEP, it is necessary to provide the algorithm with an initial and a final structure of the reaction, and with a preliminary set of intermediate structures, representing the reaction coordinate, denoted herein as 'replicas'. The starting and final structures have been extrapolated by QM/MM molecular dynamics simulations reported in previous work[26,28] involving different redox states of the Mn cluster and Tyr_Z. The dynamic properties of the same QM region (220 atoms; Supplementary Fig. 18), both in the S_3 state and after Tyr_Z oxidation were sampled for at least 10 ps. The MM system included 37,000 atoms for all the simulated systems. Extracting the initial and final structures of the MEP calculation from QM/MM molecular dynamics simulations at finite temperature supports finding the optimal hydrogen-bond network for the water and the residues included in the simulated system. Still, we cannot exclude that an even more favourable

hydrogen-bond network could be reached, for example increasing the simulation time of the QM/MM molecular dynamics trajectory.

To properly represent all the intermediates and transition states characterizing the reaction coordinate we used 14 different replicas. Three of the 14 structures, the intermediates i, ii, and iii in Extended Data Fig. 7, were extracted from previous QM/MM molecular dynamics simulations. The remaining initial structures were obtained by linear interpolation of the cartesian coordinates between i and ii geometries and between ii and iii geometries. The MEP algorithm is meant to optimize simultaneously all these replicas such that the corresponding path satisfy the requirement of an MEP. For the first half of the MEP, from intermediate i to ii (proton relocation and O6 oxidation), the first and the last structures of the initial-guess structure were extracted from the QM/MM molecular dynamics simulation reported in ref. [28]. For the second portion of the reaction pathway (peroxide formation), the structure of the final point (iii) has been extracted from the QM/MM molecular dynamics simulation reported in ref. [26]. The MEP has been calculated using the NEB method as implemented in CP2K package[63,67,74]. The algorithm form of NEB calculation applied to our model is the improved tangent version (IT-NEB)[75]. This setup has been previously applied successfully in the study of water delivery and oxygen reorganization in the S_2 to S_3 transition of Kok cycle[70,71].

After convergence, the calculated energies of the 14 geometries correspond to the internal energy variation of the system along the reaction pathway (all the geometries are reported in Supplementary Fig. 20 and provided as Supplementary Data). In the MEP calculations the calculated energy is the variation of internal energy. We note that for the proton shuffling and peroxide formation in protein the variation of volume and pressure is expected to be negligible (PV component), therefore, the internal energy variation (ΔU) is a good approximation of the enthalpy variation (ΔH).

The internal energy difference between a specific intermediate state (i or ii) and the related transition state is therefore a good estimate of the respective activation enthalpy (ΔH*1; ΔH*2). The difference of internal energy between two intermediates (between two of the three states i, ii, and iii)

corresponds to the respective enthalpy variation ($\Delta H1$; $\Delta H2$). All the values are reported in Extended Data Fig. 7 and its caption.

Classical molecular dynamics simulations

Two classical molecular dynamics simulations have been performed to investigate the possible conformations adopted by D2-Lys317. The first simulation (simulation 1) was carried out considering both D1-Asp61 and D2-Glu312 as deprotonated. In the second simulation (simulation 2) Glu312 of the D2 subunit was set as protonated, while D1-Asp61 was still deprotonated. Apart from this difference, the two simulations are based on the same setup described in ref. [76]. Protein residues were described using the AMBER99SB force field[62] while other molecules present in the crystal structure (that is, β-carotene, chlorophyll *a*, pheophytin *a*, plastoquinone 9, heptyl 1-thiohexopyranoside, dodecyl-β-d-maltoside and the four lipids digalactosyl diacylglycerol (DGDG), monogalactosyl diacylglycerol (MGDG), phosphatidylglycerol (PG) and sulfoquinovosyl diacylglycerol (SQDG) have been described by the generalized Amber force field (GAFF)[62]. Optimization and electrostatic potential analysis were performed by using Gaussian 03 at the Hartree–Fock level with the 6–31G* basis set. The protonation state of the histidines bound to haem molecules, or directly interacting with iron atoms or the magnesium atom in chlorophylls was chosen accordingly with their relative orientation in the X-ray structure. The other titratable residues were considered in their standard protonation state with the only exception of Glu312 of the D2 subunit in simulation 2 considered protonated. The PSII structure was embedded into a membrane bilayer composed by dioleoylphosphatidylcholine (DOPC) lipids described by the GAFF-based force field developed by Siu et al.[77]. The system was then solvated in a box with dimensions 27.0 × 16.3 × 14.2 nm using TIP3p water model[78]. Molecular dynamics simulations were performed using the GROMACS software package[79]. Long-range electrostatic interactions were calculated using particle mesh Ewald method[80], with a grid spacing of 0.12 nm and a short-range cutoff of 1.0 nm. The LINCS algorithm[81] was applied to constrain the bond lengths of the hydrogen atoms to a constant value. A time step of 2 fs was used for numerical integration of the equations of motion. The temperature was kept constant by coupling the system to a

Nose–Hoover thermostat (298 K) with a coupling time constant[64,65] $\tau_T = 0.1$ ps. The system was also weakly coupled to a pressure bath (1 bar) with a coupling time constant $\tau_P = 1.0$ ps, using Parrinello–Rahman barostat[82,83]. The final system was composed by almost 650,000 atoms. The two molecular dynamics simulations were carried out for 50 ns in NPT ensemble.

Reporting summary

Further information on research design is available in the Nature Portfolio Reporting Summary linked to this article.

Data availability

The complete step-scan data obtained for 230.000 sequences of 10 laser flashes applied to dark-adapted PSII is available in form of averaged time courses of the detector signal for all 334 mirror positions and 10 exciting laser flashes per mirror position (at Zenodo: https://doi.org/10.5281/zenodo.7681840). We furthermore provide the spectrum used for correction of the heat artefact at the same location. The coordinates of the 14 MEP structures are provided as a Supplementary Data file in standard PDB format. Source data are provided with this paper.

Code availability

Two short Python toolboxes used to correct time-resolved Fourier transform data of high-activity PSII membrane particles from spinach for starting population and cycle inefficiency (miss factor) and to perform a global fit of a dataset to generate DAS are available at Zenodo (https://doi.org/10.5281/zenodo.7682034).

References

1. Kok, B., Forbush, B. & McGloin, M. Cooperation of charges in photosynthetic O_2 evolution - I. A linear four-step mechanism.

Photochem. Photobiol. **11**, 457–475 (1970).

2. Junge, W. Oxygenic photosynthesis: history, status and perspective. *Q. Rev. Biophys.* **52**, e1 (2019).

3. Fischer, W. W., Hemp, J. & Johnson, J. E. Manganese and the evolution of photosynthesis. *Orig. Life Evol. Biosph.* **45**, 351–357 (2015).

4. Cox, N., Pantazis, D. A. & Lubitz, W. Current understanding of the mechanism of water oxidation in photosystem II and its relation to XFEL data. *Annu. Rev. Biochem.* **89**, 795–820 (2020).

5. Noguchi, T., Suzuki, H., Tsuno, M., Sugiura, M. & Kato, C. Time-resolved infrared detection of the proton and protein dynamics during photosynthetic oxygen evolution. *Biochemistry* **51**, 3205–3214 (2012).

6. Shimada, Y., Kitajima-Ihara, T., Nagao, R. & Noguchi, T. Role of the O4 channel in photosynthetic water oxidation as revealed by fourier transform infrared difference and time-resolved infrared analysis of the D1-S169A mutant. *J. Phys. Chem. B* **124**, 1470–1480 (2020).

7. Mausle, S. M. et al. Activation energies for two steps in the S-2 → S-3 transition of photosynthetic water oxidation from time-resolved single-frequency infrared spectroscopy. *J. Chem. Phys.* **153**, 215101 (2020).

8. Rappaport, F., Blanchard-Desce, M. & Lavergne, J. Kinetics of electron transfer and electrochromic change during the redox transition of the photosynthetic oxygen-evolving complex. *Biochim. Biophys. Acta* **1184**, 178–192 (1994).

9. Junge, W., Haumann, M., Ahlbrink, R., Mulkidjanian, A. & Clausen, J. Electrostatics and proton transfer in photosynthetic water oxidation. *Philos. Trans. R. Soc. B* **357**, 1407–1418 (2002).

10. Haumann, M. et al. Photosynthetic O_2 formation tracked by time-resolved x-ray experiments. *Science* **310**, 1019–1021 (2005).

11. Klauss, A., Haumann, M. & Dau, H. Alternating electron and proton transfer steps in photosynthetic water oxidation. *Proc. Natl Acad. Sci.*

USA **109**, 16035–16040 (2012).

12. Gerencser, L. & Dau, H. Water oxidation by photosystem II: H_2O−D_2O exchange and the influence of pH support formation of an intermediate by removal of a proton before dioxygen creation. *Biochemistry* **49**, 10098–10106 (2010).

13. Zahariou, G., Chrysina, M., Petrouleas, V. & Ioannidis, N. Can we trap the metalloradical intermediate during the S-state transitions of photosystem II? An EPR investigation. *FEBS Lett.* **588**, 1827–1831 (2014).

14. Zahariou, G. & Ioannidis, N. Theoretical study of the EPR spectrum of the S3TyrZ• metalloradical intermediate state of the O2-evolving complex of photosystem II. *Photosynth. Res.* **130**, 417–426 (2016).

15. Zaharieva, I., Dau, H. & Haumann, M. Sequential and coupled proton and electron transfer events in the S2 → S3 transition of photosynthetic water oxidation revealed by time-resolved X-ray absorption spectroscopy. *Biochemistry* **55**, 6996–7004 (2016).

16. Zaharieva, I. & Dau, H. Energetics and kinetics of S-state transitions monitored by delayed chlorophyll fluorescence. *Front. Plant. Sci.* **10**, 386 (2019).

17. Debus, R. J. Identifying carboxylate ligand vibrational modes in photosystem II with QM/MM methods. *Proc. Natl Acad. Sci. USA* **113**, 12613–12615 (2016).

18. Nakamura, S. & Noguchi, T. Quantum mechanics/molecular mechanics simulation of the ligand vibrations of the water-oxidizing Mn_4CaO_5 cluster in photosystem II. *Proc. Natl Acad. Sci. USA* **113**, 12727–12732 (2016).

19. Brahmachari, U. & Barry, B. A. Dynamics of proton transfer to internal water during the photosynthetic oxygen-evolving cycle. *J. Phys. Chem. B* **120**, 11464–11473 (2016).

20. Barth, A. Infrared spectroscopy of proteins. *Biochim. Biophys. Acta* **1767**, 1073–1101 (2007).

21. Hussein, R. et al. Structural dynamics in the water and proton channels of photosystem II during the S2 to S3 transition. *Nat. Commun.* **12**, 6531 (2021).

22. Wikstrom, M., Sharma, V., Kaila, V. R., Hosler, J. P. & Hummer, G. New perspectives on proton pumping in cellular respiration. *Chem. Rev.* **115**, 2196–2221 (2015).

23. Sugitani, R., Medvedev, E. S. & Stuchebrukhov, A. A. Theoretical and computational analysis of the membrane potential generated by cytochrome *c* oxidase upon single electron injection into the enzyme. *Biochim. Biophys. Acta* **1777**, 1129–1139 (2008).

24. Lu, J. X. & Gunner, M. R. Characterizing the proton loading site in cytochrome *c* oxidase. *Proc. Natl Acad. Sci. USA* **111**, 12414–12419 (2014).

25. Kern, J. et al. Structures of the intermediates of Kok's photosynthetic water oxidation clock. *Nature* **563**, 421–425 (2018).

26. Narzi, D., Capone, M., Bovi, D. & Guidoni, L. Evolution from S_3 to S_4 state of the oxygen evolving complex in photosystem II monitored by QM/MM dynamics. *Chem. Eur. J.* **24**, 10820–10828 (2018).

27. Suga, M. et al. Light-induced structural changes and the site of O=O bond formation in PSII caught by XFEL. *Nature* **543**, 131–135 (2017).

28. Capone, M., Guidoni, L. & Narzi, D. Structural and dynamical characterization of the S-4 state of the Kok–Joliot's cycle by means of QM/MM molecular dynamics simulations. *Chem. Phys. Lett.* **742**, 137111 (2020).

29. Siegbahn, P. E. M. Nucleophilic water attack is not a possible mechanism for O–O bond formation in photosystem II. *Proc. Natl Acad. Sci. USA* **114**, 4966–4968 (2017).

30. Shoji, M., Isobe, H., Shigeta, Y., Nakajima, T. & Yamaguchi, K. Concerted mechanism of water insertion and O_2 release during the S4 to S0 transition of the oxygen-evolving complex in photosystem II. *J. Phys. Chem. B* **122**, 6491–6502 (2018).

31. Siegbahn, P. E. A structure-consistent mechanism for dioxygen formation in photosystem II. *Chem. Eur. J.* **14**, 8290–8302 (2008).

32. Siegbahn, P. E. O–O bond formation in the S_4 state of the oxygen-evolving complex in photosystem II. *Chemistry* **12**, 9217–9227 (2006).

33. Siegbahn, P. E. Mechanisms for proton release during water oxidation in the S2 to S3 and S3 to S4 transitions in photosystem II. *Phys. Chem. Chem. Phys.* **14**, 4849–4856 (2012).

34. Allgöwer, F., Gamiz-Hernandez, A. P., Rutherford, A. W. & Kaila, V. R. I. Molecular principles of redox-coupled protonation dynamics in photosystem II. *J. Am. Chem. Soc.* **144**, 7171–7180 (2022).

35. Guerra, F., Siemers, M., Mielack, C. & Bondar, A. N. Dynamics of long-distance hydrogen-bond networks in photosystem II. *J. Phys. Chem. B* **122**, 4625–4641 (2018).

36. Li, H. J. et al. Capturing structural changes of the S_1 to S_2 transition of photosystem II using time-resolved serial femtosecond crystallography. *IUCrJ* **8**, 431–443 (2021).

37. Narzi, D., Bovi, D. & Guidoni, L. Pathway for Mn-cluster oxidation by tyrosine-Z in the S_2 state of photosystem II. *Proc. Natl Acad. Sci. USA* **111**, 8723–8728 (2014).

38. Retegan, M. et al. A five-coordinate Mn(iv) intermediate in biological water oxidation: spectroscopic signature and a pivot mechanism for water binding. *Chem. Sci.* **7**, 72–84 (2016).

39. Shoji, M. et al. Large-scale QM/MM calculations of the $CaMn_4O_5$ cluster in the S3 state of the oxygen evolving complex of photosystem

II. Comparison between water-inserted and no water-inserted structures. *Faraday Discuss.* **198**, 83–106 (2017).

40. Wang, J., Askerka, M., Brudvig, G. W. & Batista, V. S. Crystallographic data support the carousel mechanism of water supply to the oxygen-evolving complex of photosystem II. *ACS Energy Lett.* **2**, 2299–2306 (2017).

41. Yang, K. R., Lakshmi, K. V., Brudvig, G. W. & Batista, V. S. Is deprotonation of the oxygen-evolving complex of photosystem II during the S1 → S2 transition suppressed by proton quantum delocalization? *J. Am. Chem. Soc.* **143**, 8324–8332 (2021).

42. Amin, M. et al. Proton-coupled electron transfer during the S-state transitions of the oxygen-evolving complex of photosystem II. *J. Phys. Chem. B* **119**, 7366–7377 (2015).

43. Kuroda, H. et al. Proton transfer pathway from the oxygen-evolving complex in photosystem II substantiated by extensive mutagenesis. *Biochim. Biophys. Acta* **1862**, 148329 (2021).

44. Cox, N. & Messinger, J. Reflections on substrate water and dioxygen formation. *Biochim. Biophys. Acta* **1827**, 1020–1030 (2013).

45. de Lichtenberg, C. & Messinger, J. Substrate water exchange in the S2 state of photosystem II is dependent on the conformation of the Mn_4Ca cluster. *Phys. Chem. Chem. Phys.* **22**, 12894–12908 (2020).

46. Ugur, I., Rutherford, A. W. & Kaila, V. R. I. Redox-coupled substrate water reorganization in the active site of photosystem II—the role of calcium in substrate water delivery. *Biochim. Biophys. Acta* **1857**, 740–748 (2016).

47. Risch, M. et al. Water oxidation by amorphous cobalt-based oxides: in situ tracking of redox transitions and mode of catalysis. *Energy Environ. Sci.* **8**, 661–674 (2015).

48. Nong, H. N. et al. Key role of chemistry versus bias in electrocatalytic oxygen evolution. *Nature* **587**, 408–413 (2020).

49. Zaharieva, I. et al. Water oxidation catalysis—role of redox and structural dynamics in biological photosynthesis and inorganic manganese oxides. *Energy Environ. Sci.* **9**, 2433–2443 (2016).

50. Dau, H. & Haumann, M. Eight steps preceding O–O bond formation in oxygenic photosynthesis—a basic reaction cycle of the photosystem II manganese complex. *Biochim. Biophys. Acta* **1767**, 472–483 (2007).

51. Schiller, H. & Dau, H. Preparation protocols for high-activity photosystem II membrane particles of green algae and higher plants, pH dependence of oxygen evolution and comparison of the S_2-state multiline signal by X-band EPR spectroscopy. *J. Photochem. Photobiol. B* **55**, 138–144 (2000).

52. Iuzzolino, L., Dittmer, J., Dörner, W., Meyer-Klaucke, W. & Dau, H. X-ray absorption spectroscopy on layered photosystem II membrane particles suggests manganese-centered oxidation of the oxygen-evolving complex for the S_0–S_1, S_1–S_2, and S_2–S_3 transitions of the water oxidation cycle. *Biochemistry* **37**, 17112–17119 (1998).

53. Styring, S., Sjöholm, J. & Mamedov, F. Two tyrosines that changed the world: Interfacing the oxidizing power of photochemistry to water splitting in photosystem II. *Biochim. Biophys. Acta* **1817**, 76–87 (2012).

54. Greife, P., Schönborn, M. & Dau, H. Supplementary Data for 'The electron–proton bottleneck of photosynthetic oxygen evolution'. *Zenodo* https://doi.org/10.5281/zenodo.7681840 (2023).

55. Greife, P. Analysis code for 'The electron-proton bottleneck of photosynthetic oxygen evolution'. *Zenodo* https://doi.org/10.5281/zenodo.7682034 (2023).

56. Schuth, N. et al. Inhibitory and non-inhibitory NH_3 binding at the water-oxidizing manganese complex of photosystem II suggests

possible sites and a rearrangement mode of substrate water molecules. *Biochemistry* **56**, 6240–6256 (2017).

57. Dilbeck, P. L. et al. The mutation D1-D61N in *Synechocystis* sp. PCC 6803 allows the observation of pH-sensitive intermediates in the formation and release of O_2 from photosystem II. *Biochemistry* **51**, 1079–1091 (2012).

58. Eyring, H. The activated complex in chemical reactions. *J. Chem. Phys.* **3**, 107–115 (1935).

59. Guo, Y. et al. Unusual kinetics of thermal decay of dim-light photoreceptors in vertebrate vision. *Proc. Natl Acad. Sci. USA* **111**, 10438–10443 (2014).

60. Bao, H. & Burnap, R. L. Structural rearrangements preceding dioxygen formation by the water oxidation complex of photosystem II. *Proc. Natl Acad. Sci. USA* **112**, E6139–E6147 (2015).

61. Hornak, V. et al. Comparison of multiple amber force fields and development of improved protein backbone parameters. *Proteins* **65**, 712–725 (2006).

62. Wang, J. M., Wolf, R. M., Caldwell, J. W., Kollman, P. A. & Case, D. A. Development and testing of a general amber force field. *J. Comput. Chem.* **25**, 1157–1174 (2004).

63. Laino, T., Mohamed, F., Laio, A. & Parrinello, M. An efficient real space multigrid OM/MM electrostatic coupling. *J. Chem. Theory Comput.* **1**, 1176–1184 (2005).

64. Nose, S. A unified formulation of the constant temperature molecular-dynamics methods. *J. Chem. Phys.* **81**, 511–519 (1984).

65. Hoover, W. G. Canonical dynamics—equilibrium phase–space distributions. *Phys. Rev. A* **31**, 1695–1697 (1985).

66. Bovi, D., Narzi, D. & Guidoni, L. Magnetic interactions in the catalyst used by nature to split water: a DFT plus U multiscale study on the

Mn_4CaO_5 core in photosystem II. *New J. Phys.* **16**, 015020 (2014).

67. VandeVondele, J. et al. QUICKSTEP: Fast and accurate density functional calculations using a mixed Gaussian and plane waves approach. *Comput. Phys. Commun.* **167**, 103–128 (2005).

68. Becke, A. D. A new mixing of Hartree–Fock and local density–functional theories. *J. Chem. Phys.* **98**, 1372–1377 (1993).

69. Lee, C. T., Yang, W. T. & Parr, R. G. Development of the Colle–Salvetti correlation-energy formula into a functional of the electron-density. *Phys. Rev. B* **37**, 785–789 (1988).

70. Capone, M., Bovi, D., Narzi, D. & Guidoni, L. Reorganization of substrate waters between the closed and open cubane conformers during the S_2 to S_3 transition in the oxygen evolving complex. *Biochemistry* **54**, 6439–6442 (2015).

71. Capone, M., Narzi, D., Bovi, D. & Guidoni, L. Mechanism of water delivery to the active site of photosystem II along the S_2 to S_3 transition. *J. Phys. Chem. Lett.* **7**, 592–596 (2016).

72. Krewald, V. et al. Metal oxidation states in biological water splitting. *Chem. Sci.* **6**, 1676–1695 (2015).

73. Cox, N., Pantazis, D. A., Neese, F. & Lubitz, W. Biological water oxidation. *Acc. Chem. Res.* **46**, 1588–1596 (2013).

74. Hutter, J., Iannuzzi, M., Schiffmann, F. & VandeVondele, J. CP2K: atomistic simulations of condensed matter systems. *Wiley Interdiscip. Rev. Comput. Mol. Sci.* **4**, 15–25 (2014).

75. Henkelman, G. & Jonsson, H. Improved tangent estimate in the nudged elastic band method for finding minimum energy paths and saddle points. *J. Chem. Phys.* **113**, 9978–9985 (2000).

76. Narzi, D., Mattioli, G., Bovi, D. & Guidoni, L. A spotlight on the compatibility between XFEL and ab initio structures of the oxygen

evolving complex in photosystem II. *Chem. Eur. J.* **23**, 6969–6973 (2017).

77. Siu, S. W., Vacha, R., Jungwirth, P. & Bockmann, R. A. Biomolecular simulations of membranes: physical properties from different force fields. *J. Chem. Phys.* **128**, 125103 (2008).

78. Jorgensen, W. L., Chandrasekhar, J., Madura, J. D., Impey, R. W. & Klein, M. L. Comparison of simple potential functions for simulating liquid water. *J. Chem. Phys.* **79**, 926–935 (1983).

79. Van der Spoel, D. et al. GROMACS: fast, flexible, and free. *J. Comput. Chem.* **26**, 1701–1718 (2005).

80. Darden, T., York, D. & Pedersen, L. Particle mesh Ewald—an *N*.log(*N*) method for Ewald sums in large systems. *J. Chem. Phys.* **98**, 10089–10092 (1993).

81. Hess, B., Bekker, H., Berendsen, H. J. C. & Fraaije, J. G. E. M. LINCS: a linear constraint solver for molecular simulations. *J. Comput. Chem.* **18**, 1463–1472 (1997).

82. Nose, S. & Klein, M. L. Constant pressure molecular-dynamics for molecular-systems. *Mol. Phys.* **50**, 1055–1076 (1983).

83. Parrinello, M. & Rahman, A. Polymorphic transitions in single-crystals—a new molecular-dynamics method. *J. Appl. Phys.* **52**, 7182–7190 (1981).

84. Capone, M., Narzi, D. & Guidoni, L. Mechanism of oxygen evolution and Mn_4CaO_5 cluster restoration in the natural water-oxidizing catalyst. *Biochemistry* **60**, 2341–2348 (2021).

Acknowledgements

The FTIR step-scan experiment on PSII was developed by B. Süss, M. Görlin and P. Chernev; we thank them for their basic and indispensable contributions to development of the experiment. The authors thank Y.

Zilliges, Z. R. Pérez and J. Hantke for photobioreactor operation (for growth of *T. elongatus*) and preparation of the cyanobacterial thylakoid membranes; and R. Burnap and M. Haumann for stimulating discussions and critical reading of early manuscript versions. P.G., M.S., R.A. and H.D. gratefully acknowledge financial support by the Deutsche Forschungsgemeinschaft (DFG, German Research Foundation) provided to the collaborative research centre on Protonation Dynamics in Protein Function (SFB 1078, project A4/Dau) and under Germany's Excellence Strategy–EXC 2008/1–390540038–UniSysCat. M.C., D.N. and L.G. are grateful for the computational resources provided by the Partnership for the Advanced Computing in Europe (PRACE, project Pra14_3574) and CINECA computer centre (project IsC37_QMMMS3S4).

Funding

Open access funding provided by Freie Universität Berlin.

Author information

Author notes

1. These authors contributed equally: Paul Greife, Matthias Schönborn, Matteo Capone

Authors and Affiliations

1. Department of Physics, Freie Universität, Berlin, Germany

   Paul Greife, Matthias Schönborn, Ricardo Assunção & Holger Dau

2. Department of Information Engineering, Computer Science and Mathematics, University of L'Aquila, L'Aquila, Italy

   Matteo Capone

3. Department of Physical and Chemical Sciences, University of L'Aquila, L'Aquila, Italy

Matteo Capone, Daniele Narzi & Leonardo Guidoni

Contributions

H.D. and L.G. designed the experimental and computational research, respectively. M.S. optimized the FTIR step-scan experiments and collected the data. P.G. analysed the FTIR data. R.A. collected and analysed the O_2 polarography data. M.C. and D.N. performed the computational research. H.D., L.G. and P.G. wrote the paper.

Corresponding authors

Correspondence to Leonardo Guidoni or Holger Dau.

Ethics declarations

Competing interests

The authors declare no competing interests.

Peer review

Peer review information

Nature thanks Dimitrios Pantazis and the other, anonymous, reviewer(s) for their contribution to the peer review of this work. Peer reviewer reports are available.

Additional information

Publisher's note Springer Nature remains neutral with regard to jurisdictional claims in published maps and institutional affiliations.

Extended data figures and tables

Extended Data Fig. 1 Experimental setup, timing scheme, and infrared data confirming synchronized reaction-cycle advancement.

a. Schematic representation of the experimental setup. A standard FTIR instrument was modified with an extended, air-tight sample chamber to harbor the automated sample exchange system and combined with a pulsed nanosecond laser. After removal of water vapor from ambient air (dry air generator), the dry gas stream flooded the sample changer. Within the sample changer the temperature was kept a constant 10 °C by a flow of cold nitrogen gas. Stepping motors moving the sample state in x-y direction facilitated laser-flash excitation (and data collection) at 1800 spots of dark-adapted PSII samples. **b**. Timing scheme of the experiment. At each sample spot, 10 sequential flashes were applied while the interferometer had been set to a specific mirror position. The IR detector recorded 8 ms before each flash, 130 ms after each flash and waited 570 ms between the flashes without recording data. Once the detector had finished recording after the tenth flash, the sample changer moved to a 'fresh' dark-adapted sample spot and the interferometer mirror moved to a new position within about 1 s. The 10-flash sequence was applied again at the new positions and the whole timing sequence was repeated numerous times. **c**. By application of 10 sequential laser flashes, the PSII can cycle up to 2.5 times through its S-state cycle. The synchronized advancement in the S-state cycle is verified by a period-of-four pattern in the infrared absorption changes (here averaged from 50–130 ms after the laser flash for 4 selected wavenumbers). Solid lines show the data points and the grey crosses represent a simulation using the deconvolved S-States with the derived miss factor and starting populations. Scale bars correspond to 25 μOD.

Extended Data Fig. 2 Select infrared transients demonstrating that previously identified rate constants are resolved also in the step-scan FTIR experiment.

a. Transients at select wavenumbers for the four deconvolved S-state transitions. These transients are shown to demonstrate that previously identified reaction kinetics are recoverable in this work. Smooth colored

lines represent multi-exponential simulation (least-square fit) of the IR transients. Grey dashed lines mark the identified time constants while grey transients show the respective simulated contributions to the total transient. In each panel, the respective pre-flash level is indicated by a black line. The complete set of simulation parameters can be found in Supplementary Table 2. **b**. S-state cycle with previously determined time constants values (see Supplementary Table 3) and those found in this work (in parenthesis).

Extended Data Fig. 3 Infrared spectra at various times after application of the laser that initiates the oxygen-evolution transition.

The grey line shows the spectral changes induced by the 3rd laser flash applied to dark-adapted PSII. The colored lines are corrected (deconvolved) for imperfect advancement in the S-state cycle as detailed in the Supplementary Material.

Extended Data Fig. 4 Carbonyl band spectra and IR transients between 1695 and 1750 cm^{-1} for the oxygen-evolution transition (S_3->S_4->S_0).

a. Decay-associated spectra of the 340 µs component and of the 2.5 ms component, the latter before (grey line) and after (green line) correction for acceptor side contributions. The acceptor side correction results in three positive peaks for the 2.5 ms component, indicating that band shift cannot explain these three peaks at 1730 cm^{-1}, 1722 cm^{-1} and 1707 cm^{-1}. **b**. Spectra at selected times for the oxygen-evolution transition induced by the 3rd laser flash before (grey lines) and after (colored lines) deconvolution. The high level of similarity indicates that in this spectral region the deconvolution correction is uncritical as it hardly modifies the 3rd-flash data. **c**. Transients displaying reversible behaviour of the 340 µs and 2.5 ms phases reflecting carboxylate deprotonation and reprotonation. **d**. Transient changes assignable to acceptor side contributions. All scale bars correspond to 25 µOD. For details on correction for acceptor side contributions and S-state deconvolution, see Supplementary Information.

Extended Data Fig. 5 Time-resolved O_2-polarography and determination of activation energy of the O_2-formation step for cyanobacterial PSII from *T. elongatus*.

The time courses (transients) of O_2-evolution were (i) measured by time-resolved O_2-polarography for a PSII layer deposited by centrifugation on a bare platinum electrode and (ii) simulated on grounds of a physical diffusion model, including a least-square fit of the simulation parameters (see Methods section). The complete set of simulation parameters is provided in Supplementary Fig. 6. **a**. O_2-evolution transients at temperatures ranging from −5 °C to +40 °C. Each transient was obtained by averaging all the O_2-transients induced by 230 flashes of visible light. **b**. The same transients as shown before but normalized at the respective peak value. In **c** and **d**, selected transients are shown (black symbols) with their respective fit results (colored lines), either with original amplitudes (in c) or normalized to unity (in d). **e**. Arrhenius plot of τ_{ox}, the time constant (reciprocal rate constant) of the oxygen evolution reaction. This plot delivers an Arrhenius activation energy, E_{act}, of 335+/−10 meV (7.73+/−0.23 kcal/mol) with a pre-exponential frequency factor, A, of $2.2 \cdot 10^8$ s^{-1}. After determination of activation energy and pre-exponential factor following the classical approach of Arrhenius, the enthalpy of activation (H_{act}), entropy of activation (S_{act}) were determined using the Eyring equation of transition-state theory (also called Eyring-Polanyi equation) with a transmission coefficient of unity, resulting in values of 310+/−9 meV (7.15+/−0.21 kcal/mol) for H_{act} and of 284+/−9 meV (6.55+/−0.21 kcal/mol) for T_0S_{act} (with T_0 = 20 °C). The applicability of transitions state theory is discussed in Supplementary Information SII.8. The error bars provide the standard deviation of the mean value calculated for three independent experiments at each temperature; the confidence intervals of the energy values are derived from the probable error in the slope of the regression line (broken line).

Extended Data Fig. 6 The two most stable hydrogen-bonds of protonated O6 (in both S_3 and S_3' state).

Upon oxidation of Tyr_Z (Tyr161), the relative stability of the two reported conformers is reversed, conformer-**a** becoming more stable than conformer-**b**, thus favouring the oxyl radical formation as described elsewhere[26]. In both cases, the deprotonated Asp61 is stably interacting with the W1 water molecule. Relevant distances are highlighted by thin lines and reported in both panels for comparison. Manganese atoms are shown in pink, calcium as cyan sphere, oxygen in red, carbon in cyan, and hydrogen in white.

Extended Data Fig. 7 Atomic and electronic rearrangements leading to peroxide formation.

The top panels show molecular sketches of the atomic and electronic motions associated with the energy barriers to overcome along the peroxide formation reaction shown in the bottom panel. The values for the indicated enthalpies of activation and stabilization are: ΔH^*_1, +7.0 kcal/mol; ΔH^*_2, +5.8 kcal/mol; ΔH_1, −19 kcal/mol; ΔH_2, +1 kcal/mol .

Extended Data Fig. 8 Complete picture of events in the oxygen-evolution transition.

Proton and electron transfers are highlighted by blue and red arrows, whereas relocations of heavy atoms are indicated by black arrows. Substrate oxygen atoms (O5 and O6) are depicted in red. The mechanism of the steps 1–5 was investigated in the present study, while the events occurring between the steps 5 and 7 (i.e. the release of molecular oxygen after the peroxide bond formation and the Mn_4CaO_5 cluster restoration) were described in ref. [84]. The events in the transition from **7** to **8** are plausible, but currently not backed up by calculations. The eight panels illustrate the following sequence of events: Oxidation of Tyr161 in the S_3 state, which is coupled to the proton transfer from Tyr161 to His190 (**1**), induces a conformational change involving the side chain of Lys317, resulting in the approach of Lys317 to Glu312 and deprotonation of Glus312 (**2**) within about 340 μs after the laser flash. Within the next 2.5 ms, the transfer of one electron from the O6 atom to Tyr161 coupled to a concerted Grotthus-type relocation of three protons (**3**), resulting in S_4 formation by radicalization of O6 coupled to protonation of Asp61 (**4**). Thereafter, the O6 radical forms a

peroxide bond with the oxygen atom O5 (**5**) and the subsequent deprotonation of Asp61 and release of molecular oxygen. The vacancy site formed by the oxygen evolution step is rapidly refilled with a water molecule coordinated to the Ca^{2+} ion, with simultaneous proton transfer to the hydroxide ion bound to Mn4, and insertion of W5 into the coordination sphere of Ca^{2+} (**6**). The restoration of the Mn_4CaO_5 in the S_0 state is completed by the deprotonation of a water molecule coordinated to Mn4, relocation of Lys317 close to Asp61, and protonation of Glu312 (**7** and **8**).

Extended Data Fig. 9 Conformations sampled by D1-Asp61, D2-Glu312, and D2-Lys317.

a. Sticks representation of the Mn_4Ca cluster and neighboring residues (Asp61, Glu65, Glu312 and Lys317) for the two-flash state (S_3 state) of Photosystem II from the crystallographic model of Kern et al. (PDB ID: 6DHO). A Cl^- ion as well as two water oxygens are also shown as balls. **b**. Distributions of distances between Lys317 and the two residues Asp61 and Glu312 sampled along 50 ns of classical MD simulation with both Asp61 and Glu312 deprotonated (simulation for S_1 geometry). **c**. Scheme of a representative configuration of Asp61, Glu65, Glu312 and Lys317 sampled in the S_1 simulation. In this configuration Lys317 is in close contact with deprotonated Glu312. **d**. Distributions of distances between Lys317 and the two residues Asp61 and Glu312 sampled along 50 ns of classical MD simulation with deprotonated Asp61 and protonated Glu312 (simulation for S_2). **e**. Scheme of a representative configuration of Asp61, Glu65, Glu312 and Lys317 sampled in the S_2 simulation. Lys317 strongly interacts with Asp61, while protonated Glu312 interacts with Glu65.

Supplementary information

Supplementary Information

Supplementary information on the methods and a supplementary discussion for both the step-scan FTIR experiments and the computational chemistry. Moreover, a scheme detailing Fig. 1c is presented. The file includes

supplementary text sections, 22 supplementary figures and 3 supplementary tables. An internal table of contents shows the order of the supplementary elements.

Reporting Summary

Peer Review File

Supplementary Data

Text file containing the complete coordinates (including H atoms) of all 14 structures obtained by the MEP calculation. The coordinates are provided in PDB data format; the 14 coordinate sets are sequentially listed within the text file.

Supplementary Video

Coupled proton and redox chemistry leading to O–O bond formation. The video shows the atomic displacement associated with the MEP calculation, with focus on the Mn_4Ca-oxo complex and its immediate ligand environment. First, the O6 oxyl radical is formed by coupled proton movement and electron transfer to the Tyr_Z radical. Second, the O6 radical forms a peroxide bond with the neighbouring O5. The included amino acid residues are displayed with labels in Supplementary Fig. 18. The video was obtained for the 14 MEP structures by interpolation.

Source data

Source Data Fig. 1

Source Data Fig. 2

Rights and permissions

Open Access This article is licensed under a Creative Commons Attribution 4.0 International License, which permits use, sharing, adaptation, distribution and reproduction in any medium or format, as long as you give appropriate credit to the original author(s) and the source, provide a link to the Creative Commons licence, and indicate if changes were made. The images or other third party material in this article are included in the article's Creative Commons licence, unless indicated otherwise in a credit line to the material. If material is not included in the article's Creative Commons licence and your intended use is not permitted by statutory regulation or exceeds the permitted use, you will need to obtain permission directly from the copyright holder. To view a copy of this licence, visit http://creativecommons.org/licenses/by/4.0/.

Reprints and Permissions

About this article

Cite this article

Greife, P., Schönborn, M., Capone, M. *et al.* The electron–proton bottleneck of photosynthetic oxygen evolution. *Nature* **617**, 623–628 (2023). https://doi.org/10.1038/s41586-023-06008-5

- Received: 28 December 2021
- Accepted: 23 March 2023
- Published: 03 May 2023
- Issue Date: 18 May 2023
- DOI: https://doi.org/10.1038/s41586-023-06008-5

Share this article

Anyone you share the following link with will be able to read this content:

Get shareable link

Sorry, a shareable link is not currently available for this article.

Copy to clipboard

Provided by the Springer Nature SharedIt content-sharing initiative

Structural evidence for intermediates during O_2 formation in photosystem II

- Asmit Bhowmick
- Rana Hussein
- Vittal K. Yachandra

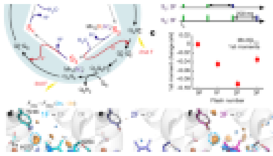
Nature Article Open Access 03 May 2023

Clues to how water splits during photosynthesis

- Dimitrios A. Pantazis

Nature News & Views 03 May 2023

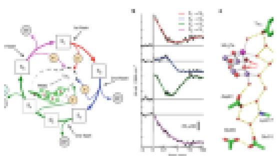
This article was downloaded by **calibre** from https://www.nature.com/articles/s41586-023-06008-5



Structures of the intermediates of Kok's photosynthetic water oxidation clock

07 November 2018

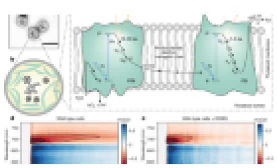
Jan Kern, Ruchira Chatterjee, … Vittal K. Yachandra



The electron–proton bottleneck of photosynthetic oxygen evolution

03 May 2023

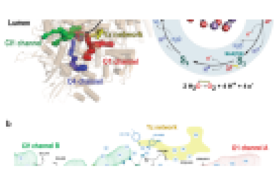
Paul Greife, Matthias Schönborn, … Holger Dau



Photosynthesis re-wired on the pico-second timescale

22 March 2023

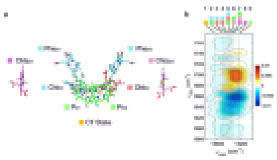
Tomi K. Baikie, Laura T. Wey, … Jenny Z. Zhang



[Structural dynamics in the water and proton channels of photosystem II during the S2 to S3 transition]

11 November 2021

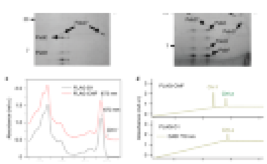
Rana Hussein, Mohamed Ibrahim, … Junko Yano



[The initial charge separation step in oxygenic photosynthesis]

27 April 2022

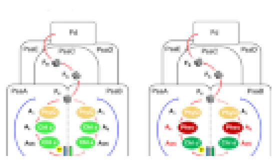
Yusuke Yoneda, Eric A. Arsenault, … Graham R. Fleming



[Chlorophyll f synthesis by a super-rogue photosystem II complex]

09 March 2020

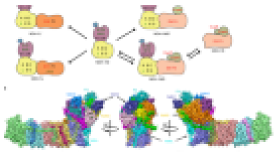
Joko P. Trinugroho, Martina Bečková, … Peter J. Nixon



[Structure of the far-red light utilizing photosystem I of Acaryochloris marina]

20 April 2021

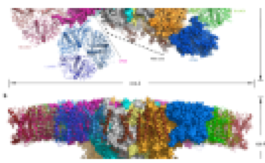
Tasuku Hamaguchi, Keisuke Kawakami, … Yasuhiro Kashino



Structural insights into NDH-1 mediated cyclic electron transfer

14 February 2020

Chunli Zhang, Jin Shuai, … Ming Lei



Structural insight into light harvesting for photosystem II in green algae

25 November 2019

Xin Sheng, Akimasa Watanabe, … Zhenfeng Liu

- Article
- Open Access
- Published: 03 May 2023

Structural evidence for intermediates during O_2 formation in photosystem II

- Asmit Bhowmick,
- Rana Hussein,

- Isabel Bogacz,
- Philipp S. Simon,
- Mohamed Ibrahim,
- Ruchira Chatterjee,
- Margaret D. Doyle,
- Mun Hon Cheah,
- Thomas Fransson,
- Petko Chernev,
- In-Sik Kim,
- Hiroki Makita,
- Medhanjali Dasgupta,
- Corey J. Kaminsky,
- Miao Zhang,
- Julia Gätcke,
- Stephanie Haupt,
- Isabela I. Nangca,
- Stephen M. Keable,
- A. Orkun Aydin,
- Kensuke Tono,
- Shigeki Owada,
- Leland B. Gee,
- Franklin D. Fuller,
- Alexander Batyuk,
- Roberto Alonso-Mori,
- James M. Holton,
- Daniel W. Paley,
- Nigel W. Moriarty,
- Fikret Mamedov,
- Paul D. Adams,
- Aaron S. Brewster,
- Holger Dobbek,
- Nicholas K. Sauter,
- Uwe Bergmann,
- Athina Zouni ,
- Johannes Messinger ,
- Jan Kern,
- Junko Yano &

- …
- Vittal K. Yachandra

Show authors

Nature **volume 617**, pages 629–636 (2023)

- 13k Accesses
- 255 Altmetric
- Metrics details

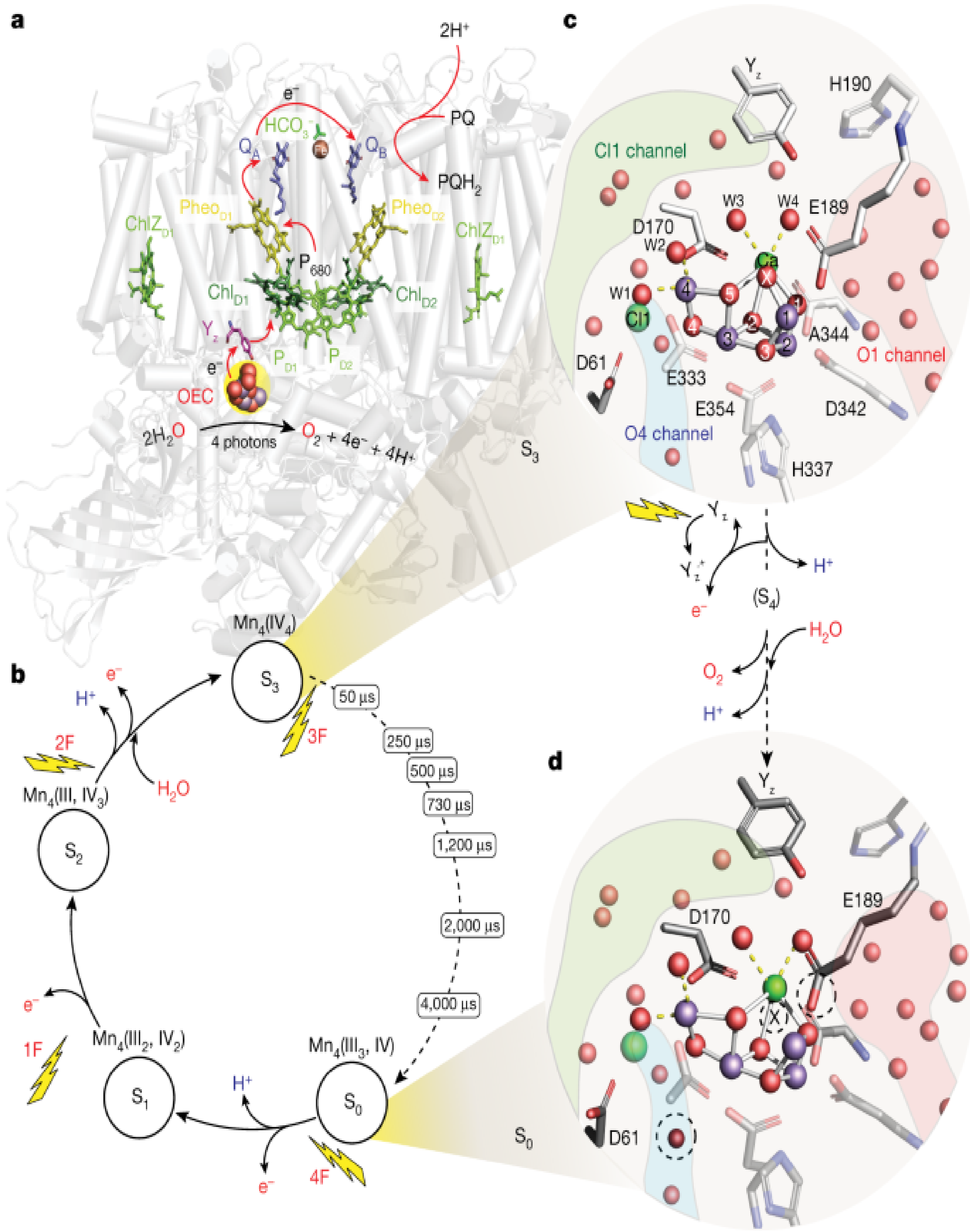
Abstract

In natural photosynthesis, the light-driven splitting of water into electrons, protons and molecular oxygen forms the first step of the solar-to-chemical energy conversion process. The reaction takes place in photosystem II, where the Mn_4CaO_5 cluster first stores four oxidizing equivalents, the S_0 to S_4 intermediate states in the Kok cycle, sequentially generated by photochemical charge separations in the reaction center and then catalyzes the O–O bond formation chemistry[1,2,3]. Here, we report room temperature snapshots by serial femtosecond X-ray crystallography to provide structural insights into the final reaction step of Kok's photosynthetic water oxidation cycle, the $S_3 \rightarrow [S_4] \rightarrow S_0$ transition where O_2 is formed and Kok's water oxidation clock is reset. Our data reveal a complex sequence of events, which occur over micro- to milliseconds, comprising changes at the Mn_4CaO_5 cluster, its ligands and water pathways as well as controlled proton release through the hydrogen-bonding network of the Cl1 channel. Importantly, the extra O atom O_x, which was introduced as a bridging ligand between Ca and Mn1 during the $S_2 \rightarrow S_3$ transition[4,5,6], disappears or relocates in parallel with Y_z reduction starting at approximately 700 µs after the third flash. The onset of O_2 evolution, as indicated by the shortening of the Mn1–Mn4 distance, occurs at around 1,200 µs, signifying the presence of a reduced intermediate, possibly a bound peroxide.

Main

Serial femtosecond X-ray crystallography at X-ray free electron lasers (XFELs)[7] enabled us to collect crystallography data of photosystem II (PS II) in real time as the reaction progresses at physiological temperature. The four photon-induced water-oxidation reaction in PS II (Fig. 1a,b) was initiated with multiple visible laser flashes. Using this capability, intermediate S-state structures (S_0, S_1, S_2 and S_3) have been studied[4,5,8,9,10] that revealed the structural changes of the oxygen evolving complex (OEC) of PS II, which is a functional unit composed of the Mn_4CaO_5 cluster and its water–ligand environment (Fig. 1c,d)[2,11]. Recently, we collected snapshot data at several time points during the $S_2 \rightarrow S_3$ transition, the step in which one substrate water is introduced into the cluster. The study[6] suggested the sequence of Mn oxidation, incorporation of an extra oxygen bridge (O_x or O6 in Suga et al.[10]) between the open coordination site at Mn1 and Ca (forming Mn_4CaO_5-O_x in S_3), the potential entry path for substrate water and the proton release with its gating mechanism[6,12]. The XFEL studies also clearly established that the electronic and geometric structure of the OEC obtained by these measurements is unaffected by X-ray photoelectrons under the conditions used[6,8,13].

Fig. 1: An overview of PS II and the electron donor site where water oxidation takes place.



a, The structure of PS II with the membrane-embedded helices and the membrane extrinsic regions on the lumenal side of PS II shown in gray. The main electron transfer components are shown in colour, which include the reaction center chlorophylls (P680), pheophytins, acceptor quinones Q_A and

Q_B, redox-active tyrosine Y_z and the catalytic Mn_4CaO_5 cluster. The Y_z and Mn_4CaO_5 cluster are the cofactors of the electron donor site. **b**, Kok cycle of the water oxidation reaction taking place at the donor site that is sequentially driven by charge separations in the reaction center P680 induced by the absorption of photons (nanosecond light flashes, 1F–4F) in the antenna system of PS II. Room temperature X-ray crystallography data were collected at the time points indicated during the $S_3 \rightarrow S_0$ transition. **c**,**d**, The structure of the OEC in the S_3 (**c**) and S_0 (**d**) states and the sequence of events occurring between them. Mn, purple; Ca^{2+}, green; O, red. W1, -2, -3 and -4 are water ligands of Mn4 and Ca. The relevant channels for water and proton transfer (O1, O4 and Cl1) are indicated as red, blue and green shaded areas, respectively. The dotted circles mark structural differences between the S_3 and S_0 states.

In the current study, we investigate the oxygen evolving step of Kok's water oxidation cycle (Fig. 1b), the $S_3 \rightarrow [S_4] \rightarrow S_0$ transition (Fig. 1c,d). In dark-adapted PS II samples, this transition is initiated by the third visible laser flash. The OEC is oxidized in this step from the all-Mn(IV) S_3 state to the proposed highly reactive S_4 state with formal oxidation states of $Mn(IV)_4O^{\square}$ or $Mn(IV)_3(V)$. This initiates O–O bond formation and O_2 release, and the now vacant binding site is filled by a new water substrate forming the lowest oxidation state of the cluster (S_0). This multistep process, which also involves the release of two protons, has the longest time constant among the S-state transitions, and its kinetics depend on the species and sample preparation[14,15,16,17,18,19].

To provide structural insight into this complex reaction step and specifically, the important interplay between the Mn_4CaO_5 cluster and its protein–water environment (Fig. 1c,d), we collected room temperature crystallography data of PS II at seven different time points during the $S_3 \rightarrow S_0$ transition, ranging from 50 µs to 4 ms after initiating this transition (Fig. 1b). All datasets have resolutions between 2.00 and 2.16 Å (Extended Data Tables 1 and 2).

The S_3 state was populated by illumination of dark-adapted PS II microcrystals with two in situ visible nanosecond laser flashes (2F in Fig.

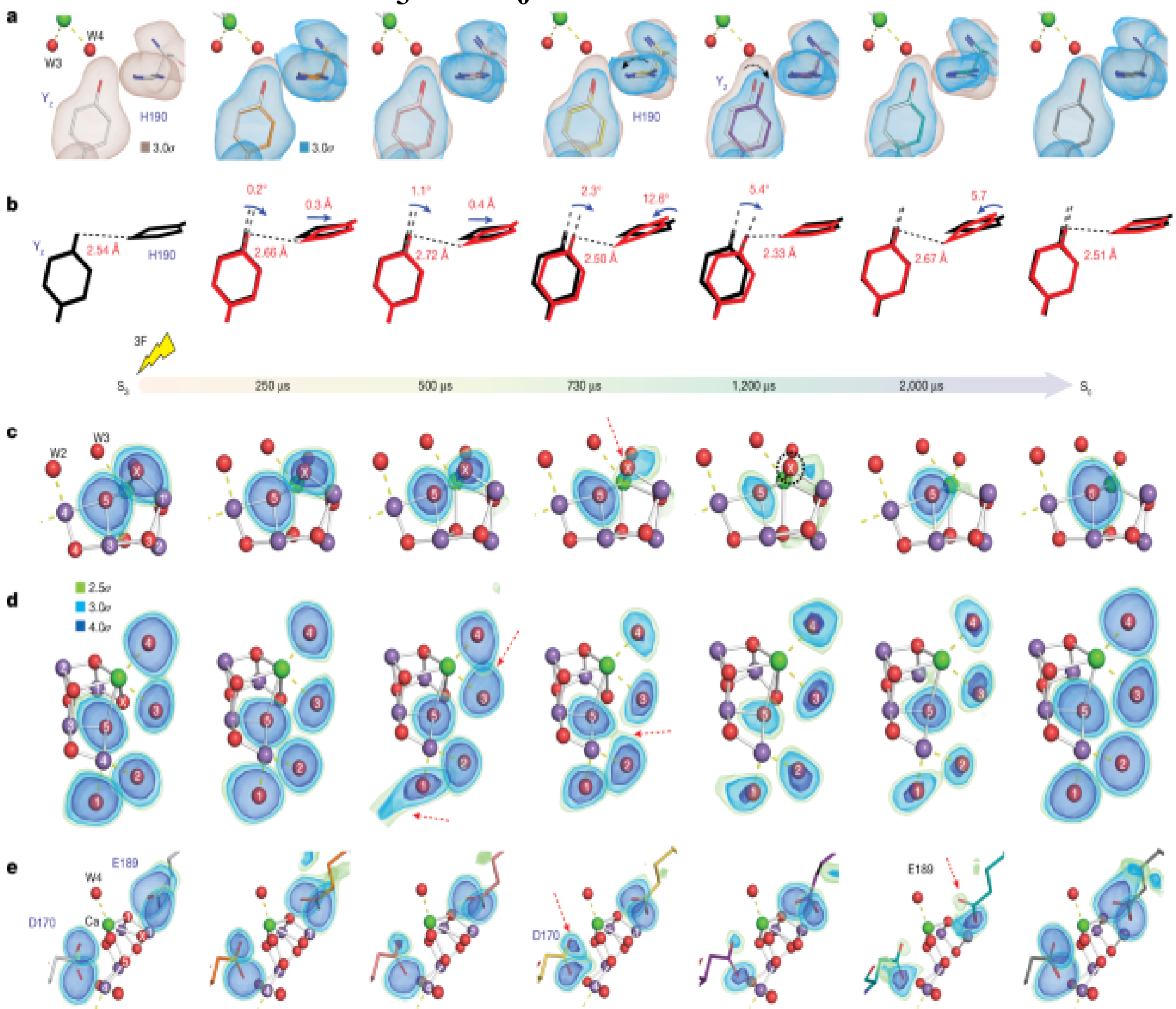
1b)[4], in which the interval between flashes was 200 ms to account for acceptor quinone Q_A and Q_B kinetics and efficiently drive S-state transitions. The time points between the S_3 and S_0 states were generated by giving the third visible pump laser flash at various delay times (Δt) before the crystals were exposed to the femtosecond XFEL pulse (the time labels in Fig. 1b). While our illumination protocol achieves the highest possible populations of particular S states, there is a higher mixing of S-state populations with increasing flash number due to intrinsic PS II-specific inefficiencies ('misses') (Methods)[20]. We model this distribution in a multicomponent model during structural refinement, with the 'primary' component being the centers that advance from the S_3 to S_0 state. The 'secondary' and 'tertiary' components are the known starting and end points: for example, the decreasing S_3 population and at longer delay times, the increasing S_0 population from centers that have completed the transition (Methods and Extended Data Table 3 have details). We note that the primary component at each time point may consist of a mixture of multiple structures, which are intermediates between S_3 and S_0. All results discussed below correspond to these refined primary components from monomer I (chains annotated as uppercase in the deposited structures).

OEC and the Y_Z region

Figure 2 shows the omit map density of selected atoms at the OEC and its surroundings of the refined population at the time points ($\Delta t = 250$, 500, 730, 1,200 and 2,000 μs) after the third flash (we use the nomenclature of 3F(Δt μs)). To visualize the sequence of events during the $S_3 \rightarrow [S_4] \rightarrow S_0$ transition, we follow the changes in three areas: Y_z and D1-H190 (Fig. 2a,b) and O_x and O5 (Fig. 2c), as well as the water ligands W1–W4 (Fig. 2d) and two carboxylate ligands of the Mn_4CaO_5/Mn_4CaO_5-O_x cluster that bridge between Mn and Ca (Fig. 2e). Additionally, selected atomic distance changes are shown in Fig. 3, including the earlier (50 μs) and later (4,000 μs) time point data.

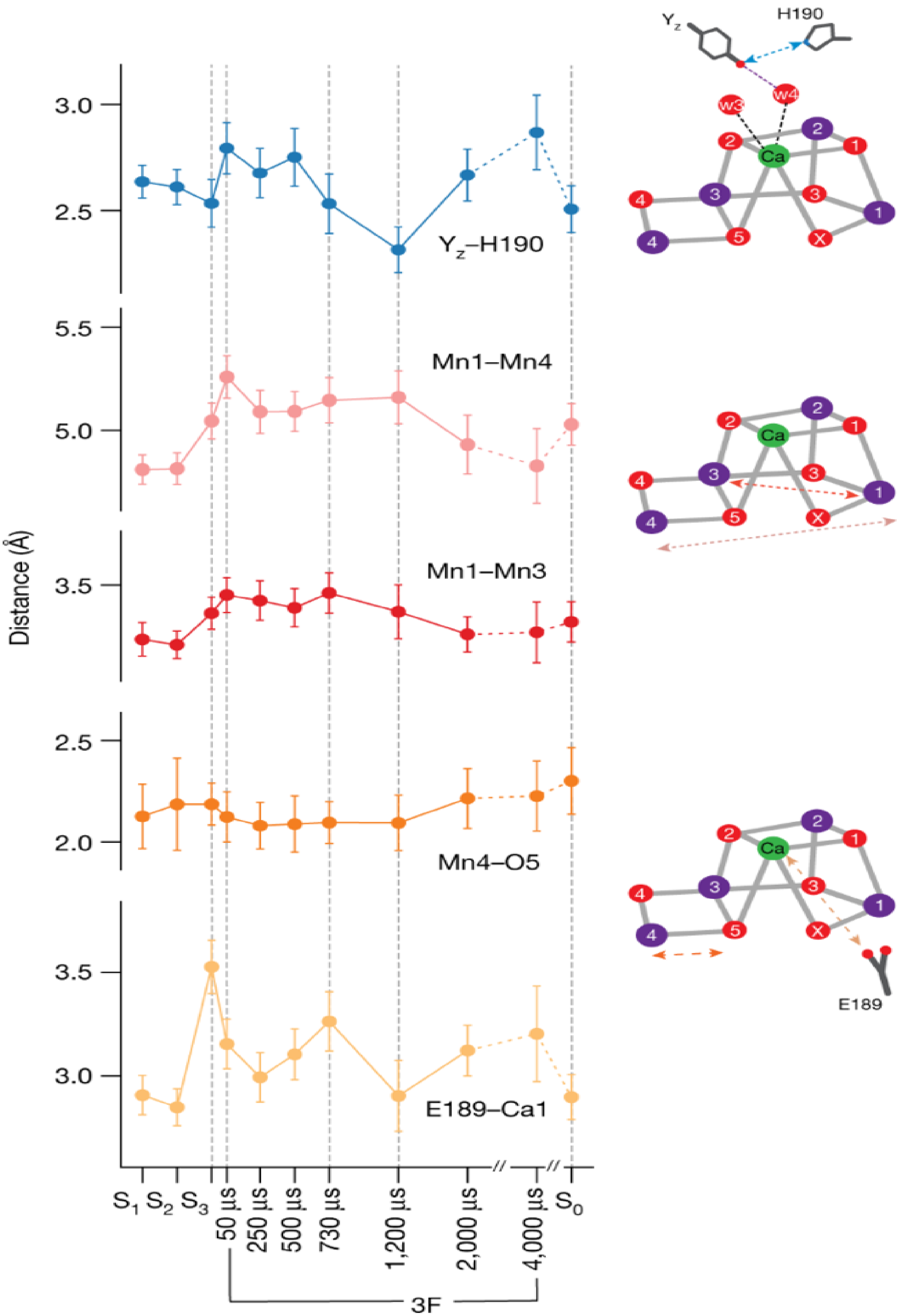
Fig. 2: m$F_{obs} - DF_{calc}$ electron density omit map of key components of the redox active donor site of PS II at five time points along the $S_3 \rightarrow S_0$

transition as well as the S_3 and S_0 states.



a, Residues D1-Y161 (Y_z) and D1-H190. The omit map from the S_3 state reference is shown in light brown for comparison with the time point data (blue). **b**, A simplified representation of the structural changes observed at the Y_z region. **c**, Omit density of atoms O5 and O_x of the OEC. **d**, Omit density of atoms O5 and the terminal water ligands W1, W2, W3 and W4 of the OEC. **e**, Omit density of carboxylate oxygen atoms of D1-E189 and D1-D170. All omit maps shown in **a** and **c**–**e** were generated by omitting the atom or residue of interest individually, and only the primary component (that is, the state that is advancing to S_0) was used. Notable features are highlighted with red arrows and black dashed circle. All omit maps shown are contoured at 2.5σ, 3σ and 4σ using the colour scheme annotated in **d** for easier visualization. See also Supplementary Information Video 1.

Fig. 3: Distance changes between selected atoms/residues in the OEC during the $S_3 \rightarrow S_0$ transition.



Yz–H190
Mn1–Mn4
Mn1–Mn3
Mn4–O5
E189–Ca1
Distance (Å)
3.0
2.5
5.5
5.0
3.5
2.5
2.0
3.5
3.0
S1 S2 S3 50 µs 250 µs 500 µs 730 µs 1,200 µs 2,000 µs 4,000 µs S0
3F
Yz
H190
w3
w4
Ca
E189

All distances are taken from the refined component of each time point (that is, the state that is advancing to the S_0 state). Error bars are calculated from the end/rapid approach described in Methods and are an upper limit. Data here are shown as mean values ± standard deviation. The error bars for each time point were obtained from $n = 100$ independent END/RAPID refinements. More details about the END/RAPID procedure can be found in Methods. Dashed arrows in the schematics of the OEC on the right indicate the location of the individual distances. Mn is shown as purple spheres, and O is shown as red spheres.

The distance between Y_z and D1-H190 has been established previously to be an indicator of the oxidation state of Y_z[6]. In the reduced state, a strong hydrogen bond between Y_z and D1-H190 leads to a short distance of about 2.6 Å. Upon oxidation of Y_z by $P680^+$, the phenolic proton of Y_z is transferred to D1-H190, the distance increases to 2.8 Å and a movement of the His ring plane is observed (Fig. 2b). Our data show that the distance already increases between the S_3 data and the first time point (50 µs), indicating that Y_z is fully oxidized by this time (Fig. 3). Thereafter, this distance remains constant until 500 µs and returns to the base level between 730 and 1,200 µs. Thus, the data demonstrate that \({{\rm{Y}}}_{{\rm{z}}}^{\mathrm{ox}}\) reduction by the Mn_4CaO_5-O_x cluster starts only after around 500 µs (Extended Data Table 4)[16,21,22] and appears to be complete by the 1,200-µs time point. Additional distance changes between Y_z and His190 are observed at 2,000 and 4,000 µs, which may be due to the rearrangement of the hydrogen bonding network related to the last proton release but are not well understood currently. Interestingly, a shift in the position of a Tyr residue next to the special pair Chl upon light excitation was previously noted in time-resolved crystallography data of the purple bacterial reaction center and interpreted as originating from a change in the hydrogen-bonding interactions of this Tyr upon deprotonation[23].

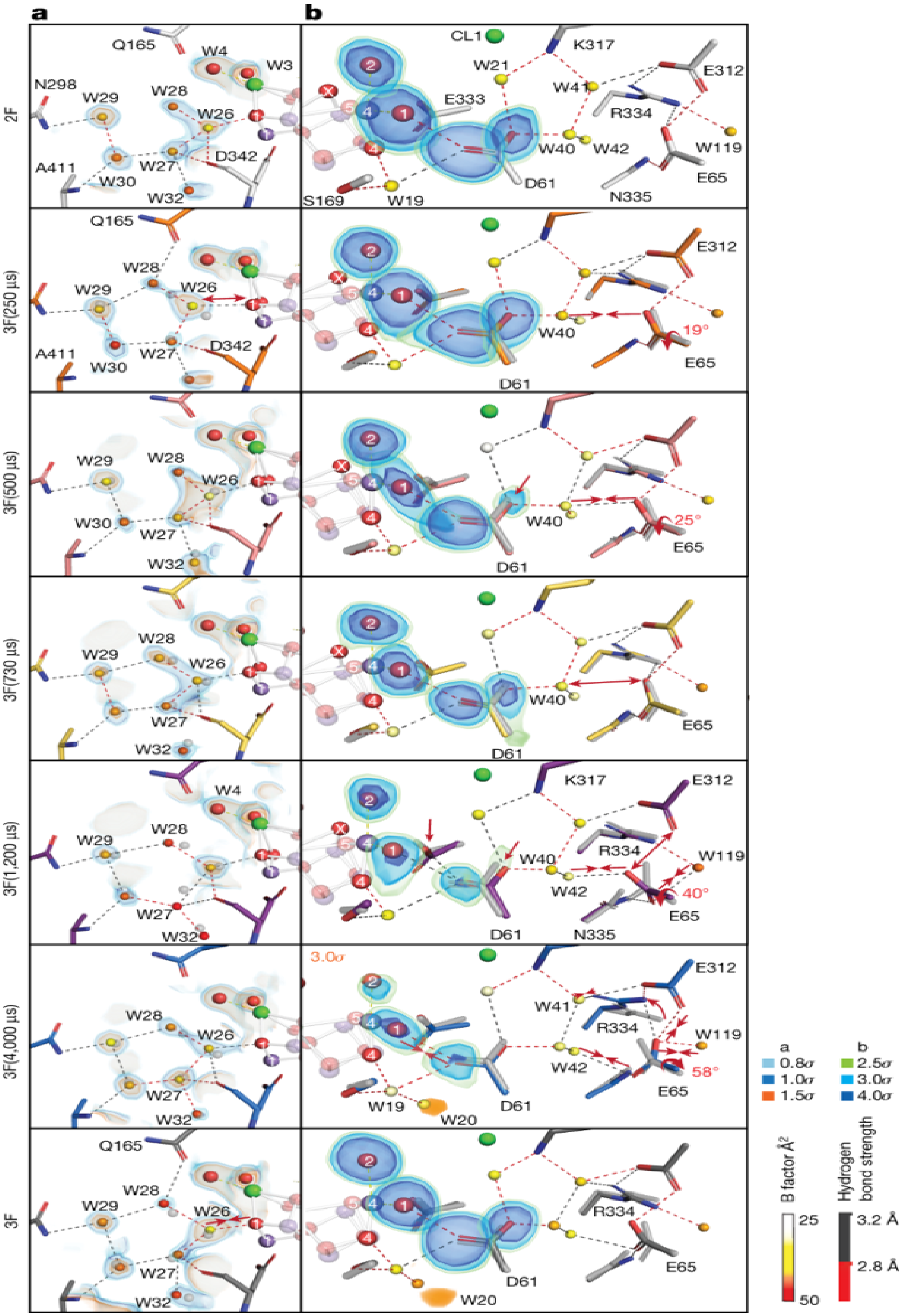
The extra oxygen O_x, present in the S_3 state, is lost upon S_0 formation, indicating that O_x may participate in the O–O bond formation, and changes in its density probably inform on the onset of this process. For tracing the O_x population, O_x was eliminated from the OEC model, and its omit map

density is shown in Fig. 2c. O5 was separately omitted, allowing comparison of their densities (see also Extended Data Fig. 1). The O_x omit density becomes asymmetric starting at 250 µs, with a clear reduction in intensity after 500 µs and dropping to the noise level between 1,200 and 2,000 µs, and O_x can only be modeled with a population of less than 20% in the 2,000 µs time point. The O_x intensity changes occur concomitantly with ${{\rm{Y}}}_{{\rm{z}}}^{\mathrm{ox}}$ reduction, indicating that the O–O bond formation occurs between 500 and 1,200 µs. During the entire $S_3 \rightarrow [S_4] \rightarrow S_0$ transition, the O5 density remains approximately constant, except for a decrease of its electron density at 1,200 µs.

Additional markers for the presence of O_x in the cluster are Mn–Mn distances. As reported previously, the Mn1–Mn4 distance increases during the $S_2 \rightarrow S_3$ transition due to the insertion of O_x (ref. [6]). Figure 3 shows that the Mn1–Mn4 distance remains elongated in the 3F structures until 1,200 µs (Methods has a more detailed analysis) and then declines over the next 3 ms to attain the same value as seen in the S_1 and S_2 states. A similar trend is also seen in the Mn1–Mn3 distance. Thus, there is a delay between the onset of O–O bond formation (500–730 µs based on the changes observed for Y_z and O_x) and the time when the Mn–Mn distances start to decrease (1,200 µs). The finding indicates that during this period, a water oxidation intermediate likely exists before the release of O_2.

Changes in shape and intensities are observed for the omit map density of the water ligands W1–W4, which are displayed in Fig. 2d. Specifically, a slight elongation of the O5 density toward W2 and a slight elongation of the W4 density toward W3 are observed at 250 µs. This latter trend continues, and at 500 µs, an overlap of the W3 and W4 densities is seen, with an $mF_{obs} - DF_{calc}$ peak (F_{obs} and F_{calc} are the experimental and model structure factors respectively, while m and D are weighting factors) at 2.5σ between W3 and W4 (Extended Data Fig. 2). At the same time point, the W1 density becomes extended toward D1-D61 and W19, indicating a higher mobility of W1. We speculate that all these motions are related to the deprotonation of the OEC and proton transfer toward the Cl1 channel (see the next section and Fig. 4).

Fig. 4: Structural changes in select regions of the water and proton channels of PS II during the $S_3 \rightarrow S_0$ transition.


a
b
2F
3F(250 µs)
3F(500 µs)
3F(730 µs)
3F(1,200 µs)
3F(4,000 µs)
3F
Q165
W4
W3
N298
W29
W28
W26
W27
W30
W32
A411
D342
CL1
K317
E312
W21
W41
E333
R334
W40
W42
W119
D61
E65
N335
S169
W19
W20
19°
25°
40°
58°
3.0σ
a
0.8σ
1.0σ
1.5σ
b
2.5σ
3.0σ
4.0σ
B factor Å²
25
50
Hydrogen bond strength
3.2 Å
2.8 Å

a, The terminus of the O1 channel near the OEC that includes the group of five waters (W26–W30) in this region. Overlaid is the $2mF_{obs} - DF_{calc}$ electron density map contoured at 0.8σ, 1.0σ and 1.5σ. **b**, The O4 and Cl1 channels (branch A) that include the D1-D61 and D1-E65/D2-E312 region that is suggested to function as a proton gate. Overlaid are $mF_{obs} - DF_{calc}$ omit maps for W1, W2 and D61 shown at 2.5σ, 3.0σ and 4.0σ. Also shown is the F_{obs}(time point) − F_{obs}(2F) difference density map within a 1.5-Å radius of W19/W20/W48 in the O4 channel at 3σ (orange map). The observed rotation angle at the side chain of E65 at particular time points is calculated with respect to the corresponding side chain position at the 2F state. Major changes are highlighted with an arrow or dashed circle. All waters are coloured by their B factors according to the diverging colour scheme shown in the figure. Important hydrogen-bond interactions are shown with a binary colour scheme to indicate strength (distance < 2.8 Å is red and 2.8–3.2 Å is gray).

At 730 µs, the O5, W2 and W3 densities become anisotropic, all pointing toward a region between these three oxygen atoms (Fig. 2d), which indicates increased mobility of these ligands. At the same time, the O_x density is also highly anisotropic. This movement of all four oxygen atoms is likely related to the formation of the water oxidation intermediate. We note that accurate modeling of the O_x position will require higher-resolution data. At 1,200 µs, the densities for all the terminal water ligands (W1–W4) and the bridging O5 become weakest. A comparison of these omit map densities within the OEC with that of the O2 atom, which is believed to not play a prominent role in the $S_3 \rightarrow S_0$ step, shows that the reduction of the density is specific to these five atoms (W1–W4 and O5) and O_x (Extended Data Fig. 1). The overlap of the O5, W2 and W3 densities is no longer observed at 1,200 µs.

At 2,000 µs after the third flash, the O5 omit map density is restored considerably compared with the S_3 and S_0 states, but omit map densities of the waters W1–W4 have not yet reached a similar level and remain elongated. We note a similar overlap of W1/W2 as observed at 500 µs. This could indicate the onset of the second proton release, known to occur in the $S_3 \rightarrow S_0$ transition, after the binding of a water that refills the vacant site formed by O_2 release[21,24,25]. Interestingly, the elongated shape of the W3

density persists even in the S_0 state, which we modeled previously with two possible positions of W3 (ref. [4]).

Figure 2e shows that the D1-D170 and D1-E189 ligands, which both bridge between an Mn and Ca, change their conformation during O_2 formation and release. Consistent with the high mobility observed for the W1 and W2 water ligands, the connection between D1-D170 and Ca appears to be weakened between 730 and 2,000 μs and is only fully restored at the S_0 state (3F(200 ms)).

From 1,200 to 4,000 μs, several structural changes occur, which are reversed upon formation of the stable S_0 state (3F(200 ms)). These include the increase of the Y_z–D1-H190, Ca–D1-E189 and Mn4–O5 distances, as well as a decrease of the Mn1–Mn4 and Mn1–Mn3 distances. Most of these changes are indicative of O_2 release and/or water insertion via the Ca ion[26,27], possibly from the O1 channel (see below). This indicates that O_2 release and refilling of the cluster by bulk water and resetting of the catalytic center occur over an extended timescale.

Water and proton channels

PS II has several hydrophilic channels that extend from the OEC to the lumenal side of the thylakoid membrane[11,28,29,30,31], and some of these are proposed to play a critical role in transporting protons and substrate waters during the catalytic cycle (O1, O4 and Cl1 channels are shown in Fig. 1)[24,32,33]. In our recent study of the $S_2 \rightarrow S_3$ transition[12], we assigned the O1 channel, which extends from the O1 and Ca of the OEC to the bulk, to be a substrate water channel and the Cl1 channel, which extends from W1 and W2 of the OEC to the bulk, to be a proton release channel during the $S_2 \rightarrow S_3$ transition[6]. The $S_3 \rightarrow S_0$ transition also involves the insertion of one substrate water into the OEC and the release of two protons to the bulk; it has been suggested that one proton is released before the O–O bond formation and the other after the rebinding of a water molecule to the OEC[24,25,34].

Figure 4 shows the time point data for the O1 and the Cl1/O4 channels near the OEC during the $S_3 \rightarrow S_0$ transition. The electron density of water molecules in the O1 channel in the vicinity of the OEC changes substantially as shown in the $2mF_{obs} - DF_{calc}$ maps (Fig. 4a), similar to what was observed during the $S_2 \rightarrow S_3$ transition[6]. Waters W27, W28 and W32 (Supplementary Table 1 has water numbering) have low electron density and high B factors (about 50 $Å^2$) (Extended Data Fig. 3) relative to the more stable waters, such as W29 (B factor of about 37 $Å^2$), in particular at 1,200 µs. We interpret this as an indication of the high mobility of these waters and hypothesize that this region could serve as the inlet for the substrate water that refills the OEC after the release of molecular oxygen[12]. We, therefore, propose that PS II uses the O1 channel for the substrate intake in both the $S_2 \rightarrow S_3$ and $S_3 \rightarrow S_0$ transitions. Among the group of five waters (W26–30) ('water wheel' in ref. [6]), W26 shows high electron density throughout the transition, with a substantially elevated density at 500 µs. As W26 is within hydrogen-bonding distance to O1 of the OEC, this interaction may be important for balancing the charge on the cluster, when the OEC advances through the last oxidation step (that is, S_4 state formation) and the subsequent four-electron reduction to form the S_0 state.

Changes are also observed in the Cl1 channel. At 250 µs, the D1-E65 residue rotates by 19° toward W40, resulting in shortening the distance between D1-E65 and W40 by 0.3 Å (Fig. 4b). This is the time point when the O_x density starts to become asymmetric, which is even more pronounced at 500 µs (Fig. 2c). At 500 µs, the W1 omit map density also becomes elongated toward the region of D1-D61 and W19 (Fig. 4b). This coincides with a decrease of the D1-D61 carboxylate oxygen density that is within hydrogen bond distance of W40 and a shortening of the distance between W40 and D1-E65 by 0.5 Å due to rotation (25°) of the side chain. Consequently, a continuous hydrogen bond network is formed that connects the OEC to the D1-E65/D2-E312 region. We speculate that the changes are related to the first proton transfer from the OEC toward the Cl1 channel. These changes are reversed by the 730-µs time point (Fig. 4b). An early deprotonation event has also been suggested by other studies using different methods, with time constants that range from 50 to 300 µs (that is, before the last oxidation event; the transient S_4 state formation)[15,16,17,21,24,34,35].

At 1,200 µs, the D1-E65 residue rotates toward W40 for the second time during this transition, accompanied by a shortening of the W42–D1-E65 distance by 0.4 Å. Thus, a hydrogen bond network from the OEC to the D1-E65/D2-E312 region, similar to what we observed at 500 µs, is reformed at this time point. The D1-E65/D2-E312 distance elongates from roughly 2.6 to roughly 3.2 Å, which points to a substantial weakening of the interaction, likely forming a configuration that can accept the next proton. This change coincides with the time at which the O_x electron density decreases below the detection level in the omit map (Fig. 2), and the W28, W27 and W32 densities decrease in the O1 channel (Fig. 4a). We interpret this series of changes to be related to the onset of the recovery process of the Mn_4CaO_5 cluster (that is, initiated by the insertion of water into the OEC along with a deprotonation). At 2,000 and 4,000 µs, the side chain of D1-E65 is rotated almost 40° from its position in the S_3 structure toward W119 (Fig. 4b). The distance D1-E65–W119 is around 2.5 Å, suggesting a shared proton or very tight interaction between these two groups. D1-R334 also moves by 20°, forming a hydrogen-bonding interaction with W41.

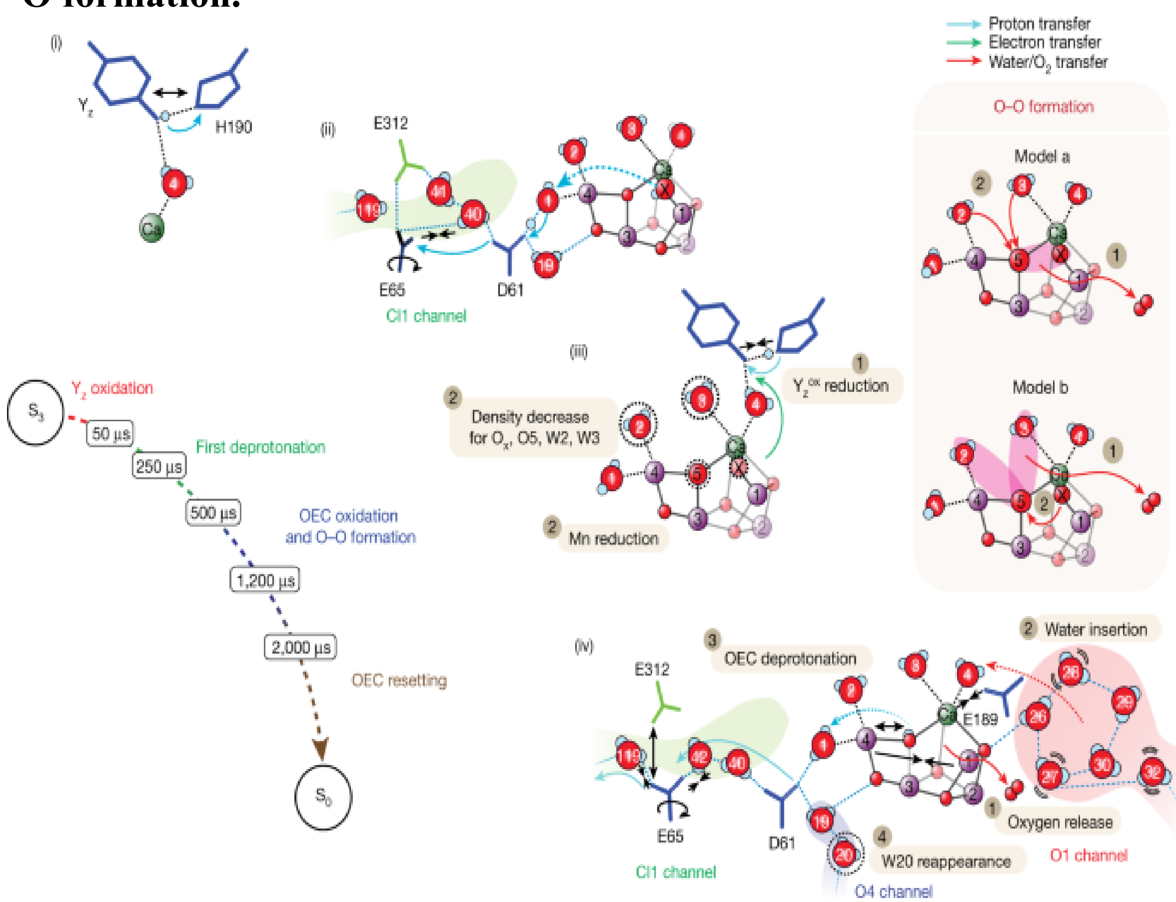
The changes around the D1-E65/D2-E312 region are indicative of the proton release to the bulk since they are reminiscent of what we observed for proton release during the $S_2 \rightarrow S_3$ transition[12]. In the $S_3 \rightarrow S_0$ transition, we hypothesize that the earlier changes of this region (250–730 µs) are related to the first proton transfer and that the later changes (1,200–4,000 µs) are related to the second proton transfer from the OEC to the bulk, through D1-D61[36,37] via the rotation of D1-E65. Thus, the current result suggests that the D1-E65/D2-E312 region functions as a gate for proton release twice during the $S_3 \rightarrow S_0$ transition.

W20, which forms a tight hydrogen bonding network with O4 via W19 in the O4 channel, disappears during the $S_1 \rightarrow S_2$ transition and reappears in the S_0 state[4]. Its return during the $S_3 \rightarrow S_0$ transition is therefore an indicator for the full recovery of the S_0 state. The first clear indication of the return of W20 is found in the $F_{obs}(4{,}000\ \mu s) - F_{obs}(2F)$ difference map (orange density in Fig. 4b), and it was modeled at 40% occupancy in the 4,000-µs refined component. This implies that the W20 restoration happens in the later stage of the OEC recovery.

Sequence of events during $S_3 \rightarrow S_0$

The snapshots of the structures of PS II during the $S_3 \rightarrow S_0$ transition show the sequence and the progression of each of the events at multiple locations with different time constants. The structural changes can be broadly grouped into four sections with different onset times and kinetics, as shown in Fig. 5; they are the redox state changes of Y_z, first deprotonation, OEC oxidation and O_2 formation and the complete recovery and resetting of the Kok clock in the S_0 state.

Fig. 5: Schematic of the $S_3 \rightarrow S_0$ transition and proposed mechanism for O–O formation.



The sequence of events (i–iv) leading to the first deprotonation event, the molecular oxygen release, the water insertion and the second deprotonation event. The OEC atoms are shown in purple (Mn), green (Ca) and red (O). The O1 channel is shown in red, the O4 channel is in blue and the Cl1

channel in green. The ligands of the OEC and the residues forming the water–proton channels are coloured based on the subunit they belong to (D1, blue; D2, green). Possible pathways for proton (cyan arrow), water (red dashed arrow), oxygen (red solid arrow) and electron (green arrow) transfer are depicted. Notable features are highlighted with black arrows. The right tan box shows the suggested models (model a and model b) for O–O bond formation. Oxygen highlighted with magenta indicates the candidate atoms for O–O formation.

In the S_3 state, all four Mn are formally in the (+IV) oxidation state. We note that oxidation of ligand instead of Mn (formation of oxyl or an oxo–oxyl bond) during the $S_2 \rightarrow S_3$ transition has been suggested in the literature[5], but this is not in line with the room temperature X-ray emission spectroscopy (XES) data, which show the oxidation of Mn[6,13]. Upon the third flash, the oxidation of Y_z occurs by donation of an electron to $P680^+$ after the charge separation at the reaction center chlorophylls. A distance increase between Y_z and D1-H190 is observed in comparison with the S_3 state in 3F(50 μs) (Figs. 3 and 5(i)). This change is assigned to the ${\rm{Y}}_{\rm{z}}^{\mathrm{ox}}$ formation, which is known to occur within 30 μs after photoexcitation[38], and related proton translocation between ${\rm{Y}}_{\rm{z}}^{\mathrm{ox}}$ and D1-H190.

The ${\rm{Y}}_{\rm{z}}^{\mathrm{ox}}$ formation triggers the first deprotonation event likely during the time period of 200–500 μs[15,16,17,24,34,39]. We observed the start of the rotation of D1-E65, which is proposed to be part of the proton gate, and the formation of the hydrogen bond pathway from the OEC to this region at 250 μs. Along with these changes, the electron densities at W1 and D61 become more prominent at 500 μs (Figs. 2d and 4b), potentially related to a proton release from the OEC to the proton gate residues D1-E65 and D2-E312 (Fig. 5(ii)).

In the early stage of the 500- to 1,200-μs period, the last oxidation event (transient S_4 state formation, with $Mn(IV)_4O^{□}$ or $Mn(IV)_3(V)$) occurs, and subsequently, the reduction of Mn takes place (Fig. 5(iii)). The O–O bond formation should be triggered by this final oxidation event of the OEC to the potentially short-lived S_4 state. The change in distance we observe for Y_z–

D1-H190 between 500 and 730 μs suggests that the reduction of $\mathrm{Y}_{\mathrm{z}}^{\mathrm{ox}}$ takes place during this time, through the electron transfer from the OEC to Y_z. After the transient formation of S_4, the four-electron reduction may proceed in one step with the O–O bond formation and immediate release of O_2 or in two steps with the presence of an intermediate before the release of molecular oxygen from the OEC. In the latter case, a peroxo species formed by an initial two-electron reduction appears most likely as an intermediate.

Our data show that there is a delay between the onset of O–O bond formation (500–730 μs) as indicated by the Y_z–D1-H190 distance/rotation and the decrease of the O_x electron density and the onset of the O_2 release supported by the Mn1–Mn4 distance contraction (1,200 μs). This onset time for O_2 release is also in line with studies of O_2 evolution[22,40]. The delay indicates that there is an intermediate state, possibly a peroxide-like species, pointing toward the two-step electron reduction mechanism.

Several O–O bond formation sites have been proposed in the literature based on theoretical studies (Fig. 5)[3,41,42,43,44,45,46,47,48,49]. Among these, O5–O_x best account for our data because of their proximity and the reduced occupancy of O5 around 1,200 μs (Fig. 5, model a). However, two other possibilities in which O5 reacts with either W2 or W3 and O_x replaces O5 cannot be excluded at this time (Fig. 5, model b). While other mechanisms that do not involve O5 cannot be ruled out, there is no clear evidence to support those in the current data.

At 1,200 μs, the O_x omit map density is below the 2.5σ threshold, indicating that a predominant fraction of O_x has shifted from its original position in the cluster. The contraction of the Mn1–Mn4 and Mn1–Mn3 distances starting at this time point suggests that the onset of O_2 release happens around this time. Once O_2 is released, refilling of the cluster with a new substrate water seems to occur immediately. This is based on the observation that there is no missing oxygen density besides O_x, although the omit map densities of all the terminal waters (W1–W4) and bridging O5 are weakened at 1,200 μs.

The data support that the O_2 release and refilling of the site are highly coordinated and occur likely via a terminal water already ligated to the OEC.

At both 2,000 and 4,000 µs (Fig. 5(iv)), O_x density is within the noise level, which implies that Mn1 becomes predominantly five coordinate. Mn4 is six coordinate, although the Mn4–O5 interaction is weak (2.2–2.3 Å), suggesting that O5 may be a hydroxide. The Ca–D1-E189 distance is still more elongated at these time points than in the S_0 state. Other slow recoveries are observed in the Y_z region (Fig. 2b), the 'water wheel' (Fig. 4a) and the proton gate regions (D1-E65/D2-E312) (Fig. 4b). We hypothesize that a water from the 'water wheel' region in the O1 channel, similar to the $S_2 \rightarrow S_3$ transition[6,12], replaces the terminal water ligand of the OEC. The changes in the proton gate region might indicate the deprotonation of the newly inserted water[36]. Concomitantly, the amino acid coordination environment, the hydrogen bonding network around the OEC and the waters in the channels reset to the S_0 state. This includes recovery of W20 in the O4 channel, which is proposed to be involved in proton release during the $S_0 \rightarrow S_1$ transition[4,50].

In the current study, room temperature snapshots of PS II structures through the final step of Kok's clock ($S_3 \rightarrow [S_4] \rightarrow S_0$) reveal details of the molecular processes for photosynthetic water oxidation. Until now, these processes were interpreted largely based on kinetic studies. Importantly, the results reported here provide experimental support for a two-step reduction mechanism of the Mn_4CaO_5-O_x cluster upon the O–O bond formation and O_2 release with a transient intermediate, most likely a bound peroxide. This is a major step forward toward understanding the chemistry of the water oxidation reaction. The results also show how biological catalysts, such as the OEC in PS II, enable multielectron/multiproton reactions through the interplay between the metal center, the protein environment and the water network. The active role of the microenvironment in natural enzymes provides inspiration for how to control such reactions in artificial photosynthetic systems that can be made from earth-abundant elements.

Methods

Sample preparation

The X-ray diffraction measurements of 20- to 60-µm crystals prepared from PS II dimers of *Thermosynechococcus vestitus* (previously named *Thermosyncechococcus elongatus*) were performed in 100 mM 2-(*N*-morpholino)ethanesulfonic acid, pH 6.5, 100 mM ammonium chloride and 35% (wt/vol) PEG 5000 (refs. [51,52]). PS II crystal suspension, at about 0.5–1.2 mM chlorophyll (Chl) concentration, was loaded into a syringe (Hamilton gastight syringe, 1 ml) and dark adapted for 1 h before data collection. Membrane inlet mass spectroscopy (MIMS) was used to determine the O_2 evolution, turnover parameters and S-state populations[4,6]. The PS II crystals showed no Mn (II) contamination based on XES and electron paramagnetic resonance measurements[53] and exhibited an activity of 2500 ± 100 µmol O_2 (mg(Chl) × h)$^{-1}$.

Sample injection and illumination

Acoustic droplet ejection[54] was used in combination with the Drop-on-Tape sample delivery method[55]. For capturing the stable intermediates S_2, S_3 and S_0, each droplet of the crystal suspension was illuminated by 120-ns laser pulses at 527 nm using an Nd:YLF (yttrium lithium fluoride) laser (Evolution, Coherent) at Linac Coherent Light Source (LCLS) or by 8-ns laser pulses at 532 nm using a combination of two Nd:YAG (yttrium aluminium garnet) lasers (Minilite, Continuum) at Spring-8 Angstrom Compact free electron Laser (SACLA) via three fiber-coupled outputs with a delay time of 200 ms between each illumination and of 200 ms between the last illumination and the X-ray probe, similar to what was used previously to accommodate the acceptor quinone Q_A and Q_B kinetics and efficiently drive S-state transitions[4,6,55]. We implemented a feedback control system of the belt speed and deposition delay, and the flashing delay and droplet phase were adjusted accordingly[55]. To achieve time delays shorter than 200 ms between illumination and the X-ray probe, a fourth ‘free space’ laser was utilized. This was either an Opolette 355 LD laser (Opotek, 530-nm wavelength, 7-ns pulse width) at the macromolecular femtosecond crystallography/LCLS instrument or an NT230 OPO laser system (530-nm wavelength, 5-ns pulse width, EKSPLA Co.) at SACLA. This free space

laser was triggered to be synchronized with the X-ray pulse with an adjustable delay that was set between 50 and 4,000 μs for this study. The laser was guided with optics to the X-ray interaction spot, and its position was fine-tuned for each delay time to ensure that the laser spot position coincides with the position of the sample droplet at the selected delay timing. At the XFELs, a light intensity of 120 ± 10 mJ per cm^2 was applied as O_2 evolution was found to be saturated at 70 mJ per cm^2 for the dimensions and concentrations of samples used in our experiments[4]. A light intensity of 120 mJ per cm^2 corresponds to about 140 photons absorbed per PS II monomer in the front 5-μm layer of the crystal and approximately 9 photons per PS II monomer when assuming a 60-μm thickness of the crystal (which is the upper size limit of the crystals used in this study) for the back 5-μm layer. This photon density ensures saturation over the entire crystal volume, even in the case of two crystals stacked on top of each other in the laser beam. Given a minimum pulse length of 5 ns and 35 Chl per PS II monomer, the light intensity used averages to 0.8 photons per (Chl and nanosecond) for the front and 0.05 photons per (Chl and nanosecond) for the back part of the crystal. If a PS II center is undergoing charge separation, additional photons absorbed by the internal antenna Chl are rapidly dissipated in the form of fluorescence with an average fluorescence lifetime of around 0.5–1 ns, hence preventing any overexcitation of the reaction center or causing any heating artefacts.

X-ray data collection

The crystallography data were collected at various facilities, and details are listed in Supplementary Table 2. The experimental beam conditions and detector configurations used to collect each dataset are also tabulated. The sample was delivered into the X-ray interaction region using the previously described Drop-on-Tape setup[55]. Illumination conditions for populating different S states are detailed in ref. [4].

X-ray diffraction data processing

The data collected for the different illumination states were processed using the program dials.stills_process with a target unit cell of a = 117.0 Å, b =

221.0 Å, $c = 309.0$ Å, $\alpha = \beta = \gamma = 90°$ and the space group $P2_12_12_1$. Bragg spots were integrated to the edge of the detector. A Kapton absorption correction due to the conveyor belt of our sample delivery system was applied to each integrated Bragg spot, taking into account the droplet size, tape thickness, tape angle and the position of the diffraction spots on the detector with respect to the crystal position. Before integration, we also performed ensemble refinement of the crystal and detector parameters using the program cctbx.xfel.stripe_experiment, which has been shown to narrow the unit cell distribution and improve the final isomorphous difference maps[56]. Finally, the intensities were merged using the program cctbx.xfel.merge, which applies a per-image resolution cutoff and filtering of the lattices using a unit cell threshold of 1% from the reference model. To merge the reflections, we use the best practices described in ref. [57]. The unit cells and number of lattices merged for each dataset are tabulated in Extended Data Tables 1 and 2.

Final merged datasets were acquired for the 2F, 3F(50 µs), 3F(250 µs), 3F(500 µs), 3F(730 µs), 3F(1,200 µs), 3F(2,000 µs), 3F(4,000 µs) and 3F(200 ms) states to resolutions between 2.16 and 2.0 Å, obtained by merging between 6,659 and 39,199 lattices (Extended Data Tables 1 and 2). The final merged datasets before model building were also scaled on a per-resolution bin basis to a reference dataset (in this case, the reference dataset is the PS II dataset published in PDB ID code 7RF1)[12]. This allows us to conduct a more accurate comparison of $mF_{obs} - DF_{calc}$ omit maps and $2mF_{obs} - DF_{calc}$ maps between different datasets.

Model building and map calculation

Each dataset was refined using a high-resolution PS II structure (1.89 Å) that was published in a previous work (PDB ID code 7RF1)[12] as the starting point using the program phenix.refine[58]. The refinement is done in several stages. First, the B factors of the starting model are set to 30, and all waters and the atoms of the OEC are removed. An initial rigid body refinement coupled with refinement of *xyz* coordinates and isotropic B factors was done for 15 cycles to adjust the model into the unit cell. Next, the OEC atoms are added back and refined with custom bonding restraints for several cycles.

We also use custom bonding restraints for chlorophyll-*a* (to allow correct placement of the Mg relative to the plane of the porphyrin ring) and unknown lipid-like ligands (steric acid) in the refinement. After initial refinement of the OEC + protein complex, waters were added to the model using the phenix.refine water picking protocol as well as manual placement of waters via coot[59] and doing multiple cycles of refinement.

At this stage, we split the model in the vicinity of the OEC and the OEC itself (only protein and OEC atoms) into multiple components (Extended Data Table 3). The split was done only in parts of chains A/a, C/c and D/d. The rationale and population of the components in each time point used are described in the section Estimating population distribution in each time point. In each dataset, the primary conformer (defined as the intermediate that is advancing from S_3 to S_0) is refined using a strategy of reciprocal *xyz* + isotropic B-factor refinement. For the secondary/tertiary components (whose structures are known as they are either in the S_3 or S_0 state), only the group B factors are adjusted (group_adp strategy in phenix.refine) to adjust them to the resolution of the dataset. For the remaining part of the model that is not split, regular reciprocal *xyz* refinement and isotropic B-factor refinement are performed in tandem for multiple cycles. All waters (except for the terminal waters ligated to the OEC; that is, W1–W4) were refined as a single component.

The refinement of the OEC in the primary component of the multicomponent model was done using custom restraints that were used to model the S_3 state. However, for all the time points, we used slightly looser estimated s.d. values for the restraints (0.1 Å for bonds, 10° for angles) to allow the OEC atoms during refinement to move toward where the electron density is optimally modeled and reduce strain in the refinement while at the same time maintaining the overall shape of the cluster. The OEC in the S_0 state was modeled with restraints used for our previously published S_0 state structure. The restraints used to model the OEC atoms in the time points have been provided as text files (schemes 1–3 in Supplementary Data).

Estimating population distribution in each time point

The S-state population distribution in the $S_3 \rightarrow S_0$ transition is a heterogeneous distribution consisting of (1) centers that are advancing from the S_3 to S_0 state, (2) centers that are lagging behind by one transition and hence, are advancing from the S_2 to S_3 state and (3) centers that have transitioned over to the S_0 state. While the majority of centers are in category (1), due to the intrinsic inefficiencies ('misses') of the Kok cycle in PS II[20], a certain fraction of centers is in category (2). In addition, after a certain time in the S_3–S_0 transition, a substantial number of centers will have formed the stable S_0 state (category (3)).

Given this context, it is important to account for this population heterogeneity in our structural modeling to obtain accurate electron density maps and models. We do this by splitting up our structural model near the active site region (including the OEC) into multiple components. The primary component in each dataset is category (1), which is the intermediate transitioning from S_3 to S_0. The nature of the secondary and tertiary components depends on the dataset under consideration. In each dataset, the coordinates/isotropic B factors of only the primary component are refined (category (1)). The secondary and tertiary component structures are modeled from known or previously deposited structures and only adjusted for resolution using a group B-factor refinement. The identity of the secondary (and tertiary if used) component depends on which time point is being processed. For example, in the 3F(50 μs) dataset, a two-component model is constructed with the 2F(50 μs) model coordinates/B factors being used for the secondary component. In the 3F(1,200 μs) data, we use a three-component model with the secondary and tertiary components being the S_0 and S_3 states. The populations for each of the components in the various time points are given in Extended Data Table 3. We used numbers available in the literature to perform a kinetic analysis yielding an estimate of the population distribution. Since populations below 10% are in the noise level for structural refinement, we adjusted our populations to avoid any conformer with such low populations.

The population distribution in each of the metastable S states has been previously determined using the MIMS technique. In our work, the starting 2F state, which is generated by illuminating with two visible lasers with a

flash interval of 200 ms, consists of approximately 65% S_3 state and 35% S_2 state based on studies conducted on crystals. With the third visible flash, the $S_3 \rightarrow S_0$ transition is initiated. The reader is referred to the extended data in ref. [4] for more details on how the S-state populations for each of the flash states were estimated, accounting for miss parameters calculated from XES and MIMS data, and crossillumination (this was negligible at the speed of the tape and deposition frequency of the acoustic droplet ejection that was used in the present study). All the results described in this paper are from monomer I (chains annotated as uppercase in the published structures). Similar trends are observed for monomer II (chains annotated as lowercase).

Estimating the effect of population on the Mn1–Mn4 distance

The Mn1–Mn4 distance stays elongated until 3F(1,200 μs) in the intermediate undergoing the $S_3 \rightarrow S_0$ transition, after which a decrease is seen in the next 3 ms. We tested the robustness of the elongated distance at 3F(1,200 μs) by constructing an alternative hypothesis to explain this observation, postulating that it could be due to two separate populations in the primary component: (1) increased Mn1–Mn4 distance due to misses that form additional S_3 or (2) decreased Mn1–Mn4 distance (with/without disappearance of O_x) that is a property of the intermediate undergoing the $S_3 \rightarrow S_0$ transition. We modeled this scenario by increasing the S_3 population from 35 to 55% and decreasing the primary component (with/without O_x) from 40 to 20% in the 3F(1,200 μs) time point. The resulting refinement gave Mn1–Mn4 distances of 5.14 Å (with O_x) and 5.09 Å (without O_x). Both numbers are similar to the distance given in Fig. 3 and within the measurement error. The tests thus show no contraction compared with the S_3 state and allow us to reject the hypothesis. We reiterate that the S_3 population estimate of 35% in the 3F(1,200 μs) time point is well established using multiple independent experiments as detailed in the previous section and past publications.

Estimated positional precision

To estimate the positional precision of the OEC atoms and the surrounding amino acids for each time point, we used the END/RAPID procedure[60], similar to what was previously employed[6]. Briefly, in this method, we perturb the structure factors by a random amount in between $\pm(\mathrm{m}F_{\mathrm{obs}} - \mathrm{D}F_{\mathrm{calc}})$. The atomic coordinates of the final model for that time point are also perturbed by a small amount to allow the model to explore greater phase space (only the primary conformer is perturbed). Subsequently, 100 such synthetic datasets are generated for each time point, and they are then each refined separately. From the ensemble of these refined datasets, we can estimate the error associated with the distance metric of interest. The obtained errors should be considered an upper bound as the introduced perturbations in the structure factors are an overestimate of the true errors in the experiment.

Implementation details can be found at https://bl831.als.lbl.gov/END/RAPID/end.rapid/Documentation/end.rapid.Manual.htm.

$\mathrm{m}F_{\mathrm{obs}} - \mathrm{D}F_{\mathrm{calc}}$ difference omit density

All $\mathrm{m}F_{\mathrm{obs}} - \mathrm{D}F_{\mathrm{calc}}$ omit maps shown in the manuscript were generated using the phenix.polder program and using the normal omit map coefficients from the output.mtz file (not polder map coefficients)[61]. For peak height calculation wherever stated, we used custom python scripts that average the $\mathrm{m}F_{\mathrm{obs}} - \mathrm{D}F_{\mathrm{calc}}$ omit map value about a 0.5-Å radius of the atom of interest.

Reporting summary

Further information on research design is available in the Nature Portfolio Reporting Summary linked to this article.

Data availability

The atomic coordinates and structure factors have been deposited in the Protein Data Bank, www.pdb.org (PDB codes 8EZ5 for the 2F data; 8F4D for the 3F(50 μs) data; 8F4E for the 3F(250 μs) data; 8F4F for the 3F(500

μs) data; 8F4G for the 3F(730 μs) data; 8F4H for the 3F(1,200 μs) data; 8F4I for the 3F(2,000 μs) data; 8F4J for the 3F(4,000 μs) data; 8F4K for the 3F(200 ms) data and 8F4C for the 2F-alternate data). The raw X-ray free electron laser data have been deposited in the Coherent X-Ray Imaging Database, www.cxidb.org (ID 215).

Code availability

The open source programs dials.stills_process, cctbx.xfel GUI, cctbx.xfel.stripe_experiment, cctbx.xfel.merge and legacy program cxi.merge are distributed with DIALS packages available at http://dials.github.io. Instructions and details for using these programs can be found in refs. [56,57] with further documentation available at http://cci.lbl.gov/xfel. Figures shown in the paper were rendered using the PyMOL software v.2.5 (ref. [62]). Custom code used for calculating peak height values is publicly available at https://github.com/asmit3/eden(ref. [63]).

References

1. Kok, B., Forbush, B. & McGloin, M. Cooperation of charges in photosynthetic O_2 evolution. 1. A linear four-step mechanism. *Photochem. Photobiol.* **11**, 457–475 (1970).

2. Yano, J. & Yachandra, V. K. Mn_4Ca cluster in photosynthesis: where and how water is oxidized to dioxygen. *Chem. Rev.* **114**, 4175–4205 (2014).

3. Cox, N., Pantazis, D. A., Neese, F. & Lubitz, W. Biological water oxidation. *Acc. Chem. Res.* **46**, 1588–1596 (2013).

4. Kern, J. et al. Structures of the intermediates of Kok's photosynthetic water oxidation clock. *Nature* **563**, 421–425 (2018).

5. Suga, M. et al. An oxyl/oxo mechanism for oxygen-oxygen coupling in PSII revealed by an x-ray free-electron laser. *Science* **366**, 334–338 (2019).

6. Ibrahim, M. et al. Untangling the sequence of events during the $S_2 \rightarrow S_3$ transition in photosystem II and implications for the water oxidation mechanism. *Proc. Natl Acad. Sci. USA* **117**, 12624–12635 (2020).

7. Brändén, G. & Neutze, R. Advances and challenges in time-resolved macromolecular crystallography. *Science* **373**, eaba0954 (2021).

8. Kern, J. et al. Simultaneous femtosecond X-ray spectroscopy and diffraction of photosystem II at room temperature. *Science* **340**, 491–495 (2013).

9. Young, I. D. et al. Structure of photosystem II and substrate binding at room temperature. *Nature* **540**, 453–457 (2016).

10. Suga, M. et al. Light-induced structural changes and the site of O=O bond formation in PSII caught by XFEL. *Nature* **543**, 131–135 (2017).

11. Umena, Y., Kawakami, K., Shen, J.-R. & Kamiya, N. Crystal structure of oxygen-evolving photosystem II at a resolution of 1.9 Å. *Nature* **473**, 55–60 (2011).

12. Hussein, R. et al. Structural dynamics in the water and proton channels of photosystem II during the S_2 to S_3 transition. *Nat. Commun.* **12**, 6531 (2021).

13. Fransson, T. et al. Effects of x-ray free-electron laser pulse intensity on the Mn $K\beta_{1,3}$ x-ray emission spectrum in photosystem II—a case study for metalloprotein crystals and solutions. *Struct. Dyn.* **8**, 064302 (2021).

14. Babcock, G. T., Blankenship, R. E. & Sauer, K. Reaction-kinetics for positive charge accumulation on water side of chloroplast photosystem II. *FEBS Lett.* **61**, 286–289 (1976).

15. Rappaport, F., Blanchard-Desce, M. & Lavergne, J. Kinetics of electron transfer and electrochromic change during the redox transitions of the photosynthetic oxygen-evolving complex. *Biochim. Biophys. Acta Bioenerg.* **1184**, 178–192 (1994).

16. Razeghifard, M. R. & Pace, R. J. EPR kinetic studies of oxygen relaese in thylakoids and PSII membranes: a kinetic intermediate in the S_3 to S_0 transition. *Biochemistry* **38**, 1252–1257 (1999).

17. Gerencsér, L. & Dau, H. Water oxidation by photosystem II: H_2O-D_2O exchange and the influence of pH support formation of an intermediate by removal of a proton before dioxygen creation. *Biochemistry* **49**, 10098–10106 (2010).

18. Dilbeck, P. L. et al. The D1-D61N mutation in *Synechocystis* sp. PCC 6803 allows the observation of pH-sensitive intermediates in the formation and release of O_2 from photosystem II. *Biochemistry* **51**, 1079–1091 (2012).

19. Noguchi, T. Fourier transform infrared difference and time-resolved infrared detection of the electron and proton transfer dynamics in photosynthetic water oxidation. *Biochim. Biophys. Acta Bioenerg.* **1847**, 35–45 (2015).

20. Han, G., Chernev, P., Styring, S., Messinger, J. & Mamedov, F. Molecular basis for turnover inefficiencies (misses) during water oxidation in photosystem II. *Chem. Sci.* **13**, 8667–8678 (2022).

21. Haumann, M. et al. Photosynthetic O_2 formation tracked by time-resolved x-ray experiments. *Science* **310**, 1019–1021 (2005).

22. Bao, H. & Burnap, R. L. Structural rearrangements preceding dioxygen formation by the water oxidation complex of photosystem II. *Proc. Natl Acad. Sci. USA* **112**, E6139–E6147 (2015).

23. Wöhri, A. B. et al. Light-induced structural changes in a photosynthetic reaction center caught by Laue diffraction. *Science* **328**, 630–633 (2010).

24. Noguchi, T., Suzuki, H., Tsuno, M., Sugiura, M. & Kato, C. Time-resolved infrared detection of the proton and protein dynamics during photosynthetic oxygen evolution. *Biochemistry* **51**, 3205–3214 (2012).

25. Suzuki, H., Sugiura, M. & Noguchi, T. Monitoring proton release during photosynthetic water oxidation in photosystem II by means of isotope-edited infrared spectroscopy. *J. Am. Chem. Soc.* **131**, 7849–7857 (2009).

26. Tso, J., Sivaraja, M. & Dismukes, G. C. Calcium limits substrate accessibility or reactivity at the manganese cluster in photosynthetic water oxidation. *Biochemistry* **30**, 4734–4739 (1991).

27. Kim, C. J. & Debus, R. J. One of the substrate waters for O_2 formation in photosystem II is provided by the water-splitting Mn_4CaO_5 cluster's Ca^{2+} ion. *Biochemistry* **58**, 3185–3192 (2019).

28. Murray, J. W. & Barber, J. Structural characteristics of channels and pathways in photosystem II including the identification of an oxygen channel. *J. Struct. Biol.* **159**, 228–237 (2007).

29. Ho, F. M. & Styring, S. Access channels and methanol binding site to the $CaMn_4$ cluster in Photosystem II based on solvent accessibility simulations, with implications for substrate water access. *Biochim. Biophys. Acta* **1777**, 140–153 (2008).

30. Gabdulkhakov, A. et al. Probing the accessibility of the Mn_4Ca cluster in photosystem II: channels calculation, noble gas derivatization, and cocrystallization with DMSO. *Structure* **17**, 1223–1234 (2009).

31. Vassiliev, S., Zaraiskaya, T. & Bruce, D. Exploring the energetics of water permeation in photosystem II by multiple steered molecular dynamics simulations. *Biochim. Biophys. Acta Bioenerg.* **1817**, 1671–1678 (2012).

32. Ishikita, H., Saenger, W., Loll, B., Biesiadka, J. & Knapp, E. W. Energetics of a possible proton exit pathway for water oxidation in photosystem II. *Biochemistry* **45**, 2063–2071 (2006).

33. Service, R. J., Hillier, W. & Debus, R. J. Evidence from FTIR difference spectroscopy of an extensive network of hydrogen bonds near the oxygen-evolving Mn_4Ca cluster of photosystem II involving

D1-Glu65, D2-Glu312, and D1-Glu329. *Biochemistry* **49**, 6655–6669 (2010).

34. Klauss, A., Haumann, M. & Dau, H. Alternating electron and proton transfer steps in photosynthetic water oxidation. *Proc. Natl Acad. Sci. USA* **109**, 16035–16040 (2012).

35. Allgöwer, F., Gamiz-Hernandez, A. P., Rutherford, A. W. & Kaila, V. R. I. Molecular principles of redox-coupled protonation dynamics in photosystem II. *J. Am. Chem. Soc.* **144**, 7171–7180 (2022).

36. Capone, M., Narzi, D. & Guidoni, L. Mechanism of oxygen evolution and Mn_4CaO_5 cluster restoration in the natural water-oxidizing catalyst. *Biochemistry* **60**, 2341–2348 (2021).

37. Debus, R. J. Evidence from FTIR difference spectroscopy that D1-Asp61 influences the water reactions of the oxygen-evolving Mn_4CaO_5 cluster of photosystem II. *Biochemistry* **53**, 2941–2955 (2014).

38. Renger, G. Mechanism of light induced water splitting in photosystem II of oxygen evolving photosynthetic organisms. *Biochim. Biophys. Acta Bioenerg.* **1817**, 1164–1176 (2012).

39. Ishida, N. et al. Biosynthetic exchange of bromide for chloride and strontium for calcium in the photosystem II oxygen-evolving enzymes. *J. Biol. Chem.* **283**, 13330–13340 (2008).

40. Assuncao, R., Zaharieva, I. & Dau, H. Ammonia as a substrate-water analogue in photosynthetic water oxidation: influence on activation barrier of the O_2-formation step. *Biochim. Biophys. Acta Bioenerg.* **1860**, 533–540 (2019).

41. Siegbahn, P. E. Structures and energetics for O_2 formation in photosystem II. *Acc. Chem. Res.* **42**, 1871–1880 (2009).

42. Sproviero, E. M., Gascon, J. A., McEvoy, J. P., Brudvig, G. W. & Batista, V. S. Quantum mechanics/molecular mechanics study of the

catalytic cycle of water splitting in photosystem II. *J. Am. Chem. Soc.* **130**, 3428–3442 (2008).

43. Rummel, F. & O'Malley, P. J. How nature makes O_2: an electronic level mechanism for water oxidation in photosynthesis. *J. Phys. Chem. B* **126**, 8214–8221 (2022).

44. Guo, Y., Zhang, B., Kloo, L. & Sun, L. Necessity of structural rearrangements for O-O bond formation between O5 and W2 in photosystem II. *J. Energy Chem.* **57**, 436–442 (2021).

45. Messinger, J. Evaluation of different mechanistic proposals for water oxidation in photosynthesis on the basis of Mn_4O_xCa structures for the catalytic site and spectroscopic data. *Phys. Chem. Chem. Phys.* **6**, 4764–4771 (2004).

46. Nilsson, H., Cournac, L., Rappaport, F., Messinger, J. & Lavergne, J. Estimation of the driving force for dioxygen formation in photosynthesis. *Biochim. Biophys. Acta* **1857**, 23–33 (2016).

47. Rapatskiy, L. et al. Detection of the water-binding sites of the oxygen-evolving complex of Photosystem II using W-band ^{17}O electron-electron double resonance-detected NMR spectroscopy. *J. Am. Chem. Soc.* **134**, 16619–16634 (2012).

48. Davis, K. M. et al. Rapid evolution of the photosystem II electronic structure during water splitting. *Phys. Rev. X* **8**, 041014 (2018).

49. Yamaguchi, K. et al. Geometric, electronic and spin structures of the $CaMn_4O_5$ catalyst for water oxidation in oxygen-evolving photosystem II. Interplay between experiments and theoretical computations. *Coord. Chem. Rev.* **471**, 214742 (2022).

50. Sakashita, N., Ishikita, H. & Saito, K. Rigidly hydrogen-bonded water molecules facilitate proton transfer in photosystem II. *Phys. Chem. Chem. Phys.* **22**, 15831–15841 (2020).

51. Hellmich, J. et al. Native-like Photosystem II superstructure at 2.44 Å resolution through detergent extraction from the protein crystal. *Structure* **22**, 1607–1615 (2014).

52. Ibrahim, M. et al. Improvements in serial femtosecond crystallography of photosystem II by optimizing crystal uniformity using microseeding procedures. *Struct. Dyn.* **2**, 041705 (2015).

53. Fransson, T. et al. X-ray emission spectroscopy as an in situ diagnostic tool for X-ray crystallography of metalloproteins using an X-ray free-electron laser. *Biochemistry* **57**, 4629–4637 (2018).

54. Roessler, C. G. et al. Acoustic injectors for drop-on-demand serial femtosecond crystallography. *Structure* **24**, 631–640 (2016).

55. Fuller, F. D. et al. Drop-on-demand sample delivery for studying biocatalysts in action at X-ray free-electron lasers. *Nat. Methods* **14**, 443–449 (2017).

56. Brewster, A. S. et al. Improving signal strength in serial crystallography with *DIALS* geometry refinement. *Acta Crystallogr. D Struct. Biol.* **74**, 877–894 (2018).

57. Brewster, A. S., Young, I. D., Lyubimov, A., Bhowmick, A. & Sauter, N. K. Processing serial crystallographic data from XFELs or synchrotrons using the cctbx.xfel GUI. *Comput. Crystallogr. Newsl.* **10**, 22–39 (2019).

58. Liebschner, D. et al. Macromolecular structure determination using X-rays, neutrons and electrons: recent developments in. *Phenix. Acta Crystallogr. D Struct. Biol.* **75**, 861–877 (2019).

59. Emsley, P., Lohkamp, B., Scott, W. G. & Cowtan, K. Features and development of *Coot*. *Acta Crystallogr. D Struct. Biol.* **66**, 486–501 (2010).

60. Lang, P. T., Holton, J. M., Fraser, J. S. & Alber, T. Protein structural ensembles are revealed by redefining X-ray electron density noise. *Proc. Natl Acad. Sci. USA* **111**, 237–242 (2014).

61. Liebschner, D. et al. Polder maps: improving OMIT maps by excluding bulk solvent. *Acta Crystallogr. D Struct. Biol.* **73**, 148–157 (2017).

62. Schrödinger, LLC. The PyMOL Molecular Graphics System, version 1.8 (2015).

63. Bhowmick A. asmit3/eden: release v.0.1.1. Zenodo https://doi.org/10.5281/zenodo.7734707 (2023).

Acknowledgements

We thank K. Sauer (1931–2022) for his interest in this research and for many discussions about photosynthetic water oxidation. We thank R. Massad, M. Kretzschmar, P. Sinnott, J. Blaschke, A. Britz, S. Carbajo, C. de Lichtenberg, L.-C. Kao, L. Lassalle, D. Liebschner, D. Mendez, F. Moss, E. Pastor, C. Pham, B. Poon, K. D. Sutherlin and I. D. Young for support during sample preparation, data collection and processing. We thank the support staff at LCLS/SLAC, SACLA/Japan, SSRL and ALS. This work was supported by the Director, Office of Science, Office of Basic Energy Sciences (OBES), Division of Chemical Sciences, Geosciences, and Biosciences of the Department of Energy (DOE) (J.Y., V.K.Y. and J.K.) for X-ray spectroscopy and crystallography data collection and analysis, and methods development for photosynthetic systems was supported by the National Institutes of Health (NIH; grants GM055302 (V.K.Y.) for photosystem II biochemistry, GM110501 (J.Y.) and GM126289 (J.K.) for instrumentation development for X-ray free electron laser (XFEL) experiments and GM117126 (N.K.S.) for development of computational protocols for XFEL data). N.K.S. acknowledges support from the Exascale Computing Project (grant 17-SC20-SC), a collaborative effort of the DOE Office of Science and the National Nuclear Security Administration. Germany's Excellence Strategy (project EXC 2008/1-390540038 (A.Z., H.D. and S.H.)) coordinated by TU Berlin and the German Research Foundation via the Collaborative Research Center SFB1078 (Humboldt Universität zu Berlin), TP A5 (A.Z., H.D., M.I., R.H. and J.G.) and Vetenskapsrådet (grants 2016-05183 (J.M.) and 2020-03809 (J.M.)) as well as Energimyndigheten (grant 45421-1 (J.M.)) are acknowledged for support. R.H. acknowledges support from a Caroline von Humboldt Stipendium,

Humboldt Universität zu Berlin. C.J.K. acknowledges support from the NIH (NRSA fellowship award F32GM142218). This research used resources of NERSC, a User Facility supported by the Office of Science, DOE (contract DE-AC02-05CH11231). XFEL data were collected at LCLS/SLAC, Stanford and SACLA, Japan. The XFEL experiments at SACLA were performed at BL2 with the approval of the Japan Synchrotron Radiation Research Institute (proposals 2018B8089, 2019A8081 and 2019B8067). Testing of crystals and various parts of the setup was carried out at synchrotron facilities that were provided by the ALS in Berkeley and SSRL in Stanford, funded by the DOE OBES. The SSRL Structural Molecular Biology Program is supported by the DOE OBER and the NIH (grant P41GM103393). Use of the LCLS and SSRL, SLAC National Accelerator Laboratory is supported by the DOE, Office of Science, OBES (contract DE-AC02-76SF00515), and structural biology work at the LCLS is supported by the NIH (grant P41GM139687; the Rayonix detector was funded by grant S10 OD023453).

Author information

Author notes

1. Mohamed Ibrahim

   Present address: Institute of Molecular Medicine, University of Lübeck, Lübeck, Germany

2. These authors contributed equally: Asmit Bhowmick, Rana Hussein, Isabel Bogacz, Philipp S. Simon

Authors and Affiliations

1. Molecular Biophysics and Integrated Bioimaging Division, Lawrence Berkeley National Laboratory, Berkeley, CA, USA

   Asmit Bhowmick, Isabel Bogacz, Philipp S. Simon, Ruchira Chatterjee, Margaret D. Doyle, In-Sik Kim, Hiroki Makita, Medhanjali Dasgupta, Corey J. Kaminsky, Miao Zhang, Isabela I. Nangca, Stephen

M. Keable, James M. Holton, Daniel W. Paley, Nigel W. Moriarty, Paul D. Adams, Aaron S. Brewster, Nicholas K. Sauter, Jan Kern, Junko Yano & Vittal K. Yachandra

2. Department of Biology, Humboldt Universität zu Berlin, Berlin, Germany

Rana Hussein, Mohamed Ibrahim, Julia Gätcke, Stephanie Haupt, Holger Dobbek & Athina Zouni

3. Molecular Biomimetics, Department of Chemistry — Ångström, Uppsala University, Uppsala, Sweden

Mun Hon Cheah, Petko Chernev, A. Orkun Aydin, Fikret Mamedov & Johannes Messinger

4. Department of Theoretical Chemistry and Biology, KTH Royal Institute of Technology, Stockholm, Sweden

Thomas Fransson

5. Japan Synchrotron Radiation Research Institute, Hyogo, Japan

Kensuke Tono & Shigeki Owada

6. RIKEN SPring-8 Center, Hyogo, Japan

Kensuke Tono & Shigeki Owada

7. Linac Coherent Light Source, SLAC National Accelerator Laboratory, Menlo Park, CA, USA

Leland B. Gee, Franklin D. Fuller, Alexander Batyuk & Roberto Alonso-Mori

8. Department of Biochemistry and Biophysics, University of California, San Francisco, CA, USA

James M. Holton

9. SSRL, SLAC National Accelerator Laboratory, Menlo Park, CA, USA

   James M. Holton

10. Department of Bioengineering, University of California, Berkeley, CA, USA

   Paul D. Adams

11. Department of Physics, University of Wisconsin–Madison, Madison, WI, USA

   Uwe Bergmann

12. Department of Chemistry, Umeå University, Umeå, Sweden

   Johannes Messinger

Contributions

R.A-.M., N.K.S., U.B., A.Z., J.M., J.K., J.Y. and V.K.Y. designed the experiment. R.H., M.I., R.C., M.D., M.Z., J.G., S.H., I.I.N., A.Z. and J.K. prepared samples. R.C., M.H.C., T.F., J.G., S.H., A.O.A. and F.M. characterized sample activity. K.T., S.O., L.B.G., F.D.F., A.Batyuk and R.A-.M. prepared and operated the X-ray free electron laser (XFEL) beam lines. I.B., P.S.S., P.C., I.-S.K., H.M., F.D.F. and J.K. developed, tested and ran the sample delivery system. A.Bhowmick, R.H., I.B., P.S.S., M.I., R.C., M.D.D., M.H.C., T.F., P.C., I.-S.K., H.M., M.D., C.J.K., M.Z., J.G., S.H., S.M.K., K.T., S.O., L.B.G., F.D.F., A.Batyuk, R.A-.M., D.W.P., A.S.B., N.K.S., U.B., A.Z., J.M., J.K., J.Y. and V.K.Y. performed the XFEL experiment. A.Bhowmick, J.M.H., D.W.P., N.W.M., P.D.A., A.S.B. and N.K.S. developed new software for data processing. A.Bhowmick, M.D., S.M.K., D.W.P., A.S.B. and N.K.S. processed XFEL data. A.Bhowmick, R.H., I.B., P.S.S., M.I., M.D.D., H.D., N.K.S., A.Z., J.M., J.K., J.Y. and V.K.Y. analysed and interpreted data. A.Bhowmick, R.H., I.B., P.S.S., M.D.D., A.Z., J.M., J.K., V.K.Y. and J.Y. wrote the manuscript with input from all authors.

Corresponding authors

Correspondence to Athina Zouni, Johannes Messinger, Junko Yano or Vittal K. Yachandra.

Ethics declarations

Competing interests

The authors declare no competing interests.

Peer review

Peer review information

Nature thanks Richard Neutze, Dimitrios Pantazis, and the other, anonymous, reviewers(s) for their contribution to the peer review of this work.

Additional information

Publisher's note Springer Nature remains neutral with regard to jurisdictional claims in published maps and institutional affiliations.

Extended data figures and tables

Extended Data Fig. 1 $mF_{obs} - DF_{calc}$ electron density omit map of relevant atoms in the OEC for time points along the $S_3 \rightarrow S_0$ reaction.

For comparison of the peak height level, the omit map of the oxygen atom, O2, is also shown. Omit maps for each atom were generated by individually omitting the atom only in the primary conformer in each dataset. The maps are shown at contour levels of 2.5, 3 and 4σ. (a) Omit maps of O_X, O5 and

O2 (b) Omit maps of W1, W2, W3, W4 and O2. A clear reduction in omit map peak height of O_X, O5, W1, W2, W3, W4 is observed with respect to the reference O2 omit map between 730–2000 μs.

Extended Data Fig. 2 $mF_{obs} - DF_{calc}$ electron density map near the OEC region in the 3F(500 μs) time point.

The map is shown at a contour level of 2.5σ (in yellow). Electron density is observed at this level in-between W3 and W4 (see red arrow), possibly indicating a transient water motion that was also corroborated by the overlap of the omit map densities. For comparison, the individual omit maps of W3 and W4 are also overlaid at 2.5, 3 and 4σ (color scheme same as in Fig. 2 in main text). Stronger electron density is also observed around W1/D61 possibly related to motion involving a proton transfer as discussed in the main text related to Fig. 2. Electron density around the O1 is possibly related to changes observed in the W26-W30 (referred to as the 'water wheel' region) in this time point (discussed in main text related to Fig. 4).

Extended Data Fig. 3 Comparing B-factors of key waters in the water wheel region of the O1 channel in the $S_3 \rightarrow S_0$ transition (W27, W28, W32) against a reference water (W29) for time points shown in Fig. 4 in the main text.

The B-factor distribution of all the channel waters are overlaid for each time point for comparison. The y-axis values of the marker points for the 4 waters are just placeholders. There is a stark shift in the relative B-factor values of W27, W28 and W32 in the 3F(1200 μs) time point which coincides with the disappearance of O_X.

Extended Data Table 1 Data collection, merging and refinement statistics (2F, 2F-alternate, 3F(50 μs), 3F(250 μs), 3F(500 μs))
Extended Data Table 2 Data collection, merging and refinement statistics (3F(730 μs), 3F(1200 μs), 3F(2000 μs), 3F(4000 μs), 3F(200 ms))
Extended Data Table 3 The estimated population distribution and identity of each of the conformers used in the multi-component modeling of the datasets

Extended Data Table 4 Source data for the plots shown in Fig. 3 of the main text

Supplementary information

Supplementary Tables

Supplementary Tables 1 and 2.

Reporting Summary

Supplementary Data

This zipped folder contains Supplementary Schemes 1–3: Restraints used for modeling the OEC in the $S_3 \rightarrow S_0$ transition.

Supplementary Video 1

Video showing the various changes at the OEC in the $S_3 \rightarrow S_0$ transition. High-resolution version available at: https://drive.google.com/file/d/1d4fMKBcYUdenqajlXo3J-a8lU5eaUxe3/view?usp=share_link.

Rights and permissions

Open Access This article is licensed under a Creative Commons Attribution 4.0 International License, which permits use, sharing, adaptation, distribution and reproduction in any medium or format, as long as you give appropriate credit to the original author(s) and the source, provide a link to the Creative Commons licence, and indicate if changes were made. The images or other third party material in this article are included in the article's Creative Commons licence, unless indicated otherwise in a credit line to the material. If material is not included in the article's Creative Commons licence and your intended use is not permitted by statutory regulation or exceeds the permitted use, you will need to obtain permission directly from

the copyright holder. To view a copy of this licence, visit http://creativecommons.org/licenses/by/4.0/.

Reprints and Permissions

About this article

Cite this article

Bhowmick, A., Hussein, R., Bogacz, I. *et al.* Structural evidence for intermediates during O_2 formation in photosystem II. *Nature* **617**, 629–636 (2023). https://doi.org/10.1038/s41586-023-06038-z

- Received: 18 November 2022
- Accepted: 31 March 2023
- Published: 03 May 2023
- Issue Date: 18 May 2023
- DOI: https://doi.org/10.1038/s41586-023-06038-z

Share this article

Anyone you share the following link with will be able to read this content:

Get shareable link

Sorry, a shareable link is not currently available for this article.

Copy to clipboard

Provided by the Springer Nature SharedIt content-sharing initiative

The electron–proton bottleneck of photosynthetic oxygen evolution

- Paul Greife
- Matthias Schönborn
- Holger Dau

Nature Article Open Access 03 May 2023

Clues to how water splits during photosynthesis

- Dimitrios A. Pantazis

Nature News & Views 03 May 2023

This article was downloaded by **calibre** from https://www.nature.com/articles/s41586-023-06038-z

| Section menu | Main menu |

Amendments & Corrections

- **Author Correction: Population dynamics of head-direction neurons during drift and reorientation** [04 May 2023]
- **Author Correction: CFTR function, pathology and pharmacology at single-molecule resolution** [04 May 2023]
- **Author Correction: Apolipoprotein E controls cerebrovascular integrity via cyclophilin A** [05 May 2023]
- **Publisher Correction: 2D fin field-effect transistors integrated with epitaxial high-k gate oxide** [03 May 2023]

- Author Correction
- Open Access
- Published: 04 May 2023

Author Correction: Population dynamics of head-direction neurons during drift and reorientation

- Zaki Ajabi ,
- Alexandra T. Keinath,
- Xue-Xin Wei &
- …
- Mark P. Brandon

Show authors

Nature **volume 617**, page E10 (2023)

- 333 Accesses
- 1 Altmetric
- Metrics details

The Original Article was published on 22 March 2023

Correction to: *Nature* https://doi.org/10.1038/s41586-023-05813-2
Published online 22 March 2023

In the version of this article initially published, there was a typographical error in the seventh sentence of the Methods “Surgeries” subsection, where in the text now reading “One week after injection, a 0.5-mm-diameter gradient refractive index (GRIN) relay lens (Go!Foton) was implanted above the ADN (AP, –1.05; ML, 0.8; DV, −3),” the AP coordinate “–1.05” originally read “1.8.” The error has been corrected in the HTML and PDF versions of the article.

Author information

Author notes

1. Zaki Ajabi

   Present address: Department of Neurobiology, Harvard Medical School, Boston, MA, USA

Authors and Affiliations

1. Department of Psychiatry, Douglas Hospital Research Centre, McGill University, Verdun, Quebec, Canada

   Zaki Ajabi, Alexandra T. Keinath & Mark P. Brandon

2. Integrated Program in Neuroscience, McGill University, Montreal, Quebec, Canada

   Zaki Ajabi & Mark P. Brandon

3. Department of Neuroscience, University of Texas at Austin, Austin, TX, USA

   Xue-Xin Wei

4. Department of Psychology, University of Texas at Austin, Austin, TX, USA

   Xue-Xin Wei

5. Center for Perceptual Systems, University of Texas at Austin, Austin, TX, USA

Xue-Xin Wei

6. Center for Theoretical and Computational Neuroscience, University of Texas at Austin, Austin, TX, USA

Xue-Xin Wei

Corresponding authors

Correspondence to Zaki Ajabi or Mark P. Brandon.

Rights and permissions

Open Access This article is licensed under a Creative Commons Attribution 4.0 International License, which permits use, sharing, adaptation, distribution and reproduction in any medium or format, as long as you give appropriate credit to the original author(s) and the source, provide a link to the Creative Commons license, and indicate if changes were made. The images or other third party material in this article are included in the article's Creative Commons license, unless indicated otherwise in a credit line to the material. If material is not included in the article's Creative Commons license and your intended use is not permitted by statutory regulation or exceeds the permitted use, you will need to obtain permission directly from the copyright holder. To view a copy of this license, visit http://creativecommons.org/licenses/by/4.0/.

Reprints and Permissions

About this article

Cite this article

Ajabi, Z., Keinath, A.T., Wei, XX. *et al.* Author Correction: Population dynamics of head-direction neurons during drift and reorientation. *Nature* **617**, E10 (2023). https://doi.org/10.1038/s41586-023-06126-0

- Published: 04 May 2023
- Issue Date: 18 May 2023
- DOI: https://doi.org/10.1038/s41586-023-06126-0

Share this article

Anyone you share the following link with will be able to read this content:

Get shareable link

Sorry, a shareable link is not currently available for this article.

Copy to clipboard

Provided by the Springer Nature SharedIt content-sharing initiative

---

This article was downloaded by **calibre** from https://www.nature.com/articles/s41586-023-06126-0

- Author Correction
- Open Access
- Published: 04 May 2023

Author Correction: CFTR function, pathology and pharmacology at single-molecule resolution

- Jesper Levring,
- Daniel S. Terry,
- Zeliha Kilic,
- Gabriel Fitzgerald,
- Scott C. Blanchard &
- …
- Jue Chen

Show authors

Nature **volume 617**, page E11 (2023)

- 442 Accesses
- 1 Altmetric
- Metrics details

The Original Article was published on 22 March 2023

Correction to: *Nature* https://doi.org/10.1038/s41586-023-05854-7
Published online 16 February 2023

In the version of this article initially published, the name of Scott C. Blanchard was missing the middle initial. The omission has been corrected in the HTML and PDF versions of the article.

Author information

Authors and Affiliations

1. Laboratory of Membrane Biology and Biophysics, The Rockefeller University, New York, NY, USA

   Jesper Levring & Jue Chen

2. Department of Structural Biology, St. Jude Children's Research Hospital, Memphis, TN, USA

   Daniel S. Terry, Zeliha Kilic & Scott C. Blanchard

3. Department of Physiology and Biophysics, Weill Cornell Medicine, New York, NY, USA

   Gabriel Fitzgerald

4. Howard Hughes Medical Institute, The Rockefeller University, New York, NY, USA

   Jue Chen

Corresponding authors

Correspondence to Scott C. Blanchard or Jue Chen.

Rights and permissions

Open Access This article is licensed under a Creative Commons Attribution 4.0 International License, which permits use, sharing, adaptation, distribution and reproduction in any medium or format, as long as you give appropriate credit to the original author(s) and the source, provide a link to the Creative Commons license, and indicate if changes were made. The images or other third party material in this article are included in the article's Creative Commons license, unless indicated otherwise in a credit line to the material. If material is not included in the article's Creative Commons license and your intended use is not permitted by statutory regulation or exceeds the permitted use, you will need to obtain permission directly from the copyright holder. To view a copy of this license, visit http://creativecommons.org/licenses/by/4.0/.

Reprints and Permissions

About this article

Cite this article

Levring, J., Terry, D.S., Kilic, Z. *et al.* Author Correction: CFTR function, pathology and pharmacology at single-molecule resolution. *Nature* **617**, E11 (2023). https://doi.org/10.1038/s41586-023-06115-3

- Published: 04 May 2023
- Issue Date: 18 May 2023
- DOI: https://doi.org/10.1038/s41586-023-06115-3

Share this article

Anyone you share the following link with will be able to read this content:

Get shareable link

Sorry, a shareable link is not currently available for this article.

Copy to clipboard

Provided by the Springer Nature SharedIt content-sharing initiative

---

This article was downloaded by **calibre** from https://www.nature.com/articles/s41586-023-06115-3

| Section menu | Main menu |

- Author Correction
- Published: 05 May 2023

Author Correction: Apolipoprotein E controls cerebrovascular integrity via cyclophilin A

- Robert D. Bell,
- Ethan A. Winkler,
- Itender Singh,
- Abhay P. Sagare,
- Rashid Deane,
- Zhenhua Wu,
- David M. Holtzman,
- Christer Betsholtz,
- Annika Armulik,
- Jan Sallstrom,
- Bradford C. Berk &
- …
- Berislav V. Zlokovic

Show authors

Nature **volume 617**, page E12 (2023)

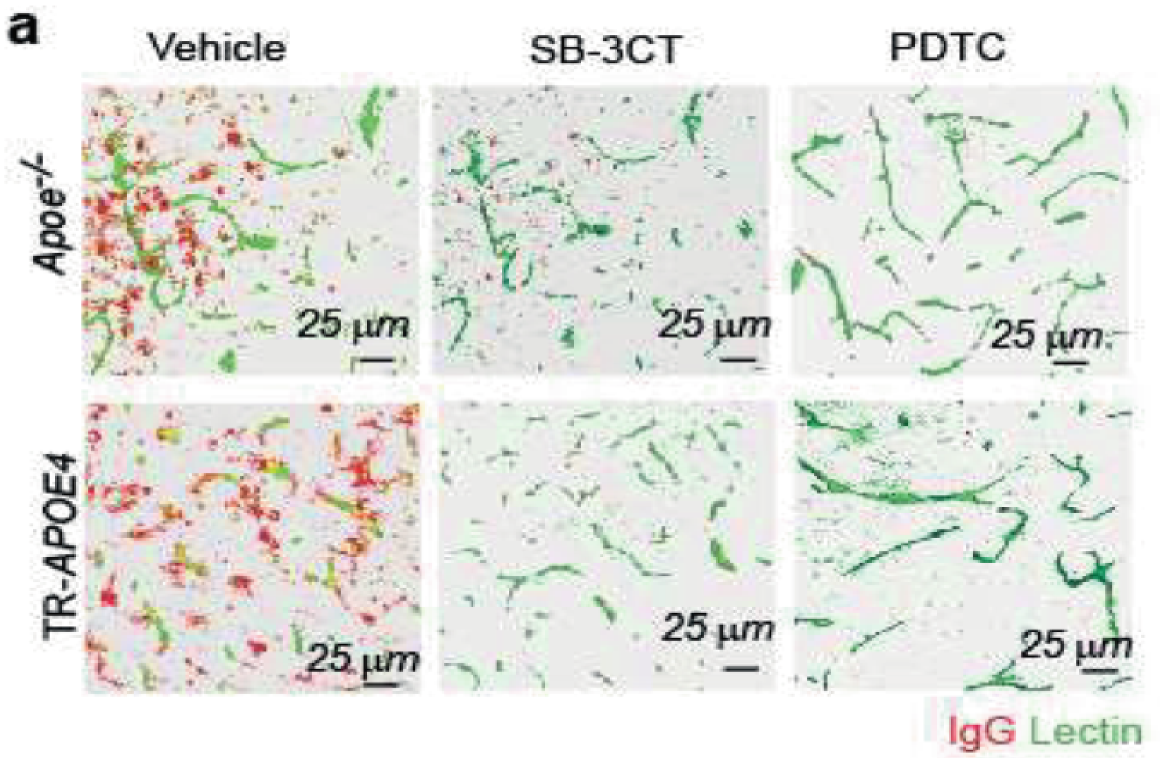
- 994 Accesses
- 11 Altmetric
- Metrics details

The Original Article was published on 16 May 2012

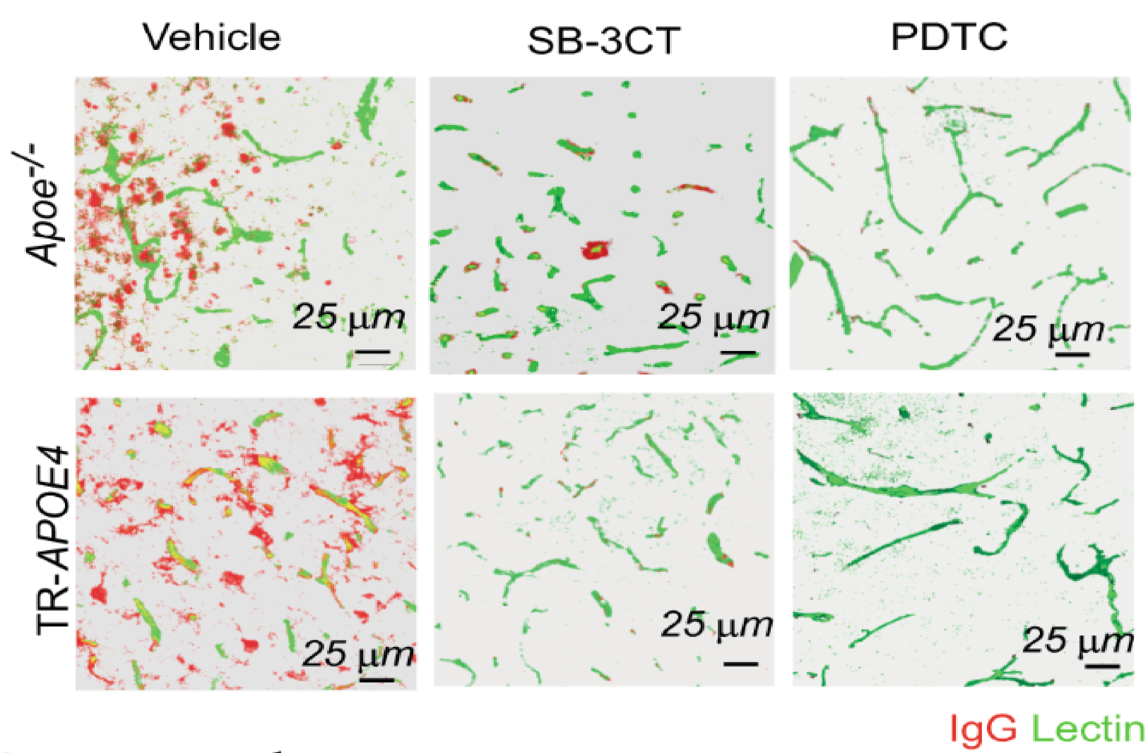
Correction to: *Nature* https://doi.org/10.1038/nature11087 Published online 16 May 2012

The original version of the Supplementary Information associated with this article contained an error in Supplementary Fig. 4a. The representative image shown in Supplementary Fig. 4a from the *Apoe*$^{-/-}$ mouse treated with SB-3CT was incorrect. The adjacent negative no IgG-stained control brain section (lectin-stained only) from the same *Apoe*$^{-/-}$ vehicle treated animal was mistakenly used for this panel during preparation of the manuscript. The correct version of Supplementary Fig. 4a, shown in Fig. 1, replaces the original image:

Fig. 1: Original incorrect version and corrected version of Supplementary Fig. 4a



Original, incorrect panel



Correct panel

.

Author information

Authors and Affiliations

1. Center for Neurodegenerative and Vascular Brain Disorders, University of Rochester Medical Center, Rochester, New York, USA

   Robert D. Bell, Ethan A. Winkler, Itender Singh, Abhay P. Sagare, Rashid Deane, Zhenhua Wu, Jan Sallstrom & Berislav V. Zlokovic

2. Aab Cardiovascular Research Institute, University of Rochester Medical Center, Rochester, New York, USA

   Robert D. Bell & Bradford C. Berk

3. Department of Neurology, Hope Center for Neurological Disorders, Knight Alzheimer's Disease Research Center, Washington University School of Medicine, Saint Louis, Missouri, USA

   David M. Holtzman

4. Division of Vascular Biology, Department of Medical Biochemistry and Biophysics, Karolinska Institutet, Stockholm, Sweden

   Christer Betsholtz & Annika Armulik

5. Institute of Neuropathology, University Hospital Zürich, CH-8091, Zürich, Switzerland

   Annika Armulik

6. Center for Neurodegeneration and Regeneration, Zilkha Neurogenetic Institute and Department of Physiology and Biophysics, University of Southern California, Keck School of Medicine, Los Angeles, California, USA

Berislav V. Zlokovic

Corresponding author

Correspondence to Berislav V. Zlokovic.

Rights and permissions

Reprints and Permissions

About this article

Cite this article

Bell, R.D., Winkler, E.A., Singh, I. *et al.* Author Correction: Apolipoprotein E controls cerebrovascular integrity via cyclophilin A. *Nature* **617**, E12 (2023). https://doi.org/10.1038/s41586-023-06118-0

- Published: 05 May 2023
- Issue Date: 18 May 2023
- DOI: https://doi.org/10.1038/s41586-023-06118-0

Share this article

Anyone you share the following link with will be able to read this content:

Get shareable link

Sorry, a shareable link is not currently available for this article.

Copy to clipboard

Provided by the Springer Nature SharedIt content-sharing initiative

This article was downloaded by **calibre** from https://www.nature.com/articles/s41586-023-06118-0

- Publisher Correction
- Published: 03 May 2023

Publisher Correction: 2D fin field-effect transistors integrated with epitaxial high-*k* gate oxide

- Congwei Tan,
- Mengshi Yu,
- Junchuan Tang,
- Xiaoyin Gao,
- Yuling Yin,
- Yichi Zhang,
- Jingyue Wang,
- Xinyu Gao,
- Congcong Zhang,
- Xuehan Zhou,
- Liming Zheng,
- Hongtao Liu,
- Kaili Jiang,
- Feng Ding &
- …
- Hailin Peng

Show authors

Nature **volume 617**, page E13 (2023)

- 432 Accesses
- 2 Altmetric

- Metrics details

The Original Article was published on 22 March 2023

Correction to: *Nature* https://doi.org/10.1038/s41586-023-05797-z
Published online 22 March 2023

In the version of this article initially published, there were labelling errors in Fig. 2e(i), where the red text currently reading “004” appeared as “\(00\bar{6},\)” and in Fig. 4c, where the *y*-axis label currently reading “IDS (mA μm^{-1})” appeared as “IDS (μA μm^{-1}).” The errors have been corrected in the HTML and PDF versions of the article.

Author information

Author notes

1. These authors contributed equally: Congwei Tan, Mengshi Yu, Junchuan Tang, Xiaoyin Gao

Authors and Affiliations

1. Center for Nanochemistry, Beijing Science and Engineering Center for Nanocarbons, Beijing National Laboratory for Molecular Sciences, College of Chemistry and Molecular Engineering, Peking University, Beijing, China

   Congwei Tan, Mengshi Yu, Junchuan Tang, Xiaoyin Gao, Yichi Zhang, Jingyue Wang, Congcong Zhang, Xuehan Zhou, Liming Zheng, Hongtao Liu & Hailin Peng

2. Center for Multidimensional Carbon Materials, Institute for Basic Science, Ulsan, South Korea

   Yuling Yin & Feng Ding

3. School of Materials Science and Engineering, Ulsan National Institute of Science and Technology, Ulsan, South Korea

Yuling Yin & Feng Ding

4. State Key Laboratory of Low-Dimensional Quantum Physics, Department of Physics, Tsinghua University, Beijing, China

Xinyu Gao & Kaili Jiang

5. Tsinghua-Foxconn Nanotechnology Research Center, Tsinghua University, Beijing, China

Xinyu Gao & Kaili Jiang

Corresponding author

Correspondence to Hailin Peng.

Rights and permissions

Reprints and Permissions

About this article

Cite this article

Tan, C., Yu, M., Tang, J. *et al.* Publisher Correction: 2D fin field-effect transistors integrated with epitaxial high-*k* gate oxide. *Nature* **617**, E13 (2023). https://doi.org/10.1038/s41586-023-06093-6

- Published: 03 May 2023
- Issue Date: 18 May 2023
- DOI: https://doi.org/10.1038/s41586-023-06093-6

Share this article

Anyone you share the following link with will be able to read this content:

Get shareable link

Sorry, a shareable link is not currently available for this article.

Copy to clipboard

Provided by the Springer Nature SharedIt content-sharing initiative

This article was downloaded by **calibre** from https://www.nature.com/articles/s41586-023-06093-6